G.10 Vol. 1

CONTRACTOR
LIBRARY

Advanced TIROS-N Program

NOAA-KLM System Design Report (SDR)

Vol. 1

Contract No. NAS5-30350 (Item 39)
Issued: 30 August 1990

Prepared for:
National Aeronautics and Space Administration
Goddard Space Flight Center
Greenbelt, Maryland 20771

Prepared by:
General Electric Company
Astro-Space Division
P.O. Box 800
Princeton, New Jersey 08543

CONTRACTOR
LIBRARY

Preface

This document was prepared under the Advanced TIROS-N Program contract NAS5-30350 in accordance with the requirements stated for Contract Data Requirements List (CDRL) Item 39, NOAA-KLM System Design Report (SDR).

TABLE OF CONTENTS

Section		Page
1.0	INTRODUCTION AND SUMMARY	l-l
	1.1 Introduction	l-l
	1.2 System Summary	l-l
	1.2.1 Mission	l-l
	1.2.2 Spacecraft	l-2
2.0	MISSION DESCRIPTION	2-l
	2.1 ATN-KLM Requirements	2-l
	2.2 Instrument Payload	2-l
	2.3 Mission Operations	2-l
	2.3.1 Mission	2-l
	2.3.2 Orbit Characteristics	2-l
	2.3.3 Implication of Orbit Characteristics	2-9
	2.3.4 HRPT and APT Contact	2-9
	2.3.5 Launch Window	2-15
	2.3.6 Orbit Accuracies	2-15
	2.3.7 Multi-Spacecraft Operations	2-15
	2.4 Launch Vehicle Interface	2-19
	2.5 Radiation	2-19
	2.5.1 Environment	2-19
	2.5.2 Damage Shielding	2-22
3.0	SYSTEM DESCRIPTION	3-l
	3.1 Physical Configuration	3-l
	3.1.1 External Arrangements	3-l
	3.1.2 Internal Arrangement	3-l
	3.2 Functional Groups	3-l
	3.2.1 Equipment Family Tree	3-l
	3.2.2 Software Family Tree	3-2
	3.3 System Interfaces	3-2
	3.3.1 Mechanical	3-2
	3.3.1.1 Alignment	3-2
	3.3.2 Electrical Interfaces	3-13
	3.3.2.1 Harness	3-14
	3.3.2.2 Control Signals	3-14
	3.3.2.3 Telemetry Signals	3-15
	3.3.2.4 Power and Grounding	3-24
	3.4 Spacecraft Characteristics	3-33
	3.5 Ascent Guidance and Control	3-33
	3.6 Structure	3-33
	3.7 Thermal Design	3-36
	3.8 Attitude Determination and Control System	3-37
	3.9 Reaction Control	3-37
	3.10 Electrical Power and Distribution	3-38
	3.11 Data-Handling	3-38
	3.11.1 TIP	3-39
	3.11.2 Manipulated Information Rate Processor (MIRP)	3-39
	3.11.3 Digital Tape Recorders (DTRs)	3-39
	3.11.4 Cross Strap Unit (XSU)	3-40
	3.11.5 AMSU Information Processor (AIP)	3-40

TABLE OF CONTENTS (Continued)

Section		Page
	3.12 Communications	3-41
	3.12.1 S-Band Data Transmitters	3-41
	3.12.2 S-Band Transmitter Antennas	3-41
	3.12.3 Dual G-STDN Receiver/Demodulator and Antenna	3-41
	3.12.4 VHF Real-Time Transmitters	3-43
	3.12.5 VHF Real-Time Antenna	3-43
	3.12.6 Beacon Transmitters	3-43
	3.12.7 Beacon Antenna	3-43
	3.12.8 UHF DCS and SARP Antenna	3-43
	3.12.9 SARR L-Band Transmit Antenna	3-44
	3.12.10 SARR Receive Antenna	3-44
	3.12.11 Launch and Emergency Transmitter	3-44
	3.12.12 Launch and Emergency Antenna	3-44
	3.13 Command and Control	3-44
	3.13.1 Redundant Crystal Oscillator	3-44
	3.13.2 Controls Interface Unit	3-45
	3.13.3 CIU Annex	3-45
	3.13.4 Controls Power Converter	3-45
	3.13.5 Central Processing Units	3-45
	3.13.6 Signal Conditioning Unit	3-46
	3.13.7 Decryption/Authentication Unit	3-46
	3.14 Flight Software	3-47
4.0	SPACECRAFT SUBSYSTEMS	4-l
	4.1 General	4-l
	4.2 Structure	4.2-l
	4.2.1 System Description	4.2-l
	4.2.1.1 Satellite Coordinate System	4.2-2
	4.2.1.2 Launch Configuration	4.2-2
	4.2.1.3 Orbit Configuration	4.2-2
	4.2.1.4 Mass Properties	4.2-2
	4.2.2 System Requirements	4.2-5
	4.2.2.1 Interface Requirements	4.2-5
	4.2.2.2 Design Requirements	4.2-8
	4.2.3 Structural Analysis	4.2-10
	4.2.3.1 Introduction	4.2-10
	4.2.3.2 Analytical Model Overview	4.2-11
	4.2.3.3 Static Analysis	4.2-14
	4.2.4 Structure Component Description	4.2-16
	4.2.4.1 Instrument Mounting Platform	4.2-16
	4.2.4.2 Equipment Support Module	4.2-27
	4.2.4.3 Truss	4.2-35
	4.2.4.4 RCS Support Structure	4.2-39
	4.2.4.5 Adapter	4.2-42
	4.2.4.6 Solar Array and Solar Support	4.2-42
	4.2.4.7 Antennas	4.2-54
	4.2.4.8 V-Band Assembly	4.2-55
	4.3 Reaction Control Subsystem	4.3-l
	4.3.1 System Description	4.3-l
	4.3.1.1 High Pressure Nitrogen Subsystem	4.3-l

TABLE OF CONTENTS (Continued)

Section	Page
4.3.1.2 Low Pressure Nitrogen Subsystem	4.3-3
4.3.1.3 Hydrazine Subsystem	4.3-4
4.3.2 Functional Description	4.3-4
4.3.2.1 Mission Operation	4.3-4
4.3.2.2 Weight and Power Requirements	4.3-8
4.3.2.3 Telemetry	4.3-9
4.3.3 Component Description	4.3-9
4.3.3.1 Hydrazine Thruster	4.3-9
4.3.3.2 Propellant Tank	4.3-15
4.3.3.3 Nitrogen Thruster	4.3-19
4.3.3.4 Pressurant Tank	4.3-21
4.3.3.5 Pressure Regulator	4.3-21
4.3.3.6 Pressure Transducer	4.3-22
4.3.3.7 Fill and Drain Valve	4.3-24
4.3.3.8 Hydrazine Isolation Valve	4.3-27
4.3.3.9 Latch Valve	4.3-28
4.3.3.10 Relief Valve	4.3-29
4.3.3.11 In-Line Filters	4.3-31
4.3.3.12 Propellant Manifold Assemblies	4.3-31
4.4 On-Orbit Attitude Determination and Control Subsystem	4.4-l
4.4.1 Requirements	4.4-l
4.4.2 Subsystem Description	4.4-l
4.4.2.1 Hardware Components	4.4-l
4.4.2.2 Software Components	4.4-4
4.4.2.3 Operating Modes	4.4-4
4.4.2.4 Coordinate Systems	4.4-7
4.4.3 Attitude Determination	4.4-8
4.4.3.1 Roll and Pitch Attitude Determination	4.4-9
4.4.3.2 Yaw Attitude Determination	4.4-12
4.4.3.3 Attitude Rate Determination	4.4-15
4.4.4 Attitude Control	4.4-16
4.4.4.1 Acquisition and Reacquisition	4.4-16
4.4.4.2 Normal Operation	4.4-20
4.4.4.3 Magnetic Momentum Unloading	4.4-20
4.4.5 Disturbance Environment	4.4-31
4.4.5.1 AVHRR	4.4-31
4.4.5.2 HIRS	4.4-31
4.4.5.3 AMSU	4.4-31
4.4.5.4 Tape Recorders	4.4-38
4.4.5.5 SBUV	4.4-38
4.4.6 Control Loop Stability	4.4-38
4.4.7 Pointing Accuracy	4.4-48
4.4.8 Hardware Components	4.4-73
4.4.8.1 Earth Sensor Assembly (ESA)	4.4-73
4.4.8.2 Inertial Measurements Unit	4.4-112
4.4.8.3 Sun Sensor Assembly (SSA)	4.4-174
4.4.8.4 Reaction Wheel Assembly	4.4-187
4.4.8.5 Magnetic Torquing Coils	4.4-202
4.5 Thermal Control Subsystem	4.5-l
4.5.1 Thermal Requirements	4.5-3

TABLE OF CONTENTS (Continued)

Section	Page
4.5.2 Design Philosophy	4.5-3
4.5.3 Thermal Control Elements Description	4.5-3
4.5.3.1 Passive Thermal Control Elements	4.5-3
4.5.4.1 Instrument Mounting Platform (IMP)	4.5-28
4.5.4.2 Equipment Support Module (ESM)	4.5-31
4.5.4.3 ESM/RSS Connection Truss	4.5-32
4.5.4.4 Reaction Control Equipment Support Structure (RSS)	4.5-35
4.5.4.5 Spacecraft/Launch Vehicle Adapter	4.5-38
4.5.4.6 Solar Array Assembly and Support (SAA/S)	4.5-38
4.5.5 Thermal Control Subsystem Telemetry	4.5-39
4.5.5.1 Operational Status Telemetry	4.5-39
4.5.5.2 TCS Temperature Telemetry	4.5-40
4.6 Power Subsystem	4.6-l
4.6.1 Power Subsystem Description	4.6-l
4.6.2 Power Subsystem Operation	4.6-4
4.6.2.1 Normal Three-Battery Operation	4.6-5
4.6.2.2 Two-Battery Operation	4.6-5
4.6.2.3 Battery Reconditioning	4.6-6
4.6.3 Reliability and Redundancy Features	4.6-8
4.6.4 Power Subsystem Performance	4.6-9
4.6.4.1 Launch Mode	4.6-9
4.6.4.2 Mission Mode	4.6-11
4.6.5 Equipment Description	4.6-30
4.6.5.1 Solar Array	4.6-30
4.6.5.2 Solar Array Drive/Array Drive Electronics	4.6-55
4.6.5.3 Solar Array Telemetry Commutator Unit (SATCU)	4.6-76
4.6.5.4 Batteries	4.6-82
4.6.5.5 Battery Reconditioning Unit (BRU)	4.6-93
4.6.5.6 Power Control Electronics (PCE)	4.6-100
4.6.5.7 Controls Power Converter	4.6-131
4.7 Communications Subsystem	4.7-l
4.7.1 Communications Links	4.7-5
4.7.1.1 Ascent and Early-Orbit Links	4 . 7 - 5
4.7.1.2 Operational Links	4.7-18
4.7.2 Communications Subsystem Component Description	4.7-23
4.7.2.1 S-Band Transmitters (STX-1, -2, -3, -4)	4.7-23
4.7.2.2 VHF Real-Time Transmitters (VTX-1, -2)	4.7-25
4.7.2.3 VHF Beacon Transmitter (BTX-1, -2)	4.7-27
4.7.2.4 G-STDN Command Receiver-Demodulator (GRD)	4.7-31
4.7.2.5 Deleted	4.7-39
4.7.2.6 S-Band Antenna (SBA-1, -2, -3)	4.7-39
4.7.2.7 S-Band Omni Antenna (SOA)	4.7-40
4.7.2.8 VHF Real-Time Antenna (VRA)	4.7-42
4.7.2.9 UHF Data Collection System Antenna (UDA)	4.7-44
4.7.2.10 VHF Beacon Antenna (BA)	4.7-45
4.7.2.11 Search and Rescue Receiving Antenna (SRA)	4.7-48
4.7.2.12 Search and Rescue L-Band Antenna (SLA)	4.7-50
4.7.2.13 RF Components	4.7-53
4.8 Data Handling Subsystem	4.8-l
4.8.1 Data Handling Subsystem Description	4.8-l

TABLE OF CONTENTS (Continued)

Section	Page
4.8.1.1 Subsystem Functions	4.8-l
4.8.1.2 Component Functions	4.8-l
4.8.2 TIROS Information Processor (TIP)	4.8-7
4.8.2.1 TIP Description	4.8-7
4.8.2.2 Data Handling Requirements	4.8-8
4.8.2.3 Telemetry Formats	4.8-8
4.8.2.4 Function Description	4.8-18
4.8.2.5 Flexibility	4.8-33
4.8.2.6 Physical Description	4.8-34
4.8.3 Manipulated Information Rats Processor (MIRP)	4.8-35
4.8.3.1 Requirements	4.8-35
4.8.3.2 Description	4.8-45
4.8.4 Digital Tape Recorders	4.8-57
4.8.4.1 Requirements	4.8-57
4.8.4.2 Description	4.8-57
4.8.4.3 Summary of DTR Characteristics	4.8-60
4.8.5 Cross Strap Unit (XSU)	4.8-61
4.8.5.1 Cross Strap Unit (XSU) Requirements	4.8-61
4.8.5.2 General Description	4.8-61
4.8.5.3 Summary of Characteristics	4.8-69
4.8.6 AMSU Information Processor (AIP)	4.8-70
4.8.6.1 AMSU Information Processor (AIP) Requirements	4.8-70
4.8.6.2 General Description	4.8-70
4.8.6.3 Summary of AIP Characteristics	4.8-88
4.9 Command and Control	4.9-l
4.9.1 Command and Control Description	4.9-l
4.9.2 Equipment Description	4.9-3
4.9.2.1 Redundant Crystal Oscillator	4.9-3
4.9.2.2 Controls Interface Unit (CIU)	4.9-8
4.9.2.3 Standard Controls Processor	4.9-77
4.9.2.4 Signal Conditioning Unit	4.9-106
4.9.2.5 Controls Power Converter	4.9-126
4.9.2.6 Controls Interface Annex	4.9-131
4.9.2.7 Decryption/Authentication Unit (DAU)	4.9-136
4.10 Spacecraft Software Organization	4.10-l
4.10.1 System Overview	4.10-l
4.10.2 Overall Organization of the FSS	4.10-l
4.10.2.1 Definition of Executable Modules	4.10-2
4.10.2.2 Load Package Organization	4.10-5
4.10.2.3 Priority Levels and Interrupts	4.10-6
4.10.3 Program Operation	4.10-6
4.10.3.1 Ascent Mode Operations	4.10-6
4.10.3.2 Handover Mode Operations	4.10-9
4.10.3.3 Orbit Mode Operations	4.10-9
4.10.4 Mode Control and Executive Software	4.10-10
4.10.4.1 Operational Philosophy	4.10-11
4.10.4.2 Mode Switching	4.10-11
4.10.5 Command and Control Software	4.10-16
4.10.6 Attitude Determination and Control Subsystem Software	4.10-23

TABLE OF CONTENTS (Continued)

Section		Page
4.10.6.1	System Description	4.10-23
4.10.6.2	Earth Sensor Read Software	4.10-24
4.10.6.3	Digital Filter Software (DFS)	4.10-28
4.10.6.4	Attitude Determination Software (ADS)	4.10-30
4.10.6.5	Attitude Control Software (ACS)	4.10-48
4.10.6.6	Magnetic Momentum Unloading Software (MMUS)	4.10-64
4.10.6.7	Solar Array Drive Control Software (SADCS)	4.10-71
4.10.6.8	Geometric Data Software (GEODAT)	4.10-76
4.10.7	Power System Description	4.10-97
4.10.7.1	System Description	4.10-97
4.10.7.2	Functional Description	4.10-98
4.10.8	Module Characteristics	4.10-105
4.10.8.1	ACS (Attitude Control Software)	4.10-105
4.10.8.2	ADACTEST (ADACS Test Software)	4.10-106
4.10.8.3	ADS (Attitude Determination Software)	4.10-107
4.10.8.4	AGS (Ascent Guidance Software)	4.10-108
4.10.8.5	ATMUL (Automatic Thruster Momentum Unloading)	4.10-108
4.10.8.6	CARP (CPU Alarm Response Program)	4.10-109
4.10.8.7	CMDPRO (Command Processor Software)	4.10-109
4.10.8.8	CTES (Cycle Thermal Control Elements)	4.10-110
4.10.8.9	CTEL (CPU Telemetry)	4.10-110
4.10.8.10	CVQI (Command Verify Queue Input)	4.10-110
4.10.8.11	CVQO (Command Verify Queue Output)	4.10-110
4.10.8.12	CYCLE (Cycle Executive Software)	4.10-110
4.10.8.13	DFS (Digital Filter Software)	4.10-111
4.10.8.14	ESRS (Earth Sensor Software)	4.10-111
4.10.8.15	FATN (Arctangent Function)	4.10-112
4.10.9.16	FCOS (Cosine Function)	4.10-112
4.10.9.17	FMAG (Vector Magnitude Function)	4.10-112
4.10.9.18	FROT3 (3-axis rotation of a vector)	4.10-112
4.10.9.19	FSIN (Sine Function)	4.10-112
4.10.9.20	FRST (Square Root Function)	4.10-112
4.10.9.21	GDUMP (General Dump)	4.10-112
4.10.9.22	GEODAT (Geodetic Data Software)	4.10-113
4.10.9.23	HAND (Handover Software)	4.10-113
4.10.9.24	ITEST (Instruction Test)	4.10-113
4.10.9.25	LIBRY Software Library Functions)	4.10-114
4.10.9.26	MEMCHK (Memory Checksum)'	4.10-114
4.10.9.27	MMUS (Magnetic Momentum Unloading Software)	4.10-114
4.10.9.28	MODE (CPU Mode Control Executive)	4.10-115
4.10.9.29	NULS (Nitrogen Momentum Unloading Software)	4.10-115
4.10.9.30	PMS (Power Management Software)	4.10-116
4.10.9.31	POPS (Power On Processor Software)	4.10-116
4.10.9.32	PRIVMOV (Privileged Mode Software)	4.10-117
4.10.9.33	PSSS (Power Survival State Software)	4.10-117
4.10.9.34	Recovers (Recovery Software)	4.10-117
4.10.9.35	RTP (Real Time Processor)	4.10-117
4.10.9.36	RWACS (Reaction Wheel Control Software)	4.10-118
4.10.9.37	SADBIAS	4.10-118
4.10.9.38	SADCS (Solar Array Drive Control Software)	4.10-118

TABLE OF CONTENTS (Continued)

Section		Page
	4.10.9.39 SADTEST (Solar Array Drive Test Software)	4.10-118
	4.10.9.40 SCPRO (Stored Command Processor)	4.10-118
	4.10.9.41 SOPS (Standby CPU Operations Software)	4.10-119
	4.10.9.42 STESM (Software to Establish a Safe Mode)	4.10-119
	4.10.9.43 TCNTRL (Thruster Control Software)	4.10-120
	4.10.9.44 TIKS (Timed Tasks)	4.10-120
	4.10.9.45 TIREX (TIROS-N Executive Software)	4.10-120
	4.10.9.46 TNPOOL (TIROS-N COMPOOL)	4.10-121
	4.10.9.47 TSRS (TIP Subcom Read Software)	4.10-121
	4.10.9.48 XPOPS	4.10-122
	4.11 Instruments	4.11-l
	4.11.1 Advanced Very High Resolution Radiometer	4.11-l
	4.11.2 High Resolution Infrared Radiation Sounder	4.11-8
	4.11.3 Advanced Microwave Sounding Unit	4.11-16
	4.11.3.1 AMSU-Al	4.11-16
	4.11.3.2 AMSU-A2	4.11-16
	4.11.3.3 AMSU-B	4.11-16
	4.11.4 Data Collection and Platform Location System	4.11-31
	4.11.5 Space Environment Monitor	4.11-38
	4.11.5.1 Total Energy Detector	4.11-38
	4.11.5.2 Medium Energy Proton Electron Detector	4.11-38
	4.11.5.3 Data Processing Unit	4.11-38
	4.11.5.4 SEM Component Location	4.11-38
	4.11.6 Solar Backscatter Ultraviolet Spectral Radiometer	4.11-44
	4.11.7 Search and Rescue Repeater	4.11-50
	4.11.8 Search and Rescue Processor with Memory	4.11-54
	4.12 Ascent Guidance Software	4.12-l
	4.12.1 Guidance Software Development	4.12-l
	4.12.1.1 Introduction	4.12-1
	4.12.1.2 General Requirements	4.12-4
	4.12.1.3 Navigation and Open Loop Guidance	4.12-5
	4.12.1.4 Closed Loop Guidance Equations	4.12-19
	4.12.1.5 Curve Fit Accuracy	4.12-48
	4.12.2 Control System Analysis (TBD)	4.12-49
	4.12.3 Ascent Guidance Software Mechanization	4.12-50
	4.12.3.1 System Definition	4.12-50
	4.12.3.2 Level 11 Interrupt Requirements (Telemetry)	4.12-52
	4.12.3.3 Level 9 Interrupt Requirements (IMU Data)	4.12-52
	4.12.3.4 Level 6 Interrupt (2/Sec Computations)	4.12-70
	4.12.3.5 AGS Startup Routine	4.12-80
	4.12.4 Telemetry (TBD)	4.12-84
5.0	ADVANCED TIROS-N AEROSPACE GROUND EQUIPMENT (ATNAGE)	5-1
	5.1 General ATNAGE Architecture	5-1
	5.2 ATNAGE Equipment Groups	5-1
	5.2.1 Stationary AGE (SAGE)	5-1
	5.2.1.1 Computers	5-2
	5.2.1.2 Nine-Track Tape Recorders	5-9
	5.2.1.3 Alpha-Numeric Display Terminals	5-9
	5.2.1.4 Line Printers	5-9

TABLE OF CONTENTS (Continued)

Section	Page
5.2.1.5 Multiprocessor Communications Adapter	5-10
5.2.1.6 Time Code Reader/Generator	5-10
5.2.1.7 Moving Head Disk	5-10
5.2.1.8 Digital-to-Analog System	5-11
5.2.1.9 Strip Chart Recorders	5-11
5.2.1.10 Printing Terminals	5-12
5.2.2 Spacecraft Simulator	5-12
5.2.3 Spacecraft Support Racks	5-12
5.3 Displays	5-12
5.3.1 HRPT Display	5-12
5.3.2 APT Display	5-14
5.4 ATNAGE Interfaces	5-14
5.4.1 Spacecraft Power	5-14
5.4.2 Spacecraft Radio Frequency	5-15
5.4.2.1 Analog Data Storage	5-16
5.4.2.2 Uplink Data Generation and Verification	5-16
5.4.2.3 Downlink Data Acquisition and Display	5-18
5.4.3 IRIG Clock	5-21
5.4.4 General Purpose Measurements	5-22
5.4.5 DCS/SARP-2 Special Test Equipment (DCS/SARP-2 STE)	5-23
5.4.6 SARR Special Test Equipment (SARR STE)	5-23
5.5 Frame Synchronizers	5-23
5.5.1 GE Frame Synchronizers	5-23
5.5.2 EMR Frame Synchronizers	5-23
5.6.1 ATNAGE System Overview	5-24
5.7 ATNAGE Subsystems	5-29
5.7.1 HRI Subsystem	5-29
5.7.1.1 Background Program Description	5-32
5.7.1.2 Foreground Program Description	5-33
5.7.2 Bus and Support	5-33
5.7.3 ATLAS and Support	5-33
5.7.3.1 ATLAS System	5-33
5.7.3.2 ATLAS Support Subsystem	5-34
5.7.4 LRI and Support Subsystems	5-35
5.7.4.1 Real-Time Low-Rate Instrument Processor	5-35
5.7.4.2 TIP Long Lines	5-36
5.7.4.3 DCS/SAP STE	5-36
5.7.4.4 Off-Line (Support) Processing	5-36
5.7.5 ATSIM and Support	5-36
5.8 Subsystem Interfaces	5-37
5.8.1 HRI/BUS Interface	5-37
5.8.1.1 Computer B to Computer A	5-38
5.8.1.2 Computer A to Computer B	5-38
5.8.2 BUS/LRI Interface	5-38
5.8.3 HRI/LRI Interface	5-40
5.8.4 BUS/ATLAS Interface	5-40
5.8.5 ATSIM/BUS Interfaces	5-40
5.8.6 ATSIM/HRI Interfaces	5-40

LIST OF ILLUSTRATIONS

Figure		Page
1.1-1	Summary of Characteristics of ATN-KLM Satellite	l-3
1.2-1	ATN-KLM Functional Block Diagram	l-5
2.3.2-l	Sun-Node Configuration for Pairing an Afternoon Ascending Node Orbit with a Morning Ascending Node Orbit	2-5
2.3.2-2	Seasonal Variations in Scene Illumination for a Morning Descending-Node Sun-Synchronous Orbit	2-6
2.3.2-3	Seasonal Variations in Scene Illumination for an Afternoon Ascending-Node Sun-Synchronous Orbit	2-7
2.3.2-4	Geometry of a Sun-Synchronous Orbit, Morning Descending Node	2-8
2.3.2-5	Geometry of a Sun-Synchronous Orbit, Afternoon Ascending Node	2-8
2.3.3-l	Seasonal Variation of Spacecraft Sun Angle for 833 km (450 nmi) Orbits	2-10
2.3.3-2	Time in Eclipse for Morning Descending-Node Orbits [833 km (450 nmi) Orbits]	2-11
2.3.3-3	Time in Eclipse for Afternoon Ascending-Node Orbits [833 km (450 nmi) Orbits]	2-11
2.3.3-4	Nodal Drift Rate Error Versus Mean Altitude Error	2-12
2.3.3-5	Nodal Drift Rate Error Versus Inclination Error	2-12
2.3.3-6	Typical Ground Contact Boundaries for 833 km (450 nmi) Orbit	2-13
2.3.3-7	Ground Station Contact Time Versus Longitude of Ascending Node	2-13
2.3.3-8	Keyhole Pattern	2-14
2.3.4-l	HRPT and APT Contact Regions	2-16
2.3.4-2	HRPT and APT Contact Frequency	2-17
2.3.4-3	BRPT and APT Contact Frequency	2-18
2.4-l	Launch Vehicle/Payload Mechanical Interface	2-20
2.4-2	ATN-KLM Launch Vehicle Configuration	2-21
2.5.2-l	Ionization vs. Shielding	2-27
3.1.1-l	ATN-KLM Spacecraft Configuration	3-3
3.1.2-l	ATN-KLM Internal Layout	3-5
3.2.1-la	Equipment Family Tree	3-7
3.2.1-lb	Equipment Family Tree	3-9
3.2.2-l	Software Family Tree	3-11
3.3.1-1	Sensor IMP Mounting	3-12
3.3.2-l	Clock and Sync Distribution	3-16
3.3.2-2	CMOS to CMOS Interface	3-17
3.3.2-3	TTL to CMOS Interface	3-18
3.3.2-4	CMOS to LPTTL Interface	3-19
3.3.2-5	CMOS to CMOS High Speed Interface	3-20
3.3.2-6	CMOS LPTTL High Speed Interface	3-21
3.3.2-7	Interface Receiving Circuit with Hysteresis	3-22
3.3.2-8	Typical Relay Drive Configurations	3-23
3.3.2-9	TIP Orbital Mode Format - NOAA-KLM	3-25
3.3.2-10	TIP Dump Mode Format - NOAA-KLM	3-26
3.3.2-11	Dwell Mode	3-27
3.3.2-12	TIP Boost Mode Format for NOAA-KLM	3-28

LIST OF ILLUSTRATIONS (Continued)

Figure		Page
3.3.2-13	AIP Data	3-29
3.3.2-14	ATN-KLM Grounding	3-32
4.2.1-l	ATN-KLM Spacecraft and Coordinate System	4.2-l
4.2.1-2	ATN-KLM Launch Configuration	4.2-3
4.2.1-3	ATN-KLM Orbit Configuration	4.2-5
4.2.3-l	ATN-KLM Analytical Model	4.2-10
4.2.3-2	IMP Finite Element Model	4.2-11
4.2.3-3	ESM Finite Element Model	4.2-12
4.2.3-4	Truss Finite Element Model	4.2-13
4.2.3-5	RSS Finite Element Model	4.2-13
4.2.3-6	Adapter Finite Element Model	4.2-14
4.2.3-7	ESM Top Panel	4.2-19
4.2.4-l	IMP General Arrangement	4.2-19
4.2.4-2	IMP Details	4.2-20
4.2.4-3	IMP Attachment Details	4.2-21
4.2.4-4	IMP Mounting Configuration	4.2-22
4.2.4-5	IMP Louver Assembly	4.2-23
4.2.4-6	IMP Louver Assembly Detail	4.2-24
4.2.4-7	IMP Sunshade	4.2-25
4.2.4-8	IMP Sunshade, Fixed	4.2-26
4.2.4-9	IMU Flex Mount	4.2-27
4.2.4-10	Typical Instrument Mount Showing Conical Bushing	4.2-27
4.2.4-11	Plastic Dowel	4.2-28
4.2.4-12	ESM Structure	4.2-28
4.2.4-13	ESM Panel Louvers	4.2-30
4.2.4-14	ESM Internal Arrangement	4.2-31
4.2.4-15	ESM Front Panel	4.2-33
4.2.4-16	ESM Bottom Panel	4.2-34
4.2.4-17	ESM Panel Inserts	4.2-35
4.2.4-18	AMSU-Al Installation	4.2-36
4.2.4-19	MEPED Installation	4.2-37
4.2.4-20	Truss Configuration	4.2-37
4.2.4-21	Truss to ESM and RSS Interfaces	4.2-38
4.2.4-22	Truss Interface Hardware	4.2-38
4.2.4-23	TED Installation	4.2-39
4.2.4-24	VRA Installation on Truss	4.2-40
4.2.4-25	RSS Layout	4.2-40
4.2.4-26	AKM Mounting Ring	4.2-41
4.2.4-27	Detail of AKM Attachment to RSS	4.2-41
4.2.4-28	RSS Assembly	4.2-43
4.2.4-29	Apogee Kick Motor Assembly	4.2-44
4.2.4-30	Booster Adapter	4.2-45
4.2.4-31	Solar Panel Substrates	4.2-45
4.2.4-32	Solar Array Support	4.2-46
4.2.4-33	Solar Array Deployment Mechanism	4.2-47
4.2.4-34	SAS Short Boom and Cant Hinges	4.2-48
4.2.4-35	Solar Array - Launch Configuration	4.2-49
4.2.4-36	SAD Restraint	4.2-51
4.2.4-37	Solar Panel Hinge Design	4.2-53
4.2.4-38	Solar Panel Deployment Sequence	4.2-53

LIST OF ILLUSTRATIONS (Continued)

Figure		Page
4.2.4-39	SAS Deployment Sequence	4.2-54
4.2.4-40	VRA and UDA Deployment	4.2-55
4.2.4-41	UDA in Launch Configuration	4.2-56
4.2.4-42	Search and Rescue Receiving Antenna Installation	4.2-57
4.2.4-43	SRA Deployment	4.2-58
4.2.4-44	SRA Phase 1 Hold-Down	4.2-58
4.2.4-45	SRA Phase 2 Release Mechanism	4.2-59
4.2.4-46	ATN-KLM V-Band Assembly	4.2-60
4.3.1-1	Apogee Kick Motor (AKM)	4.3-2
4.3.1-2	Reaction Control Equipment (RCE) Schematic Diagram	4.3-2
4.3.2-l	RCE Mission Requirements	4.3-7
4.3.3-l	MR-104A Hydrazine Thruster	4.3-10
4.3.3-2	Propellant Valve	4.3-13
4.3.3-3	MR-104A Vacuum Thrust vs. Feed Pressure	4.3-16
4.3.3-4	MR-104A REA Steady-State Performance Characteristics	4.3-17
4.3.3-5	Minimum N_2H_4 Thruster Performance	4.3-18
4.3.3-6	Impulse Bit vs. Thrust	4.3-18
4.3.3-7	MR-104A REA Pulse-Mode Performance vs. Throat Temperature	4.3-19
4.3.3-8	RCE Propellant Tank	4.3-20
4.3.3-9	Cold Gas Thruster	4.3-21
4.3.3-10	Pressurant Tank	4.3-22
4.3.3-11	Cross Section, Pressure Regulator	4.3-23
4.3.3-12	Pressure Transducer	4.3-25
4.3.3-13	Fill and Drain Valve	4.3-26
4.3.3-14	Hydrazine Isolation Valve	4.3-27
4.3.3-15	Latch Valve	4.3-28
4.3.3-16	Relief Valve	4.3-30
4.3.3-17	Filter, N_2H_4 Fill and Drain	4.3-32
4.3.3-18	Filter, Low Pressure GN2 Fill and Drain	4.3-33
4.3.3-19	Filter, High Pressure GN2 Fill and Drain	4.3-34
4.3.3-20	Filter, Nitrogen Engine Inlet	4.3-35
4.3.3-21	Filter, Pressure Regulator Inlet	4.3-36
4.4.2-l	ADACS Configuration Block Diagram	4.4-2
4.4.2-2	ESA Detector Configuration	4.4-3
4.4.2-3	Attitude Control Mode Switching	4.4-5
4.4.3-l	ESA Data Word Format	4.4-9
4.4.3-2	Earth Penetration Geometry	4.4-10
4.4.3-3	ESA Mounting Configuration	4.4-12
4.4.3-4	Sun Sensor Geometry	4.4-13
4.4.4-l	Normal Acquisition From 0.5 Radian Roll Angle, 0.25 Radian Pitch Angle	4.4-19
4.4.4-2	Yaw Gyrocompassing Acquisition	4.4-19
4.4.4-3	ATN Magnetic Momentum Unloading Regions	4.4-22
4.4.4-4	TIROS KLM Magnetic Momentum Unloading System Performance 22 deg S/A Cant Angle Summer Solstice	4.4-25
4.4.4-5	TIROS KLM Magnetic Momentum Unloading System Performance 22 deg S/A Cant Angle Equinox	4.4-25
4.4.4-6	TIROS KLM Magnetic Momentum Unloading System Performance 22 deg S/A Cant Angle Winter Solstice	4.4-26

LIST OF ILLUSTRATIONS (Continued)

Figure		Page
4.4.4-7	TIROS KLM Magnetic Momentum Unloading System Performance 37 deg S/A Cant Angle Summer Solstice	4.4-26
4.4.4-8	TIROS KLM Magnetic Momentum Unloading System Performance 37 deg S/A Cant Angle Equinox	4.4-27
4.4.4-9	TIROS KLM Magnetic Momentum Unloading System Performance 37 deg S/A Cant Angle Winter Solstice	4.4-27
4.4.4-10	TIROS KLM Magnetic Momentum Unloading System Performance 22 deg S/A Cant Angle Equinox +1 Min Orbit Period Uncertainty	4.4-29
4.4.4-11	TIROS KLM Magnetic Momentum Unloading System Performance 22 deg S/A Cant Angle Equinox -1 Min Orbit Period Uncertainty	4.4-29
4.4.4-12	TIROS KLM Magnetic Momentum Unloading System Performance 37 deg S/A Cant Angle Equinox +1 Min Orbit Period Uncertainty	4.4-30
4.4.4-13	TIROS KLM Magnetic Momentum Unloading System Performance 37 deg S/A Cant Angle Equinox -1 Min Orbit Period Uncertainty	4.4-30
4.4.5-l	HIRS Scan Timing Diagram	4.4-36
4.4.5-2	AMSU-Al Torque Profile (both units combined)	4.4-37
4.4.5-3	AMSU-A2 Torque Profile (compensated 85%)	4.4-37
4.4.5-4	AMSU-AB Torque Profile (uncompensated)	4.4-38
4.4.5-5	Tape Recorder Momentum Profile	4.4-39
4.4.6-l	Yaw Control Loop Block Diagram - Nominal and Coast Mode	4.4-43
4.4.6-2	Yaw Control Loop - YGC Mode	4.4-43
4.4.6-3	Yaw Control Loop Block Diagram - Search and Rate Nulling Modes	4.4-44
4.4.6-4	Roll Control Loop Block Diagram - Nominal Mode	4.4-44
4.4.6-5	Roll Control Loop Block Diagram - YGC Mode	4.4-45
4.4.6-6	Roll Control Loop Block Diagram - Rate Nulling and Search Modes	4.4-45
4.4.6-7	Roll Control Loop Block Diagram - Coast Mode	4.4-46
4.4.6-8	Pitch Control Loop Block Diagram - Nominal Mode	4.4-46
4.4.6-9	Pitch Control Loop Block Diagram - YGC Mode	4.4-47
4.4.6-10	Pitch Control Loop Block Diagram - Rate Nulling and Search Modes	4.4-47
4.4.6-11	Pitch Control Loop Block Diagram - Coast Mode	4.4-48
4.4.6-12	10 Hz Digital Filter Frequency Response	4.4-52
4.4.6-13a	Nominal Mode - Yaw Open Loop Response	4.4-64
4.4.6-13b	Nominal Mode - Roll Open Loop Response	4.4-65
4.4.6-13c	Nominal Mode - Pitch Open Loop Response	4.4-66
4.4.6-14a	RN/Search Mode - Yaw Open Loop Response	4.4-67
4.4.6-14b	RN/Search Mode - Roll Open Loop Response	4.4-68
4.4.6-14c	RN/Search Mode - Pitch Open Loop Response	4.4-69
4.4.6-15a	YGC Mode - Yaw Open Loop Response	4.4-70
4.4.6-15b	YGC Mode - Roll Open Loop Response	4.4-71
4.4.6-15c	YGC Mode - Pitch Open Loop Response	4.4-72
4.4.8-l	Earth Sensor Assembly Functional Block Diagram	4.4-74
4.4.8-2	ESA Sensor Fields of View	4.4-75
4.4.8-3	Sensor Basic Principle and Derivation	4.4-76
4.4.8-4	Processing Electronics Functional Block Diagram	4.4-80
4.4.8-5	ESA External Configuration	4.4-81
4.4.8-6	ESA Mounting Adapter	4.4-82
4.4.8-7	ESA Coordinate System Definition	4.4-82

LIST OF ILLUSTRATIONS (Continued)

Figure		Page
4.4.8-8	ESA Cross-Sectional Configuration	4.4-84
4.4.8-9	Optical Ray Paths	4.4-85
4.4.8-10	Detector Assembly Block	4.4-88
4.4.8-11	Six-Junction Thermopile Detector	4.4-89
4.4.8-12	ORS Assembly	4.4-90
4.4.8-13	Optical Assembly Spectral Response	4.4-93
4.4.8-14	Signal vs Apparent Earth Temperature	4.4-93
4.4.8-15	Pitch and Roll Error at Null vs Latitude (400 nmi)	4.4-94
4.4.8-16	Pitch and Roll Error at Null vs Latitude (450 nmi)	4.4-95
4.4.8-17	Pitch and Roll Error at Null vs Latitude (500 nmi)	4.4-95
4.4.8-18	Detectors and Commutator Simplified Schematic Diagram	4.4-97
4.4.8-19	Analog Waveforms	4.4-98
4.4.8-20	Preamplifier Schematic Diagram	4.4-99
4.4.8-21	Preamplifier Detector Noise	4.4-100
4.4.8-22	Analog Processor Gain Bandwidth Characteristic	4.4-100
4.4.8-23	Analog to Digital Converter Functional Block Diagram	4.4-101
4.4.8-24	Up/Down Converter Basic Principle	4.4-102
4.4.8-25	Analog to Digital Converter Frame Timing	4.4-103
4.4.8-26	Analog to Digital Converter Detailed Timing	4.4-104
4.4.8-27	ORS Controller Functional Block Diagram	4.4-106
4.4.8-28	ORS Controller Timing	4.4-107
4.4.8-29	ESA Output vs ORS Ball Temperature	4.4-107
4.4.8-30	Data Processor Functional Block Diagram	4.4-108
4.4.8-31	Data Processor Timing	4.4-109
4.4.8-32	Power Supply Functional Block Diagram	4.4-110
4.4.8-33	ESA Interface Diagram	4.4-111
4.4.8-34	IMU Interfaces	4.4-112
4.4.8-35	IMU Functional Block Diagram	4.4-113
4.4.8-36	Gyro Channel Transfer Function, Ascent Mode	4.4-120
4.4.8-37	Gyro Transfer Function Parameters	4.4-121
4.4.8-38	Gyro Transfer Function, Orbit Mode	4.4-123
4.4.8-39	Accelerometer Closed-Loop Transfer Function	4.4-124
4.4.8-40	Accelerometer Loop Block Diagram	4.4-126
4.4.8-41	IMU Mounting Base	4.4-127
4.4.8-42	IMU Exploded View	4.4-128
4.4.8-43	IMU	4.4-129
4.4.8-44	DC Power Supplies, Block Diagram	4.4-132
4.4.8-45	Primary/Backup DC Power Supply Switching	4.4-133
4.4.8-46	Transformer, Rectifiers, and Filters (Primary or Backup) Block Diagram	4.4-135
4.4.8-47	Spin Motor Power Supply Block Diagram	4.4-137
4.4.8-48	Phasing for Gyro Spin Motor Excitation	4.4-138
4.4.8-49	Primary AC Power Supply Failure Detection and Automatic Switchover	4.4-138
4.4.8-50	Gyro and Associated Circuitry	4.4-140
4.4.8-51	Equivalent Decommutator Circuit and Waveforms	4.4-142
4.4.8-52	Orbit Loop Gyro Test	4.4-144
4.4.8-53	Accelerometer and Rebalance Loop	4.4-145
4.4.8-54	Precision Pulser	4.4-147
4.4.8-55	Digitizer Functional Schematic	4.4-148

LIST OF ILLUSTRATIONS (Continued)

Figure		Page
4.4.8-56	Digitizer Waveforms	4.4-149
4.4.8-57	Timer Board Functional Diagram	4.4-149
4.4.8-58	Input Board Functional Diagram	4.4-150
4.4.8-59	Output Board Functional Diagram	4.4-151
4.4.8-60	Clock Input Section	4.4-152
4.4.8-61	CP, CP/Waveforms	4.4-152
4.4.8-62	Bit Time Counter	4.4-153
4.4.8-63	Power On Set Pulse	4.4-153
4.4.8-64	Bit Time Counter Start Up	4.4-154
4.4.8-65	32 kHz Counter	4.4-154
4.4.8-66	32 kHz Counter Waveforms	4.4-155
4.4.8-67	Digitizer Signal Generator	4.4-155
4.4.8-68	Digitizer Signals	4.4-156
4.4.8-69	Gyro Data Registers and Precounters	4.4-157
4.4.8-70	Data Storage and Accumulation Cycle	4.4-158
4.4.8-71	Digitizer Data Registers Store/Shift (Ascent Mode)	4.4-159
4.4.8-72	CPS Generation	4.4-159
4.4.8-73	CPS Waveforms	4.4-160
4.4.8-74	Countdown to 10 Hz Circuit	4.4-161
4.4.8-75	Countdown to 10 Hz Waveforms	4.4-161
4.4.8-76	Dump, Data Ready and 10 Hz Sync	4.4-162
4.4.8-77	Dump, Data Ready and 10 Hz Sync/Waveforms	4.4-163
4.4.8-78	Data Accumulator	4.4-163
4.4.8-79	Status Data Register	4.4-165
4.4.8-80	Output Buffer Section	4.4-166
4.4.8-81	IMU Block Temperature Control	4.4-168
4.4.8-82	DTG-IMU Thermal Mockup Test - Sensor Block Thermocouples	4.4-169
4.4.8-83	DTG-IMU Thermal Mockup Test - Gyro Thermocouples	4.4-170
4.4.8-84	IMU Turn-On from 77" Ambient	4.4-170
4.4.8-85	Sun Sensor Assembly Simplified Block Diagram	4.4-174
4.4.8-86	Sun Sensor Assembly Basic Principle of Operation	4.4-175
4.4.8-87	SSD External Configuration with Baffle	4.4-177
4.4.8-88	SSE External Configuration	4.4-177
4.4.8-89	SSD Mounting Adapter	4.4-178
4.4.8-90	SSA Coordinate System and Field of View Definition	4.4-178
4.4.8-91	Sun Sensor Unit Assembly	4.4-179
4.4.8-92	SSA Functional Block Diagram	4.4-182
4.4.8-93	Binary Number Correlation	4.4-183
4.4.8-94	Binary Code Bit Pattern Modification for Non-Ambiguous Data	4.4-183
4.4.8-95	Photocell Output as a Function of Sun Angle for a Single Photocell in the Quadrature Configuration	4.4-185
4.4.8-96	SSA Data Timing	4.4-186
4.4.8-97	Reaction Wheel Assembly Mounting Geometry	4.4-188
4.4.8-98	Reaction Wheel Assembly Interface Diagram	4.4-189
4.4.8-99	RWA Equivalent Mathematical Model	4.4-190
4.4.8-100	RWA Motor Torque vs Speed Characteristics	4.4-192
4.4.8-101	RWA Reaction Torque vs Speed Characteristic	4.4-193
4.4.8-102	RWA Cutaway View	4.4-195
4.4.8-103	RWA Side View	4.4-196
4.4.8-104	RWA Block Diagram	4.4-198

LIST OF ILLUSTRATIONS (Continued)

Figure		Page
4.4.8-105	RWA Power Controller Simplified Schematic	4.4-199
4.4.8-106	Commutation Control Loop Simplified Schematic Design	4.4-200
4.4.8-107	Torque Control Loop	4.4-201
4.4.8-108	Pulse Width Modulator	4.4-203
4.4.8-109	Momentum Torquing Coil, Schematic Diagram	4.4-203
4.4.8-110	RYC Momentum Coil Configuration	4.4-205
4.4.8-111	PTC Momentum Coil Configuration	4.4-206
4.4.8-112	Momentum Torquing Coils, Mounting Orientation	4.4-206
4.5.3-l	Multi-layer Thermal Blanket - Basic Construction	4.5-9
4.5.3-2	Dual Thermal Controller	4.5-12
4.5.3-3	Differential Thermal Controller	4.5-12
4.5.3-4	Dual TCE Functional Block Diagram	4.5-14
4.5.3-5	Dual TCE Operation	4.5-14
4.5.3-6	Sample Dual TCE Bridge Circuit	4.5-15
4.5.3-7	Dual TCE Bridge Operation	4.5-15
4.5.3-8	Differential TCE Functional Block Diagram	4.5-17
4.5.3-9	Differential TCE Operation	4.5-17
4.5.3-10	Differential TCE Bridge Circuit	4.5-18
4.5.3-11	Differential TCE Bridge Operation	4.5-18
4.5.3-12	Vane Thermal Louver Assembly	4.5-22
4.5.3-13	Vane Louver Blade Actuator Assembly'	4.5-23
4.5.3-14	Vane Louver Heat Transfer Characteristics	4.5-24
4.5.3-15	Vane Louver Actuation Characteristics	4.5-25
4.5.3-16	Pinwheel Thermal Louver	4.5-26
4.5.3-17	Pinwheel Louver Blade	4.5-26
4.5.3-18	Pinwheel Louver Actuator	4.5-27
4.5.3-19	Pinwheel Radiator/Guard Ring Assembly	4.5-28
4.6.1-1	Power Subsystem Functional Block Diagram	4.6-2
4.6.2-l	Regulation Profile	4.6-5
4.6.2-2	Battery Charging Method	4.6-6
4.6.2-3	Reconditioning in 100% Sun	4.6-7
4.6.2-4	Reconditioning in Eclipse Orbits	4.6-8
4.6.4-l	Battery State-of-Charge Timeline, Titan Launch	4.6-10
4.6.4-2	Orbit Timeline Used for Load Analysis	4.6-19
4.6.4-3	Power Profile for a Typical Orbit	4.6-20
4.6.4-4	Thermal Subsystem Electrical Loading	4.6-20
4.6.4-5	Energy Balance Computer Model	4.6-24
4.6.4-6	Power Subsystem Load Capability	4.6-25
4.6.5-l	Incidence Angle vs. Sun Angle - No Rotational Offset	4.6-30
4.6.5-2	Aluminum Skin Solar Panel Cross Section	4.6-31
4.6.5-3	Solar Cell Electron Damage Coefficients	4.6-36
4.6.5-4	Solar Cell Proton Damage Coefficients	4.6-36
4.6.5-5	Short-Circuit Current and Open-Circuit Voltage Changes with Radiation	4.6-38
4.6.5-6	Baseline Solar Cell I-V Characteristics @ 28°C	4.6-40
4.6.5-7	Degraded Solar Cell I-V Curves @ 28°C	4.6-40
4.6.5-8	Solar Array Current Availability	4.6-41
4.6.5-9	Solar Array Temperatures at Boundary Sun Angles	4.6-42
4.6.5-10	Maximum Solar Array Temperature Versus Sun Angle	4.6-43
4.6.5-11	Solar Array Partial Shunt Regulator Circuits	4.6-43

LIST OF ILLUSTRATIONS (Continued)

Figure		Page
4.6.5-12	Partial Shunt Performance	4.6-44
4.6.5-13	Maximum Partial Shunt Heat Dissipation	4.6-45
4.6.5-14	NOAA KLM Solar Array Telemetry Locations	4.6-47
4.6.5-15	APS Sensor Circuit	4.6-48
4.6.5-16	Solar Cell Load Current and Load Voltage Sensor Circuits	4.6-49
4.6.5-17	Solar Array Voltage Sensor Circuit	4.6-49
4.6.5-18	Solar Array Bus Voltage Sensor Circuit	4.6-50
4.6.5-19	Solar Array Hinge Deployment Sensor Circuits	4.6-51
4.6.5-20	Solar Array High Temperature Sensor Circuit	4.6-51
4.6.5-21	Solar Array Low Temperature Sensor Circuit	4.6-52
4.6.5-22	Solar Cell Short Circuit Current Sensor Circuit	4.6-52
4.6.5-23	Partial Shunt Voltage Sensor Circuit	4.6-53
4.6.5-24	Shunt Heat Sink High Temperature Sensor Circuit	4.6-54
4.6.5-25	Shunt Heat Sink Low Temperature Sensor Circuit	4.6-54
4.6.5-26	Solar Array Drive/Array Drive Electronics Interface Diagram	4.6-55
4.6.5-27	SAD Functional Block Diagram	4.6-56
4.6.5-28	ADE Functional Block Diagram	4.6-57
4.6.5-29	Array Drive Electronics Construction	4.6-60
4.6.5-30	Solar Array Drive	4.6-61
4.6.5-31	SAD Actuator	4.6-62
4.6.5-32	Slip Ring and Brush Configuration	4.6-64
4.6.5-33	SAD Component Flow	4.6-65
4.6.5-34	Command Decoder and Clock Generator	4.6-66
4.6.5-35	Resolver Interface	4.6-66
4.6.5-36	Sequence Generator	4.6-68
4.6.5-37	Forward/Reverse State Diagrams	4.6-69
4.6.5-38	Base Drive Bridge Circuit	4.6-70
4.6.5-39	Position and Status Monitoring Block Diagram	4.6-71
4.6.5-40	Sequencer State Diagram	4.6-73
4.6.5-41	Sequencer Timing Diagram	4.6-73
4.6.5-42	Pulse Generator-Timing Diagram	4.6-74
4.6.5-43	Power Switching Functional Block Diagram	4.6-75
4.6.5-44	SATCU Interface Diagram	4.6-77
4.6.5-45	SATCU Physical Configuration	4.6-78
4.6.5-46	SATCU Functional Block Diagram	4.6-79
4.6.5-47	SATCU Commutator Block Diagram	4.6-80
4.6.5-48	Battery Functional Block Diagram	4.6-84
4.6.5-49	Battery Bonded Cell Module	4.6-86
4.6.5-50	Typical Battery Pack Physical Configuration	4.6-87
4.6.5-51	Battery Cell Voltage	4.6-88
4.6.5-52	Life Prediction of NiCd Batteries in Low Earth Orbit	4.6-89
4.6.5-53	Minimum Charge/Discharge Ratios	4.6-90
4.6.5-54	Nominal Battery Voltage Limits	4.6-91
4.6.5-55	BRU Functional Block Diagram	4.6-94
4.6.5-56	PCB Assembly Outline	4.6-97
4.6.5-57	BRU Outline Drawing	4.6-98
4.6.5-58	BRU Interface Diagram	4.6-99
4.6.5-59	PCE Functional Block Diagram	4.6-102
4.6.5-60	Battery Charge Assembly Construction	4.6-111
4.6.5-61	BCA Radiator Construction	4.6-112

LIST OF ILLUSTRATIONS (Continued)

Figure		Page
4.6.5-62	Power Supply External Construction	4.6-113
4.6.5-63	Power Supply Internal Construction	4.6-114
4.6.5-64	Mode Control Functional Block Diagram	4.6-116
4.6.5-65	Regulated +28V Bus I-V Characteristics	4.6-116
4.6.5-66	BVR Functional Block Diagram	4.6-118
4.6.5-67	PWM Boost Regulator Waveforms	4.6-120
4.6.5-68	Typical Boost Regulator Efficiency	4.6-121
4.6.5-69	Charge Regulator Functional Block Diagram	4.6-122
4.6.5-70	Nominal Battery Voltage Limits	4.6-123
4.6.5-71	Partial Shunt Operations	4.6-124
4.6.5-72	Mode Control Functional Block Diagram	4.6-125
4.6.5-73	Mode Control Failure Detector Functional Block Diagram	4.6-127
4.6.5-74	Charge Regulator Failure Detector Functional Block Diagram	4.6-129
4.6.5-75	Controls Power Converter Functional Block Diagram	4.6-134
4.6.5-76	DC-to-DC Converter Functional Block Diagram	4.6-134
4.6.5-77	Controls Power Converter Outline Drawing	4.6-137
4.7-l	Communication Subsystem Block Diagram	4.7-2
4.7-2	Ascent and Early-Orbit RF Communications Link Summary	4.7-4
4.7-3	Operational RF Communications Link Summary	4.7-4
4.7-4	Command Data Waveform	4.7-5
4.7-5	Spectrum Control Characteristics (S-Band, APT, and VHF TIP)	4.7-8
4.7-6	Net Gain at DCS Receiver·RF Interface Connector	4.7-9
4.7-7	Net Gain at SARR 121.5-MHz Receiver RF Interface Connector	4.7-10
4.7-8	Net Gain at SARR 243-MHz Receiver RF Interface Connector	4.7-10
4.7-9	Net Gain at SARR 406.05 MHz RF Interface Connector	4.7-11
'4.7-10	Net Gain at SARP-M Receiver RF Interface Connector	4.7-11
4.7-11	Antenna Gain for LO-Watt 1544.5-MHz Transmitter at SARR Interface Connector	4.7-13
4.7.1-1	Ground Station Contact in 450-nmi Orbit	4.7-14
4.7.1-2	RF Paths Between the Satellite and the ATNAGE II at WTR	4.7-15
4.7.1-3	TIROS-N Boost Telemetry Signal Strength at WTR	4.7-16
4.7.1-4	VHF Beacon Coverage Areas for Positive Link Margin (Operational Orbit)	4.7-23
4.7.2-l	S-Band Transmitter (STX)	4.7-23
4.7.2-2	S-Band Transmitter Block Diagram	4.7-27
4.7.2-3	S-Band Transmitter Interfaces	4.7-27
4.7.2-4	VHF Real-Time Transmitter Outline Drawing	4.7-28
4.7.2-5	VHF Real-Time Transmitter Block Diagram	4.7-30
4.7.2-6	VHF Real-Time Transmitter Interfaces	4.7-31
4.7.2-7	VHF Beacon Transmitter Outline Drawing	4.7-32
4.7.2-8	Beacon Transmitter Block Diagram	4.7-34
4.7.2-9	Beacon Transmitter Interfaces	4.7-35
4.7.2-10	G-STDN Command Receiver-Demodulator	4.7-36
4.7.2-11	G-STDN Command Receiver-Demodulator Block Diagram	4.7-38
4.7.2-12	G-STDN Command Receiver-Demodulator Interfaces (Each Unit)	4.7-38
4.7.2-13	S-Band Antenna	4.7-39
4.7.2-14	S-Band Antenna Free-Space Minimum Gain	4.7-40
4.7.2-15	Antennules for the S-Band Omni Antennas	4.7-41
4.7.2-16	S-Band Omni Antennule Free-Space Minimum Gain	4.7-42

LIST OF ILLUSTRATIONS (Continued)

Figure		Page
4.7.2-17	VHF Real-Time Antenna	4.7-42
4.7.2-18	VRA Free-Space Minimum Gain	4.7-43
4.7.2-19	UHF Data Collection System Antenna	4.7-44
4.7.2-20	UDA Free-Space Minimum and Maximum Gain	4.7-46
4.7.2-21	VHF Beacon Antenna	4.7-47
4.7.2-22	BA Tuning Details	4.7-48
4.7.2-23	Search and Rescue Receiving Antenna	4.7-49
4.7.2-24	SRA Block Diagram	4.7-50
4.7.2-25	SRA Free-Space Minimum Gain	4.7-51
4.7.2-26	Search and Rescue L-Band Antenna	4.7-52
4.7.2-27	SLA Free-Space Minimum Gain	4.7-53
4.7.2-28	RF Filter RFF-1 Outline Drawing	4.7-56
4.7.2-29	RF Filter RFF-1 Attenuation Characteristics	4.7-57
4.7.2-30	RF Filter RFF-2 and RFF-3 Outline Drawing	4.7-57
4.7.2-31	RF Filter RFF-2 Attenuation Characteristics	4.7-58
4.7.2-32	RF Filter RFF-3 Attenuation Characteristics	4.7-58
4.7.2-33	RF Filter RFF-4 Outline Drawing	4.7-59
4.7.2-34	RF Filter RFF-4 Attenuation Characteristics	4.7-59
4.7.2-35	RF Filter RFF-5 Outline Drawing	4.7-60
4.7.2-36	RF Filter RFF-5 Attenuation Characteristics	4.7-60
4.7.2-37	DCS/SARP-M Diplexer Outline Drawing	4.7-61
4.7.2-38	GFN Outline Drawing	4.7-62
4.7.2-39	GFN Absolute Response vs. Frequency	4.7-63
4.7.2-40	RF Switch	4.7-63
4.8.1-1	Data Handling Subsystem, Functional View	4.8-2
4.8.2-l	TIP Interface Diagram	4.8-9
4.8.2-2	TIP Orbital Mode Format - NOAA-KLM	4.8-13
4.8.2-3	TIP Boost Mode Format for NOAA-KLM	4.8-14
4.8.2-4	TIP Subcom Frame Format	4.8-15
4.8.2-5	TIP Functional Block Diagram	4.8-19
4.8.3-l	MIRP Operational Configuration	4.8-35
4.8.3-2	MIRP Interface Diagram	4.8-37
4.8.3-3	Relative Phasing of MIRP Output Frames	4.8-41
4.8.3-4	HRPT/LAC Output Frame Formats	4.8-41
4.8.3-5	GAC Output Frame Format	4.8-42
4.8.3-6	MIRP Block Diagram	4.8-46
4.8.3-7	TIP Data Processing	4.8-49
4.8.3-8	HRPT/LAC Memory Block Diagram	4.8-51
4.8.3-9	MIRP APT Channel, Digital Block Diagram	4.8-53
4.8.4-l	DTR Electrical Interfaces	4.8-58
4.8.5-l	XSU Block Diagram	4.8-62
4.8.5-2	Mode Command Logic	4.8-65
4.8.5-3	DHS Data Paths	4.8-67
4.8.5-4	XSU Mode Status Telemetry	4.8-68
4.8.6-l	AIP Interface Diagram	4.8-71
4.8.6-2	AIP Block Diagram	4.8-75
4.8.6-3	AIP Output Format	4.8-76
4.8.6-4	AIP/AMSU Digital Interface	4.8-78
4.8.6-5	AIP/AMSU Data Input Sequence	4.8-79

LIST OF ILLUSTRATIONS (Continued)

Figure		Page
4.8.6-6	MIRP Data Transfer Timing	4.8-80
4.8.6-7	Cross-Strap Unit Data Transfer Waveforms	4.8-81
4.8.6-8	AIP Input/Output Timing	4.8-81
4.8.6-9	AIP Generated Sync Signals	4.8-82
4.8.6-10	A2/A5 Processor Board Block Diagram	4.8-82
4.8.6-11	AMSU Data Buffer Block Diagram	4.8-83
4.8.6-12	AMSU Memory R/W Switching	4.8-84
4.8.6-13	TIP Data Buffer Block Diagram	4.8-85
4.8.6-14	TIP R/W Memory Switching	4.8-86
4.8.6-15	Timing Generator	4.8-87
4.9.1-1	Coxnand and Control Subsystem Block Diagram	4.9-2
4.9.2-l	Redundant Crystal Oscillator Functional Block Diagram	4.9-3
4.9.2-2	RXO Physical Configuration	4.9-7
4.9.2-3	RXO Internal View	4.9-7
4.9.2-4	Oven Temperature Controller	4.9-7
4.9.2-5	CIU Functional Block Diagram	4.9-10
4.9.2-6	CIU Design Organization	4.9-12
4.9.2-7	CIU Physical Configuration	4.9-17
4.9.2-8	Power Turn-On Monitor Circuits	4.9-19
4.9.2-9	Uplink Processor Interface Diagram	4.9-22
4.9.2-10	Command Formats	4.9-24
4.9.2-11	UP Block Diagram	4.9-26
4.9.2-12	UP Flow Chart	4.9-27
4.9.2-13	UP Data Register Flow	4.9-28
4.9.2-14	TIROS KLM Hamming Code Decoder (32,25) for the CIU Uplink Processor	4.9-34
4.9.2-15	Uplink Processor Status Word Format	4.9-35
4.9.2-16	CIU Decoded Command Circuit	4.9-39
4.9.2-17	Clock Divider/Time Code Counter Block Diagram	4.9-40
4.9.2-18	Data Trunk Buffer Block Diagram	4.9-42
4.9.2-19	CIU Timing, IPR Data (To CPU>	4.9-43
4.9.2-20	CIU Timing, OPR Data (From CPU)	4.9-44
4.9.2-21	Invalid Address Detector Functional Diagram	4.9-47
4.9.2-22	Interrupt Sequencer Logic and State Diagram	4.9-48
4.9.2-23	Simplified CPU Select and Bus Switch Logic	4.9-51
4.9.2-24	Data/Interrupt Steering Logic Functional Schematic	4.9-52
4.9.2-25	Serial Output Buffer State Diagram	4.9-59
4.9.2-26	Serial Output Buffer Signal Timing	4.9-59
4.9.2-27	Serial Input Buffer State Diagram	4.9-62
4.9.2-28	Serial Input Buffer Signal Timing	4.9-62
4.9.2-29	RWA Torque Output Logic and Circuitry	4.9-66
4.9.2-30	RWA Speed Measurement Timing Diagram	4.9-68
4.9.2-31	IMU Data Special Processing	4.9-70
4.9.2-32	IMU Data Input Timing, Boost Mode	4.9-71
4.9.2-33	IMU Data Input Timing, Orbit Mode	4.9-72
4.9.2-34	Boost Mode CPU Telemetry SOB Timing Diagram	4.9-75
4.9.2-35	SCP-234FT Interface Diagram	4.9-78
4.9.2-36	CPU Configuration	4.9-79
4.9.2-37	CPU Microprogram Address Generator	4.9-80
4.9.2-38	Conditional Branch Logic	4.9-82

LIST OF ILLUSTRATIONS (Continued)

Figure		Page
4.9.2-39	Microprogram Flow, CMA Instruction	4.9-83
4.9.2-40	CPU Iteration Counter	4.9-84
4.9.2-41	CPU Clock Generator	4.9-85
4.9.2-42	CPU I/O Section	4.9-86
4.9.2-43	Interface Unit, CIU I/O Section	4.9-87
4.9.2-44	CPU Priority Interrupt Section	4.9-89
4.9.2-45	CIU Interrupt Logic	4.9-89
4.9.2-46	Alarm/Interrupt Routines	4.9-91
4.9.2-47	CPU Status Register	4.9-92
4.9.2-48	CPU Alarm Sequencer	4.9-93
4.9.2-49	START Microprogram Routine	4.9-94
4.9.2-50	CPU Memory Address Generator	4.9-95
4.9.2-51	CPU ALU Section	4.9-98
4.9.2-52	Memory Subsystem Block Diagram	4.9-102
4.9.2-53	R-W Memory Correction Diagram	4.9-104
4.9.2-54	Interface Diagram of the Memory	4.9-105
4.9.2-55	Signal Conditioning Unit Interface Diagram	4.9-107
4.9.2-56	SCU Relay Driver Circuits	4.9-108
4.9.2-57	CPU Power Controller State Diagram	4.9-110
4.9.2-58	scu Physical Configuration	4.9-112
4.9.2-59	scu Functional Block Diagram	4.9-113
4.9.2-60	scu Power Controller Schematic Diagram	4.9-114
4.9.2-61	scu Power Inhibit Schematic Diagram	4.9-114
4.9.2-62	CPU Power Controller Circuit Diagram	4.9-115
4.9.2-63	CPU Power Controller State Diagram	4.9-116
4.9.2-64	EED Bus Controller Schematic Diagram	4.9-117
4.9.2-65	Typical Momentum Coil Driver Circuit Diagram	4.9-119
4.9.2-66	Typical Thruster Signal Conditioner Circuit Diagram	4.9-120
4.9.2-67	Typical RCE Heaters Power Controller Circuit Design	4.9-121
4.9.2-68	Latch Valve Controller Schematic Diagram	4.9-122
4.9.2-69	Typical Ordnance Signal Conditioner Circuit Diagram	4.9-122
4.9.2-70	Liftoff Flag Signal Conditioner Circuit Diagram	4.9-125
4.9.2-71	Controls Power Converter Functional Block Diagram	4.9-128
4.9.2-72	DC to DC Converter Functional Block Diagram	4.9-128
4.9.2-73	Controls Power Converter Outline Drawing	4.9-130
4.9.2-74	Control Interface Annex (CXU) Block Diagram	4.9-132
4.9.2-75	Data Transfer Timing Diagram	4.9-133
4.9.2-76	CXU Control and Output Logic	4.9-134
4.9.2-77	Typical Output Buffer Configuration	4.9-135
4.9.2-78	CXU Outline	4.9-137
4.9.2-79	DAU Block Diagram	4.9-138
4.9.2-80	Cipher/Decrypt Text	4.9-139
4.9.2-81	DAU Box Interface Diagram	4.9-140
4.9.2-82	DAU Functional State Diagram	4.9-146
4.9.2-83	DAU I/O Signal Timing	4.9-149
4.9.2-84	Uplink Functional Block Diagram	4.9-150
4.9.2-85	Uplink Format (Encrypted)	4.9-150
4.10.2-l	Temporal Phases of Software Operation	4.10-6
4.10.2-2	Orbit Phase Software Hierarchy	4.10-8
4.10.4-l	CPU MODE States	4.10-12

LIST OF ILLUSTRATIONS (Continued)

Figure		Page
4.10.5-l	Command & Control Software, Functional Block Diagram	4.10-17
4.10.5-2	Uplink Processor Status Word	4.10-18
4.10.5-3	Uplink Word Format	4.10-18
4.10.5-4	Command Format	4.10-19
4.10.5-S	Stored-Command-Table Format	4.10-21
4.10.5-6	GDUMP Interfaces	4.10-23
4.10.6-l	Generalized Flow for Data Transfers Between Buffer 425 and ESRS	4.10-25
4.10.6-2	Relative Timing of MODE, ESRS, ADS and ACS	4.10-26
4.10.6-3	ESRS Input/Output Requirements	4.10-27
4.10.6-4	DFS Input/Output Requirements	4.10-31
4.10.6-s	ADS Functional Diagram	4.10-32
4.10.6-4	Format of IMU Status Word	4.10-36
4.10.6-7	Format of GRFAIL and NAVL	4.10-36
4.10.6-8	Gyro to Payload Transformation	4.10-37
4.10.6-9	Format of GTPIND	4.10-38
4.10.6-10	Attitude Control Mode Switching	4.10-43
4.10.6-11	ADS Input/Output Requirements	4.10-47
4.10.6-12	ACS Functional Diagram	4.10-49
4.10.6-13	Search Mode Processing Using QUW and QLW	4.10-54
4.10.6-14	Structure of RWA Command Word	4.10-58
4.10.6-15	ACS Input/Output Requirements	4.10-63
4.10.6-16	Momentum Polarity Criteria Spacecraft	4.10-66
4.10.6-17	MMUS Input/Output Requirements	4.10-71
4.10.6-18	SADCS Input/Output Requirements	4.10-75
4.10.6-19	Sun Cone and Clock Angles	4.10-80
4.10.6-20	Sun Sensor Geometry	4.10-80
4.10.6-21	Transformation from the I Frame to the G Frame	4.10-84
4.10.6-22	Transformation from the D Frame to the I Frame	4.10-86
4.10.6-23	SSA Transfer Function	4.10-91
4.10.6-24	ESA Cluster Geometry	4.10-92
4.10.6-25	GEODAT Interface Block Diagram	4.10-95
4.10.7-l	PMS Interface Block Diagram	4.10-99
4.11.1-l	AVHRR/3 Outline Drawing	4.11-l
4.11.1-2	AVHRR/3 Simplified Block Diagram	4.11-3
4.11.2-1	HIRS/3 Functional Block Diagram	4.11-9
4.11.2-2	HIRS/3 Outline Drawing	4.11-11
4.11.3-1	AMSU-Al Functional Block Diagram	4.11-17
4.11.3-2	AMSU-Al Outline Drawing	4.11-19
4.11.3-3	AMSU-A2 Functional Block Diagram	4.11-23
4.11.3-4	AMSU-A2 Outline Drawing	4.11-24
4.11.3-5	AMSU-B Functional Block Diagram	4.11-27
4.11.3-6	AMSU-B Outline Drawing	4.11-28
4.11.4-1	DCS-2 Simplified Block Diagram	4.11-32
4.11.4-2	DCS-2 RPU 'Outline Drawing	4.11-33
4.11.4-3	DCS-2 SPU Outline Drawing	4.11-34
4.11.5-1	TED Simplified Block Diagram	4.11-39
4.11.5-2	MEPED Simplified Block Diagram	4.11-39
4.11.5-3	DPU Simplified Block Diagram	4.11-39
4.11.5-4	SEM DPU Outline Drawing	4.11-40

LIST OF ILLUSTRATIONS (Continued)

Figure		Page
4.11.5-5	SEM MEPED Outline Drawing	4.11-40
4.11.5-6	SEM TED Outline Drawing	4.11-41
4.11.6-1	SBUV/2 Electrical Block Diagram	4.11-45
4.11.6-2	SBUV/2 Outline Drawing	4.11-47
4.11.8-1	SARP-2 Simplified Block Diagram	4.11-55
4.11.8-2	SARP-2 RPU Outline Drawing	4.11-56
4.11.8-3	SARP-2 SPU Outline Drawing	4.11-57
4.12.1-1	Alignment Loop	4.12-8
4.12.1-2	Coordinate Systems	4.12-9
4.12.1-3	Navigation Block Diagram	4.12-14
4.12.1-4	Gravity Error Due to Square Root Approximation (TIROS-N SAR)	4.12-15
4.12.1-5	Coordinate Systems Detail-Thrusters	4.12-18
4.12.1-6	On-Off Phase Plane Description	4.12-19
4.12.1-7	On-Off Control Logic	4.12-19
4.12.1-8	Simplified Guidance System Block Diagram	4.12-21
4.12.1-9	Guidance Mode Sequence	4.12-21
4.12.1-10	Powered Flight Predictor Block Diagram	4.12-25
4.12.1-11	Acceleration Curve Fits	4.12-26
4.12.1-12	Need for Alternate Predictor	4.12-30
4.12.1-13	Error Policy Geometry	4.12-32
4.12.1-14	Steering Policy and Time-to-Go Geometry	4.12-34
4.12.1-15	Time-To-Cutoff Diagram	4.12-38
4.12.1-16	Coast Adjust Policy Geometry	4.12-41
4.12.1-17	Coast Adjust Guidance Functional Diagram, Part 1	4.12-44
4.12.1-18	Coast Adjust Guidance Functional Diagram, Part 2	4.12-44
4.12.1-19	Position Pointing Geometry	4.12-45
4.12.1-20	Errors in Inertial Velocity to Go from Curve Fits, ARM Stage (TIROS-N SAR)	4.12-49
4.12.3-1	Pre-Launch Vehicle Configuration	4.12-50
4.12.3-2	Vehicle Checkout Orientation Capability	4.12-51
4.12.3-3	Alignment Loop Block Diagram	4.12-52
4.12.3-4	Telemetry Interrupt (Level 11)	4.12-53
4.12.3-5	Level 9 Interrupt Flow Diagram	4.12-54
4.12.3-6	Gyro Data Processing Flow Diagram	4.12-55
4.12.3-7	Controls Equations	4.12-56
4.12.3-8	Control Filter Equations	4.12-56
4.12.3-9	Control System Switch Line Characteristics	4.12-57
4.12.3-10	On-Off Logic Flow Diagram	4.12-57
4.12.3-11	Accelerometer Data Processing Flow Diagram	4.12-59
4.12.3-12	Telemetry Store	4.12-60
4.12.3-13	Orthonormalize	4.12-60
4.12.3-14	50/sec to 2/sec Logic Flow Diagram	4.12-61
4.12.3-15	Initialization (TBD)	4.12-63
4.12.3-16	Closed Loop Test Flow Diagram (TBD)	4.12-64
4.12.3-17	Controls Test Flow Diagram (TBD)	4.12-66
4.12.3-18	Control Test Attitude Error Pattern	4.12-67
4.12.3-19	Navigation Test	4.12-68
4.12.3-20	Manual Controls Test (TBD)	4.12-68
4.12.3-21	Liftoff Detection/Alignment (TBD)	4.12-69

LIST OF ILLUSTRATIONS (Continued)

Figure		Page
4.12.3-22	Alignment Logic Flow Diagram	4.12-71
4.12.3-23	Level 6 Interrupt Logic Flow Diagram	4.12-72
4.12.3-24	Navigation and Gravity Flow Diagrams	4.12-73
4.12.3-25	Closed Loop Guidance Flow Diagram	4.12-75
4.12.3-26	Powered Flight Predictor Flow Diagram	4.12-76
4.12.3-27	Guidance Error Flow Diagram	4.12-78
4.12.3-28	Guidance Steering Flow Diagram	4.12-79
4.12.3-29	Sequencer Routine Flow Diagram	4.12-81
4.12.3-30	AGS Start Up Logic	4.12-83
4.12.4-1	Ascent Guidance Telemetry Master Frame Format	4.12-84
5.2.1-1a	ATNAGE II Hardware Configuration (Part A): ATNAGE II For ATN-KLM	5-3
5.2.1-1b	ATNAGE II Hardware Configuration (Part B): ATNAGE II For ATN-KLM	5-5
5.2.1-1c	ATNAGE II Hardware Configuration (Part C): ATNAGE II For ATN-KLM	5-7
5.2.3-1	Spacecraft Support Rack (SSR) Functional Configuration	5-13
5.4.2-1	Analog Data Record/Playback Configuration	5-17
5.4.2-2	Uplink Data Modulation Format	5-17
5.6.1-1a	SAGE Hardware System Configuration	5-25
5.6.1-1b	ATNAGE Computer Support Hardware System Configuration	5-27
5.7.1-1	HRI Subsystem Organization	5-30
5.7.3-1	ATLAS Subsystem Organization	5-35
5.8.1-1	HRI/BUS Interface	5-39

LIST OF TABLES

Table		Page
2.1-1	ATN-KLM Requirements	2-2
2.2-l	Instrument Complement	2-3
2.3.2-l	Orbital Parameters	2-4
2.3.5-l	A Sun Angle for 10 Minutes A Launch Time (Degrees/10 Minutes)	2-19
2.5.1-1	Trapped Proton Environment	2-22
2.5.1-2	Trapped Electron Environment	2-23
2.5.1-3	Orbit Attenuated Solar Flare Proton Fluences	2-24
2.5.1-4	Total Integral LET Spectra for Solar Maximum for Cosmic-Ray Flux of Galactic Origin	2-25
2.5.1-5	Total Integral LET Spectra for Solar Minimum for Cosmic-Ray Flux of Galactic Origin	2-26
3.3.2-l	Interface Test Data	3-24
3.3.2-2	Telemetry Characteristics	3-30
3.3.2-3	Regulated Bus Interface Characteristics	3-31
3.4-l	ATN-KLM Spacecraft Characteristics and Performance	3-34
3.4-2	Weight Breakdown and Mass Properties	3-36
3.11.3-1	Transport Unit Bit Rates and Capacity	3-40
3.12-1	Communications Link Summary	3-42
4.2-l	ATN-KLM Weight Summary	4.2-6
4.2.1-2	Inertia Report ATN-KLM	4.2-7
4.2.2-l	ATN-KLM Payload Alignment Parameters	4.2-9
4.2.2-2	Instrument Alignment Tolerances	4.2-9
4.2.3-l	Environmental Loads and Structural Design Criteria, ATN-KLM	4.2-15
4.2.3-2	ATN-KLM Loading Configurations	4.2-15
4.2.3-3	Stress Analysis Summary For ATN-KLM ESM	4.2-17
4.2.3-4	Stress Analysis Summary For ATN-KLM RSS	4.2-18
4.2.4-l	ATN-KLM System Deployment Ordnances	4.2-51
4.2.4-2	ATN-KIM System Deployment Mechanisms	4.2-52
4.3.1-1	High Pressure Nitrogen Component Pressure Levels	4.3-3
4.3.1-2	Low Pressure *Nitrogen* Component Pressure Levels	4.3-4
4.3.1-3	Hydrazine Component Pressure Levels	4.3-5
4.3.2-l	RCE Mission Operations	4.3-6
4.3.2-2	RCE Weight and Power Summary	4.3-8
4.3.3-l	Design Summary - MR-104A REA	4.3-11
4.3.3-2	Hydrazine Thruster Valve Characteristics	4.3-12
4.3.3-3	MR-104A REA Nominal Steady-State Performance Characteristics	4.3-14
4.3.3-4	Nitrogen Thruster Valve Characteristics	4.3-19
4.3.3-5	Pressure Regulator Operational Characteristics	4.3-24
4.3.3-6	Pressure Transducer Characteristics	4.3-24
4.3.3-7	Fill and Drain Valve Characteristics	4.3-25
4.3.3-8	Hydrazine Isolation Valve Characteristics	4.3-27
4.3.3-9	Latch Valve Characteristics	4.3-28
4.3.3-10	Relief Valve Characteristics	4.3-29
4.4.2-l	Decision Table - ADACS Mode Determination	4.4-6
4.4.2-2	Search Mode Decision Table	4.4-8
4.4.3-l	ESA Attitude Calculations	4.4-11
4.4.4-l	Unloading Thresholds	4.4-21

LIST OF TABLES (Continued)

Table		Page
4.4.4-2a	Magnetic Momentum Unloading Logic, Polar	4.4-23
4.4.4-2b	Magnetic Momentum Unloading Logic, East/West	4.4-23
4.4.4-3	Nominal Compensation Constants	4.4-23
4.4.4-4	Summary Reaction Wheel Speeds	4.4-28
4.4.4-5	Magnetic Coil Duty Cycles	4.4-28
4.4.5-l	Worst Case Total Environmental Disturbance Body Torque Fourier Coefficients, Afternoon Ascending Orbit	4.4-32
4.4.5-2	Worst Case Total Environmental Disturbance Body Torque Fourier Coefficients, Morning Ascending Orbit	4.4-33
4.4.5-3	Environmental Disturbance Analysis Parameters	4.4-34
4.4.5-4	ATN-KLM External Disturbances	4.4-35
4.4.5-5	Tape Recorder Momentum Characteristics	4.4-39
4.4.6-l	Fixed Base Natural Frequencies of the Solar Array	4.4-40
4.4.6-2	Fixed Base Natural Frequencies of the SAR	4.4-40
4.4.6-3	Free-Free Natural Frequencies of the Spacecraft (Rigid Body Spacecraft With Solar Array and SAR)	4.4-40
4.4.6-4	TIROS KLM Spacecraft Inertias	4.4-41
4.4.6-5	TIROS KLM Solar Array Flextural Properties	4.4-42
4.4.6-6	Definition of Variables	4.4-49
4.4.6-7	System Constants	4.4-50
4.4.6-8	PID Controller Gains	4.4-53
4.4.6-9	Transfer Function Definitions	4.4-54
4.4.6-10a	Stability Margins Nominal Mode - 22" Cant Angle	4.4-55
4.4.6-10b	Stability Margins Nominal Mode - 37" Cant Angle	4.4-56
4.4.6-11a	Stability Margins RN/Search Mode - 22° Cant Angle	4.4-57
4.4.6-11b	Stability Margins RN/Search Mode - 37" Cant Angle	4.4-58
4.4.6-12a	Stability Margins YGC Mode - 22° Cant Angle	4.4-59
4.4.6-12b	Stability Margins YGC Mode - 37" Cant Angle	4.4-60
4.4.6-13a	Stability Margins Coast Mode - 22' Cant Angle	4.4-61
4.4.6-13b	Stability Margins Coast Mode - 37" Cant Angle	4.4-62
4.4.6-14	Closed Loop Control System Bandwidths	4.4-63
4.4.7-l	ADACS Error Budget	4.4-73
4.4.8-l	Earth Sensor Assembly Characteristics	4.4-81
4.4.8-2	Optical Component Characteristics	4.4-86
4.4.8-3	Error Summary Chart	4.4-92
4.4.8-4	ESA Data Format	4.4-109
4.4.8-5	IMU Operating Modes	4.4-117
4.4.8-6	IMU Design Characteristics	4.4-118
4.4.8-7	Gyro Channel Performance Characteristics, Ascent Mode	4.4-119
4.4.8-8	Gyro Channel Performance Characteristics, Orbit/Maneuver Mode	4.4-122
4.4.8-9	Accelerometer Channel Performance	4.4-125
4.4.8-10	IMU Thermal Control Heater Power Requirements	4.4-169
4.4.8-11	Status Word Contents	4.4-174
4.4.8-12	Sun Sensor Assembly Characteristics	4.4-176
4.4.8-13	SSA Performance Summary	4.4-180
4.4.8-14	Sun Sensor Assembly Output Data Code	4.4-187
4.4.8-15	RWA Mathematical Model Nomenclature Parameters	4.4-191
4.4.8-16	Reaction Wheel Assembly Design Characteristics	4.4-194
4.4.8-17	Momentum Coil Characteristics	4.4-204

LIST OF TABLES (Continued)

Table		Page
4.4.8-18	Momentum Coil Winding Characteristics	4.4-205
4.5-l	Thermal Control Subsystem (TCS) Parameters	4.5-l
4.5.1-1	Temperature Limits and Predictions - IMP	4.5-4
4.5.1-2	Temperature Limits and Predictions - ESM	4.5-5
4.5.1-3	Temperature Limits and Predictions - RSS AND SAS	4.5-7
4.5.3-l	ATN-KLM Principal Thermal Control Finishes	4.5-8
4.5.3-2	ATN-KLM Thermal Conduction Control Materials	4.5-9
4.5.3-3	Thermal Multilayer Insulation Blankets	4.5-10
4.5.3-4	ATN-KLM TCE Controller Usage	4.5-13
4.5.3-5	Ribbon Heater Characteristics	4.5-20
4.5.3-6	TCE Controller Heater Usage	4.5-21
4.5.4-l	IMP Thermal Provisions	4.5-29
4.5.4-2	ESM Thermal Provisions	4.5-33
4.5.4-3	RSS Thermal Provisions	4.5-36
4.5.5-l	TCE Controller Status Telemetry List	4.5-41
4.5.5-2	RCE C/D Heater System Status Telemetry	4.5-43
4.5.5-3	TCS Temperature Telemetry List	4.5-44
4.6.1-1	Power Subsystem Components Size and Weight Summary	4.6-3
4.6.4-l	Estimated Ascent Load Power Requirements, Titan Launch	4.6-10
4.6.4-2	Component Operating Currents	4.6-12
4.6.4-3	Orbit Average Power Requirements	4.6-17
4.6.4-4	Eclipse Time Duration Versus Spacecraft Sun Angle	4.6-21
4.6.4-5	Computer Inputs For Power Analysis	4.6-22
4.6.4-6	TIROS KLM Power Summary	4.6-26
4.6.4-7	Peak Continuous Current in CDA Contact	4.6-27
4.6.4-8	Regulated Bus Interface Characteristics	4.6-29
4.6.5-l	Trapped Proton Environment	4.6-33
4.6.5-2	Trapped Electron Environment	4.6-34
4.6.5-3	Orbit Attenuated Solar Flare Proton Fluences	4.6-35
4.6.5-4	TIROS KLM Solar-Cell Fluence - Two-Year Mission	4.6-37
4.6.5-5	Solar Array Degradation Factors	4.6-37
4.6.5-6	Solar Array Parameters	4.6-39
4.6.5-7	Solar Cell Temperature Coefficients	4.6-41
4.6.5-8	Solar Array Thermal Properties	4.6-42
4.6.5-9	Solar Array Telemetry	4.6-46
4.6.5-10	Solar Array Drive/Array Drive Electronics Performance Summary	4.6-58
4.6.5-11	Array Drive Electronics Characteristics	4.6-58
4.6.5-12	Solar Array Drive Characteristics	4.6-59
4.6.5-13	Solar Array Drive Train Parameters	4.6-61
4.6.5-14	Solar Array Drive Slip Ring Characteristics	4.6-62
4.6.5-15	SAD Status Format	4.6-72
4.6.5-16	Solar Array Angle Output Code	4.6-72
4.6.5-17	SAD Speed and Direction Control	4.6-76
4.6.5-18	SATCU Design Parameters	4.6-80
4.6.5-19	SATCU Commutated Telemetry Sequence	4.6-81
4.6.5-20	Battery Characteristics	4.6-85
4.6.5-21	NOAA KLM Battery Performance	4.6-92
4.6.5-22	BRU Design Characteristics	4.6-96
4.6.5-23	BRU Telemetry	4.6-99

LIST OF TABLES (Continued)

Table		Page
4.6.5-24	BRU Relay Drive Signal Characteristics	4.6-100
4.6.5-25	PCE Control Signals	4.6-104
4.6.5-26	V/T Limit Signal Response	4.6-105
4.6.5-27	Charge Rate Control Signal Response	4.6-106
4.6.5-28	Battery Connect/Disconnect Relay Control Signal Response	4.6-107
4.6.5-29	Redundant Equipment Selection Control Signal Response	4.6-108
4.6.5-30	PSE and BCA Design Specifications	4.6-109
4.6.5-31	Available Fused Power From PSE	4.6-129
4.6.5-32	PCE Analog Telemetry	4.6-130
4.6.5-33	PCE Multi-Level Analog Telemetry	4.6-131
4.6.5-34	PCE Discrete Telemetry	4.6-132
4.6.5-35	Controls Power Converter Design Characteristics	4.6-136
4.6.5-36	Typical CPC Mode Telemetry	4.6-137
4.7-l	Communications Subsystem Components	4.7-3
4.7-2	Ascent and Early-Orbit Communications Link Characteristics Summary	4.7-6
4.7-3	Operational Link Summary	4.7-7
4.7-4	Maximum EM1 Level into the DCS RF Interface Connector	4.7-9
4.7-5	Maximum Satellite Transmitter Power Levels into the SARP-M and SARR Receiver RF Interface Connectors	4.7-12
4.7-6	Maximum Levels Out of the SARR Transmitter RF Interface Connector	4.7-13
4.7.1-1	S-Band Command Link Analysis (Random Satellite Attitude)	4.7-17
4.7.1-2	VHF Beacon Real-Time Link Analysis (Random Satellite Attitude)	4.7-17
4.7.1-3	S-Band Command Link Analysis (Operational Orbit)	4.7-19
4.7.1-4	VHF Beacon Real-Time Link Analysis (Operational Orbit)	4.7-20
4.7.1-5	S-Band Downlink Analysis (Operational Orbit)	4.7-21
4.7.1-6	VHF APT Real-Time Link Analysis (Operational Orbits)	4.7-22
4.7.2-l	S-Band Transmitter Characteristics (STX-1, -2, -3)	4.7-24
4.7.2-2	S-Band Transmitter Characteristics (STX-4)	4.7-26
4.7.2-3	VHF Real-Time Transmitter Characteristics	4.7-29
4.7.2-4	Beacon Transmitter Characteristics	4.7-33
4.7.2-5	Command Receiver-Demodulator Characteristics	4.7-37
4.7.2-6	S-Band Antenna Characteristics	4.7-40
4.7.2-7	S-Band Omni Antennule Characteristics	4.7-41
4.7.2-8	VRA Characteristics	4.7-43
4.7.2-9	UHF Data Collection System Antenna Characteristics	4.7-45
4.7.2-10	VHF Beacon Antenna Characteristics	4.7-47
4.7.2-11	Search and Rescue Receiving Antenna Characteristics	4.7-49
4.7.2-12	Search and Rescue L-Band Antenna Characteristics	4.7-52
4.7.2-13	RF Filters - Characteristics	4.7-54
4.7.2-14	DCS/SARP-M Diplexer Attenuation Characteristics	4.7-61
4.7.2-15	RF Switch Characteristics	4.7-64
4.7.2-16	Antenna Hybrid Characteristics	4.7-64
4.7.2-17	RF Cable Characteristics	4.7-65
4.8.2-l	TIP Salient Characteristics	4.8-10
4.8.2-2	TIP Orbital Mode Data Handling Requirements	4.8-11
4.8.2-3	TIP Boost Mode Data Handling Requirements	4.8-12
4.8.3-l	HRPT/LAC/GAC/Header Structure	4.8-42

LIST OF TABLES (Continued)

Table		Page
4.8.4-l	DTR Modes, Commands and Power	4.8-59
4.8.6-l	AIP Input Signals	4.8-72
4.8.6-2	AIP Output Signals	4.8-74
4.8.6-3	AIP Modes	4.8-77
4.9.2-l	RXO Failure Truth Table	4.9-5
4.9.2-2	RXO Design Characteristics	4.9-6
4.9.2-3	CIU Design Characteristics	4.9-16
4.9.2-4	CIU Buffers	4.9-18
4.9.2-5	Uplink Command Reject/Accept Criteria	4.9-29
4.9.2-6	UP Processor Status Words	4.9-36
4.9.2-7	CIU Decoder Commands	4.9-37
4.9.2-8	Clock Divider Outputs	4.9-40
4.9.2-9	Time Code Counter Synchronization	4.9-41
4.9.2-10	I/O Address Word Format and Mode Control	4.9-46
4.9.2-11	Interrupt Assignments	4.9-49
4.9.2-12	Data/Interrupt Cross Strap Steering Summary	4.9-53
4.9.2-13	Serial Transfer Clock (102.4 kHz) Source Selection	4.9-54
4.9.2-14	Buffer Address Assignment	4.9-55
4.9.2-15	Serial Output Buffer Status Codes	4.9-60
4.9.2-16	Serial Input Buffer Status Codes	4.9-63
4.9.2-17	Memory Address Modes	4.9-96
4.9.2-18	Microprogram Addressed Memory Locations	4.9-97
4.9.2-19	Hardware Multiply	4.9-100
4.9.2-20	R/W Memory Reserved Addresses	4.9-103
4.9.2-21	Memory Address Space Map	4.9-103
4.9.2-22	Relay Driver Characteristics	4.9-109
4.9.2-23	SCU Design Characteristics	4.9-111
4.9.2-24	SCU Ordnance Firing Signals	4.9-123
4.9.2-25	Flag Signal Generation	4.9-125
4.9.2-26	SCU Discrete Telemetry	4.9-127
4.9.2-27	Controls Power Converter Design Characteristics	4.9-130
4.9.2-28	Typical CPC Mode Telemetry	4.9-131
4.9.2-29	Telemetry Word Contents (For One Redundant Side)	4.9-141
4.10.2-l	Priority Levels, Interrupts, and Program Execution - Orbit Mode Control CPU	4.10-7
4.10.4-l	CPU Software States	4.10-13
4.10.6-l	Decision Table - Quadrant Use	4.10-34
4.10.6-2	Decision Table - Submode Determination	4.10-45
4.10.6-3	Attitude Control Laws	4.10-52
4.10.6-4	Search Rate Decision Table	4.10-55
4.10.6-5	MMUS Turn On/Off Criteria	4.10-67
4.10.6-6	Compensation Term Table	4.10-68
4.10.6-7	MMUS Output Format	4.10-69
4.10.6-8	ADE Status Word and SAD Modes	4.10-72
4.10.6-g	SAD Direction and Speed Commands as s Function of Error	4.10-74
4.10.6-10	SAD Command Word	4.10-74
4.10.6-11	Uplinked Inputs to GEODAT	4.10-77
4.10.6-12	GEODAT Program Constants	4.10-82
4.10.6-13	GEODAT Calibration Constants	4.10-93
4.10.6-14	Data Inputs to GEODAT Other than the Ephemeris Table	4.10-96

LIST OF TABLES (Continued)

Table		Page
4.10.6-15	Data Outputs of GEODAT	4.10-96
4.10.6-16	Control Inputs of GEODAT	4.10-97
4.10.6-17	Control Outputs of GEODAT	4.10-97
4.10.7-l	KLM Summary	4.10-98
4.11.1-l	AVHRR/3 Optical Parameters	4.11-4
4.11.1-2	AVHRR/3 Electrical Parameters	4.11-5
4.11.1-3	AVHRR/3 Mechanical Parameters	4.11-6
4.11.1-4	AVHRR/3 Thermal Parameters	4.11-7
4.11.2-1	HIRS/3 Optical Parameters	4.11-12
4.11.2-2	HIRS/3 Electrical Parameters	4.11-13
4.11.2-3	HIRS/3 Mechanical Parameters	4.11-14
4.11.2-4	HIRS/3 Thermal Parameters	4.11-15
4.11.3-1	AMSU-Al Optical Parameters	4.11-20
4.11.3-2	AMSU-Al Electrical Parameters	4.11-21
4.11.3-3	AMSU-Al Mechanical Parameters	4.11-22
4.11.3-4	AMSU-Al Thermal Parameters	4.11-22
4.11.3-5	AMSU-A2 Optical Parameters	4.11-24
4.11.3-6	AMSU-A2 Electrical Parameters	4.11-25
4.11.3-7	AMSU-A2 Mechanical Parameters	4.11-26
4.11.3-8	AMSU-A2 Thermal Parameters	4.11-26
4.11.3-9	AMSU-B Optical Parameters	4.11-29
4.11.3-10	AMSU-B Electrical Parameters	4.11-29
4.11.3-11	AMSU-B Mechanical Parameters	4.11-30
4.11.3-12	AMSU-B Thermal Parameters	4.11-30
4.11.4-l	DCS-2 System Parameters	4.11-35
4.11.4-2	DCS-2 Electrical Parameters	4.11-36
4.11.4-3	DCS-2 Mechanical Parameters	4.11-37
4.11.4-4	DCS-2 Thermal Parameters	4.11-37
4.11.5-l	SEM Field of View Parameters	4.11-41
4.11.5-2	SEM Electrical Parameters	4.11-42
4.11.5-3	SEM Mechanical Parameters	4.11-42
4.11.5-4	SEM Thermal Parameters	4.11-43
4.11.6-1	SBUV/2 Spectral Parameters	4.11-48
4.11.6-2	SBUV/2 Electrical Parameters	4.11-48
4.11.6-3	SBUV/2 Mechanical Parameters	4.11-49
4.11.6-4	SBUV/2 Thermal Parameters	4.11-49
4.11.7-1	SARR Input Parameters	4.11-50
4.11.7-2	SARR Output Parameters	4.11-51
4.11.7-3	SARR Electrical Parameters	4.11-52
4.11.7-4	SARR Mechanical Parameters	4.11-53
4.11.7-S	SARR Thermal Parameters	4.11-53
4.11.8-1	SARP-2 System Parameters	4.11-58
4.11.8-2	SARP-2 Electrical Parameters	4.11-59
4.11.8-3	SARP-2 Mechanical Parameters	4.11-59
4.11.8-4	SARP-2 Thermal Parameters	4.11-60
4.12.1-1	Guidance Modes	4.12-22
4.12-4	Controls Coefficient Table Format	4.12-58
4.12-5	Guidance Curve FIT Coefficients Table	4.12-65
4.12.3-2	Sequencer Table Formats	4.12-82
4.12.4-1	AGS Telemetry Parameters (TBD)	4.12-84

LIST OF TABLES (Continued)

Table		Page
4.12.4-2	Vehicle Discrete 1 (Word 29) Telemetry Bit Assignments (TBD)	4.12-84
4.12.4-3	Vehicle Discrete 2 (Word 30) Telemetry Bit Assignments (TBD)	4.12-84
5.4.2-l	Downlink PCM Data	5-15
5.4.2-2	APT Downlink	5-15
5.4.2-3	Command Uplink	5-16
5.4.2-4	Real-Time TIP Signal Characteristics	5-18
5.4.2-5	APT Signal Characteristics	5-18
5.4.2-6	Real-Time GAC Signal Characteristics	5-18
5.4.2-7	Real-Time AIP Signal CHaracteristics	5-19
5.4.2-8	HRPT (Real-Time AVHRR) Signal Characteristics	5-19
5.4.2-9	Spacecraft Recorder Dump (S-Band Link) Signal Characteristics	5-19
5.4.3-l	ATNAGE IRIG Time Code Input	5-22
5.4.4-l	ATNAGE Measurement Capabilities (In DC Voltage)	5-22
5.7.1-1	DKØ Contiguous Files	5-32
5.8.5-l	Input/Output Interface Characteristics	5-41

Blank Page

SECTION 1.0

INTRODUCTION AND SUMMARY

1.1 INTRODUCTION

This report, the System Design Report (SDR), documents the design of the ATN-KIM Spacecraft. The spacecraft design has been generated in response to the requirements of Goddard Space Flight Center Specification GSFC S-480-25.

Considerable documentation of the spacecraft exists beyond this report. Among the pertinent documents are: subsystem specifications, component specifications, CDR packages, a General Instrument Interface Specification, Unique Interface Specifications, and the Programming and Control Handbook.

The SDR describes the spacecraft as a system segment. It also includes discussions of all GFE and detailed discussions of all spacecraft components and of the ATN Aerospace Ground Equipment (ATNAGE). The ATN-KIM spacecraft design is based on heritage from the ATN-HIJ spacecraft.

Figure 1.1-l provides a summary of ATN-KIM characteristics.

1.2 SYSTEM SUMMARY

1.2.1 MISSION

ATN-KIM is the fourth variation of the latest generation of polar orbiting operational environmental satellite systems. It provides an economical and stable platform for the advanced instruments to be used in making measurements of the earth's atmosphere, its surface, its cloud cover, and proton and electron fluxes near the earth.

As a part of this mission the spacecraft also has the ability to receive, process and retransmit data from free-floating balloons, buoys and remote automatic observation stations distributed around the globe. The instrument complement includes: (1) the Advanced Very High Resolution Radiometer (a six channel imaging line scan sensor); (2) vertical sounders (consisting of four separate instruments - the High Resolution Infrared Radiation Sounding Unit, and three Advanced Microwave Sounding Unit Modules); (3) a Space Environment Monitor, comprised of two units; (4) a Data Collection System; (5) a Search and Rescue Processor; (6) a Search and Rescue Repeater; and (7) a Solar Backscatter Ultraviolet Spectral Radiometer. Other payloads may be added or substituted, but the ten listed above form the KIM baseline.

The nominal orbit will be circular with either a 450 nmi or a 470 nmi altitude, a 102 minute period, and sun-synchronous inclination of approximately 99". The spacecraft will be launched from the WTR to provide for either a 0730 LMT (nominal) Descending Node (DN) or 1340 LMT (nominal) Ascending Node (AN). The initial injection can result in drifts from sun-synchronism so that the spacecraft has been designed to operate over the following LMT ranges: 0600-1120 DN or 1240-1800 AN.

1.2.2 SPACECRAFT

The ATN-KLM spacecraft is an integrated system designed to provide for injection into, and operation in, a nominal 450 nmi or 470 nmi circular sun-synchronous orbit after separation from the Titan II launch vehicle. The spacecraft, including the Apogee Kick Motor (AKM), in the launch configuration is 165 inches high and 74 inches in diameter. On orbit, with the AKM and reaction control equipment expended, the satellite has a dry weight of 3231.8 lb. The ATN-KLM spacecraft incorporates an attitude control subsystem that integrates the ascent and control hardware with on-orbit attitude control system. During injection, an integrated three axis, gyro-accelerometer package and central processor are used for ascent navigation and guidance and control of the Star 37 XFP (19% offloaded.) solid propellant AKM and combined hydrazine/nitrogen Reaction Control Equipment (RCE) after first stage separation. After acquisition, spacecraft attitude is maintained to $\pm 0.2°$ in 3 axes with a zero momentum system which uses a static infrared horizon sensor to measure pitch and roll attitudes, gyros to provide attitude information about the yaw axis via sun sensor updates, and reaction wheels with magnetic unloading to supply control torques. A single axis oriented 181 square foot solar array, rotated continuously about the orbit normal, will support at least 870 watts of orbit average satellite load power for two years over a 0" to 80" sun-angle range. The command subsystem provides a two kbs S-Band link with a G-STDN (NRZ-M) format. On-board data handling and recording is primarily digital. The communications links include: (1) a real-time S-Band digital link for continuous transmission of high resolution video and all low rate data; (2) a real-time VHF link for continuous analog transmission of medium resolution video; (3) an S-Band digital playback link for recovery of all recorded data by the two existing CDA stations; (4) a digital VHF beacon downlink for continuous transmission of telemetry and low rate data; (5) an S-Band command uplink; (6) a UHF Data Collection uplink; (7) an S-Band digital playback link for recorded low rate data to European ground station; (8) three UHF search and rescue uplinks; (9) an L-Band search and rescue downlink; and (10) an Air Force-compatible S-Band launch, data and emergency downlink.

The functional block diagram for the spacecraft is shown in Figure 1.2-1.

ATN-KLM

SATELLITE AND MISSION ORBIT CHARACTERISTICS

Size

- 185 inches high by 74 inches diameter (excluding solar array)

Configuration Type

- Multisectioned stack
  - — Instrument Mounting Platform
  - — Equipment Support Module
  - — Reaction Control Support Structure

Weight

- On orbit: 3251.8 lbs
- At liftoff: 4920.0 lbs

Power (orbit average load capability)

- 0° sun angle: 880 watts
- 80° sun angle: 870 watts

Operational Sun Angle

- 0° to 80°

Lifetime

- Goal of greater than 2 years

Nominal Altitude

- 450 nmi (833 km) or 470 nmi (870 km)

Orbit Inclination

- 98.739 degrees for 450 nmi or 98.899 degrees for 470 nmi

bit O'Clock Angle (Nominal)

- 07:30 descending node
- 13:40 ascending node

WEIGHT BREAKDOWN & MASS PROPERTIES

Assembly	Estimated Weight (lbs)
Structure	736.8
Thermal	77.3
ADACS (dry)	185.6
Power	527.1
Communications	58.7
Command and Control	68.9
Data Handling	39.9
GFE (GFE margin)	982.5 (67.2)
Harness	233.0
AKM Burnout	145.6
Balance Weight & S/C Margin	49.8
Ballast	146.6
Spacecraft Dry Weight	3251.8
N_2H_4	62.8
GN_2	10.4
AKM Expendables	1595.0
Spacecraft at Liftoff	4920.0

S-Band Data Links

- 1698 MHz 1702.5 MHz, 1707 MHz
- To CDA stations, HRPT stations, and European stations
- Split phase, or NRZ data with PSK modulation
- 2.6, 1.33 and 0.3327 Mbps

S-Band Telemetry Link

- 1702.5 MHz
- 16.64 kbps, 8.32 kbps
- Split phase data with PSK modulation

S-Band Launch Telemetry Link

- 2247.5 MHz
- To AF SCF Stations and ARIA
- Split phase data with PSK modulation
- 16.64 kbps or 8.32 kbps

VHF APT Real-Time Link

- 137.5 or 137.62 MHz
- To APT stations
- 2400 Hz baseband
- AM/FM modulation

VHF Beacon Link

- 137.35 MHz, and 137.77 MHz
- To CDA stations, TIP stations, and in early orbit and emergency to European station
- Split phase data with PSK modulation
- 8320 bps

Command Link

- 2025 MHz
- From CDA stations; also in emergency from WTR
- 2 kbps

DCS Uplink

401.65 MHz

- From Platforms
- Split Phase PSK
- 400 bps

SAR Uplink

- 121.5, 243, and 406.05 MHz (FM/AM)
- 406.025 MHz (Split Phase PSK)
- From emergency transmitters

SAR Downlink

- 1544.5 MHz (PM)
- To Local Stations
- PM Modulations

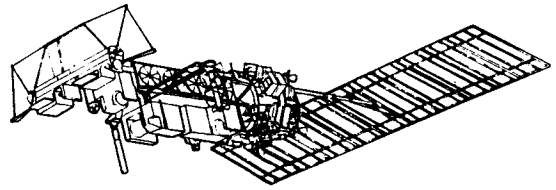

SUBSYSTEM CHARACTERISTICS

Attitude Determination and Control

- Zero momentum system
- Reaction wheel control with magnetic momentum unloading
- Earth stabilized
- Three-axis determination and
- $\leq \pm 0.2°$ control
- $\leq \pm 0.10°$ attitude knowledge
- $\leq \pm 0.35°$/second pitch/yaw rates
- $\leq \pm 0.15°$/second roll rates

Reaction Control

- Monopropellant hydrazine system, used for:
  - — Control during AKM burn
  - — Orbit injection velocity trim
- Gaseous Nitrogen System, used for:
  - — Hydrazine pressurization
  - — Coast control
  - — Control during Δ V maneuvers
  - — Momentum unloading

Apogee Kick Motor

- STAR - 37XFP 19% Off Loaded

Thermal Control

- Passive control components
  - — Blankets, finishes, insulators, shades
- Active control components
  - — Pinwheel and vane louvers,
  - — heaters, control electronics

Power and Distribution

- Boost-Discharge DET system
- +28V, 10V regulated voltages
- Single-axis oriented solar array 181 ft²
- 880 - W orbit avg. load capability
- Three 47 Ah batteries

POWER SUMMARY (0° sun angle)

Subsystem	DC Power (Watts)
Instruments	450.0
Attitude Control	61.9
Data Handling	21.2
Thermal	162.0
Command	33.2
Communications	66.3
Power	22.8
Power Required	817.4
EOL Spacecraft Power Available	879.9

Data Handling

- Low data rate processing:
  - — Flexible low rate data formatter and telemetry processor
  - — Boost, orbit, dwell dump modes
  - — 8320 bps (orbit)
  - — 16,640 bps (boost)
  - — 16,640 bps TIP/AMSU data
  - — TLM; 512 analog, 352 bilevel digital B, 16 serial digital A word channels
- High data rate processing:
  - — High rate data formatter and processor
  - — Performs multiplexing, formatting, resolution reduction, geometric correction functions
  - — Analog APT; global data (66.54 kbps); HRPT data (665.4 kbps); local data (665.4 kbps) outputs
- Data Storage:
  - — 5 GFE digital data recorders
  - — Record 8.32 kbps - 230.5 min.
    16.64 kbps - 115 min.
    66.54 kbps - 111 min.
    665.40 kbps - 11.1 min.
  - — Playback 1.3308 Mbps - 5.6 min.
    332.7 kbps - 5.8 min.
    2.6616 Mbps - 2.8 min.

Command and Control

- Command link bit rate: 2 kbps
  - — Effective commanding rate: 30 - 80 words/sec.
- Message Types
  - — CPU Data
  - — CIU decoded commands: 28 hardware capacity, 28 implemented
  - — CPU decoded commands:
    - CIU pulses and levels 384 hardware capacity, 349 implemented
    - CXU pulses and levels - 196 hardware capacity, 123 implemented
    - Serial Mode Commands
- Stored Commands
  - — table capacity: 2300 commands
  - — time tag: 1.0 sec granularity 36 hour clock

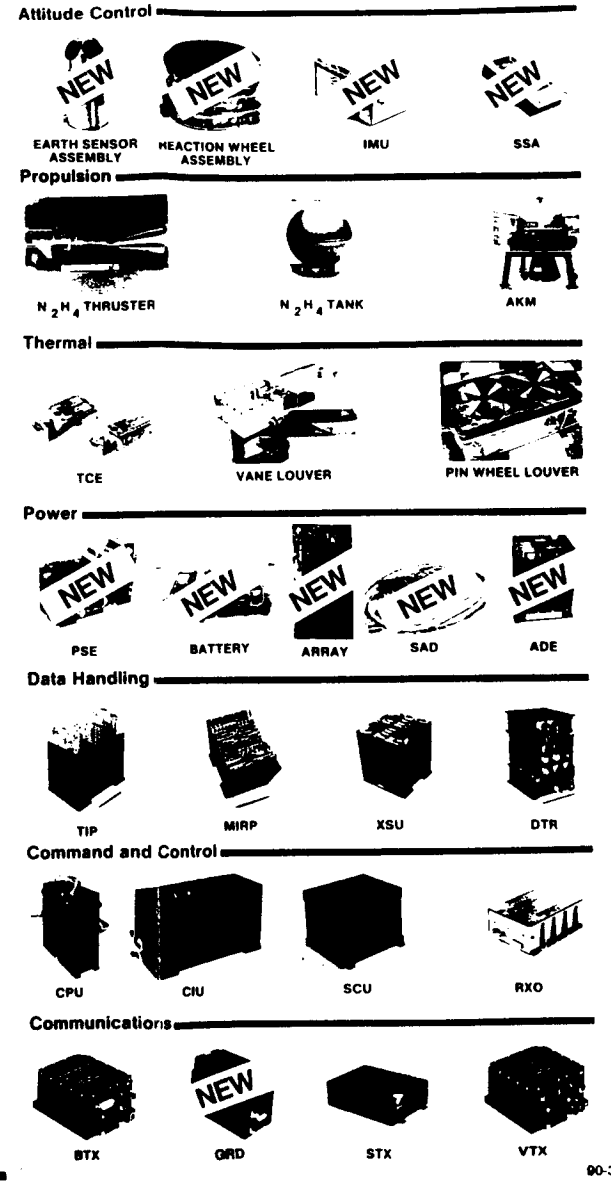

90-380

Figure 1.1-1. Summary of Characteristics of ATN-KLM Satellite

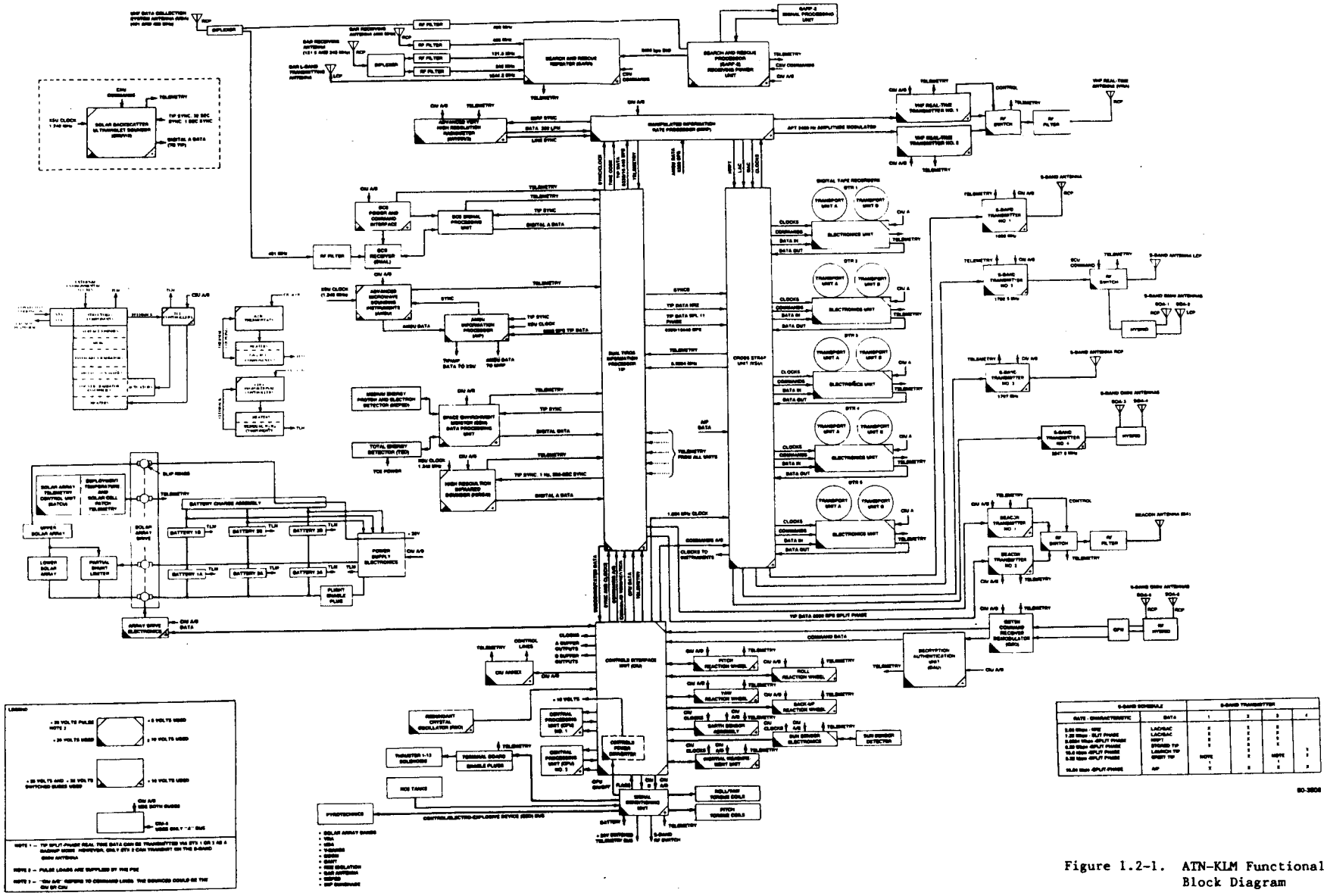

Figure 1.2-1. ATN-KLM Functional Block Diagram

Blank Page

SECTION 2.0

MISSION DESCRIPTION

2.1 ATN-KLM REQUIREMENTS

The mission objectives for ATN-KLM are based primarily on both national and international meteorological needs and reflect the leading participation of the United States in the World Weather Program, the operational global weather observation, communication, and processing system. The meteorological data needs applicable to the polar orbiting operational satellite, have led to specific operating requirements for the ATN-KLM systems. These meteorological data needs and the performance requirements they invoke are shown in Table 2.1-1. Note how-various data needs directly impact three categories of performance requirements: sensor, spacecraft and operational requirements. The data needs are described in terms of several parameters including data type, timeliness, coverage, frequency, and accuracy. Each of these needs results in one or more specific requirements.

2.2 INSTRUMENT PAYLOAD

Table 2.2-l lists the major characteristics of the ATN-KLM instrument complement.

2.3 MISSION OPERATIONS

2.3.1 MISSION

The mission of the ATN-KLM spacecraft derives from the Environmental Data Needs shown in Table 2.1-1. This table shows how the stated needs result in a series of requirements placed upon the instruments, the spacecraft and the operational system. The instrument requirements result, in turn, in the instrument complement given in Table 2.2-l.

The basic configuration of the spacecraft is influenced by the instrument requirements, principally their optical or RF view factors and their thermal view factor requirements. The remaining spacecraft components support the Environmental Data Needs in terms of resultant Spacecraft Requirements or Operational Requirements as shown in Table 2.1-1. These components support the mission in terms of housekeeping or system support functions.

2.3.2 ORBIT CHARACTERISTICS

The Advanced TIROS-N (ATN) spacecraft are designed to operate in a sun-synchronous orbit at an altitude of 833 km (450 nmi) or 870 km (470 nmi). The nominal parameters and 3σ high and low limits for these two orbits are given in Table 2.3.2-l. The operational system configuration consists of a pair

TABLE 2.1-1. ATN-KLM REQUIREMENTS

Environmental Data Needs	Instrument Requirements	Spacecraft Requirements	Operational Requirements
I.A. Provide day and night image information on: Cloud cover distribution Could top temperature Moisture pattern Ice Snow Surface temperature (accuracy 1°C absolute, 0.5°C relative)	o Six spectral channels with resolution of 0.9 km (0.5 nmi). o Radiometric accuracy ≤digitization to 10 bits	o Stable platform: ±0.2° earth pointing accuracy. Jitter rate ≤0.035°/sec in pitch and yaw and ≤0.015°/sec in roll. Attitude determination ≤0.1°. o Processor algorithms specified	Sun synchronous orbit with mean local sun angle of 0° to 80°
B. Provide above data: 1. Globally for central processing 2. To APT class direct readout stations, globally 3. To HRPT class direct readout stations, globally 4. On selected area basis for central processing		o High rate data processor: processor reduces resolution to 3.7 km (2 nmi). o Recorder system capability for global data 428 minutes o S-band communications links with EIPR >+38 dbm. Recorder capability for high resolution data.	
C. Coverage of above data of entire earth twice daily	o Contiguous and continuous scanning	Process data over ±56° nadir angle	
II.A. Provide vertical temperature and moisture profiles of the atmosphere (accuracy 1°K and 10%, respectively) from Earth's surface up to 50 km	o Obtain measure of radiation emitted from earth's atmosphere. o 19 channels from 3.7-15 μm (1 visible channel).	Low-rate processor AMSU Information Processor (AIP)	Two spacecraft system at 833 km or 870 km altitude (450 or 470 nmi)
B. Provide above data globally with grid spacing of 400 km (216 nmi), even in presence of clouds.	o Spatial resolutions (IFOV) ~1.5°(tropospheric channels) o Resolution ~10° (microwave and stratospheric channels)	Record system capability for 428 minutes.	
C. Provide continuous real-time transmission of radiances to local stations.		Real-time low rate data link	
III.A. Collection of meteorological data from fixed in situ platforms outside the range of GOES	o Receive and format data	Record system capability for 428 minutes. Antenna capability for earth coverage.	
B. Collection of meteorological data from free-floating in situ platforms, including platform position, globally.	o Processing of data to extract position information		Non-integral numbers of orbits per day
IV. Timeliness of data: receipt of data for inclusion in NMC products.			Playback to European ground station.
V. Measure proton and electron flux density and total particulate energy deposition.			
VI. Provide total ozone concentration and vertical distribution of ozone in the atmosphere (accuracy 1% and 5%, respectively)	o Measure the solar irradiance and the backscattered solar radiation from the Earth over the spectral range 160 to 400 nanometers.	Low-rate processor	Afternoon orbit satellite.
VII. Operational Systems	≥ Highly reliable	Highly reliable	

I. is provided by the AVHRR/3
II. is provided by the HIRS/3, AMSU-A1, AMSU-A2, AMSU-B
III. is provided by the DCS
V. is provided by the SEM-2
VI. is provided by the SBUV/2

SECTION 2.0

MISSION DESCRIPTION

2.1 ATN-KLM REQUIREMENTS

The mission objectives for ATN-KLM are based primarily on both national and international meteorological needs and reflect the leading participation of the United States in the World Weather Program, the operational global weather observation, communication, and processing system. The meteorological data needs applicable to the polar orbiting operational satellite, have led to specific operating requirements for the ATN-KLM systems. These meteorological data needs and the performance requirements they invoke are shown in Table 2.1-1. Note how various data needs directly impact three categories of performance requirements: sensor, spacecraft and operational requirements. The data needs are described in terms of several parameters including data type, timeliness, coverage, frequency, and accuracy. Each of these needs results in one or more specific requirements.

2.2 INSTRUMENT PAYLOAD

Table 2.2-1 lists the major characteristics of the ATN-KLM instrument complement.

2.3 MISSION OPERATIONS

2.3.1 MISSION

The mission of the ATN-KLM spacecraft derives from the Environmental Data Needs shown in Table 2.1-1. This table shows how the stated needs result in a series of requirements placed upon the instruments, the spacecraft and the operational system. The instrument requirements result, in turn, in the instrument complement given in Table 2.2-1.

The basic configuration of the spacecraft is influenced by the instrument requirements, principally their optical or RF view factors and their thermal view factor requirements. The remaining spacecraft components support the Environmental Data Needs in terms of resultant Spacecraft Requirements or Operational Requirements as shown in Table 2.1-1. These components support the mission in terms of housekeeping or system support functions.

2.3.2 ORBIT CHARACTERISTICS

The Advanced TIROS-N (ATN) spacecraft are designed to operate in a sun-synchronous orbit at an altitude of 833 km (450 nmi) or 870 km (470 nmi). The nominal parameters and 3σ high and low limits for these two orbits are given in Table 2.3.2-1. The operational system configuration consists of a pair

TABLE 2.1-1. ATN-KLM REQUIREMENTS

Environmental Data Needs	Instrument Requirements	Spacecraft Requirements	Operational Requirements
I.A. Provide day and night image information on: Cloud cover distribution Could top temperature Moisture pattern Ice Snow Surface temperature (accuracy 1°C absolute, 0.5°C relative)	o Six spectral channels with resolution of 0.9 km (0.5 nmi). o Radiometric accuracy ≤digitization to 10 bits	o Stable platform: ±0.2° earth pointing accuracy. Jitter rate ≤0.035°/sec in pitch and yaw and ≤0.015°/sec in roll. Attitude determination ≤0.1°. o Processor algorithms specified	Sun synchronous orbit with mean local sun angle of 0° to 80°
B. Provide above data: 1. Globally for central processing 2. To APT class direct readout stations, globally 3. To HRPT class direct readout stations, globally 4. On selected area basis for central processing		o High rate data processor: processor reduces resolution to 3.7 km (2 nmi). o Recorder system capability for global data 428 minutes o S-band communications links with EIPR >+38 dbm. Recorder capability for high resolution data.	
C. Coverage of above data of entire earth twice daily	o Contiguous and continuous scanning	Process data over ±56° nadir angle	
II.A. Provide vertical temperature and moisture profiles of the atmosphere (accuracy 1°K and 10%, respectively) from Earth's surface up to 50 km	o Obtain measure of radiation emitted from earth's atmosphere. o 19 channels from 3.7-15 μm (1 visible channel).	Low-rate processor AMSU Information Processor (AIP)	Two spacecraft system at 833 km or 870 km altitude (450 or 470 nmi)
B. Provide above data globally with grid spacing of 400 km (216 nmi), even in presence of clouds.	o Spatial resolutions (IFOV) ~1.5°(tropospheric channels) o Resolution ~10° (microwave and stratospheric channels)	Record system capability for 428 minutes.	
C. Provide continuous real-time transmission of radiances to local stations.		Real-time low rate data link	
III.A. Collection of meteorological data from fixed in situ platforms outside the range of GOES	o Receive and format data	Record system capability for 428 minutes. Antenna capability for earth coverage.	
B. Collection of meteorological data from free-floating in situ platforms, including platform position, globally.	o Processing of data to extract position information		Non-integral numbers of orbits per day
IV. Timeliness of data: receipt of data for inclusion in NMC products.			Playback to European ground station.
V. Measure proton and electron flux density and total particulate energy deposition.			
VI. Provide total ozone concentration and vertical distribution of ozone in the atmosphere (accuracy 1% and 5%, respectively)	o Measure the solar irradiance and the backscattered solar radiation from the Earth over the spectral range 160 to 400 nanometers.	Low-rate processor	Afternoon orbit satellite.
VII. Operational Systems	Highly reliable	Highly reliable	

I. is provided by the AVHRR/3
II. is provided by the HIRS/3, AMSU-A1, AMSU-A2, AMSU-B
III. is provided by the DCS
V. is provided by the SEM-2
VI. is provided by the SBUV/2

TABLE 2.2-1. INSTRUMENT COMPLEMENT (NOAA KLM CLASS)

	Basic Resolution	Sensitivity NEΔT (°K)	Aperture Diameter (in)	Scan Mode	Scan Angle (deg)	Weight (lb)	Power (W)
Imagers							
AVHRR/3	1.3 mrad	0.12	8	Rotating	125.5	69	27.0
0.58 - 0.68 μm 0.725 - 1.00 μm 1.58 - 1.64 μm 3.55 - 3.93 μm 10.3 - 11.30 μm 11.5 - 12.50 μm							
Temperature Sounders							
AMSU - 20 Channels							
AMSU-A2 (channels 1,2)	50 km	0.3	11	30 steps 3.3° each	±48.33	110.0	37.0
AMSU-A1 (channels 3-15)						112.0	88.0
A1-1	50 km	0.25 (ch 6,7,9) 0.4 (ch 10,11) 0.6 (ch 12) 0.8 (ch 13) 1.20 (ch 14) 0.5 (ch 15)	6	30 steps 3.3° each	±48.33		
A1-2	50 km	0.4 (ch 3) 0.25 (ch 4,5,8)	6	30 steps 3.3° each	±48.33		
AMSU-B (channels 16-20)	17 km	1.0 (ch 16-19) 1.2 (ch 20)	12	90 steps 1.1° each	±49.5	132.0	90.0
HIRS/3 - 20 channels	1.4°	NEΔN 0.03 to 0.96 (ch 1-12 0.0002 to 0.003 (ch 13-19)	5.9	56 Steps 1.8° each	±49.5	73.0	22.8
1 visible 0.69 μm 7 shortwave 3.7 to 4.6 μm 12 longwave 6.5 to 15 μm							
DCS	N/A	N/A	N/A	N/A	N/A	85.4	26.5
SEM	N/A	N/A	N/A	N/A	N/A	33.7	14.8
SBUV/2	160 km x 160-400nm 160 km		N/A	N/A	N/A	86.0	17.0
SARR	N/A	N/A	N/A	N/A	N/A	35.6	57.0
SARP	N/A	N/A	N/A	N/A	N/A	54	19
					TOTAL →	790.7 (LBS)	399.1 (W)

[* → INSTRUMENT MASS (LB): 812 LBS TYPICALLY BUDGETED] → ACCOUNTS FOR "ASSOCIATED "

TABLE 2.3.2-1. ORBITAL PARAMETERS

Parameter	833 km (450 nmi) Nominal Orbit			870 km (470 nmi) Nominal Orbit		
	Lower 3σ Limit	Nominal Value	Upper 3σ Limit	Lower 3σ Limit	Nominal Value	Upper 3σ Limit
Altitude (km)	815	833	852	852	870	889
Inclination (degrees)	98.889	98.739	98.589	99.049	98.899	98.749
Nodal Period (minutes)	101.193	101.584	101.975	101.975	102.368	102.760
Nodal Regression (degree/orbit)	25.298	25.396	25.494	25.494	25.592	25.690
Nodal Precession Rate (degree/day)	1.0114	0.9856	0.9601	1.0111	0.9856	0.9605
Orbits Per Day	14.230	14.175	14.121	14.121	14.067	14.013
Nodal Time (Operational Limits)	0600 to 1050 (descending node) 1300 to 1800 (ascending node)					
Nodal Time (Nominal)	0730 (descending node) 1340 (ascending node)					

of satellites, each orbiting in a different plane and at a different altitude (one satellite at 833 km; the other at 870 km). The ascending nodes of each of the two planes are separated by approximately 90 degrees to achieve the quadrature orbit geometry depicted in Figure 2.3.2-1. As shown, one spacecraft is in an afternoon ascending node orbit and the other is in a morning descending node orbit (afternoon and morning are defined by the location of the nodal crossings relative to the sun's position). This orbit arrangement provides global coverage for the sounding mission, and optimizes the global coverage in the visible spectrum. The orbit period difference resulting from the 37 km (20 nmi) altitude separation assures that ground station conflicts associated with the simultaneous viewing of both spacecraft will have a minimum impact on the operational mission.

For the KLM satellite series, as for the previous generation of operational meteorological (or environmental) satellites, a sun-synchronous orbit has been selected because it is near-polar for global coverage and provides the least variation of solar illumination at the spacecraft and at the observed earth scene. This last characteristic derives from the near constancy of the geometry between the orbit plane and the sun vector. By achieving the correct combination of altitude and orbit inclination (the nominal value in Table 2.3.2-1), the orbit will precess about the geographic North Pole in the same direction (West to East) and at the same annual rate as the apparent sun's motion relative to the earth. Table 2.3.2-1 also shows the effect on period, nodal regression, nodal precession, and orbits per day for the worst case combinations of the 3-sigma limits of orbit altitude and inclination. This is depicted in Figures 2.3.2-2 and 2.3.2-3 for the morning descending node and afternoon ascending node orbit planes, respectively. The figures also show how ground scene illumination is affected by changes in season. Such seasonal variations also have an impact on illumination at the spacecraft.

For a nominal sun-synchronous orbit, i.e., one that precesses at a rate of 0.9856 degrees/day or 360 degrees/year, the scene and spacecraft illumination

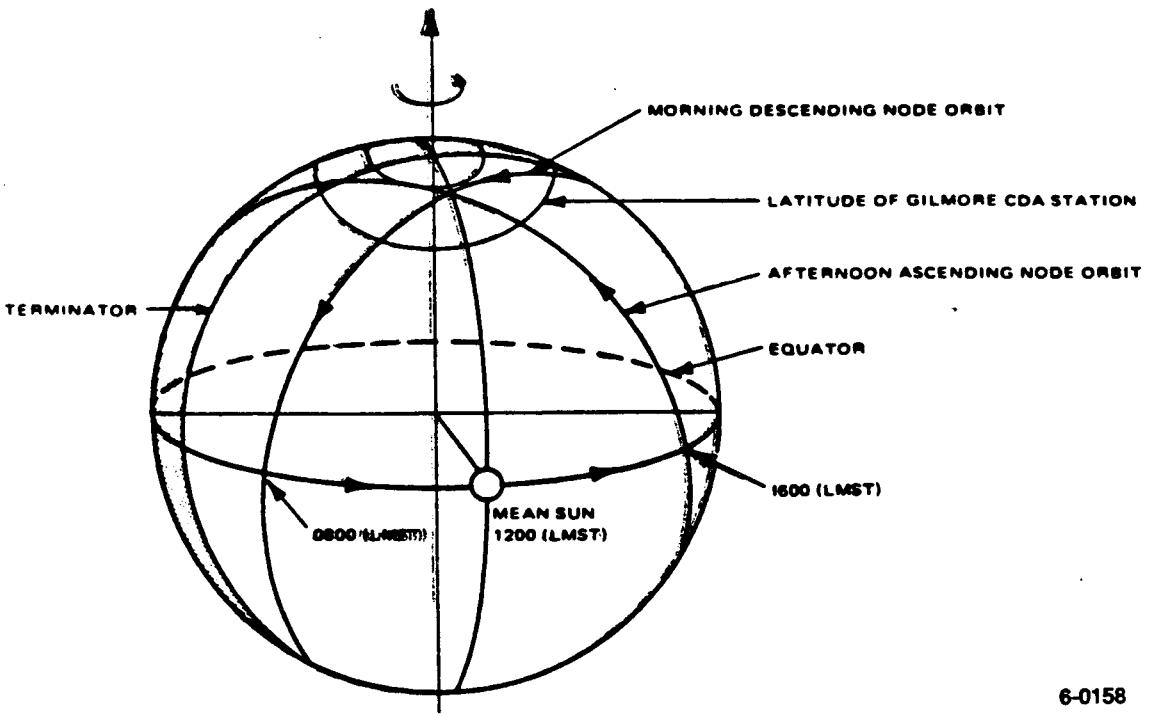

Figure 2.3.2-1. Sun-Node Configuration for Pairing an Afternoon Ascending Node Orbit with a Morning Ascending Node Orbit

conditions vary throughout the year, but repeat on a yearly cycle. The changes during the year occur because the apparent sun's motion in the ecliptic plane is non-uniform whereas the satellite orbit precession is uniform relative to the equatorial plane. The parameter that determines the actual illumination time histories is the orbit o'clock angle. This is the angle between the ascending or descending node and the "mean sun"* vector. For a perfect sun-synchronous orbit, the orbit o'clock angle remains constant. Furthermore, the Local Mean Sun Time (LMST) of the nodal crossing is the orbit o'clock angle, This is shown in Figures 2.3.2-4 and 2.3.2-5 for the morning descending node and afternoon ascending node orbits, respectively. (The difference between the actual sun longitude and the mean sun longitude has been exaggerated for clarity.)

Selection of the target orbit o'clock angle and orbit altitude (i.e., launch trajectory) uniquely determines the liftoff time independent of launch date.

*To afford a uniform time reference on the earth's globe, a "fictitious sun" was invented, referred to as the "mean sun". This "mean sun" moves eastward around the celestial equator at a strictly uniform rate, completing 360 degrees in a year. The angle between the "mean sun" and an earth longitude determines the Local Mean Sun Time (LMST) at that longitude.

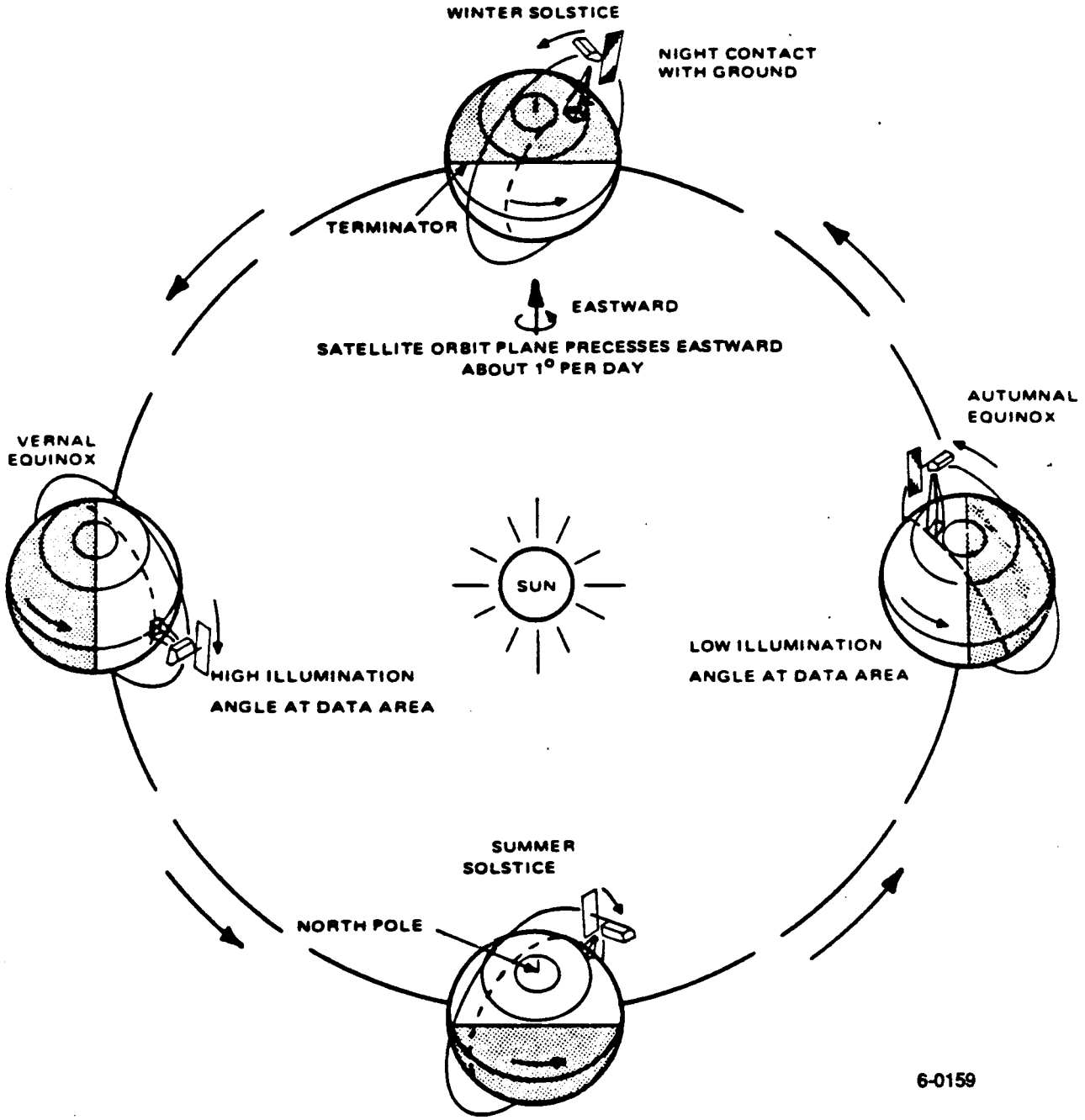

Figure 2.3.2-2. Seasonal Variations in Scene Illumination for a Morning Descending-Node Sun-Synchronous Orbit

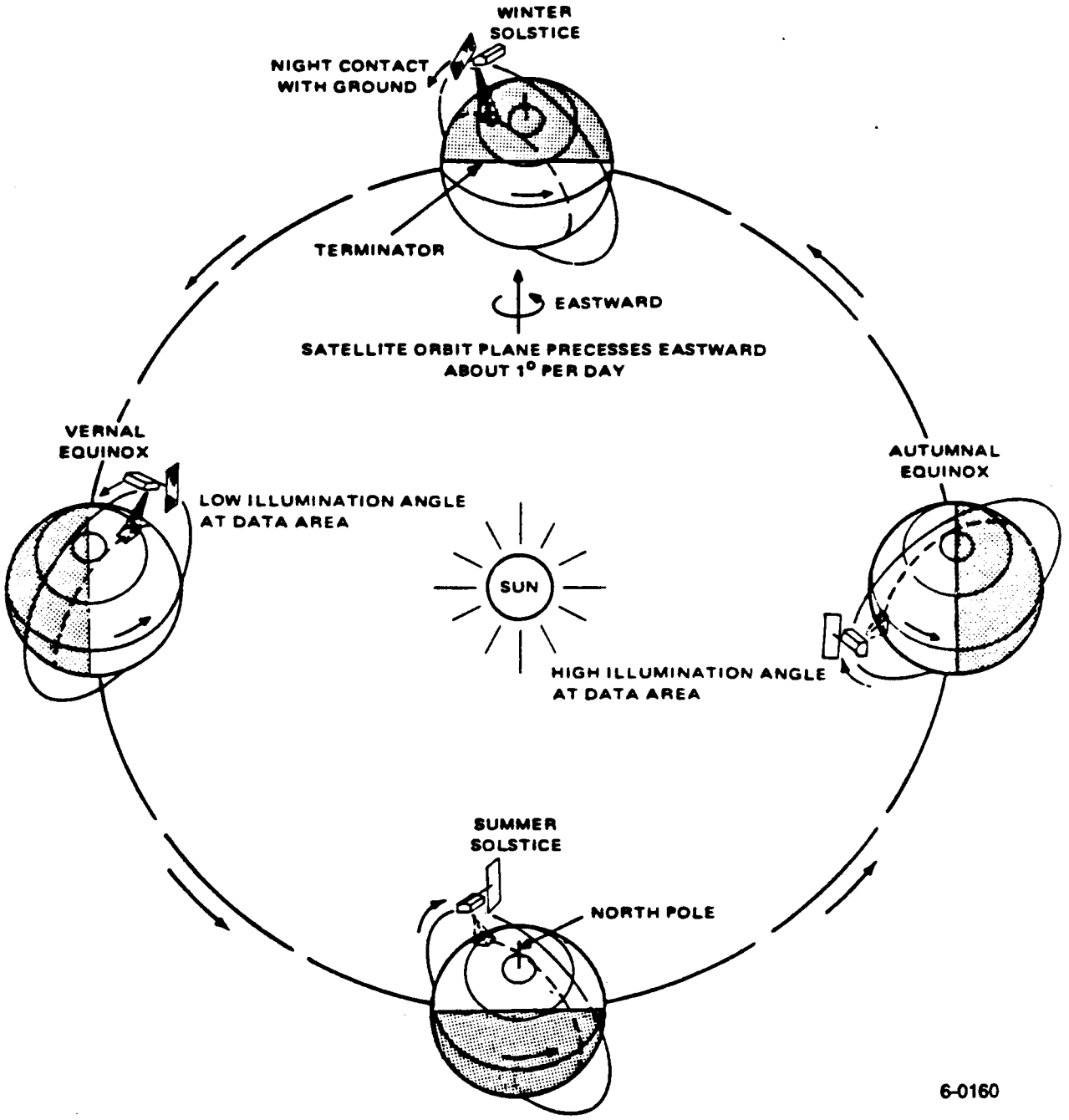

Figure 2.3.2-3. Seasonal Variations in Scene Illumination for an Afternoon Ascending-Node Sun-Synchronous Orbit

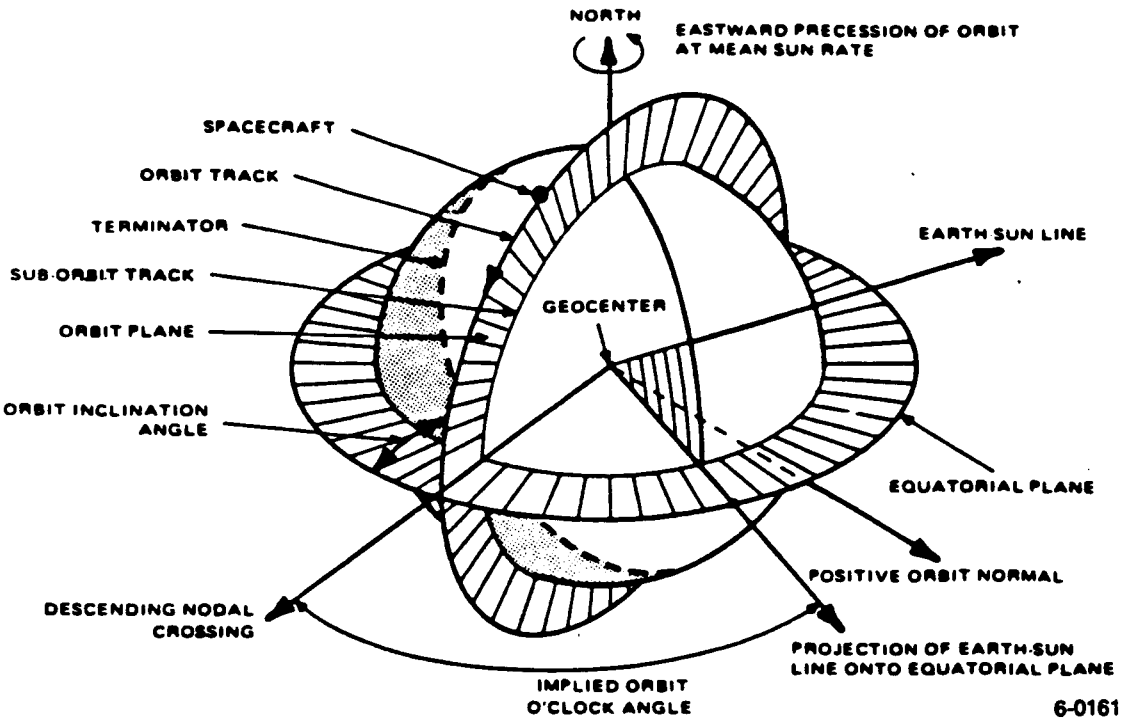

Figure 2.3.2-4. Geometry of a Sun-Synchronous Orbit, Morning Descending Node

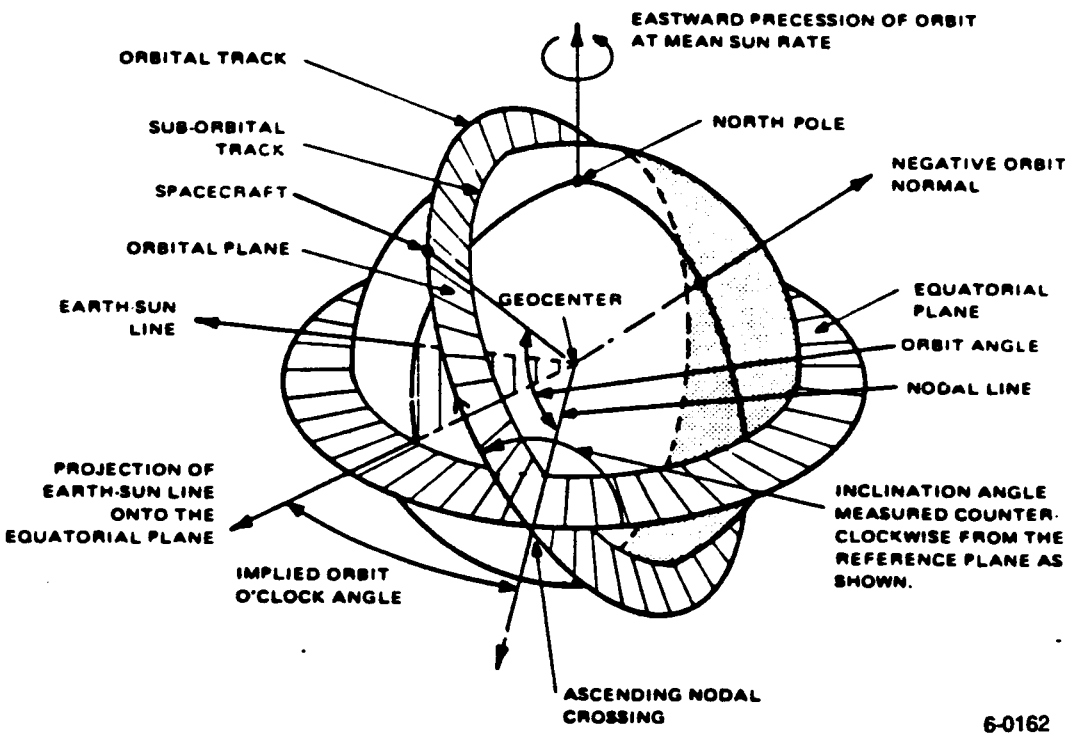

Figure 2.3.2-5. Geometry of a Sun-Synchronous Orbit, Afternoon Ascending Node

2.3.3 IMPLICATION OF ORBIT CHARACTERISTICS

In normal mission mode operation, the parameter that defines the spacecraft illumination condition and most significantly affects the thermal and power subsystem performance is the angle between the pitch axis and the sun vector. Since the pitch axis is controlled to be within 0.2 degrees (in roll and yaw) of the orbit normal at all times, this spacecraft sun angle is, for all practical purposes, the angle between the orbit normal and the sun vector. This angle remains constant over an orbit but varies with season (or calendar date) and orbit o'clock angle. These variations are shown in Figure 2.3.3-1. The time the spacecraft spends in eclipse per orbit also varies with calendar date and orbit o'clock angle (see Figures 2.3.3-2 and 2.3.3-3). Both sun angle and eclipse duration also depend on orbit altitude, but for the small difference in nominal altitude, 37 km (20 nmi), the effect is second order.

The attainment of a perfect sun-synchronous orbit depends upon a unique pairing of altitude and inclination. Errors in either of these parameters cause changes in the sun-synchronous nodal drift rate (0.9856 degrees/day). Such errors may be separately evaluated and algebraically combined to determine the overall departure from the synchronous condition.

The effects on nodal drift rate of variations in the nominal altitude and inclination angle are shown in Figures 2.3.3-4 and 2.3.3-5 respectively. Such departure from the nominal nodal drift rate will cause a change in the orbit-o'clock angle.

The approximate times (in minutes after the ascending node) during which satellite contact can be made at the various ground stations are plotted in Figure 2.3.3-6 for the 833 km (450 nmi) orbit. [The 870 km (470 nmi) orbit causes a slight increase in these contacts.] A plot of net contact time as a function of the longitude of the ascending node is shown in Figure 2.3.3-7 for the 833 km (450 nmi) orbit. The contact starts and ends with the satellite five degrees above the horizon at the Wallops Island and European stations, and five degrees above the horizon or above the terrain at the Alaska station. Figure 2.3.3-8 shows this "keyhole" pattern.

For ascending-node longitudes in the range of 134 degrees East to 188 degrees East, neither the Wallops Island nor the Fairbanks, Alaska station will be in contact with the satellite for at least five minutes.* Thus, the spacecraft, with 25.4 degrees between successive ascending nodes, could go three successive (missed) orbits with marginal ground station contact. Normally, there will be only two missed orbits every 14 orbits. When this "missed orbit" condition exists, data playback will be performed during the next orbit in which adequate ground station contact time is available.

2.3.4 HRPT AND APT CONTACT

The frequency and duration of the HRPT and APT contacts depends upon the ground station latitude and local terrain as well as on the orbital characteristics of the spacecraft. Arbitrarily defining a contact as a portion of a pass during

*A ground station contact time of five minutes has been established as the minimum time required to perform satellite acquisition, playback-command transmission, and data playback (2.5 minutes for a full recorder).

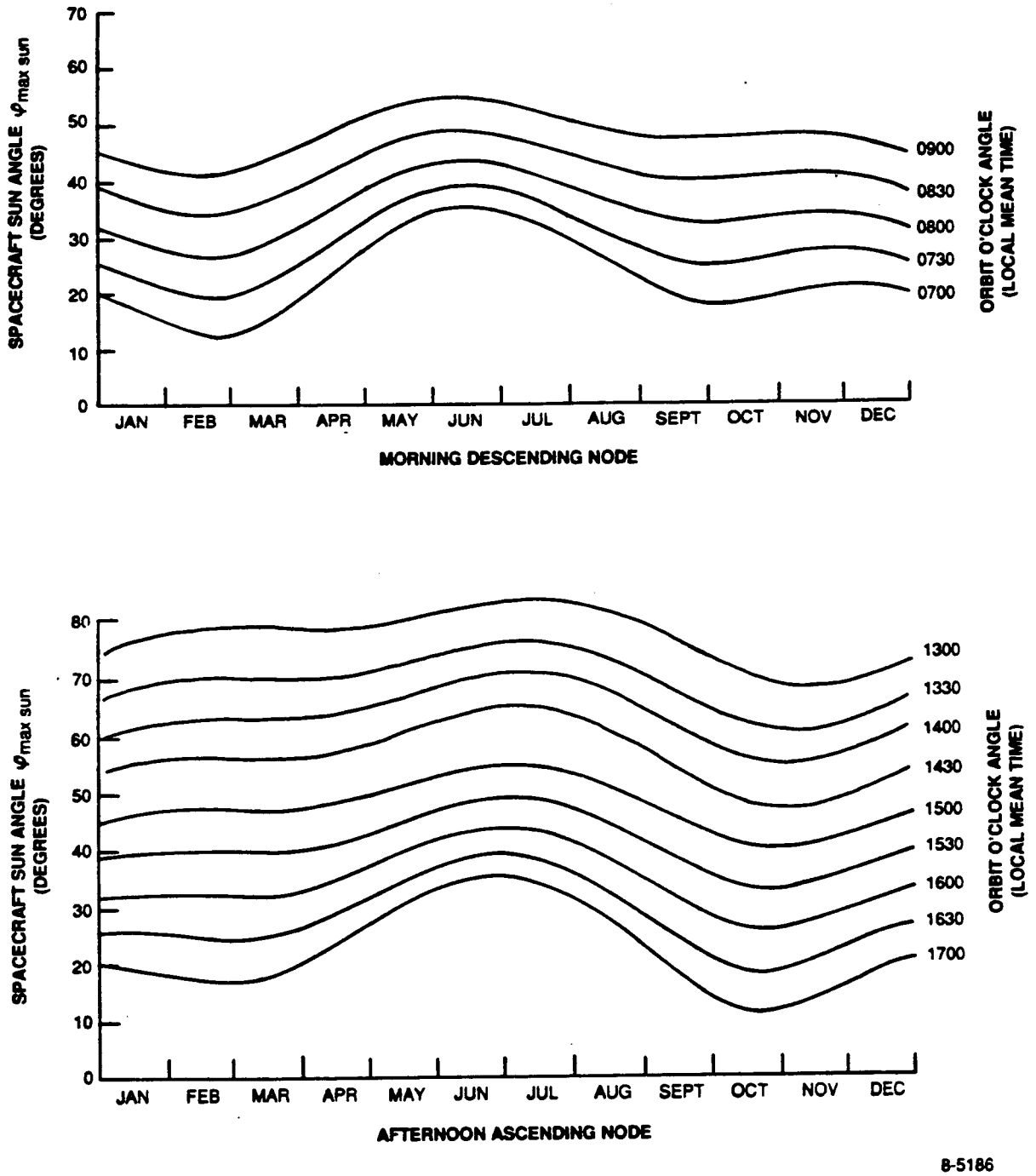

Figure 2.3.3-1. Seasonal Variation of Spacecraft Sun Angle for 833 km (450 nmi) Orbits

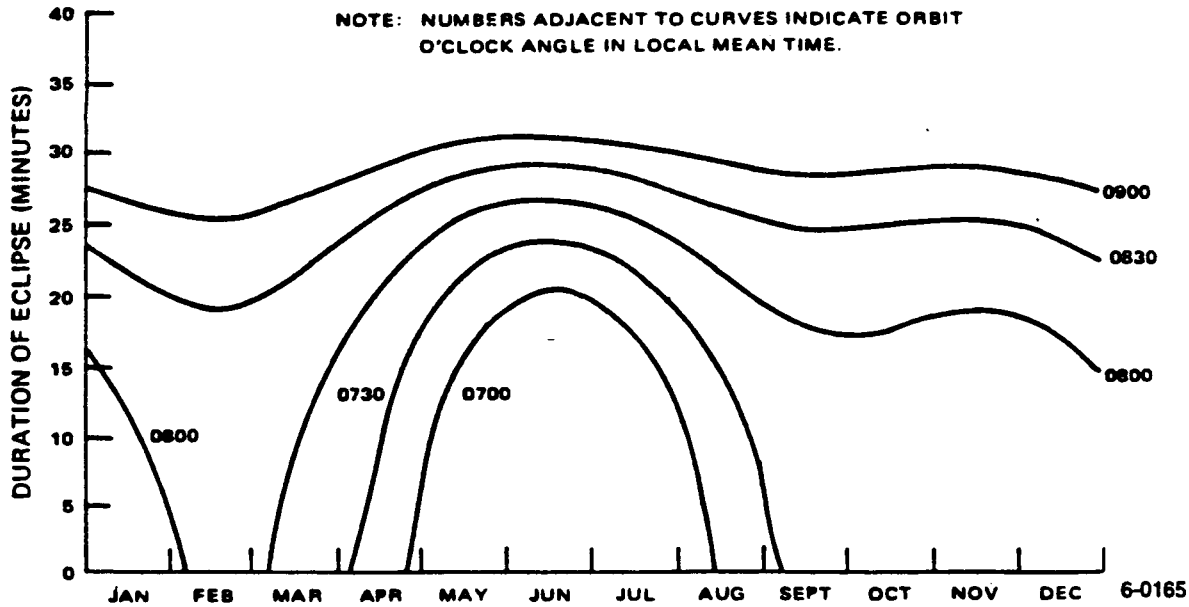

Figure 2.3.3-2. Time in Eclipse for Morning Descending-Node Orbits [833 km (450 nmi) Orbits]

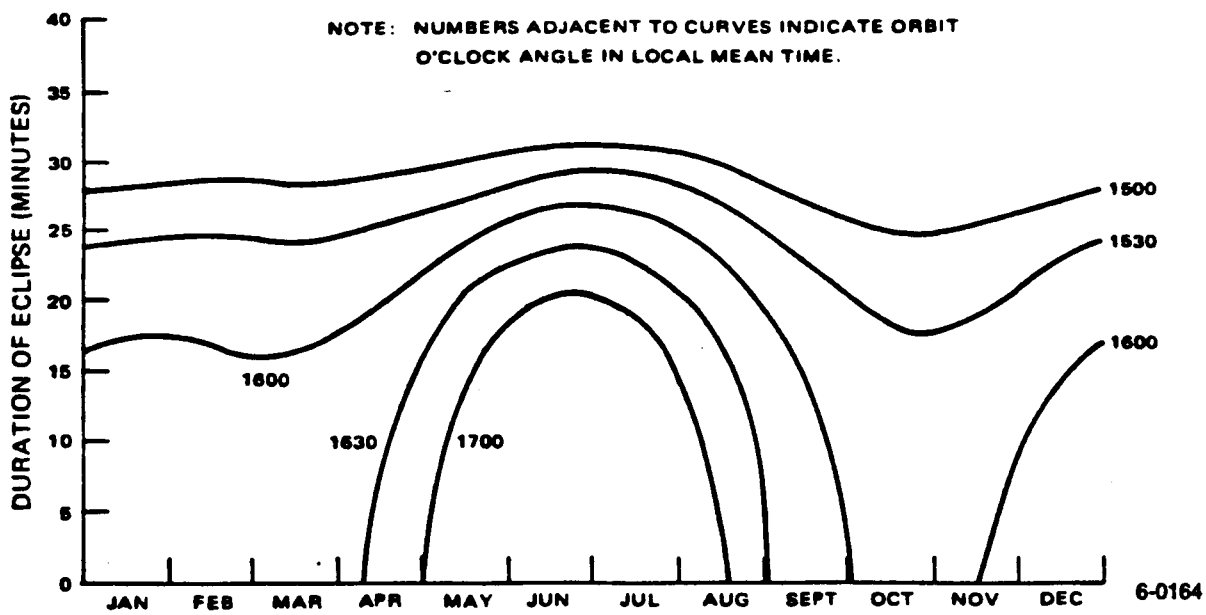

Figure 2.3.3-3. Time in Eclipse for Afternoon Ascending-Node Orbits [833 km (450 nmi) Orbits]

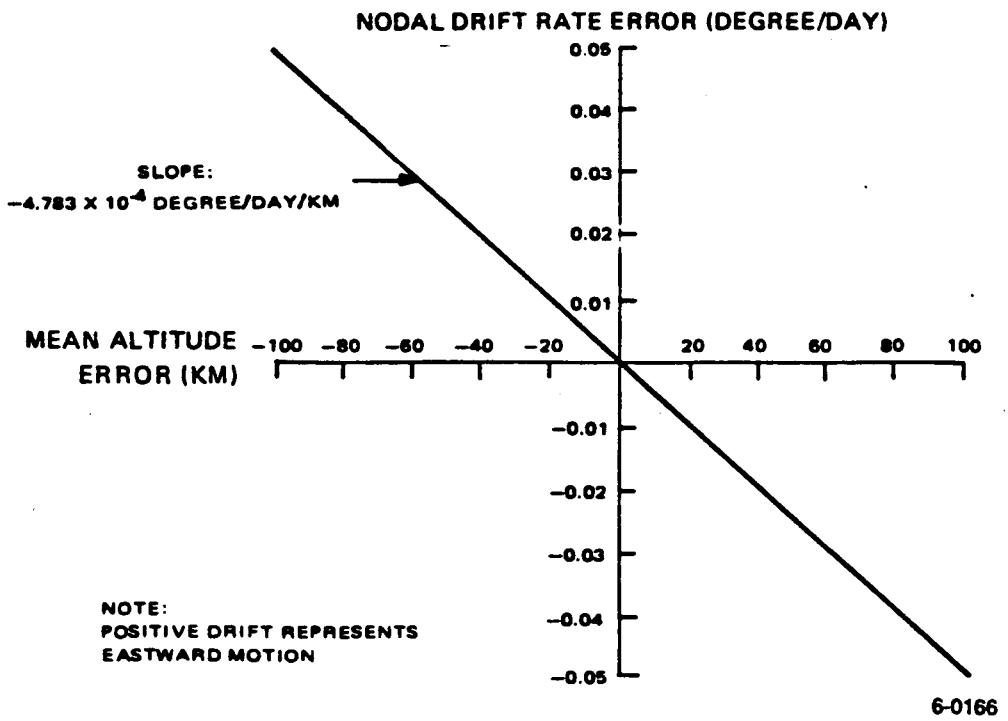

Figure 2.3.3-4. Nodal Drift Rate Error Versus Mean Altitude Error

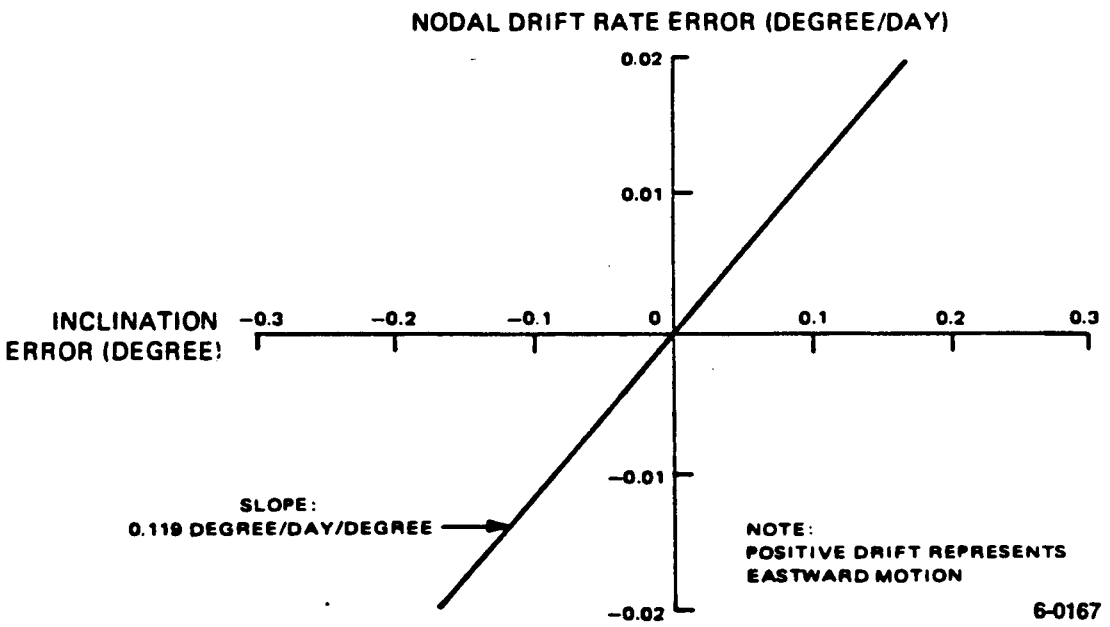

Figure 2.3.3-5. Nodal Drift Rate Error Versus Inclination Error

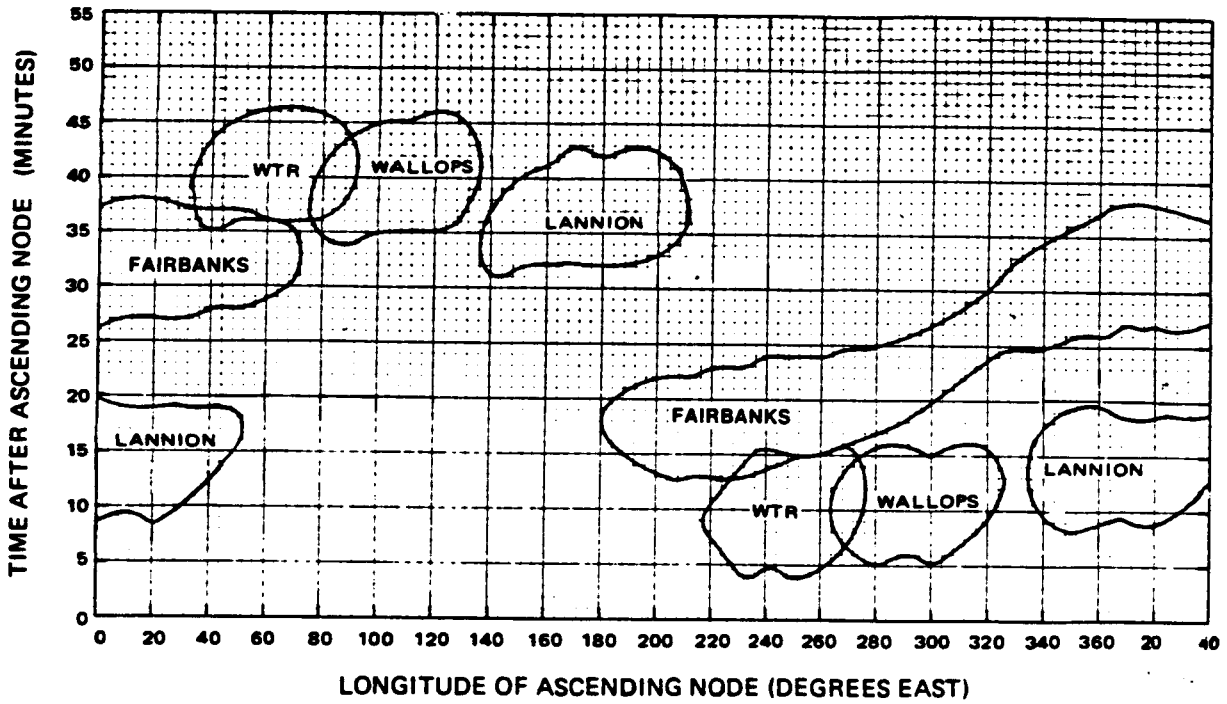

Figure 2.3.3-6. Typical Ground Contact Boundaries for 833 km (450 nmi) Orbit

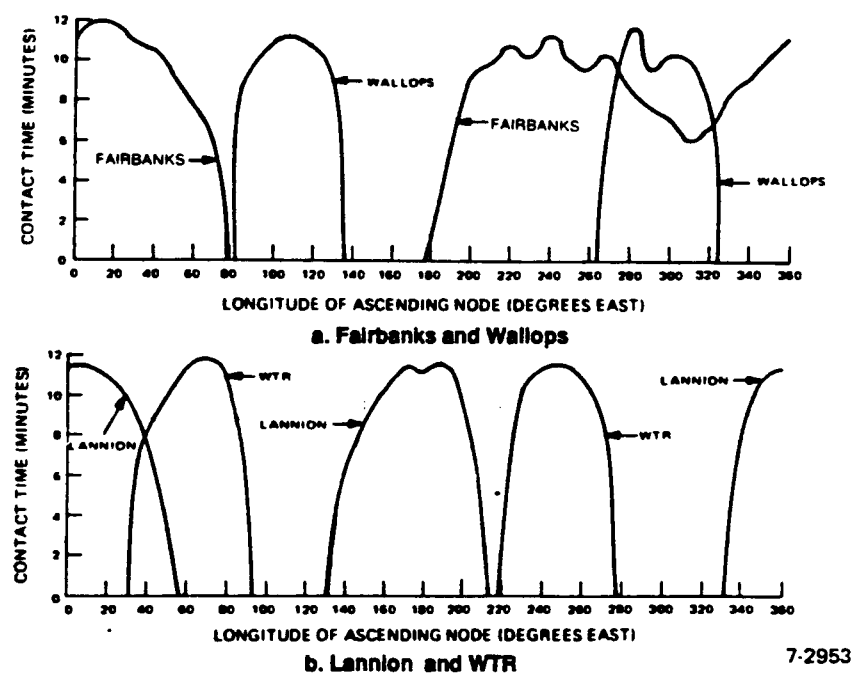

Figure 2.3.3-7. Ground Station Contact Time Versus Longitude of Ascending Node

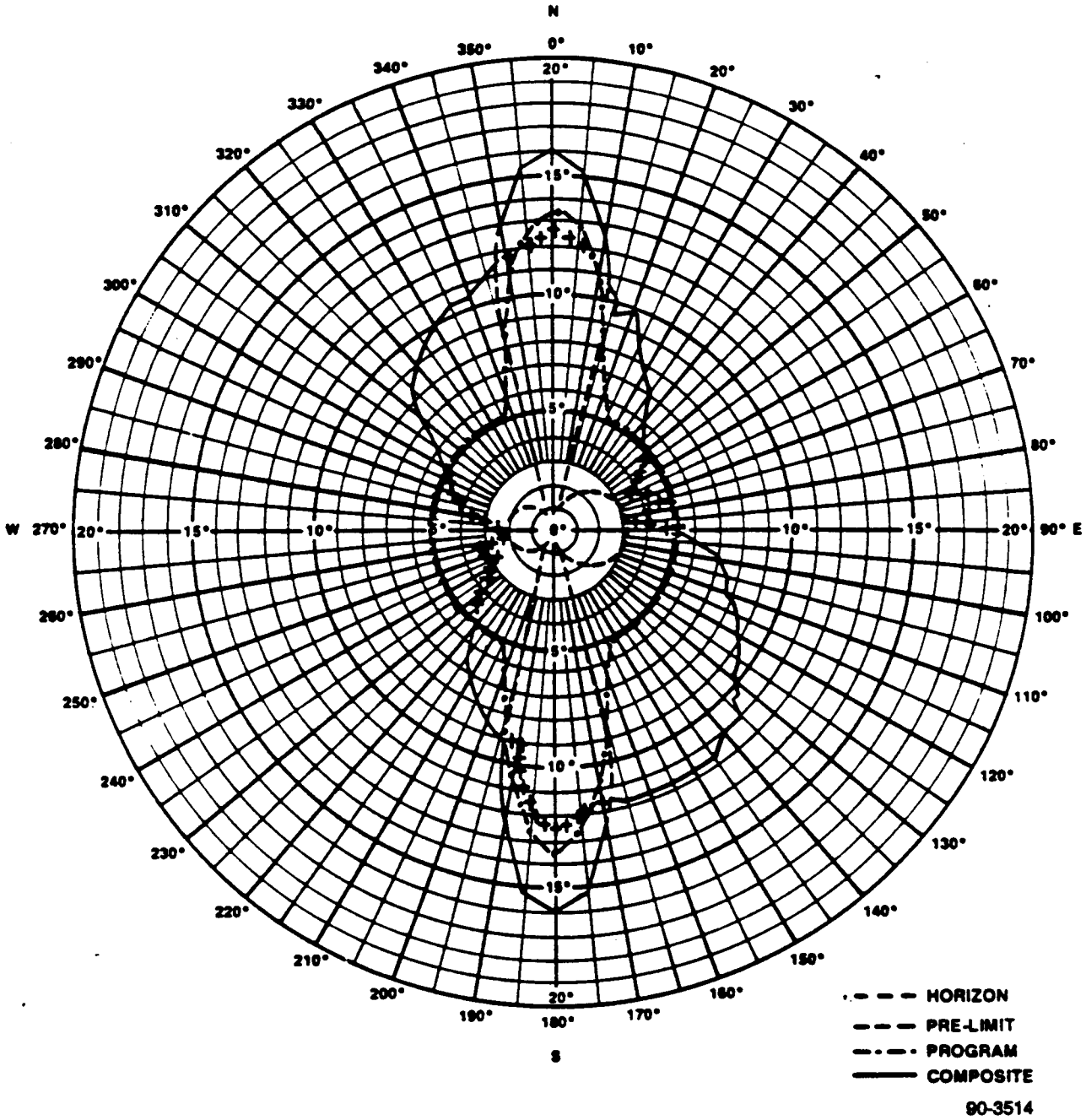

Figure 2.3.3-8. Keyhole Pattern

which the satellite is in a direct line of sight for at least five minutes at a ground elevation of at least 10°, Figure 2.3.4-1 shows regions of contact for an arbitrarily located station at any of five different latitudes. The figure shows the total number of contacts per day (i.e., per 360° change in longitude as the ascending node moves westward at about 25.4° per orbit) to be the sum of ascent pass contacts and descent pass contacts. Figure 2.3.4-2 shows the frequency of only a given number of contacts per day for the various latitudes while Figure 2.3.4-3 shows frequency of at least N contacts per day as a function of latitude. Continental U.S. stations have a 69% to 100% probability of at least 3 contacts on any particular day, and a 65% to 100% chance of at least 4 contacts, depending on the exact latitude.

2.3.5 LAUNCH WINDOW

The effect of the launch window on the mission is the change in the orbit sun angle - the angle between the orbit normal and the earth-sun vector - caused by launching at other than the nominal time. This effect varies with orbit o'clock angle and with time of year. The typical angle change for a 10-minute change in launch time is shown in Table 2.3.5-1.

2.3.6 ORBIT ACCURACIES

Stage two shutdown orbit parameter errors result from several causes. Booster guidance errors at stage two shutdown are propagated to error in apogee of the ascent eclipse. The pointing accuracy and timing of the apogee kick-burn also affect the accuracy of the resulting orbit. The orbital plane inclination error is established primarily by the booster stage two shutdown conditions and is thus relatively small. The AKM is used to remove a small cross-track bias. Spacecraft guidance contribution to inclination error is small. A hydrazine orbit velocity trim burn will have negligible effect on reducing inclination error, but can remove part of the altitude error.

The 3σ orbit parameter errors for the ATN-KLM spacecraft are 450 or 470 $\pm$10 nmi altitude, $\pm$0.15 degrees inclination, and <30 nmi apogee to perigee difference.

These injection errors cause the nodal precession rate to change from the nominal value, with the end result being a gradual deviation of the sun angle from the nominal value. Whether the sun angle increases or decreases depends on the sign of the error and on whether the orbit has a morning descending node or an afternoon ascending node. The effect of the eccentricity error is small compared to the effect caused by the inclination or altitude errors.

2.3.7 MULTI-SPACECRAFT OPERATIONS

ATN-KLM system, in its full operational mode, will have two spacecraft in orbit at any given time. Operation of the two CDA stations and the data transfer through the ground data handling system will require appropriate planning to permit checkout of each spacecraft without disrupting the flow of data from one or more operations. There are four operational S-Band frequencies, two APT frequencies and two beacon frequencies available to allow communication with different spacecraft to be over different frequencies. A common command frequency is used, but each command includes a unique spacecraft address to differentiate between spacecraft if more than one is in view.

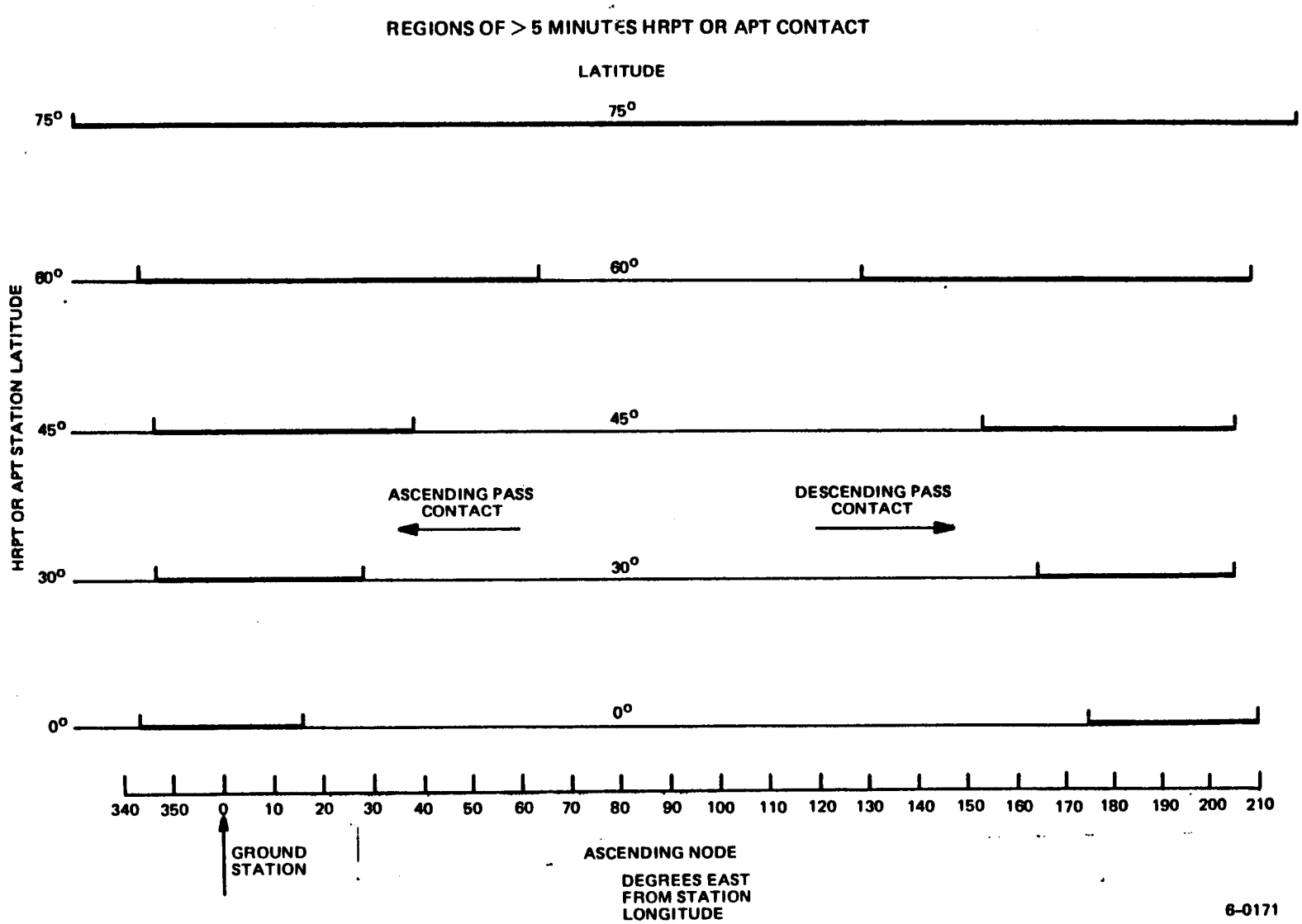

Figure 2.3.4-1. HRPT and APT Contact Regions

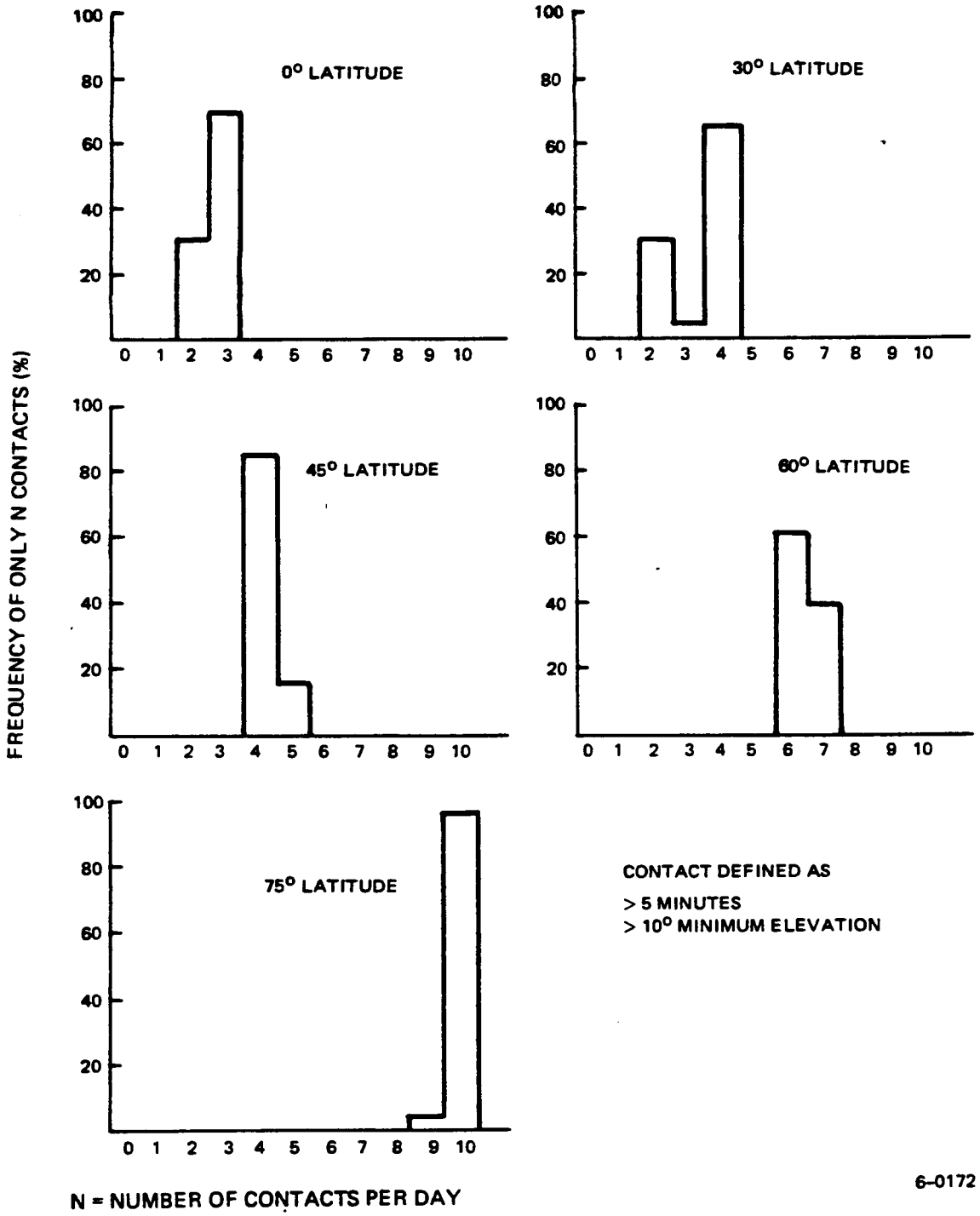

Figure 2.3.4-2. HRPT and APT Contact Frequency

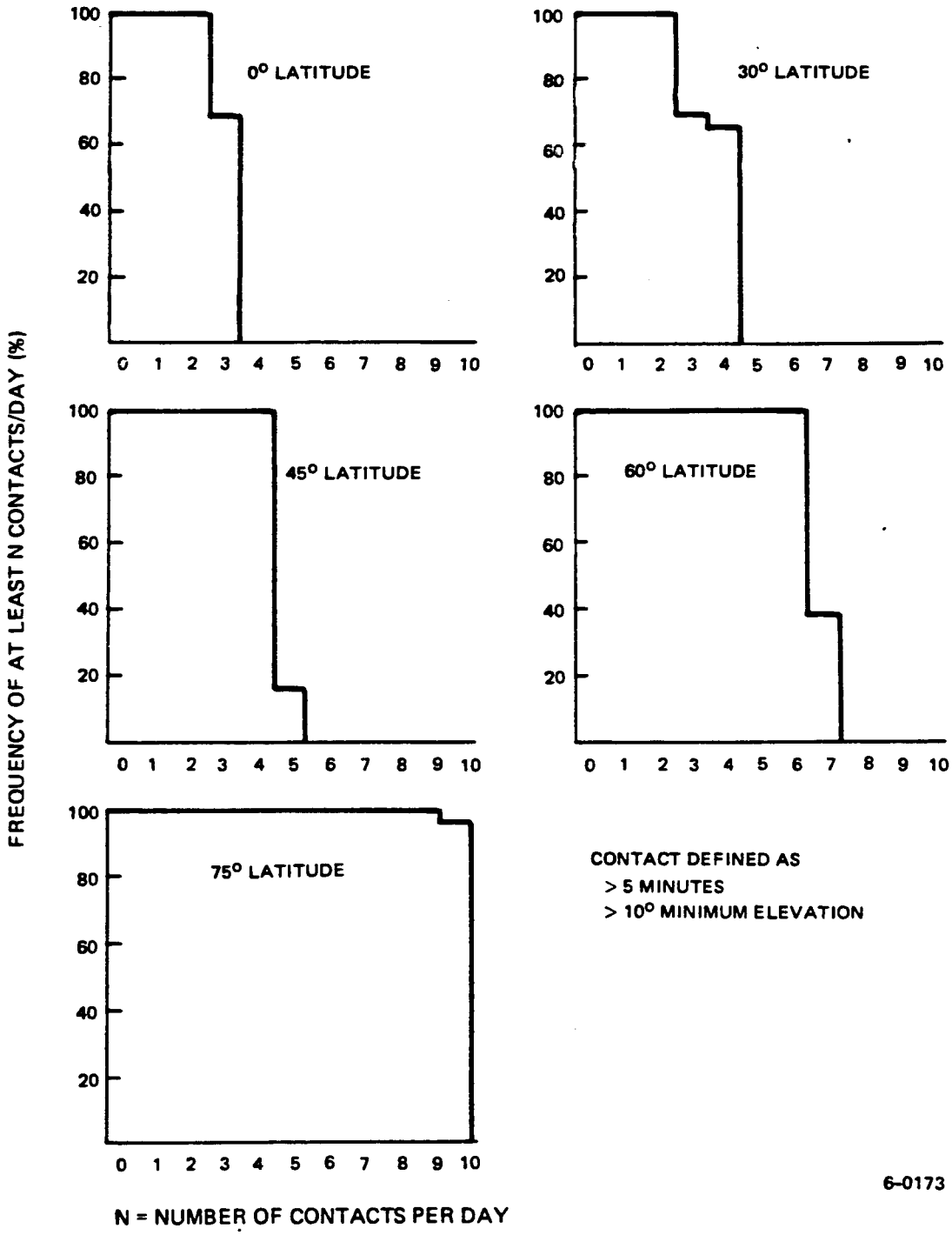

Figure 2.3.4-3. HRPT and APT Contact Frequency

TABLE 2.3.5-1. Δ SUN ANGLE FOR 10 MINUTES Δ LAUNCH TIME (DEGREES/10 MINUTES)

Descending Node Time	January 1	March 5	June 20	October 20
0600 - 0700	0.85	1.42	0.44	2.57
0700 - 0800	1.95	2.46	1.37	2.44
0800 - 0900	2.13	2.48	1.86	2.48
0900 - 1000	2.35	2.44	2.11	2.44
Ascending Node Time	**January 1**	**March 1**	**July 1**	**October 17**
1700 - 1800	1.02	2.48	0.60	1.33
1600 - 1700	1.99	2.46	1.40	2.46
1500 - 1600	2.18	2.50	1.86	2.46
1400 - 1500	2.26	2.46	2.02	2.46

2.4 LAUNCH VEHICLE INTERFACE

Figure 2.4-1 presents an interface drawing for ATN-KLM. It depicts a 120 inch diameter by 20 foot fairing whose 15° conical section begins at station 75.151.

The conical section starts above the uppermost part of the SRA. The IMP thus uses the reduced fairing diameter with an envelope of approximately 80 inches in diameter.

The spacecraft mechanical interface with the standard Titan-II launch vehicle is at station 207.55. The attachment is via a pattern of 88 bolts. This requires a short adapter section to provide a transition from the bolted joint to the vee clamp ring at the separation plane.

Figure 2.4-2 shows the launch vehicle in its erected position with all major stations noted.

2.5 RADIATION

2.5.1 ENVIRONMENT

The trapped particle environment used in the TIROS K, L, M Program is from the GSFC X-600-87-11 study.* The information found in Tables 2.5.1-1 through 2.5.1-5 and Figure 2.5.2-1 are based on the same source. Tables 2.5.1-1 and

*E.G. Stassinopoulos, J.M. Barth, and R.L. Smith, "METSAT Charged Particle Environment Study Revised Edition, Method 2" NASA Goddard Space Flight Center, August 1987, GSFC X-600-87-11.

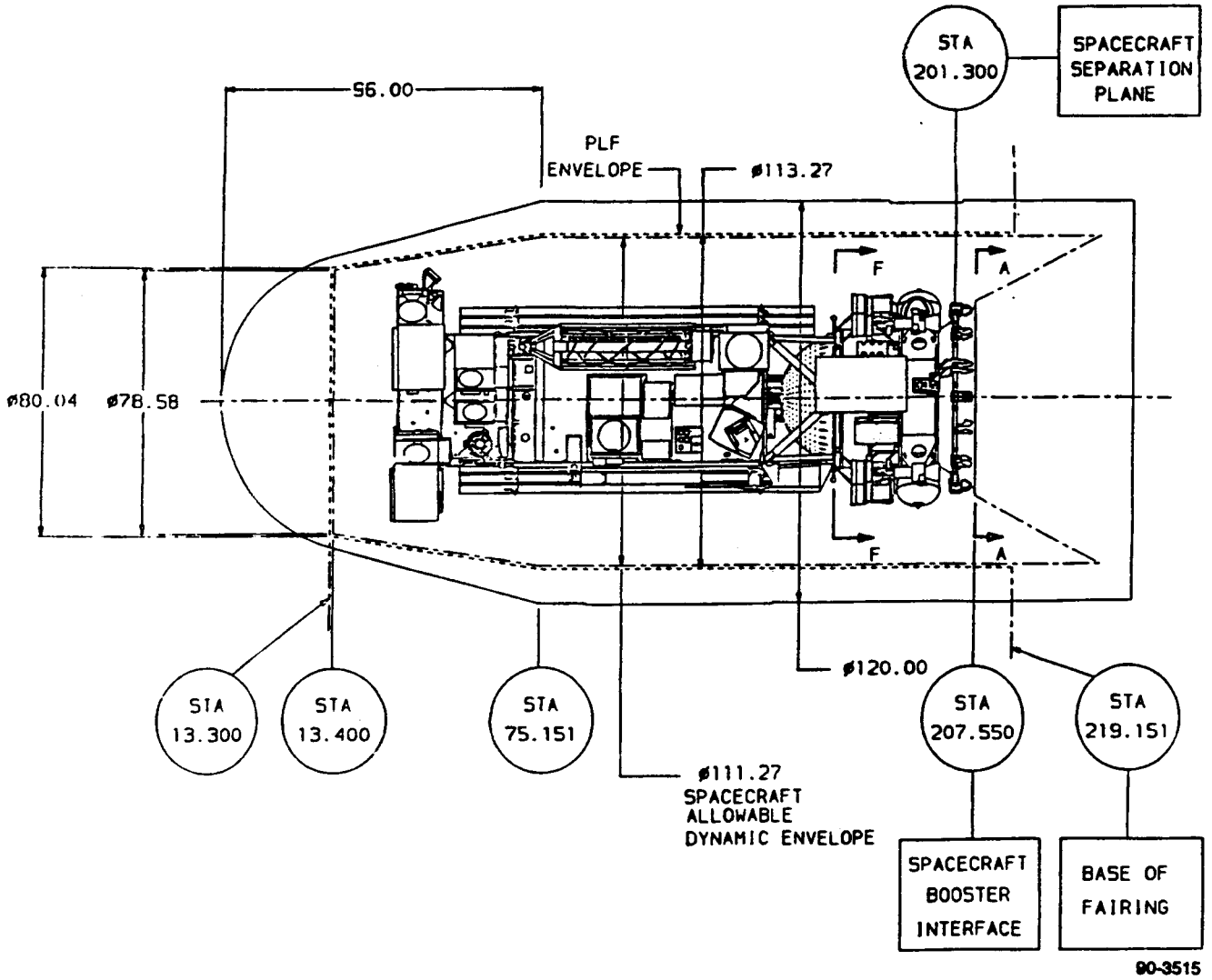

Figure 2.4-1. Launch Vehicle/Payload Mechanical Interface

2.5.1-2 list average orbit-integrated spectral distributions for both protons and electrons. Table 2.5.1-3 lists magnetospherically-attenuated solar flare proton fluences for the number of anomalously large events corresponding to the indicated confidence levels. Tables 2.5.1-4 and 2.5.1-5 list total (all 28 elements) integral Linear Energy Transfer (LET) spectra (for solar maximum and solar minimum) emerging at the center of an aluminum solid sphere of various thickness (gm/cm^2). The LET spectra is obtained for combined orbit-attenuated cosmic ray spectra of all heavy ions for atomic number less than 29. For example, in Table 2.5.1-4, column four lists LET spectra (particle/cm^2-day) for devices inside the spacecraft having a wall thickness of 0.50 gm/cm^2 (73 MILS). For total integral LET values ranging from 3.98E + 00 MeV/cm to 1.00E + 05 MeV/cm.

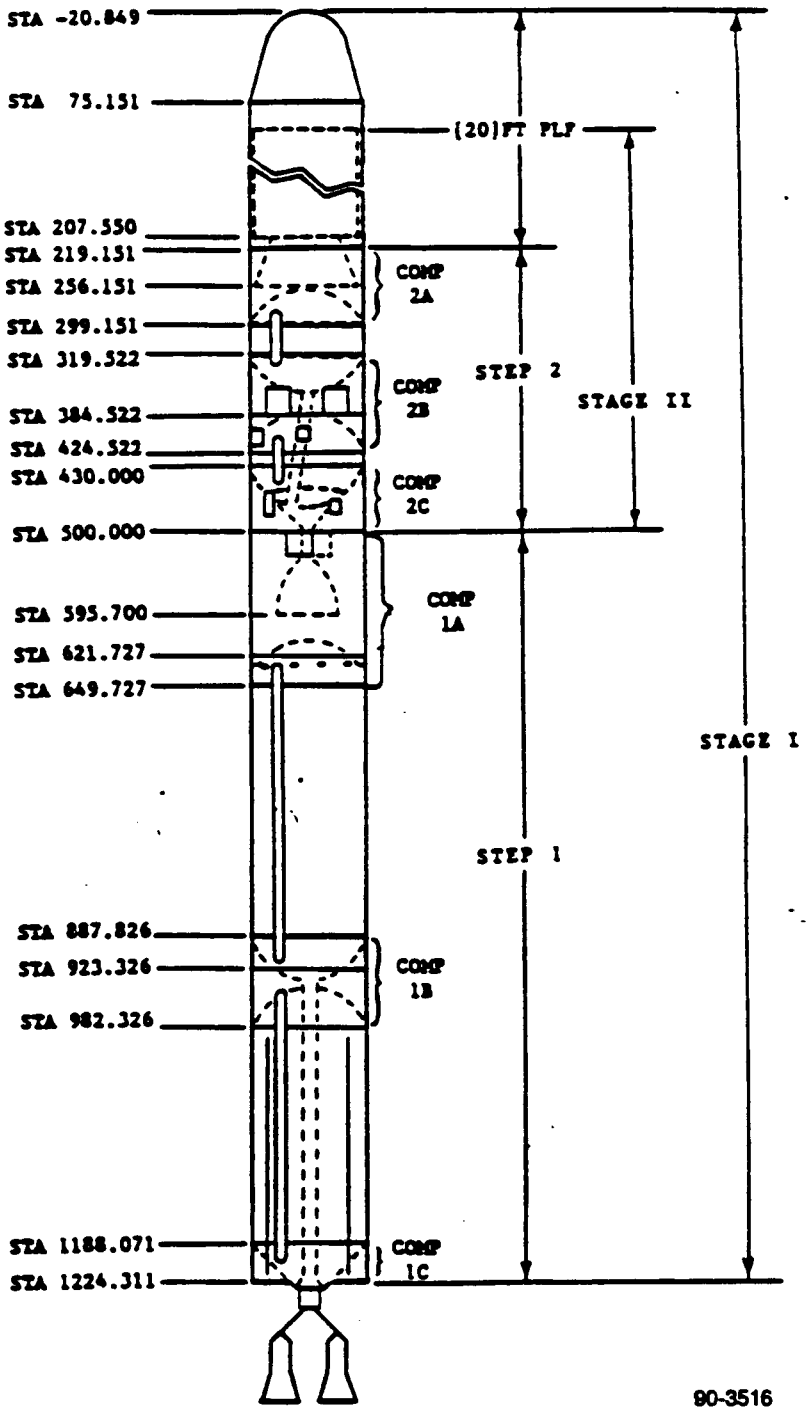

Figure 2.4-2. ATN-KLM Launch Vehicle Configuration

TABLE 2.5.1-2. TRAPPED ELECTRON ENVIRONMENT

(Orbit-Integrated, Omnidirectional, Internal Fluxes)
Inclination = 99°, Circular Orbit, Solar Maximum

	Average No. of Particles/cm^2-day		
Energy (Mev)	Inner Zone L, <2.8	Outer Zone L, >2.8	Total
0.10	3.100E10	8.057E09	3.906E10
0.50	6.615E08	1.432E08	2.094E09
0.80	1.446E08	6.879E08	8.326E08
1.00	7.467E07	4.701E08	5.447E08
1.25	4.532E07	3.071E08	3.523E08
1.50	2.761E07	2.023E08	2.298E08
1.75	1.828E07	1.321E08	1.504E08
2.00	1.213E07	8.667E07	9.879E07
2.25	8.173E06	5.772E07	6.590E07
2.50	5.517E06	3.861E07	4.412E07
2.75	2.265E06	2.441E07	2.667E07
3.00	9.458E05	1.547E07	1.642E07
3.25	2.945E05	9.632E06	9.927E06
3.50	9.349E04	6.010E06	6.104E06
3.75	3.060E04	3.473E06	3.505E06
4.00	8.320E04	2.019E06	2.027E06
4.50	1.890E02	5.956E05	5.958E05
5.00	0.00	1.628E05	1.629E05
5.50	0.00	3.594E04	3.594E04
6.00	0.00	5.152E04	5.151E03
6.50	0.00	6.242E01	6.243E01
7.00	0.00	0.00	0.00

TABLE 2.5.1-1. TRAPPED PROTON ENVIRONMENT

(Orbit-integrated, Omnidirectional, Integral Fluxes)
Perigee = 852 km, Apogee = 852 km, Inclination = 99°

Energy (MeV)	Averages No. of Particles/cm^2-day
2	2.453E 07
3	2.051E 07
4	1.801E 07
5	1.632E 07
6	1.512E 07
8	1.371E 07
10	1.262E 07
15	1.128E 07
20	1.022E 07
25	9.613E 06
30	9.057E 06
35	8.623E 06
40	8.216E 06
45	7.832E 06
50	7.470E 06
60	6.786E 06
80	5.625E 06
100	4.685E 06
150	2.877E 06
200	1.798E 06
250	1.112E 06
300	6.918E 05
350	4.333E 05
400	2.724E 05
500	1.088E 05

2.5.2 DAMAGE SHIELDING

Surface damage in semiconductor devices is due to the trapping of ionization charge in the passivating layers of silicon dioxide or other types of insulators. This effect is the dominant damage effect in MOS type transistors or ICs. Under certain operating conditions, surface damage can dominate the total radiation damage in bipolar transistors or ICs. Since both electrons and protons in trapped radiation belts produce ionization charge within spacecraft materials or devices, the charge deposited by these particles must be calculated in order to evaluate and design against radiation damage to spacecraft components and materials (e.g., glasses, thermal or optical coatings, insulators, and structural materials). The approach to this evaluation is to calculate dose-depth curves for electrons and protons in aluminum. These curves give the absorbed dose in units of RADS versus equivalent thickness of aluminum in MILS for a space environment specified for the spacecraft mission and duration (see Figure 2.5.2-1).

TABLE 2.5.1-3. ORBIT ATTENUATED SOLAR FLARE PROTON FLUENCES

for Cutoff Dipole Shell of 5 Earth Radii
(Omnidirectional, Integral Intensities) Circular Orbit, Inclination 99°
Solar Maximum

	Total No. of Particles/cm^2 for a Mission Duration of 2 Years		
	Confidence level Q (%)*		
	80-87	88-96	97-99
Energy (MeV)	No. of Anomalously Large Events Predicted (1)	(2)	(3)
10.0	3.402E09	6.804E09	1.021E10
20.0	2.479E09	4.958E09	7.437E09
30.0	1.791E09	3.582E09	5.373E09
40.0	1.279E09	2.558E09	3.837E09
50.0	9.058E08	1.812E09	2.717E09
60.0	6.369E08	1.274E09	1.911E09
70.0	4.474E08	8.948E08	1.342E09
80.0	3.135E08	6.269E08	9.404E08
90.0	2.189E08	4.379E08	6.568E08
100.0	1.527E08	3.054E08	4.581E08

*Q denotes the degree of confidence assigned to the results, namely that for the specified mission duration; the calculated fluences are the smallest values that will not be exceeded by actually encountered intensities.

TABLE 2.5.1-4. TOTAL INTEGRAL LET SPECTRA FOR SOLAR MAXIMUM FOR COSMIC-RAY FLUX OF GALACTIC ORIGIN

LET				TOTAL INTEGRAL LET SPECTRA IN UNITS OF #/CM**2*DAY (FOR ALL 28 ELEMENTS) BEHIND SPHERICAL ALUMINUM SHIELDS FOR COSMIC RAY FLUXES OF NORMAL INCIDENCE, FOR THICKNESSES (GM/CM**2)							
MEV/CM	MEV.CM**2/G	PC/CM +	PC.CM**2/G +*	0.01	0.05	0.10	0.50	1.00	3.00	5.00	10.00
1.00E+05	4.17E+04	4.55E+03	1.89E+03	0.00E+00	0.00E+00	0.00E+00	0.00E+00	0.00E+00	0.00E+00	0.00E+00	0.00E+00
7.94E+04	3.31E+04	3.61E+03	1.50E+03	0.00E+00	2.52E-04	1.22E-04	6.20E-05	6.23E-05	6.70E-05	6.37E-05	6.13E-05
6.31E+04	2.63E+04	2.87E+03	1.20E+03	1.15E-03	1.59E-02	7.73E-03	3.96E-03	3.93E-03	4.15E-03	4.02E-03	3.83E-03
5.01E+04	2.09E+04	2.28E+03	9.49E+02	2.65E-02	3.55E-02	1.81E-02	9.30E-03	9.14E-03	9.67E-03	9.45E-03	8.97E-03
3.98E+04	1.66E+04	1.81E+03	7.54E+02	8.39E-02	6.23E-02	3.43E-02	1.82E-02	1.80E-02	1.90E-02	1.86E-02	1.77E-02
3.16E+04	1.32E+04	1.44E+03	5.98E+02	1.47E-01	9.98E-02	5.98E-02	3.42E-02	3.42E-02	3.63E-02	3.57E-02	3.39E-02
2.51E+04	1.05E+04	1.14E+03	4.75E+02	2.17E-01	1.50E-01	9.83E-02	6.14E-02	6.13E-02	6.56E-02	6.49E-02	6.14E-02
2.00E+04	8.33E+03	9.09E+02	3.79E+02	2.91E-01	2.12E-01	1.51E-01	1.04E-01	1.03E-01	1.10E-01	1.09E-01	1.03E-01
1.58E+04	6.58E+03	7.18E+02	2.99E+02	3.89E-01	3.09E-01	2.38E-01	1.79E-01	1.78E-01	1.91E-01	1.90E-01	1.81E-01
1.26E+04	5.25E+03	5.73E+02	2.39E+02	5.30E-01	4.52E-01	3.74E-01	3.03E-01	3.07E-01	3.25E-01	3.23E-01	3.09E-01
1.00E+04	4.17E+03	4.55E+02	1.89E+02	7.53E-01	6.84E-01	5.99E-01	5.21E-01	5.28E-01	5.56E-01	5.54E-01	5.32E-01
7.94E+03	3.31E+03	3.61E+02	1.50E+02	1.13E+00	1.07E+00	9.82E-01	9.02E-01	9.15E-01	9.57E-01	9.57E-01	9.09E-01
6.31E+03	2.63E+03	2.87E+02	1.20E+02	1.76E+00	1.73E+00	1.63E+00	1.56E+00	1.58E+00	1.63E+00	1.63E+00	1.54E+00
5.01E+03	2.09E+03	2.28E+02	9.49E+01	3.22E+00	3.19E+00	3.09E+00	3.02E+00	3.05E+00	3.10E+00	3.08E+00	2.90E+00
3.98E+03	1.66E+03	1.81E+02	7.54E+01	6.27E+00	6.25E+00	6.14E+00	6.06E+00	6.09E+00	6.11E+00	6.01E+00	5.65E+00
3.16E+03	1.32E+03	1.44E+02	5.98E+01	1.73E+01	1.73E+01	1.72E+01	1.70E+01	1.70E+01	1.68E+01	1.64E+01	1.54E+01
2.51E+03	1.05E+03	1.14E+02	4.75E+01	4.82E+01	4.81E+01	4.80E+01	4.79E+01	4.77E+01	4.70E+01	4.59E+01	4.37E+01
2.00E+03	8.33E+02	9.09E+01	3.79E+01	5.79E+01	5.79E+01	5.78E+01	5.77E+01	5.75E+01	5.66E+01	5.54E+01	5.28E+01
1.58E+03	6.58E+02	7.18E+01	2.99E+01	7.00E+01	6.99E+01	6.99E+01	6.98E+01	6.96E+01	6.86E+01	6.72E+01	6.40E+01
1.26E+03	5.25E+02	5.73E+01	2.39E+01	8.10E+01	8.09E+01	8.09E+01	8.08E+01	8.06E+01	7.95E+01	7.79E+01	7.42E+01
1.00E+03	4.17E+02	4.55E+01	1.89E+01	9.49E+01	9.48E+01	9.48E+01	9.48E+01	9.46E+01	9.33E+01	9.15E+01	8.70E+01
7.94E+02	3.31E+02	3.61E+01	1.50E+01	1.25E+02	1.25E+02	1.25E+02	1.25E+02	1.24E+02	1.23E+02	1.21E+02	1.15E+02
6.31E+02	2.63E+02	2.87E+01	1.20E+01	1.60E+02	1.59E+02	1.59E+02	1.60E+02	1.59E+02	1.57E+02	1.55E+02	1.48E+02
5.01E+02	2.09E+02	2.28E+01	9.49E+00	1.84E+02	1.84E+02	1.85E+02	1.85E+02	1.84E+02	1.82E+02	1.79E+02	1.72E+02
3.98E+02	1.66E+02	1.81E+01	7.54E+00	2.23E+02	2.23E+02	2.24E+02	2.23E+02	2.23E+02	2.20E+02	2.17E+02	2.08E+02
3.16E+02	1.32E+02	1.44E+01	5.98E+00	2.65E+02	2.66E+02	2.66E+02	2.66E+02	2.65E+02	2.62E+02	2.58E+02	2.47E+02
2.51E+02	1.05E+02	1.14E+01	4.75E+00	4.19E+02	4.19E+02	4.21E+02	4.19E+02	4.18E+02	4.14E+02	4.09E+02	3.95E+02
2.00E+02	8.33E+01	9.09E+00	3.79E+00	4.81E+02	4.81E+02	4.87E+02	4.81E+02	4.79E+02	4.75E+02	4.69E+02	4.54E+02
1.58E+02	6.58E+01	7.18E+00	2.99E+00	5.97E+02	5.97E+02	6.11E+02	5.98E+02	5.96E+02	5.91E+02	5.85E+02	5.68E+02
1.26E+02	5.25E+01	5.73E+00	2.39E+00	6.67E+02	6.74E+02	6.89E+02	6.68E+02	6.65E+02	6.60E+02	6.54E+02	6.38E+02
1.00E+02	4.17E+01	4.55E+00	1.89E+00	7.35E+02	7.44E+02	7.52E+02	7.23E+02	7.20E+02	7.15E+02	7.10E+02	6.94E+02
7.94E+01	3.31E+01	3.61E+00	1.50E+00	7.77E+02	7.80E+02	7.86E+02	7.51E+02	7.48E+02	7.44E+02	7.40E+02	7.24E+02
6.31E+01	2.63E+01	2.87E+00	1.20E+00	8.38E+02	8.39E+02	8.42E+02	8.03E+02	7.99E+02	7.96E+02	7.92E+02	7.80E+02
5.01E+01	2.09E+01	2.28E+00	9.49E-01	9.21E+02	9.21E+02	9.24E+02	8.82E+02	8.78E+02	8.77E+02	8.74E+02	8.65E+02
3.98E+01	1.66E+01	1.81E+00	7.54E-01	1.10E+03	1.10E+03	1.11E+03	1.06E+03	1.06E+03	1.06E+03	1.06E+03	1.05E+03
3.16E+01	1.32E+01	1.44E+00	5.98E-01	1.41E+03	1.41E+03	1.41E+03	1.37E+03	1.36E+03	1.36E+03	1.36E+03	1.36E+03
2.51E+01	1.05E+01	1.14E+00	4.75E-01	2.04E+03	2.04E+03	2.04E+03	1.99E+03	1.99E+03	1.99E+03	1.98E+03	1.97E+03
2.00E+01	8.33E+00	9.09E-01	3.79E-01	3.44E+03	3.44E+03	3.44E+03	3.39E+03	3.39E+03	3.38E+03	3.36E+03	3.35E+03
1.58E+01	6.58E+00	7.18E-01	2.99E-01	9.13E+03	9.13E+03	9.13E+03	9.09E+03	9.09E+03	9.09E+03	9.07E+03	9.03E+03
1.26E+01	5.25E+00	5.73E-01	2.39E-01	9.27E+03	9.27E+03	9.27E+03	9.24E+03	9.23E+03	9.25E+03	9.23E+03	9.21E+03
1.00E+01	4.17E+00	4.55E-01	1.89E-01	9.58E+03	9.58E+03	9.58E+03	9.54E+03	9.55E+03	9.57E+03	9.57E+03	9.56E+03
7.94E+00	3.31E+00	3.61E-01	1.50E-01	1.05E+04	1.05E+04	1.05E+04	1.05E+04	1.05E+04	1.05E+04	1.05E+04	1.06E+04
6.31E+00	2.63E+00	2.87E-01	1.20E-01	1.25E+04	1.25E+04	1.25E+04	1.25E+04	1.25E+04	1.26E+04	1.26E+04	1.26E+04
5.01E+00	2.09E+00	2.28E-01	9.49E-02	1.99E+04	1.99E+04	1.99E+04	1.98E+04	1.99E+04	1.99E+04	2.00E+04	2.00E+04
3.98E+00	1.66E+00	1.81E-01	7.54E-02	8.32E+04	8.32E+04	8.32E+04	8.32E+04	8.32E+04	8.32E+04	8.32E+04	8.31E+04

* THESE UNITS APPLY ONLY TO SILICON TARGETS
\+ THESE UNITS ARE DENSITY DEPENDENT; LISTED FOR SILICON TARGET

TABLE 2.5.1-5. TOTAL INTEGRAL LET SPECTRA FOR SOLAR MINIMUM FOR COSMIC-RAY FLUX OF GALACTIC ORIGIN

LET				TOTAL INTEGRAL LET SPECTRA IN UNITS OF #/CM**2*DAY (FOR ALL 28 ELEMENTS) BEHIND SPHERICAL ALUMINUM SHIELDS FOR COSMIC RAY FLUXES OF NORMAL INCIDENCE, FOR THICKNESSES (GM/CM**2)							
MEV/CM	MEV.CM**2/G	PC/CM +	PC.CM**2/G +*	0.01	0.05	0.10	0.50	1.00	3.00	5.00	10.00
1.00E+05	4.17E+04	4.55E+03	1.89E+03	0.00E+00	0.00E+00	0.00E+00	0.00E+00	0.00E+00	0.00E+00	0.00E+00	0.00E+00
7.94E+04	3.31E+04	3.61E+03	1.50E+03	0.00E+00	5.25E-04	2.98E-04	1.88E-04	1.96E-04	2.00E-04	1.84E-04	1.60E-04
6.31E+04	2.63E+04	2.87E+03	1.20E+03	1.92E-03	3.32E-02	1.89E-02	1.19E-02	1.24E-02	1.25E-02	1.16E-02	1.00E-02
5.01E+04	2.09E+04	2.28E+03	9.49E+02	4.60E-02	7.46E-02	4.42E-02	2.80E-02	2.87E-02	2.91E-02	2.73E-02	2.37E-02
3.98E+04	1.66E+04	1.81E+03	7.54E+02	1.52E-01	1.34E-01	8.47E-02	5.59E-02	5.75E-02	5.82E-02	5.45E-02	4.70E-02
3.16E+04	1.32E+04	1.44E+03	5.98E+02	2.79E-01	2.25E-01	1.55E-01	1.11E-01	1.16E-01	1.17E-01	1.09E-01	9.35E-02
2.51E+04	1.05E+04	1.14E+03	4.75E+02	4.33E-01	3.54E-01	2.64E-01	2.05E-01	2.15E-01	2.17E-01	2.04E-01	1.73E-01
2.00E+04	8.33E+03	9.09E+02	3.79E+02	6.14E-01	5.28E-01	4.20E-01	3.52E-01	3.66E-01	3.70E-01	3.47E-01	2.94E-01
1.58E+04	6.58E+03	7.18E+02	2.99E+02	8.84E-01	8.17E-01	6.94E-01	6.18E-01	6.43E-01	6.56E-01	6.14E-01	5.23E-01
1.26E+04	5.25E+03	5.73E+02	2.39E+02	1.30E+00	1.27E+00	1.14E+00	1.07E+00	1.12E+00	1.13E+00	1.06E+00	9.04E-01
1.00E+04	4.17E+03	4.55E+02	1.89E+02	2.02E+00	2.02E+00	1.89E+00	1.85E+00	1.92E+00	1.93E+00	1.82E+00	1.56E+00
7.94E+03	3.31E+03	3.61E+02	1.50E+02	3.24E+00	3.30E+00	3.19E+00	3.18E+00	3.29E+00	3.28E+00	3.10E+00	2.65E+00
6.31E+03	2.63E+03	2.87E+02	1.20E+02	5.35E+00	5.52E+00	5.40E+00	5.48E+00	5.60E+00	5.54E+00	5.24E+00	4.47E+00
5.01E+03	2.09E+03	2.28E+02	9.49E+01	9.96E+00	1.02E+01	1.01E+01	1.02E+01	1.04E+01	1.01E+01	9.55E+00	8.15E+00
3.98E+03	1.66E+03	1.81E+02	7.54E+01	1.90E+01	1.93E+01	1.92E+01	1.94E+01	1.95E+01	1.89E+01	1.78E+01	1.52E+01
3.16E+03	1.32E+03	1.44E+02	5.98E+01	4.43E+01	4.46E+01	4.45E+01	4.46E+01	4.46E+01	4.29E+01	4.06E+01	3.58E+01
2.51E+03	1.05E+03	1.14E+02	4.75E+01	9.83E+01	9.86E+01	9.85E+01	9.88E+01	9.85E+01	9.54E+01	9.15E+01	8.31E+01
2.00E+03	8.33E+02	9.09E+01	3.79E+01	1.22E+02	1.22E+02	1.22E+02	1.22E+02	1.22E+02	1.18E+02	1.13E+02	1.02E+02
1.58E+03	6.58E+02	7.18E+01	2.99E+01	1.51E+02	1.52E+02	1.52E+02	1.52E+02	1.52E+02	1.47E+02	1.40E+02	1.27E+02
1.26E+03	5.25E+02	5.73E+01	2.39E+01	1.84E+02	1.85E+02	1.85E+02	1.86E+02	1.85E+02	1.78E+02	1.70E+02	1.53E+02
1.00E+03	4.17E+02	4.55E+01	1.89E+01	2.29E+02	2.29E+02	2.29E+02	2.30E+02	2.29E+02	2.20E+02	2.10E+02	1.88E+02
7.94E+02	3.31E+02	3.61E+01	1.50E+01	3.00E+02	3.01E+02	3.01E+02	3.02E+02	3.00E+02	2.90E+02	2.77E+02	2.48E+02
6.31E+02	2.63E+02	2.87E+01	1.20E+01	3.87E+02	3.88E+02	3.88E+02	3.89E+02	3.87E+02	3.74E+02	3.59E+02	3.23E+02
5.01E+02	2.09E+02	2.28E+01	9.49E+00	4.64E+02	4.65E+02	4.66E+02	4.68E+02	4.65E+02	4.50E+02	4.32E+02	3.89E+02
3.98E+02	1.66E+02	1.81E+01	7.54E+00	5.77E+02	5.78E+02	5.81E+02	5.82E+02	5.78E+02	5.59E+02	5.37E+02	4.86E+02
3.16E+02	1.32E+02	1.44E+01	5.98E+00	7.20E+02	7.22E+02	7.24E+02	7.24E+02	7.18E+02	6.97E+02	6.69E+02	6.08E+02
2.51E+02	1.05E+02	1.14E+01	4.75E+00	1.02E+03	1.02E+03	1.02E+03	1.02E+03	1.01E+03	9.90E+02	9.59E+02	8.87E+02
2.00E+02	8.33E+01	9.09E+00	3.79E+00	1.17E+03	1.17E+03	1.19E+03	1.18E+03	1.17E+03	1.14E+03	1.11E+03	1.03E+03
1.58E+02	6.58E+01	7.18E+00	2.99E+00	1.41E+03	1.41E+03	1.44E+03	1.42E+03	1.41E+03	1.39E+03	1.35E+03	1.27E+03
1.26E+02	5.25E+01	5.73E+00	2.39E+00	1.56E+03	1.58E+03	1.61E+03	1.58E+03	1.57E+03	1.55E+03	1.51E+03	1.44E+03
1.00E+02	4.17E+01	4.55E+00	1.89E+00	1.73E+03	1.76E+03	1.78E+03	1.73E+03	1.72E+03	1.71E+03	1.68E+03	1.60E+03
7.94E+01	3.31E+01	3.61E+00	1.50E+00	1.93E+03	1.94E+03	1.96E+03	1.90E+03	1.90E+03	1.89E+03	1.87E+03	1.79E+03
6.31E+01	2.63E+01	2.87E+00	1.20E+00	2.22E+03	2.23E+03	2.24E+03	2.17E+03	2.17E+03	2.17E+03	2.15E+03	2.08E+03
5.01E+01	2.09E+01	2.28E+00	9.49E-01	2.72E+03	2.73E+03	2.74E+03	2.67E+03	2.67E+03	2.68E+03	2.64E+03	2.58E+03
3.98E+01	1.66E+01	1.81E+00	7.54E-01	3.70E+03	3.71E+03	3.71E+03	3.64E+03	3.63E+03	3.63E+03	3.59E+03	3.51E+03
3.16E+01	1.32E+01	1.44E+00	5.98E-01	5.17E+03	5.17E+03	5.19E+03	5.11E+03	5.09E+03	5.08E+03	5.02E+03	4.92E+03
2.51E+01	1.05E+01	1.14E+00	4.75E-01	7.68E+03	7.69E+03	7.70E+03	7.63E+03	7.61E+03	7.58E+03	7.53E+03	7.38E+03
2.00E+01	8.33E+00	9.09E-01	3.79E-01	1.18E+04	1.18E+04	1.19E+04	1.18E+04	1.18E+04	1.18E+04	1.17E+04	1.15E+04
1.58E+01	6.58E+00	7.18E-01	2.99E-01	2.13E+04	2.13E+04	2.13E+04	2.13E+04	2.13E+04	2.13E+04	2.13E+04	2.10E+04
1.26E+01	5.25E+00	5.73E-01	2.39E-01	2.25E+04	2.25E+04	2.25E+04	2.24E+04	2.25E+04	2.26E+04	2.26E+04	2.24E+04
1.00E+01	4.17E+00	4.55E-01	1.89E-01	2.48E+04	2.48E+04	2.48E+04	2.48E+04	2.49E+04	2.51E+04	2.51E+04	2.51E+04
7.94E+00	3.31E+00	3.61E-01	1.50E-01	3.13E+04	3.13E+04	3.13E+04	3.13E+04	3.14E+04	3.15E+04	3.16E+04	3.17E+04
6.31E+00	2.63E+00	2.87E-01	1.20E-01	4.35E+04	4.35E+04	4.35E+04	4.34E+04	4.35E+04	4.36E+04	4.37E+04	4.36E+04
5.01E+00	2.09E+00	2.28E-01	9.49E-02	7.56E+04	7.56E+04	7.56E+04	7.55E+04	7.56E+04	7.56E+04	7.53E+04	7.49E+04
3.98E+00	1.66E+00	1.81E-01	7.54E-02	1.94E+05	1.94E+05	1.94E+05	1.94E+05	1.94E+05	1.94E+05	1.94E+05	1.92E+05

* THESE UNITS APPLY ONLY TO SILICON TARGETS
\+ THESE UNITS ARE DENSITY DEPENDENT: LISTED FOR SILICON TARGET

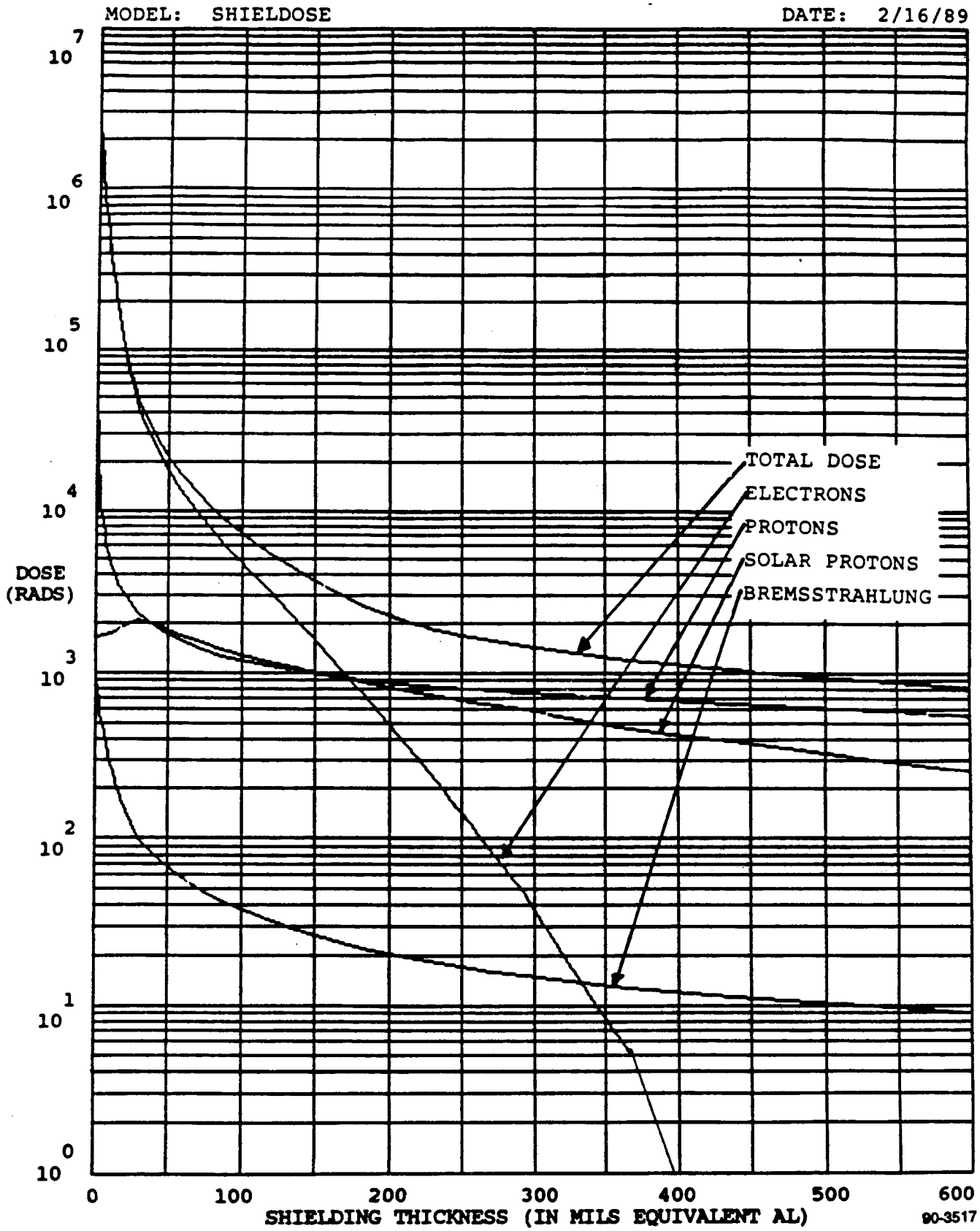

Figure 2.5.2-1. Ionization vs. Shielding

Blank Page

SECTION 3.0

SYSTEM DESCRIPTION

3.1 PHYSICAL CONFIGURATION

3.1.1 EXTERNAL ARRANGEMENTS

Figure 3.1.1-1 shows the configuration of the spacecraft. The structure itself consists of four major components: the Reaction Control Equipment Support Structure (RSS), the Equipment Support Module (ESM), the Instrument Mounting Platform (IMP), and the Solar Array (SA). A short launch vehicle adapter joins the spacecraft to the Titan II launch vehicle.

The AVHRR/3 and HIRS/3 are mounted on the IMP which is the primary mounting surface for the earth-viewing instruments. The AMSU-A1 is mounted to the ESM top panel. The AMSU-A2, AMSU-B, and SBUV/2 instruments are mounted to the ESM earth-facing (front) panel. The DCS-2 and the SARP-2 are mounted inside the ESM. The SEM has boxes in various locations.

The attitude determination sensors (the Inertial Measurement Unit, the Earth Sensor Assembly, and the Sun Sensor Assembly) are also mounted on the IMP. As such, it may be said that the IMP is controlled to the desired orientation and the rest of the spacecraft follows along.

At launch, the solar array is stowed on the back panels of the ESM.

3.1.2 INTERNAL ARRANGEMENT

The arrangement of components within the spacecraft is depicted in Figure 3.1.2-1. Insofar as possible they have been grouped to satisfy the following criteria:

- Maintain functional proximity to reduce harness lengths and to ease integration and checkout.
- Combine power dissipations and duty cycles of neighboring components, so that a narrow range of temperatures will be experienced.
- Arrange components and panels such that they tend to statically balance the spacecraft.

3.2 FUNCTIONAL GROUPS

3.2.1 EQUIPMENT FAMILY TREE

GE Drawing 3278201 (Rev. A), shown in Figures 3.2.1-1a and 3.2.1-1b, is an equipment tree for the spacecraft. This tree provides a breakdown of the components used to fabricate a spacecraft. It identifies the number of components used and the performance specification number for each component.

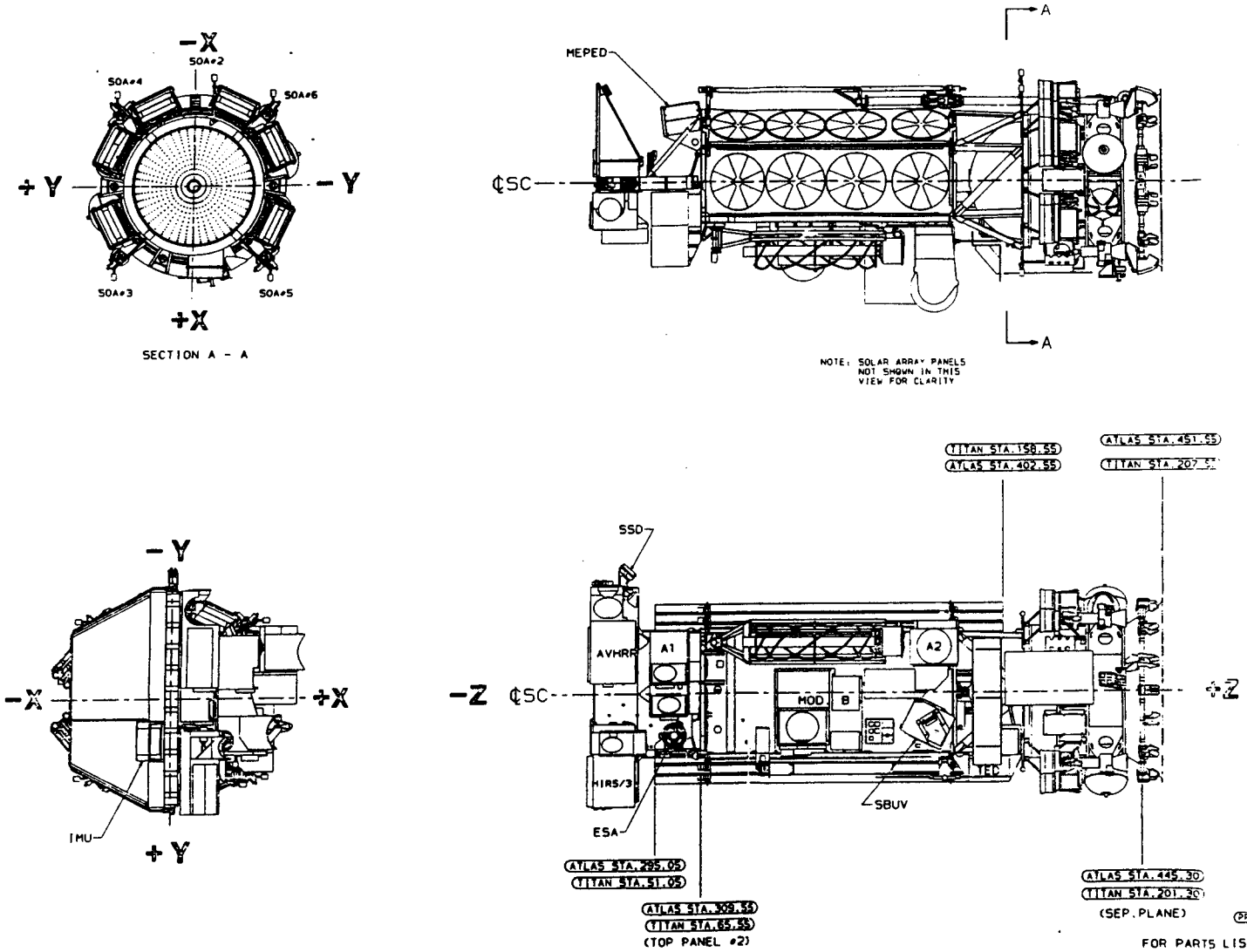

Figure 3.1.1-1. ATN-KLM Spacecraft Configuration

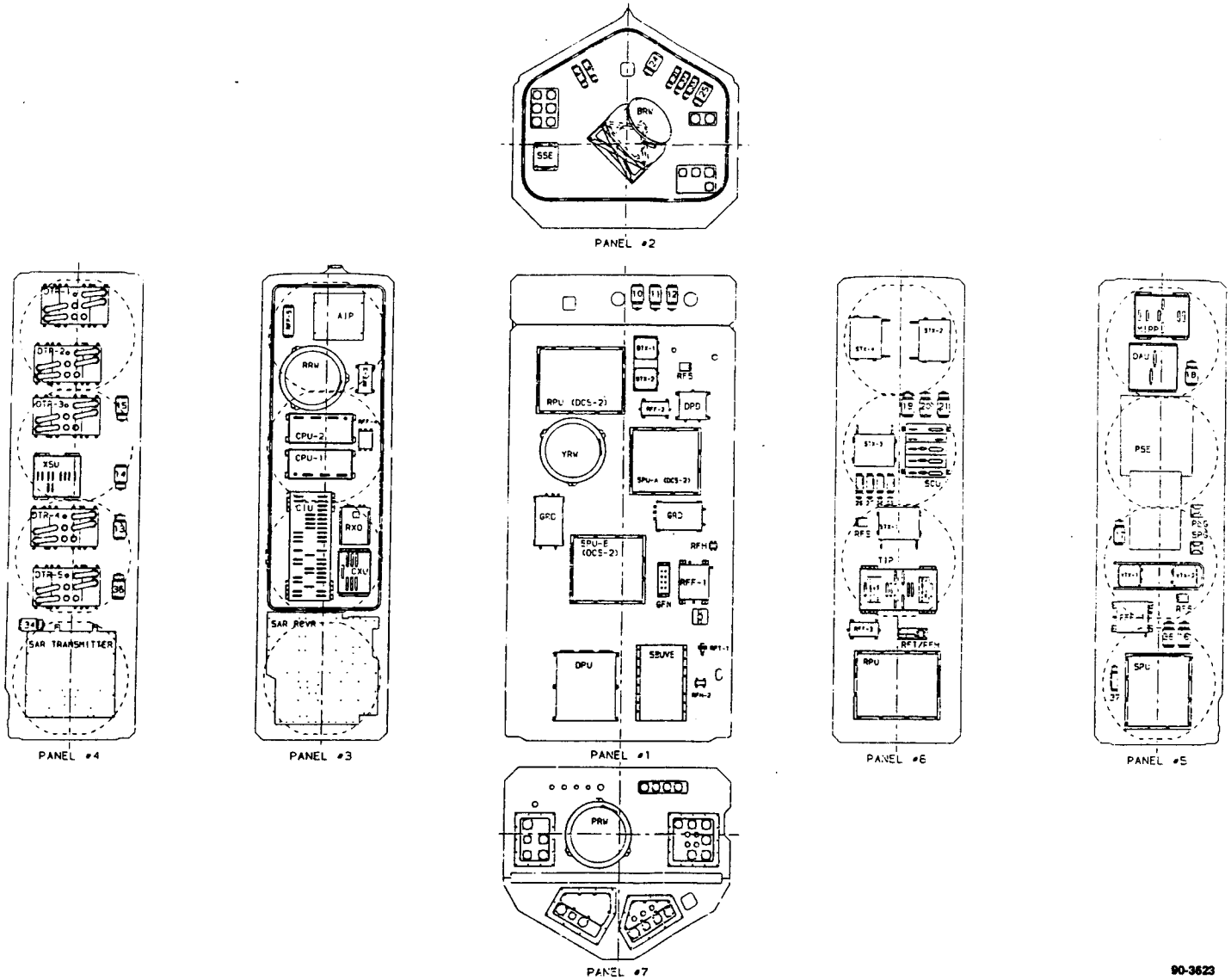

90-3623

Figure 3.1.2-1. ATN-KLM Internal Layout

THE FOLLOWING DRAWING IS ON THE NEXT TWO PAGES.

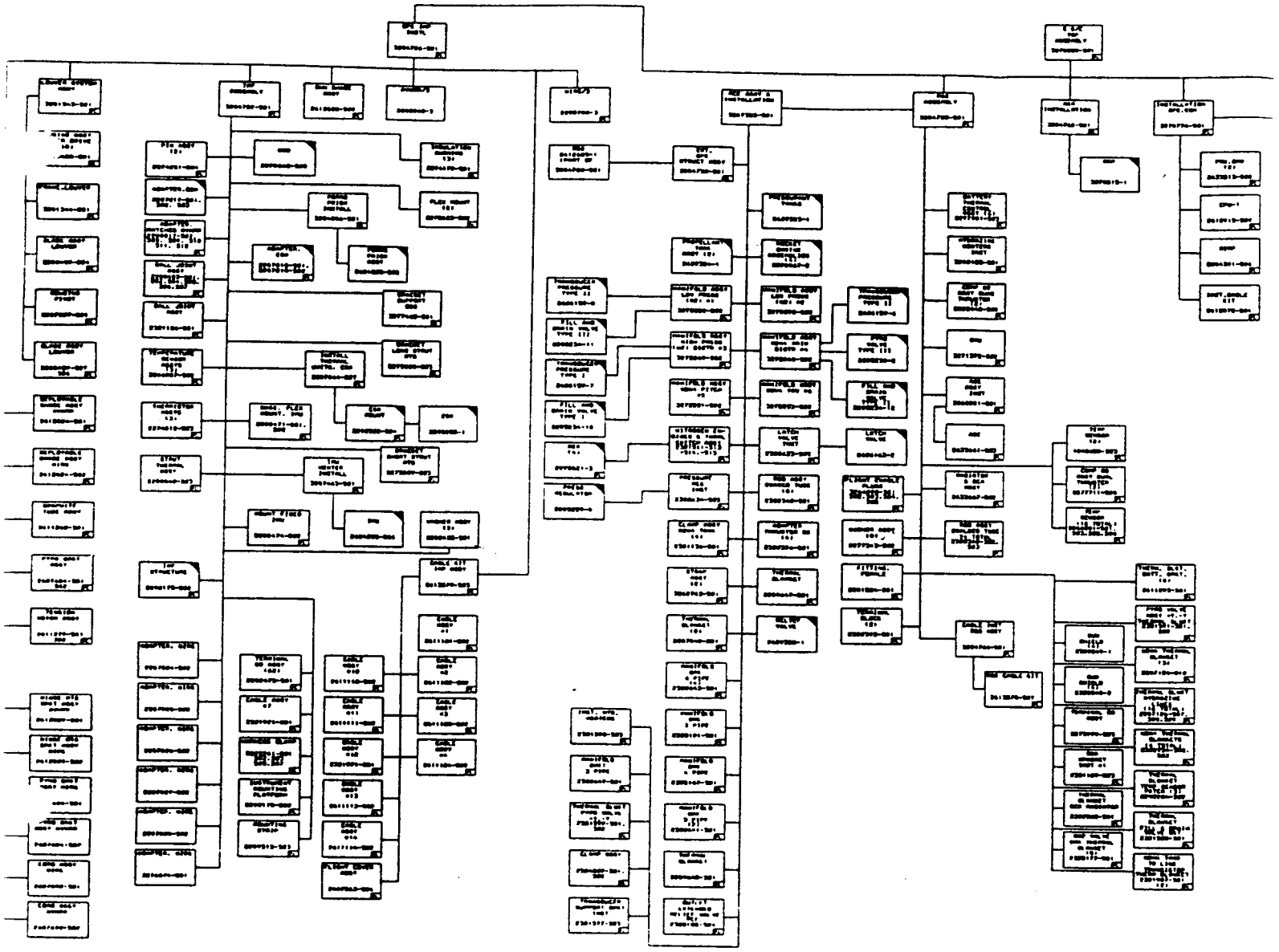

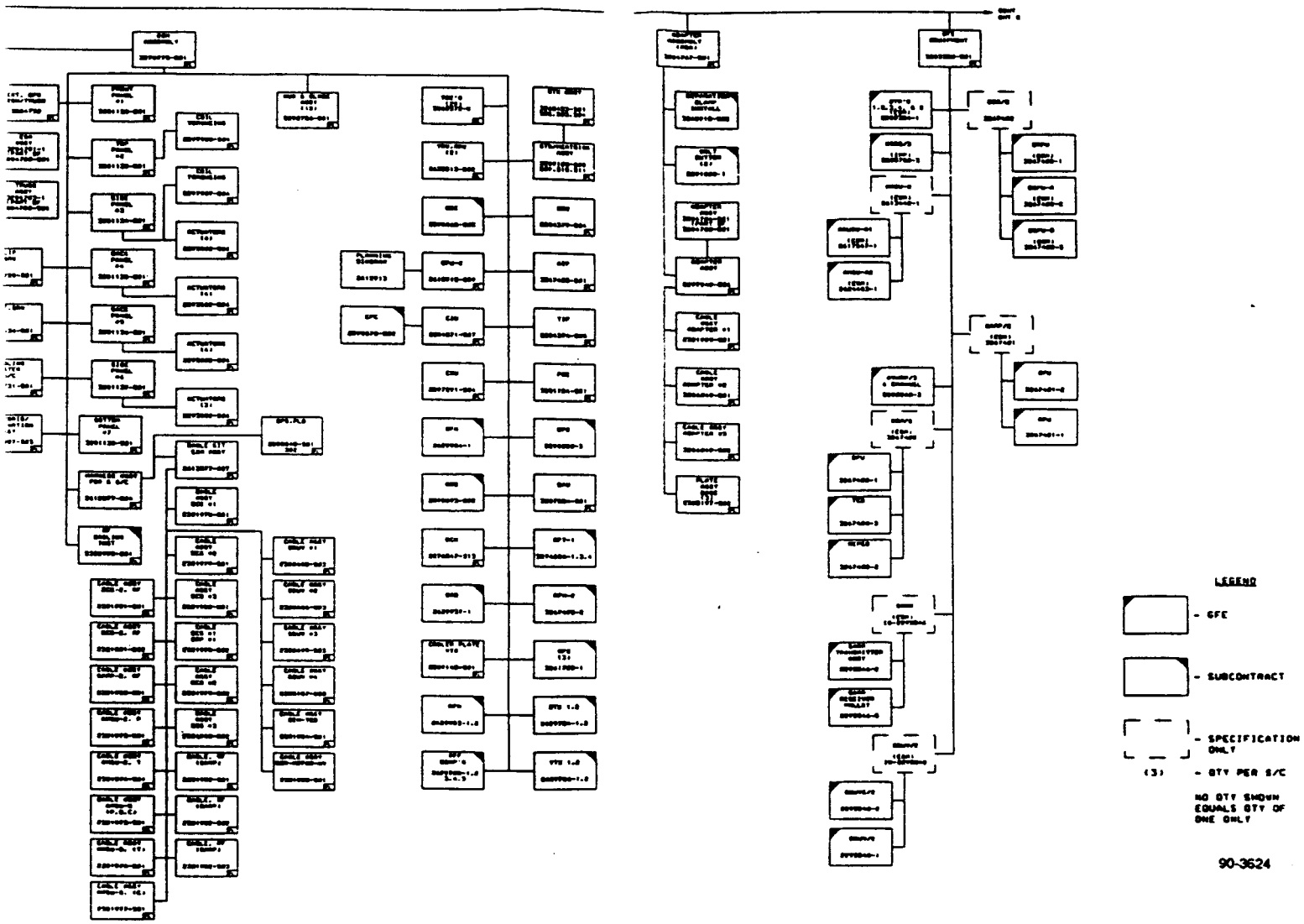

Figure 3.2.1-1a. Equipment Family Tree (Sheet 1 of 2)

THE FOLLOWING DRAWING IS ON THE NEXT TWO PAGES.

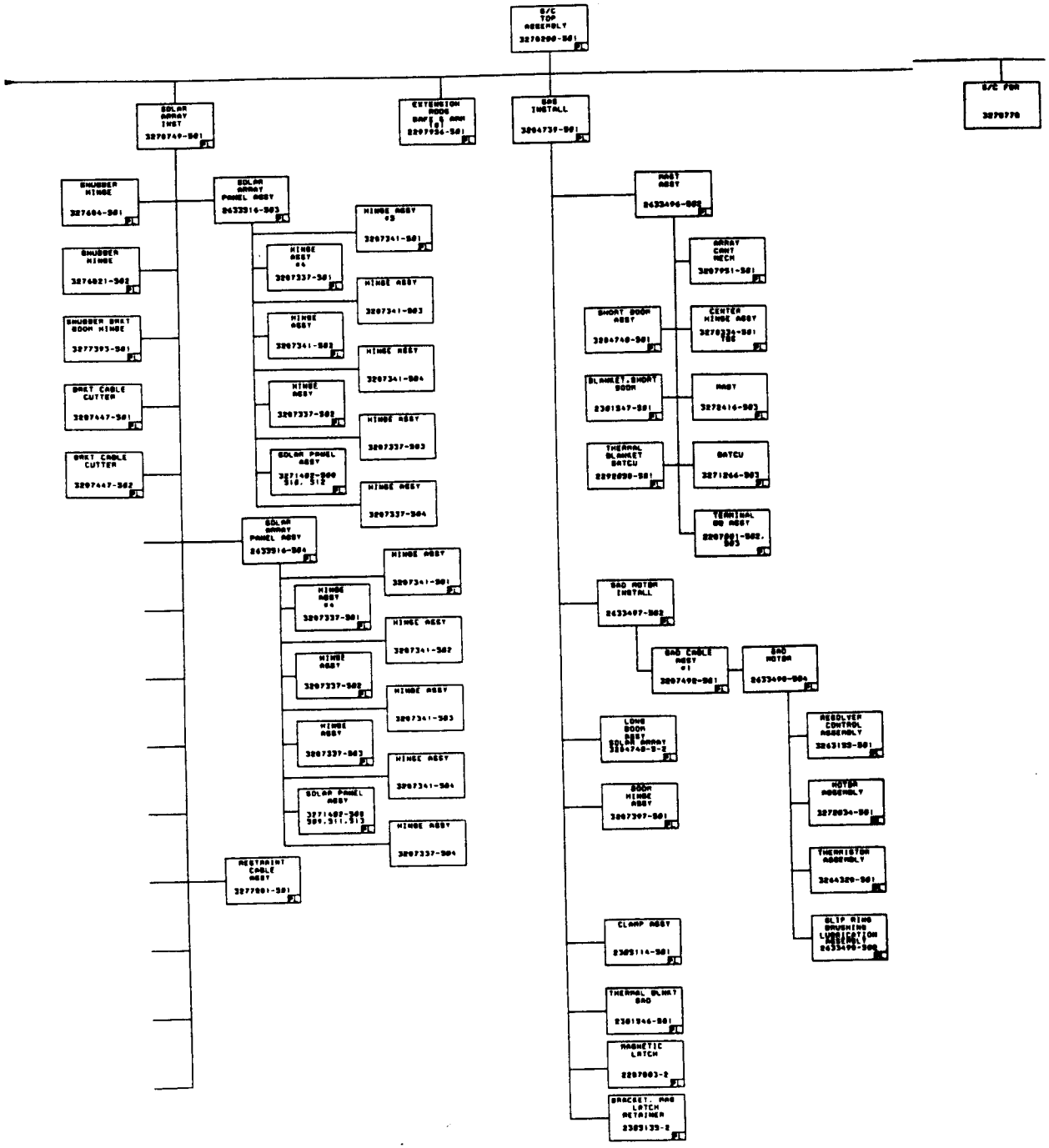
S/C TOP ASSEMBLY 3270200-501
S/C PDR 3270770
SOLAR ARRAY INST 3270749-501
EXTENSION RODS BAY 1 & ARM 1,2 3207936-501
SAD INSTALL 3204739-501
SNUBBER HINGE 3276604-501
SNUBBER HINGE 3276021-502
SNUBBER BRKT BOOM HINGE 3277393-501
BRKT CABLE CUTTER 3207447-501
BRKT CABLE CUTTER 3207447-502
SOLAR ARRAY PANEL ASSY 2633316-503
HINGE ASSY #3 3207341-501
HINGE ASSY #4 3207337-501
HINGE ASSY 3207341-503
HINGE ASSY 3207341-502
HINGE ASSY 3207341-504
HINGE ASSY 3207337-502
HINGE ASSY 3207337-503
SOLAR PANEL ASSY 3271402-500 510, 512
HINGE ASSY 3207337-504
SOLAR ARRAY PANEL ASSY 2633316-504
HINGE ASSY 3207341-501
HINGE ASSY #4 3207337-501
HINGE ASSY 3207341-502
HINGE ASSY 3207337-502
HINGE ASSY 3207341-503
HINGE ASSY 3207337-503
HINGE ASSY 3207341-504
SOLAR PANEL ASSY 3271402-508 509,511,513
HINGE ASSY 3207337-504
RESTRAINT CABLE ASSY 3277001-501
MAST ASSY 2633496-502
ARRAY CANT MECH 3207951-501
SHORT BOOM ASSY 3204740-501
CENTER HINGE ASSY 3270334-501 TBC
BLANKET, SHORT BOOM 2301547-501
MAST 3278416-503
THERMAL BLANKET BATCU 2292090-501
BATCU 3271244-503
TERMINAL BD ASSY 2207001-502, 503
SAD MOTOR INSTALL 2633497-502
SAD CABLE ASSY #1 3207498-501
SAD MOTOR 2633490-504
RESOLVER CONTROL ASSEMBLY 3263193-501
MOTOR ASSEMBLY 3278034-501
THERMISTOR ASSEMBLY 3264320-501
SLIP RING BRUSHING LUBRICATION PANEL 2633490-505
LONG BOOM BRKT SOLAR ARRAY 3204740-5-2
BOOM HINGE ASSY 3207307-501
CLAMP ASSY 2305114-501
THERMAL BLNKT SAD 2301546-501
MAGNETIC LATCH 2207003-2
BRACKET, MAG LATCH RETAINER 2305133-2

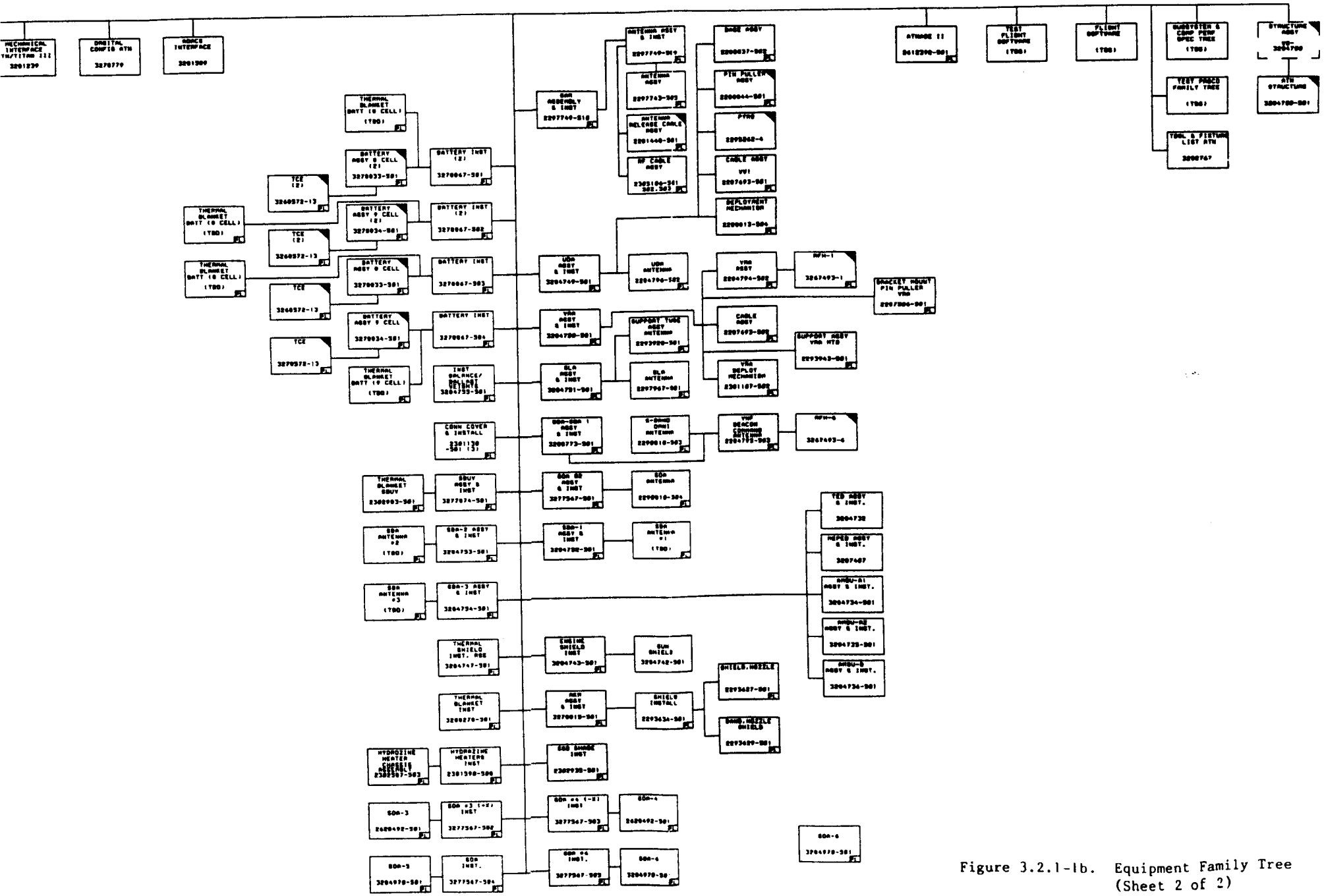

Figure 3.2.1-1b. Equipment Family Tree (Sheet 2 of 2)

Blank Page

Drawing ~~72~~

~~70~~ #73

Blank Page

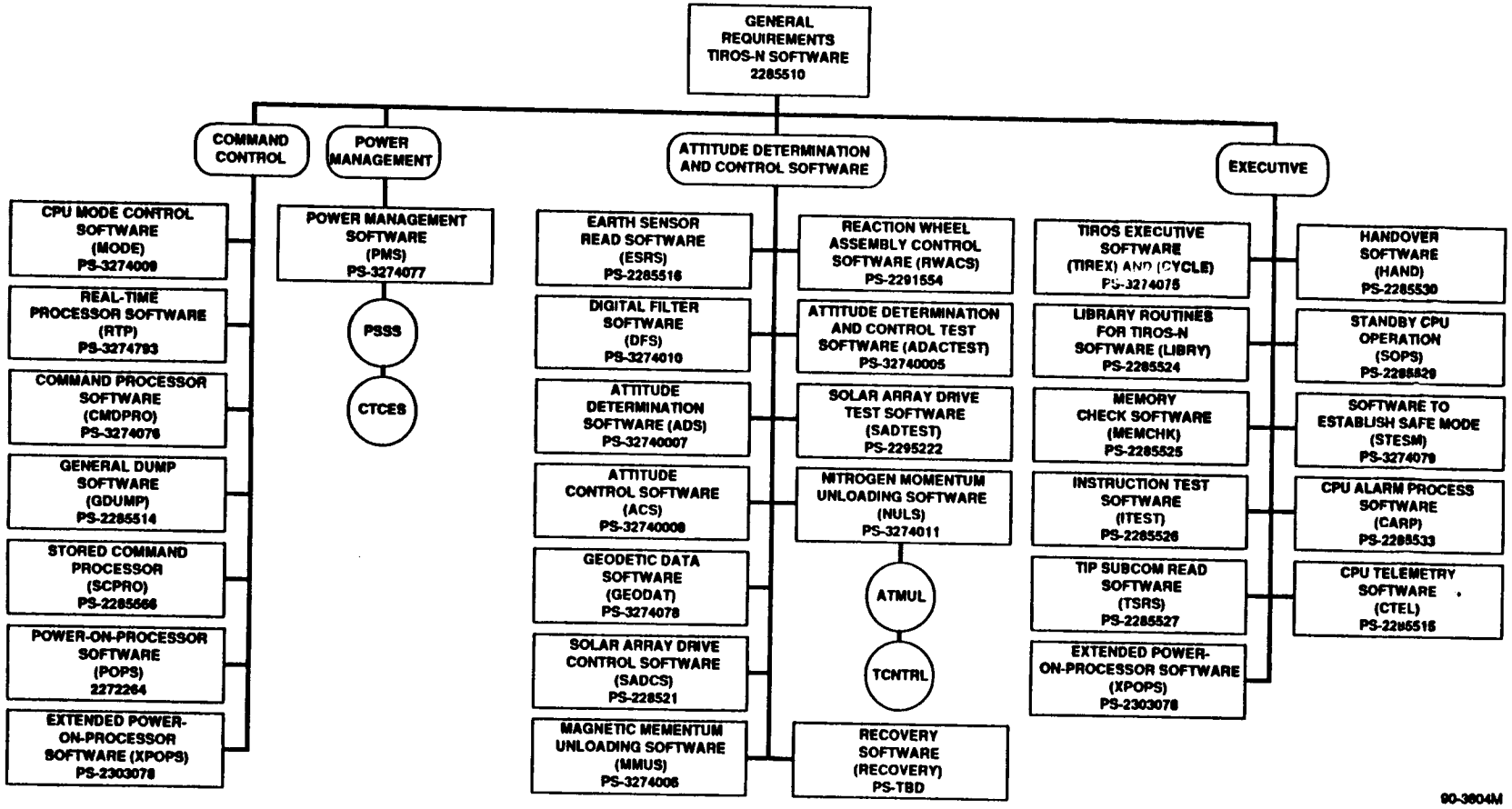

Figure 3.2.2-1. Software Family Tree

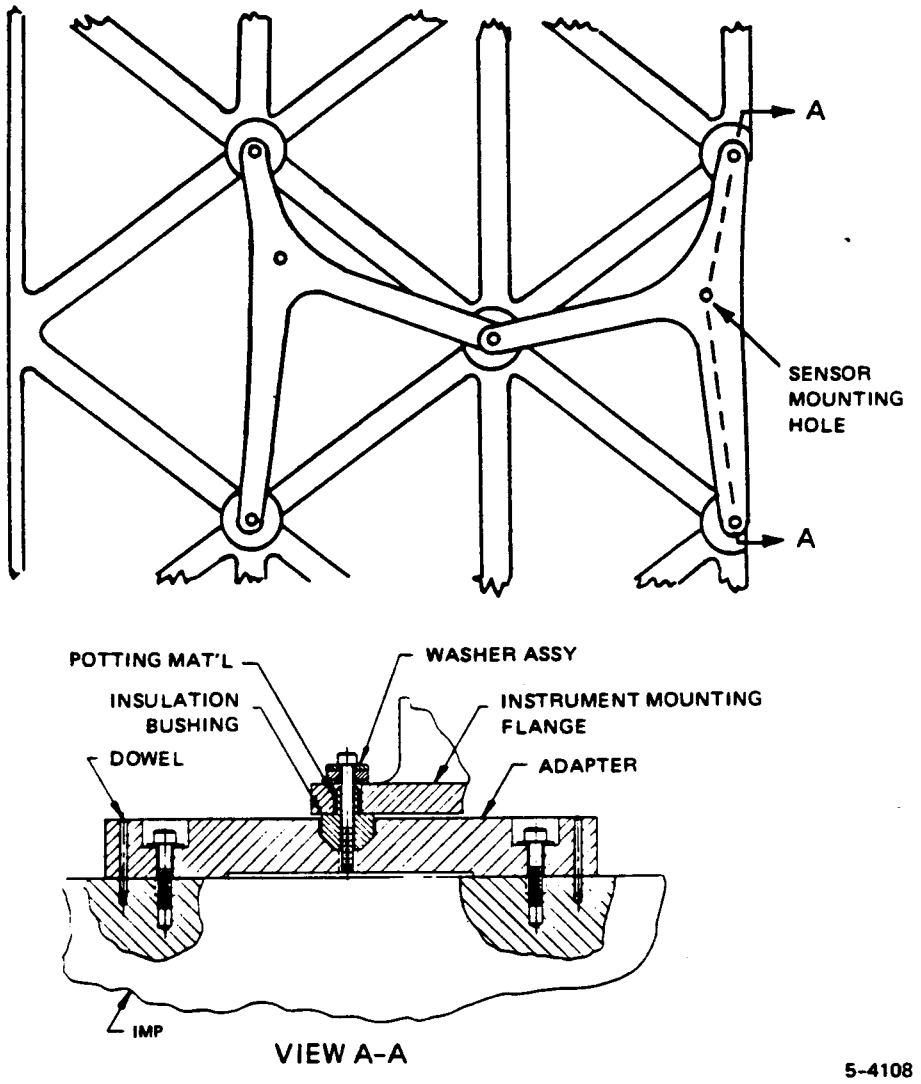

Figure 3.3.1-1. Sensor IMP Mounting

The majority of the alignment requirements exist in the orbital mode of operation. The GFE sensors requiring alignment to the primary reference frame are the AVHRR/3, AMSU-A1, SBUV/2 and HIRS/3. AMSU-A2 and AMSU-B will be aligned to the AMSU-A1 in order to meet the AMSU in-orbit co-registration requirement. The orbital attitude control equipment requiring alignment are the ESA, IMU, and SSD. Previous analysis has shown that the REA's magnetic coils, antennas, and SEM instruments can meet 1° - 2° alignment requirements without optical measurements if the spacecraft body alignments are maintained.

The spacecraft system requirements specify that the spacecraft reference axes be maintained within ±0.1 degree of the local geodetic reference and the AVHRR/3 optical axes within ±0.1 degree of the spacecraft reference axes to eliminate ground data processing.

The AVHRR/3 has the tightest alignment requirement of 0.1° between the AVHRR/3 optical axes and the spacecraft primary axes. The in-orbit alignment requirement between the AMSU-A1 optical axes and the spacecraft primary axes is 0.23°. AMSU-A2 and AMSU-B each have an in-orbit alignment requirement of 0.30° between their optical axes and the spacecraft primary axes. The alignment requirements for the SBUV/2 and HIRS/3 is 0.5°. The spacecraft mechanical tolerances are such that the AVHRR/3 may require shimming after optically determining its alignment.

The AMSU-A1 instrument will require shimming about the X and Y axes to meet the initial alignment placement requirement of 0.05 degree with respect to the ESA. AMSU-A2 and AMSU-B will require shimming about the Y and Z axes and rotating about the X axis to align them to AMSU-A1 to within 0.05 degree.

Alignment of the optical axes to the sensor reference axes is determined from the instrument data package for that sensor. The sum of this value and the reference axes to spacecraft primary axes must be less than the defined initial position.

The system requirements for ascent are that the IMU be aligned with the propulsive units on the spacecraft and that its azimuth position relative to true North at the time of liftoff be known. A 1.0° alignment requirement for the spacecraft axes to IMU is satisfactory for the spacecraft propulsive units. This requirement is met by maintaining mechanical tolerances.

To determine the IMU's azimuth position relative to true North, accurate knowledge of the Porro Prism alignment is required. This knowledge requirement is 0.017° azimuth between the Porro Prism and IMU cube for any elevations around 18°. Placement is required to assure that the Porro Prism can be viewed accurately from the theodolite pad. The line of sight of the Porro Prism is 5° 53" from +Y towards -X and 37° 11" from -X towards +Z. The top roof axis should also be aligned approximately parallel to the spacecraft Y-X plane.

In order to make the AVHRR/3 installation more positionally repeatable, the mounting adapter has tapered holes to accept a tapered bushing. When the AVHRR/3 yaw adjustment has been made, potting compound is injected onto the space between the tapered bushing and the oversized hole in the AVHRR/3 foot. Subsequent removal of the AVHRR/3 takes the tapered bushing with it and allows precise positioning when the sensor is reinstalled. AMSU-A1 and -A2 have alignment pins for position repeatability.

3.3.2 ELECTRICAL INTERFACES

The ATN-KLM spacecraft operates with an unregulated bus (battery) voltage of 18.7 volts to 26 volts. Various units require power from the regulated PSE +28 volt bus, the +28V PSE pulse load bus, the +28V PSE instrument analog telemetry bus, the +5 volt bus generated by the CIU and XSU, and the 10 volt bus in the CPC. A power summary of the individual units is included in Section 4.6. In addition to the power interfaces between spacecraft units, there are command and control signals which cause units to operate and there are telemetry signals monitoring whether the unit operation is proper or not.

3.3.2.1 Harness

To organize the spacecraft harness, five categories of signals were established: (1) power and control signals, (2) high level signals, (3) low level signals, (4) electro explosive device signals, and (5) high frequency signals. These signals are functionally grouped into three harness bundles, wherever feasible, and routed for minimum mutual inductance: (a) power and control, (b) telemetry, (c) ordnance.

Many spacecraft connectors are lightweight metal shell Microdot connectors. These are supplied with short wires already attached to the plugs and sockets. Connection to the harness is through the use of solder splicing contained within heat shrinkable tubing. High reliability MIL-C-24308, MS27500 and NB(X)E series connectors are also utilized. Except as noted below, the minimum wire size used in the harness is AWG #24. ESM panels 3, 4, 5, and 6 and TCE heater and louver circuits use #26 wires potted to the panel.

The RFI-sealed shielding properties of the ESM are such that minimum harness shielding is necessary within the ESM. Major exceptions are fast clock TRIAX and data lines. For immunity to spurious signals, the ordnance harness uses shielded twisted pairs. RF output lines use flexible metal coaxial cables for maximum radiation efficiency.

Necessary wiring external to the ESM is RFI-beaded and covered with shield braid for EMI considerations and heat reflective tape for thermal considerations. Thermal soakback from the motor requires the RSS cables, which present large areas subject to this effect, to be covered with silver heat reflective tape and additional thermal blankets if necessary. External cables are designed for ease of installation and removal.

Throughout the harness, current loop areas are minimized whenever possible by routing return lines next to outgoing lines so as to reduce dipole torquing. Interconnecting wires on the solar array are considered an integral part of the array, not part of the harness.

3.3.2.2 Control Signals

Spacecraft control signals consist of clock or timing signals, command signals, and other control signals. There are two types of command signals: pulse discretes and level discretes. Each control signal is a single unbalanced bi-level which is transferred from and received by either standard COS/MOS CD4000 series or TTL SN54 (or equivalent) family logic. Each control signal is referenced to its interface ground, which in turn returns to spacecraft single point ground.

The standard is full COS/MOS to COS/MOS interfacing with ON (Data 1) = 0.0 $\pm$0.2 volts and OFF (Data 0) = 10.0 $\pm$0.7 volts referenced to spacecraft ground. For the Sun Sensor and Digital Tape Recorders, COS/MOS to TTL interface circuits (ON = 0.0 $\pm$0.3 volts, OFF = 5.0 $\pm$0.3 volts) or TTL to COS/MOS (ON = 0.0 +1.3, -0.2, OFF = 10.0 $\pm$0.7 volts) referenced to spacecraft ground are used.

The interfaces can be grouped into three categories: high clock rate, fast, and slow. Clock signals ranging from 2Hz to 2.6616 MHz result from frequency synthesis and frequency division in the CIU and XSU. The clock distribution paths are shown in Figure 3.3.2-1. The primary clock source is the 5.12 MHz RXO signal. Synchronization signals with periods ranging from 0.1 second to 256 seconds result from frequency division of the above clocks in the CIU, IMU, and TIP. They are also shown in Figure 3.3.2-1. The AVHRR/3 line sync tracks the AVHRR/3 scan motor position which is synchronous with one of the above clocks.

Clocks with rates above 100 kHz fall under the "high clock rate" interface category. "Fast" applies to interfaces transferring signals with pulse widths less than 250 microseconds or where symmetry is required. Under this category are digital A control signals and control signals between the CIU and TIP and between the TIP and MIRP. "Slow" interfaces are any other interfaces powered by the spacecraft +10 volt bus, with pulse widths greater than 250 microseconds, but not requiring symmetry. The two types of slow commands are level discrete and pulse discrete. For level discrete commands, the ON level, when activated, is applied full time until commanded OFF. Pulse discretes are issued as 0.5 second to 1.5 second pulses from the CIU or 60 $\pm$ 5 millisecond pulses from the CIU Annex. The XSU supplies 5V power to the DTRs.

Receiving circuits for all noise-sensitive signals, including (as a minimum) all slow interface clocks and TTL interface clocks, use feedback latching to prevent oscillation in the receiving unit.

Figures 3.3.2-2 through 3.3.2-8 show the standard interfaces and their characteristics. Table 3.3.2-1 is ambient temperature test data for the interface circuits.

3.3.2.3 Telemetry Signals

Verification that selected equipment is operating within prescribed limits is the function of the telemetry. The telemetry format includes digital and analog housekeeping telemetry, digital A telemetry (low-rate instrument data), time code, CPU memory dump, CPU telemetry, and command verification as shown in Figures 3.3.2-9 through 3.3.2-12 for TIP data and in Figure 3.3.2-13 for AIP data.

Housekeeping telemetry is used to determine if operation of a unit is nominal, to predict unit failures, and to diagnose failures. Housekeeping telemetry can be retrieved in one of two modes: orbital mode, which monitors parameters relative to on-orbit operation, and boost mode, which concentrates on those parameters pertaining to the boost phase of the mission. Digital housekeeping telemetry (also referred to as discrete, bilevel, or digital B) consists of single bit digital status and operation monitors. Analog housekeeping telemetry points monitor key temperatures and voltages throughout the spacecraft. Table 3.3.2-2 gives the Analog and Digital B telemetry characteristics.

Certain voltages and temperatures, as well as cold space and hot target calibration levels in the instruments, are digitized at the source. Under control of the TIP (or AIP) sequencer PROM, they are output to TIP (or AIP) using digital A control signals. There the data is multiplexed into the desired TIP (or AIP) bit stream. The digital A words are transferred 8 bits at a time.

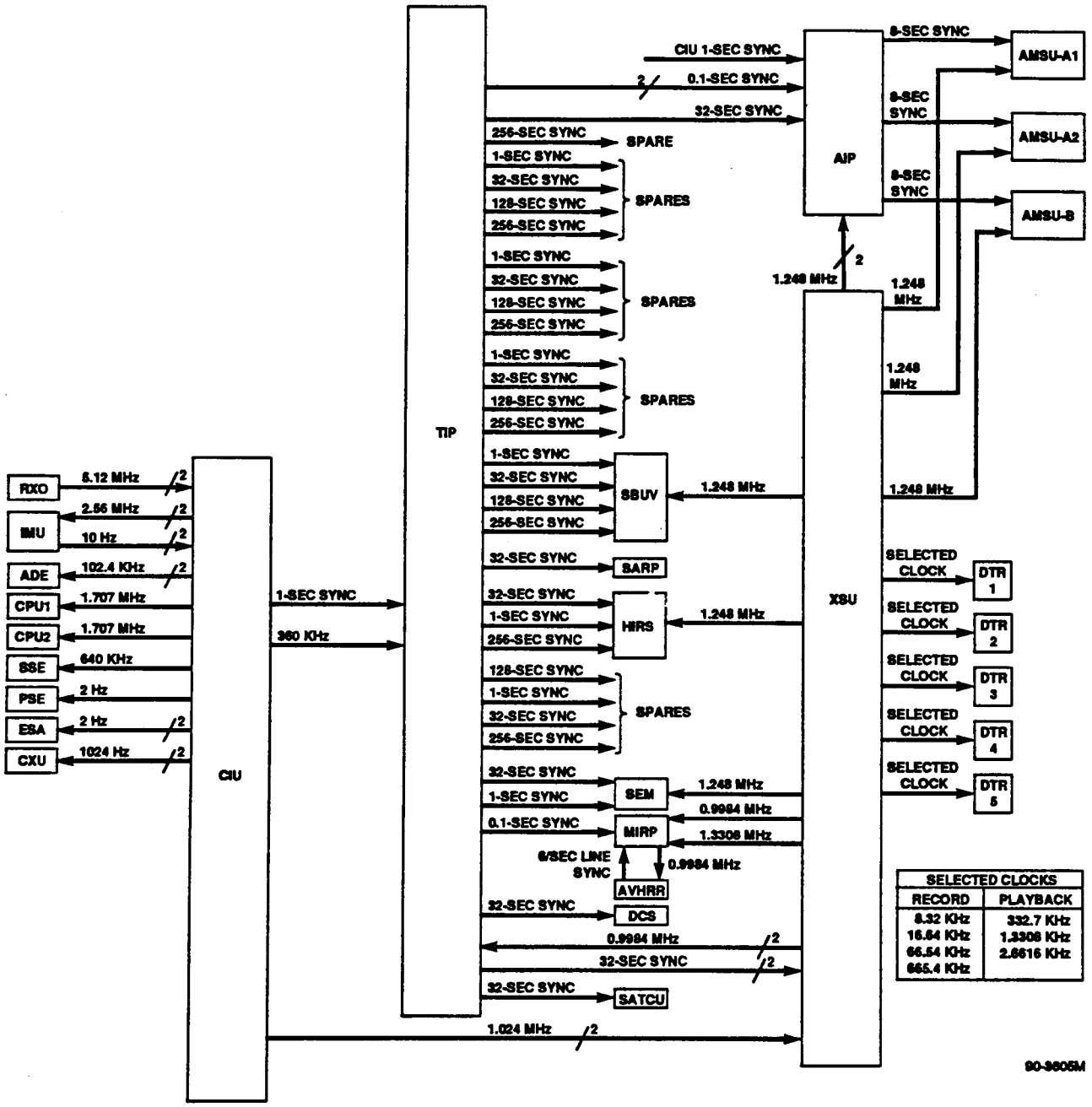

Figure 3.3.2-1. Clock and Sync Distribution

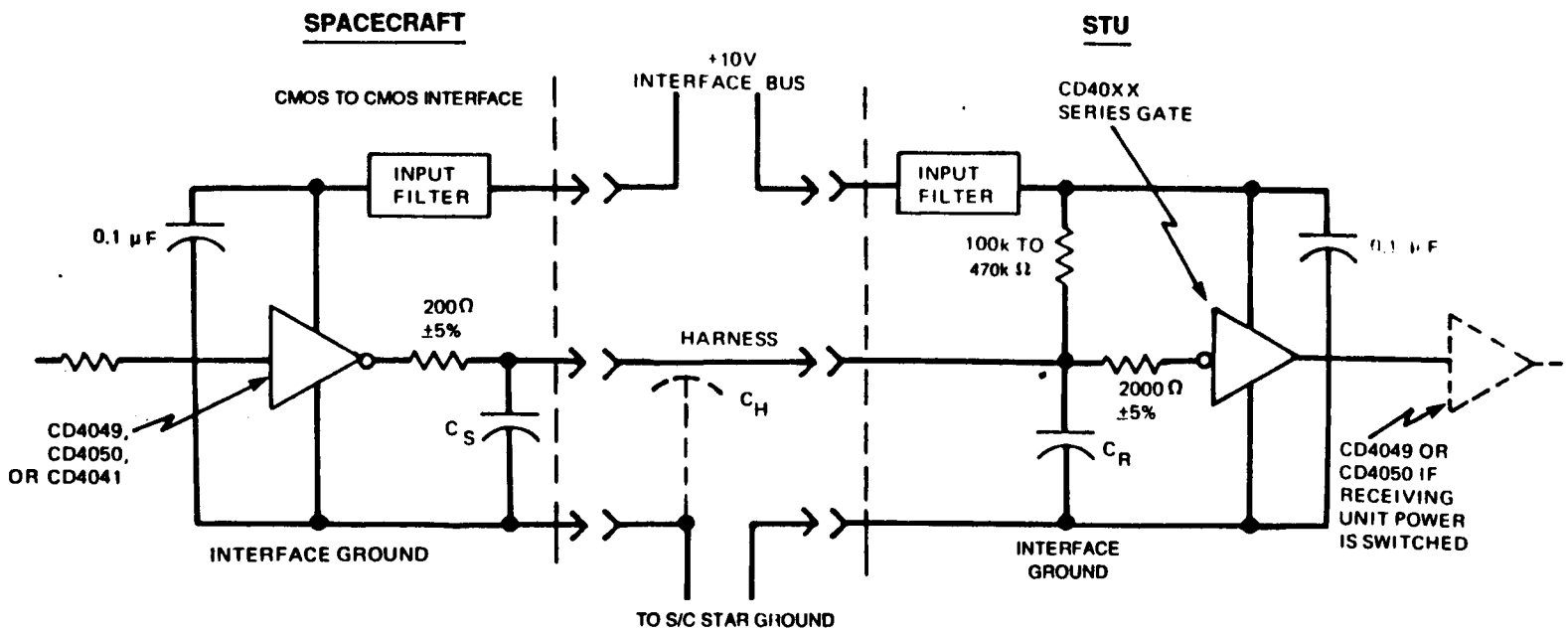

CMOS TO CMOS INTERFACE CHARACTERISTICS					
CKT TYPE	C_S (pF)	C_R (pF)	TR/TF MIN (μs)	TR/TF MAX (μs)	TD MAX (μs)
FAST	270 ±5%	470 ±5%	0.3	2.0	1.0

NOTE: MAX VALUES INCLUDE 500 pF CABLE CAPACITY (C_H).

8-4630

Figure 3.3.2-2. CMOS to CMOS Interface

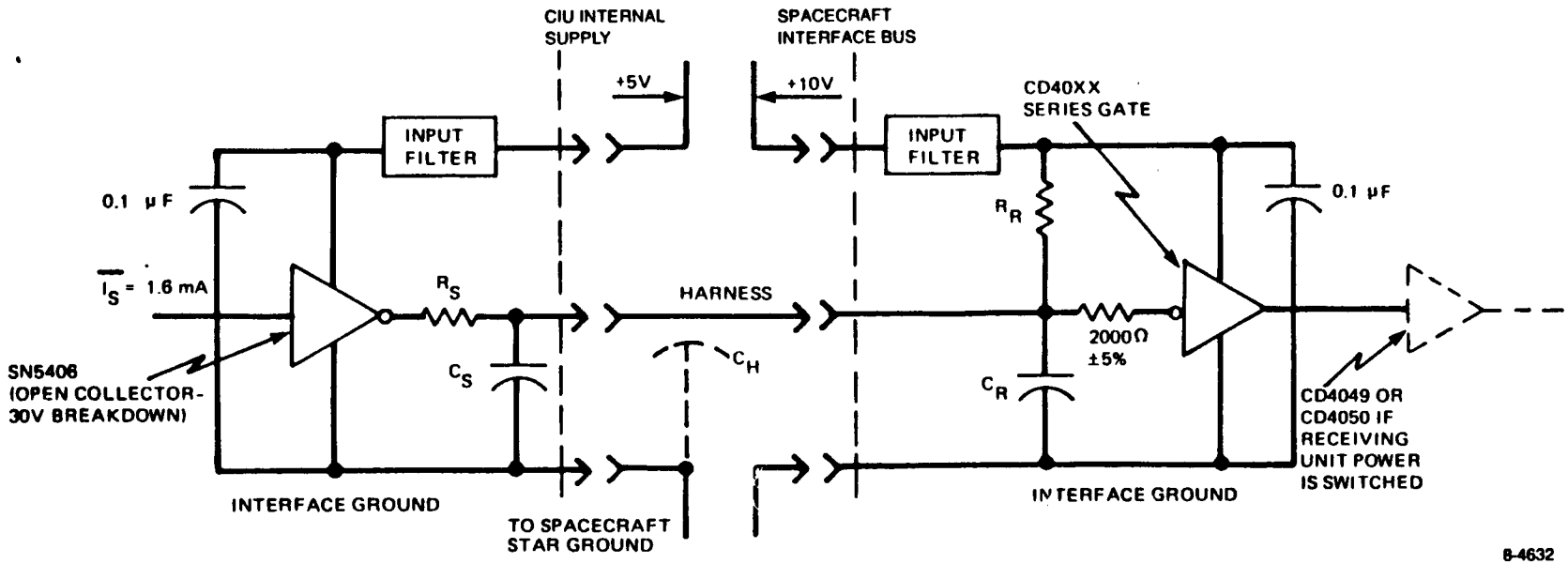

NOTE: USE OF THIS INTERFACE REQUIRES TIROS PMO APPROVAL

TTL TO CMOS INTERFACE CHARACTERISTICS										
CKT TYPE	C_S (pF)	R_S (OHMS)	C_R (pF)	R_R (OHMS)	TR MAX (μs)	TR MIN (μs)	TF MAX (μs)	TF MIN (μs)	TD MAX (0 TO +10V)	TD MAX (+10V TO 0)
SLOW	5600 ±10%	200 ±5%	5600 ±10%	3000 ±5%	100	80	7.0	5.0	60 μs	5.0 μs
FAST	560 ±5%	39 ±5%	470 ±5%	620 ±5%	3.0	1.5	0.5	0.1	1.5	0.5

NOTE: MAX VALUES INCLUDE 500 pF CABLE CAPACITY (C_H)

Figure 3.3.2-3. TTL to CMOS Interface

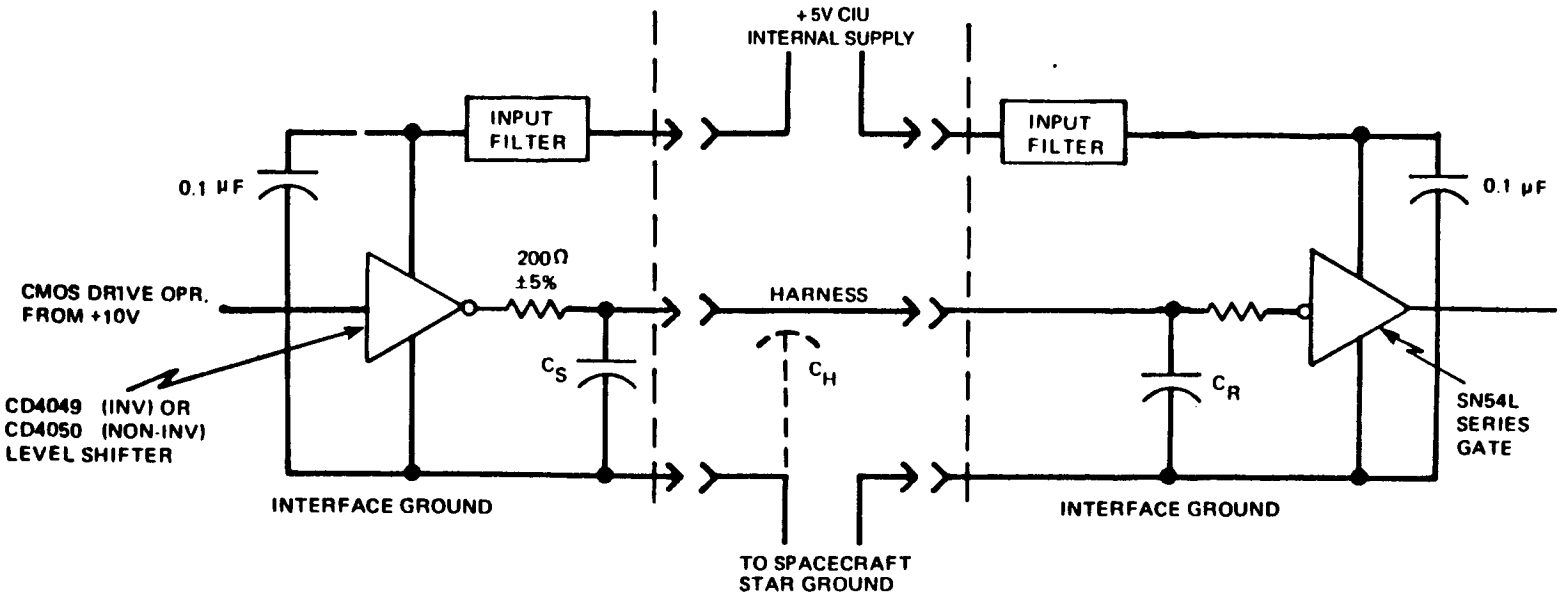

NOTE: USE OF THIS INTERFACE REQUIRES TIROS PMO APPROVAL

CMOS TO LPTTL INTERFACE CHARACTERISTICS						
CKT TYPE	C_R (pF)	C_S (pF)	TR MAX (μs)	TF MAX (μs)	TD MAX (+5V TO 0) μsec	TD MAX (0 TO +5V) μsec
SLOW	5600 ±10%	5600 ±10%	38.0	11.0	10.0 μs	11.0 μs
FAST	470 ±5%	270 ±5%	3.0	1.0	1.0	1.0

NOTE: MAX VALUES INCLUDE 500 pF CABLE CAPACITY (C_H)

8-4679

Figure 3.3.2-4. CMOS to LPTTL Interface

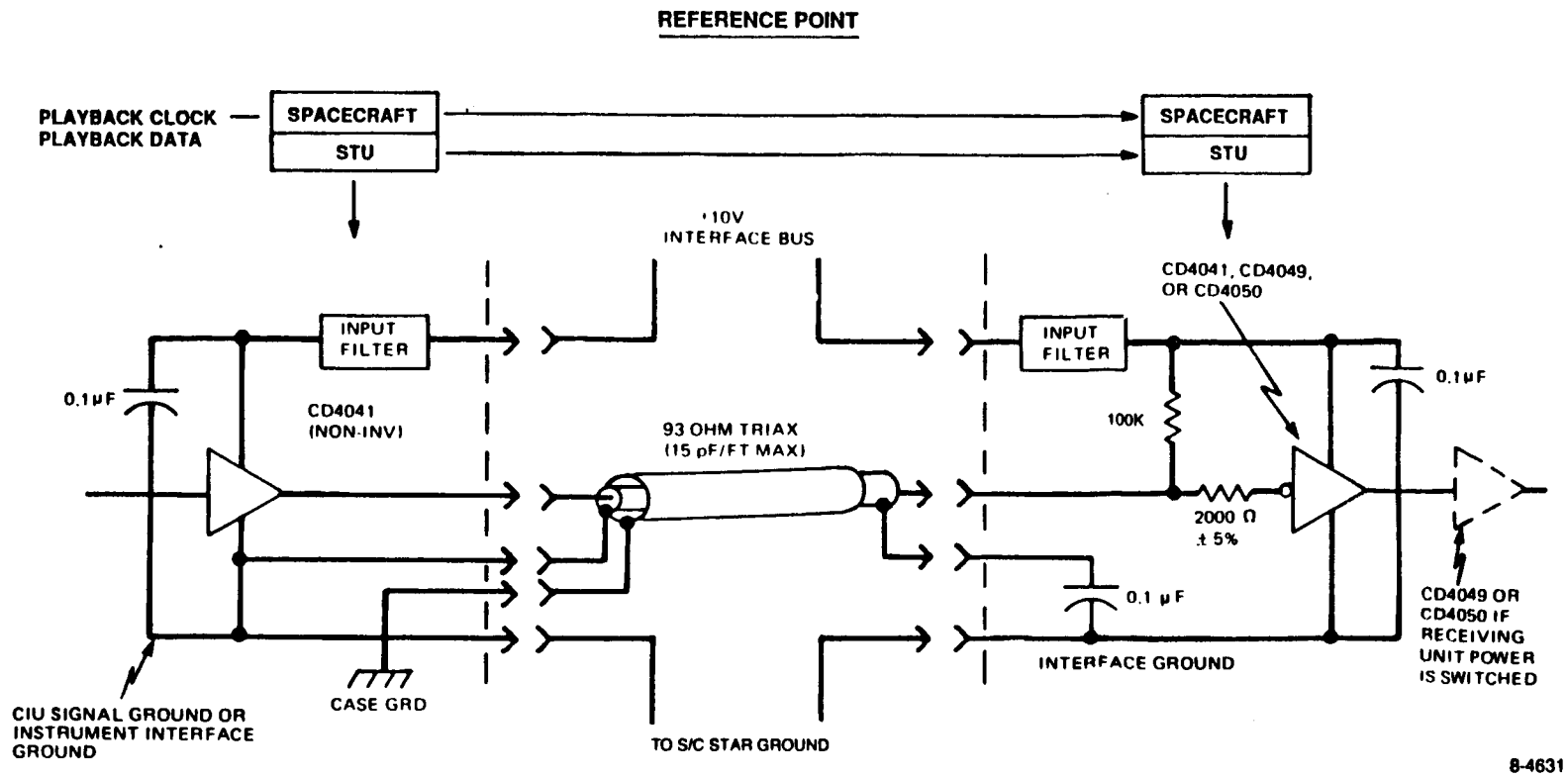

Figure 3.3.2-5. CMOS to CMOS High Speed Interface

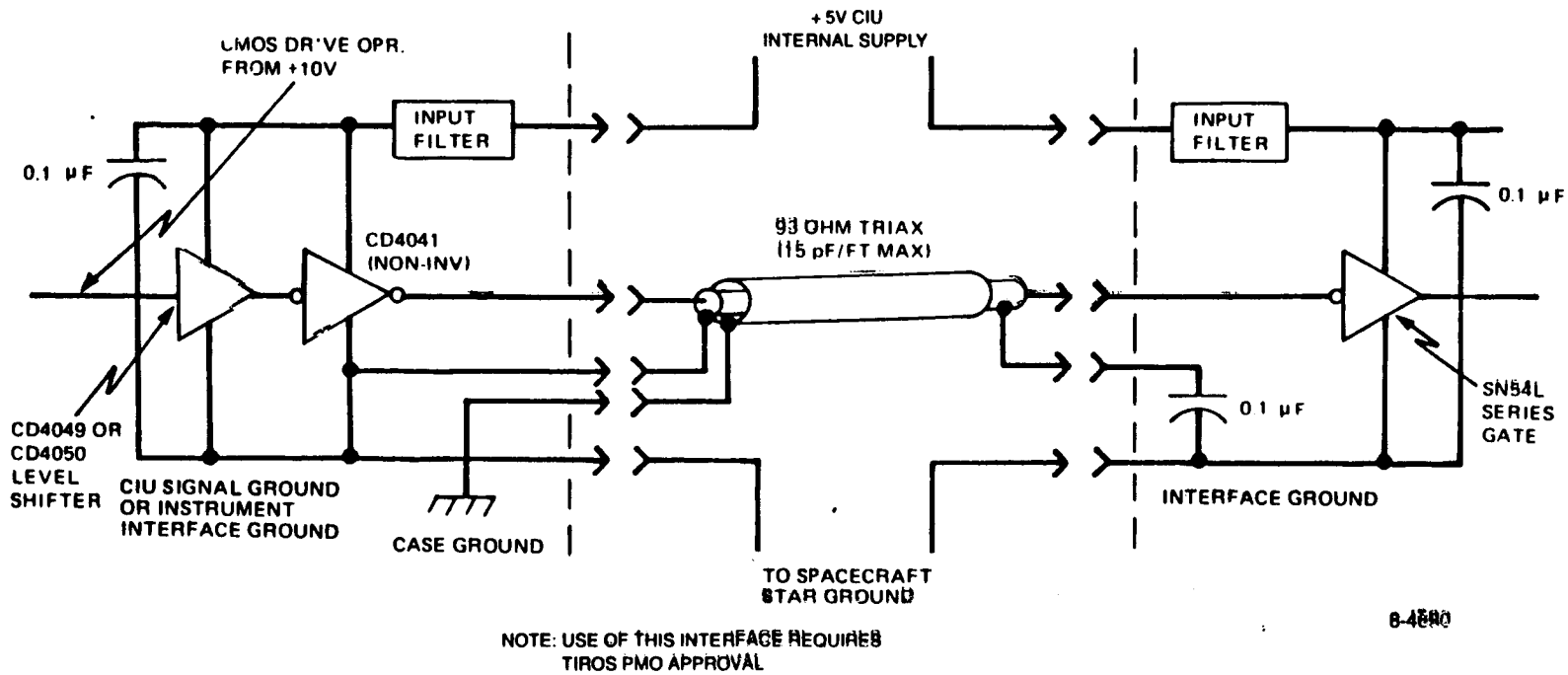

Figure 3.3.2-6. CMOS LPTTL High Speed Interface

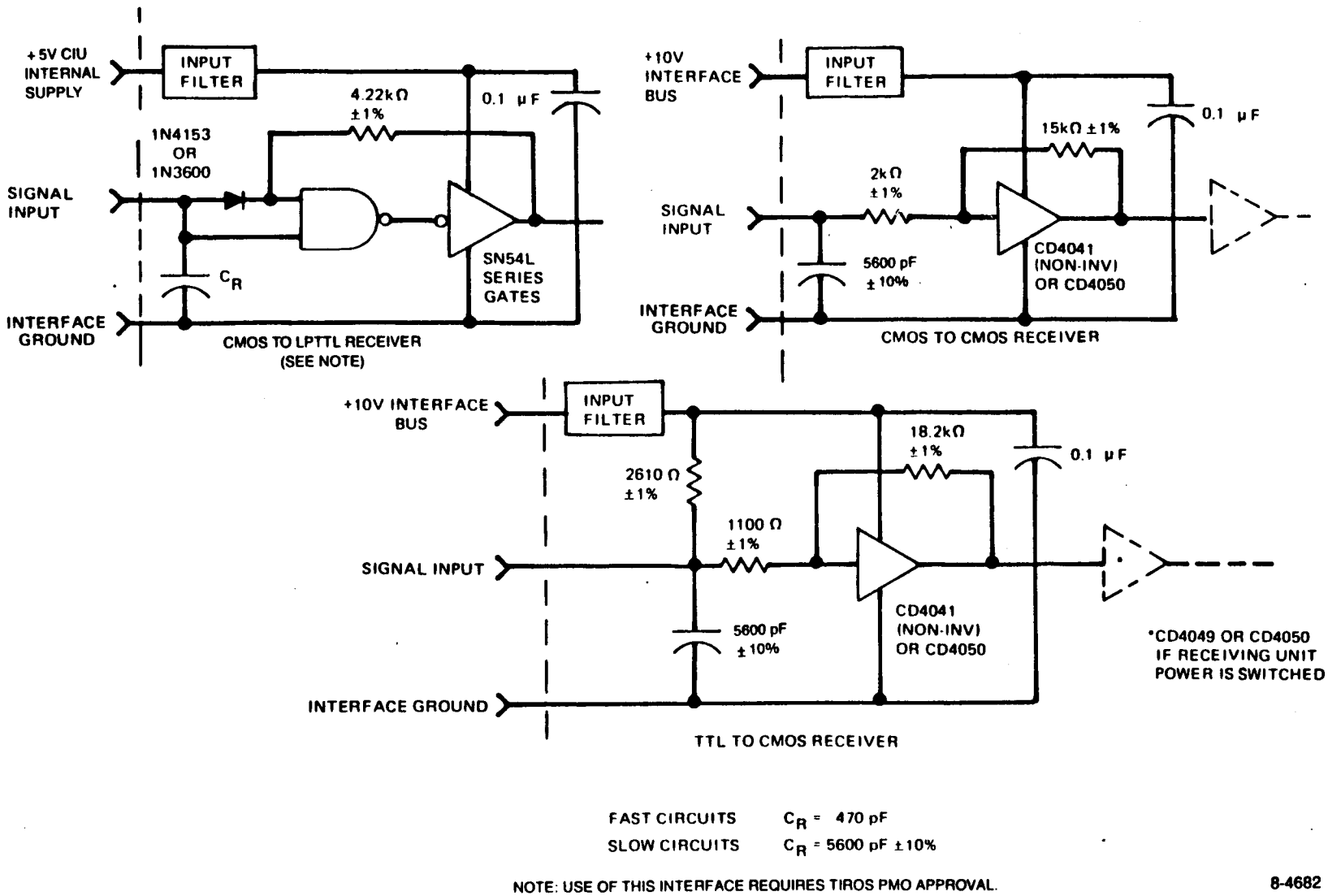

FAST CIRCUITS C_R = 470 pF
SLOW CIRCUITS C_R = 5600 pF ±10%

NOTE: USE OF THIS INTERFACE REQUIRES TIROS PMO APPROVAL.

8-4682

Figure 3.3.2-7. Interface Receiving Circuit with Hysteresis

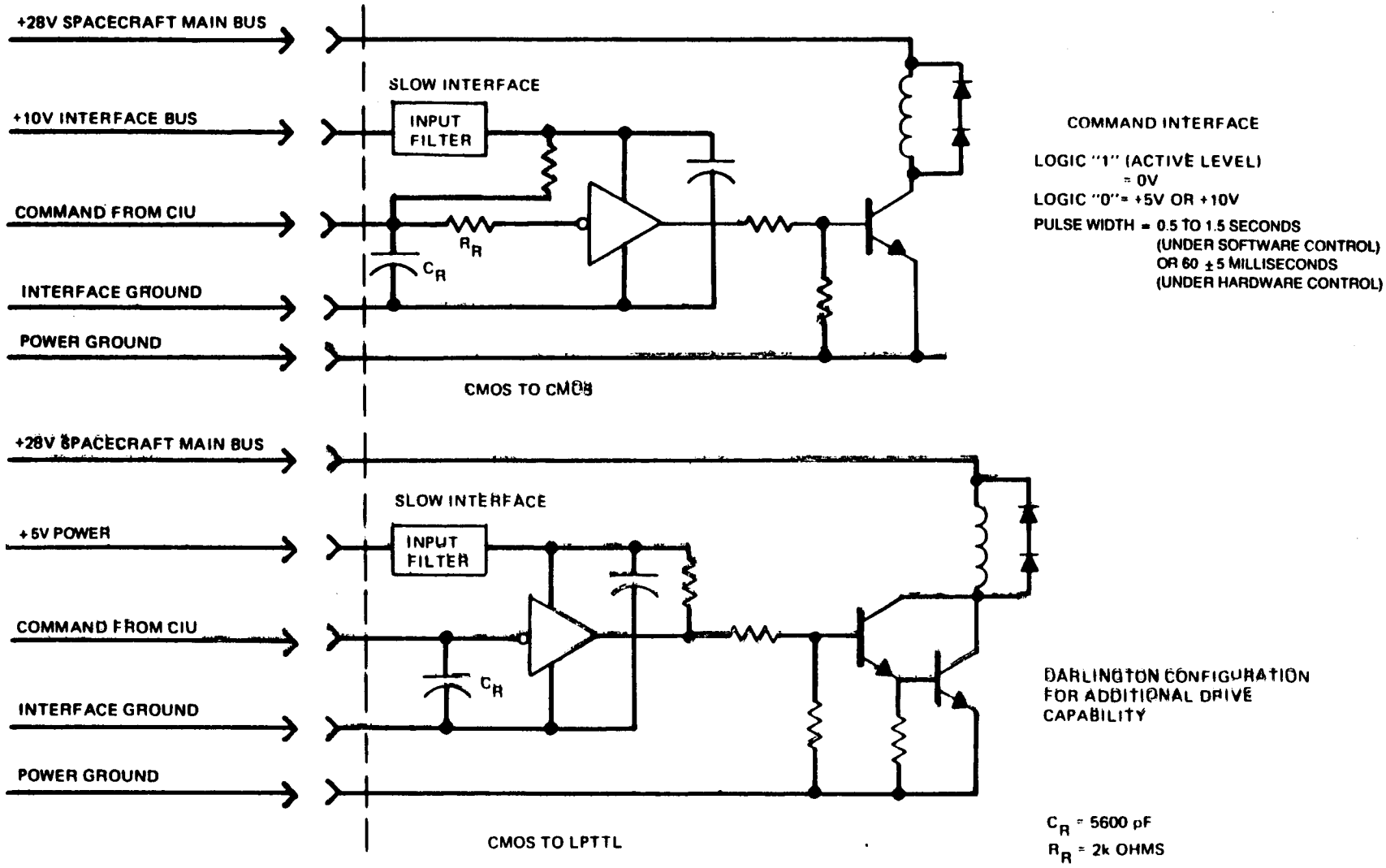

NOTE: USE OF THE 5 VOLT INTERFACE REQUIRES APPROVAL OF THE TIROS PMO.

Figure 3.3.2-8. Typical Relay Drive Configurations

TABLE 3.3.2-1. INTERFACE TEST DATA

CKT Type	TR (μSEC)	TF (μSEC)	TD (1-0) (μSEC)	TD (0-1) (μSEC)
• CMOS to CMOS				
Slow	7.0 (12.0)	7.0 (12.0)	3.3 (8.0)	2.05 (8.0)
Fast	0.8 (2.0)	0.5 (2.0)	0.54 (1.0)	0.34 (1.0)
High Speed	0.04	0.04	0.2	0.2
• TTL to CMOS				
Slow	85 (100)	5.0 (7.0)	32 (60)	1.8 (5.0)
Fast	1.7 (3.0)	0.15 (0.5)	0.68 (1.5)	0.1 (0.5)
• CMOS to LPTTL				
Slow	7.6 (38.0)	4.6 (11.0)	4.0 (11.0)	1.6 (10.0)
Fast	0.9 (3.0)	0.45 (1.0)	0.5 (1.0)	0.24 (1.0)
High Speed	0.12	0.1	0.17	0.14
( ) WORST CASE VALUES				

In orbit mode, housekeeping telemetry is combined with low-rate instrument data in the TIP and output at 8.32 kbps to a beacon transmitter for real time transmission, and to the MIRP to be combined with AVHRR/3 data for real time output, and to be recorded with both LAC and GAC data. The TIP data can also be recorded for playback to a European station during CDA blind orbits. TIP data is combined with AMSU data in the AIP for either real-time or playback transmission.

3.3.2.4 Power and Grounding

Central power distribution is provided by the spacecraft as an unregulated bus and four regulated buses. The unregulated bus is tied directly to the battery and typically varies between 19 and 25.5 volts. This is used primarily for ordnance devices. Primary regulated power is distributed at +28V. This is used for primary power by all spacecraft units. A +28 volt pulse load bus is provided for powering items which are high transient loads, such as stepper motors and heaters. A switched +28 volt bus is provided from the +28 volt main bus in order to power certain telemetry circuits so that temperature telemetry can be obtained even when the instrument is off. Additionally, a regulated interface bus is provided at +10 volts. This is used only to power interface drivers and receivers for the transfer of data and control signals between spacecraft units.

The interface characteristics of the regulated buses are summarized in Table 3.3.2-3.

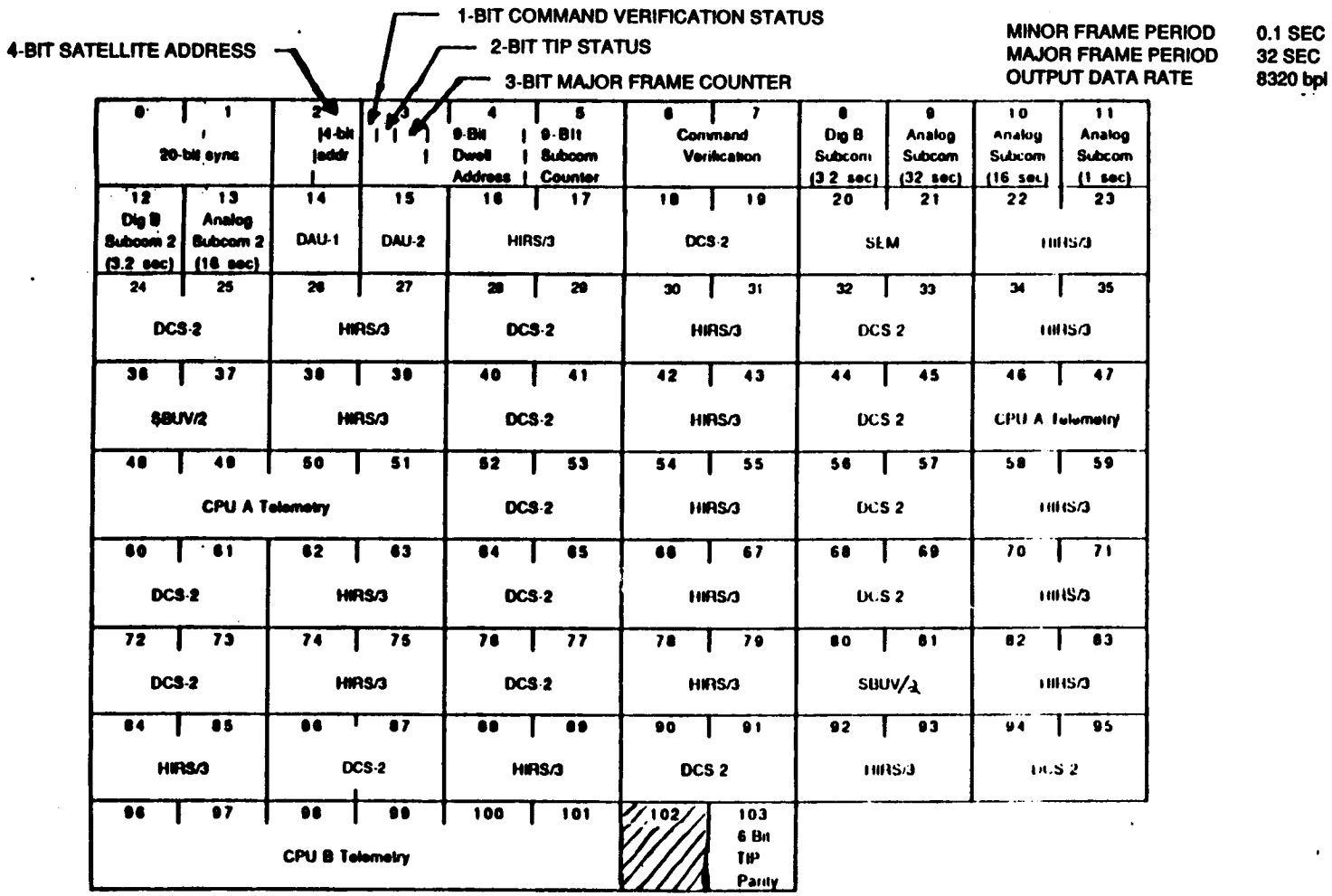

NOTES
- NUMBER IN UPPER LEFT HAND CORNER INDICATES MINOR FRAME WORD NUMBER.
- TIME CODE DATA APPEARS DURING MINOR FRAME "0" WORD LOCATIONS 8 THROUGH 12.
- ///// WORD LOCATIONS ARE SPARE AND CONTAIN CODE 01010101.

90-3606M

Figure 3.3.2-9. TIP Orbital Mode Format - NOAA-KLM

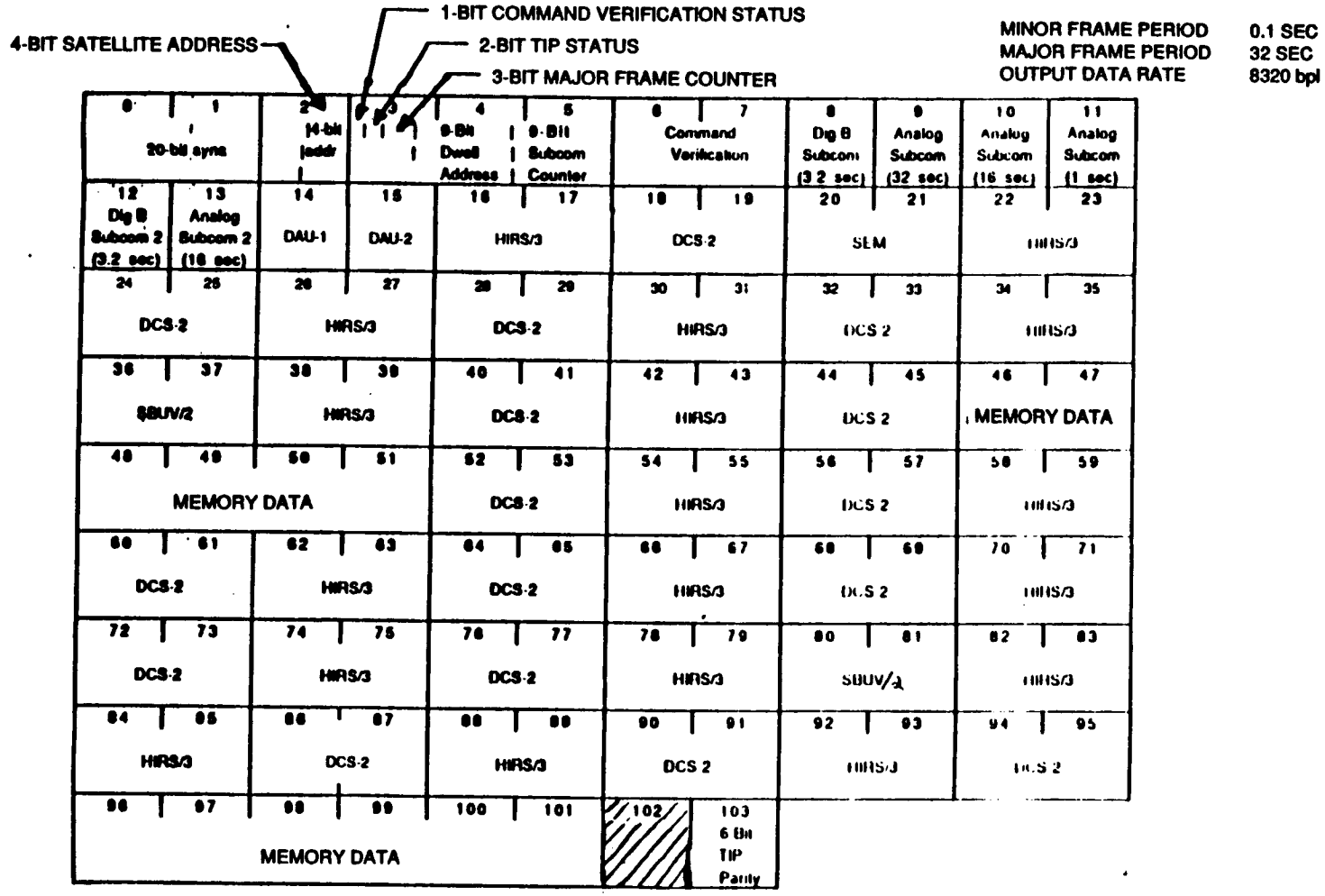

NOTES
- NUMBER IN UPPER LEFT HAND CORNER INDICATES MINOR FRAME WORD NUMBER.
- TIME CODE DATA APPEARS DURING MINOR FRAME "0" WORD LOCATIONS 8 THROUGH 12.
- ///// WORD LOCATIONS ARE SPARE AND CONTAIN CODE 01010101.

90-3607

Figure 3.3.2-10. TIP Dump Mode Format - NOAA-KLM

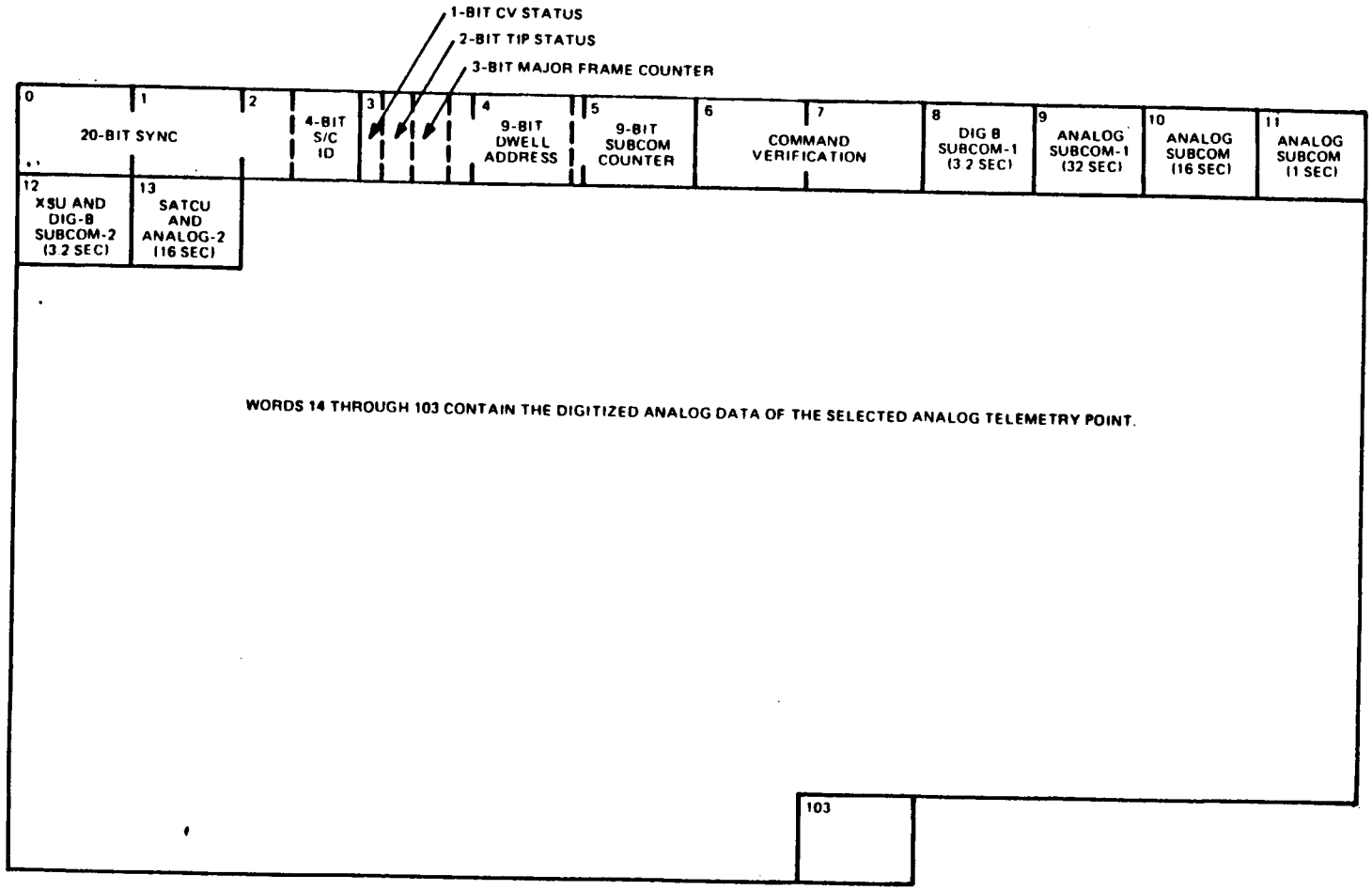

NOTES: 1) NUMBER IN UPPER LEFT HAND CORNER INDICATES MINOR FRAME WORD NUMBER
2) TIME CODE DATA APPEARS DURING MINOR FRAME "0" WORD LOCATIONS 8 THROUGH 12
3) MINOR FRAME PERIOD--0.1 SECOND
MAJOR FRAME PERIOD--32 SECONDS
OUTPUT DATA RATE--8.32 kbps

5-4057

Figure 3.3.2-11. Dwell Mode

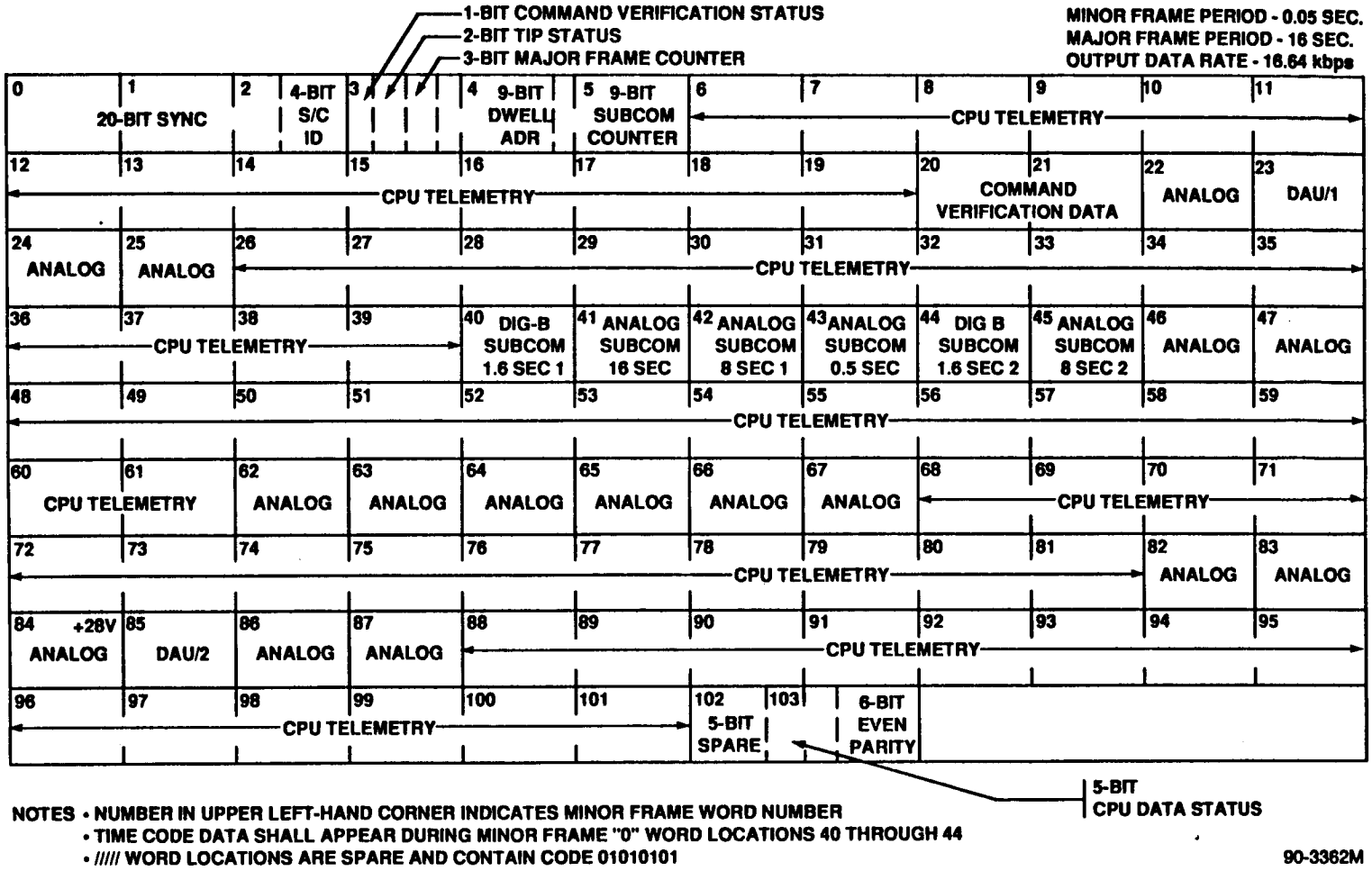

Figure 3.3.2-12. TIP Boost Mode Format for NOAA-KLM

0	1	2	3	4	5	6	7	8	9	10	11	12	13	14	15	16	17	18	19	20	21	22	23		
22-BIT SYNC			///	MINOR FRAME COUNTER (0-79)	SEE NOTE	///////		AMSU-A1 (WORDS 8 THROUGH 33)																	
24	25	26	27	28	29	30	31	32	33	34	35	36	37	38	39	40	41	42	43	44	45	46	47		
AMSU - A1										AMSU - A2 (WORDS 34 THROUGH 47)*															
48	49	50	51	52	53	54	55	56	57	58	59	60	61	62	63	64	65	66	67	68	69	70	71		
AMSU - B (WORDS 48 THROUGH 97)																									
72	73	74	75	76	77	78	79	80	81	82	83	84	85	86	87	88	89	90	91	92	93	94	95		
AMSU - B (WORDS 48 THROUGH 97)																									
96	97	98	99	100	101	102	103	104	105	106	107	108	109	110	111	112	113	114	115	116	117	118	119		
AMSU - B		//////////////////////				6-BIT PARITY AMSU	20-BIT SYNC		4-BIT SATELLITE ADDRESS	SEE NOTE	6-BIT DWELL ADDRESS	SUBCOM COUNTER 9-BITS	COMMAND VERIFICATION		DIG B SUBCOM (3.2 SEC)	ANALOG SUBCOM (32 SEC)	ANALOG SUBCOM (16 SEC)	ANALOG SUBCOM (1 SEC)	DIG B SUBCOM 2 (3.2 SEC)	ANALOG SUBCOM 2 (16 SEC)	DAU 1	DAU 2	HIRS / 3		
120	121	122	123	124	125	126	127	128	129	130	131	132	133	134	135	136	137	138	139	140	141	142	143		
HIRS / 3	DCS - 2		SEM		HIRS / 3		DCS - 2		HIRS / 3		DCS - 2		HIRS / 3		DCS - 2		HIRS / 3		SBUV / 2		HIRS / 3		DCS - 2		
144	145	146	147	148	149	150	151	152	153	154	155	156	157	158	159	160	161	162	163	164	165	166	167		
DCS - 2	HIRS / 3		DCS - 2		CPU A TELEMETRY						DCS - 2		HIRS / 3		DCS - 2		HIRS / 3		DCS - 2		HIRS / 3		DCS - 2		
168	169	170	171	172	173	174	175	176	177	178	179	180	181	182	183	184	185	186	187	188	189	190	191		
DCS - 2	HIRS / 3		DCS - 2		HIRS / 3		DCS - 2		HIRS / 3		DCS - 2		HIRS / 3		SBUV		HIRS / 3		HIRS / 3		DCS - 2		HIRS / 3		
192	193	194	195	196	197	198	199	200	201	202	203	204	205	206	207										
HIRS / 3	DCS - 2		HIRS / 3		DCS - 2		CPU B TELEMETRY						/////	6-BIT TIP PARITY (TIP)	6-BIT TIP PARITY (AIP)										

2-BIT CPU DATA STATUS

NOTES:
- NUMBER IN UPPER LEFT HAND CORNER INDICATES MINOR FRAME WORD NUMBER
- LAST TWO BITS OF WORD 2 ARE 00
- /// WORD LOCATIONS ARE SPARE AND CONTAIN CODE 01010101
- FIRST SIX BITS OF WORD 5 ARE 000000. LAST TWO BITS ARE 8-SECOND FRAME COUNTER
- WORDS 103 THROUGH 206 ARE IDENTICAL TO A TIP ORBITAL MODE MINOR FRAME'S WORDS 0 THROUGH 103
- 106

1 BIT CV ST	2 BIT TIP ST	3-BIT MAJOR FRAME COUNTER

MINOR FRAME PERIOD - 0.1 SECOND
OUTPUT DATA RATE - 16.64 KBPS

90-0735M

Figure 3.3.2-13. AIP Data

TABLE 3.3.2-2. TELEMETRY CHARACTERISTICS

Analog	
Parameter	**Value**
Signal Type	Analog
Signal Level	0 to +5.12 Volts referenced to signal ground
Frequency Response	DC to 200 Hz
Output Configuration	Single ended, DC coupled, referenced to signal ground*
Output Impedance	2.0 KΩ, minimum; 15.0 KΩ, maximum
Load Impedance	2 megohms, minimum
Source/Sink Current	1 microamp, maximum
Overrange Limits	-15.0V to + 15.0 Volts**
Discrete (Bi-Level)	
Parameter	**Value**
Signal Level:	
Data "1" (low)	$0.0 \begin{smallmatrix}+0.5\\-0.1\end{smallmatrix}$ volts
Data "0" (High)	+5.0 ± 0.7 volts
Frequency Response	DC - 200 Hz
Output Configuration	Single-ended, DC coupled, referenced to signal ground*
Output Impedance	15.0 KΩ, maximum, 2.0 KΩ, minimum
Source/Sink Current	1 microamp, maximum
Overrange Limits	-15.0V to +15.0 Volts**

*Referenced, but not necessarily tied to signal ground

**Maintaining proper output impedance

TABLE 3.3.2-3. REGULATED BUS INTERFACE CHARACTERISTICS

Parameter	+28-V Main Bus	Pulse Load Bus	+10-V Common Bus
Bus Voltage	+28.0 V	+28.0 V	+10.0 V
Regulation	+0.56/-0.30 V	±0.56	±0.5 V
Output Impedance	< 0.16Ω (dc to 100 kHz)	< 0.2Ω (dc to 100 kHz)	< 1.0Ω (dc to 10 MHz)
Load Current	45.0A* max. from BVR alone 57.0A* max. from BVR and SA	0-23.25A	100-800 mA
Voltage Ripple	150 mV p-p or 200 mV p-p including dead bands (dc to 100 kHz)	200 mV p-p (dc to 100 kHz)	250 mV p-p (dc to 10 MHz)
Transient Response	500 mV p-p for 7.5A ΔI	600 mV p-p for 2.1 A ΔI; 1.6 V p-p for 6.0 A ΔI	1 V pk
Voltage Range	+16 V to +38 V	+16 V to +38 V	+9 V to +15 V
Redundancy	Automatic Failure Detection & switchover for: • Mode Controller • Phase Control Circuit • Charge Regulator 4 out of 5 BVR Channel Redundancy	Same as Main Bus	Redundant Converters; Diode OR'ed
Source Unit	PSE	PSE	CPC

*Includes Pulse Load Current

The general grounding philosophy is shown in Figure 3.3.2-14. Separate returns are provided in each unit for: +28V power, internal signal power, +10 volt interface power, chassis ground, and shield ground, +28V analog telemetry ground, and pulse load bus ground. All grounds are isolated, to the extent possible, within each unit. Except for +10 volt returns and pulse load returns, which go back to the source box, each ground is returned to a spacecraft "single point" ground plate on individual conductors.

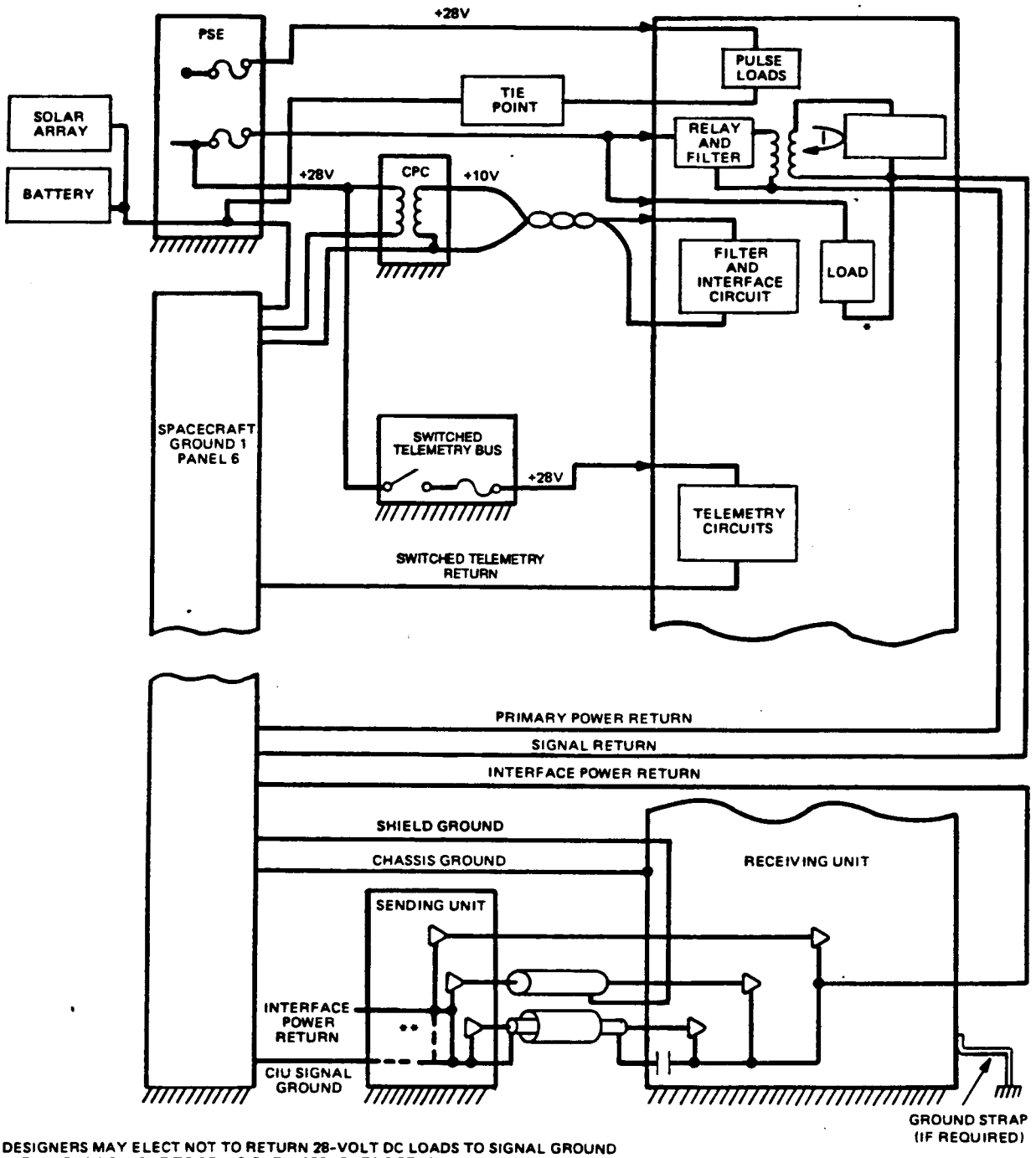

* DESIGNERS MAY ELECT NOT TO RETURN 28-VOLT DC LOADS TO SIGNAL GROUND WITHIN THE BOX, BUT TO BRING OUT A SEPARATE RETURN.

**DOTTED LINES INDICATE THAT THE CIRCUIT RETURN CAN BE CONNECTED TO THE INTERFACE POWER RETURN OR TO THE CIU SIGNAL GROUND.

9-2690

Figure 3.3.2-14. ATN-KLM Grounding

3.4 SPACECRAFT CHARACTERISTICS

A summary of the spacecraft characteristics and performance is shown in Table 3.4-1. The system weight breakdown and Mass Properties are given in Table 3.4-2. A tabular listing of the power requirements for launch, survival and mission mode is contained in Section 4.6.

3.5 ASCENT GUIDANCE AND CONTROL

The ATN-KLM guidance and control during ascent is provided by the ascent hardware and the Ascent Guidance Software (AGS). The hardware consists of an Inertial Measurement Unit (IMU) which contains triads of rate-integrating gyros and accelerometers, providing body rate and acceleration data to the Central Processing Unit (CPU) which, with a stored set of equations, operates on this data to generate the flight profile. After separation from the Titan II booster, control is provided by a mixed hydrazine/nitrogen Reaction Control System (RCE) attached to the spacecraft. The RCE provides spacecraft control during the solid stage (AKM) burn, provides a velocity trim burn after orbit insertion, and is used to orient the spacecraft and provide control during the deployments. The hydrazine system and the accelerometers are deactivated after handoff to the orbital control system. Any remaining nitrogen is usable on-orbit for backup control.

The Ascent Guidance Software (AGS) is developed by the McDonnell Douglas Corporation for ASD. It contains a set of guidance equations which are used to force the vehicle to fly the trajectory profile stored in the CPU, and it is used to provide the necessary ascent event sequence discretes.

The Titan provides guidance during the booster phase. The spacecraft navigates during this phase and uses its own state vectors resulting from this navigation to provide navigation and guidance for the AKM burn. The system thus insures proper ignition attitude for the AKM. The axial accelerometer is used to sense the total AKM and RCE Δ V to insure that the nominal value is achieved.

3.6 STRUCTURE

The mission configuration of the structure is composed of 4 major elements: the RCE Support Structure (RSS), the Equipment Support Module (ESM), the Instrument Mounting Platform (IMP), and the Solar Array (SA). The structure is assembled as shown in Figure 3.1.1-1. In addition, a transition ring adapter is required to interface the spacecraft with the booster's payload adapter.

The IMP is the primary mounting surface for earth viewing payload. It is approximately 65 inches by 31.5 inches by 4 inches thick and is cantilevered from the center of the top ESM panel via a 4 point mount with its broad face perpendicular to the satellite X axis. The IMP is machined from a 7075-T73 aluminum alloy plate.

The upper ESM structure is a pentagon 77.71 inches high that is developed from a hexagon prism measuring 43.5 inches across the points, with one apex removed. It is constructed of seven honeycomb panels which cover the riveted, machined-member magnesium alloy frame. The earth-viewing face of this module is used to support antennas and instruments. The electronic equipment is mounted on the internal sides of seven panels.

TABLE 3.4-1. ATN-KLM SPACECRAFT CHARACTERISTICS AND PERFORMANCE

Parameter	Description
Lifetime	Goal of greater than 2 years
Operational Sun Angle	0 to 80°
Configuration	Multi-sectioned stack
Size	165 inches long by 74 inches in diameter (4.19m x 1.88m)
Weight (Normal, On Orbit)	Approximately 3251.8 lbs
Attitude Control	Zero momentum Earth stabilized Earth and solar reference Reaction wheel control Magnetic Unloading, GN_2 Backup
Control Accuracy	$< \pm 0.2°$
Knowledge with Ground Processing	$< \pm 0.1°$
Rates	$< \pm 0.035°$/second pitch $< \pm 0.035°$/second yaw $< \pm 0.015°$/second roll
Orbit Attainment	Spacecraft navigation from liftoff Titan II guidance and control up through separation Spacecraft attitude control after separation Apogee velocity kick Spacecraft ΔV trim
Reaction Control	N_2 (2-lb thrust) (8.9 N) N_2H_4 (98-lb thrust) (435.9 N)
Thermal Control	Passive (blankets, finishes, materials) Active (pinwheel and vane louvers, heaters)

TABLE 3.4-1. ATN-KLM SPACECRAFT CHARACTERISTICS AND PERFORMANCE (Continued)

Parameter	Description
Power	Direct energy transfer Partial shunt array control Boost discharge 870 watts orbit average max. load power available at 2-year EOL at 80° sun angle, 880 watts at 0° sun angle
Command	S-Band, NRZ-M (STDN 2025.0 MHz, 16 kHz Subcom 2 KB/sec
Command Capacity	1200 realtime (approx. 360 implemented) ι 2300 stored
Communications	Beacon: 137.35 and 137.77 MHz 0.5 watts EOL APT: 137.5 and 137.62 MHz, 5 watts EOL S-Band: 1698 MHz, 6.35 watts EOL S-Band: 1702.5 MHz, 6.35 watts EOL S-Band: 1707 MHz, 6.35 watts EOL Command Receiver: 2025.0 MHz DCS Receiver: 401.65 MHz S-Band TLM: 1702.5 MHz S-Band Ascent and Emergency: 2247.5 MHz, 5.25 EOL SARP Receiver: 406.025 MHz SARR Receiver: 121.5 MHz, 243 MHz, 406.05 MHz SARR: 1544.5 MHz, 10 watts

TABLE 3.4-2. WEIGHT BREAKDOWN AND MASS PROPERTIES

Assembly	Estimated Weight (lbs)
Structure	736.8
Thermal	77.3
ADACS (dry)	185.6
Power	527.1
Communications	58.7
Command and Control	68.9
Data Handling	39.9
GFE (GFE Margin)	982.5 (67.2)
Harness	233.0
AKM Burnout	145.6
Balance Weight & S/C Margin	49.8
Ballast	146.6
Spacecraft Dry Weight	3251.8
N_2H_4	62.8
GN_2	10.4
AKM Expendables	1595.0
Spacecraft at Liftoff	4920.0

The lower ESM structure is a titanium alloy truss arrangement connecting the upper ESM module to the RSS at six points, and enclosing the upper portion of the AKM.

The RSS is a riveted, reinforced aluminum alloy shell, approximately 41 inches in diameter by 32.5 inches long. It is composed of an aluminum skin reinforced externally by four machined aluminum rings and internally by eighteen aluminum ribs. The lower ring mates with the transition ring adapter and is clamped to it with a V-band assembly. The top ring mates with the ESM truss. The intermediate rings both stiffen the shell and support concentrated loads from the battery packs, the propellant tanks, the pressurant tanks, the array drive electronics and the battery charge assembly. The RCE equipment is attached to the outer shell.

The solar array is a single-axis, sun-tracking array with 181 square feet of area. It is composed of 10 panels, each of which is 107.5 inches by 24.2 inches.

After deployment, the array is supported from the RSS through the main boom, solar array drive, and the array mast. The array is canted 37° for a morning orbit mission or 22° for an afternoon orbit mission with respect to the boom axis (orbit normal). During orbit operations, the array rotates continuously about the main boom once each orbit, so as to remain directed toward the sun.

3.7 THERMAL DESIGN

The Thermal Control Subsystem consists of both active and passive thermal control equipment. During both acquisition and mission modes, the thermal control subsystem will maintain unit temperatures within the general limits of 5°C to 25°C.

Passive thermal control is effected by the appropriate use of multi-layered insulation blankets, thermal shielding, special finishes and thermal conduction control materials.

The two major elements of the active portion of the thermal control subsystem are heaters and louver-controlled radiators. There are two types of louvers: vane louvers and pinwheel louvers. Both are controlled by Thermal Control Electronics units.

3.8 ATTITUDE DETERMINATION AND CONTROL SYSTEM

The on-orbit Attitude Determination and Control System (ADACS) provides three-axes geodetic pointing of the spacecraft. The ADACS is a zero momentum system consisting of reaction wheel control based on solar observations, an earth sensor and inertial position for reference. The static Earth Sensor Assembly (ESA) and Sun Sensor Assembly (SSA), together with the IMU-derived rates, furnish the attitude reference. Control torquing is accomplished by an orthogonal set of reaction wheels (RWA) which are backed up by a fourth skewed wheel. Secular momentum accumulation due to external disturbances is unloaded by actuation of magnetic torquing coils. Interfacing of ADACS signals is handled by the CIU and SCU with processing occurring within the redundant CPUs. Acquisition/re-aquisition control, and momentum desaturation are performed automatically by the flight software. All update requirements are compatible with a single ground station contact per week. In line with the integrated spacecraft design philosophy, the Inertial Measurement Unit (IMU) required for the ascent phase is also utilized during on-orbit operation. Considerable redundancy is provided in each portion of the system.

The ADACS provides attitude control of the spacecraft reference axes to within $\pm 0.2°$ (3σ) of the local geodetic vertical attitude reference system. Furthermore, knowledge of spacecraft attitude is obtainable, after the fact, to an accuracy of $\pm 0.1°$ in all axes. The rates of change of angles defining the orientation of spacecraft axes with respect to the reference axes do not exceed $\pm 0.035°$/sec. in pitch and yaw and $\pm 0.015°$/sec in roll.

3.9 REACTION CONTROL

The Reaction Control Equipment (RCE) is responsible for roll and pitch/yaw control during the ascent coast phases and AKM burn, for assisting in stage separation, and for final injection velocity trim and attitude stabilization prior to hand-over to the on-orbit attitude control system.

RCE consists of two hydrazine tanks, two cold N_2 gas tanks, valves and piping, four hydrazine thrusters, eight nitrogen thrusters, hydrazine propellant, and nitrogen pressurant/propellant.

The two N_2 storage tanks hold a maximum total of 9.4 lbs. of N_2. The tanks supply nitrogen as pressurant to the hydrazine fuel tanks and to roll, pitch, and yaw thrusters for use as propellant. The four N_2 roll thrusters each supply a nominal thrust of 2.0 lbs. The nitrogen thrusters can operate in a steady state or pulse mode.

Two N_2H_4 tanks have a total maximum expellable propellant weight of 65.4 lbs. at 98% expulsion efficiency. An elastomer bladder separates the hydrazine from the nitrogen pressurant. A single thruster is capable of 98 pounds thrust and with all four engines operating simultaneously a nominal 64.5 lb thrust per engine is produced. The hydrazine thrusters provide the ΔV for stage separation. During injection motor burn, the hydrazine thrusters are operated in pulsed mode for steering. Final orbit velocity trim is also performed by the hydrazine thrusters.

3.10 ELECTRICAL POWER AND DISTRIBUTION

Electrical Power is provided by a boost-discharge Direct Energy Transfer (DET) system. The primary power source is a single axis oriented Solar Array and the secondary source is a set of Nickel Cadmium Batteries. Output from the power subsystem consists of the buses listed in Table 3.3.2-3. The major components are the Solar Array Batteries, Power Supply Electronics (PSE), Battery Charge Assembly (BCA), Solar Array Drive (SAD), Array Drive Electronics (ADE), and Pulse Load Regulator (PLR).

The SAD (controlled by ADE) rotates the 181 ft^2 solar array, canted at 37° or 22° to the orbit normal, once per orbit so that it continually faces the sun. The array supplies more than ample current through slip-rings to the PSE during normal daytime operation. Excess power is used to recharge the batteries, if necessary. Power above that required by spacecraft loads and battery charging is dissipated by partial shunts which reduce the total Solar Array output to that required by the spacecraft. Total orbit average load capability for the system is 870 W EOL after 2 years with an 80° sun angle. The three Batteries (42 AH each) supply the spacecraft power through the Boost Regulator during dark portions of each orbit and augment the Solar Array during peak load conditions during daylight portions. The mode control senses +28 Vdc regulated bus voltage and operates the partial shunts and/or charge regulator as required. The Controls Power Converter (CPC) changes +28 Vdc regulated power to +10 Vdc regulated power which is used to power interface circuits. The PSE also provides a heavily filtered +28 Vdc pulse load for powering stepper motors and heaters.

Automatic switchover occurs from primary to backup circuitry for the Boost Regulator, Charge Regulator, and Mode Control in response to signals from the failure detection circuits. Either primary or backup may be selected by ground command. Commandable battery charge and discharge disconnect relays are provided. Full circuit redundancy also exists in the ADE and partial shunts.

3.11 DATA HANDLING

The data handling subsystem consists of: the dual TIROS Information Processor (TIP), a status telemetry and low rate data processor; the Manipulated Information Rate Processor (MIRP), a high rate data processor; the AMSU Information Processor (AIP), a low rate data processor; a set of five digital Tape Recorders (DTR), and a Cross-Strap Unit (XSU). This equipment processes all data handled by the spacecraft in the course of its mission. The TIP performs the telemetry and low rate instrument data commutation function. The AIP combines inputs from the three AMSU instruments with TIP data. The MIRP transforms the data from the AVHRR/3 into forms more suitable for transmission

to earth, and multiplexes it with the TIP and AIP data. The DTRs selectively record TIP, AIP or MIRP data for playback to ground stations. The XSU effects the interface switching and sequencing required to appropriately route the data streams from the TIP, AIP, and MIRP through the recorders (if required) to the various transmitters.

3.11.1 TIP

The TIROS Information Processor multiplexes instrument data signals and status telemetry into one 8320 bps signal (operational mode) or 16,640 bps signal (boost mode). Inputs to the TIP include: low rate instrument data housekeeping telemetry, and CPU data. This data is time division multiplexed into a format determined by a stored program in a ROM within the TIP. The TIP can operate in any of three modes: a mission mode, a boost mode, and a dwell mode.

The TIP output data stream is directed to: the beacon link, for continuous real time transmission; the digital recorders during multiple blind orbits, for playback to a ground station in Europe; and the MIRP, for multiplexing with the AVHRR/3 data.

3.11.2 MANIPULATED INFORMATION RATE PROCESSOR (MIRP)

The function of the Manipulated Information Rate Processor (MIRP) is to buffer, process, and format digital data from five of the six AVHRR/3 channels into the required three output formats. The five selected AVHRR/3 channels produce 10240 words of earth data per scan. The scan rate is 6 revolutions per second and each word has 10 bits. The MIRP contains large memories to: (1) permit a continuous output of earth scan data during the time the AVHRR/3 is viewing space, and (2) manipulate the earth scan data into the desired digital signals. The three MIRP output formats are:

(1) High Resolution Video (LAC and HRPT)

(2) Real Time Medium Resolution Video, (APT) and

(3) Global Stored Data (GAC).

The TIP and AMSU data are multiplexed into the high resolution and global stored output formats.

3.11.3 DIGITAL TAPE RECORDERS (DTRs)

Five digital tape recorders serve to store the mission data. Four recorders are required to support the mission: two recorders are required for the Global Area Coverage (GAC) data during the multiple blind orbit condition (they are also used for recording the TIP output for playback to the European station during these orbits); two more are required for selectively recording high-resolution Local Area Coverage (LAC) data during these orbits. A fifth recorder is carried for redundancy.

All recorders are identical. Each contains two identical transport units and a common electronics unit. The capacity and bit rates of each transport are given in Table 3.11.3-1.

TABLE 3.11.3-1. TRANSPORT UNIT BIT RATES AND CAPACITY

Data	Record		Playback	
	Time Minutes	Bit Rate KB/s	Time Minutes	Bit Rate KB/s
TIP Orbit Data	225.0	8.32	5.6	332.7
TIP Boost Data (or AIP Data)	113.0	16.64	5.6	332.7
GAC	113.0	66.54	5.6	1330.8
			2.8	2661.6
LAC	11.3	665.4	5.6	1330.8
			2.8	2661.6

The highest rate playback is in NRZ-L format. The others are in split-phase-L. At the CDA pass following multiple blind orbits the GAC and LAC data are played back at the highest rate, two recorders in parallel.

The playback data is routed through the Cross Strap Unit (XSU) to two of the three S-band transmitters for transmission as PSK signals. In less crowded passes, serial playback may be used.

3.11.4 CROSS STRAP UNIT (XSU)

The XSU provides data switching, command transfer to the DTRs and clock synthesis.

Data switching permits recording GAC, LAC, TIP, or AIP Data on any of the five DTRs, playing back from any DTR to any STX, connecting the MIRP High Resolution Picture Transmission (HRPT) data to any STX, and connecting the TIP data to STX #2 and STX #4. Two or more DTRs may receive the same data. Two or more STXs may receive the same data. STX #2 can be connected by command to an omni antenna; however, STX #1 and STX #3 cannot.

The XSU distributes mode commands to all DTRs. It receives the commands from the CIU.

The XSU synthesizes all clocks used by the Data Handling Subsystem and by the GFE sensors. The clock input to the synthesizer is from the CIU, which derives the clock by dividing down the 5.12 MHz RXO clock.

3.11.5 AMSU INFORMATION PROCESSOR (AIP)

The AMSU Information Processor accepts sensor data from AMSU-A1, AMSU-A2, and AMSU-B, combines it with TIP data, minor and major frame counters, a synchronization pattern, and parity check bits to form a 16.64 kbps AIP data stream which is sent to the XSU for real-time transmission or recording for later playback. The AIP also performs a switching function to cause either AIP data (including TIP) or TIP data by itself to be sent to the XSU. The AIP also provides the means for supplying AMSU data to the MIRP to be included in the MIRP outputs described in Section 3.11.2.

3.12 COMMUNICATIONS

The primary communications links that comprise the communications system are (1) S-Band Playback downlink to the CDA stations, (2) S-Band Real-Time downlink, (3) VHF Real-Time downlink, (4) VHF Beacon downlink, (5) S-Band Command uplink, (6) the Data Collection uplink, and (7) S-Band Playback downlink to the European ground station, (8) S-band launch and emergency downlink, (9) Search and Rescue Processor uplink, (10) Search and Rescue Repeater uplinks, (11) Search and Rescue Repeater downlink.

The communications links are summarized in Table 3.12-1.

3.12.1 S-BAND DATA TRANSMITTERS

The three S-Band data transmitters provide:

- high resolution real time transmission
- transmission of global stored data
- transmission of high resolution stored data
- transmission of stored sounder data

These three transmitters operate at 1698, 1702.5 and 1707 MHz with PSK modulation. Each transmitter is coupled to one of the three S-Band quadrifilar antennas. The transmitters have 6.35 watt EOL RF output. Normally one transmitter is used continuously with split-phase PSK for HRPT. A second transmitter is used for sequentially transmitting GAC and LAC in a randomized NRZ format to the CDA stations in the single orbit data dump cases, and it used to transmit stored TIP data in split-phase PSK format to the European ground station. In the multi-orbit data dumps, two transmitters are used to playback recorders in parallel. The third transmitter, which supports the multiple missed orbit stored data transmission, is used to back-up the real time transmitter or the primary stored data transmitter, in case of a transmitter failure.

3.12.2 S-BAND TRANSMITTER ANTENNAS

Three bifolium quadrifilar S-Band data antennas are used. Each is connected to one of the three S-Band data transmitters. The circularly polarized antennas, with a nominal directivity gain of -4 dBci at nadir and +3.0 dBci at 63 degrees off-axis (earth's horizon), are used for the S-Band real-time link and the two S-Band playback links.

During the ascent phase, S-Band transmitter number 2 can be connected to S-Band omni directional antennas to provide spacecraft telemetry if required. A second set of S-Band omni-directional antennas is permanently connected to S-Band transmitter number 4 and is used for the launch and emergency link.

3.12.3 DUAL G-STDN RECEIVER/DEMODULATOR AND ANTENNA

The command signal is Phase Modulated (PM) on a carrier at 2025.0 MHz. The modulating signal is a 16 kHz subcarrier modulated by 2 kbps split-phase-level data.

TABLE 3.12-1. COMMUNICATIONS LINK SUMMARY

Link	Carrier Frequency	Information Signal	Baseband Bandwidth	Modulation	Subcarrier Frequency
1. Command	2025.0 MHz	Digital Commands	2 kbps	NRZ-M	16 kHz
2. Beacon	137.77 MHz and 137.35 MHz	Sounder Data, Spacecraft Attitude Data, Time Code, Housekeeping Telemetry. Memory Verification All from TIP.	8320 bps	Split-phase PSK	
3. VHF Real Time	137.5 MHz and 137.62 MHz	Medium Resolution Video Data from MIRP.	~ 2 kHz	AM/FM	2.4 kHz
4. S-Band Real Time	1698 or 1707 MHz	High Resolution Video Data and TIP data from MIRP.	665.4 kbps	Split-phase PSK	
5. S-Band Playback to CDAs	1698, 1702.5 or 1707 MHz	High Resolution Video Data from MIRP, Medium Resolution Video Data from MIRP	2.6616 Mbps	Randomized NRZ-PSK	
6. Data Collection	401.65 MHz	Data from Earth based platforms and balloons.	400 bps	Split-phase PSK	
7. S-Band Sounder Playback	1698; 1702.5 or 1707 MHz	TIP data recovered from tape recorders.	332.7 kpbs	Split-phase PSK	
8. Launch/Emergency	2247.5 MHz	TIP data during ascent & orbital emergencies	8.32 kbps 16.64 kbps	Split-phase	
9. SARP uplink	406.025 MHz	Distress messages	400 bps	Split-phase PSK	
10. SARR uplink	121.5, 243, 406.05 MHz	Distress messages			
11. SARR downlink	1544.5 MHz	Distress messages			

The Command Antennas, RF Filters, and Dual Command Receiver recover the signal. Both command receivers operate simultaneously and continuously. The outputs of both receivers are cross-strapped externally to the two Command Demodulators. The Command Receiver-Demodulator provides two isolated sets of outputs. Each set of five separate output lines are provided to the CIU and DAU containing 1, 0 NRZ-M data, command clock, command enable level, and command return.

The G-STDN receivers are permanently connected to a set of S-band omni-directional antennas via a hybrid network.

3.12.4 VHF REAL-TIME TRANSMITTERS

The VHF Real Time Transmitter has a 5 watt (RF) output and operates at a pre-selected frequency of 137.5 or 137.62 MHz. (The dual frequency assignment reduces the problem of interference when two spacecraft are in orbit.) One of the two redundant transmitters is powered at all times such that the Real Time Medium Resolution video output from the MIRP is transmitted continuously.

One transmitter or the other is coupled to the VHF Real Time Quadrifilar Antenna via an RF Switch. Modulation is AM on a 2.4 kHz subcarrier, which in turn, frequency modulates the carrier.

3.12.5 VHF REAL-TIME ANTENNA

A 1/2 turn, 1/2 wavelength, four element quadrifilar providing a cardiod pattern serves as the VHF Real-Time Antenna. Designed to operate at 137 MHz the circularly polarized antenna has a nominal directivity gain of +4.5 dBci at nadir and +0.0 dBci at 63° off-axis (~ earth horizon).

3.12.6 BEACON TRANSMITTERS

Two redundant VHF Beacon transmitters are connected to the beacon antenna via an RF switch assembly. One transmitter is continuously split-phase modulated with the TIP output. the orbital data rate is 8.32 Kb/s. Dual frequency assignments of 137.35 MHz and 137.77 MHz reduce the problem of interference when two spacecrafts are in orbit.

3.12.7 BEACON ANTENNA

The beacon antenna is a VHF dipole producing, nominally, an isotropic pattern. The antenna is mounted on the earth-facing panel of the ESM. The beacon transmitters are connected to the antenna via an RF switch.

3.12.8 UHF DCS AND SARP ANTENNA

A single right-hand circularly polarized quadrifilar antenna is used to provide DCS signals at 401.65 MHz and SARP signals at 406.025 MHz to the respective instrument receivers. The antenna has a minimum gain of -10.2 dBci at nadir and -4.6 dBci at 60 degrees off axis.

3.12.9 SARR L-BAND TRANSMIT ANTENNA

A quadrifilar L-Band antenna is used to transmit to search-and-rescue user terminals the distress signals received by the spacecraft's two search-and-rescue instruments. The SARR L-Band transmit antenna is connected to the SARR transmitter operating at 1544.5 MHz. The left-hand circularly polarized antenna has a nominal gain of +4.0 dBci at nadir and -1.0 dBci at 60 degrees off axis.

3.12.10 SARR RECEIVE ANTENNA

The SARR receive antenna is a nest of two concentric quadrifilar structures designed to pick up search-and-rescue distress signals at 121.5 MHz, 243 MHz, and 406.05 MHz for retransmission by the SARR. The SARR receive antenna is right-hand circularly polarized. It has a minimum gain of -0.4 dBli at nadir for 121 MHz and -8.4 dBli at nadir for 243 MHz and 406 MHz. At 60 degrees from nadir, minimum gain is -8.4 dBli at 121 MHz, -6.2 dBli at 243 MHz, and -9.6 dBli at 406 MHz.

3.12.11 LAUNCH AND EMERGENCY TRANSMITTER

A 5.25 watt EOL S-band transmitter (STX-4) operating at 2247.5 MHz is used for launch telemetry and for spacecraft emergencies. The data normally transmitted is the 8.32 kbps (orbit mode)/16.64 kbps (boost mode) TIP data.

3.12.12 LAUNCH AND EMERGENCY ANTENNA

The antennas for STX-4 are quadrifilar omnis with right-hand circular polarization on each of the two antennules. Estimated gain is greater than -18 dBci over 95% of a sphere and greater than -10 dBci over 70% of the sphere.

3.13 COMMAND AND CONTROL

The Command and Control Subsystem performs the functions of decoding ground commands which have been received and demodulated, storing certain commands to be executed at a later time, transforming valid decoded commands into control or driving signals, and providing various spacecraft units with +10 Vdc regulated interface power. Major units comprising the Command and Control Subsystem are the Redundant Crystal Oscillator (RXO), Signal Conditioning Unit (SCU), two Central Processing Units (CPU), Controls Interface Unit (CIU), a CIU Annex (CXU), a Decryption/Authentication Unit (DAU), and a Controls Power Converter (CPC) which is physically located within the CIU.

3.13.1 REDUNDANT CRYSTAL OSCILLATOR

One of two crystal oscillators (designated primary and backup) is used as a highly stable 5.12 MHz frequency source. Although both oscillators are continuously operating (from separate 24 voltage regulators and in separate ovens), only one is selected for use at any given time. Failure detector circuitry monitors the primary and backup amplitudes and primary oven temperature and provides automatic switchover in the event of a failure. The switchover truth table is such that one of the oscillators is selected for use

no matter what failures have been detected. If the backup oscillator is functioning, it can be selected by ground command, even in the absence of any RXO output at all.

3.13.2 CONTROLS INTERFACE UNIT

The Controls Interface Unit is a dual unit which can be functionally divided into six blocks: power turn-on monitors, CPU interface controllers, clock and timing generators, uplink processors, I/O bus control logic, and I/O circuits.

Clock frequencies are provided by the CIU to other portions of the CIU, to both CPUs and to other spacecraft units. A Time Code Counter is provided to allow either CPU to determine "real time".

Command messages and other data from the Command Receiver-Demodulator are received by the CIU, decoded, and, if appropriate, sent to one of the CPUs.

Data and control signals from other parts of the CIU or from various spacecraft units are received, buffered and transmitted to the appropriate CPU. Control signals from the various spacecraft units are sent to the CPU in the form of flags or priority interrupts.

The CIU takes data and control signals from the CPU, buffers them, and transmits them to various spacecraft units or to other portions of the CIU for appropriate action.

Software in the CPU controls cross-strap switching (in the CIU) of certain interface lines to permit selective connection of either CPU to either of two interface trunks.

3.13.3 CIU ANNEX

The CIU Annex is a redundant extension to the CIU output buffer capability. It has redundant sides for interfacing with the CIU, and redundant output buses. Equivalent buffers on both buses are automatically updated simultaneously.

3.13.4 CONTROLS POWER CONVERTER

The Controls Power Converter is a dual dc-to-dc converter and is physically located within the CIU box. Each converter accepts +28 Vdc as input and outputs +10 Vdc to the CPU and associated logic in the CIU, and -10 Vdc to the CIU. A common +10 volt bus is provided by OR'ing from either converter. This common bus provides power to all spacecraft units requiring +10 volts for interface purposes.

3.13.5 CENTRAL PROCESSING UNITS

The two Central Processing Units each contain the spacecraft main memory and facilities for interfacing with the memory and for performing arithmetic and logical operations. The major sections are the memory, Arithmetic and Logic Unit (ALU), Memory Address Generator (MAG), and Control.

The Control board has microprogram control logic contained in a Control Read Only Memory. This contains instruction steps for the various control routines.

Interrupt and error control logic which affect the processing order are also contained on the Control board. I/O interface logic allows the CPU to transmit data and address words to the CIU and receive status and data words from the CIU.

The ALU and MAG interface directly with the memory section. The arithmetic unit performs arithmetic operations on operands fetched from memory. The MAG contains memory interface logic. It fetches instructions and operands from memory, loads new programs and data into memory, and performs the necessary timing and control operations for the main memory.

Two 16K word memory boards are used in each CPU. The memory boards contain the address and output drives, a Read-Only-Memory, and a Read-Write Memory. Each memory location contains, in addition to the 16 data bits 6 specially encoded bits which are used to correct an error in the 16 data bits. The memory is thus single error correcting and multiple error detecting, or fault tolerant.

3.13.6 SIGNAL CONDITIONING UNIT

Power switching for the CIU, for the momentum unloading coils, for the Reaction Control thruster valves, for RCE heaters, and for the various ordnance devices is the function of the Signal Conditioning Unit (SCU). The SCU also provides interface signal conditioning between the Ascent Phase Equipment and the satellite. Power switching is accomplished through extensive use of latching and non-latching relays and associated drives which are located primarily in the SCU. The relays either source current from the batteries, from the +28 volt bus, or sink current to ground.

Three types of signal conditioning are performed by the SCU. Low level control signals are converted to medium power coil driving output signals (up to 1.5 amps at +28 volts). Low level control signals are converted to high current output signals for firing ordinance devices requiring 4.5 amps or less all-fire current. This power is taken from the spacecraft unregulated Battery bus. Status signal conditioning circuits convert low level inputs to low level outputs compatible with the CIU, TIP and the spacecraft umbilical.

The SCU switches power to initiate separation from the Titan and to ignite the AKM. A flag signal is sent to the CIU to indicate liftoff.

3.13.7 DECRYPTION/AUTHENTICATION UNIT

The NOAA-KLM spacecraft include the capability to operate the command uplink in either a "clear" mode or an encrypted/authenticated mode. The Decryption/Authentication Unit (DAU) accepts uplink messages from the spacecraft receiver/demodulator and passes clear authenticated text to the CIU. An automatic provision exists to return to the clear mode if no commands are received for a preset period of time.

3.14 FLIGHT SOFTWARE

The flight software is an integral part of the spacecraft. It is a subsystem which performs critical tasks in all phases of the mission. During ascent, the software operates in conjunction with hardware to provide guidance and navigation computation and CPU telemetry. Once in orbit, all attitude control and command control functions rely on software. Because of software's central role in the system, changes in the hardware subsystems may require changes in software.

The spacecraft includes two Central Processing Units (CPUs) in a redundant configuration. The software residing in the CPUs consists of a number of interrelated modules which can be grouped into four major categories:

- Command and Control Software (C&CS)
- Attitude Determination and Control Subsystem (ADACS) software
- Ascent Guidance System Software (AGS)
- The Electrical Power Subsystem Software

Identical software is loaded into each CPU. Normal on-orbit operation calls for one CPU to run Attitude Determination and Control, and for the other CPU to run portions of Attitude Determination as a standby. Each CPU is separately addressable. Command and control can be effected from either CPU, but the non-control CPU can affect only non-redundant buffers on the CIU bus on which it resides. One CPU is designated as the Control CPU, and has ultimate control of the two-processor system.

The command and control subsystem utilizes a multi-processor, multi-tasking approach. Executive control is provided by a configuration of hardware and software. Some tasks are invoked by synchronous or asynchronous hardware interrupts; other tasks are scheduled by software executive control, based on the state of the system and the external commands.

The attitude control operates on a 0.5-second cycle, with data collection and some processing at a higher rate of 10 Hz. The command system is adapted to this 0.5-second cycle. Real-time commands are processed as received; stored commands are executed with one-second granularity. The software executive (CYCLE) module operates from the 10-Hz interrupts from the Inertial Measurement Unit (IMU), and "calls" the other routines as required by the mode and state of the system. The attitude determination and control routines run on a time-sequenced basis with a 0.5-second cycle.

The CPU interface with the spacecraft is through the Controls Interface Unit (CIU) through a set of two buses. Most functions are redundant on the two buses, and either CPU can be placed on either bus. Thus, all functions can be accomplished either directly or by switching buses. A hardware "watchdog" system in the CIU will transfer control away from a CPU if its does not report "OK" on a periodic basis. This system is designed to detect both temporary and permanent faults. In the event of a fault in one CPU, all operations, both on-line and standby, can be performed by the remaining CPU.

The software is designed around the "unified-load-package" (ULP) concept. All required functions are included in the package, and the software is identical for both CPUs. This concept provides full flexibility in assigning the functions of the CPUs and allows for full automatic switching of CPU functions if and when necessary. The ULP concept extends to the ascent phase as well; AGS is included in the package.

Blank Page

SECTION 4.0

SPACECRAFT SUBSYSTEMS

4.1 GENERAL

This section of the report provides detailed descriptions of the components that comprise the ATN-KLM spacecraft, their requirements, performance and design. Where available and applicable, the qualification history of the component has been included. This history is largely derived from TIROS-N and ATN spacecraft programs where with same or similar components have been used.

Appropriate application software as well as executive and ADACS software are discussed in Section 4.10 of this report.

Blank Page

4.2 STRUCTURE

4.2.1 SYSTEM DESCRIPTION

The structure subsystem (STS) provides the foundation to support the remainder of the spacecraft subsystems and instruments during the pre-launch, launch, and orbital phases of the ATN-KLM mission. In addition, the mechanical aspects of components such as the solar array and antennas are included in this subsystem.

As shown in Figure 4.2.1-1, the subsystem segments are:

a. An instrument mounting platform (IMP) designed to support instruments and attitude control sensors with viewing requirements.

b. An equipment support module (ESM) designed to support the spacecraft electronics and sensors not located on the IMP.

c. A reaction control subsystem support structure (RSS) designed to support the reaction control equipment and the apogee kick motor (AKM). A titanium truss connects the ESM to the RSS, and provides structural support and thermal isolation.

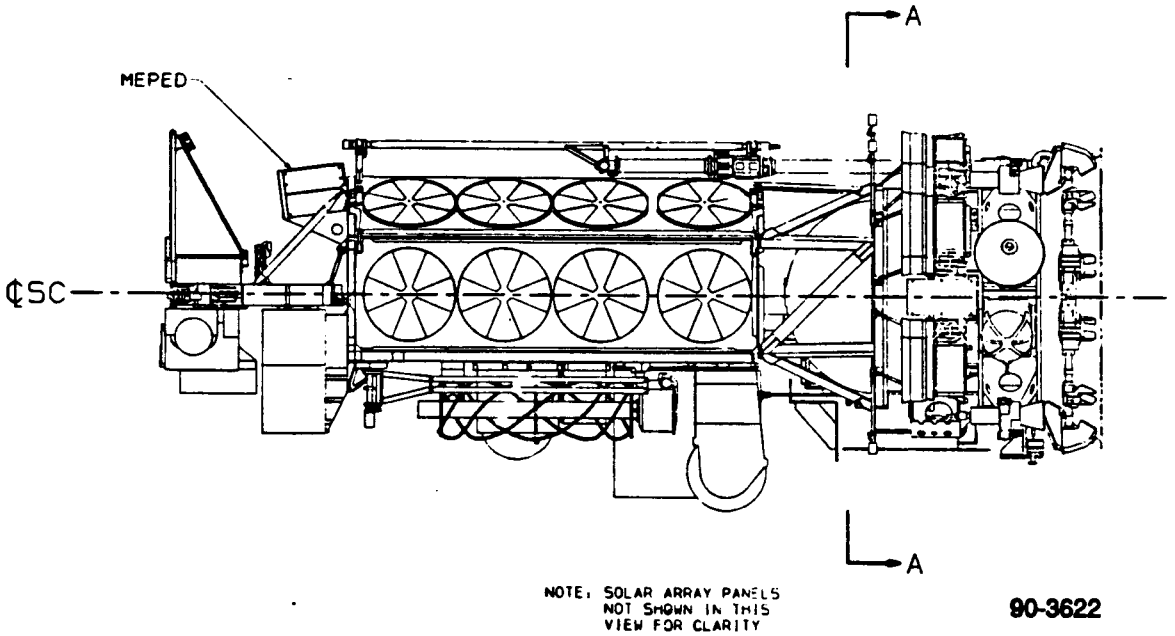

Figure 4.2.1-1. ATN - KLM Spacecraft and Coordinate System

d. A booster adapter, which provides a mechanical interface between the spacecraft structure and the launch vehicle.

e. Mechanical components such as the solar array and solar array support, antennas, and the marmon separation clamp system.

4.2.1.1 Satellite Coordinate System

A right-hand, body-fixed coordinate system is used for reference purposes. The origin of the system is located on the plane of separation between the spacecraft and the booster with the X-axis normal to the earth-facing side of the spacecraft, and the positive sense toward the earth. The Z-axis is normal to the separation plane and passes through the center of the separation ring. The positive sense of the Z-axis is in the direction traveled in moving from the IMP to the RSS. The Y-axis is normal to the X and Z axes to form the right-handed orthogonal coordinate-system shown in Figure 4.2.1-1.

4.2.1.2 Launch Configuration

At lift-off, the solar array panels are stowed on the two ESM apex panels are held in place with a pair of wrap-around cables. The UDA, SAR, and VRA are folded against the spacecraft and are held with retractable pins. The deployable portion of the IMP sunshade is stowed. The spacecraft assembly is attached to the Titan II booster through the adapter, and the entire system fits inside the static envelope. The ATN-KLM spacecraft launch configuration is shown in Figure 4.2.1-2.

4.2.1.3 Orbit Configuration

After achieving the specified orbit, but prior to handover, the solar array, IMP sunshade, and antennas are deployed, resulting in the orbital configuration shown in Figure 4.2.1-3. The solar array has completed a series of motions described in Section 4.2.4.6.4 and is now positioned off the +Z end of the spacecraft and is supported by a long boom (along the array rotation axis), and canted at either 22 or 37 degrees. The UDA, SAR, and VRA are rotated from their launch configurations to positions parallel to the +X axis so that they point towards the earth. The +Y portion of the IMP sunshade deploys 116 degrees and the -Y portion of the sunshade deploys 131 degrees.

4.2.1.4 Mass Properties

The system weight allocation by subsystem is given in Table 4.2.1-1, including the required allotment for the GFE components. The structure is approximately 15 percent of the total launch weight. System inertias and center of gravity (CG) locations for various conditions are indicated for reference in Table 4.2.1-2. The X and Y axis components of the center of gravity of the system in its lift-off configuration is controlled by balance and ballast weights at the RSS and ESM so that the C.G. is fixed within 0.030 inches of the spacecraft centerline. No attempt is made to control the Z-axis component of the CG because the launch system is relatively insensitive to small changes in Z.

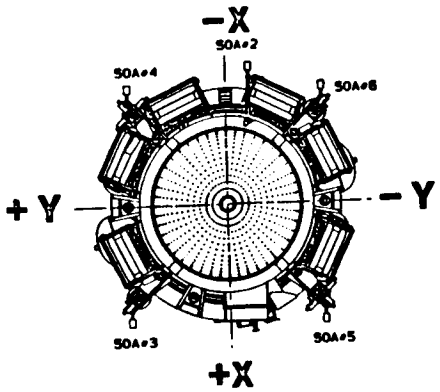

SECTION A - A

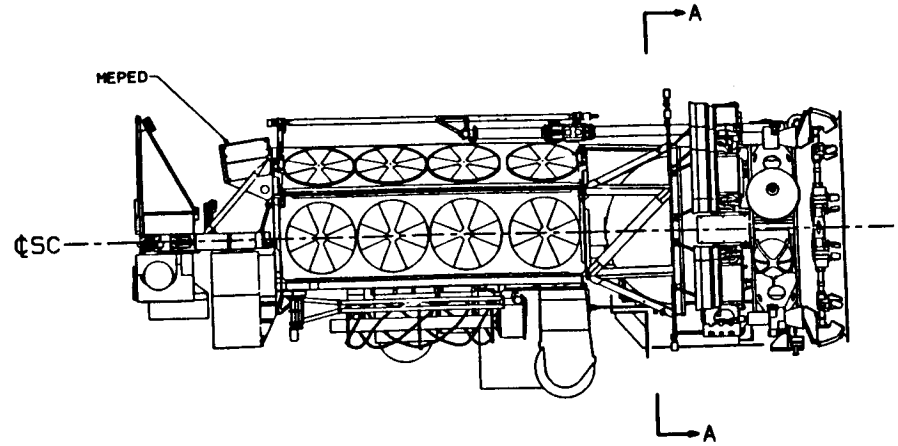

NOTE: SOLAR ARRAY PANELS NOT SHOWN IN THIS VIEW FOR CLARITY

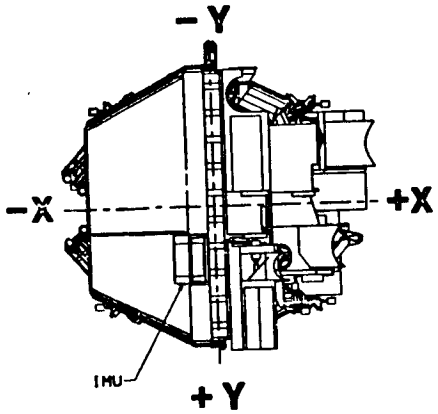

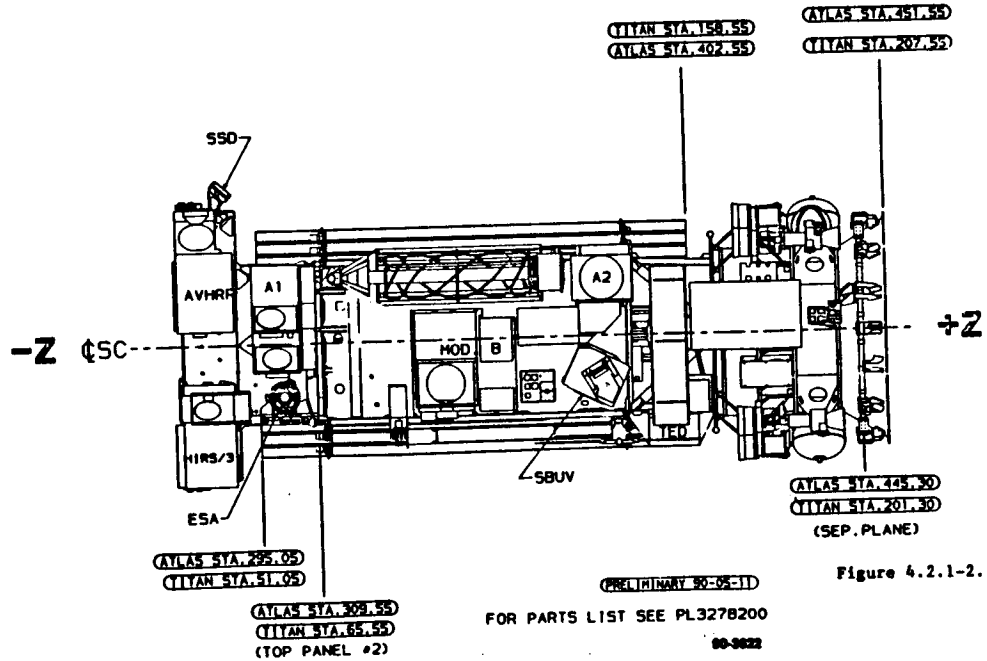

FOR PARTS LIST SEE PL3278200

90-3022

Figure 4.2.1-2. ATN-KLM Launch Configuration

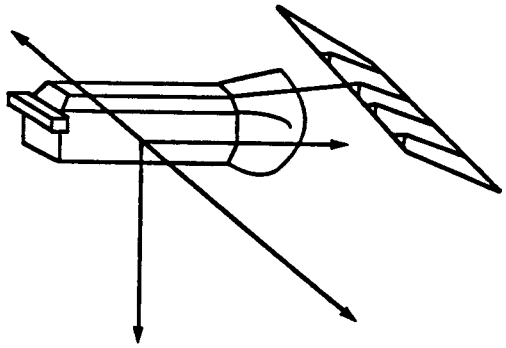

AXIS	MISSION
+X	EARTH FACING
-X	
+Y	
-Y	VELOCITY VECTOR
+Z	ORBIT NORMAL
-Z	

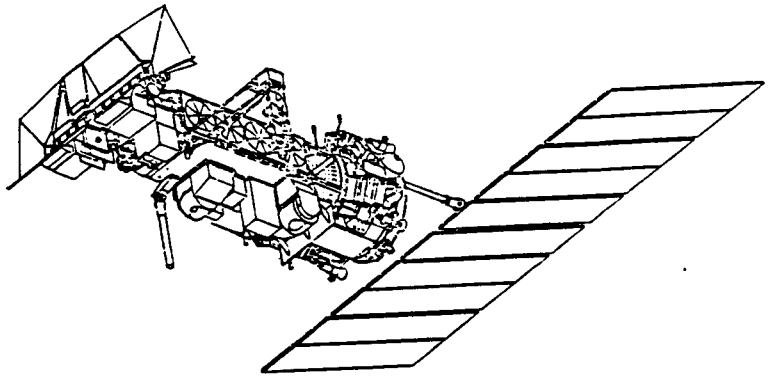

90-3539M

Figure 4.2.1-3. ATN-KLM Orbit Configuration

4.2.2 SYSTEM REQUIREMENTS

The ATN-KLM structure is required to support the meteorological payload and all other subsystems to form an integrated spacecraft that satisfies the specified mission requirements of GSFC S-480-25. In addition, the structure is designed to meet the reliability and quality requirements of GSFC S-480-26 and the performance requirements of GE ASD PS-3267544.

The integrated structural components are designed to provide the required mounting accuracy for the payload sensor system, and, to maintain this alignment throughout the launch, ascent, and orbital phases of the mission.

4.2.2.1 Interface Requirements

The spacecraft structural subsystem is compatible with the Titan II launch vehicle system in accordance with Interface Control Document ICD-T11-25004 and GE ASD 3281239. The structure subsystem also supports the Solid Rocket Motor. The empty casing is retained during the mission.

TABLE 4.2-1. ATN-KLM WEIGHT SUMMARY

Assembly	Estimated Weight (lbs)
Structure	736.8
Thermal	77.3
ADACS (Dry)	185.6
Power	527.1
Communications	58.7
Command and Control	68.9
Data Handling	39.9
GFE (GFE Margin)	982.5 (67.2)
Harness	233.0
AKM Burnout	145.6
Balance Weight & S/C Margin	49.8
Ballast	146.6
Spacecraft Dry Weight	3251.8
N_2H_4	62.8
GN_2	10.4
AKM Expendables	1595.0
S/C at Liftoff	4920.0

4.2.2.1.1 Booster

The booster interface is via an adapter cone, which mates with the standard General Dynamics Titan II booster interface cone. The spacecraft will separate at the forward end of the adapter using a V-band, marmon clamp system. The spacecraft will also be designed to fit inside the physical envelope of the booster heatshield.

4.2.2.1.2 Payload

The mechanical, electrical, thermal, fields-of-view and other interfaces of the following specifications are satisfied.

GE ASD IS-3267415 KLM General Instrument Interface Specification

GE ASD IS-2280260 Interface - Advanced Very High Resolution Radiometer/3 (AVHRR/3)

GE ASD IS-3267402 Interface - Data Collection System (DCS-2)

GE ASD IS 2280264 Interface - Solar Environment Monitor (SEM)

GE ASD IS-2285780 Interface - High Resolution Infrared Sounder/3 (HIRS/3)

GE ASD IS-2280354 Interface - Digital Tape Recorder

GE ASD IS-2295546 Interface - Search and Rescue Repeater (SARR)

GE ASD IS-3267401 Interface - Search and Rescue Processor (SARP-2)

GE ASD IS-2295548 Interface - Solar Backscatter Ultraviolet Sounding Unit (SBUV/2)

GE ASD IS-2617547 Interface - Advanced Microwave Sounding Unit Module A1 (AMSU-A1)

GE ASD IS-2624483 Interface - Advanced Microwave Sounding Unit Module A2 (AMSU-A2)

GE ASD IS-2613442 Interface - Advanced Microwave Sounding Unit Module A3 (AMSU-A3)

TABLE 4.2.1-2. INERTIA REPORT ATN-KLM

	(Pounds)	Center-of-Gravity (Inches)			Moments (Inch-Pound-Second^2)			Products (Inch-Pound-Second^2)		
Condition	S/C Weight	-X	-Y	-Z	I_x	I_y	I_z	I_{xz}	I_{yz}	I_{xy}
Lift-off	4914.1	0.0	0.0	-62.1	27811.0	28004.0	4736.0	-369.0	-57.0	-1.0
AKM Ignition	4798.3	0.0	0.0	-63.6	26517.0	26749.0	4575.0	-369.0	-57.0	-13.0
AKM Burnout	3203.4	0.0	0.0	-77.9	20748.0	20981.0	3889.0	-369.0	-57.0	-13.0
End of ΔV Trim	3181.9	0.0	0.0	-78.3	20451.0	20724.0	3839.0	-369.0	-57.0	-26.0
Post Solar Array Panel Deployment	3181.3	-0.4	0.0	-76.6	25239.0	22789.0	6859.0	-702.0	-51.0	-16.0
Post Solar Array Boom Deployment	3181.3	-0.5	0.0	-65.0	37962.0	35574.0	6922.0	-3640.0	-118.0	-16.0
Post Solar Array Cant-22°	3181.3	-0.1	0.0	-64.9	38074.0	35580.0	6814.0	-2988.0	-119.0	-17.0
Post Solar Array Cant-37°	3181.3	-0.3	0.0	-64.9	37971.0	35660.0	6998.0	-3111.0	-111.0	-19.0
Post SRA Deployment S/A 22°	3181.3	-0.1	-0.4	-65.3	38611.0	35838.0	7146.0	-3051.0	149.0	-94.0
Post SRA Deployment S/A 37°	3181.3	-0.2	-0.4	-65.3	38507.0	35918.0	7300.0	-3174.0	157.0	-96.0
Post UDA & VRA Deployment S/A 22°	3182.3	0.0	-0.5	-65.2	38633.0	35883.0	7146.0	-3053.0	140.0	-102.0
Post UDA & VRA Deployment S/A 37°	3182.3	-0.2	-0.5	-65.2	38529.0	35963.0	7330.0	-3176.0	148.0	-103.0
Shipping Weight	2841.3	0.4	0.0	-83.2	18061.0	18261.0	3542.0	-349.0	-52.0	-24.0
S/C w/o Solar Array and AKM	2968.8	1.6	0.0	-76.3	20595.0	20575.0	3542.0	-621.0	-54.0	-1.0

4.2.2.1.3 Spacecraft Subsystems

The spacecraft structure is designed to support all the subsystems. The equipment is placed in the structure so that full consideration is given to: heat dissipation, harness lengths, and sensor fields-of-view. The equipment is also placed to satisfy the mass properties requirements. All equipment mounted externally satisfies the clearance requirements of the booster fairing.

The solar array and support subsystem is designed to withstand the mission environments and to satisfy the requirements imposed by the electrical power subsystem. The solar array exhibits dynamic characteristics that are compatible with the on-orbit stability requirements of the Attitude Control and Reaction Control subsystems.

All antennas are placed so that each particular viewing-angle and RF pattern requirement is satisfied. Except for the UDA, VRA, and SRA, which are deployable, each antenna has a fixed mounting base.

4.2.2.2 Design Requirements

4.2.2.2.1 Loads and Stiffness

The principle design requirements for strength, rigidity and other characteristics are to provide sufficient support during Launch/Ascent and permit proper spacecraft operation during the orbital mission.

4.2.2.2.2 Design Levels

At the limit load, the structure is designed to have sufficient stiffness to withstand simultaneously the 110% limit loads, applied temperature and other accompanying environmental phenomena for each design condition without experiencing excessive elastic or plastic deformation. Allowable material strengths used in design reflect the effects of load, temperature and time associated with the design environment. The yield and ultimate values are in accordance with MIL-HDBK-5.

At ultimate load, the structure is designed to withstand simultaneously the ultimate loads, applied temperature and other accompanying environmental phenomena without failure or excessive deformation.

The margin of safety is defined as: $MS = (1/R) - 1$ where R is the ratio of applied load (or stress, when applicable) to the allowable load (or stress). The factor R includes the effects of combined loads or stresses (interaction). It is a criterion for structural design that no margin of safety be less than zero.

4.2.2.2.3 Test Levels

The structure is designed to withstand the test levels specified in GSFC S-480-25 and GE ASD Specification PS-3267544, and is tested to the dynamic and acoustical levels stipulated.

4.2.2.2.4 GFE Alignment

As will be discussed in more detail in Section 4.2.4.1, the Instrument Mounting Platform (IMP) provides a stable base for mounting the GFE sensors. The IMP-mounted sensors are the AVHRR/3 and the HIRS/3. The MEPED, AMSU-A1, -A2 and -B, and the SBUV/2 mount to the ESM. The TED instrument is located at the +Y side of the truss.

Tables 4.2.2-1 and 4.2.2-2 list the values for placement accuracy, placement knowledge, and the instrument alignment tolerances. The spacecraft structure was not designed specifically to meet the AMSU alignment requirements which are an artifact of their locations on the ESM.

TABLE 4.2.2-1. ATN-KLM PAYLOAD ALIGNMENT PARAMETERS

Sensor	Placement Accuracy* [degrees]
AVHRR/3	0.1
AMSU-A1	0.05
AMSU-A2	0.10
AMSU-B	0.10
HIRS/3	0.50
MEPED	5.0
TED	5.0
SBUV	0.50
ESA	Ref.

*Instrument optical axis to spacecraft reference. All values are ± per axis.

TABLE 4.2.2-2. INSTRUMENT ALIGNMENT TOLERANCES

SBUV/2	AVHRR/3	HIRS/3	AMSU-A1	AMSU-A2	AMSU-B	SEM	
0.005"	0.005"	0.001"	0.005"	0.005"	0.005"	0.001"	• PLANARITY OF INSTRUMENT MOUNTING FEET
							• OPTICAL AXIS TO MOUNTING SURFACE HOLE PATTERN
0.25°	0.07°	0.25°	0.20°	0.20°	TBD	1.0°	- MOUNTING SURFACE
0.25°	0.2°	0.25°	0.20°	0.20°	TBD	1.0°	- MOUNTING HOLES
0.1°	0.0029°	0.01°	0.1°	0.1°	0.1°	1.0°	• OPTICAL AXIS TO UNIT REFERENCE MEASUREMENT
0.05°	0.0057°	0.05°	0.05°	0.05°	05.0°	1.25°	• CHANGE IN OPTICAL AXIS TO MOUNTING SURFACE DUE TO QUAL. ENVIRONMENT
N/A	0.0057°	N/A	0.05°	0.05°	0.05°	0.25°	• CHANGE IN OPTICAL AXIS TO UNIT REFERENCE DUE TO QUAL. ENVIRONMENT

The data in Tables 4.2.2-1 and 4.2.2-2 were used to derive tolerances for installing instruments. Using specially toleranced GFE drill fixtures, which relate the centerlines of instrument fields-of-view to the instrument footprint to within the tolerances given in Table 4.2.2-2, one can install

the mounting devices (inserts or IMP adaptors) to the desired accuracy. In all cases, the spacecraft reference is the ESA field-of-view (represented by a special ESA fixture mounted to the IMP).

Following mechanical installation and alignment, the instruments' mirror and/or cube positions are measured by a theodolite to determine instrument placement to within the knowledge values of Table 4.2.2-1. The SEM (MEPED and TED) instrument, which has no optical reference and a relatively large knowledge value, will not be measured.

4.2.3 STRUCTURAL ANALYSIS

4.2.3.1 Introduction

The analysis of the ATN-KLM structure verifies that the stiffness and strength of the design are sufficient to meet the qualification requirements for the Titan II launch vehicle as well as the on-orbit performance requirements. The analysis is based on the configuration shown in Figure 4.2.3-1 and the qualification loads defined for the Titan II environment.

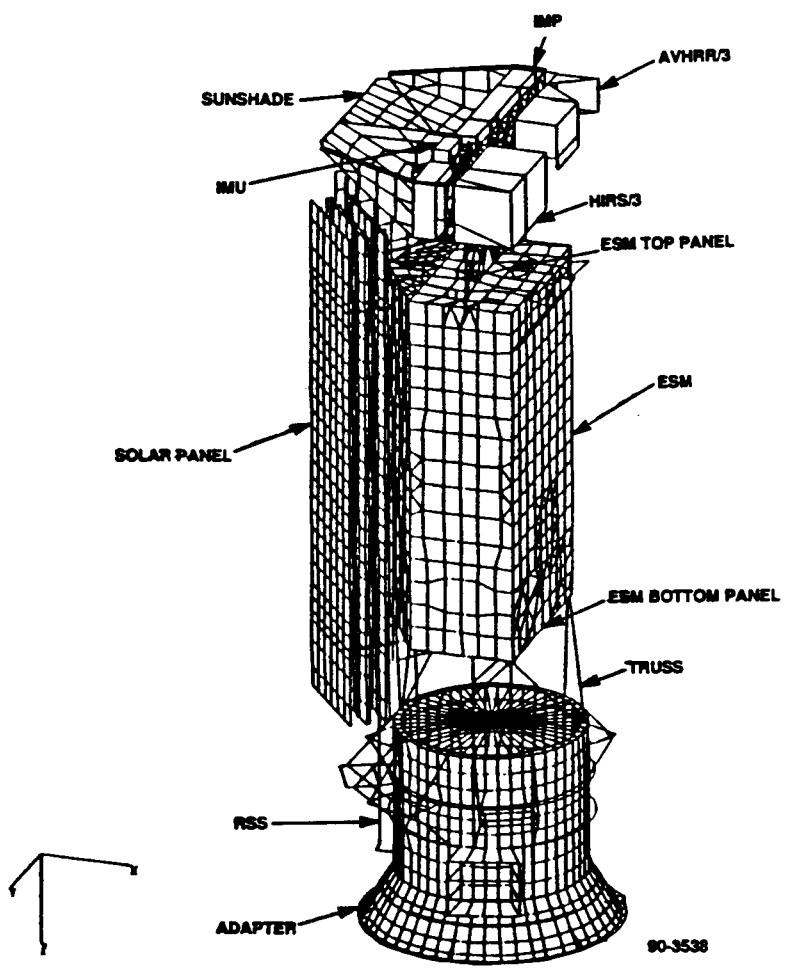

Figure 4.2.3-1. ATN-KLM Analytical Model

The point masses and inertias used in the model are determined from the Mass Properties Computer Program for segments of the spacecraft along the thrust axis. The subsection masses are further distributed over the mode points that define each subsection. This procedure results in a reliable mass distribution between the finite element model and the spacecraft in its launch configuration. The structure is then analyzed for both static and dynamic loadings, and the more critical load cases are selected for detailed stress analyses.

4.2.3.2 Analytical Model Overview

The ATN-KLM spacecraft consists of four primary sections: IMP, ESM/Truss, RSS, and adapter. Each section's analytical representation enables recovery of element loads that define the structural load contours. The NASTRAN refined finite element model (RFEM) consists of 4815 grid points representing 6823 structural elements. The RFEM weight is 4901.00 lbs which includes the booster adapter weight. Thus, the spacecraft is modelled with a weight slightly different than nominal. This difference is caused by the model mass placement constraints of the mass properties program, and is of no consequence. The adapter weight is included since the model defines the launch configuration.

The instrument mounting platform (IMP) is a thick, stiff, machined aluminum part to which the precision electro-optical sensors are attached. Beam and plate elements simulate the sensors, and the mass distribution preserves each component's center of gravity. In the present RFEM, shown in Figure 4.2.3-2, the IMP is represented by 257 grids defining 378 structural elements.

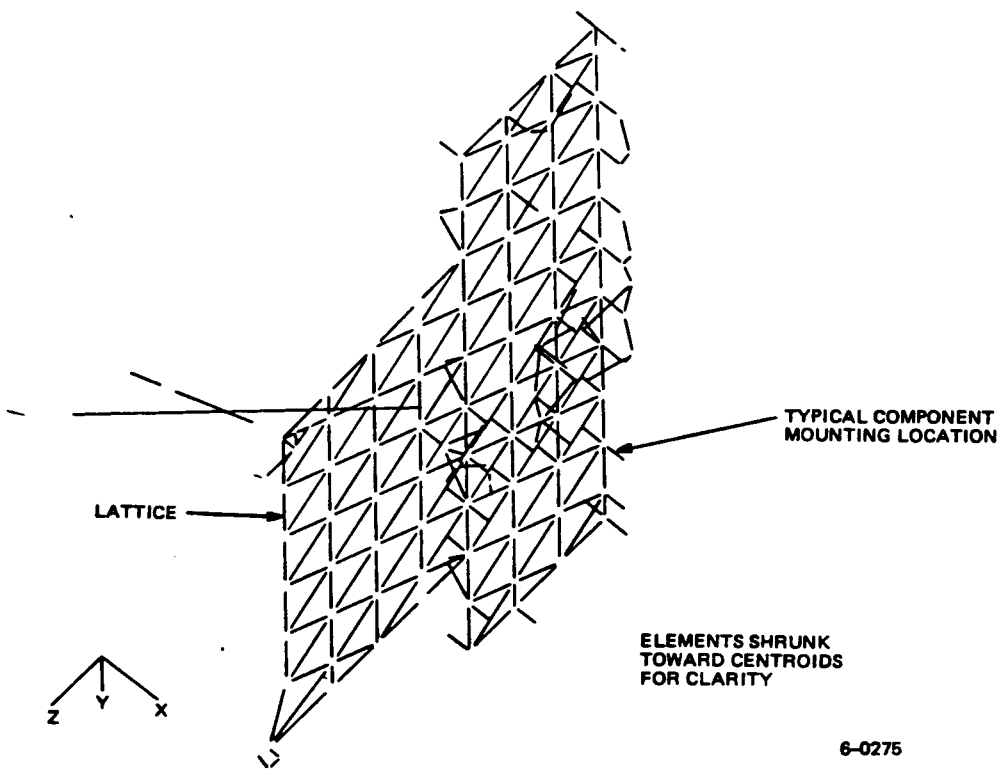

Figure 4.2.3-2. IMP Finite Element Model

The equipment support module (ESM) consists of honeycomb panel assemblies with aluminum frames. Equipment is attached to the panels both inside and out. In the present RFEM, shown is Figure 4.2.3-3, the ESM is represented by 561 grids defining 784 structural elements.

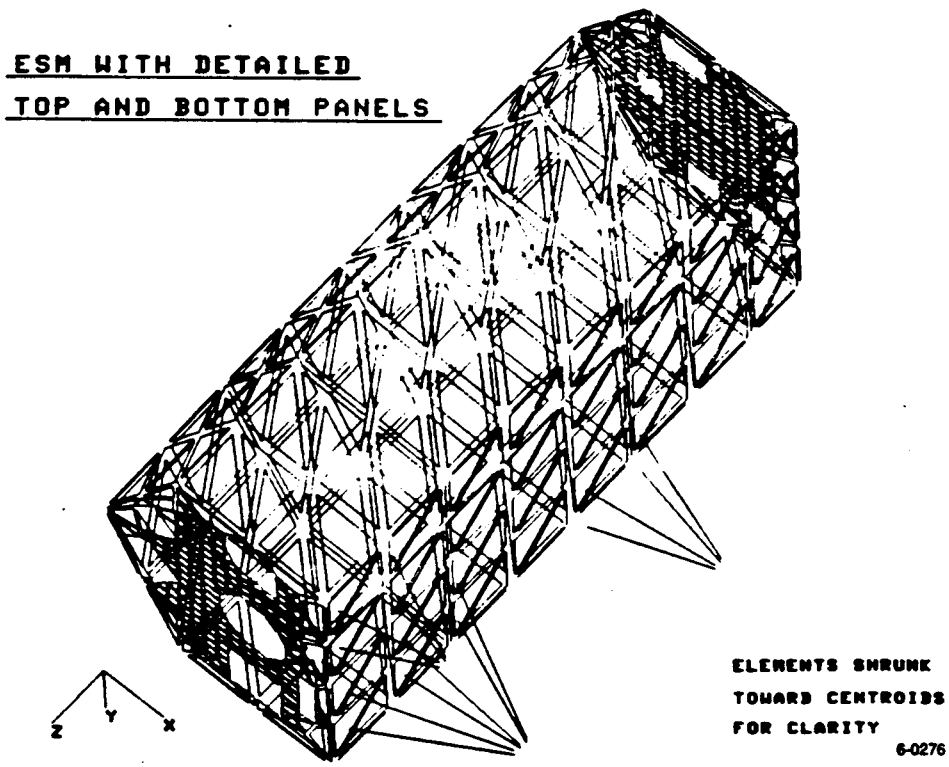

Figure 4.2.3-3. ESM Finite Element Model

The truss is a welded titanium frame that provides structural continuity between the ESM and Reaction Control Subsystem Support Structure through a welded titanium frame. It is bolted to the adjacent sections, with the interior of the frame occupied by the upper hemisphere of the apogee kick motor. Figure 4.2.3-4 defines the analytical representation of eleven beam elements.

The RSS is a longitudinally and circumferentially stiffened sheet metal cylinder with intermediate and end rings. The lower ring mates with the booster adapter and forms the separation plane between the launch vehicle and spacecraft. All structural components are aluminum. Figure 4.2.3-5 defines the analytical representation of 194 grids and 361 elements.

The adapter is the mechanical interface between the Titan II booster and the ATN spacecraft. It is an aluminum cone with end rings to provide rigidity. The lower portion of the adapter bolts permanently to the booster, while the upper section is held to the RSS by a steel restraining band (Marmon V-band assembly). In the present RFEM, shown in Figure 4.2.3-6, the adapter is defined by 168 grids and 288 elements.

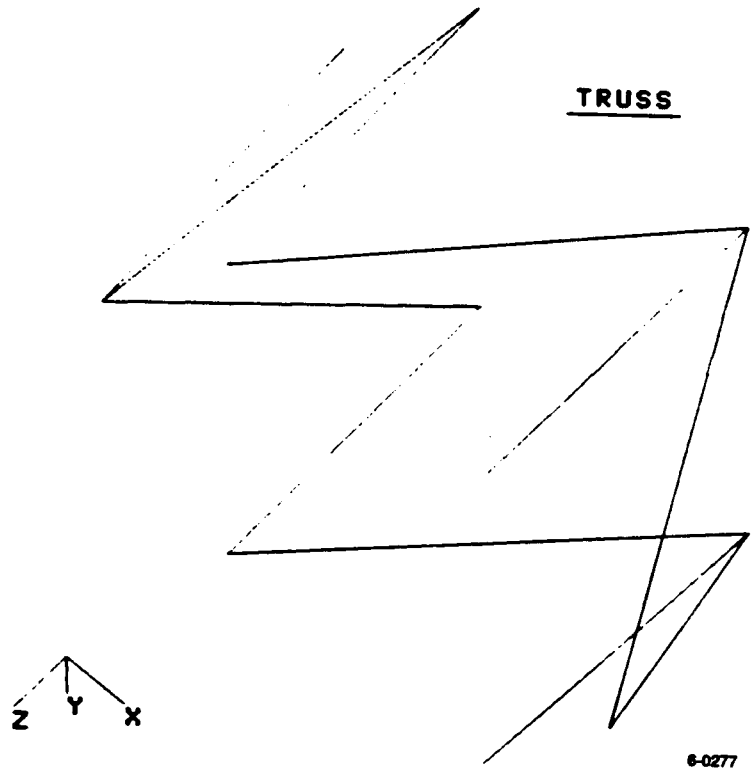

Figure 4.2.3-4. Truss Finite Element Model

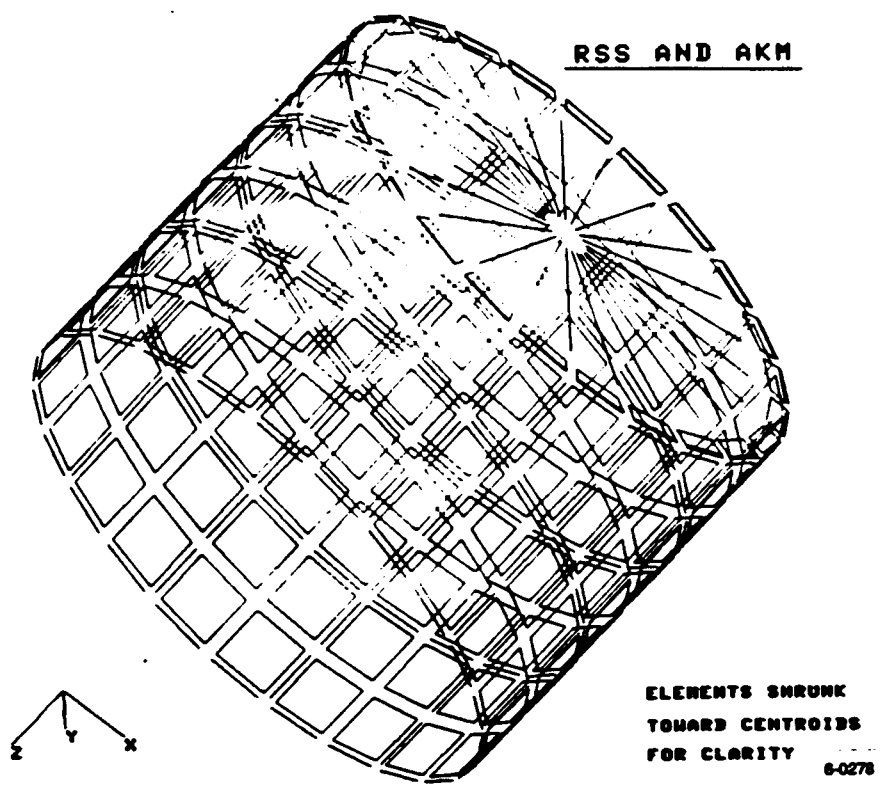

Figure 4.2.3-5. RSS Finite Element Model

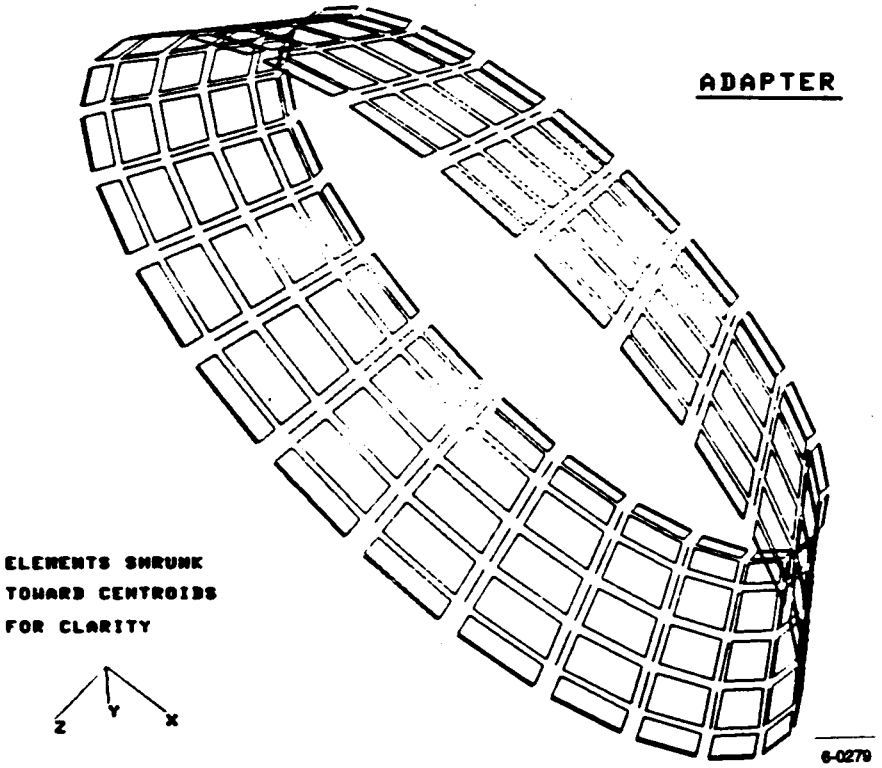

Figure 4.2.3-6. Adapter Finite Element Model

4.2.3.3 Static Analysis

The static loads in the primary structural components are determined from the NASTRAN three dimensional refined finite element model shown in Figure 4.2.3-1. The structure is modeled in sufficient detail to account for local eccentricities at the RSS/truss interface, at the ESM frame/panel interface, and at the upper adapter ring. Detailed subsystem simulations are used to determine the local load distributions as well as dynamical response.

The design limit loads are defined in Table 4.2.3-1 for the BECO/SECO and lift-off/flight winds conditions. The design limit values are taken to be a factor of 1.15 below qualification values in order to minimize weight.

Design integrity is appraised by applying the ascent loads supplied by General Dynamics Corporation (GDC) to the structure finite element model in order to determine the internal load distribution.

The ATN-KLM Stress Analysis Report contains the results of the complete structural analysis performed for the ATN-KLM spacecraft. Lift-off loading conditions defined in the reference and shown in Table 4.2.3-2 were applied to the ATN-KLM structural model, and the resulting internal member loadings were evaluated. Wherever possible, the stress analysis is done by classical methods using a conservative approach. The results of these analyses indicated that the ATN-KLM design is adequate. Tables 4.2.3-3 and 4.2.3-4 summarize the safety margins associated with ATN-KLM for those areas where modifications occurred. Figure 4.2.3-7 shows the ESM top panel.

TABLE 4.2.3-1. ENVIRONMENTAL LOADS AND STRUCTURAL DESIGN CRITERIA, ATN-KLM

	Design Limit (Note 9)				Qualification			
	S/C Longitudinal (Z)	S/C Lateral X	S/C Lateral Y	Ref.	Longitudinal (Z)	S/C Lateral X	S/C Lateral Y	Ref.
Lift-Off (Note 1)	-0.65 +3.9	±3.9	±3.9	Note 5	-0.75 min +4.5 max	±4.5	±4.5	Ref. 1, pp. 20, 43, 111; Ref. 2, p. 27
Maximum Air Loads (Note 1)	+1.3 Min +3.9 max	±3.26	±3.26		+1.5 min +4.5 max	±3.75	±3.75	Ref. 1, pp. 20, 43, 111; Ref. 2, p. 27
Stage I (Note 1)	-3.9 min +11.7 max	±3.9	±3.9	Note 5	-4.5 min +13.5 max	±4.5	±4.5	Ref. 1, pp. 20, 43, 111; Ref. 2, p. 27
Stage II (Note 1)	-5.2 min +15.6 max	±2.6	±2.6	Note 5	-6.0 min +18.0 max	±3.0	±3.0	Ref. 1, pp. 20, 43, 111; Ref. 2, p. 27
Sine Vibrations	1.0g, 5-200 Hz (.5" D.A. Max)	2.3g peak Shaped input, 5-200 Hz		Note 6	1.0g, 5-200 Hz (.5" D.A. Max)	2.3g peak Shaped input, 5-200 Hz		Ref. 1, p.26
Acoustic Internal	137.4 dB (OA), 1 min.			Note 6	137.4 (OA), 1 min.			Ref. 1, p.19
Transportation	See Note 7			—	—			—
Shock	See Ref.			Ref. 1, pp. 20, 111	See Ref.			Ref. 1, pp. 20, 111
Structural Stiffness and Frequency	See Notes 2 and 3			—	—			—

NOTES:

(1) For static accelerations, longitudinal and either lateral X or lateral Y g's act simultaneously; positive static longitudinal g's produce compression in spacecraft.
(2) At design limit loads, no contact or interference is permitted between adjacent parts of spacecraft, or between spacecraft and heat shield or booster (Ref. 2, p. 19).
(3) The ATN-KLM shall have a minimum lateral natural frequency of 10.0 Hz (Ref. 2, p.19).
(4) Qual loads = 1.5 x flight loads.
(5) Design limit load = qualification load/1.15 (static loading only; Ref. 2, p. 27).
(6) Design limit load = qualification load/(Protoflight levels, sine and acoustic loadings).
(7) Shall be controlled to be significantly less severe than flight conditions (Ref. 1, pp. 17 & 111; Ref. 2, p. 21
(8) For spacecraft structure:
(a) Design yield = 1.15 x design limit (Ref. 2, p. 15).
(b) Design ultimate = 1.25 x design limit (Ref. 2, p. 15; Ref. 1, p. 43

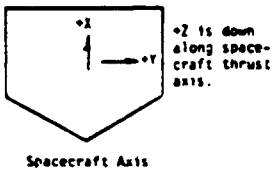

REFERENCES:

1. GSPC Specification S-480-25
2. GE ASD Performance Specification PS-3267544.

TABLE 4.2.3-2. ATN-KLM LOADING CONFIGURATIONS

Loc	Ctr of Imp			Top of ESM			ESM/Truss PL			Truss/RSS PL			Separation PL		
Case \ Dir	Z	X	Y	Z	X	Y	Z	X	Y	Z	X	Y	Z	X	Y
Liftoff	2.68	±3.93	±3.20	2.60	±2.42	±2.43	2.40	±0.73	±0.80	2.24	±0.51	±0.47	2.07	±0.55	±0.50
Stage I	6.73	±4.49	±0.19	6.68	±2.37	±0.17	6.65	±0.68	±0.11	6.63	±0.56	±0.08	6.61	±0.65	±0.08
Stage II	8.94	±0.65	±0.67	8.70	±0.39	±0.27	8.52	±0.46	±0.20	8.33	±0.19	±0.12	8.33	±0.27	±0.13

Notes:

- Point Flight G's per General Dynamics, used to define load cases
- Directions are Spacecraft References Axes:
  Z is longitudinal
  X is pitch
  Y is yaw
- X, Y and Z G's are simultaneous
- Pos Z direction G's produce compression in structure
- G's are opposite direction to accelerations

4.2.4 STRUCTURE COMPONENT DESCRIPTION

As noted earlier, the spacecraft consists of four separable modules (IMP, ESM/Truss, RSS, and Adapter) as well as mechanical components such as the solar array and solar array support, antennas, and the marmon separation clamp system. The GFE payload is located as described below:

a. IMP mounted Payload: AVHRR/3, HIRS/3

b. ESM mounted Payload (external): SBUV/2, MEPED, SARR, AMSU-A1, AMSU-A2, AMSU-B

c. ESM mounted Payload (internal): DCS-2, DPU, SARP-2, SBUVE

d. Truss mounted Payload: TED

The structure components are described in detail in this section.

4.2.4.1 Instrument Mounting Platform

The IMP is a modified isogrid machined plate of 7075-T73 aluminum consisting primarily of a pattern of open triangular areas with hollow node intersections. The primary structural section bounding the open triangle and blending into the hollow node consists of a flanged 0.030 inch thick web. The platform's tee shape allows its lower portion to fit between the stowed solar panels while providing the maximum equipment mounting space on the upper portion. Earth-viewing sensors on the upper portion radiate from their baseplates through the

TABLE 4.2.3-3. STRESS ANALYSIS SUMMARY FOR ATN-KLM ESM

Item No.	Name	Ref Dwg No.	Critical load	Critical Stress	MS
1	ESM Frame	3284702	Quasi-Stltic Load Case 1	Various	≥0.09
2	ESM Front Panel (#1)	3284706	Quasi-Static Load Case 2	Face Wrinkling	0.95
3	ESM Front Panel (#1)	3284706	Quasi-Static Load Case 1	Core Shear	0.70
4	ESM Top Panel (#2)	3284705	NOAA-H Sine Test Input	Face Wrinkling	0.84
5	ESM Top Panel (#2)	3284705	NOAA-H Sine Test Input	Core Shear	1.46
6	ESM Panel (#3)	3284707	NOAA-H Sine Test Input	Face Wrinkling	0.98
7	ESM Panel (#3)	3284707	Quasi-Static Load Case 1	Core Shear	3.91
8	ESM Panel (#4)	3284708	Quasi-Static Load Case 4	Face Wrinkling	0.98
9	ESM Panel (#4)	3284708	NOAA-H Sine Test Input	Core Shear	2.20
10	ESM Panel (#5)	3284708	Quasi-Static Load Case 3	Face Wrinkling	0.86
11	ESM Panel (#5)	3284708	NOAA-H Sine Test Input	Core Shear	1.33
12	ESM Panel (#6)	3284707	NOAA-H Sine Test Input	Face Wrinkling	0.27
13	ESM Panel (#6)	3284707	NOAA-H Sine Test Input	Core Shear	1.26
14	ESM Bottom Panel (#7)	3284709	Quasi-Static Load Case 2	Face Wrinkling	1.45
15	ESM Bottom Panel (#7)	3284709	NOAA-H Sine Test Input	Core Shear	3.56

TABLE 4.2.3-4. STRESS ANALYSIS SUMMARY FOR ATN-KLM RSS

Item No.	Name	Ref Dwg No.	Critical load	Critical Stress	MS
1	RSS Skin	3284126	Quasi-Static Load Case 3	Compression Buckling	0.68
2	RSS Stiffener	3277005	Quasi-Static Load Case 2	Crippling	0.98
3	RSS Ring-Lower On Flare	3284125	Quasi-Static Load Case 2	Crippling	1.26
4	Engine Adapter Ring	3272408	Quasi-Static Z=+12G	Torsion Yield	0.60
5	Engine Adapter Bolts (NAS135IN3-10)	3272408	Quasi-Static Z=+12G	Tensile Yield	0.38
6	RSS Skin Rivets	3284127	Quasi-Static Load Case 2	Rivet Shear	0.37
7	RSS Skin Rivets	3284127	Quasi-Static Load Case 1	Hi-LOK Ultimate	0.23
8	RSS Skin HI-LOKS on Lower Ring	3284127	Quasi-Static Load Case 4	Bearing Yield	1.11
9	RSS Truss Fitting Fastener to Skin	3277006	Quasi-Static Load Case 2	Hi-LOK Shear	0.25
10	RSS Truss Fitting HI-LOK to Skin	3277006	Quasi-Static Load Case 2	Bearing Yield	0.10

open triangles in the platform and through the louver subsystem mounted on the (-X) side of the IMP. The overall size of the machined platform is 65.5 inches wide by 31.8 inches high by 4 inches thick. The main features are shown in Figures 4.2.4-1 and 4.2.4-2.

The IMP is located near the center of the ESM top panel, with the broad face perpendicular to the satellite +X axis. Attitude control and payload sensors which must be accurately co-aligned are mounted on the IMP. The IMP mounted ESA is the primary spacecraft reference to which the remainder of the instruments are aligned. Misalignments due to thermal distortions are minimized by the IMP mounting point designs.

Ball joints and struts provide the attachments between the IMP and the ESM. This four-point attachment, shown in Figure 4.2.4-3 provides a support system which allows differential thermal expansion between the ESM and the IMP without introducing a bending moment in the IMP. Thermal isolation between the IMP and the ESM is provided by Polycarbafil insulation bushings between the ends of the supports and the IMP. The platform is supported at its base by two types of ball joints. One support has a single ball and is the only fixed point between

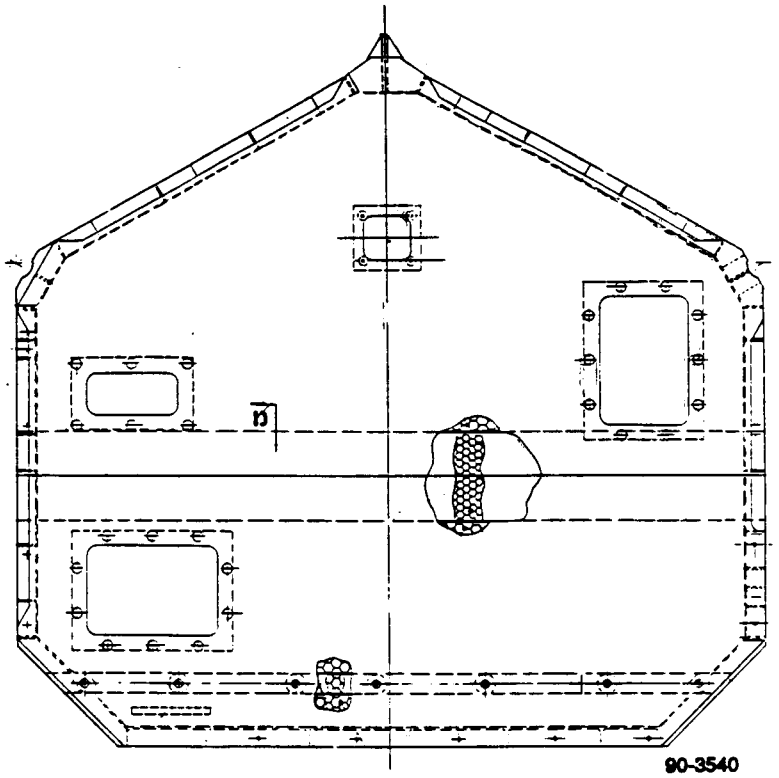

Figure 4.2.3-7. ESM Top Panel

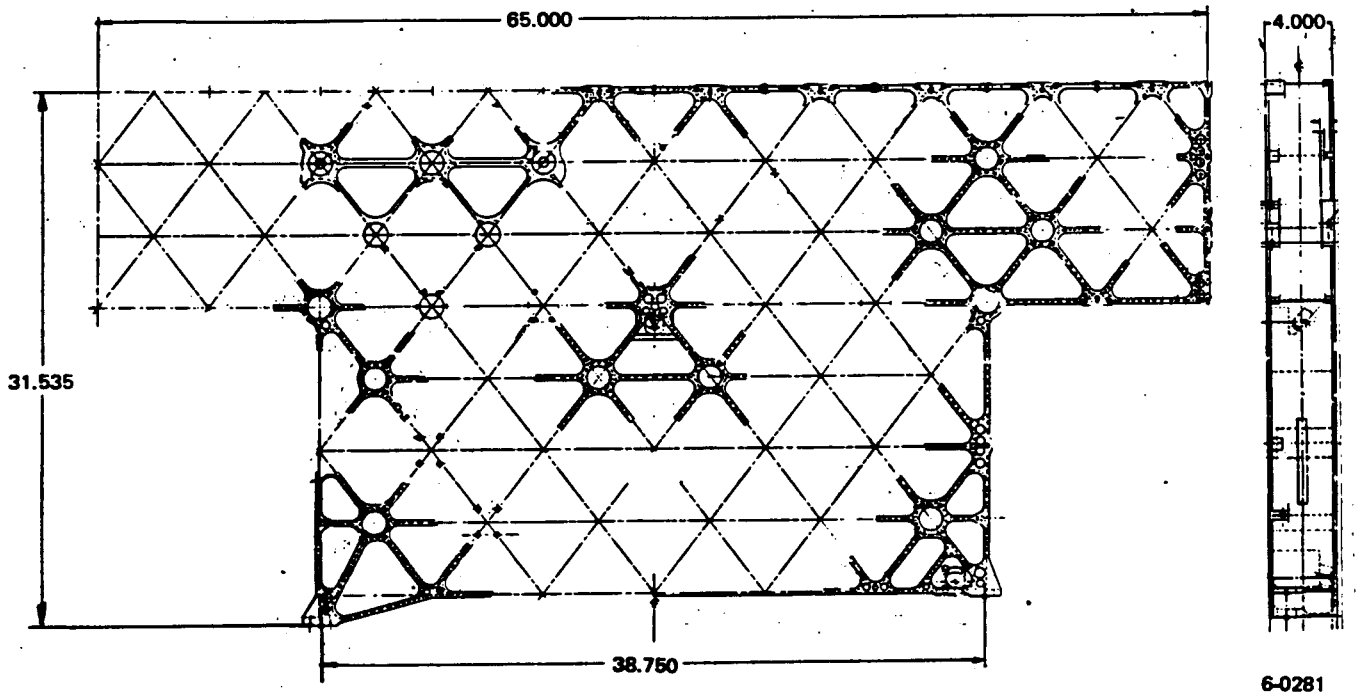

Figure 4.2.4-1. IMP General Arrangement

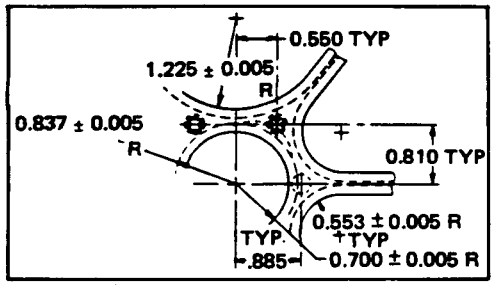

A. TYPICAL HOLLOW MODE

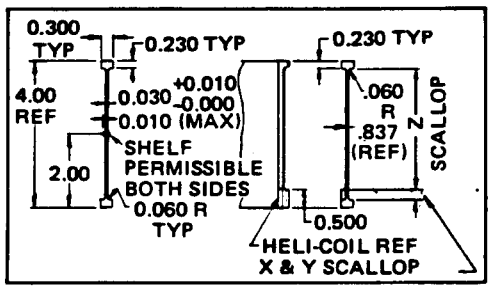

B. TYPICAL WEB

6-0282

Figure 4.2.4-2. IMP Details

the IMP and the ESM. The other support consists of two ball joints having a threaded interconnection that provides platform adjustment about the fixed ball. Two thin wall 7075-T73 aluminum alloy struts with ball joints at both ends complete the support system. A typical ball joint assembly is shown in Figure 4.2.4-4.

The louver system (shown in Figure 4.2.4-5) and the sunshade complete the major subassemblies mounted to the IMP. The AVHRR/3 and HIRS/3 louver groups are mounted within a polished aluminum frame on the upper portion of the platform. Figure 4.2.4-6 shows one set of louvers with their drive assemblies.

The sunshade consists of three sections: a fixed shade, and two deployable shades. See Figures 4.2.4-7 and 4.2.4-8. The fixed shade is designed to fit within the static fairing envelope and provide -X shading. The fixed sunshade also supports the deployable sections in both the stowed and deployed configuration and also provides the proper thermal coupling between the IMP sensors and space. The shade is constructed of polyurethane foam panels with aluminized Kapton® skins. These panels are bonded and fastened to a polished aluminum reinforcement frame which is insulated from the louver frame by Polycarbafil washers.

The deployable sunshades provides ±Y shading to the AVHRR/3 and HIRS/3 cooler doors. The shades stow neatly inside the spacecraft fairing along the ±Y sides of the spacecraft. Each deployable sunshade consists of two battens, a hinge assembly, and one shade membrane. The battens are fabricated from 0.25x0.50x32

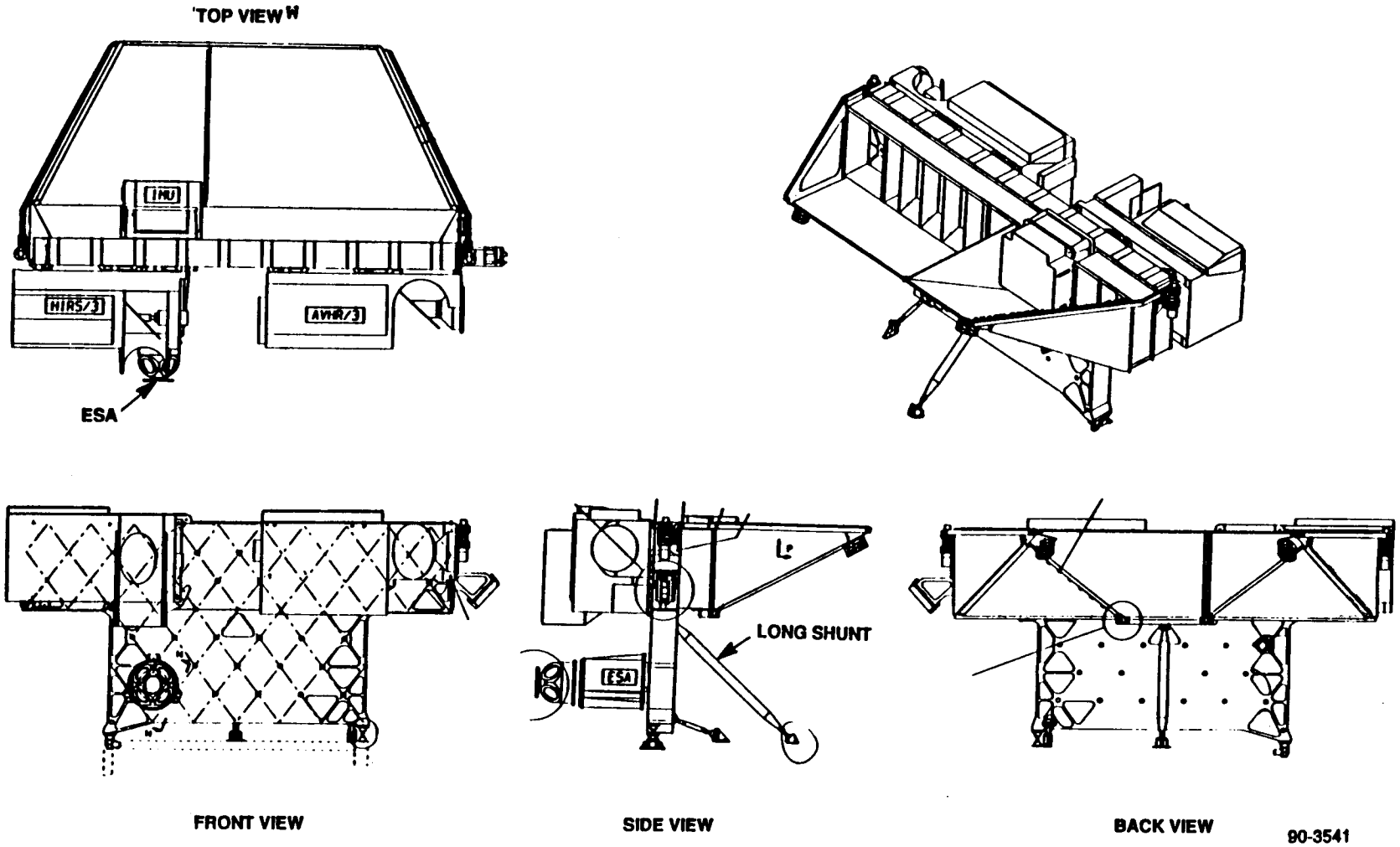

Figure 4.2.4-3. IMP Attachment Details

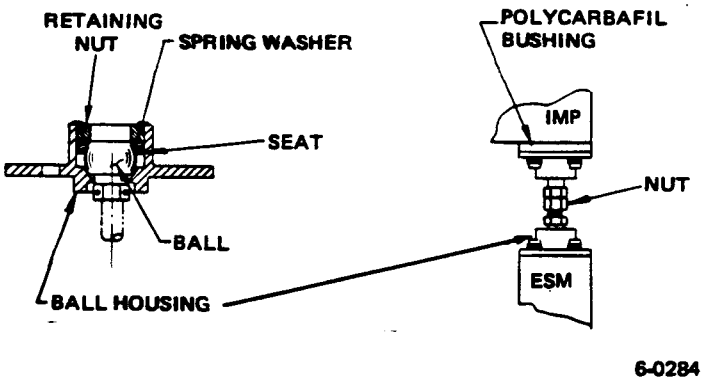

Figure 4.2.4-4. IMP Mounting Configuration

inch silicone-coated Kevlar® laminate. The purpose of the battens is to support the membrane in the stowed and deployed configurations. The shade membrane is made from two-ply, 1 mil thick, reinforced black Kapton®, and attaches directly to the the battens and fixed shade. The deployable shades are actuated by pyrotechnic devices that sever Kevlar® cords, thus allowing the battens to deploy.

Adapters are used to locate the instrument mounting pattern with respect to the IMP grid, thus providing instrument placement on a universal mounting surface. The IMU, which operates at a substantial temperature differential from the IMP is mounted on insulating bushings in a set of one fixed and two flexible mounts. The flexible mounts (see Figure 4.2.4-9) are thick blade-shaped supports which support loads in two directions, but which will deflect under load in the third direction. The flexible mounts are oriented so that the direction of maximum flexibility is along the line passing through the fixed mount. This provides support along any axis while relieving thermal expansion between support points.

Instruments, adapters, and ball joint assemblies are fastened to the IMP with high strength 6AL-4V titanium alloy bolts. A typical adapter is shown in Figure 4.2.4-10. This adapter is fabricated from 7075-T73 aluminum and has threaded inserts to mount the instruments, as well as clearance holes for mounting to the platform. The AVHRR/3 and IMU have conical bushing interfaces with the adapters for alignment maintenance. These conical bushings are potted after alignment and become part of the instrument feet. Adapters located on the louver-controlled area of the platform are black anodized.

The ESA and SSD alignment is maintained by plastic (epoxy) dowels as shown in Figure 4.2.4-11. The dowel assembly and its temporary screw and washer is installed in the adapter with a press fit. After alignment, the gap formed within the oversize hole in the mounting foot is potted making the tapered sleeve part of the mounting foot.

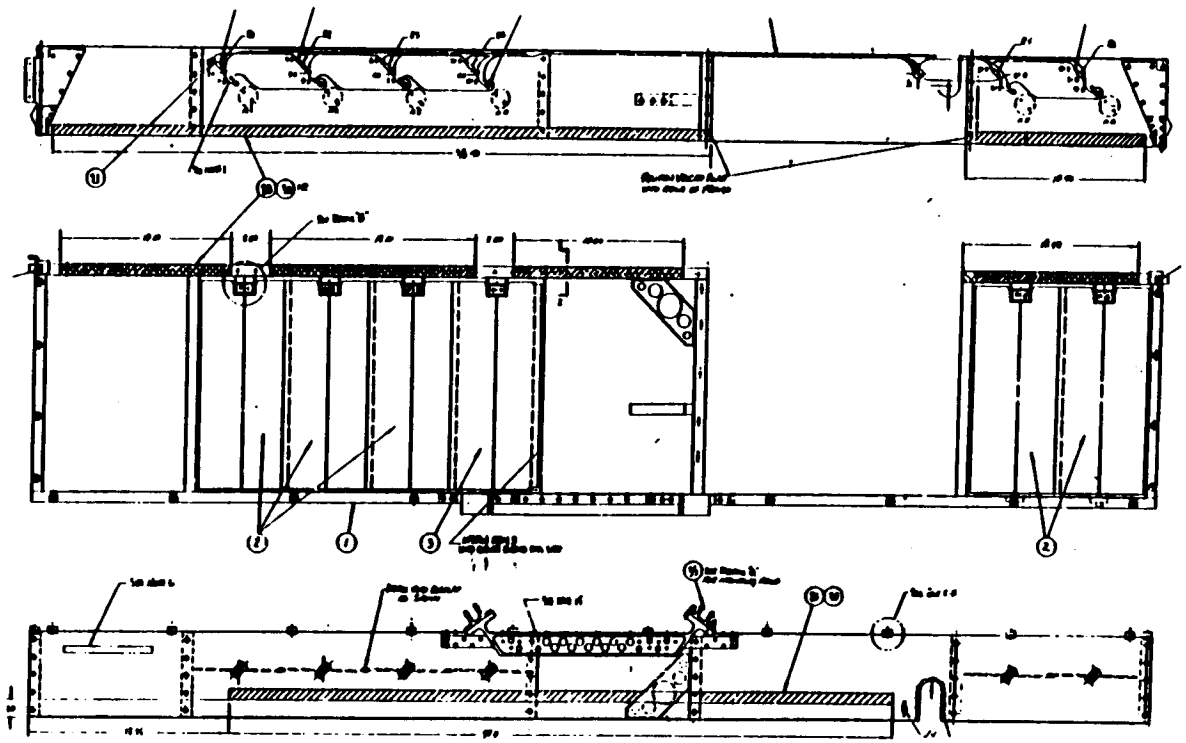

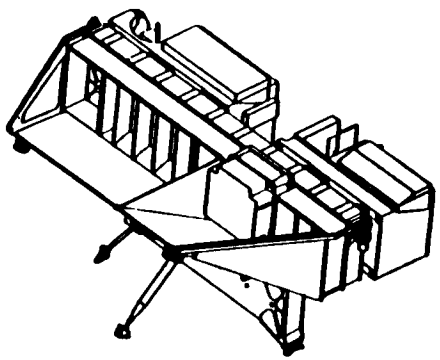

Figure 4.2.4-5. IMP Louver Assembly

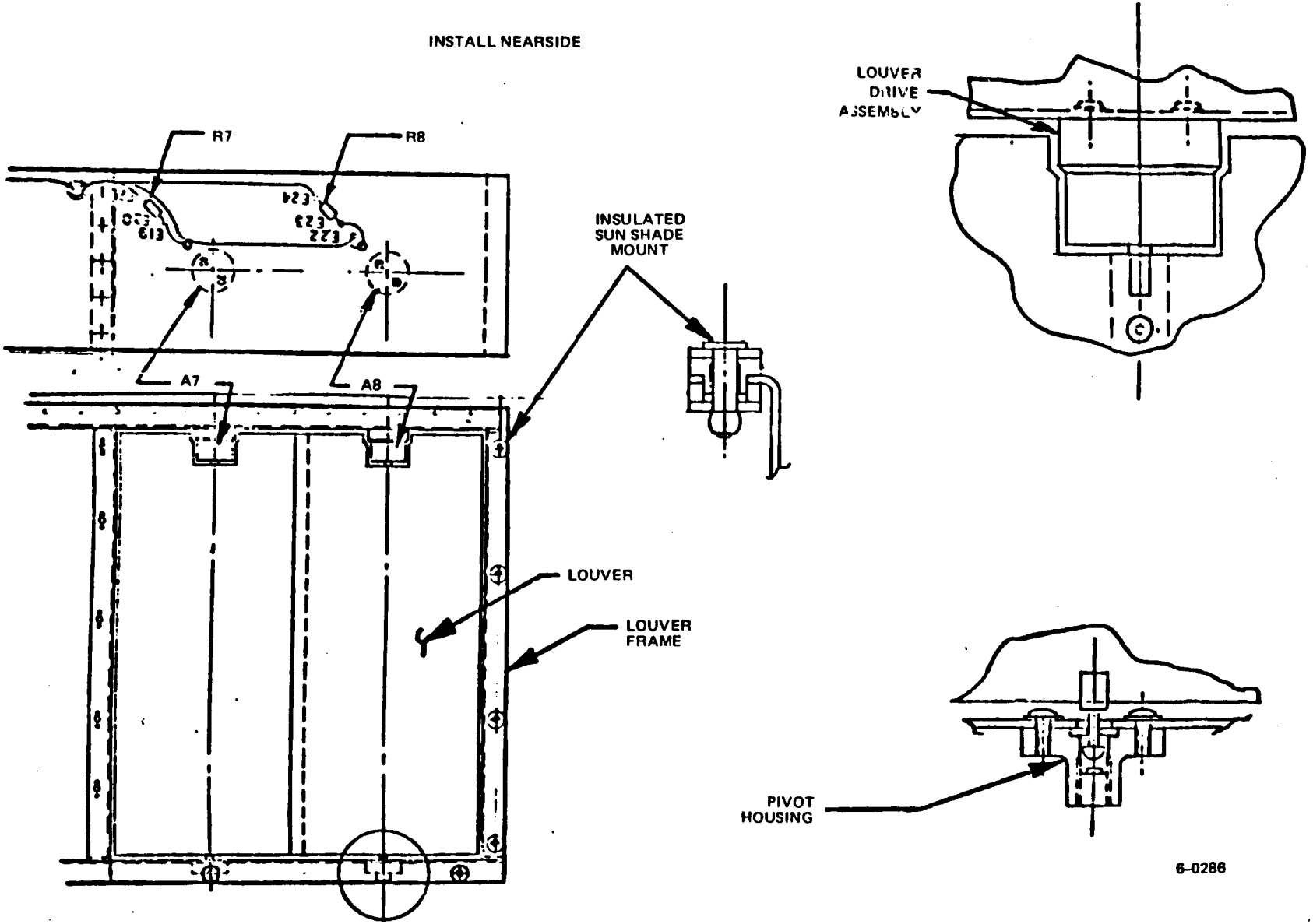

Figure 4.2.4-6. IMP Louver Assembly Detail

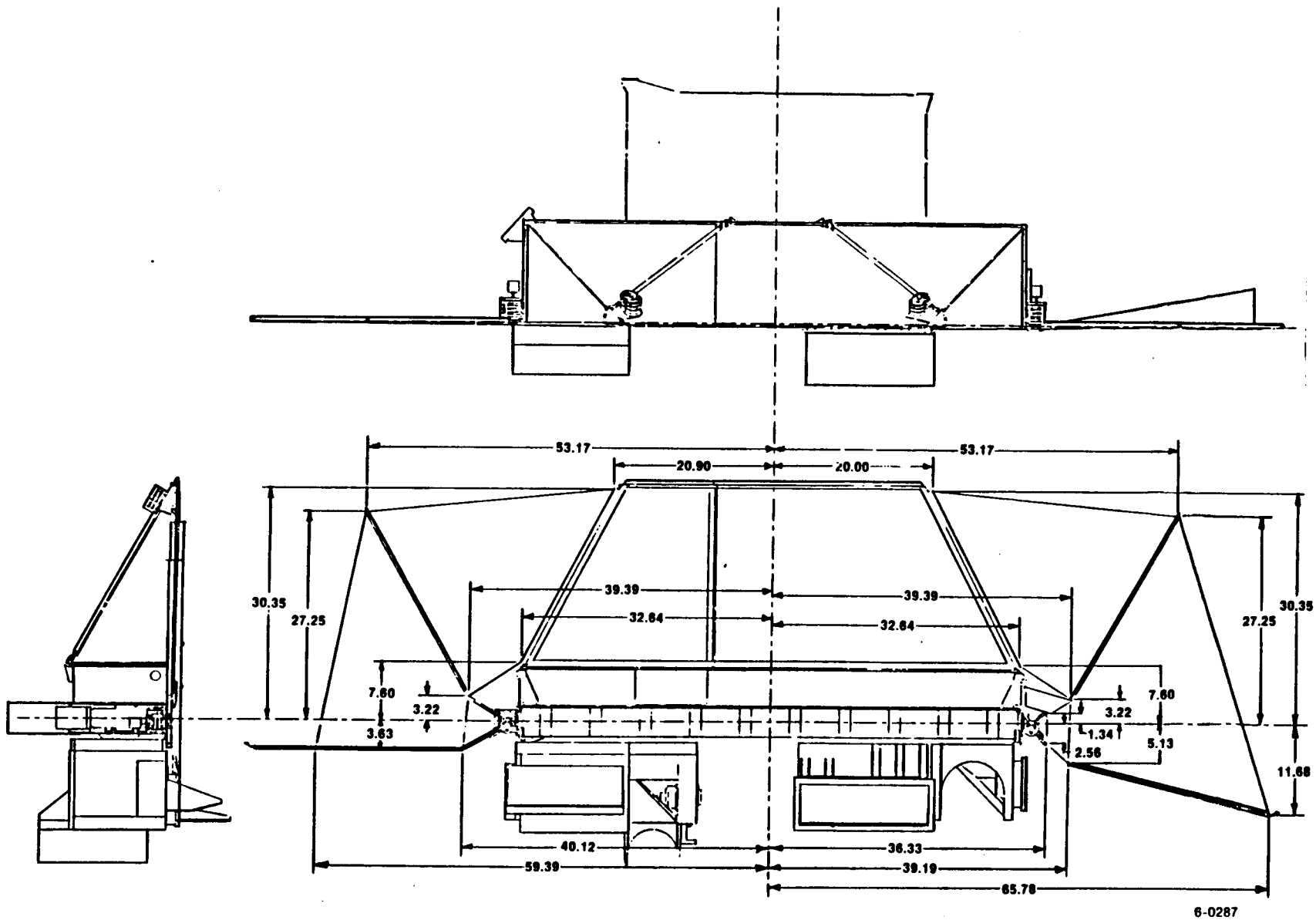

Figure 4.2.4-7. IMP Sunshade

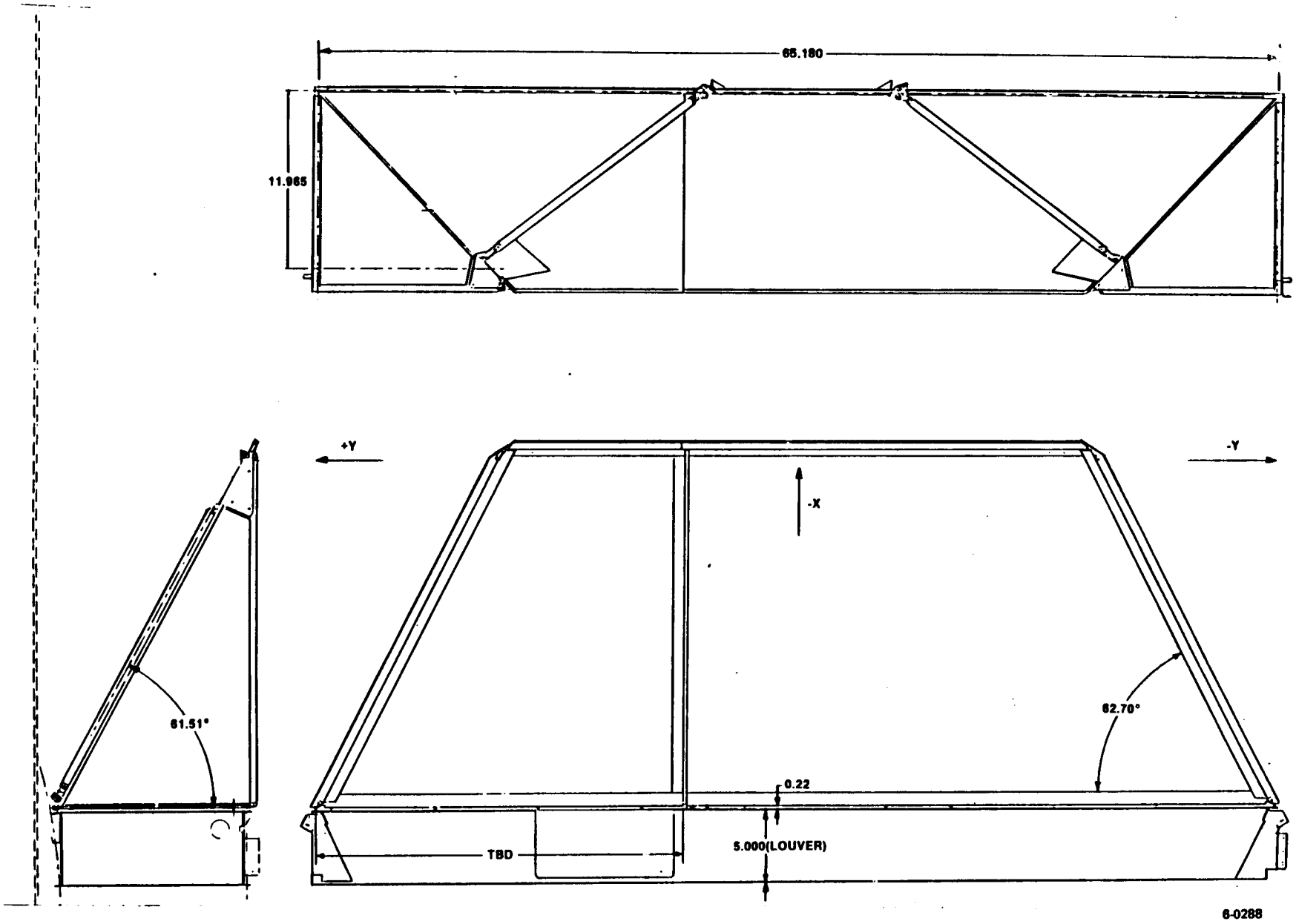

Figure 4.2.4-8. IMP Sunshade, Fixed

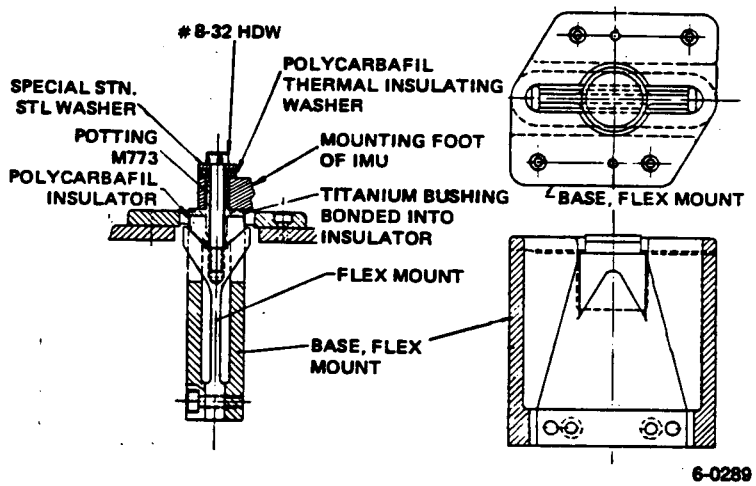

Figure 4.2.4-9. IMU Flex Mount

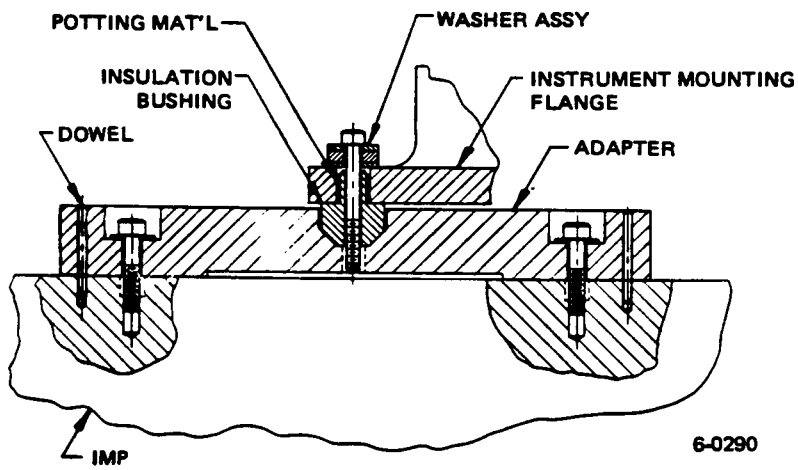

Figure 4.2.4-10. Typical Instrument Mount Showing Conical Bushing

Instrument alignment is provided in two stages: in the first stage, a mechanical alignment locates and fastens dowels in all adapters. In the second stage, an optical alignment is performed to position and verify the locations of all instruments relative to the ESA. Except for the AVHRR, which has critical alignment requirements, and thus is shimmed, tolerance budgeting between the adapters and the machined platform has provided a design which meets the alignment placement requirements without the use of shims at either the instrument to adapter interfaces or the adapter to platform interfaces. The adapters are mounted as a set for each instrument by a locating fixture. This fixture is aligned to the ESA fixture prior to pinning. This mechanical alignment results in a platform with adapters fully aligned to the primary reference adapters prior to any instrument mounting or optical alignment.

4.2.4.2 Equipment Support Module

The ESM structure, shown in Figure 4.2.4-12 is approximately 99.5-inches high and would fit within a hexagonal prism measuring approximately 43.5 inches across the points. The upper 77.2 inches has the shape of a pentagon which is

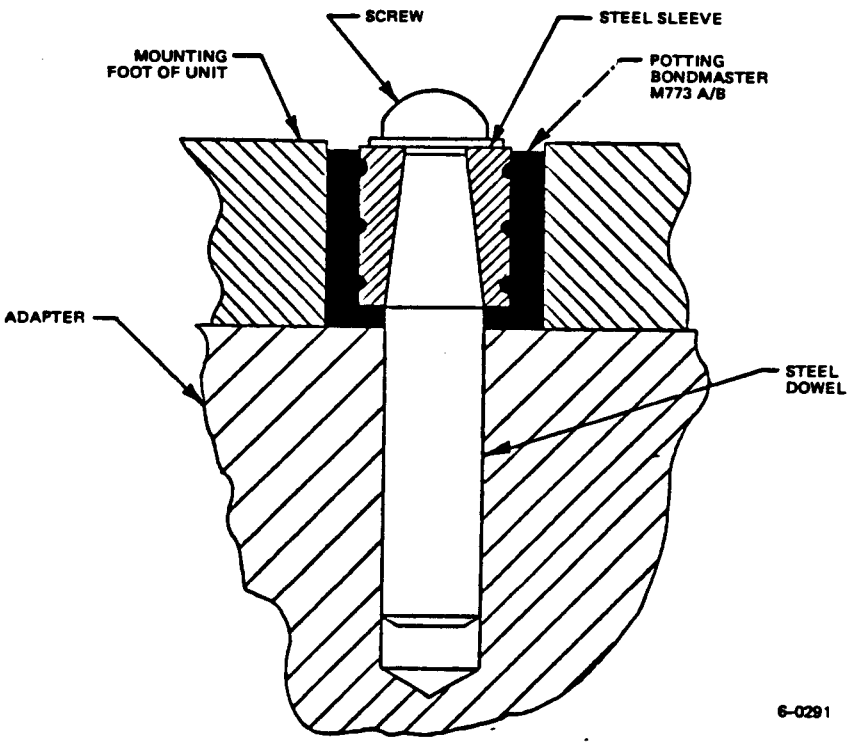

Figure 4.2.4-11. Plastic Dowel

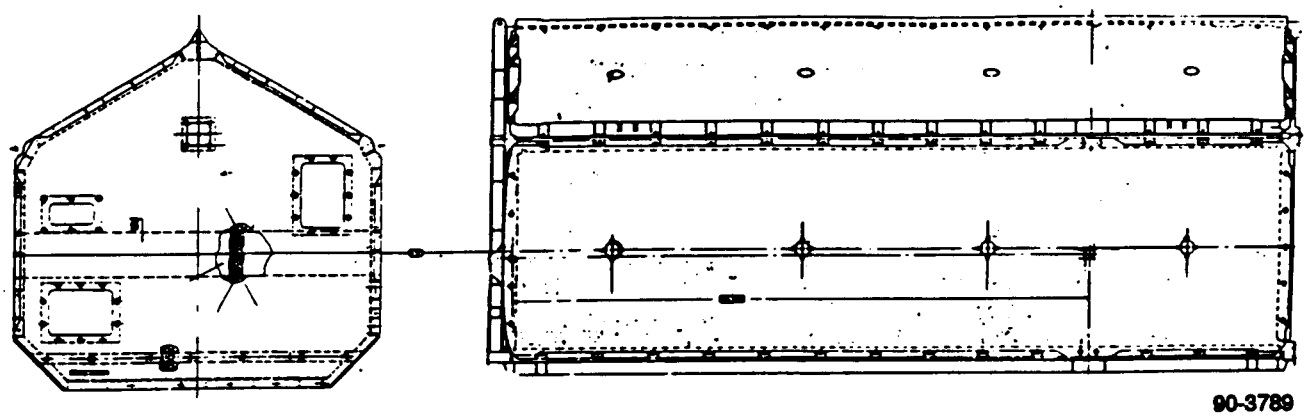

Figure 4.2.4-12. ESM Structure

formed by removing an apex from the hexagon. This section is covered with honeycomb panels that support most of the electronic equipment, antennas, the stowed solar array, and some of the sensors.

The major item supported by the ESM is the IMP. Ball joint ended struts, including one fixed support, as described in Section 4.2.4.1, are attached to the frame, top panel, and the side panels. Extruded square tubes, built-in to the associated ESM panels, distribute the load. In addition to the IMP, the ESM supports nearly all of the spacecraft's electronic components, the SBUV the MEPED, and the AMSU-A1, -A2, and -B sensors as well as the the UDA, SAR, SLA, BDA, and one set of SOA antennas. An additional set of SOA antennas is located on the RSS/Truss interface.

Active thermal controllers (pinwheel louvers and radiators, shown in Figure 4.2.4-13) and blankets are attached to the external surfaces of the four ESM side panels to control the internal temperatures. Blankets are used on the top (-Z) and front (earth-facing) panels.

At its lower (+Z) end, the ESM is supported by the truss section described in Section 4.2.4.3. The ESM to truss interface is a five-point planar joint secured with one 0.25 inch diameter 17-4 ph stainless bolt and two 0.375 inch diameter alloy steel bolts at each interface point.

The ESM frame is a riveted, machined-member structure 99.5 inches high which would fit inside a 43.5 inch diameter cylinder. The upper frame members supporting the ESM panels are fabricated from 7075-T7351 aluminum alloy angle extrusions, the lower truss interface fittings in the RSS are machined from 7075-T73 aluminum alloy.

The upper part of the frame is a pentagon, 77.2 inches high, formed from a regular hexagon by removing one apex. The locations of the fastening holes in the frame for attaching the ESM panels, the solar panels, and the RSS is controlled by matching drill jigs. Hard points for spacecraft handling are machined into the frame. Lightweight, high strength 6AL-4V titanium bolts are used to fasten the ESM panels to the frame.

The ESM frame accuracy is controlled so that the edge members and the solar panel mounting holes are held perpendicular to the RSS mounting plane to within 0.020 inch. Flatness of the truss mounting plane is held to within 0.005 inch.

The seven ESM panels are bonded honeycomb sandwich structures which cover the frame members and support some of the sensors and most of the electronic equipment of the spacecraft, and is arranged as shown in Figure 4.2.4-14.

The ESM front panel, shown in Figure 4.2.4-15 is approximately 37.3 inches wide by 75.5 inches long; it supports the SBUV/2, AMSU-A2, AMSU-B, and the BDA, SAR, SLA and UDA antennas on its external surface, and various electronic equipment on its interior surface. The top panel, shown in Figure 4.2.4-7 is a pentagon approximately 37.3 inches wide by 34.9 inches long; it supports two of the IMP struts and resists the lateral load from the fixed IMP support point. The AMSU-A1 and MEPED are supported on brackets off the top panel. There are four side panels which are approximately 21.3 inches wide by 76.5 inches long. Two of these panels support the longitudinal loads of the IMP

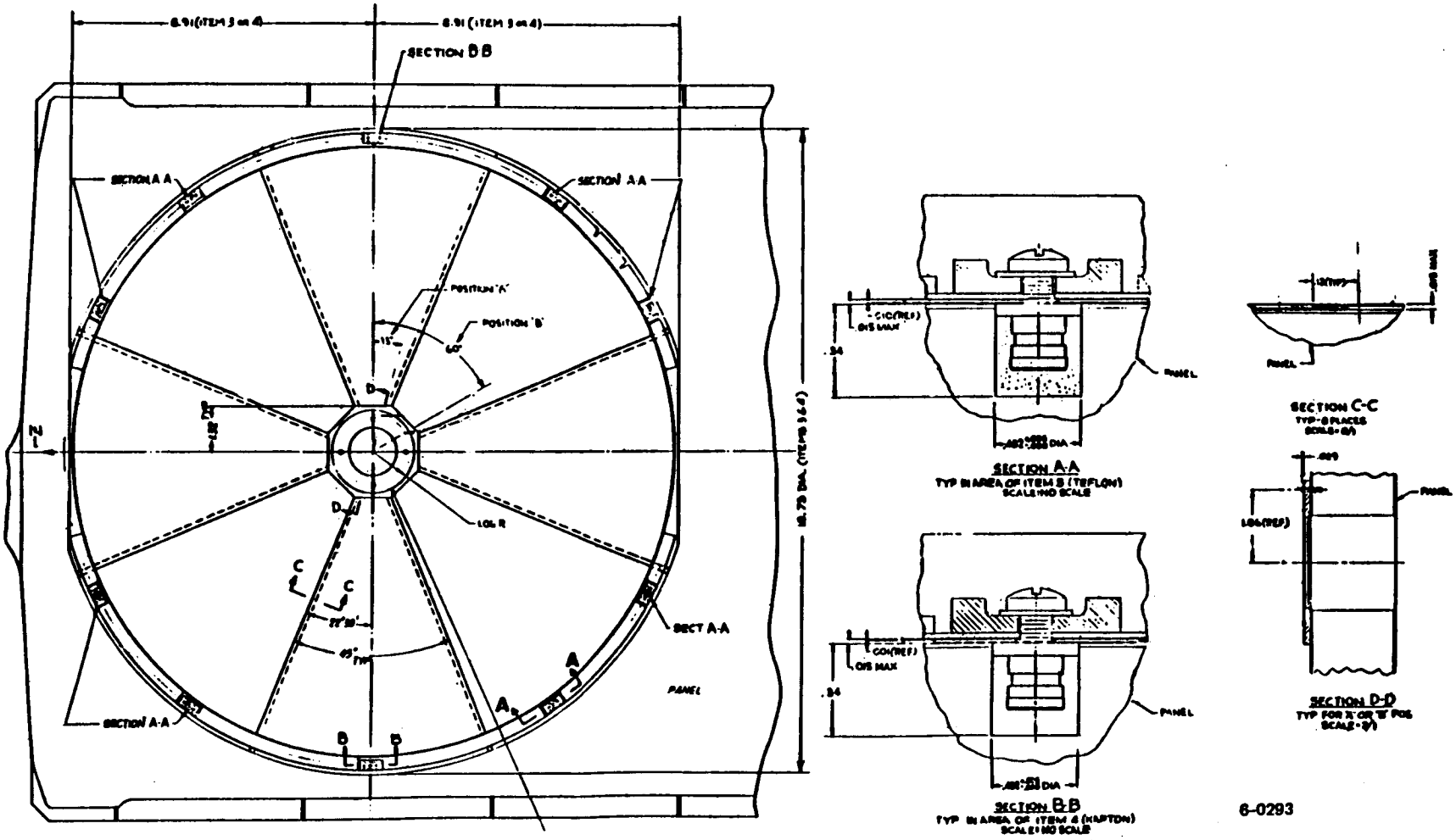

Figure 4.2.4-13. ESM Panel Louvers

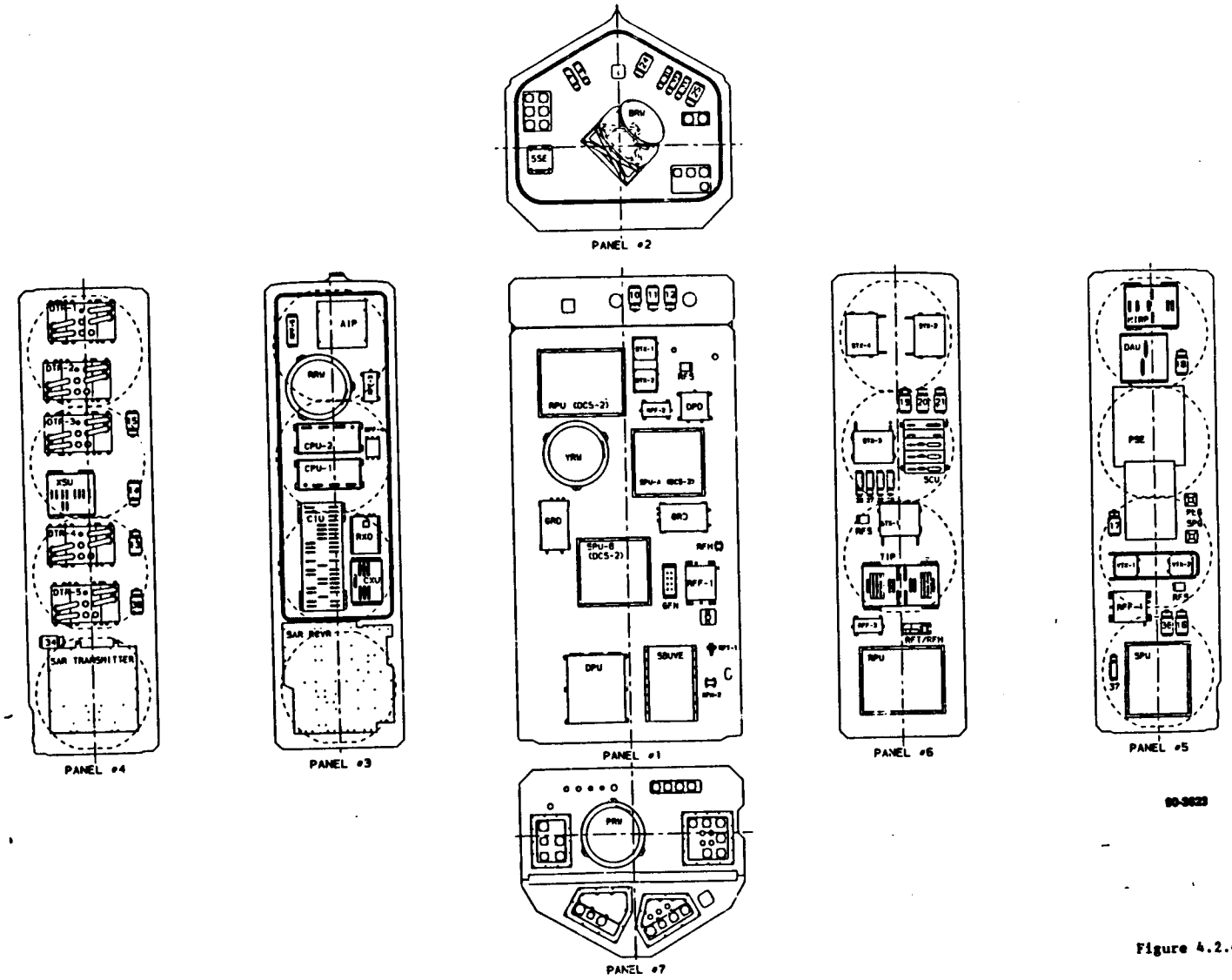

Figure 4.2.4-14. ESM Internal Arrangement

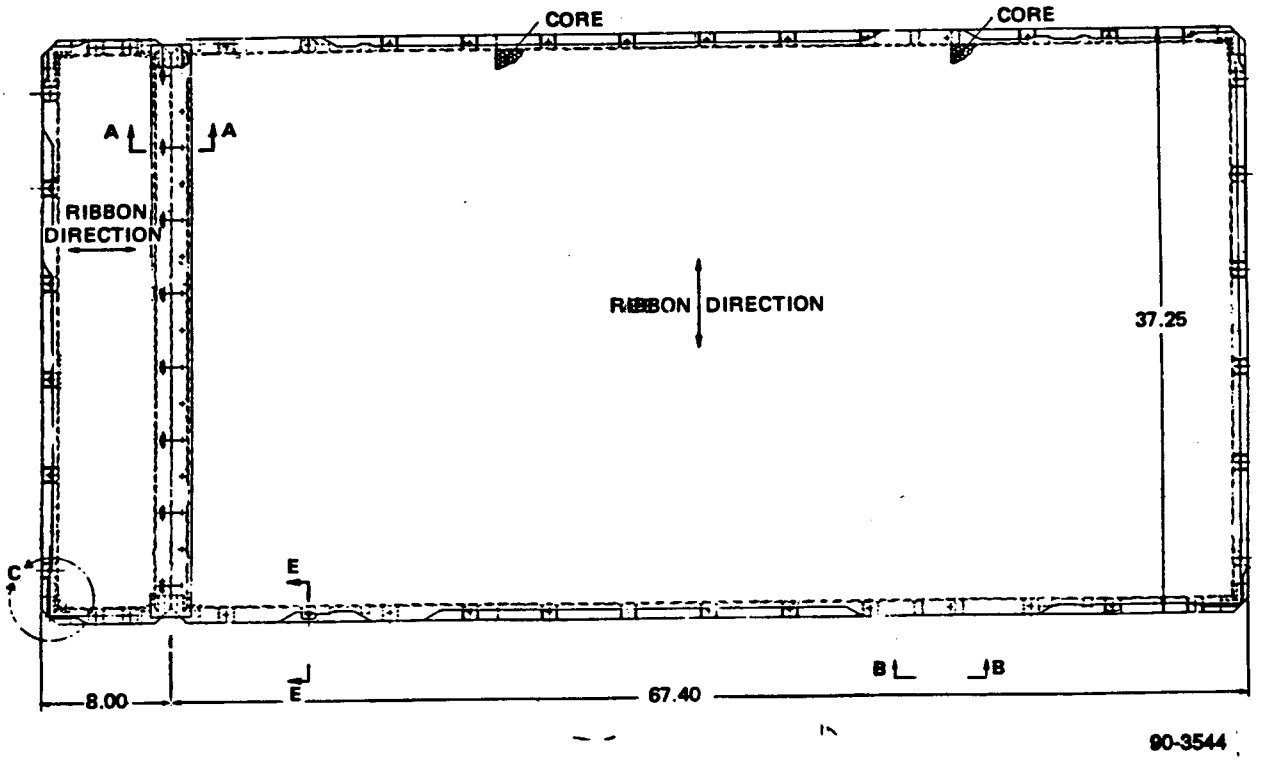

Figure 4.2.4-15. ESM Front Panel

panel. All of the side panels have mounting and blind clearance holes for the pinwheel thermal controller; mounting holes for the solar array panels are provided in the edges of panels 3 and 6.

Except for thickness of material sections all the ESM panels are constructed in the same manner and of the same materials. All panels contain a honeycomb core of 5052-H39 aluminum with a cell size 0.25 inch constructed from 0.001 inch thick foil. All panel skins are 7075-T73 aluminum alloy sheet. The top and four side panels are all constructed with 1.25 inch thick cores. The top panel skin is 0.025 inch thick. Panels 4 and 5 each have 0.010 inch thick skins and panels 3 and 6 have 0.030 inch thick skins. The front panel has 0.012 inch thick skins and a 1.25 inch core. The bottom panel shown in Figure 4.2.4-16, uses 0.012 inch thick skins and a 0.50 thick core as well as 7075-T73 0.050 thick sheet edge members and is used primarily as a harness bulkhead between the RSS and ESM. All panels except the bottom have electronic boxes mounted on their inboard surfaces and require machined 7075-T73 aluminum alloy edge members which act as hard points for panel to frame fastening. Panel aluminum substrate materials are joined using rivets and adhesives. The adhesives used consist of American Cyanamid FM-123-2 modified epoxy adhesive to bond the skin to the core, American Cyanamid FM-37 modified epoxy foam to bond the edge members to the core, and 615 corefil syntactic foam to close-off the edges of holes. The American Starch M668 modified epoxy polyamid compound and CH16 catalyst are used to bond the edge flanges around the pinwheel and harness holes.

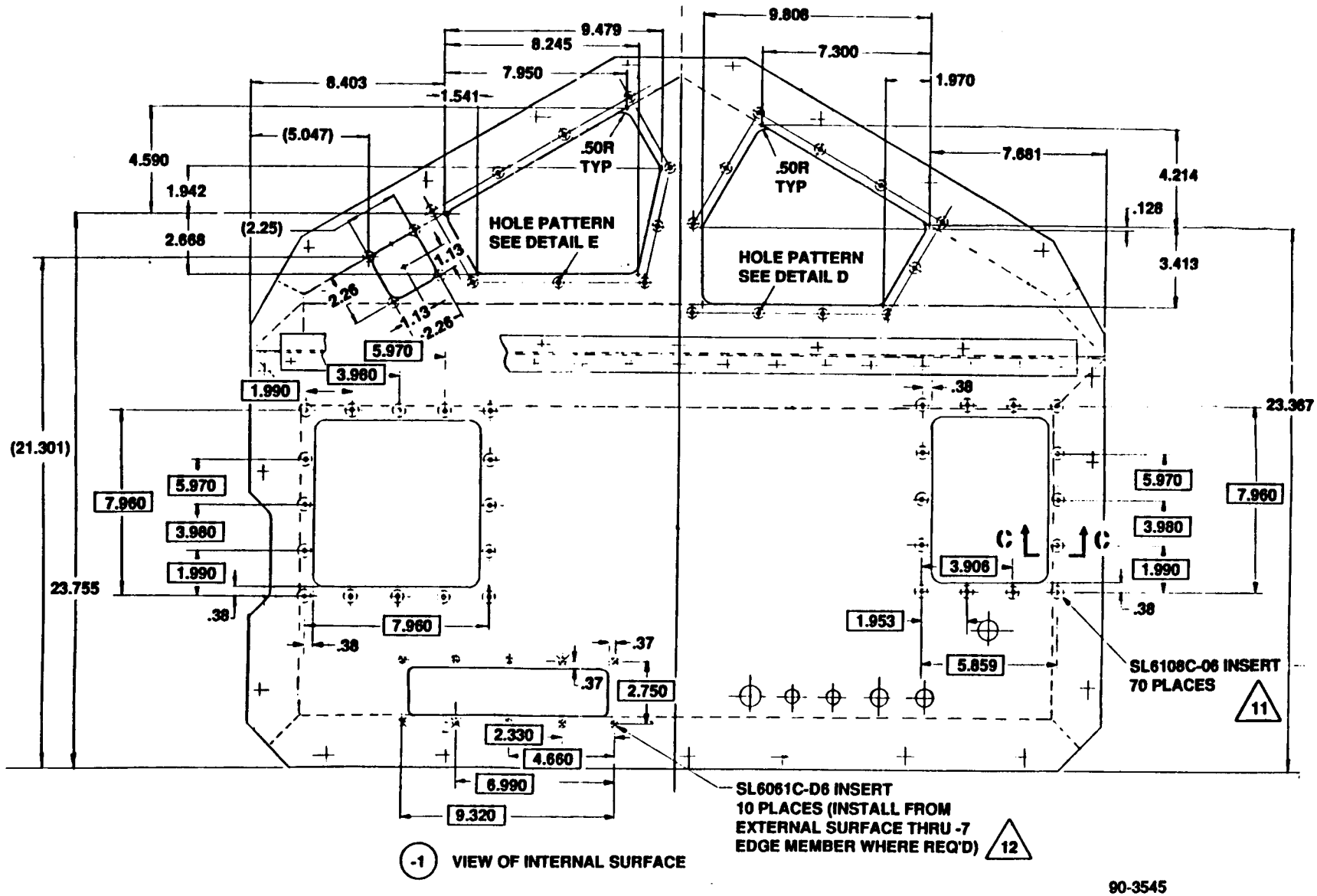

Figure 4.2.4-16. ESM Bottom Panel

Inserts used in the honeycomb panels consist of two basic types, as shown in Figure 4.2.4-17. A captive floating nut type of light weight potted inserts, each of which can support a minimum load of 350 pounds safely, is used to attach most components to the ESM honeycomb panels. These inserts are potted in place with Shur-Loc Corporation SLE3010 syntactic foam. The floating nut insert can be selected with thread sizes that range from 6-32 to 10-32. Tangs on the insert pierce the honeycomb skin during installation, and thus provide a grounded box mounting.

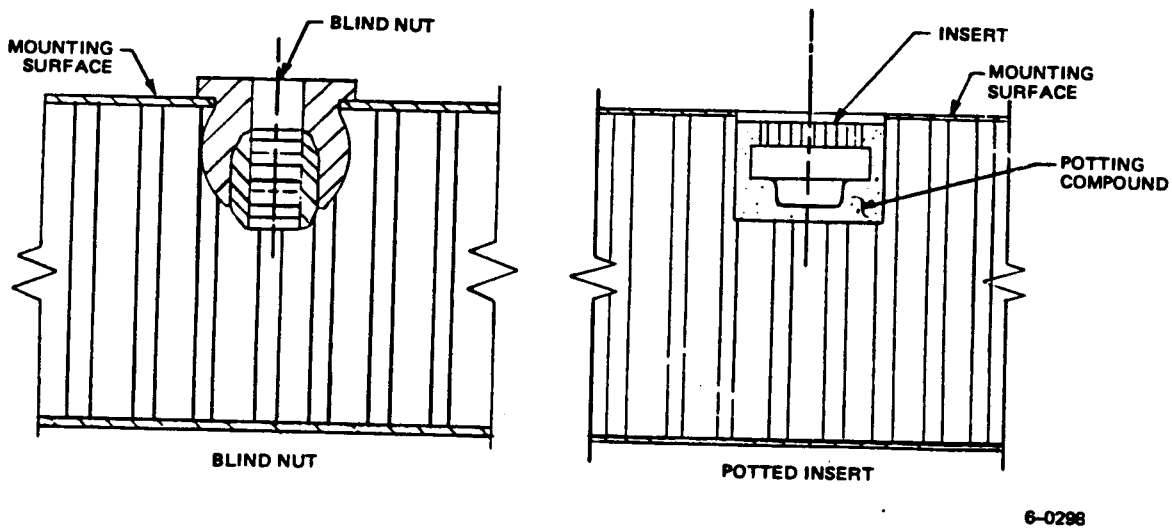

Figure 4.2.4-17. ESM Panel Inserts

The blind nut, the second type of honeycomb insert, is an extremely light weight insert that can support a twenty five pound load safely. This insert is used to fasten light-weight items as TCE units, connector brackets, component boards, the spacecraft harness, and the torquing coils.

Two of the sensors, the AMSU-A1 and the MEPED, are mounted on special brackets that attach to the ESM top and front panels. The AMSU-A1 mounting configuration is shown in Figure 4.2.4-18. An overhang is needed and thus brackets have been added to share some of the support loads into the earth facing panel. The sensor is isolated thermally from the ESM panel and overhung support brackets. The MEPED is mounted on a bracket assembly off the -X end of the top (-Z) panel. This configuration is shown in Figure 4.2.4-19.

4.2.4.3 Truss

The truss is an eleven element substructure fabricated from titanium extrusions and plate stock shown as in Figure 4.2.4-20. A special extrusion (tee) of 6AL-4V is machined to final size to form the beam members, while 6AL-4V plates of varying thickness form the corner gussets and attachment point fittings. All welds are double-sized (mostly double fillet type) for increased weldment strength.

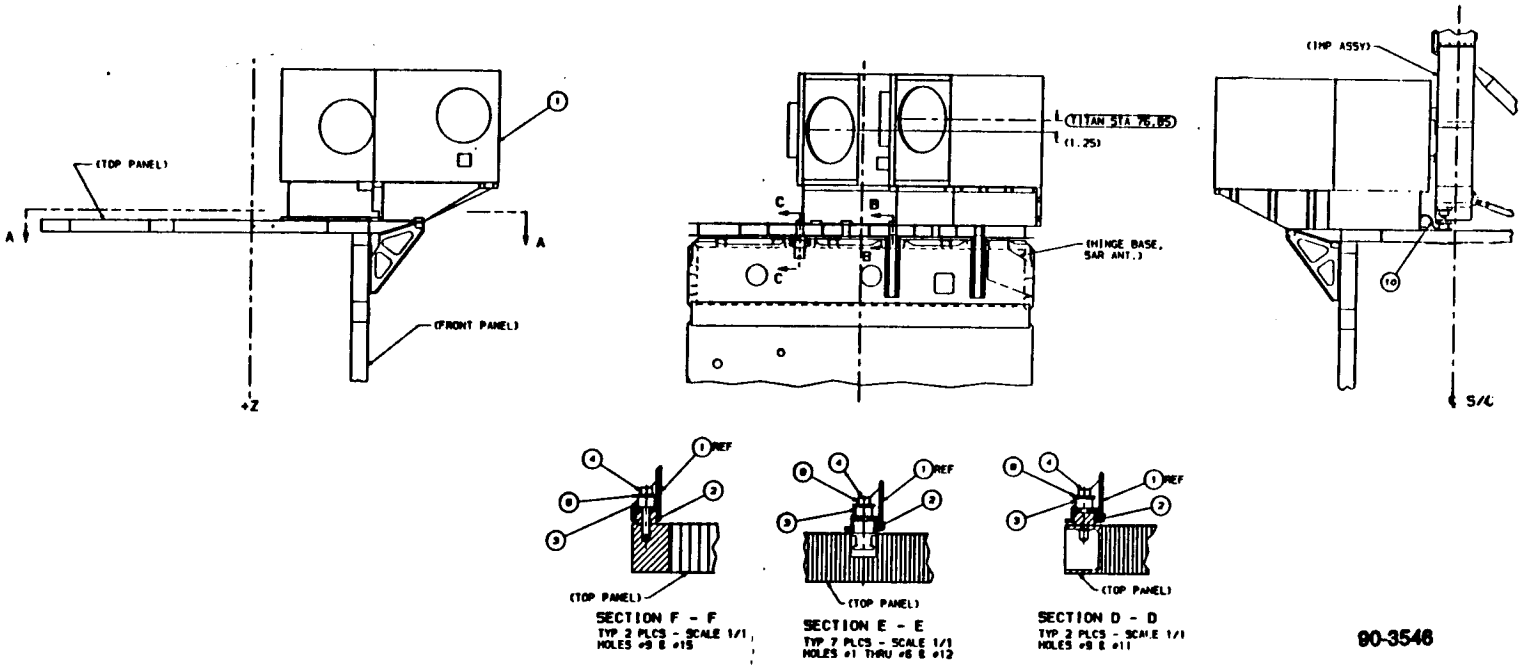

Figure 4.2.4-18. AMSU-A1 Installation

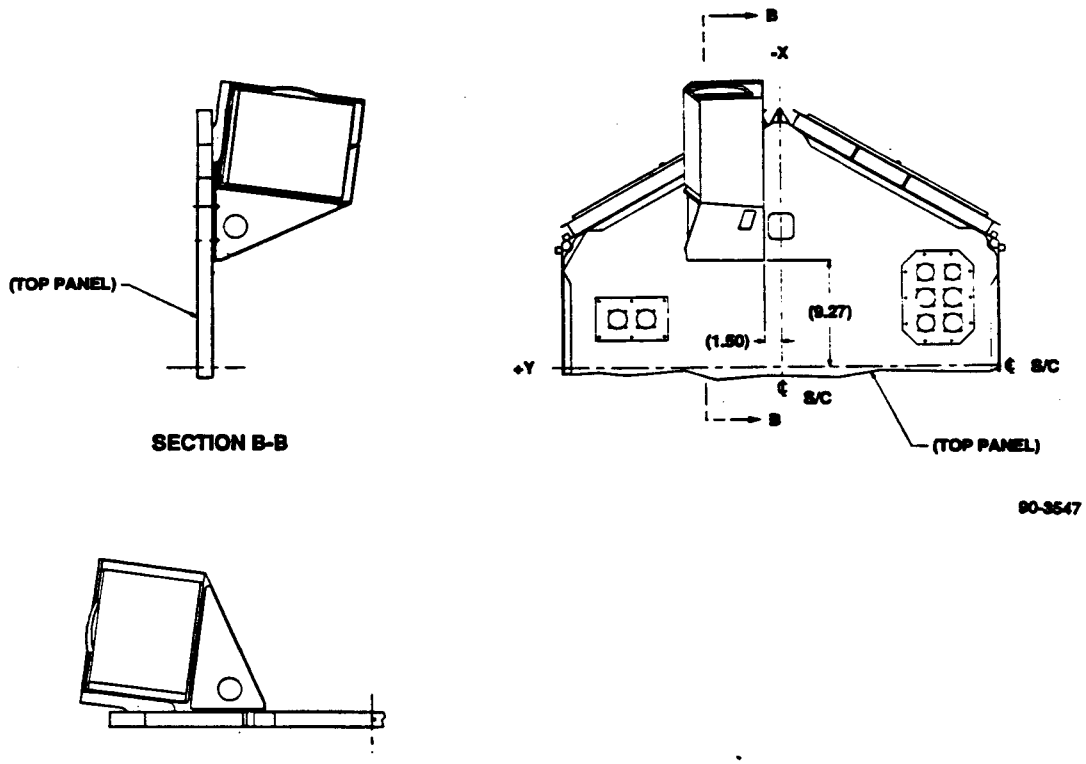

Figure 4.2.4-19. MEPED Installation

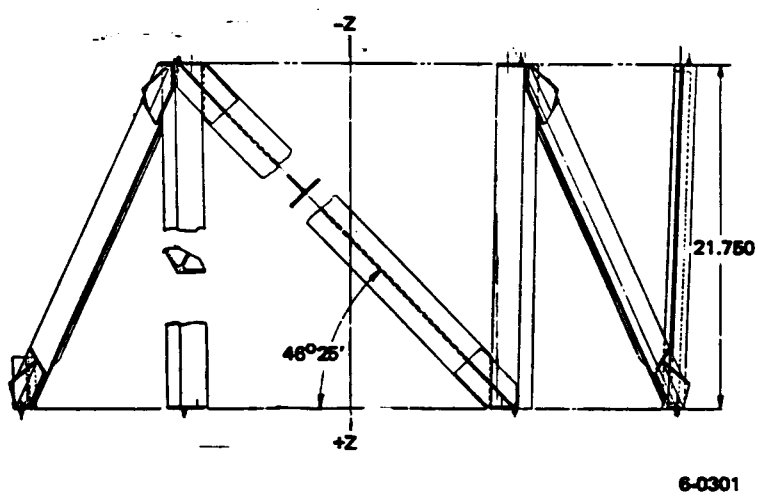

Figure 4.2.4-20. Truss Configuration

The truss supports and thermally isolates the ESM at its upper (-Z) interface plane through five attachment points. At its lower (+Z) end, the truss is supported by the RSS through a six-point circular attachment made with a 0.25 inch diameter dowel pin and two 0.375 diameter high strength alloy steel bolts at each point. See Figures 4.2.4-21 and 4.2.4-22. The truss also acts as the support structure for the TED and VRA as shown in Figures 4.2.4-23 and 4.2.4-24 respectively.

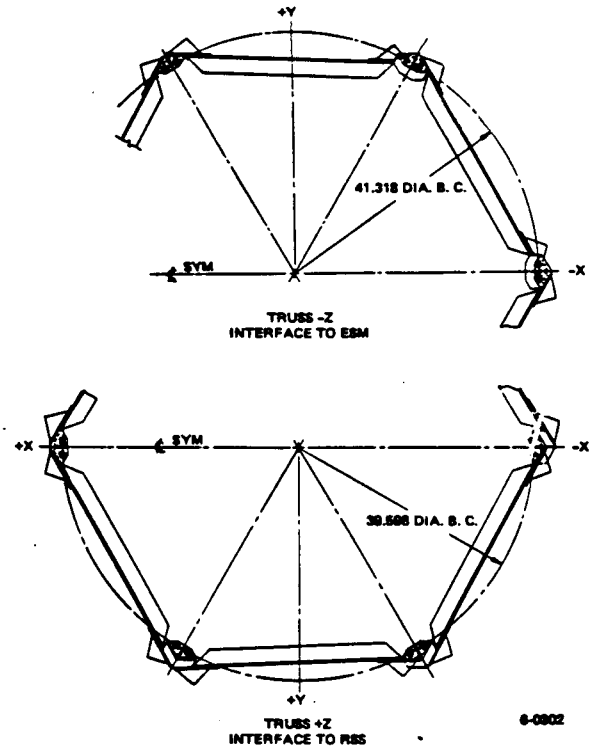

Figure 4.2.4-21. Truss to ESM and RSS Interfaces

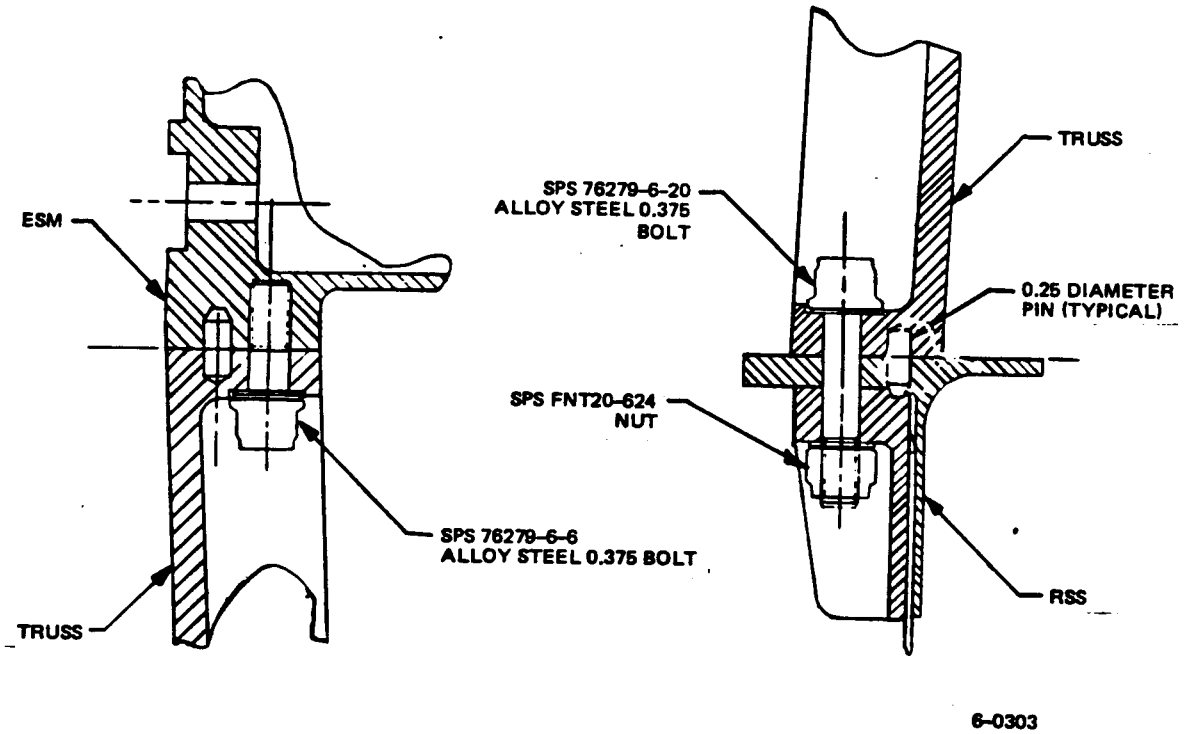

Figure 4.2.4-22. Truss Interface Hardware

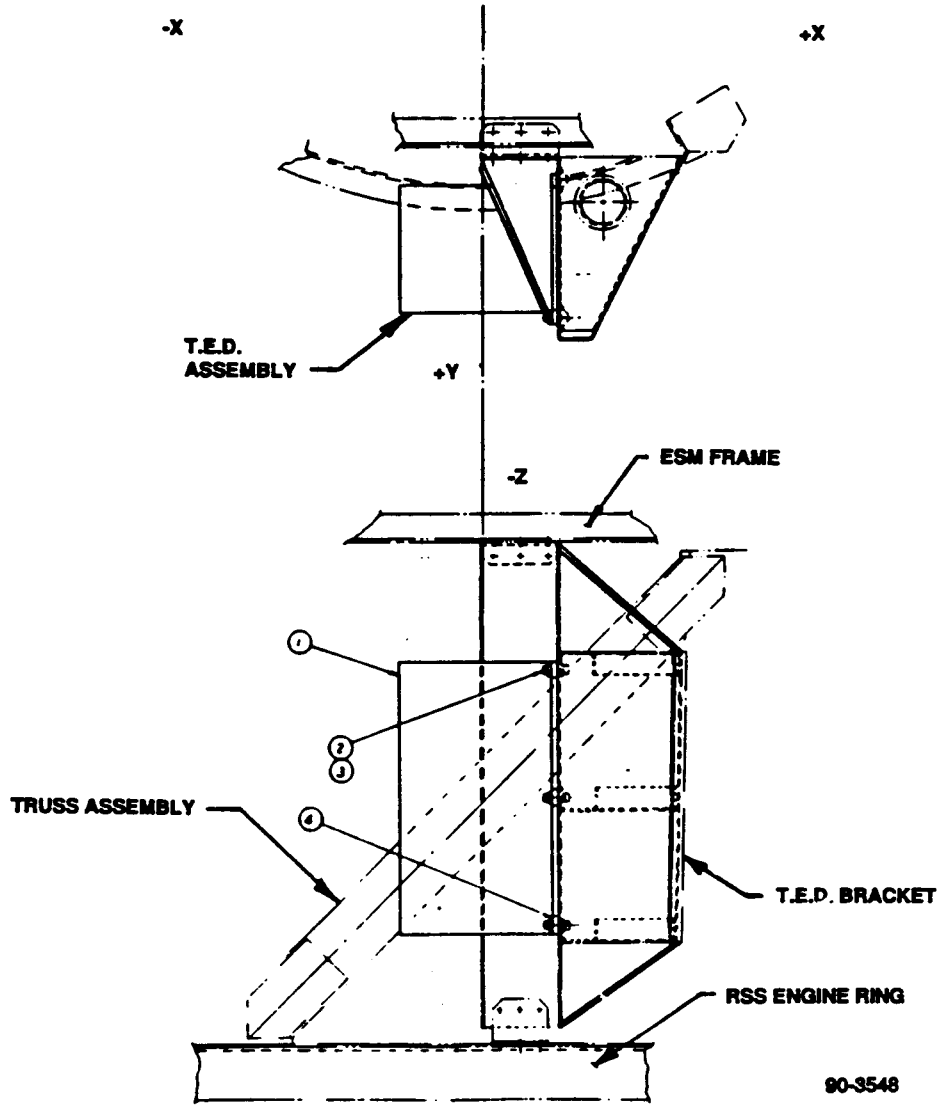

Figure 4.2.4-23. TED Installation

4.2.4.4 RCS Support Structure

The RSS, shown in Figure 4.2.4-25 is a riveted, reinforced aluminum alloy shell, approximately 41 inches in diameter by 32.5 inches long, which supports the ESM, Apogee Kick Motor (AKM), Solar Array Support (SAS), and Reaction Control Subsystem (RCS). The RSS consists of a 0.120 inch thick skin of 7075-T73 aluminum reinforced externally by four machined rings and internally by twenty-two 7075-T7351 ribs. The end rings are forged from 7075-T7352 aluminum alloy. The lower ring mates with the Booster Adapter assembly and is clamped to it with a V-band clamp assembly. The top ring mates with the AKM engine mounting ring shown in Figure 4.2.4-26 and supports the ESM/Truss. The intermediate rings both stiffen the shell and act as mounting surfaces to support the batteries, propellant and pressurant tanks, the Array Drive Electronics, the Battery Charge Assembly, and RCS equipment. The internal ribs add stiffness to the shell and support the balance/ballast weights.

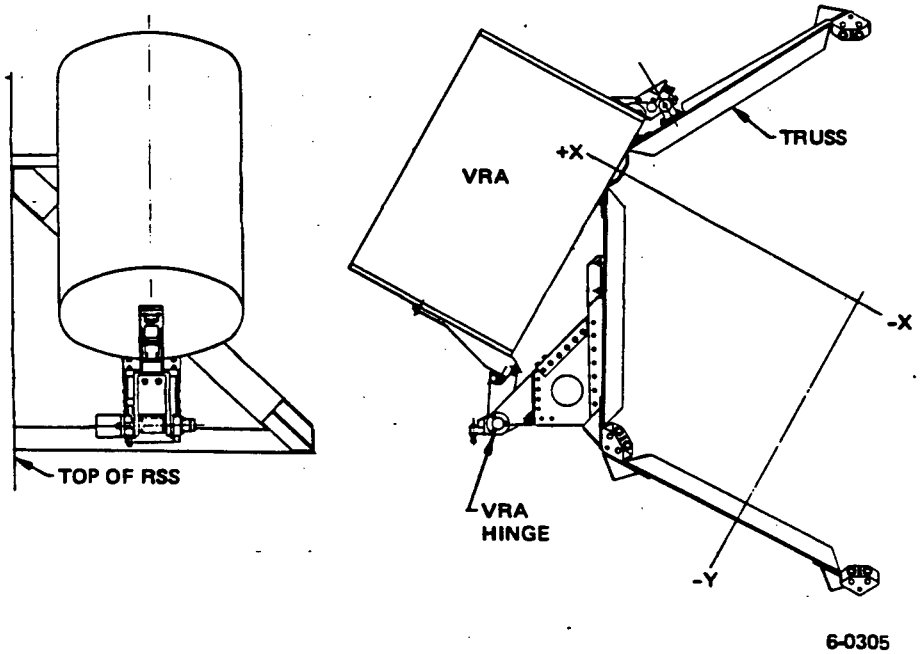

Figure 4.2.4-24. VRA Installation on Truss

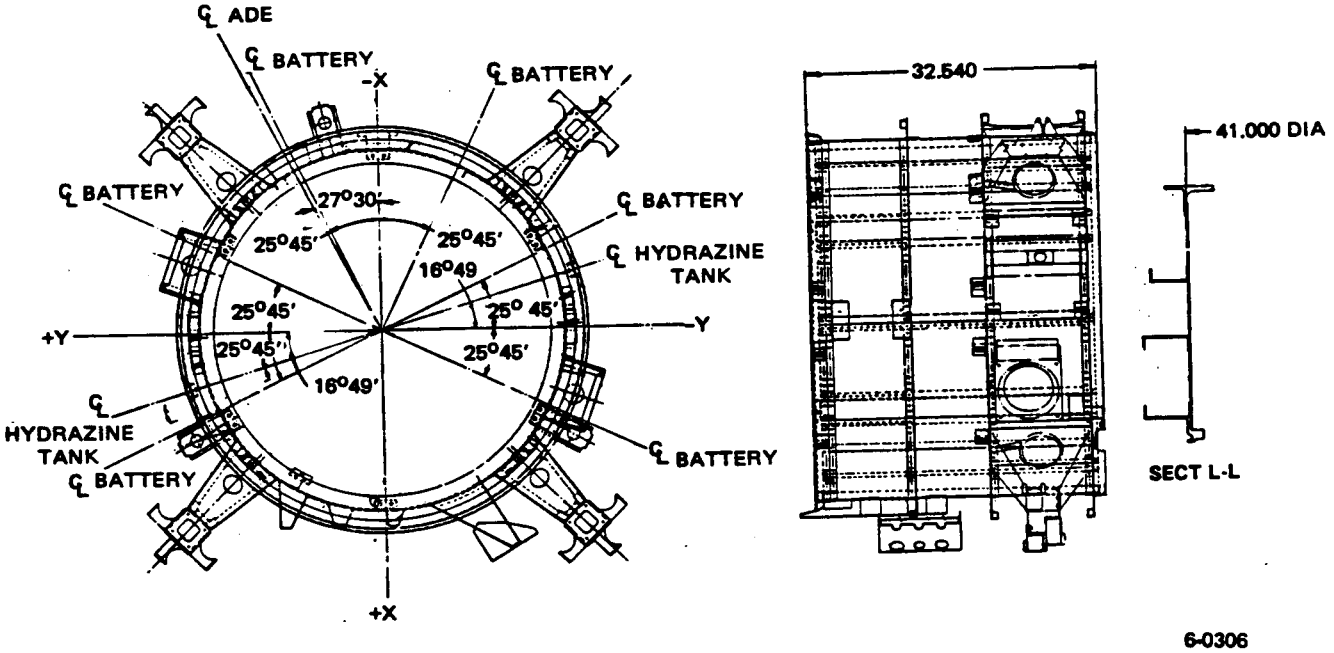

Figure 4.2.4-25. RSS Layout

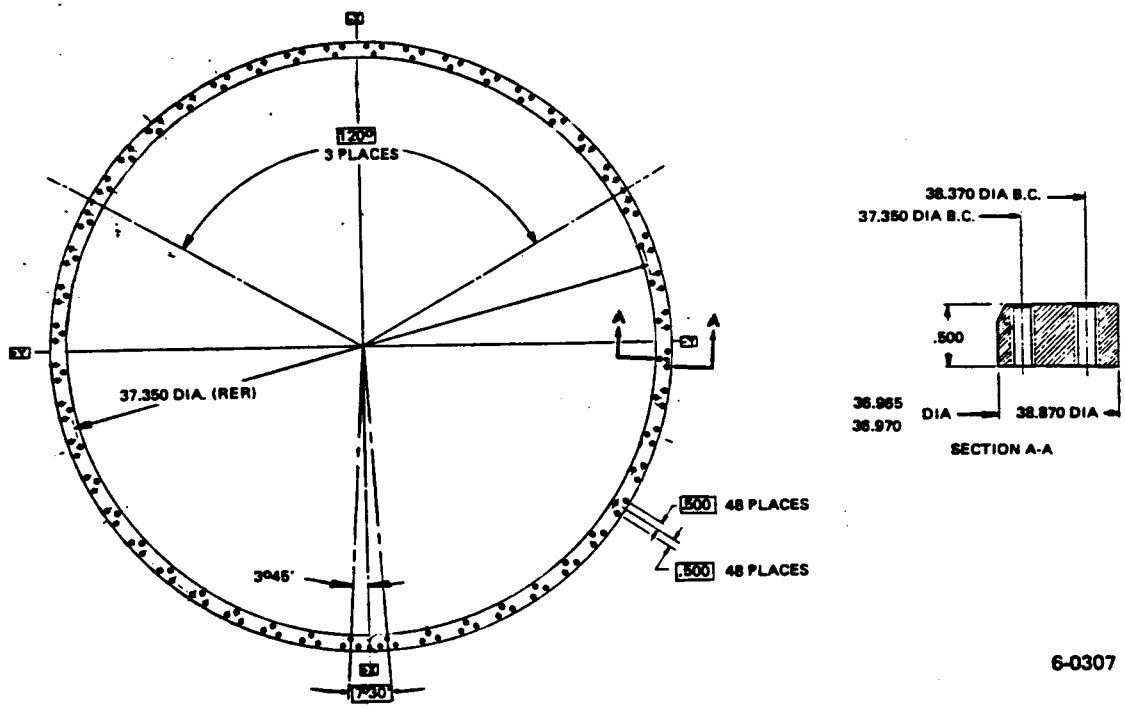

Figure 4.2.4-26. AKM Mounting Ring

Many minor brackets are fastened to the outer shell of the RSS to provide support for such items as the three breakaway connectors at the separation plane, the RCS fill and drain valves, the spacecraft umbilical connector, and the RCS manifolds.

Forty-eight 6AL-4V titanium bolts hold the AKM to the RSS as shown in Figure 4.2-27. A pilot diameter on the AKM Engine Mounting Ring fits into a mating diameter in the RSS which accurately locates the Z axis alignment of the AKM in the RSS structure. The X and Y axis orientation is achieved by lining up two pilot holes, one in the AKM ring and the other in the RSS.

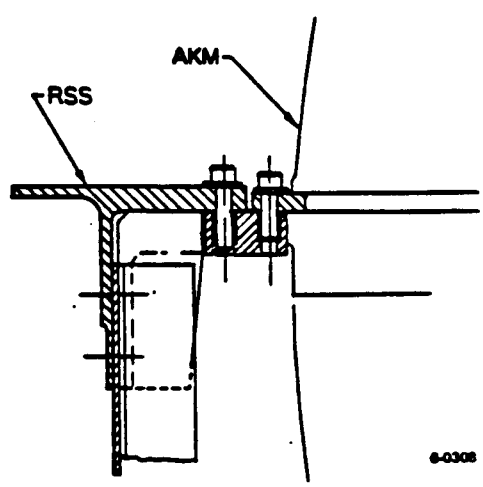

Figure 4.2.4-27. Detail of AKM Attachment to RSS

Concentricity between the second stage separation mating surface on the bottom ring and the internal diameter on the top ring is held to within 0.030 inch. Parallelism of the flanges of the top and the bottom ring is held to within 0.010 inch. Flatness of these rings is held to 0.004 inch. The mounting surfaces of the thruster brackets are held parallel to the separation plane to within 0.002 inch. The RSS assembly is shown in Figure 4.2.4-28, while the Apogee Kick Motor Assembly is depicted in Figure 4.2.4-29.

4.2.4.5 Adapter

The adapter, shown in Figure 4.2.4-30 is a reinforced aluminum conical shell, 10 inches high, which supports the spacecraft on the booster, and provides electrical connection and V-band clamp actuation. It is a riveted, stiffened sheet metal structure with a 0.210 inch thick aluminum alloy 7075-T7351 skin reinforced externally by twenty eight 7075-T7351 aluminum angle ribs. These are in line with the RSS ribs when the two assemblies are mated. The upper and lower rings are forged from 7075-T7352 aluminum, machined to form the required mating configuration to the spacecraft and booster interfaces. The mating surfaces are held parallel to within 0.010 inch and concentricity between the V-band clamp diameter and the booster bolt circle diameter is held to within 0.010 inch. A keyway in the upper ring and a sighting hole in the lower ring permits the spacecraft to be accurately located with respect to the booster. The adapter includes six hardpoints on the lower ring that provide the capability to lift the assembled spacecraft plus adapter as a unit.

Three separation plane connectors are mounted on three brackets attached to the upper end of the adapter and mate with similar connectors and brackets mounted on the RSS. The V-band assembly with its actuator squibs, lanyards, and pulldown springs is also supported at the top of the adapter structure.

4.2.4.6 Solar Array and Solar Support

A 181 square foot solar array is positioned (on-orbit) off the +Z end of the spacecraft and supported by a long boom that in turn is supported by the RSS. The solar array structure and its supporting hardware are described in the following section.

4.2.4.6.1 Solar Array

The ATN-KLM spacecraft uses a sun-following solar array which, after deployment, measures approximately 9 feet wide by 16 feet long. The solar array and the array support hardware have been designed to meet a set of fundamental requirements:

- Support the large array structure within heat shield constraints during launch.
- Deploy the array to its on-orbit configuration.
- Provide the appropriate structural characteristics for proper interface with the attitude control system.

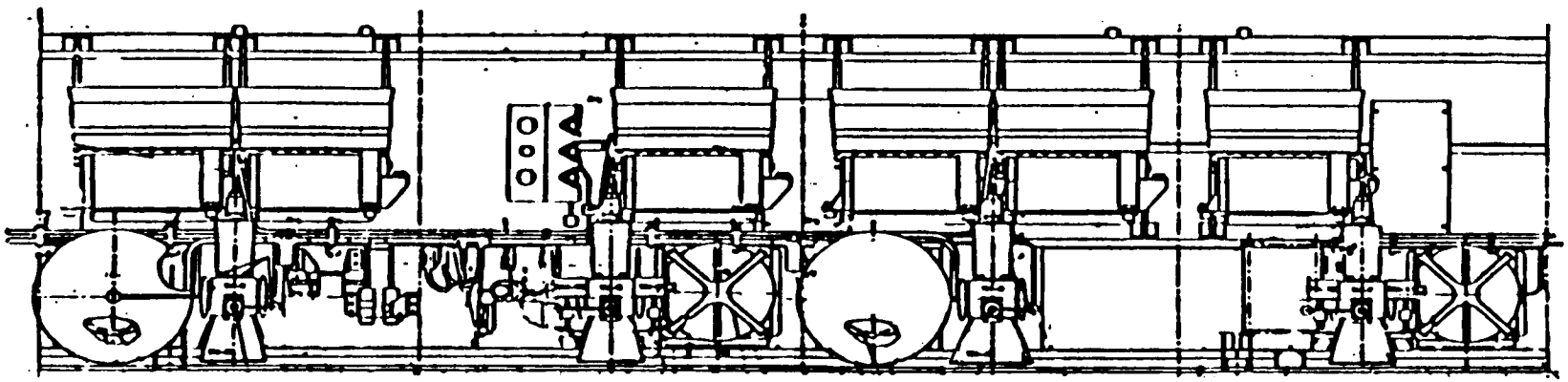

90-3549

Figure 4.2.4-28. RSS Assembly

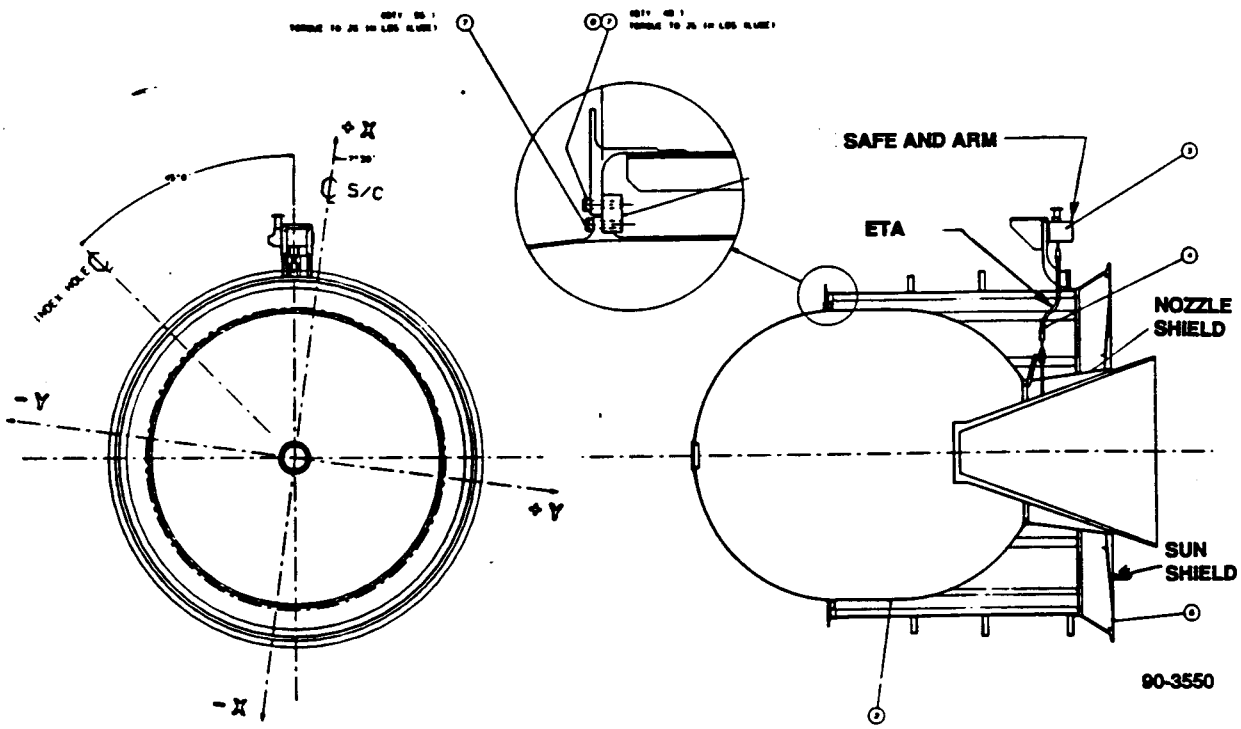

Figure 4.2.4-29. Apogee Kick Motor Assembly

The orbital configuration of the solar array is shown in Figure 4.2.1-3. Note the position of the array with respect to the main satellite body. The array center of gravity (also the center of rotation) is located 91.1 inches behind the RSS separation ring (in the +Z direction), and 24.6 inches above the spacecraft centerline (in the -X direction). The array is canted at either 22 or 37 degrees to a line through the main boom, which is normal to the XY plane. During orbital operations, the array rotates relative to the main boom once each orbit.

The solar array consists of ten separate but identical solar panels joined together by hinges. After deployment, the solar array is supported by the main (long) boom, solar array drive, short boom, and the array mast.

The solar array structure consists of ten reinforced honeycomb panels which are hinged to each other along their long edges. As shown in Figure 4.2.4-31, each panel is approximately 24 inches wide by 107.5 inches long by 1.25 inches thick. When deployed, the array is approximately 242 inches long by 107.5 inches wide. The center point of the array is attached a short boom, which in turn is attached to the solar array drive which, is attached to the main boom. The other end of the main boom is attached to a pivot point near the separation plane of the RSS. In its deployed configuration, the nearest edge of the solar array is approximately 52 inches from the separation plane in the +Z direction; the overall deployed satellite length is increased to 294.8 inches.

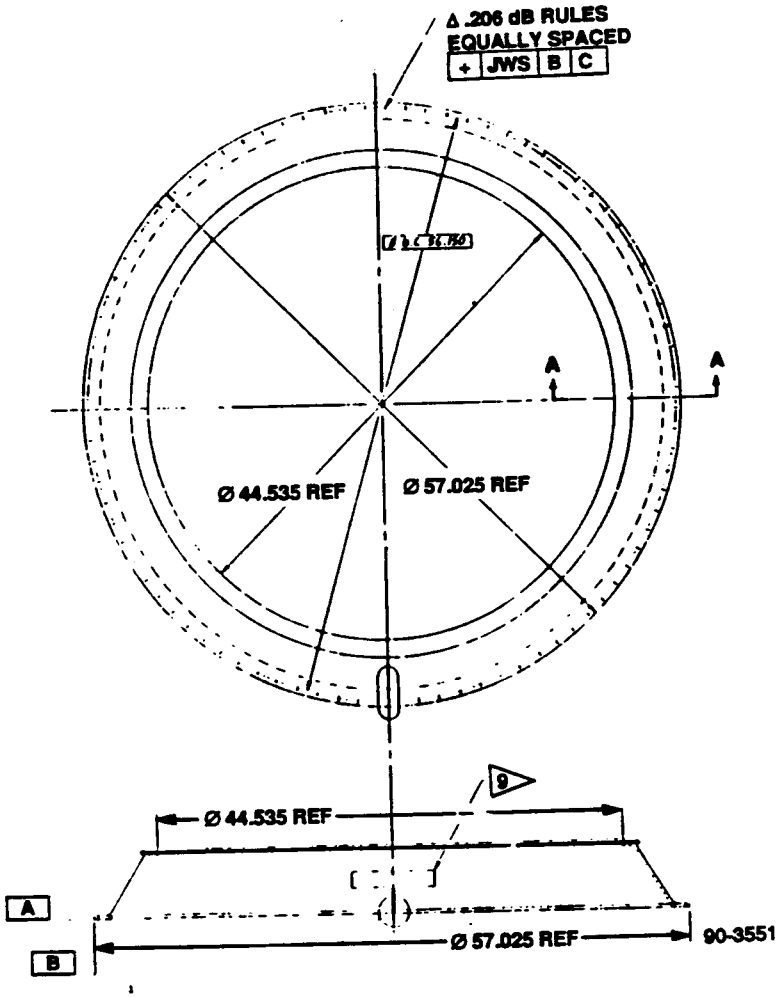

Figure 4.2.4-30. Booster Adapter

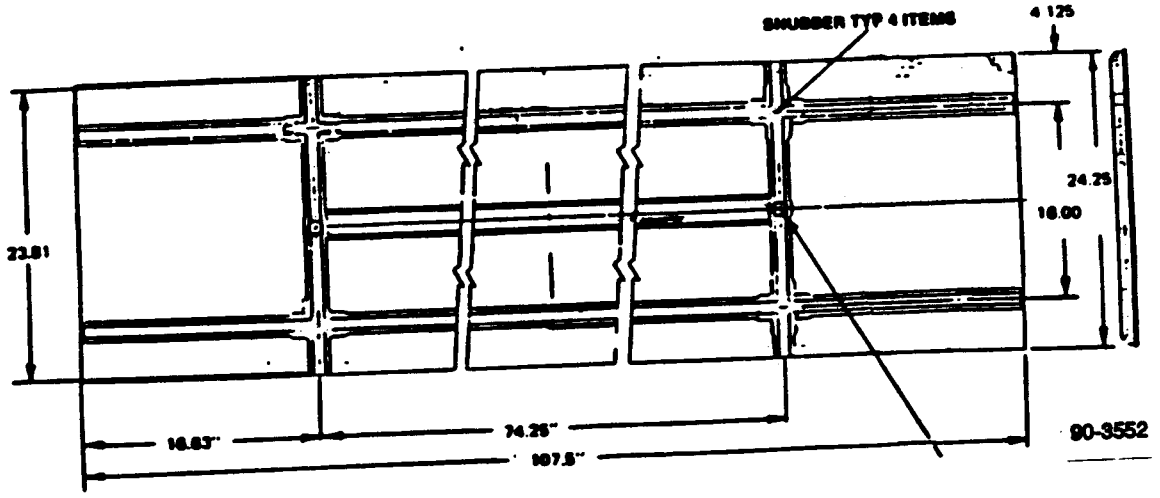

Figure 4.2.4-31. Solar Panel Substrates

Each panel is constructed of a honeycomb plate bonded to a riveted sheet metal reinforcing frame or stiffener. The honeycomb structure is a sandwich panel consisting of two 0.0037 inch thick 5052-H19 aluminum alloy skins bonded to a 0.25 inch thick "egg-crate" honey-comb panel with a cell size of 0.25 inch; the cells are formed from a 0.0007 inch thick ribbon of 5052-H39 aluminum alloy. The skin on the solar cell side has 0.002 inch thick white Tedlar skin bonded to it in order to electrically isolate the solar cells from the panel.

The skin to core adhesive is an American Cyanamid FM-73M modified epoxy adhesive. The edges of the honeycomb panel are closed off by a 0.0085 inch thick 7075-T73 aluminum alloy channel bonded to the core by American Cyanamid FM-37 modified epoxy foam. The edges of the hole through the panel are closed off by Dexter TO-1000 syntactic foam using an epoxy resin. The core ribbon and edge member channels are perforated.

The reinforcing frame or stiffener is fabricated from hat-sectioned members of 7075-T73 aluminum alloy. At the joints and other hard points, magnesium fittings are riveted into the frame. The frame is bonded to the honeycomb panel with an American Starch M688 modified epoxy polyamid compound and CH-16 catalyst.

4.2.4.6.2 Solar Array Support

The solar array support (SAS) provides the means for attaching the solar array to the RSS. As shown in Figure 4.2.4-32, the solar array support consists of a main deployment mechanism, the main boom, the array cant mechanism, and the array mast. In addition to the structural characteristics discussed here, the main deployment mechanism and array cant mechanism provide actions required during deployment, which is discussed in Section 4.2.4.6.4.

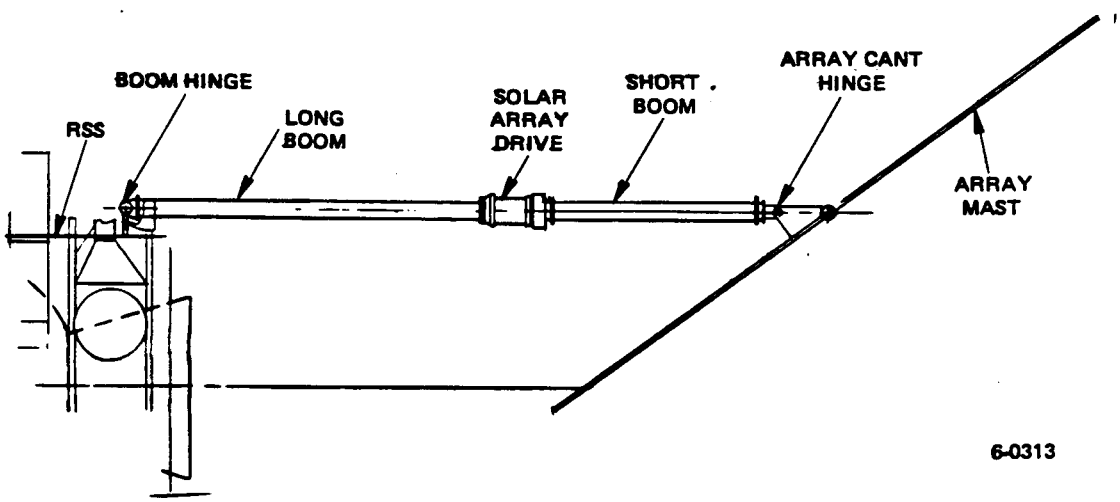

Figure 4.2.4-32. Solar Array Support

The solar array is a cantilever with respect to the RSS. A bracket is used to ensure that the loads are shared among RSS internal stiffeners. After deployment is completed, a two-point support for the main boom is created by the main deployment mechanism and the associated stop, as shown in Figure 4.2.4-33. The main deployment mechanism restrains forces in the X and Y

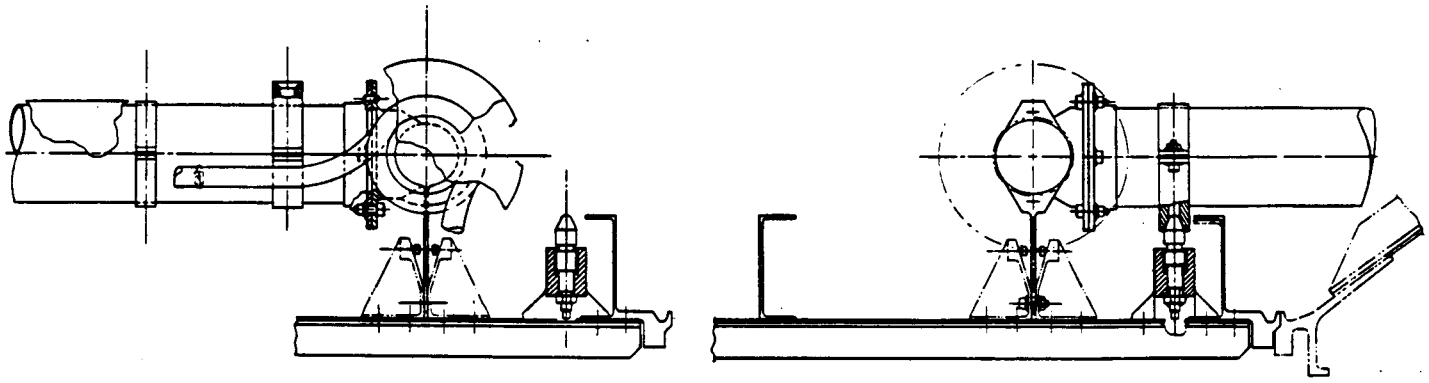

Figure 4.2.4-33. Solar Array Deployment Mechanism

coordinates and moments about X and Z; the end of deployment stop restrains forces in all directions as well as moments about Z. This combination creates a hard mounting between the boom and the RSS.

The main boom is a 2.5 inch tube with 0.125 inch wall thickness fabricated from 6061-T6 aluminum. The 47.35 inch long boom provides the support from the main deployment mechanism out to the solar array drive. The main boom has welded end flanges to allow rigid attachment to mating parts.

The solar array drive is flange-mounted to the end of the main boom, but is thermally insulated from the boom by a Polycarbafil spacer at the flange interface and by sleeve insulators around the bolts.

The shaft of the solar array drive is connected to a short boom 28.6 inches long which in turn is attached to the array cant mechanism actuator which provides the array cant at deployment. The SAS short boom and cant hinges are shown in Figure 4.2.4-34. Thermal insulation between the solar array drive and the short boom is provided by a Polycarbafil spacer at the flange interface and by sleeve insulators around the bolts.

A 1.25 inch square seamless mast provides the structural connection from the array cant mechanism to the center of the solar array. This mast, made from 6061-T6 aluminum, is a rigid element providing load paths to each panel hinge line (located at the panel stiffeners). The individual hinges carry the loads from one panel to another.

All rotating mechanisms have end-of-travel locks which preclude opening in response to perturbations while the spacecraft is in orbit. Furthermore, each rotating mechanism has sufficient stored energy in the spring at end of travel to hold the device closed against its stop, thus providing a clearance-free, rigid link between adjacent structural elements.

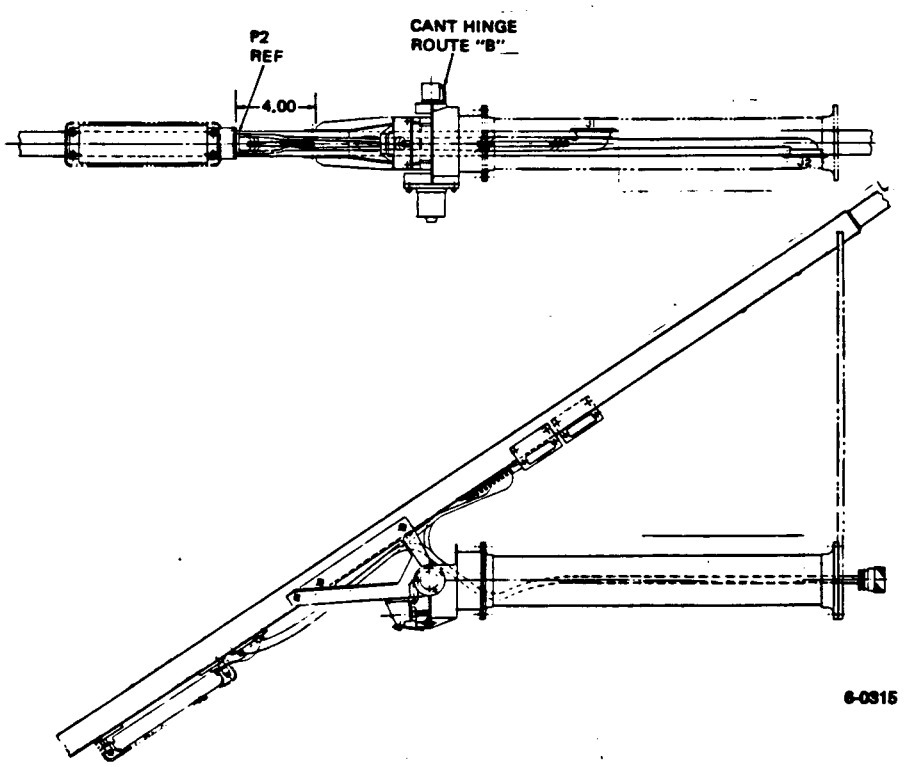

Figure 4.2.4-34. SAS Short Boom and Cant Hinges

4.2.4.6.3 Array Stowage

The launch configuration of the solar array is different from the orbital configuration, for two reasons:

- The solar array panels are folded together for launch to fit within heat shield constraints;
- The system must survive the launch environment, which is severe by comparison with the on-orbit loadings.

Figure 4.2.4-35 illustrates the launch configuration of the solar array and solar array support. The two packs of five panels are folded against the ESM. The panels are held in this position and loaded against the back of the ESM by two stainless steel cables which wrap around the panels. Each cable is comprised of two sections, one section inter- faces with the solar array panels and the other interfaces with the release initiators. The sections are connected with two turnbuckles that are used to tension the cable once it is in place.

All surfaces making contact with the cables are coated with Tufram, a low friction, Teflon based treatment the results in cable tension being evenly distributed around the perimeter. Guides built in the solar array hinges and panels hold the cable in position and maintain clearance between the cable and the solar cells. Most of the loads introduced by the cable tension are carried

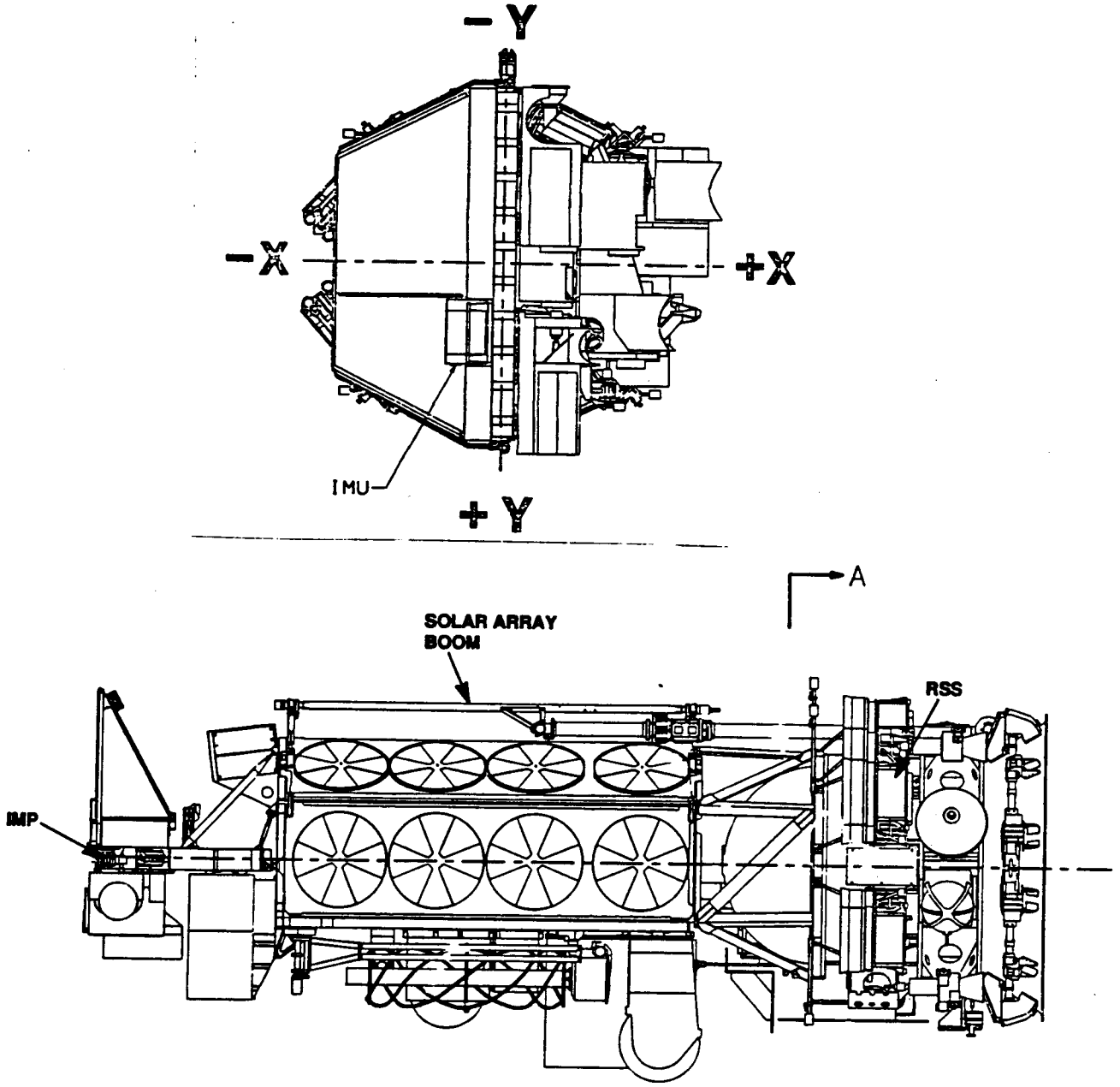

NOTE: SOLAR ARRAY PANELS NOT SHOWN IN THIS VIEW FOR CLARITY

90-3508

Figure 4.2.4-35. Solar Array - Launch Configuration

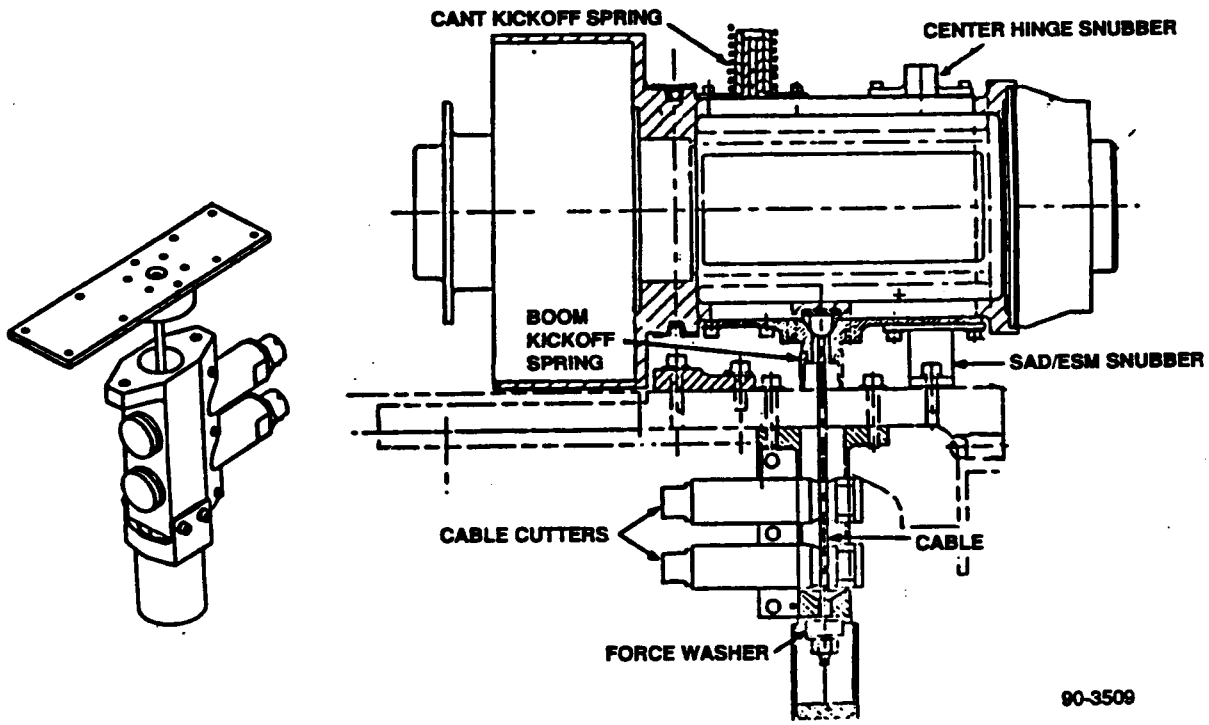

Figure 4.2.4-36. SAD Restraint

TABLE 4.2.4-1 ATN-KLM SYSTEM DEPLOYMENT ORDNANCES

Event	Device	Vendor	GE Part	Bridge-wires	Devices per System
Solar Array Cable	Cable Cutter	Hi-Shear	2629571-1	1*	4
Solar Array Boom	Cable Cutter	Hi-Shear	2629571-1	1	1
Solar Array Cant	Cable Cutter	Hi-Shear	2295362-X	2	2
VRA	Cable Cutter	Hi-Shear	2629571-1	2	1
UDA	Pin Puller	Hi-Shear	2308208-X	2	1
SRA	Bolt Cutter	Hi-Shear	2295362-X	1*	1
Sunshade	Cord Cutter	Hi-Shear	2295362-X	2	4

*2 BRIDGEWIRES/SQUIB, but only one is used.

The deployment mechanisms used in the deployment sequence are listed in Table 4.2.4-2. Each deployment motion is driven by a spring-loaded rotary mechanism; the deployment rate is governed by a silicone DC510 fluid-filled rotary vane damper. The dampers have a temperature dependent coefficient of

TABLE 4.2.4-2. ATN-KLM SYSTEM DEPLOYMENT MECHANISMS

Item	Dwg. No.	Rotation [deg]	Torque (Stowed) [in-lb]	Torque (Deployed) [in-lb]	Friction (Stowed) [in-lb]	Friction (Deployed) [in-lb]	Damping Rate [in-lb/rad/s]		Deployment Time [sec]	
							30°C	0°C	30°C	0°C
Center	3287334	42	TBD	TBD	TBD	TBD	TBD	TBD	TBD	TBD
Interpanel #2	TBD	48	TBD	TBD	TBD	TBD	TBD	TBD	TBD	TBD
Interpanel #3	TBD	180	TBD	TBD	TBD	TBD	TBD	TBD	TBD	TBD
Interpanel #4	3287337	180	TBD	TBD	TBD	TBD	TBD	TBD	TBD	TBD
Interpanel #5	3287341	180	TBD	TBD	TBD	TBD	TBD	TBD	TBD	TBD
Cant Hinge	3287951	22 or 37	TBD	TBD	TBD	TBD	TBD	TBD	TBD	TBD
Boom Hinge	3287397	180	TBD	TBD	TBD	TBD	TBD#	TBD	TBD	TBD
UDA	2288813	90	12.0	7.5	2.5	1.47	64	193	12.9	39.0
VRA	2288819	90	12.0	7.0	2.5	2.2	64	193	12.9	39.0
SRA Ø1	2297747	90	62.0	40.0	3.0	2.2	392	858	12.7	27.8
SRA Ø2	2293929	90	44.0	23.0	3.0	2.2	392	858	20.1	43.9
Sunshade(+Y)	2612804	117	NA*	NA	NA	NA	23	72	10.0	18.0
Sunshade(-Y)	2612804	138	NA	NA	NA	NA	23	72	11.3	20.3

*Estimates not available at time of publication.
#Temperature compensated, torque sensitive.

damping. The phase 3 damper is temperature compensated, but exhibits variation due to torque. The worst case operating temperature of the dampers is 0°C to 17°C.

4.2.4.6.4.1 Phase 1 and 2, Panel Deployment. Phase 1 and 2 are initiated by the release of the two restraint cables wrapped around the solar array. These are released separately so that stored energy in the bowed panels is lessened before total release. Two cable cutters (Hi-Shear SL1013-6) are used for each cable; each cutter uses a single power cartridge (Hi-Shear PC-12). Phases 1 and 2 release one band each; after the second band is cut, the panels are free to deploy.

Deployment is accomplished via spring-loaded hinges, two of which are between each pair of Solar Array panels. To one hinge is assembled a damper, to the other is mounted a potentiometer. A typical hinge design is illustrated in

Figure 4.2.4-37. The ends of the hinge are fitted into the hat-sectioned stiffeners on the back of the solar panels and pinned and bolted in place. A deployment spring selected for a specific hinge line provides both the deployment energy and the necessary end-of-travel residual loading to maintain the hinge position during perturbations while in orbit. The damper is a rate-sensitive device which fixes the deployment time.

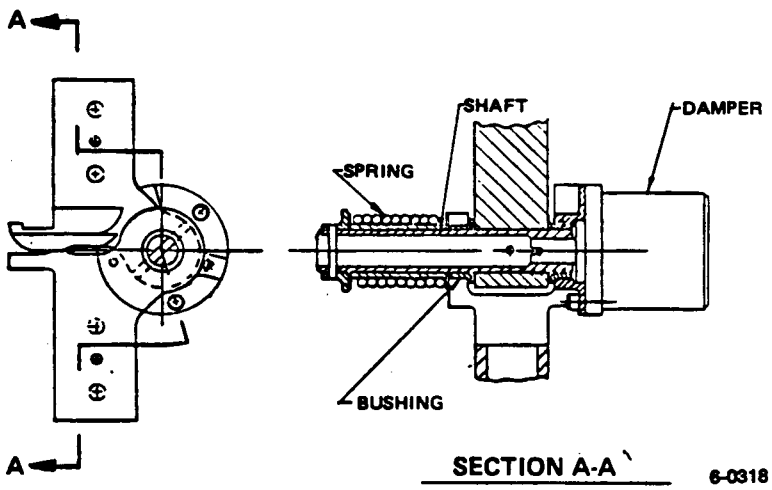

Figure 4.2.4-37. Solar Panel Hinge Design

Each hinge group employs a different spring and damper combination because of end-of-travel requirement differences; therefore, the deployment times for the individual panels are not identical. Figure 4.2.4-38 shows the general deployment sequence.

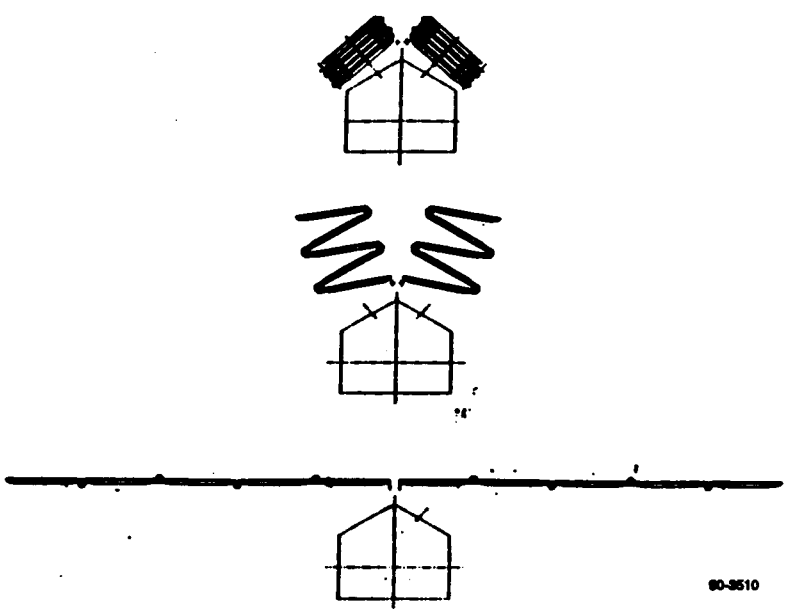

Figure 4.2.4-38. Solar Panel Deployment Sequence

4.2.4.6.4.2 Phase 3, Main Deployment. Prior to Phase 3, the panels have completed their deployment and are planar, parallel to the spacecraft YZ plane. The Phase 3 deployment is a rotation of the SAS about the RSS to its flight position behind the spacecraft; this action is shown in Figure 4.2.4-39. Phase 3 is initiated by releasing the Solar Array Drive from its attachment to the truss. Two independent bolt cutters are fired; the inboard bolt cutter is fired first to achieve release redundancy. A kick-off spring is located at the SAD attachment point to begin the deployment. A magnetic latch provides hinge rigidity at the completion of deployment.

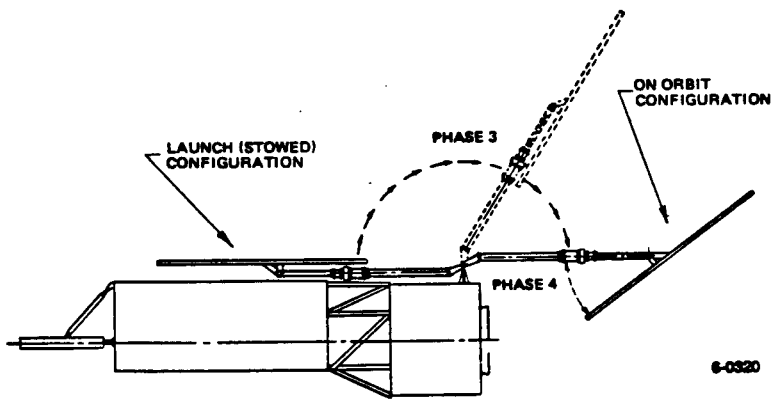

Figure 4.2.4-39. SAS Deployment Sequence

4.2.4.6.4.3 Phase 4, Array Cant Deployment. Prior to Phase 4, the (SAS) rotation is completed and locked in place. The Phase 4 deployment is the 22 or 37 degree canting of the solar array with respect to the spacecraft YZ plane, as shown in Figure 4.2.4-39. During all steps up to this point the array has been held parallel to the axis of the main boom. A pin puller is used to initiate Phase 4. As soon as the pin retracts, the array is free to rotate under the influence of the array cant mechanism.

It is similar to the main deployment mechanism except for the mounting arrangement, damper, and the sensing potentiometer.

4.2.4.7 Antennas

All antenna deployment mechanisms and deployment ordnances are described in Tables 4.2.4-1 and 4.2.4-2.

4.2.4.7.1 VRA

The launch configuration of the VRA Antenna is shown in Figure 4.2.1-35. The antenna is folded against the truss. The base of the antenna is attached to the deployment mechanism, which in turn is attached to the truss. The opposite end of the antenna is constrained to the spacecraft with a pin puller (Hi-Shear SP1105). The antenna bracket which is engaged with the pin puller is pre-loaded to prevent gapping during launch. The VRA deployment sequence is shown in Figure 4.2.4-40.

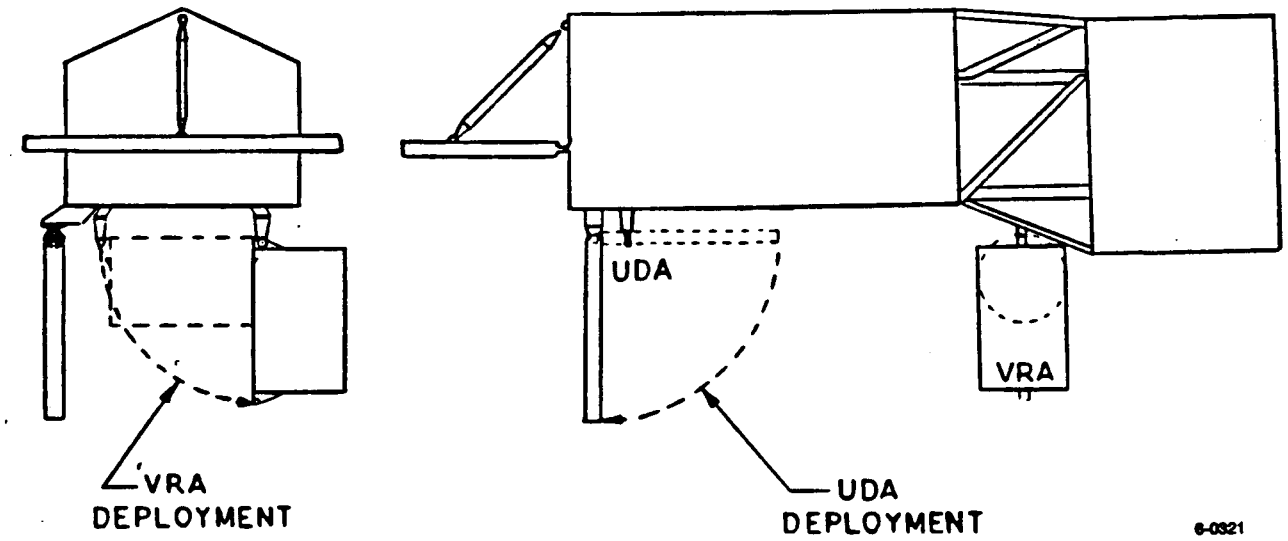

Figure 4.2.4-40. VRA and UDA Deployment

4.2.4.7.2 UDA

Shown in Figure 4.2.4-41 is the UDA antenna in the launch configuration. The antenna is folded against the ESM and attached to the front panel. The deployment mechanism is mounted to the base of the antenna. The mechanism is also attached to an offset bracket which is bolted to the spacecraft. The antenna is caged to the spacecraft at approximately the c.g. of the radiating element. The caging and release mechanism is a pin puller (Hi-Shear SP1105). The UDA Deployment sequence is shown in Figure 4.2.4-40.

4.2.4.7.3 SRA

The Search and Rescue Receiving Antenna (SRA) shown in Figure 4.2.4-42 is stowed on the -Y side of the front panel in a 6061-T6 aluminum alloy welded cradle which acts as the antenna support structure upon deployment. The SRA deployment shown in Figure 4.2.4-43 occurs in two phases. The first phase is initiated by a bolt cutter (Hi-Shear SL1047, see Figure 4.2.4-44) which releases the cradle/antenna assembly from the front panel where it is stowed parallel to the Z axis. The assembly pivots 90° in the YZ plane completing first phase deployment parallel to the spacecraft Y axis.

The second phase deployment begins during the first phase when the assembly has swept an arc of approximately 72°. At this point the antenna is released to deploy out of the cradle by a cable and latch mechanism actuated by the first phase hinge. The second phase deployment is completed as the antenna rotates 90° from the deployed cradle to a position approximately 45 inches from the ESM, and parallel to the X axis. The Phase 2 mechanism is shown is Figure 4.2.4-45.

4.2.4.8 V-Band Assembly

4.2.4.8.1 Operation

The payload is held to the booster adapter by V-blocks installed across the interface flanges. The blocks are attached to two piece circumferential band assemblies held in tension by two 5/16 inch high strength steel bolts. Separation occurs when either bolt is severed by 2631523-1 separation nut.

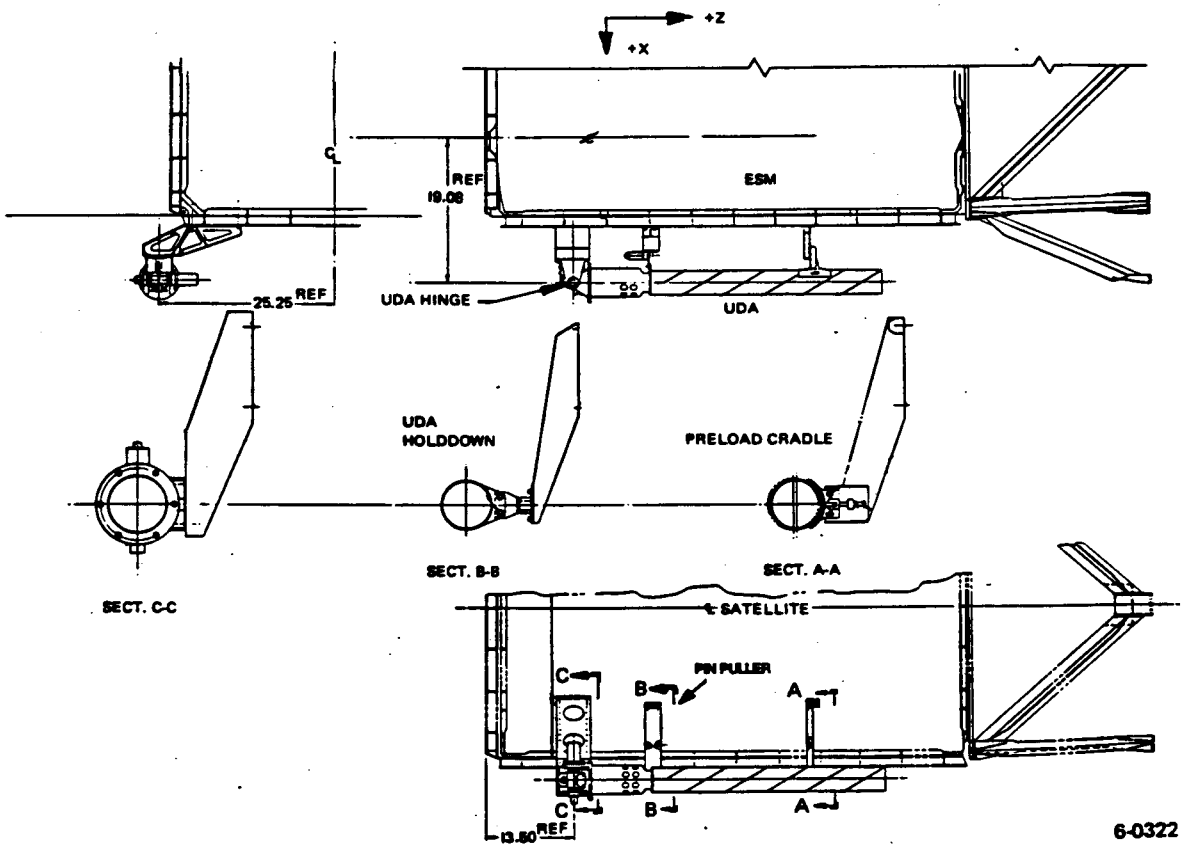

Figure 4.2.4-41. UDA in Launch Configuration

The separation bolt cutter consists of a steel knife contained in a cylindrical steel body. Prior to separation, the knife is held in place by a shear pin installed through both the knife and body. The knife is driven by gas pressure generated by an electrically initiated pressure cartridge assembly. When the cartridge is initiated, gas pressure builds up behind the knife, causing it to shear the pin and sever the bolt. The knife and gas are contained within the cutter body and the severed bolt is retained on the band assemblies. The 1B94542-1 bolt cutters have initiators which are not normally taken out of the assemblies.

Springs and lanyards are attached to the adapter assembly. The springs move the V-blocks off the flanges so that the stages are free to separate. The lanyard retaining system prevents the band assemblies from extending beyond the separation plane and prevents radial travel beyond specified limits.

4.2.4.8.2 Configuration

The V-blocks are machined from a 7075-T7351 aluminum hand forging. The band is constructed from 301 1/2 hard stainless steel per MIL-S-5059. The end fittings are machined from 7075-T7351 rolled bar per QQ-A-225/9. The high-strength

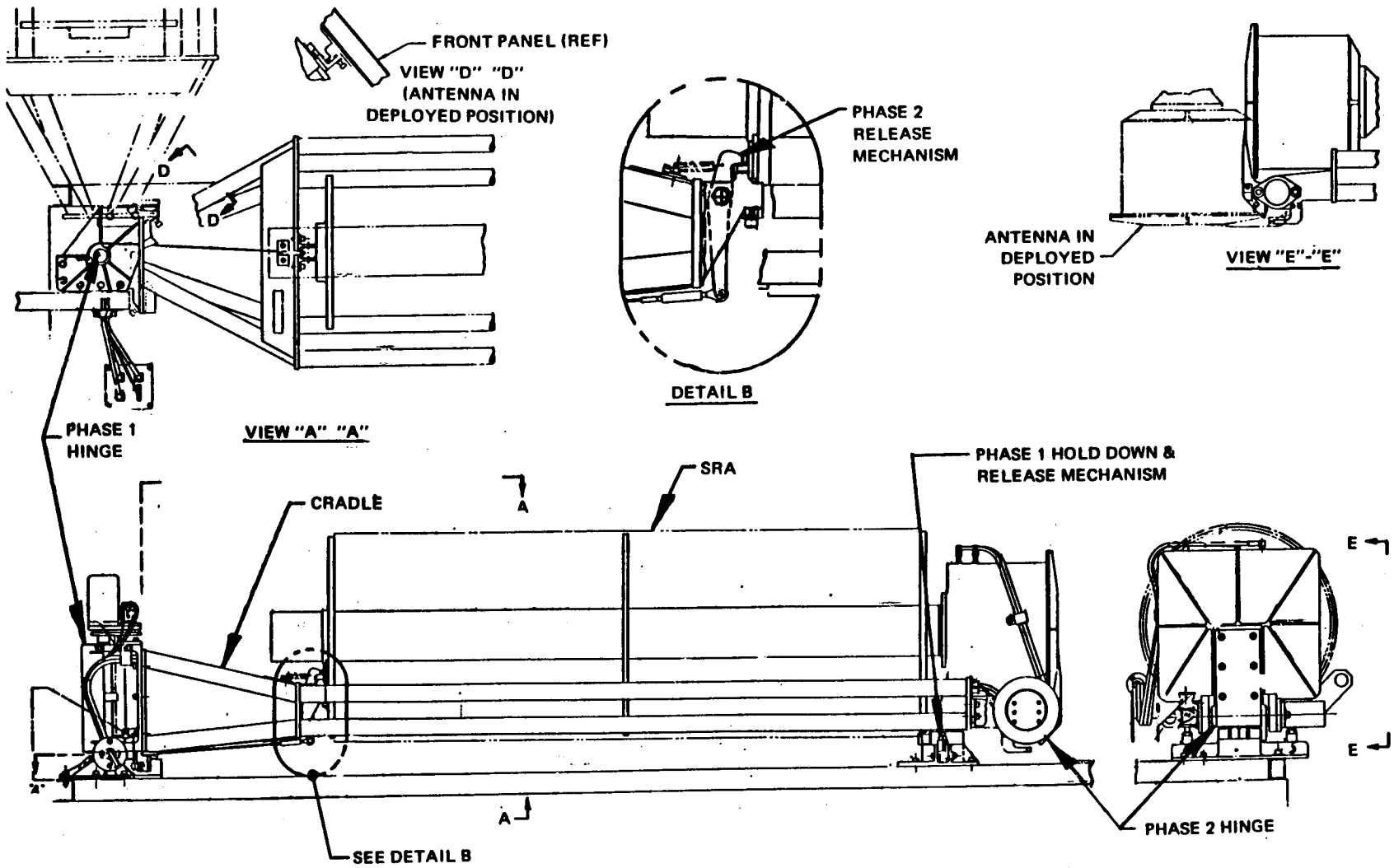

Figure 4.2.4-42. Search and Rescue Receiving Antenna Installation

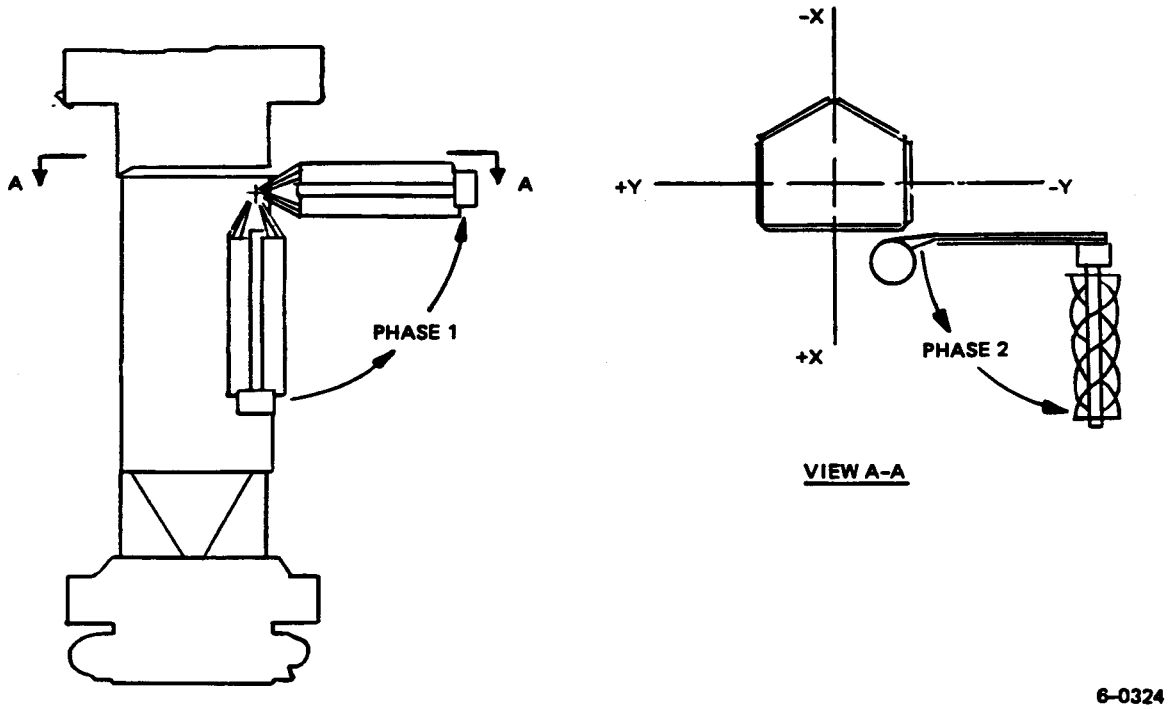

Figure 4.2.4-43. SRA Deployment

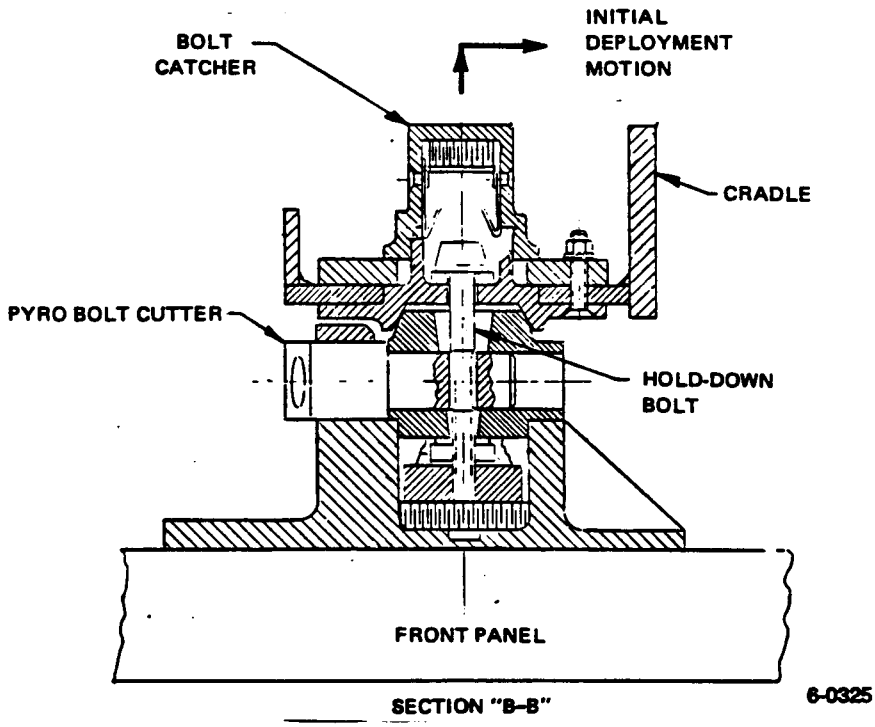

Figure 4.2.4-44. SRA Phase 1 Hold-Down

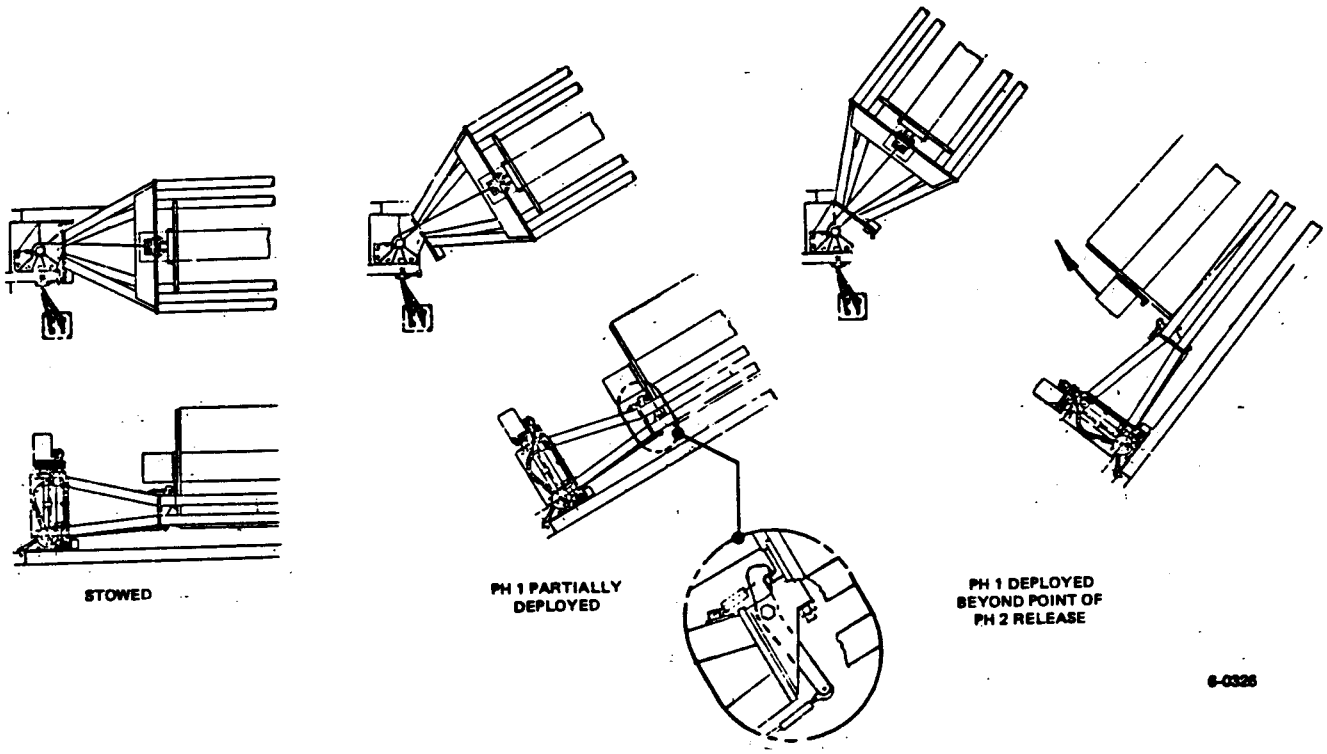

Figure 4.2.4-45. SRA Phase 2 Release Mechanism

bolts are constructed to MS21250 standards, except that the shear requirement is waived and the tensile strength is 170,000 PSI minimum and 200,000 PSI maximum. The band is formed to a radius slightly larger than the installed radius. This is done to reduce stresses and also to provide a slight spring characteristic to the band. The V-band assembly is shown in Figure 4.2.4-46. The 20 V- Blocks are mounted in slotted holes in the band. While the assembly is being preloaded, compressor driven air chisels tap the V-blocks to overcome friction and to reduce the shear loads in the V-block attachment hardware.

The band assemblies were designed specifically for the ATN Program and adequate strength margins were incorporated in the design. The lowest margin obtained during analysis was 0.03 and was associated with the separation bolt.

4.2.4.8.3 Installation

The band is installed to a tension of 6950 ± 50 lbs. Strain gauge instrumented bolts are used to ensure that the proper preload band tension is achieved. The strain gauge output is processed by a computer, which computes the actual tension in the band. The accuracy of the total force measuring system is approximately ± 1% of the actual load. The installation procedure provides a technique to assure even tension within the band. Reference MDAC ID23123 Installation Requirements, Separation System.

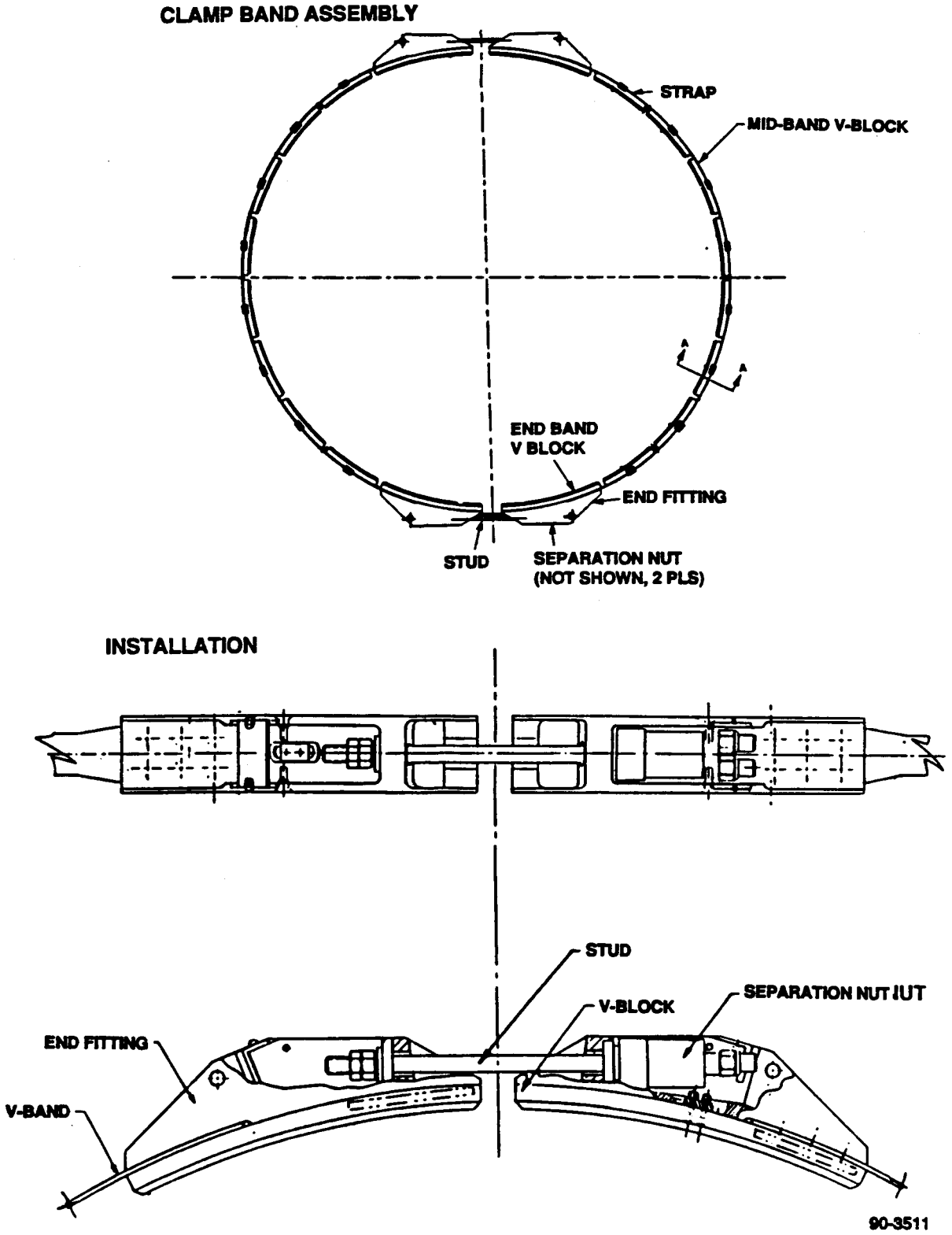

Figure 4.2.4-46. ATN-KLM V-Band Assembly

Blank Page

4.3 REACTION CONTROL SUBSYSTEM

4.3.1 SYSTEM DESCRIPTION

The Titan II launch vehicle performs all the guidance and control functions. From liftoff to spacecraft separation attitude control, the Reaction Control Subsystem (RCS) provides for the velocity correction, steering and trim during the separation period from the Titan booster and the subsequent ascent mode coast phase, as well as during Apogee Kick Motor (AKM) burn. The RCS functions also provide for the spacecraft attitude orientation and stabilization during the deployment stages of the spacecraft solar array and other appendages.

The RCS consists of a solid rocket AKM which supplies the primary orbit injection velocity requirement for the satellite after booster separation. The NOAA-K,L,M AKM will be the Thiokol STAR-37XFP solid rocket motor. It provides the major source of impulse required to circularize the satellite orbit after attaining the required orbit altitude from the launch vehicle.

Figure 4.3.1-1 shows the major components of the AKM. The total impulse of the motor is 459,696 pound-seconds. The motor is initiated by a software command signal from the CIU.

The reaction control subsystem is equipped with a dual propellant system consisting of a regulated cold gas nitrogen (GN_2) subsystem and a monopropellant hydrazine (N_2H_4) subsystem. This dual propellant system is identified as the Reaction Control Equipment (RCE) system. Figure 4.3.1-2 shows schematically the components of the RCE. The components are assembled around the periphery of the RSS which also supports the AKM. The AKM is configured in the center of the annulus. The entire assembly fits within a 60-inch diameter envelope. Other non-RCE components such as batteries, antennas, and electronic boxes are located within the constraints of the RCE manifold routing.

4.3.1.1 High Pressure Nitrogen Subsystem

The high pressure GN_2 is loaded in two 4,500 psia rated pressurant tanks located symmetrically on the vehicle assembly. Sufficient GN_2 is stored in these tanks to provide the required total impulse for the cold-gas thrusters, as well as providing the ullage pressurant for the hydrazine propellant tanks. These titanium tanks have an average volume of 430 in^3 each and carry a combined total GN_2 load of 9.4 pounds. The outlets of these tanks are welded to a common high pressure manifold. The manifold distributes the GN_2 to a pressure regulator, which reduces the pressure to a nominal value of 480 psia. Other items that are an integral part of the high pressure group are the high pressure GN_2 fill/drain valve, pressure transducer, and pressurant tank temperature sensors.

A pressure relief valve is not provided in the high pressure GN_2 system since there is no source that can exceed the maximum pressure provided by the GSE. During the ground filling operations, pressure relief is provided by the GSE.

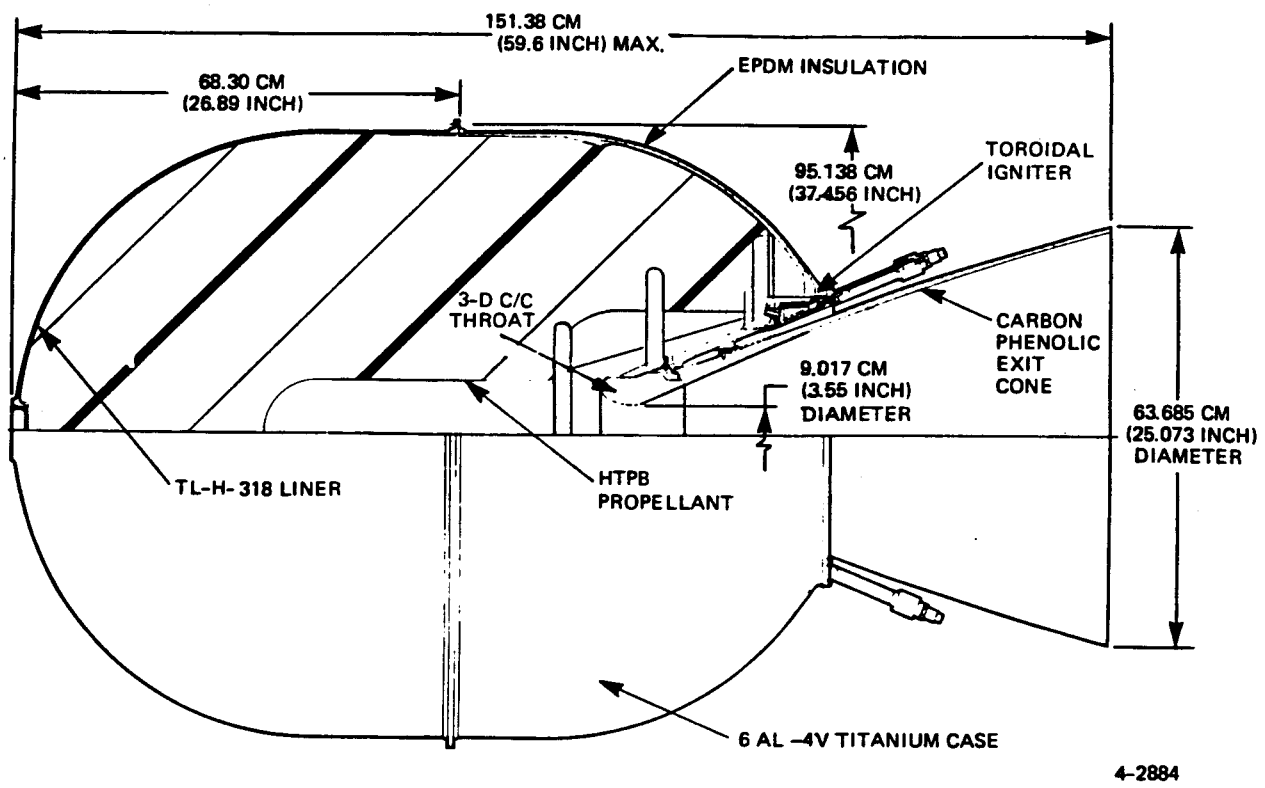

Figure 4.3.1-1. Apogee Kick Motor (AKM)

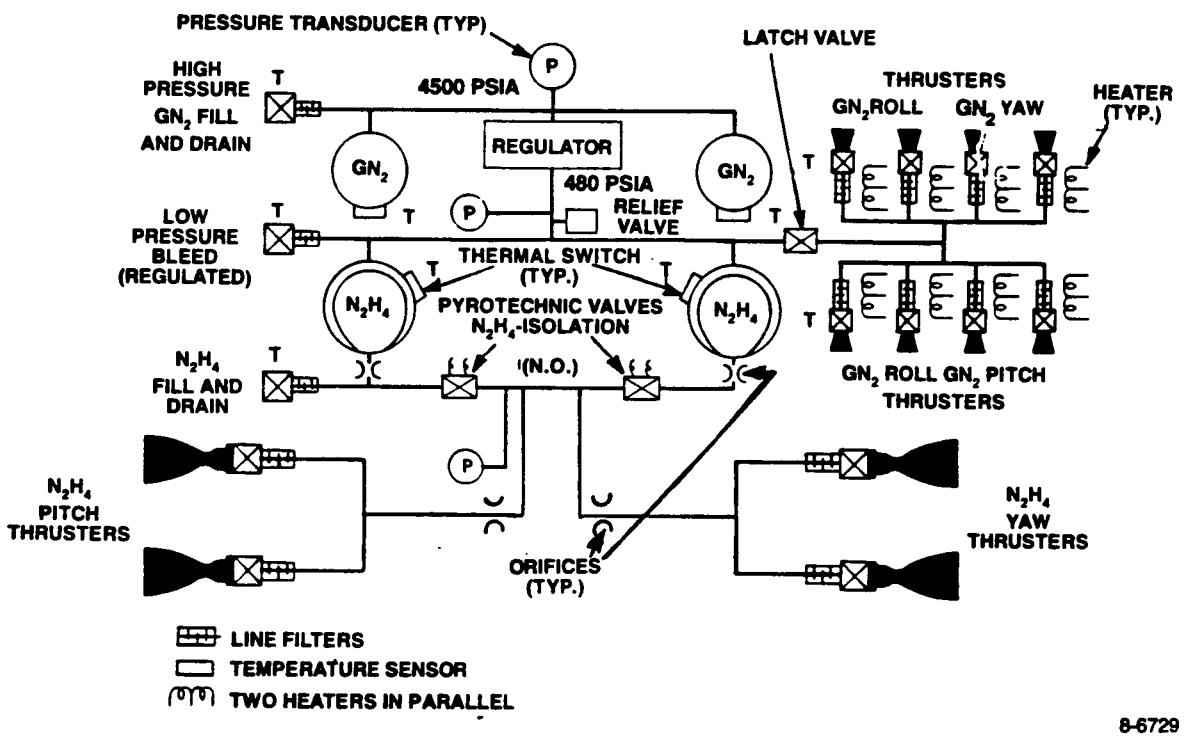

Figure 4.3.1-2. Reaction Control Equipment (RCE) Schematic Diagram

The high pressure manifolds are fabricated from 0.035 inch thick wall tubing made from 304L stainless steel. Total external leakage from the entire system is less than an equivalent 30 SCC/hr GN_2 at a maximum operating pressure of 4,500 psia when measured at the assembled RCE subsystem level.

The high pressure subsystem operating, proof and burst pressures are presented in Table 4.3.1-1. The proof pressure is the pressure to which every component is tested, and the burst pressure is the pressure at which every component has been qualified.

TABLE 4.3.1-1. HIGH PRESSURE NITROGEN COMPONENT PRESSURE LEVELS

Component (High Pressure GN_2)	Operating Pressure (at liftoff) (psia)	Proof Pressure (psia)	Burst Pressure (psia)
Fill Valve	4500	6750	18000
Tank	4500	6750	9000
Regulator (High Side)	4500	6750	18000
Pressure Transducer	4500	6750	18000
Lines and Fittings	4500	9000	18000
Filter	4500	9000	18000

4.3.1.2 Low Pressure Nitrogen Subsystem

The nominal low operating pressure is regulated to 480 psia nominal pressure. The low pressure nitrogen output from the regulator is distributed by manifolding to the cold-gas thrusters and the hydrazine propellant tanks. A mechanical relief valve is incorporated on the low pressure output side of the pressure regulator to ensure that the pressure in the low pressure GN_2 manifold will never exceed a maximum of TBD psia. Of the eight cold-gas thrusters, four provide roll control and are operated in coupled pairs; the remaining four thrusters, which provide for pitch and yaw control, are not coupled and operate singularly. These cold-gas thrusters are rated at 2.0 $\pm$0.1 lbs thrust in vacuum. The latch valve provides a commandable means for controlling the GN_2 flow to the cold-gas thrusters; this valve may be commanded from the ground to open or close. A low pressure bleed valve and pressure transducer are also included. The low pressure manifolds are fabricated from 0.025 inch wall thickness tubing made from 304L stainless steel.

To minimize the potential for pressurant leakage, the GN_2 system manifolds are of all welded construction except for the connections at the regulator. These two connections are mechanical fittings with ethylene propylene rubber O-ring seals. The mechanical fittings were retained because the aluminum regulator body is not compatible for welding to the stainless steel plumbing using conventional techniques.

Filter assemblies are provided at the GN_2 high pressure and low pressure fill and drain valves. The pressure regulator contains a filter.

The low pressure side operating proof and burst pressures are presented in Table 4.3.1-2.

TABLE 4.3.1-2. LOW PRESSURE NITROGEN COMPONENT PRESSURE LEVELS

Component (Low Pressure GN_2)	Operating Pressure (at liftoff) (psig)	Proof Pressure (psig)	Burst Pressure (psig)
Regulator (low side)	480	990	1980
Thruster	480	1035	2020
Tank	480	TBD	TBD
Pressure Transducer	480	900	2400
Latch Valve	480	900	2200
Relief Valve	480	1010	2020
Bleed Valve	480	900	2400
Lines and Fittings	480	960	1920
Filter	480	1010	2020

4.3.1.3 Hydrazine Subsystem

The major components of the hydrazine group are the propellant tanks and the four hydrazine monopropellant thrusters. The two hydrazine propellant tanks incorporate positive expulsion diaphragms and provide for a minimum usable propellant volume of 864 in^3 or 31.5 pounds per tank each. Temperature sensors are provided on each tank. Matched trim orifices are incorporated at the propellant tank outlets to avoid shifts in the vehicle center of gravity due to a usage misbalance. A pressure transducer is also included on this side to monitor pressure during ground loading and to check on propellant consumption during operation in space. After completion of the hydrazine system functions, and following the orbit insertion velocity trim burn, pyrotechnic isolation valves are closed in the feed line from each of the two tank outlets to isolate the residual propellant from the subsystem and thrusters.

The hydrazine manifold is also of all welded construction. Filter assemblies are welded at the thruster inlets to preclude inadvertent contamination which could result in leakage at the valve seats. Filter assemblies are also provided at the hydrazine fill and drain coupling for added protection.

The hydrazine manifolding is pressurized by the diaphragm within the tanks to a nominal 480 psig at 70°F by the low pressure GN_2 system regulator. The hydrazine system low pressure operating, proof and burst pressures are presented in the Table 4.3.1-3.

4.3.2 FUNCTIONAL DESCRIPTION

4.3.2.1 Mission Operation

The RCE provides propulsive torques to the vehicle, thus providing three-axis control during ascent; the RCE is operational from spacecraft/SLV separation until handoff from the ascent to the orbital control system. The RCE also provides propulsive torques as required to maintain spacecraft momentum below specific maximum levels for the duration of the mission.

TABLE 4.3.1-3. HYDRAZINE COMPONENT PRESSURE LEVELS

Component (Low Pressure N_2H_4)	System Nominal Pressure (at liftoff) (psig)	Proof Pressure (psig)	Burst Pressure (psig)
Tank	480	TBD	TBD
Fill/Drain Valve	480	900	2400
Pressure Transducer	480	3000	9600
Isolation Valve	480	900	2400
Thruster	480	900	2400
Filter	480	1010	2020
Lines and Fittings	480	1010	2020

The following propulsive functions are provided during this time from separation through final orbit acquisition and trim:

- Separation of satellite from Titan II booster
- Attitude control during separation and subsequent coast period
- Attitude control during AKM burn for orbit injection
- Orbital ΔV correction and trim
- Attitude control during orbital ΔV correction
- Attitude control during coast following orbit injection
- Orientation of spacecraft for mission requirements
- Attitude control during spacecraft deployments
- Final trim of spacecraft attitude and attitude rates prior to hand off to the on-orbit attitude control system

Following completion of these primary propulsion functions, the hydrazine thrusters are inhibited from further operations.

After orbit insertion, the spacecraft can command GN_2 thrusters to fire as required to stabilize the spacecraft attitude and reduce body rates to within the operational range of the reaction wheels.

The mission operation of the thrusters as a function of the nominal time line is listed in Table 4.3.2-1. Throughout the mission, roll control is provided by the cold gas thrusters. However, the pitch and yaw cold gas thrusters are inhibited from operating during booster separation, AKM burn, and ΔV maneuvers; pitch and yaw control during these maneuvers is accomplished by either on- or off-pulsing of the hydrazine thrusters.

As shown in Table 4.3.2-1, there are several possible combinations of N_2H_4 thruster firings, which, because of the different mass flow rate requirements, result in different thruster operating pressures.

The RCE provides for single thrust mode operation from the hydrazine thrusters, and the engines are qualified in the range of 40 to 100 lbf.

TABLE 4.3.2-1. RCE MISSION OPERATIONS

Maneuver	N_2H_4 Thruster	N_2 Thruster
Spacecraft/Titan Separation	4 Thrusters Simultaneously Burn for 4 seconds	ON Pulsing for Roll Torques
Post Separation Control	ON Pulsing for Pitch and Yaw Torques	ON Pulsing for Roll Torques
Coast Period	- -	ON Pulsing for Roll, Pitch, and Yaw Torques
Pre-AKM Thruster Warm-up	4 Thrusters Simultaneous on Pulse for .5 sec	- -
AKM Burn	ON Pulsing for Pitch and Yaw Torques	ON Pulsing for Roll Torques
Orbit Velocity Trim	4 Thrusters ON Simultaneously with OFF Pulsing for Pitch and Yaw Torques	ON Pulsing for Roll Torques
Coast Period	- -	ON Pulsing for Roll, Pitch, and Yaw Torques
N_2H_4 Isolation	- -	- -
Yaw and Roll Maneuvers	- -	GN_2 ON Pulsing for Roll, Pitch, and Yaw Torques
Initial N_2H_4 Line Vent	4 Thrusters ON Simultaneously for 0.5 Seconds Repeated 10 times	- -
Final Pointing	- -	GN_2 ON Pulsing for Roll, Pitch and Yaw Torques
Handover	- -	- -

Figure 4.3.2-1 shows the RCE mission requirements and includes prelaunch, ascent and on-orbit phases. The propulsive functions are shown after the first stage separation. This propulsion system is mounted on and supported by the RCE Support Structure (RSS), which is a cylindrical, reinforced aluminum alloy shell, approximately 38 inches inside diameter by 32.5 inches long. After this shell is painted and taped the RCE is installed as components which are then connected by stainless steel tubing.

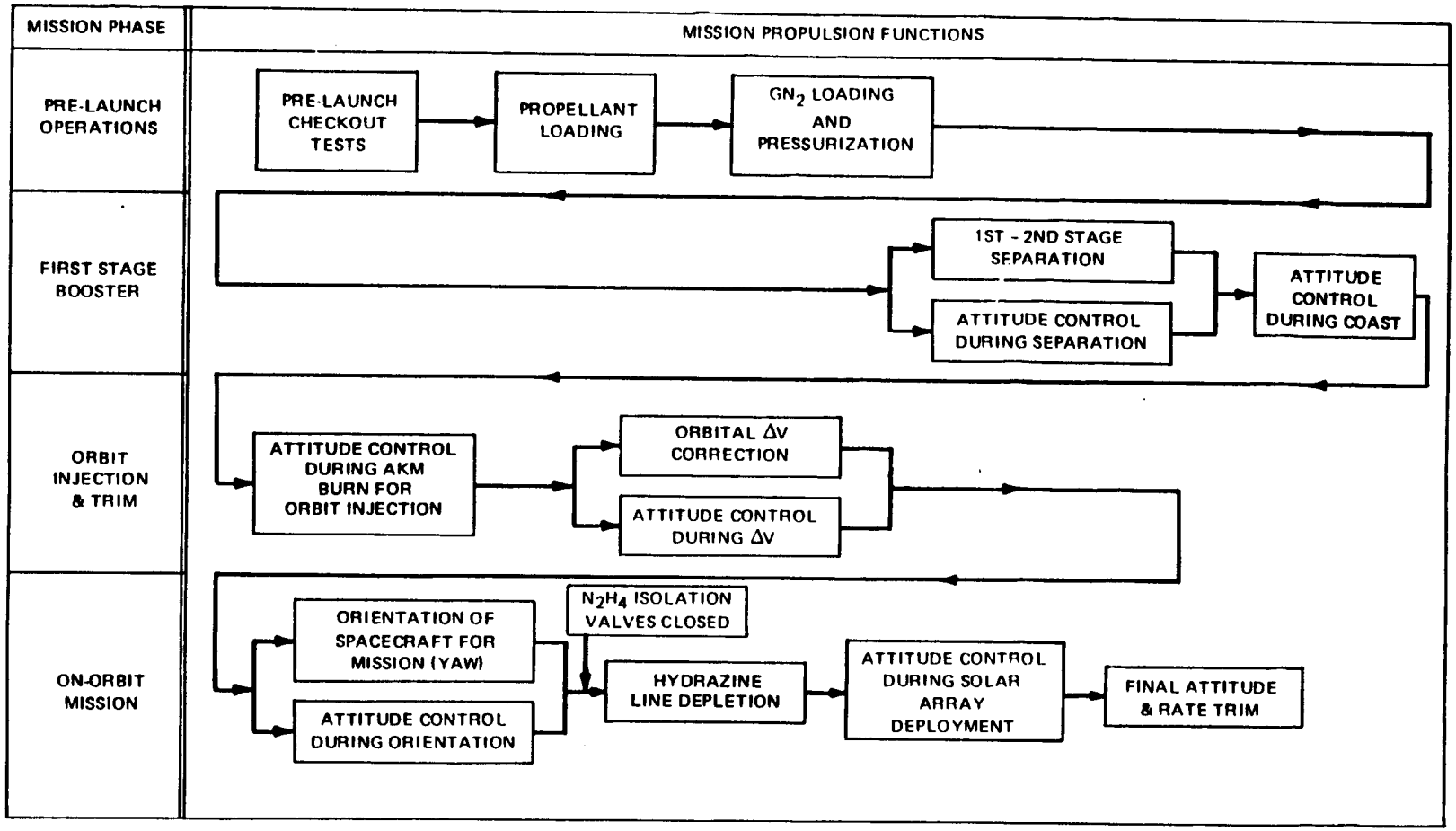

Figure 4.3.2-1. RCE Mission Requirements

4.3.2.2 Weight and Power Requirements

The RCS component weights and power requirements are shown in Table 4.3.2-2.

TABLE 4.3.2-2. RCE WEIGHT AND POWER SUMMARY

Component	Quantity	(Weight Pounds)**	Power (Watts)*
Propellant Tank	2	12.0	--
N_2H_4 Thruster	4	19.68	30***
Pressurant Tank	2	14.8	--
N_2 Thruster	8	4.94	30***
Regulator	1	2.27	--
Pressure Transducer	3	1.39	0.3
Fill and Drain Valves	3	1.10#	--
Filters	16	0.14	--
Manifold, GN_2 High	--	0.72	--
Manifold, GN_2 Low	--	2.68	--
Manifold, N_2H_4	--	5.00	--
Isolation Valve, N_2H_4	2	1.54	48****
Relief Valve	1	0.40	--
Latch Valve	1	1.23	--
Total		67.89	--

*Power for each component.
** Weight for total quantity of components
*** A Maximum of 6 thrusters on at one time, 4 N_2H_4 for Δ V and 2 N_2 for roll control, can occur during ascent.
**** One shot, dual bridgewire squibs, 3.5 amperes minimum all-fire current per bridgewire.
# 1.10 lbs consists of (1) Type I, 0.5 lbs; (1) Type II, 0.35 lbs; (1) Type III, 0.35 lbs.

4.3.2.3 Telemetry

A telemetry indication of the operating GN_2 pressure is provided by a pressure transducer in the high pressure lines and another pressure transducer in the low pressure lines. With the RCE pressurized to the proper pre-launch operating pressure, the telemetry output is approximately +5V (high pressure) and +3.5V (low pressure).

A telemetry indication of the operating N_2H_4 pressure is provided by a pressure transducer in the hydrazine lines. Under normal operating conditions the telemetry output is approximately +4.5V.

4.3.3 COMPONENT DESCRIPTION

4.3.3.1 Hydrazine Thruster

The hydrazine thruster incorporated in the NOAA-K,L,M spacecraft is the Rocket Research company MR-104A, 100 lbf Rocket Engine Assembly (REA) shown in Figure 4.3.3-1. The thruster consists of: 1) a thruster chamber assembly comprising an injector for supplying and distributing propellant radially into the annular catalyst bed, catalyst bed supports, a pressure shell, and a lightweight high-altitude nozzle of 54:1 expansion ratio; 2) a single-seat solenoid actuated (normally closed) propellant valve; 3) an inlet tube assembly with a trim orifice to adjust pressure schedules; and 4) a mounting structure to interface with the RSS mounting points.

The engine is trimmed to produce a 100-lbf thrust level at 308-psia inlet pressure. A design summary of the engine is contained in Table 4.3.3-1.

The overall length of the engine from the mount interface to the nozzle exit is 13.08 inches. The maximum diameter of the engine is 5.67 inches at the nozzle exit.

Mounting to the NOAA-K,L,M spacecraft is provided by four 0.212-inch diameter clearance holes equally spaced at 2.6 inches per side. The outside diameter of the interface flange for mounting of the REA to the structure is 4.25 inches. The mounting structure is 6061-T6 aluminum gold irridite conversion-coated and painted white for thermal control with S13G-LO.

The propellant inlet to the solenoid valve is 0.375-inch outside diameter tube of 0.028-inch wall thickness with the end prepared for welding.

The thrust chamber assembly is composed of an injector, radial flow catalyst bed, thrust chamber body and nozzle assembly, internal chamber body heat shield, and support structure. The chamber/nozzle body, catalyst bed end closures, heat shield, and support structure are fabricated from Inconel 625. The catalyst bed retaining cylinders are fabricated from Hastelloy B and the injector Rigimesh elements are fabricated from Haynes 25. The injector body is fabricated from Inconel 600.

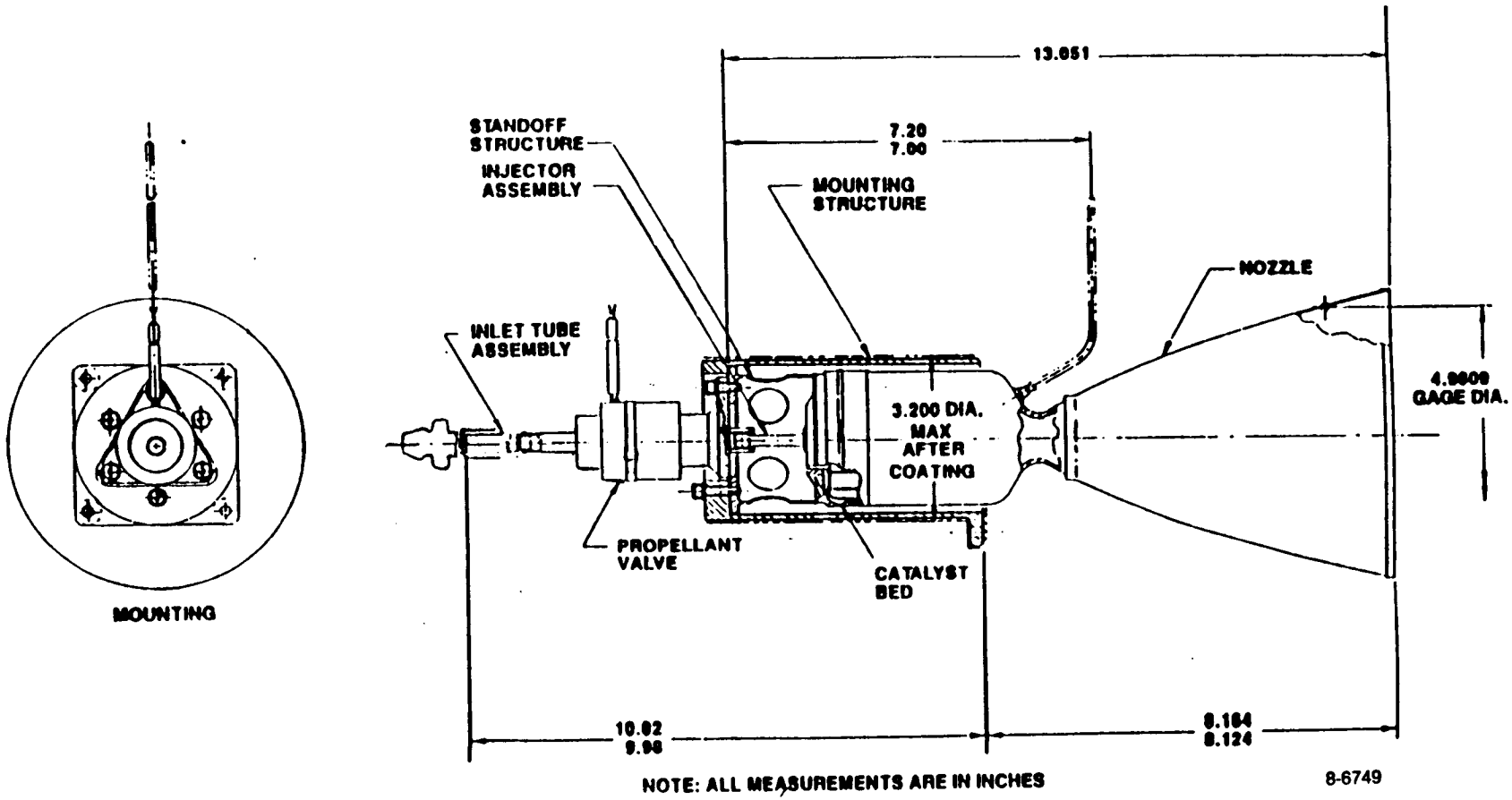

Figure 4.3.3-1. MR-104A Hydrazine Thruster

TABLE 4.3.3-1. DESIGN SUMMARY - MR-104A REA

Parameter	Description
Catalyst	
Inner Bed	Shell 405 15 to 18-mesh granules
Outer Bed	RRC LCH-202 14 to 18-mesh granules
Radial bed length	
Inner Bed	0.3 inches
Outer Bed	0.3 inches
Total radial bed length	0.6 inches
Axial bed length	3.0 inches
Nozzle	80% Bell Contoured
Expansion ratio	54:1
Throat diameter	0.762 inches
Exit diameter	5.608 inches
Materials	
Thrust chamber/nozzle	Inconel 625
Injector	Inconel 600
Catalyst bed end supports	Inconel 625
Catalyst bed cylinders	Hastelloy B
Support structure	Inconel 625
Internal Heat Shield	Inconel 625
Weight	
Thrust Chamber Assembly	4.90 lbm
Power	
Propellant valve	30 watts at 28 Vdc and 70°F

The propellant valve/injector feed-tube interface includes redundant EPR O-rings for sealing. Four individual manifolds intersect the downstream end of the feed tube at an acute angle to reduce thermal stresses and to supply propellant to the injection elements. Propellant flows through the four manifold passages to tapered manifolds, which are machined longitudinally along the injector body, and then flows through the Rigimesh injection element into the catalyst bed. The 0.167 to 0.164 inch diameter passages are sized to preclude plume propagation under low flow conditions that might occur due to valve seat leaks. The Rigimesh material used in the injector consists of two layers of 12-by-64 mesh Haynes 25 wire screen sintered and pressed together to a plate thickness of 0.041 inch. The mean pore opening of the Rigimesh material is approximately 100 microns in diameter, producing a finely atomized spray that aids rapid dispersion and vaporization of the propellant in the catalyst bed.

The material breaks up the propellant into many fine low momentum streams, minimizing catalyst loss. The injector approach used on the 100 lbf engine produces very low local momentum injection into the catalyst bed which is significant in minimizing attrition.

The catalyst bed is divided into two concentric annular sections: the inner bed is 14-18 mesh Shell 405 catalyst of 0.3-inch radial depth. The outer bed is 14-18 mesh catalyst of 0.3-inch radial depth and employs RRC LCH-202 catalyst. The LCH-202 catalyst used in the outer catalyst bed is manufactured by RRC on the same alumina carrier as that on which Shell 405 is made.

Each catalyst bed is held radially by a circular bed cylinder that is slotted perpendicular to the engine axis by 0.014-inch wide slots. The slots convert the cylinders into low-spring rate/high-temperature springs that absorb expansion differentials in the axial direction. Axial containment of the catalyst is provided by bed closures at each end with grooves to positively retain the bed cylinders.

The thrust chamber body is machined from Inconel 625 bar stock to an expansion ratio of approximately 5:1. A nozzle extension spun from Inconel 625 Sheet stock is Tungsten Inert Gas (TIG) welded to the chamber body to provide the overall chamber/nozzle assembly and expansion ratio of 54:1.

The inside of the chamber body contains a two-piece liner, fabricated from Inconel 625 sheet stock, that serves to limit the maximum chamber body temperature, allowing use of Inconel 625 for the chamber body with high stress margins. The liner is dimpled to provide a standoff distance from the chamber wall. The forward liner is TIG welded to the upstream bed closure and the aft liner is TIG welded to the convergent section of the nozzle.

The support structure is fabricated from Inconel 625 bar stock and serves the dual purpose of providing thermal isolation between the thrust chamber and propellant valve as well as providing structural support for the thrust chamber, attachment of the solenoid valve, and mounting structure. The propellant valve is attached to the forward flange of the mount structure by three No. 10 screws. The support structure is TIG welded to the thrust chamber closure. During the welding operation, tooling holds the nozzle centerline perpendicular to the mounting flange such that the required thrust alignment is maintained. A final skim machine cut may be made across the support structure mount flange if required to hold precise thrust vector alignment.

The propellant valve is solenoid-actuated single-seat valve manufactured by Wright Components, Inc. (WCI). The main function of the valve is to provide shutoff of propellant flow (no leakage) between command pulses and reliable/repeatable delivery of propellant on command during either steady-state or pulse-mode operation. The hydrazine thruster valve characteristics are listed in Table 4.3.3-2.

TABLE 4.3.3-2. HYDRAZINE THRUSTER VALVE CHARACTERISTICS

Parameter	Value
Power required (at +28 V and 70°F)	34 watts
Pull-in Voltage	<20 V @ 500 psia
Drop-out Voltage	>1.3 V @ 52 lbf
Leak Rate (scc/Hour of GN_2)	<3
Cycle life	20,000 wet

The propellant valve is shown in Figure 4.3.3-2 in its closed or deenergized position. Pressure forces and spring forces act to maintain the valve in the closed position. The plunger assembly is stopped mechanically; thus, the

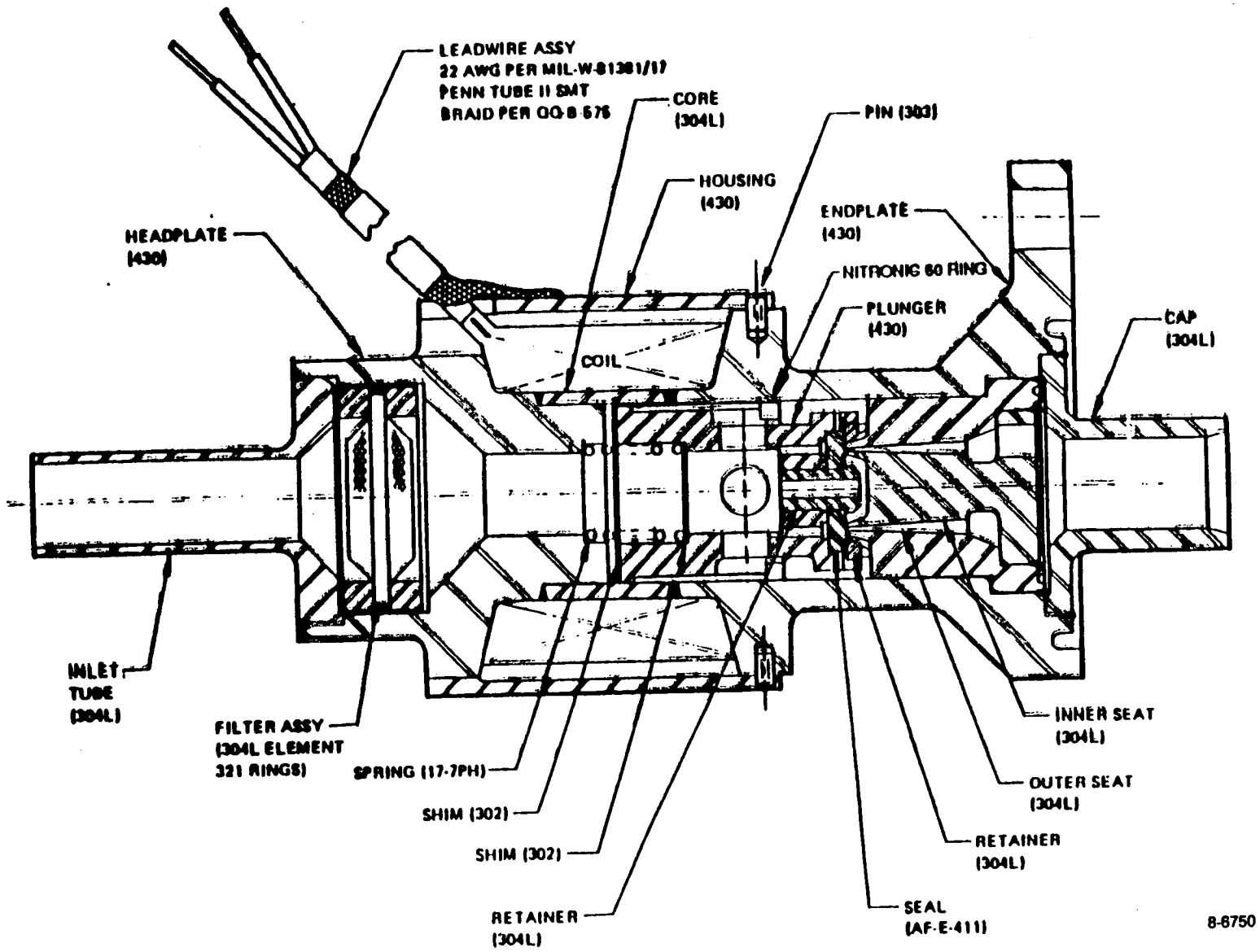

Figure 4.3.3-2. Propellant Valve

impression of the seat into the soft-seat insert is controlled such that no cutting or abrading can occur on the soft-seat insert material. Clearance grooves are cut in the plunger insert cavity to allow for any swelling that may occur in the seat areas and to prevent entrapment of fluids.

Upon energizing the coil, the plunger assembly will move to the open position thereby allowing propellant to flow through the valve inlet and around the valve seat. Propellant flow will continue until the valve is deenergized. Upon deenergizing of the coil, the plunger will move to the closed position and form a positive seal against the seat. The action of the spring pressure will cause the plunger to move to the closed position.

The valve is made of corrosive-resistant steel with the spool assembly and inlet parts joined by electron-beam welding methods. The steels used are types 302,304L, 430, 347 and 17-7 pH. The magnetic portions of the solenoid are type 430 CRES, and the nonmagnetic core is type 304L CRES. The coil consists of Class 200 magnet wire per Federal Specification J-W-1177/14A and is impregnated with low outgassing epoxy to ensure that, under vibration and acceleration, the coil windings will not short out as result of breakdown of wire film insulation.

The soft-seat insert is made from AFE-411 elastomer and is contained within the plunger assembly. The amount of elastomeric compression is closely controlled to ensure that no permanent deformation takes place as a result of valve actuation or continued seating of the elastomer insert on the valve seat. This is achieved by making certain that the spring load, together with the pressure loading, is never fully carried by the elastomer insert, but is jointly carried by plunger/seat (metal to metal) and the insert.

The nominal steady-state performance characteristics of the MR-104A REA are summarized in Table 4.3.3-3 for flowing inlet pressures of 350 and 100 psia.

TABLE 4.3.3-3. MR-104A REA NOMINAL STEADY-STATE PERFORMANCE CHARACTERISTICS

Performance Parameter	Characteristics	
	Inlet Pressure = 350.0 psia	Inlet Pressure = 100.0 psia
Propellant Temperature, °F	70.0	70.0
Trim Orifice Pressure Drop, psid	126.4	21.4
Valve Pressure Drop, psid	40.6	6.9
Injector Pressure Drop, psid	19.7	3.3
Catalyst Bed Pressure Drop, psid	22.5	11.1
Stagnation Pressure Loss, psid	7.5	3.1
Stagnation Chamber Pressure, psia	133.4	54.2
Flow Rate, lbm/sec	0.472	0.184
Ammonia Disassociation, %	53.4	60.1
Characteristic Velocity,ft/sec	4,340.0	4,306.0
Vacuum Thrust Coefficient	1.7238	1.7044
Vacuum Thrust, lbf	109.7	42.0
Vacuum Specific Impulse, lbf-sec/lbm	232.5	228.1

The nominal steady-state vacuum thrust characteristics of the engine are shown graphically in Figure 4.3.3-3 as a function of flowing inlet pressure to the engine. As noted in Table 4.3.2-2, the engine produces a nominal thrust level of 109.7 lbf at a flowing inlet pressure of 350 psia and 42.0 lbf at a flowing inlet pressure of 100 psia.

The nominal vacuum specific impulse characteristics of the MR-104A REA are shown graphically in Figure 4.3.3-4 as a function of flowing inlet pressure for propellant temperatures of 40°F to 120°F. At a propellant temperature of 70°F the nominal vacuum specific impulse is 232.5 and 228.1 lbf-sec/lbm for flowing inlet pressures of 350 and 100 psia, respectively. The vacuum specific impulse as a function of thrust is shown in Figure 4.3.3-5.

The impulse bit delivered by the REA is a function of the pulse width, duty cycle, and feed pressure. Impulse-bit data is presented in Figure 4.3.3-6 for pulse widths of 100 ms and 60 ms at 180 ms off-times over the thrust range.

The pulse-mode performance characteristics of the MR-104A REA are summarized in Figure 4.3.3-7 for a duty cycle of 0.020 second on-time and 5 seconds off-time, at a flowing inlet pressure of 350 psia. The transient performance is plotted as a function of throat temperature. Under equilibrium pulsing the engines performance at this duty cycle is 202.3 lbf-sec/lbm.

4.3.3.2 Propellant Tank

The propellant tank consists of three main elements; the tank shell, the expulsion diaphram, and the stem pipe outlet, as shown in Figure 4.3.3-8. Low pressure N_2 is introduced into the tank through an inlet port on the forward end of the tank; the N_2 exerts a force on the diaphram which in turn acts on the hydrazine propellant. As hydrazine is consumed, the constant pressure N_2 forces the diaphram hydrazine to be expelled from the aft end of the tank.

All of the N_2 pressurant in the propellant tanks can be utilized by the cold gas thrusters, although the system is sized and loaded so that none of the N_2 in the propellant tank is needed for control.

The tank shell is fabricated from 6AL4V titanium. Two hemispheres are spun formed and subsequently welded to a center girth ring. The girth ring contains a machined boss which taper fits into the RCE Support Structure; the girth ring is used to remove all axial shear loading on the propellant tank. Radial loads are removed by turn-buckle clamps attached to the forward and aft inlet/outlet fittings. The tank outside diameter is 13.2 inches.

The diaphram is a TBD material, which is used for the containment of hydrazine. The diaphram is designed (and tested) to withstand, without rupture, a 100 psia pressure on either the N_2 or N_2H_4 side while the opposite side is at zero psi. Additionally, leakage through the diaphram is less than 140 scc per hour with a Δ p of 100 psig on the N_2 side and 0 psig on the N_2H_4 side.

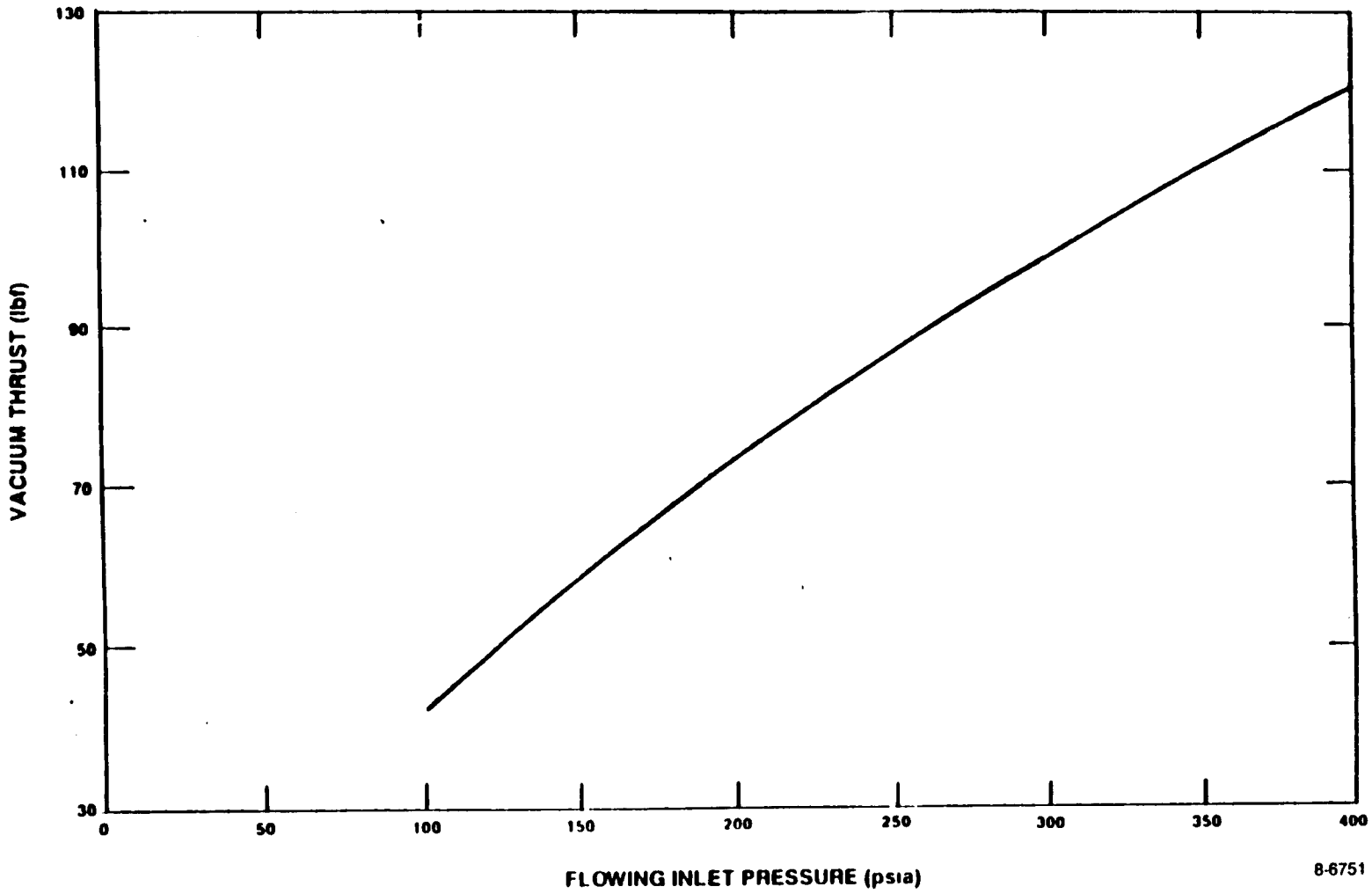

Figure 4.3.3-3. MR-104A Vacuum Thrust vs. Feed Pressure

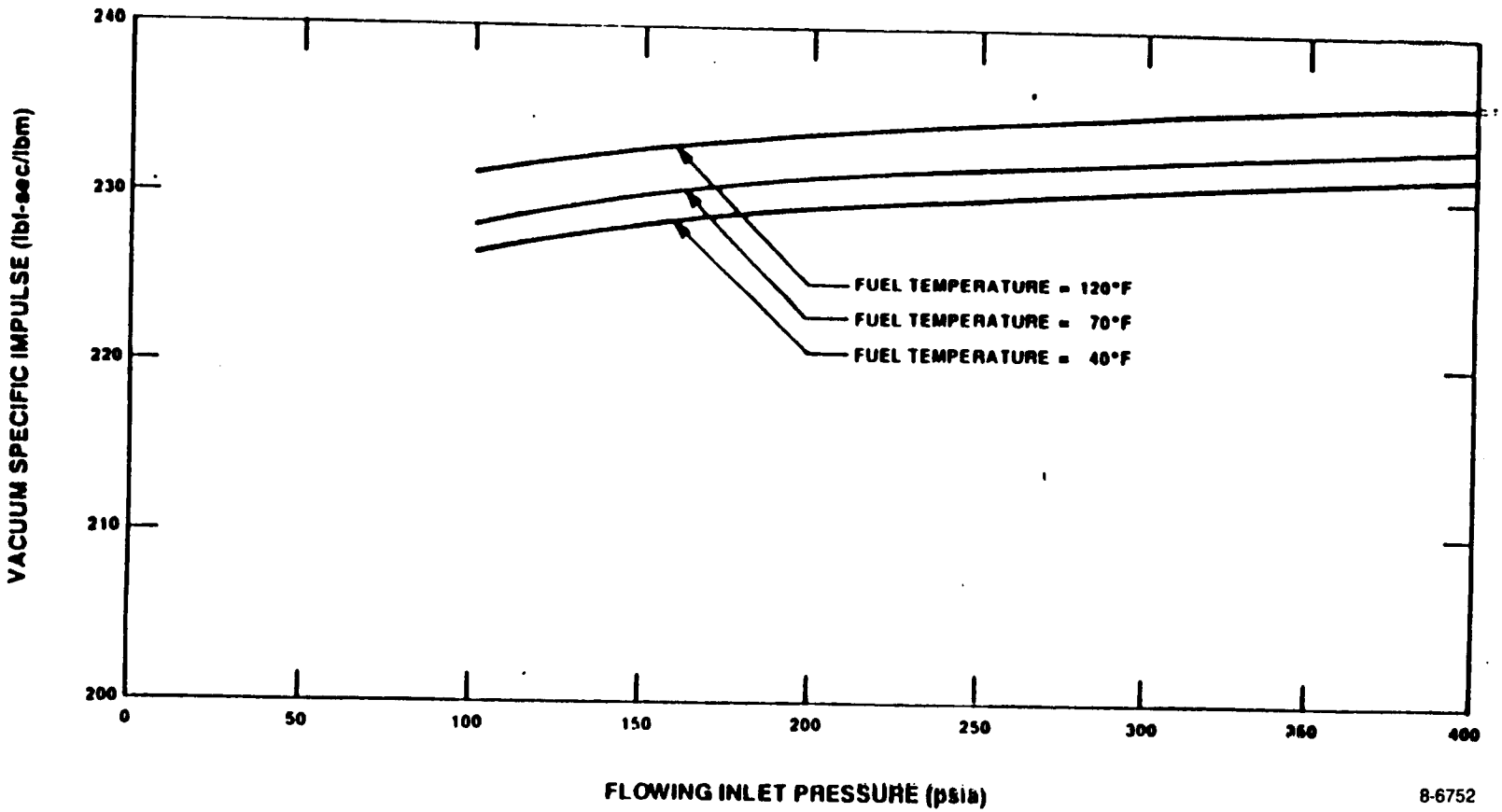

Figure 4.3.3-4. MR-104A REA Steady-State Performance Characteristics

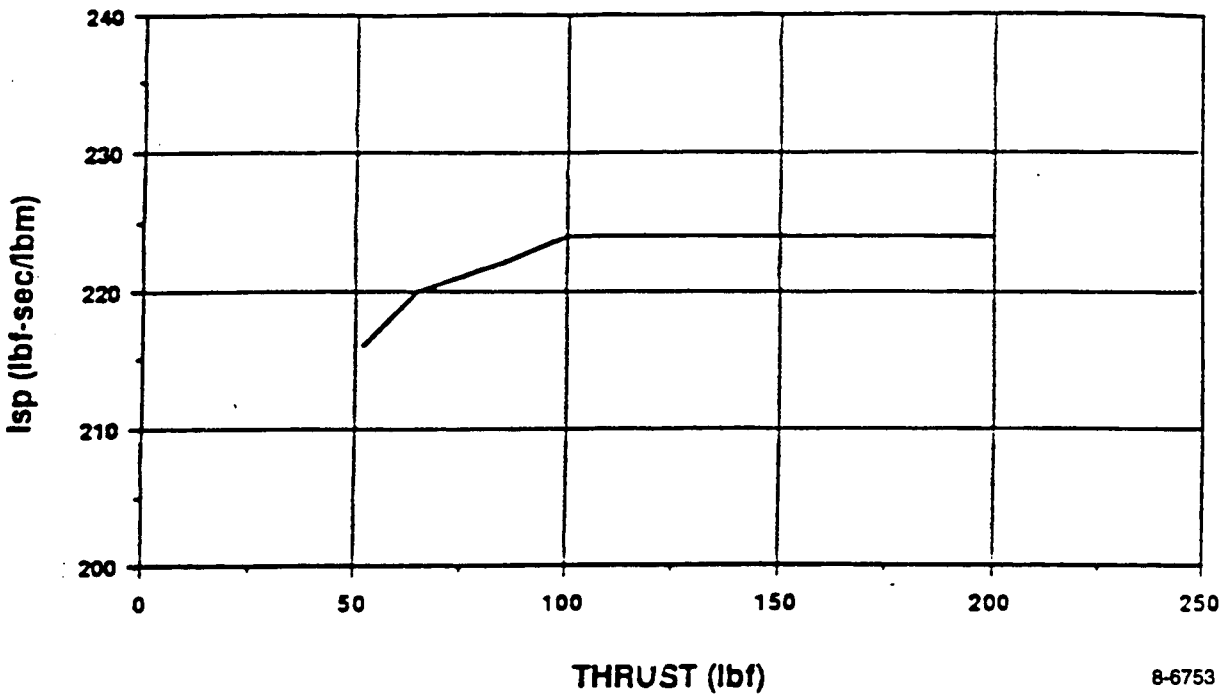

Figure 4.3.3-5. Minimum N_2H_4 Thruster Performance

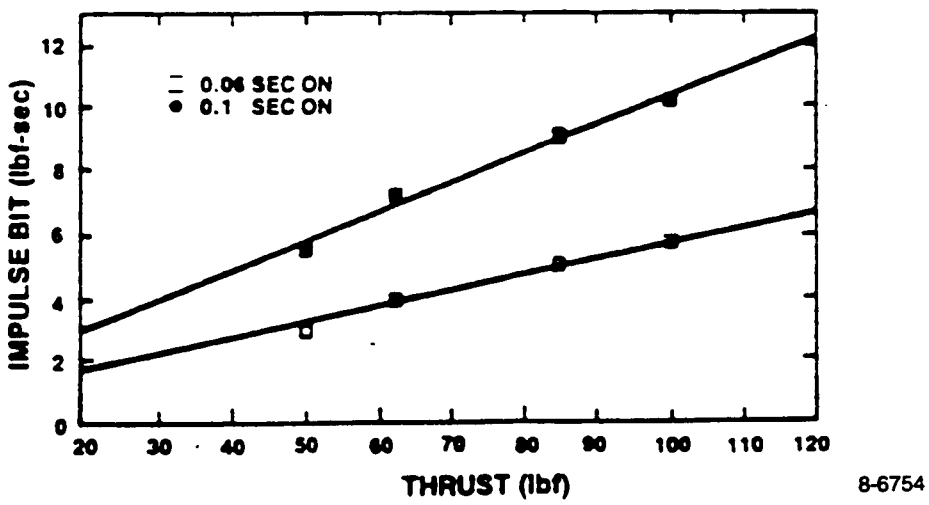

Figure 4.3.3-6. Impulse Bit vs. Thrust

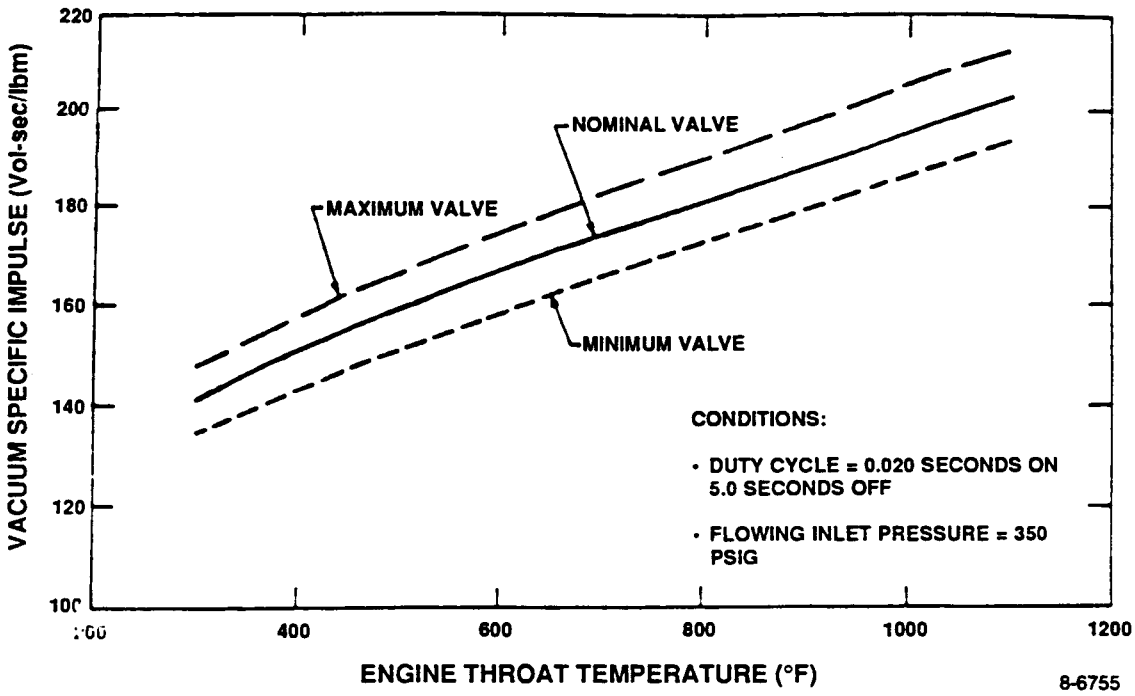

Figure 4.3.3-7. MR-104A REA Pulse-Mode Performance vs. Throat Temperature

4.3.3.3 Nitrogen Thruster

The 2 lbf cold gas GN_2 thruster consists of a solenoid-operated valve and a supersonic nozzle with an expansion ratio of 44 to 1, as shown in Figure 4.3.3-9. The thruster operates at a pressure of 480 psig over a temperature range of -45 to +150°F. The valve operating characteristics are shown in Table 4.3.3-4. The thruster opening and closing response is less than 18 ms to 90% of rated thrust and closing response is less than 10% of rated thrust. The valve is constructed from ARMCO iron, 10.8 mild steel, nickel plated 302 stainless steel spring, and an ethylene propylene copper coil O-ring.

TABLE 4.3.3-4. NITROGEN THRUSTER VALVE CHARACTERISTICS

Parameter	Value
Operating Pressure (nominal)	480 psig
Thrust Level	2.0± 0.1 lbf
Power Required (at +28 V and +70°F)	30 watts
Pull in Voltage	<2 Vdc
Drop Out Voltage	>2 Vdc
Leak Rate (internal)	<0.5scc/hr GN_2

The thruster steady state specific impulse, Isp, is at least 65 seconds. A minimum impulse bit of 0.05 lb-sec is obtainable within a tolerance of ±10%.

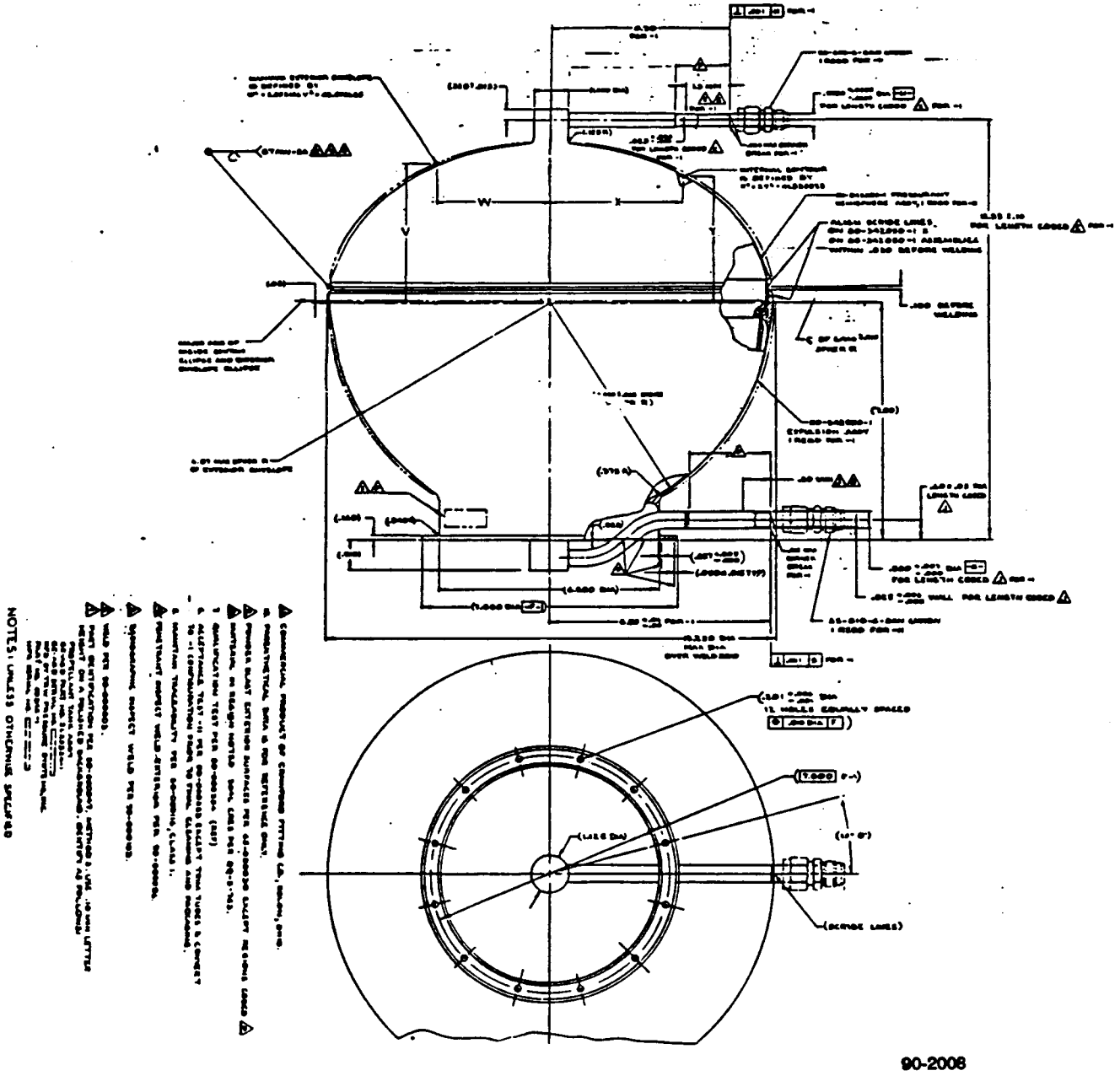

Figure 4.3.3-8. RCE Propellant Tank

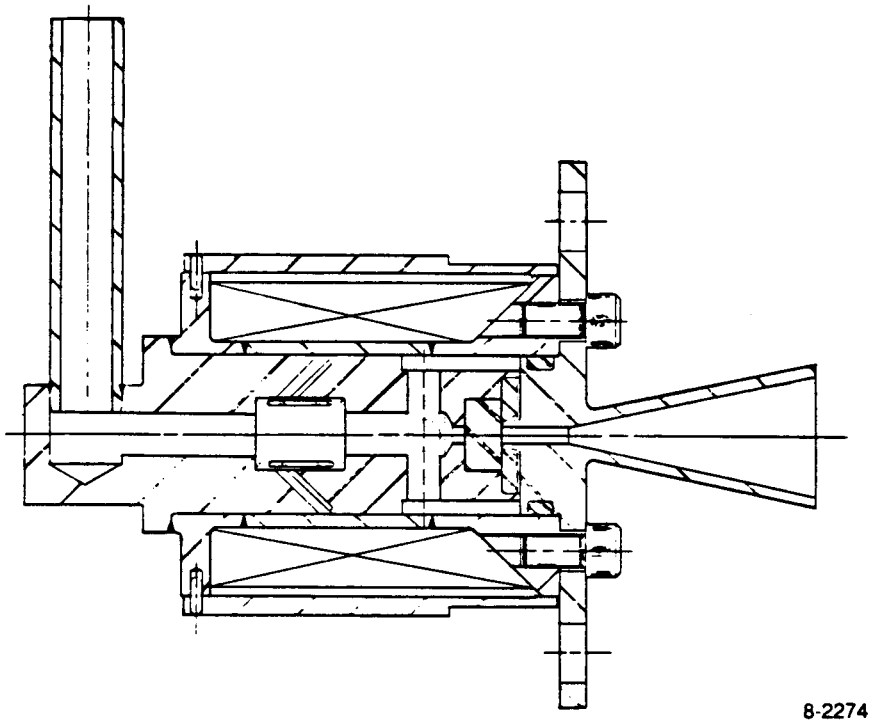

Figure 4.3.3-9. Cold Gas Thruster

4.3.3.4 Pressurant Tank

Two spherical pressure tanks are provided. Sufficient GN_2 is stored to provide propellant pressurization throughout the mission, in addition to providing GN_2 for full mission control requirements. Each GN_2 tank is fabricated from 6AL4V titanium and has a nominal internal Volume of 430 in^3. The external diameter of each tank is 9.75 inches. The pressurant tank is shown in Figure 4.3.3-10.

4.3.3.5 Pressure Regulator

The pressure regulator performs the function of reducing the high pressure GN_2 supply to a 480 psia working pressure in the low pressure system. The regulator selected is manufactured by Futurecraft, Inc. and is depicted in cross section in Figure 4.3.3-11. From the cross section, it is evident that the regulator is a three-stage design, featuring dual fault tolerant series regulation. The regulator consists of a first, or roughing stage coaxial regulator followed by two series redundant regulator stages. A dual fault tolerant design is selected to meet range safety criteria and requirements at the U.S. launch sites..

The first regulation stage features an axial poppet and seat design contained within a Nitronic 60 stainless steel. Seat material is ethylene propylene O-rings with teflon backup. The first stage poppet is opened through the

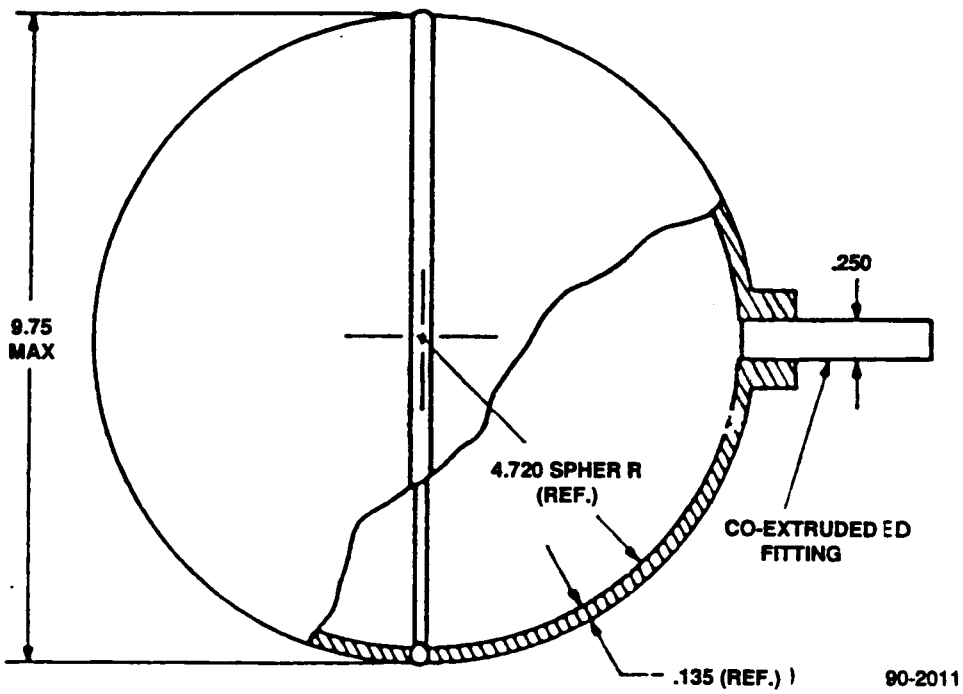

Figure 4.3.3-10. Pressurant Tank

action of a Belleville spring washer stack. Most of the second and third stage components, including the main housing and poppet spools, are made of 7075-T7351 aluminum alloy for weight savings and fast, balanced regulator response. Poppets are opened through the action of parallel chrome vanadium die springs of custom grind and electrolic nickel plating. Seat material is ethylene propylene with teflon backup. Tube stubs are 304L CRES material to meet the RCE manifold materials.

Functional characteristics of the regulator are shown in Table 4.3.3-5.

4.3.3.6 Pressure Transducer

Three pressure transducers are provided as part of the telemetry subsystem. One transducer monitors the high pressure nitrogen (Type I); the second transducer monitors the low pressure nitrogen (Type II); the third transducer monitors the hydrazine side (Type III). The operating characteristics of the pressure transducers are listed in Table 4.3.3-6. The pressure transducer is shown in Figure 4.3.3-12. The transducer output is directly proportional to the nitrogen line pressure, and hence provides a checkpoint for proper pressurant loading as well as constant flight telemetry.

The pressure transducer is manufactured by Statham. The outer case and pressure fitting are made from stainless steel to give high strength, low weight, and good corrosion resistance for use in severe environments. The unit consists of a machined diaphragm to which four active strain gauges are attached with added electronics for signal and conditioning.

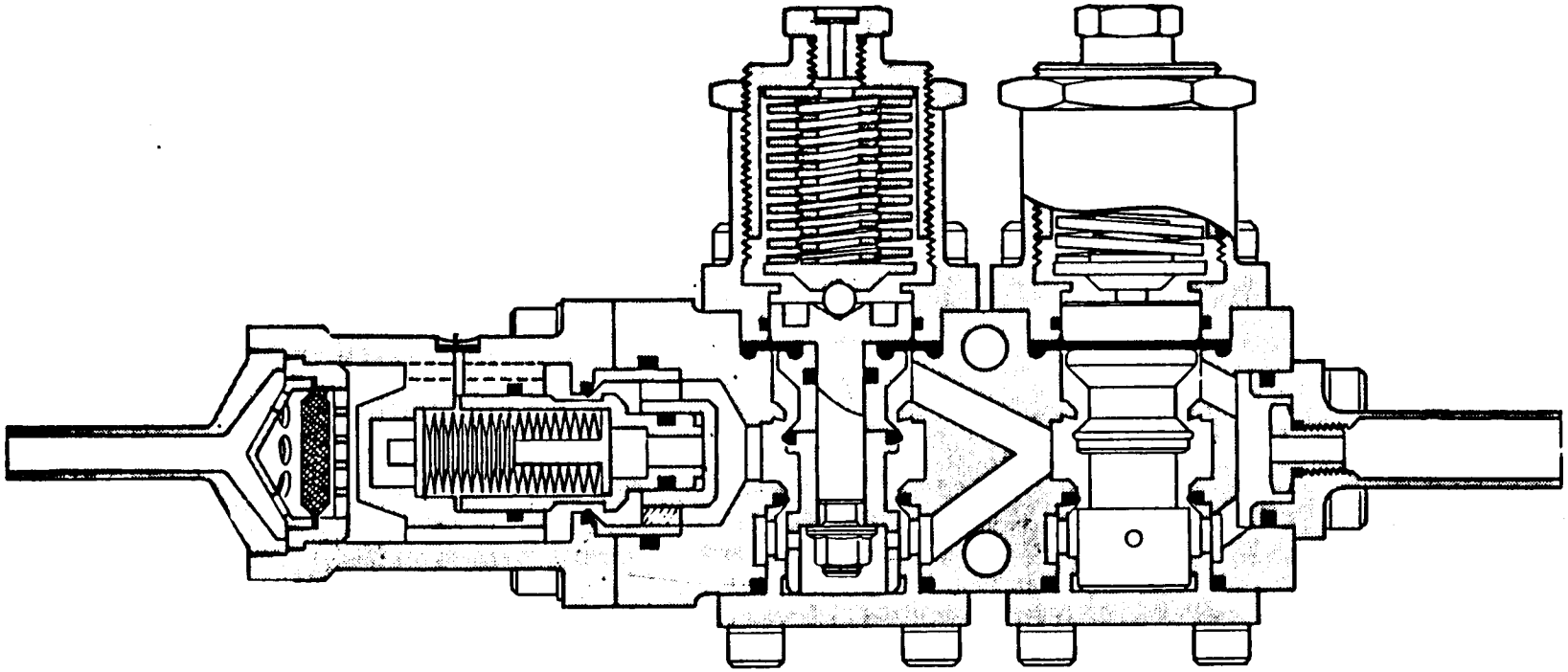

Figure 4.3.3-11. Cross Section, Pressure Regulator

TABLE 4.3.3-5. PRESSURE REGULATOR OPERATIONAL CHARACTERISTICS

Parameter	Value			
Type	Three-stage regulator with integral filter and outlet flow control orifice. Second and third stage are precision series redundant regulators.			
Media	Gaseous nitrogen			
Pressure Characteristics	Operating	Proof	Burst	(psia)
A. Inlet Pressure	4500	9000	18,000	
B. Outlet Pressure	477 ±7	990	1,980	
Stage Settings				
A. 1st Stage (roughing)	650			
B. 2nd Stage (secondary)	487 ±7			
C. 3rd Stage (primary)	477 ±7			
Design Cycle Life	100,000 cycles			

TABLE 4.3.3-6. PRESSURE TRANSDUCER CHARACTERISTICS

Parameter	Performance	
	High Pressure (Type I)	Low Pressure (Type II & III)
Nominal Operating Pressure (psig)	4500	600
Maximum Overload (psig)	6750	900, Type II 2500, Type III
Temperature Compensation Range (°F)	-30 to +130	-30 to +130
Maximum Thermal Sensitivity (%/°F)	0.1	0.1
Maximum Thermal Zero Shift (%FS/°F)	0.015	0.015
Non-linearity and Hysteresis (%FS)	±0.75	±0.75
Accuracy (min) at 24-32 Vdc (%FS/V)	±0.1	±0.1
Output Voltage (Vdc)	5.0 ±0.1	5.0 ±0.1
Output Noise, Maximum (mVp-p)	15	15
Over Range Limit (Vdc)	-1 to +7	-1 to +7
Zero Balance (%)	± 2	± 2

4.3.3.7 Fill and Drain Valve

Three fill and drain couplings as shown in Figure 4.3.3-13 are provided in the manifolding. Two fill and drain couplings are provided in the gaseous nitrogen manifolds for filling and draining the GN_2. One fill and drain coupling is provided in the N_2H_4 manifold to allow filling and draining of the propellant. The operating characteristics of the fill and drain valves are listed in Table 4.3.3-7.

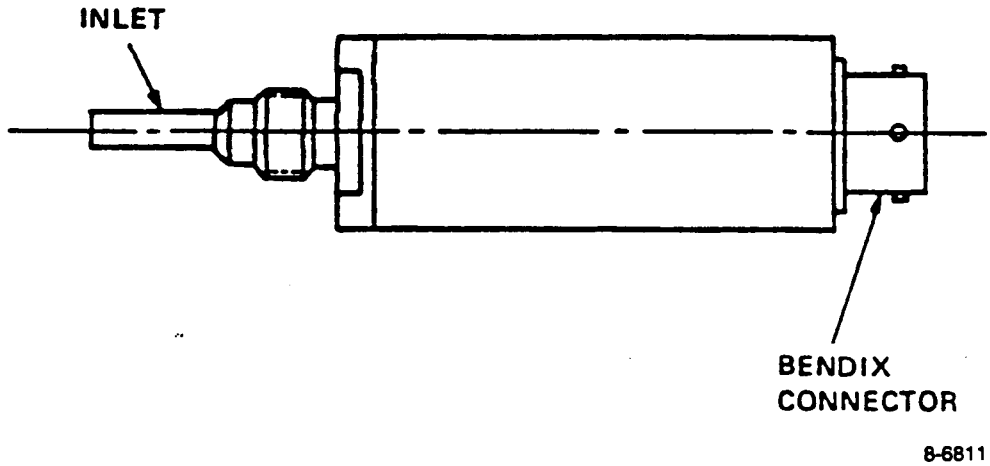

Figure 4.3.3-12. Pressure Transducer

TABLE 4.3.3-7. FILL AND DRAIN VALVE CHARACTERISTICS

Parameter	GN_2, High Type I	GN_2, Low Type III	N_2H_4 Type II
System Operating Pressure (psig)	4500	TBS	TBS
Proof Pressure (psig)	6750	900	900
Burst Pressure (psig)	18,000	2,400	2,400
Leakage (scc/sec He)			
Cap Off	1 X 10 -5	1 X 10-5	1 X 10-5
Cap On	1 X 10 -6	1 X 10-6	1 X 10-6
Cycle Life (minimum	100	100	100
Operating Fluids - Operational	GN_2	GN_2	N_2H_4
Operating Fluids - Testing	GN_2	GN_2	N_2H_4 & GN_2
Materials			
Body	304L SS	304L SS	304L SS
Poppet	17-4PH cond. H-900 SS	17-4PH cond. H-900 SS	17-4PH cond H-900 SS
Pin & Balls	440C SS	440C SS	440C SS
O-Rings	EPR	EPR	EPR

The high pressure and low pressure fill and drain valves are identical to the hydrazine fill and drain valve, except for the inlet fitting. The fittings are varied to ensure mating with the proper source. Each valve is labeled and fitted with a color coded cap. Red is hydrazine, green is low pressure, and silver is high pressure.

The Pyronetics, Inc. Model 1831 fill and drain valve is a small stainless steel, in-line, flange-mounted, manually operated valve. The primary sealing functio: of the Model 1831 valve is accomplished by a poppet engaging a tapered seat in the valve body, which forms a metal to metal seal. Three pins are utilized to prevent the poppet from rotating radially as the poppet is moved

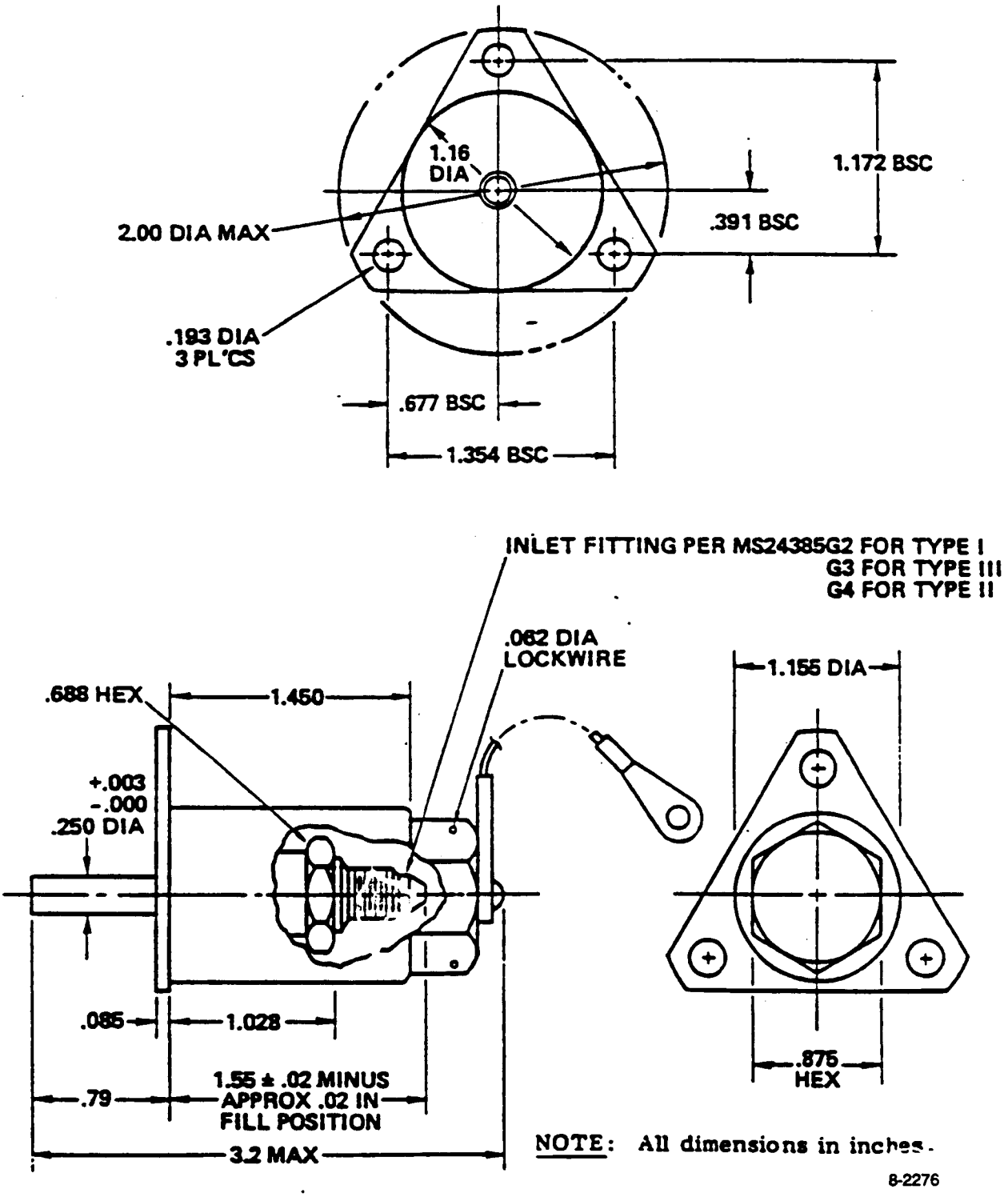

Figure 4.3.3-13. Fill and Drain Valve

along the longitudinal axis by rotating the retainer nut. Turning the retainer nut clockwise and tightening 30 ±5 inch pounds (3.39 ±0.6 N-m) seals the valve. Conversely, turning the retainer counterclockwise disengages the poppet from the tapered body seat and allows flow. The purpose of the O-ring and backup ring on the poppet is to prevent an external leak path when the valve is in the open mode. Thus, the O-ring is exposed to the working fluid only in the open valve position.

4.3.3.8 Hydrazine Isolation Valve

After the hydrazine engines have completed their mission, two pyrotechnic-actuated isolation valves are commanded closed; the valves are located in the propellant line immediately downstream of each hydrazine tank. Actuation of the valves irreversibly isolates the hydrazine from the propellant manifold and thrusters to prevent large scale disturbances in the event of thruster valve or manifold leaks or inadvertent fire commands to the engines. The operating characteristics of the valve are listed in Table 4.3.3-8. The N_2H_4 isolation valve is shown in Figure 4.3.3-14. Inadvertant latch value operation after propellant loading will isolate the tank from the tank drain and pressure monitor.

TABLE 4.3.3-8. HYDRAZINE ISOLATION VALVE CHARACTERISTICS

Parameter	Performance
Pressure Drop (Open)	<10 psid at 2.9 pps N_2H_4
Maximum Squib No-Fire Current	1.0 amp for 5 minutes
Maximum Squib No-Fire Power	1.0 watt for 5 minutes
Minimum All Fire	4.0 amps/bridgewire,<10 ms
Bridge Wire Resistance	1.0 +0.2 ohms -0.1

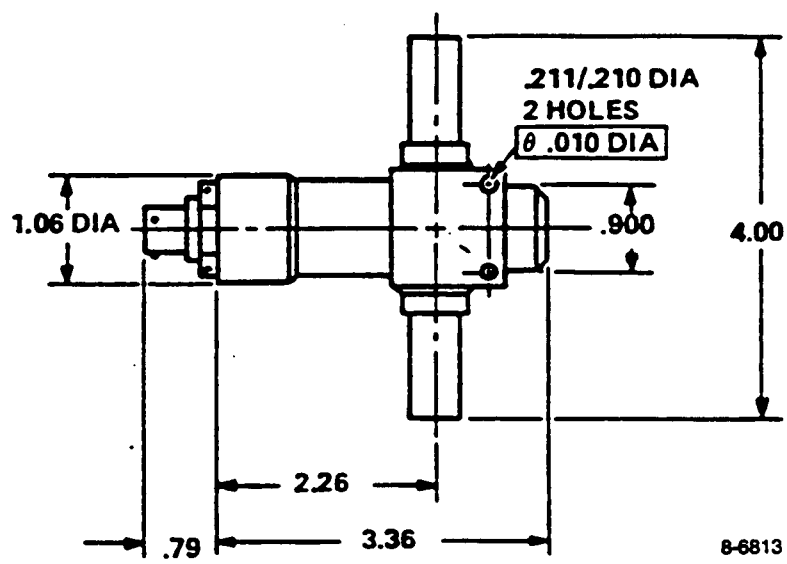

Figure 4.3.3-14. Hydrazine Isolation Valve

4.3.3.9 Latch Valve

The latch valve shown in Figure 4.3.3-15 is included in the manifold leading to the 8 nitrogen thrusters to provide a series-redundant seal against nitrogen leakage from the thrusters during the mission life. The operating characteristics of the latch valve are given in Table 4.3.3-9. The latch valve is manufactured by Hydraulic Research, Part No. 48003300. It is a torque motor actuated design with latching forces supplied by permanent magnets in both the open and closed positions. The torque motor is isolated from the fluid passages by a flexible tube.

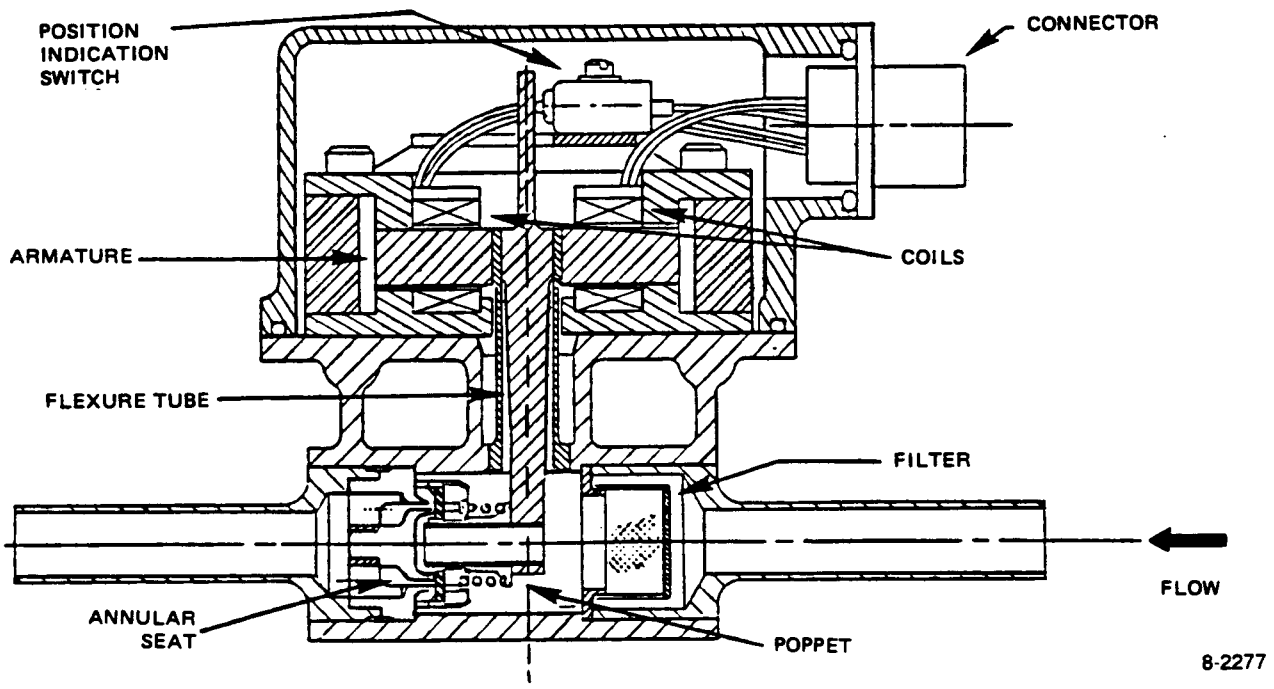

Figure 4.3.3-15. Latch Valve

TABLE 4.3.3-9. LATCH VALVE CHARACTERISTICS

Parameter	Value
Operating Pressure (nominal)	480 psig
Internal Leakage	1 scc/hr GN_2
Opening Response	20 ms
Closing Response	20 ms
Voltage Range	28 $\pm$1 Vdc
Power	70 W at 28 VDC
Cycle Life	20,000
Proof Pressure	900 psig
Burst Pressure	2200 psig
Weight	1.35 lb

The materials of construction are:

Housing	- Stainless steel 304L CRES QQ-S-763
Poppet Seal	- AF-E-411, ethylene propyleneterpolymer
Flexible Tube	- 17-7-PH CRES AMS 5673 steel

4.3.3.10 Relief Valve

The NOAA KLM relief valve is being reevaluated. A final design has not been selected to date. The typical relief valve shown in Figure 4.3.3-16 (TBD) is a direct pressure-actuated, spring-loaded poppet assembly which vents externally through a zero-net-thrust port. A Carleton Controls Relief Valve (RCA P/N 2295728) is usually installed in the RCE to provide system relief in the event of a rise in system pressure on the low pressure GN_2 side of the RCE. It is sized to protect the propellant tank and the low pressure system from overpressure during normal spacecraft temperature excursions during ground processing or flight.

The relief valve design is known as the inverted relief, the reliability of which is enhanced because the spring pressure is not forcing the valve stem on the seat. Rather, the spring works on the piston, inside of which is a spring loaded poppet. Inlet pressure works on the piston diameter and compresses the spring. When increased pressure causes the piston to pick up the end of the valve stem, the valve has reached its cracking pressure of TBD psig maximum. The valve is of all-stainless-steel design with an elastomeric Kynar seat. The maximum pressure required to operate the relief valve is TBD psig; the relief reset pressure is set at TBD psig. The operation characteristics of the relief valve are given in Table 4.3.3-10.

TABLE 4.3.3-10. RELIEF VALVE CHARACTERISTICS

Parameter	Value
Operating Pressure	TBD psig
Relief Cracking Pressure	TBD psig
Reseat Pressure	TBD psig
Vent Flow Rate, Minimum	TBD scfm at TBD psig
Internal Leakage	TBD scc/hr GN_2 at TBD psig
Proof Pressure	TBD psia
Burst Pressure	TBD psia
Life	TBD cycles
Weight	TBD lb

TBD

Figure 4.3.3-16. Relief Valve

4.3.3.11 In-Line Filters

There are three types of filter assemblies in the RCE system. Their locations are:

- Inlet to GN_2 engine assemblies
- Inlet to N_2H_4 engine assemblies
- The three fill and drain valves

The characteristics are to prevent contaminants larger than 25 microns from reaching the nitrogen engines, hydrazine thrusters, and the system via any of the three fill valves.

Figures 4.3.3-17, 4.3.3-18, 4.3.3-19, 4.3.3-20 and 4.3.3-21 show typical filter assemblies. The materials of construction are 304 CRES stainless steel and a twilled Dutch weave wire cloth for the filter element.

4.3.3.12 Propellant Manifold Assemblies

There are six propellant tubing manifolds that serve as flow passages for the propellants to the different RCE components. They are fabricated from 0.035" and 0.025" wall, 304L stainless steel tubing, which is a low-weight, high strength material. The manifolds are of all welded construction except for the component interfaces which are mechanical connections to provide ease of replacement and maintenance of the components.

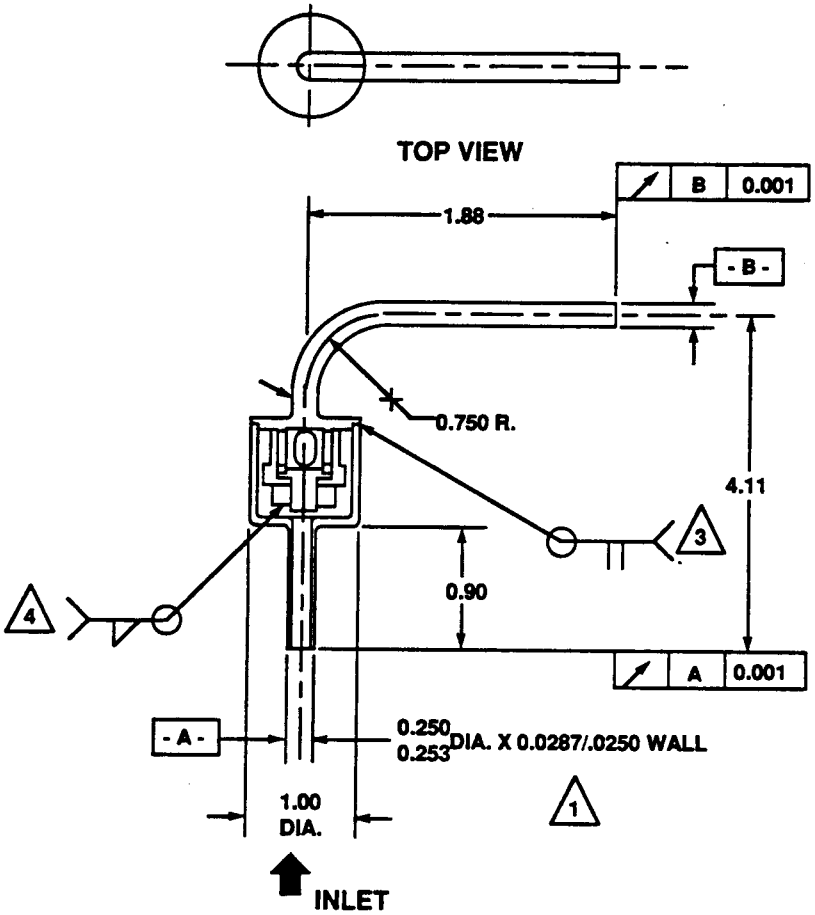

SPECIFICATIONS

END CONNECTION	0.253/0.250 DIA. X 0.0287/0.0250 WALL
OPEN PRESSURE	505 A
PROOF PRESSURE	2 X OPERATION PRESSURE
BURST PRESSURE	4 X OPERATING PRESSURE
FILTRATION RATING	25 MICRONS ABSOLUTE
COLLAPSE PRESSURE	OPERATING PRESSURE ACROSS THE ELEMENT MIN
FLUID COMPATIBILITY	N_2H_4, H_2O, IPA, GN_2 & GHe
FLOW RATE	0.010 LBM/SEC
DP (CLEAN)	10 PSID
EXTERNAL LEAKAGE	1 X C^{-6} SCC/SEC GHe
CUSTOMER NAME	GE
WEIGHT	0.16 LBM

90-2013M

Figure 4.3.3-17. Filter, N_2H_4 Fill and Drain

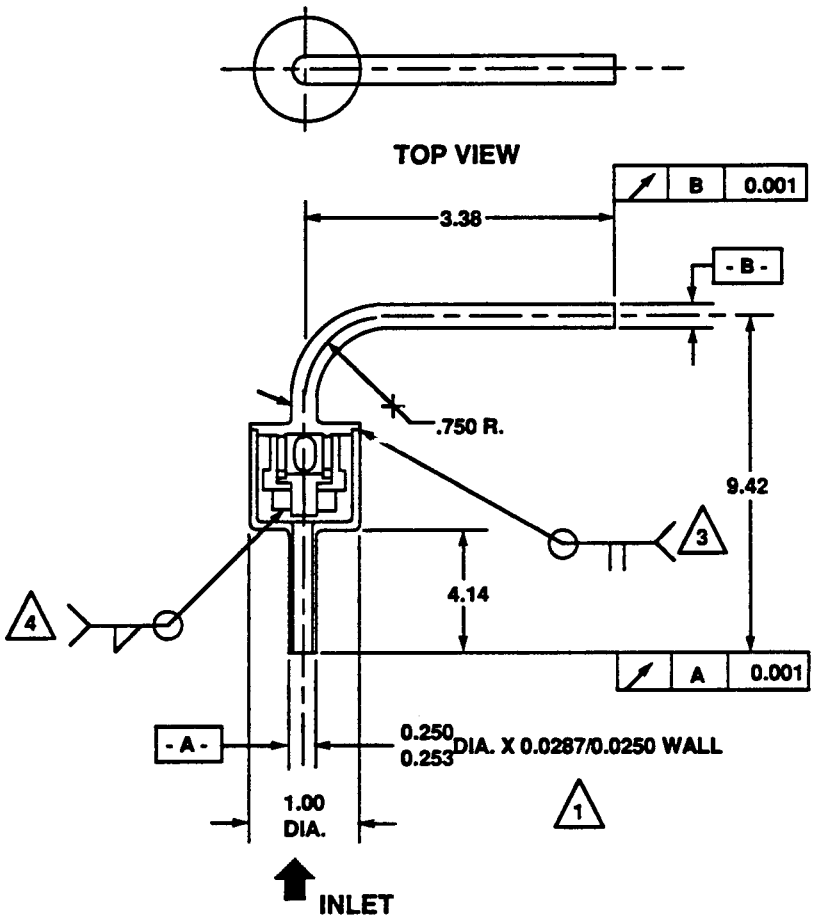

SPECIFICATIONS

END CONNECTION	0.253/0.250 DIA. X 0.0287/0.0250 WALL
OPEN PRESSURE	505 A
PROOF PRESSURE	2 X OPERATION PRESSURE
BURST PRESSURE	4 X OPERATING PRESSURE
FILTRATION RATING	25 MICRONS ABSOLUTE
COLLAPSE PRESSURE	OPERATING PRESSURE ACROSS THE ELEMENT MIN
FLUID COMPATIBILITY	N_2H_4, H_2O, IPA, GN_2 & GHe
FLOW RATE	0.010 LBM/SEC
DP (CLEAN)	10 PSID
EXTERNAL LEAKAGE	1 X C^{-6} SCC/SEC GHe
CUSTOMER NAME	GE
WEIGHT	0.21 LBM

90-2016M

Figure 4.3.3-18. Filter, Low Pressure GN_2 Fill and Drain

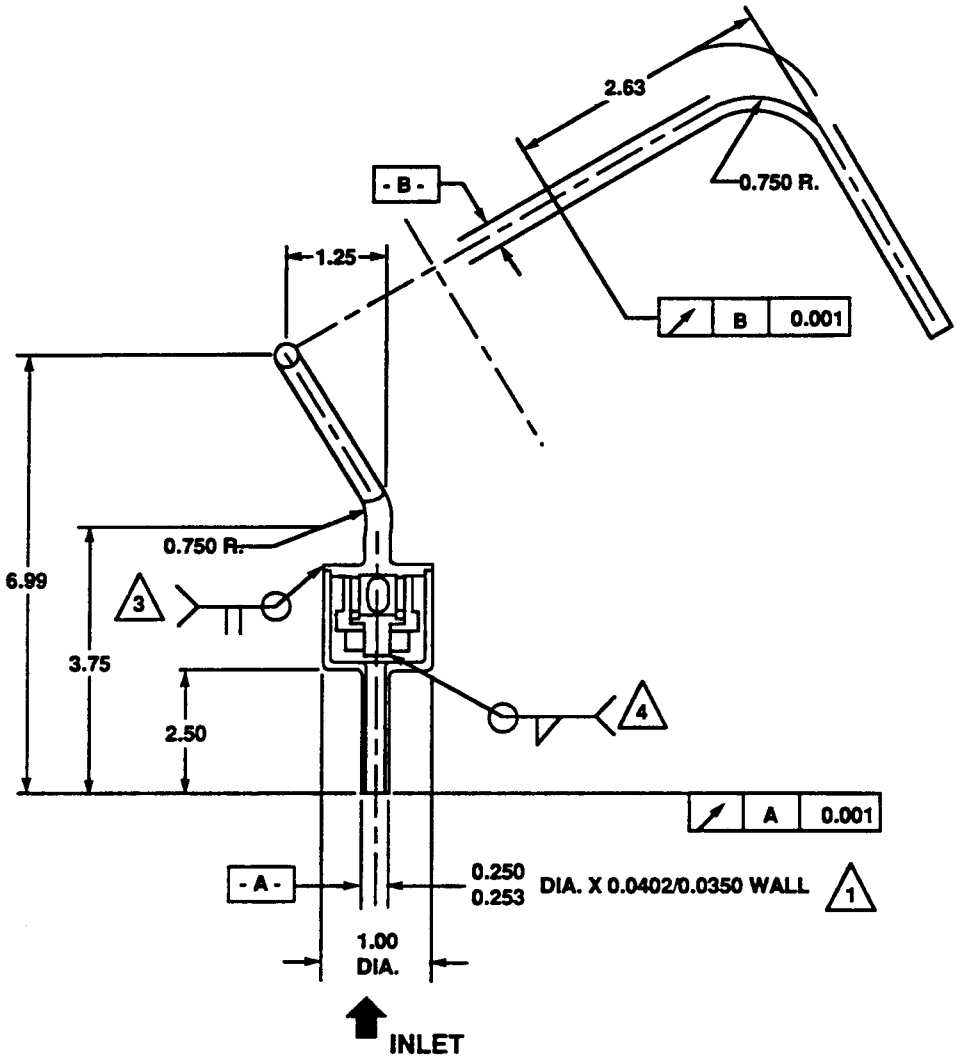

SPECIFICATIONS

END CONNECTION	0.253/0.250 DIA. X 0.0402/0.0350 WALL
OPEN PRESSURE	505 A
PROOF PRESSURE	2 X OPERATION PRESSURE
BURST PRESSURE	4 X OPERATING PRESSURE
FILTRATION RATING	25 MICRONS ABSOLUTE
COLLAPSE PRESSURE	OPERATING PRESSURE ACROSS THE ELEMENT MIN
FLUID COMPATIBILITY	N_2H_4, H_2O, IPA, GN_2 & GHe
FLOW RATE	0.010 LBM/SEC
ΔP (CLEAN)	10 PSID
EXTERNAL LEAKAGE	1 X C^{-6} SCC/SEC GH_2
CUSTOMER NAME	GE
WEIGHT	0.27 LBM

90-2017M

Figure 4.3.3-19. Filter, High Pressure GN_2 Fill and Drain

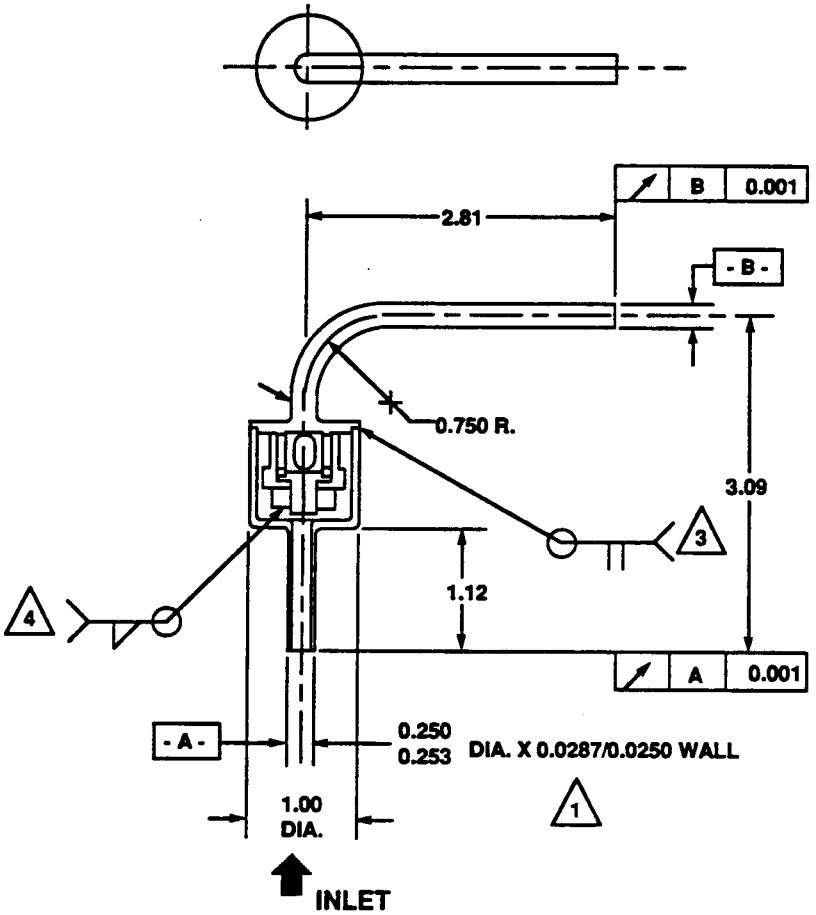

SPECIFICATIONS

END CONNECTION	0.253/0.250 DIA. X 0.0287/0.0250 WALL
OPEN PRESSURE	505 A
PROOF PRESSURE	2 X OPERATION PRESSURE
BURST PRESSURE	4 X OPERATING PRESSURE
FILTRATION RATING	25 MICRONS ABSOLUTE
COLLAPSE PRESSURE	OPERATING PRESSURE ACROSS THE ELEMENT MIN
FLUID COMPATIBILITY	N_2H_4, H_2O, IPA, GN_2 & GHe
FLOW RATE	0.010 LBM/SEC
DP (CLEAN)	10 PSID
EXTERNAL LEAKAGE	1 X C^{-6} SCC/SEC GHe
CUSTOMER NAME	GE
WEIGHT	0.16 LBM

90-2018M

Figure 4.3.3-20. Filter, Nitrogen Engine Inlet

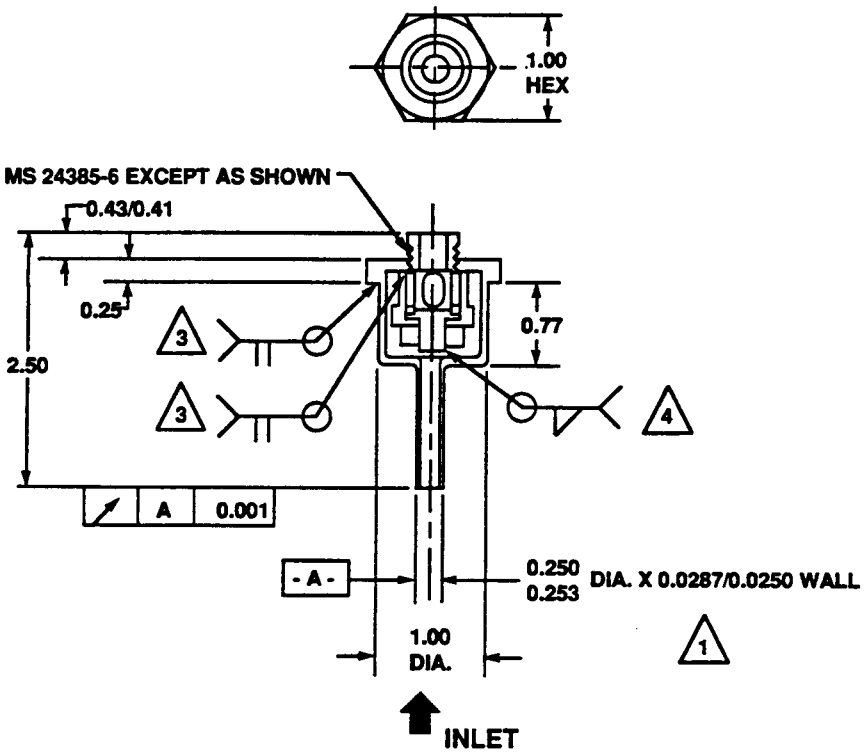

SPECIFICATIONS

END CONNECTION	0.253/0.250 DIA. X 0.0287/0.0250 WALL
OPEN PRESSURE	505 A
PROOF PRESSURE	2 X OPERATION PRESSURE
BURST PRESSURE	4 X OPERATING PRESSURE
FILTRATION RATING	25 MICRONS ABSOLUTE
COLLAPSE PRESSURE	OPERATING PRESSURE ACROSS THE ELEMENT MIN
FLUID COMPATIBILITY	N_2H_4, H_2O, IPA, GN_2 & GH_2
FLOW RATE	0.010 LBM/SEC
DP (CLEAN)	10 PSID
EXTERNAL LEAKAGE	1 X C^{-6} SCC/SEC GHe
CUSTOMER NAME	GE
WEIGHT	0.21 LBM

90-2019M

Figure 4.3.3-21. Filter, Pressure Regulator Inlet

Blank Page

4.4 ON-ORBIT ATTITUDE DETERMINATION AND CONTROL SUBSYSTEM

The on-orbit Attitude Determination and Control Subsystem (ADACS) provides three axis pointing of the spacecraft by utilizing multiwheel control based upon an earth sensor reference for pitch and roll and an inertial reference with sun sensor updates for yaw. Initial acquisition, reacquisition, and momentum desaturation are all automatically performed.

4.4.1 REQUIREMENTS

The ADACS is required to provide the attitude determination and control capability needed to maintain each spacecraft reference axis within 0.2 degree (3σ) of the local geodetic reference in the presence of external environmental disturbances (aerodynamic drag, gravity gradient, solar radiation pressure, and residual magnetics), uncompensated angular momentum of payload instruments, and solar array disturbances. The ADACS must also maintain the spacecraft coordinate reference such that the error rates; i.e., the spacecraft rates exclusive of orbital rate motion, about the pitch and yaw axes are less than 0.035 degree/sec (3σ), and the error rate about the roll axis is less than 0.015 degree/sec. Knowledge of the spacecraft reference axes orientation with respect to the local geodetic reference is required to within 0.1 degree (3σ) per axis using ground processed data.

4.4.2 SUBSYSTEM DESCRIPTION

The ADACS is a three axis stabilized zero momentum control subsystem, configured as shown in the block diagram in Figure 4.4.2-1, which consists of the following major hardware and software items:

Hardware Components

- One Earth Sensor Assembly (ESA)
- One Sun Sensor Assembly (SSA)
- Four Reaction Wheel Assemblies (RWA's)
- Two Roll/Yaw Magnetic Torquing Coils (RYC's)
- Two Pitch Magnetic Torquing Coils (PTC's)
- One Inertial Measurement Unit (IMU)
- Eight Nitrogen Thrusters and Valves

Software Components

- Earth Sensor Read Software (ESRS)
- Digital Filter Software (DFS)
- Attitude Determination Software (ADS)
- Geometric Data Software (GEODAT)
- Attitude Control Software (ACS)
- Magnetic Momentum Unloading Software (MMUS)
- Solar Array Drive Control Software (SADCS)
- Nitrogen Momentum Unloading Software (NULS)

4.4.2.1 Hardware Components

The ESA is a static infrared horizon sensor designed to operate over an altitude range of 400 to 500 nautical miles with optimum sensitivity in the 14 - 16 micron (CO_2) band. As shown in Figure 4.4.2-2, the ESA nominally

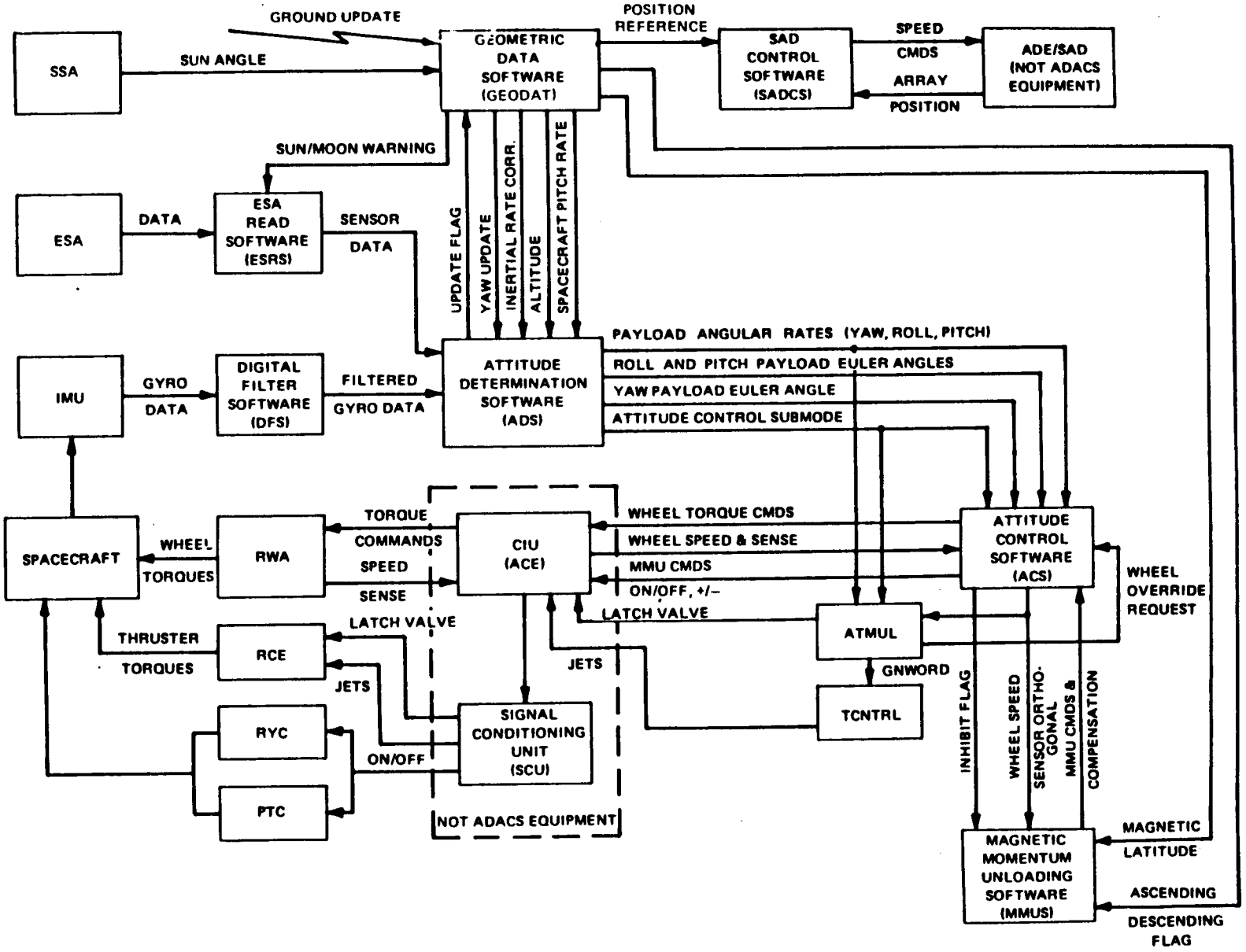

Figure 4.4.2-1. ADACS Configuration Block Diagram

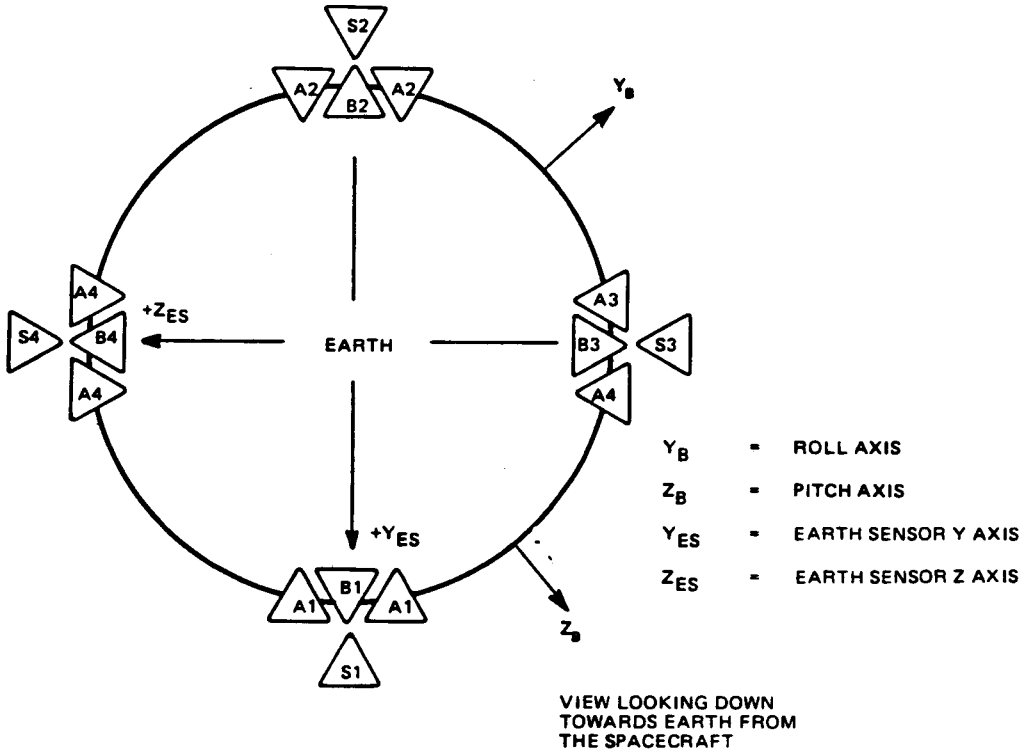

Figure 4.4.2-2. ESA Detector Configuration

centers the earth's disk between four independent detectors, which view a segment of the horizon in each of four quadrants. Four corresponding sets of digital horizon measurement data are obtained and provided to the on-board data processors for pitch and roll attitude determination to an accuracy of 0.1 degree (3σ). The field-of-view geometry of the detectors and optics was chosen to provide attitude data that is independent of levels of earth radiance.

The SSA is a single-axis digital sun sensor that measures the component of the sun angle between the spacecraft pitch axis (+Z) and the projection of the earth-sun line on the pitch-roll (YZ) plane. The measured sun-angle component is used (together with pitch, roll, and skew gyro data and stored ephemeris data) to calculate yaw attitude error. The calculated error is used as the primary source for correcting gyro-derived yaw attitude data during the on-earth modes of operation.

The RWA's provide active attitude control by generating reaction torques about the three orthogonal spacecraft axes. Three of the RWA's are orthogonally mounted to produce torques about each of the three primary spacecraft axes; the fourth RWA is canted at an angle of approximately 54.7 degrees with respect to each of the orthogonal axes so that $1/\sqrt{3}$ of its torque resolves into all three axes. The fourth RWA is normally idle but is brought into use if one of the three orthogonal RWA's fails. Each RWA is capable of storing 240 in-lb-sec of angular momentum.

The pitch and roll/yaw magnetic torquing coils provide the capability for unloading accumulated satellite momentum. The counteraction of external disturbance torques results in the accumulation of angular momentum in the three

operating reaction wheels; momentum unloading torques are developed, as required, through the interaction of the earth's magnetic field with dipoles generated by applying DC voltages of appropriate sign to magnetic coils on board the spacecraft.

The ADACS contains three dual-axis, rate integrating gyros which are packaged as a part of the inertial measurement unit (IMU). The gyros provide a measure of the attitude rates about each of the three spacecraft reference axes for control loop damping and for deriving yaw attitude during the periods between sun sensor readings. Digital integrated rate signals are made available at a 10 Hz rate in orbit mode.

The ADACS utilizes the GN_2 thrusters of the reaction control subsystem to assist with the unloading of momentum that has been acquired from unusually high disturbances. The two pound force thrusters can be automatically activated whenever the total momentum exceeds a constant threshold. If the nitrogen supply has been depleted, then the ADACS can still acquire the earth, provided the momentum is within the saturation limits of the RWA's.

4.4.2.2 Software Components

The ADACS software components are described in Section 4.10.6.

4.4.2.3 Operating Modes

There are seven operating modes in the ADACS. They are designated: Rate Nulling (RN), Search, Yaw Gyrocompassing (YGC), Nominal (NOM), Despin, Spindamp, and Coast. RN, Search, and YGC comprise the control modes during acquisition (or re-acquisition); NOM is the normal operating control mode; spindamp and despin comprise the attitude recovery modes; and Coast is a rate holding mode which is entered in the event of an ESA outage while controlling in NOM. The ADACS software is automatically initialized at the conclusion of the ascent control phase, commencing operation in the RN mode. All subsequent mode switching is automatically controlled by the ADACS software with the exceptions of the transfer from YGC to NOM, the bi-directional transfer from RN to spindamp, and the bi-directional transfer from spindamp to despin which are only effected upon ground command. The relationship between the modes is illustrated in Figure 4.4.2-3 and is defined by the decision table in Table 4.4.2-1.

In the RN mode, the satellite roll, pitch, and yaw axes are stabilized in space with no preferred orientation relative to the local geodetic reference. Control is provided by damping out the sensed gyro rates as corrected for orbital motion. Stabilization is considered to be effected when the error rates about all three control reference axes are simultaneously below 0.014 deg/sec for a 10 second period. (Pitch rate must be within 0.014 deg/sec of orbital rate.)

If the spacecraft's angular momentum is beyond the capacity of the Reaction Wheel Assemblies (RWAs) the normal mode Earth re-acquisition system cannot be used and the TIROS-KLM attitude recovery system is activated by the ground. The spindamp mode uses the RWAs to transform the spacecraft's initial tumbling motion into a spinning motion about the roll axis, and damps the nutational motion during the momentum transfer. The Pitch Torquing Coils (PTC) are then used to orient the spin axis close to the orbit normal. In the despin mode

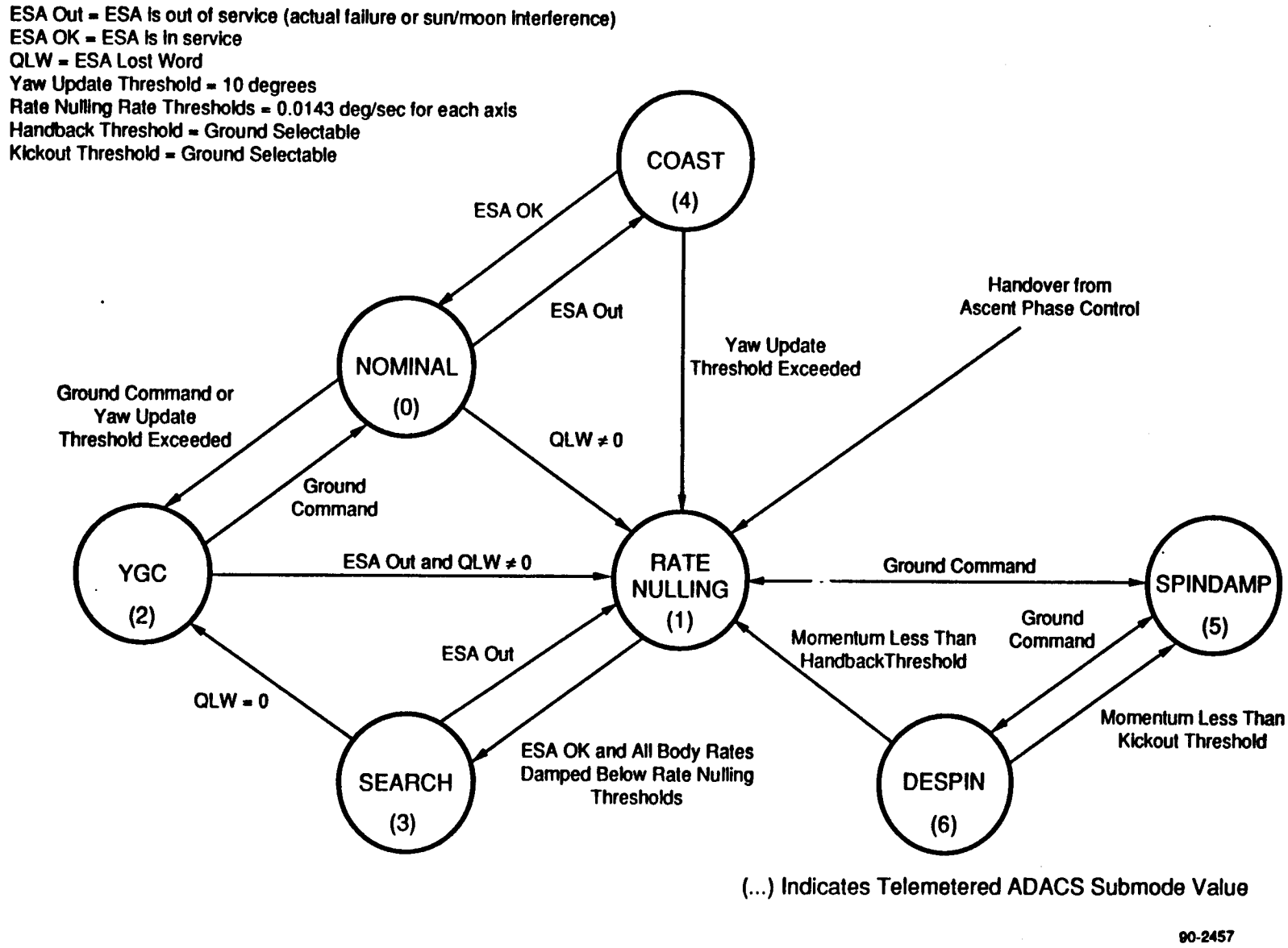

Figure 4.4.2-3. Attitude Control Mode Switching

TABLE 4.4.2-1. DECISION TABLE - ADACS MODE DETERMINATION

SUBMODE ON LAST CYCLE	NOM	NOM	NOM	NOM	NOM	CST	CST	CST	RN	RN	RN	RN	SRCH	SRCH	SRCH	YGC	YGC	YGC	YGC	SDMP	SDMP	DSPN	DSPN	DSPN
ESAOUT	NO	YES	NO	NO	NO	YES	YES	NO	NO	YES	—	NO	NO	YES	NO	NO	YES	NO	NO	NO	NO	—	NO	YES
QLW (NOT ZERO IS QUAD LOST)	0	—	NOT 0	0	0	—	—	—	—	—	—	—	NOT 0	—	0	0	—	NOT 0	0	—	—	—	—	—
RATES KILLED	—	—	—	—	—	—	—	—	NO	—	YES	—	—	—	—	—	—	—	—	—	—	—	—	—
GROUND COMMAND	—	—	—	—	—	—	—	—	—	—	—	YES	—	—	—	NO	—	—	YES	YES	YES	—	YES	—
UPDATE LIMIT	NO	—	—	YES	NO	NO	YES	—	—	—	—	—	—	—	—	—	—	—	—	—	—	—	—	—
FYGC	—	—	—	—	SET	—	—	—	—	—	—	—	—	—	—	—	—	—	—	—	—	—	—	—
MOMENTUM OK	—	—	—	—	—	—	—	—	—	—	—	NO	—	—	—	—	—	—	—	YES	NO	YES	NO	YES
SUBMODE SHALL BE	NOM	CST	RN	YGC	YGC	CST	RN	NOM	RN	RN	SRCH	SDMP	SRCH	RN	YGC	YGC	RN	RN	NOM	RN	DSPN	RN	SDMP	SDMP

90-3805M

SYMBOL	DEFINITION
—	DO NOT CARE
NOM	NOMINAL MODE
CST	COAST MODE
RN	RATE NULLING MODE
SRCH	SEARCH MODE
YGC	YAW GYROCOMPASSING MODE
SDMP	SPINDAMPING MODE
DSPN	DESPIN MODE
FYCG	FORCED YGC CONDITION

the Roll/Yaw coil (RYC) is used to reduce the total angular momentum so that the normal mode Attitude Determination and Control Subsystem (ADACS) can re-acquire the Earth.

Once the satellite attitude has been stabilized in space, but is unknown, the subsystem enters the Search mode. In this mode fixed pitch and/or roll torquing rates are developed (with the yaw axis rate still nulled) to rotate the ESA such that it searches for the earth and acquires the proper pitch and roll attitude as shown in Figure 4.4.2-2. The earth acquisition (torquing) rate commands are generated according to the status of the four ESA quadrants relative to the earth's horizon as delineated in Table 4.4.2-2.

Following earth acquisition, the proper yaw-axis attitude is achieved by means of gyrocompassing, using a linear combination of the sensed rotation rates about the roll and yaw axes as the control reference. While in YGC the pitch and roll attitude is maintained by processing the ESA signal outputs as in the Nominal mode.

In NOM, the control loops utilize proportional plus integral plus rate control laws with the ESA supplying the pitch and roll references, the gyros and SSA providing the yaw reference, and the gyros providing three axis rate information for rate damping. In the event of an ESA outage while controlling in NOM, the ADACS automatically switches into the Coast mode. Yaw attitude in Coast is controlled by the NOM mode yaw attitude control law; pitch and roll are controlled identically to RN with the exception that the knowledge of yaw attitude is accounted for in the gyro rate corrections.

4.4.2.4 Coordinate Systems

The coordinate reference frames used by the ADACS are as follows:

1. IMU Gyro Axes: [X/Y, Y/Z, X/Z]
2. Local Vertical Geodetic Frame: $[X_G, Y_G, Z_G]$
3. Body Frame: $[X_B, Y_B, Z_B]$

The local geodetic reference represents the nominal required directions for the spacecraft body coordinate reference. The X_G axis is a line through the origin of the body coordinate reference and normal to the reference geoid (an ellipsoid with center at the center of mass of the earth and with a mean equitorial radius of 6378145 meters and an inverse flattening of 298.25) on the near side. The Z_G axis is a line normal to the X_G axis and to the instantaneous inertial velocity vector. The positive sense of Z_G lies on the sunlit side of the plane formed by X_G and the instantaneous inertial velocity vector. The Y_G axis completes the right hand orthogonal basis.

TABLE 4.4.2-2. SEARCH MODE DECISION TABLE

ESA Quadrant Status				Acquisition Pitch (ω_{CZ})	Command Rate Roll (ω_{CY})	Notes
4	3	2	1			
0	0	0	0	0	0	ESA Locked on Earth-Nominal Pitch and Roll Control
0	0	0	1	+B	+C	
0	0	1	0	-B	-C	
0	0	1	1	-	-	Geometrically Excluded
0	1	0	0	-B	+C	
0	1	0	1	0	+C	
0	1	1	0	-B	0	
0	1	1	1	-B	+C	
1	0	0	0	+B	-C	
1	0	0	1	+B	0	
1	0	1	0	0	-C	
1	0	1	1	+B	-C	
1	1	0	0	-	-	Geometrically Excluded
1	1	0	1	+B	+C	
1	1	1	0	-B	-C	
1	1	1	1	$\pm$A	0	Rate Command Shall Be + For + pitch momentum and - For - pitch momentum

1 = Quadrant Lost
0 = Quadrant on Earth

A = 0.300 deg/sec = .005236 r/s
B = 0.150 deg/sec = .002618 r/s
C = 0.090 deg/sec = .001571 r/s

The body frame is a body fixed coordinate reference which is controlled to correspond to the axes of the geodetic frame. The Z_B (pitch) axis is normal to the separation plane with the positive sense toward the positive orbit normal. The X_B (yaw) axis is normal to the earth facing side of the spacecraft with the positive sense directed toward the earth. The Y_B (roll) axis is normal to the X_B and Z_B axes, completing the right hand orthogonal triad, with the positive sense of Y_B nominally opposite to the instantaneous velocity vector of the satellite.

4.4.3 ATTITUDE DETERMINATION

The design approach to meeting the requirement of attitude determination was to utilize a passive horizon sensor to provide pitch and roll information and a passive sun sensor to provide yaw information. The ESA images the earth's disk onto four detector assemblies such that, in nominal attitude, the detectors are

receiving equal energy from the earth's horizon in all four quadrants. A comparison of the amount of energy in each quadrant allows a determination of the satellite pitch and roll attitude errors. The SSA obtains a reading of the satellite sun angle once each orbit. This data is then utilized along with gyro data to derive the yaw attitude error.

4.4.3.1 Roll and Pitch Attitude Determination

The roll and pitch spacecraft Euler angles are derived from processed ESA output data. Figure 4.4.2-2 illustrates the ESA geometry under stabilized conditions. The ESA optics cause the earth to be imaged on the triangular detector configuration as shown. The A detectors of a quadrant are electrically in parallel. The A and B detectors of a quadrant are nominally earth viewing, while the S detector is nominally space viewing.

When illuminated, the ESA detectors produce output voltages which are denoted: (V_{S1}, V_{A1}, V_{B1}), (V_{S2}, V_{A2}, V_{B2}), (V_{S3}, V_{A3}, V_{B3}), (V_{S4}, V_{A4}, V_{B4}). These voltages are digitized within the ESA in the word format given in Figure 4.4.3-1.

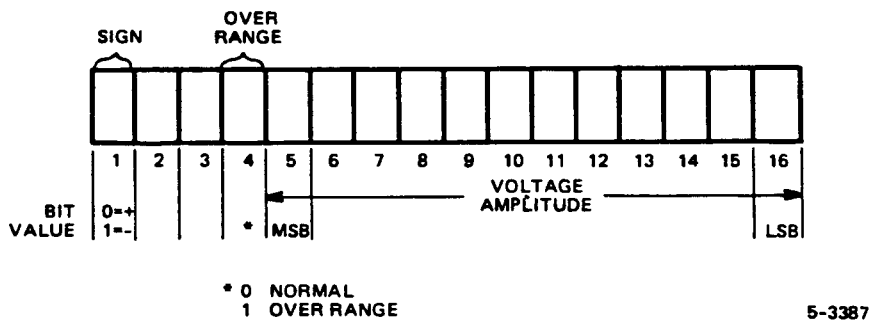

Figure 4.4.3-1. ESA Data Word Format

Each 0.5 second, these words are transmitted to the Central Processing Unit (CPU) through the Controls Interface Unit (CIU) in the sequence: V_{S3}, V_{B3}, V_{A3}, V_{S4}, V_{B4}, V_{A4}, V_{S1}, V_{B1}, V_{A1}, V_{S2}, V_{B2}, V_{A2}. Bit 1 designates voltage sign. Bits 2 and 3 are unused. Bit 4 designates an over-range condition which can occur if the sun is in the field of view of a quadrant. Bit 5 through 16 inclusive indicate voltage amplitude, with bit 5 the most significant bit.

Subsequently, quantities denoted X_n (where n = 1, 2, 3, 4) are computed for each of the four ESA quadrants. X_n is a measure of earth penetration into a quadrant and is a function of three voltages of each quadrant, denoted V_A, V_B, and V_S. Figure 4.4.3-2 illustrates the applicable geometry. X_n is calculated from a function involving the voltage of all four detectors in the nth quadrant; i.e.,

$$X_n = \frac{2(5.196°)\,[(V_{An} - V_{Sn}) + (F_{ORSSn} - F_{ORSAn})\,P_{ORS}]}{[(V_{An} + V_{Bn}) - 2V_{Sn} + (2F_{ORSAn} - (F_{ORSAn} + F_{ORSBn})\,P_{ORS}]}$$

Where n = 1, 2, 3, 4

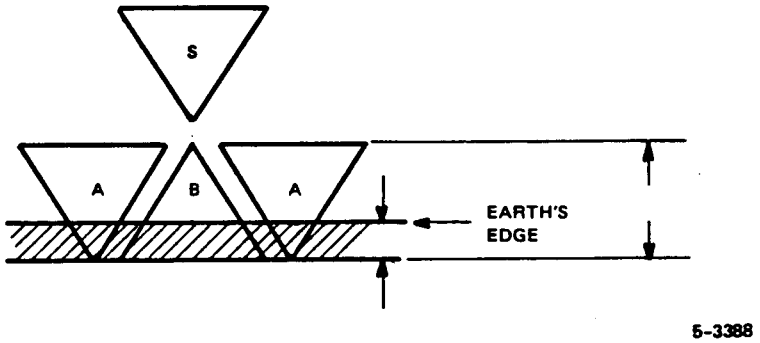

Figure 4.4.3-2. Earth Penetration Geometry

Term subscripted "ORS" represent correction factors to account for slightly different offset radiation source (ORS) radiation received by the various detectors. The ORS consists of a thermal radiator located in the common optical aperture of the sensor and is controlled by an electronic servo to drive the coldest space reference detector signal to zero. This source replaces the radiation the detectors are emitting to space and reduces the large offset signal to zero. The quantities F_{ORSAn}, F_{ORSBn}, F_{ORSSn} and P_{ORS} in the equation for calculation of X_n, are constants derived by box level calibration tests on each unit.

Using the X_n's, sensor roll and pitch are next computed. Sensor roll (A_{34}) is a function of the difference between X_3 and X_4. Sensor pitch (A_{12}) is a function of the difference between X_1 and X_2. That is,

$$A_{34} = 1/2\ (X_3 - X_4) = \text{sensor roll attitude error}$$

$$A_{12} = 1/2\ (X_1 - X_2) = \text{sensor pitch attitude error}$$

It is noted that the reading of a quadrant depends on the altitude of the satellite as well as the attitude. By using two quadrants in the above equation, the altitude dependent parts of the X values will cancel since they are the same, to a first order, for all quadrants. If a single quadrant is blocked, use is made of the two adjacent quadrant readings to estimate the altitude dependent part of the X reading of the remaining quadrant. If two adjacent quadrants are blocked, estimation of the altitude dependent part of the X readings is not possible from the sensor measurements. In this case, the blocked quadrants are handled by estimating their altitude dependent X value by the computational algorithm.

$$XAVE = 2.797680952 - 0.02903600\ (h - 450)$$

where h is the satellite altitude in nautical miles above the earth subpoint. Table 4.4.3-1 summarizes the ESA attitude calculations for the various operating conditions.

ESA roll and pitch sensing axes are not identical to the corresponding payload axes. The relationship between these axes is as shown in Figure 4.4.3-3. Because of this difference in alignment, a transformation between ESA sensing and payload axes is required to derive payload roll and pitch Euler angles from ESA sensor angles (A_{34}, A_{12}).

TABLE 4.4.3-1. ESA ATTITUDE CALCULATIONS

Normal (Four Quadrant) Operation		
	$A_{12} = 1/2\ (X_1 - X_2)$	
	$A_{34} = 1/2\ (X_3 - X_4)$	
	Degenerate Operation	
Missing Quadrant	Three Quadrant Operation	Two Quadrant Operation
1	$A_{12} = -X_2 + \frac{X_3 + X_4}{2}$	$A_{12} = -X_2 + XAVE$
2	$A_{12} = -X_1 + \frac{X_3 + X_4}{2}$	$A_{12} = -X_1 + XAVE$
3	$A_{34} = -X_1 + \frac{X_1 + X_2}{2}$	$A_{34} = -X_4 + XAVE$
4	$A_{34} = -X_1 + \frac{X_1 + X_2}{2}$	$A_{34} = -X_3 + XAVE$

This transformation is given by:

$$\begin{bmatrix} -\alpha_{ZP} \\ -\alpha_{YP} \end{bmatrix} = \begin{bmatrix} T_{PE22} \\ T_{PE32} \end{bmatrix} \begin{bmatrix} T_{PE23} \\ T_{PE33} \end{bmatrix} \begin{bmatrix} +A_{12} \\ -A_{34} \end{bmatrix} + \begin{bmatrix} T_{PE21} \\ T_{PE31} \end{bmatrix}$$

where T_{PEij} = elements of T_{PE} matrix

α_{ZP} = spacecraft pitch Euler angle

α_{YP} = spacecraft roll Euler angle

The elements of $[T_{PE}]$ are determined from alignment measurements of the sensor and payload relative to spacecraft body axes. For the nominal alignment of the ESA and the payload relative to spacecraft body axes, the matrix has the following elements:

$$[T_{PE}] = \begin{bmatrix} 1 & 0 & 0 \\ 0 & .7071 & .7071 \\ 0 & -.7071 & .7071 \end{bmatrix}$$

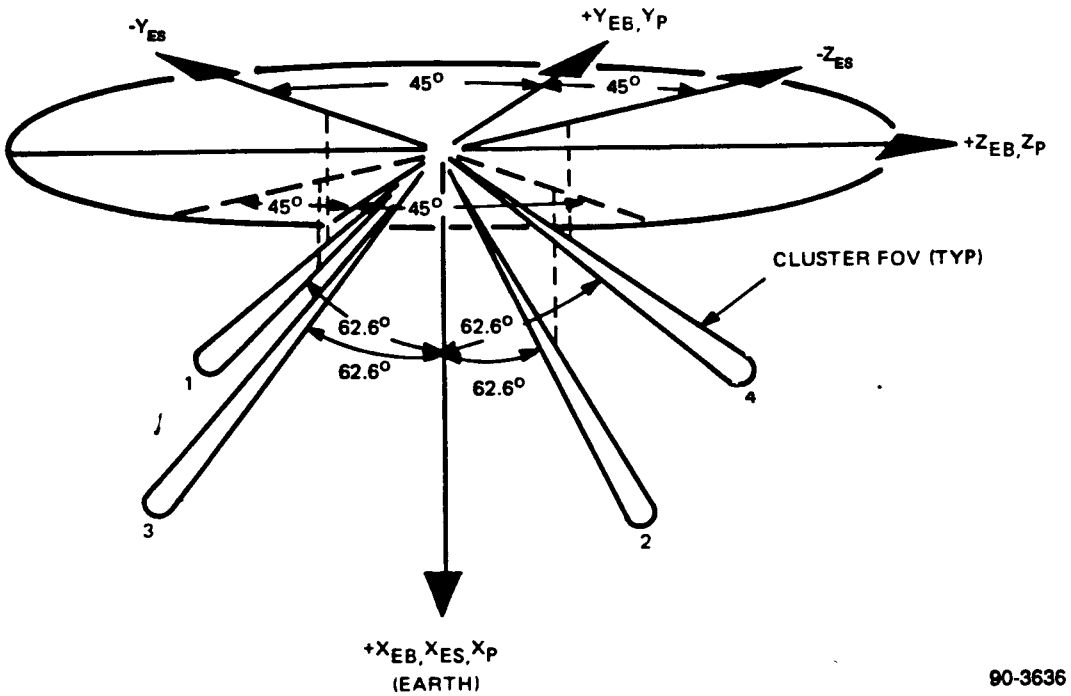

Figure 4.4.3-3. ESA Mounting Configuration

4.4.3.2 Yaw Attitude Determination

Yaw attitude is re-initialized (updated) once per orbit by using a Sun Sensor Assembly (SSA) and IMU gyro signals to provide a yaw attitude error. The method for deriving the updated yaw attitude reference is as follows.

Orbital motion of the geodetic reference axis system is such that a line from the spacecraft to the sun lies on a cone whose axis is the positive Z geodetic axis (Z_G) as shown in Figure 4.4.3-4. From this geometry, it is clear that the sun line crosses the Y_G, Z_G plane twice per orbit, and on one of these occasions, the sun line will also lie within the field of view of the SSA. Figure 4.4.3-4 outlines this geometry for the spacecraft aligned with the geodetic axis system. The SSA center line lies nominally in the spacecraft $+Y_B$, $+Z_B$ plane at an angle of 47.5 degrees from the $+Z_B$ axis.

In the software within the Geometric Data (GEODAT) subroutine, the coordinates of the sun vector are calculated each 0.5 second in the geodetic reference system.

At a time when the sun vector is calculated to lie within $\pm 0.5°$ of the Y_G, Z_G plane and also within the SSA field of view, sun angles are read. Ten such readings are taken, 0.5 second apart. These readings are denoted η_K (K = 1, 2, 3, ...10). From each reading there is subtracted the calculated expected sun angle (η'). The result, denoted $\Delta\psi_K$, is a measure of the yaw attitude error; i.e.,

$$\Delta\psi_K = (\eta_K - \eta'); \text{ where } \eta_K = \text{SSA reading}, \quad \eta' = \text{expected sun angle}$$

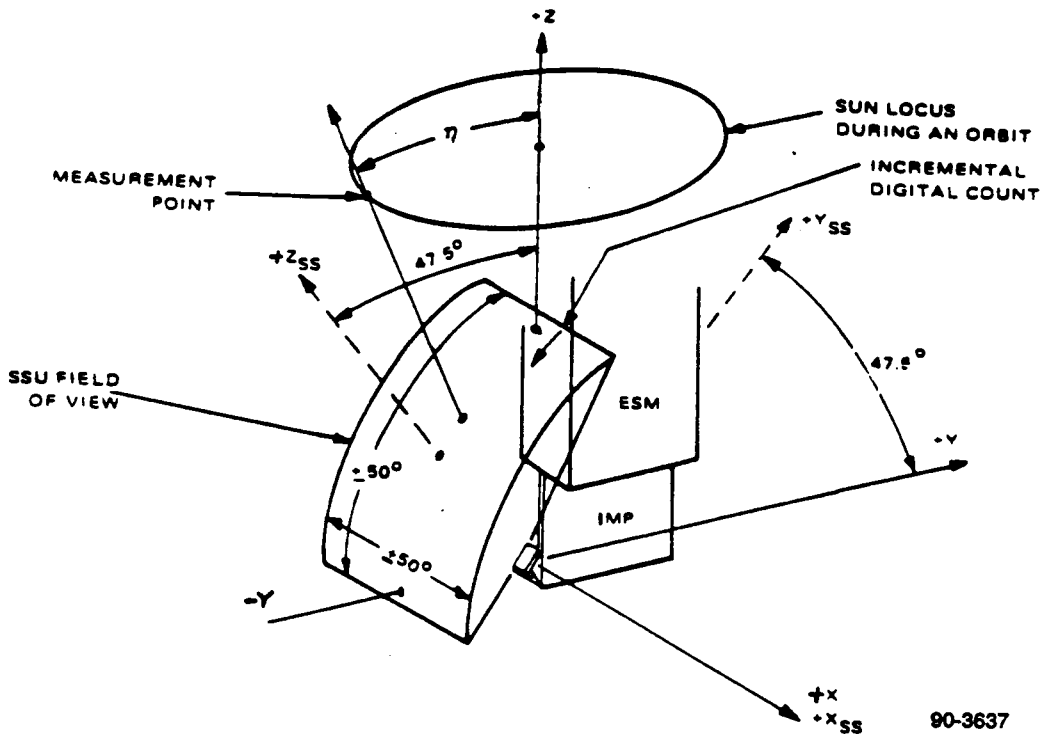

Figure 4.4.3-4. Sun Sensor Geometry

The angle used for yaw update, $\Delta\psi_{AVG}$, is the average of ten $\Delta\psi_K$'s; i.e,

$$\Delta\psi_{AVG} = \frac{\sum_{K=1}^{10} \Delta\psi_K}{10}$$

Attitude changes subsequent to this update, and until the following update, are derived from the yaw, roll, and pitch gyro outputs (or alternately any skew configuration) after appropriate combination. The error in these attitude changes, summed with the initialization value, constitutes the yaw attitude error.

In general, the gyro pulse counts from the yaw, roll, and pitch gyros, representing the integral of the rate outputs of these gyros, are sampled at a 10 Hz rate. For each gyro, these pulse counts are next passed through a digital filter to provide attenuation at structural bending frequencies. Next, summation of the filtered pulse counts is performed over 0.5 second intervals and then multiplied by a pulse weight of approximately 0.15 arc sec per pulse. Constant bias terms are then added to the result. The pulse weights and bias terms are gyro dependent constants derived during IMU calibration, which is done not more than 120 days prior to launch.

In general, the gyro input axes will not lie exactly along the X, Y, Z payload axes. Therefore, each gyro will sense rates about all body axes. Based upon alignment measurements expressing the orientation of gyro input axes relative to body axes, a matrix is used to decouple the angular increments.

Because the yaw angular increment is based on the output of three gyros, the error in the derived yaw angle is influenced by uncompensated bias drifts in all three of these gyros. In order to partially correct for this effect, a gyro bias correction (bx) is calculated at each SSA update and used until the next update. The actual correction used at any time is a combination of individual bias estimates, which are derived and applied as follows:

1. Prior to the first yaw attitude update, the only correction used is the ground-calibrated gyro biases, resulting in a delta correction of zero; i.e., bx = 0

2. α_{xp1} denotes the initial update yaw angle and α_{xp2} denotes the subsequent update angle, one orbit later. Between these two updates, the bias correction used is bx = 0. Let t1 denote the first update time and t2 denote the second update time. If a bias correction has been available for use during the interval t1 to t2, its value would be obtained from the equation:

$$\alpha_{xp2} = \alpha_{xp1} + bx\ (t2 - t1)$$

or

$$bx_{t2} = \frac{(\alpha_{xp2} - \alpha_{xp1})}{(t2 - t1)}$$

[(t2 - t1) corresponds very nearly to the orbital period].

This value is best estimate which can be used over the next interval, t2 to t3. In practice, the value of bx over the interval t2 to t3 is:

$$bx_{(t_2 - t_3)} = \frac{4bx_{t2}}{4}$$

3. At t3, a new update is obtained, α_{xp3}, and a new bias correction estimate is found from:

$$bx_{t3} = \frac{(\alpha_{xp3} - \alpha_{xp2})}{(t3 - t2)}$$

4. The bias correction used over the next interval is given by a combination of bx_{t2} and bx_{t3}, specifically,

$$bx_{(t_3 - t_4)} = \frac{3bx_{t2} + bx_{t3}}{4}$$

5. Over the next two intervals, the bias corrections used are:

$$bx\ (t4 - t5) = \frac{2bx_{t2} + bx_{t3} + bx_{t4}}{4}$$

$$bx_{(t5 - t6)} = \frac{bx_{t2} + bx_{t3} + bx_{t4} + bx_{t4}}{4}$$

where bx_{t6} is defined in a similar manner as bx_{t2}, bx_{t3}, bx_{t4}, and bx_{t5}.

This pattern of using the average of the four most recent bias correction estimates is subsequently followed.

An additional compensation term is applied to the gyro-bias-corrected yaw angular increment every 0.5 second to account for precession of the yaw geodetic reference axis resulting from earth's oblateness effects. This compensation term is of the form:

$$\Delta\alpha_{xp} = -K (\sin \beta) \Delta t$$

where β = spacecraft orbit angle with respect to the ascending node

Δt = 0.5 second

K = a constant (function of orbit inclination, rate and radius, and the zonal harmonics coefficient J_2).

$$K = \frac{3m\ J_2\ r_{eq}^2\ \sin(2i)}{2hr^3}$$

where $\mu = 1.406 \times 10^{16}\ ft^3/sec^2$

$J_2 = 0.00108228$

$r_{eq} = 2.0903 \times 10^7$ ft

$r = 2.3637 \times 10^7$ ft @ 450 n.mi. altitude

$h = \omega_o r^2$ ($\omega_o = 1.032 \times 10^{-3}$ rad/sec)

$i = 98.7$ degrees

4.4.3.3 Attitude Rate Determination

Attitude rate terms are utilized to provide damping in the control loops. The necessary body rates are determined by means of a second order rate derivation scheme operating on the gyro angular increments (in the payload frame) summed over 0.5 second intervals. For yaw, the angular increments utilized for rate derivation are those already compensated for gyro bias (SSA-updated) as well as orbit precession effects. For roll and pitch, the derived body rates are corrected for the derived (from IMU calibration tests and from on-orbit gyro data analysis) bias terms. In addition, the derived pitch body rate is corrected for the nominal orbital pitch rate.

4.4.4 ATTITUDE CONTROL

4.4.4.1 Acquisition and Reacquisition

The spacecraft is considered as acquired when the ESA provides pitch and roll attitude error signals and the yaw axis is under gyro derived yaw control, with sun sensor updates. The process of achieving this condition after handover from ascent mode control is termed acquisition with reacquisition being the re-establishment of the acquired state after a temporary loss of lock. Reacquisition is possible for a spacecraft momentum of up to 160 in-lb-sec. If this vector corresponded to one of the RWA axes, a margin of 80 in-lb-sec would exist for maneuvering the satellite since the RWA's have a capacity of approximately 240 in-lb-sec. In the acquisition (or reacquisition) sequence, the satellite body rates are nulled by the RN control mode, earth search and acquisition (pitch and roll) is effected by the Search mode followed by gyrocompassing for yaw capture and finally ground commanded switchover to NOM yaw control mode.

At handover, attitude errors will nominally be less than ± 1 degree on each axis and the rates, corresponding to less than 6 in-lb-sec momentum per axis, will be less than 0.012 deg/sec in roll and yaw and less than 0.06 deg/sec in pitch. The Solar Array Drive (SAD) is unpowered. The propulsion system,prior to handover, controls the pitch axis (roll axis in ascent language) with a torque of 130 in-lb (2080 in-oz), whereas the array drive friction torque is about 28 in-oz. Therefore, the array for all practical purposes is disconnected from the body (in its single degree of freedom). The result is that the limit cycle control will cycle faster with greater propellant consumption and negligibly increased displacement limits for the fine mode time before hand-over. However, the array and body will move together within a few seconds after the cessation of thrusting and at handover with a momentum not greater than the specified 6 in-lb-sec per axis.

The worst-case combination of pitch axis inertial rate at handover (0.06 deg/sec) combined with orbital rate could result in an over-all relative rate of 0.12 deg/sec between the earth's image and the ESA. Allowing for a maximum initial pitch error of ± 1 degree, the ESA pitch linear error range may be exceeded at handover, automatically calling for a programmed acquisition search rate of at least 0.15 deg/sec. The Search (earth acquisition) and Gyrocompassing modes are sequentially entered when the ESA provides usable data. If this is not the case (a temporary ESA outage), the Rate Nulling mode is entered automatically.

The three payload gyro signals, ω_{px}, ω_{py}, ω_{pz}, corrected by the latest gyro bias estimates, are used in the rate nulling control loops that will be shown in Figures 4.4.6-3, 4.4.6-6, and 4.4.6-10. These loops are unconditionally stable Type 1 controls, with stability margins shown in Tables 4.4.6-11a and 4.4.6-11b. When all of the axis rates are simultaneously less than 0.014 deg/sec for 10 seconds, the spacecraft is considered to be stabilized with respect to inertial space, with almost all the momentum stored in the RWA's. The nulling amplitude-time thresholds were chosen to assure that the rate nulling event is achieved in the presence of gyro noise and structural modes with low damping.

After Rate Nulling, Search mode acquisition is automatically commenced. The Search mode uses the same control logic as Rate Nulling except the rate to be controlled to is the commanded scan rate, as determined by the ESA state, rather than zero. Earth acquisition proceeds according to the logic of Table 4.4.2-2 which may be entered at any state. Following a nominal handover and after the spacecraft rates have been nulled, three or four ESA quadrants should be viewing the earth. The condition in Search mode that a given quadrant views the earth is satisfied when:

$$V_S > \varepsilon_1$$

or

$$V_B - V_S > \varepsilon_2$$

where V_B is the signal from the B detector
V_S is the signal from the S detector

ε_1 and ε_2 are the signal threshold values chosen to be consistent with the signal variation due to noise, bias, and other second order effects.

Pitch axis scan is initiated if no quadrants view the earth; for this condition, grazing angles are large and acquisition is just as simple as when one or more quadrants initially view the earth. The initial scan direction, in this case, is in the direction which reduces pitch wheel speed.

The earth's image moves at the orbital rate (0.06 deg/sec) with respect to the inertially fixed spacecraft. Pitch and roll acquisition rates have been chosen at 0.15 deg/sec 0.15 to provide reasonably fast acquisition with little overshoot, thereby minimizing the control logic.

Due to the geometry, a scan about any axis from an initial arbitrary attitude will always result in at least one earth sensor set viewing the earth.

During acquisition and in steady-state operation, the sun may interfere with the normal ESA data. This interference from the sun is handled in several ways. First, ephemeris data generates a flag which voids data from a quadrant when the sun vector or moon vector is within 12 degrees of the cluster center line of sight. The software is not able to predict sun/moon interference when operating in Rate Nulling of Search Modes. However, when the rates are nulled, the probability that one of the twelve A or B ESA segments views the sun is only 0.005. Secondly, if a segment should view the sun, its output register would go to over-range, immediately indicating this condition. If the sun were on the edge of a segment such that a false earth indication occurred, the spacecraft would move according to Table 4.4.2-2 and the detector would go into over-range or off the sun. Both of these are transient conditions with no deleterious effects.

Upon earth acquisition with yaw indeterminate, the sun moving radially off the horizon and on the edge of a detector could conceivable "pull" the spacecraft off the earth. This would persist until the sun was about 9 degrees off the horizon, at which time the two orthogonal sensors would leave the earth and a second earth acquisition free of sun interference would occur. This is the worst-case sun interference effect possible.

When all four ESA quadrants pass the conditions for viewing the earth, the ADACS switches to the yaw gyrocompassing (YGC) mode and yaw stabilization is initiated. When sufficiently stabilized, switchover to the nominal ADACS yaw mode will be accomplished by ground command after a sun update of the yaw gyro has occurred.

The roll and yaw gyros (or appropriate skew substitution) furnish the required information for gyrocompassing. The derived yaw payload axis rate, ω_{xp}, obtained after processing from the yaw gyro (or roll gyros), furnishes the damping term in the control law, whereas the derived roll payload axis rate, ω_{yp}, supplies proportional information. A block diagram of the gyrocompassing control will be shown in Figure 4.4.6-2.

The applicable control law for gyrocompassing yaw axis control is:

$$T_{CXG} = -[K_{g2}\ \omega_{XPD} + K_{g1}\ \omega_{YPD_{LIM}}]$$

where T_{CXG} (volts) = momentum wheel torque command voltage

ω_{XPD} = derived yaw payload axis rate in rad/sec

$\omega_{YPD_{LIM}} = \pm \frac{K_{g2}}{K_{g1}}\ \omega_{XPD_{LIM}}$

$\omega_{XPD_{LIM}}$ = desired yaw payload axis rate limit equal to $\pm 1.5 \times 10^{-3}$ rad/sec

K_{g2} & K_{g1} = control law gains in volts/rad/sec

The earth acquisition sequence (rate nulling mode → search mode → yaw gyrocompassing mode) has been studied with the aid of a simulation program that contains the rigid body spacecraft dynamics and a logically equivalent version of the flight software. Simulation results show that convergence will take place from any attitude with a maximum time (including yaw acquisition) of about one hour provided the initial spacecraft momentum is within the saturation limits of the RWA's. With a single point ESA failure (the ESA is usable with a failure of any one quadrant or any two adjacent quadrants), acquisition takes longer, but convergence is assured. The simulation results of a normal pitch and roll acquisition sequence is shown in Figure 4.4.4-1. Simulation results showing a typical YGC yaw acquisition are given in Figure 4.4.4-2.

The solar array drive loop is stable under all conditions and can acquire from any initial condition. The desired position of the array is determined by the software, and the appropriate rate commands are selected to keep the array pointing at the predicted sun position.

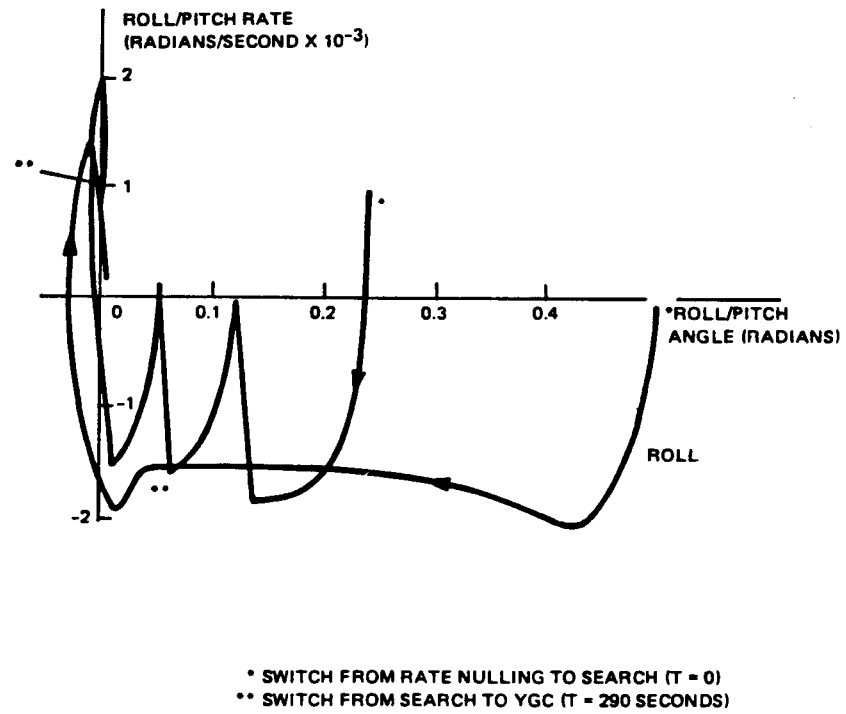

5-3391

Figure 4.4.4-1. Normal Acquisition From 0.5 Radian Roll Angle, 0.25 Radian Pitch Angle

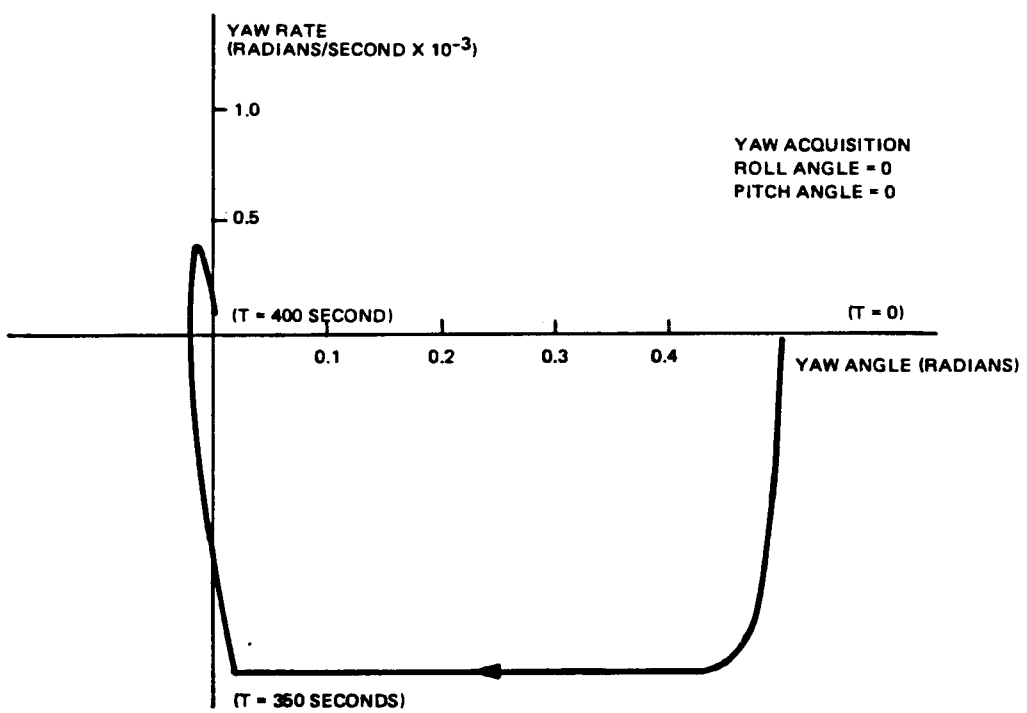

5-3392

Figure 4.4.4-2. Yaw Gyrocompassing Acquisition

4.4.4.2 Normal Operation

Figure 4.4.2-1 depicts a functional block diagram of the ADACS, together with its principal interfaces. The required control torques are generated by three (nominally the orthogonal set) of the four RWA's with torque commands computed in the ACS based upon ESA, gyro, and SSA data as processed by the ADS. The ACS computed torque commands obey the following control law for each body reference axis:

$$T_{Cn} = K_n \left[K_{1n}\alpha_n + K_{2n}\dot{\alpha}_n - K_{5n}\delta_n + K_{3n}\int(\alpha_n - \delta_n)\,dt\right]$$

where n = x, y, z

α_n = spacecraft Euler angles

δ_n = magnetic compensation (see Table 4.4.6-7).

$K_x = +1$, $K_y = -1$, $K_z = -1$

All other gains are provided in Table 4.4.6-7.

The integral terms in the control laws are limited to a magnitude of 1.2 volts; i.e., whenever an integral reaches a magnitude of 1.2 volts, the integration reverses. In addition, integration is inhibited whenever wheel power or current saturation occurs as indicated by a signal from the RWA.

The computed torque command signal consists of an 8-bit word (plus a sign bit). To improve torque granularity on a time average basis, one of four possible dither bits is added to the torque command prior to truncation to the 8-bit word.

The dither bits are 1/8, 3/8, 5/8, and 7/8 of the minimum torque command word quantum and are sequentially selected on successive computation cycles.

Wheel torque commands are transmitted to the RWA, with the command to any given RWA limited to ± 5.1 volts in magnitude via the CIU. The CIU converts the digital wheel torque commands to the equivalent voltage levels for input to the RWA motor drive circuitry at half second intervals.

4.4.4.3 Magnetic Momentum Unloading

The primary means of angular momentum unloading is magnetic. Redundant sets of air-core coils, when activated, generate control dipoles which react against the earth's magnetic field to develop the requisite unloading torques in accordance with the following vector equation.

$\vec{T}$ =	$\vec{M}$	X	$\vec{B}$
Torque	Coil Dipole		Earth's Field

The Roll-Yaw Coils (RYC) generate dipoles aligned with the spacecraft Z-axis to produce transverse, Roll/Yaw (Y/X-axes) unloading torques via interaction with the orbit-plane component of the earth's field. By like motor action, the Pitch Torquing Coils (PTC), generating Y-axis aligned dipoles, produce pitch (Z axis) unloading torques.

Magnetic Momentum Unloading (MMU) on any given spacecraft axis is initiated whenever three conditions are simultaneously satisfied; namely (1) that the ADACS is in an operating mode which permits unloading (MMU is inhibited whenever the ADACS is in the YGC mode with a roll rate exceeding 0.00014 rad/sec, the RN mode, or the Search mode, or whenever wheel testing is in progress), (2) that the spacecraft is in a region where the magnetic field is suitably oriented, and (3) that the equivalent wheel speed magnitude along a body reference axis exceeds the threshold conditions of Table 4.4.4-1. Momentum unloading for the spacecraft roll and pitch axes takes place within ±24 degrees of the geomagnetic poles. For the spacecraft yaw axis, MMU takes place when both the roll axis momentum and yaw axis momentum exceed the respective threshold conditions while the spacecraft is within the region between 20°N and 55°N magnetic latitude and between 20°S and 55°S magnetic latitude. The magnetic coil operating regions and unloading logic are shown in Figure 4.4.4-3, and listed in Tables 4.4.4-2a and b. The unloading logic is based upon the polarity of the body momentum and is independent of the reaction wheel body alignments.

TABLE 4.4.4-1. UNLOADING THRESHOLDS

Polar Unloading Region				
Axis	On Threshold		Off Threshold	
	(in-lb-sec)	(rpm)	(in-lb-sec)	(rpm)
Roll	21.0	525	20.0	500
Pitch	31.0	775	30.0	750
East/West Unloading Region				
Axis	On Threshold		Off Threshold	
	(in-lb-sec)	(rpm)	(in-lb-sec)	(rpm)
*Roll	21.0	525	20.0	500
*Yaw	8.0	200	7.0	175

*The stored momentum on both roll and yaw axes must exceed their respective thresholds before RYC activation can occur.

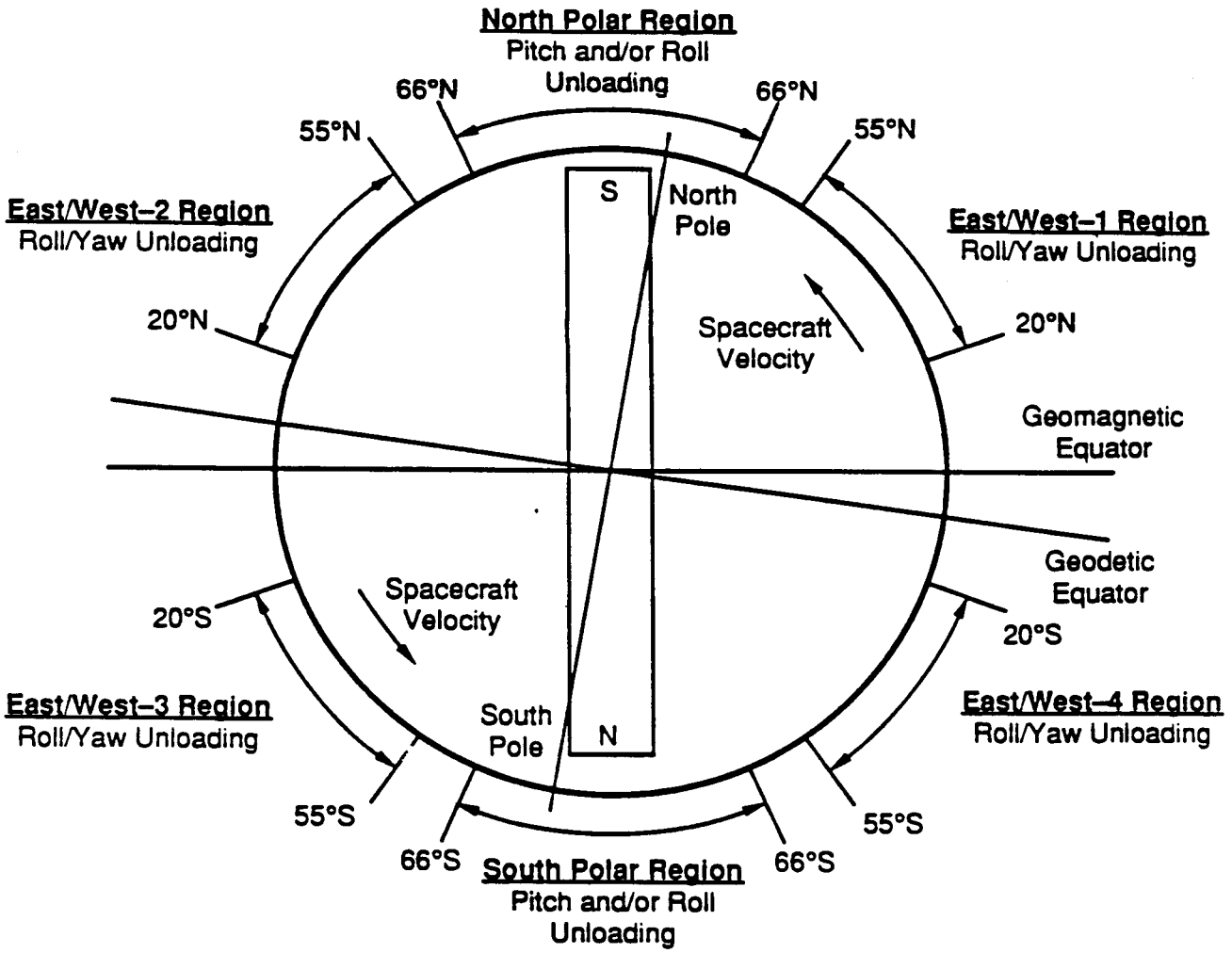

Note: Latitudes shown are referenced to the Geomagnetic equator

90-3638

Figure 4.4.4-3. ATN Magnetic Momentum Unloading Regions

TABLE 4.4.4-2a. MAGNETIC MOMENTUM UNLOADING LOGIC, POLAR

Polar Unloading Region Logic			
Body Momentum Polarity		Dipole Polarity	
		North Polar Region	South Polar Region
Roll Axis	+	On-	On+
	-	On+	On-
Pitch Axis	+	On+	On-
	-	On-	On+

TABLE 4.4.4-2b. MAGNETIC MOMENTUM UNLOADING LOGIC, EAST/WEST

East/West Unloading Region Logic					
Body Momentum Polarity		RYC Dipole Polarity			
Roll	Yaw	E/W-1	E/W-2	E/W-3	E/W-4
+	+	On-	Off	On+	Off
-	-	On+	Off	On-	Off
+	-	Off	On-	Off	On+
-	+	Off	On+	Off	On-

To keep dipole turn-on transient effects on spacecraft attitude to a minimum, extra compensation terms are introduced in the wheel control laws whenever such a turn-on command is generated. The values of the ground loaded compensation constants, which are a function of the magnetic field strength and the coil dipole magnitude, are given in Table 4.4.4-3.

TABLE 4.4.4-3. NOMINAL COMPENSATION CONSTANTS

Unloading Axis	Compensation Constant - δ_n (Radians)	Compensation Gain - K_{5n} (Volts/Rad)
Yaw	1.952×10^{-6}	38400
Roll	3.979×10^{-6} (Poles) 2.429×10^{-4} (East-West)	44400
Pitch	1.963×10^{-3}	4320

Momentum unloading performance was verified in a computer simulation which assumed a circular orbit and perfect attitude determination and control loops for each of the spacecraft axes. For all computer runs, worst case external disturbance torques were assumed, with the absence of solar pressure torques during eclipse portions of the orbit ignored. The performance of the magnetic momentum unloading system was determined using Summer Solstice, Equinox, and Winter Solstice total environmental disturbances for afternoon ascending orbit and morning descending orbit spacecraft. Even with the worst disturbance torques, the largest magnetic torquer duty cycle is only 26.4%, and the spacecraft momentum levels are maintained well within the reaction wheel limits. The magnetic momentum unloading system performs satisfactorily for over 20 orbits with a ±1 minute orbit period uncertainty.

A FORTRAN program modelling the Earth's magnetic field, the environmental disturbances, and the unloading logic was used to evaluate the magnetic momentum unloading system performance. Figures 4.4.4-4, 4.4.4-5, and 4.4.4-6 show the performance for a 22° solar array cant angle during Summer Solstice, Equinox and Winter Solstice. Figures 4.4.4-7, 4.4.4-8, and 4.4.4-9 show the performance for a 37° solar array cant angle. The minimum wheel speed (momentum level) requirements was met for both satellite configurations and for all seasonal environmental disturbances. The per-orbit speed ranges for all the different cases are listed in Table 4.4.4-4 and are well within the reaction wheel speed range.

The magnetic coil duty cycle during momentum unloading is defined in two ways: on-time/orbit and on-time/maximum on time. The maximum on-time for the Y axis PTC coil is 1,622 seconds (the sum of the time the spacecraft spends in the North and South Polar momentum unloading regions, and the maximum on-time for the Z-axis RYC coil is 3,986 seconds (the sum of the time the spacecraft spends in all six momentum unloading regions. Table 4.4.4-5 lists the duty cycles for each magnetic coil for each spacecraft configuration and season. The largest on-time/maximum on-time duty cycle for the Y axis PTC coil is 10.4% and the largest on-time/maximum on-time duty cycle for the Z axis RYC coil is 26.4%.

- Effect of Poor Initial Ephemerides

Following handover in the vicinity of the descending node, Magnetic Momentum Unloading System (MMU) must proceed on the basis of poor initial ephemeris information. A poor ephemeris is defined as one with an uncertainty of ±1 minute in orbital period. This corresponds to an error in mean altitude of the orbit of about ±25 n.mi., which is much worse than the expected booster performance of ±10 n.mi. This uncertainty in orbit period has a secular effect on the spacecraft pitch axis of shifting the orbit angle by 3.6 degrees per revolution. Initial uncertainties in orbit inclination and the location of the ascending node (with respect to the intersection of the geographic and geomagnetic equators) are relatively unimportant as far as the operation of the momentum unloading subsystem is concerned.

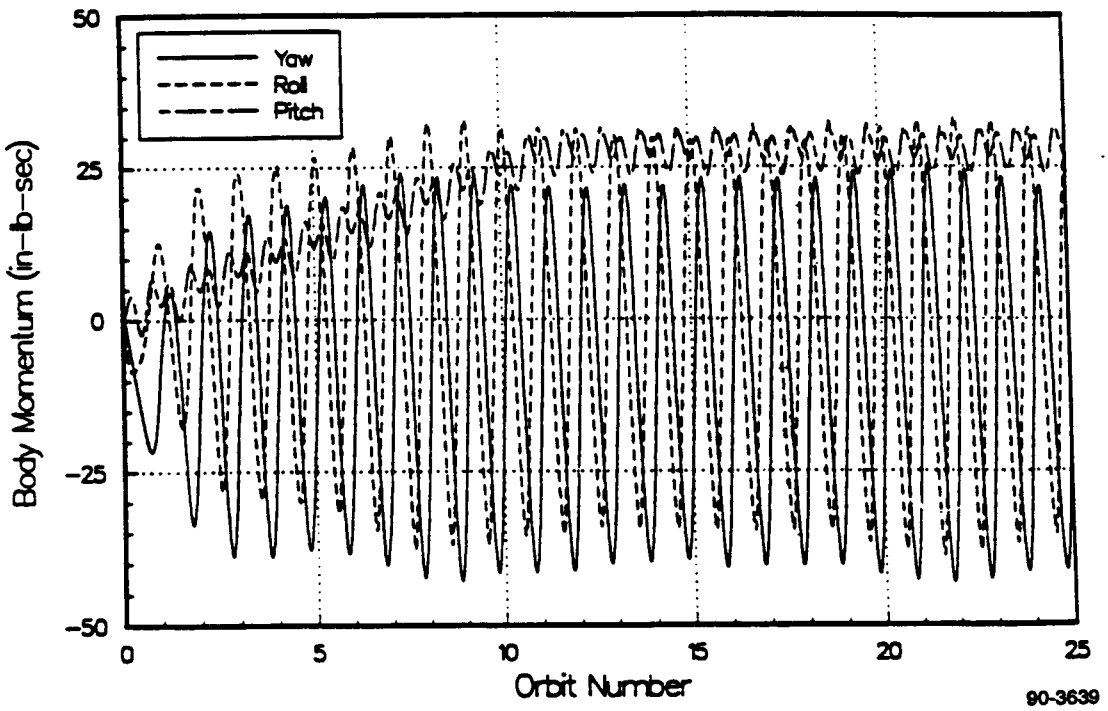

Figure 4.4.4-4. TIROS KLM Magnetic Momentum Unloading System Performance 22 deg S/A Cant Angle Summer Solstice

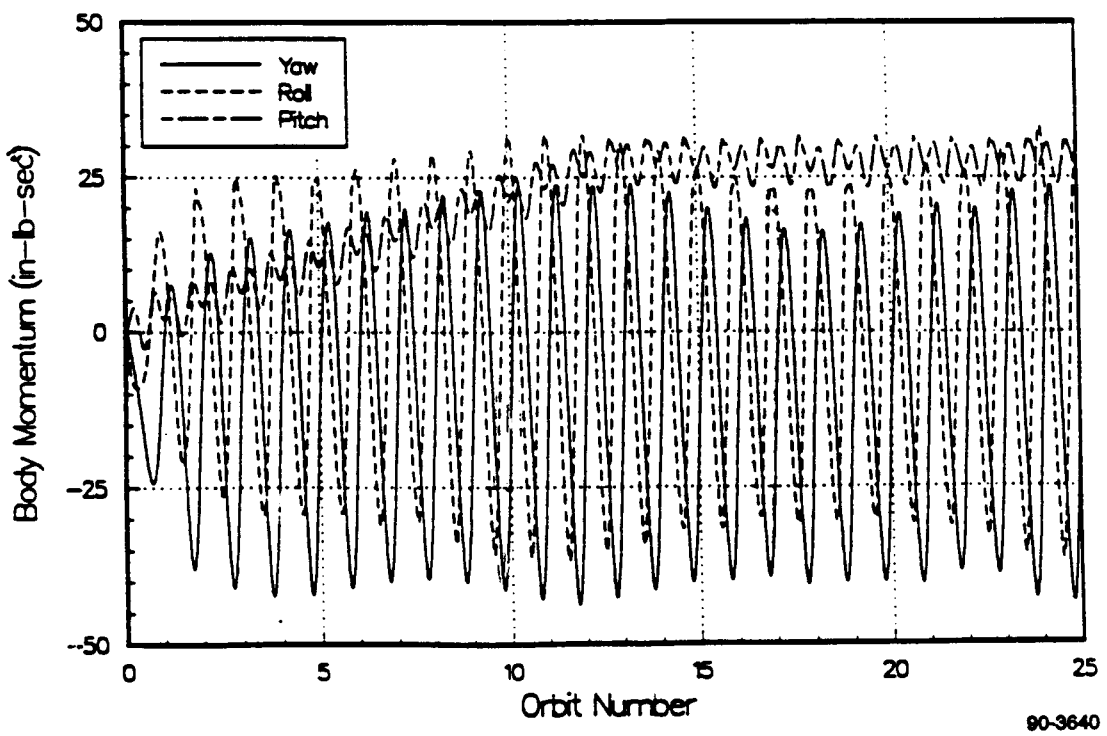

Figure 4.4.4-5. TIROS KLM Magnetic Momentum Unloading System Performance 22 deg S/A Cant Angle Equinox

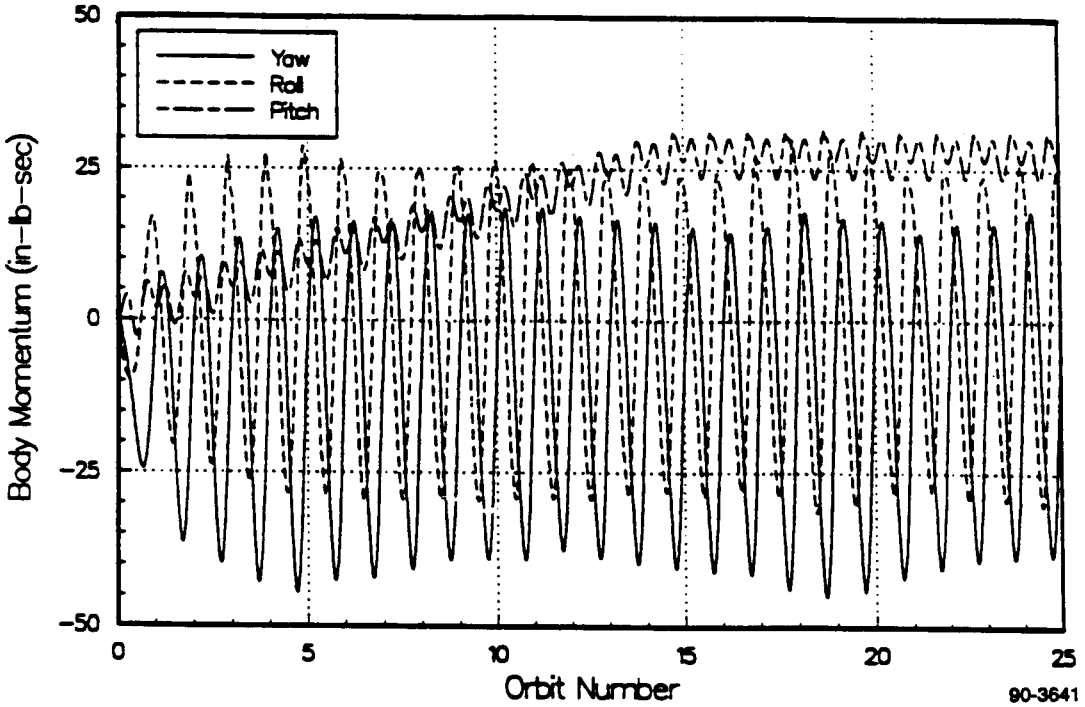

Figure 4.4.4-6. TIROS KLM Magnetic Momentum Unloading System Performance 22 deg S/A Cant Angle Winter Solstice

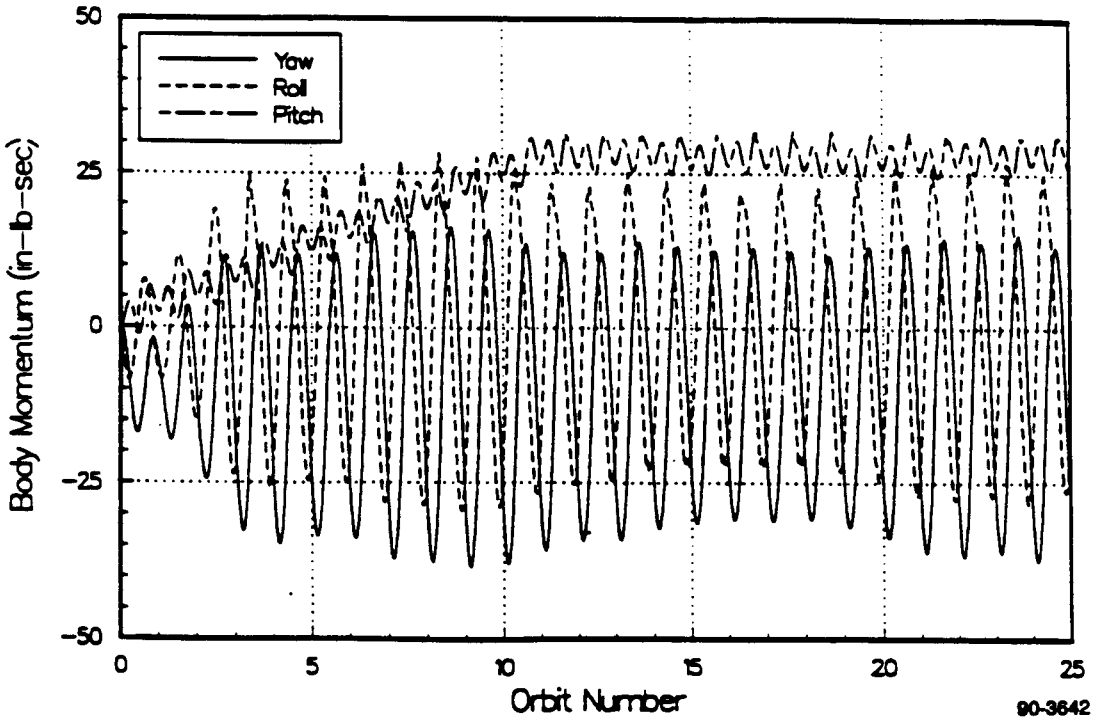

Figure 4.4.4-7. TIROS KLM Magnetic Momentum Unloading System Performance 37 deg S/A Cant Angle Summer Solstice

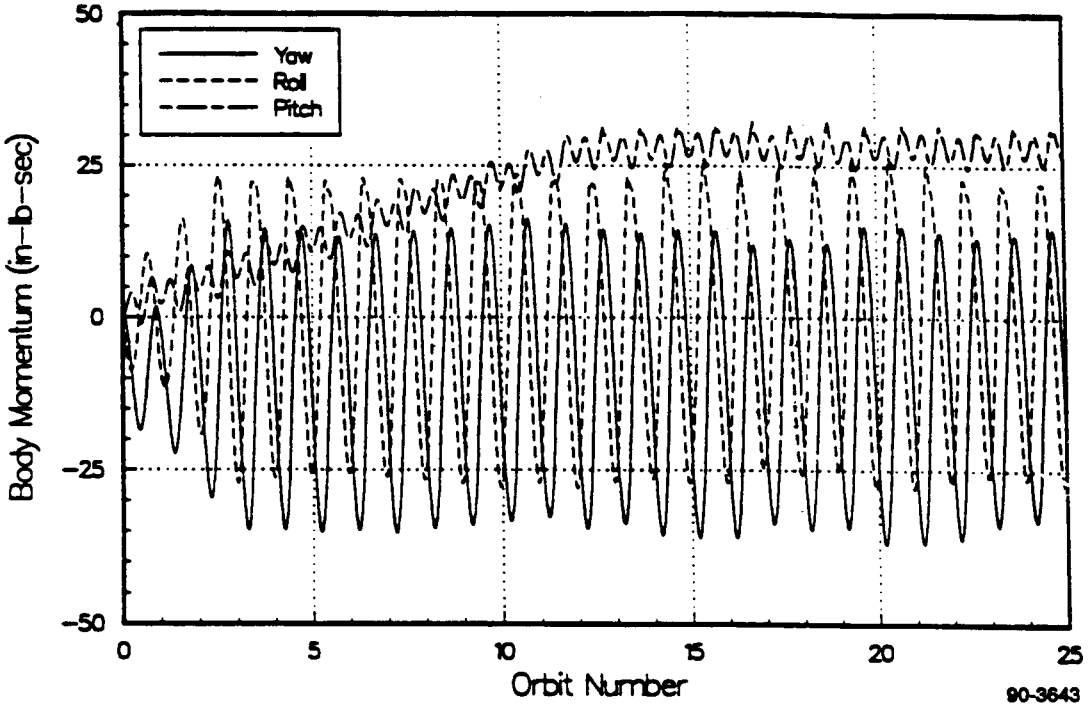

Figure 4.4.4-8. TIROS KLM Magnetic Momentum Unloading System Performance 37 deg S/A Cant Angle Equinox

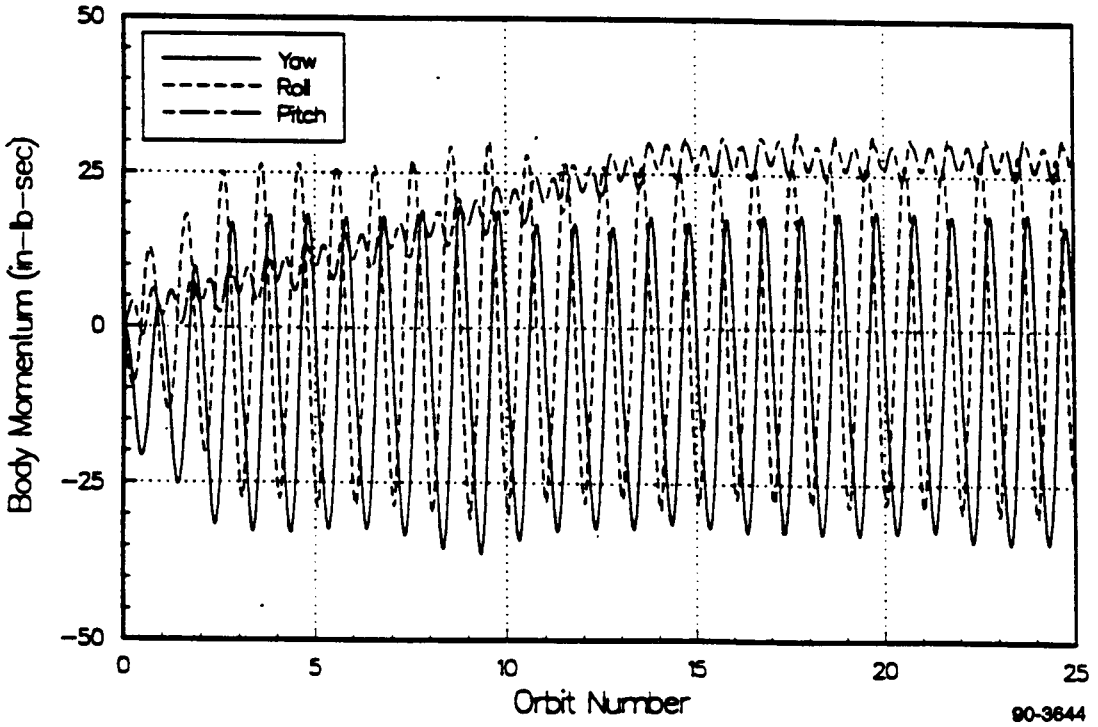

Figure 4.4.4-9. TIROS KLM Magnetic Momentum Unloading System Performance 37 deg S/A Cant Angle Winter Solstice

TABLE 4.4.4-4. SUMMARY REACTION WHEEL SPEEDS

Array Cant Angle	Season	Wheel Speed Ranges (rpm)					
		Yaw		Roll		Pitch	
		Min	Max	Min	Max	Min	Max
22°	Summer	-625	1075	825	-975	-600	-825
	Equinox	-625	1100	825	-975	-575	-800
	Winter	-450	1125	750	-800	-600	-800
37°	Summer	-400	950	700	-750	-600	-800
	Equinox	-375	925	650	-700	-625	-825
	Winter	-500	925	750	-800	-600	-800

TABLE 4.4.4-5. MAGNETIC COIL DUTY CYCLES

Array Cant Angle	Season	Duty Cycle			
		On-Time/Orbit Time (%)		On-Time/Max. On-Time (%)	
		Y Axis Coil	Z Axis Coil	Y Axis Coil	Z Axis Coil
22°	Summer	2.7	14.7	10.0	22.5
	Equinox	2.2	17.3	8.3	26.4
	Winter	1.7	15.2	6.3	23.1
37°	Summer	2.8	9.3	10.4	14.1
	Equinox	2.3	10.9	8.5	16.6
	Winter	1.7	9.1	6.5	13.8

Figures 4.4.4-10 and 4.4.4-11 show the magnetic momentum unloading system performance for a 22° solar array cant during Equinox with a 1 minute orbit period uncertainty and a -1 minute orbit period uncertainty. Figures 4.4.4-12 and 4.4.4-13 show the magnetic momentum unloading system performance for a 37° solar array cant during Equinox with a' 1 minute orbit period uncertainty and a -1 minute orbit period uncertainty. The magnetic coil duty cycles are greatest during Equinox, and thus, the magnetic momentum unloading system performance will degrade more at Equinox than at any other season for a given orbit period uncertainty.

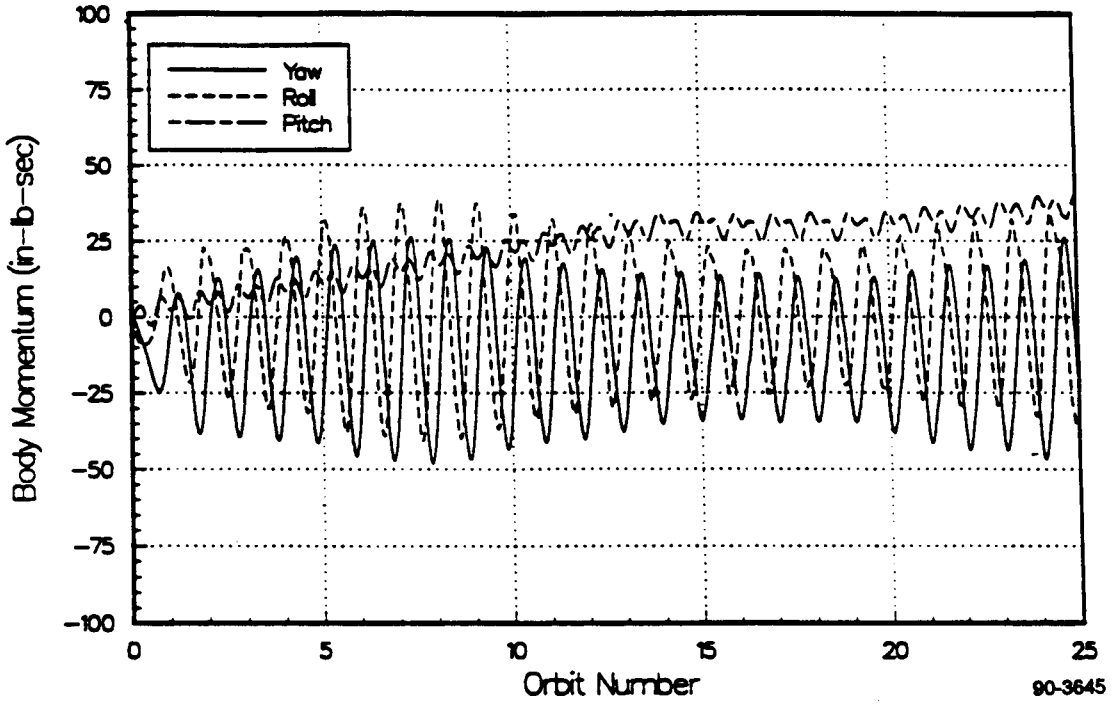

Figure 4.4.4-10. TIROS KLM Magnetic Momentum Unloading System Performance 22 deg S/A Cant Angle Equinox +1 Min Orbit Period Uncertainty

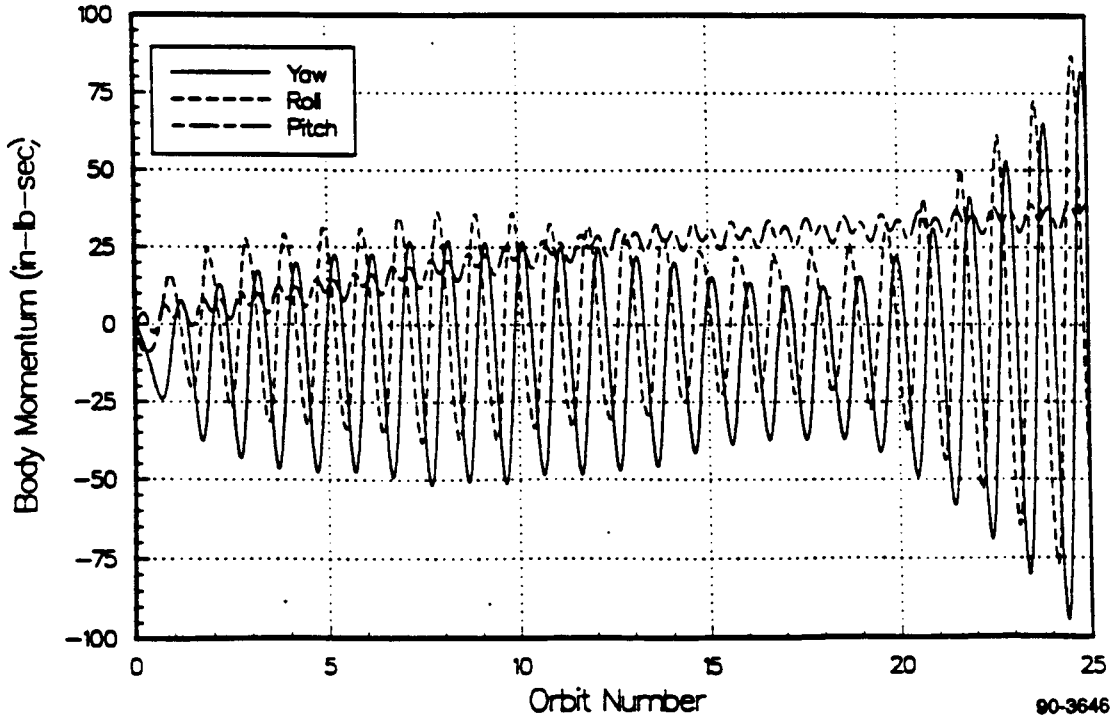

Figure 4.4.4-11. TIROS KLM Magnetic Momentum Unloading System Performance 22 deg S/A Cant Angle Equinox -1 Min Orbit Period Uncertainty

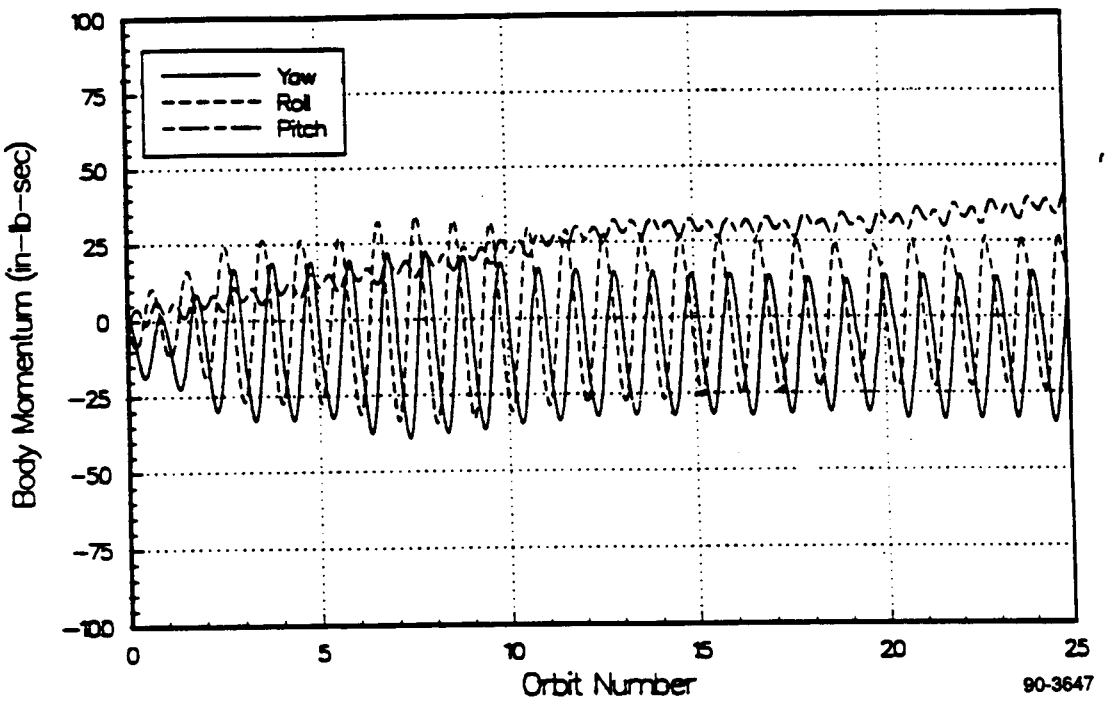

Figure 4.4.4-12. TIROS KLM Magnetic Momentum Unloading System Performance 37 deg S/A Cant Angle Equinox +1 Min Orbit Period Uncertainty

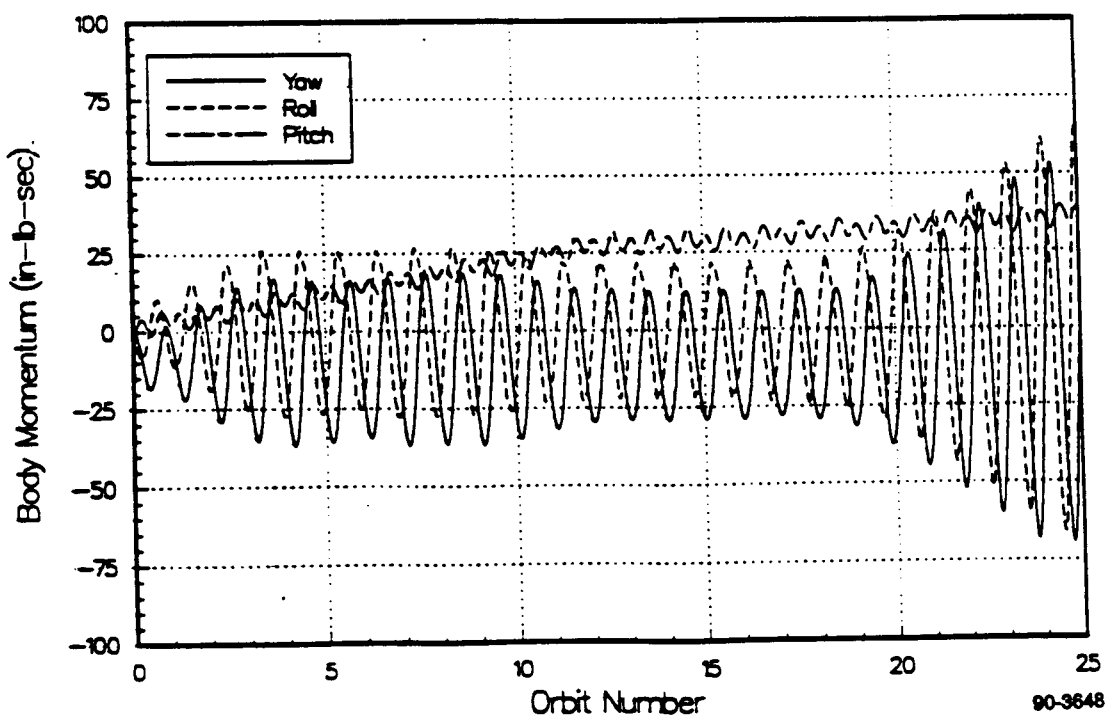

Figure 4.4.4-13. TIROS KLM Magnetic Momentum Unloading System Performance 37 deg S/A Cant Angle Equinox -1 Min Orbit Period Uncertainty

4.4.5 DISTURBANCE ENVIRONMENT

ATN satellites will be subjected to disturbances from the following external influences: gravient gradient, solar radiation pressure (ignoring periods when the sun is eclipsed by the earth), residual magnetic dipoles (5.0 atm^2 along each spacecraft axis), and aerodynamic forces. The worst case torque summation is described by the following Fourier series for each spacecraft axis, where the Fourier coefficients are listed in Tables 4.4.5-1 and 4.4.5-2.

$$T_{ext} = a_o + \sum_{n=1}^{4} a_n \cos(n\beta) + \sum_{n=1}^{4} b_n \sin(n\beta)$$

where, T_{ext} = External Disturbance Torque (in-lb);
b = Orbit angle measured from the ascending node.

The parameters used in the determination of the environmental disturbance torques are listed in Table 4.4.5-3. The peak torques are listed in Table 4.4.5-4 for 22° and 37° Solar Array Cant Angles.

In addition to the influence of external torques, the satellite will also be subjected to internal disturbances produced by payload instruments and tape recorders. With the exception of some of the recorder disturbances, all payload disturbances are nominally along the roll axis. A summary of the internal disturbances is discussed in the following paragraphs.

4.4.5.1 AVHRR

Continuously rotating instrument with an uncompensated angular momentum of 2.375 in-lb-sec along the -Y axis.

4.4.5.2 HIRS

The HIRS is a step scan instrument with a slew mode calibration cycle and a flyback return after each scan line as shown in the timing diagram of Figure 4.4.5-1. The slew/scan and flyback rotations are directed along the positive and negative Y-axis, respectively. The maximum angular momentum associated with the respective operating modes are:

Mode	$\|H\|$ max (in-lb-sec)
Slew	0.0150
Scan	0.0050
Flyback	0.0124

Additionally, the HIRS has a continuously rotating filter wheel with an angular momentum of 2 in-lb-sec directed along the negative Z-axis.

4.4.5.3 AMSU

The Advanced Microwave Sounding Unit (AMSU) is comprised of four scanning modules, namely, two AMSU-A1 modules, one AMSU-A2 module and one AMSU-B module. The scan axis of each of the modules is nominally aligned with the spacecraft roll axis. The AMSU-A1 and AMSU-A2 modules have the same scan

TABLE 4.4.5-1. WORST CASE TOTAL ENVIRONMENTAL DISTURBANCE BODY TORQUE FOURIER COEFFICIENTS, AFTERNOON ASCENDING ORBIT

Array Angle	Season	Body Axis	Fourier Coefficients (micro in-lbs)								
			a_0	a_1	a_2	a_3	a_4	b_1	b_2	b_3	b_4
22°	Summer Solstice	Yaw	36	322	383	51	-18	2174	-889	-480	-68
		Roll	-10995	1786	-849	-105	187	2197	-220	-160	-19
		Pitch	389	-781	63	7	-6	-1874	5969	77	5
	Equinox	Yaw	-200	761	157	3	32	2648	-1087	-587	-84
		Roll	-11156	2106	-1038	-128	228	1538	28	13	9
		Pitch	346	-701	22	-2	3	-1955	6000	98	8
	Winter Solstice	Yaw	-453	1230	-84	-47	87	2322	-951	-514	-73
		Roll	-11045	1886	-908	-112	200	834	292	197	41
		Pitch	299	-614	-23	-11	13	-1903	5980	84	6

TABLE 4.4.5-2. WORST CASE TOTAL ENVIRONMENTAL DISTURBANCE BODY TORQUE FOURIER COEFFICIENTS, MORNING ASCENDING ORBIT

Array Angle	Season	Body Axis	Fourier Coefficients (micro in-lbs)								
			a_0	a_1	a_2	a_3	a_4	b_1	b_2	b_3	b_4
37°	Summer Solstice	Yaw	68	323	360	51	-22	-1663	500	570	116
		Roll	-9340	-786	400	199	-98	2195	-219	-160	-20
		Pitch	396	-775	56	7	-6	-1173	5499	-92	-24
	Equinox	Yaw	-168	762	134	4	29	-2041	610	696	142
		Roll	-9191	-1030	488	244	-119	1537	29	12	9
		Pitch	350	-691	13	-2	4	-1111	5475	-109	27
	Winter Solstice	Yaw	-421	1230	-107	-47	83	-1781	534	610	124
		Roll	-9293	-862	427	213	-104	834	293	196	40
		Pitch	303	-603	-32	-12	14	-1157	5493	-97	-25

TABLE 4.4.5-3. ENVIRONMENTAL DISTURBANCE ANALYSIS PARAMETERS

Parameter		Value	Units
Spacecraft Altitude (a)		2734000	ft
Earth Radius (r_e)		20891000	ft
Geocentric Gravitational Constant (μ)		1.407644E+16	ft^3/s^2
Orbit Eccentricity (e)		0	n/a
Atmospheric Density @ Spacecraft Altitude (ρ_e)		2.27E-17	$slugs/ft^3$
Drag Coefficient (C_d)		2	n/a
Solar Pressure Constant (P_0)	Summer	9.39E-08	lb_f/ft^2
	Equinox	9.72E-08	lb_f/ft^2
	Winter	1.004E-07	lb_f/ft^2
Sun Angle (γ)	Summer	23.5	degrees
	Equinox	0	degrees
	Winter	-23.5	degrees
Geomagnetic Dipole Moment (M_e)		1.96E+16	$slug\text{-}ft^3/Amp\text{-}s^2$
Inclination of Earth's Magnetic Field (i_m)		11.4	degrees
Orbit Inclination (i)		98.7	degrees
Orbit Clock Angle (κ)	Morning Descending Orbit	53*	degrees
	Afternoon Ascending Orbit	68†	degrees

* The nominal morning descending orbit clock angle is 22.5°. A 53° orbit clock angle produces the worst case environmental disturbances for a morning descending orbit satellite.

† The nominal afternoon ascending orbit clock angle is 25°. A 68° orbit clock angle produces the worst case environmental disturbances for an afternoon ascending orbit satellite.

TABLE 4.4.5-4. ATN-KLM EXTERNAL DISTURBANCES

22 Degree Solar Array Cant Angle

Disturbance Source	Peak Torque (in-lb) X	Y	Z
Aerodynamics	0.00035	0.0	0.00006
Gravity Gradient	0.0	0.011	0.0065
Residual Magnetics	0.0009	0.0016	0.0018
Solar Radiation	0.0033	0.0035	0.0030

37 Degree Solar Array Cant Angle

Disturbance Source	Peak Torque (in-lb) X	Y	Z
Aerodynamics	0.0003	0.0	0.00004
Gravity Gradient	0.0	0.011	0.006
Residual Magnetics	0.0009	0.0016	0.0018
Solar Radiation	0.0030	0.0024	0.0020

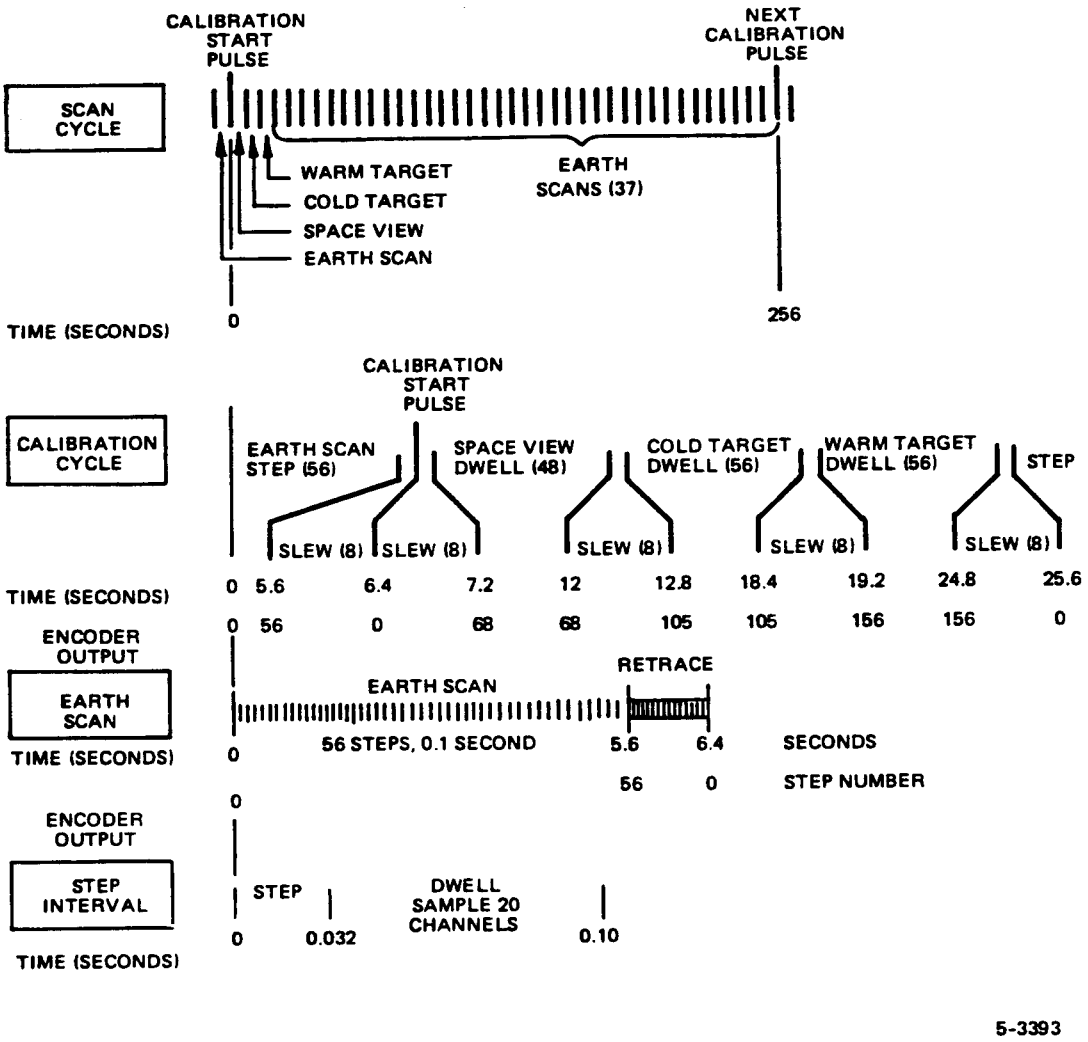

Figure 4.4.5-1. HIRS Scan Timing Diagram

profile and operate synchronously. The AMSU-B module has a different scan profile; however the start of its scan profile is synchronized with that of the AMSU-A1 and AMSU-A2 modules. The reaction torque profiles for each module are shown in Figures 4.4.5-2 through 4.4.5-4.

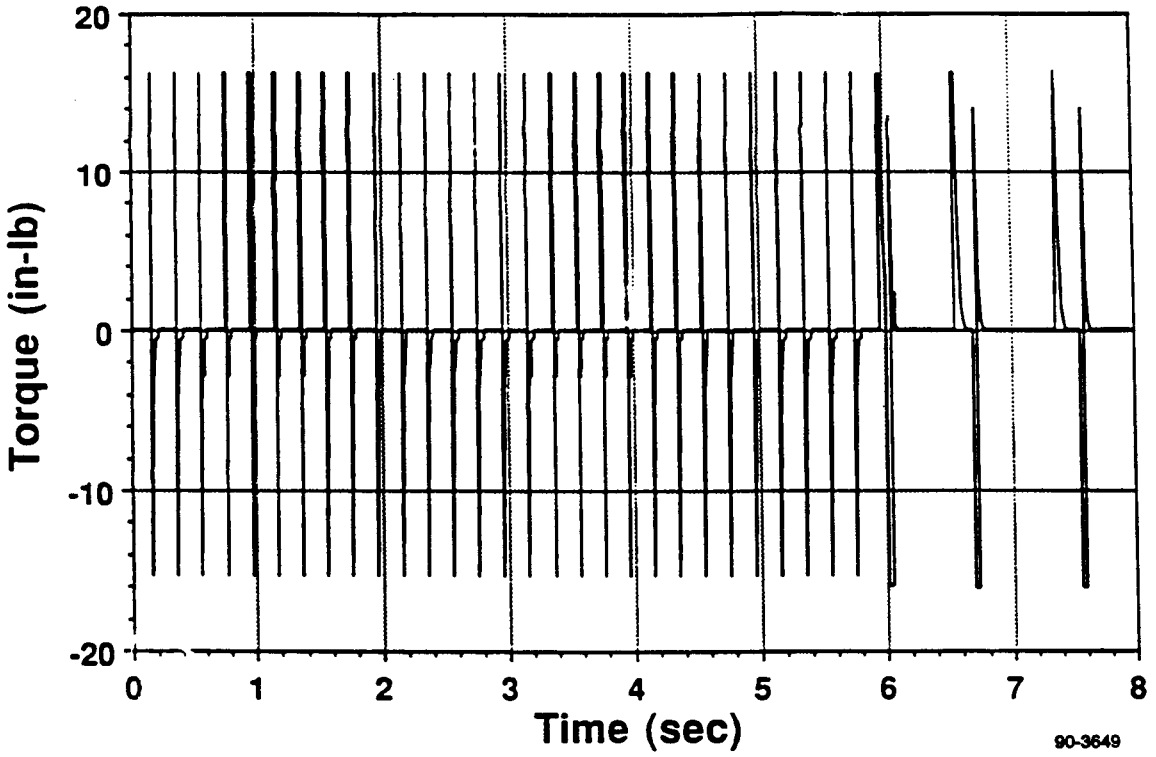

Figure 4.4.5-2. AMSU-A1 Torque Profile (both units combined)

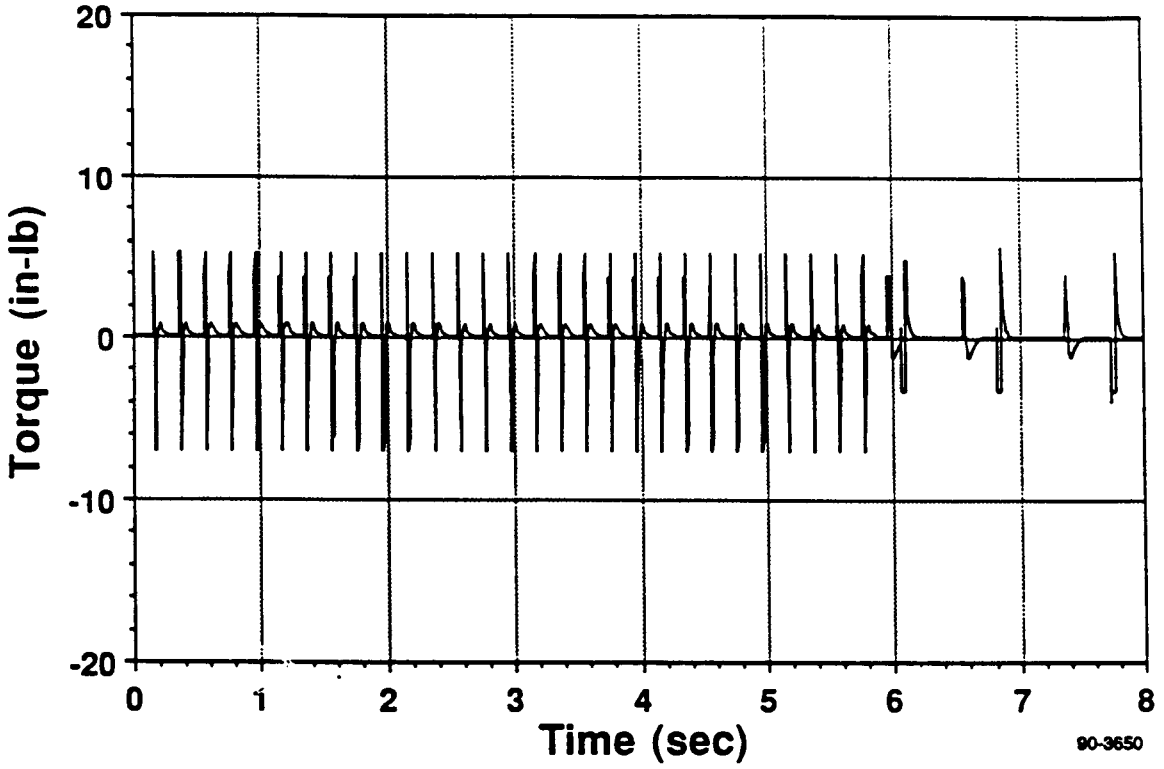

Figure 4.4.5-3. AMSU-A2 Torque Profile (compensated 85%)

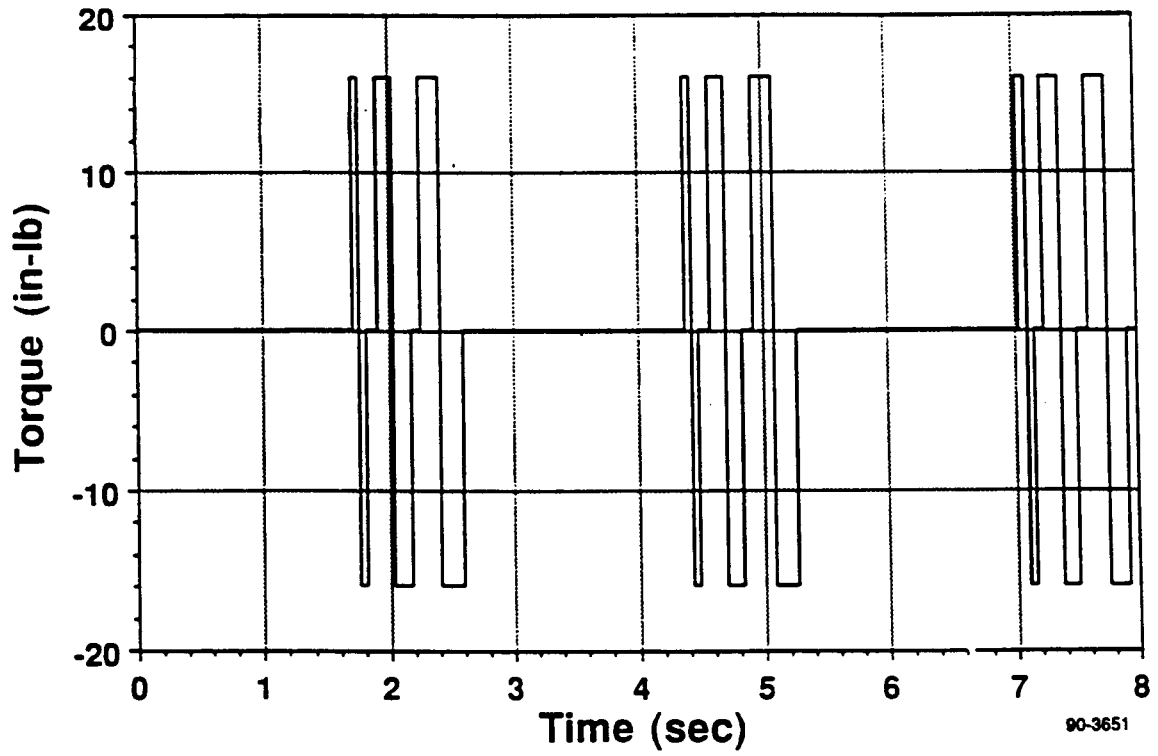

Figure 4.4.5-4. AMSU-AB Torque Profile (uncompensated)

4.4.5.4 Tape Recorders

Each ATN spacecraft will carry a complement of five Digital Tape Recorder (DTRs) which can operate at any of several tape speeds. The momentum axis of the five units will lie in the transverse plane, which bisects the -X, -Y axes and is parallel to the Z axis, with a momentum profile for record or playback as shown in Figure 4.4.5-5. The peak amplitude and duration of the waveform is a function of tape speed with typical parameters as defined in Table 4.4.5-5.

4.4.5.5 SBUV

The SBUV is fixed instrument. However, it will deploy a diffuser on an occasional basis. It will not induce angular momentum in excess of 0.5 in-lb-sec on any axis.

4.4.6 CONTROL LOOP STABILITY

A linear stability analysis has been performed for all the operating modes (Rate Nulling (RN/Search, Yaw Gyrocompassing (YGC), Nominal and Coast) with the solar array cant at two cant angles (22° and 37°) and three rotation angles (0°, 45° and 90°). The stability analysis may be separated into two areas; namely (1) structural dynamics in terms of the system mass properties, system frequencies, and array shapes and (2) dynamic stability with control loops active.

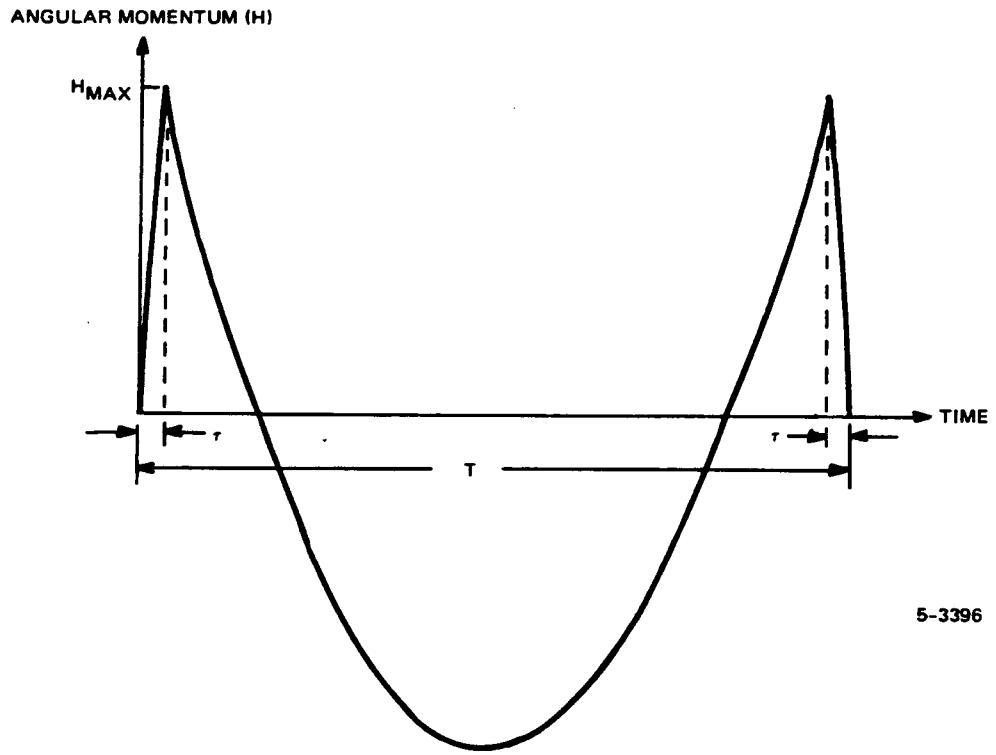

Figure 4.4.5-5. Tape Recorder Momentum Profile

TABLE 4.4.5-5. TAPE RECORDER MOMENTUM CHARACTERISTICS

$\|H\|$ max (in-lb-sec)	τ (min)	τ (sec)	Tape Speed (IPS)	Comment
7.5×10^{-5}	100	0.05	0.87	Primary Record Speed
7.5×10^{-4}	10	0.5	8.7	
3.0×10^{-3}	2.5	2.0	34.8	Primary Playback Speed

The structural dynamics was modeled as a rigid main body with an articulated flexible appendage (the solar array) attached to the spacecraft structure by a flexible boom, and a nonarticulated appendage (the Search and Rescue antenna). The Solar Array flex was modeled for two cant angles (22° and 37°) and three rotation angles (0°, 45°, and 90°). The natural frequencies of the solar array fixed at the base of the boom are as listed in Table 4.4.6-1. The natural frequencies of the SAR fixed at the base of the boom are as listed in Table 4.4.6-2. The system natural frequencies (the frequency of the free-free model of the spacecraft with the solar array at the zero degree position), and SAR is listed in Table 4.4.6-3. The damping coefficient associated with the fundamental frequency of the spacecraft shall be 0.0015.

TABLE 4.4.6-1. FIXED BASE NATURAL FREQUENCIES OF THE SOLAR ARRAY

22 degrees Cant Angle		37 degrees Cant Angle	
Mode	Frequency (Hz)	Mode	Frequency (Hz)
1	0.345	1	0.347
2	0.440	2	0.439
3	0.635	3	6.473
4	1.200	4	1.126
5	1.222	5	1.173
6	1.899	6	1.899
7	2.246	7	2.128
8	3.603	8	3.622
9	4.885	9	4.682
10	5.569	10	5.073
11	7.042	11	7.042
12	9.976	12	9.472
13	10.056	13	10.576
14	10.690	14	10.750

TABLE 4.4.6-2. FIXED BASE NATURAL FREQUENCIES OF THE SAR

Mode	Frequency (Hz)
1	2.36
2	2.72
3	5.76
4	6.50

TABLE 4.4.6-3. FREE-FREE NATURAL FREQUENCIES OF THE SPACECRAFT (RIGID BODY SPACECRAFT WITH SOLAR ARRAY AND SAR)

22 degrees Cant Angle		37 degrees Cant Angle	
Mode	Frequency (Hz)	Mode	Frequency (Hz)
1	0.407	1	0.405
2	0.495	2	0.457
3	0.762	3	0.764
4	1.256	4	1.225
5	1.361	5	1.283
6	1.899	6	1.883
7	2.333	7	2.223
8	3.527	8	3.579

Linearized mass, damping and stiffness matrices were derived for each solar array orientation from the modal and mass properties data using the Mass Stiffness and Damping Matrix Generation Program (MSDGEN). The resulting mass, stiffness and damping matrices modeled the first three solar array flexural modes. The state space transfer functions for the spacecraft dynamics were derived at each solar array position from these matrices. These transfer functions were then used in a series of MATLAB programs to analyze the stability of each control system operating mode. Tables 4.4.6-4 and Table 4.4.6-5 summarize the spacecraft inertia and flex data.

TABLE 4.4.6-4. TIROS KLM SPACECRAFT INERTIAS

Inertias (in-lb-sec2)	22° Cant Angle			37° Cant Angle		
	Rotation Angle			Rotation Angle		
	0°	45°	90°	0°	45°	90°
Ixx	37054	35692	34329	36902	35612	34320
Iyy	34341	35675	36965	34396	35639	36813
Izz	6883	6854	6781	7090	7043	6925
Ixy	115.6	-1218	166.3	116.2	-1117	198.5
Ixz	3056	2891	2493	3368	3111	2491
Izz	-352	-750	-914.9	-352	-971.6	-1228

A series of MATLAB programs were utilized to analyze the open loop stability of the yaw, roll and pitch loops, each with the other two loops closed. Each program modeled the linearized control system block diagram for each operating mode as shown in Figures 4.4.6-1 thru 4.4.6-11. The definitions of the variables used in the block diagrams are listed in Table 4.4.6-6. Table 4.4.6-7 lists the numerical values of the fixed parameters in the various block diagrams and the control loop gains.

In each model, the control system was closed around the spacecraft dynamics. Since the stepper motor drive is an open loop controller that essentially fixes the solar array to the body, Solar Array Drive (SAD) dynamics were not modeled. The structural filters and PID controllers for each control loop used in the analysis are given in Figure 4.4.6-12 and Table 4.4.6-8. Table 4.4.6-9 defines the transfer functions used to model the gyro, RWA, and earth sensor hardware dynamics together with the sample and hold and the computational delay components of the control system.

The results of the frequency domain stability analysis are presented in Tables 4.4.6-10 through 4.4.6-13. The tables listed the rigid body gain and phase margins and the degree of flex mode attenuation for each control axes in each operating mode for 22° and 37° solar array cant angles and 0°, 45°, and 90° solar array rotation angles. Table 4.4.6-14 specifies the closed loop system bandwidth for each operating mode.

Bode and Nichols chart plots are shown for one typical case from Table 4.4.6-10 through 4.4.6-12 for each operating mode. Figure 4.4.6-13 shows the yaw, roll and pitch responses for the Nominal mode. Figure 4.4.6-14 shows the yaw, roll and pitch responses for the RN/Search mode. Figure 4.4.6-15 show the yaw, roll and pitch responses for the YGC mode. Each figure is for solar array cant and

TABLE 4.4.6-5. TIROS KLM SOLAR ARRAY FLEXTURAL PROPERTIES

Mode	Solar Array Cant Angle	Solar Array Rotation Angle	Fixed Base Modal Frequency (rad/s)	Modal Coupling Coefficients (in-lb-sec2)		
				Yaw	Roll	Pitch
1	22°	0°	2.1697	-30.4924	0.0000	47.4389
2			2.7677	100.9086	-0.0004	29.4732
3			3.9899	-0.0620	-103.9894	0.2577
1	22°	45°	2.1697	-21.5614	21.5615	47.8942
2			2.7677	71.3527	-71.3535	27.4169
3			3.9899	-71.4065	-74.4373	-8.9479
1	22°	90°	2.1697	0.0001	30.4924	49.0395
2			2.7677	-0.0007	-100.9086	22.2444
3			3.9899	-100.9581	-3.0925	-12.9119
1	37°	0°	2.1820	46.0719	0.0000	-40.2847
2			2.7598	90.5409	-0.0003	41.6921
3			4.0674	-0.1085	-100.4889	0.2388
1	37°	45°	2.1820	32.5777	-32.5778	-40.9063
2			2.7598	64.0217	-64.0224	39.8025
3			4.0674	-67.3271	-72.6458	-8.2935
1	37°	90°	2.1820	-0.0002	-46.0719	-42.4698
2			2.7598	-0.0007	-90.5409	35.0492
3			4.0674	-95.1696	-5.4271	-11.9676

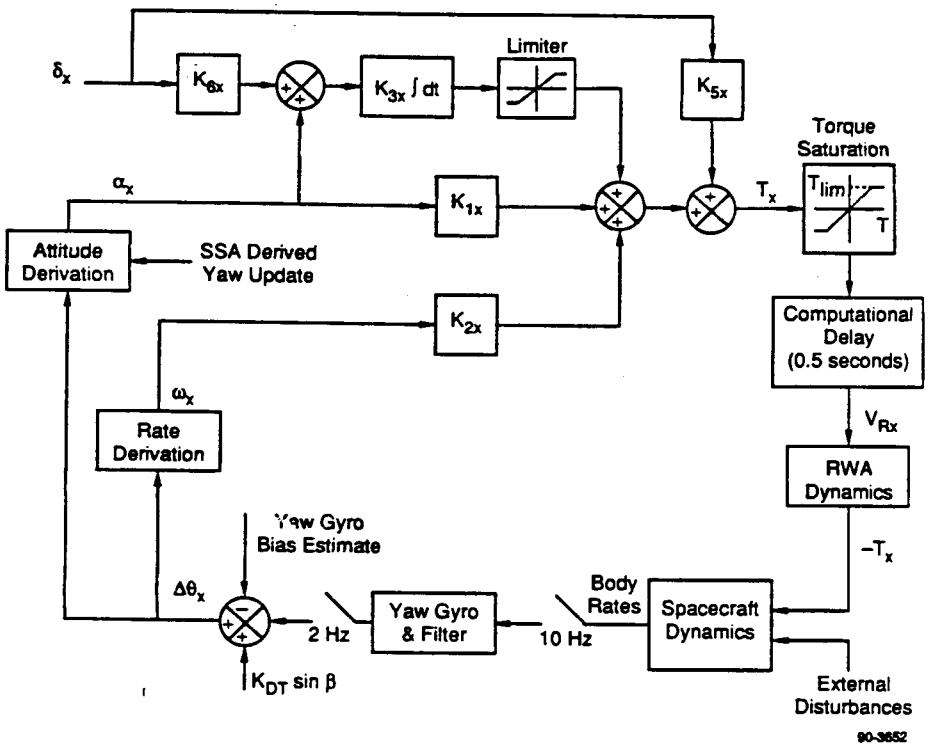

Figure 4.4.6-1. Yaw Control Loop Block Diagram - Nominal and Coast Mode

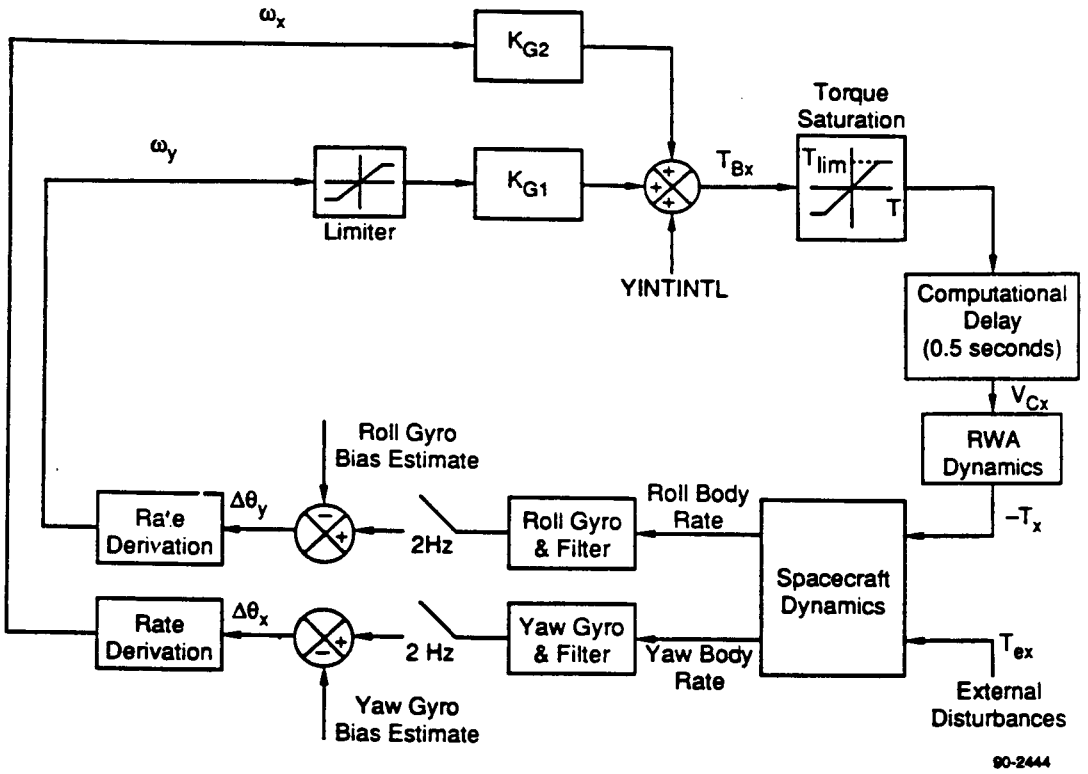

Figure 4.4.6-2. Yaw Control Loop - YGC Mode

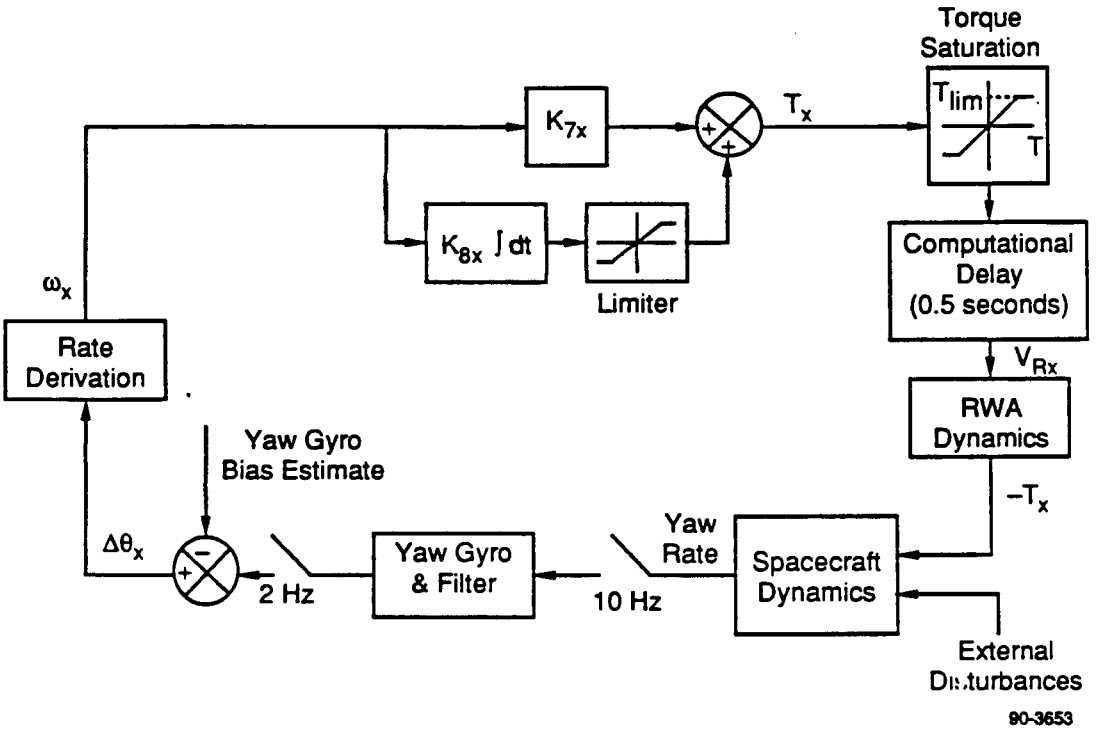

Figure 4.4.6-3. Yaw Control Loop Block Diagram - Search and Rate Nulling Modes

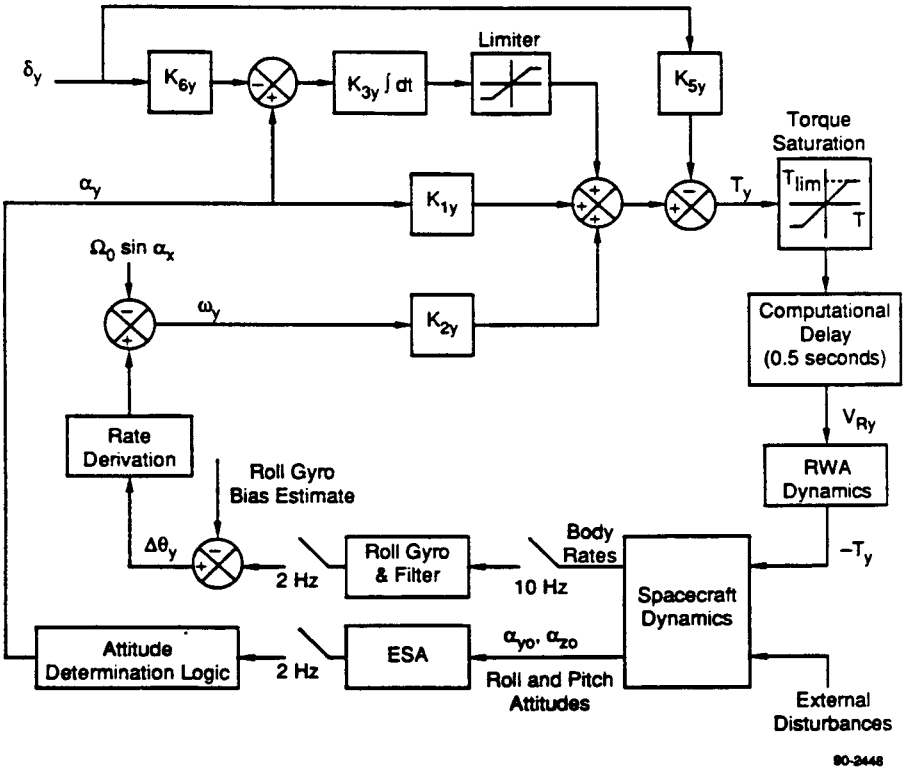

Figure 4.4.6-4. Roll Control Loop Block Diagram - Nominal Mode

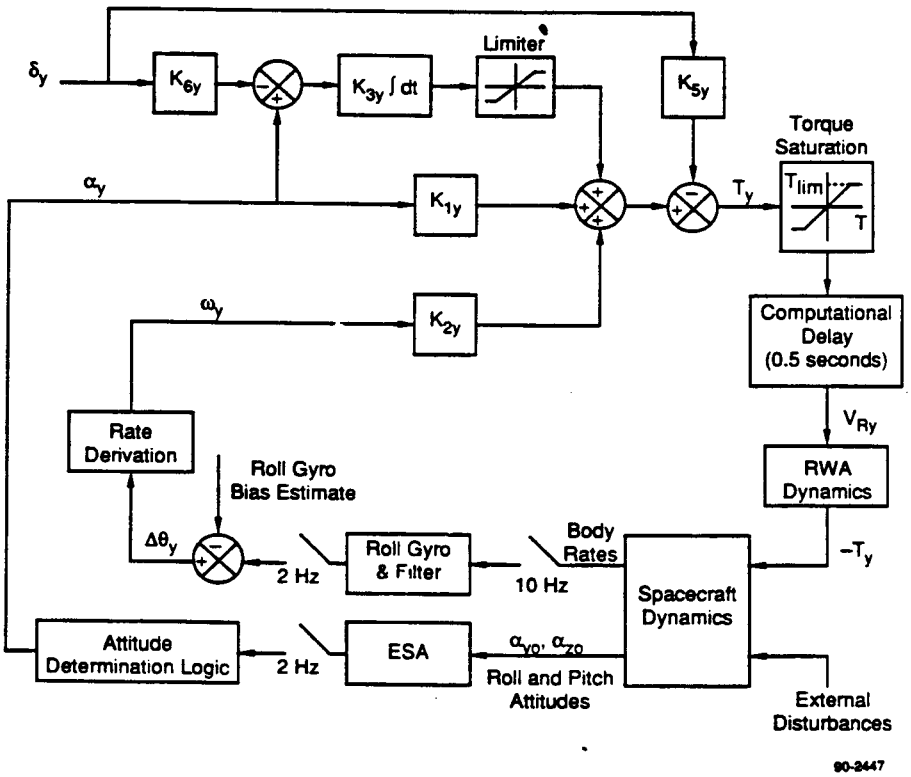

Figure 4.4.6-5. Roll Control Loop Block Diagram - YGC Mode

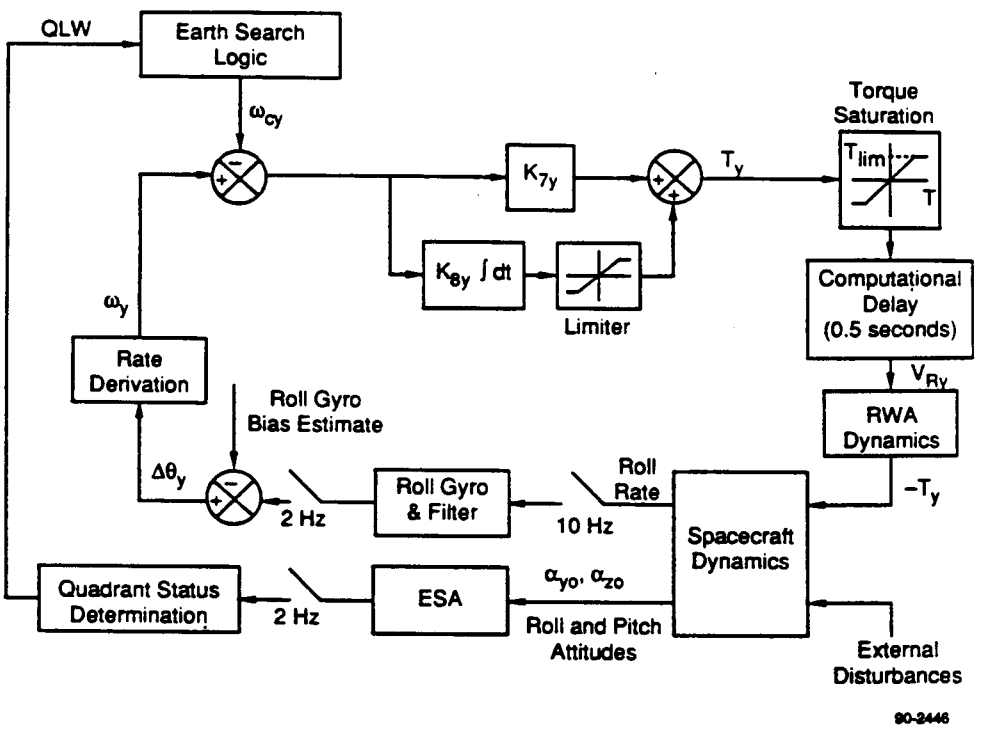

Figure 4.4.6-6. Roll Control Loop Block Diagram - Rate Nulling and Search Modes

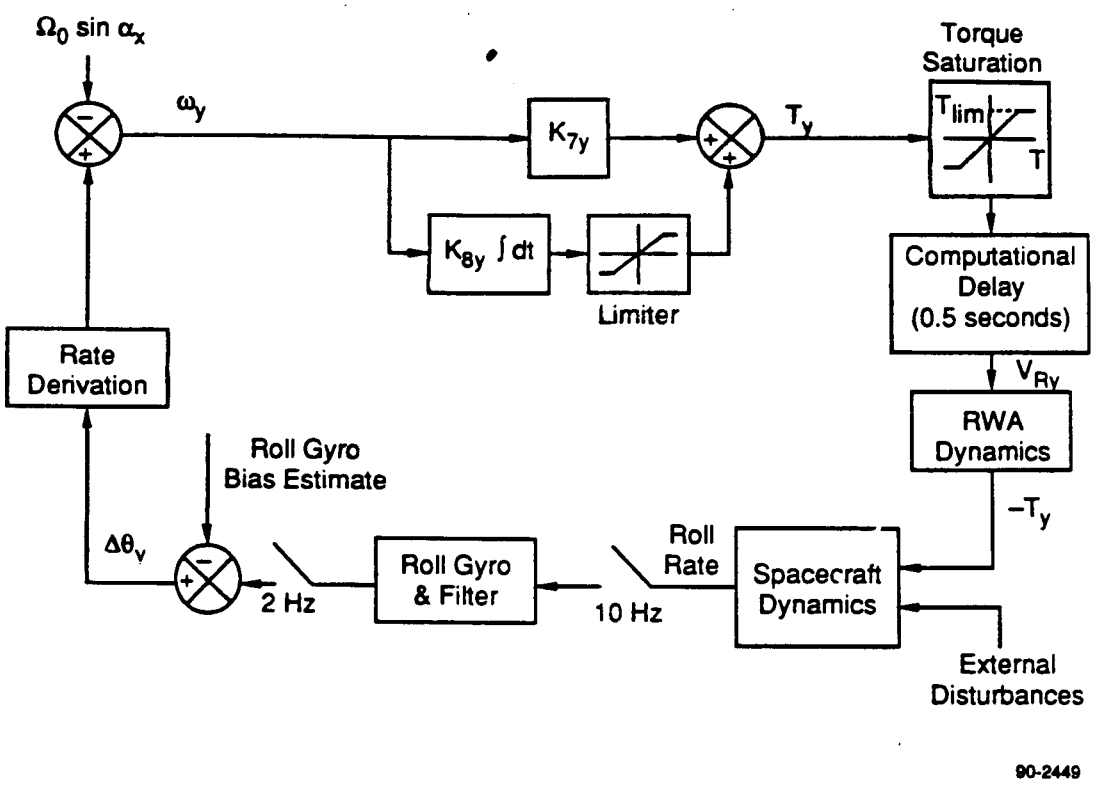

Figure 4.4.6-7. Roll Control Loop Block Diagram - Coast Mode

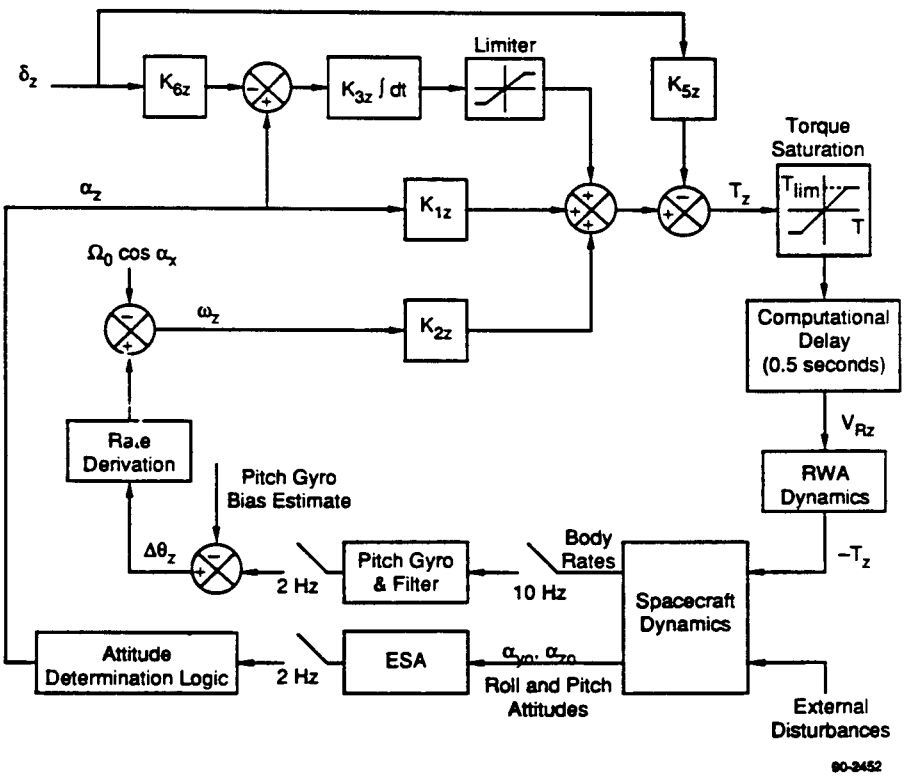

Figure 4.4.6-8. Pitch Control Loop Block Diagram - Nominal Mode

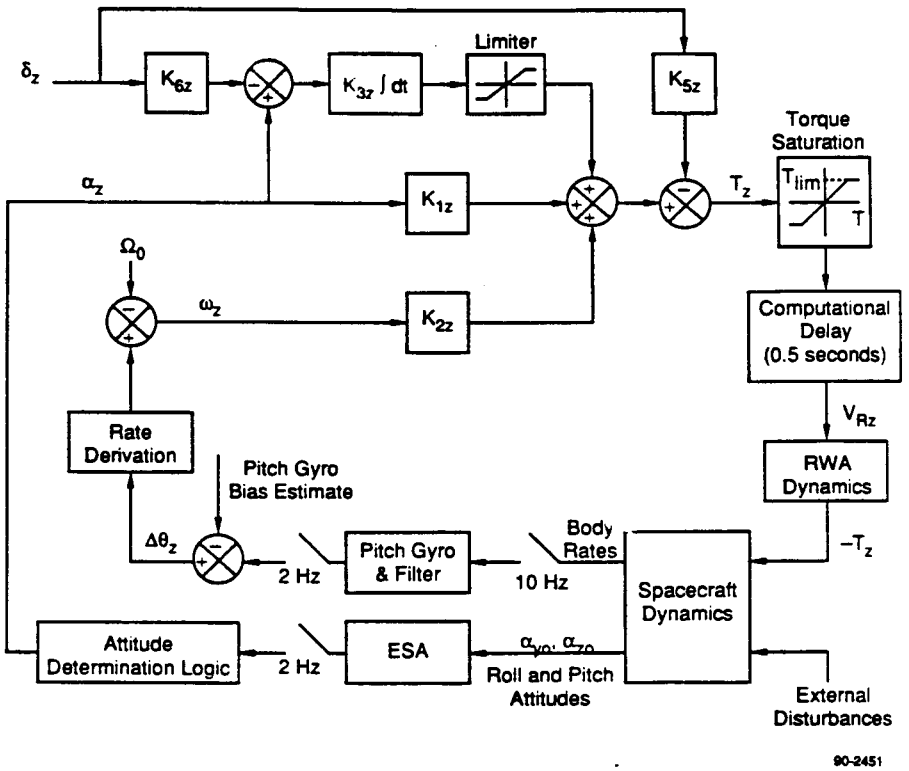

Figure 4.4.6-9. Pitch Control Loop Block Diagram - YGC Mode

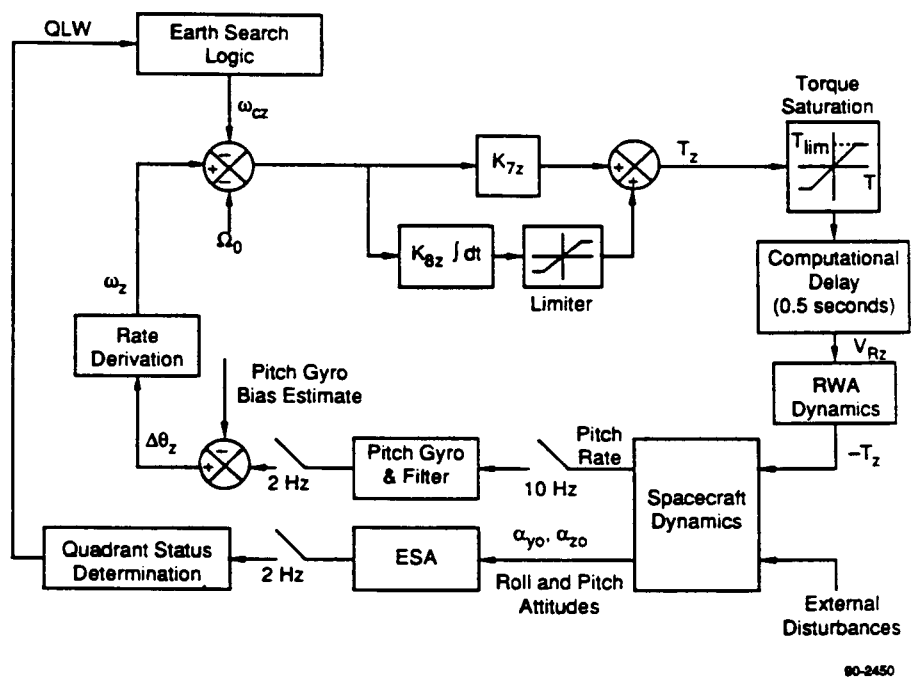

Figure 4.4.6-10. Pitch Control Loop Block Diagram - Rate Nulling and Search Modes

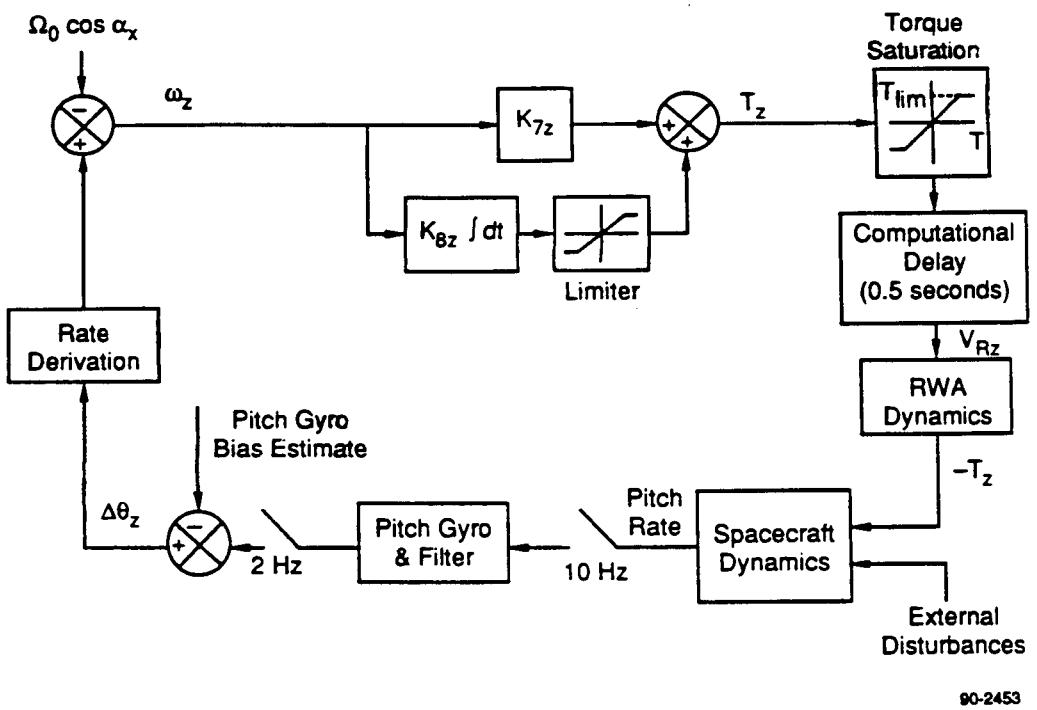

Figure 4.4.6-11. Pitch Control Loop Block Diagram - Coast Mode

rotation angles of 22° and 0° with the modal frequencies reduced by 25%. The other combinations of solar array cant and rotation angles presented in Table 4.4.6-10 through 4.4.6-12 give similar plots.

4.4.7 POINTING ACCURACY

The satellite pointing error is the total misalignment of the body reference axes with respect to the local geodetic reference frame. The contributors of this error are: attitude determination, alignment, attitude control, and ephemeris. The attitude determination errors consist of instrument errors and subsystem performance errors; the alignment errors are those uncertainties between the body reference and the sensing axes. Attitude control errors are subsystem performance related only, and ephemeris errors are primarily a function of the ground based determination of the satellite location. Combining these factors as the sum of a bias error, a long term variation, and a short term variation, the spacecraft pointing is shown by Table 4.4.7-1 to remain within 0.2 degree per axis of the local geodetic reference.

TABLE 4.4.6-6. DEFINITION OF VARIABLES

Variable	Definition
α_{XO}	True spacecraft yaw attitude
$\Delta\theta_X$	Gyro-derived yaw angle increment
α_{YO}	True spacecraft roll attitude
α_Y	ESA-derived roll attitude error
$\Delta\theta_Y$	Gyro-derived roll angle increment
α_{ZO}	True spacecraft pitch attitude
α_Z	ESA-derived pitch attitude error
$\Delta\theta_Z$	Gyro-derived pitch angle increment
ω_X	Gyro-derived yaw body rate
ω_Y	Gyro-derived roll body rate
ω_Z	Gyro-derived pitch body rate
T_{BX}	Yaw axis body torque
T_{BY}	Roll axis body torque
T_{BZ}	Pitch axis body torque
T_{CX}	Yaw axis control torque command
T_{CY}	Roll axis control torque command
T_{CZ}	Pitch axis control torque command
V_{CX}	Yaw axis wheel torque command voltage
V_{CY}	Roll axis wheel torque command voltage
V_{CZ}	Pitch axis wheel torque command voltage
T_{EX}	External yaw axis disturbance torque
T_{EY}	External roll axis disturbance torque
T_{EZ}	External pitch axis disturbance torque
T_{EX}	External yaw axis disturbance torque
T_{EY}	External roll axis disturbance torque
T_{EZ}	External pitch axis disturbance torque

TABLE 4.4.6-7. SYSTEM CONSTANTS

Symbol	Definition	Value	Units
K_{1X}	Yaw Proportional Gain	2044.0	Volts/rad
K_{2X}	Yaw Rate Gain	22630.0	Volts per rad/sec
K_{3X}	Yaw Integral Gain	46.7	Volts/rad-sec
K_{5X}	Magnetic Compensation Gain-Yaw	38400.	Volts/rad
K_{6X}	Magnetic Compensation Integral Gain-Yaw	1.0	-
K_{7X}	Rate Nulling Gain-Yaw	15330.0	Volts per rad/sec
K_{8X}	Rate Nulling Integral Gain-Yaw	481.8	Volts/rad
K_{1Y}	Roll Proportional Gain	1920.0	Volts/rad
K_{2Y}	Roll Rate Gain	21600.0	Volts per rad/sec
K_{3Y}	Roll Integral Gain	44.4	Volts/ rad-sec
K_{5Y}	Magnetic Compensation Gain-Roll	44400.	Volts/rad
K_{6Y}	Magnetic Compensation Integral Gain-Roll	1.0	-
K_{7Y}	Rate Nulling Gain-Roll	12600.	Volts per rad/sec
K_{8Y}	Rate Nulling Integral Gain-Roll	396.0	Volts/rad
K_{1Z}	Pitch Proportional Gain	300.3	Volts/rad
K_{2Z}	Pitch Rate Gain	3913.0	Volts per rad/sec
K_{3Z}	Pitch Integral Gain	6.55	Volts/ rad-sec
K_{5Z}	Magnetic Compensation Gain-Pitch	4320.	Volts/rad
K_{6Z}	Magnetic Compensation Integral Gain-Pitch	1.0	-
K_{7Z}	Rate Nulling Gain-Pitch	3185.0	Volts per rad/sec
K_{8Z}	Rate Nulling Integral Gain-Pitch	134.7	Volts/rad
L1	Wheel Torque Command Voltage Limit	± 5.1	Volts

TABLE 4.4.6-7. SYSTEM CONSTANTS (Continued)

Symbol	Definition	Value	Units
L2	Integral Term Limit		
	Nominal Mode - All Axes Gyrocompass Mode - Roll/Pitch Axes Coast Mode - Yaw Axis	± 1.2	Volts
	Rate Nulling/Search Modes - All Axes Coast Mode - Roll/Pitch Axes	± 10.0	Volts
δ_X	Yaw Axis Magnetic Compensation Constant	1.952×10^{-6}	Rad
δ_Y	Roll Axis Magnetic Compensation Constant	Poles: 3.979×10^{-6} E/W: 2.429×10^{-6}	Rad Rad
δ_Z	Pitch Axis Magnetic Compensation Constant	1.963×10^{-5}	Rad
K_{g1}	Gyrocompass Position Gain	71540.	Volts per rad/sec
K_{g2}	Gyrocompass Rate Gain	6570.	Volts per rad/sec
RRL	Roll Rate Limit	$\pm 1.5 \times 10^{-3} \times \frac{K_{g2}}{K_{g1}}$	rad/sec
Ω_0	Nominal Pitch Rate	1.032×10^{-3}	rad/sec
ω_{CY}	Roll Axis Acquisition Velocity Command	$\pm 1.571 \times 10^{-3}$	rad/sec
ω_{CZ}	Pitch Axis Acquisition Velocity Command	$+2.618 \times 10^{-3}$ (See Note 1)	rad/sec
FYAWB	Spacecraft Yaw Orientation Flag	-1	-
NOTE 1:	$\pm 2\ \omega_{CZ}$, if ESA sees sky only.		

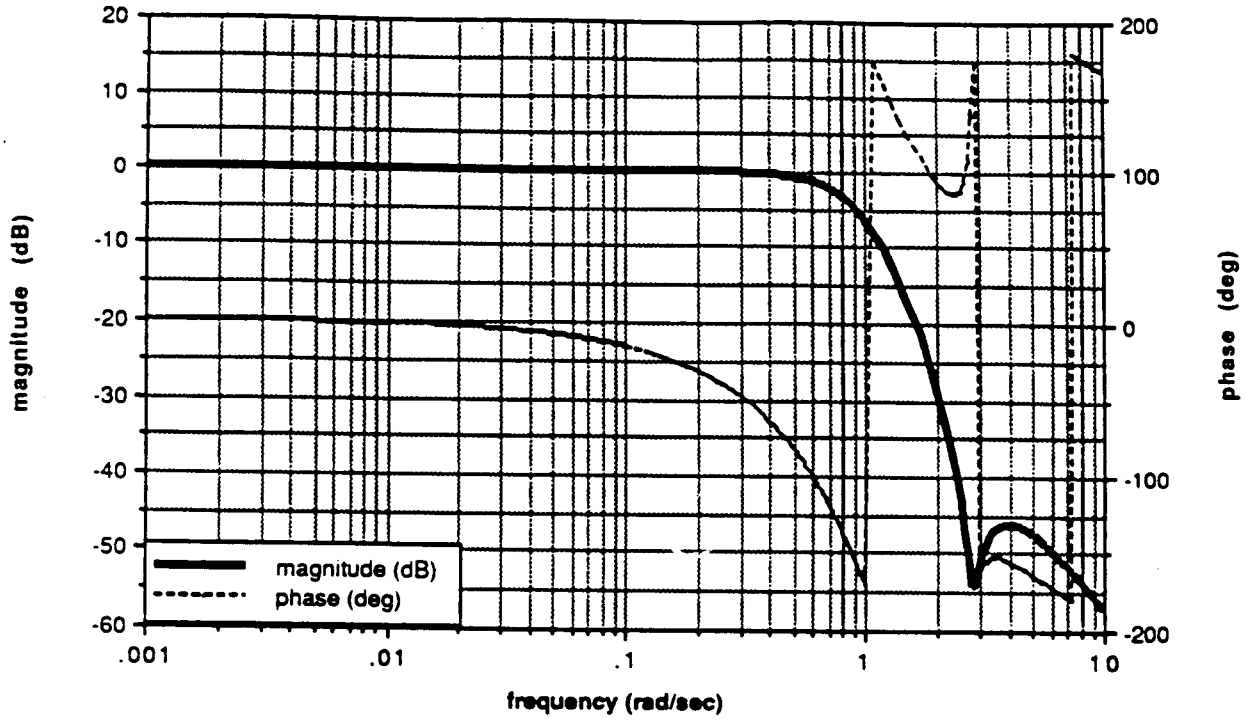

The filter coefficients are:

N0 = 0.0	D0 = 1.0
N1 = 0.0007142385	D1 = -3.7024205
N2 = -0.0007005459	D2 = 5.1500229
N3 = -0.0005417667	D3 = -3.1897158
N4 = 0.0006343945	D4 = 0.7422197

Where the z-domain transfer function is:

$$G(z) = \frac{N0 + N1.z^{-1} + N2.z^{-2} + N3.z^{-3} + N4.z^{-4}}{D0 + D1.z^{-1} + D2.z^{-2} + D3.z^{-3} + D4.z^{-4}}$$

The equivalent s-domain transfer function is:

$$G(s) = \frac{0.1554s^2 + 0.0438s + 1.2341}{s^4 + 2.9811s^3 + 4.4436s^2 + 3.3118s + 1.2341}$$

90-3654

Figure 4.4.6-12. 10 Hz Digital Filter Frequency Response

TABLE 4.4.6-8. PID CONTROLLER GAINS

Spacecraft Operating Mode	Yaw			Roll			Pitch		
	Kr V/(rad/s)	Kp V/rad	Ki V/(rad-s)	Kr V/(rad/s)	Kp V/rad	Ki V/(rad-s)	Kr V/(rad/s)	Kp V/rad	Ki V/(rad-s)
Nominal	22630	2044	46.7	21600	1920	44.4	3913	300	6.6
RN/Search	15330	482	0	12600	396	0	3185	135	0
YGC	6570	71540	0	21600	1920	44.4	3913	300	6.6
Coast	22630	2044	46.7	12600	396	0	3185	135	0

TABLE 4.4.6-9. TRANSFER FUNCTION DEFINITIONS

Component	Transfer Function
Gyro	$\frac{23.94^2}{s^2 + 2\,(0.707)\,(23.94)\,s + 23.94^2}$
RWA	$\frac{326\ s}{1 + 1910\ s}$
Earth Sensor	$\frac{e^{-0.4\ s}}{1 + 0.6\ s}$
Computational Delay	$e^{-0.1\ s}$
Sample And Hold	$\frac{1 - e^{-0.5\ s}}{0.5\ s}$

TABLE 4.4.6-10a. STABILITY MARGINS NOMINAL MODE - 22° CANT ANGLE

Array Angle (deg)	Modal Frequencies	Axis	Gain Margins (dB)			Phase Margin (deg)
			Low	High	Flex	
0	Nominal	Yaw	11.0	12.4	32.8	28.0
		Roll	12.7	11.8	36.2	34.0
		Pitch	12.8	12.9	11.6	37.0
45	Nominal	Yaw	11.3	12.1	36.4	29.0
		Roll	12.4	12.2	27.7	33.0
		Pitch	12.8	12.8	11.8	37.0
90	Nominal	Yaw	11.5	11.8	30.3	29.0
		Roll	12.1	12.5	21.4	33.0
		Pitch	12.9	12.8	11.2	37.0
0	Reduced By 25%	Yaw	11.0	12.5	12.7	28.0
		Roll	12.7	11.9	21.4	34.0
		Pitch	12.8	13.0	3.4	37.0
45	Reduced By 25%	Yaw	11.3	12.1	16.0	29.0
		Roll	12.4	12.2	19.7	33.0
		Pitch	12.8	13.0	2.7	37.0
90	Reduced By 25%	Yaw	11.5	11.8	28.5	29.0
		Roll	12.1	12.6	13.5	33.0
		Pitch	12.9	12.9	2.7	37.0

TABLE 4.4.6-10b. STABILITY MARGINS NOMINAL MODE - 37° CANT ANGLE

Array Angle (deg)	Modal Frequencies	Axis	Gain Margins (dB)			Phase Margin (deg)
			Low	High	Flex	
0	Nominal	Yaw	11.1	12.3	28.9	29.0
		Roll	12.7	11.9	37.3	34.0
		Pitch	12.6	13.0	15.0	37.0
45	Nominal	Yaw	11.3	12.0	33.1	29.0
		Roll	12.4	12.2	22.6	33.0
		Pitch	12.6	13.0	14.4	37.0
90	Nominal	Yaw	11.5	11.8	31.4	29.0
		Roll	12.2	12.4	17.1	33.0
		Pitch	12.7	12.9	14.9	37.0
0	Reduced By 25%	Yaw	11.1	12.4	7.7	29.0
		Roll	12.7	11.9	22.2	34.0
		Pitch	12.6	13.2	5.5	37.0
45	Reduced By 25%	Yaw	11.3	12.1	12.7	29.0
		Roll	12.4	12.2	14.7	33.0
		Pitch	12.6	13.1	5.8	37.0
90	Reduced By 25%	Yaw	11.5	11.8	29.8	29.0
		Roll	12.2	12.5	8.1	33.0
		Pitch	13.1	13.1	5.4	37.0

TABLE 4.4.6-11a. STABILITY MARGINS RN/SEARCH MODE - 22° CANT ANGLE

Array Angle (deg)	Modal Frequencies	Axis	Gain Margins (dB)			Phase Margin (deg)
			Low	High	Flex	
0	Nominal	Yaw	-	16.8	36.2	55.0
		Roll	-	18.1	34.0	54.0
		Pitch	-	15.8	30.5	49.0
45	Nominal	Yaw	-	16.5	39.8	55.0
		Roll	-	18.7	40.0	53.0
		Pitch	-	15.7	31.1	49.0
90	Nominal	Yaw	-	16.2	33.7	55.0
		Roll	-	18.8	34.4	53.0
		Pitch	-	15.7	30.8	49.0
0	Reduced By 25%	Yaw	-	16.9	16.1	55.0
		Roll	-	18.2	32.0	54.0
		Pitch	-	15.9	8.3	49.0
45	Reduced By 25%	Yaw	-	16.5	19.4	55.0
		Roll	-	18.5	28.2	53.0
		Pitch	-	15.9	7.7	49.0
90	Reduced By 25%	Yaw	-	16.2	31.9	55.0
		Roll	-	18.9	21.9	53.0
		Pitch	-	15.8	7.7	49.0

TABLE 4.4.6-11b. STABILITY MARGINS RN/SEARCH MODE - 37° CANT ANGLE

Array Angle (deg)	Modal Frequencies	Axis	Gain Margins (dB)			Phase Margin (deg)
			Low	High	Flex	
0	Nominal	Yaw	-	16.7	32.2	55.0
		Roll	-	18.1	34.8	54.0
		Pitch	-	16.0	26.3	49.0
45	Nominal	Yaw	-	16.8	36.5	55.0
		Roll	-	18.4	40.7	53.0
		Pitch	-	15.9	26.7	49.0
90	Nominal	Yaw	-	16.2	34.8	55.0
		Roll	-	18.7	37.1	53.0
		Pitch	-	15.9	27.2	49.0
0	Reduced By 25%	Yaw	-	16.8	11.1	55.0
		Roll	-	18.2	32.8	54.0
		Pitch	-	16.1	9.8	49.0
45	Reduced By 25%	Yaw	-	16.5	16.1	55.0
		Roll	-	18.5	22.4	53.0
		Pitch	-	16.0	10.2	49.0
90	Reduced By 25%	Yaw	-	16.6	33.1	55.0
		Roll	-	18.8	15.8	53.0
		Pitch	-	16.0	9.7	49.0

TABLE 4.4.6-12a. STABILITY MARGINS YGC MODE - 22° CANT ANGLE

Array Angle (deg)	Modal Frequencies	Axis	Gain Margins (dB)			Phase Margin (deg)
			Low	High	Flex	
0	Nominal	Yaw	-	24.6	43.6	86.0
		Roll	12.7	11.8	36.2	34.0
		Pitch	12.8	12.9	11.6	37.0
45	Nominal	Yaw	-	24.3	47.2	85.0
		Roll	12.4	12.2	27.7	33.0
		Pitch	12.8	12.8	11.8	37.0
90	Nominal	Yaw	-	24.0	41.1	85.0
		Roll	12.1	12.5	21.4	33.0
		Pitch	12.9	12.8	11.2	37.0
0	Reduced By 25%	Yaw	-	24.7	23.4	86.0
		Roll	12.7	11.9	21.4	34.0
		Pitch	12.8	13.0	3.4	37.0
45	Reduced By 25%	Yaw	-	24.4	26.8	85.0
		Roll	12.4	12.2	19.7	33.0
		Pitch	12.8	13.0	2.7	37.0
90	Reduced By 25%	Yaw	-	24.0	39.2	85.0
		Roll	12.1	12.6	13.5	33.0
		Pitch	13.0	12.9	2.7	37.0

TABLE 4.4.6-12b. STABILITY MARGINS YGC MODE - 37° CANT ANGLE

Array Angle (deg)	Modal Frequencies	Axis	Gain Margins (dB)			Phase Margin (deg)
			Low	High	Flex	
0	Nominal	Yaw	-	24.5	39.6	85.0
		Roll	12.7	11.8	37.3	34.0
		Pitch	12.6	13.0	15.0	37.0
45	Nominal	Yaw	-	24.2	43.8	85.0
		Roll	12.4	12.2	22.6	33.0
		Pitch	12.6	13.0	14.4	37.0
90	Nominal	Yaw	-	24.0	42.1	85.0
		Roll	12.2	12.4	17.1	33.0
		Pitch	12.7	12.9	14.9	37.0
0	Reduced By 25%	Yaw	-	24.6	18.5	85.0
		Roll	12.7	11.9	22.2	34.0
		Pitch	12.6	13.2	5.5	37.0
45	Reduced By 25%	Yaw	-	24.3	23.4	85.0
		Roll	12.4	12.2	14.7	33.0
		Pitch	12.6	13.1	5.8	37.0
90	Reduced By 25%	Yaw	-	24.0	40.5	85.0
		Roll	12.2	12.5	8.1	33.0
		Pitch	12.7	13.1	5.4	37.0

TABLE 4.4.6-13a. STABILITY MARGINS COAST MODE - 22° CANT ANGLE

Array Angle (deg)	Modal Frequencies	Axis	Gain Margins (dB)			Phase Margin (deg)
			Low	High	Flex	
0	Nominal	Yaw	11.0	12.4	32.8	28.0
		Roll	-	18.1	34.0	54.0
		Pitch	-	15.8	30.5	49.0
45	Nominal	Yaw	11.3	12.1	36.4	29.0
		Roll	-	18.7	40.0	53.0
		Pitch	-	15.7	31.1	49.0
90	Nominal	Yaw	11.5	11.8	30.3	29.0
		Roll	-	18.8	34.4	53.0
		Pitch	-	15.7	30.8	49.0
0	Reduced By 25%	Yaw	11.0	12.5	12.7	28.0
		Roll	-	18.2	32.0	54.0
		Pitch	-	15.9	8.3	49.0
45	Reduced By 25%	Yaw	11.3	12.1	16.0	29.0
		Roll	-	18.5	28.2	53.0
		Pitch	-	15.9	7.7	49.0
90	Reduced By 25%	Yaw	11.5	11.8	28.5	29.0
		Roll	-	18.9	21.9	53.0
		Pitch	-	15.8	7.7	49.0

TABLE 4.4.6-13b. STABILITY MARGINS COAST MODE - 37° CANT ANGLE

Array Angle (deg)	Modal Frequencies	Axis	Gain Margins (dB)			Phase Margin (deg)
			Low	High	Flex	
0	Nominal	Yaw	11.1	12.3	28.9	29.0
		Roll	-	18.1	34.8	54.0
		Pitch	-	16.0	26.3	49.0
45	Nominal	Yaw	11.3	12.0	33.1	29.0
		Roll	-	18.4	40.7	53.0
		Pitch	-	15.9	26.7	49.0
90	Nominal	Yaw	11.5	11.8	31.4	29.0
		Roll	-	18.7	37.1	53.0
		Pitch	-	15.9	27.2	49.0
0	Reduced By 25%	Yaw	11.1	12.4	7.7	29.0
		Roll	-	18.2	32.8	54.0
		Pitch	-	16.1	9.8	49.0
45	Reduced By 25%	Yaw	11.3	12.1	12.7	29.0
		Roll	-	18.5	22.4	53.0
		Pitch	-	16.0	10.2	49.0
90	Reduced By 25%	Yaw	11.5	11.8	29.8	29.0
		Roll	-	18.8	15.8	53.0
		Pitch	-	16.0	9.7	49.0

TABLE 4.4.6-14. CLOSED LOOP CONTROL SYSTEM BANDWIDTHS

Mode	Bandwidth (rad/s)		
	Yaw	Roll	Pitch
Nominal	0.17	0.17	0.17
RN/Search	0.11	0.09	0.12
YGC	0.05	0.17	0.17
Coast	0.17	0.09	0.12

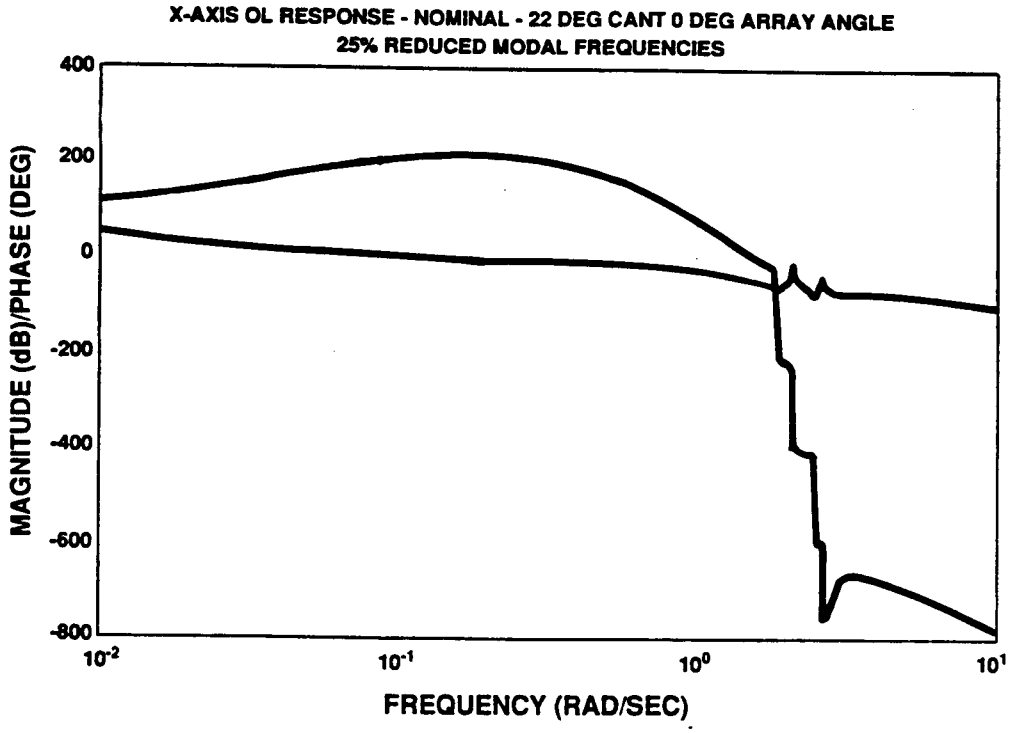

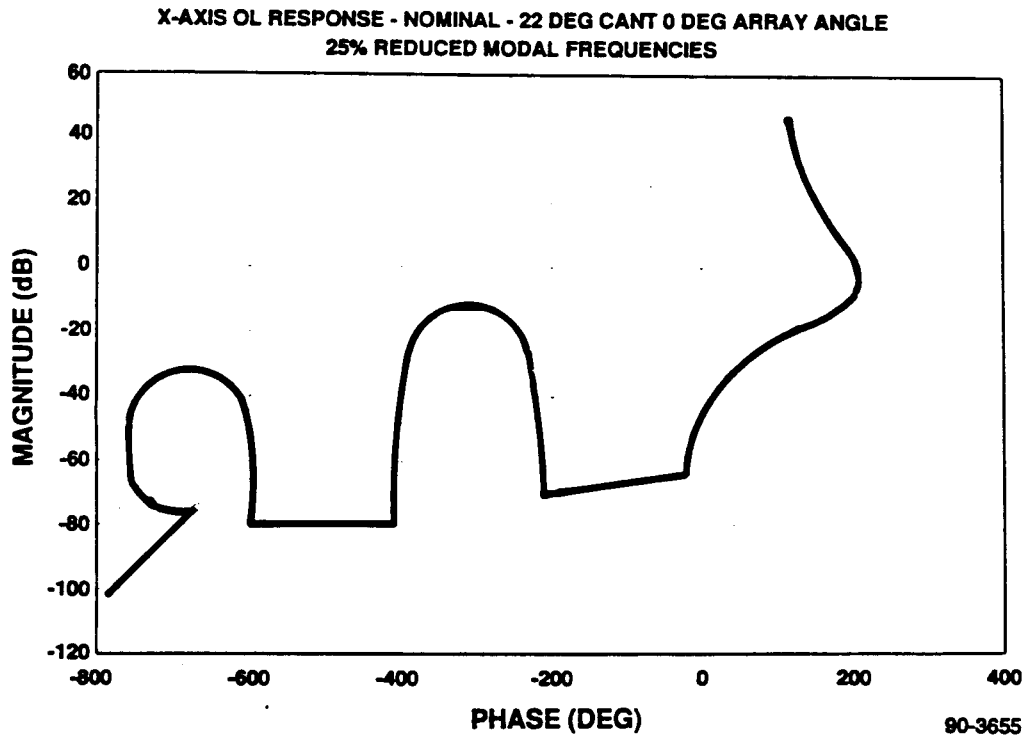

Figure 4.4.6-13a. Nominal Mode - Yaw Open Loop Response

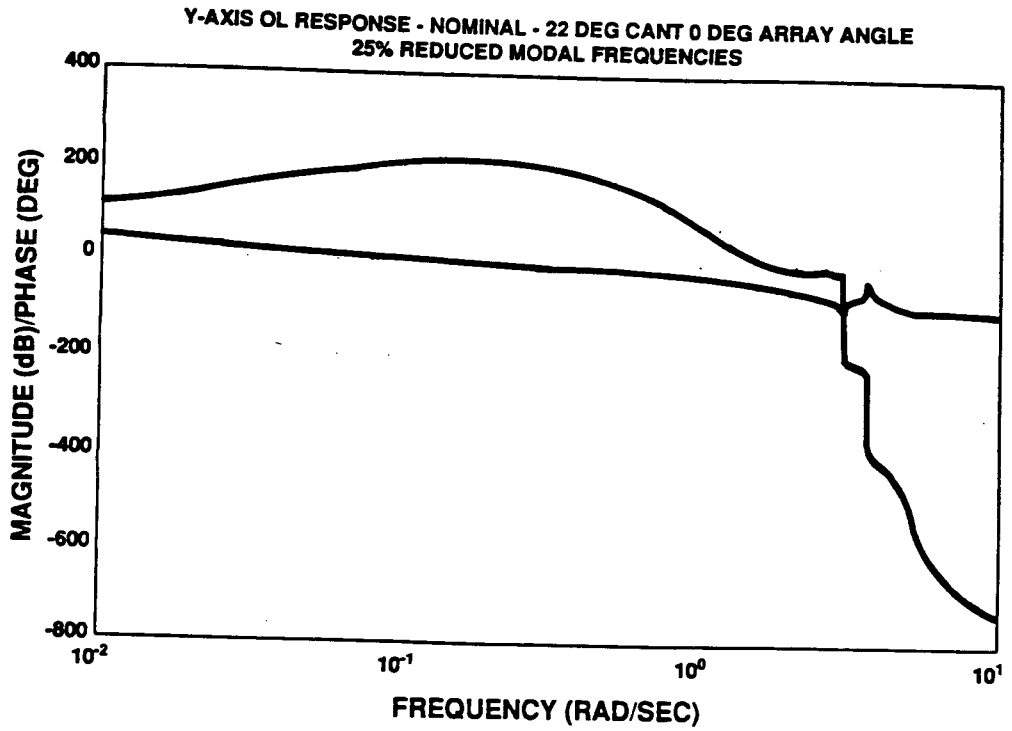

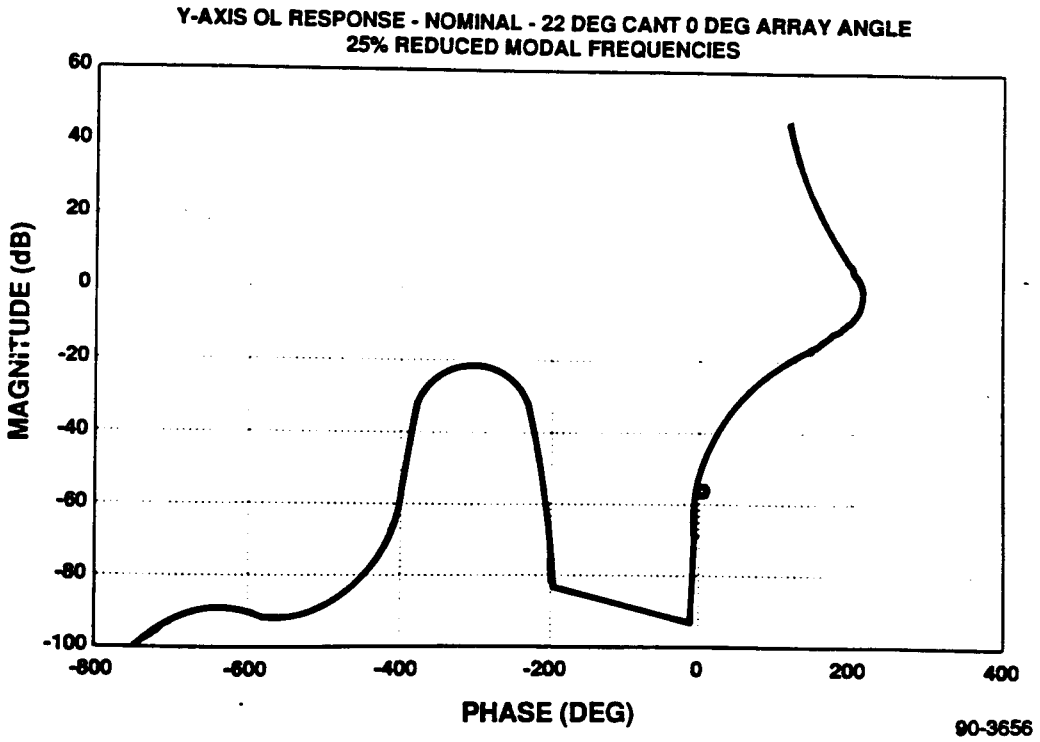

Figure 4.4.6-13b. Nominal Mode - Roll Open Loop Response

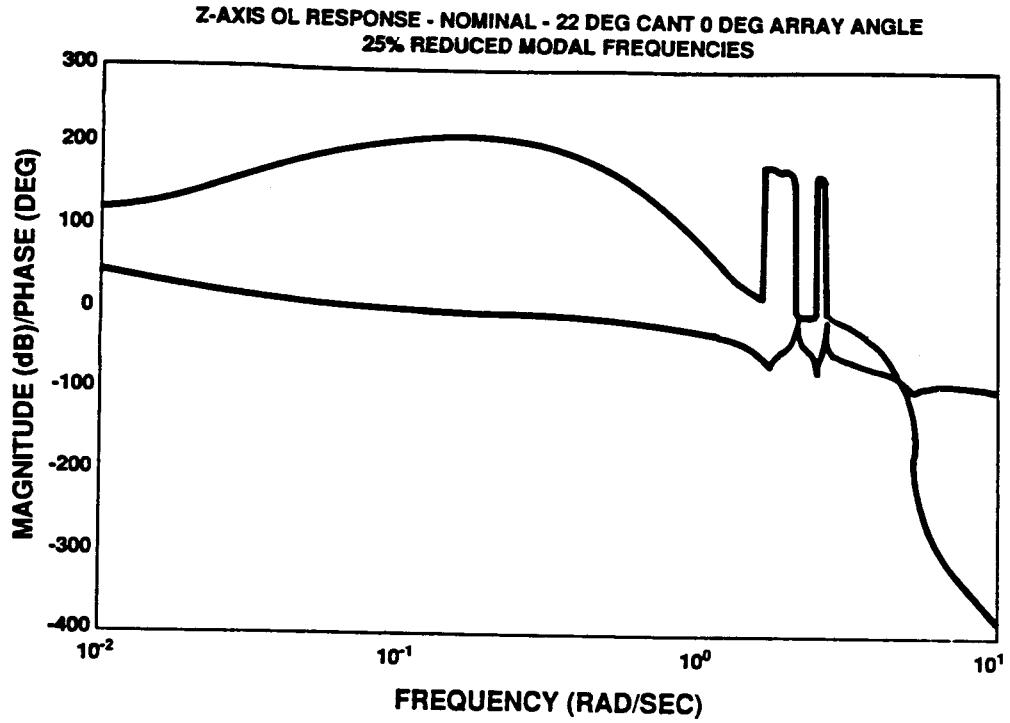

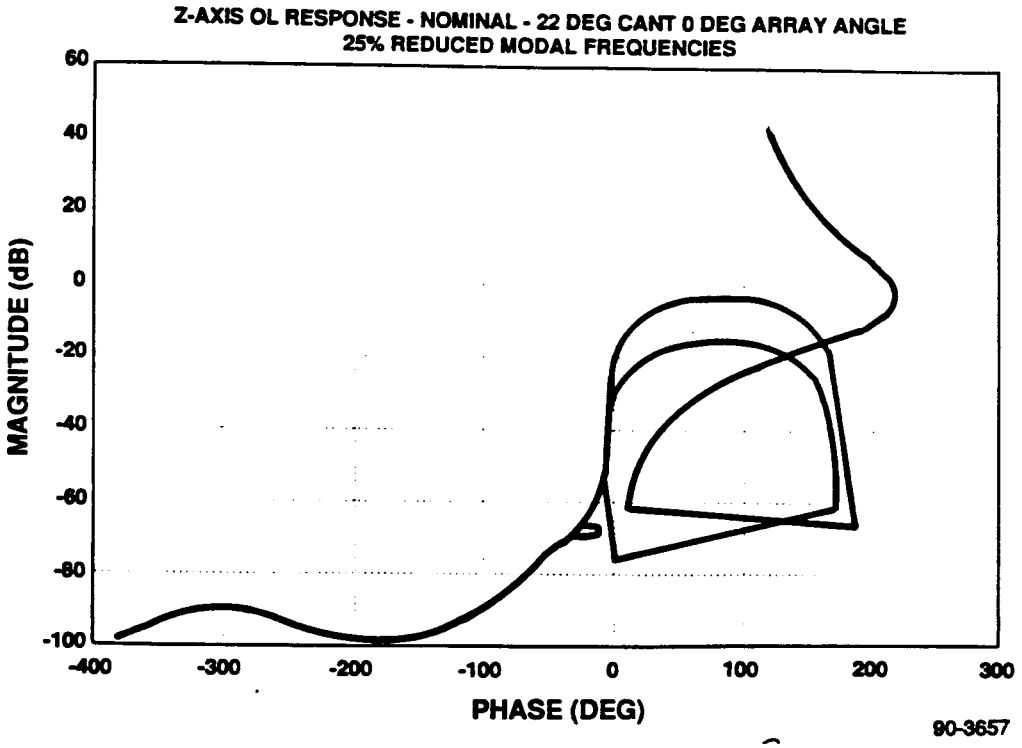

Figure 4.4.6-13c. Nominal Mode - Pitch Open Loop Response

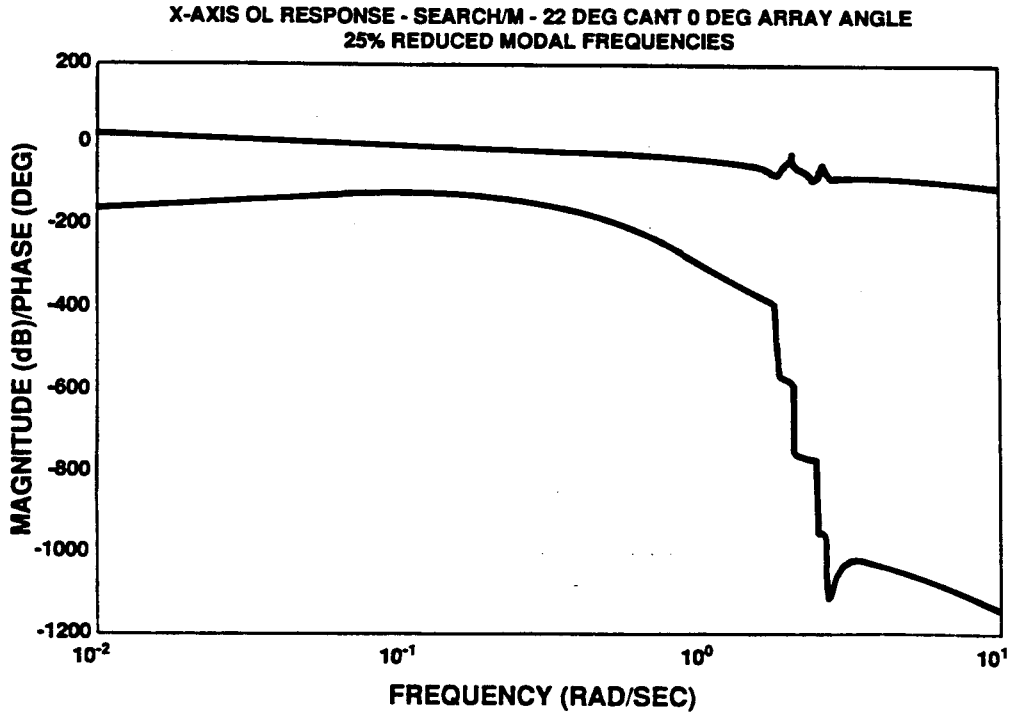

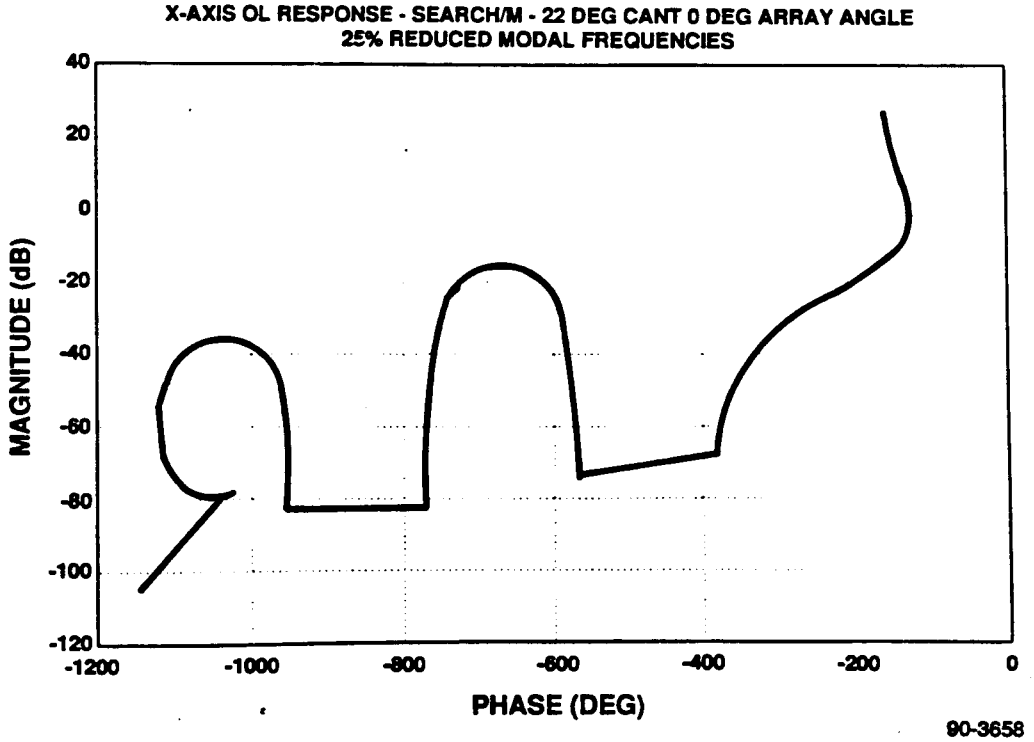

Figure 4.4.6-14a. RN/Search Mode - Yaw Open Loop Response

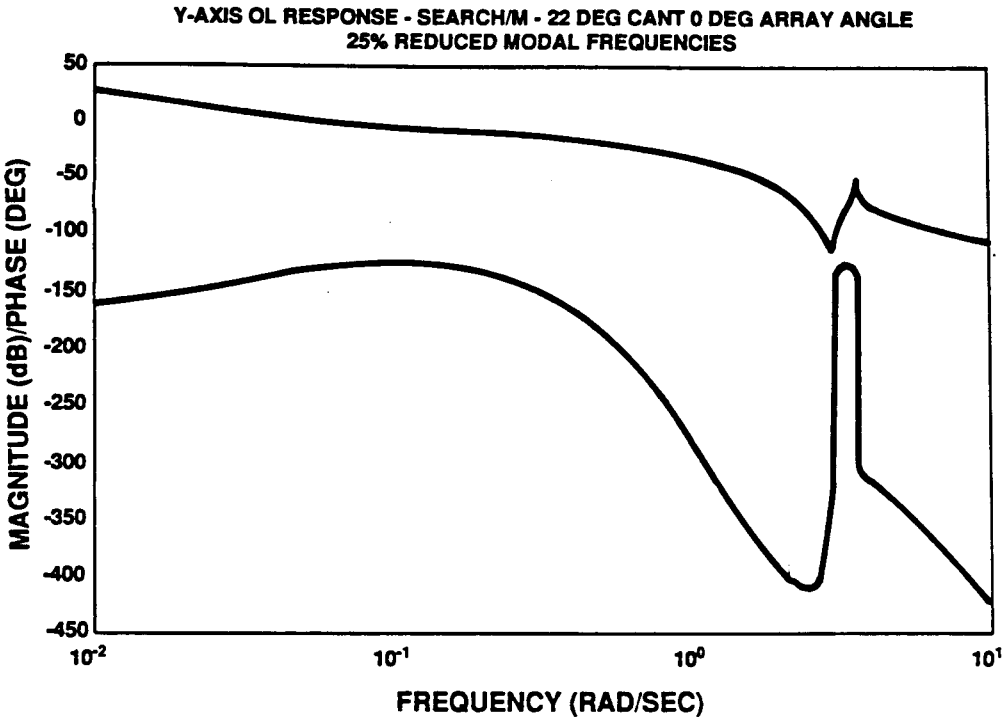

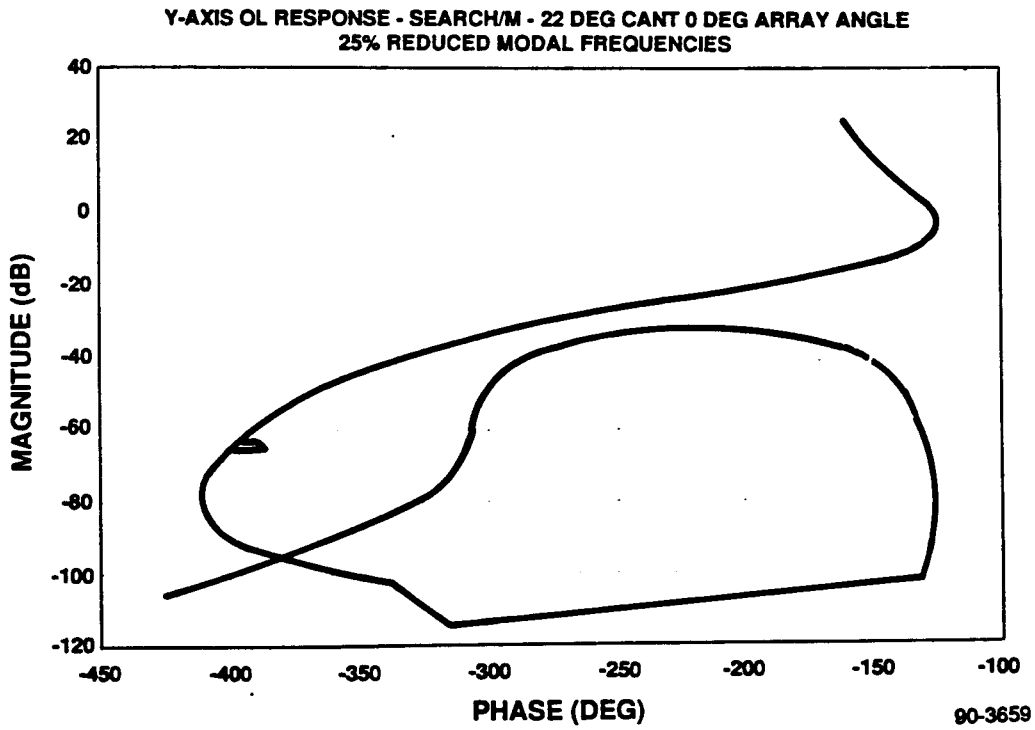

Figure 4.4.6-14b. RN/Search Mode - Roll Open Loop Response

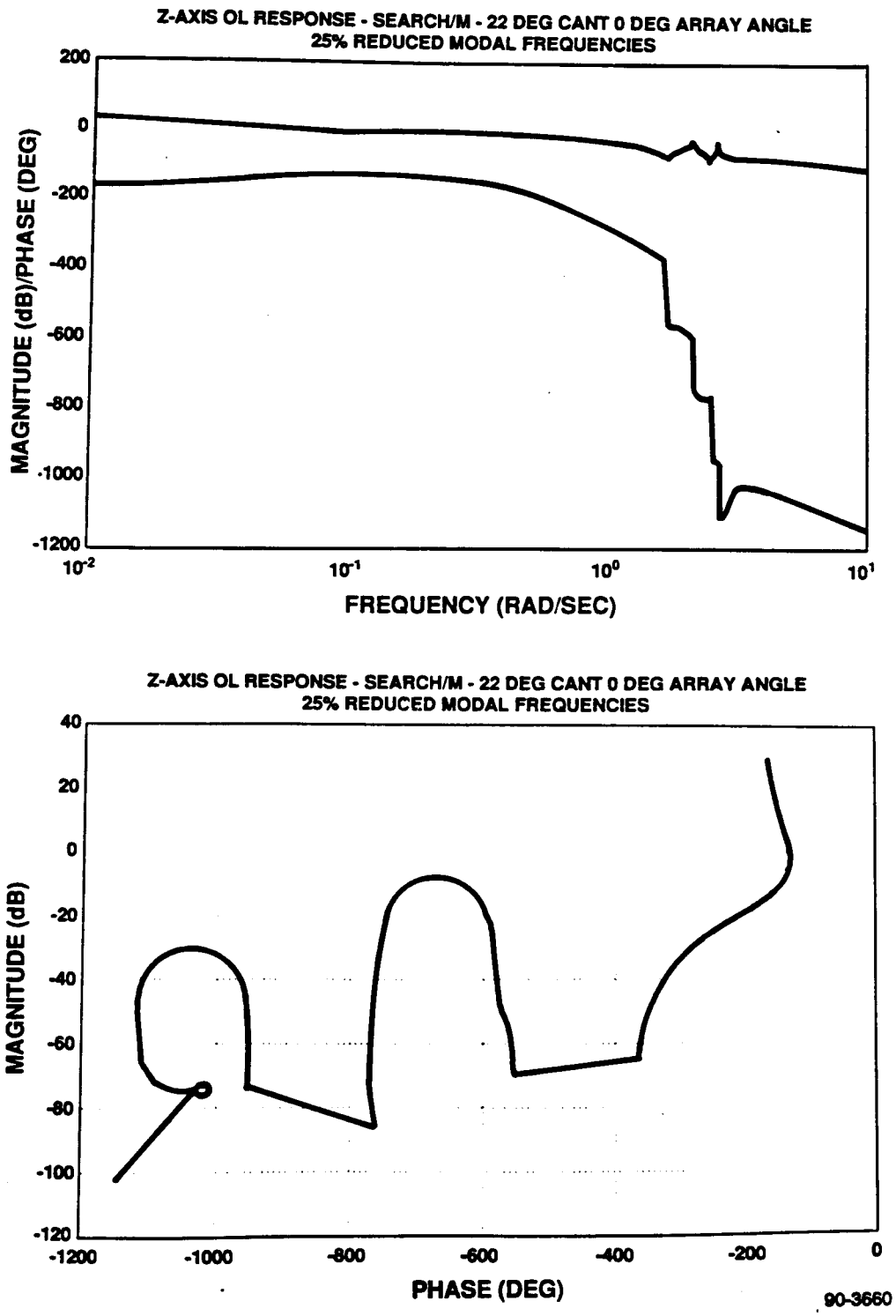

Figure 4.4.6-14c. RN/Search Mode - Pitch Open Loop Response

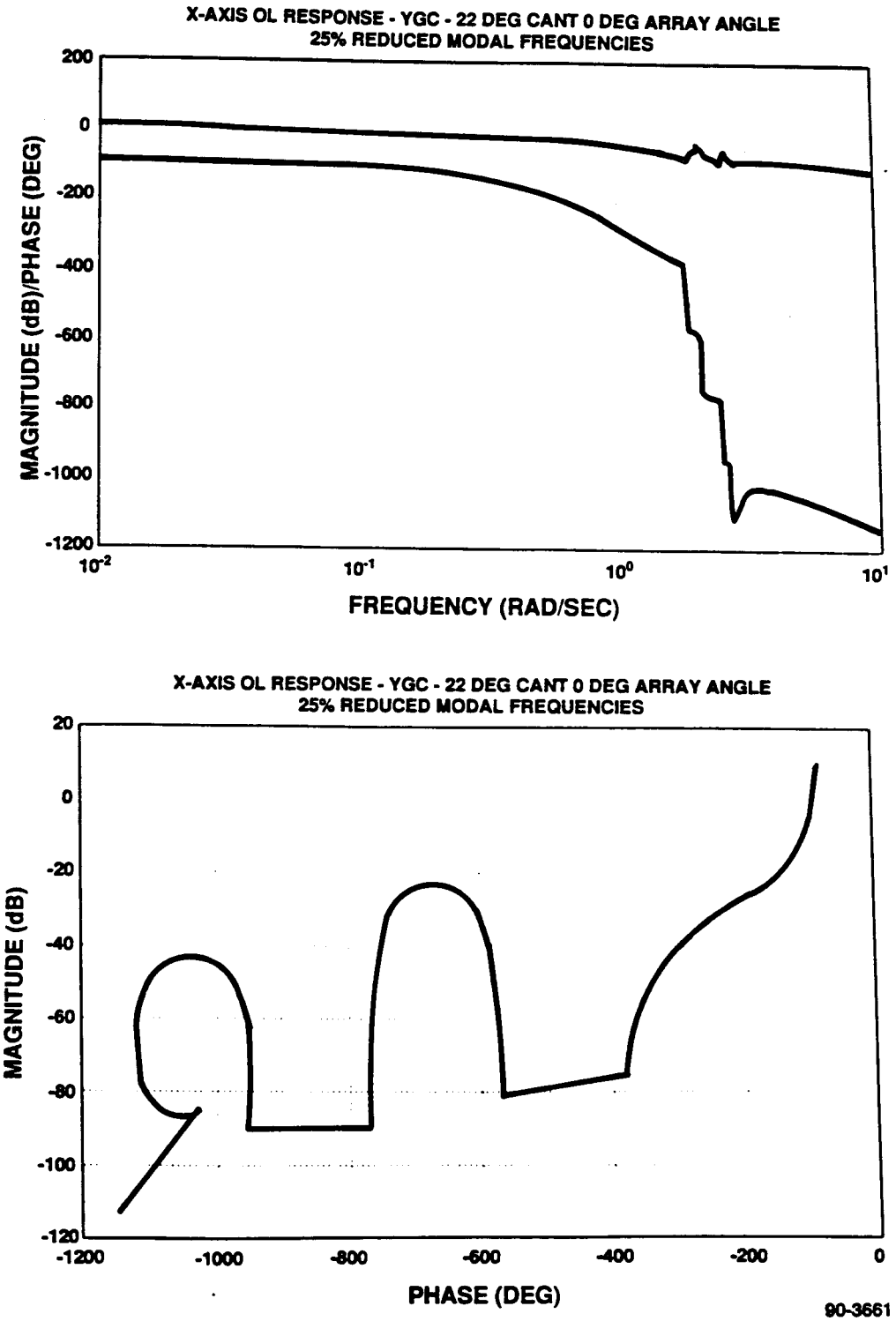

Figure 4.4.6-15a. YGC Mode - Yaw Open Loop Response

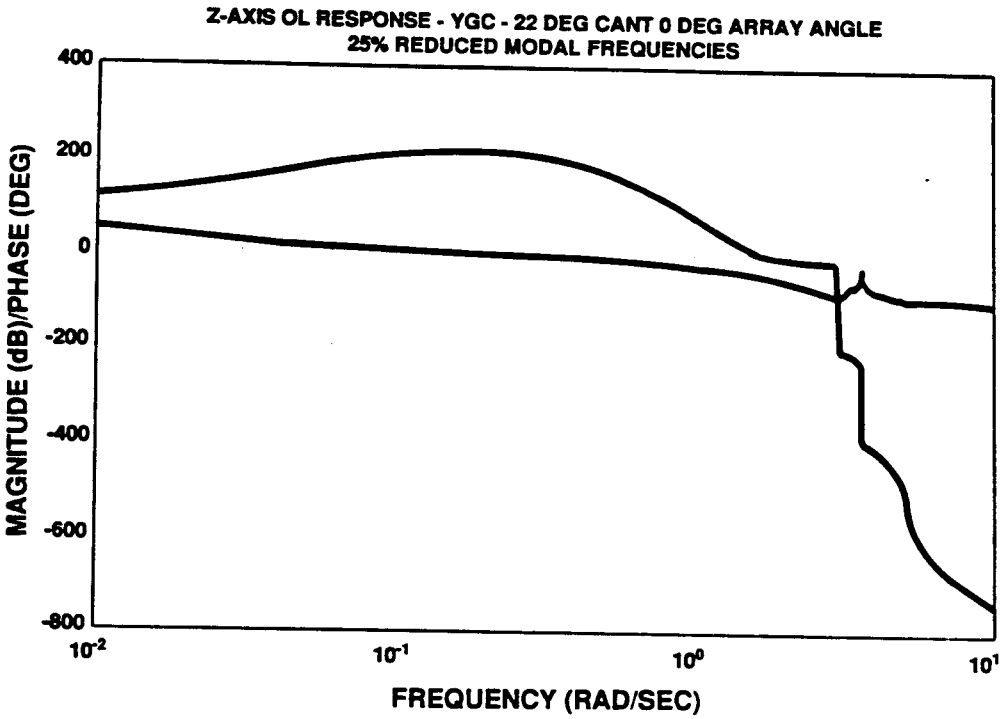

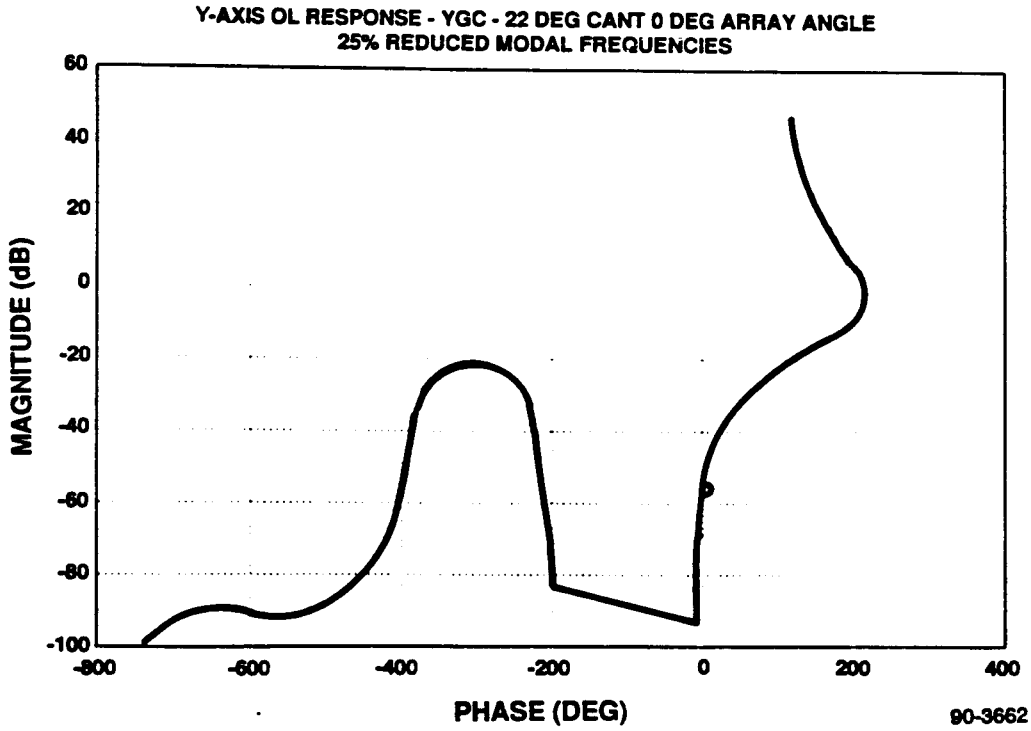

Figure 4.4.6-15b. YGC Mode - Roll Open Loop Response

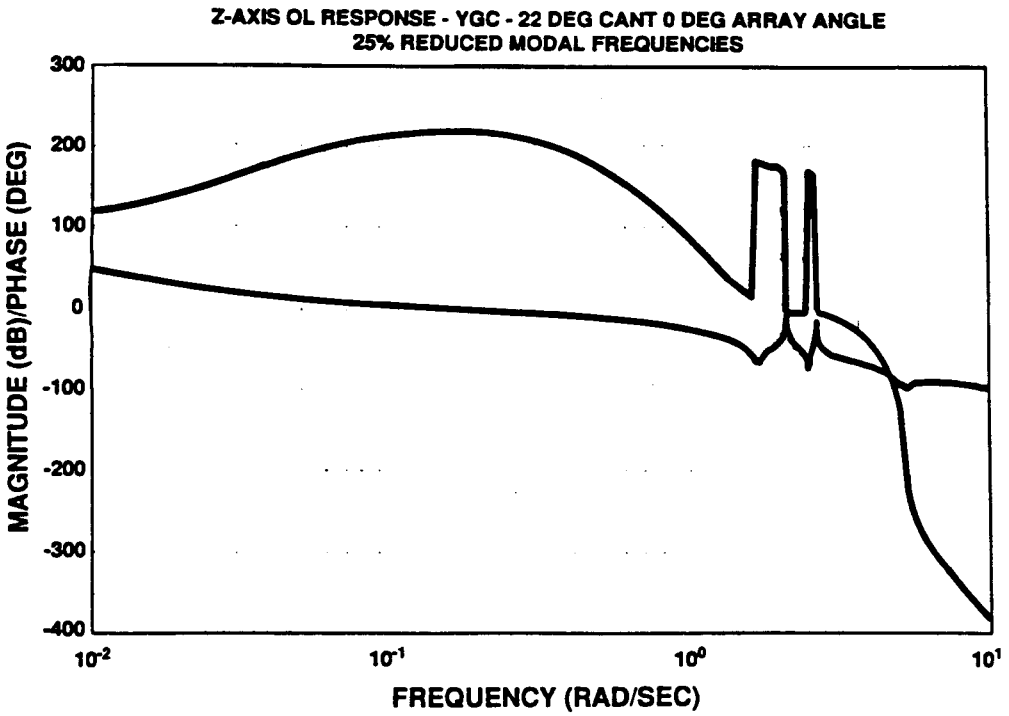

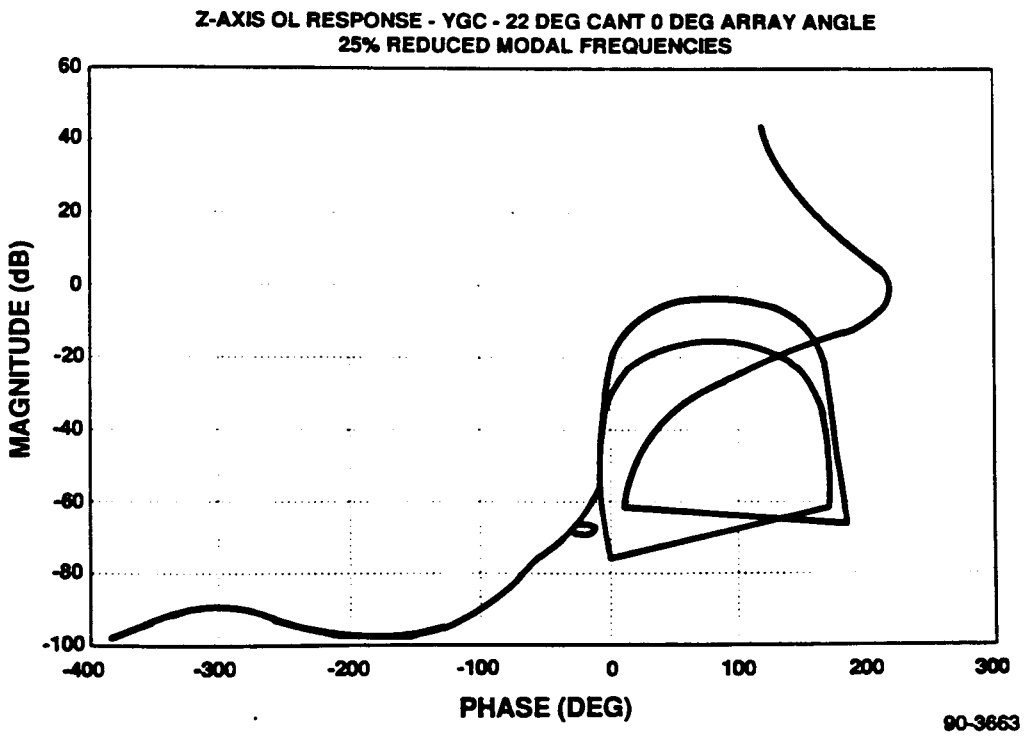

Figure 4.4.6-15c. YGC Mode - Pitch Open Loop Response

TABLE 4.4.7-1. ADACS ERROR BUDGET

	Yaw (degrees)	Roll (degrees)	Pitch (degrees)
Bias			
ESA Alignment		0.025	0.025
SSA Alignment	0.008		
RSS Bias	0.008	0.025	0.025
Long Term Varying			
ESA Long Term Errors		0.064	0.087
Earth Oblateness		0.019	0.019
Uncompensated Gyro Drift	0.019		
Integrated Gyro Random Drift	0.027		
SSA Long Term Varying	0.038		
Ephemeris Uncertainty	0.064		
Attitude Control Tolerances	0.100	0.100	0.100
RSS Long Term Varying	0.129	0.120	0.134
Short Term Varying			
ESA Short Term Errors		0.033	0.033
Solar Array Stepping			0.002
Solar Array Rate Change	0.001	0.001	0.010
AMSU (A1, A2 and B)	0.005	0.010	0.005
All Other Instruments		0.010	
RSS Short Term Varying	0.005	0.036	0.035
Total Pointing Uncertainty	0.142	0.181	0.194
Pointing Requirement	0.200	0.200	0.200
Margin	0.058	0.019	0.006

4.4.8 HARDWARE COMPONENTS

4.4.8.1 Earth Sensor Assembly (ESA)

The Earth Sensor Assembly (ESA) provides spacecraft pitch and roll data to the Attitude Determination and Control subsystem. The ESA is a static infrared horizon sensor designed to operate over an altitude range of 400 to 500 nautical miles with optimum sensitivity in the 14 to 16 micron (CO_2) band. The ESA independently views a segment of the horizon in. each of four quadrants; four corresponding sets of digital horizon measurement data are obtained and provided to the on-board data processors for pitch and roll attitude determination to an accuracy of better than 0.1 degree (3 sigma). The field of view geometry of the detectors and optics was chosen to provide attitude data that is independent of levels of earth radiance.

A major design feature of the ESA is an offset radiation source (ORS) which reduces the net radiation loss to space from each of the four optical channels to near zero. This radiometric biasing of the sensor reduces errors arising from variations in detector responsivity and permits more accurate processing of differential radiant signals containing attitude information.

An overall simplified functional block diagram of the ESA is shown in Figure 4.4.8-1. A commutator is used to sample each of the 12 detector assembly outputs to produce a 25 Hz pulse train. A low-noise preamplifier provides the proper drive levels for the analog to digital converter. The digitized radiance signals are then formatted and provided on request to the Controls Interface Unit. The digitized radiance signals from the four space-viewing

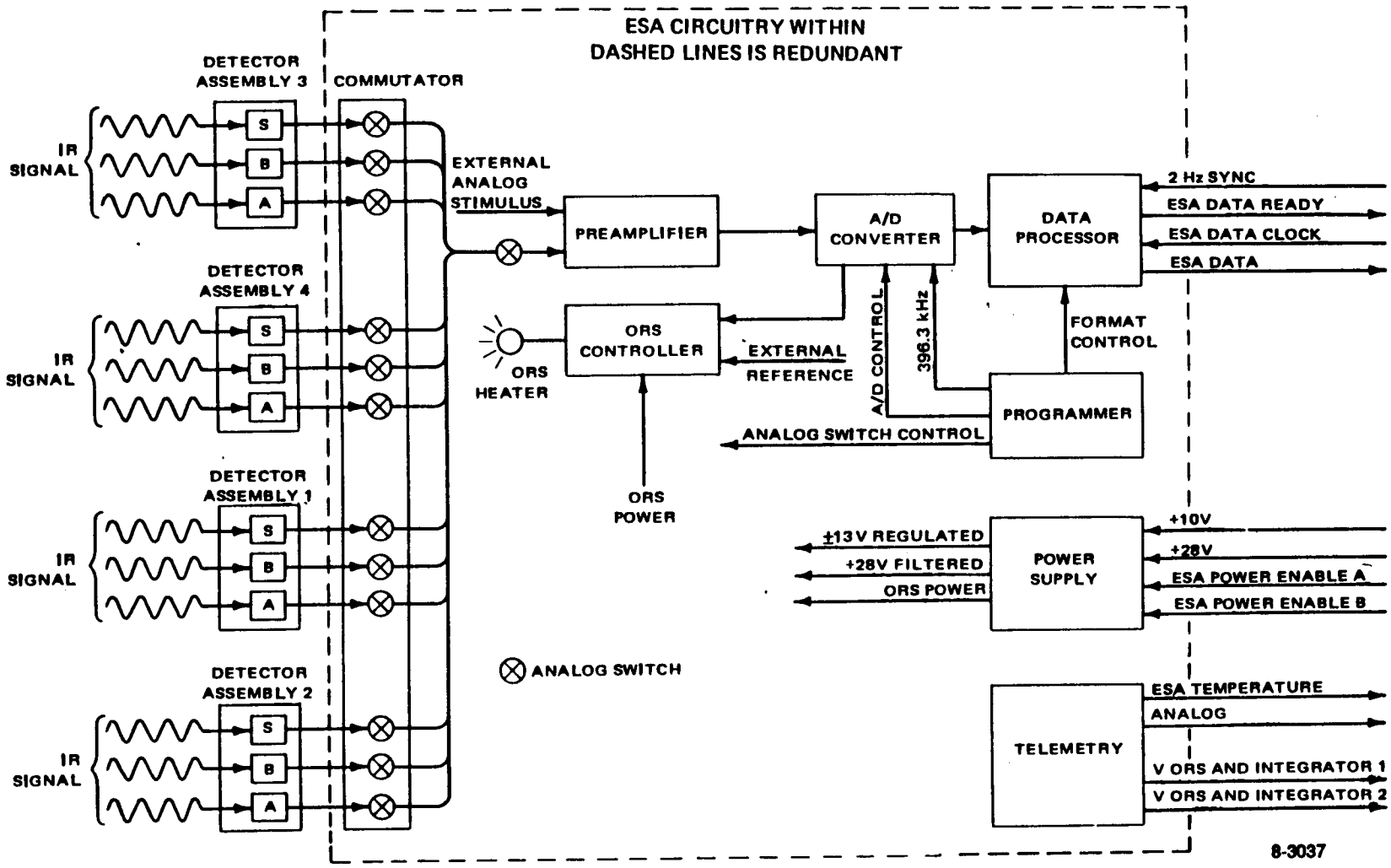

Figure 4.4.8-1. Earth Sensor Assembly Functional Block Diagram

detectors are also fed from the A/D converter to the ORS controller, where they are used to regulate the amount of heat (radiance) generated by the ORS. Analog signal switching, A/D conversion, and formatting of the output data is under the control of the programmer.

4.4.8.1.1 Design Description

The ESA has four objective lenses which focus segments of the horizon on four detector assemblies as shown in Figure 4.4.8-2. Each detector assembly is equivalent to a four channel dc radiometer sharing a common objective lens. An individual channel consists of a six-element thermopile detector placed behind a tetrahedron shaped optical cavity.

Triangular field lenses are located at the entrance of the four optical cavities in each detector assembly. These lenses restrict the view angle of the detectors to the solid angle subtended by the objective. This unique optical configuration projects the four triangular fields of view, established by the field lenses, toward the earth's horizon. Band-pass filters are deposited on the field lenses to limit the sensitivity of each optical channel to energy in the 14 to 16 micron spectral band.

To compensate for the radiation lost to space from the detectors, an offset radiation heat source (ORS) is incorporated. The ORS heater is controlled by the most negative output from the four space-viewing detectors, with the heater power varied until the most negative signal is nulled. The ORS thereby provides a radiation bias to the detectors, offsetting the radiation lost to space.

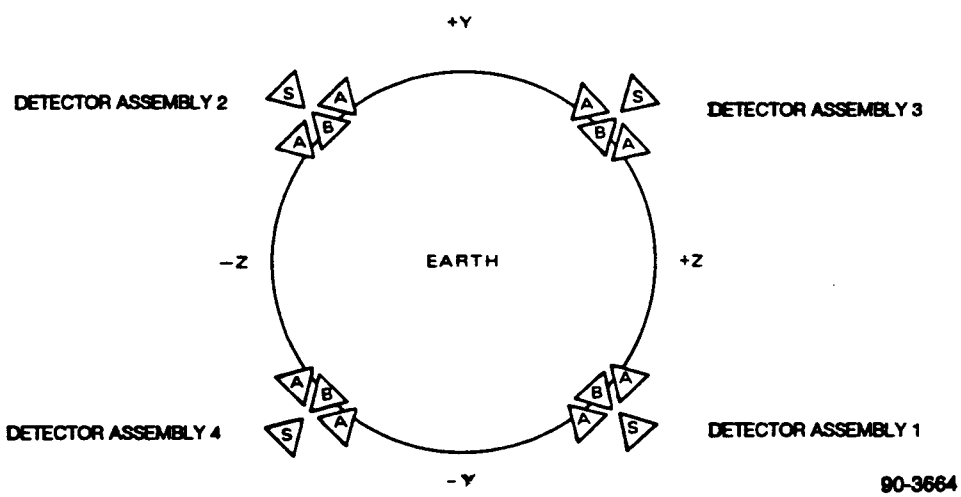

Figure 4.4.8-2. ESA Sensor Fields of View

4.4.8.1.1.1 Design Approach

4.4.8.1.1.1.1 Basic Design Concept. The basic principle of operation of the ESA is a "double-triangle" concept as shown in Figure 4.4.8-3. The simple geometric relationship that exists between the A and B fields of view independently establishes the horizon with respect to the sensor for each of the four

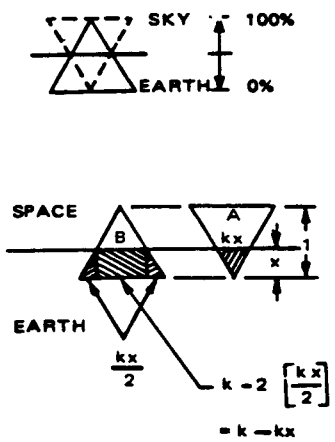

$$\text{AREA}_A = \frac{(kx)(x)}{2} = \frac{kx^2}{2} = k(0.5x^2)$$

$$\text{AREA}_B = \frac{Kx^2}{2} + x[k - kx] = kx - \frac{Kx^2}{2} = k(x - 0.5x^2)$$

$$\text{VOLTAGE}_A = K[N]k(0.5x^2)$$

$$\text{VOLTAGE}_B = K[N]k(x - 0.5x^2)$$

$$\frac{V_A}{V_B} = \frac{K[N]k(0.5x^2)}{K[N]k(x - 0.5x^2)} = \frac{0.5x^2}{x - 0.5x^2}$$

$$V_A\, x - 0.5x^2\, V_A = 0.5x^2\, V_B$$

$$0.5x^2(V_B + V_A) = V_A\, x$$

$$0.5x = \frac{V_A}{V_B + V_A}$$

$$x = \frac{2V_A}{V_A + V_B} = V_x$$

8-3039

Figure 4.4.8-3. Sensor Basic Principle and Derivation

horizon segments viewed. The S field of view contained in each field of view cluster provides a space radiation reference measurement.

The field of view geometry was chosen to provide attitude data that is independent of levels of earth radiance. The outputs of the two A field detectors within each detector assembly are connected in parallel to minimize errors from radiance gradients along the horizon. Since both the A and B fields sense essentially the same segment of the horizon, errors from radiance gradients in the direction perpendicular to the horizon are also reduced. This "double-triangle" measurement technique enables the ESA to measure pitch and roll attitude to an accuracy of better than 0.1° (3 sigma).

The 12 independent detector outputs (three in each of the four detector assemblies) are sequentially sampled by a low-level MOS-FET commutator. After amplification, the outputs are converted to 16-bit digital words and supplied to the spacecraft data processor for attitude computation.

4.4.8.1.1.1.2 Radiation Compensation. A thermopile output is proportional to the difference in temperature between its active and reference junctions. Junctions viewing space or cold earth radiate heat and become colder than their reference junctions; the result is a large amplitude detector output. Changes in the horizon image within this field would appear as small changes in this large negative voltage, producing a problem of detecting a small change in a large voltage.

To circumvent this problem, the output of a space viewing detector is used to subtract out the large negative signals generated in the horizon viewing detectors. If a detector with perfectly matched responsivities were available, no other corrections would be necessary; however, detectors can only be matched imperfectly (approximately 1 percent) and further means of reducing space generated voltages are required. One correction is accomplished by using an offset radiation source (ORS) to compensate for heat lost to space by the detectors.

The offset radiation source consists of a thermal radiator located in the common optical aperture of the sensors and controlled by an electronic servo to drive the most negative space reference detector signal to zero. The space viewing detector, in addition to providing a reference for the horizon sensing detector, also acts as the error sensor for the ORS electronic servo. The radiation source, about 0.2 inch in diameter, is enclosed in a reflective spherical housing; this source replaces the radiation the detectors are emitting to space and reduces the large offset signal to zero.

Germanium lenses image the ORS heater into four 23 mm diameter field mirrors that are cemented to the rear surface of each objective lens. The ORS field mirrors image the Germanium lenses onto the four field lenses in the corresponding detector assembly. Since the ORS is imaged on the field mirror and not the field lenses themselves, any variations in the ORS heater emittance will be uniformly distributed over the field lenses.

An Irtran 2 ball, used as the radiation source, is heated by a resistance element that is conductively attached to the underside of the ball. Irtran 2 was selected to conserve electrical power by spectrally limiting the energy emitted by the heaters. The emittance of Irtran 2 is high in the spectral pass band; at wavelengths below 12 microns, it is very transparent and therefore a poor emitter. To achieve the required radiance compensation, the Irtran 2 must be controlled at 430°K (157°C) for an ambient temperature of 27°C. To further conserve radiation loss, the source is surrounded by a polished, spherical, gold-plated enclosure. Radiation from the source is reflected back upon itself except for the area occupied by the four Germanium ORS lenses.

The ORS radiation received by each of the detectors, to a first order approximation, is the same. However, because of manufacturing tolerances, non-uniformity of transmission of the lens materials, temperature gradients, differences between detector assemblies and other minor variations, the corresponding detector outputs will not be matched to the degree necessary to achieve the overall accuracy. Fine adjustment occulting screw shanks are therefore provided on the upper ORS housing, directly behind the four lenses. The location of these screws is such that each one intersects only the radiation directed to a single detector cavity. Because each screw shank is located behind and close to an ORS lens, it will form a blurred image on one detector field lens. The screws are engaged in and heat sunk to the aluminum upper enclosure and therefore are maintained at approximately ambient ESA temperature, which is well below the ORS source temperature. Consequently, the radiation received by each detector will be diminished in proportion to the occulted area of each of the screw shanks.

4.4.8.1.1.1.3 Thermal Design. The susceptibility of a static sensor employing thermopile detectors to thermally caused errors was a major consideration in the system design. This restriction applied not only between detector substrates but to the components in the viewing (optical) path of the detectors as well. Ideally, all detectors receive exactly the same radiation from the instrument interior and the optical elements.

The four optical cavities are contained within the same detector block to achieve an extremely small temperature gradient between the four detectors in each cluster. If a temperature gradient should exist on the main support casting of the ESA, such as from the sun impinging on one side of the ESA or

from a gradient on the vehicle mounting flange, the resulting gradients on the detector assembly are negligibly small. This is achieved by a two-stage thermal isolation design. The optical cavity block is mounted using two foamed epoxide (Eccostock R20) sleeves placed over the two trunnions of the block; the sleeves are than clamped to a one-piece aluminum cradle that is mounted to a thermally isolated mounting ring. This thermal ring is attached to the main casting by four insulating standoffs made from the same foamed epoxide material. Four cradles and detector cavity assemblies are mounted to the ring for the four optical channels.

The main casting, thermal ring, cradle, and detector block are all made from aluminum, are relatively massive, and are effectively excellent thermal shunts. The four standoffs and two sleeves on each cavity block have large thermal impedances. The temperature gradient on the thermal ring, caused by a gradient on the main casting, will be diminished by the ratio of the thermal impedances of the ring and standoffs; this gradient is reduced further by the cradle. Finally, the gradient is made negligibly small by the impedance ratio of the cavity block and sleeves.

Thermal conduction of the detector leads has also been considered. The 0.005 inch diameter lead wires are relatively long, of equal length, and terminated on the thermal ring in a common location; therefore, their gradient contribution is negligible.

Radiation interchange between the detector assembly block and its surroundings is minimized by gold plating the exterior surfaces to achieve a low emissivity. The thermal ring and cradle are also gold plated. The inner surfaces of the main casting and upper housing of the ESA are blackened with paint, which serves to reduce the gradient on the housing and provide a more uniform heat sink to the critical components.

The results of a thermal analysis indicate that, if a very conservative 1°C temperature gradient is assumed on the main casting and upper housing, it will result in less than 0.001°C gradient on the detector assembly block. The effect of even this small gradient will not be fully realized; the B and S detectors are symmetrically located between the two A detectors, and the system error is proportional to the temperature difference between the B and S detectors and the average of the two A detectors. If the gradient is assumed to be linear between the detector/cavity assembly trunnions, it is apparent that no signal error would be produced by this thermal condition.

A thermal analysis was performed on the ORS assembly; the results are summarized as follows:

- 250 milliwatts power is required for the spherical Irtran 2 source to reach 157°C in a vacuum;
- The time constant of the temperature rise is approximately 37 minutes;
- The temperature of the upper and lower enclosures is within 3°C of the ESA ambient temperature;

- The maximum temperature difference from the top to the bottom of the Irtran heater is 0.3°C; and,

- Approximately one-third of the power input is radiated and transmitted through the four ORS field lenses.

4.4.8.1.1.1.4 Electronic Processing. Careful design is necessary to insure equal radiation on the thermopile detectors from the optical elements of the sensor and it is equally important to avoid offsets in the electrical output signals. Changes in leakage current, voltage levels, and gain between channels must be eliminated. A functional block diagram of the processing electronics is shown in Figure 4.4.8-4.

Only one electronic processing channel is used and all the detector outputs are multiplexed into this channel, thus automatically eliminating many causes of channel asymmetry. Restricting the sampling rate and keeping the detector impedances relatively low forestalls any memory or cross-coupling effects (incomplete discharge between samples). Thus the fidelity of the balance achieved by the optical and thermal design is maintained by the electronic processing circuitry.

4.4.8.1.1.2 Operating Modes. Power to the ESA is controlled in response to 2 control signals from the Command and Control Subsystem:

- ESA Power Enable A
- ESA Power Enable B

The ESA Power Enable A control signal sets latching relays to connect the power and signal leads to the side A set of redundant electronics and to disconnect the power and signal leads from side B set of electronics. Similarly, the ESA Power Enable B control signal sets latching relays to connect the side B electronics and to disconnect the side A electronics.

Note that either side A or side B in the ESA is always turned on; no provision is made for turning off the ESA.

4.4.8.1.1.3 Design Characteristics. The design characteristics of the ESA are summarized in Table 4.4.8-1.

4.4.8.1.1.4 Physical Description. The ESA is contained within a single cylindrical housing as shown in Figure 4.4.8-5. The ESA is installed on the spacecraft using the mounting adapter shown in Figure 4.4.8-6; the ESA is inserted into the mounting adapter and attached to it at the mounting flange. The mounting adapter is attached to the IMP near the -Y, -Z corner.

The relationship between the spacecraft reference axes (X, Y, Z) and the ESA sensing axes (X_{es}, Y_{es}, Z_{es}) is shown in Figures 4.4.8-5 and 4.4.8-7. As shown, the $-Y_{es}$ and $-Z_{es}$ axes are in the Y-Z plane and are displaced 45° with respect to the spacecraft -Z and +Y reference axes, respectively.

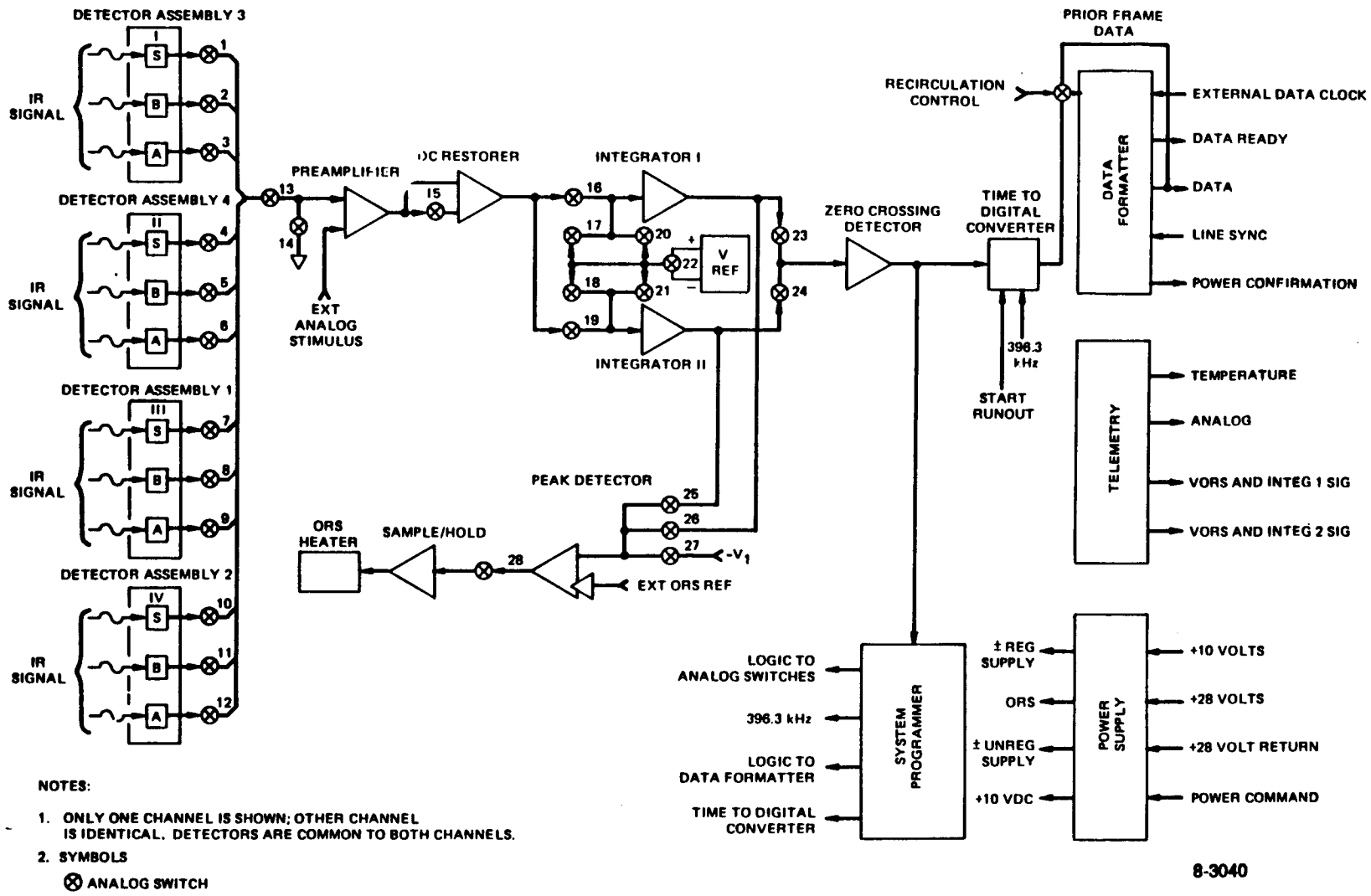

NOTES:

1. ONLY ONE CHANNEL IS SHOWN; OTHER CHANNEL IS IDENTICAL. DETECTORS ARE COMMON TO BOTH CHANNELS.
2. SYMBOLS
   ⊗ ANALOG SWITCH

Figure 4.4.8-4. Processing Electronics Functional Block Diagram

TABLE 4.4.8-1. EARTH SENSOR ASSEMBLY CHARACTERISTICS

Characteristic	Value
Design Concept	Static 4-quadrant IR horizon sensor
Spectral Band	14 to 16 microns (CO_2 band)
Detector Field of View	Triangular, 6° on a side
Field of View Center	62.6° from +X axis
Accuracy (3σ at 450 nmi)	
Pitch	0.070°
Roll	0.052°
Data Output	Digital
Warm-Up Time	20 minutes
Redundancy	Dual set of electronics
Size	Approximately 7.28 diameter X 13.5 long
Weight	8.9 lbs
Power	1.35 Watts at +28 Vdc

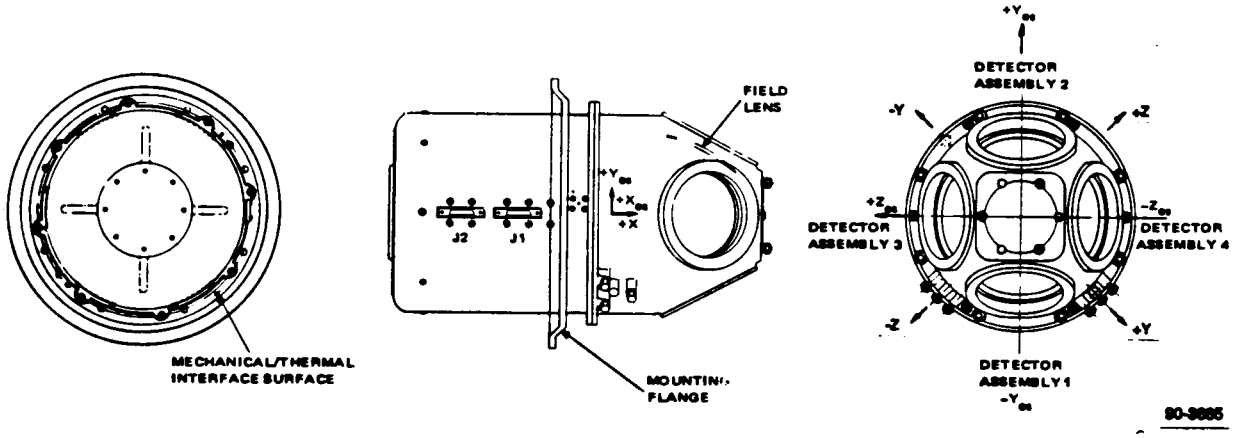

Figure 4.4.8-5. ESA External Configuration

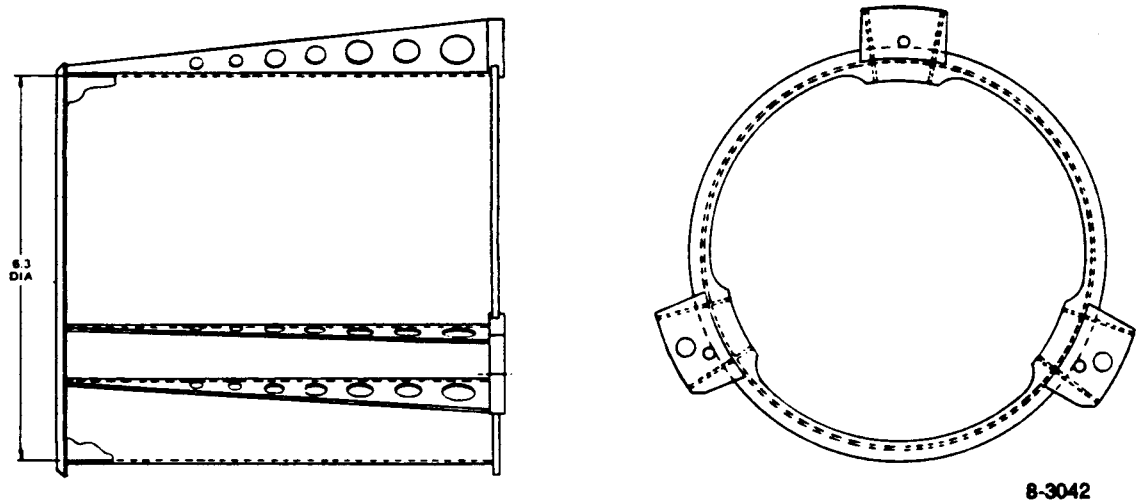

Figure 4.4.8-6. ESA Mounting Adapter

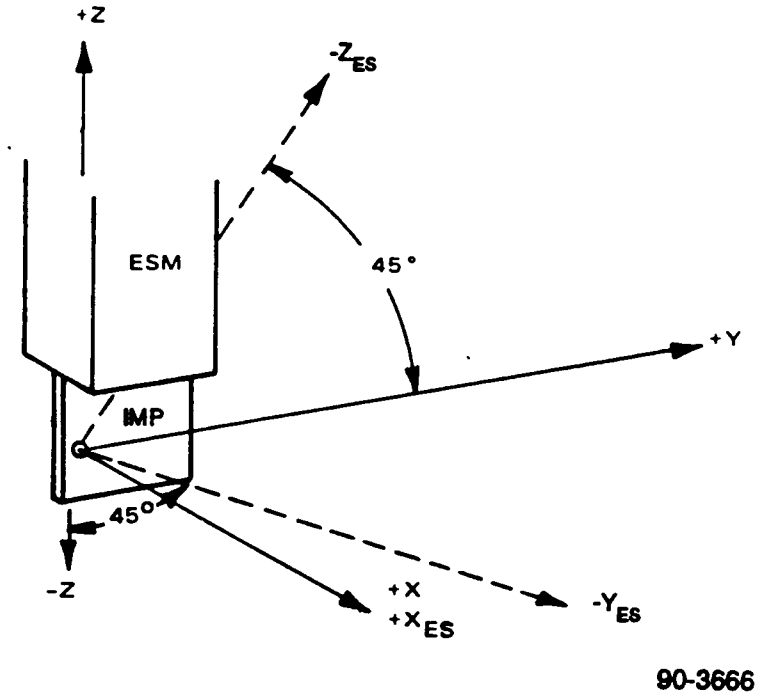

Figure 4.4.8-7. ESA Coordinate System Definition

The internal configuration of the ESA is shown in Figure 4.4.8-8. This figure shows the major mechanical, optical, and thermal components of the ESA.

4.4.8.1.1.4.1 Mechanical Components. The major mechanical components of the ESA are:

- Main support casting
- Upper housing casting
- Thermal ring
- Preamplifier board
- ORS assembly
- Electronics module
- Detector assemblies

Within the ESA, a centrally located main support casting serves as the primary structural member to which most of the major subassemblies are mounted. This casting also provides the main interface mounting flange to the ESA mounting adaptor. The casting consists of a tubular center, a flat plate, and an outer ring; eight radial ribs provide axial as well as radial stiffness. The main support casting is fabricated from A356-T6 aluminum with a nominal wall thickness of 0.05 inch.

The upper housing casting is cylindrical in the lower section and a truncated pyramid shape in the upper section to provide the mounting surfaces for the four objective lenses, cells and retaining rings. This casting is also fabricated from A356-T6 aluminum with a nominal wall thickness of 0.050 inch.

The thermal ring has a modified 'T' shaped cross section, and is attached to the main support casting by four insulating standoffs. The thermal ring provides a very stiff and light weight mounting surface for the four detector assemblies with their mounting cradles.

The preamplifier board is supported near the outside of its periphery by the four insulating standoffs that support the thermal ring. The standoffs are sectioned to clamp the board about midway along their length. Near its center, the board is attached directly to the main casting.

The ORS assembly is mounted to the main casting near the center of the ESA; the ORS field mirrors are mounted on the back of the objective lenses.

The electronics module is mounted to the rear side of the main casting, with the printed circuit boards stacked parallel to each other. The power supply board is circular and mounted to the end of the stack; a thin aluminum cover encloses the electronics module. Vents, with fine wire mesh screening, allow the unit to 'breathe' and to evacuate when entering a vacuum environment.

The electronics module is designed so the printed circuit boards provide most of the structural support. Four corner posts, attached to the main section casting at one end, serve to form a frame for a box-like structure. A parallel stack of 10 boards is mounted within this structure. The two outer circuit boards and 2 aluminum shear plates enclose the box on four sides; the

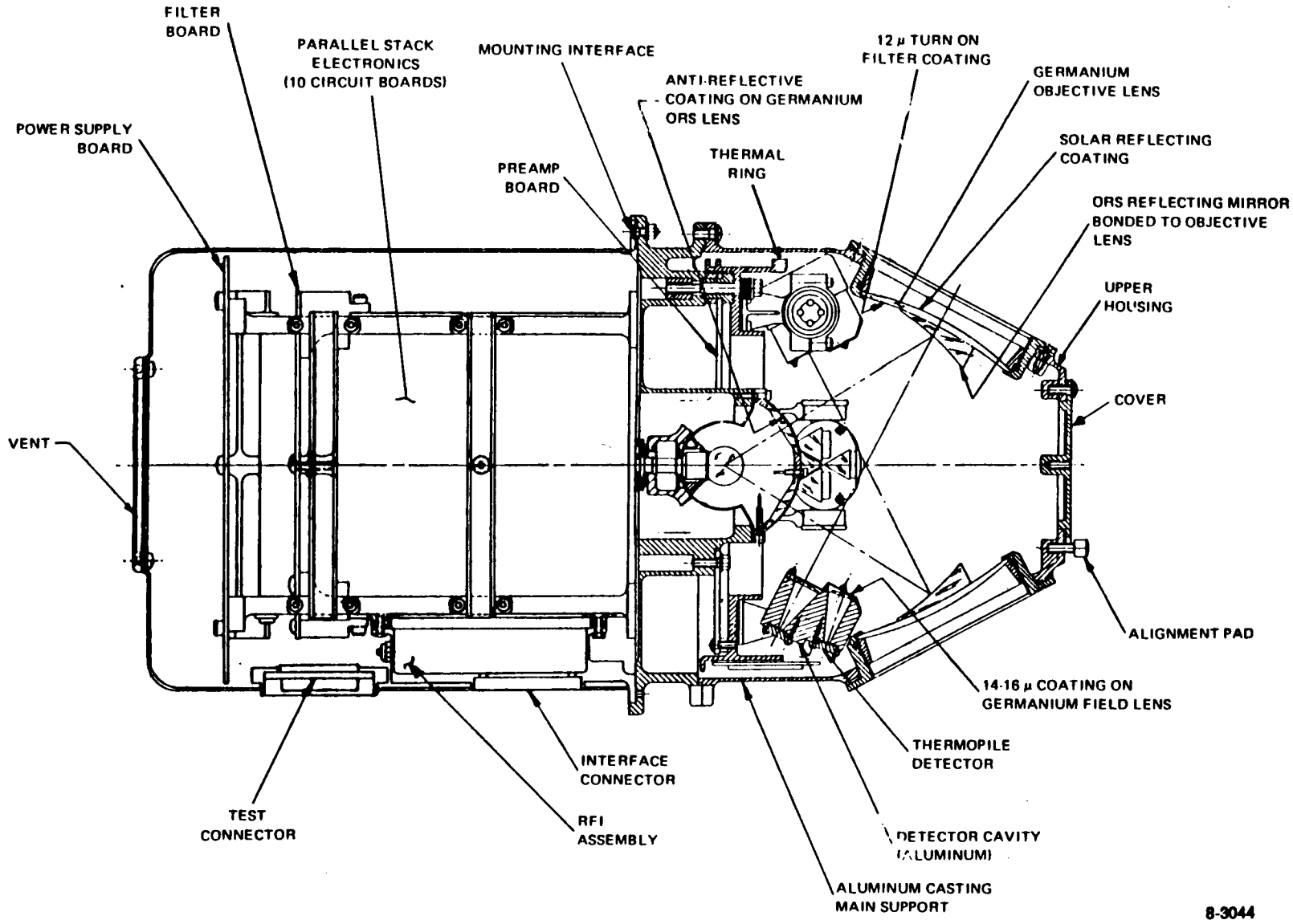

Figure 4.4.8-8. ESA Cross-Sectional Configuration

remaining eight enclosed circuit boards are supported along two edges of the shear plates. The shear plates also provide support to the wire harness and are used for attaching the RFI shield box of the main input connector to the housing. A support rod, with spacers between each board, passes through the center of all 10 boards to minimize "oil-canning"; it is attached at both ends to two channel-shaped bridges that span between the corner posts on both ends. The power supply is mounted at four points to the ends of the corner posts as well as three points across the center for a total of seven mounting points.

Although its primary function is not structural support, the outer thin walled housing does assist in increasing the package stiffness. Attachment points are located around its flange for attachment to the main casting, to the center of both support bridges, to the corner posts just below the power supply, and to the RFI box.

4.4.8.1.1.4.2 Optical Components. The major optical components in the ESA are:

- Objective lens
- Detector assembly
- ORS assembly

These optical components and the principal ray paths between them are shown in Figure 4.4.8-9. The major optical component characteristics are shown in Table 4.4.8-2.

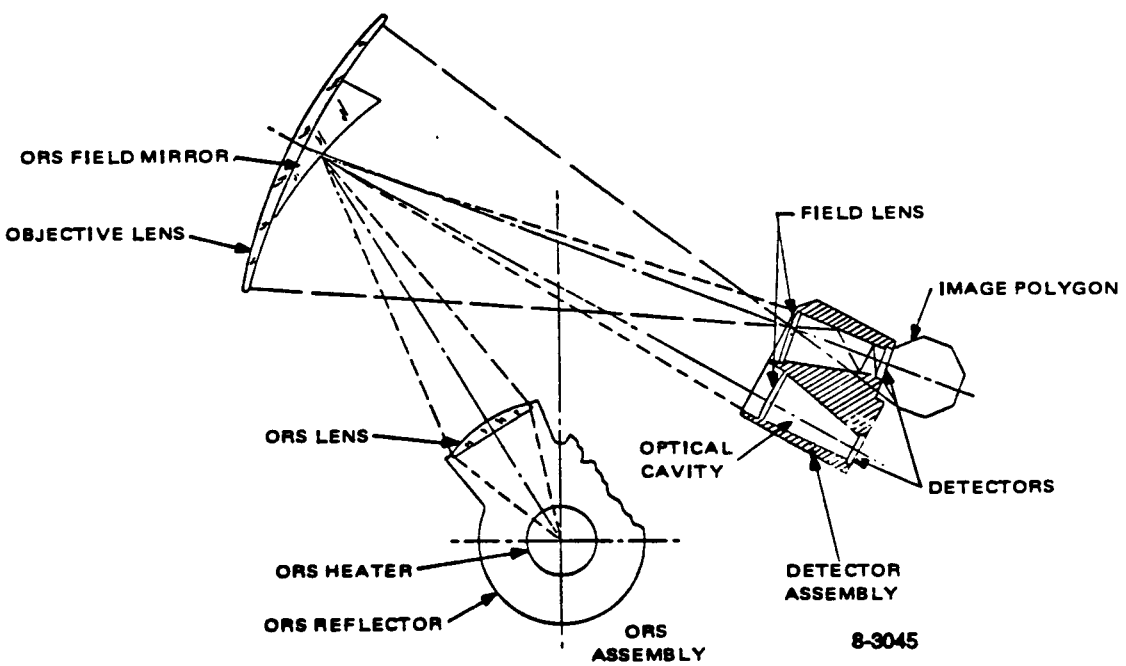

Figure 4.4.8-9. Optical Ray Paths

TABLE 4.4.8-2. OPTICAL COMPONENT CHARACTERISTICS

Parameter	Value
Objective Lens	
Diameter	59 mm
Material	Germanium
Focal Length	f/1.7
Front Surface Coating	Reflect 80% of solar energy in 0.4 to 2.4μ spectral band
Rear Surface Coating	Reflect solar energy and block transmission in 1.8 to 12μ spectral band
Field Lens	
Size	Equilateral triangle 10.74 mm high
Material	Germanium
Clear Aperture	3.43 mm
Lens Coating	Bandpass, 14 to 16μ
Optical Cavities	
Focal Length	f/0.5
Detectors	
Type	6-Element thermopile
Active Materials	Bismuth and tellurium
Active Area	Equilateral triangle, 2.5 mm each side
Responsivity	30 volts per watt
Resistance	13,000 ohms
Time Constant	600 ms in vacuum
ORS Lens	
Diameter	20 mm
Material	Germanium
ORS Field Mirror	
Diameter	23 mm
Material	Germanium
Reflective Surface	Evaporated gold
Reflectance	>97% within 12 to 18μ band

4.4.8.1.1.4.2.1 Objective Lenses. The 4 f/1.7 germanium objective lenses form images of the horizon on the field lenses located at the front of each detector assembly. The front surface of each 59 mm diameter objective lens is coated to reflect 80% of the sun's energy in the 0.4 to 2.4 micron spectral band. The rear surface is coated to reflect solar energy and to block transmission in the 1.8 to 12 micron spectral band.

The upper housing provides the mounting support for the four objective lenses, cells, and retaining rings. The cells and retainers are made from beryllium to match the coefficient of expansion of the germanium objective lens. The exposed exterior surfaces of these parts are polished and coated with gold to reduce solar absorption.

4.4.8.1.1.4.2.2 Detector Assembly. Each of the four detector assemblies contains 4 field lenses, four tetrahedron-shaped optical cavities, and four detectors. A photograph of a single detector assembly is shown in Figure 4.4.8-10. The gold coated and polished surfaces of the optical cavities are achieved by an epoxy optical replication technique. The four tetrahedron cavities are machined slightly oversize into the 6061-T6 aluminum block by an electric discharge machining (EDM) operation. An optically polished stainless steel male master that conforms to the exact final shape of the cavity is first coated with a release agent, followed by an evaporated gold coat. Epoxy is applied to the surfaces of the block as well as the outer surface of the plated master and the master is inserted into the cavity. After the epoxy has cured, the master can be removed from the block; the release agent allows the separation of the master and the gold. The result is that the gold surface is cemented to the block and the inside surfaces conform to the original configuration of the master.

The central axis of the four cavities all converge at a point that corresponds to the nodal point of the objective lens. The field lenses, containing the bandpass filter coating, are cemented into recesses at the top of each of the cavities using Armstrong A12 cement. The detectors are mounted at the opposite (small) end of the cavity using three shoulder screws that serve to precisely locate the detector with respect to the cavity. A 2-mil copper shim is bonded between the detector substrate and the face of the cavity; a thermally conductive adhesive provides good thermal contact.

Thermopile detectors are employed in the ESA because they are well suited for unchopped dc radiometry. The thermopile output is a direct measure of its radiant exchange, and the output is not superimposed on a large electrical bias.

A triangular detector was chosen due to the geometry of the optics. This type of detector is very efficient because its active junctions are centrally located and the reference junctions are located about the periphery of the active junctions. This design was also desirable because it minimizes variations in responsivity across the active area of the thermopile.

The detector contains six junction pairs as shown in Figure 4.4.8-11. The active junctions lie in the target area enclosed in an equalateral triangle 2.5 millimeters on a side, while the reference junctions are outside the target area and are in thermal contact with the detector substrate which acts as a

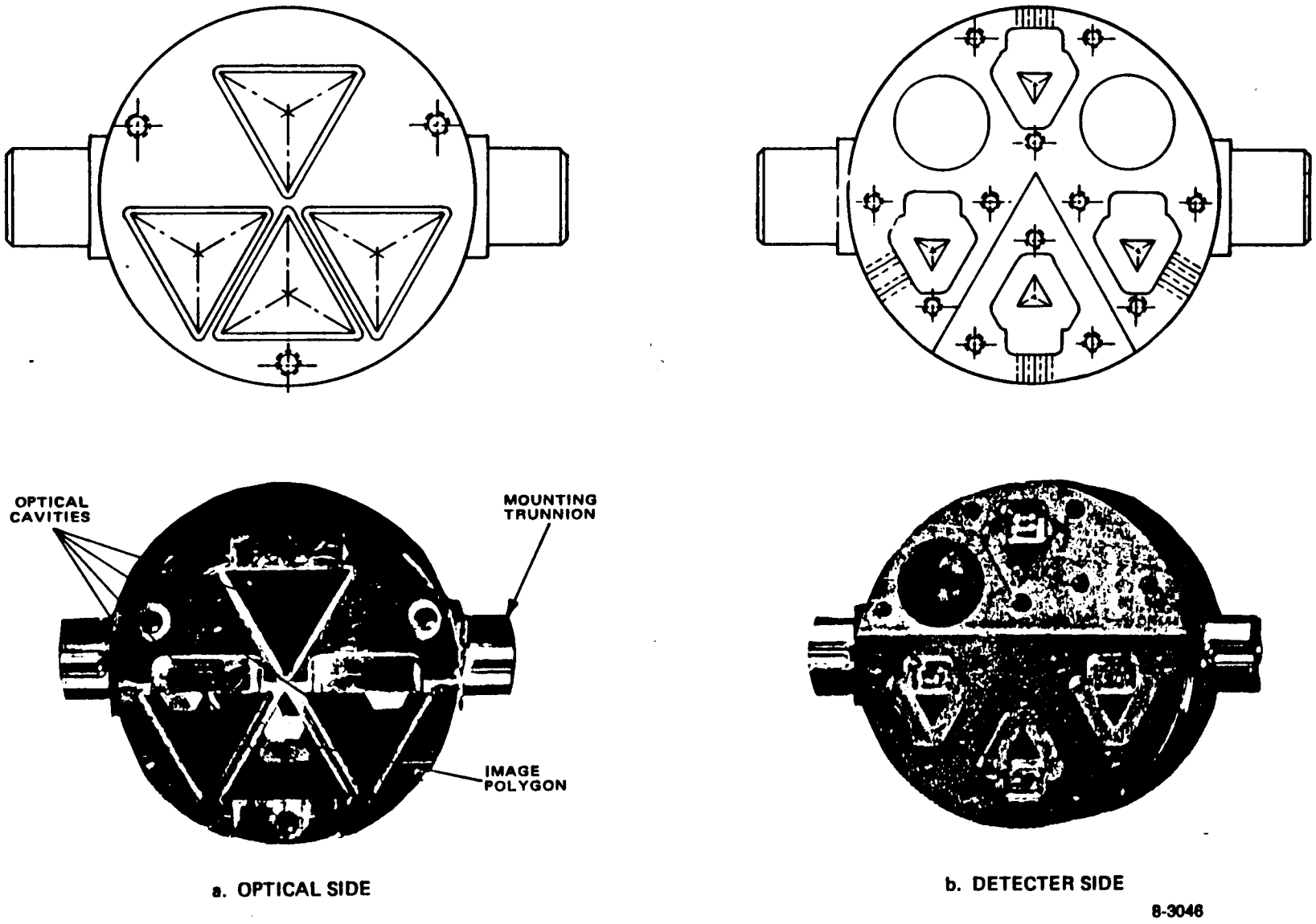

Figure 4.4.8-10. Detector Assembly Block

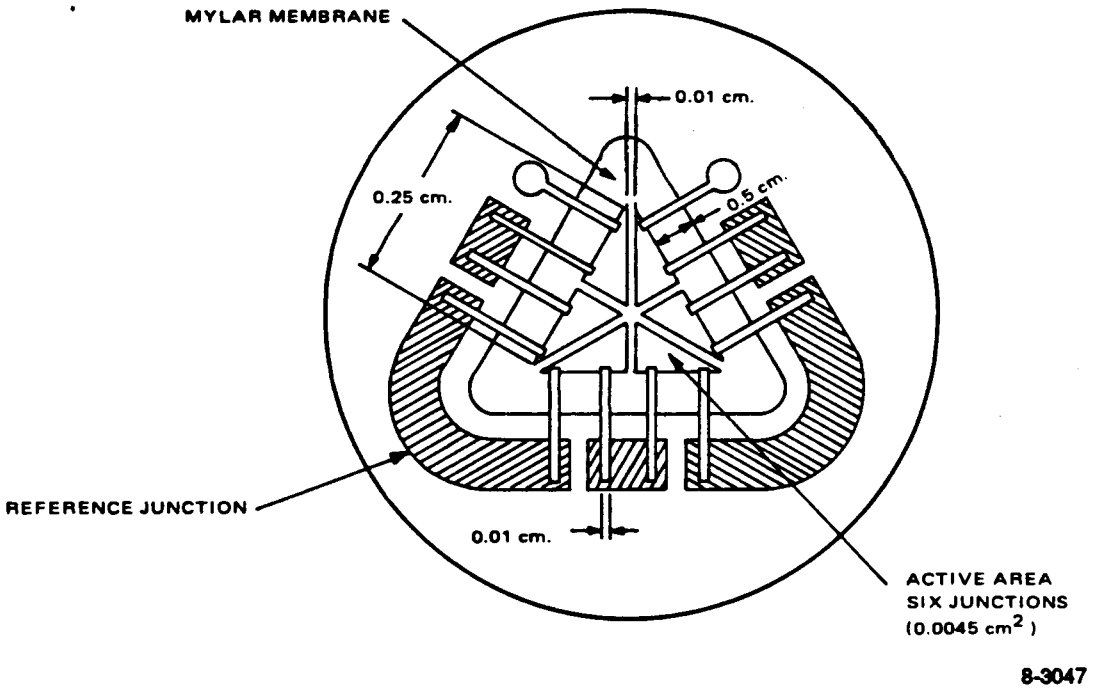

Figure 4.4.8-11. Six-Junction Thermopile Detector

common heat sink. The thermocouple materials are bismuth and tellurium, electrically joined by a gold pattern. The target area is coated with a special black paint for maximum emissivity with minimum added thermal capacity. The entire vacuum-deposited pattern is supported on a mylar film. All junctions are connected in series; the resulting output voltage is directly proportional to the difference in temperature between the active junctions exposed to the radiation and the heat sink to which the reference junctions are tied.

The thermopile exhibits a nominal responsivity of 30 volts per watt, a resistance of 13,000 ohms, and a time constant of 600 milliseconds when operating in a vacuum. The horizon sensor uses 16 identical thermopile detectors of this type.

4.4.8.1.1.4.2.3 ORS Assembly. The ORS assembly consists of a single radiation source and 4 field lenses for collimating this source into four radiation beams. The associated ORS field mirrors are cemented to the back surface of the ESA objective lenses. The physical configuration of the ORS assembly is shown in Figure 4.4.8-12.

An Irtran 2 ball is used as the radiation source; power to heat the ORS is obtained from a resistive heater that is conductively attached to the underside of the ball. The heater consists of two redundant Dale Electronics RWR 81 beryllium oxide core resistors encased in a Kovar housing. One of the end caps of each resistor is silver brazed to the housing to provide a good thermal path from the resistor core to the housing and, in turn, to the source. Dow Corning 307 silicone molding compound is used to encapsulate the resistors within the housing to provide further support to the resistors and leads.

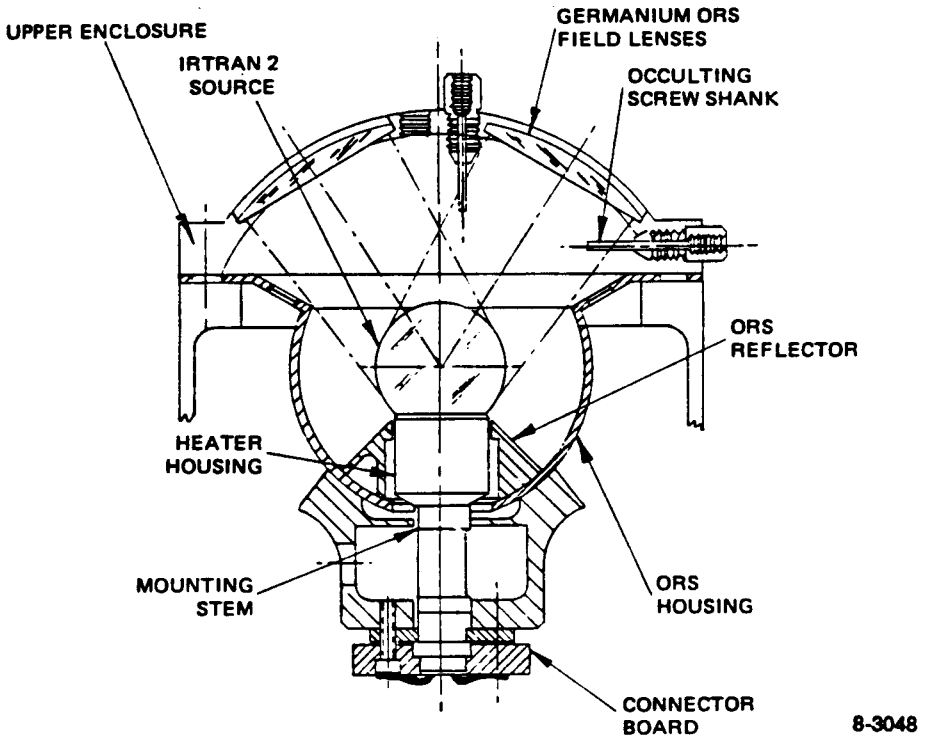

Figure 4.4.8-12. ORS Assembly

Full redundancy is achieved with two resistive heaters, only one of which is powered at any one time. Four leads are brought out, two from the ends of the resistors and two brazed to the inside surface of the housing. All materials used in the heater assembly are capable of continuous operation at temperatures in excess of the maximum temperature required to heat the source.

The heater and source are supported by a stem made of high temperature plastic (Vespel SP-1 Dupont). A high temperature epoxy (Eccobond 104) is used to attach the source to the heater and to the stem. The stem, in turn, is attached to the lower half of the spherical enclosure that surrounds the source. The mounting area is kept to a minimum to minimize the thermal impedance between the stem and the lower enclosure. Three protrusions on the stem contact the enclosure for radial support and a narrow flange is clamped to provide axial support.

The specular finish on the inside spherical surface of the lower enclosure, which is greater than a hemisphere, is achieved by copper electroforming onto a polished aluminum ball. The aluminum is leached away by a caustic solution, leaving the copper shell that is then gold plated. The upper enclosure that provides for mounting of the four ORS field lenses is machined, polished, and gold-plated aluminum. The four Germanium lenses are cemented to the aluminum housing using Armstrong A12 adhesive.

Twelve ORS adjustment screws are situated radially around the periphery of the upper ORS enclosure. These screws occult the two A fields and the B field of each of the four detector assemblies. Access holes are provided in the thermal

ring and the upper main housing to permit adjustments from outside of the ESA. However, this adjustment must be made when the ESA is contained in a vacuum environment because of the reduced responsivity caused by convection currents.

Four additional screws are located on the top of the upper ORS housing. These screws occult the four S fields and are reached through the access cover on the front end of the Earth Sensor Assembly. Adjustment of the four S fields is not as critical as that of the A and B fields.

The design of the ORS assembly minimizes the possibility of contamination. Each of the occulting screws is threaded into an insert with its shank extending through a close-fitting sleeve. Particles that may be produced on the threads are therefore confined within the insert. Fine mesh screened holes are located around the electroformed enclosure to permit evacuation of the source, to allow the unit to breathe, and to prevent the entry of foreign particles.

4.4.8.1.1.5 Performance Summary. The performance accuracy of the ESA is a function of the signal produced by an incremental attitude change, the overall ESA system noise level, and errors arising from earth radiance variations. Each of the above performance factors is discussed in the following paragraphs; Table 4.4.8-3 lists all significant sources of ESA error and summarizes its performance accuracy.

The spectral band of the ESA is determined by the filter on the lens and by the absorption of the germanium optical elements. The filter is approximately 1.7μ wide and, when combined with the rest of the optical assembly, has the spectral response shown in Figure 4.4.8-13.

The apparent temperature of the earth in the 15μ CO_2 band will be within the range of 200°K to 250°K. This spectral response has an integrated radiance of 1.026×10^{-4} W/cm^2 steradian for a 200°K earth. The clear aperture for the earth signal is 14.11 cm^2 and the signal factor is 0.86 x 0.83 = 0.714 (due to the cavity effective reflectivity and cavity obscuration at the detector end). The field of view (FOV) is an equilateral triangle 6.0° on an edge, or 15.59 deg^2 or $15.59 \times 0.01745^2 = 0.0047$ steradians. The signal for a 200°K apparent earth temperature is therefore 1.026×10^{-4} W/cm steradians x 14.11 cm^2 x 0.0047 x 0.714 = 4.9 μW. Figure 4.4.3-14 shows the signal as a function of apparent earth temperature.

The 6-element triangular thermopile array selected for this application has a responsivity of 30 V/W; for a fully illuminated field of view, this results in a minimum signal level of 147 μV.

The minimum signal change at null for an 0.1° attitude change will occur in the A detector for a 200°K earth at the highest altitude (500 nmi). The response of field of view A at its midpoint is 147 μV/5.2° = 28.3 μV/degree, giving a 2.8 μV signal change for 0.1° attitude change. For a 500 nmi altitude the horizon will actually only illuminate 1.2° of field of view A, at which point the response of A will be 1.2°/2.6° or 0.462 times its response at mid-point. The worst case signal change for 0.1° attitude change will therefore be 2.8 x 0.462 = 1.3 μV. Noise from the detector preamplifier combination has been measured to be 0.25 μV rms.

TABLE 4.4.8-3. ERROR SUMMARY CHART

Significant Error Source	3σ Performance Accuracy (Degrees)		
	400 nmi	450 nmi	500 nmi
Radiance Variation			
Pitch	0.082	0.058	0.041
Roll	0.057	0.033	0.025
Responsivity Difference*	0.030	0.029	0.038
Detector and Preamplifier Noise (0.75 μV, 3σ)	0.012	0.023	0.062
Alignment	0.015	0.015	0.015
Stray Junctions (0.15 μV, 3σ)	--	--	--
Temperature Difference Between Cavities	--	--	--
Temperature Difference Between Cavities and Substrates	--	--	--
Temperature Gradient Across Objective Lens	--	--	--
RSS of Above Errors			
Pitch	0.089	0.070	0.085
Roll	0.067	0.052	0.078

*Responsivity correction to better than 1% will reduce these errors

The ESA output, as a function of spacecraft attitude, has been optimized for an altitude of 450 nmi with an additional requirement for good linearity out to ±1.0° at 400 nmi and 500 nmi. These considerations led to the choice of a triangular field of view 6° on an edge, with an angle between the center of the field of view and the spacecraft +X axis of 62.60°. This field of view allows for the 2.8° required due to the variation in angle with altitude change, plus 1° additional coverage at each extreme altitude.

The system transfer functions and null errors depends upon the variation of radiance over the earth's surface; therefore, an earth model must be used to determine the anticipated performance in actual orbit. The computer program used permits the radiance at any altitude above the horizon and at all points on the earth's surface to be determined; the result is then used to compute the radiance received by fields of view A and B, from which attitude errors can also be computed.

The model used is based on horizon profiles computed from the spectral band shown in Figure 4.4.8-13 for January, April, July and October in the northern hemisphere. No reliable data exists for the southern hemisphere; it was

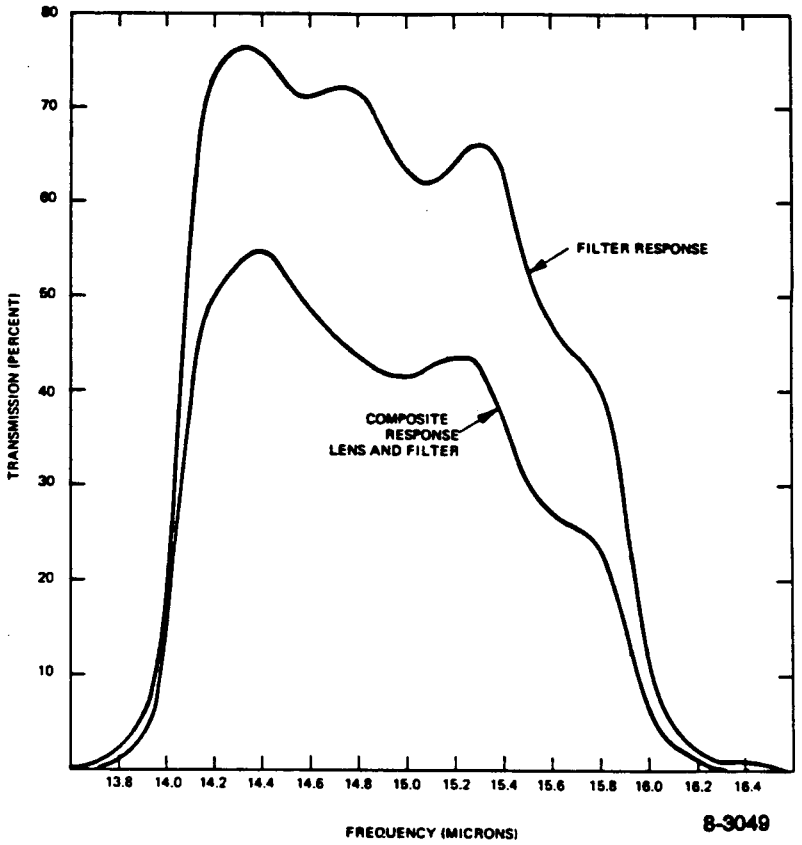

Figure 4.4.8-13. Optical Assembly Spectral Response

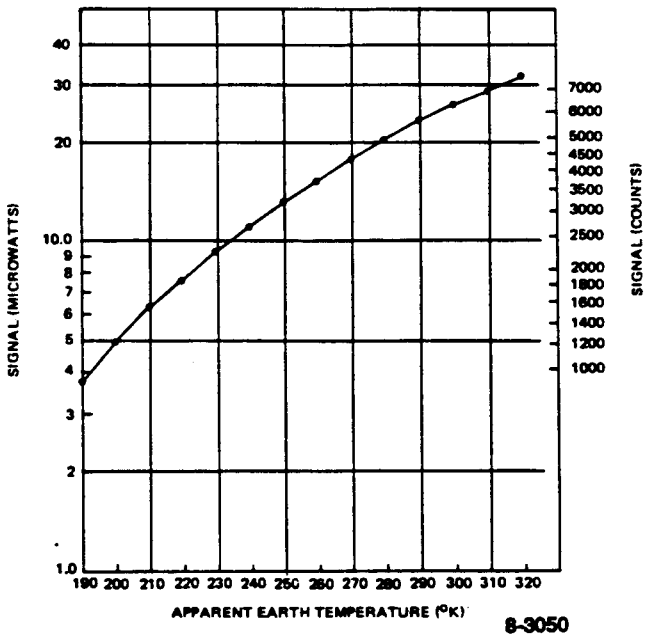

Figure 4.4.8-14. Signal vs Apparent Earth Temperature

assumed that the southern hemisphere model is the same as the northern hemisphere model of six months earlier. Various space measurements have indicated that radiance in the 15μ CO_2 band varies with latitude and season but does not vary appreciably with longitude. The earth model therefore assumes that, since the field of view is 5.2° in the direction perpendicular to the horizon, the transfer function should theoretically be linear out to ±2.0° at 450 nmi and out to 2.6° - 1.4° or ±1.2° at the extremes in altitude, 400 nmi and 500 nmi. Actually, the thickness of the horizon itself as seen from space degrades this characteristic somewhat.

For the January orbit, the southern hemisphere was simulated by July radiance data from the northern hemisphere. For the April orbit, October northern hemisphere data was used to simulate the southern hemisphere condition. July and October orbits would therefore have error plots identical to those shown for January and April, but with a 180° phase shift. Signal versus apparent earth temperatures are shown in Figure 4.4.8-14.

The earth simulation computer program was used to compute pitch and roll errors due to radiance variations for 400, 450, and 500 nmi for an orbit inclination of 98.7° and for the fields of view rotated 45° with respect to the vehicle pitch and roll axes. These are shown, respectively, in Figures 4.4.8-15, 4.4.8-16, and 4.4.8-17.

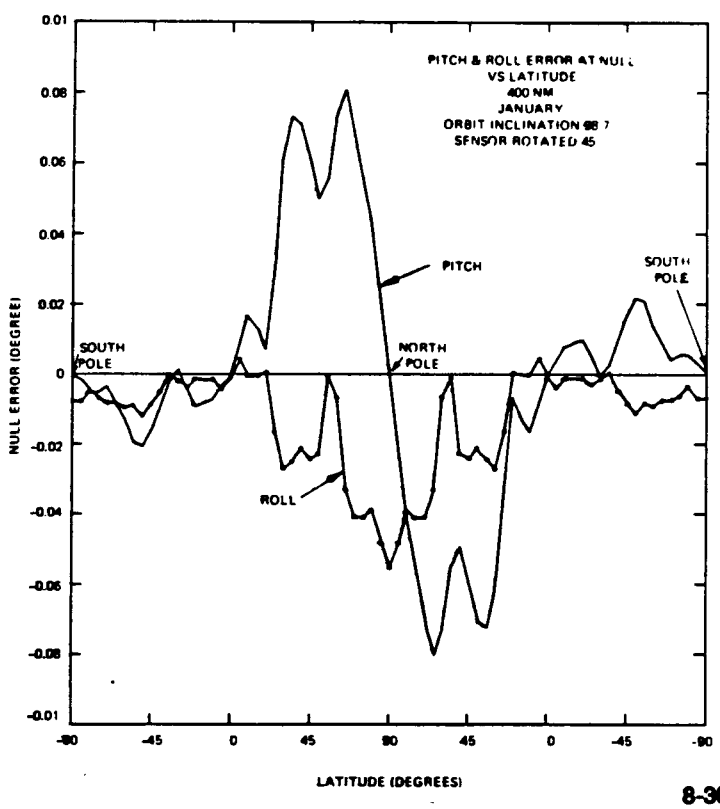

8-3051

Figure 4.4.8-15. Pitch and Roll Error at Null vs Latitude (400 nmi)

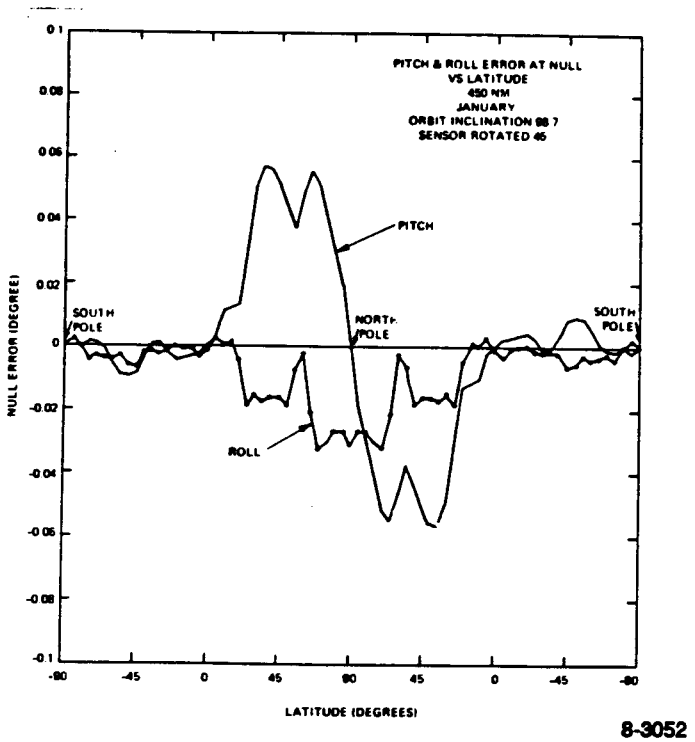

Figure 4.4.8-16. Pitch and Roll Error at Null vs Latitude (450 nmi)

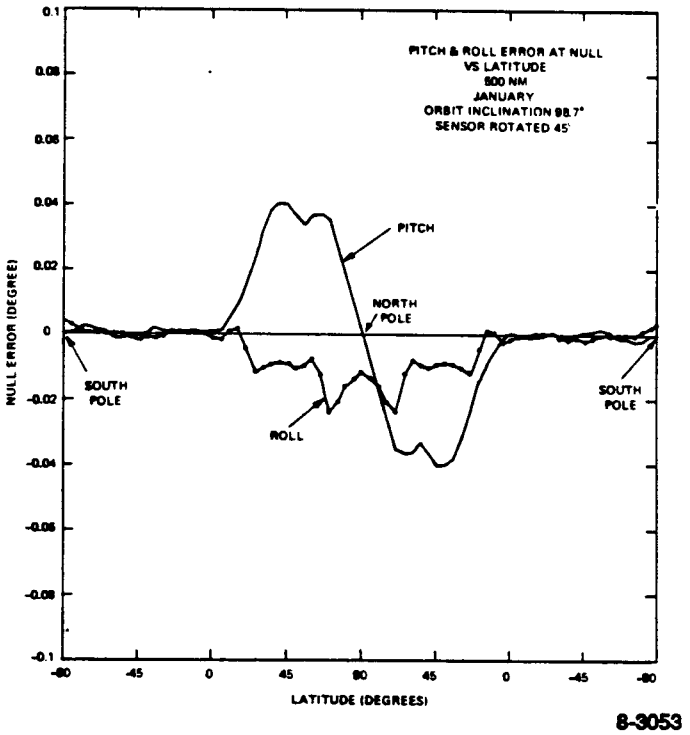

Figure 4.4.8-17. Pitch and Roll Error at Null vs Latitude (500 nmi)

4.4.8.1.2 Functional Description

4.4.8.1.2.1 Optics. The four Germanium objective lenses form images of the earth's horizon on the field lenses in each detector assembly. The four optical bundles crisscross in the center of the upper housing.

The field lenses are mounted at the entrance of each optical condensing cavity. They limit the acceptance angle of the detector to the solid angle subtended by the objective lens. In addition, the field lenses and optical cavities scramble the horizon image at the detector to prevent possible non-uniform detector response from degrading the linearity of the system transfer function.

The ORS assembly provides a controlled radiative input to the detectors which offsets the radiation loss to space from each of the detectors, thus reducing the net radiation loss to near zero. Radiant energy from the single ORS source is collimated into four beams by the ORS field lenses; the 4 field mirrors on the back of the objective lenses then fold and project the ORS beam onto the field lenses in the detector assemblies.

The detector assemblies are placed with their field stops located in the focal plane of the associated objective lens. The tetrahedron shaped optical cavities serve as f/0.5 condensing elements to provide optical gain by illuminating the detector over a full two μsteradians. As shown in Figure 4.4.8-9, the two extreme (dashed) rays that cross at the center of the upper field lens define the tetrahedron's image polygon. All rays that pass through the objective lens and intersect the image polygon reach the detector.

4.4.8.1.2.2 Detector Assembly. Each detector assembly contains four detectors; two A field detectors, one B field detector, and one S (space) field detector, as shown in Figures 4.4.8-2 and 4.4.8-18. The two A field detectors are connected in parallel.

Each thermopile detector provides an output voltage which is a direct measure of the temperature difference between the set of active junctions and the associated set of reference junctions. The output dc level is therefore directly proportional to the radiation exchange between the detector and any object within its field of view.

While the ESA electronics is totally redundant and immune to single point failure modes, the 16 detectors are not redundant. Therefore, a failed S detector (open or shorted) is prevented from assuming control of the ORS heater drive by the ESA electronics (commutator and dc restorer). Without these provisions, a failed S detector could cause the ORS heater to saturate all detectors, which in turn would cause the electronics to produce over-range counts for all 12 output words; this condition would not be overcome by switching to the redundant ESA channel.

4.4.8.1.2.3 Commutator. The amplitude of signals derived from the detectors ranges from approximately 10 μV to 1 mV. An MOS FET commutator as shown in Figure 4.4.8-18 is used to sample the detector array output. Each detector output is sampled for a period of 20 msec; during the 20 msec period between each detector sample, the output of the commutator is shunted to 0 volts. The resulting wave form is a 25 Hz pulse train containing the individual outputs of the 12 thermopile detectors, as shown in Figure 4.4.8-19. The pulse train is repetitive at a frame rate of approximately 2 Hz.

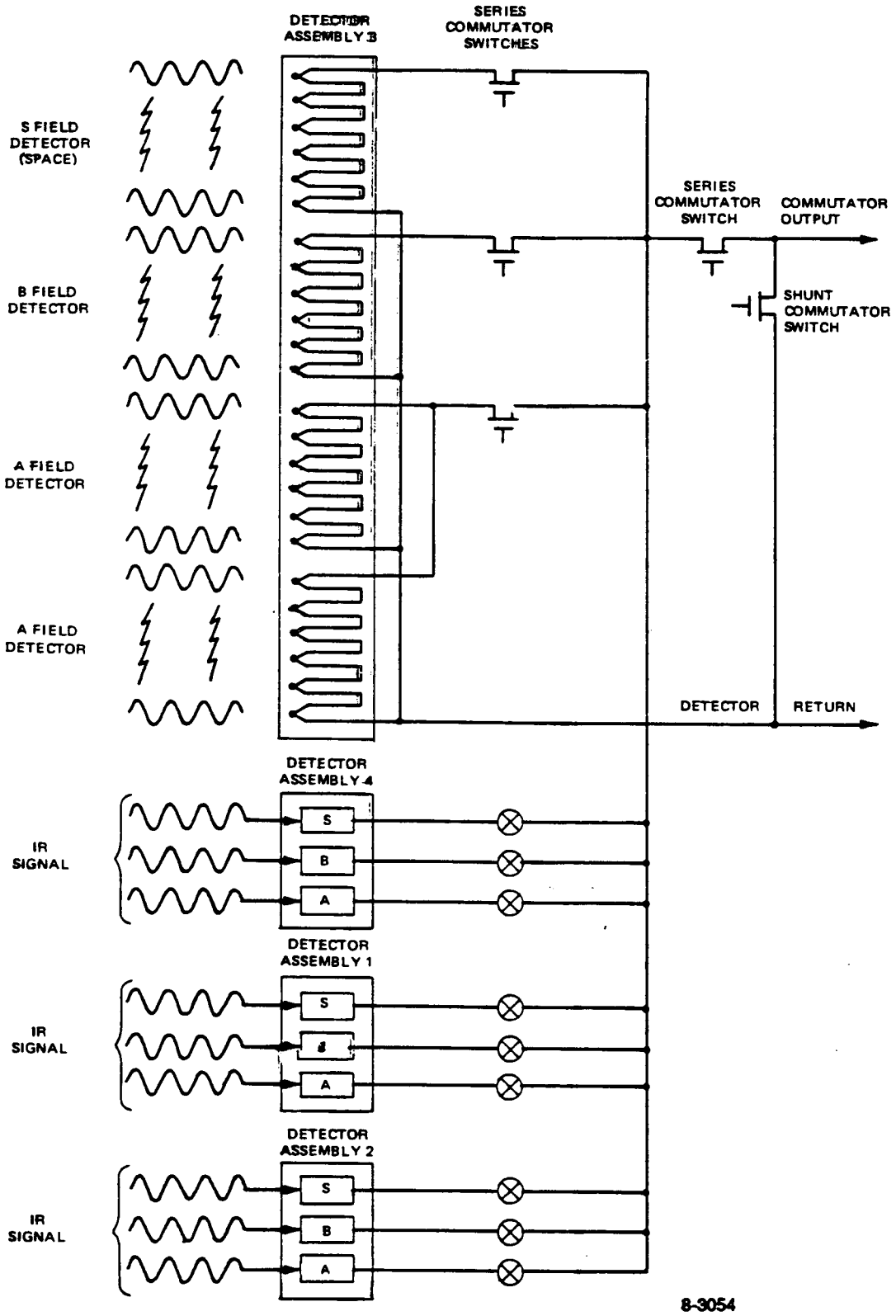

Figure 4.4.8-18. Detectors and Commutator Simplified Schematic Diagram

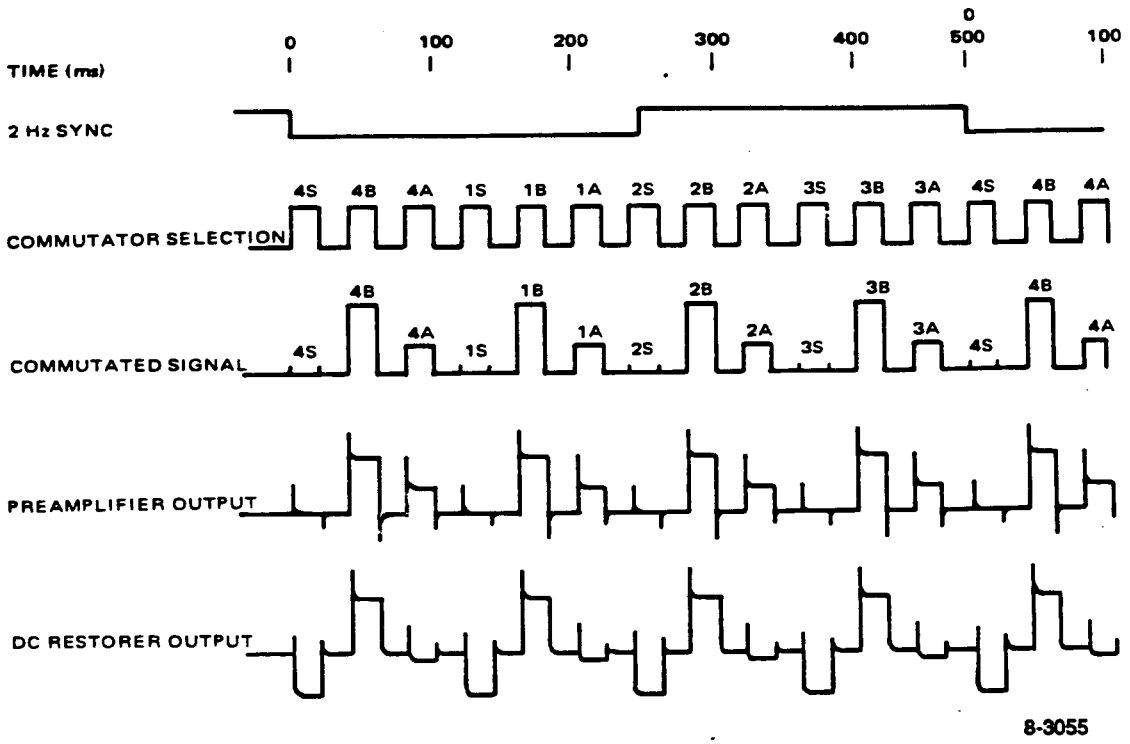

Figure 4.4.8-19. Analog Waveforms

In the process of sampling each detector, the commutator produces a voltage spike that is superimposed onto the detector signal. The spike is a result of capacitively coupling the FET gating drive signals. (Note that for an open-circuited detector, the spike will not decay; this will manifest itself as an over-range positive output count for the faulty detector. If this is an S detector, the ORS heater drive would then be controlled by one of the three remaining S detectors.) The commutator spike signal is orders of magnitude greater than the sampled detector signals and would produce erroneous information if it were not removed. These spikes are effectively removed in the A/D converter by not integrating during the spikes.

4.4.8.1.2.4 Preamplifier. A low-noise FET preamplifier as shown in Figure 4.4.8-20 amplifies the commutator output to provide an adequate level for driving the analog to digital converter.

The preamplifier noise characteristics are shown in Figure 4.4.8-21. With a system bandpass of 25 Hz centered at 25 Hz, the preamplifier will increase the system noise by approximately 3 dB. This increase in noise is primarily due to the amplifier feedback resistor. A reduction in the value of the resistor would reduce the low-frequency performance of the amplifier, thus degrading system performance.

The preamplifier gain-bandwidth characteristics are shown in Figure 4.4.8-22. The preamplifier provides sufficient gain prior to the dc restorer circuit so that any noise introduced by the restorer does not increase the system noise level. The preamplifier frequency response has been selected to provide faithful reproduction of the detector signal and to maintain the fidelity of the

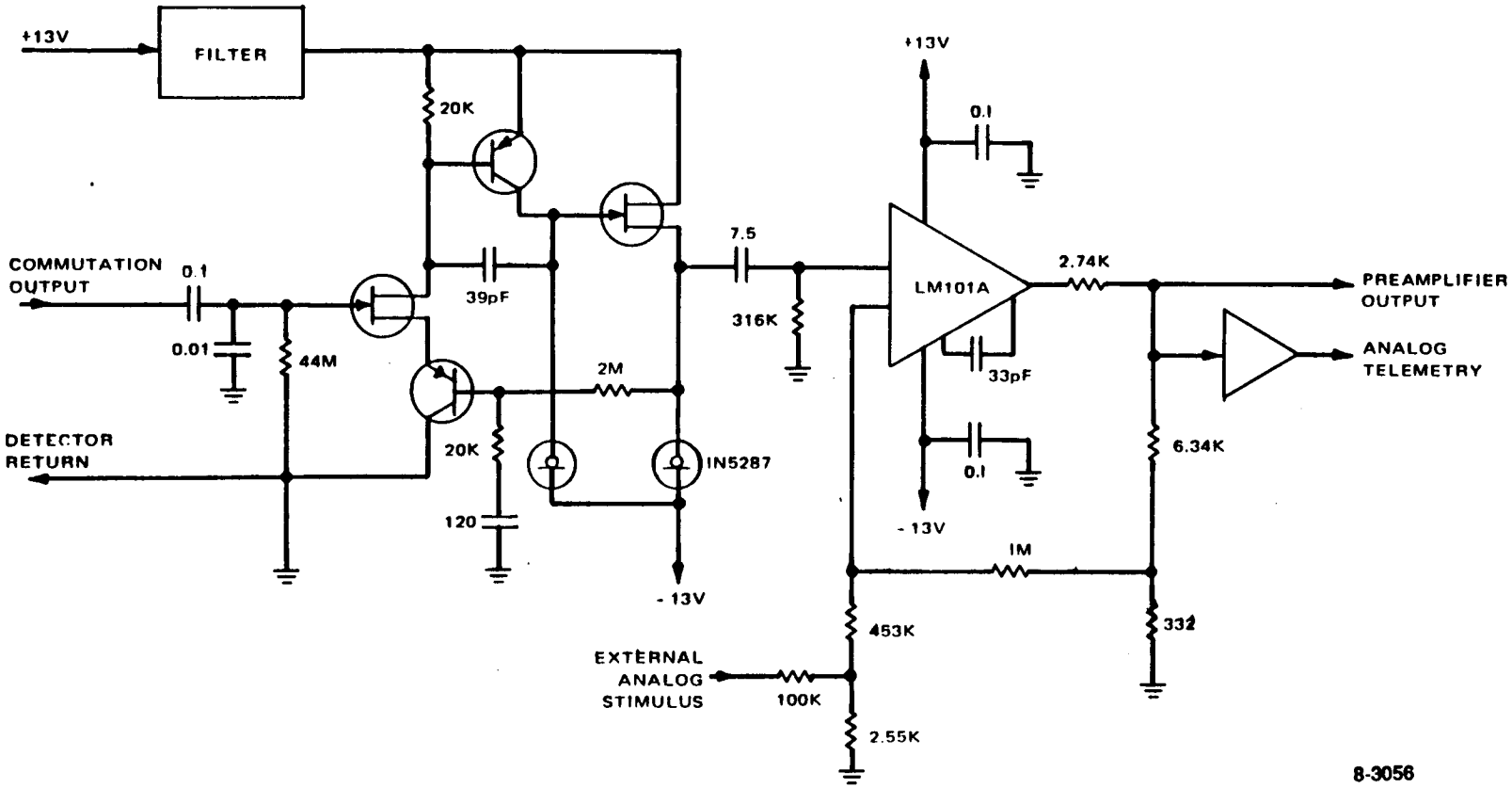

Figure 4.4.8-20. Preamplifier Schematic Diagram

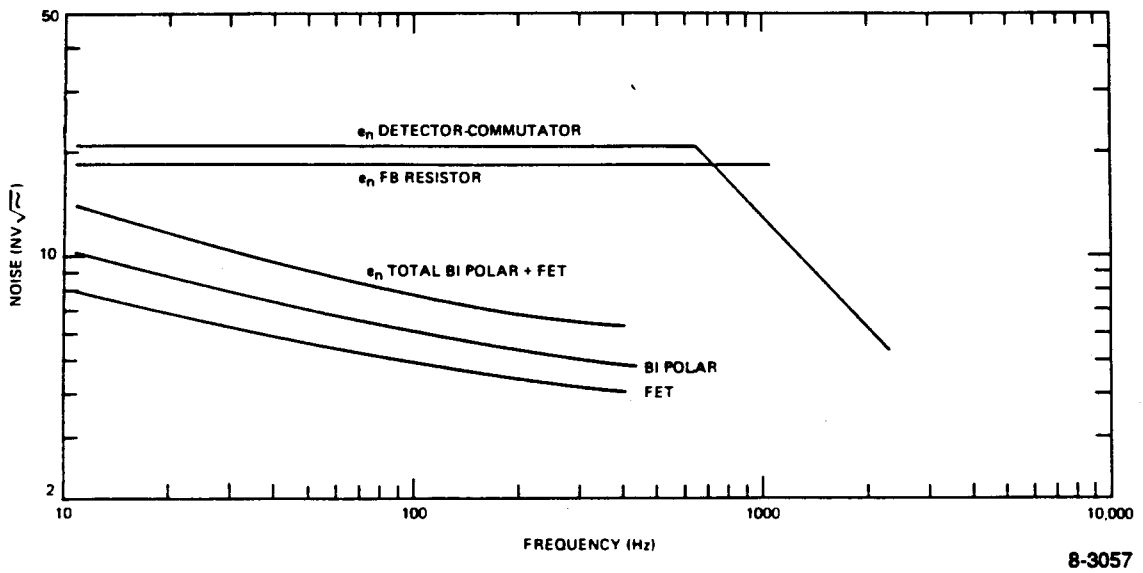

Figure 4.4.8-21. Preamplifier Detector Noise

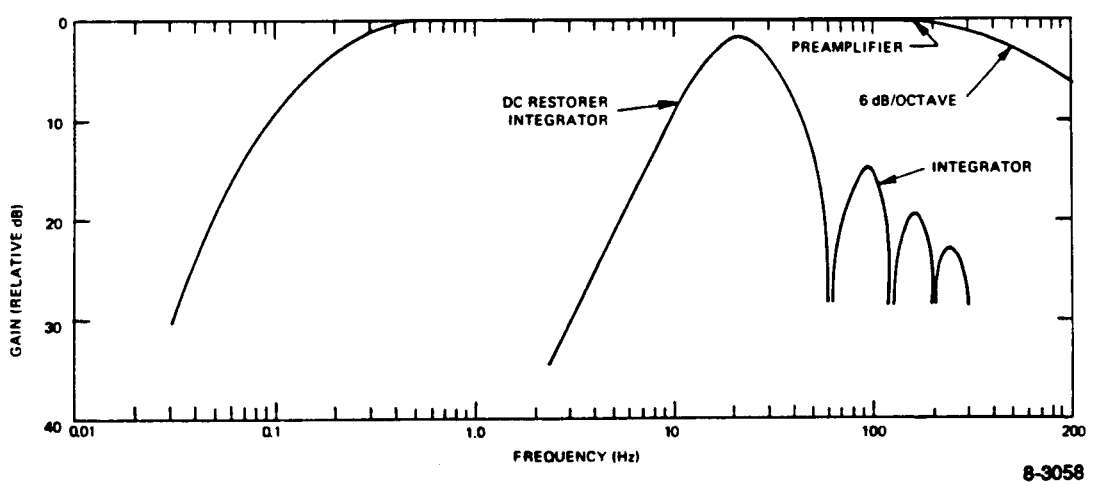

Figure 4.4.8-22. Analog Processor Gain Bandwidth Characteristic

transient spikes produced by the commutator drive signals. By not allowing the preamplifier to distort the commutator transient spikes, their contribution to system error can be easily eliminated in the A/D converter.

4.4.8.1.2.5 Analog to Digital Converter. The analog to digital (A/D) converter digitizes each analog detector signal and provides an output in the form of a 16 bit word containing 12 data bits, one sign bit, and one over-range bit.

As shown in Figure 4.4.8-23, the A/D converter consists essentially of a dc restorer, two integrators used alternately to satisfy the timing constraints, a zero-crossing detector, and a frequency counter. A buffer register is used for temporary storage of the resultant digital word.

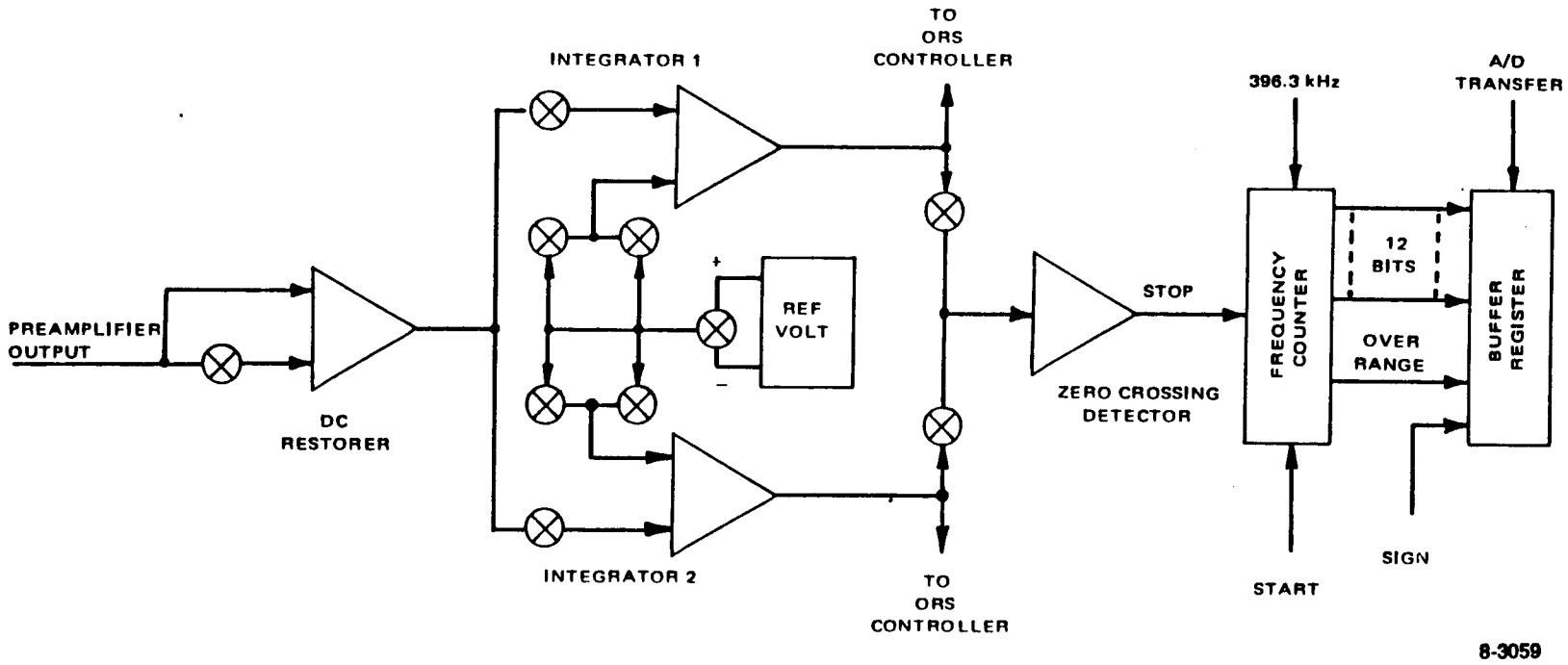

Figure 4.4.8-23. Analog to Digital Converter Functional Block Diagram

The dc restorer provides a gain of -0.5 for the ground reference and a gain of 1 for the detector sample (see Figure 4.4.8-4; MOS switch 15 is closed during the detector sample).

At the input to the dc restorer, a fixed dc bias is added so that a 0 volt output, due to a shorted detector, will be above the voltage cutoff point of the ORS heater drive. Nominally, the cutoff point of the ORS drive is set, at time of assembly, at +100 counts. When the fixed bias of +200 counts is added to the outputs of all detectors, the output of the shorted detector is +200 counts, or 100 counts above the cutoff point of the ORS drive. Therefore, if the shorted detector is an S detector, the other 3 S detectors will normally produce lower counts and will have control of the ORS drive.

The A/D converter is a conventional up/down converter using a pulse width modulation integration technique; the basic principle of operation of this type of converter is shown in Figure 4.4.8-24. The analog signal is integrated for a fixed time interval, after which the accumulated integrator level is proportional to the analog signal amplitude. After this fixed time interval, a frequency counter is started and a reference voltage of opposite polarity is switched into the integrator. This reference voltage is then integrated at a constant slope until a zero-crossing is detected, at which point the frequency counter is stopped.

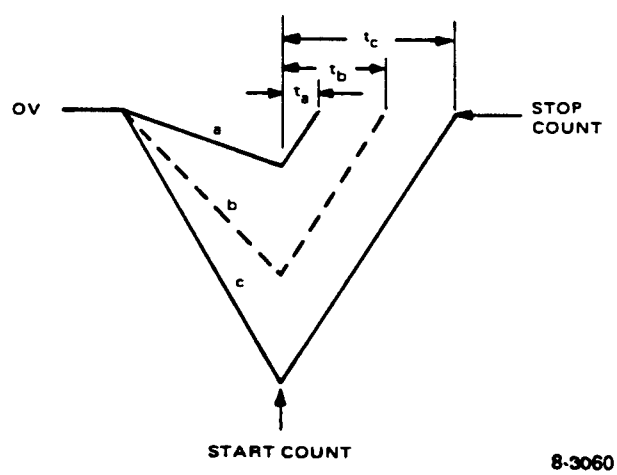

Figure 4.4.8-24. Up/Down Converter Basic Principle

The reference integration time and therefore the frequency counter content is directly proportional to the analog signal amplitude.

The detailed operation of the A/D converter is shown in Figures 4.4.8-25 and 4.4.8-26. Note that the integrators are placed in a "hold" configuration during the initial 5 ms period in each 20 ms sample period. This "hold" period prevents the commutation spikes from being integrated with the detector signal.

The integrating aperture of integrators 1 and 2 consists of three consecutive samples, each having a 15 msec duration; integrate ground reference, integrate detector sample, and integrate ground reference. The technique of producing an integrating aperture containing a ground reference (gain = -0.5) prior to and subsequent to each detector sample (gain = 1) eliminates any baseline drift or transient that is linear with time during a complete integration aperture.

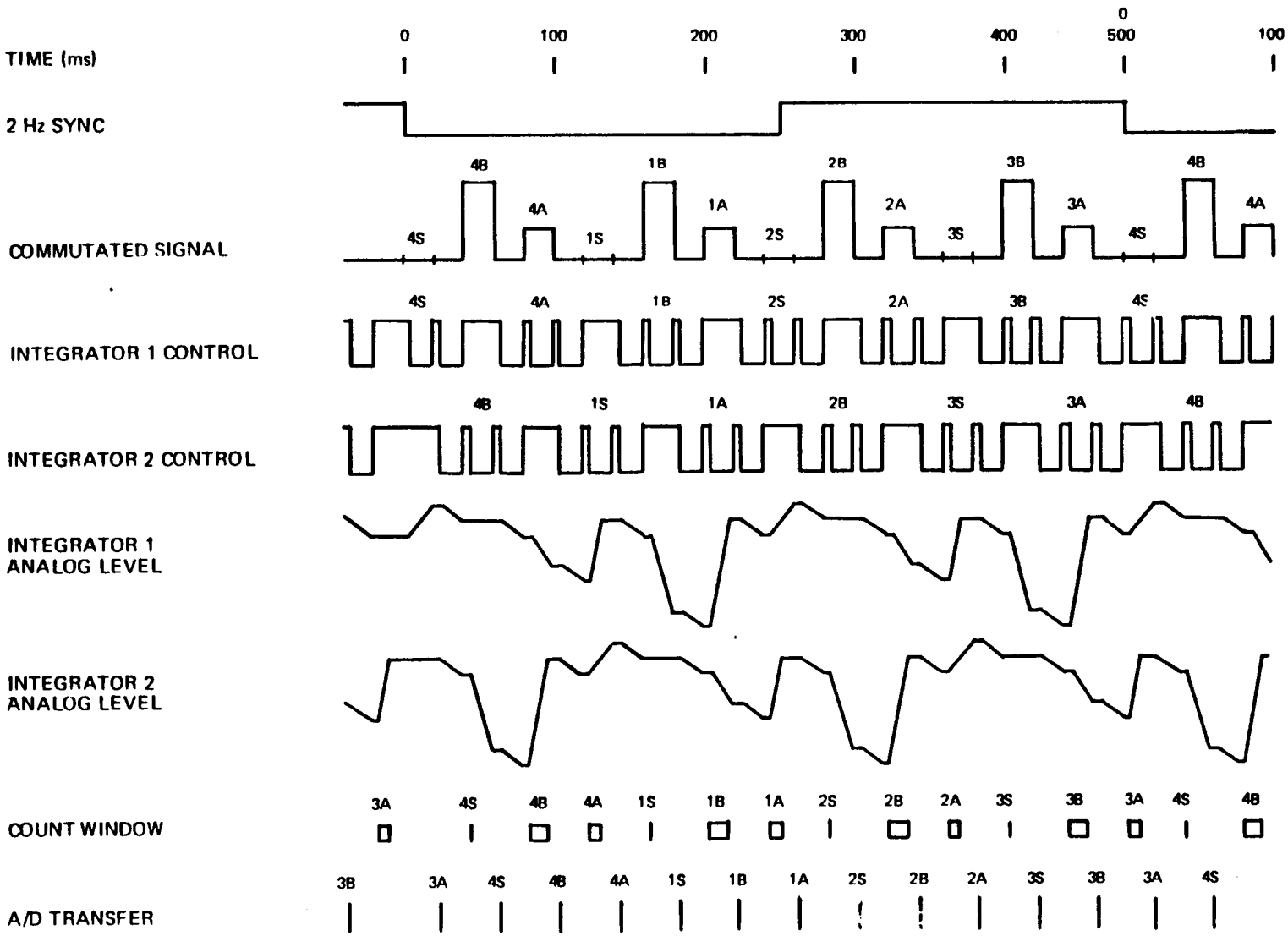

Figure 4.4.8-25. Analog to Digital Converter Frame Timing

8-3061

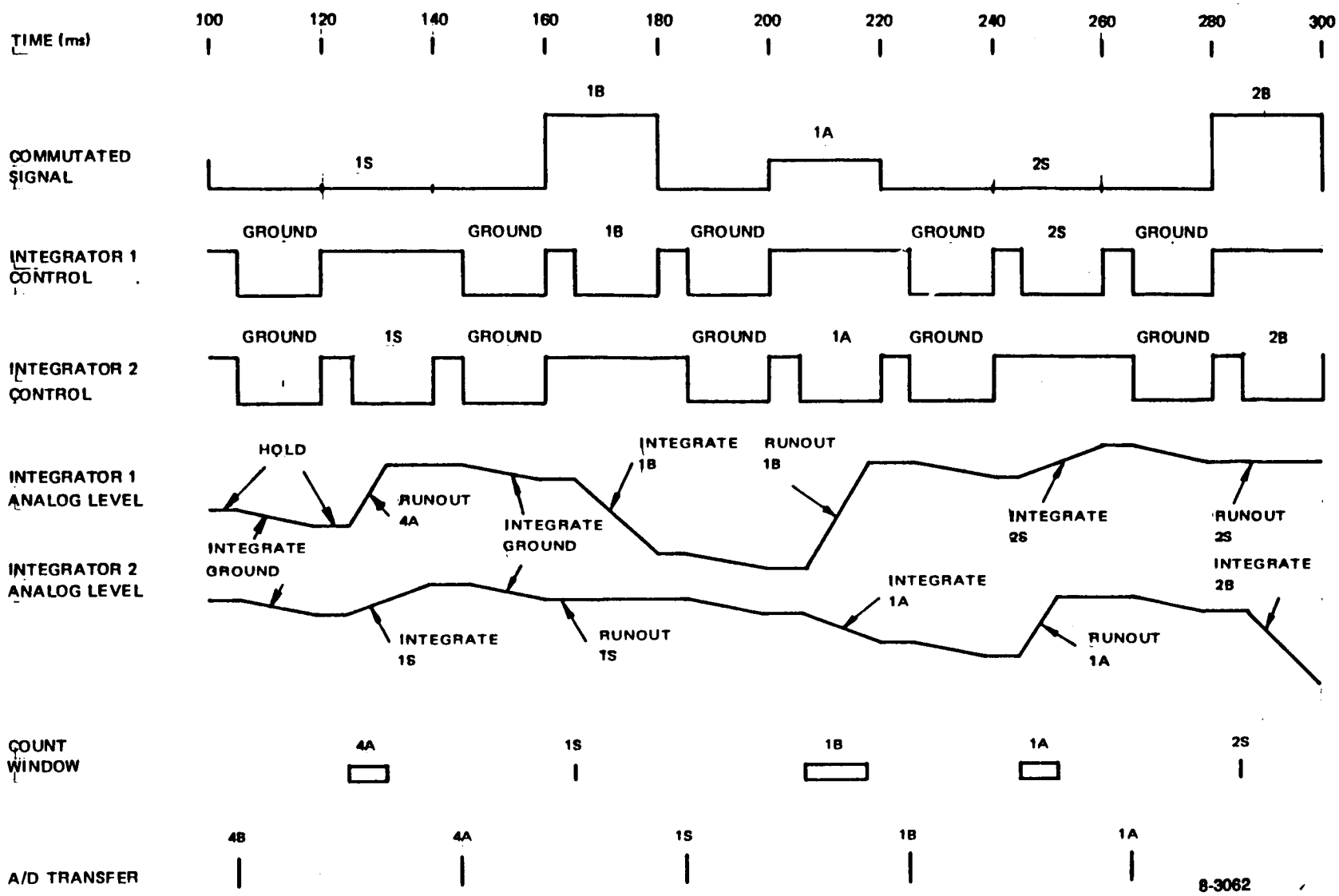

Figure 4.4.8-26. Analog to Digital Converter Detailed Timing

If a non-linear baseline drift occurs, such as is associated with the output "settling" of an RC network after being driven by a step input, the integrator responds only to the "curvature" (or second derivative) of the transient; this feature makes this configuration especially immune to low-frequency memory error and low-frequency noise.

Operation of the A/D conversion is as follows. During the integrate aperture time, T_1, the output V_o of the integrator increases linearly with time. The integrator output at the end of T_1 is $V_{o1} = V_i + V_s (T_1/R_c)$ where V_i is the initial voltage on the integrator and V_s is the detector signal.

At the completion of time T_1, a reference voltage, V_R, having a polarity opposite to V_s, is integrated until the output of the integrator again becomes V_i. The time required for this second operation is the desired information, T_x. The period of this integration is:

$$T_x = T_1 \left(\frac{V_S}{V_R} \right)$$

Thus, not only is T_x linearly related to V_s, but it is also completely independent of both the integration time constant RC, and the integrator offset voltage.

The output of the zero-crossing detector changes state each time the integrator voltage crosses 0 volts. Thus, by starting a counter with the V_R signal and stopping it when the integrator output crosses zero volts, a binary number proportional to V_s is obtained.

Conversion of the output from integrators 1 and 2 is alternately effected during 20 millisecond intervals once every 40 milliseconds. During each 20 millisecond A/D conversion interval, the number of 396.3 kHz clock pulses available for counting is 8192; the 12 bit counter used for A/D conversion can therefore achieve a full scale output in 10 milliseconds.

The anticipated normal maximum A/D output count is +3200, corresponding to a 250°K apparent earth target filling the full detector field of view. The anticipated normal minimum A/D output count is +100, corresponding to space filling the full detector field of view; the expected normal range of counts is therefore +100 to +3200.

Automatic ranging is provided for both positive and negative signals that exceed the normal operating conditions. During initial warm-up, all detectors produce very large negative signals. A digital sampling system continually monitors the output of each space detector signal. Whenever a space detector signal of a particular detector assembly produces a negative signal, the system automatically ranges to a 0.5 scale factor for that entire detector assembly (S, B, and A detectors), insuring linear system operation during warm-up or ORS malfunction. By allowing each detector assembly to perform independently, erroneous cross-coupling information is eliminated. An indication of the negative overrange condition is provided by the sign bit in the output data for that detector assembly.

Positive overranging occurs when the normal positive-going detector signal exceeds a full count, 4096. In the event that positive overranging occurs, the overrange bit goes to a 1; the system scale factor is halved and the counter recycles. This condition should occur only when the sun is in the sensor field of view.

4.4.8.1.2.6 Offset Radiation Source Controller. The ORS circuitry samples the output of integrator 1 and integrator 2 at the completion of each space detector integrate period, as shown in Figures 4.4.8-27 and 4.4.8-28.

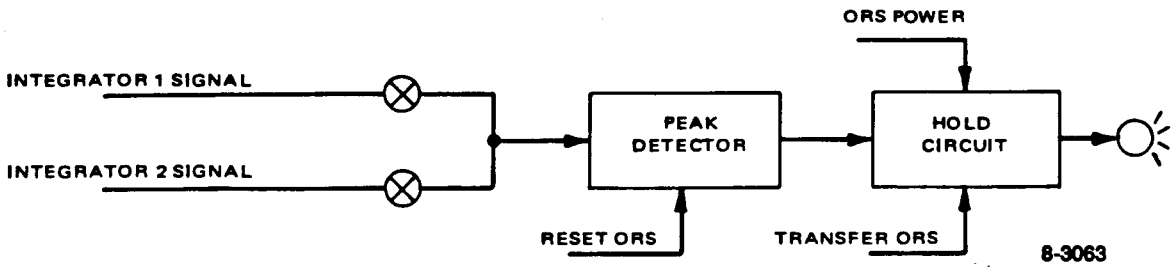

Figure 4.4.8-27. ORS Controller Functional Block Diagram

Each integrated space detector signal is amplified and peak detects to obtain the most negative space signal, which defines the space detector that is certain to be viewing space. The peak detector is reset to a negative reference voltage at the beginning of each frame period, then detects the most positive signal obtained from all four of the space detector samples (the most positive integrator signal represents the most negative space signal). At the completion of the integrate period for detector 3A, the peak detected signal is transferred to a hold circuit; the output of the hold circuit provides the drive to the ORS heater element during the next data frame. At the completion of the signal transfer, the sample switch opens and the peak detector is again reset to a negative reference. The reset is maintained for the duration of the period prior to the second 4S ground reference sample.

The overall electro-optical gain of the ORS channel is approximately 50 (static) and approximately 100 (dynamic). The time constant of the heater is approximately 30 seconds. With a 0.5 second sampling system, overall loop stability is easily achieved.

Figure 4.4.8-29 provides transfer function curves to determine the ESA output and ORS heater power as a function of ORS ball temperature for ESA operating temperatures of -5°C, +10°C, and +25°C.

4.4.8.1.2.7 Programmer. The master clock for the ESA is derived from a low power COS/MOS oscillator operating at 396.3 kHz. The 396.3 kHz is used directly for clocking the frequency counter associated with the A/D converter; the 396.3 kHz signal is also divided down as required to perform logic and analog gating operations.

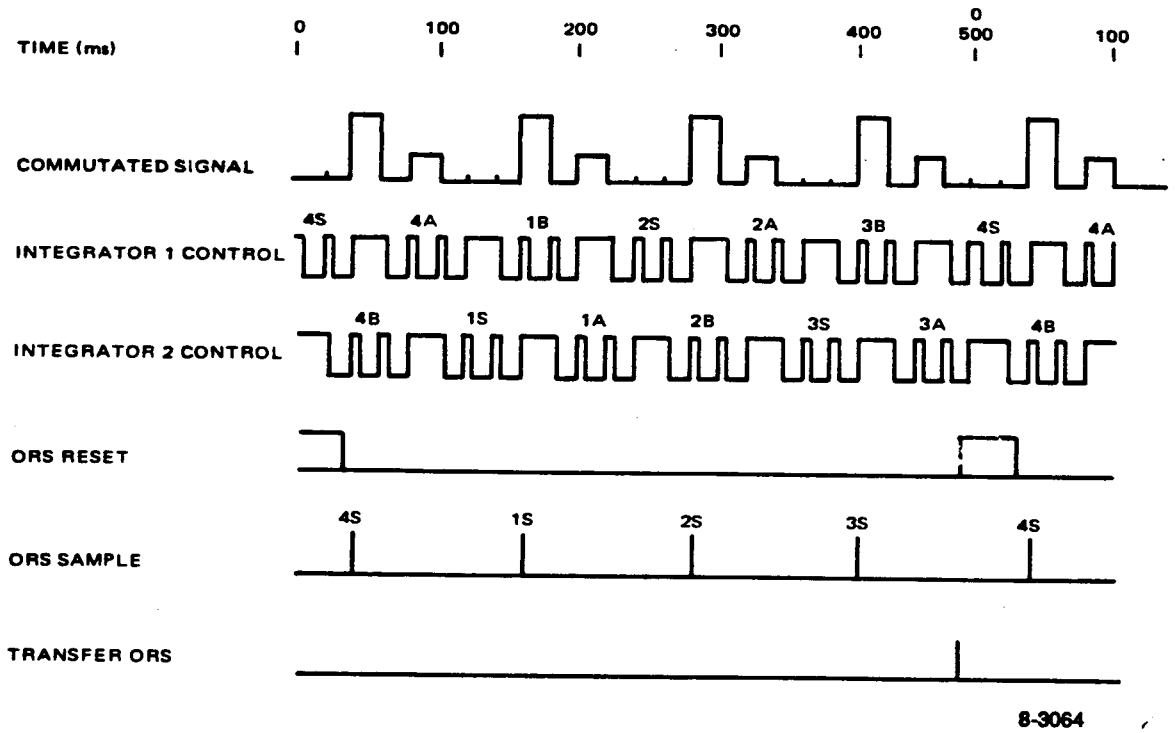

Figure 4.4.8-28. ORS Controller Timing

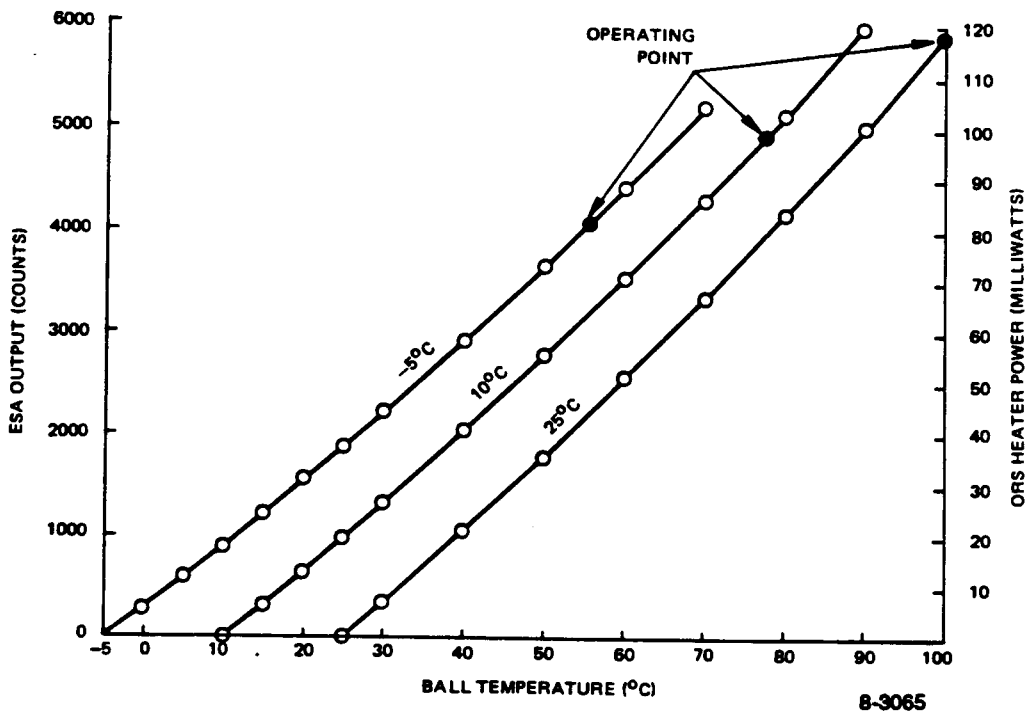

Figure 4.4.8-29. ESA Output vs ORS Ball Temperature

4.4.8.1.2.8 Data Processor and Data Interfaces. The data processor provides the data storage and handling required for providing the ESA data to the Controls Interface Unit. As shown in Figure 4.4.8-30, the data processor consists of a buffer register for temporary data storage and a 48-bit register for assembling the data into three word groups. Both of these registers are controlled by the programmer.

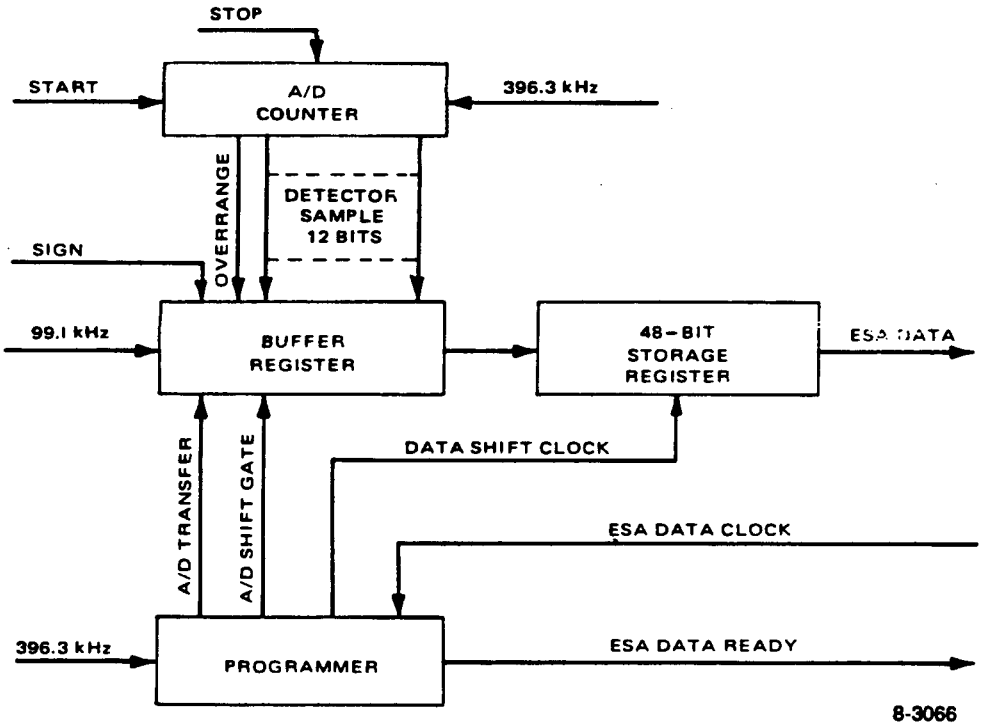

Figure 4.4.8-30. Data Processor Functional Block Diagram

The data processor timing is shown in Figure 4.4.8-31. The 12-bit output of the A/D converter and the sign and over-range bits are parallel loaded into the buffer register at the completion of each A/D conversion. Immediately after this, a 161.5 μsecond shift gate timing bracket that encompasses 16 clock pulses (at 99.1 kHz, which is 396.3 divided by 4) is generated and used to shift the buffer contents into the 48-bit storage register.

An ESA Data Ready signal is initiated 5 milliseconds after the completion of each A integrate period (four Data Ready signals per frame). The ESA Data Ready signal indicates that three 16 bit words containing, in sequence, the S, B, and A field information of a particular detector assembly are ready for retrieval by the CIU. The ESA Data is then shifted out in synchronism with the ESA Data Clock signal supplied by the CIU; the format of each data word is as shown in Table 4.4.8-4. The three data words are recirculated in the ESA output buffers such that the data may be clocked out a number of times on command. A data blanking gate limits the data retrieval period to 35 milliseconds.

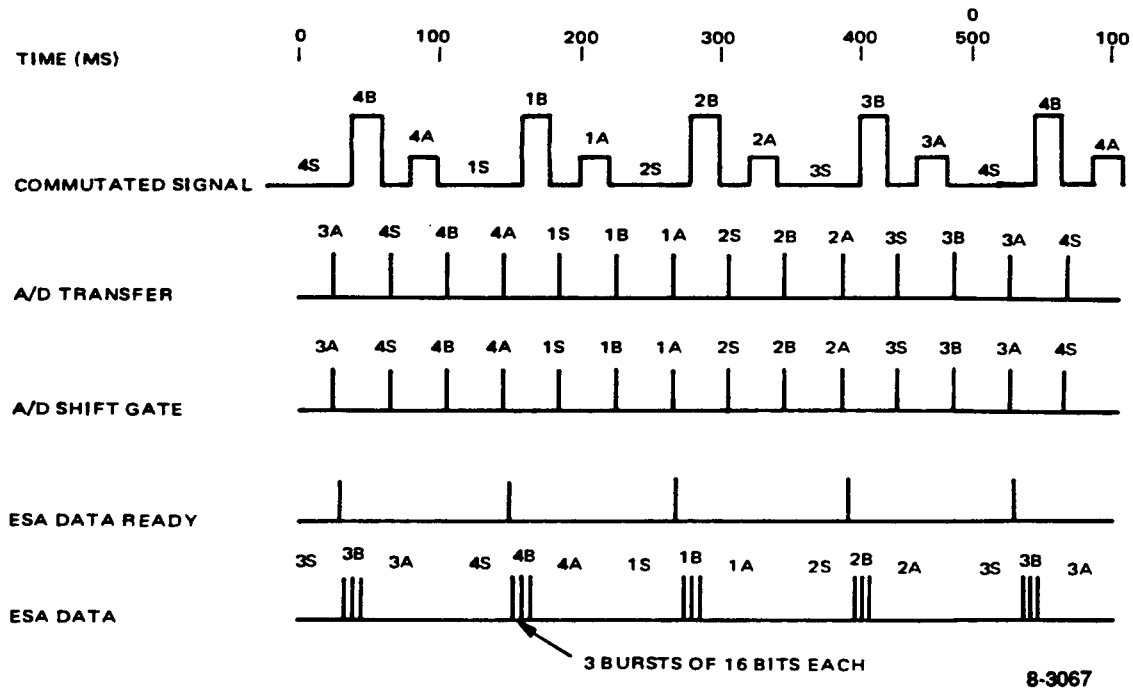

Figure 4.4.8-31. Data Processor Timing

TABLE 4.4.8-4. ESA DATA FORMAT

Bit	Function
1	Sign bit; 0 = positive, 1 = negative
2	0
3	0
4	Overrange bit; 0 = normal, 1 = overrange
5	MSB ESA Data
6	
7	
8	
9	
10	
11	
12	
13	
14	
15	
16	LSB

4.4.8.1.2.9 Power Supply. The power supply provides the regulated ±13 volts required in the digital and analog electronics circuitry. As shown in Figure 4.4.8-32, the power supply consists of an EMI filter, a line filter, power switching to provide power to either one of the redundant electronics, and a dc to dc converter.

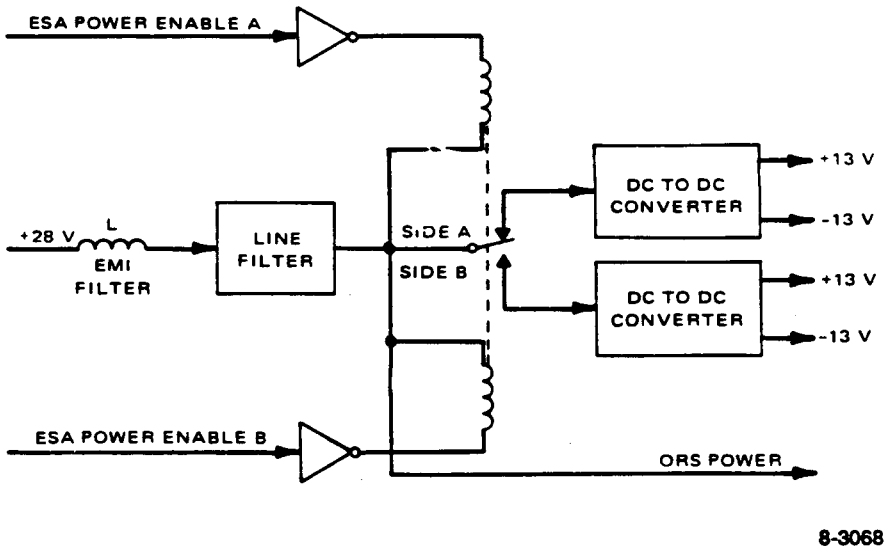

Figure 4.4.8-32. Power Supply Functional Block Diagram

4.4.8.1.2.9.1 DC to DC Converter. The dc to dc converter consists of an oscillator driving a saturable core reactor, a starter circuit, rectifiers, and regulators to provide the regulated ±13 volts. Each regulator consists of a series pass transistor, a driver transistor for line regulation, and zener diode reference.

Power efficiency within the converter is maintained high by using a very low loss core material in the transformer, a starter circuit that is inactivated after the oscillator starts, low capacity winding techniques, and current limiting during switching.

4.4.8.1.2.9.2 A/D BiPolar Reference Voltage Generator. The stable dc bipolar reference voltage used in the A/D converter is generated by referencing the output of a programmable operational amplifier to a low temperature coefficient zener diode. A logic signal from the A/D converter controls the polarity of the reference generator.

4.4.8.1.2.10 ESA/Spacecraft Interfaces. As shown in Figure 4.4.8-33, the ESA provides for completely redundant data and power interfaces; there is one set for side A, and another set for side B. Both interfaces are powered and there is internal power control logic in each side, but only the interface associated with the enabled side of the ESA will be active. There is a status signal from each interface to indicate which side of the ESA is active.

4.4.8.1.3 Telemetry

4.4.8.1.3.1 ESA Temperature Telemetry. ESA temperature telemetry is provided by a pair of thermistors bonded to the thermal ring inside the ESA. The bias voltage for the thermistors is obtained through a constant current diode from the filtered +28 volt supply. There is a separate telemetry channel for each side of the ESA.

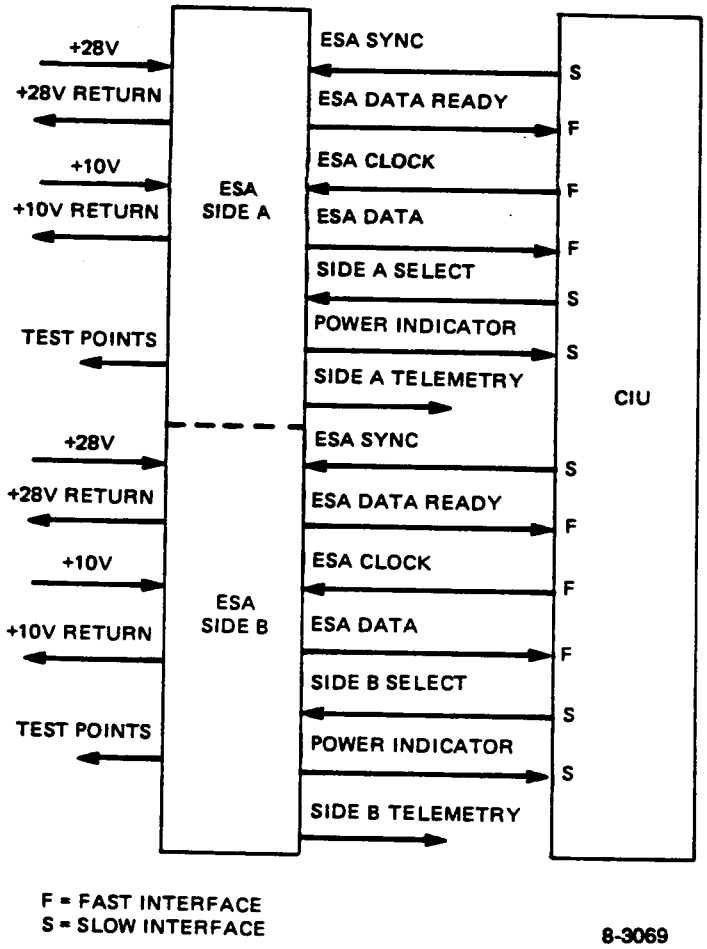

Figure 4.4.8-33. ESA Interface Diagram

4.4.8.1.3.2 Analog Side A Telemetry. The analog detector signal available at the output of the side A preamplifier is conditioned and provided as a telemetry output signal.

4.4.8.1.3.3 Analog Side B Telemetry. The analog detector signal available at the output of the side B preamplifier is conditioned and provided as a telemetry output signal.

4.4.8.1.3.4 ORS Voltage and Integrator 1A Telemetry. With side B selected, this telemetry point provides a zero volt indication. With side A selected, this telemetry point provides the ORS heater voltage telemetry combined with the output signal from integrator 1 in side A.

4.4.8.1.3.5 ORS Voltage and Integrator 2A Telemetry. With side B selected, this telemetry point provides a zero volt indication. With side A selected, this telemetry point provides the ORS heater voltage telemetry combined with the output signal from integrator 2 in side A.

4.4.8.1.3.6 ORS Voltage and Integrator 1B Telemetry. With side A selected, this telemetry point provides a zero volt indication. With side B selected, this telemetry point provides the ORS heater voltage telemetry combined with the output signal from integrator 1 in side B.

4.4.8.1.3.7 ORS Voltage and Integrator 2B Telemetry. With side A selected, this telemetry point provides a zero volt indication. With side B selected, this telemetry point provides the ORS heater voltage telemetry combined with the output signal from integrator 2 in side B.

4.4.8.2 Inertial Measurements Unit

The Inertial Measurements Unit (IMU) provides the capability for determining satellite angular rates about the roll, yaw, and pitch axes, and during ascent, operation linear accelerations along the spacecraft X, Y, and Z axes. During the ascent phase, the angular and linear rates are utilized to derive any required guidance corrections. During in-orbit operation, the angular rates are used to derive three-axis attitude corrections required to maintain the desired earth orientation.

Figure 4.4.8-34 shows the interfaces between the IMU and other spacecraft components. Power is supplied from the spacecraft regulated +28 Vdc buses and a spacecraft regulated +10 Vdc. The Controls Interface Unit (CIU) (part of the spacecraft Command and Control subsystem) provides all of the IMU input control signals and the basic 2.56-MHz clock input. The IMU supplies to the CIU a 10-Hz synchronizing signal and a digital bit stream in the form of eight 16-bit words representing angular and linear motion in three axes, and IMU status data. Telemetry data are supplied to the TIROS Information Processor (TIP) as analog or discrete value signals.

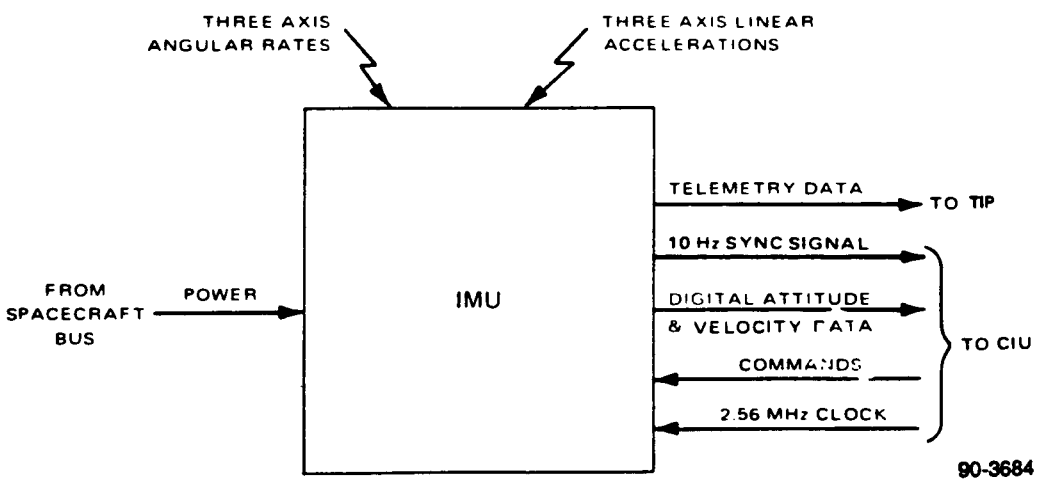

Figure 4.4.8-34. IMU Interfaces

4.4.8.2.1 Design Description

The IMU circuitry is housed in a single sealed container located on the space-facing side of the spacecraft Instrument Mounting Platform. Figure 4.4.8-35 is a functional block diagram of the IMU.

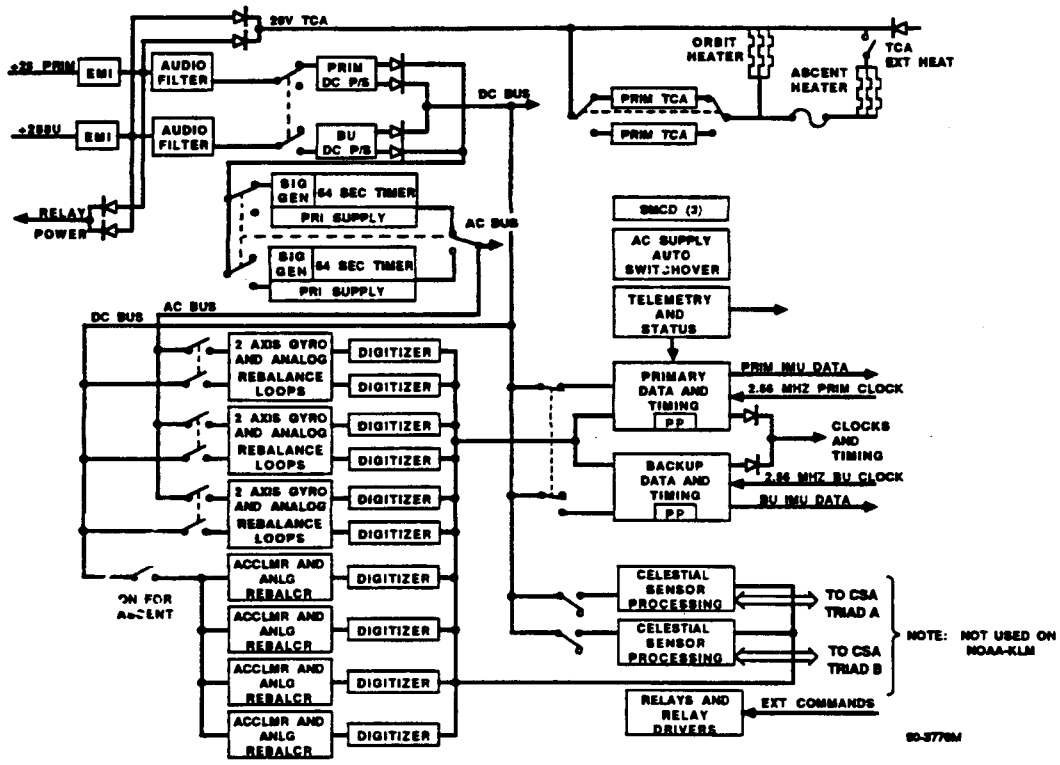

Figure 4.4.8-35. IMU Functional Block Diagram

The 28 Vdc power from the spacecraft regulated bus is filtered and applied to either of two identical temperature control amplifiers, and to either of two identical dc power supplies (via contacts of a primary/backup relays). The IMU is normally operated in the primary mode; however, the dc power supply primary/backup relay is operated automatically to switch to the backup supply in the event of a detected failure in the primary dc power supply. Switchover from backup to primary operation can only be be accomplished by command from the CIU. Each of the dc power supplies provides all power at the various voltages required for IMU operation.

The ac power required for IMU operation is provided by either of two identical ac power supplies. As with the dc supplies, the primary ac power supply is normally in use, as selected by a primary/backup relay. Switchover is accomplished automatically on detection of a failure in the primary ac power supply, and can also be accomplished by command from the CIU. Switchover from the backup to the primary supply can only be accomplished by command from the CIU.

Angular rates in each of the three spacecraft axes are detected by a configuration of three dry tuned, two-degree of freedom gyros (X, Y, Z). Each gyro can be turned on or off individually; normally, all three are turned on sequentially. With all three operating properly, redundant data from each of the spacecraft axes (X, Y, Z) are available. In the event that any one of the three gyros fails, the remaining two still provide angular data for all three axis.

Each of the three gyros requires two analog rebalance loops and two digitizers, with the digital outputs (representing increments of attitude) supplied to both the primary and backup data processing circuitry.

During operation in the ascent mode, linear accelerations along the three spacecraft axes are detected by four Q-Flex accelerometers (three orthogonal and one skewed). Again, each accelerometer channel includes an analog rebalance loop and a digitizer, with the digital outputs (representing increments of velocity) supplied to both the primary and backup data processing circuitry. Only data from the three orthogonal accelerometers are used during ascent operations. The redundancy provided by the skewed accelerometer can not be utilized during ascent since there is no way to conclusively determine a failure. It is included in the IMU for use on another program.

Two identical precision pulsers (a primary and a backup) supply the precision timing signals required for digitizer operation. Selection is governed by the operating data channel mode (primary or backup).

The data processing circuitry samples the digital data inputs at the proper rates and times, and processes the samples to provide 16-bit digital words in the proper sequence. In the I/O and buffer circuitry (also redundant), the words are formatted and multiplexed with a 16-bit status word to provide a data output (from either the primary or backup circuitry) consisting of eight 16-bit digital data words.

All timing within the IMU is controlled by timing signals developed by either of two identical clock countdown chains (again, a primary and a backup). The basic input to each chain is a redundant 2.56-MHz clock signal from the CIU.

4.4.8.2.1.1 Design Approach. The approach to the IMU is defined in terms of six major areas:

- Inertial sensing
- Loop closure
- Analog-to-digital conversion
- Digital data processing
- Supporting functions
- Temperature control

4.4.8.2.1.1.1 Inertial Sensing. Spacecraft angular rates about the three orthogonal axes (pitch, roll, and yaw) are sensed by three Teledyne SDG-5 dry tuned two-degree of freedom gyros. The angular rate about a particular axis is sensed by the gyro associated with that axis, and electrical signals proportional to the rate are generated. The three gyros are mounted to sense rates about the three orthogonal axes; since each gyro has two sensitive input axes, redundant data about all three orthogonal axes is available when all gyro channels are operating.

During ascent operations, linear accelerations along the three orthogonal axes are sensed by four Q-Flex accelerometers. Acceleration along a particular axis is sensed by the accelerometer associated with that axis, and an electrical signal proportional to the acceleration is generated. Three of the four accelerometers are mounted to sense accelerations along the three orthogonal axes; the fourth accelerometer is mounted in a skewed direction such that it senses accelerations along all three orthogonal axes.

4.4.8.2.1.1.2 Loop Closure. Analog loop closure (rebalance) is utilized for each of the three gyros and four accelerometers. Each gyro rebalance loop utilizes switching of both gain and scale factor to optimize resolution, dynamic range, and frequency response in both ascent and orbit modes. Switchover from the ascent mode to the orbit mode may be accomplished with a single command from the CIU; however, redundant orbit mode commands are provided.

4.4.8.2.1.1.3 Analog-to-Digital Conversion. The analog output from each gyro and accelerometer rebalance loop is converted to a pulse rate by a digitizer (a precision voltage to pulse rate converter). The digitizer consists of a precision electronic integrator whose output logically "steers" a pulse from a train of precision restoring pulses into the integrator input. This process results in a variable frequency pulse train, each pulse representing the sensing of a precise value of integrated rotational rate or linear acceleration. Thus, the gyro pulses represent attitude increments, and accelerometer pulses represent velocity increments.

4.4.8.2.1.1.4 Digital Data Processing. The digital pulses from each gyro and accelerometer channel are accumulated for a fixed time interval: 20 milliseconds (50 Hz) in the ascent mode and 100 milliseconds (10 Hz) in the orbit mode. At the end of each interval, the net pulse count is made available for transfer to the CIU.

In addition to the gyro net count data, status data from the IMU is made available for the CIU. Gyro spin motor power status, gyro self-test status, and precision pulse generator selection status (required for scale factor selection) are among the items included in the status data. In the ascent mode, accumulated data net counts from each of the four accelerometer channels are also made available to the CIU. In the orbit mode, the accelerometer data is replaced with dummy data from the CSA.

All data made available to the CIU are presented serially for transfer under CIU control. A total of 128 data bits are available, arranged as eight 16-bit words.

4.4.8.2.1.1.5 Supporting Functions. The IMU is designed to provide all supporting functions internally, with only spacecraft power (+28 Vdc and +10 Vdc), fundamental 2.56-MHz clock signals (from the CIU), and operating mode commands (from the CIU) required as inputs.

The IMU also provides a 10-Hz synchronization signal to the CIU with the IMU in either the ascent or the orbit mode. The leading edge of the signal is used to synchronize the overall spacecraft timing of the CIU, Earth Sensor, telemetry, software, etc.

4.4.8.2.1.1.6 Temperature Control. The temperature of the IMU inertial block, which contains the gyros and accelerometers, is controlled by a thermal control assembly and associated heaters during both ascent and orbit operation.

4.4.8.2.1.2 Operating Modes. Prior to launch, the IMU is turned on when spacecraft power is turned on, and it remains on during ascent and throughout the on-orbit mission duration.

All operating modes of the IMU are listed in Table 4.4.8-5, together with a brief explanation of each and the conditions under which mode is used. Each mode is controlled by a separate command pulse from the IMU which actuates latching relays.

4.4.8.2.1.3 Design Characteristics. The major design characteristics of the IMU are summarized in Table 4.4.8-6.

4.4.8.2.1.3.1 Gyro Channels. The IMU gyro channel performance requirements differ for the ascent and orbit modes, and are considered separately. Table 4.4.8-7 summarizes the IMU gyro channel performance characteristics in the ascent mode. As shown, gyro and digitizer thermal coefficients are significant error sources in both bias and scale factor uncertainty. These terms are dominant because of the relatively large range of chassis temperature ($\pm$10°F in the worst case) prior to launch.

Figure 4.4.8-36 shows the gyro transfer function in the ascent mode. Figure 4.4.8-37 presents the block diagram model (and pertinent parameter values) of the gyro analog torque rebalance loops on which the gyro transfer function is based; the parameter values are given for both the ascent and orbit modes of gyro operation.

Table 4.4.8-8 summarized the gyro channel performance characteristics in the orbit mode, and Figure 4.4.8-38 shows the transfer function in the orbit mode. Gyro fixed bias stability is significantly better in the orbit mode than in the ascent mode. This is a direct consequence of the change in digitizer pulse weight (gyro channel scale factor) between two modes. The fixed bias stability reflects the uncertainty in initial bias estimates which might exist at the transfer from ascent mode to orbit mode and is not in any way indicative of the variation which is required or expected after convergence of steady state on-orbit operation.

Similarly, the scale factor stability represents the uncertainty which is initially expected at the ascent/orbit transfer. As the thermal transient of the launch decays and the gyros return to the controlled temperature, the scale factor uncertainty will become slightly less.

Actual scale factor linearity performance is based on test. At the low rates involved, a significant portion of the apparent non-linearity must be attributed to gyro random bias performance and the resultant data scatter.

Estimated gyro input axis alignment uncertainty, relative to the IMU mounting surface, is the same for ascent and orbit modes. The present estimate of this critical uncertainty is $\pm$55 arc-seconds (3 sigma). This value is within the system allocation of $\pm$60 arc-seconds (3 sigma) for this error source.

Random drift performance at the gyro level is specified at 0.02 degree per hour (3σ), 0.1 to 0.5 Hz; between 0.001 Hz and 0.1 Hz, the single sided power spectral density of the random drift is less than 2.0×10^{-4} $(\text{deg/hr})^2/\text{Hz}$.

In addition to the performance parameters given in Table 4.4.8-8, orbit performance can be affected by IMU sensitivity to environmental variations. The environments which are potentially troublesome are magnetic fields, thermal variations, and applied voltage variations.

TABLE 4.4.8-5. IMU OPERATING MODES

Command	Operation	Conditions/Comments
X Gyro Channel On/Off Y Gyro Channel On/Off Z Gyro Channel On/Off	• Power applied to channel by ON command, removed by OFF command • Start spin motor voltage = 45 volts rms • Run spin motor voltage = 35 volts rms	All gyros are turned on prior to launch, and remain on unless a failure is detected
Ascent/Orbit	• Ascent Mode -Accelerometer channels enabled • Orbit Mode -Accelerometer channels disabled -Gyro channel scale factor decreased by factor of 30 -Gyro channel transfer functions changed -10 Hz sampling rate selected	• Set to ascent mode prior to launch • Commanded to orbit mode by CIU at handover -50 Hz sampling rate
Primary/Backup DC Power Supply	• Primary -Spacecraft primary +28 Vdc applied to primary supply only • Backup - Spacecraft backup +28 Vdc applied to backup supply only	• Normal operation with primary supply • Switch to backup will occur automatically on detection of failure in primary supply • Return to primary supply only by command
Primary/Backup Data Processing	• Primary -Primary data channel selected -Primary clock countdown chain selected -Primary I/O and buffer channel selected • Backup -Backup data channel, clock countdown chain, and I/O and buffer channel selected	• Normal operation with primary data processing • Switched only by command

TABLE 4.4.8-5. IMU OPERATING MODES (Continued)

Command	Operation	Conditions/Comments
XA Gyro Channel Test On/Off YA Gyro Channel Test On/Off ZA Gyro Channel Test On/Off XB Gyro Channel Test On/Off YB Gyro Channel Test On/Off ZB Gyro Channel Test On/Off	• When commanded ON, stimulus is applied to analog rebalance loop of appropriate channel	• Used to verify gyro channel operation
Primary/Backup AC Supply	• Primary -Primary spin motor supply and signal generator enabled • Backup -Backup spin motor supply and signal generator enabled	• Normal operation with primary supply • Switch to backup will occur automatically on detection of failure in primary supply • Return to primary supply only by command

TABLE 4.4.8-6. IMU DESIGN CHARACTERISTICS

Gyros	
Number	3 (each gyro has 2 sensitive input axes)
Type	Strapdown, Rate Integrating
Model	Teledyne SDG-5 Dry Tuned
Rate Response Range	±15°/sec (ascent) ±1.0°/sec (orbit)
Accelerometers	
Number	4 (3 orthogonal, 1 skew)
Type	Flexible Seismic Pendulum
Model	Sundstrand "Q" Flex
Response Range	±23.7 g
Power Requirements	
Ascent	69.6 W
Orbit	50.1 W
Size	13.15 x 11.85 x 8.6 inches
Weight	39.14 lb

TABLE 4.4.8-7. GYRO CHANNEL PERFORMANCE CHARACTERISTICS, ASCENT MODE

Parameter	Requirement	Principal Error Contributions
G-Insensitive Bias	±10°/hr (Maximum)	None. Initial calibration to achieve
G-Insensitive Bias Stability (240 day)	±0.65°/hr (3σ)	Gyro stability, digitizer stability, digitizer thermal coefficient
G-Insensitive Bias Stability (24 hour)	±0.2°/hr (3σ)	Gyro stability, digitizer thermal coefficient
G-Sensitive Bias	±8°/hr/g (Maximum)	None. Gyro calibration to achieve
G-Sensitive Bias Stability (240 day)	±0.60°/hr/g (3σ)	Gyro stability, gyro thermal coefficient
G-Sensitive Bias Stability (3 hour)	±0.05°/hr/g (3σ)	Gyro thermal coefficient
Rate Range	±15°/sec (Minimum)	Worst case tolerance buildup
Scale Factor	1.83 arc-sec/pulse ±5%	None. Initial calibration to achieve
Scale Factor Stability (240 day)	±600 ppm (3σ)	Gyro stability, gyro thermal coefficient, digitizer stability, digitizer thermal coefficient
Scale Factor Linearity	±400 ppm (3σ)	Gyro linearity
Frequency Response	Nominal Response per Fig. 4.4.1-3	None. Requirement generated from nominal design values
Alignment	±0.5 degree (Maximum)	Gyro tolerance, gyro mount machining
Alignment Uncertainty	±60 arc-sec (3σ)	Gyro stability, sensor block stability
Hangoff	30.6 arc-sec/deg/sec (Maximum)	None. Steady state hangoff is zero as a result of integrator in sync loop
Anisoelastic Drift	±0.10°/hr/g^2 (Maximum)	Gyro, package transmissibility

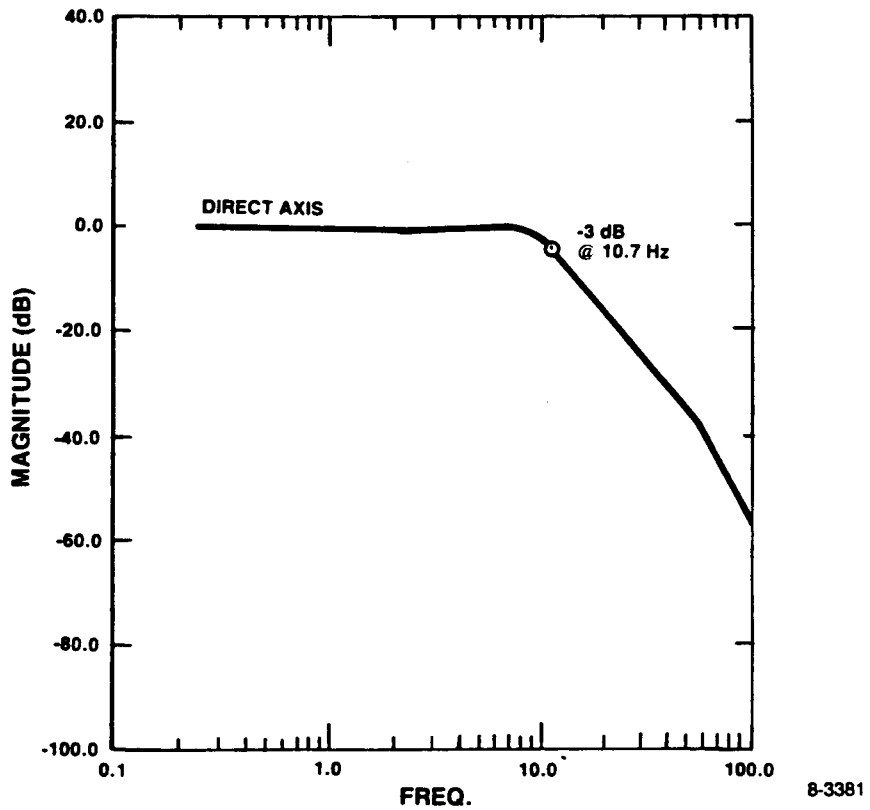

Figure 4.4.8-36. Gyro Channel Transfer Function, Ascent Mode

Sensitivity to these variations does not necessarily result in degraded orbit performance, depending on the nature of the environmental variation. A constant uncertainty in any of these environments do not pose a problem, if such variations are not large enough to dominate the gyro channel random drift performance. The most troublesome variations are those which occur in a deterministic manner, either as periodic functions of orbit frequency or as aperiodic steps or shifts in the environment.

Magnetic field variations include both periodic components at orbit frequency due to the earth's magnetic field, and step changes due to magnetic momentum unloading coils. Unloading field steps will have a significant component at orbit frequency. To minimize errors due to magnetic fields, each gyro includes integrally fitted mu-metal shielding.

Thermal variations are known to occur at orbit frequency due to the cyclic heat input to the IMU by the earth's albedo. The resultant cyclic temperature variations of the gyros and their associated electronics causes both bias and scale factor shifts. Passive control of the IMU surface temperature proved insufficient; active control of gyro temperature is included in the ascent and orbit mode operating configurations.

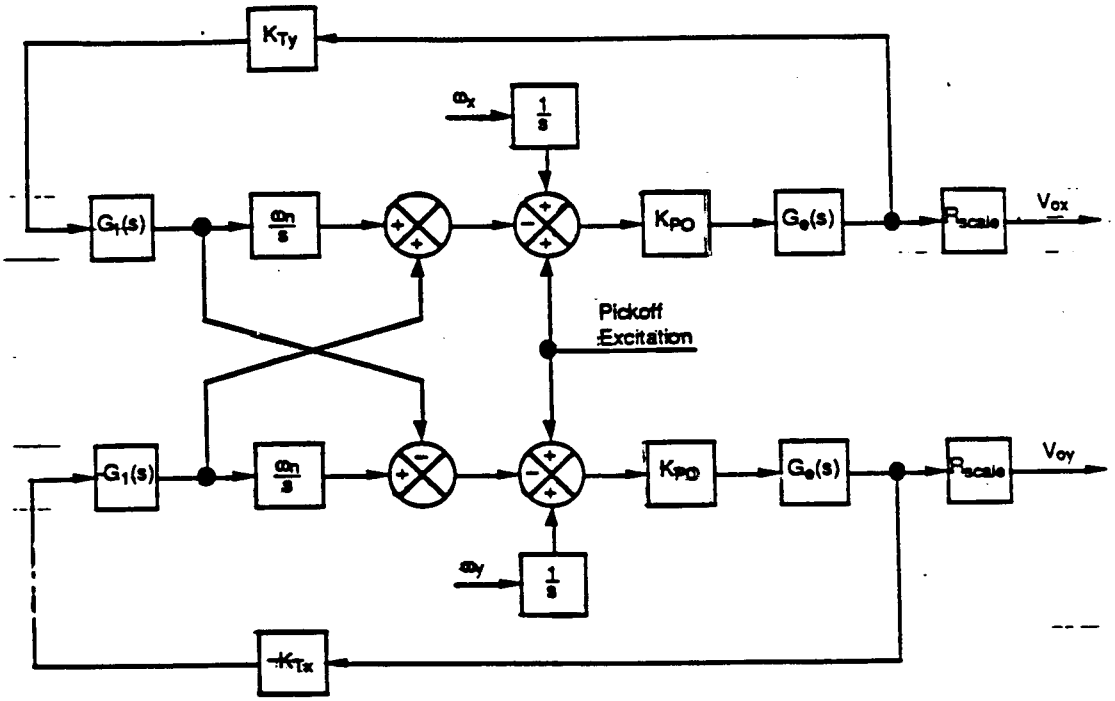

$$G_e(s) = \frac{K_d K_i K_f K_{gc} K_p (1 + s\,\tau_{lead})}{s(1 + s\,\tau_{lag})\left(\frac{s^2}{\omega_f^2} + \frac{2\,\delta_f\, s}{\omega_f} + 1\right)}$$

$$G_1(s) = \frac{1}{\omega_n H \left(\frac{s^2}{\omega_n^2} + \frac{2\,\delta_n\, s}{\omega_n} + 1\right)}$$

Parameter	Description	Units	Orbit Mode	Ascent Mode
V_{ox}, V_{oy}	Output	volts	—	—
ω_x, ω_y	Input angular rate	rad/sec	—	—
ω_n	Nutation frequency	rad/sec	1100	1100
H	Gyro rotor angular momentum	gm cm^2/sec	10^6	10^6
δ_n	Gyro damping ratio	—	0.003	0.003
K_{Tx}, K_{Ty}	Torquer gain	dyne cm amp	8.5×10^5	8.5×10^5
K_{po}	Pickoff gain	V_{rms}/rad	1000	1000
K_d	Demodulator and filter gain	V_{dc}/V_{rms}	−1.23	−1.23
K_i	Integrator gain	V/sec/V	−0.677	−0.677
K_f	Second order filter	V/V	−1	−1
K_{gc}	Gain change	V/V	−0.503*	−1.258*
K_p	Power amplifier	amp/V	0.0541*	0.0541*
R_{scale}	Readout resistance	ohms	555*	18.5*
τ_{lag}	Integrator lag time constant	seconds	0.0133	0.0133
τ_{lead}	Integrator lead time constant	seconds	0.861	0.861
ω_f	Second order filter natural frequency	rad/sec	321	321
δ_f	Second order filter damping ratio	—	0.716	0.716

* The nominal value is listed herein. The actual value is selected to compensate for gyro unique performance characteristics.

90-3686

Figure 4.4.8-37. Gyro Transfer Function Parameters

TABLE 4.4.8-8. GYRO CHANNEL PERFORMANCE CHARACTERISTICS, ORBIT/MANEUVER MODE

Parameter	Requirement	Principal Error Contributions
G-Insensitive Bias	±10°/hr (Maximum)	None. Initial calibration to achieve
G-Insensitive Bias Stability (240 day)	±0.30°/hr (3σ)	Gyro Stability
G-Insensitive Bias Stability (24 hr)	±0.070°/hr (3σ)	Gyro Stability
G-Insensitive Bias Stability (8 hrs)	±0.025°/hr (3σ)	Gyro Stability
G-Insensitive Bias Stability (Launch 7 day)	±.30°/hr (3σ)	Gyro Stability
Rate Range	±1800°/hr (Minimum)	Gyro channel scale factor. Calibration to achieve
Scale Factor	0.061 arc-sec/pulse ±5%	None. Initial calibration to achieve
Scale Factor Stability (240 day)	±375 ppm (3σ)	Gyro stability, gyro thermal coefficient, digitizer stability, digitizer thermal coefficient
Scale Factor Non-Linearity	±300 ppm to 300°/hr and ±600 ppm from 300 to 1800°/hr	Digitizer linearity/symmetry, random drift
Scale Factor Asymmetry	±(200 ppm + 40 ppm/(°/sec of input rate) (3σ)	Digitizer
Frequency Response	Nominal Response per Fig. 4.4.1-5	None. Requirement generated from from nominal design values
Alignment	±0.5 degree (Maximum)	Gyro tolerance, gyro mount machining
Alignment Uncertainty	±60 arc-sec (3σ)	Gyro stability, sensor block stability
Hangoff	108 arc-sec/deg/sec (Maximum)	None. Steady state hangoff is zero as a result of integrator in sync loop

TABLE 4.4.8-8. GYRO CHANNEL PERFORMANCE CHARACTERISTICS, ORBIT/MANEUVER MODE (Continued)

Parameter	Requirement	Principal Error Contributions
Random Drift	0.04°/hr (3σ) for frequencies between 0.1 Hz and 0.5 Hz. Between 0.001 Hz and 0.1 Hz, the single sided, random drift power spectral density shall be $<3.6 \times 10^{-4}(°/hr)^2/Hz$	Gyro performance. See text.
Magnetic Sensitivity	±0.15°/hr/gauss	Gyro performance

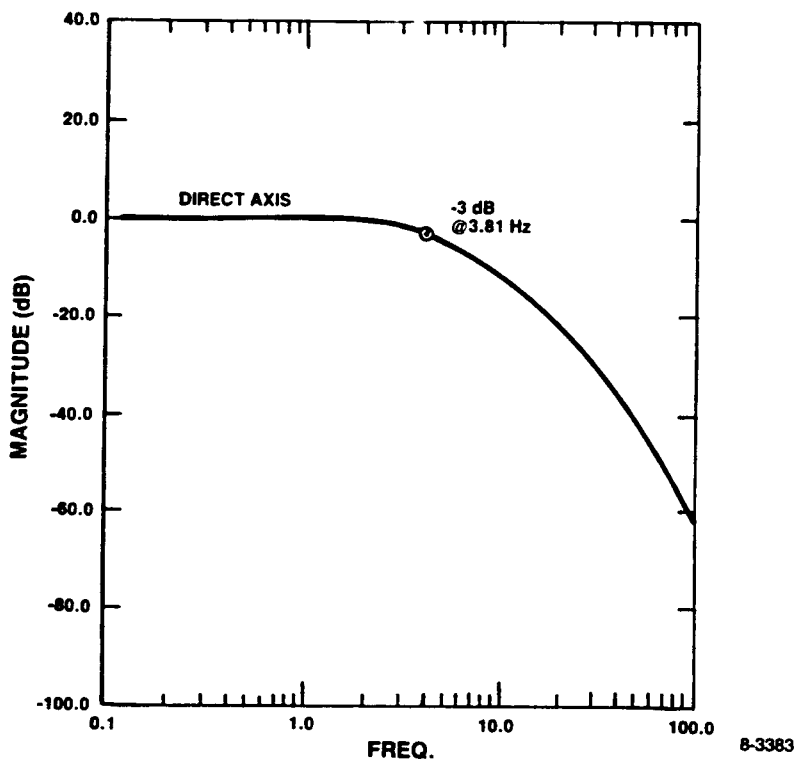

Figure 4.4.8-38. Gyro Transfer Function, Orbit Mode

Variations on the 28 Vdc bus occur at orbit frequency due to the solar panels being alternately sunlit and shaded. The changes occur in a step fashion as the spacecraft enters and leaves the earth's shadow. This variation requires additional regulation in the gyro spin motor supply to avoid step changes in gyro bias. The regulation included in the IMU effectively eliminates this potential error source.

4.4.8.2.1.3.2 Accelerometer Channels. Table 4.4.8-9 summarizes the accelerometer channel performance requirements. Projected performance against the PA coupling requirements is zero. Discussions with the accelerometer vendor have verified that the Q-Flex unit is essentially immune to error from this source. These terms are caused by anomalies in the compliance of the device. The proof mass of the Q-Flex is constrained against acceleration in the pendulous axis. Any deflection must result from tension in these beams, which are formed as an integral part of the proof mass assembly. Past efforts to evaluate these terms have yielded data that were characteristic only of alignment uncertainty and input axis rectification.

Figure 4.4.8-39 shows the nominal accelerometer transfer function exclusive of scale factor error effects. Figure 4.4.8-40 presents the block diagram model and pertinent parameter values on which the accelerometer transfer function is based.

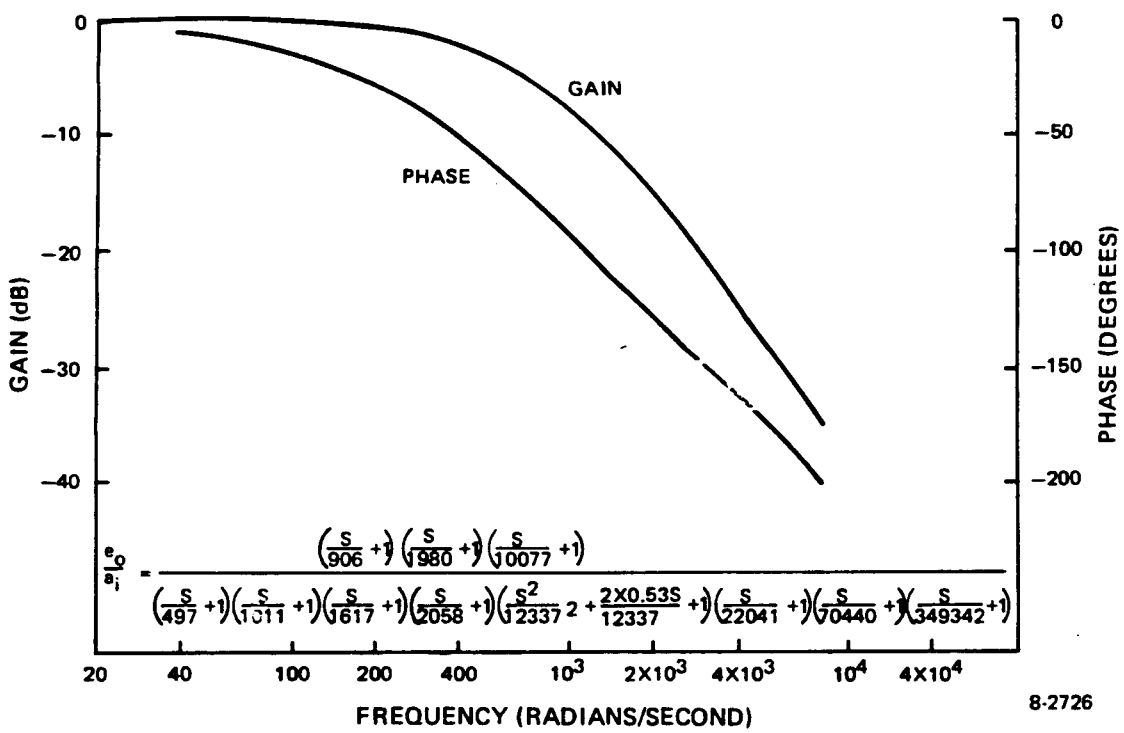

Figure 4.4.8-39. Accelerometer Closed-Loop Transfer Function

4.4.8.2.1.4 Physical Description. The IMU is designed as a flexible structure that protects the sensor and electronics from the severe vibration and yet is stable and lightweight, utilizing modular construction and proven packaging techniques. It consists of an investment cast chassis structure that contains plug-in printed circuit boards for the ac and dc power supplies and support electronics, and an inertial sensor block with pig-tailed connectors.

The IMU assembly is secured to the spacecraft IMP by means of an interface adapter. This mounting base is hardmounted via three high-strength fasteners. Figure 4.4.8-41 shows the adapter construction features and support pylons for the four-point external isolator mounting of the IMU.

TABLE 4.4.8-9. ACCELEROMETER CHANNEL PERFORMANCE

Parameter	Requirement	Principal Error Contributions
Null Bias	±0.020 g (Maximum)	None. Initial calibration to achieve
Bias Stability (30 minutes)	±80 μg (3σ)	Accelerometer stability digitizer thermal coefficient
Bias Stability (3 hour)	±400 μg (3σ)	Accelerometer stability, digitizer thermal coefficient
Bias Stability (240 day)	±700 μg (3σ)	Accelerometer stability, digitizer stability
Bias Stability (Across vibration)	±700 μg (3σ)	Accelerometer stability
Range	±21 g (Minimum)	Worst case tolerance
Scale Factor	0.023 ft/sec/pulse ±5%	None. Initial calibration to achieve
Scale Factor Error (240 day)	±600 ppm (3σ)	Accelerometer linearity and scale factor stability
Scale Factor Asymmetry	400 ppm (3σ)	Accelerometer scale factor symmetry
Frequency Response	Nominal Response per Fig. 4.4.1-6	None. Requirement generated design values
Vibropendulous Bias	±4700 μg (3σ)	Accelerometer mechanism
Input Rectification Bias	±5200 μg (3σ)	Accelerometer mechanism
Alignment (IA to Cube)	±1.0 degree (Maximum)	Accelerometer tolerance, accelerometer mount machining
Alignment Uncertainty	±0.5 mrad (3σ)	Accelerometer stability
IA/PA Cross Coupling (includes hangoff)	60 $\mu g/g^2$ (Maximum)	Deterministic error due to finite loop bandwidth
IA/OA Cross Coupling PA/OA Cross Coupling	±300 $\mu g/g^2$ (3σ)	Accelerometer compliance terms
2nd Order Nonlinear Effects (g^2)	±50 $\mu g/g^2$ (3σ)	No known mechanism

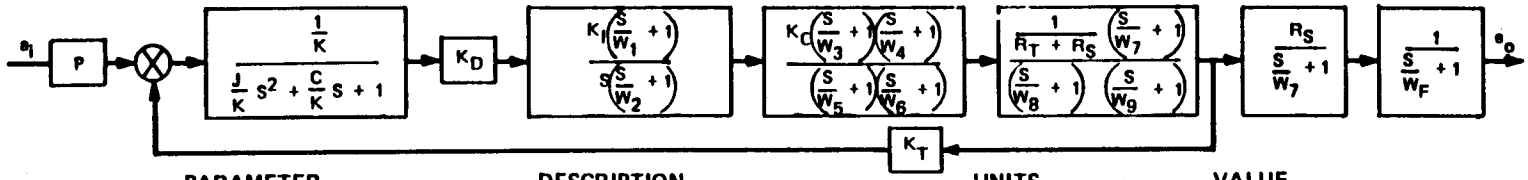

PARAMETER	DESCRIPTION	UNITS	VALUE
a_i	Input acceleration	g	–
P	Pendulous scale factor	dyne cm/g	580
J	Pendulum inertia	gm–cm^2	0.5
C	Pendulum damping	dyne cm sec	1500
K	Pendulum elastic restraint	dyne cm/rad	4060
K_D	Detector gain	amp/rad	0.05
K_I	Integrator gain	volt/amp-sec	4.55×10^7
W_1	Integrator zero	rad/sec	1.98×10^3
W_2	Integrator pole	rad/sec	4.55×10^4
K_C	Compensation gain	volt/volt	3.8
W_3, W_4	Compensation zeros	rad/sec	906, 10077
W_5, W_6	Compensation poles	rad/sec	3704, 3.49×10^5
R_T	Torquer resistance	ohm	170
R_S	Sampling resistance	ohm	130
W_7	Load zero	rad/sec	1876.2
W_8, W_9	Load poles	rad/sec	3402, 55140
W_F	Filter pole	rad/sec	497
K_T	Torquer constant	dyne cm/amp	4.35×10^5
G	Loop gain $= K_D K_I K_C K_T / K (R_T + R_S)$	sec^{-1}	3.0875×10^6

8-2727

Figure 4.4.8-40. Accelerometer Loop Block Diagram

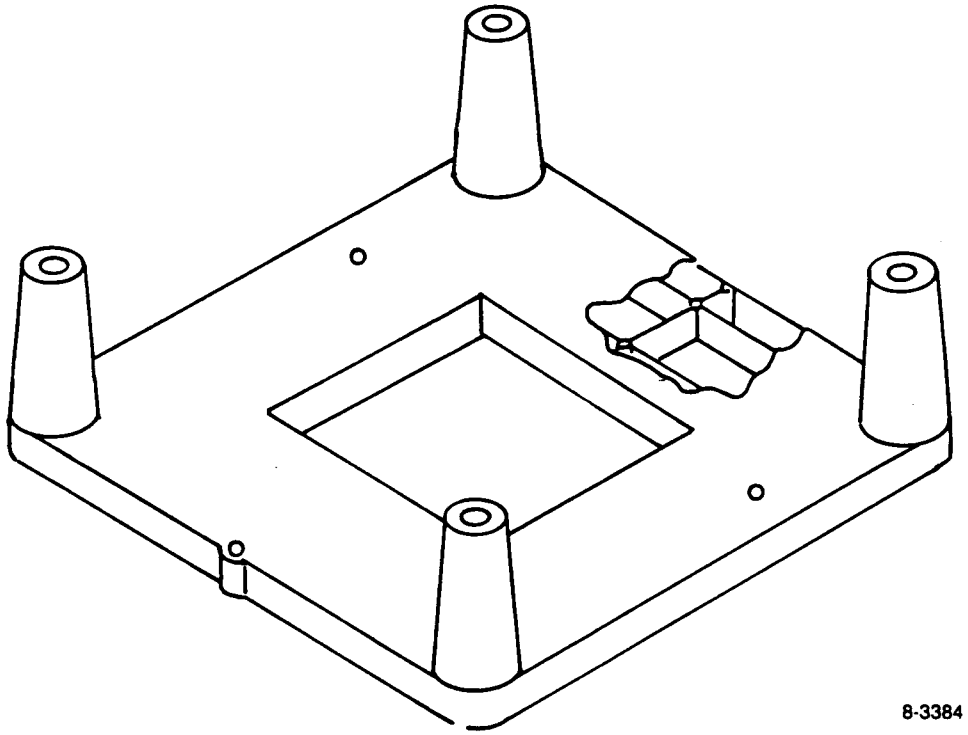

Figure 4.4.8-41. IMU Mounting Base

4.4.8.2.1.4.1 Chassis Structure. The chassis assembly houses the electronics and supports the inertial block. The chassis has a four-point center of gravity mount to the interface adapter through external isolators. The isolators have a resonant frequency of 120 Hz and a Q of 3.5 and provide vibration protection for the gyros.

The chassis structure has five modularized compartments: one for the inertial block, one for the spin motor supply and chassis mounted components, one for the dc supply printed circuit cards, one for the 21 support electronics cards, and one for the EMI filter.

Figure 4.4.8-42 is an exploded view of the IMU, and Figure 4.4.8-43 shows a photograph of the IMU.

4.4.8.2.1.4.2 Inertial Block. The inertial block assembly contains all components that must be aligned. The components are hard mounted to the block, and the block is temperature controlled. This technique removes any unstable insulators under the components and minimizes the component to component gradient changes. Also, it requires only one temperature control assembly, thus simplifying the electronics, although two are provided for redundancy.

The inertial block consists of a cast block, three gyros, four accelerometers, an optical cube, temperature control components, and some electronic circuits. The block provides pre-aligned interfaces by which the gyros, accelerometers, and optical cube are aligned to each other as well as to the main chassis. Gyros and accelerometers are inserted in cavities, positioned against their respective reference surfaces, and bolted through their flanges. The inertial block to chassis interface is a three point mount.

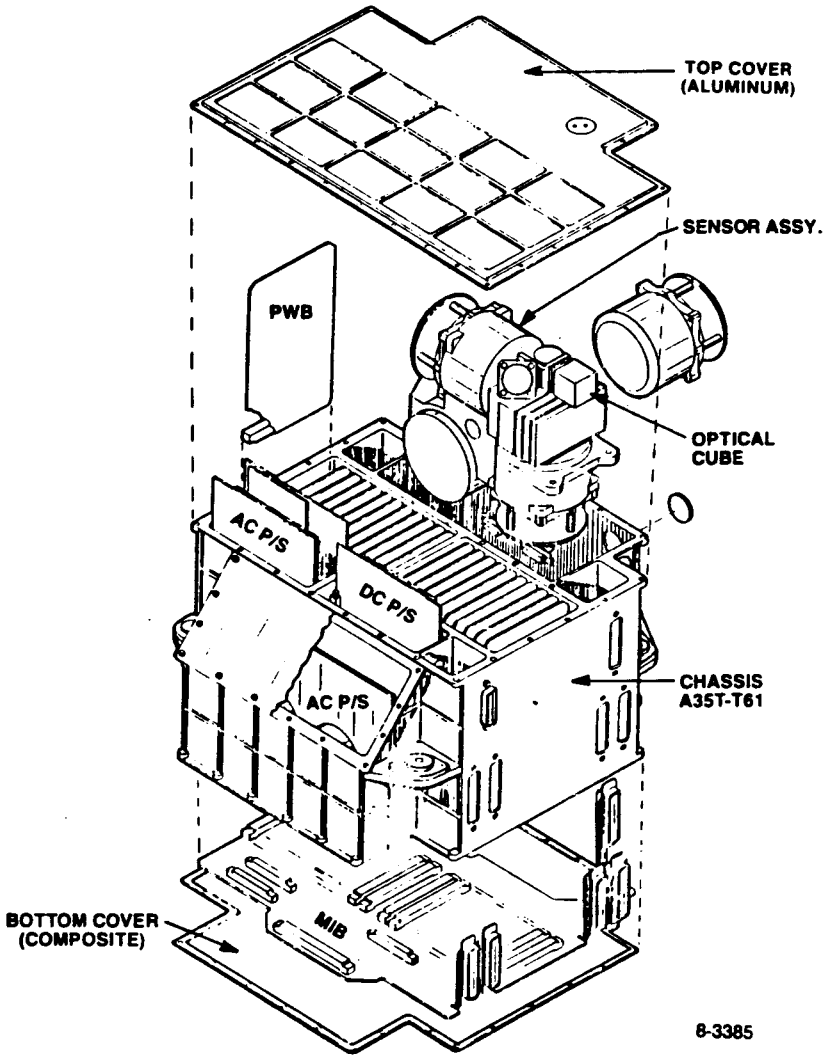

Figure 4.4.8-42. IMU Exploded View

The use of the aluminum optical cube in an aluminum inertial sensor block eliminates the differential expansion problem usually encountered with a glass to aluminum interface. Optical surfaces on the cube are diamond machined.

For temperature control, the block has a heater element inserted in each foot to minimize gradient changes. Three temperature sensors are mounted on the block. One for each of the two TCAs and one for the Block Temperature Telemetry circuit. Redundant precision pulser circuits are also mounted on the block to take advantage of the temperature control.

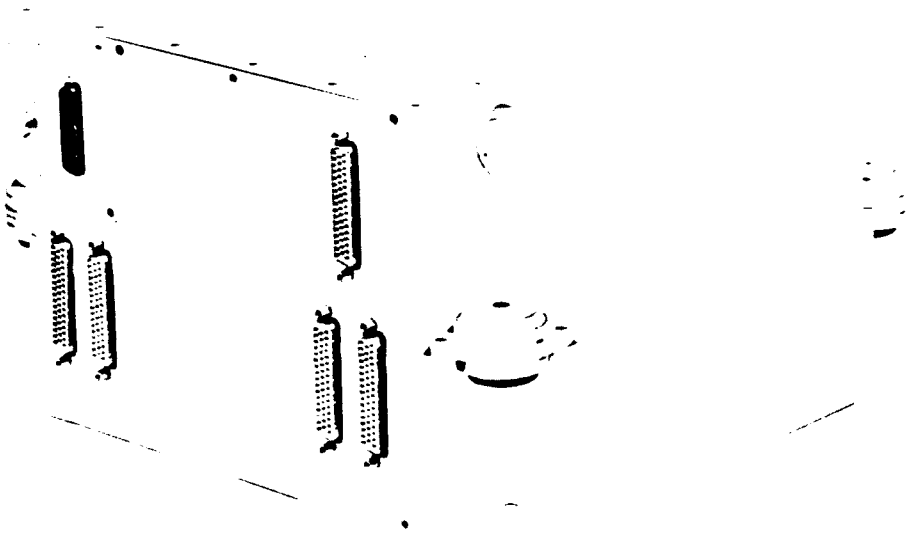

Figure 4.4.8-43. IMU

8801-162

4.4.8.2.1.4.3 Electronic Packaging. The IMU electronics are packaged into three major subassemblies and interconnected by a single master interconnect board as follows:

- The main chassis assembly contains the major portion of the electronics on printed circuit boards, houses most of the harness assembly, and contains an interconnect cavity for chassis mounted circuits, as well as five of the six IMU connectors.

- The dc power supply assembly is separately packaged, off to the side of the main circuit board compartments and contains the other IMU connectors.

- The inertial block assembly is separately packaged and is mounted on one end of the main chassis assembly.

The 21 circuit boards housed in the main chassis assembly are mounted in Birtcher card guides. The master interconnect board provides the electrical interfaces between circuit boards and with other IMU components.

The IMU uses custom printed circuit boards for all plug-in subassemblies. All but four assemblies in the main chassis compartment are simple two-sided boards using plated through holes to increase reliability. The remaining assemblies (timer, input, and output boards) are five layer designs, but interior layers are used only for ground connections (two planes) and power connections. Redundant plated through holes are provided when connections are required to internal layers from components mounted on the board surface; the redundant

hole does not suffer the thermal shock of the component soldering process and thus is less susceptible to circuit path failures at the connection to the internal layer. The gyro loop boards are equipped with a copper ground plane (but no power plane) to provide a heat transfer path cor components that heat up at high input angular rates.

A single master interconnect board assembly provides all interconnections between the circuit boards and with other IMU components. This assembly is an eight-layer printed circuit board, mounted primarily in the circuit board housing.

The dc power supply assembly is packaged in a separate compartment which is further subdivided for each circuit board. The major elements in the dc power supply assembly are:

- EMI filter box assembly, with IMU connector J6
- Four circuit boards mounted in Birtcher guides

The circuit boards are equipped with an aluminum heat sinks and are slightly larger than circuit boards in the main chassis assembly. The dc supply boards use the same type of connector as the other boards. The cover has an access cutout for the IMU J6 connector.

As described previously, the inertial block is a single block, configured to accept and accurately maintain alignment of the inertial components. The major elements packaged in this assembly are the three gyros, the four accelerometers, two precision pulsers, an optical cube, and temperature control elements. The optical cube is the IMU alignment reference, and is mounted permanently and accurately to the block.

4.4.8.2.1.4.4 Weight. The estimated weight of the IMU is 39.15 pounds.

4.4.8.2.1.4.5 Thermal Characteristics. The IMU is thermally insulated from its mounting surface, the IMP. The IMP is a stable platform and cannot tolerate heat input from the IMU. Heat is dissipated from the IMU by radiation to deep space from its -Z and -X external surfaces. Such heat dissipation is accomplished by a thermal control coating on the IMU and a thermal hood placed over the IMU.

The primary purpose of the hood is to protect the IMU from direct and reflected sunlight. The shroud opening faces normal to the orbit plane, so that the only varying heat load input to the IMU is the earth albedo entering the aperture and the shadowing of the hood by the solar array. The IMU has a thermal control coating of white paint on the exterior surfaces; the paint has an emittance of approximately 0.9 and an absorptance of approximately 0.2.

An inertial block temperature controller is incorporated to control the gyro operating temperature. This controller consists of six cartridge heaters and redundant temperature sensors embedded in the block, and a temperature control amplifiers. The output transistor for this amplifier is mounted on the spin motor supply chassis rather than the block to allow for more stable thermal control.

The IMU is calibrated during assembly so that approximately 6 watts of heater power are used at the nominal interface condition. Total available heater power is 12 watts to allow for control margin over the orbital and mission life variations.

In the event that a gyro channel failure requires that it be turned off, cartridg heaters can make up about 2 watts of power per gyro so that control over the entire ambient range can be maintained.

In the ascent mode, a heater capacity of about 25 watts is provided to assure active control over the more demanding environments on the launch pad and during boost. This additional authority is provided by connecting an additional heater set in parallel with the orbit mode heaters, using an ascent mode relay contact.

4.4.8.2.2 Functional Description

A block diagram of the IMU was shown in Figure 4.4.8-35. In brief, the IMU utilizes power from the spacecraft +28 Vdc bus and +10 Vdc bus to provide all voltages in the IMU itself. The dc voltages are provided by a redundant dc power supply, the ac voltages by a redundant ac power supply. Switchover from the primary supply to the backup supply is accomplished by signals from the CIU or, in the case of the dc supply, automatically upon detection of a failure in the primary dc supply. The ac power is coupled, via relays controlled by CIU signals, to each of three dynamically tuned, two-degree of freedom gyros. The three gyros are mounted to detect angular rates about the spacecraft X, Y, and Z axes. Each gyro includes two analog rebalance loops and digitizers which provide variable frequency pulse train outputs, each pulse representing an attitude increment in the specific axis. These pulses are accumulated for a fixed time period, and the count is provided to the CPU. In the ascent mode, the IMU also provides similar data on linear acceleration in each of three orthogonal axes (the spacecraft X, Y, and Z axes) with a fourth accelerometer mounted at a 54.736 degree angle to each of the axes. The data processing circuitry and output buffer circuitry are also redundant, with switching accomplished by signals from the CIU.

4.4.8.2.2.1 <u>DC Power Supplies</u>. The dc power supply functions are contained on four printed circuit boards: the primary and back-up dc supplies, the input filter/relay board, and the primary dc supply failure detector.

4.4.8.2.2.1.1 <u>Input Filter/Relay Functions</u>. Figure 4.4.8-44 shows a block diagram of the dc power supplies. The primary and back-up spacecraft 28V bus lines enter the IMU at the EMI filters, which reside in a separate compartment in the IMU. From here the buses are routed to the Input Filter/Relay Board where they pass through the contacts of the IMU off relay and the audio filters. The primary/backup dc supply selection relay, also located on this board, applies the filtered +28V to its appropriate dc supply. (The IMU power off relay is used only during ground testing and is energized via the ground support equipment.) The selection between primary and back-up dc supplies is accomplished with the Primary/Backup DC selection relay, a bi-directional latching relay which can be commanded by the CIU. A primary dc on signal from the CIU causes the primary 28 Vdc to be applied to the primary dc power supply; a backup dc ON signal from the CIU causes the backup 28 Vdc to be applied to the backup dc power supply. In addition, if a failure occurs in the primary

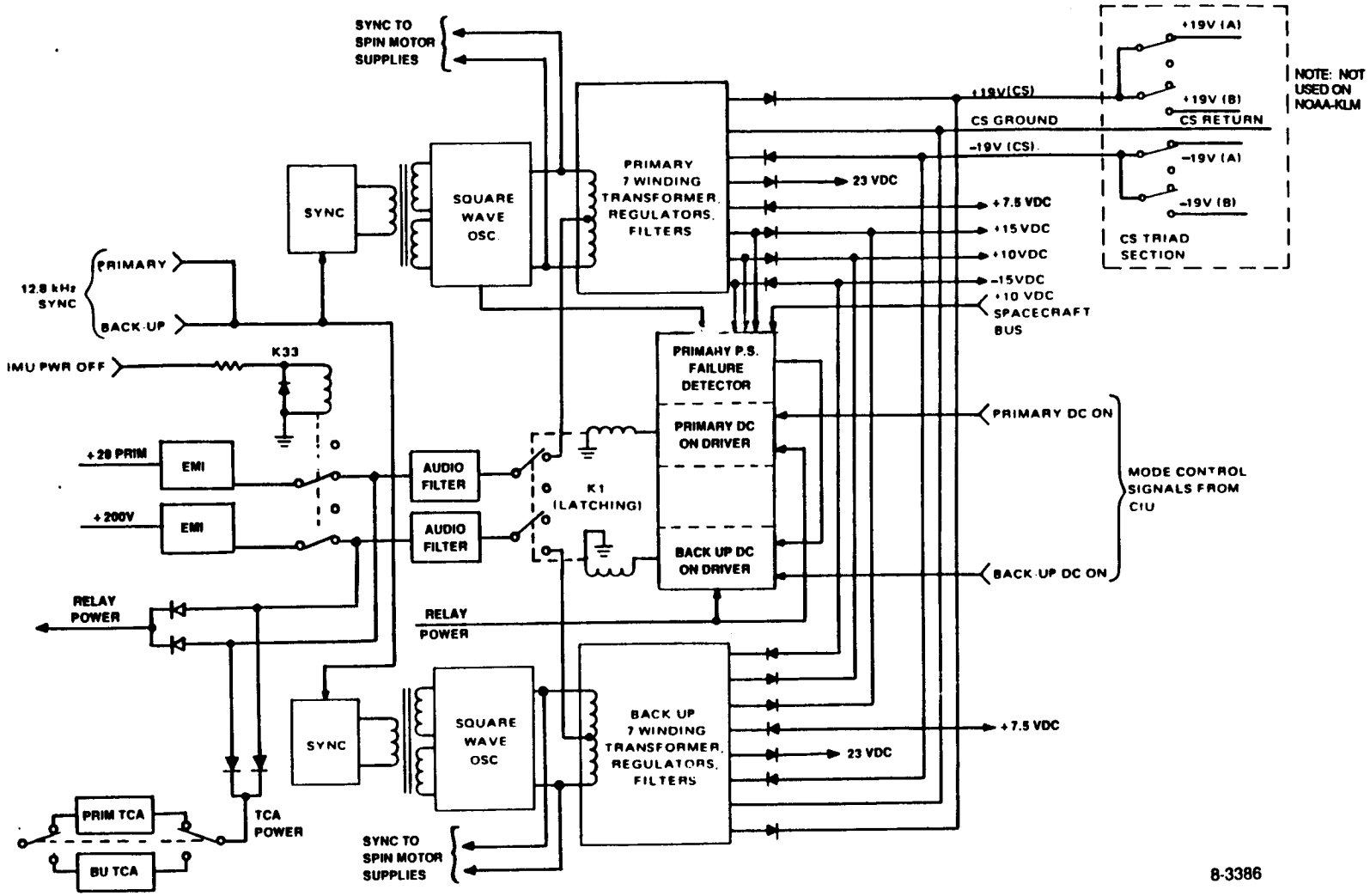

Figure 4.4.8-44. DC Power Supplies, Block Diagram

supply during operation in the primary mode, the failure detection circuitry causes an automatic switchover to the backup supply.

The Input Filter/Relay board also supplies 28V to the relays and TCAs. Each of these voltages is the diode-OR of the primary and backup 28V lines before the audio filter. A relay on this board also provides switching between primary and backup TCAs.

4.4.8.2.2.1.2 Primary Power Supply Failure Detection. The failure detection circuitry is designed such that a failure in the primary dc must last for at least 6 milliseconds (nominal) before switchover is initiated (precluding "nuisance" switchovers resulting from transients). The time required for switchover in the event of an actual failure is approximately 70 milliseconds, measured from the start of the failure until backup supply voltages are within the specified limits.

The DC Supply Failure Detector receives its power from the +15 Vdc supply output and the +28 Vdc relay power (see Figure 4.4.8-45). The failure detector monitors three dc voltages: +10V, +15V, -15V, with the trip levels set to 20% below the nominal values. The failure detector also monitors a 12.8 kHz signal from one of the secondary windings of the primary dc-dc converter transformer. This voltage is proportional to the transformer flux that produces all power supply output voltages; the loss of this signal represents the loss of the basic dc-dc converter action. If this voltage should go to zero for approximately 20 ms, or if one of the dc voltages should drop below the trip level, a single-shot pulse is produced automatically to switch the relay from the primary dc supply to the backup dc supply.

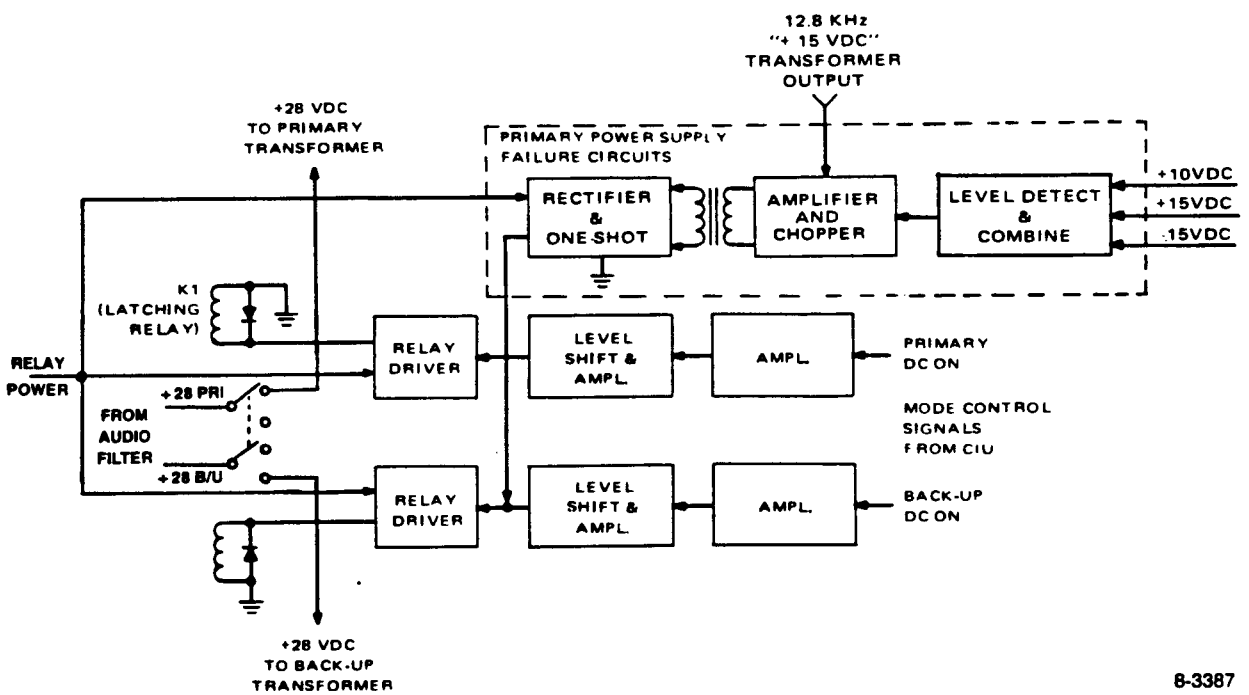

Figure 4.4.8-45. Primary/Backup DC Power Supply Switching

The DC Supply Failure Detector Board also contains the circuitry that generates the sync signals for the timing transformers from the 12.8 kHz logic signal. The two 12.8 kHz logic square waves, one from the primary data channel, the other from the backup, are diode-OR'd so that either signal can drive both the primary and backup circuits. The driver circuits each contain a 4041 CMOS buffer which generates an in-phase and an inverted signal, each ac coupled to a 2N2222A drive transistor connected to one of the timing transformer windings.

The DC Supply Failure Detector also contains telemetry circuits for the +15 Vdc, -15 Vdc, +10 Vdc, and the three spin motor supply phases. The telemetry outputs are proportional to the rms. Values of the voltages being monitored. The relay driver circuits for the Primary/Backup DC ON commands are located on this board.

4.4.8.2.2.1.3 Transformer and Transformer Input. In each dc power supply, the +28 Vdc power is fed to a free-running square wave oscillator whose natural frequency is slightly less than 12.8 kHz. A 12.8 kHz sync signal derived from the CIU is amplified and transformer coupled into the square wave oscillator to synchronize the dc power supply frequency at exactly 12.8 kHz. The synchronized oscillator drives an isolation transformer that has 7 output windings (see Figure 4.4.8-46). The outputs of the windings are each full-wave rectified and filtered. Three of the seven dc voltages thereby produced are analog regulated by means of an IC regulator and chassis mounted pass transistors.

Each of these regulators incorporates protective current limiting. Five of the dc voltages produced are referenced to a common ground that serves as the IMU logic, spin motor, and signal ground. Two other dc voltages have a common isolated ground for power supplied to the celestial sensor circuitry. The dc voltages for each dc power supply are described below.

The +23 Vdc supply is not regulated; it is used only to power the IC regulator for the +15V output.

The ±15 Vdc supplies are derived from separate windings, analog regulated with current limiting protection, and referenced to the IMU dc signal ground. The ±15 Vdc are the main power source for the analog circuits; the ±15 Vdc are widely distributed through the IMU.

A +10 Vdc supply is derived from a separate winding, and analog regulated with current limiting protection. This voltage is extensively used throughout the IMU for CMOS circuits, other than the interface circuits powered by the spacecraft +10 Vdc.

Each power supply has a +7.5 Vdc winding. This voltage is not regulated, and is referenced to the dc power supply ground. The 7.5 Vdc is used to power the 12.8 kHz sync circuit and the -15 Vdc IC regulator. The only use of this voltage external to the dc power supply is for telemetry. Each +7.5 Vdc voltage is conditioned separately for telemetry as an indication of which supply (primary or backup) is selected.

All other regulated voltages from the dc power supply chassis (±15 Vdc, +10 Vdc) are diode-OR'd between the primary and backup dc supplies. Telemetry conditioning is performed downstream of the diode-OR so that telemetry readings of these signals will reflect the voltage derived from the active supply.

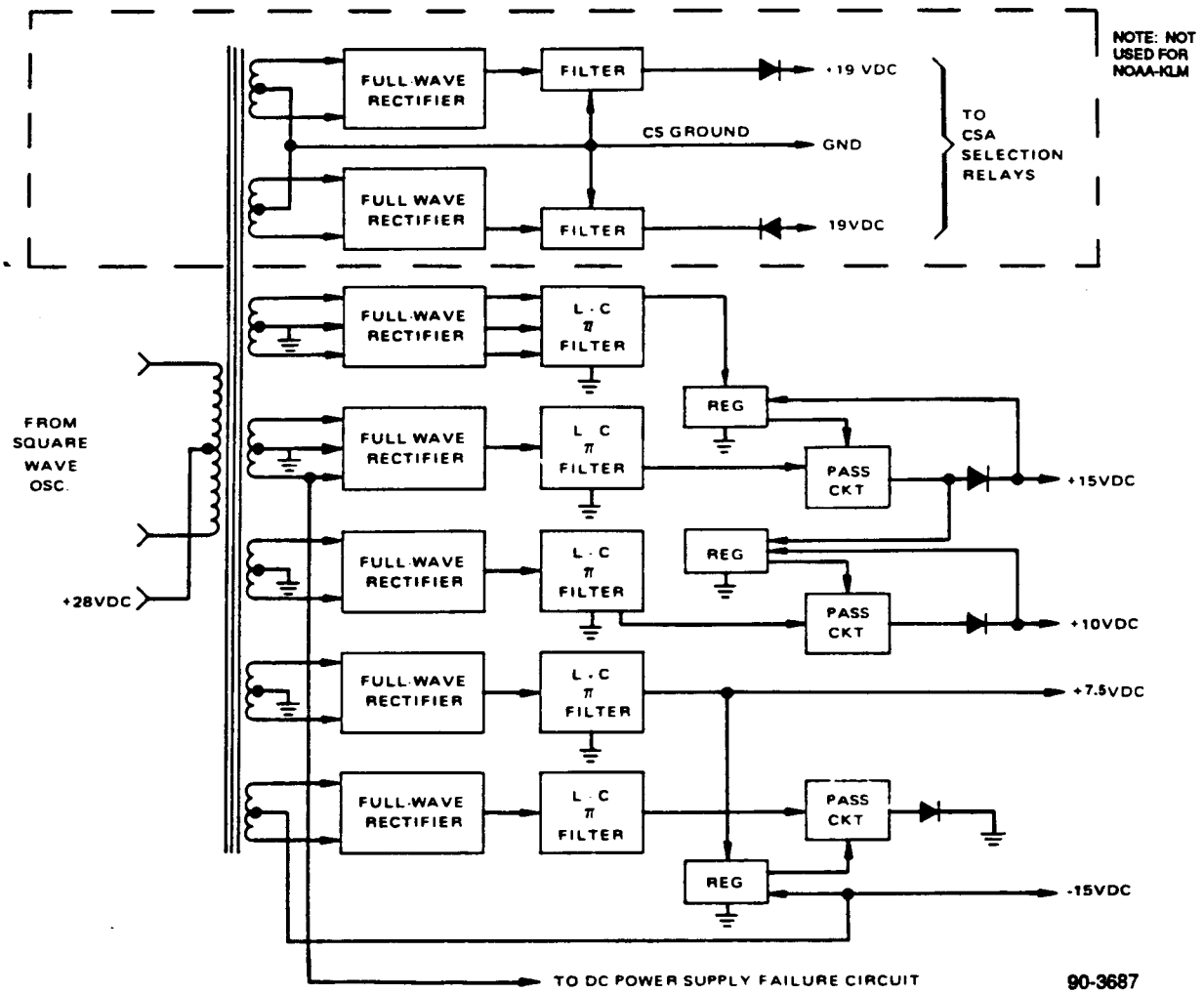

Figure 4.4.8-46. Transformer, Rectifiers, and Filters (Primary or Backup) Block Diagram

4.4.8.2.2.1.4 Spin Motor Supply Sync Voltage. Each dc supply also provides two 12.8 kHz converter sync signals to the spin motor supplies. Each spin motor supply has its own dc-dc converter for generation of dc voltages dedicated to the spin motor supply circuits. The converter sync signals are applied to the primary side of the dc supply dc-dc converter transformer by the converter drive circuitry, and consist of two square waves, 180 degrees out-of-phase, 56V in amplitude.

4.4.8.2.2.2 Spin Motor Power Supplies. The IMU incorporates two identical spin motor supplies (a primary and a backup) to power the gyro spin motors. Switching between primary and backup supplies is accomplished by latching relays at the input and output, with the primary supply normally on, as commanded from the CIU. The backup supply will be switched into the circuit to replace the primary supply: (a) automatically if a failure is detected in

the primary supply; or (b) a Backup AC Power Supply On command is received from the CIU. A Primary AC On command must be received from the CIU to return to operation with the primary supply.

4.4.8.2.2.2.1 Spin Motor Supply Operation. Figure 4.4.8-47 is a block diagram of the spin motor power supply. Each spin motor supply is capable of providing three 400 Hz square waves to the gyro spin motor windings. The square waves are phase shifted by 120 degrees so that the voltage across any two gyro spin motor windings (line-to-line) is a quasisinewave. Figure 4.4.8-48 depicts the relative phasing of these outputs. The supplies are capable of providing two output amplitudes: a 45 Vrms line-to-line start voltage and a 35 Vrms line-to-line run voltage. The inputs to the spin motor supplies are the dc-dc converter drive signals, and the +28 Vdc and +10 Vdc from the dc supplies and three 400 Hz logic square waves from the timer board. The outputs of the spin motor supply dc-dc converters are diode-OR'd and relay switchable so that either the primary or backup spin motor supply can run off either dc supply.

Each gyro receives its spin motor supply voltage through a dedicated double-pole, triple-throw relay; thus, spin motor power can be applied to each gyro separately via external commands. A small transformer in series with one phase of each gyro's spin motor supply voltage provides a current proportional to the spin motor current which is used by the spin motor current detector. The spin motor supply also provides a high impedance output signal for each phase for the spin motor supply telemetry and failure detection circuitry.

The 400 Hz timing signals from the timer logic board are each gated with the output of a latch comprised of CMOS NOR gates. Short circuit protection is provided by a comparator that trips when the current through a 0.1 ohm sensing resistor exceeds a maximum current of 2.2A. When the comparator output goes low, signifying a short circuit, the latch is reset, thus disabling the 400 Hz timing signals and shutting off the spin motor supply. The comparator circuit contains hysteresis to avoid intermittent short circuit cut-offs.

Each spin motor supply has its own gyro start command input which goes to a high logic level (+10V) during the 64-second gyro start period. While this input is high, the high voltage spin motor supply output is applied to the gyros. This allows a faster runup time for the gyros, also permitting the motors to be operated in an "overmagnetized" state which results in lower power consumption and increased running torque margin for the 35 Vrms run condition. When the start command is at logic low (0V), the spin motor supply will output 35 Vrms run voltage to the gyros. The spin motor supplies operate in run mode except during the initial 64-second start period for a gyro. The 64-second gyro start command is generated by the 64-second timer located on the Spin Motor Timers & Relays Board in response to a CIU Gyro Start command.

4.4.8.2.2.2.2 Failure Detection and Automatic Switchover. As shown in Figure 4.4.8-47, the spin motor supply provides high impedance outputs for the spin motor telemetry and failure detection circuits. The spin motor supply voltage is divided down in amplitude by the telemetry circuits before being applied to the failure detection circuits in order to avoid having high voltage square waves running through the motherboard. Figure 4.4.8-49 is a block diagram of the spin motor supply failure detector circuit, which is located on the Signal Generator/Spin Motor Supply Failure Detector Board.

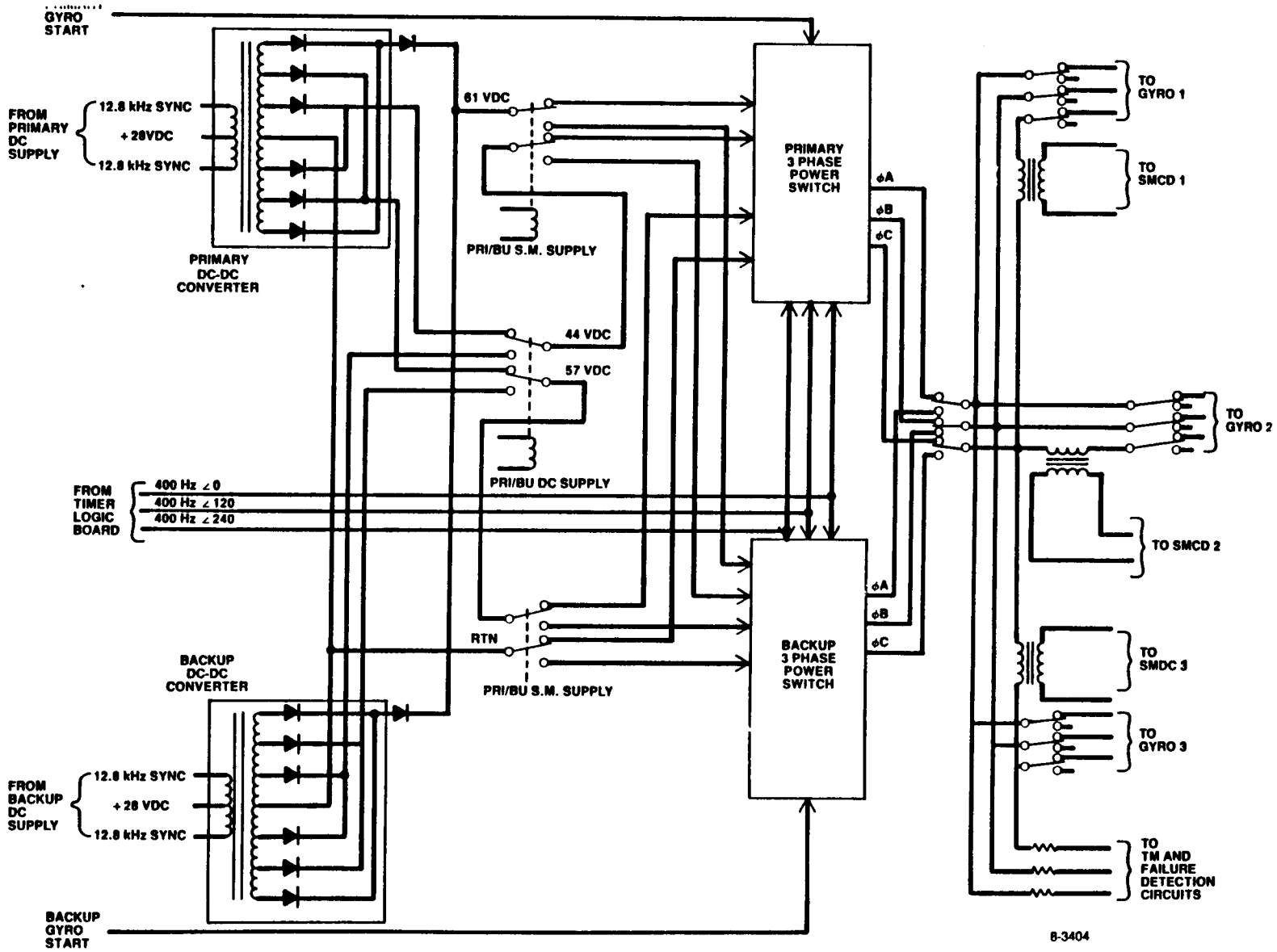

Figure 4.4.8-47. Spin Motor Power Supply Block Diagram

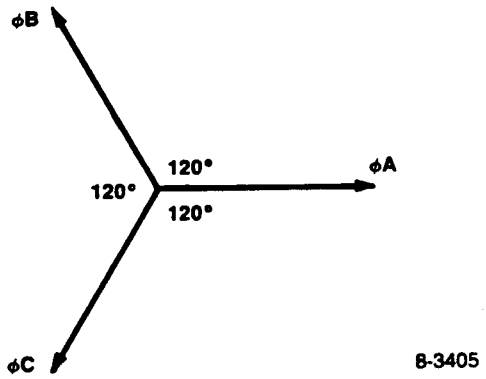

Figure 4.4.8-48. Phasing for Gyro Spin Motor Excitation

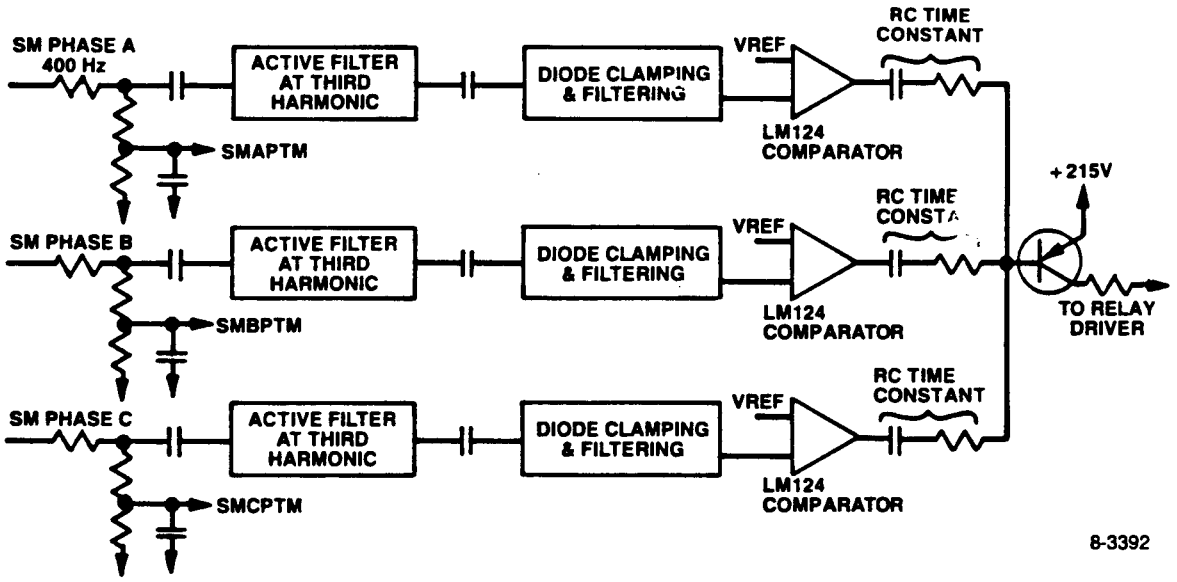

Figure 4.4.8-49. Primary AC Power Supply Failure Detection and Automatic Switchover

The detector circuit is tuned to the third harmonic of the supply voltage, which is a square wave. If the supply voltage should fail, then the spin motor will run down, generating a sinusoidal back emf. Since the detector is sensitive to the third harmonic, it differentiates between the square wave supply voltage, which has a third harmonic, and the spin motor sinusoidal back emf, which does not have any harmonics. If the monitor circuit detects a failure in any of the three primary voltage supplies, it will output a signal to the backup ac supply on mode switching circuit, which will then switch the relays to the backup ac supply. The failure detector circuit will switch at a spin motor voltage of no less than approximately 20 volts rms at the gyros, which will assure synchronous operation of all the spin motors. The failure detector circuit has been designed to provide a delay of approximately 100 ms from the time a failure is detected until the start of the switching pulse.

Once the backup supply is operating, a command from the CIU is required to return to the primary supply.

4.4.8.2.2.3 Gyros and Associated Circuitry. The IMU contains three gyros, each with two analog rebalance loops and a spin motor current detector. The signal generator power supply which furnishes the excitation for generating unbalance signals is common to all 3 gyros. Figure 4.4.8-50 is a block diagram of one of the three gyros and its associated circuitry.

4.4.8.2.2.3.1 Gyro Signal Generator Power Supply. As shown in Figure 4.4.8-50, the signal generator power supply is redundant, with either the primary or the backup generator in use at any given time. Each supply is powered on with and operates in conjunction with a specific ac power supply (i.e., primary or backup). The signal generator circuits are located on the signal generator/spin motor supply failure detector board.

Each signal generator supply receives a 32 kHz square wave (at a relative phase angle of -90°) from the count down circuitry. The required phase shift is obtained by a select in test resistor. This phase and gain tailoring is accomplished for a given set of 3 gyros. Thereafter, the signal generator supply and the 3 gyros must be maintained as a matched set. An IC preamplifier and a push-pull power amplifier are incorporated to provide adequate power to drive the signal generation windings of the 3 gyros in parallel. The proper signal generator output is selected in conjunction with selection of the associated spin motor power supply. The 2 outputs are also fed to half wave rectifiers, filters and voltage dividers to provide telemetry signals indicating which of the ac power supplies is on, with a nominal 4.5 Vdc for the on channel. (This circuit does not provide the voltage for bit 15 of the IMU status word. Rather, status bit 15 is obtained from the relay utilized to switch the +28 Vdc and +10 Vdc for the ac power supplies.) The combination of a spin motor supply and a signal generator supply is referred to as an ac supply.

4.4.8.2.2.3.2 Gyro. Each of the three gyros is a Teledyne, SDG-5, dry tuned, strapdown, two-degree of freedom unit. The three gyros are mounted to measure rates about the spacecraft X, Y, and Z orthogonal axes; thus, rates about each spacecraft axis are sensed by two different gyros, providing redundancy. Each gyro channel (consisting of a gyro, its associated spin motor current detector, and its associates analog rebalance loops and digitizers) is turned on and off as a complete, independent entity via signals from the CIU.

The three gyros are mounted on the IMU inertial block. This block is temperature stabilized prior to spacecraft launch, and is temperature controlled during both ascent and orbit operation (throughout the mission).

The Teledyne SDG-5 dry tuned gyro is a two axis rate integrating device. Its high angular momentum and low speed (1000000 gm-cm*2/sec at 100 revolutions/sec) make the gyro stable with respect to noise and error torques, but also physically large (3 in. dia x 3 in. long, 2.3 pounds). The gyro contains no damping fluid, and the damping function must be provided by the analog rebalance electronics.

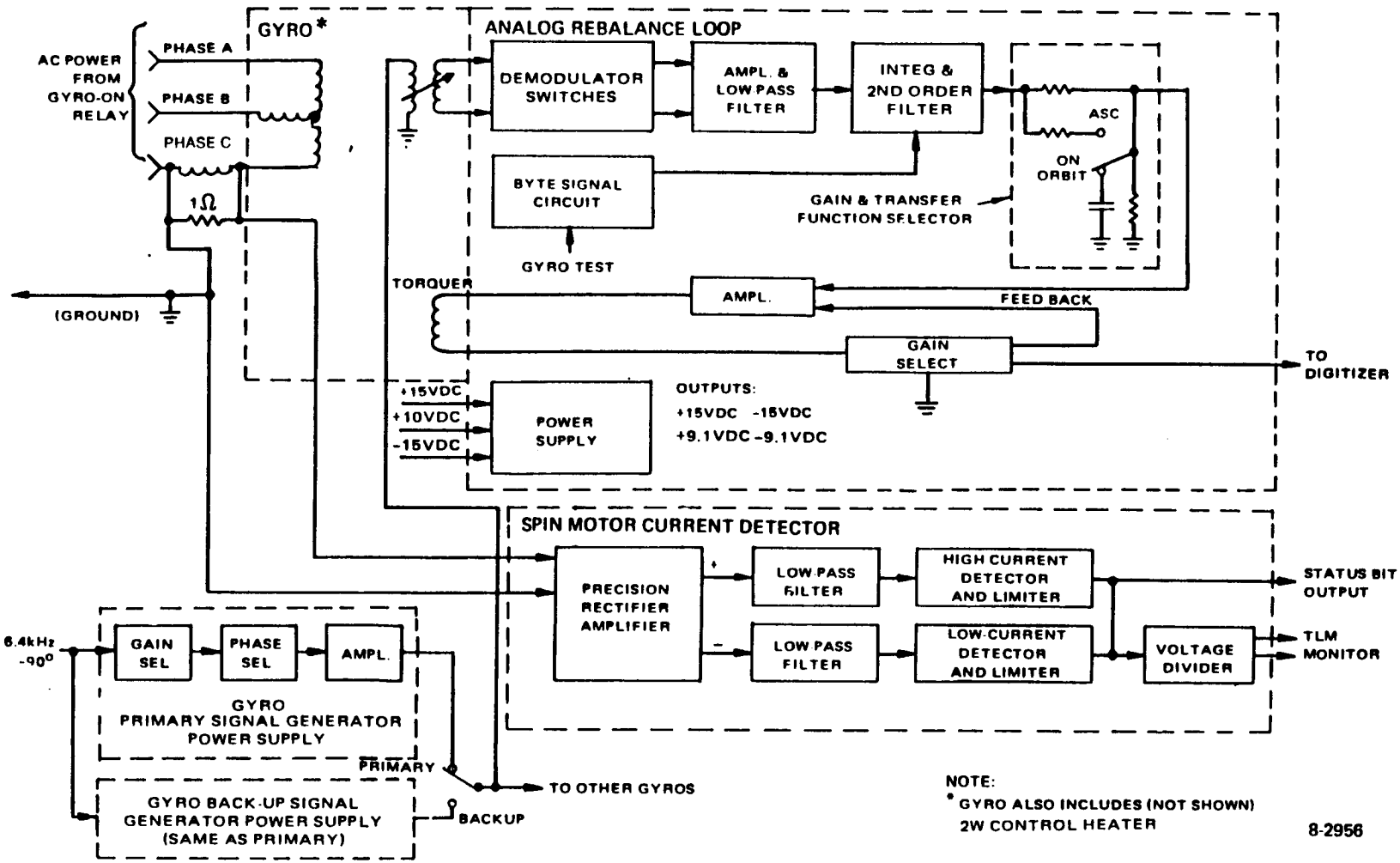

Figure 4.4.8-50. Gyro and Associated Circuitry

Since the gyro is sensitive to rotations about two axes, two analog rebalance loops are required for each gyro. Two case fixed pickoffs sense changes in the gyro case attitude and provide ac signals to the analog rebalance loops which have a phase dependent on the rotation magnitude. Two case fixed torquers are provided in each gyro to rebalance the rotor in two axes. Current passing through the torquer coils acts on the magnets in the rotor to change the rotor to case attitude. The analog rebalance loops provide current to the torquers to reduce the change in rotor to case attitude to zero. Thus, the current flow into a torquer is a direct measure of the input angular rate applied to the gyro case. Gyro temperature is maintained by electrically isolated block mounted resistance heaters controlled by a Thermal Control Assembly (TCA). The temperature is monitored by an electrically isolated, resistance-type temperature sensor.

A small current transformer in series with one leg of each gyro's spin motor provides a current proportional to the spin motor current for a 1-ohm resistor. The voltage across this known resistor is a function of spin motor current; the voltage is used as an input to the spin motor current detector.

Each gyro includes integrally fitted mu-metal magnetic shielding to minimize the effects of expected levels of periodic fields produced by the spacecraft and of the earth's magnetic field (which varies around the orbit).

The three gyros are turned on prior to launch, and should remain on (and the IMU is providing data outputs from each) throughout the ascent phase and throughout the satellite's operational life. This approach assures that temperatures are maintained within the operating range. If a gyro is turned off, a make-up heater is switched on to compensate for the gyro's lost power dissipation, thus maintaining proper block temperature.

4.4.8.2.2.3.3 Spin Motor Current Detector. The Spin Motor Current Detector (SMCD) utilizes the voltage developed across a precision resistor by the current from the secondary of the transformer in series with one of the spin motor legs to derive a signal for detecting either a high-current condition or a low-current condition. Motor current greater than a present upper limit indicates that the spin motor is operating in a non-over-magnetized state; motor current less than a preset lower limit indicates either one or more open motor windings, loss of ac input power to one or more phases, or a gyro which is off.

The motor current results in an ac signal at 400 Hz across the 1 ohm resistor. This signal is amplified, half-wave rectified, and filtered to provide two dc voltages (one positive, the other negative), each proportional to the motor current. If the motor current increases, the positive output increases until the high current detector is tripped. Similarly, as the motor current decreases, the negative output decreases (becomes less negative) until the low current detector is tripped. The two level detector outputs are "wire-OR'd" to provide a bilevel output signal. This voltage level is converted in the logic circuitry to a status bit which is "0" when the motor is not operating properly and "1" when the current indicates over-magnetized operation of the spin motor, which is the normal condition. Such a status bit is generated for each of the three spin motors and is included in the IMU output. The SMCD also provides an analog telemetry output which is a dc voltage proportional to the rms value of the motor current.

The SMCD circuitry contains select in test resistors in the current detectors; thus, the SMCD is matched to a specific gyro and cannot be interchanged without re-matching.

4.4.8.2.2.3.4 Analog Rebalance Loop. The analog rebalance loop utilizes the 32 kHz ac signals from the gyro's pick-offs to develop signals which: (a) rebalance the gyro; and (b) provide an output to the digitizer for the particular gyro. Power for the loops is supplied only when the particular gyro is commanded on. The power input is ±15 Vdc.

As discussed previously, the pickoff output (and input to the rebalance loop) is a 32 kHz ac signal whose phase (0° or 180°) is dependent on the direction of gyro precession and whose amplitude is proportional to the amount of precession (amplitude of the angular rate). This signal is fed to a demodulator switch. This circuit acts like a bi-directional full-wave rectifier, producing bipolar outputs. Figure 4.4.8-51 shows an equivalent diagram of the circuit and the associated waveforms for the two possible input phases. The input signal is either in phase (case 1) or 180° out of phase (case 2) with the switching. The outputs are two full-wave rectified signals of opposite polarity, the polarity of each output depending on the phase of the input. Regardless of polarity, the amplitude of the two outputs is proportional to the amplitude of the input. (This amplitude is, in turn, proportional to the amount of rotor to case movement, or case rotation.)

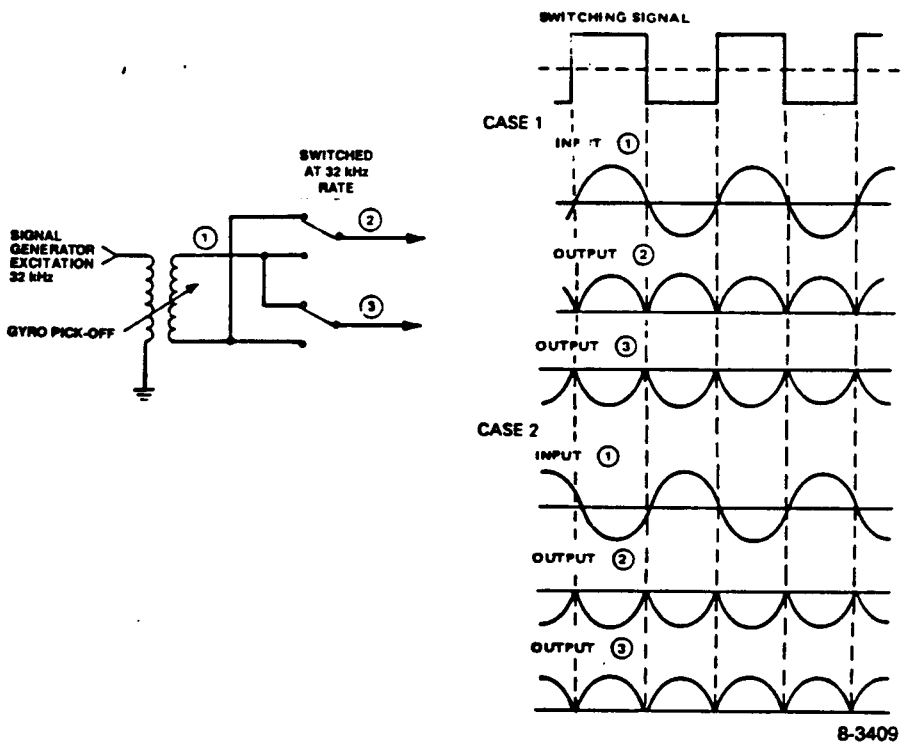

Figure 4.4.8-51. Equivalent Decommutator Circuit and Waveforms

The switch output signals are amplified, filtered, and combined to provide a single output voltage whose polarity is dependent on the phase of the pickoff output and whose amplitude is proportional to the amplitude of the pickoff

output. This signal is applied to the lead/lag amplifier which integrates the steady state hangoff angle to null and helps to provide the proper frequency response for the entire loop. The second order low-pass filter also helps determine the loop frequency response. The gain change amplifier allows switching of the electronics gain between its ascent mode and orbit mode values. The power stage supplies rebalance current to the gyro torquer. this rebalance current is proportional to the input angular rate, and the voltage developed by this current across the readout resistors serves as the input to the digitizer circuitry.

4.4.8.2.2.3.5 Gyro Loop Self-Test. The gyro loop test is mechanized to provide a functional check of the IMU gyros and loop electronics. The test is commanded by a discrete signal to the IMU from the CIU. When the test is commanded on, a fixed voltage is introduced into the gyro forward loop electronics. The voltage is sufficiently large that the electronics will saturate, yet sufficiently small that the loop can recapture. The electronics output at this point falls to near zero; however, the loop is disturbed in the sense that the rotor is displaced from its normal operating position. When the test is commanded off, the stimulus voltage is removed causing the electronics to saturate in the opposite polarity. The loop recaptures and the electronics output again falls to near zero.

The above description is for a normally functioning gyro and loop. An open or shorted element within the loop will alter this response so that either the saturation of the electronics output or the recapture of the loop (return to null) will not be observed. Note that the response does not depend on the precessional torque mechanism of the gyro. The test is only for the integrity of the elements within the gyro loop, hence the name loop test.

A trained observer could conceivably infer more than just a loop open or loop closed result from the test. Careful examination of the saturation rebalance time history could provide an indication of the total loop gain shifting from nominal. However, only the most gross gain changes would be evident in this test and few failures occur in this manner.

Because of the spurious output introduced during this test (and for a finite time period after it is commanded off), this test must not be performed on a gyro which is in use for attitude determination or control. To do so would result in loss of attitude reference accuracy and potential loss of vehicle stability. Also, the gyro loop test affects both axes of the dry tuned gyro, although the cross axis response is much less than the direct axis response. Thus, both axis outputs become unusable for a time during the loop test. Figure 4.4.8-52 shows the time history of loop electronics output following an on command of a gyro loop test in the orbit mode. Assuming nominal electronics and gyro parameters, the loop electronics will remain saturated for approximately 0.5 second. The telemetry signal and IMU digitizer output remain saturated slightly longer since the loop electronics has considerable overrange capability. The decay from saturation occurs over a period of several seconds.

The integral or sum of the digitizer output pulses from this transient is approximately 12,000 pulses for the direct axis; this is the equivalent of 0.2 degree of spacecraft attitude in the orbit mode.

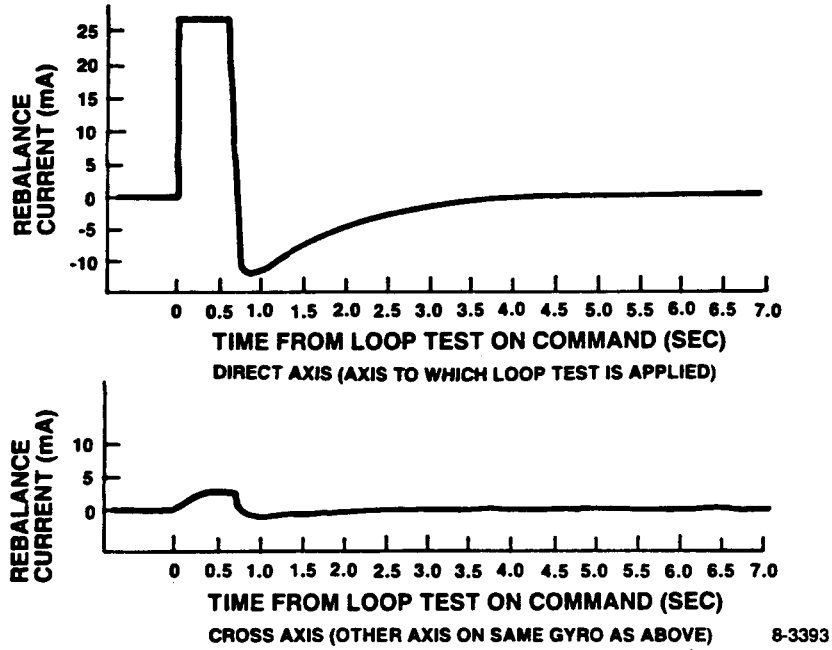

Figure 4.4.8-52. Orbit Loop Gyro Test

The transient occurring when the test is commanded off would be the mirror image of this response. Digital filtering as performed in DFLSR would not diminish the net attitude from this transient but would merely spread it out over a longer time. Because of this it is detrimental to system performance to employ the output pulses from a gyro which has been tested for a period of time even greater than the 7 seconds which Figure 4.4.8-52 would indicate, unless the digital filter were to be reinitialized.

A similar transient will occur when exercising the gyro loop test in the ascent mode, but the transient will be of shorter duration. This transient will not affect ascent performance because the test will not be employed during the boost phase. The test could potentially impact the operation of the alignment calculations prior to launch, so that sufficient recovery time will be allowed following a test or steps will be taken to isolate the alignment calculations from the test transient.

4.4.8.2.2.4 Accelerometer and Associated Circuitry. The IMU incorporates four identical Q-Flex accelerometers, each with an analog rebalance loop. The accelerometers are mounted to detect and measure linear accelerations along the spacecraft X, Y, Z and skew (54.736 degrees from each axis). During ascent only the three orthogonal accelerometers are used. The signals representing the accelerations are used for ascent mode control and stabilization. When the IMU is in orbit mode, power to the four accelerometers (and their associated digitizers) is switched off.

Each of the four Q-Flex accelerometers is a single-axis inertial device of the closed loop force balance type, with integral rebalance servo circuitry. The sensing element is a quartz flexure supported seismic pendulum with a rigidly controlled single-degree of freedom. The pendulum motion is damped by internal gas (as opposed to fluid) damping, with servo (rebalance) stabilization.

Figure 4.4.8-53 is a block diagram of the accelerometer and its associated circuitry, all contained in the accelerometer unit. The unit is mounted such that linear acceleration along the sensitive axis causes the pendulum to flex, causing an output from the proximity detector. The output is amplified and applied across a torque coil which returns the pendulum to its null position. From the torque coil, the output is coupled to a current sampling resistor and the derived voltage is supplied to the appropriate digitizer.

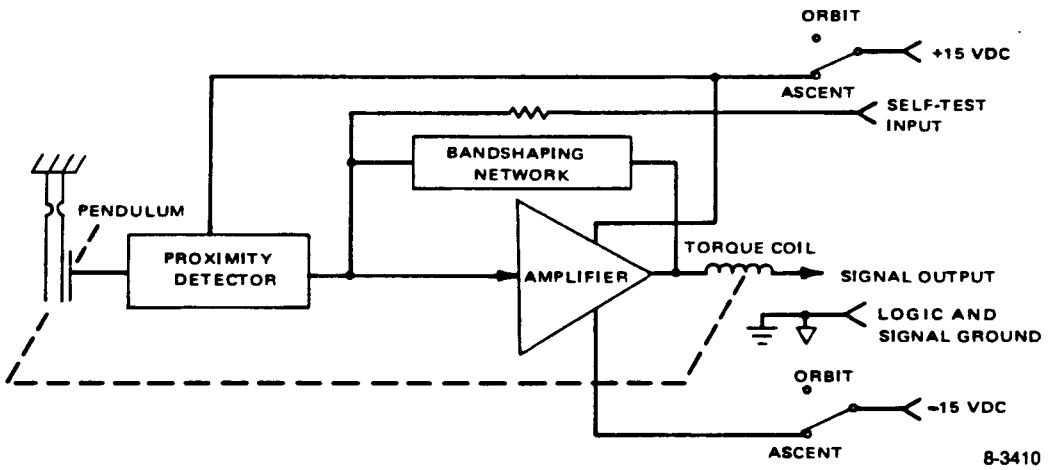

Figure 4.4.8-53. Accelerometer and Rebalance Loop

The accelerometer output is measured across a sampling resistor. The polarity of the dc output is dependent upon whether the acceleration is positive or negative (acceleration or deceleration) and the amplitude is proportional to the magnitude of the acceleration.

The accelerometer loop self-test is similar to the gyro loop self-test, it is commanded by applying a logic low to the accel test relay driver input on the accel digitizer board. Commanding the accelerometer test results in +15 Vdc applied to the accelerometer forward loop electronics.

In response to this stimulus, the accelerometer output goes to a plus full scale indication. With this level of signal the loop cannot rebalance and the full-scale indication is present as long as the test stimulus remains. Failure to achieve a full-scale output response is indicative of an electronics malfunction of the accelerometer test is in progress.

4.4.8.2.2.5 Precision Pulser. The IMU incorporates two independent precision pulsers (a primary and a backup) which utilize the clock countdown outputs to provide the high precision pulses required for digitizer operation. The amplitude and time duration of each precision pulse is accurately controlled, the amplitude as a function of a precision voltage developed from the +15 Vdc power, the duration as a function of input clock signals.

Figure 4.4.8-54 shows a block diagram of the precision pulser and the input and output waveforms. The input U square wave clock signal from the countdown circuitry is buffered and utilized to close and open individual solid state switches in sequence. The precision voltage across the switches is provided from a precision power supply. The result is the output shown in Figure 4.4.8-54. This output is coupled to all 10 digitizers in the ascent mode, and to the three gyro digitizers in the orbit mode. The precision pulser features an integrator in both loops. In the +PP loop this assures the output pulse amplitude is tightly controlled to the precision Zener reference voltage. The integrator in the -PP loop assures symmetry between the positive and negative precision pulse train amplitudes; symmetry trim is accomplished by returning a fraction of the +PP or -PP voltage as required. Note that the integral feedback assures control of the area of the pulse so that changes in timing waveforms are automatically compensated.

A backup pulser is incorporated, with the pulser output selected via relay contacts. The input power lines are also selected via relay contacts, such that power is supplied to either the primary or the backup pulser (but not both). Both pulsers are physically located on the inertial block for close temperature control.

4.4.8.2.2.6 Digitizer. The IMU incorporates 10 identical digitizers -- two for each of the three gyros and one for each of the four accelerometers. The digitizer converts the input signal, a dc voltage representing either an angular rate (from a gyro analog rebalance loop) or a linear acceleration (from an accelerometer rebalance loop), into a series of output pulses such that the sum of the pulses is proportional to the magnitude of the angular position change (or velocity).

Figure 4.4.8-55 is a block diagram of the digitizer. The torquer rebalance current in the gyro or accelerometer is sensed by a precision resistor, Rs. The dc voltage across this resistor is proportional to angular rate or linear acceleration, and is selected to achieve a specific scale factor. The voltage is resistance coupled to a precision integrator. For ground test purposes, an analog test input voltage can also be coupled to the integrator input via relay contacts. The relay is actuated by a test switch. A bias trim compensation is achieved by also summing a small offset voltage into the integrator.

The integrator output (a ramp voltage for a constant input) is coupled to a pair of level detectors. A "set" level detector provides a logic "1" to the D input of a flip-flop which is clocked at specific sample times relative to the 32 kHz precision pulse trains. The output of the flip-flop steers the proper phase of the precision pulser train into the integrator via signal gates. The integral of the precision pulse drives the integrator toward zero and thus "rebalances" the integrated rate or acceleration. Each precision pulse thus gated to the integrator represents a finite attitude increment (integral of rate) or velocity increment (integral of linear acceleration).

The flip-flop outputs are combined by logic to generate a single pulse output where the phasing of the pulse relative to the clock signals conveys the polarity of the pulse being gated. This multiplexing of the pulses is compatible with earlier designs of the pulse accumulation logic and IMU test equipment.

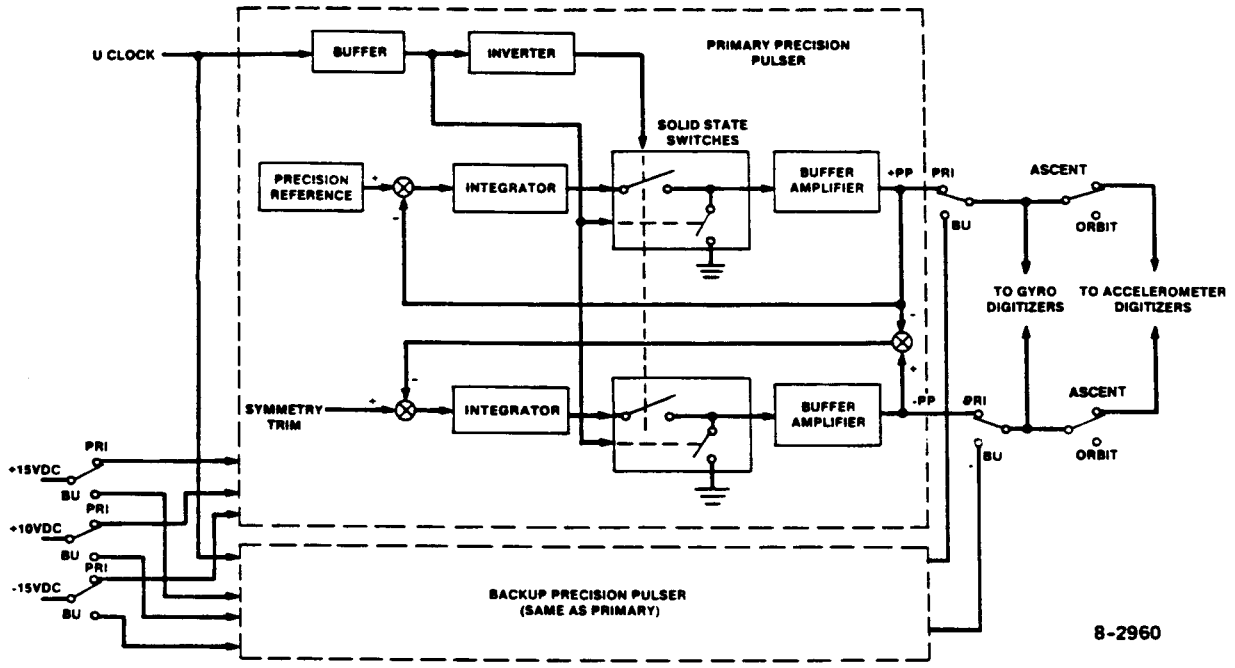

A. FUNCTIONAL BLOCK DIAGRAM

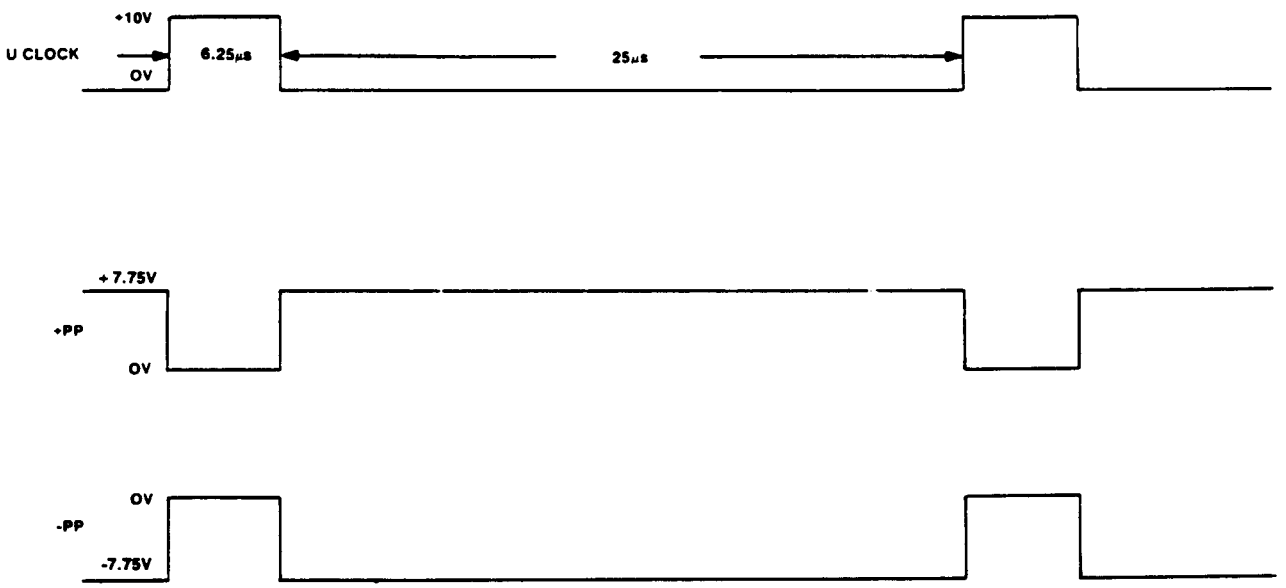

b. WAVEFORMS

8-3478

Figure 4.4.8-54. Precision Pulser

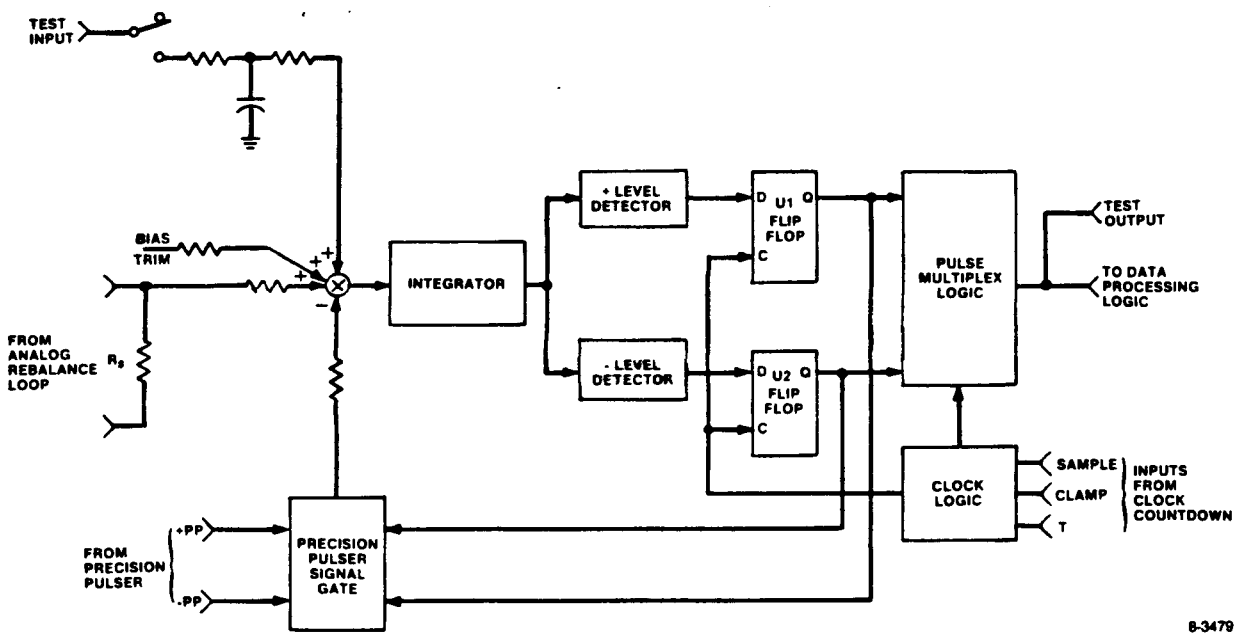

Figure 4.4.8-55. Digitizer Functional Schematic

Figure 4.4.8-56 depicts the digitizer waveforms for positive and negative input conditions. If the amplitude of the input analog voltage (and, therefore, the integrator output level) is not sufficient to trigger either level detector, there is no output to the flip-flop and, therefore, neither positive nor negative pulses are gated back to the integrator.

4.4.8.2.2.7 Digital Logic. The IMU digital logic performs the functions of timing, data accumulation, and digital data output for the IMU. These functions are distributed between three subassemblies: the timer board, the input board and the output board. Figures 4.4.8-57, 4.4.8-58, and 4.4.8-59 summarize, in block diagram form, the distribution and organization of the several subfunctions of the logic. The digital logic is redundant within the IMU and is selected by external command from the CIU (Primary Data Channel or Backup Data Channel). The Precision Pulse Generator is considered a part of the data channel and is switched by the same command.

The remainder of the logic may be separated into 13 subfunctions, each of which is described in the following sections. A slash (/) is used throughout this section to denote the logical inverse.

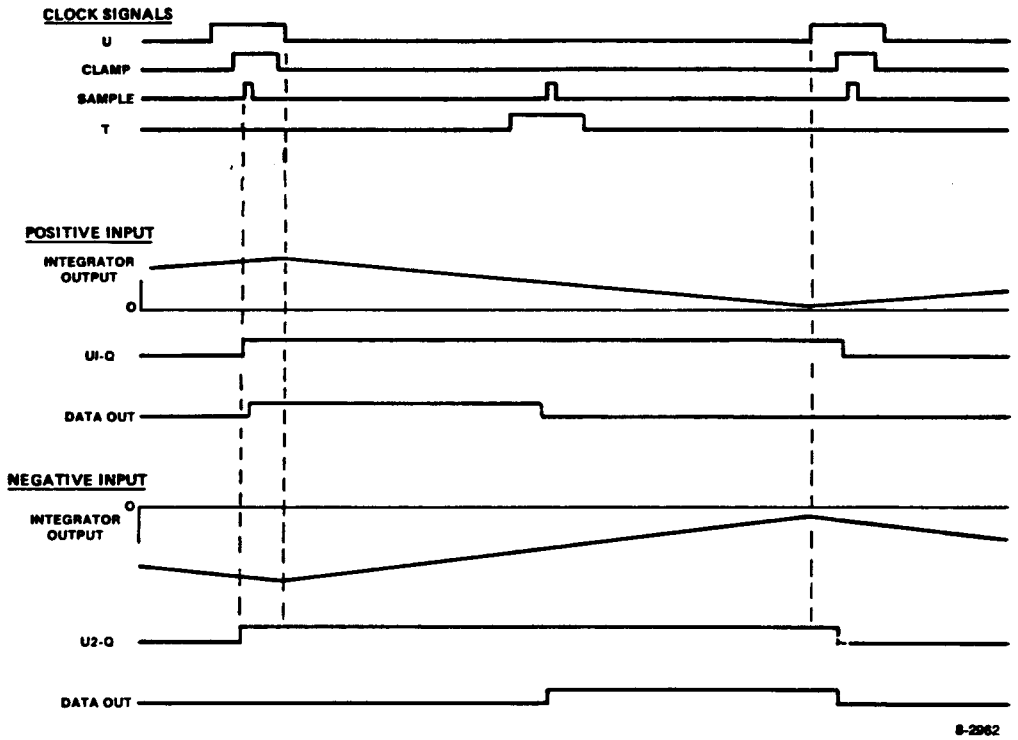

Figure 4.4.8-56. Digitizer Waveforms

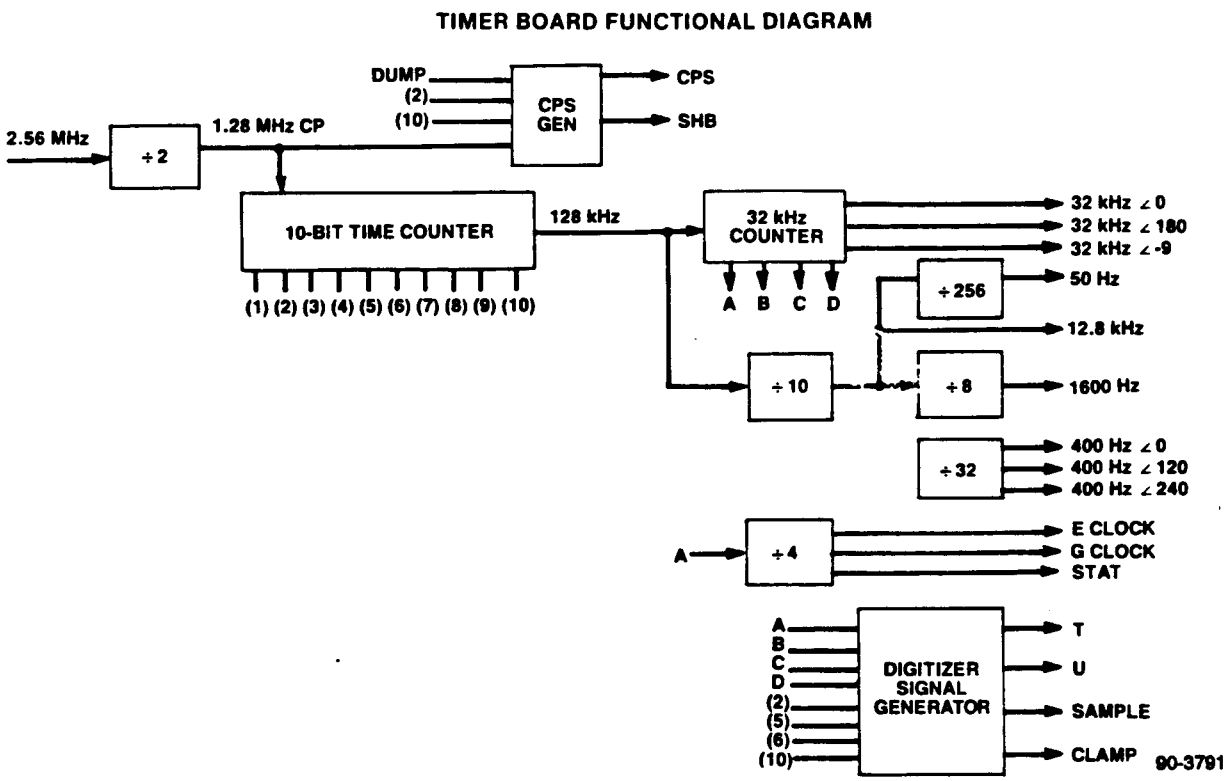

Figure 4.4.8-57. Timer Board Functional Diagram

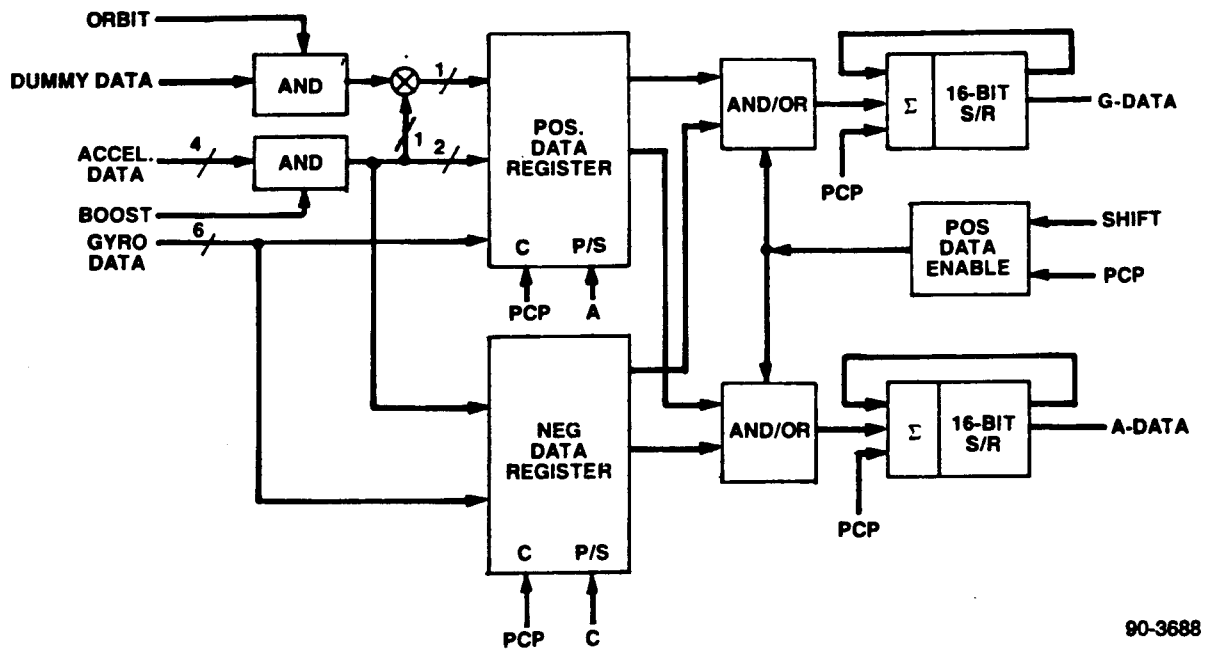

Figure 4.4.8-58. Input Board Functional Diagram

4.4.8.2.2.7.1 Clock Input Section. The IMU receives from the Controls Interface Unit (CIU) a 2.56 MHz square wave clock signals, one for each data channel. This frequency is divided down by a factor of two to generate a 1.28 MHz square wave clock and buffered for general use throughout the digital logic.

The 2.56 MHz square wave clocks arrive at the IMU logic section via connector J1 with an amplitude of +10V and a 50% duty cycle. The receiving input circuit configuration consists of a CMOS to CMOS high-speed interface receiving circuit using a CD4041UB powered from the spacecraft (S/C) +10V power as described in GE Document 2624203, Figure 3, Paragraph 3.2.1.1.1.

The second stage of the circuit consists of a CD4050B. The unique characteristic of non-transparency to the positive rail of this device provides complete power isolation between the IMU +10V logic power and the S/C +10V power used for the CD4041UB.

The 2.56 MHz frequency is subsequently divided by a factor of two using a CD4013B flip-flop and buffered by a CD4041UB. The two outputs of the CD4041UB are called CP and CP/ and are nominally 180° out-of phase. Figure 4.4.8-60 is a schematic of the clock input section. Figure 4.4.8-61 shows the basic clock waveforms.

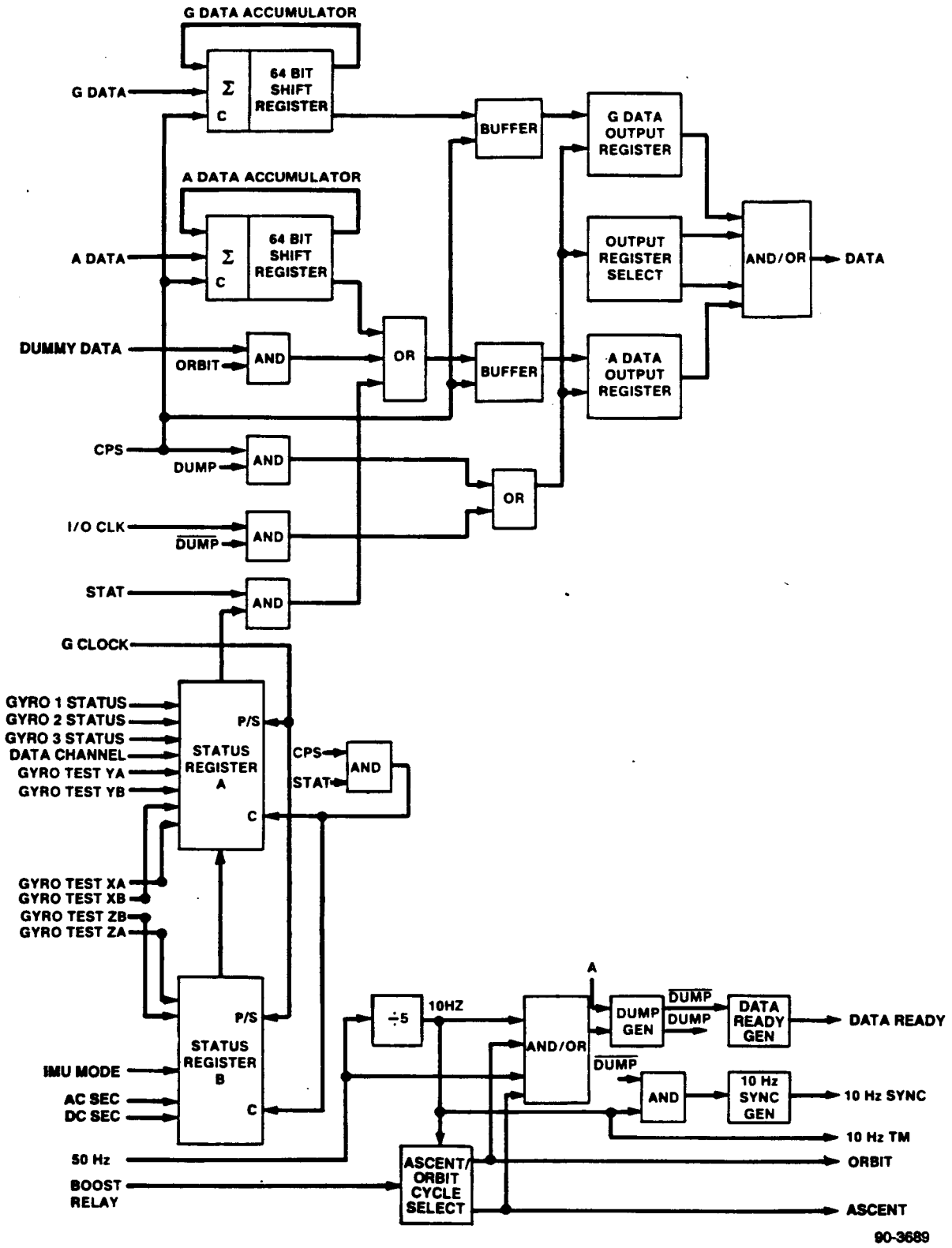

Figure 4.4.8-59. Output Board Functional Diagram

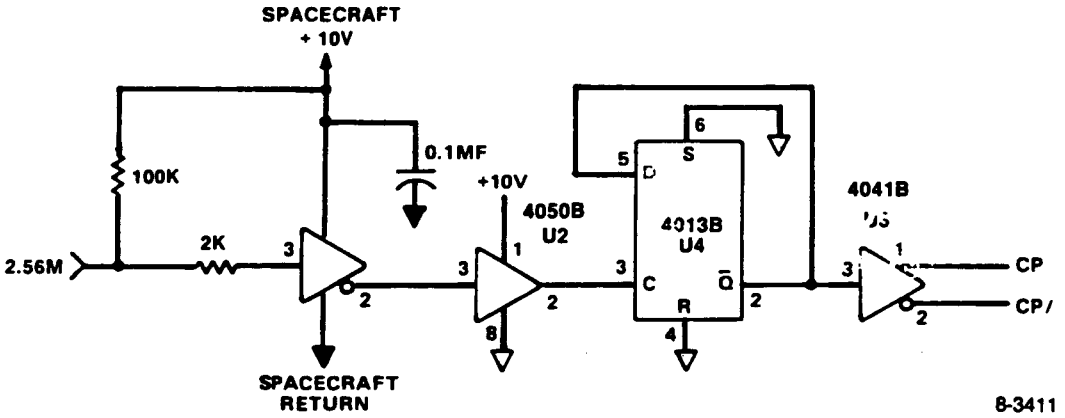

Figure 4.4.8-60. Clock Input Section

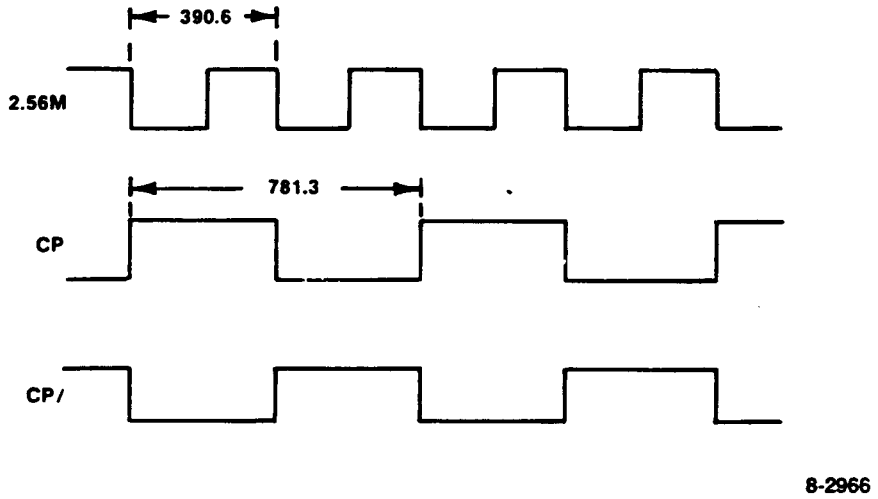

Figure 4.4.8-61. CP, CP/Waveforms

4.4.8.2.2.7.2 Bit-Time Counter. The bit-time counter generates a continuous sequence of 10 consecutive bit times, each with a duration of one CP clock cycle (781.25 sec).

The bit time counter (BTC) consists of a 10 stage Johnson type counter operating in a modulo-10 manner. It is built up from two 4-stage shift registers and two D-type flip-flops with a single logic "1" (positive pulse) circulating through the 10 stages at the rate of the CP clock (1.28 MHz). Proper initialization of the BTC at the +10V power up is assured by the use of power on set circuit at the first stage in combination with a self-clearing sequence which allows only a single positive pulse to circulate through the BTC. The BTC, including the "power on set" circuit, is shown in Figure 4.4.8-62.

Figure 4.4.8-63 shows the waveform of the "power on set" pulse. The duration of the pulse is a function of the time constant (R1 + R6)C9 and the logic "0" threshold of the CD4050B. Once the initial charge of C9 is leaked off sufficiently to go below the CD4050 threshold, the gate will turn off and remove

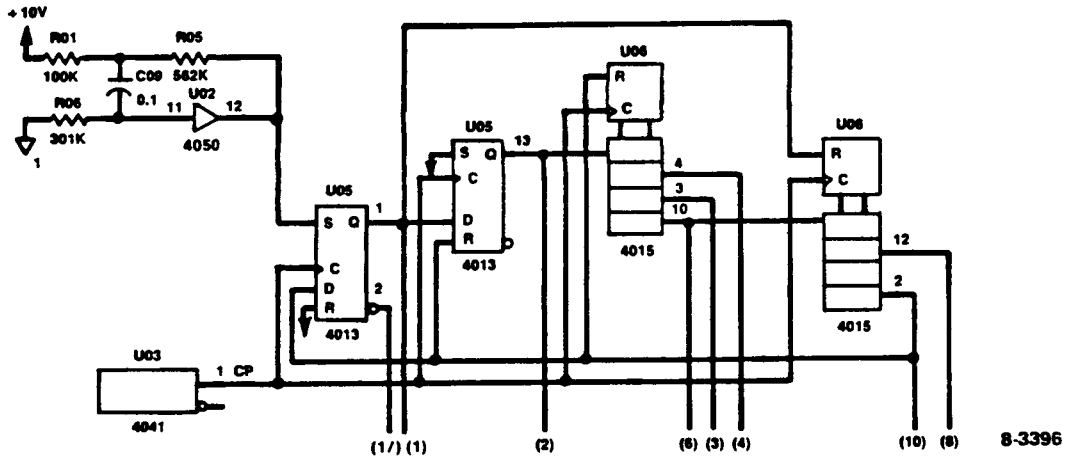

Figure 4.4.8-62. Bit Time Counter

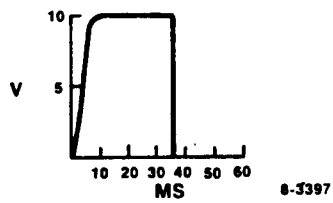

Figure 4.4.8-63. Power On Set Pulse

the logic "1" level from the pre-set input S of the flip-flop. With the component values as shown, the nominal duration of the pulse is approximately 37 ms.

During the presence of this pulse, the Q output of the U5 flip-flop is forced high, so that stages 2 through 6 of the shift register are filled with logic "1"'s by the CP clock. Stages 7 through 10 are forced to the reset or logical "0" condition by the high on the Q output of the flip-flop (refer to Figure 4.4.8-64). As soon as the "power on set" pulse disappears, the output of stage 10 is clocked into the flip-flop thus removing the forced reset for stages 2 through 6 which are filled with logical "1"'s (Figure 4.4.8-64) until the first "1" appears at the output of stage 10. This "1" level in turn forms the input to the D flip-flop and forces stages 2 through 6 to reset (Figure 4.4.8-64). The next clock pulse brings the Q output of the flip-flop high, and the remaining "1" levels of stages 7 through 10 are reset to fulfill the requirement of a single circulating "1" (Figure 4.4.8-65). The time required for proper initiation of the BTC from the end of the "power on set" pulse is thus five CP cycles long (5 x 781.25 = 3.9 μs).

4.4.8.2.2.7.3 <u>32 kHz Counter</u>. This counter divides the revolutions of the bit-time counter by an additional factor of four, so that a 32 kHz frequency is generated. Each of the 4-bit time counter revolutions within this 32 kHz frequency cycle period is to be brought out separately as a distinct signal, designated A, B, C, or D. These four phases are distributed throughout the logic for various control and timing purposes. Figure 4.4.8-65 shows the schematic for the counter; waveforms are shown in Figure 4.4.8-66.

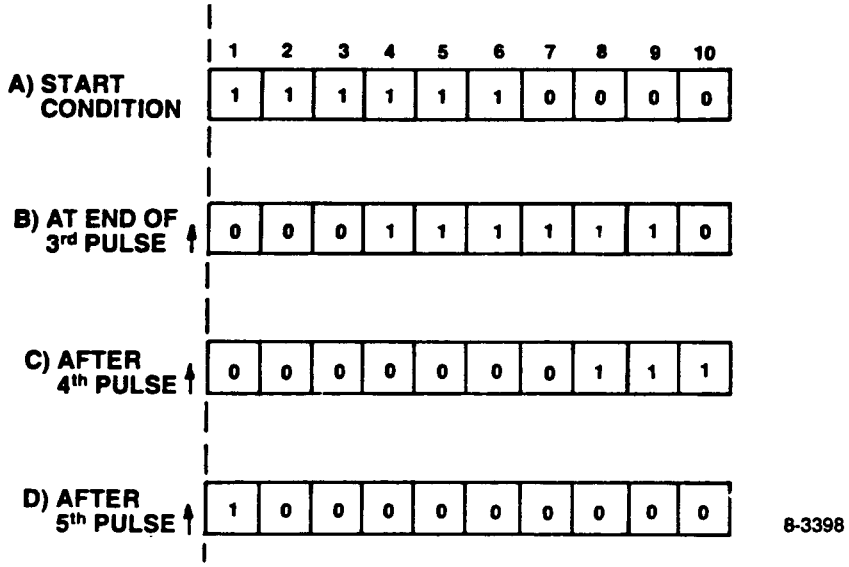

Figure 4.4.8-64. Bit Time Counter Start Up

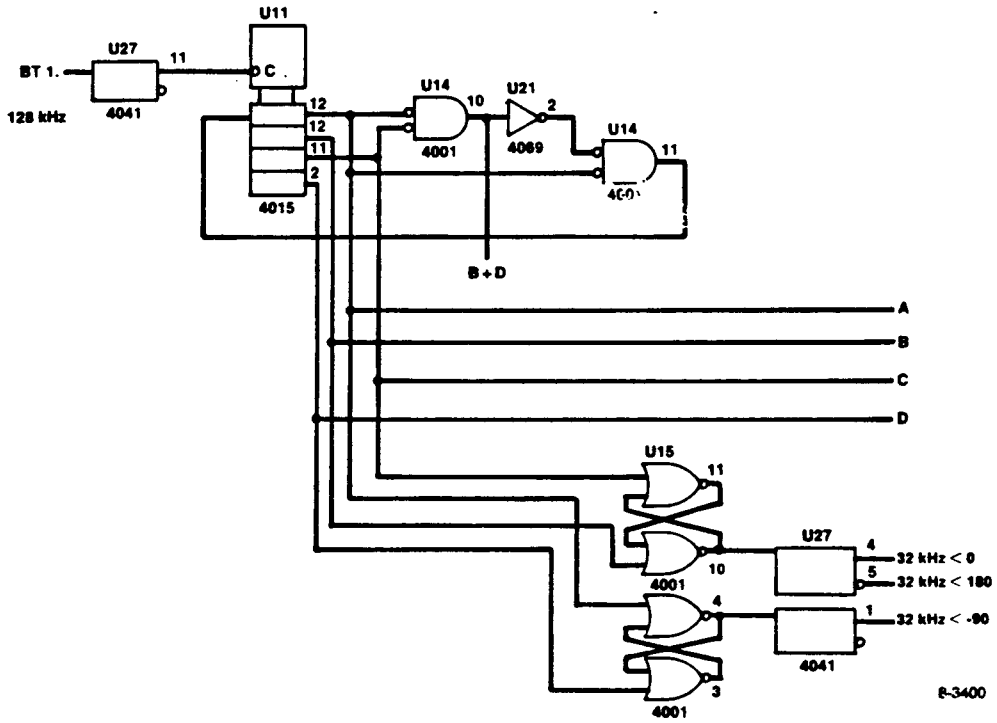

Figure 4.4.8-65. 32 kHz Counter

The 32 kHz counter operates in a similar fashion as the bit time counter, where a single positive signal is recirculated. The 32 kHz generator produces the three phases of the 32 kHz signals for the demodulators and signal generator.

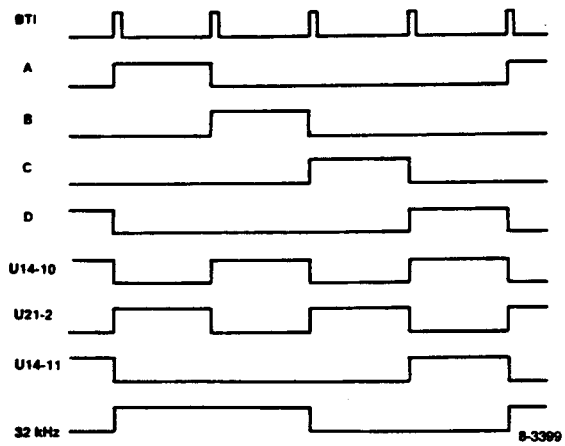

Figure 4.4.8-66. 32 kHz Counter Waveforms

4.4.8.2.2.7.4 Digitizer and Precision Pulser Signal Generation. This circuit generates the required signals for the IMU digitizer and precision pulser section by combining the outputs of the bit time counter and the 32 kHz counter, as shown in Figure 4.4.8-67.

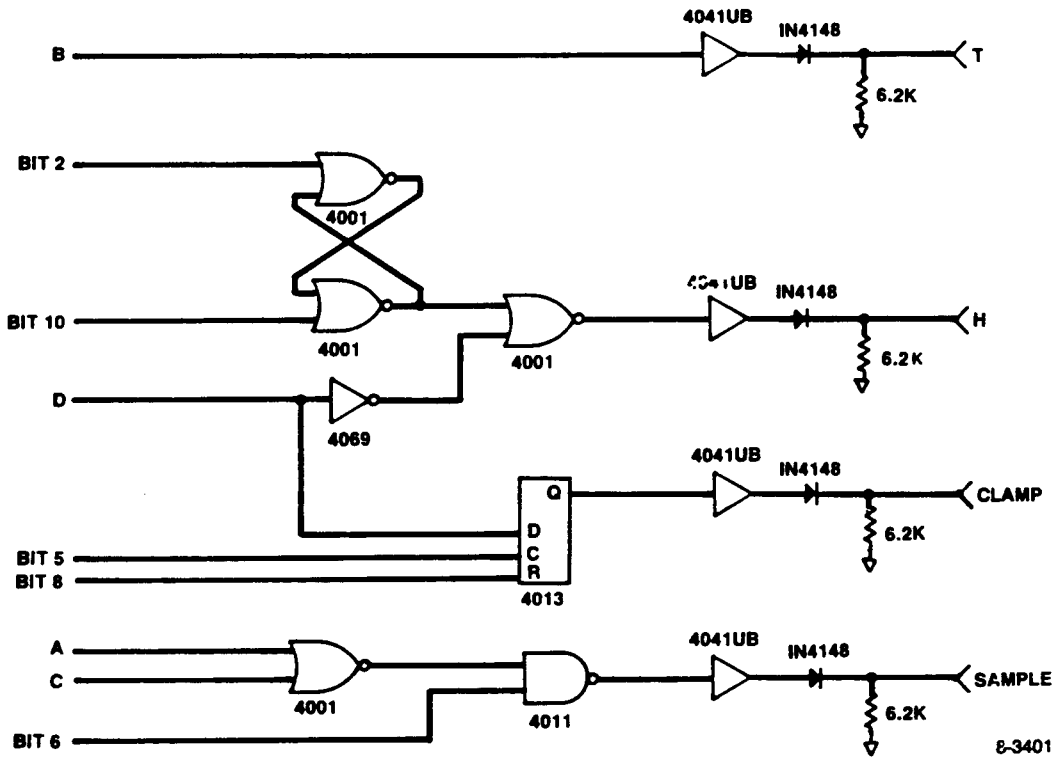

Figure 4.4.8-67. Digitizer Signal Generator

The IMU gyro and accelerometer digitizers and the precision pulser circuit require four signals of different length at a 32 kHz repetition rate. They are, for the digitizers: a 10 bit-time long signal called T during the B portion of the 32 kHz counter, a three bit-time long signal called CLAMP during

the D portion, and a single bit time long signal called SAMPLE during the B and D portions of the 32 kHz counter. The precision pulser requires a signal called U which is eight bit-times long and occurs during the D interval. The signals are generated using various outputs of the bit time counter and the 32 kHz counter as shown in Figure 4.4.8-67. Because of the multiple use of the digitizer signals (10 digitizers) and the fact that they may be generated on either set of digital logic board requires for the outputs to be diode-OR'd. The waveforms for the four signals are shown in Figure 4.4.8-68.

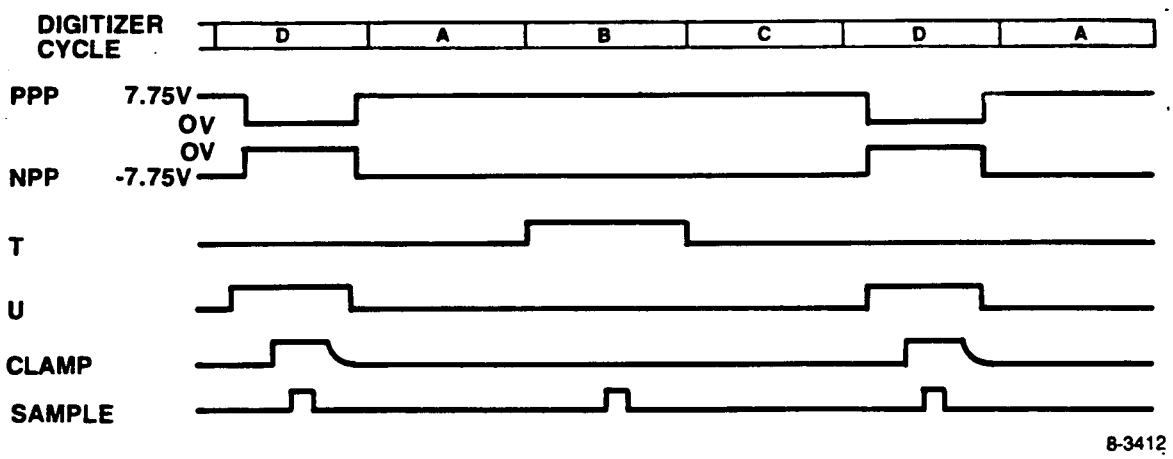

Figure 4.4.8-68. Digitizer Signals

4.4.8.2.2.7.5 Gyro and Accelerometer Data Input Registers and Pre-Counters. This circuit stores the positive and negative data received from three gyro and four accelerometer digitizers during the ascent mode and the six gyro digitizer outputs and a starcrossing event timing signal during the orbit mode. These stored data are then to be made available to the two serial adders in the correct sequence and at the correct time.

The received digitizer signals are stored in two 8-bit shift registers, one for the positive data and one for the negative data. Positive data are present at the input lines during a period overlapping the A time; negative data are present at the register inputs during a period which overlaps the C time. During a digitizer period (32 μs) either a positive or a negative input appears on any input line. The two data registers are CD4021B asynchronous registers which are transparent to the Q outputs while in the parallel entry mode, so that the Q8 and Q7 outputs present the incoming data during the whole parallel control mode. These modes are set by the A and C signals for the positive and negative registers, respectively.

The stored data are used in sets of two during each of the four quarter digitizer cycle periods A, B, C, and D. They are therefore shifted twice each of the three remaining periods that a register is not in the parallel mode (and therefore in the serial mode).

Figure 4.4.8-69 is the schematic and Figure 4.4.8-70 shows the timing diagram of the store/shift operation. Figure 4.4.8-70 shows the overlap of the positive and negative input signals received from the digitizers and their timing with respect to the A and C signals that are used for the data storage in the

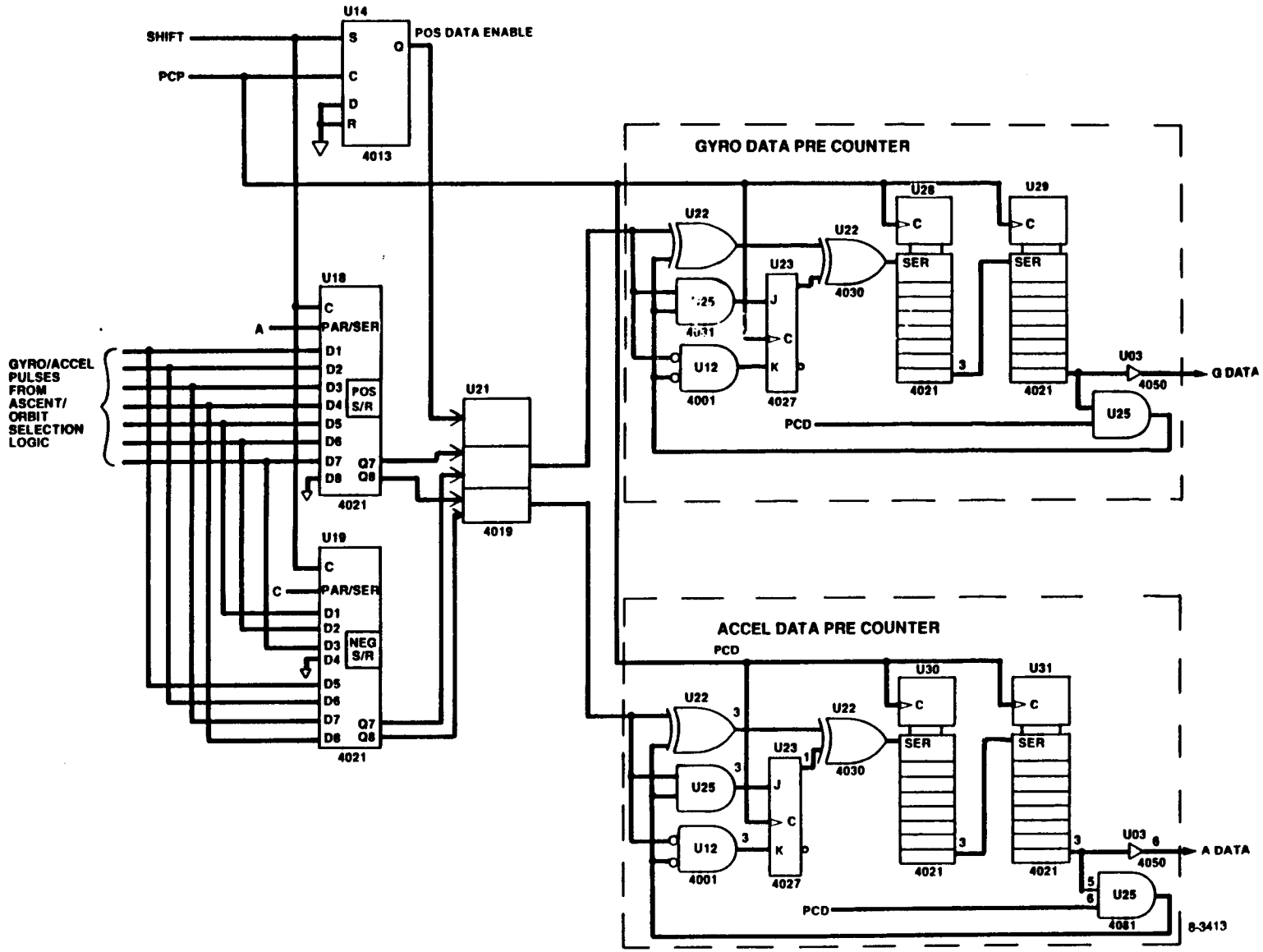

Figure 4.4.8-69. Gyro Data Registers and Precounters

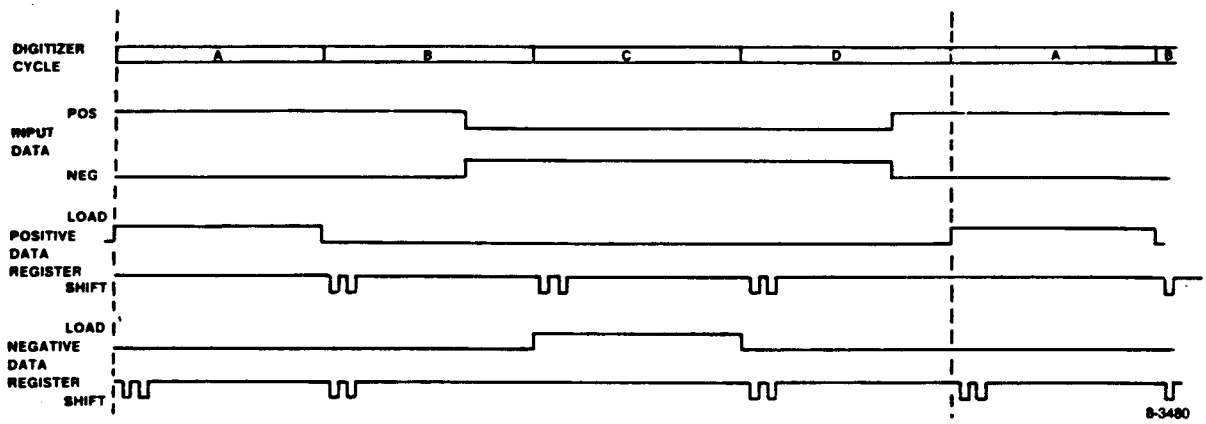

Figure 4.4.8-70. Data Storage and Accumulation Cycle

Positive Data Register and Negative Data Register respectively. When in this mode the clock input of these registers is disabled, so that during the sample time the data remain stationary. When not in the parallel entry mode, the stored data are shifted two places to the right by the shift operation. This results in a new set of data present at the Q7 and Q8 outputs at the end of the shift operation. Because of the difference in sampling time between the positive and negative data, the data are stored with an offset of four places.

To accommodate the 32 kHz digitizer frequency it was necessary to use a data precounter for data accumulation. The precounter is designed to accumulate a maximum of four gyro and accelerometer pulses before transferring them into the main accumulators. Therefore, each precounter consists of a 16-bit shift register and uses a recirculating serial addition to create four 4-bit bytes every 125 μs. The clocking of the precounter is done by the PCP clock which consists of the CP/clock and bit times 4, 6, 8 and 10.

The possibility of a positive and a negative data bit occurring at the outputs of the two registers at the same time could happen if a negative bit is followed by a positive data bit in consecutive digitizer cycles. This cannot occur since it requires a negative to positive null crossing at a slew rate in excess of a saturated gyro condition. The data positioning within the two registers resulting from the load and shift actions are shown in Figure 4.4.8-71.

4.4.8.2.2.7.6 <u>CPS Generation</u>. This circuit generates a common clock signal so that all data processing operations are controlled from one single source. The CPS clock signal is generated by gating the CP/clock with the (2 ÷ 10)/envelope, so that this clock only occurs during the 16-bit accumulation cycles. Envelope (2 ÷ 10)/is formed by the NOR gate latch (U9) which is set by bit (2) and reset by bit (10).

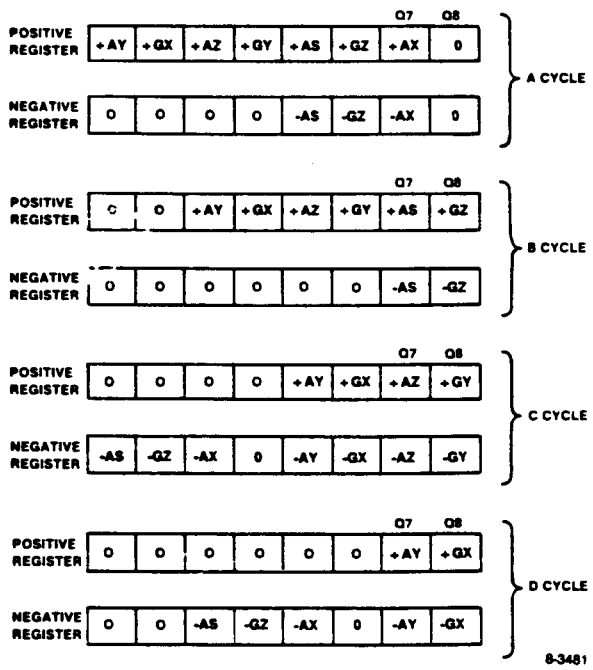

Figure 4.4.8-71. Digitizer Data Registers Store/Shift (Ascent Mode)

Figure 4.4.8-72 shows the CPS generation circuit. The CPS pulse train waveforms are shown in Figure 4.4.8-73.

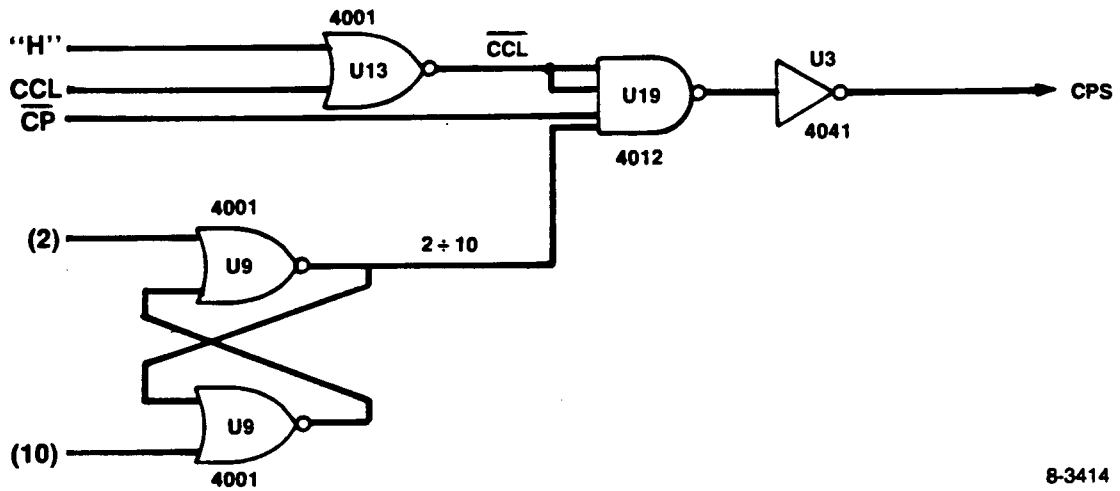

Figure 4.4.8-72. CPS Generation

4.4.8.2.2.7.7 Countdown to 10 Hz. This circuit generates a 50 Hz or 10 Hz signal for controlling the duration of the data accumulation cycle during the ascent or orbit modes, respectively.

Bit 1 (128 kHz) clocks a 10 counter which generates the 128 kHz dc-dc converter sync. This signal drives a 4024 8-bit counter which divides down by 32 to generate the 400 Hz signal, and divides down by 128 to generate the 100 Hz signal. This signal is divided by two and transmitted to the output board

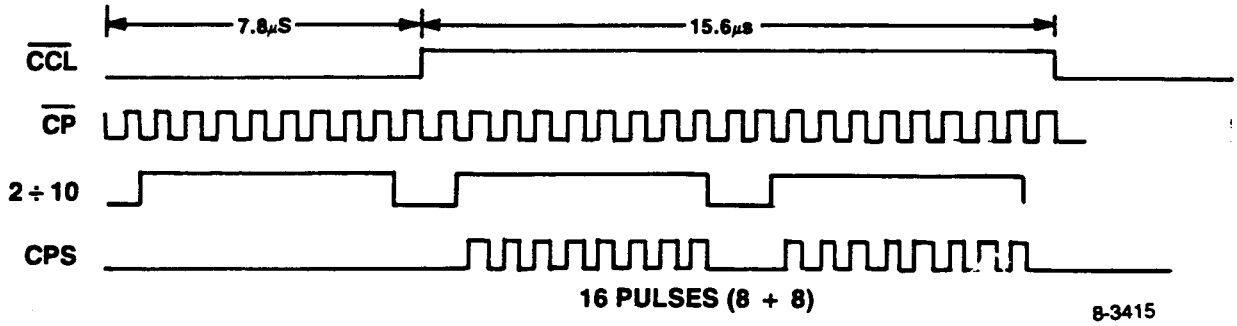

Figure 4.4.8-73. CPS Waveforms

where it is further divided by five to produce a 40/60 10 Hz signal. The 10 Hz and 50 Hz signals are then combined with the outputs of the boost relay flip-flop U22 to produce the required 10 Hz or 50 Hz signal selection.

Figure 4.4.8-74 shows the countdown circuit and frequency select circuit for the ascent and orbit modes. The associated waveforms are shown in Figure 4.4.8-75.

The divide-by-five stage operates in accordance with equations

$$Q2 + Q3 = D/$$
$$Q/ \bullet Q3 = D$$

thus producing the required 40% duty cycle waveform for the 10 Hz signal. The boost relay signal is high for the ascent mode and low for the orbit mode so that (Q • 50 Hz) or (Q/ • 10 Hz) are the two selected signals for the ascent or orbit mode data cycles, respectively.

4.4.8.2.2.7.8 Data Ready Generation. This circuitry generates a data dump cycle as a result of the occurrence of the (10 + 50) Hz signal, followed by the required "handshake" signals to initiate a data transfer to the CIU.

The leading edge of the (10 + 50) Hz signal strobes the first flip-flop. This sets the Q output high, so that the leading edge of the first E clock signal that follows will start the dump cycle, while at the same time resetting the first flip-flop. This essentially produces a one-shot with a duration equal to 125 μs. The dump signal is then inverted and used to strobe the data ready flip-flop, thus sending a logic "0" signal to the CIU. The first pulse of the I/O CLK will reset this signal, but a back up reset is provided by the combination of the next Dump signal and the G clock in case of failure of the I/O CLK to respond to the data ready signal. In addition the dump is combined with the 10 Hz signal to generate a 20 ms sync signal with a 100 ms repetition rate.

Figure 4.4.8-75 shows the generation of these functions. The (10 + 50) Hz signal is the result of a four-step countdown originating from the leading edge of the (1) signal, which is practically the same as the leading edge of

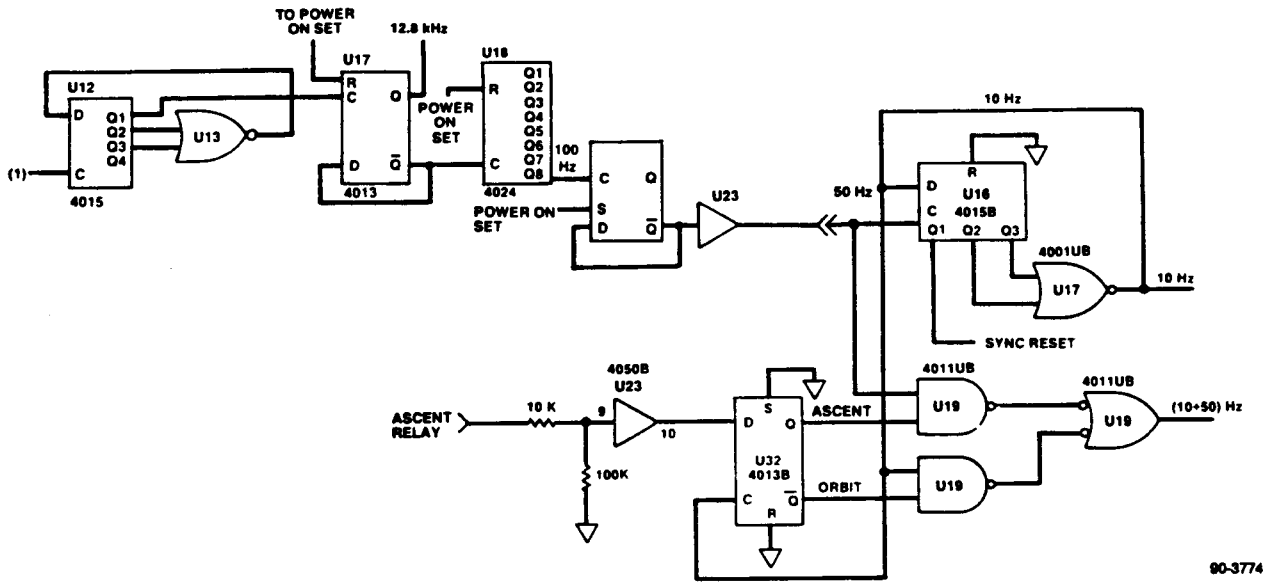

Figure 4.4.8-74. Countdown to 10 Hz Circuit

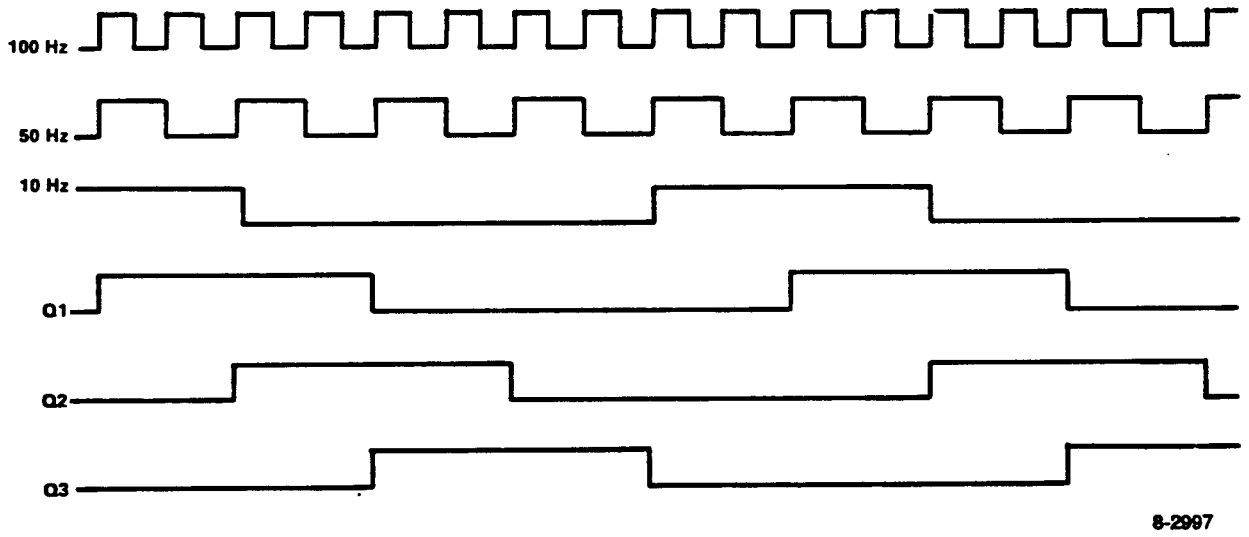

Figure 4.4.8-75. Countdown to 10 Hz Waveforms

the E clock that starts the dump cycle. Since each of the countdown stages have some delay greater than zero, the (10 + 50) Hz pulse will always lag the (1), therefore, the dump cycle will start at a constant repetition rate.

The dump signal is used to set the 10 Hz sync and data ready signals. Since this action differs by one gate delay, they will occur almost synchronously.

The sync reset signal is the Q1 output of the divide-by-5 counter. The leading edge of this signal lags the 10 Hz signal by 20 ms so that the duration of the 10 Hz sync will be approximately equal to that period.

The waveforms for the circuit shown in Figure 4.4.8-76 are shown in Figure 4.4.8-77.

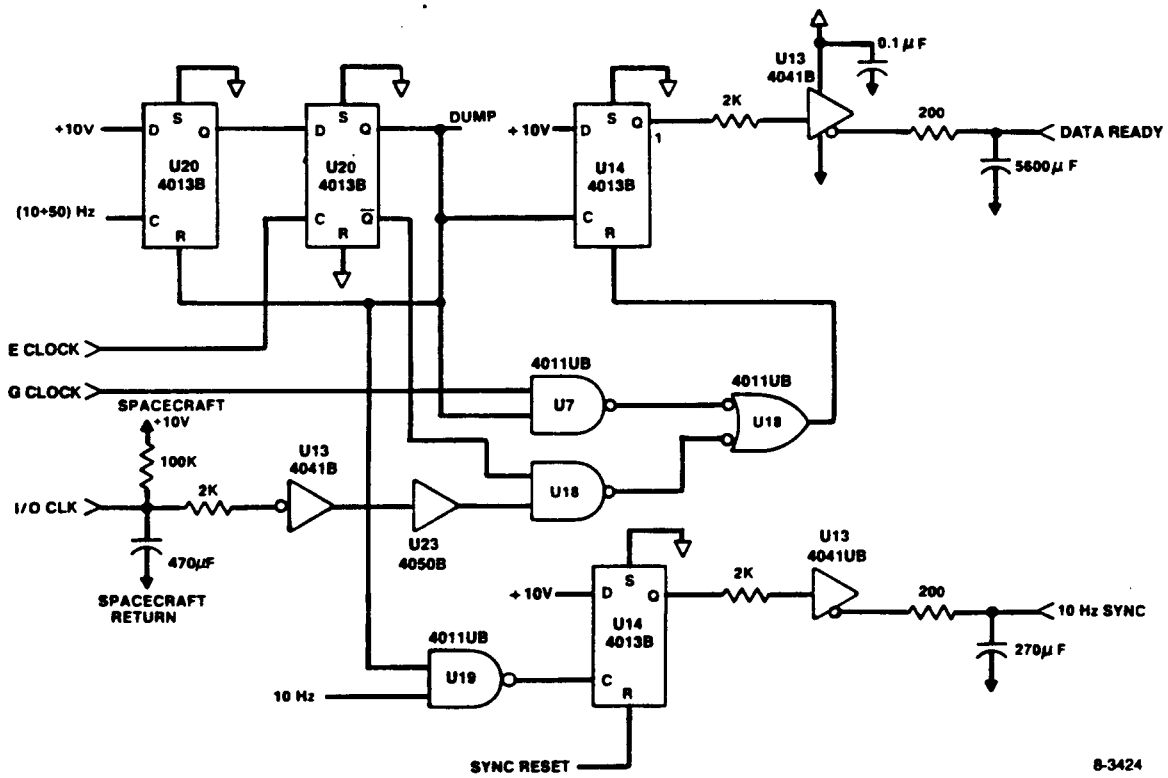

Figure 4.4.8-76. Dump, Data Ready and 10 Hz Sync

4.4.8.2.2.7.9 Data Accumulator. These circuits accumulate positive and negative gyro and accelerometer data pulses, and format them simultaneously into four separate 16-bit data words for a time period controlled by the dump signal. The data accumulator section consists of two parallel accumulator circuits, one for the gyro data and one for the accelerometer data that are stored in the positive and negative data registers. One such accumulator circuit is shown in Figure 4.4.8-78. It consists of a serial adder circuit with selected input gating and a 64-bit shift register (40318) that is connected to the adder in such a way that the contents of the shift register are presented one bit at the time at the input of the serial adder. It accumulates data that are transferred from the data precounter via a 4-bit buffer storage register such that four data words of 16-bits each are

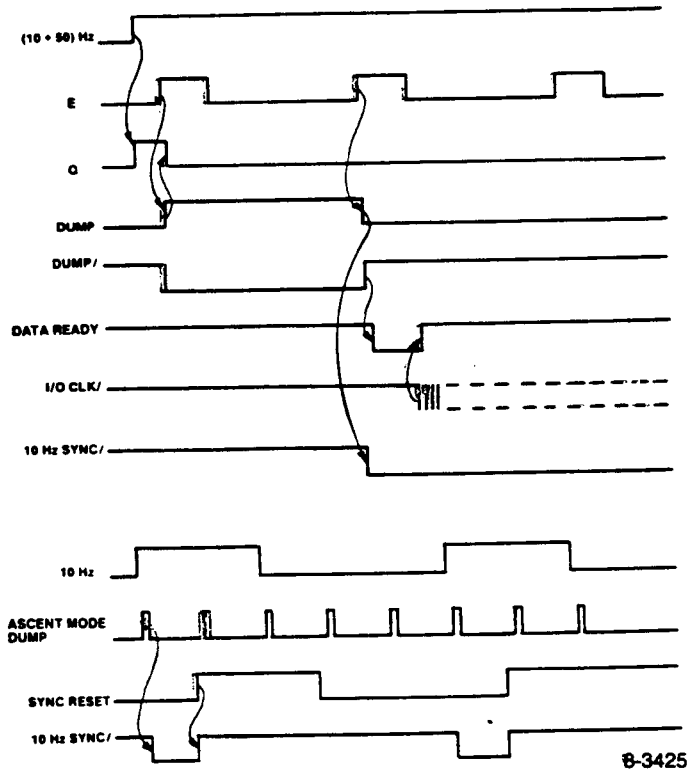

Figure 4.4.8-77. Dump, Data Ready and 10 Hz Sync/Waveforms

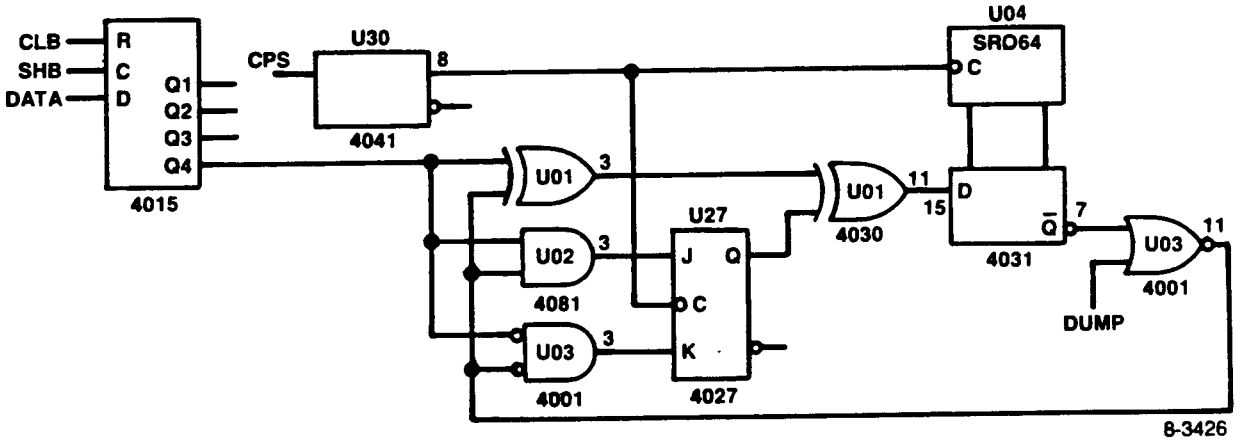

Figure 4.4.8-78. Data Accumulator

generated every 20 or 100 ms depending on the commanded data channel operating mode. All four 16-bit words are recirculated every 125 μs and are clocked by the CPS clock which consists of eight 8-bit bursts of the CP/clock.

The CPS clock consists of a 16 pulse clock burst during bit times (2 ÷ 25). This clock strobes the adder and the shift register both, while the CCL signal is used to reset the U27 carry flip-flop. During the dump period only logical "0" data are circulated to the adder input, so that while the shift register contents are transferred out, a new set of data may be entered during this cycle.

The serial adder is made up of two exclusive-OR gates in series and a carry generation circuit consisting of a flip-flop and two input gates. Serial addition must be performed LSB first for the carry action to work properly; each positive bit must be added to an LSB bit of a data word, (or by the first CPS pulse only) while the remaining CPS pulses handle any required carry action. Negative addition (subtraction of the negative data bits) in a serial adder is performed as 2's complement positive addition and so the negative data must be present during all 16 CPS pulses.

The Q/ output of the shift register produces the complement of the data word which, during dump/, is inverted by U3 into true data. The combination of this "old" data and the "new" data is then added together and re-entered in the shift register in accordance with the following truth table:

OLD	NEW	CARRY	RESULT
0	0	0	0
1	0	0	1
0	1	0	1
1	1	0	0
0	0	1	1
1	0	1	0
0	1	1	0
1	1	1	1

The carry bit must lag the adding function that causes it, which is accomplished by the inherent delay through the flip-flop. This carry flip-flop output must perform the following based on the inputs to the two input gates, called A and B. The truth table for A, B, J, K, and Q is:

A	B	J	K	Q
0	0	0	1	0
0	1	0	0	NC
1	0	0	0	NC
1	1	1	0	1

This shows that when A and B are both "1" the carry is set and will not change until both A and B are "0". This verifies correct adder function.

The last remaining carry at the end of the 16 CPS pulse burst is cleared by the CCL signal so that the carry flip-flop output is "0" prior to input to the shift register.

4.4.8.2.2.7.10 Status Register. This register stores status data prior to each dump cycle and shifts these data into the first data word slot of the A-data output register during dump.

Figure 4.4.8-79 shows the status data register. It consists of two 8-bit parallel-input, serial-output shift registers. The parallel loading is performed by the G clock. The data entered by the last G clock pulse before the start of the dump cycle are the data loaded into the output buffer. This loading is performed by the CPS clock during the (A) period of the dump cycle.

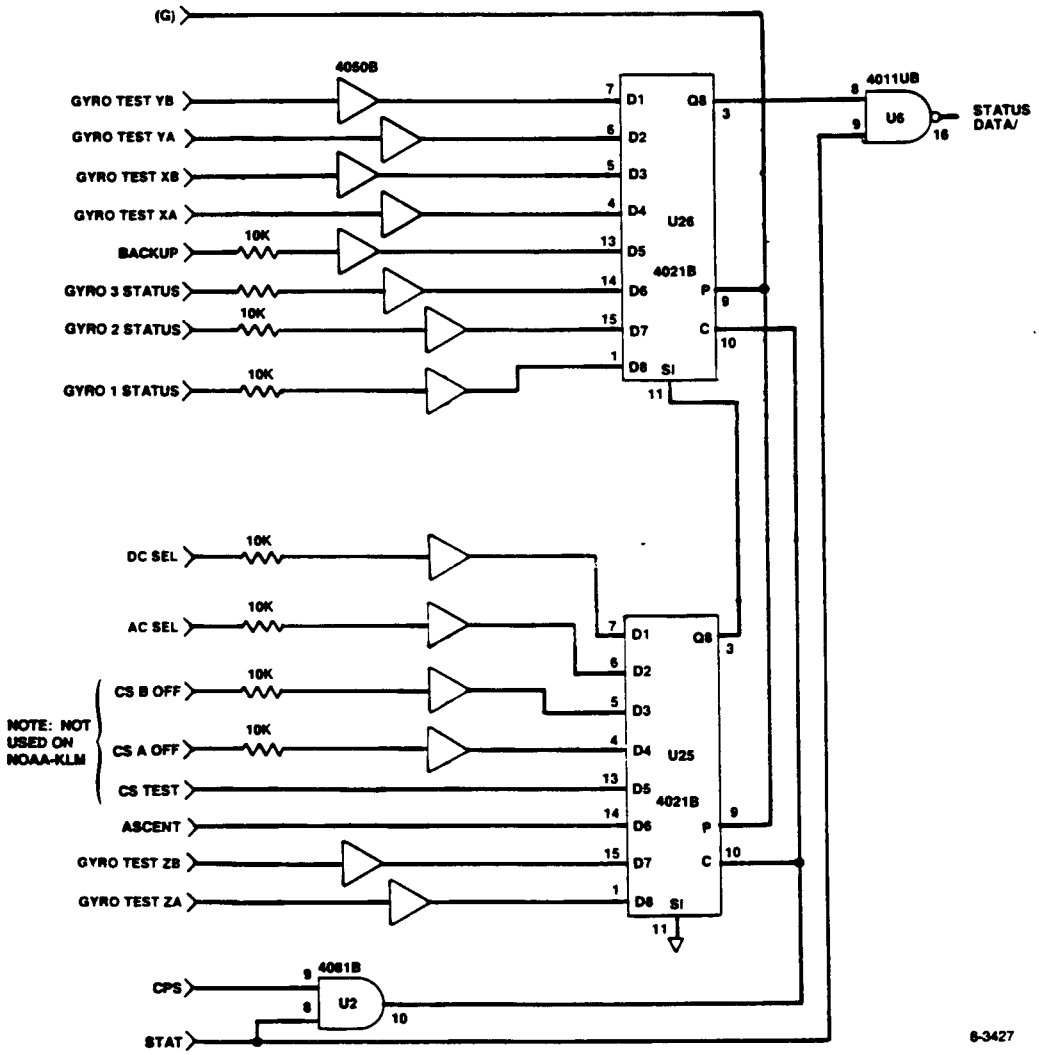

Figure 4.4.8-79. Status Data Register

All inputs to the status data registers are power isolated by the use of CD4050 level shifters. The shift registers are asynchronous parallel loading units which clock the available data at the CPS. Shifting out the data simultaneously clears the registers due to the "0" level at the serial input gate; this occurs at the CPS clock edge.

4.4.8.2.2.7.11 <u>Output Register Data Transfer</u>. This final circuit transfers the contents of all accumulators and data registers into two output registers in the correct format for outputting to the CIU. The two output registers are 64-bit shift registers. One is used exclusively for the four gyro data words (G-data) and one is used for all other data (A-data).

The A-data contents are different during the ascent and orbit modes. During ascent, they consist of the status data word followed by th three gyro data words and four accelerometer data words. The stat signal d_sables the gyro data output during the status word data transfer.

When in the orbit mode dummy data from the CSA follows the data words from all 6 gyro channels.

The data are first shifted into a set of buffer flip-flops (U8) by the CPS clock and then transferred into the output registers by the CPS. U10, a 64-bit shift register connected in a modulo 2 mode, serves as a selective enabling device for the output registers. The output registers are always maintained in a re-circulation mode except during the dump cycle when the D-input is enabled.

The I/O CLK/ from the CIU is inhibited during the dump cycle so that data outputting can occur only during dump/. Figure 4.4.8-80 shows the output register section. The first function of the circuit is ·e data transfer action from the various sources into the output register.. For the G-data transfer, gyro data are gated with the stat signal so that status data are transferred to the output buffer during the status word interval. For the A-data transfer, dummy data is gated with the orbit signal. Both the status data and the A accumulator data are shifted by the CPS positive going clock edge into the buffer flip-flop and are therefore available at the output register input at the CPS/.

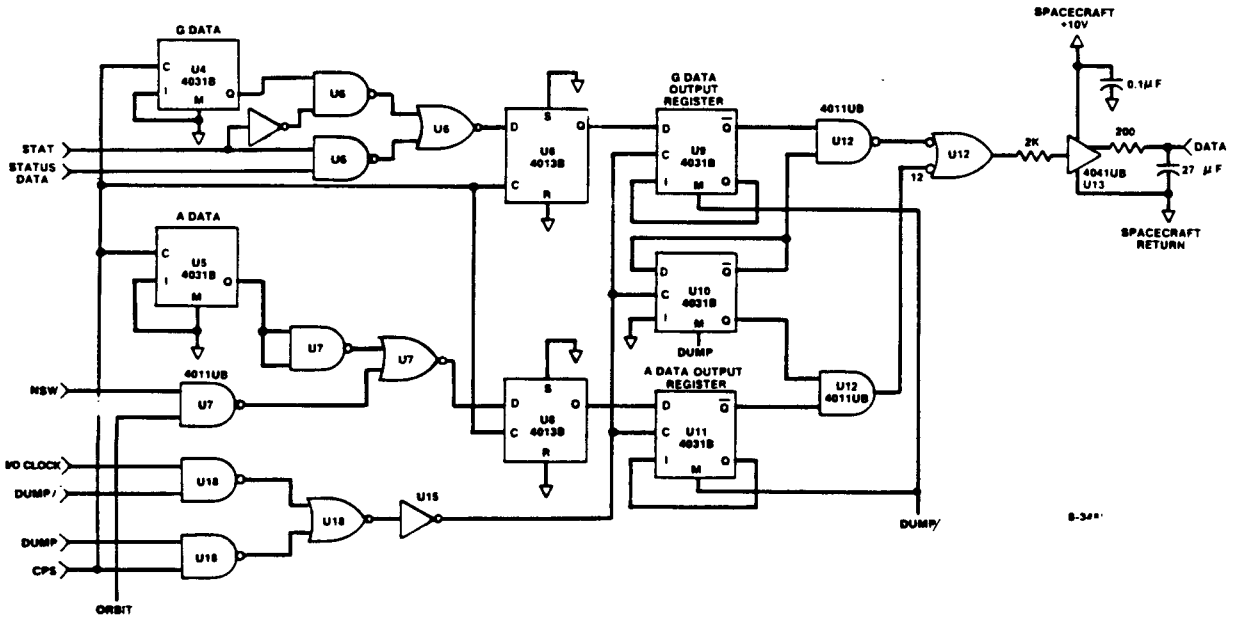

Figure 4.4.8-80. Output Buffer Section

The outputs of the two output registers are selectively enabled by the output of the 64-bit shift register U10. During dump this unit is in the re-circulation mode which enables the recirculation input. This enters 64 "0" bits into the register, so that the first 64 I/O CLK/ pulses will output 64 low signals from

the Q output and 64 high signals from the Q/ output. Because the Q/ output is fed back to the D input, the register will fill up with 64 "1" bits, thus reversing the polarity of the two outputs during the next 64 I/O CLK/ pulses. This provides the G-data to the data port first, followed by the A-data. Because both registers are in the re-circulation mode, the data will be continuously available for re-outputting if required, until the next dump cycle.

Shifting by the I/O CLK/ signal must occur by the trailing edge of the negative going clock pulse.

4.4.8.2.2.8 Thermal Control Amplifier. Figure 4.4.8-81 shows the circuitry that controls the IMU block temperature and the fine heater in each of the three gyros. Block temperature is sensed by a thermistor element which forms one leg of a bridge. The bridge output is amplified to control the effective resistance of the TCA power transistor (located on the spin motor supply chassis). In turn, this effective resistance controls the current through the selected ascent or orbit mode block heater configuration. This configuration comprises 6 resistance wound cartridge type heaters (of which three are disconnected in the orbit mode). Also, each gyro contains a 390-ohm make-up heater which is switched on whenever the gyro is turned off. Table 4.4.8-10 summarizes the power necessary to meet thermal requirements in the various operational modes.

The TCA is powered by 28 Vdc from either the spacecraft bus (via the IMU on/off relay) or an external source (via the test connector, in pre-launch test only). The operating voltage for the bridge is stabilized by a shunt voltage regulator.

During pre-launch, +28 Vdc heater power is applied through the spacecraft test connector and is diode isolated from the remainder of the IMU so that only the TCA circuits and heaters receive power. Series diodes also prevent reverse polarity voltage (should it be inadvertently applied) from reaching the TCA. Heater power is applied during pre-launch operations to temperature stabilize the inertial block, minimizing the time required to reach IMU thermal stability after the IMU and its gyros are turned on prior to launch. Typically, thermal stability is reached 90 minutes after application of block power and warm-up heaters, when the initial chassis temperature is +77°F in +70°F air. The required IMU power is 11 watts (maximum) of heater power during this thermal stabilization period.

Figures 4.4.8-82 and 4.4.8-83 show the inertial sensor block and gyros temperature response to IMU turn-on in the orbit mode. The IMU is in a vacuum with an initial temperature of 59°F (15°C). Both the sensor block and the gyros reach their steady state temperature within 150 minutes, as do the accelerometers (not shown). This is well within the 4.5-hour maximum time allowed for the IMU to reach operational performance.

IMU turn on from a 77°F (in air) start condition is shown in Figure 4.4.8-84. The specification requirement here is that the IMU reach operational performance within 120 minutes from turn on. Figure 4.4.8-84 shows that the ground based IMU gyros reach their final steady state temperatures within 90 minutes. This is different from the orbit condition because the sensor block "warm up" heaters (24W) can be energized on earth but not in orbit. The warm-up heaters are manually controlled and have thermostatic over-temperature protection.

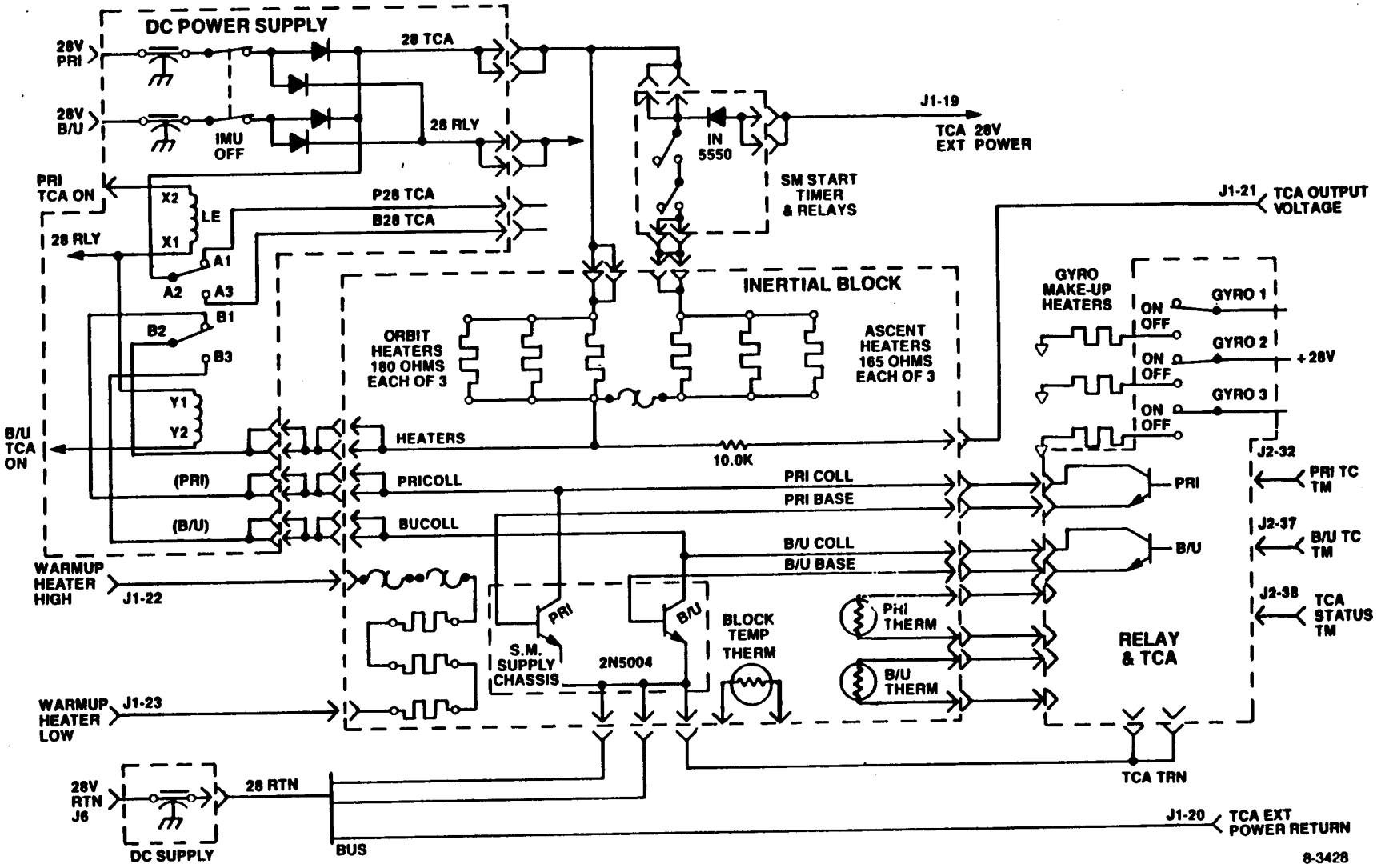

Figure 4.4.8-81. IMU Block Temperature Control

TABLE 4.4.8-10. IMU THERMAL CONTROL HEATER POWER REQUIREMENTS

Operating Mode	Power Source Position	Ascent/ Orbit Relay 180Ω	Total Block Power 165Ω	Total Heaters (watts)	Gyro Heater Power (watts)*	Warmup Heater Power (watts)	Power Control Range (watts) (max/nom**)
Pre-launch Test	External (via Test Connector	Ascent	0.45W	0.45W	2W/gyro	24W	52.5W/33.3W
		Orbit	0.9W	-	2W/gyro	24W	39W/35W
Ascent	Spacecraft Bus	Ascent	0.45W	0.45W	2W/gyro	-	28.5W/9.3W
Orbit	Spacecraft Bus	Orbit	0.9W	-	2W/gyro	-	15W/11W

*Gyro heaters turned on only when gyro is off.
**Under normal operating conditions, with TCA transistor collector at 22V (Ascent) or 20V (Orbit) max values include initial turn-on condition.

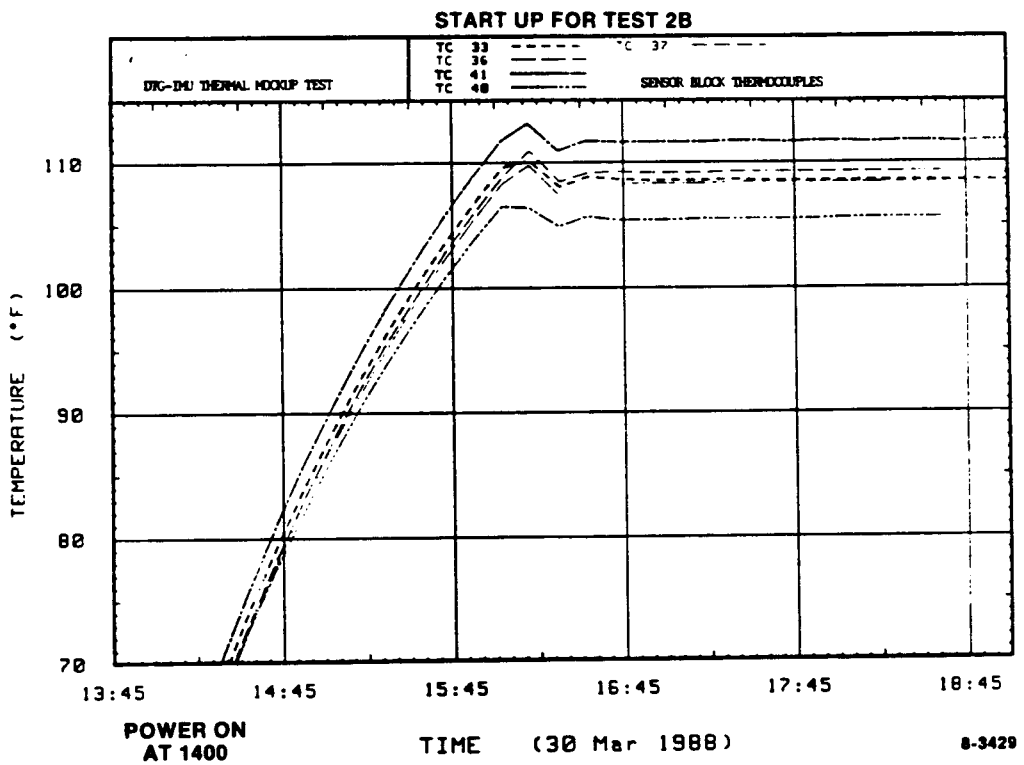

Figure 4.4.8-82. DTG-IMU Thermal Mockup Test - Sensor Block Thermocouples

Each of the three gyros contains its own 390-ohm makeup heater. The latching relay contacts that enable current through the gyro make-up heaters are set as a function of the gyro on/off commands while the IMU has operating power applied. The latched condition is maintained when operating power is removed from the IMU.

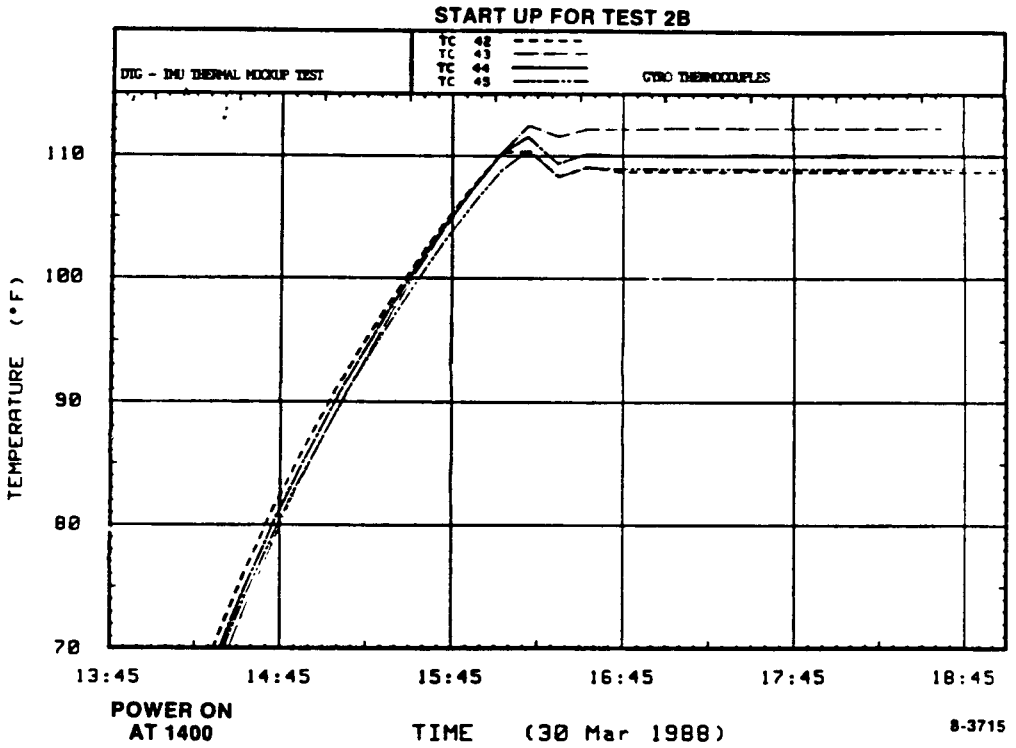

Figure 4.4.8-83. DTG-IMU Thermal Mockup Test - Gyro Thermocouples

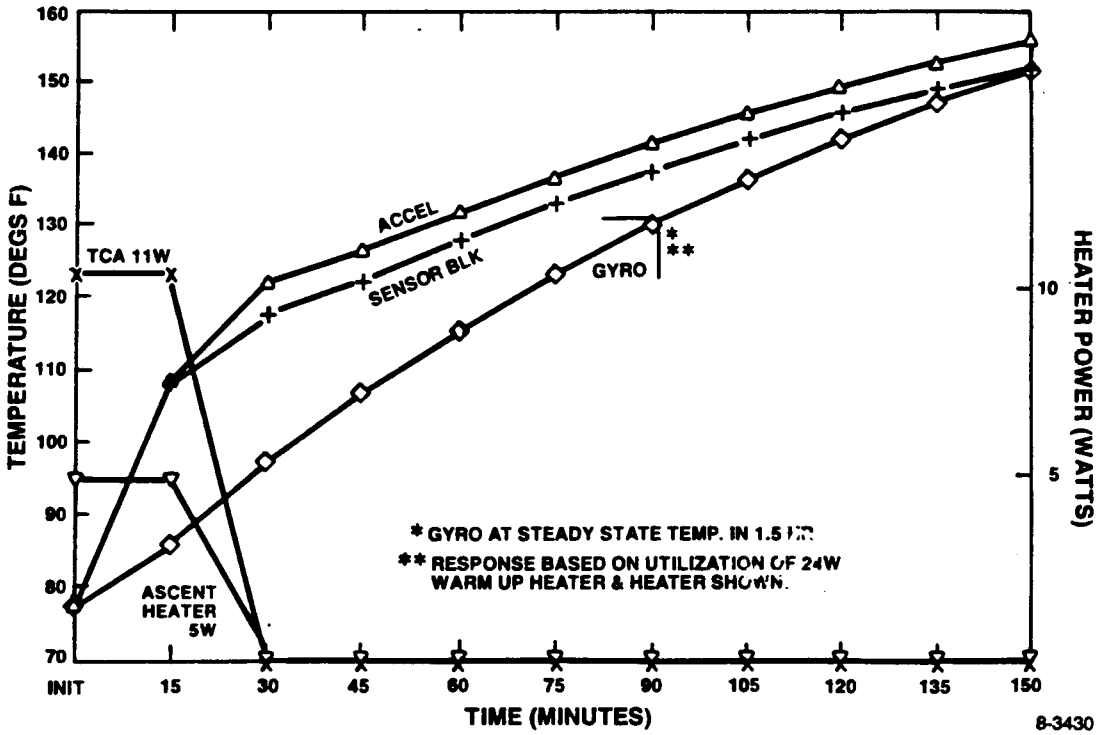

Figure 4.4.8-84. IMU Turn-On from 77° Ambient

The gyro make-up heaters have been incorporated to maintain inertial block thermal stability in the IMU by replacing 2 watts of power per gyro in the event that a gyro must be turned off. If one or more of the gyros is turned off before operating power is removed from the IMU (normally all three gyros should be turned off), the gyro makeup heaters will be enabled by closure of their latching relay contacts.

During operation in the ascent mode, the heater power control range is normally 0.7 to 25.0 watt. The TCA controls the current through the set of six heaters connected in parallel to control the inertial block temperature to 109°F. The inertial block temperature is controlled to the calibration temperature within 1.0°F during ascent.

During operation in the orbit mode, the IMU thermal interface is controlled to be within the temperature range of +48.2°F to +84.2°F (+9°C to +29°C), with orbital variations of ±1°F ±0.56°C). The orbit heater power control range is normally 5.5 watts TCA power. Actual TCA power input is approximately 0.7 watt at the highest ambient condition and 11.1 watts at the lowest ambient condition. The normal orbital block temperature is nominally controlled to +109°F (46.7°C) with an orbital gyro temperature variation of ±0.2°F.

In the unlikely event that the ascent/orbit mode relay fails so as to leave the 165-ohm heaters energized in orbit mode, the TCA will maintain normal control using only the power necessary to maintain temperature stabilization. A block mounted thermostat assures that subsequent electronics failures will not result in a temperature that would permanently damage the gyros. Similarly, dual thermostats in the warmup heater circuit preclude damage from a procedural error or hardware problem during test operations.

The electronics compensation of the TCA features an integrator in the forward path. In the steady state, the controller will thus bring the sensor to the same temperature over all ambient conditions (zero servo error). Gradients will exist, however, and it is important to minimize these effects by control of the environment so that inertial component temperatures remain near the calibration conditions.

4.4.8.2.3 Telemetry

4.4.8.2.3.1 Analog Telemetry. The IMU has 28 analog telemetry points. Of these, one point represents temperature, 10 points represent voltages, 10 points represent torquer currents, and three points represent gyro spin motor currents. The remaining two points represent data channel selection as indicated by a square wave output.

4.4.8.2.3.1.1 Temperature Telemetry. Inertial block temperature is sensed by a thermistor which forms the variable portion of a voltage divider between +15 Vdc. The divider output is amplified to give a dc telemetry output voltage proportional to block temperature.

4.4.8.2.3.1.2 Power Supply Selection Telemetry. Four telemetry points indicate selection and proper operation of certain IMU internal power supplies. These four telemetry points are:

a. Primary +7.5 Vdc power supply
b. Backup +7.5 Vdc power supply
c. Primary Signal Generator power supply
d. Backup Signal Generator power supply

The +7.5 Vdc supplies are used internally to the respective IMU power supply assemblies. They are made available for separate telemetry to provide a positive means dc power supply selection in addition to the status word bit. The signal generator power supplies are also telemetered separately as a backup verification of ac power supply selection.

The dc voltages developed for use throughout the IMU (+15 Vdc, +10 Vdc, -15 Vdc) are telemetered from points downstream of the combination of the primary and backup supply voltages. Thus, these telemetry signals reflect the status of the selected power supply.

All telemetry points are resistively isolated from the IMU circuitry and scaled to provide a nominal 4.5 Vdc output to telemetry for the nominal supply operation. In the case of the gyro spin motor supply telemetry, scaling provides 4.5 Vdc to telemetry while the supply is at the start condition (approximately 45 Vrms) and 3.5 Vdc at the spin motor run voltage (35 Vrms).

4.4.8.2.3.1.3 Current Telemetry. A total of 10 torquer current telemetry points are included. These represent gyro and accelerometer torquer currents (two torquers for each of the three gyros, one torquer for each of the four accelerometers).

The currents through the six gyro torquers and four accelerometer torquers are represented, in each case, by the voltage output from the rebalance loop to the appropriate digitizer. The six gyro torquer currents are utilized throughout mission life; the four accelerometer torquer currents (X, Y, Z, and S accelerometers) are utilized only in the ascent. In all cases, a +2.5 Vdc (nominal) output indicates zero torquer current. Also, each Spin Motor Current Detector produces a dc telemetry voltage proportional to the spin motor current.

4.4.8.2.3.1.4 Data Channel Selection Telemetry. Two data channel selection telemetry points are provided:

a. Primary data channel
b. Backup data channel

Selection and proper operation of either the primary data channel or the backup data channel is indicated by a 10 Hz square wave at the appropriate telemetry point and a steady state high or low output at the other telemetry point. This square wave is derived from the 10 Hz output of the clock countdown chain.

4.4.8.2.3.1.5 Thermal Control Assembly. An indication of the voltage supplied to the TCA heater is provided by a simple resistive voltage divider

connected in parallel with each TCA control transistor. With the TCA heater turned full on, the telemetry signal is approximately 0.5V; with the heater turned full off, the telemetry signal is approximately +4.8V. While the TCA is in control, the telemetry voltage will be at some steady state value between the two extremes. The telemetry voltage level is directly proportional to the power dissipated in the control transistor and is inversely proportional to the power dissipated in the TCA heater. The telemetry output of the disabled TCA will be 200 volts.

4.4.8.2.3.2 Discrete Telemetry. The IMU includes a total of five discrete telemetry points, of which two are utilized only in the orbit mode. These telemetry points are:

a. Gyro 1 spin motor status
b. Gyro 2 spin motor status
c. Gyro 3 spin motor status
d. TCA status
e. IMU Mode (ascent or orbit)

The status of each of the three gyro spin motors is derived from its spin motor current detector. With the spin motor current within the specified range, the telemetry output is +4.7 Vdc (nominal); outside this range, either high or low, the telemetry output is zero volts.

The IMU status point indicates whether the IMU is in the orbit, or ascent mode. With the IMU in the ascent mode, the switched +15 Vdc used to turn on the accelerometers is voltage divided to provide a telemetry output of +4.5 Vdc (nominal). A zero volt output indicates that the IMU is in the orbit mode.

The TCA status telemetry point indicates whether the primary or back-up TCA is on. The primary TCA 28V power is divided down to produce a 4.5V signal indicating primary TCA on or an 0V signal indicating back-up TCA on.

4.4.8.2.3.3 Digital Telemetry. Redundant telemetry data for the IMU are incorporated by including a 16-bit digital status word in each "frame" of the data output. Table 4.4.8-11 shows the meaning of the contents (logic "1" or "0") in each of the 16 bit positions. The 16 telemetry points are:

a. Gyro 1 spin motor status
b. Gyro 2 spin motor status
c. Gyro 3 spin motor status
d. Logic Processing Channel
e. X_P Gyro test status
f. X_B Gyro test status
g. Y_P Gyro test status
h. Y_B Gyro test status
i. Z_P Gyro test status
j. Z_B Gyro test status
k. IMU mode
l. Not Used
m. Not Used
n. Not Used
o. AC power supply selection
p. DC power supply selection

TABLE 4.4.8-11. STATUS WORD CONTENTS

Bit	Function	Logic "0" (False)	Logic "1" (True)
1	Gyro 1 Spin Motor Current	Off/Bad	On/Good
2	Gyro 2 Spin Motor Current	Off/Bad	On/Good
3	Gyro 3 Spin Motor Current	Off/Bad	On/Good
4	Logic Processing Channel	Primary	Backup
5	X_P Gyro Test	Off	On
6	X_B Gyro Test	Off	On
7	Y_P Gyro Test	Off	On
8	Y_B Gyro Test	Off	On
9	Z_P Gyro Test	Off	On
10	Z_B Gyro Test	Off	On
11	IMU Mode	Orbit	Ascent/Maneuver
12	Not Used		
13	Not Used		
14	Not Used		
15	AC Power Supply	Primary	Backup
16 (MSB)	DC Power Supply	Primary	Backup

4.4.8.3 Sun Sensor Assembly (SSA)

The Sun Sensor Assembly (SSA) is a non-redundant unit which may be commanded on or off. The unit is a single-axis digital sun sensor that measures the component of the sun angle between the spacecraft pitch axis (+Z) and the projection of the earth-sun line on the pitch-roll (YZ) plane. The sun sensor is used to re-initialize the yaw-attitude calculation once per orbit when the sun-spacecraft vector lies in the Y-Z plane, and to provide an update of the equivalent yaw gyro drift.

The SSA consists of a Sun Sensor Detector (SSD) and Sun Sensor Electronics (SSE), shown in Figure 4.4.8-85, and a stray light baffle. The SSU senses the position of the sun and provides a digital code output corresponding to the sun position component in the YZ plane; the SSE processes this digital code and provides the resulting binary data to the Controls Interface Unit on request.

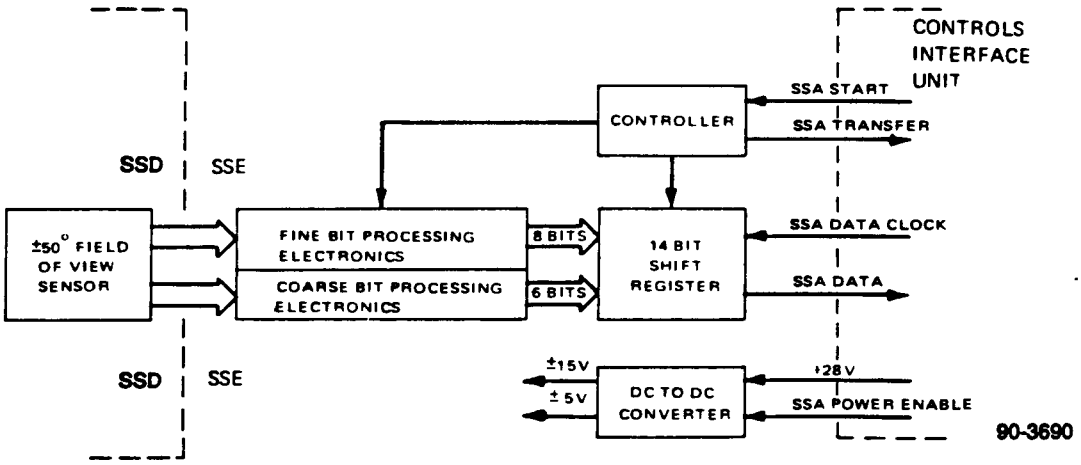

Figure 4.4.8-85. Sun Sensor Assembly Simplified Block Diagram

The SSD consists of a set of entrance slits for viewing the sun and a set of photocells on the rear surface for detecting each slit image through an overlay mask containing a light transmission pattern. The light transmission pattern translates the slit image position into a digital output code that is a function of sun angle.

The SSE accepts the detected image coarse and fine bit data from the SSU, processes it to obtain binary data, then stores the resulting 14-bit word in a shift register. The SSA Data is then serially transferred to the Controls Interface Unit on request.

The baffle is installed on the sensing side of the SSU and restricts the transverse axis field of view to $\pm 5°$.

4.4.8.3.1 Design Description

4.4.8.3.1.1 Design Approach. The basic principle of operation of the SSA is shown in Figure 4.4.8-86. Light passing through a slit on the front surface of a fused-silica reticle forms an illuminated image of the slit on the light transmission code pattern on the sensor's rear surface; the angle of incidence determines the position of this image. A silicon photocell is located behind each column of the code pattern. Light incident upon the slit and then on a clear portion of the pattern in a particular column illuminates the photocell and produces an output "one"; if the light falls on the opaque segment, the photocell is not illuminated, and an output "zero" results. The encoded sun angle bits are then amplified, processed, and transferred serially to the Controls Interface Unit.

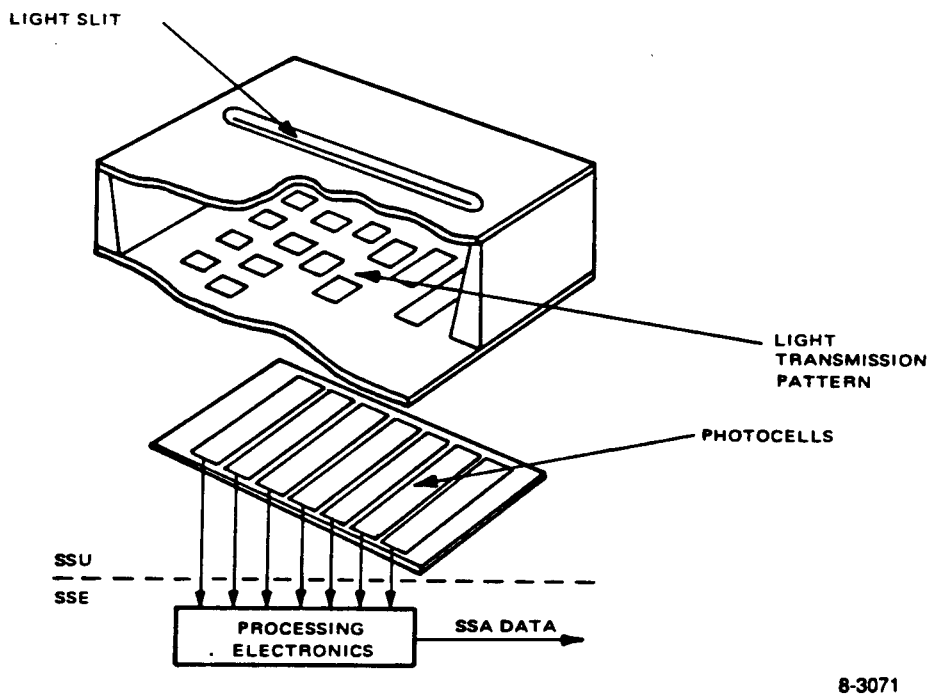

Figure 4.4.8-86. Sun Sensor Assembly Basic Principle of Operation

4.4.8.3.1.2 Operating Modes. The SSA is controlled in response to two control signals from the Command and Control Subsystem (C&CS):

- SSA Power Enable
- SSA Start

The SSA is turned on during receipt of the true level of the SSA Power Enable control signal, and is turned off during receipt of the false level. Under normal conditions the SSA is turned on just prior to a desired measurement and is turned off just after the measurement.

During the time the SSA is turned on, receipt of each SSA Start control signal results in the acquisition of a new sun angle measurement and the subsequent transfer of one digital word containing this data to the Controls Interface Unit. Under normal conditions, several SSA Start signals are generated at the time selected to yield a direct measurement of sun angle, η; the resulting series of measurements are averaged by the SSA data processing software to minimize noise effects.

4.4.8.3.1.3 Design Characteristics. The design characteristics of the SSA are summarized in Table 4.4.8-12.

TABLE 4.4.8-12. SUN SENSOR ASSEMBLY CHARACTERISTICS

Characteristic	Value
Type of Sensor	Single Axis, Digital
Type of Detector	Photocells
Field of View	100 by 10 degrees, Centered 47.5° from +Z Axis, Toward -Y Axis
Measurement Accuracy	5 arc-minutes
Data Format	Binary, 16 bits, MSB first
Active Data Bits	14
Data Bit Value	
At Center of FOV	0.49 arc-minute
At Edge of FOV	0.19 arc-minute
Mean Value	0.37 arc-minute
Size	
SSU	5.2 x 2.6 x 1.6 inches
Baffle	2.8 x 5.5 x 1.2 inches
SSE	4.6 x 4.0 x 2.0 inches
Weight	
SSU	0.71 lb
Baffle	0.21 lb
SSE	1.1 lbs
Power	0.8 Watt at +28V

4.4.8.3.1.4 Physical Description. The SSA is contained within two rectangular packages, the SSD and SSE, as shown in Figures 4.4.8-87 and 4.4.8-88. The SSD is attached to the -Y edge of the IMP using the mounting adapter shown in Figure 4.4.8-89; the SSE is mounted in the top of the Equipment Support Module, near the -Y axis.

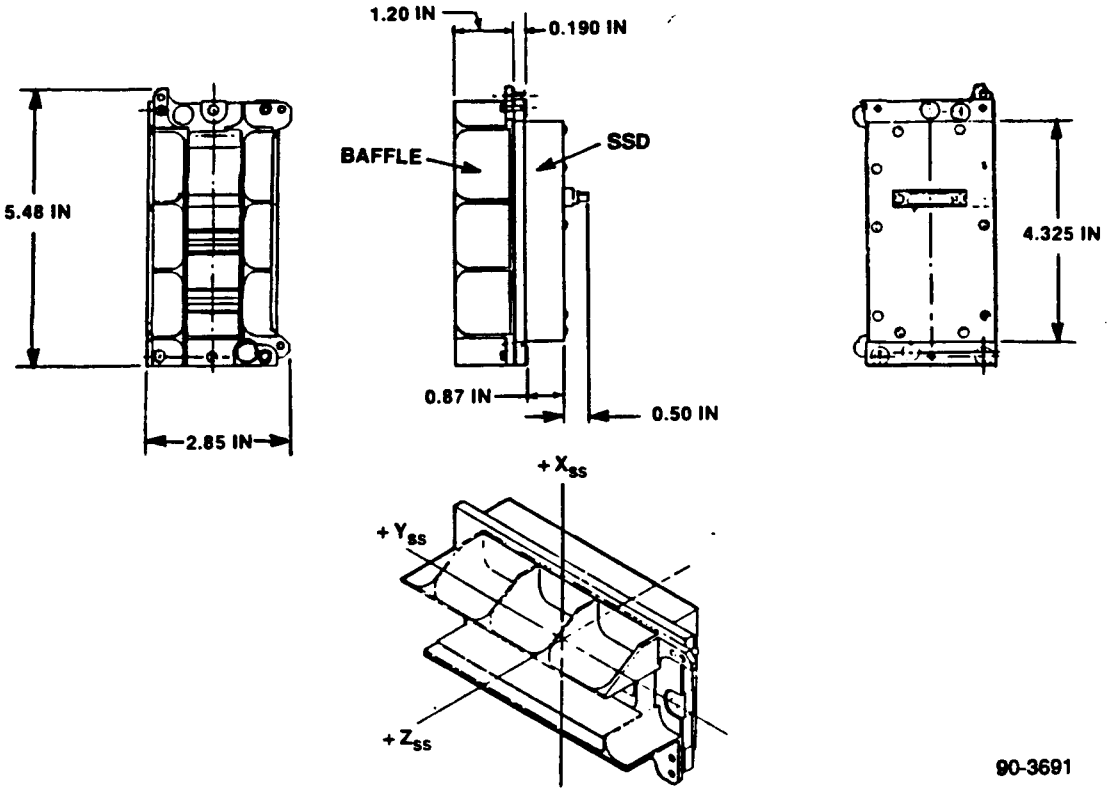

Figure 4.4.8-87. SSD External Configuration with Baffle

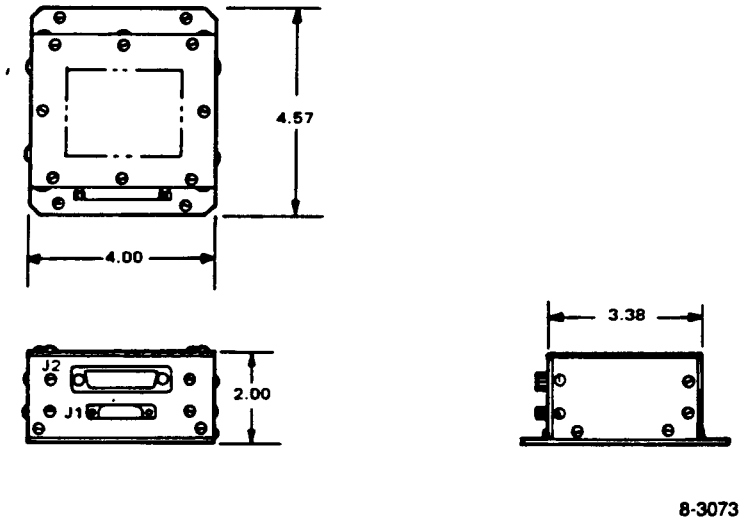

Figure 4.4.8-88. SSE External Configuration

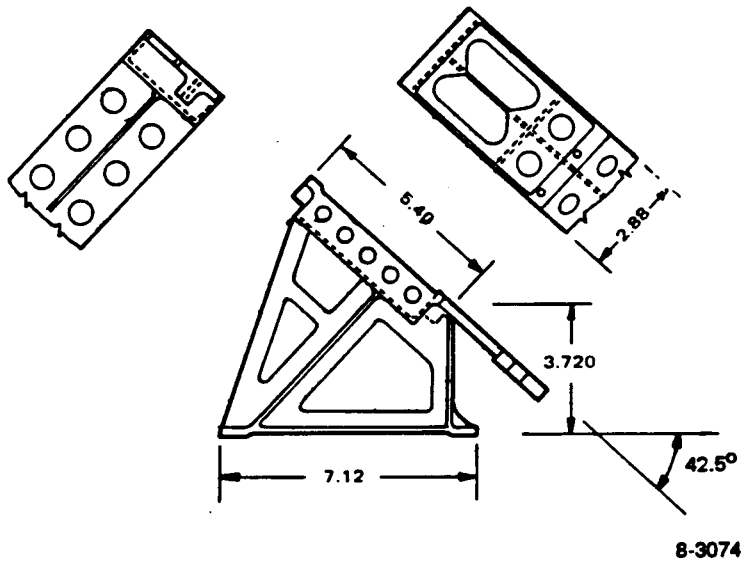

Figure 4.4.8-89. SSD Mounting Adapter

The SSA coordinate system and field of view definition is shown in Figure 4.4.8-90. The Y_{SS} and Z_{SS} sensing axes are displaced by 47.5° from the spacecraft Y and Z axes; with this displacement, the 100° by 10° field of view of the SSD includes the spacecraft +Z and -Y axes. The nominal sun angle measurement point is also shown. This measurement occurs at the predicted time when the sun is in the YZ plane on the -Y side of the spacecraft, thus obtaining a direct measurement of the sun angle, η.

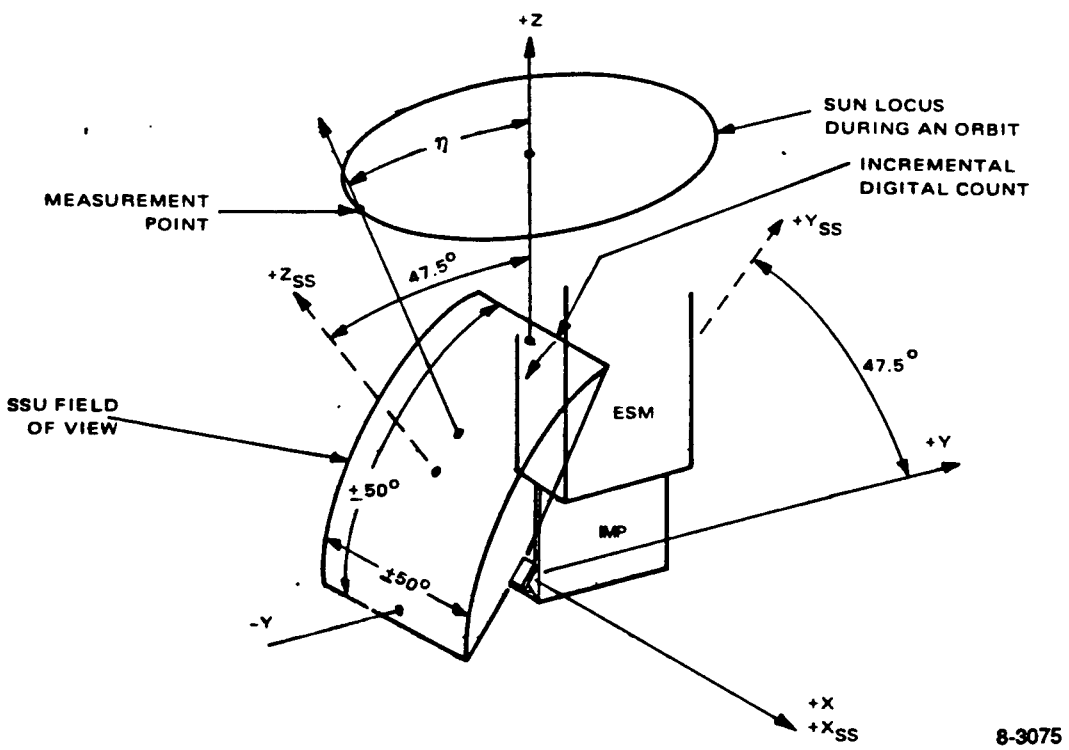

Figure 4.4.8-90. SSA Coordinate System and Field of View Definition

4.4.8.3.1.4.1 Sun Sensor Detector. The Sun Sensor Detector (SSD) is a digital sensor. As shown in Figure 4.4.8-91, the SSU contains two reticles, one coarse and one fine, each of which is constructed of two thin fused silica plates separated by a fused silica spacer. Each reticle includes an air vent to permit outgassing in a vacuum environment. The coarse reticle contains two slits for light entry, while the fine reticle contains a "grating" pattern with a number of equally spaced transparent and opaque slits. Both reticles have light transmission patterns located in the bottom plate.

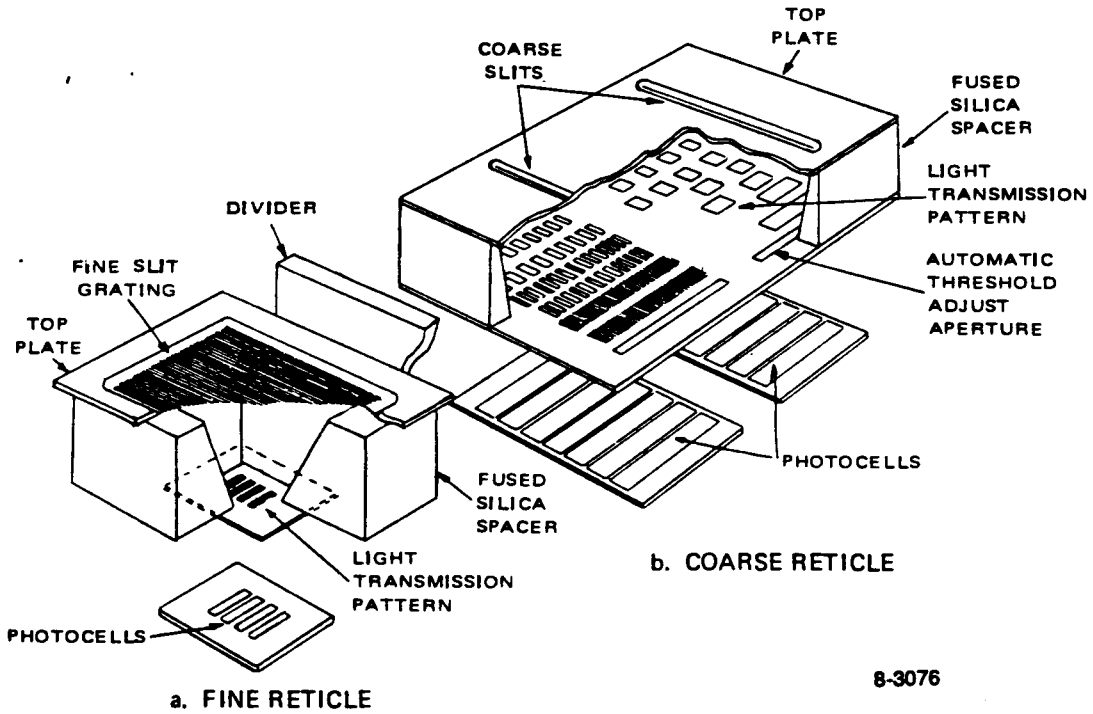

Figure 4.4.8-91. Sun Sensor Unit Assembly

In orbital operation, the SSD views the sun and forms an illuminated image of each entrance slit on the light transmission pattern. The image illuminates those photocells behind each clear (non-opaque) portion of the transmission pattern, thus producing an output digital code which is a function of sun angle.

The SSD is externally hard mounted on a bracket which is hard mounted to a temperature controlled plate (the IMP); the bracket is covered with a thermal blanket. For thermal reasons, all sides of the SSU except the connector side are covered with Dentor Silver.

4.4.8.3.1.4.2 Sun Sensor Electronics. The SSE is a standard electronics box containing all of the electronics required for processing, storing, and transferring the digital data from the SSU. This electronic circuitry and the associated ±15 and ±5 volt power supplies are mounted on five printed circuit boards.

4.4.8.3.1.4.3 Sun Sensor Baffle. The Sun Sensor Baffle is attached to the detector slit side of the SSD. The baffle limits the transverse axis clear field of view to ±5° with respect to the SSA Y-Z plane. In addition, the

baffle restricts the stray light field of view to ±30° maximum. It is made from an aluminum alloy with a black anodized exterior to eliminate glint.

4.4.8.3.1.5 Performance Summary. Table 4.4.8-13 summarizes the expected errors in the SSD; typical errors measured during qualification testing of the prototype SSA were less than ±0.025°.

TABLE 4.4.8-13. SSA PERFORMANCE SUMMARY

Source	Bias Type Errors (deg.)			Random Errors (deg.)
	Initial Uncertainties	Temperature Effects	End of Life Effects	Initial Uncertainties
Alignment with Simulated Sun	0.0015			
Angle Encoder Zero Set	0.0015			
Encoder Quantization				0.0005
Encoder Transition	0.0005			
Uniformity of Sun Beam	0.002			
Distortion in Photocell Output				0.003
Photocell Mismatch		0.002	0.002	
Electronics Harmonic Effects				0.003
Electronics Trimming	0.005	0.005	0.005	
Detector Slit and Pattern Location				0.03
Mechanical Distortion of Detector		0.010		
Alignment Uncertainty of SSU FOV centerline with respect to alignment cube	0.008			
RSS Total	0.0099	0.0114	0.0054	0.0303
Bias Total		0.0160°		
Random Total		0.0303°		
RSS Total of Bias and Random Errors		0.034°		

4.4.8.3.2 Functional Description

The SSA reads and stores the sun angle data on request and provides a serial binary output under the control of the CIU. As shown in Figure 4.4.8-92, the SSU consists essentially of a set of coarse angle measurement circuitry, a set of fine angle measurement circuitry, an output register with the associated interface circuitry, and a dc-to-dc converter.

4.4.8.3.2.1 Coarse Angle Measurement. An "early/late" technique is used to derive each coarse data bit. The "early/late" technique uses the state of the next lower binary bit (the most significant fine bit for the least significant coarse bit) to select 1 of 2 possible photocell outputs for that bit. Use of this technique automatically removes all ambiguities associated with transitions from one bit to the next.

The logic of the early/late technique can be derived by examining the table of binary numbers shown in Figure 4.4.8-93. Note that whenever the least significant bit changes from a "zero" to a "one" in the direction of increasing count, all other bits remain constant because no carries can occur; note also that whenever the least significant digit changes from "one" to "zero" in the direction of increasing count, at least one other bit must change, because a carry occurs. Therefore, bit changes in all columns may be thought of as triggered by the carries propagated when the least significant digit changes from "one" to "zero". Similarly, it can be seen that the digits in column 2 to 4 can only change when the digit in column 1 changes from "one" to "zero" in the direction of increasing count; similarly, changes in columns 3 and 4 depend on "one" to "zero" changes in column 2, etc.

The preceding relationships can be used to remove ambiguities by modifying the code pattern for each bit as shown in Figure 4.4.8-94. Note that each bit pattern of the binary code is replaced by 2 patterns, one displaced one way from the normal binary code position and the other by the same amount in the opposite direction. The horizontal lines through the pattern represent 3 possible cases for the position of the sun image produced by the entrance slit.

For illustration purposes, assume that the least significant digit, 2^0, reads "one". Then if the pattern in the next higher zone were displaced slightly in the direction of decreasing count, its reading could be erroneous if the index line were very close to a "one-to-zero" transition in the least significant (2^0) digit column. This is true because the displacement of the 2^1 pattern would anticipate the corresponding carry. If, however, the 2^1 pattern were displaced slightly in the direction of increasing count, it would read correctly when the 2^0 digit is "one".

Now assume that the least significant digit reads "zero". Then if the pattern in the next higher zone were displaced slightly in the direction of increasing count, its reading could be erroneous if the least significant bit was just past a "one-to-zero" transition; the required change in the 2^1 column would not be read. However, slight displacement of the 2^1 pattern in the direction of decreasing count assures correct reading when the 2^0 digit is "zero".

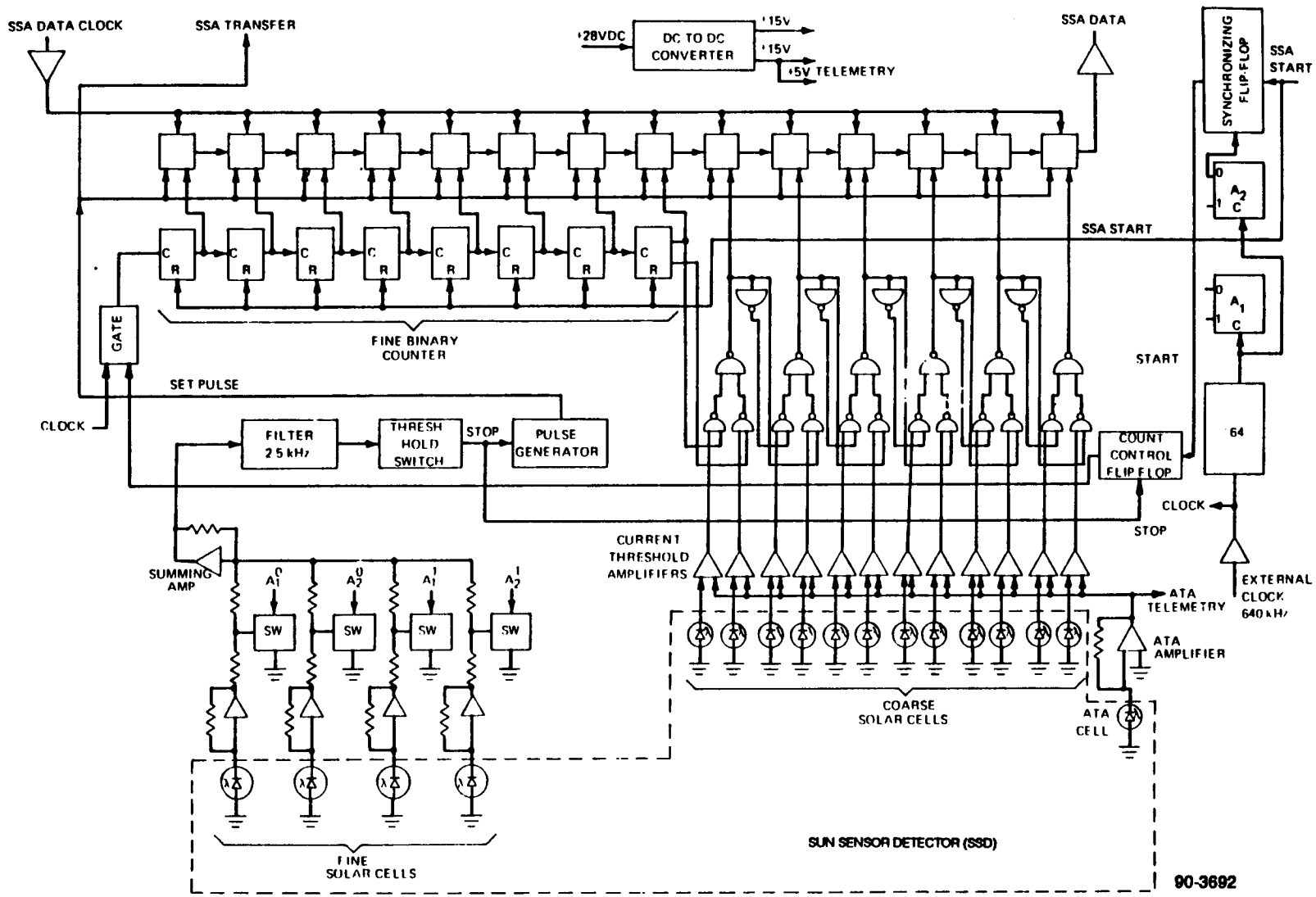

Figure 4.4.8-92. SSA Functional Block Diagram

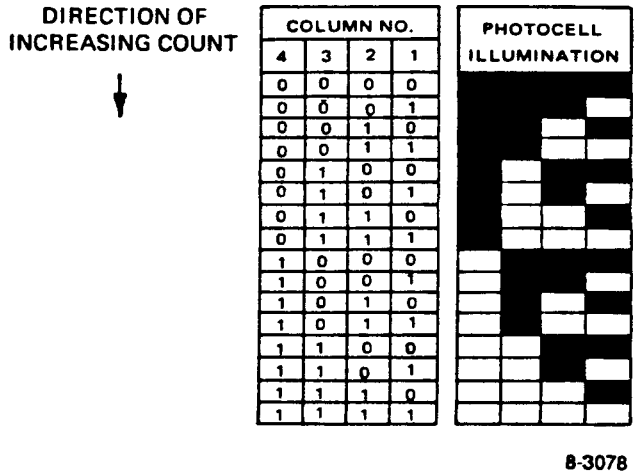

Figure 4.4.8-93. Binary Number Correlation

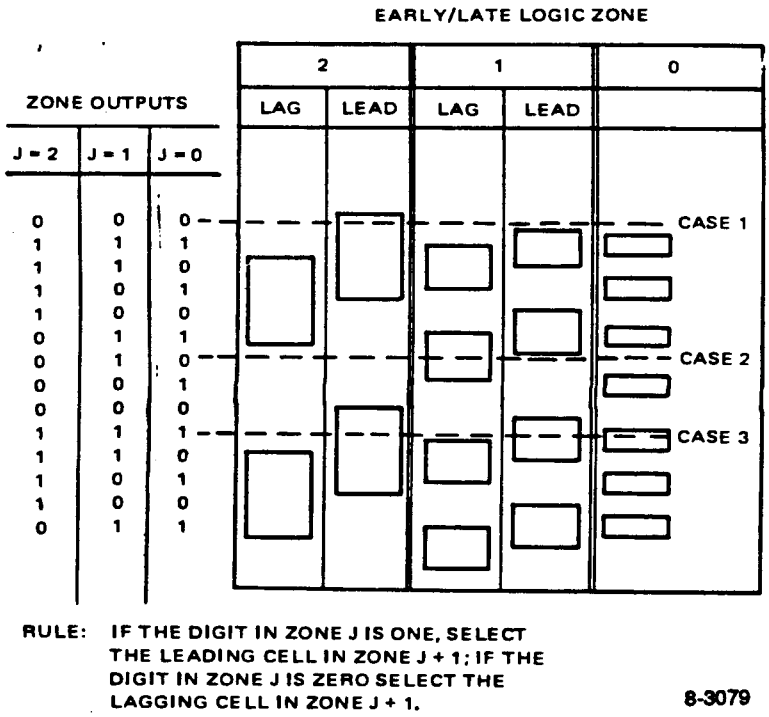

Figure 4.4.8-94. Binary Code Bit Pattern Modification for Non-Ambiguous Data

The selection of the correct pattern in any zone is made according to the following rule: If the digit in zone j is "one", select the leading pattern (displaced in the direction of increasing count) in zone j + 1; if the digit in zone j is "zero", select the lagging pattern in zone j + 1. Thus, the reading in each zone determines the pattern selection for the next higher zone, and the overall coarse angle measurement accuracy is determined by the accuracy of the least significant bit.

Two Automatic Threshold Adjust (ATA) light transmission patterns are included, only one of which is actually used. The output of the photocell beneath this

ATA pattern gives a measure of the effective light intensity at the detector, which is a function of the incident angle. The ATA cell and associated amplifier serve to set the threshold for the 12 coarse bit operational amplifiers, which are operated open loop. If the output from a photocell exceeds the output of the ATA cell, the output of the photocell amplifier is a one; if not, the output is a zero. The ATA pattern is arranged to have the full field of view of the sensor, but the slit width is half as wide as the slit widths for the data cells.

Use of the ATA cell compensates for the change of output with angle of incidence and varying satellite-sun distance, and simplifies ground calibration by eliminating the need for an accurate absolute level of illumination.

4.4.8.3.2.2 Fine Angle Measurement. The fine reticle "grating" pattern is composed of a number of equally spaced transparent and opaque slits. The bottom pattern consists of four sets of nine transparent slits spaced as in the top grating; the four sets of slits are located in space quadrature with respect to each other. As the sun scans the sensor along the measurement axis, quadrature sinusoidal outputs are produced from the photocells located beneath the four sets of slits. The period of the signal varies over the angular range (sensor field of view) and has an average value of approximately 1.5°; the output of one of the photocells is illustrated in Figure 4.4.8-95. The outputs from all four photocells can be represented as:

$$I_1 = I_o\ (1 + \cos 2\pi\alpha/\theta_o)$$
$$I_2 = I_o\ (1 + \sin 2\pi\alpha/\theta_o)$$
$$I_3 = I_o\ (1 - \cos 2\pi\alpha/\theta_o)$$
$$I_4 = I_o\ (1 - \sin 2\pi\alpha/\theta_o)$$

Where θ_o is the 1.5 degree average period of the pattern and α is the sun angle component.

If each of the four spatially phased outputs is multiplied by one of four temporally phased electrical voltages,

$$(\cos\omega t)$$
$$(\sin\omega t)$$
$$(-\cos\omega t)$$
$$(-\sin\omega t)$$

then, when the four products are added, the result is

$$\text{Cos}\ (\omega t - 2\pi\alpha/\theta_o).$$

By measuring the phase angle, $2\pi\alpha/\theta_o$, the position of the slit image can be determined in fractions of the 1.5 degree pattern space. The integral number of grating spaces is defined by the least significant bit in the coarse angle data.

The preceding method requires the generation of four accurately phased sine waves and devices for sine wave multiplication. An equivalent result is obtained by chopping each of the four fine photocell outputs with quadrature square waves derived from a chain of flip-flops counting down from the 640 kHz

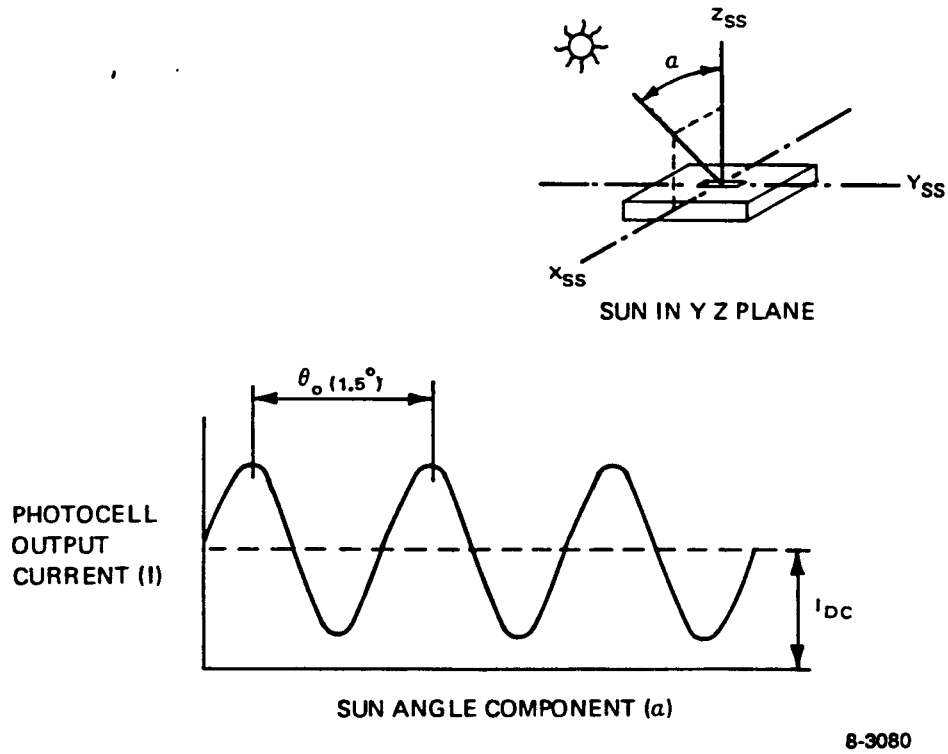

Figure 4.4.8-95. Photocell Output as a Function of Sun Angle for a Single Photocell in the Quadrature Configuration

external clock frequency reference. The chopped outputs are summed and passed through a 2.5 kHz band-pass filter to obtain the fundamental sine wave which has a phase that is an indication of the sun angle. The phase angle is measured by counting the number of reference frequency pulses that occur between the zero crossing of the phase reference signal (one of the chopping signals) and the zero crossing of the sine wave.

4.4.8.3.2.3 Data Processing and Transfer. The processing cycle is initiated after receipt of an SSA Start signal, as shown in Figure 4.4.8-96. The phase angle counter is started at the first reference signal edge after the leading edge of the SSA Start pulse, and is stopped by the zero-crossing of the 2.5 kHz signal containing the phase (sun angle) information. An SSA Transfer signal is then sent to the CIU; the most significant bit (MSB) of the binary angle readout is present on the SSA Data line at this time.

The first negative-going edge of the SSU Data Clock signal terminates the SSA Transfer signal and the following positive-going edge shifts the second MSB onto the SSA Data line. Successive positive-going edges of the SSA Data Clock signal shift all 16 bits serially onto the SSA Data output line; the 15th and 16th bits are always "zeros", since shifting is being accomplished from a 14 bit register. The binary output codes for the cases of -50 degrees, 0 degrees, and +50 degrees of sun angle component are shown in Table 4.4.8-14, along with the corresponding satellite sun angle for nominal alignment of the SSU on the

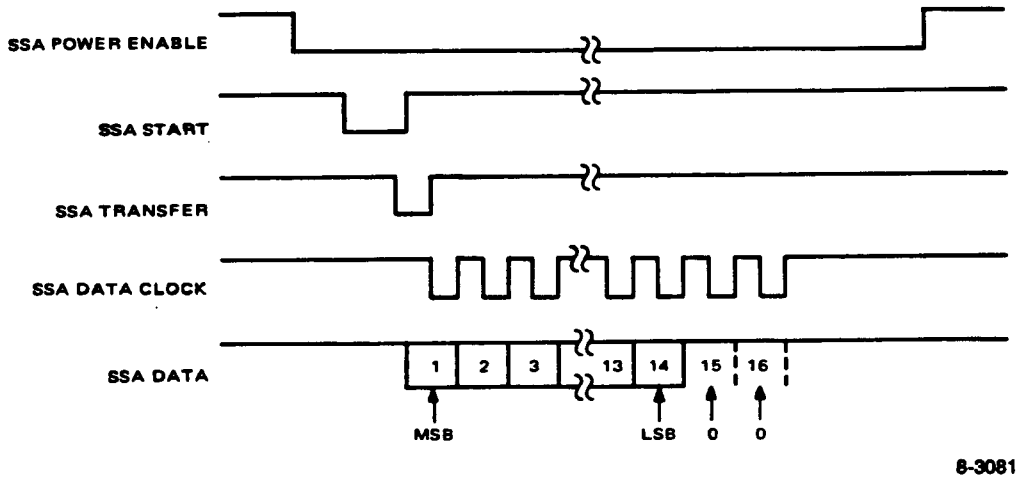

Figure 4.4.8-96. SSA Data Timing

satellite. The complete transfer function of the SSA which must be used to derive the sun angle based on the sensor reading is

$$\alpha = \tan^{-1}(N_A A_{1(M)} + A_{2(M)}) + A_{3(M)}$$

where

N_A is the decimal equivalent of the binary number from the electronics output. This number will be between 0 and 16383 ($2^{14}-1$).

$A_{1(M)}$, $A_{2(M)}$, and $A_{3(M)}$ are constants for a particular sensor.

M is the serial number of the sensor

A_1 and A_2 are dimensionless quantities and A_3 is an angle.

A_1 has a nominal value of 1.454778×10^{-4} and A_2 is nominally -1.18718. A_3 is an offset angle (with respect to the SSU mounting surface) and will be less than 0.1 degree.

For a nominal sensor when $N_A = 0°$, α is -50° and the sun is located 2.5° from the +Z axis, toward the +Y axis. When $N_A = 8192$, α is 0° and the sun is located 47.5° from the +Z axis, toward the -Y axis. For $N_A = 16{,}383$, $\alpha = +50°$ and the sun is located 7.5° from the -Y axis, toward the -Z axis.

4.4.8.3.3 Telemetry

4.4.8.3.3.1 Automatic Threshold Adjust Telemetry. The Automatic Threshold Adjust (ATA) signal is used to adjust the gain of the photocell pre-amplifiers in accordance with the radiance level sensed by a reference photocell, thus compensating for apparent radiance differences. A sample of the Automatic Threshold Adjust signal is obtained through a resistive voltage divider and provided as the output telemetry signal.

TABLE 4.4.8-14. SUN SENSOR ASSEMBLY OUTPUT DATA CODE

Sun Angle Component			Output Code															
Degrees		Decimal	MSB															LSB
Spacecraft*	SSU	Equivalent	1	2	3	4	5	6	7	8	9	10	11	12	13	14	15	16
-2.5	-50	0	0	0	0	0	0	0	0	0	0	0	0	0	0	0	0	0
+47.5	0	8192	1	0	0	0	0	0	0	0	0	0	0	0	0	0	0	0
+97.5	+50	16383	1	1	1	1	1	1	1	1	1	1	1	1	1	1	0	0

*Nominal Orientation

4.4.8.3.3.2 B+ Monitor Telemetry. A sample of the internally-generated +5 volt bus is obtained through a resistive voltage divider and provided as the output telemetry signal. With the SSA turned off, the telemetry output is 0 volts; with the SSA turned on, the output is nominally +2.5 volts.

4.4.8.4 Reaction Wheel Assembly

The Attitude Determination and Control subsystem contains four identical Reaction Wheel Assemblies which provide active attitude control by generating reaction torques about the three orthogonal spacecraft axes. Three of the RWA's are orthogonally mounted to produce torques about each of the three primary spacecraft axes; the fourth RWA is canted at an angle of 54.74 degrees with respect to each of the orthogonal axes so that $1/\sqrt{3}$ of its torque resolves into all three axes as shown in Figure 4.4.8-97. The fourth RWA is normally idle but is brought into use if one of the three orthogonal RWA's fails.

Each RWA interfaces with the Controls Interface Unit as shown in Figure 4.4.8-98.

Each RWA is individually turned on or off; torque control signals and feedback signals are connected sequentially to each RWA through a set of RWA selection logic. The time-shared digital-to-analog (D/A) converter in the CIU converts the digital Torque Magnitude signal into an analog Torque Magnitude signal for driving each RWA; the time-shared speed decode logic decodes the 3 speed signals from each RWA to provide the digital RWA Speed and Speed Direction signals required for input to the Standard Controls Processor (SCP).

4.4.8.4.1 Design Description

4.4.8.4.1.1 Design Approach. Each RWA flywheel is basically a massive Inconel rim attached to a light Beryllium hub which turns on a central shaft. This configuration maximizes the wheel inertia, thus minimizing the size and weight required.

The basic design approach is given by the mathematical model shown in Figure 4.4.8-99; the parameters are defined in Table 4.4.8-15.

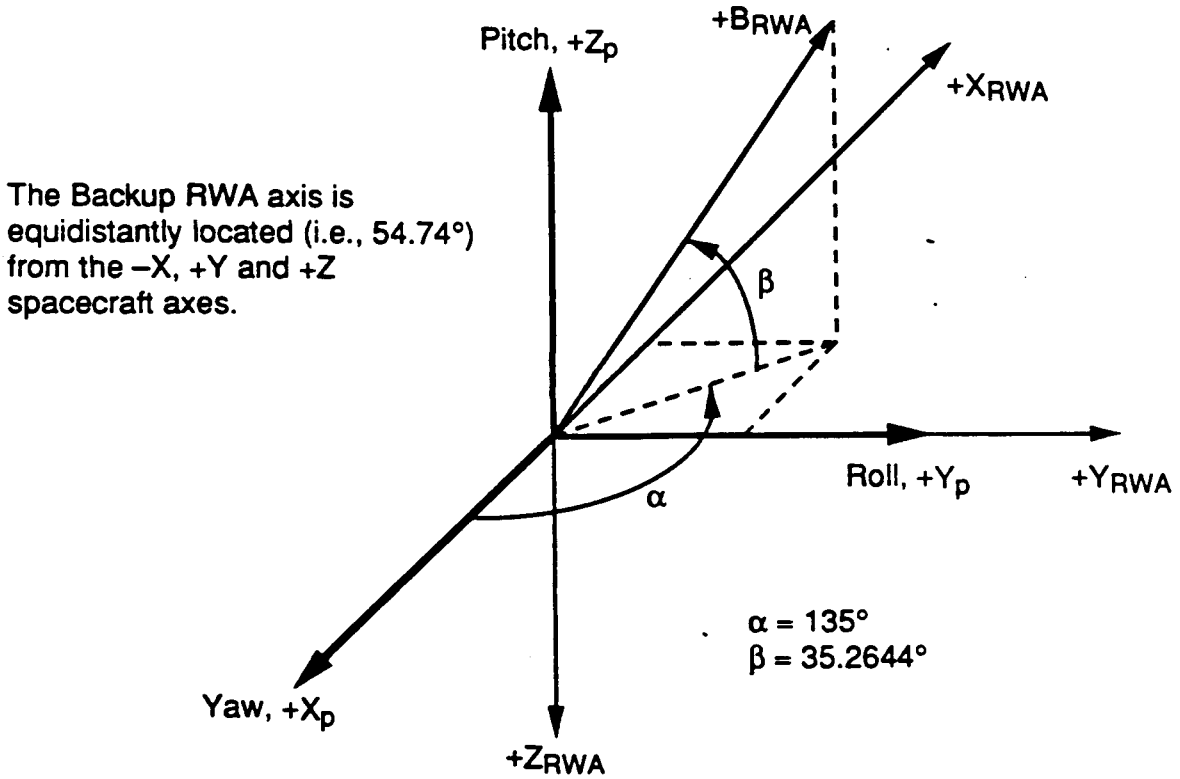

RWA	Spacecraft Axis for Positive Wheel Speed (Momentum) Polarity
Yaw	–X
Roll	+Y
Pitch	–Z
Backup	–X, +Y, +Z

90-2461

Figure 4.4.8-97. Reaction Wheel Assembly Mounting Geometry

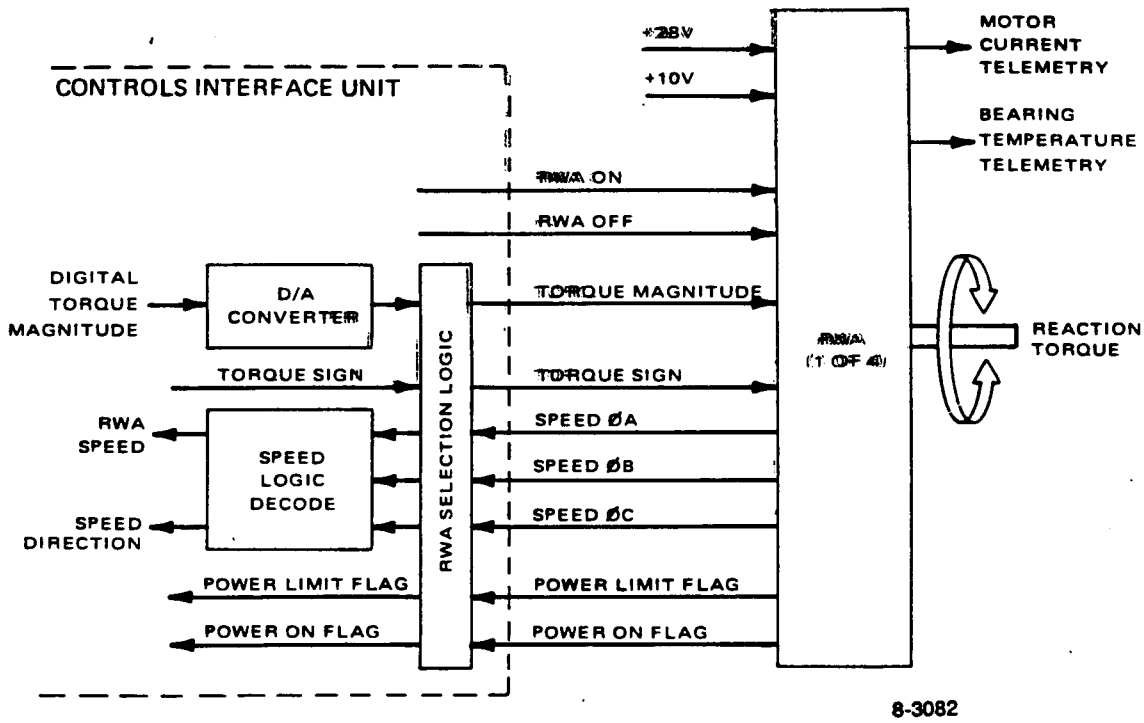

Figure 4.4.8-98. Reaction Wheel Assembly Interface Diagram

For stability analysis, it is sufficient to let

$$\frac{T_R(s)}{V_C(s)} = \frac{K\ s}{\tau_1\ s + 1}$$

where, T_R = Reaction Torque (in-lb)
V_C = Torque Command Voltage (volts)
K = Dynamic Transfer Function Gain = 326 in-lb-sec/V
τ_1 = Dynamic Transfer Function Pole = 1910 seconds
s = Laplace Operator

This configuration gives the torque versus speed characteristic shown in Figure 4.4.8-100. The RWA speed is increasing in quadrants 1 and 3 and is decreasing in quadrants 2 and 4.

Power consumption in quadrants 2 and 4 is small; the flywheel is supplying energy. In quadrants 1 and 3, the power required must come from the +28 volt bus; limits are therefore placed on operation in these quadrants:

- Average motor current is limited to 3.5 amperes maximum, which limits motor torque to 14 in-oz.
- Current drawn from the +28 volt bus is limited to 2.5 amperes. If this limit is invoked, the power limit flag is activated and sent to the CIU.
- The maximum speed of the flywheel is limited to 6400. If this limit is invoked, the power limit flag is activated and sent to the CIU.

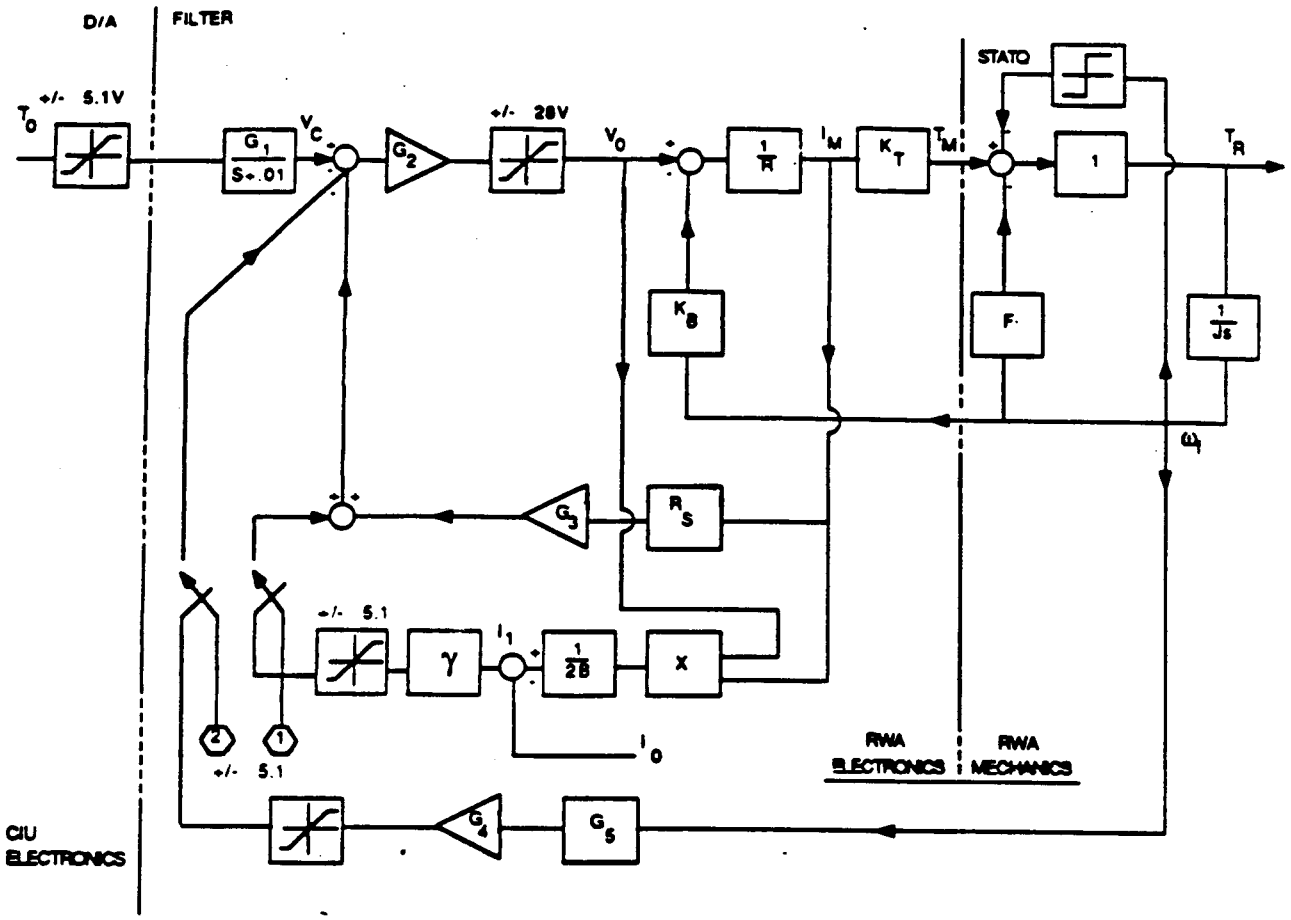

1. Power Limit Switch closes when $I_1 \geq I_0$ (I_0 = 0.95 A)
2. Speed Limit Circuit limits speed to +/- 681 R/sec under any condition.
3. Both Power and Speed limit circuits are high gain and saturate before closing.

90-2456

Figure 4.4.8-99. RWA Equivalent Mathematical Model

Note that both the motor torque and the available reaction torque are shown. The motor torque is directly related to motor current and to the Torque Magnitude signal. In the first and third quadrants when the wheel is increasing in speed and is storing energy, the available reaction torque is lower than motor torque due to mechanical torque losses and the motor back emf.

Note that both the motor torque and the available reaction torque are shown. The motor torque is directly related to motor current and to the Torque Magnitude signal. In the first and third quadrants when the wheel is increasing in speed and is storing energy, the available reaction torque is lower than motor torque due to mechanical torque losses and the motor back emf.

In the second and fourth quadrant when the wheel is decreasing in speed and is therefore giving up energy, the motor back emf aids the speed decrease; the available reaction torque can therefore be greater than the motor torque. The relationship between the reaction torque and flywheel speed is shown as a family of curves for various Torque Magnitude signal and motor current levels in Figure 4.4.8-101.

TABLE 4.4.8-15. RWA MATHEMATICAL MODEL NOMENCLATURE PARAMETERS

Parameter	Description	Nominal Value	Units
T_R	Output Reaction Torque	-	in-lb
V_C	Input Torque Command Voltage	-	volts
G_1	Filter Pre-amp Gain	1.0	V/V
G_2	Pulse Width Modulator Voltage Gain	45.0	V/V
G_3	Current Loop Feedback Gain	7.3	V/V
R_s	Current Sense Resistance	0.2	Ohm
$R^\dagger$	Total Series Motor Resistance	0.45	Ohm
K_T	Motor Torque Constant	0.252	in-lb/amp
K_B	Motor Back EMF Constant	0.0283	V-sec/rad
F	Viscous Friction Constant	0.0002	in-lb-sec/rad
J	Flywheel Assembly Inertia	0.382	in-lb-sec^2
STATQ	Static Coulomb Torque	0.0343	in-lb
Y	Power Loop Feedback Gain	100.0	V/amp
G_4	Speed Limit Circuit Feedback Gain	80.0	V/V
G_5	Speed Limit Circuit Tachometer Gain	0.014	V/(rad/sec)

† Resistance at 30°C

4.4.8.4.1.2 Operating Modes. Each RWA may be independently turned on or off; while turned on, each RWA may be controlled to produce a positive or negative torque in the range of 0 to 14 in oz.

4.4.8.4.1.2.1 RWA Power Control. Power in the RWA is switched in response to two control signals from the C&CS:

- RWA On
- RWA Off

The RWA On signal sets a latching relay to connect the +28V bus to the appropriate loads inside the RWA, thus enabling the unit. The RWA Off signal disconnects all power within the RWA except for the interface circuitry required for responding to an RWA On control signal.

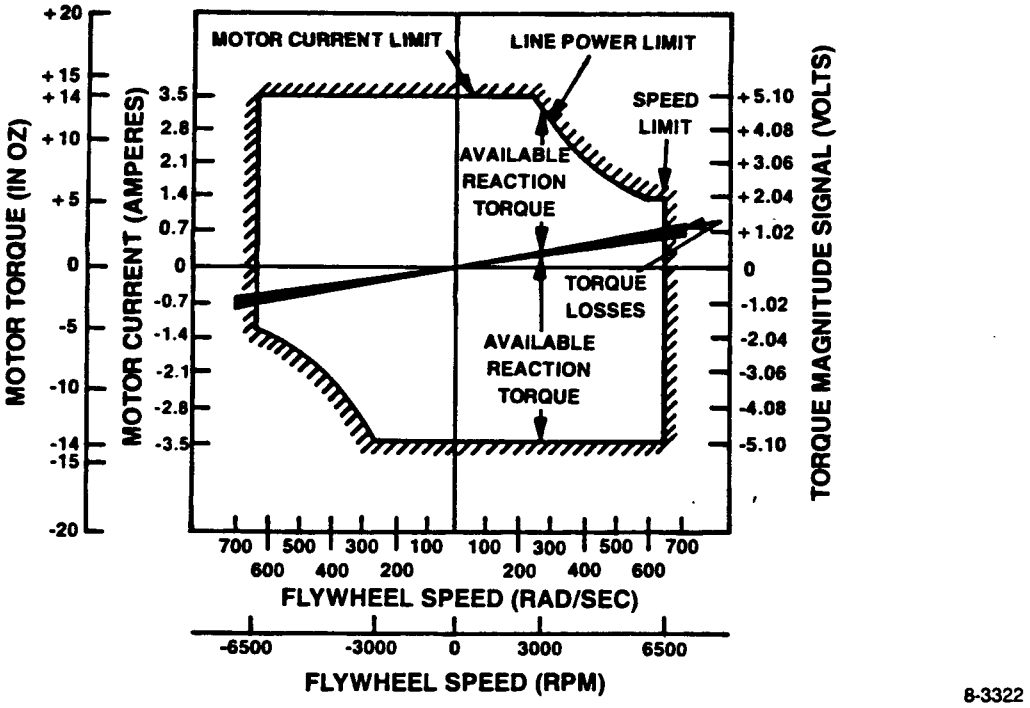

Figure 4.4.8-100. RWA Motor Torque vs Speed Characteristics

4.4.8.4.1.2.2 Torque Control. The torque exerted by the RWA on its mounting feet is generated in response to two control signals from the C&CS:

- Torque Magnitude
- Torque Sign

The amount of torque produced by the RWA is directly proportional to the Torque Magnitude signal; the direction of the torque produced is controlled by the Torque Sign signal.

4.4.8.4.1.3 Design Characteristics. The design characteristics for the RWA are summarized in Table 4.4.8-16.

4.4.8.4.1.4 Physical Description. The physical configuration of the RWA is shown as a cutaway view in Figure 4.4.8-102 and in cross-section in Figure 4.4.8-103. The major components of the RWA are the flywheel, the bearings, the drive motor, the housing, and the electronics boards.

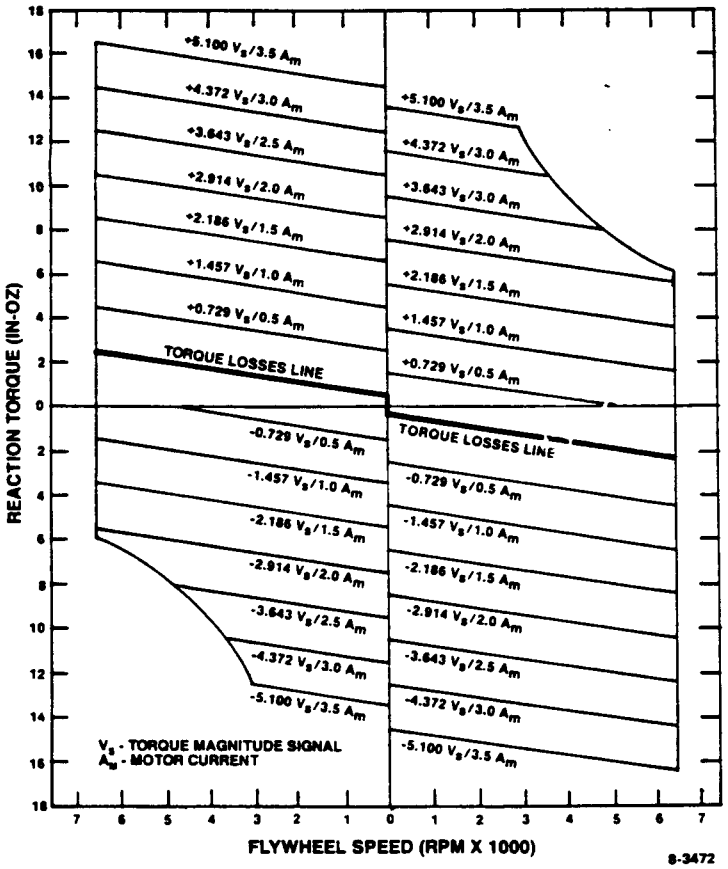

Figure 4.4.8-101. RWA Reaction Torque vs Speed Characteristic

4.4.8.4.1.4.1 Flywheel. The flywheel consists of a massive Inconel rim attached to a light Beryllium hub which turns on a set of bearings mounted on a central shaft. A tuned vibration damper consisting of an annulus of Inconel is attached to the rim by a synthetic elastomer; this serves to reduce the stresses on the bearings due to vibration during launch. To reduce the risk of Brinell marks on the bearing races, the reaction wheel is run at low speed during launch.

4.4.8.4.1.4.2 Bearings. The bearings are pre-loaded, angular-contact R103 bearings fabricated from 52100 high chrome bearing steel. The bearings are processed to inertial gyroscope standards; they are fully measured dimensionally, string lapped to the highest possible finish, microscopically examined for flaws or imperfections in the race ways or on the balls, ultrasonically cleaned and checked for wettability by the lubricant, surface treated by tri-cresyl-phosphate, and tested under the working preload on a low speed dynamometer, during which the torque "signature" is recorded for future reference.

Lubrication is by SRG-40 mineral oil; sintered polyamide ball retainers with controlled pore size and porosity form the primary oil reservoir in each bearing. A secondary sintered polyamide reservoir is mounted between the 2 bearings and sacrificial sintered polyamide reservoirs are mounted outboard. To cover the unlikely event of a leak in the enclosure, a labyrinth seal is

TABLE 4.4.8-16. REACTION WHEEL ASSEMBLY DESIGN CHARACTERISTICS

Parameter	Value
Motor	
Type	Brushless dc torque motor
Poles	16
Windings	6
Motor Torque	0 to ±14 in.-oz
Operating Speed	0 to ±628 rad/sec (6000 rpm)
Run Up/Run Down Time Constant	1910 seconds
Momentum	
Maximum (at 6000 rpm)	240 in.-lb sec
Rated (at 334 rad/sec)	128 in.-lb sec
Average (at 102 rad/sec)	39 in.-lb sec
Transfer Characteristic	2.75 in.-oz/volt
Transfer Characteristic Linearity	21%
+28V Power Requirements	
Peak	70 W
Average*	3.2 W
+10V Power Requirements	200 μW
+5V Power Requirements	None
Size	6.0 x 10.7 inches diameter
Weight	60.7 lb

*At 1000 rpm and zero reaction torque

fitted outboard of the sacrificial reservoirs. The supply of lubricant is adequate for a design life of greater than 20 years of continuous vacuum operation.

4.4.8.4.1.4.3 Drive Motor. The drive motor is a brushless dc torque motor designed for maximum efficiency and minimal torque losses. The configuration is "inside-out", with an external 16-pole Samarium Cobalt permanent magnet rotor and an internal stator consisting of 6 windings on a low-loss laminated stack.

The rotor "overhangs" or extends beyond the stator. Three fixed Hall-effect devices on the stator sense the magnetic fields from the overhung portion of the rotor. The sensed signals are used for defining present rotor position for motor commutation and for generating the 3-phase RWA Speed signals to the CIU. The Hall-effect devices are mechanically mounted 7.5 degrees apart; this corresponds to 60 electrical degrees, due to the 8-cycle effect of the 16 pole rotor.

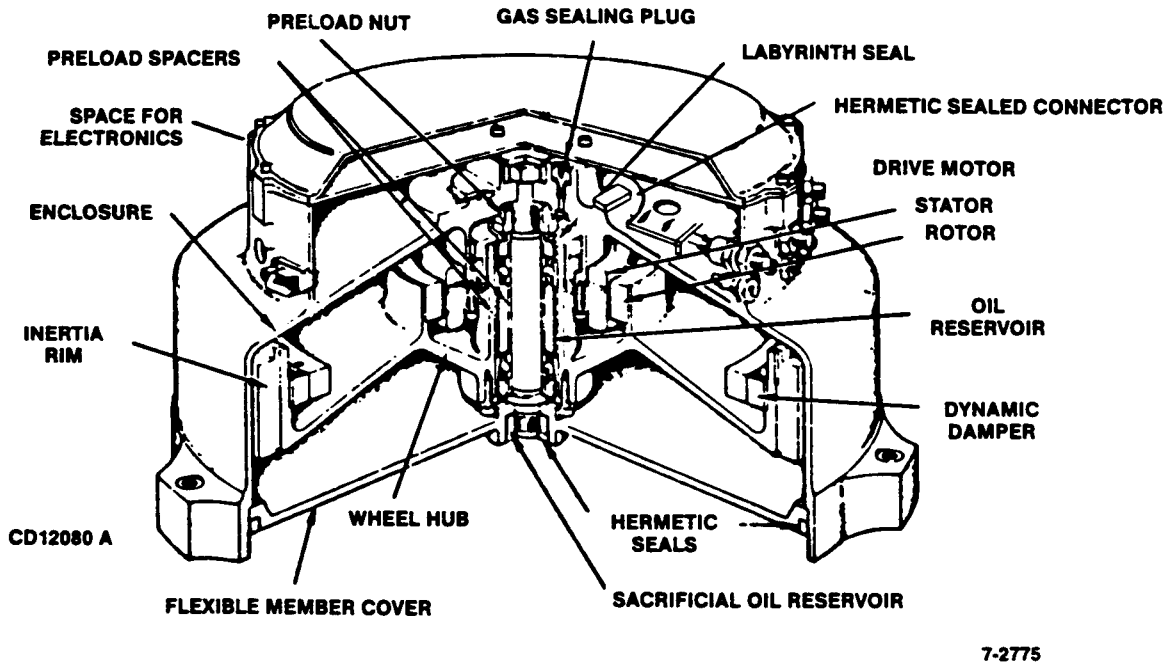

Figure 4.4.8-102. RWA Cutaway View

4.4.8.4.1.4.4 RWA Housing. The reaction wheel, bearings, and drive motor are contained in a hermetically sealed Magnesium housing containing Helium at an absolute pressure of 1.5 in Hg. The housing is sealed during assembly by metal rings cemented in grooves by an epoxy. The leads to the bi-filar stator windings and from the three Hall-effect devices are brought out to an upper compartment by hermetically sealed connectors.

The upper compartment of the housing contains the electronic circuits and components required to drive the motor and reaction wheel in response to control signals from the CIU. Most of the components are mounted to the two electronics boards; however, the six motor drive transistors, series pass transistor, six fly-back diodes and six Zener diodes for overvoltage protection, and two motor current sampling resistors are mounted on the container wall to provide a good thermal heat sink.

The RWA is mounted to the spacecraft by 3 feet spaced 120° apart around the base of the enclosure.

A thermistor is attached to the upper compartment side of the central housing to provide a telemetry indication of bearing temperature.

4.4.8.4.1.4.5 Electronics Boards. The two electronics boards contain all of the RWA electronics except for the motor drive transistors, flyback and Zener diodes, and motor current sampling resistors. The main electronics board is a circular, multilayer printed circuit board that attaches to the outboard rim of the RWA, thus forming the outboard "wall" of an enclosure; most of the electronics is mounted to this board.

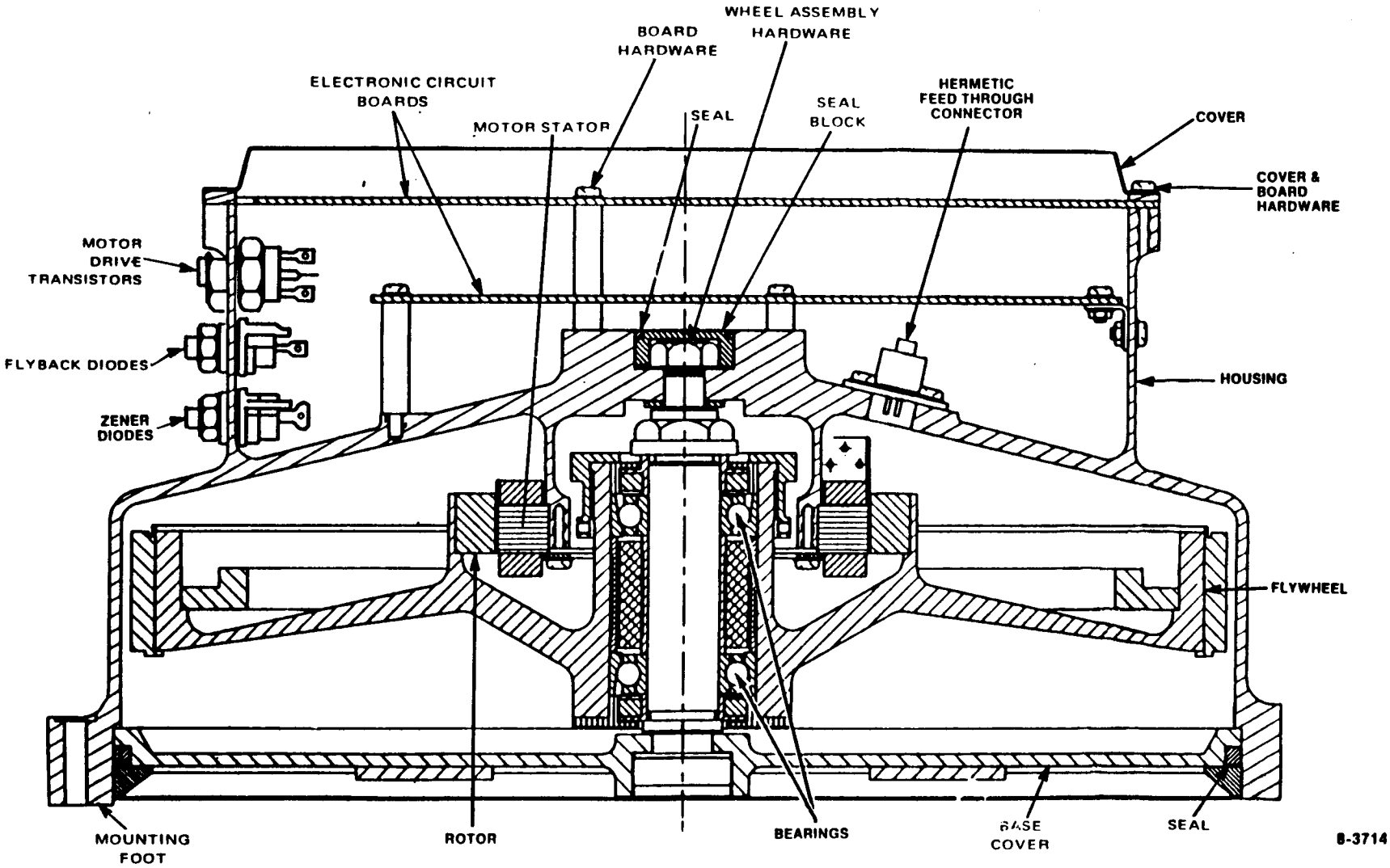

Figure 4.4.8-103. RWA Side View

The remaining board is mounted within the formed enclosure. This board contains the +10V regulator, Hall-effect detectors, and the driver circuits for the motor drive transistors.

4.4.8.4.2 Functional Description

The RWA provides a reaction torque about its mounting axis in response to a Torque Magnitude and a Torque Sign control signal from the CIU. A functional block diagram of the RWA is shown in Figure 4.4.8-104; for convenience, the functions can be grouped into several major sections:

a. Power controller;

b. Commutation control loop, including the Hall generators and associated electronics, the commutation logic, and the power amplifiers;

c. Torque control loop, including the limit detectors, summing amplifier, pulse width modulator, the commutation logic, and the power amplifiers.

The power controller either enables or disables the RWA in response to an RWA On or RWA Off control signal from the CIU. When enabled, the power controller provides a +28V switched bus to the remainder of the RWA, provides a regulated +10V to the logic, and also provides +13.6V and -6.4V reference voltages. The power controller also contains the sensing element for the line current limit detector.

The commutation control loop provides the proper commutation of current to the 6 windings in the torque motor, thus controlling motor rotation. The Hall generators are used to achieve proper commutation regardless of motor speed; the phasing of the commutation (and therefore the direction of motor torque) is controlled by the Torque Sign signal from the CIU.

The torque control loop controls the amount of current to the torque motor (and therefore motor torque) in response to the Torque Magnitude signal from the CIU. If either motor speed or line current reach a pre-assigned limit, then operation of the torque control loop is overridden such that the limit is not exceeded.

4.4.8.4.2.1 Power Controller. A simplified schematic diagram of the power controller is shown in Figure 4.4.8-105. The power controller consists essentially of a set of latching relays and enabling electronics, power line filters, a +10V regulator, and the reference voltage generator.

Latching relays switch all power to the remainder of the RWA in response to the RWA On or RWA Off control signals from the CIU. Diodes are provided on the +28V relay contacts to protect against high surge currents; the relay coils also have diodes in parallel to dissipate the inductive surge at current turn-off.

Filters are provided on all power lines to the RWA. The +10V bus is filtered by a 0.1 μF capacitor to ensure that the RWA circuits operating from this line always "see" a low source impedance. The +28V input is filtered by an inductor in the power and power return lines; the motor supply power is filtered by a single L-type low-pass filter, which limits the current ripple fed back to the spacecraft.

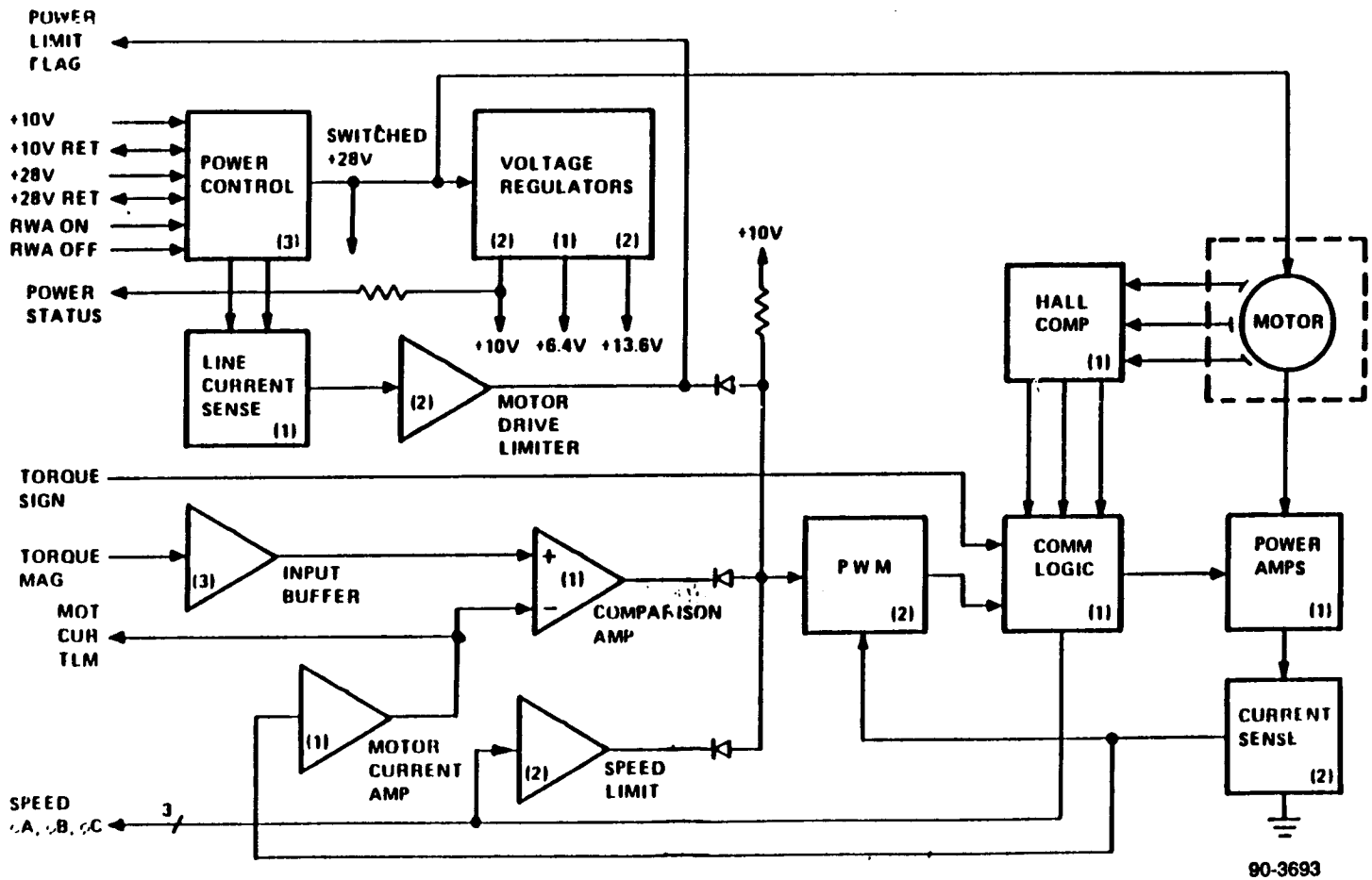

Figure 4.4.8-104. RWA Block Diagram

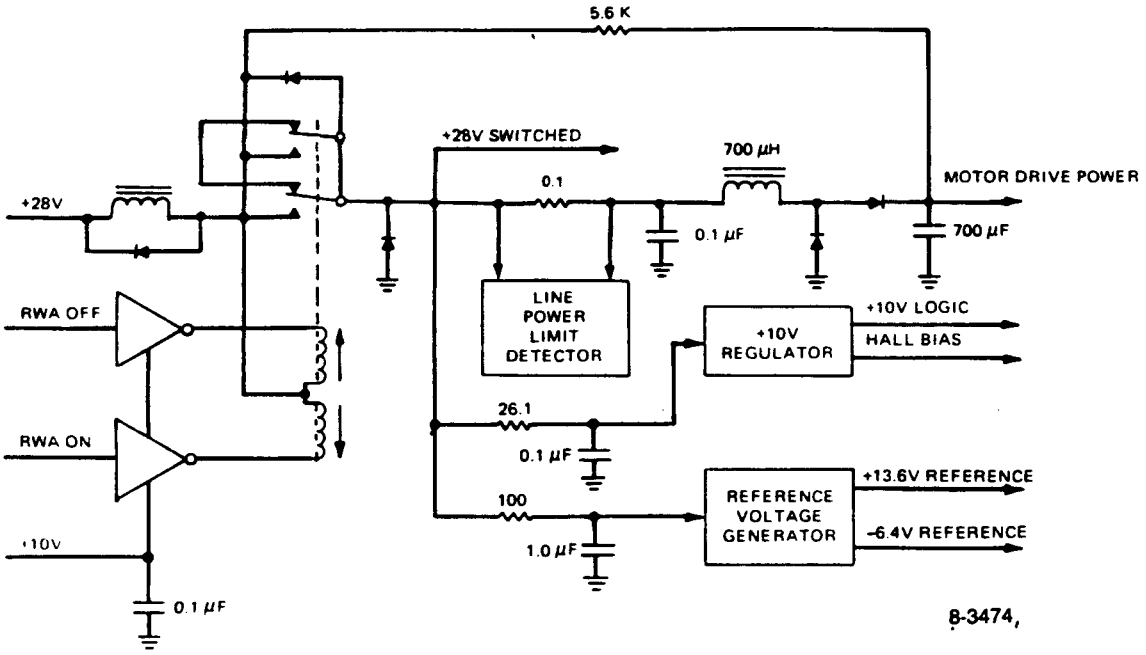

Figure 4.4.8-105. RWA Power Controller Simplified Schematic

The reference voltage generators provide reference voltages of +13.6 and -6.4V, which are used for biasing the analog control portion of the RWA.

The +10V regulator provides the Hall element bias supply voltage, which is nominally 8 to 9 volts, and provides a regulated +10V for the COS-MOS logic circuitry. The regulator is designed for rapid regulation during power turn on. Full output voltage regulation is obtained if the +28V bus is at +12V or higher; below +12V, the regulator output follows the input except for the small series element loss. Reliable COS-MOS logic operation is obtained with a regulator output of +5V, which is obtained if the +28V bus is at +6V.

4.4.8.4.2.2 Commutation Control Loop. The commutation control loop provides the proper commutation of current to the 6 windings in the torque motor at all motor speeds. A simplified schematic diagram of the commutation control loop is shown in Figure 4.4.8-106.

The position of the rotor in the torque motor is sensed by the 3 Hall generators, which are excited 8 times during each rotor revolution and are electrically spaced 60 degrees apart. The Hall generator signals are processed by the Hall comparators to produce symmetrical square waves for use in the commutation logic and in the CIU. The CIU processes these signals to determine the existing RWA speed and direction of rotation.

The commutation logic decodes the motor position signals into 6 sequential commutation channels equally spaced over 360 electrical degrees. During the decode of each channel, the pulse-width-modulated waveform is passed through a commutation drive amplifier and power amplifier to one motor winding; during the sequential decode of the other channels, the other motor windings are sequentially excited. The phasing of the sequential excitation (forward or reverse) is controlled by the Torque Sign signal from the CIU.

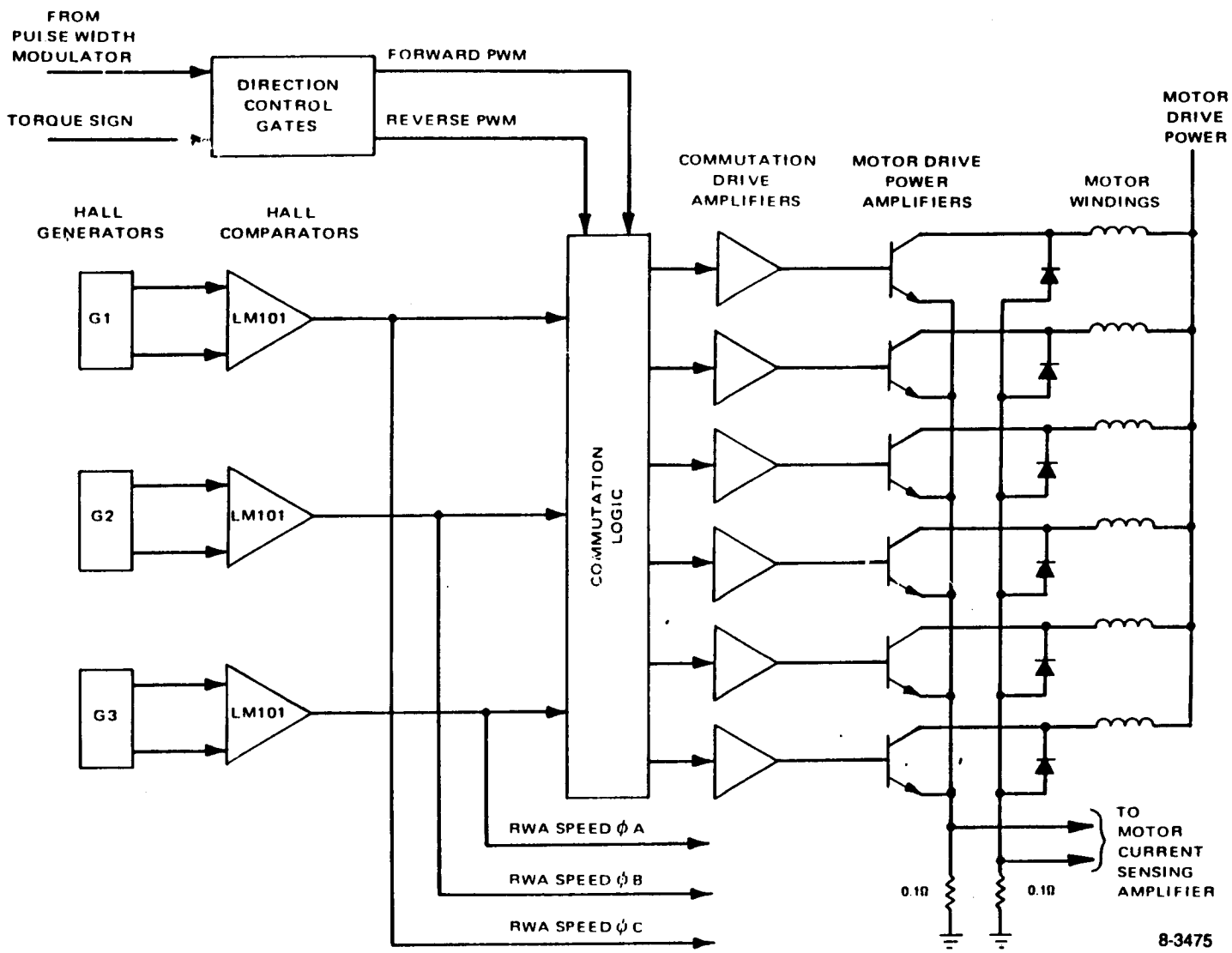

Figure 4.4.8-106. Commutation Control Loop Simplified Schematic Design

The commutation drive amplifier and power amplifier combination is designed for high speed power switching and minimum loss in the drive circuit. The drive amplifier output transistor and the power amplifier are connected as an inverted Darlington circuit. All current required for circuit operation is obtained through the motor windings; thus, no idling current is required by the driver.

4.4.8.4.2.3 Torque Control Loop. The torque control loop controls the amount of drive current to the torque motor windings, and therefore controls motor torque.

Referring to the block diagram in Figure 4.4.8-107 motor current is sensed by two 0.1 ohm resistors in series with the motor winding; current through the power transistor is sensed during acceleration, and current through the flyback diode is sensed during deceleration. The motor current signals are filtered, amplified, and applied to the torque error amplifier and the motor current telemetry circuit. The unfiltered motor current acceleration signal is also applied to the pulse width modulator.

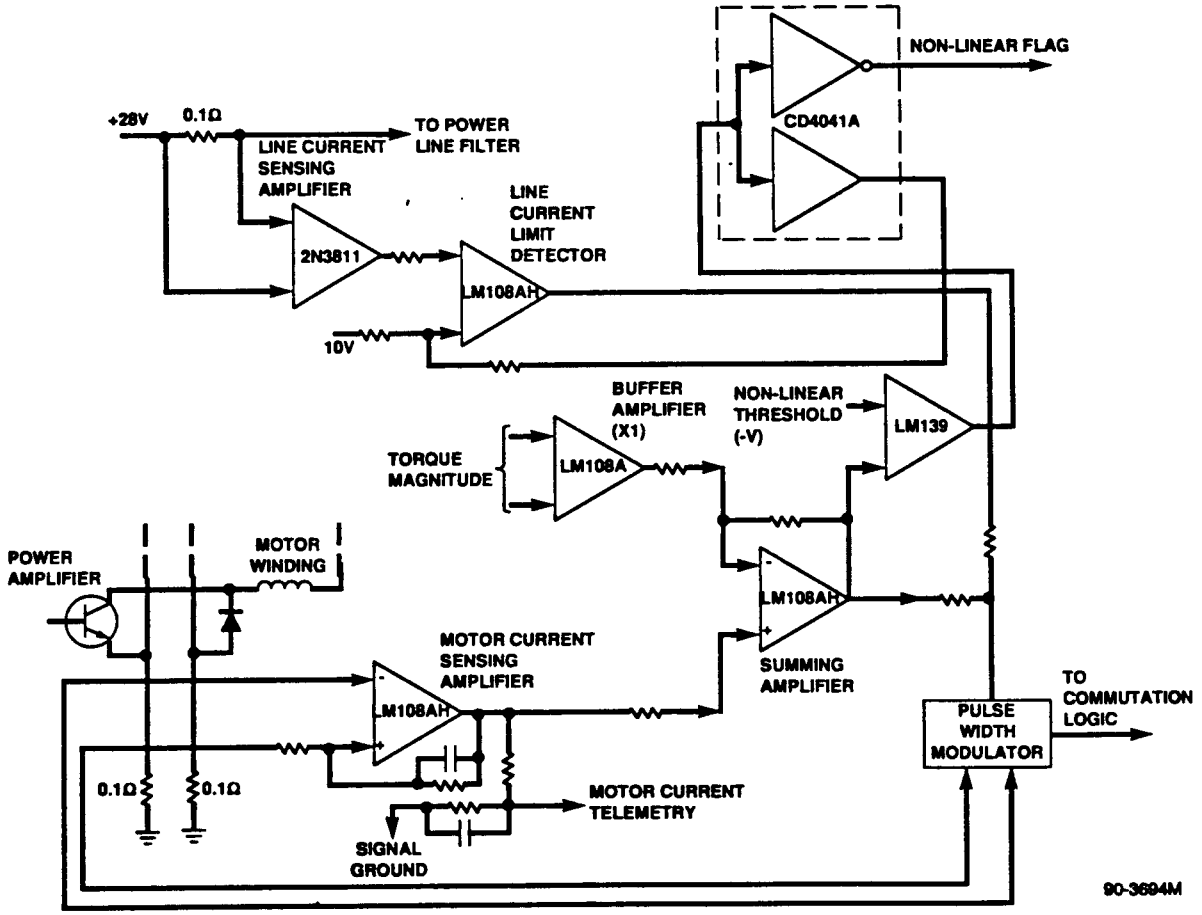

Figure 4.4.8-107. Torque Control Loop

During normal operation the only active input signals to the summing amplifier are the motor current signal and the Torque Magnitude signal from the CIU. These 2 signals are subtractively combined, then amplified to form an input to the pulse width modulator.

If an input current limit of 2.5 amperes or a speed limit of 6400 rpm is detected, then additional inputs to the pulse width modulator become active. In effect, either signal overrides or "swamps out" the Torque Magnitude signal in such a manner that motor speed or line current cannot rise above the limit value.

The pulse width modulator converts the signal from the summing amplifier into a pulse train with a duty cycle proportional to the required torque level. As shown in Figure 4.4.8-108, the pulse width modulator consists of a VCO, latching flip-flops, a hysteresis comparator, and a zero crossing detector, thus forming a free-running pulse generator operating at a nominal frequency of 10 kHz. Both the frequency and duty cycle of the generated waveform vary in proportion to the existing motor current and signals from the summing amplifier, motor speed limiter, and line power limit detector. There are two modes of PWM operation; discontinuous mode for low torque demand and continuous mode for high torque demand. This allows the RWA to produce greater torque output with lower stress on the motor drive components.

4.4.8.4.3 Telemetry

Each RWA provides two analog telemetry signals to the Telemetry subsystem:

- Bearing Temperature Telemetry
- Motor Current Telemetry

Bearing temperature telemetry is provided by a thermistor mounted in the outer compartment side of the central casting. Temperatures measured by this thermistor are not a direct measurement of bearing temperature, since the central housing is between it and the bearing; however, the temperature difference between the bearing and the thermistor will be small.

Motor current telemetry is provided by amplifying the sensed motor current signal; motor current is directly related to motor torque. Reaction torque can be derived from motor torque by using the equivalent of Figure 4.4.8-101, provided that the RWA speed is known.

4.4.8.5 <u>Magnetic Torquing Coils</u>

The magnetic torquing coils provide the necessary magnetic torques to unload (dump) angular momentum stored in the three operating reaction wheels aboard the spacecraft. There are two redundant roll/yaw torquing coils, (designated RYC1 and RYC2), both wound on a common coil form and mounted on the spacecraft such that the plane of the coils is perpendicular to the spacecraft pitch (Z) axis. There are also two redundant pitch torquing coils (designated PTC1 and PTC2) wound on a common coil form and mounted such that the plane of these coils is perpendicular to the spacecraft roll (Y) axis.

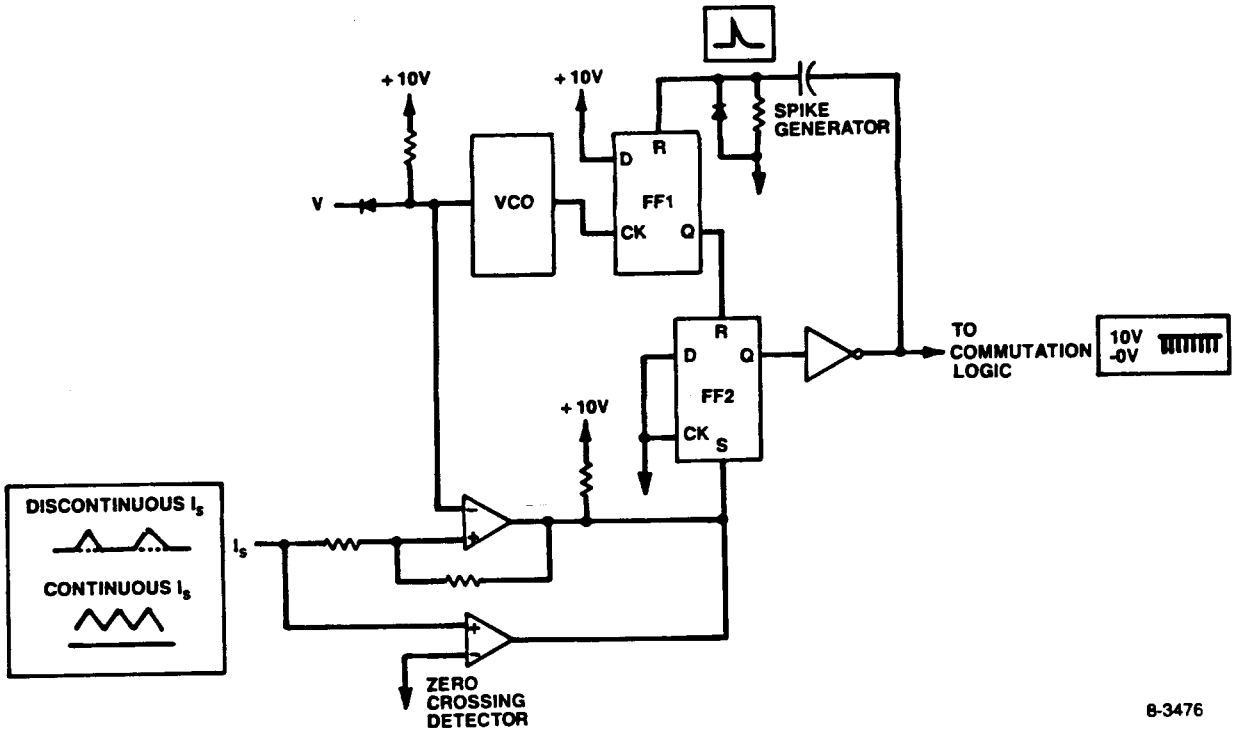

Figure 4.4.8-108. Pulse Width Modulator

4.4.8.5.1 Design Description

4.4.8.5.1.1 Design Approach. Each of the four momentum coils consists of two air-core aluminum-wire windings in parallel, as shown in Figure 4.4.8-109. Two windings are used in each coil to provide an optimum design (minimum power-weight product) using commercially available wire sizes. A 1 ohm resistor is incorporated for power protection.

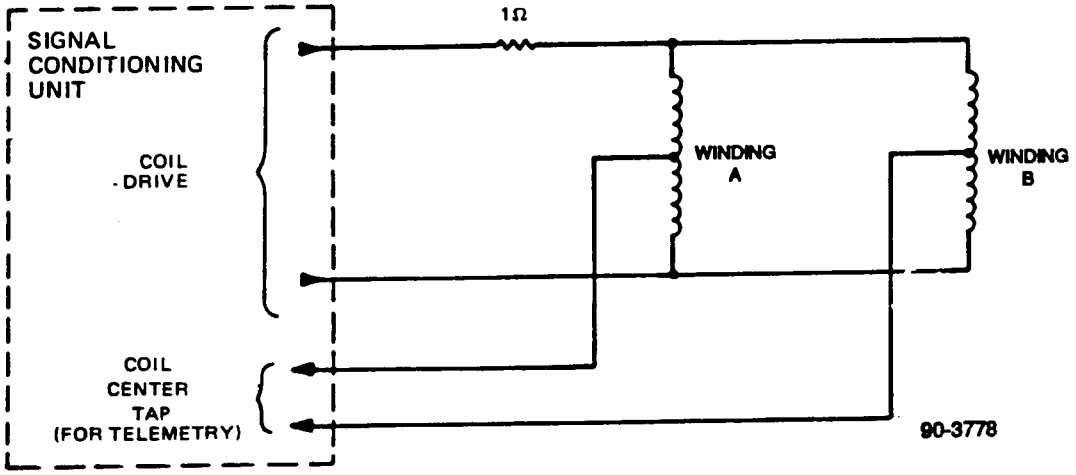

Figure 4.4.8-109. Momentum Torquing Coil, Schematic Diagram

4.4.8.5.1.2 Operating Modes. Coil drive power to the momentum coils is controlled by the SCU, which provides power in accordance with the following states:

- ON +
- OFF
- ON -

In either ON state, 28 volts is impressed across the momentum coil and its series resistor. The voltage is applied with one polarity in the ON + state; polarity is reversed in the ON - state.

4.4.8.5.1.3 Design Characteristics. The design characteristics of the RYC and PTC coils are summarized in Table 4.4.8-17 and 4.4.8-18.

The two RYC coils are wound into a single coil form as shown in Figure 4.4.8-110; the two PTC coils are wound into a single coil form as shown in Figure 4.4.8-111. The two coil forms are mounted within the Equipment Support Module (ESM) as shown in Figure 4.4.8-112.

TABLE 4.4.8-17. MOMENTUM COIL CHARACTERISTICS

Parameter	Value	
	RYC	PTC
Coil Form	Air Core	Air Core
Total Dipole (ATM^2)	62.8	29.9
Coil Plane Orientation	Perpendicular to Z axis	Perpendicular to Y axis
Power Dissipation (Watts)		
Peak	12	8
Orbit Average	4.27	2.13
Duty Cycle (Percent)	35.6	26.7
Weight (Pounds)	4.45	2.4

TABLE 4.4.8-18. MOMENTUM COIL WINDING CHARACTERISTICS

Parameter	RYC1 or RYC2		PTC1 or PTC2	
	Winding A	Winding B	Winding A	Winding B
Dipole (ATM^2)	36.8	24.2	21.4	8.5
Wire Gage (AWG)	24	26	26	30
Wire Material	Aluminum	Aluminum	Aluminum	Aluminum
Wire Current (Ampere)	0.263	0.166	0.205	0.081
Winding Resistance (Ohms) (At +20°C)	104.7	167.3	135.4	345.0
Power Dissipation (Watts)	7.37	4.63	5.73	2.27
Number of Turns	286	286	176	176
Wire Weight (Pounds)	0.935	0.587	0.475	0.189

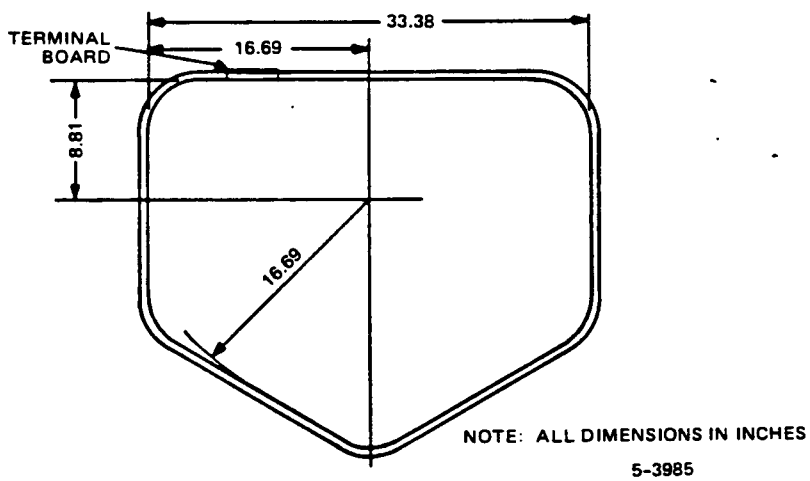

Figure 4.4.8-110. RYC Momentum Coil Configuration

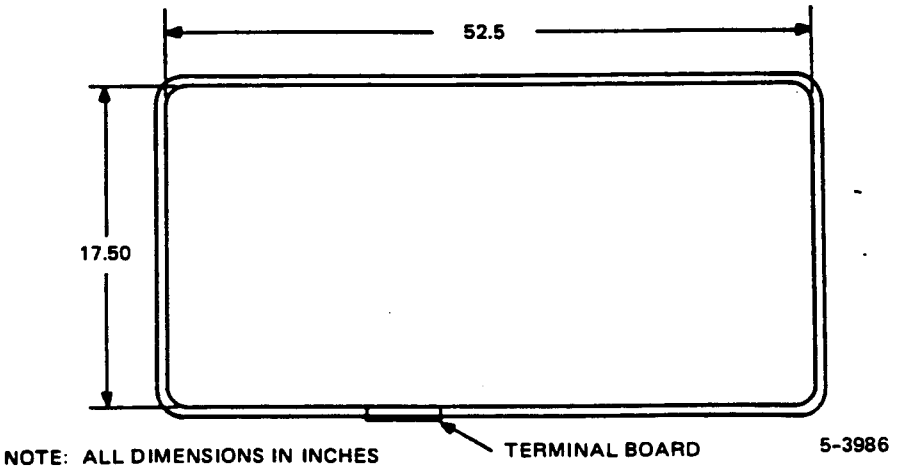

Figure 4.4.8-111. PTC Momentum Coil Configuration

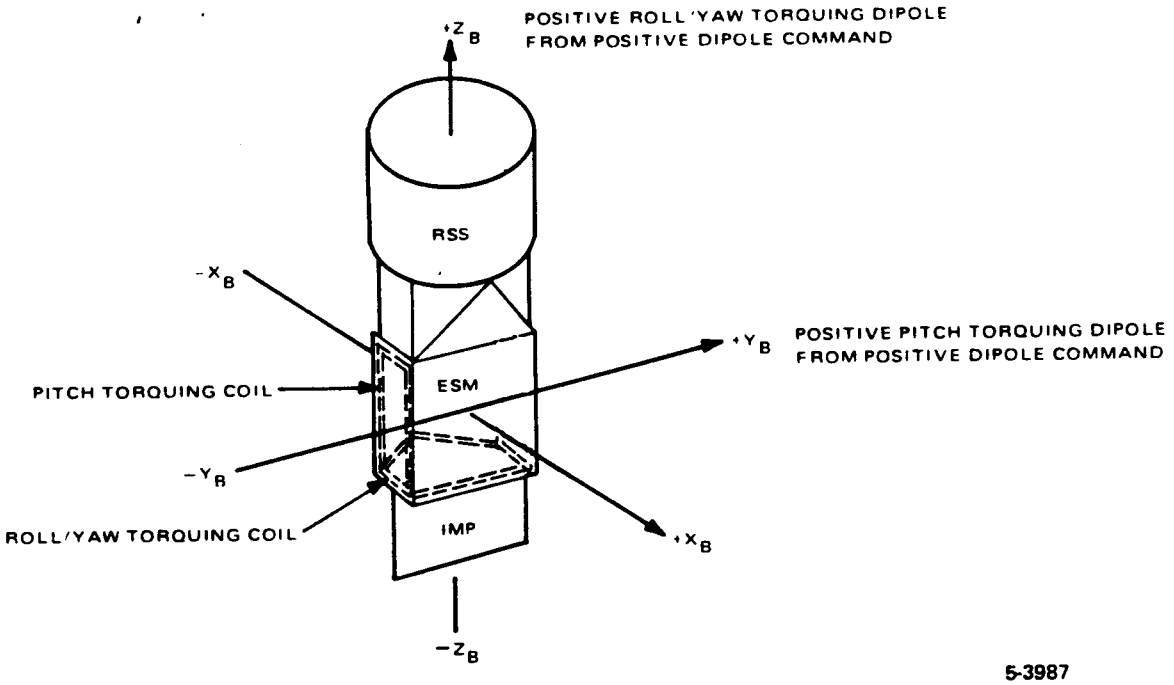

Figure 4.4.8-112. Momentum Torquing Coils, Mounting Orientation

Blank Page

4.5 THERMAL CONTROL SUBSYSTEM

The purpose of the ATN-KLM Thermal Control Subsystem (TCS) is:

(1) To maintain the ATN-KLM spacecraft bus and instrument (payload) temperatures within their allowable limits over the entire range of external environmental conditions and internal operational modes;

(2) To minimize spacecraft bus and instrument temperature excursions within these allowable limits; and

(3) To minimize thermally induced sensor misalignments in the instrument packages.

This control is operative during the pre-launch, ascent, and orbital phases of the ATN mission and is achieved by utilizing both active and passive thermal control elements. These control parameters and principles are summarily presented in Table 4.5-1.

TABLE 4.5-1. THERMAL CONTROL SUBSYSTEM (TCS) PARAMETERS

Type	Principle/Element
Passive Control	• Spacecraft Configuration • Equipment Location • Surface Finishes • Multi-layer Insulation Blankets • Shields • Sunshades • Conductors and Insulators • Telemetric Thermistors
Active Control	• TCE Controllers - Differential Type - Dual Type • Thermostats (Mechanical) • Proportional Controllers • Louver/Radiator Assemblies - Vane Type - Pinwheel Type • Heater Circuits • Control Thermistors • TCS Commands • Launch Platform Conditioning

The methods and items used to provide passive thermal control include: The basic ATN-KLM spacecraft configuration, equipment and instrument location, surface finishes, multi-layer insulation blankets, thermal and solar shields, radiators, and thermal conductors and insulators. The instrument locations, the proper selection of external surface finishes, and the use of shields

also provide for the minimization of reflected solar radiation into the instruments' radiometric fields-of-view.

The active TCS elements include: Thermal Control Electronics (TCE) units, mechanical thermostats, proportional controllers, heater circuits, and louver/radiator assemblies. The bulk of the active control is provided by TCE-controlled louver/radiator assemblies coupled with auxiliary heaters.

Temperature sensors are used for both telemetric and control purposes, and a set of spacecraft commands is available to enable and inhibit the active TCS elements.

Partial redundancy is provided in the design of the louver actuators. In the absence of active control (as produced by TCE inhibit commanding or failure), the passive response of these devices permits reduced levels of temperature control.

Total redundancy is available in both the gaseous nitrogen (A & B) heater subsystems and in the liquid hydrazine (C & D) heater subsystems on the Reaction Control Equipment.

General prelaunch temperature control is provided by air-conditioning of the launch vehicle's fairing space. Special temperature control at this time is provided for the VHF, S-Band and Search-and-Rescue Repeater (SARR) transmitters. This provision consists of a set of internal coolant lines which permit low-temperature maintenance of these units on the launch platform. The coolant lines to the two systems serving VTX-1, VTX-2, STX-1, STX-3 and the SARR transmitter are manually disconnected after prelaunch spacecraft testing is complete. A third system serving STX-2 and STX-4 is automatically disconnected at liftoff. An umbilical connector also enables power to be supplied to a heater circuit on the IMU cover. This capability is present to properly condition that unit's internal Temperature Control Amplifier (TCA) for positive IMU sensor block temperature control during ascent into orbit.

Ascent thermal control is achieved by the above mentioned prelaunch conditioning of selected equipment, by the operation of active thermal control elements, and by the use of passive control elements which reduce the thermal effects produced by Apogee Kick Motor (AKM) and Reaction Engine Assembly (REA) firings and their consequent thermal soak-backs.

The spacecraft consists of the following major assemblies:

(1) Instrument Mounting Platform (IMP);
(2) Equipment Support Module (ESM);
(3) ESM/RSS Connection Truss;
(4) Reaction Control Equipment (RCE) Support Structure (RSS);
(5) Spacecraft/Launch Vehicle Adapter; and
(6) Solar Array Assembly and Support (SAA/S).

Due to the different thermal control requirements of each assembly, their thermal designs are basically independent and utilize different control techniques. This independence has been increased by the minimization of the thermal couplings which exist between them.

4.5.1 THERMAL REQUIREMENTS

The ATN-KLM Thermal Control Subsystem has been designed to maintain all of the spacecraft structure, equipment and instrument payloads within the temperature limits given in Tables 4.5.1-1, 4.5.1-2 and 4.5.1-3. On-orbit min/max predicated temperatures are also listed. The temperatures presented are those for a mission orbital sun-angle range from 0° to 80°.

In these requirement/prediction tables, the "non-operational" temperature range defines the allowable temperature extremes which will not cause damage to the component when it is not required to operate. The "operational" temperature range defines the worst-case hot and cold temperatures allowable on the components, in orbit, while operating within specification.

All components installed in or on the satellite have a non-operating survival temperature range of at least -5°C to +45°C, except the batteries, AVHRR, and IMU. Equipment must operate successfully subsequent to, but not during, exposure to its non-operational temperature range extremes.

Temperature differences on the mounting surfaces of sensors which require accurate alignment are minimized so as not to cause misalignment greater than that specified for the individual instruments.

4.5.2 DESIGN PHILOSOPHY

The thermal design of the ATN-KLM spacecraft involves accurate temperature control of both the spacecraft structure and equipment and the instrument payloads. This requirement necessitates the use of many different thermal control elements of both active and passive type. Because the major structural modules on the spacecraft have distinctly different thermal requirements on the equipment and/or instruments they support, each module has been made nearly thermally independent in design and in the thermal control methods employed. Coupling between these modules has, therefore, been minimized.

The basic design philosophy is to ensure that each component or area of the spacecraft is regulated within its specified temperature limits with adequate margins for all ground test and mission environment exposures. This is accomplished with a minimum number of thermal control elements compatible with the constraints of reliability, weight, complexity, power usage and cost.

4.5.3 THERMAL CONTROL ELEMENTS DESCRIPTION

A listing of the thermal parameters for the ATN-KLM TCS is provided in Table 4.5-1.

4.5.3.1 Passive Thermal Control Elements

Passive thermal control is primarily achieved by the selective use of surface finishes, thermal conduction control materials, multi-layer insulation blankets, sunshades and thermal shields.

TABLE 4.5.1-1. TEMPERATURE LIMITS AND PREDICTIONS - IMP

Item	Temperature Limits				Temperature Predictions	
	Non-Operational		Operational			
	Min	Max	Min	Max	Min	Max
IMP Structure	-5	45	10	30	15.3	16.0
Long Strut	-5	45	10	30	15.8	16.2
ESA	-5	45	5	25	15.6	16.2
SSD	-5	-45	-5	35	14.0	15.8
IMU Cover	25	30	25	35	25.0	35.0
AVHRR/3 Baseplate	-5	30	10	30	13.3	15.5
HIRS/3 Baseplate	-10	30	5	25	13.5	15.7
All Temperatures in Degrees C.						

4.5.3.1.1 Thermal Control Finishes

The major thermal finishing materials used are listed in Table 4.5.3-1.

Black paint is used to optimize radiative coupling whenever sunlight is not a factor; white paints are used whenever heat is dissipated with sunlight present. White paint presents a problem, however, since its characteristics change due to UV exposure. The second-surface aluminized Teflon finish is an effective, stable radiator in the presence of sunlight. Second-surface aluminized Kapton is utilized whenever low α/ε ratios are not required.

4.5.3.1.2 Thermal Conduction Control Materials

Thermal conduction materials are applied as required to either increase or decrease the conductive coupling between units or assemblies. Materials used for this purpose are summarized in Table 4.5.3-2.

Glass-filled polycarbonate pads and washers are used whenever mechanical stability and minimal thermal conductive coupling are required. It is a tough plastic with a very low thermal conductivity (0.0005 watts/inch/C°) coupled with high tensile and compressive strengths. It also has a high resistance to creep - a property particularly useful where alignment stability is required.

It is often desirable to increase the conductive coupling between items that dissipate high power and their mounting interfaces and/or radiators. When mechanical strength or a true bonding action is required, epoxies are used; unprimed RTV is used at other locations.

4.5.3.1.3 Thermal Multi-layer Insulation Blankets

Construction details of the basic thermal insulation blanket is illustrated in Figure 4.5.3-1. The outermost layers of this blanket consist of 0.5 mil thick second-surface aluminized Kapton sheets. The sheets are reinforced with a glass cloth which is bonded to the aluminized surface with a thermosetting adhesive. These sheets sandwich 10 layers of 0.25 mil thick double-sided aluminized Mylar. Separation between these primary blanket sheets is provided by 7 mil thick, honeycomb weave Dacron netting.

TABLE 4.5.1-2. TEMPERATURE LIMITS AND PREDICTIONS - ESM

ESM Panel	Internal Equipment	Temperature Limits				Temperature Predictions	
		Non-Operational		Operational			
		Min	Max	Min	Max	Min	Max
1-Z	DCS-2/RPU	-30	60	-5	45	23.0	31.6
	BTX-1	-5	45	-5	45	27.3	36.4
	BTX-2	-5	45	-5	45	22.9	32.1
	TCE [3]	-5	45	-5	55	9.5	20.3
	RFS	-5	55	-5	55	17.6	27.6
1-ZC	DPD	-5	45	-5	45	12.6	22.1
	DCS-2/SPU-A	-30	60	-5	45	16.1	26.9
	YRW	-5	45	-5	45	16.4	26.9
	RFF-2	-5	45	-5	45	12.7	27.2
1+ZC	GRD-1	-5	45	-5	45	16.7	29.2
	GRD-2	-5	45	-5	45	15.4	28.2
	DCS-2/SPU-B	-30	60	-5	45	14.9	28.3
	RFH	-5	55	-5	55	14.9	31.8
	RFF-1	-5	55	-5	45	16.7	26.3
1+Z	SEM-2/DPU	-5	45	-5	45	16.4	31.4
	SBUVE	-5	45	-5	45	16.4	32.4
	RFT-1	-5	55	-5	55	13.6	30.5
	RFH-2	-5	55	-5	55	12.3	26.9
2	BRW	-5	45	-5	45	11.2	18.9
	SSE	-5	45	-5	45	14.1	22.3
	TCE [7]	-5	45	-5	45	2.4	17.7
3-Z	AIP	-5	45	-5	45	12.6	20.6
	RRW	-5	45	-5	45	13.1	20.7
	RFF-3	-5	45	-5	45	11.2	21.0
	RFF-5	-5	45	-5	45	11.8	20.8
3-ZC	CPU-1	-5	45	-5	45	14.8	26.2
	CPU-2	-5	45	-5	45	15.1	25.6
	RFF-4	-5	45	-5	45	11.3	24.1
3+ZC	CIU	-5	45	-5	45	12.6	26.4
	RXO	-5	45	-5	45	12.7	27.9
	CXU	-5	45	-5	45	10.1	25.0
3+Z	SARR Receiver	-5	55	0	35	12.4	25.7
4-Z	DTR-1	-5	45	0	35	12.9	15.9
	DTR-2	-5	45	0	35	10.6	15.5
4-ZC	DTR-3	-5	45	0	35	10.8	20.4
	XSU	-5	45	-5	45	11.7	22.7
	TCE [2]	-5	45	-5	45	10.4	23.5
4+ZC	DTR-4	-5	45	0	35	10.7	23.8
	DTR-5	-5	45	0	35	10.8	21.8
	TCE [2]	-5	45	-5	45	10.3	24.9

TABLE 4.5.1-2. TEMPERATURE LIMITS AND PREDICTIONS - ESM (Continued)

ESM Panel	Internal Equipment	Temperature Limits				Temperature Predictions	
		Non-Operational		Operational			
		Min	Max	Min	Max	Min	Max
4+Z	SARR Transmitter	-5	55	0	35	13.8	30.4
	TCE [1]	-5	45	-5	45	9.7	26.7
5-Z	MIRP	-5	45	-5	45	12.0	17.8
	DAU	-5	45	-5	45	13.6	21.6
	TCE [1]	-5	45	-5	45	10.0	23.8
5-ZC	PSE	-5	45	-5	45	12.5	30.7
5+ZC	PSE	-5	45	-5	45	12.5	30.7
	VTX-1	-43	65	-5	45	21.0	37.5
	VTX-2	-43	65	-5	45	13.8	30.1
	TCE [1]	-5	45	-5	45	9.9	25.9
	RFS	-5	55	-5	55	15.1	30.1
5+Z	SARP-2/SPU	-30	60	-5	45	12.4	24.1
	TCE [3]	-5	45	-5	45	10.0	28.5
	RFF-1	-5	55	-5	45	12.7	27.2
6-Z	STX-2	-43	65	-5	45	9.2	21.2
	STX-4	-43	65	-5	45	8.7	18.6
6-ZC	STX-3	-43	65	-5	45	10.1	25.9
	SCU	-5	45	-5	45	10.6	20.9
	TCE [7]	-5	45	-5	45	10.1	25.9
6+ZC	STX-1	-43	65	-5	45	23.8	40.4
	TIP	-5	45	-5	45	13.4	28.4
	RFS	-5	55	-5	45	14.5	32.0
6+Z	SARP-2/RPU	-30	60	-5	45	20.3	35.2
	RFF-3	-5	55	-5	45	14.6	30.9
	RFT/RFH	-5	55	-5	45	14.5	31.9
7	PRW	-5	45	-5	45	17.0	31.3
1	BDA	-68	67	-68	67	-70.3	46.0
	SRA	-61	66	-61	66	-4.3	10.7
	SLA	-140	64	-140	64	-58.1	16.9
	UDA	-80	108	-75	61	-6.0	25.7
	VRA	-80	64	-80	64	-51.7	68.3
	SBUV/2	-10*	30*	0*	30*	TBD	TBD
	AMSU-A2	-10*	30*	0*	30*	TBD	TBD
	AMSU-B	-10*	30*	0*	30*	TBD	TBD
2	MEPED	-10*	30*	0*	30*	TBD	TBD
	AMSU-A1	-10*	30*	0*	30*	TBD	TBD

* Spacecraft (ESM) Interface Temperature Limit; equipment listed for ESM Panel 1 and 2 is external.

TABLE 4.5.1-3. TEMPERATURE LIMITS AND PREDICTIONS - RSS AND SAS

Item	Temperature Limits				Temperature Predictions	
	Non-Operational		Operational			
	Min	Max	Min	Max	Min	Max
RSS Structure	-100	120	-90	120	-55.0	10.0
Battery Packs	-5	25	0	4	-1.0	3.1
Battery Reconditioning Units	-55	89	-55	89	-55.0	20.8
BCA Heat Sinks	-24	67	-24	65	-17.3	60.5
ADE Baseplate	-5	50	0	50	10.0	18.9
Nitrogen Engine Assemblies	-5	55	-5	45	8.0	26.0
Pressure Regulator Assembly	-5	55	-5	45	8.0	26.0
Latch Valve Assembly	-5	55	-5	45	8.0	26.0
Nitrogen Tanks	-34	71	-24	61	-50.0	10.0
Reaction Engine Assemblies	-5	55	-5	25	-5.0	16.0
Hydrazine Tanks	-34	71	5	61	9.0	39.0
Isolation Valves	-5	55	5	45	9.0	9.0
Hydrazine Lines	-5	60	5	45	9.0	23.0
TED	TBD	TBD	TBD	TBD	TBD	TBD
C/D Controller Chassis	-35	40	-30	30	TBD	TBD
Solar Array					77.2	-79.3
Partial Shunt Assemblies	-65	110	-65	110	-61.0	97.0
SATCU	-34	71	-24	-61	11.0	42.0
SAD	-5	45	0	40	9.1	37.6

TABLE 4.5.3-1. ATN-KLM PRINCIPAL THERMAL CONTROL FINISHES

Coating/Finish	Application	Absorptivity (α)		Emissivity (ε)	
		Min.	Max.	Min.	Max.
Black Paint (Chemglaze Z-306)	Rear of solar panels, internal surfaces of ESM panels, ESM boxes and inside RSS	0.93	0.96	0.85	0.90
White Paint (IITRI S-13GLO)	BCA, non-ESM radiators and IMU	0.20	0.40	0.84	0.88
Second-Surface Aluminized Teflon Sheet (10 mil)	ESM radiators	0.13	0.20	0.80	0.85
Second-Surface Aluminized Teflon Sheet (2 mil)	External surfaces of sun shields	0.13	0.18	0.62	0.67
Second-Surface Aluminized Kapton Sheet (0.5 mil) Reinforced with Dacron Cloth	Exposed ESM insulation blankets	0.32	0.37	0.50	0.55
Clear Anodize	RSS sun shield	0.30	0.70	0.60	0.80
Etched Titanium	Nitrogen tanks, AKM, Truss	0.25	0.55	0.55	
Front-Surface Aluminized Kapton Sheet (1 mil)	Exposed surfaces of Pinwheel louver blades, inside of IMP sunshade and inside RSS	0.08	0.15	0.02	0.05
Second-Surface Aluminized Kapton Sheet (1 mil)	Pinwheel louver blades (front and rear surfaces), and outside surfaces of IMP sunshade	0.35	0.39	0.60	0.65
Denton Silver	Sun sensor	0.05	0.07	0.02	0.04
Gold	Bi-metal housing of vane type louvers	0.19	0.25	0.02	0.05
Second-Surface Aluminized Teflon Sheet (5 mil)	RSS structure	0.14	0.20	0.75	0.79

A 2 mil thick layer of second-surface aluminized Teflon is added to the outboard layer of this basic blanket whenever it is required to minimize the effects of solar loading. Blankets for the IMP, battery packs, the IMP-ESM long and short struts, ESA and ADE, and some RCE components include this additional layer.

Except for those blankets associated with the SEM-TED and its local environment, the spacecrafts' blankets are not electrically grounded.

TABLE 4.5.3-2. ATN-KLM THERMAL CONDUCTION CONTROL MATERIALS

Type Material	Thermal Characteristic	Use Location
Glass-filled polycarbonate pads and washers	Provide high thermal resistance	1) At mounting interface between IMP and IMU, at support struts 2) Between RSS and Batteries, BCA and ADE 3) Between RSS and hydrazine tanks. 4) Between Solar Array Boom/ SAD
Epoxy EC 2850-GT	Electrical insulator, moderate thermal conductor	Bonding of BCA Heat Sinks to BCA Radiator
Unprimed RTV	Improves thermal conductance across high power equipment mounting interfaces	At mounting interfaces of ESM transmitters, tape recorders, PSE, and other high power dissipation units.
Doubler Plates, Aluminum	High thermal conductivity	Thermally couples BTX-1 to BTX-2 and VTX-1 to VTX-2
G-10 Glass Epoxy	Low thermal conductivity	ESM/instrument interfaces

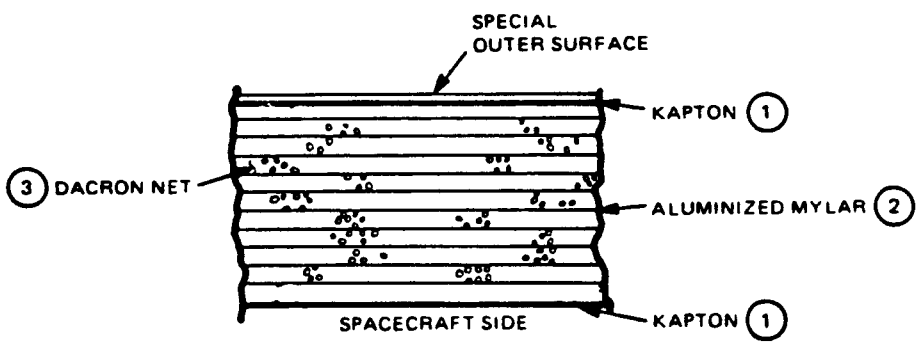

6-0476

Item

1 0.5 mil KAPTON film, aluminized and reinforced on one side; the reinforcement, a composition B107 glass cloth, is bonded to the aluminized surface with a thermosetting adhesive. KAPTON substrate is outboard.

2 0.25 mil MYLAR film, aluminized on both sides.

3 7 ±1 mil DACRON netting, honeycomb weave. 9 layers used.

Figure 4.5.3-1. Multi-layer Thermal Blanket - Basic Construction

Table 4.5.3-3 lists the outer surface and effective thermal properties of the thermal blankets. Blanket assembly and attachment to spacecraft surfaces are accomplished through sewing, button fasteners, hook/pile fasteners and tapes.

TABLE 4.5.3-3. THERMAL MULTILAYER INSULATION BLANKETS

Outer Surface	Outer Layer Surface Properties		Effective Blanket Properties		
	α	ε	α	ε	α/ε
Aluminized Teflon	0.13-0.18	0.62-0.67	0.007-0.017	0.02-0.05	0.194-0.290
Aluminized Kapton	0.36-0.41	0.66-0.69	0.02-0.03	0.02-0.05	0.52-0.62
Black Kapton	0.90	0.86	---	0.02-0.05	---

Thermal properties are affected by:

- Open blanket ends
- Blanket stitching
- Penetrations for fasteners
- Ratio of stitched area to total area

4.5.3.1.4 Thermal Shields and Sunshades

Thermal shields and sunshades are used where protection from solar, AKM plume, and soak-back heating is required or desirable. The major thermal shields and sunshades provided are:

- ESM-RSS Connection Truss: The lateral areas of this truss are covered with a set of six 3-ply thermal shields. The outermost layer of this shield is a 5 mil thick, second-surface aluminized Teflon sheet. On missions which carry SBUV instruments, this layer will be replaced by a reinforced black Kapton sheet on those shields which could reflect sunlight into that instrument's radiometric field-of-view. These shields provide sun shielding of the +Z ESM panel (Panel 7) during on-orbit operation and protect the stowed solar array panels from the high radiative heat flux off the contained AKM hemisphere during the mission's ascent phase. Truss shields local to the SEM-2/TED are required to be electrically grounded.

- ESM Panel 7: The AKM/RSS viewing side of this honeycomb panel is finished with a low emittance, vapor-deposited gold taping. Its inboard viewing side is finished with a high emittance, black paint. This shield radiatively isolates the ESM from the RSS/AKM thermal environment. It also provides for RFI shielding.

- IMP: The IMP sunshade consists of both fixed and deployable components. The purpose of this sunshade system is to prevent direct solar loading onto the IMP louver assembly and the AVHRR/3 and HIRS/3 radiant cooler doors. The fixed component of the sunshade is composed of 0.25" thick open-cell urethane foam sheets sandwiched between 1 mil thick sheets of aluminized Kapton film. The internal film which views the IMP louver system is aluminized on both sides. The external film is aluminized on the side which is bonded to the foam material. The deployable components (±Y wings) of this sunshade are fabricated from two 1 mil thick, reinforced black Kapton sheets.

4.5.3.2.1 Thermal Control Electronics (TCE)

Two types of TCE's are used -- dual TCE's and differential TCE's. Both types can be enabled or inhibited by ground command. The maximum output power is specified as 30 watts; the power dissipated in the TCE depends on the power output of the unit, but is specified as 1 watt maximum.

The dual TCE operates in a dual thermal controller as shown in Figure 4.5.3-2. This controller consists of a dual TCE unit, a heater, a thermistor temperature sensor, a heat radiating surface (radiator), and a louver actuator. The thermistor senses the temperature of the body which is to be controlled; the TCE then actuates either a heater or a louver actuator or does nothing at all, depending on whether the sensed temperature is lower, higher or in the dead band temperature range, respectively. The cooler is activated by heating a bimetallic element, which in turn opens a louver and allows the radiating surface to radiate heat to the space sink.

The differential TCE operates in a differential thermal controller as shown in Figure 4.5.3-3. This controller consists of a differential TCE unit, a heater, 2 thermistor temperature sensors, a reference body, and a controlled body. The controlled body has a fixed radiating surface which is sized such that the controlled body tries to run cooler than the reference body for all orbital conditions; the TCE then supplies just enough power to maintain the controlled body temperature at the temperature of the reference body.

At times when only heating is required, a differential TCE (with 1 of the thermistors replaced by a fixed resistor) can be used to control the power to the heater. When a differential TCE is used with a fixed resistor, the TCE will give a 50% duty cycle when the thermistor resistance equals that of the fixed resistor.

The ATN-KLM TCE configuration is given in Table 4.5.3-4.

<u>Dual TCE Operation</u>

The dual TCE activates either a heater or a louver cooler in accordance with the temperature sensed by a single thermistor. As shown in Figure 4.5.3-4, the dual TCE consists essentially of a power switch, a sawtooth generator, a thermistor temperature sensor, a control bridge circuit, 2 external heater elements, and 2 operational amplifier driver circuits for the heaters. The design is such that both external heater elements can never be powered at the same time.

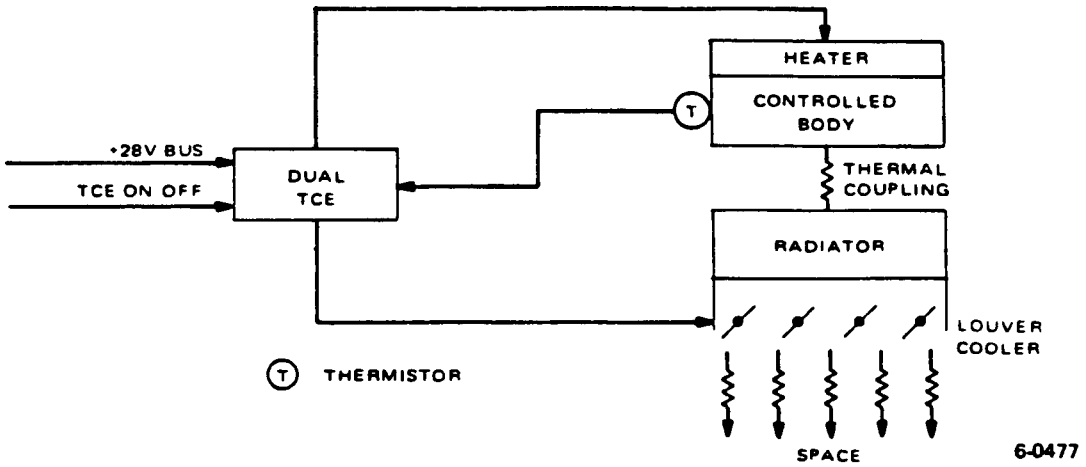

Figure 4.5.3-2. Dual Thermal Controller

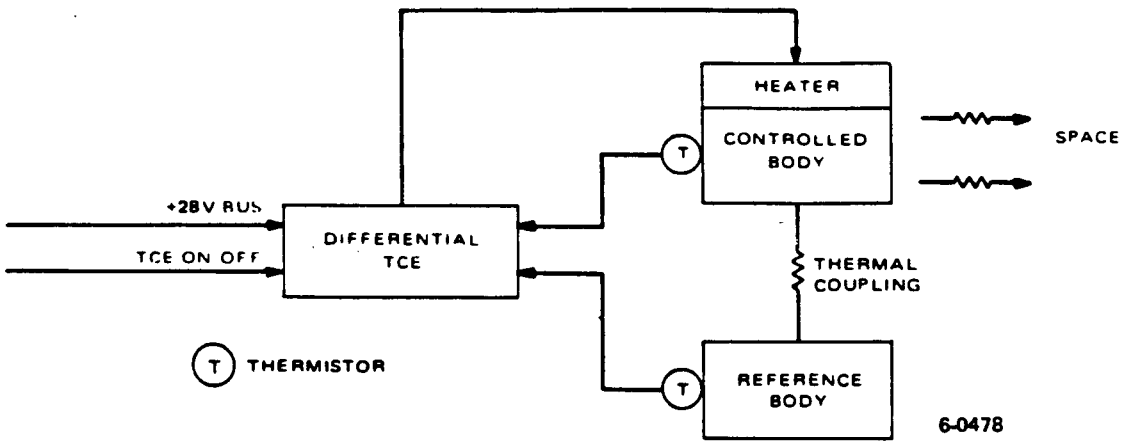

Figure 4.5.3-3. Differential Thermal Controller

The dual TCE uses a pulse width modulation technique to provide the operating characteristics shown in Figure 4.5.3-5. The TCE power output to the louver heating element starts to turn on (minimum duty cycle) at the louver set point temperature (T_S) and can be full on (maximum duty cycle) at a temperature 1°C higher. The louver power output is linearly proportional to temperature in the region between full-off and full-on. The maximum power output for the louver control portion of the circuit is 5 watts; the maximum power used on the spacecraft is 0.45 watt. During manufacturing, the temperature set point T_S is adjustable from 0°C to +21°C (by changing externally mounted resistors).

The TCE power output to the heater starts to turn on at the heater temperature set point ($T_S - \Delta T$). The heater set point is always below the cooler set point (T_S) by the temperature differential ΔT, which will be no less than 0.5°C to insure that the heater and louver portions of the circuit are never on at the same time. The heater output can also be full on 1°C below the heater

TABLE 4.5.3-4. ATN-KLM TCE CONTROLLER USAGE

TCE No.	Controlled Item (Controller Type)	Set Point (°C)		TIP Status Telemetry Channel	
		Heater	Louver	Heater	Louver
1	Battery 1A (3)	0	2	201	209
2	Battery 1B (3)	0	2	217	225
3	Battery 2A (3)	0	2	233	241
4	Battery 2B (3)	0	2	81	89
5	Battery 3A (3)	0	2	432	440
6	Battery 3B (3)	0	2	448	456
7					
8	Long Strut (2)	*	*	207	*
9	ESA (1)	15	*	215	*
10	ESM 3+ZC (3)	5	10	82	90
11	ESM 3-ZC (3)	5	10	162	170
12	ESM 3-Z (3)	5	10	178	186
13	ESM 4+ZC (3)	5	10	194	202
14	ESM 4-ZC (3)	5	10	210	218
15	ESM 4-Z (3)	5	10	226	234
16	ESM 5+ZC (3)	5	10	242	8
17	ESM 5-ZC (3)	5	10	16	24
18	ESM 5-Z (3)	5	10	32	40
19	ESM 6+ZC (3)	5	10	48	56
20	ESM 6-ZC (3)	5	10	64	72
21	ESM 6-Z (3)	5	10	80	88
22					
23					
24	AVHRR/3 (3)	13	15	192	200
25	HIRS/3 (3)	13	15	208	216
26	IMU (1)	34	*	224	*
27	ADE (1)	10	*	232	*
28	SAD (1)	10	*	240	*
29	TED (1)	-20	*	3	*
30					
31	MEPED (1)	-20	*	19	*
32	IMP +X (1)	15	*	27	*
33	IMP -X (1)	15	*	35	*
34	ESM 4+Z (3)	5	10	387	392
35	ESM 3+Z (3)	5	10	400	408
36	ESM 5+Z (3)	5	10	416	424
37	ESM 6+Z (1)	5	*	467	*

NOTES Controller Type (1) Heater (Fixed-Temperature Differential)
(2) Differential
(3) Dual

See also Table 4.5.5-1.

* Parameter Not Applicable

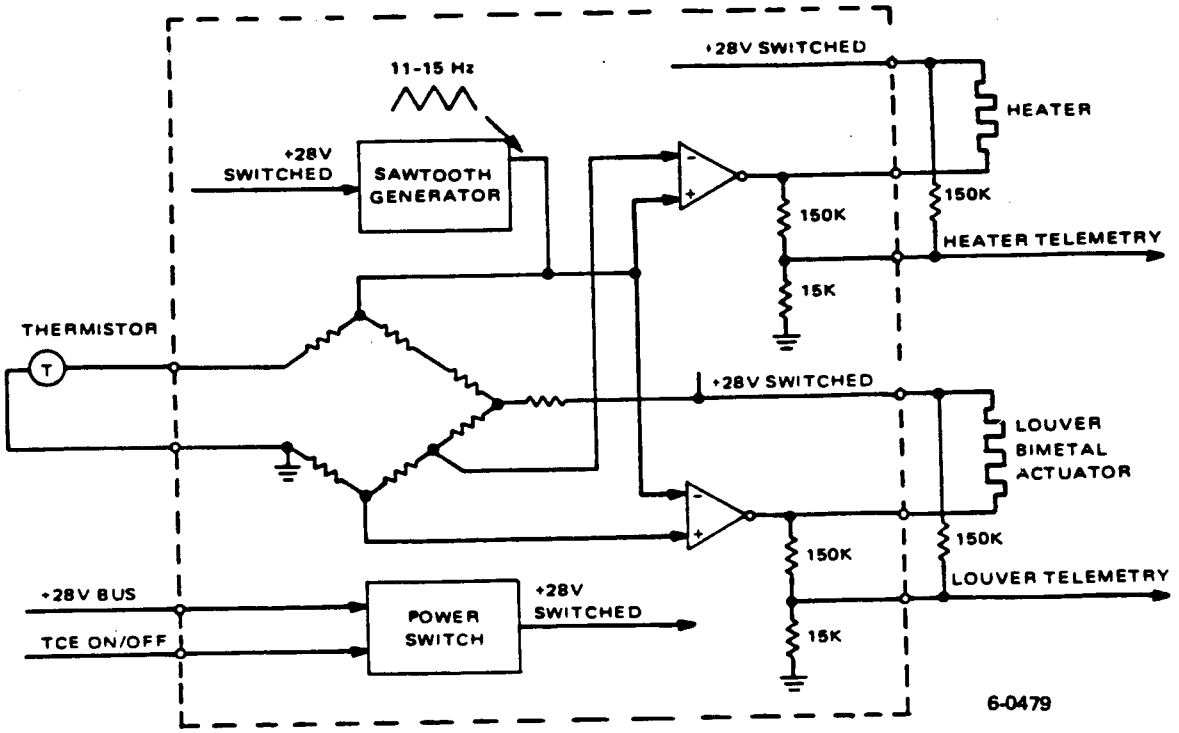

Figure 4.5.3-4. Dual TCE Functional Block Diagram

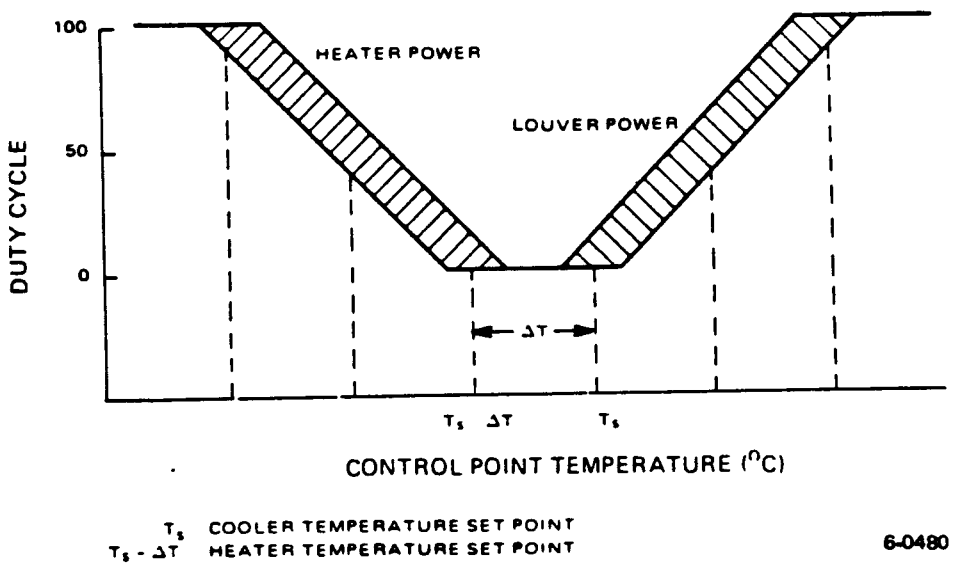

Figure 4.5.3-5. Dual TCE Operation

set point temperature; however, circuit limitations allow only the heater circuit or the louver circuit to be adjusted for this full power switch in 1°C. The other circuit will then be slightly different. The average power output or duty cycle is linearly proportional to temperature in the region between full off and full on. The maximum power output capability of the heater circuit is 30 watts; the maximum power used in flight is 24 watts. During manufacturing, the heater set point temperature is adjustable from 0°C to +21°C.

During manufacturing, the dead band temperature range (ΔT) is also adjustable from 0°C to 15°C. As mentioned above, however, ΔT will never be set to less than 0.5°C.

The key to a more detailed understanding of the dual TCE is the control bridge circuit, shown in greater detail in Figures 4.5.3-6 and 4.5.3-7. Note that the circuit arrangement is the same as shown earlier in Figure 4.5.3-4.

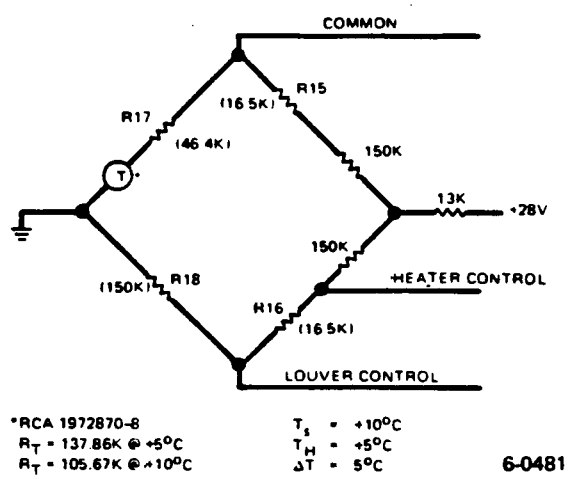

Figure 4.5.3-6. Sample Dual TCE Bridge Circuit

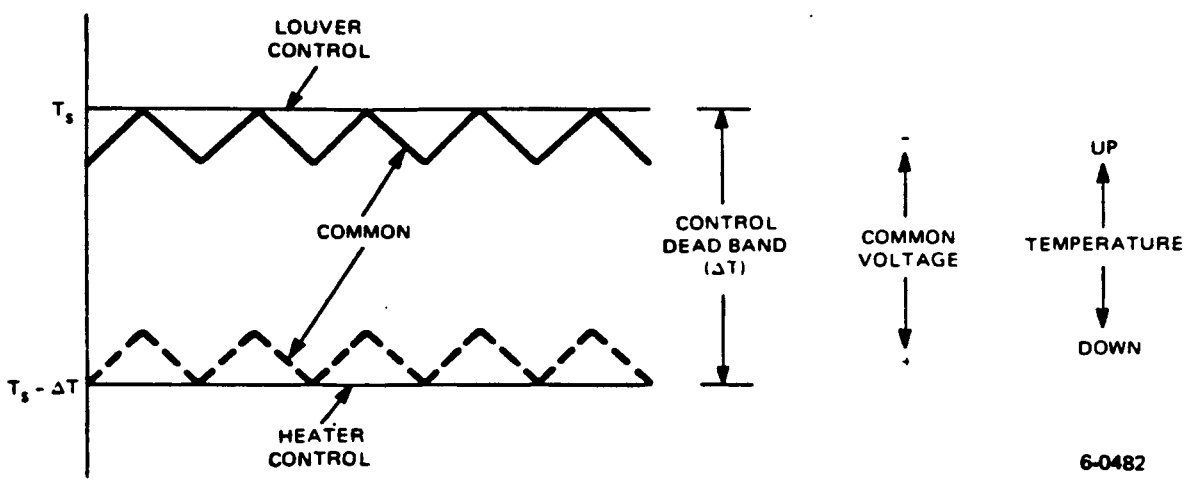

Figure 4.5.3-7. Dual TCE Bridge Operation

The heater control and louver control tap points in the bridge are in a fixed voltage divider; these 2 control signals are therefore fixed dc levels. The voltage potential between the heater and louver control points controls the TCE dead band; R16 is selected to give the proper ΔT.

The bridge side with the common tap point also has the control thermistor in one leg. The thermistor resistance varies with temperature; therefore, the dc level present at the common tap point also varies with temperature. Note that this dc level also has the sawtooth waveform superimposed. The amplitude of the sawtooth waveform controls the temperature band over which the TCE switches from no output power to full output power; the amplitude is normally adjusted so that this full power switch occurs in 1°C.

During factory testing, bridge resistor R17 is selected so that the TCE just begins to supply power to the louver at T_S; this is shown by the solid common line in Figure 4.5.3-7. If the temperature then goes higher, the thermistor resistance decreases, the common tap point dc level becomes more negative, and progressively more power is delivered to the louver.

Similarly, bridge resistor R16 is selected so that the TCE just begins to supply power to the heater at $T_S - \Delta T$; this is shown by the dashed common line. If the temperature then goes lower, the thermistor resistance increases, the common tap point dc level becomes more positive, and progressively more power is delivered to the heater.

To complete the bridge resistor selection criteria, R18 is set to 150K in all present applications but would be adjusted upwards if R_T were greater than 150K at T_S. To balance the bridge, R18 must be approximately equal to R17 plus R_T at T_S. For bridge symmetry, R15 is simply set equal to R16.

Differential TCE Operation

The differential TCE activates a single heater in accordance with the temperature difference sensed by a pair of thermistors. As shown in Figure 4.5.3-8, the differential TCE consists essentially of a power switch, a sawtooth generator, a pair of thermistor temperature sensors, a control bridge circuit, and an operational amplifier that activates a single external heater.

The differential TCE uses a pulse width modulation technique to provide the operating characteristics shown in Figure 4.5.3-9. The heater output starts to turn on (minimum duty cycle) when the controlled body temperature is approximately 0.2°C lower than the reference body temperature. It is full on (maximum duty cycle) when the controlled body temperature is approximately 0.2°C higher than the reference body temperature. The output power is linearly proportional to the temperature differential in the region between full off and full on. The maximum power output capability of the heater output is 30 watts; the maximum power used in flight is 16 watts.

The key to a more detailed understanding of the differential TCE is the control bridge circuit, shown in greater detail in Figures 4.5.3-10 and 4.5.3-11.

With proper design, the controlled body always tries to run cooler than the reference body. Under active TCE control, however, just enough heat is supplied to maintain the controlled body temperature at the same value as the reference body.

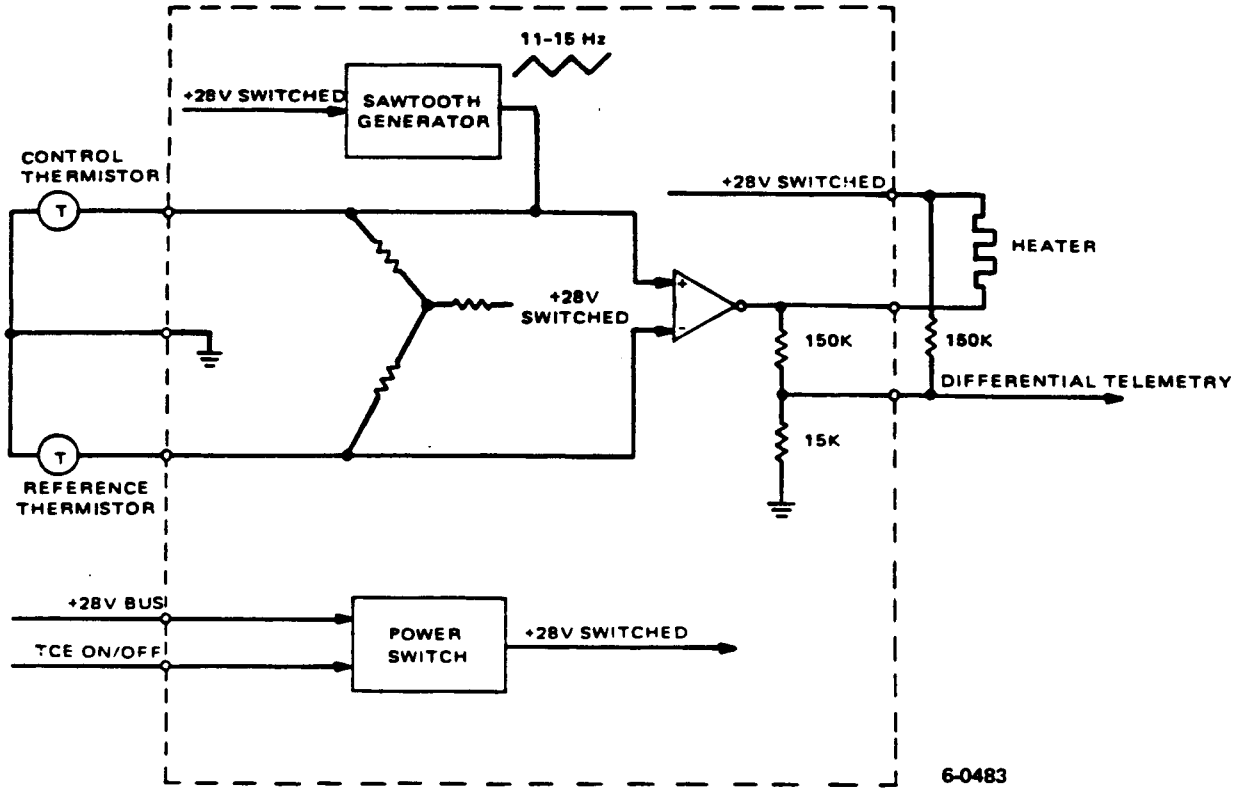

Figure 4.5.3-8. Differential TCE Functional Block Diagram

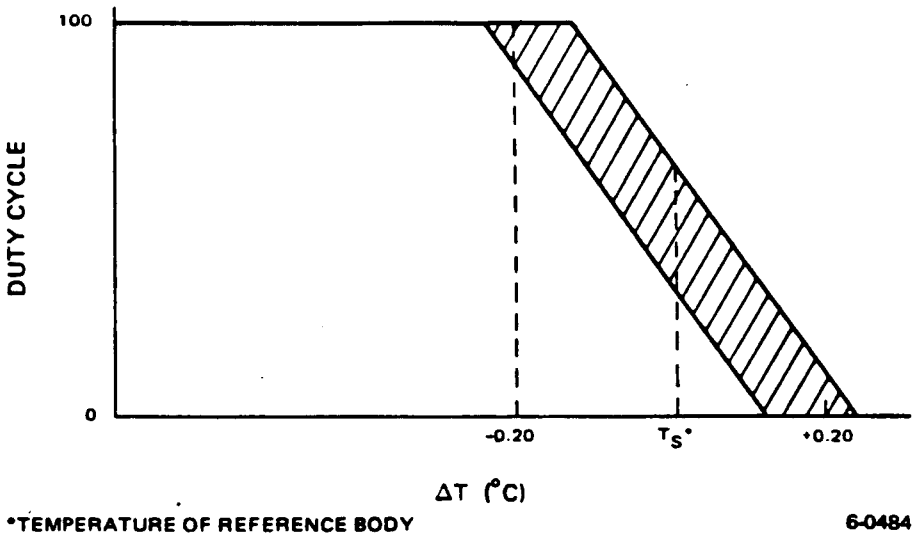

Figure 4.5.3-9. Differential TCE Operation

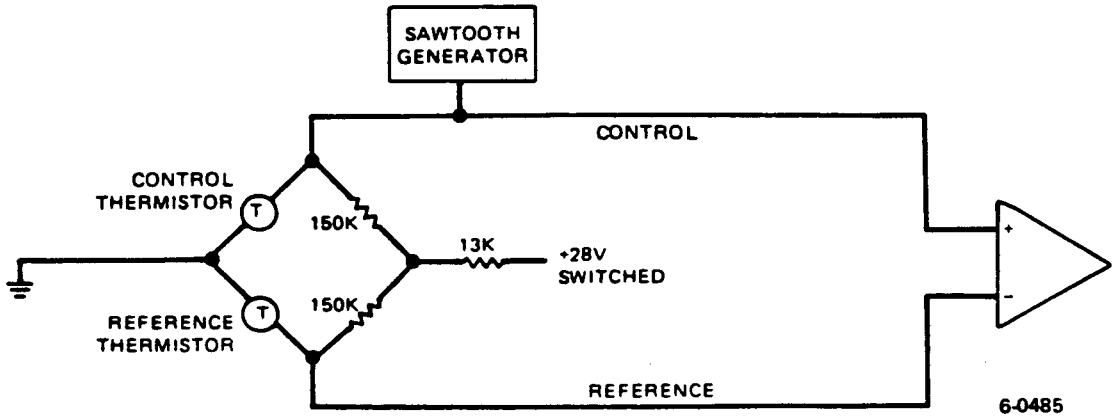

Figure 4.5.3-10. Differential TCE Bridge Circuit

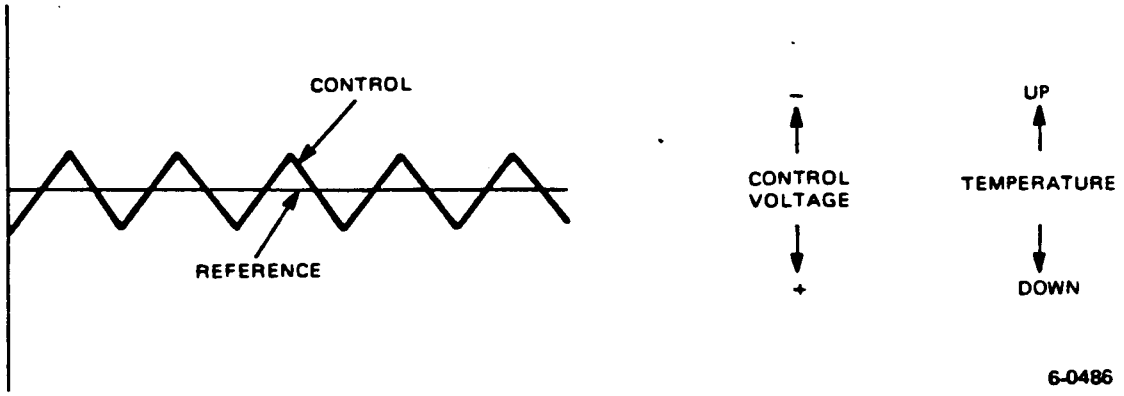

Figure 4.5.3-11. Differential TCE Bridge Operation

If both bodies are at the same temperature, the bridge will be balanced and the TCE will be operating with a 50% duty cycle, supplying half the available power to the heater; this condition is shown in Figure 4.5.3-11. If the controlled body temperature then tries to go colder, thermistor resistance will increase, the control dc level will become more positive, and progressively more power is delivered to the heater. Similarly, if the controlled body temperature tries to go warmer, progressively less power is delivered to the heater.

4.5.3.2.2 RCE A/B, C/D and BRU Heating Systems

RCE A/B Heating Systems

The active components within these subsystems are heaters and mechanical thermostats.

The heating elements are type RW80S wire-wound resistors. The latch valve and the eight nitrogen thrusters (NEA's) utilize a single resistor as a heater; the pressure regulator uses two such elements connected in parallel. Each

thermostat is connected to a single enabling relay (A or B) within the Command and Control Subsystem (C&CS). Enabling (disabling) the A relay results in the enabling (disabling) of all the 10 thermostats connected to it (the A heater subsystem). Identical command capability is present for the B subsystem.

The thermostat activation temperature for the A subsystem is approximately 15.5°C; it is approximately 10°C for the B subsystem.

Total power dissipation for the A and B subsystems are the same: 17.9W. This is distributed among the controlled components as follows. Pressure regulator: 3.1W; latch valve: 2.0W; and 1.6W per nitrogen thruster.

RCE C/D Heating Systems

Propellant freezing and freeze/thaw cycling in the unvented portion of the RCE hydrazine subsystem is prevented by active heating of those subsystem components which could retain residual hydrazine. These components are the propellant tanks (2), tank-to-isolation-valve lines (2), and isolation valves (2).

This control is implemented on each of these 6 RCE components by conductively isolating each of them from the RSS, by using multilayer insulation blankets, and by attaching a redundant pair of local heater circuits (designated C and D) to each component. Each heater circuit is regulated by remote, unique proportional controllers responsive to a unique sensor (control thermistor) located on the affected component. There are a total of 12 sensor/heater pairs - 6 components x 2 systems (C and D). Two spacecraft commands allow enabling and inhibiting of the complete set of 6 C-system triples. An identical commanding scheme exists for the D-system. The C-system maintains component temperatures at approximately 15°C, while the D-system maintenance level is approximately 9°C. The controllers are located on a special chassis which is mounted on the ESM/RSS connection truss.

Both film-type heating elements (propellant tanks and lines) and wire-wound resistors (isolation valves) are used as dissipating elements.

These subsystems maintain nearly constant temperature levels in the affected components. This characteristic is produced by the proportional-type control provided by the subsystem's controllers.

Both subsystems are capable of supplying a maximum heating power of approximately 20W. This maximum power is distributed among the affected components as follows: 12W per propellant tank; 5W per propellant line; and 3W per isolation valve.

4.5.3.2.3 Thermal Heaters

Two kinds of heating elements are used aboard the ATN spacecraft:

- Wire-wound resistors are used within the RCE A/B and C/D heating systems; the TCE-controlled IMP heaters also use these elements.

- Thin film ribbon heaters are used with all TCE controllers (except for the IMP) for both local area heating and for driving the bi-metallic louver actuators.

A summary of the ribbon heater characteristics is given in Table 4.5.3-5. Table 4.5.3-6 lists the TCE-controlled heaters used on-board the ATN spacecraft. Where more than one heater is used, the heaters are usually connected in parallel to provide redundancy. All heaters except those which drive the louver actuators are mounted with M777 epoxy; the actuator heaters are bonded with a dry, thin-film, heat reactive adhesive.

TABLE 4.5.3-5. RIBBON HEATER CHARACTERISTICS

Parameter	Characteristics
Insulation Materials	Kapton/FEP
Heater Element	Non-Inductive, Nichrome or Cupro-nickel
Heater Leads	24 or 30 AWG stranded, Kapton Insulated*
Heater Thickness	0.010 max. except 0.065 max. over leads
Lead Length	12.00 min.
Lead Pull Strength	3.0 lbs min.
Heater Bend Radius	0.1 radius or greater
Insulation Resistance	1000 megohms min. at 500 VDC
Temp. Range, Operating	-200°C to 232°C
Temp. Range, Non-operating	-200°C to 260°C
Power Density	Up to 70 watts/square inch when properly heat sunk
Weight	Less than 0.25 grams per square inch
Finish	Aluminum foil on bonded side**
Heat Distribution	Uniform

*Actuator heaters are Teflon insulated
**Actuator heaters are not finished

4.5.3.2.4 Thermal Louvers

There are 2 types of thermal louvers used on the spacecraft -- pinwheel louvers and vane louvers. Each type is used in conjunction with an appropriate radiator.

Pinwheel louvers move in a plane parallel to the radiator surface; vane type louvers open and close like a venetian blind in front of the radiator. Vane louvers are more efficient than pinwheel louvers because the pinwheel blade must cover a non-radiator surface as it moves to expose a radiator. Pinwheel louvers must be used where vane motion is restricted.

TABLE 4.5.3-6. TCE CONTROLLER HEATER USAGE

TCE No.	Heater Location	Quantity and Type*	Resistance (ohms)	Maximum Power** (watts)
1	BATTERY 1A	1-16	51.2	14.8
2	BATTERY 1B	1-16	51.2	14.8
3	BATTERY 2A	1-16	51.2	14.8
4	BATTERY 2B	1-16	51.2	14.8
5	BATTERY 3A	1-16	51.2	14.8
6	BATTERY 3B	1-16	51.2	14.8
7				
8	LONG STRUT	1-4	445.0	1.7
9	ESA	1-14	145.0	5.2
10	ESM 3+ZC	4-27	51.7	14.6
11	ESM 3-ZC	3-27	69.0	11.0
12	ESM 3-Z	2-18	74.5	10.2
13	ESM 4+ZC	4-19	70.25	10.8
14	ESM 4-ZC	4-19	70.25	10.8
15	ESM 4-Z	4-19	70.25	10.8
16	ESM 5+ZC	2-27	103.5	7.3
17	ESM 5-ZC	2-27	103.5	7.3
18	ESM 5-Z	2-9	59.5	12.7
19	ESM 6+ZC	2-9	59.5	12.7
20	ESM 6-ZC	4-19	70.25	10.8
21	ESM 6-Z	2-9	59.5	12.7
22				
23				
24	AVHRR/3	GFE	31.4	24.1
25	HIRS/3	GFE	32	24
26	IMU	2-27	103.5	7.3
27	ADE	2-27	103.5	7.3
28	SAD	1-17	180.0	4.2
29	TED	GFE		7.6
30				
31	MEPED	GFE		9.2
32	IMP +X	13	70.3	10.8
33	IMP -X	18	48.0	15.8
34	ESM 4+Z	2-9	59.5	12.7
35	ESM 3+Z	1-30	59.2	12.8
36	ESM 5+Z	2-9	59.5	12.7
37	ESM 6+Z	2-9	59.5	12.7

*Type refers to RCA part number of heating element per RCA
Specification Control Drawing 2280052.
**Heater circuit voltage = 27.5 volts.

The louvers are actuated by means of a bimetallic element attached to the louver drive shaft. The temperature of the bimetallic element is controlled by a heater bonded to it. When the TCE supplies power to the heater, the bimetallic element heats up and moves the louver blade, allowing heat to be radiated from the controlled body.

Vane Thermal Louvers

The vane thermal louver consists of a heater actuated bimetallic actuator assembly, a foam sandwich louver blade reinforced with a fiberglass quill, and a support bracket, as shown in Figure 4.5.3-12. The actuator assembly is shown in detail in Figure 4.5.3-13. The blades are surrounded by a thermal fence, which helps control radiative coupling between the controlled surface and external sources or sinks.

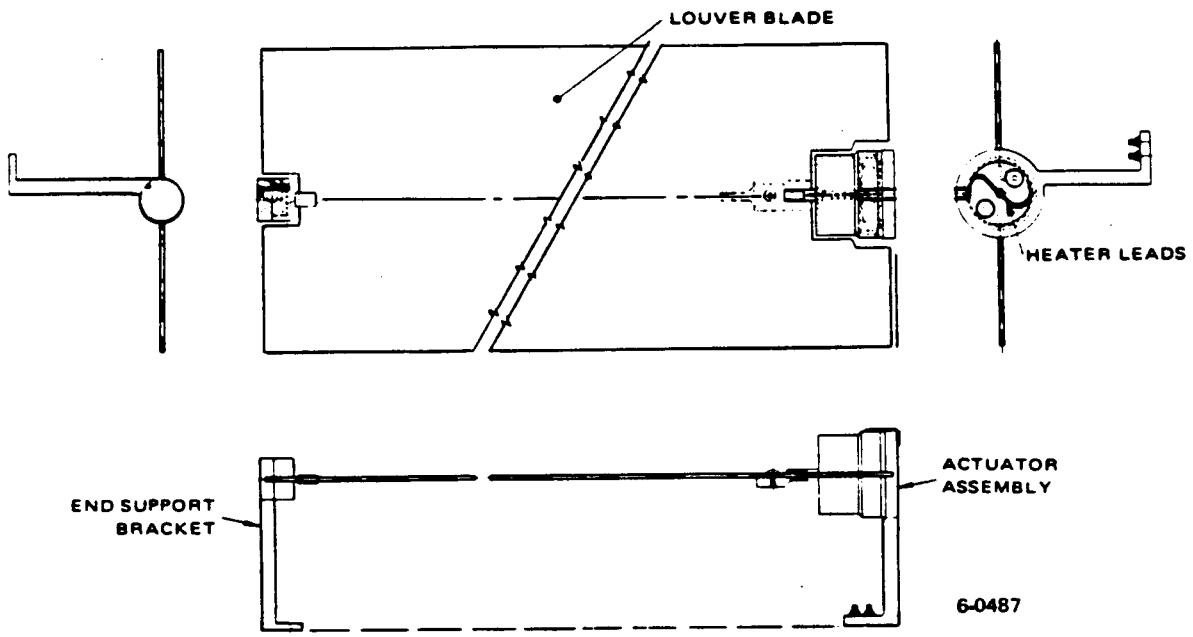

Figure 4.5.3-12. Vane Thermal Louver Assembly

The actuator bimetallic element is heated by a TCE-controlled heater strip which is bonded directly to it. When the TCE calls for cooling, the TCE supplies power to the heater which heats the bimetallic element and causes the louver to open. When no power is supplied to the heater, the bimetallic element approaches the mounting bracket temperature; under normal operating conditions, this causes the louver to close. The mounting bracket is strongly coupled to its mounting surface (the controlled radiating surface), and is always at or near the mounting surface temperature.

The actuator assembly contains stop elements which limit the louver rotation at the fully closed and fully open position (90° of angular rotation). The bimetallic element is sized to rotate 90° when its average temperature changes

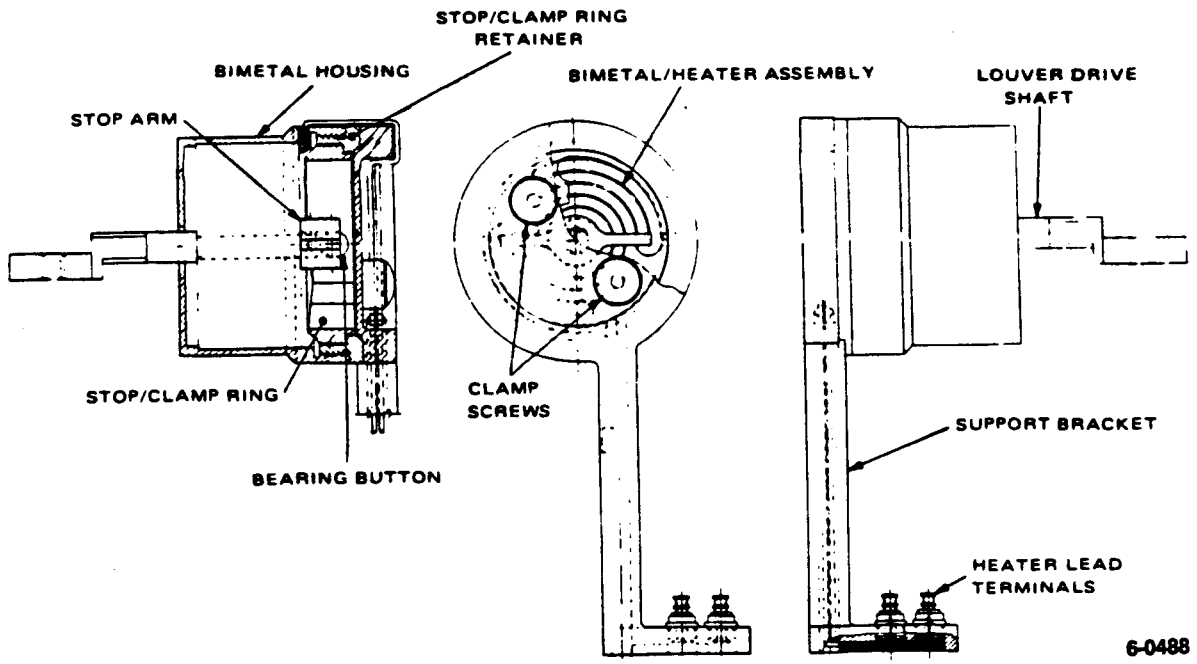

Figure 4.5.3-13. Vane Louver Blade Actuator Assembly

10°C. A louver drive shaft is mounted at the center of the bimetallic coil; the shaft drives the louver blade as the bimetallic element uncoils.

The louver blade consists of a foam sandwich structure with a fiberglass quill in the center. The foam is 100-pore, open cell flexible polyurethane. The fiberglass quill is machined on one end to mate with and provide attachment to the louver drive shaft; the other end has a bonded-on, ball-end pivot, which is captured by the end support bracket such that it cannot pull out during vibration. The end support bracket supports the "free" end of the louver blade and constrains it during the launch environment. The support bracket holds the ball end of the pivot in a Delrin AF cup, which minimizes friction during ground testing and flight.

The blade facing materials can be varied to provide the best decoupling between the radiator and space, depending on the radiation field in which the louver must operate. The vane louvers usually do not receive solar radiation; therefore, the front surface is aluminized Kapton with the aluminum facing out. This surface has a high α/ε. With a low emissivity, the energy loss from this vane will be low when the vane is closed.

The Louver Transfer Ratio (LTR) for this type of louver is shown in Figure 4.5.3-14. LTR is the ratio of heat radiated with louvers to heat radiated without louvers. This type of louver is very efficient; it has a fully closed LTR of approximately 0.1 (with no cutouts in the blade), and a fully open LTR of approximately 0.95. The transfer ratio is not zero when the vane is closed because the vane has a finite emittance. The transfer ratio is also not 1.0 when the vane is completely open (90°), since the edge-on vane still blocks part of the radiator field of view.

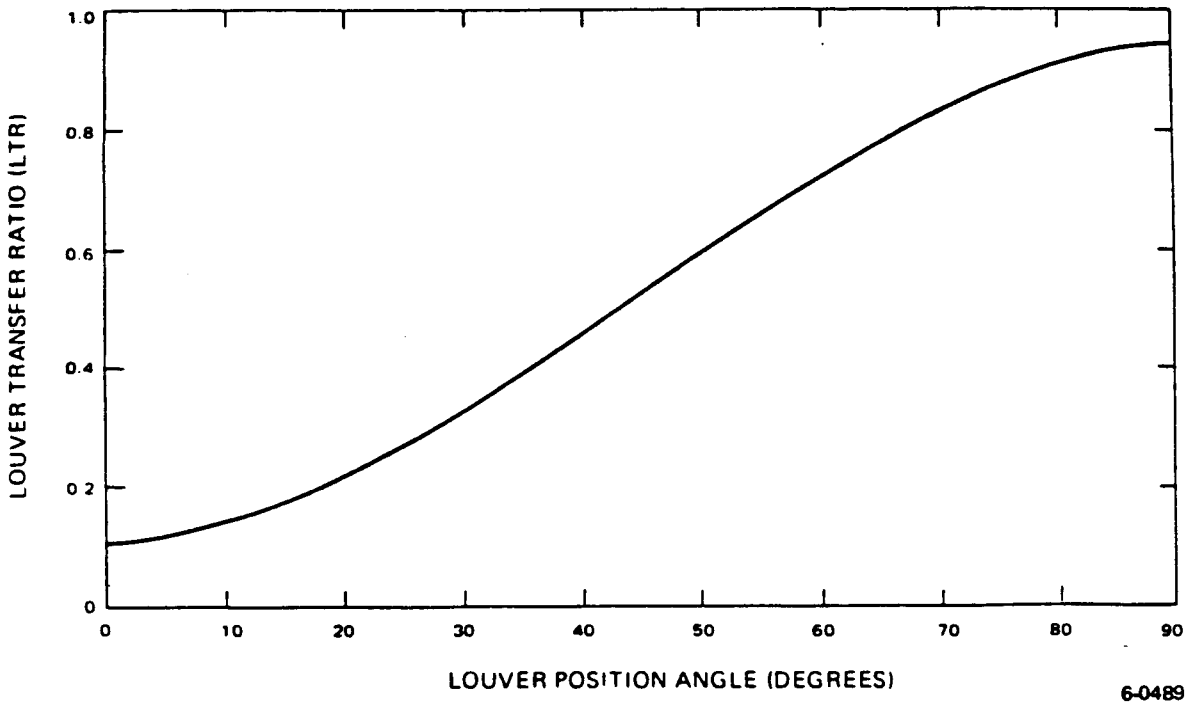

Figure 4.5.3-14. Vane Louver Heat Transfer Characteristics

The louver position versus the mounting interface temperature is shown in Figure 4.5.3-15. This assumes that the interface temperature is maintained at each value until the louver responds. In the active mode (TCE activated), the louver goes from fully closed to fully open with a thermal interface temperature change of approximately 1°C. This range may vary depending on TCE characteristics. If the active mode has failed or has been deactivated, the louver will operate passively at a higher temperature.

The blade will fully open when the actuator temperature changes by 10°C. Theoretically it would be desirable to have the blade start to open at the set point temperature (T_S). Practically, this is not feasible because of the variation in the thermal coupling for increasing and decreasing interface temperature (hysteresis). To insure correct active operation, the louver actuators are adjusted so that passive actuation starts 5°C higher than T_S. This is accomplished by setting the unit during test at atmospheric pressure so that the blade starts to move at a temperature lower than the TCE set point.

A thermal fence of foam sandwich material surrounds the louvers to prevent excessive heat leakage when the louvers are closed and also to provide some shielding against direct solar input to the louvers. The outer layer of the foam sandwich material is second-surface aluminized Teflon when sun shielding is needed. When the thermal fence serves as a sun shield, the top of the fence is flared out at a 10° angle to reflect solar energy away from the louvers and radiators.

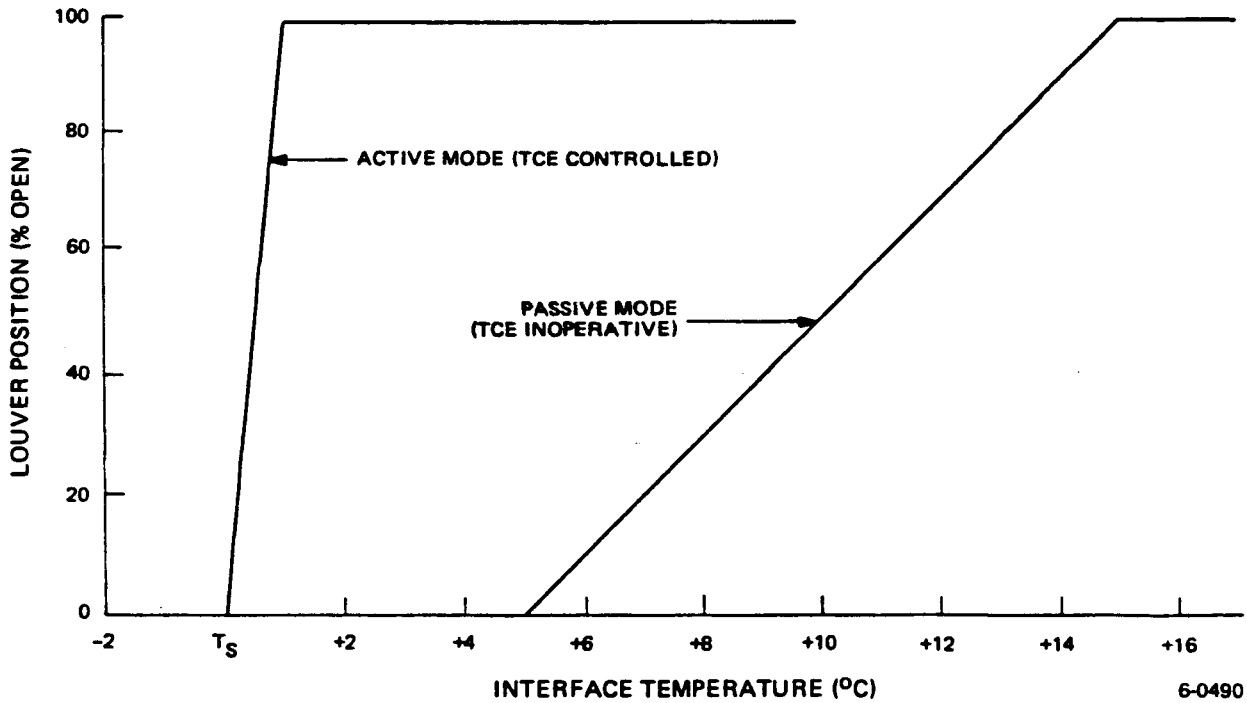

Figure 4.5.3-15. Vane Louver Actuation Characteristics

Pinwheel Thermal Louvers

The pinwheel louver consists of a 4 lobed louver blade, an actuator assembly, a guard ring, and a special radiator pattern, as shown in Figure 4.5.3-16. These louvers are used on ESM panels 3, 4, 5, and 6 to increase the power dissipation range. This type of louver is used on the ESM panels due to its low mechanical profile (less than 0.5 inch, which permits mounting under the stowed solar panels). The louvers have a passive actuation temperature at which they will start to open without TCE power; this temperature is the louver set point temperature plus 3°C.

The pinwheel louver blade is shown in detail in Figure 4.5.3-17. The louver blade consists of a fiberglass hub, foam sandwich blades, a fiberglass support framework, and a single sided aluminized Kapton film outer shield. The outer shield shields the hub and blades from most of the external environment; this is necessary to prevent wide variations in hub and blade temperatures, which in turn would affect the bimetallic element temperature and thus its response.

The pinwheel actuator assembly is shown in detail in Figure 4.5.3-18. The actuator assembly consists of a bimetallic element, heater strip, drive shaft assembly, bimetallic element housing, outer housing, clamp ring, stop element, and 2 Delrin AF bushings. The heater strip is bonded directly to the bimetallic element, which in turn is bonded into the bimetallic housing.

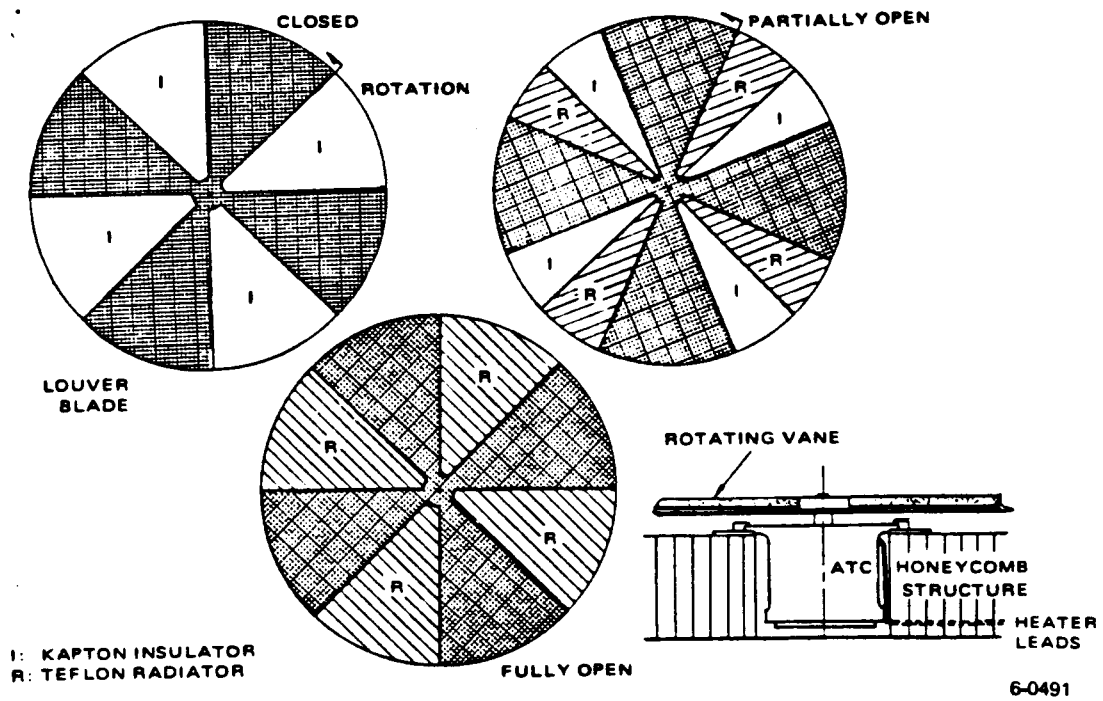

Figure 4.5.3-16. Pinwheel Thermal Louver

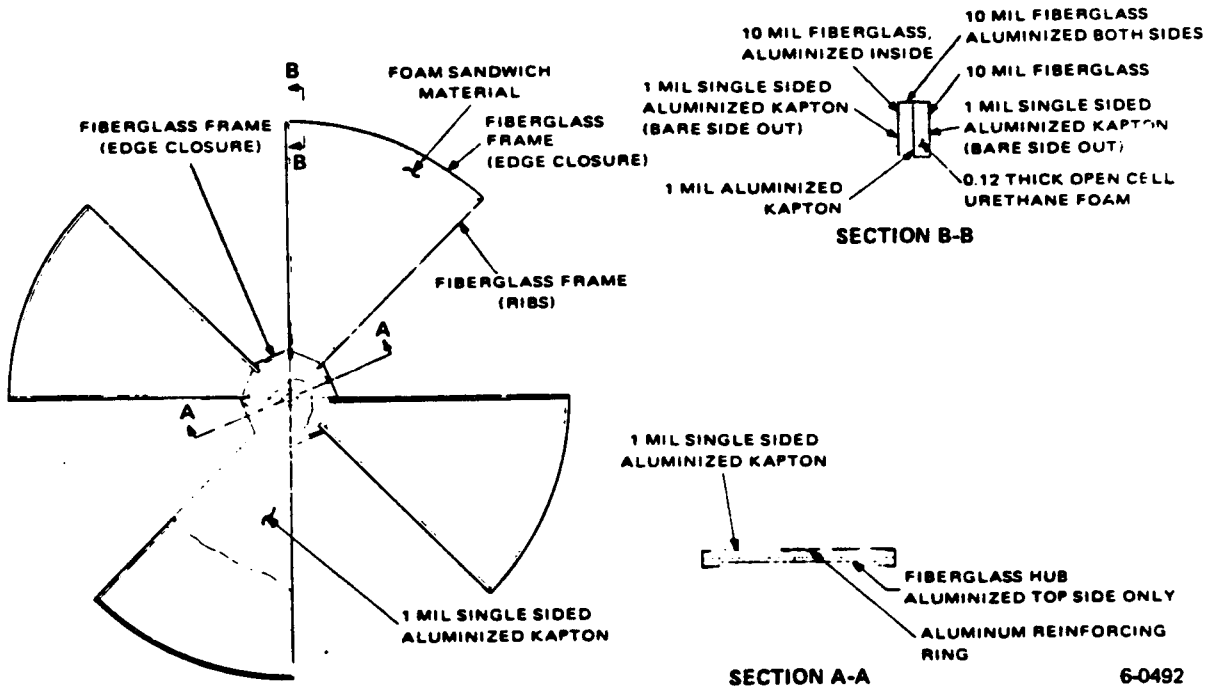

Figure 4.5.3-17. Pinwheel Louver Blade

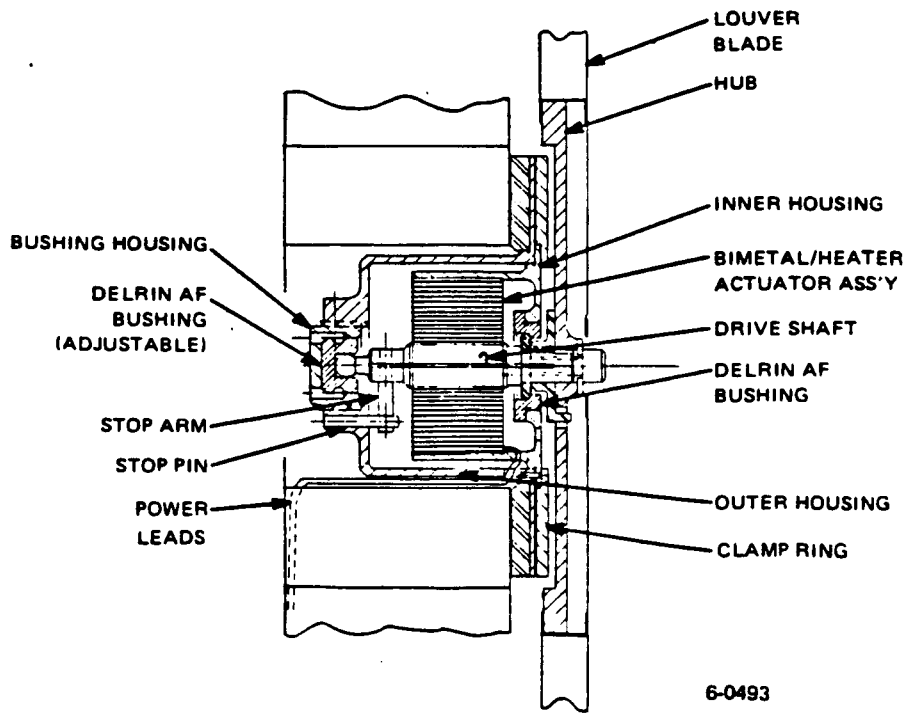

Figure 4.5.3-18. Pinwheel Louver Actuator

The drive shaft assembly is attached to the inner coil of the bimetallic element and carries the stop arm and two bearing surfaces which ride in the Delrin AF bushings, one of which is mounted in bimetallic housing. The bimetallic housing mounts inside the outer housing, which contains the stop element and an adjustable Delrin AF bushing. The whole assembly mounts in a hole in the ESM honeycomb panel and is held in place with a clamp ring. The actuator passive set point is adjusted by loosening the clamp ring, rotating the housing, then retightening the clamp ring.

The stop elements limit the blade rotation at the fully closed and fully open positions (45° of angular rotation). The actuator operation is the same as for the vane louver actuator except that a temperature change of 15°C is required to drive the louver from the fully closed to fully open position.

The Delrin AF bushings are adjusted during assembly to limit the drive shaft axial movement to 10 mils. The bushings also provide low torque louver blade support during 1 g testing; this minimizes the 1 g testing error.

The radiator/guard ring assembly is shown in detail in Figure 4.5.3-19. The radiator consists of a guard ring for louver blade protection and alternating radiator segments of 10 mil second surface aluminized Teflon and 1 mil first surface aluminized Kapton. The Teflon areas are the radiating areas and have a low solar absorptance value ($\alpha < 0.2$). The aluminized Kapton areas are the low emittance areas, which act as insulation when the louvers are closed. The louver blade covers the Teflon areas when in the closed position, and covers the Kapton areas when in the open position.

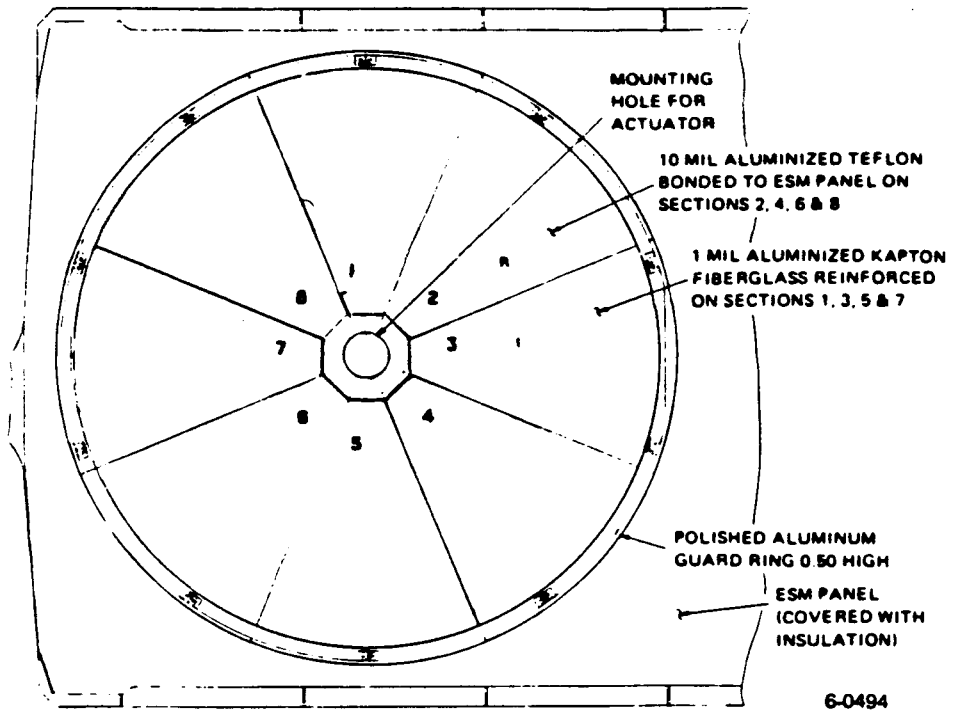

Figure 4.5.3-19. Pinwheel Radiator/Guard Ring Assembly

With the pinwheel louver open, the radiating capacity is approximately 25 to 30 watts. With the louver closed, approximately 5 to 7 watts are radiated. The heat rejection rate is linearly proportional to the louver position.

4.5.4.1 Instrument Mounting Platform (IMP)

The thermal provisions for the IMP and for the IMP-mounted instruments are summarized in Table 4.5.4-1. The open construction of the basic platform (shown in Figures 4.2.4-1 and 4.2.4-3) allows the baseplate of any IMP-mounted instrument to be used as a radiator to the space environment. The construction also retains adequate inter-structure thermal (conductive) coupling to reduce structure thermal gradients.

The IMP provides mounting for the AVHRR/3, IMU, HIRS/3, SSD and ESA. A six-vane, venetian-blind type louver assembly covers the open structure opposite the mounting areas (baseplates) of the AVHRR/3 and the HIRS/3. Multi-layer insulation blankets enclose the remainder of the structure.

The outermost layer of each blanket is a 2-mil thick, second surface, aluminized teflon sheet. The IMP is thermally isolated from the ESM at its attachment points, and the temperature of its blanketed central support strut is maintained near to the IMP structure temperature. This latter control is provided by a differential type TCE controller. The structure temperature, itself, is maintained above 14°C by two heater-type controllers.

TABLE 4.5.4-1. IMP THERMAL PROVISIONS

Item	Item-IMP Attachment	Thermal Control Methods	TCE Set Point		Item Orbit Average Power	Radiator Area
			Htr	Lvr		
IMP Structure	-	A E F	15	-	0	0
Long Strut	Ball Joint Insulators	C E	*	-	0	0
Short Strut	Ball Joint Insulators	E	-	-	0	0
Y-Axis Joints	Ball Joint Insulators	E	-	-	0	0
Porro Prism	Bracket with PC Isolators	E	-	-	0	0
ESA	Bracket with PC Isolators	A E H	15	-	1.2	9.0
SSD	Bracket with Hard Mounting	E H	-	-	0	0
IMU	PC Conical Seats	A D E F H	30	-	31.0	136.5
AVHRR/3	Hard Mounting	B D E F G H I	13	15	28.1	210.2
HIRS/3	Hard Mounting	B D E F G H I	13	15	22.6	127.1

A Heater-type TCE Controller
B Dual-type TCE Controller
C Differential-type TCE Controller
D Internally (Vendor-provided) Controlled Heaters
E Multi-layer Insulation Blanket(s)
F Fixed Sunshade
G Deployable Sunshade
H Passive (Fixed-Area) Radiator
I Louver/Radiator Assembly

PC: Glass-filled Polycarbonate
HTR: Heater
LVR: Louver
Temperatures in degrees C; Power in watts; Areas in sq. inches.

A three component sunshade (Figure 4.2.4-7) consisting of a main, fixed sunshade (Figure 4.2.4-8) and two deployable (±Y) wings is attached to the IMP and IMP louver assembly frame. The fixed sunshade shields the louver vanes and frame, the instrument radiator baseplates, and the IMU from direct solar irradiation for orbital sun-angles less than 80°. This shade is constructed from a foam sheet material sandwiched between an outer layer of second-surface

Kapton-aluminum and an inner layer of double-sided aluminized Kapton. The purpose of the deployable components of the sunshade is to minimize direct insolation on the -X faces of the AVHRR/3 and HIRS/3 radiant cooler doors. These flexible shades are each constructed from two reinforced, black Kapton sheets.

Instruments provided with louver-modulated radiators (baseplates) are conductively coupled to the IMP via special spider adapters and are provided with internal heating elements. Such a configuration permits maintenance of the baseplate temperature at a temperature near to that of the IMP structure at all times. This regulation is provided for each instrument by a single, dual-type TCE controller. With this near constant IMP/instrument interface temperature (15°C), thermal blankets and fixed radiators located on other surfaces of the package passively maintain the instrument within its allowable temperature limits.

The ESA, attached to a mounting bracket which is thermally isolated from the IMP, is essentially under passive thermal control. A small, fixed-area radiator and a multi-layer insulation blanket establish this control. An attached heating element, driven by a heater type TCE controller, prevents the ESA temperature from falling below 14°C.

The SSD is attached to a small mounting bracket which is clamped to the IMP structure. The complete assembly is covered with multi-layer insulation blankets. Its exposed sensor area is covered with a special silver finish. These passive elements maintain the detector temperature near to the temperature of the IMP structure.

The IMU is thermally isolated from the IMP via a special mounting technique and is finished with a white paint. The -X faces of the package and segments of adjacent faces are exposed to the local spacecraft and space environments, while the other surface areas are covered with a multi-layer thermal blanket. Primary thermal control for the IMU is provided by an internal Temperature Control Amplifier (TCA) which closely regulates the temperature of the IMU's sensor support block (near 47°C). The TCA controls block-mounted heaters which are capable of supplying maximum powers of approximately 24.0 watts during the mission ascent phase and 6.7 watts during normal, on-orbit operations. Heating elements attached to the exposed external -X surface of the IMU cover maintain the average on-orbit cover temperature near 30°C. This latter heater is regulated by a heater-type TCE controller. With this external control, the TCA operates near the midpoint of its dynamic control range ensuring positive regulation of the sensor block temperature. The external heater power required to maintain the specified cover temperature is dependent on the basic electrical dissipation within the IMU and is adjusted by the application of small multi-layer insulation blankets (patches) to the exposed radiator surfaces. The on-orbit performance goal is to have the TCE controller supply 45% of its maximum power (a 45% duty cycle) while the TCA is near the midpoint of its control range.

The IMU also contains a gyro make-up heater on its sensor support block. This heater is automatically activated when any gyro is commanded off-line and is deactivated by any gyro turn-on command. The power provided is equal to the dissipation within a single gyro assembly.

An additional external heater circuit on the -X face of the IMU chassis cover provides means for preconditioning the IMU TCA voltage (power output) prior to liftoff. This heater is used as necessary to achieve an immediate prelaunch TCE voltage near 8V. This action promotes positive TCA control of the sensor block temperature during the mission ascent phase.

4.5.4.2 Equipment Support Module (ESM)

The basic form of the ESM is that of an orthogonal prism with pentagonal cross-section. The module is constructed from thick aluminum honeycomb panels over an aluminum framework. The lateral panels (faces) of the prism (designated No. 1, No. 3, No. 4, No. 5 and No. 6) are parallel to the Z axis of the spacecraft; the end panels (No. 2 and No. 7) are perpendicular to that axis. The pentagonal cross-section is derived from that of a regular hexagon by the replacement of two adjacent edges with a single edge (chord). The edge so constructed corresponds to panel No. 1.

On-orbit, the +Z axis of the spacecraft is maintained parallel to the positive orbit normal, and the +X axis (coincident with the outward normal to panel No. 1) is continuously directed to the earth. These constraints place the spacecraft velocity in the direction of the spacecraft's -Y axis (parallel to the outward normal to panel No. 3). In addition, the five lateral panels of the module are always perpendicular to the orbital plane, while the two end panels are always parallel to the plane.

The nominal 450-nm altitude and 98.7° inclination of the spacecraft's circular orbit (plus launch constraints) produce a potential orbital sun-angle range from 0° to 80° for the ATN mission. (The orbital sun-angle, OSA, is defined to be the angle between the positive orbit normal and the direction to the sun.) This OSA range yields orbital fractional sun-times ranging from 1.000 ($0° \leq OSA \leq 27.8°$) to 0.657 (OSA = 80°). The motion of the earth-oriented ATN in its orbit induces an apparent solar rotation about the spacecraft's +Z axis in a direction counter to that of the spacecraft's motion. The lateral ESM panels are, thus, successively exposed to and occulted from solar irradiation as the spacecraft traverses its orbit.

The surface of panel No. 2 is parallel to the orbit plane, but under normal conditions, the sun never enters the half-space determined by its outward normal. Panel No. 7 is not exposed to the space environment, but views the volume enclosed by the ESM/RSS connection truss.

4.5.4.2.1 Internal Equipment Thermal Control

The lateral ESM panels (exclusive of panel No. 1) are partitioned into a total of 16 thermal control zones. (See Figure 4.2.4-14.) Internally, these zones measure approximately 20 inches x 20 inches and, except for the zone designated 6+Z, thermal control for each is provided by a unique dual type TCE controller. These 15 zones accommodate pinwheel type louver/radiator assemblies on their outboard surfaces and heaters on their inboard sides. Zone 6+Z is serviced by a single heater type TCE controller. All external, space exposed, ESM surfaces not occupied by louver assemblies or spacecraft equipment are covered with a multi-layer insulation blanket. The outermost layer of this blanket is a

0.5-mil thick, second-surface, Kapton-aluminum sheet. The external surface of panel No. 7 is finished with a vapor-deposited gold tape. All exposed inboard surfaces and the equipment are covered with a black paint.

This configuration provides closely regulated temperature control of the internally mounted ESM equipment. When fully open, each louver/radiator assembly at 15°C can radiate approximately 25.6 watts of equipment dissipation to the space environment with no external loading. When fully closed, a minimum dissipation of 5.5 watts is required to maintain a temperature of 5°C in any thermal control zone.

The thermal control features of the ESM and internally mounted ESM equipment are given in Table 4.5.4-2.

Panel No. 7 acts as a thermal shield which minimizes ESM heat leakage and protects the ESM from the high radiative heat flux emanating from the AKM housing during the ascent soak-back period. The titanium fabricated ESM/RSS connection truss also serves to decouple this panel from local external thermal influences.

4.5.4.2.2 External Equipment Thermal Control

The external surface of ESM panels No. 1 and No. 2 provide mounting for additional spacecraft equipment and instruments.

The earth-oriented panel No. 1 accommodates an assortment of the ATN antennas. Thermal control of these components is completely passive, being accomplished by means of insulative spacers, multilayer insulation blankets, and special surface finishes.

4.5.4.3 ESM/RSS Connection Truss

This truss provides housing for part of the AKM case and supports the SEM Total Energy Detector (TED) and RCE C/D heater subsystem controller chassis. The open, titanium construction of the truss additionally serves to reduce the ESM-to-RSS thermal coupling. (See Figure 4.2.4-20.)

The RCE heater controller chassis is located on the earth-facing side of the truss. It provides mounting for that system's controller modules. Its basic configuration consists of two parallel, rectangular plates separated by C-channels. The controller modules and other dissipating elements are mounted on the inside surface of the outboard plate; the outside surface of this plate, which serves as a radiator, is covered with a 2-mil thick, second surface, teflon-aluminum sheet. Additional C-channels attached to the inboard plate provide for mounting of the chassis directly to the truss structure.

Both of the above items are protected from the AKM thermal soak-back by the intervention of multilayer insulation blankets between their mounting brackets and the enclosed connection truss volume. A low emittance tape is also applied to the truss elements in the vicinity of the mounting points.

TABLE 4.5.4-2. ESM THERMAL PROVISIONS

ESM Panel	Internal Equipment	TCE Controller	Orbital Average Power Dissipation (Watts)		
			Min	Nom	Max
1-Z	DCS-2/RPU	None	0.00		20.00
	BTX-1		7.24		7.24
	BTX-2		0.04		0.04
	TCE [3]		0.30		0.30
	RFS		0.00		0.00
1-ZC	DPD	None	0.00		0.00
	DCS-2/SPU-A		0.00		5.00
	YRW		3.13		3.13
	RFF-2		0.00		0.00
1+ZC	GRD-1	None	2.00		2.00
	GRD-2		2.00		2.00
	DCS-2/SPU-B		0.00		5.00
	RFH		0.00		0.00
	RFF-1		0.00		0.00
1+Z	SEM-2/DPU	None	0.00		5.40
	SBUVE		0.00		9.00
	RFT-1		0.00		0.00
	RFH-2		0.00		0.00
2	BRW	None	0.05		0.05
	SSE		1.28		1.28
	TCE [7]		0.70		0.70
3-Z	AIP	12	0.03		3.33
	RRW		3.13		3.13
	RFF-3		0.00		0.00
	RFF-5		0.00		0.00
3-ZC	CPU-1	11	6.00		8.50
	CPU-2		6.00		8.50
	RFF-4		0.00		0.00
3+ZC	CIU	10	14.50		14.50
	RXO		3.90		3.90
	CXU		0.35		0.35
3+Z	SARR Receiver	35	0.00		10.60
4-Z	DTR-1	15	8.62		*
	DTR-2		0.00		*
4-ZC	DTR-3	14	0.00		*
	XSU		3.59		*
	TCE [2]		0.20		0.20
4+ZC	DTR-4	13	0.00		*
	DTR-5		0.00		0.17
	TCE [2]		0.20		0.20
4+Z	SARR Transmitter	34	0.10		23.50
	TCE [1]		0.10		0.10

TABLE 4.5.4-2. ESM THERMAL PROVISIONS (Continued)

ESM Panel	Internal Equipment	TCE Controller	Orbital Average Power Dissipation (Watts)		
			Min	Nom	Max
5-Z	MIRP	18	5.89		5.89
	DAU		5.49		5.49
	TCE [1]		0.10		0.10
5-ZC	PSE	17	9.10		*
5+ZC	PSE	16	(9.10)		(*)
	VTX-1		0.04		13.50
	VTX-2		0.04		0.00
	TCE [1]		0.10		0.10
	RFS		0.00		1.00
5+Z	SARP-2/SPU	36	0.00		17.00
	TCE [3]		0.30		0.30
	RFF-1		0.00		0.00
6-Z	STX-2	21	0.04		*
	STX-4		0.04		0.04
6-ZC	STX-3	20	0.04		*
	SCU		0.10		0.10
	TCE [7]		0.70		0.70
6+ZC	STX-1	19	0.04		19.40
	TIP		2.71		2.71
	RFS		0.00		1.00
6+Z	SARP-2/RPU	37	0.00		17.00
	RFF-3		0.00		0.00
	RFT/RFH		0.00		0.00
7	PRW	None	3.13		3.13
1	SRA	None	0	0	0
	SLA		0	0	0
	UDA		0	0	0
	VDA		0	0	0
	SBUV/2		0.0	3.0	3.0
	AMSU-A2		0.0	34.6	34.6
	AMSU-B		0.0	90.0	90.0
2	MEPED	31	0.0	3.7	3.7
	AMSU-A1		0.0	81.4	81.4

Additionally, these shields protect the folded solar array panels from the high radiative heat flux off the contained AKM hemisphere during the soak-back period and prevent exposure of ESM Panel No. 7 to solar irradiation.

4.5.4.4 Reaction Control Equipment Support Structure (RSS)

The thermal control features of the RSS and of the RSS-mounted equipment are summarized in Table 4.5.4-3. Equipment arrangement on the RSS is given in Figure 4.2.4-29.

The RSS is a cylindrical structure which houses the AKM and provides support for the RCE. In addition, it provides mounting for the six battery packs, the Battery Charge Assembly (BCA), three Battery Reconditioning Units (BRUs), and the Solar Array Drive Electronics (ADE). Before deployment of the Solar Array Assembly, the RSS offers support to that major assembly's long boom, Solar Array Drive (SAD) and mast. The long boom of the SAA is hinged near the +Z end of the -X side of the RSS. A primary function of the RSS thermal design is to limit the heat transfer to the above equipment and assemblies during the period immediately following AKM ignition.

Externally, the basic RSS is finished with a 5-mil thick, second surface, teflon-aluminum tape. The initially low ratio of solar absorptance to thermal emittance offered by this finish can cause low on-orbit structure temperatures. Contamination acquired during the ascent phase and degradation from exposure to solar ultraviolet irradiation, however, quickly increase the surface's solar absorptance. This change results in more moderate on-orbit RSS temperatures.

Internally, the basic RSS is finished with a black paint. Approximately 50% of this surface is covered by a thermal shield. The black paint serves to maximize the exposed RSS radiative couplings, and this provides for more uniform on-orbit RSS temperatures. The thermal shield decouples the RSS from the AKM housing. During ascent, it attenuates the effects of AKM thermal soak-back; on-orbit, it prevents heating of the RSS due to radiative exchange with the spent AKM housing which is subject to direct solar irradiation. The shield is fabricated from a 1-mil thick, aluminized Kapton sheet, and its aluminized side faces the AKM.

A solar shield covers the annular gap between the AKM nozzle and the +Z circumference of the RSS. This shield prevents the entrance of solar radiation into the interstitial clearance volume and minimizes the deposition of contaminants onto the RSS internal surfaces. The external surface of this shield is finished with a clear anodic coating; the internal finish is polished aluminum.

4.5.4.4.1 Reaction Control Equipment (RCE)

The nitrogen thrusters (8), pressure regulator (1) and latch valve (1) of the RCE are conductively isolated from the RSS and are enclosed in multilayer insulation blankets. This configuration minimizes both internal heat loss and heat gain from variable, external sources. A redundant pair (designated A and B) of thermostatically controlled heater circuits is attached to each of these 10 RCE components — a total of 20 thermostat/heater pairs at 2 pairs (A and B) per component. These active elements maintain component temperatures above 5°C. The mechanical thermostats cycle their associated heaters ON/OFF to achieve this purpose. Two spacecraft commands provide for the enabling or the

TABLE 4.5.4-3. RSS THERMAL PROVISIONS

Item	Item-RSS Attachment	Thermal Control Methods	Orbit Average Power			Item Radiator Area
			Min	Nom	Max	
RSS Structure	-	A	0	0	0	0
Battery Pack [6]	Struts with PC Isolators	B C D G	9.1	10.2	10.2	83.0
Battery Reconditioning Unit [3]	Bracket with PC Isolators	B C F J	0	0	16.5	87.5
BCA/Radiator	Bracket with PC Isolators	B C F	0	18.9	18.9	455.4
ADE	Bracket with PC Isolators	B C E F	2.3	2.3	2.3	8.0
Nitrogen Engine Assembly [8]	Bracket with PC Isolators	C H	0	0	0	0
Pressure Regulator Assembly	Bracket with PC Isolators	C H	0	0	0	0
Latch Valve Assembly	Bracket with PC Isolators	C H	0	0	0	0
Nitrogen Tank [2]	Hard Mounted	-	0	0	0	0
Reaction Engine Assembly [4]	Hard Mounted	B C	0	0	0	0
Hydrazine Tank [2]	Bracket with PC Isolators	C I	0	0	0	0
Isolation Valve [2]	Bracket with PC Isolators	C I	0	0	0	0
Hydrazine Line [2]	Bracket with PC Isolators	C I	0	0	0	0
TED	G-10 Spacers	C E F	0.0	1.1	1.1	TBD
C/D Controller Chassis	PC Isolators	A C F	0.0	8.0	10.0	50.0
Solar Array	PC Isolators	F	-	-	-	(Array)
Partial Shunt Assembly [70]	G-10 Sheet from Solar Array	F	-	-	-	11.8
SATCU	G-10 Spacers	C	0.6	0.6	0.6	0
SAD	PC Isolators from SA Boom	C E F	6.3	6.3	10.8	20.8

[ ] Quantity
A Teflon/Aluminum Taping
B IITRI S13-G/LO
C Multi-layered Insulation Blanket
D Dual-type TCE Controller
E Heater-type TCE Controller
F Passive (Fixed-Area) Radiator
G Louver/Radiator Assembly
H A/B Heater System
I C/D Heater System
J Thermostatted Heater
K Thermal Shield

inhibiting of the complete set of 10 A units, and an identical commanding capability is available for the complete B set. The ON actuation temperature for the A set is approximately 12°C; for the B set, this value is approximately 8°C.

Propellant freezing and freeze/thaw cycling in the unvented portion of the RCE hydrazine subsystem is prevented by active heating of those subsystem components which could retain residual hydrazine. These components are the propellant tanks (2), tank to isolation valve lines (2) and isolation valves proper (2).

This control is implemented on each of these 6 RCE components by conductively isolating each of them from the RSS, by using multi-layer insulation blankets, and by attaching a redundant pair of local heater circuits (designated C and D) to each component. Each heater circuit is regulated by remote, unique proportional controllers responsive to a unique sensor (control thermistor) located on the affected component. There are a total of 12 sensor/heater pairs - 6 components x 2 systems (C and D). Two spacecraft commands allow enabling and inhibiting of the complete set of 6 C-system triples. An identical commanding scheme exists for the D-system. The C-system maintains component temperatures at approximately 15°C, while the D-system maintenance level is approximately 9°C. The controllers are located on a special chassis which is mounted on the ESM/RSS connection truss.

All remaining RCE components, e.g., the Fill/Drain Valve Assembly, are hard mounted to the RSS. Components located on the RSS, but properly belonging to other spacecraft systems, are afforded thermal isolation from that structure and are provided with independent thermal control. The control techniques used for these components are described below.

4.5.4.4.2 Battery Packs

Although located at different azimuthal positions around the RSS circumference, each of the six battery packs has the same thermal control provisions. This is possible because of the active character of the basic thermal design. The design utilizes a dual type TCE controller which regulates both a heater and a louver/radiator assembly. The anti-solar (-Z) surface of the pack is finished with a white paint and is used as a radiator. This radiator is covered by the TCE-controlled louver assembly (two louver vanes per assembly). The remaining surfaces are covered by a multi-layer insulation blanket. The outermost layer of this blanket is a 2-mil thick, second surface, teflon-aluminum sheet. The TCE-controlled heater is applied to the +Z surface of the pack beneath the blanket. The above combination of elements prevents battery pack temperatures from falling below 0°C under normal on-orbit conditions.

4.5.4.4.3 Battery Charge Assembly (BCA)

The BCA consists of a flat, earth-oriented, radiator plate which accommodates three Battery Charge Units near the center of its active radiating surface. Its reverse (inboard) surface is covered by a multi-layer insulation blanket which further decouples the BCA from the RSS and attenuates the effect of AKM thermal soak-back during spacecraft ascent. The active radiator surface and

the three charging units are finished with a white paint. Special techniques for heat-sinking these units to the radiator plate are also employed. These considerations and the radiator sizing prevent excessively high temperatures at peak battery charging times; the earth-directed orientation prevents excessively low temperatures during orbital nighttime and at times of minimal battery charging.

4.5.4.4.4 Battery Reconditioning Unit (BRU)

The three BRUs are located at distinct positions around the RSS.

4.5.4.4.5 Array Drive Electronics

Thermal control of the Solar Array Drive Electronics (ADE) includes a small, fixed-area radiator located on the unit's outboard face. This radiator is finished with white paint. The remaining external surface area is covered with a multi-layer insulation blanket. These passive elements are complemented with a heater type TCE controller which maintains the ADE baseplate temperature above 9°C.

4.5.4.5 Spacecraft/Launch Vehicle Adapter

The adapter section thermal environment during launch consists of conduction coupling to the RSS and the first stage booster, radiation coupling to the heat shield, second stage motor, RSS, and first stage booster, and aerothermal heating after heat shield separation.

At launch, all initial temperatures are at the air conditioning temperature of approximately 20°C. Heat inputs during launch consist of the radiation heating from heat shield (this is negligible), aerothermal heating after heat shield separation (this is also negligible) and prior to first stage/second stage separation, and conduction heating from first stage.

Since the adapter is simply a mechanical adapter and stays with the first stage, its temperature is relatively unimportant and does not vary much from lift-off to second stage separation. Hence, the thermal design of adapter assembly is of minor concern.

4.5.4.6 Solar Array Assembly and Support (SAA/S)

This assembly consists of a Solar Array (SA), a mast assembly, the Solar Array Drive (SAD), and a long support boom. The mast assembly includes an array cant mechanism, the Solar Array Telemetry Commutator Unit (SATCU), and a short boom. Partial Shunt Assemblies (PSAs) are also mounted to the rear surface of the SA. Each panel includes seven such assemblies.

When deployed, the normal to the active surface of the SA is at an angle of 54° from the assembly's axis of rotation. This axis is parallel to the Z axis of the spacecraft but is radially displaced from it a distance of 24.6 inches. The fully extended array can produce extensive solar shadowing on many other spacecraft assemblies particularly for low orbital sun-angles.

4.5.4.6.1 Solar Array (SA)

This assembly consists of ten solar-cell panels interconnected by locking hinges with dampers. The dampers are covered with vapor-deposited aluminum tape to limit predeployment cooling. On orbit, overall thermal control is achieved in a passive manner. The anti-sun side of the array is finished with a black paint to minimize reflections into instrument sensor ports.

Power shunt components which serve to dissipate excess array generated power are mounted on heat sinks which are thermally decoupled from the backside of the array. There are 12 such heat sinks per panel (96 total).

High and low range temperature sensors used for telemetric purposes are located on the reverse side of the array near the rotational axis.

4.5.4.6.2 Mast Assembly

This assembly serves to mechanically couple the SA to its drive mechanism (SAD) and to provide mounting for the SATCU. The boom segment is thermally decoupled from the SAD with insulative spacers and is completely enclosed in a multilayer insulation blanket.

Thermal control of the SATCU is achieved by thermally isolating it from the mast assembly and by multilayer insulation blankets.

4.5.4.6.3 Solar Array Drive (SAD)

The SAD is thermally decoupled from the mast assembly and long support boom by insulative spacers. Passive thermal control of the unit is provided by a small, annular radiator (finished with a white paint), by two white-painted commutator block radiators, and by multi-layer insulation blankets. Exposed surfaces not amenable to blanketing are covered with a vapor-deposited gold tape. A heater type TCE controller is used to maintain the SAD temperature above 9°C.

4.5.4.6.4 Long Support Boom

The temperature of this item is relatively unimportant. Adequate thermal control is achieved by wrapping it in a multi-layer insulation blanket.

4.5.5 THERMAL CONTROL SUBSYSTEM TELEMETRY

Telemetry data for the TCS includes both operational status data of the active thermal control elements and basic temperature data. Operational status data is available for all of the TCE controllers, while more basic status data (enable/inhibit) is provided for the RCE A/B and C/D heating systems.

4.5.5.1 <u>Operational Status Telemetry</u>

4.5.5.1.1 TCE Controller Status

Dual type TCE controllers have two operational status telemetry points: one for the primary heating circuit, and one for the heating circuit which provides

for louver actuation. The differential-type TCEs each have a single such status point. Controller status is determined by the telemetered voltage noted at these points.

When a TCE controller is inhibited, its associated status voltages are a constant value of 0.0V. When enabled, a fully ON heater status (primary heater or louver actuator heater) is indicated by a constant telemetry value near 2.4V, while a constant value near 4.7V is representative of a fully OFF heater condition. Features incorporated in the design of the dual type TCE controller preclude the event of both of its telemetry status points to indicate the fully ON status at the same time. A fully ON primary heater status signifies that the controller is supplying maximum available heater power for maximum heating, while this status for the louver actuator heater indicates that the controlled louver assembly is fully open and is providing maximum cooling.

When a TCE is in its linear range of operation, the status voltage for that TCE oscillates between the fully ON and fully OFF values. While the relatively slow telemetry sampling interval of 32 seconds does not permit total reconstruction of the actual controller status, these data collected over an orbit or longer period of time can be used to determine the controller's average status value. This average value can be used to estimate the average power supplied to a primary heater circuit or the degree of activity of a louver assembly.

A complete list of the TCE controller status telemetry points is given in Table 4.5.5-1.

4.5.5.1.2 RCE A/B and C/D Heating System Status

Operational status for the RCE A, B, C and D heater systems only provides an indication that the respective system is enabled or is inhibited.

The digital telemetry points for these items are defined in Table 4.5.5-2.

4.5.5.2 <u>TCS Temperature Telemetry</u>

Temperature telemetry data channels for the TCS are given in Table 4.5.5-3. Temperature telemetry channels and other telemetered thermal status indicators which originate within spacecraft bus equipment and instrument packages are not included in this table.

TABLE 4.5.5-1. TCE CONTROLLER STATUS TELEMETRY LIST (1 of 3)

TCE No.	Function*	Controlled Item	TIP Telemetry Channel	Data Type	TIP Minor Frames
1	H	Battery Pack 1A	201	32	201
1	L		209	32	209
2	H	Battery Pack 1B	217	32	217
2	L		225	32	225
3	H	Battery Pack 2A	233	32	233
3	L		241	32	241
4	H	Battery Pack 2B	081	32	081
4	L		089	32	089
5	H	Battery Pack 3A	432	16-2	048 208
5	L		440	16-2	056 216
6	H	Battery Pack 3B	448	16-2	064 224
6	L		456	16-2	072 232
7	-	--	--	--	--
7	-	--	--	--	--
8	H	IMP Long Strut	207	32	207
9	H	ESA	215	32	215
10	H	ESM Zone 3+ZC	082	32	082
10	L		090	32	090
11	H	ESM Zone 3-ZC	162	32	162
11	L		170	32	170
12	H	ESM Zone 3-Z	178	32	178
12	L		186	32	186
13	H	ESM Zone 4+ZC	194	32	194
13	L		202	32	202
14	H	ESM Zone 4-ZC	210	32	210
14	L		218	32	218
15	H	ESM Zone 4-Z	226	32	226
15	L		234	32	234
16	H	ESM Zone 5+ZC	242	32	242
16	L		008	32	008

TABLE 4.5.5-1. TCE CONTROLLER STATUS TELEMETRY LIST (2 of 3)

TCE No.	Function*	Controlled Item	TIP Telemetry Channel	Data Type	TIP Minor Frames
17	H	ESM Zone 5-ZC	016	32	016
17	L		024	32	024
18	H	ESM Zone 5-Z	032	32	032
18	L		040	32	040
19	H	ESM Zone 6+ZC	048	32	048
19	L		056	32	056
20	H	ESM Zone 6-ZC	064	32	064
20	L		072	32	072
21	H	ESM Zone 6-Z	080	32	080
21	L		088	32	088
22	-	--	--	--	--
22	-		--	--	--
23	-	--	--	--	--
23	-		--	--	--
24	H	AVHRR/3	192	32	192
24	L		200	32	200
25	H	HIRS/3	208	32	208
25	L		216	32	216
26	H	IMU	224	32	224
27	H	ADE	232	32	232
28	H	SAD	240	32	240
29	H	TED	003	32	003
30	-	--	--	--	--
30	-	--	--	--	--
31	H	MEPED	019	32	019
32	H	IMP (+X)	027	32	027

TABLE 4.5.5-1. TCE CONTROLLER STATUS TELEMETRY LIST (3 of 3)

TCE No.	Function*	Controlled Item	TIP Telemetry Channel	Data Type	TIP Minor Frames	
33	H	IMP (-X)	035	32	035	
34	H	ESM Zone 4+Z	387	16-2	003	163
34	L	(SARR Transmitter)	392	16-2	008	168
35	H	ESM Zone 3+Z	400	16-2	016	176
35	L	(SARR Receiver)	408	16-2	024	184
36	H	ESM Zone 5+Z	416	16-2	032	192
36	L	(SARP-2 SPU)	424	16-2	040	200
37	H	ESM Zone 6+Z (SARP-2 RPU)	467	16-2	083	243

*Function: H = Heater
L = Louver

TABLE 4.5.5-2. RCE C/D HEATER SYSTEM STATUS TELEMETRY

Heater System	Data Type	Telemetry Channel
A	DIGB	159
B	DIGB	214
C	DIGB	223
D	DIGB	245

Telemetry Value: 0 = System Inhibited
1 = System Enabled

TABLE 4.5.5-3. TCS TEMPERATURE TELEMETRY LIST

Monitored Item	TIP Telemetry Channel	Data Type	TIP Minor Frames			
ESM Panel No. 1	361	16-1	115	275		
ESM Panel No. 2	369	16-1	114	274		
ESM Panel No. 3	377	16-1	113	273		
ESM Panel No. 4	278	16-1	071	151	231	311
ESM Panel No. 5	375	16-1	098	258		
ESM Panel No. 6	383	16-1	102	262		
IMP No. 1 (+X)	171	32	171			
IMP No. 2 (-Y)	179	32	179			
IMP No. 3 (+Y)	004	32	004			
RSS (-X,-Z) (High Range)	253	32	253			
REA No. 1 Inlet	195	32	195			
REA No. 2 Inlet	303	16-1	013	173		
REA No. 3 Inlet	287	16-1	011	171		
REA No. 4 Inlet	351	16-1	140	300		
REA No. 1 Loop	187	32	187			
REA No. 2 Loop	263	16-1	083	243		
REA No. 3 Loop	163	32	163			
RCE C/D Controller Chassis	269	16-1	056	216		
PTA-1 (-X,-Y) Hydrazine Tank	203	32	203			
PTA-1 Hydrazine Line	295	16-1	012	172		
PTA-1 Isolation Valve	343	16-1	136	296		
PTA-2 (+X,+Y) Hydrazine Tank	211	32	211			
PTA-2 Hydrazine Line	322	16-1	107	267		
PTA-2 Isolation Valve	277	16-1	005	165		
NEA No. 5 Valve	177	32	177			
NEA No. 6 Valve	030	32	030			
NEA No. 7 Valve	237	32	237			
NEA No. 8 Valve	244	32	244			
NEA No. 9 Valve	249	32	249			
NEA No. 10 Valve	221	32	221			
NEA No. 11 Valve	229	32	229			
NEA No. 12 Valve	007	32	007			
Nitrogen Pressure Regulator	251	32	251			
Nitrogen Latch Valve	250	32	250			
PT-1 (-X,+Y) Nitrogen Tank	243	32	243			
PT-2 (+X,-Y) Nitrogen Tank	235	32	235			

Blank Page

4.6 POWER SUBSYSTEM

The Power Subsystem comprises all the satellite equipment required for generation, storage, control, and distribution of electrical power. This subsystem includes a photovoltaic solar-cell array, three nickel-cadmium secondary batteries, and power conditioning electronics. The Power Subsystem elements are connected in a direct energy transfer configuration, using solar array partial-shunt regulation and a battery voltage boost regulator.

4.6.1 POWER SUBSYSTEM DESCRIPTION

A functional block diagram of the ATN-KLM Power Subsystem is given in Figure 4.6.1-1. As shown, the Power Subsystem consists of the following elements:

- Solar Array (SA)
- Solar Array Telemetry Commutator Unit (SATCU)
- Solar Array Drive (SAD)
- Array Drive Electronics (ADE)
- Batteries - three each
- Battery Charge Assembly (BCA)
- Power Supply Electronics (PSE)
- Controls Power Converter (CPC)
- Battery Reconditioning Units - three each (BRU)

The physical description of these Power Subsystem components is summarized in Table 4.6.1-1.

The solar array consists of 10 flat structurally identical solar cell panels. In space, the deployed panels are positioned into a single plane with the surface canted with respect to the spacecraft +Z axis. For a mission in which the spacecraft sun angle range is expected to be 0 to 50° (morning orbits), the cant mechanism will be preset for a 37° angle. For an afternoon mission (with a sun angle range of 40 to 80°) the cant angle will be preset for 22°. Once deployed and canted, the solar array is rotated on a boom about the Z axis once per orbit by the SAD. The rotation of the boom is such that the position of the solar array is essentially motionless in inertial space. The phasing of the array rotation is normally chosen so that the solar cell surfaces are always oriented toward the sun. However, an offset can be implemented by ground commanded changes to constants in the on-board software.

Included on the solar array panels are the partial shunt power transistors. The total partial shunt configuration consists of 140 shunt transistors (2 in parallel with each of 70 solar cell circuits). Each partial shunt circuit is across 3 parallel-connected by 58 series-connected solar cells. The function of the partial shunts is to dissipate excess solar array power by electrically mismatching the upper and lower portions of each cell circuit.

The solar array is rotated by the SAD, which also contains a set of slip rings for transferring signals and power from the solar array to the satellite. The SAD is controlled by the ADE in response to control signals from the Command and Control Subsystem (C&CS).

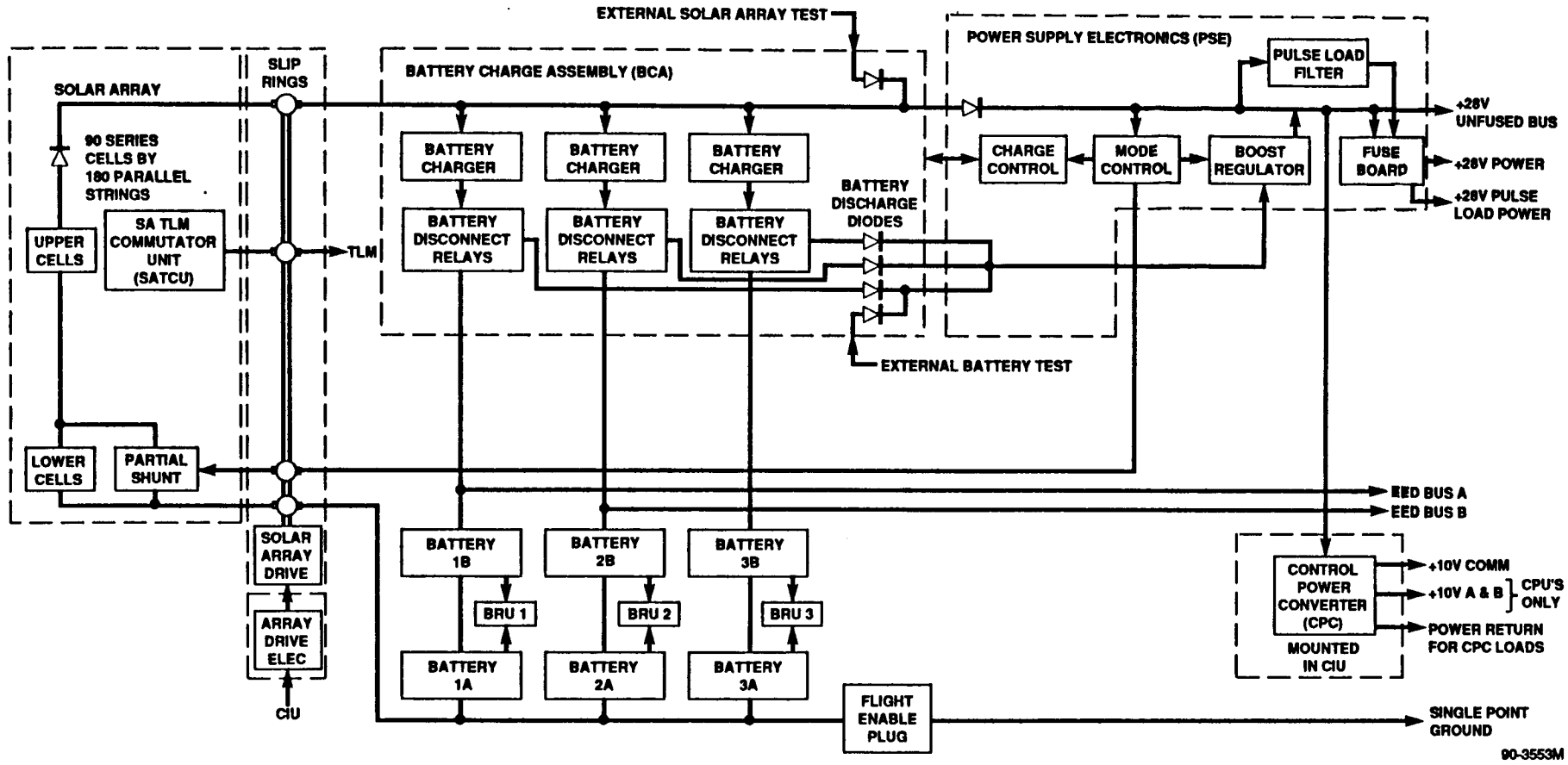

Figure 4.6.1-1. Power Subsystem Functional Block Diagram

TABLE 4.6.1-1. POWER SUBSYSTEM COMPONENTS SIZE AND WEIGHT SUMMARY

Power Subsystem Components	No. Per Satellite	Maximum Size (inches)	Maximum Weight (pounds)
Solar Array Assembly Solar Panels	10	107.5 x 24.2	18.8 each
Solar Array Drive Unit	1	6.0 dia x 13.4 long	15.9 (includes cables)
Array Drive Electronics	1	5.3 x 7.7 x 9.6	5.6
Solar Array Telemetry Commutator Unit	1	16.1 x 3.3 x 1.3	1.2
Batteries			
8-Cell Pack (BA)	3	15.2 x 8.1 x 7.4	39.6 each
9-Cell Pack (BB)	3	16.1 x 8.1 x 7.4	43.6 each
Battery Charge Assembly (Includes Radiator Plate)	1	26.7 x 16.5 x 5	25.5
Power Supply Electronics	1	25.0 x 12.0 x 13.4	43.0
Battery Reconditioning Unit	3	13.0 x 6.75 x 2.17	3.35
Controls Power Converter	1	10.0 x 5.0 x 1.0	2.2
Total Power Subsystem Weight = 541.1 pounds			

In addition to being the source for satellite power during the eclipse portion of the orbit cycle, the batteries provide supplementary electrical power during peak daytime load periods that is beyond the solar array capability. There are three batteries, each made up of 17 series-connected, 47 ampere-hour storage cells. The cells are packaged in six similarly shaped assemblies, three containing nine cells and three containing eight cells.

Each battery has an associated BRU that contains the resistors and control relays for draining the energy from the individual cells during reconditioning operations. In addition, a pull-up resistor allows initial recharge to reduce battery charge regulator thermal dissipation. BRUs are mounted on the RCE Support Structure (RSS) with outward-facing radiators.

The BCA contains the high current elements associated with charging and discharging the batteries. This includes the battery disconnect relays, the discharge diodes, the telemetry sensors for battery charge and discharge current and solar array current, and the current pass elements of the charge regulator (the remainder of the charge control electronics is in the PSE). The BCA is

physically mounted on a radiator plate that is attached to the RSS, close to the batteries and the solar array.

The Power Supply Electronics (PSE) acts as the control and distribution center for the Power Subsystem. In addition to the battery charge-control electronics, the PSE also houses the pulsewidth-modulated voltage boost regulator and mode control circuits. The PSE utilizes these elements and the partial shunts on the array to provide the primary +28-volt regulated bus, as well as a separately filtered +28-volt pulse load bus for the satellite loads. Several automatic fault detection and Power Subsystem protection features are also included within the PSE.

The Controls Power Converter (CPC) is housed within the Controls Interface Unit (CIU). It accepts its input from the +28 volt bus and provides ±10 volts of power for Command and Control Subsystem units. The CPC also supplies a +10-volt interface power bus to the other satellite subsystems.

4.6.2 POWER SUBSYSTEM OPERATION

During normal operation of the Power Subsystem, satellite load power is supplied by either the Solar Array or three 47.0-ampere-hour batteries. In sunlight, the Solar Array supplies the load power directly and provides for battery recharge via the charge regulators. When the Solar Array is in eclipse, the three batteries supply the power for the loads. The batteries are coupled to the primary +28-volt regulated bus through discharge diodes and the boost voltage regulator.

The heart of the Power Subsystem is the Mode Controller which coordinates the operation of the various regulatory elements in the subsystem. The Mode Controller automatically senses voltage changes on the primary bus and sequentially applies drive signals to the appropriate regulatory elements as shown by the regulation profile of Figure 4.6.2-1. Selection and control of the various regulatory elements are carried out within a +0.56/-0.30-volt regulation band as follows:

- When the Solar Array current is insufficient (e.g., during eclipse or when the satellite load current exceeds the available solar array current), the boost regulator is activated and provides the bus regulation.

- When the Solar Array current exceeds the load current but is less that what the three batteries require for charge, then the charge regulators become the regulatory element in the system.

- Finally, when the Solar Array current exceeds both the satellite load current and that needed by the batteries, then regulation is carried out by the action of the partial shunts. The shunt operation provides the exact Solar Array mismatch necessary to ensure the proper load and battery-charge current conditions at the regulated bus.

Battery charge control is performed by the charge regulators in order to protect the batteries from overcurrent and overvoltage conditions. They perform this function by monitoring battery charge current, voltage, and temperature parameters.

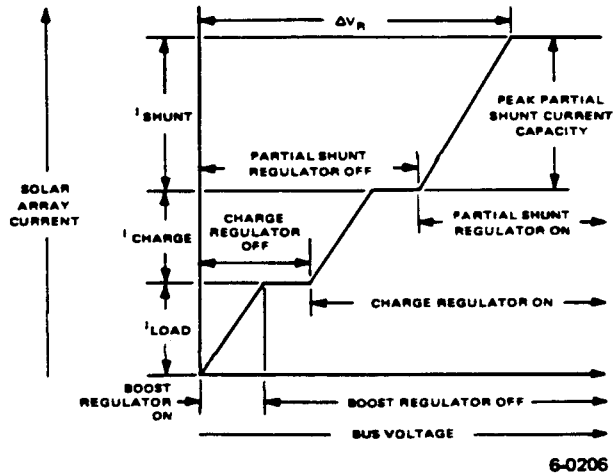

Figure 4.6.2-1. Regulation Profile

4.6.2.1 Normal Three-Battery Operation

For orbits that contain eclipse periods, battery charging is accomplished via a three-level charge regime as shown in Figure 4.6.2-2. Upon entry into sunlight in an orbit, each battery is charged in a constant current mode at an independently commanded rate of 7.5 or 10 amperes. The 7.5-ampere rate will be used when spacecraft loads are relatively light or when the eclipse durations are short. The 10.0-ampere rate will be used for heavier sensor programming and for longer eclipse durations. As a battery approaches a fully charged state, a temperature dependent Voltage Limit (VT) is imposed, which causes the charge current to taper to a lower value. The 8-VT limit values available have been selected taking into account the charge rate used, the depth of discharge, and the cell characteristics. To accommodate a shorted cell in a battery, a level shift capability is provided to shift all eight VT curves downward by 1.45 volts. This ensures that a battery with a shorted cell can continue to contribute during discharge without danger of uncontrolled overcharge during the recharge period. During the charge and discharge period, Power Management Software (PMS) monitors the battery current and provides a running tabulation of the ratio of the charge energy to the discharge energy (C/D). When the actual C/D ratio becomes equal to the desired C/D ratio, i.e., where desired C/D is a function of battery temperature, battery charging is changed from the VT-limited constant voltage mode to an 0.85-ampere constant current trickle charge rate for the balance of the sunlight period. With this charging technique, adequate recharge is achieved in a minimum period of time consistent with low overcharge rates and minimum battery heating. For orbits with no eclipse periods, batteries typically will be trickle charged continuously at the 0.85-ampere constant current rate.

4.6.2.2 Two-Battery Operation

For two-battery operation (during reconditioning or with one battery off-line due to a failure), the scenario is the same except that the constant current charge rate for orbits with eclipse periods is increased by ground command to 12.5 amperes for each battery. This is done to ensure that sufficient recharge energy can be returned to the on-line batteries during the sunlight period.

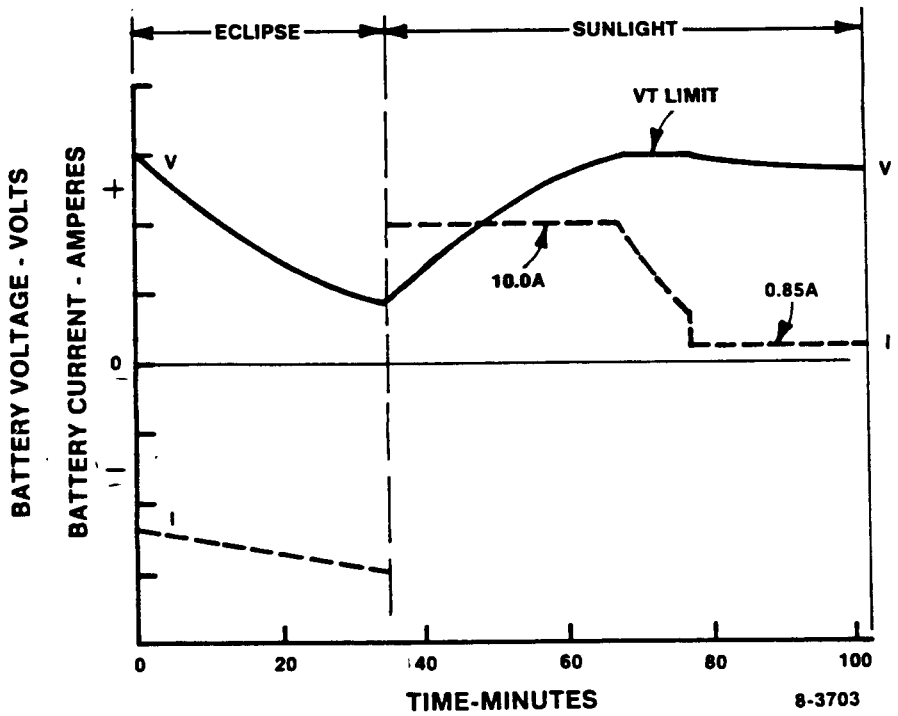

Figure 4.6.2-2. Battery Charging Method

4.6.2.3 Battery Reconditioning

Reconditioning for morning orbit spacecraft will be performed on one battery at a time, preferably during the period prior to entry into an eclipse season.

Reconditioning will be initiated by ground commanded disconnect of the charge path for the selected battery. The selected battery discharge path will then be disconnected and the let-down resistors connected across each cell by ground commands. When the battery voltage has decreased to less than 1.7 volts, the letdown resistors will be disconnected and the pull-up resistor connected by ground commands as shown in Figure 4.6.2-3. PMS control of the reconditioning battery will be enabled at this time. The battery voltage will be required to rise to 12.0 volts before the pull-up resistor is disconnected and the 0.85-ampere trickle charge rate and the battery charge path reconnection are commanded by software. Recharge at the VT-limited 12.5-ampere charge rate will be initiated when the battery voltage has risen to 22 volts. Charging will continue until full recharge is indicated by the VT-limited tapering action of the charge current and the achievement of the proper ampere-minute return.

The second and third batteries will be reconditioned in sequence using the same procedure. The entire reconditioning sequence for three batteries is expected to take about two weeks.

It is recommended that reconditioning for afternoon orbit spacecraft be performed at least once a year. Generally, it will be desirable to perform this reconditioning when the spacecraft sun angle is in the range of 50.0 to 70.0° to minimize the recharge time. However, there is no hard and fast restriction against reconditioning at other sun angles.

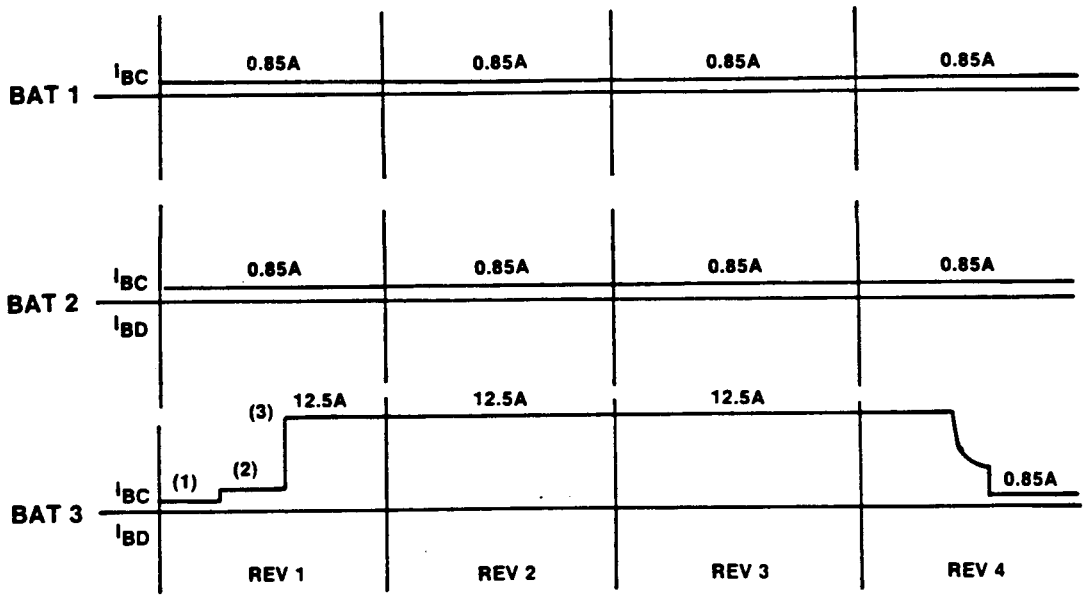

(1) PULL UP RESISTOR CHARGING: 100ma TO 150ma RANGE
(2) 0.85A TRICKLE CHARGE WHEN BATTERY VOLTAGE IS > 12.0 VOLTS
(3) 12.5A CHARGE RATE WHEN BATTERY VOLTAGE IS > 22.0 VOLTS

8-3704

Figure 4.6.2-3. Reconditioning in 100% Sun

Reconditioning will be initiated by ground commanded disconnection of the charge path for the selected battery. At that time, the initialized charge rate will be changed from 7.5 or 10.0 amperes to 12.5 amperes for the two batteries remaining on-line. The selected battery will be allowed to discharge along with the other two batteries during the next eclipse. The discharge path will then be disconnected and the let-down resistors connected across each cell by ground commands. When the battery voltage has decreased to less than 1.7 volts, the letdown resistors will be disconnected and the pull-up resistor connected by ground commands as shown in Figure 4.6.2-4. PMS control of the reconditioning battery will be enabled at this time. The battery voltage will be required to rise to 12.0 volts before the pull-up resistor is disconnected and the 0.85-ampere trickle charge rate and the battery charge path reconnection are commanded by software. Recharge at the VT-limited 12.5-ampere charge rate will be initiated when the battery voltage has risen to 22 volts and the other two on-line batteries have been fully recharged as indicated by the reduction of their charge currents to the trickle charge level. The 12.5-ampere VT-limited charge rate will be commanded automatically by PMS, and high-rate recharge will begin. During each ensuing orbit, recharge of the battery being reconditioned will be accomplished only when the on-line batteries have been fully recharged as indicated by the reduction of their charge rates to trickle charge by PMS. Reconditioning recharge will continue until full recharge is indicated by the VT-limited tapering action of the charge current and the achievement of the proper ampere-minute return.

The second and third batteries will be reconditioned in sequence using the same procedure. Reconditioning of all three batteries in the eclipse season is expected to take approximately 25 days.

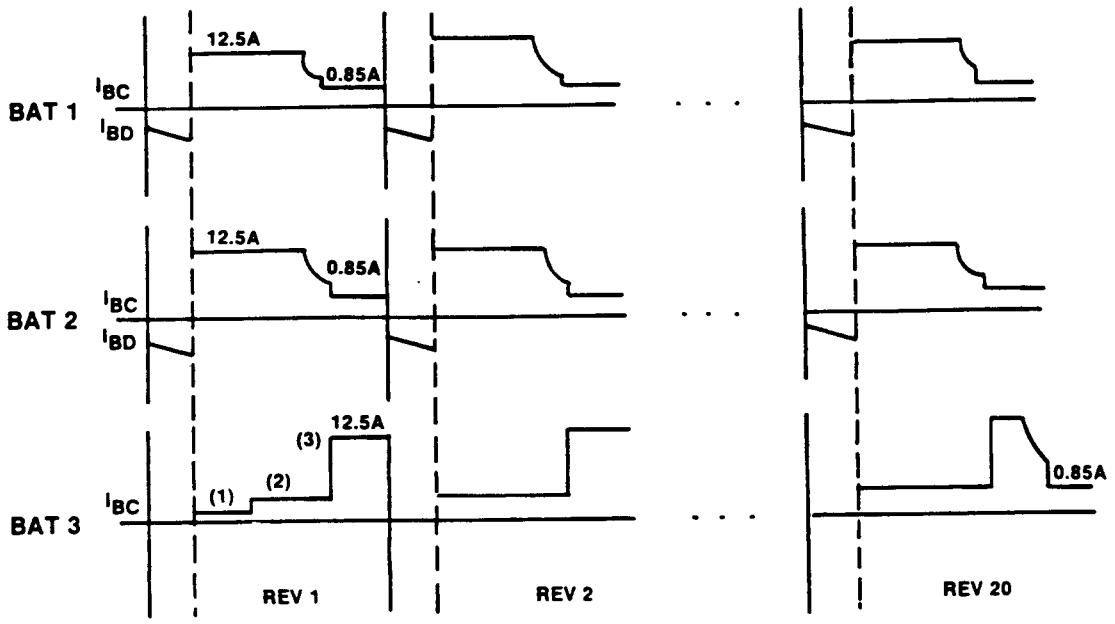

Figure 4.6.2-4. Reconditioning in Eclipse Orbits

4.6.3 RELIABILITY AND REDUNDANCY FEATURES

The Power Subsystem is configured so that no single point electronic failure can cause mission failure. Standard parts and conservative hardware design approaches are used throughout. Safety factors have been included in both the system performance estimates and the component designs to ensure reasonable margins against component degradation.

Redundancy in the solar array is provided by the multiplicity of diode isolated parallel solar cell circuits and partial shunt assemblies. Each of the 70 independent solar cell circuits has a partial shunt assembly consisting of two parallel redundant shunt transistors with a single driver transistor.

If necessary, a full spacecraft mission load can be supported with only two out of the three batteries operating. The C/4 (12.5 ampere) charge rate is provided for this purpose to assure adequate recharge capability.

Except for the power components, all elements of the boost regulator and mode controller are fully redundant. Backup elements, independent and separate from the primary elements, are automatically switched in by failure detection circuits or by ground command. The failure detection circuits are not redundant, but are designed so that any failure can result only in a loss of automatic failure detection or a false switchover to the backup unit. In the event of false switchovers, the primary units can be switched back in by ground command.

Due to the large volume and weight of the boost regulator power components, 5 parallel channels instead of completely redundant elements are provided. Any 4 of these channels can support a maximum spacecraft load.

The charge regulator for each battery has the power components located in the BCA and the control circuits in the PSE. The main current pass elements as well as the current and voltage limit feedback loops are fully redundant with separate and independent components for primary and back-up. Charge regulator failure detection is similar to the mode control/boost regulator failure detection with automatic switching from the primary to the back-up. Either the primary or back-up charger can be selected by ground command. The battery discharge diodes, also located within the BCA, are configured in a quad redundant arrangement so that 1) an open diode does not cause an open battery discharge path and 2) a battery is still diode isolated from the battery bus in the presence of a shorted diode.

The solar array drive, which has redundant motor windings, is driven by fully redundant control electronics located in the ADE. There are no automatic failure detection circuits in the ADE, but software is provided to switch sides if an array tracking error is sensed. The slip rings in the SAD are connected so that multiple parallel paths are provided for the positive and negative array buses as well as for the partial shunt drive signals.

The CPC contains two independent charge regulators that can be commanded independently on or off by the command and control subsystem. Typically, both regulators are operated at the same time so that the loss of one outside of the ground station range will not be catastrophic.

4.6.4 POWER SUBSYSTEM PERFORMANCE

4.6.4.1 Launch Mode

During the ascent phase of a Titan launch, the satellite Power Subsystem must support the loads shown in Table 4.6.4-1. The power values presented are averaged over the entire ascent period and include the transient loads caused by RCE firings and activation of short-duration ordnance devices. Taking all load requirements into account results in a predicted total average ascent load power of 229.3 watts.

The timeline of Figure 4.6.4-1 shows the state-of-charge of each of the three batteries (from time of liftoff) during a Titan launch. While still on the ground, all power requirements are supplied to the satellite Solar Array bus from an external ground power source. Batteries are kept on charge and in a "topped-off" condition. Approximately eight minutes prior to liftoff, this external power is removed and the satellite goes on internal battery power. Normally, handover occurs within 37 minutes of liftoff.

In order to assess the maximum depth-of-discharge for the batteries, the timeline for Figure 4.6.4-1 assumes a 230 watt average ascent load, and that no solar array input is available prior to handover. Furthermore, the satellite is assumed to enter a maximum-duration 35-minute eclipse immediately after handover. With these worst-case conditions imposed, the timeline demonstrates a maximum depth-of-discharge of 12.4 percent occurring at exit from eclipse.

TABLE 4.6.4-1. ESTIMATED ASCENT LOAD POWER REQUIREMENTS, TITAN LAUNCH

Subsystem/Instrument	Average Power At +28-Volt Bus (Watts)
Bus Subsystem	
Attitude Control	54.9
Data Handling	15.6
Command and Control	39.3
Communications	37.2
Thermal	33.0
Power	12.7
• Total Bus	192.7
GFE	
DTR 5 (TIP Record)	8.6
HIRS Scan	17.6
AVHRR Scan	8.2
All Other Instruments are Off (Interface Power)	2.2
• Total GFE	36.6
Total Spacecraft	229.3

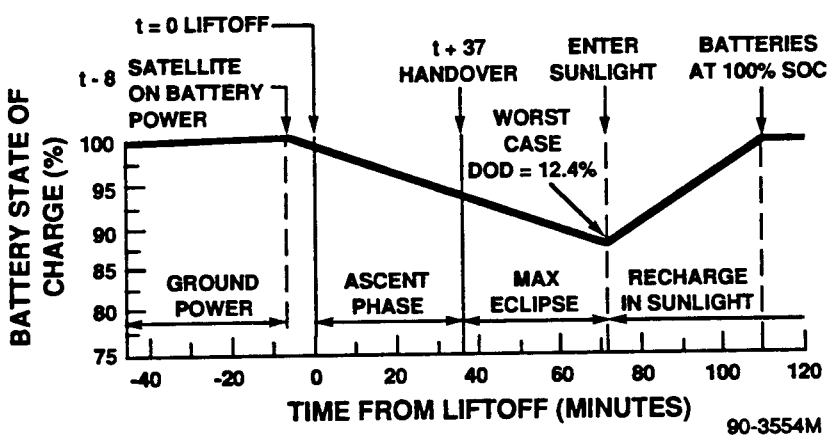

Figure 4.6.4-1. Battery State-of-Charge Timeline, Titan Launch

Batteries are restored to 100-percent state-of-charge during the sunlit period of the first orbit following handover. It is therefore quite evident that the Titan launch presents no problem for the Power Subsystem with respect to energy balance and battery depth-of-discharge.

4.6.4.2 Mission Mode

4.6.4.2.1 Load Requirements

The satellite equipment loads are summarized in Table 4.6.4-2, which presents load current values for each satellite unit (or group of related units) when in the operating mode indicated. The currents listed are based on measured performance data for those components that are presently used on the ATN satellite; in cases where there were variations in measurements for a particular component, the larger value was selected for the table entry. Specification values are used for all components for which measured data was not available. There are five load current conditions identified; the current drawn directly from each of the four spacecraft buses (28, PLB, SW TLM, and 10-volt), and the total net equivalent load referred to the primary +28 volt power regulator. Net equivalent loads were calculated assuming a power conversion efficiency factor of 65 percent for the CPC. Therefore, the total current, I_T, supplied by the PSE regulator for each load is given as:

$$I_T = I_{+28V} + I_{PLB} + I_{SW\ TLM} + 0.549 I_{10V}$$

Table 4.6.4-3 lists the predicted average power consumed by each load throughout a given orbit. These values are derived from Table 4.6.4-2 and are based on a mission profile defined by the time-lines of Figures 4.6.4-2 and 4.6.4-3.

The assumed orbit represents one that is particularly busy with a long 15-minute CDA contact and a TIP data record/playback cycle. In actual practice, recording of TIP data ordinarily takes place only during the one or two blind orbits that may occur each day for playback over Lannion, France; an orbit with both recorded TIP and CDA playback events might occur once following that blind. However, this particular orbit profile has been selected in order to provide an energy-balance analysis which is conservative.

All loads, except for that of the Thermal Control Subsystem, are assumed constant with sun angle. Thermal Control Subsystem loading, which varies as a function of sun angle as shown in Figure 4.6.4-4, is assigned to the bus power allotment. Values for the 0 degree and 80 degree boundaries, as well as the 28 and 50 degree cases, are entered in the Table.

4.6.4.2.2 Load Capability

The load capability of the ATN-KLM power system is defined as the maximum load that can be supported by the solar array, batteries, and control electronics as they function together in the system configuration shown in Figure 4.6.1-1. The solar array is required to supply the spacecraft loads directly (via the solar array power bus) during satellite daytime, plus provide proper battery recharge. When the spacecraft is in sunlight 100% of the time, the minimum acceptable battery charge rate is trickle charge (0.85 ampere per battery); however, when the spacecraft is operating in an orbit with an eclipse, the minimum battery charge rate has to be increased to a point where full battery recharge is achieved by the end of each sunlight period.

TABLE 4.6.4-2. COMPONENT OPERATING CURRENTS

Subsystem/ Component	Operating mode	28V Main Bus (mA) max avg reg	28V Main Bus (mA) peak reg	Pulse Load Bus (mA) max avg pls	Pulse Load Bus (mA) pk pls	+10V Bus (mA) 10V	+10V Bus (mA) 10V pk	SW. TLM Bus (mA)	Total Current At +28V Reg. (mA) Total I	Total Current At +28V Reg. (mA) Peak I	Comments
C&CS											
SCU	On	2.0	25.0	.0	.0	2.0	2.0	.0	3.1	26.1	
CPU(2)	Minimum Program	.0	.0	.0	.0	230.0	948.0	.0	126.4	520.9	
	Normal Program	.0	.0	.0	.0	552.0	948.0	.0	303.3	520.9	
	Maximum Program	.0	.0	.0	.0	948.0	948.0	.0	520.9	520.9	
CIU	On	5.0	5.0	.0	.0	403.0	403.0	.0	226.4	226.4	300 mA on 10V common
CXU	On	.0	.0	.0	.0	23.0	23.0	.0	12.6	12.6	
RXO	On (Nominal)	130.0	195.0	.0	.0	18.0	18.0	.0	139.9	204.9	Includes typical heater power
	On (Max Heater)	195.0	195.0	.0	.0	18.0	18.0	.0	204.9	204.9	Includes full on heater power
DAU	On	196.0	196.0	.0	.0	.0	.0	.0	196.0	196.0	
ADACS											
SSA	Off	.0	.0	.0	.0	.0	.0	.0	.0	.0	
	On	25.0	25.0	.0	.0	38.0	38.0	.0	45.9	45.9	+5V pwr supplied by CIU
ESA	On	39.0	72.0	.0	.0	5.0	5.0	.0	41.7	74.7	
RWA(4)	Off	.0	.0	.0	.0	3.0	3.0	.0	1.6	1.6	
	200 RPM (Ascent)	100.0	140.0	.0	.0	3.0	3.0	.0	101.6	141.6	
	1000 RPM	110.0	5,000.0	.0	.0	3.0	3.0	.0	111.6	5,001.6	
	2000 RPM	140.0	5,000.0	.0	.0	3.0	3.0	.0	141.6	5,001.6	
	Max Torque	2,500.0	5,000.0	.0	.0	3.0	3.0	.0	2,501.6	5,001.6	
PTC	Off	.0	.0	.0	.0	.0	.0	.0	.0	.0	
	On	286.0	307.7	.0	.0	.0	.0	.0	286.0	307.0	
RYC	Off	.0	.0	.0	.0	.0	.0	.0	.0	.0	
	On	429.0	461.0	.0	.0	.0	.0	.0	429.0	461.0	

TABLE 4.6.4-2. COMPONENT OPERATING CURRENTS (Continued)

Subsystem/ Component	Operating mode	28V Main Bus (mA) max avg reg	28V Main Bus (mA) peak reg	Pulse Load Bus (mA) max avg pls	Pulse Load Bus (mA) pk pls	+10V Bus (mA) 10V	+10V Bus (mA) 10V pk	SW. TLM Bus (mA)	Total Current At +28V Reg. (mA) Total I	Total Current At +28V Reg. (mA) Peak I	Comments
GFE											
SEM/2	Off	.0	.0	.0	.0	4.0	4.0	5.0	7.2	7.2	
	DPU	161.1	161.1	.0	.0	4.0	4.0	5.0	168.2	168.2	
	delta MEPED	164.0	164.0	.0	.0	.0	.0	.0	164.0	164.0	
	delta TED	21.0	21.0	.0	.0	.0	.0	.0	21.0	21.0	
SBUV/2	Off	.0	.0	.0	.0	16.0	16.0	4.0	12.8	12.8	
	On (Discrete)	225.0	240.0	326.0	800.0	10.0	10.0	4.0	560.5	1,049.5	Grating Mode 1
	On (Calibrate)	340.0	350.0	329.0	1,145.0	10.0	10.0	4.0	678.5	1,504.5	Grating Mode 3
SARR	Off	.0	.0	.0	.0	5.0	5.0	4.0	6.7	6.7	
	On	1,557.0	1,557.0	.0	.0	5.0	5.0	4.0	1,563.7	1,563.7	All receivers on
SARP-2	Off	.0	.0	.0	.0	10.0	10.0	2.0	7.5	7.5	
	Standby (RPU Only)	589.0	589.0	.0	.0	10.0	10.0	2.0	596.5	596.5	
	delta DRU	54.0	54.0	.0	.0	.0	.0	.0	54.0	54.0	
DTR(5)	Off	.0	.0	.0	.0	.0	.0	.0	.0	.0	XSU supplies +5V pwr.
	Standby	70.0	70.0	.0	.0	.0	.0	.0	70.0	70.0	
	Record 8.3 kB	308.0	308.0	.0	.0	.0	.0	.0	308.0	308.0	TIP record
	Record 16.4 kB	308.0	308.0	.0	.0	.0	.0	.0	308.0	308.0	Boost or AMSU/TIP record
	Record 66.5 kB	308.0	308.0	.0	.0	.0	.0	.0	308.0	308.0	GAC record
	Record 665.4 kB	348.0	348.0	.0	.0	.0	.0	.0	348.0	348.0	LAC record
	Playback 332.7 kB	613.0	613.0	.0	.0	.0	.0	.0	613.0	613.0	TIP or ASMU/TIP playback
	Playback 1330.8 kB	613.0	613.0	.0	.0	.0	.0	.0	613.0	613.0	Test only
	Playback 2661.6 kB	658.0	658.0	.0	.0	.0	.0	.0	658.0	658.0	GAC/LAC playback or fast forward
AMSU-A1	Off	.0	.0	.0	.0	10.0	10.0	7.0	12.5	12.5	
	On	3,000.0	3,500.0	214.0	1,000.0	10.0	10.0	7.0	3,226.5	4,512.5	
AMSU-A2	Off	.0	.0	.0	.0	10.0	10.0	5.0	10.5	10.5	
	On	1,000.0	1,000.0	430.0	2,000.0	10.0	10.0	5.0	1,440.5	3,010.5	

TABLE 4.6.4-2. COMPONENT OPERATING CURRENTS (Continued)

Subsystem/ Component	Operating mode	28V Main Bus (mA) max avg reg	28V Main Bus (mA) peak reg	Pulse Load Bus (mA) max avg pls	Pulse Load Bus (mA) pk pls	+10V Bus (mA) 10V	+10V Bus (mA) 10V pk	SW. TLM Bus (mA)	Total Current At +28V Reg. (mA) Total I	Total Current At +28V Reg. (mA) Peak I	Comments
Communication											
VTX-2	Off	.0	.0	.0	.0	2.5	2.5	.0	1.4	1.4	
	On	659.0	659.0	.0	.0	2.5	2.5	.0	660.4	660.4	
BTX-1	Off	.0	.0	.0	.0	2.5	2.5	.0	1.4	1.4	
	On	275.0	275.0	.0	.0	2.5	2.5	.0	276.4	276.4	BTX-1 + RF Switch
BTX-2	Off	.0	.0	.0	.0	2.5	2.5	.0	1.4	1.4	
	On	239.0	239.0	.0	.0	2.5	2.5	.0	240.4	240.4	
GRD	Standby	101.0	101.0	.0	.0	2.0	2.0	.0	102.1	102.1	
	Active	113.0	113.0	.0	.0	2.0	2.0	.0	114.1	114.1	
Power											
SAD/ADE	Off	.0	.0	.0	.0	2.0	2.0	.0	1.1	1.1	
	Normal/Slew	361.0	539.0	.0	.0	2.0	2.0	.0	362.1	540.1	
PSE/BCA	On	450.0	450.0	.0	.0	4.0	4.0	.0	452.2	452.2	Loads are shunt losses
Thermal	Ascent	393.3	393.3	786.7	786.7	.0	.0	.0	1,180.0	1,180.0	
	GAMMA = 0	1,950.0	1,950.0	3,835.0	14,935.0	.0	.0	.0	5,785.0	16,885.0	
	GAMMA = 28	960.0	960.0	2,300.0	4,200.0	.0	.0	.0	3,260.0	5,560.0	
	GAMMA = 50	1,095.0	1,095.0	2,555.0	5,110.0	.0	.0	.0	3,650.0	6,205.0	
	GAMMA = 80	860.0	860.0	2,000.0	4,000.0	.0	.0	.0	2,860.0	4,860.0	
GFE											
AVHRR/3	Off	.0	.0	.0	.0	4.0	4.0	.0	2.2	2.2	
	Operating	968.1	968.1	.0	.0	4.0	4.0	.0	970.3	970.3	
	Scan Only	289.0	289.0	.0	.0	4.0	4.0	.0	291.2	291.2	
	delta Cooler Heater	757.0	757.0	.0	.0	.0	.0	.0	757.0	757.0	
	delta Cooler Cover Deploy	.0	2,030.0	.0	.0	.0	.0	.0	.0	2,030.0	Cover deploys once, 1 sec
DCS-2	Off	.0	.0	.0	.0	10.0	10.0	2.0	7.5	7.5	
	Standby (RPU Only)	607.0	607.0	.0	.0	10.0	10.0	2.0	614.5	614.5	
	delta DRU	54.0	54.0	.0	.0	.0	.0	.0	54.0	54.0	8 DRUs typical

TABLE 4.6.4-2. COMPONENT OPERATING CURRENTS (Continued)

Subsystem/ Component	Operating mode	28V Main Bus (mA) max avg reg	28V Main Bus (mA) peak reg	Pulse Load Bus (mA) max avg pls	Pulse Load Bus (mA) pk pls	+10V Bus (mA) 10V	+10V Bus (mA) 10V pk	SW. TLM Bus (mA)	Total Current At +28V Reg. (mA) Total I	Total Current At +28V Reg. (mA) Peak I	Comments
ADACS											
IMU	Ascent	1,500.0	1,770.0	.0	.0	25.0	50.0	.0	1,513.7	1,783.7	Heater full on
	On (Nominal)	1,190.0	1,460.0	.0	.0	25.0	50.0	.0	1,203.7	1,473.7	Includes typical heater power
Data Handling											
TIP	On	65.0	65.0	.0	.0	58.0	58.0	.0	96.9	96.9	
MIRP	On	202.0	202.0	.0	.0	15.0	15.0	.0	210.2	210.2	
XSU	On (Minimum Operating)	57.5	57.5	.0	.0	31.0	31.0	.0	74.5	74.5	No DTR or STX operation
	delta, 1 STX on	36.0	36.0	.0	.0	.0	.0	.0	36.0	36.0	
	delta, 1 DTR REC	61.0	61.0	.0	.0	.0	.0	.0	61.0	61.0	
	delta, 1 DTR PBK	50.0	50.0	.0	.0	.0	.0	.0	50.6	50.0	
SATCU	On	28.0	28.0	.0	.0	.0	.0	.0	28.0	28.0	
S/C TLM	On	50.0	50.0	.0	.0	.0	.0	.0	50.0	50.0	S/C pressure, temp. TLM
AIP	Off	.0	.0	.0	.0	2.0	2.0	.0	1.1	1.1	
	On (AMSU/TIP)	118.0	118.0	.0	.0	2.0	2.0	.0	119.1	119.1	
	On (TIP)	107.0	107.0	.0	.0	2.0	2.0	.0	108.1	108.1	
Communi-cation											
STX 1-3	Off	.0	.0	.0	.0	10.0	10.0	.0	5.5	5.5	
	On	915.0	915.0	.0	.0	10.0	10.0	.0	920.5	920.5	
STX 4	Off	.0	.0	.0	.0	10.0	10.0	.0	5.5	5.5	
	On	925.0	925.0	.0	.0	10.0	10.0	.0	930.5	930.5	
VTX-1	Off	.0	.0	.0	.0	2.5	2.5	.0	1.4	1.4	
	On	695.0	695.0	.0	.0	2.5	2.5	.0	696.4	696.4	VTX-1 + RF Switch

TABLE 4.6.4-2. COMPONENT OPERATING CURRENTS (Continued)

Subsystem/ Component	Operating mode	28V Main Bus (mA) max avg reg	28V Main Bus (mA) peak reg	Pulse Load Bus (mA) max avg pls	Pulse Load Bus (mA) pk pls	+10V Bus (mA) 10V	+10V Bus (mA) 10V pk	SW. TLM Bus (mA)	Total Current At +28V Reg. (mA) Total I	Total Current At +28V Reg. (mA) Peak I	Comments
GFE											
AMSU-B	Off	.0	.0	.0	.0	10.0	10.0	10.0	15.5	15.5	
	On	2,250.0	2,250.0	960.0	2,800.0	10.0	10.0	10.0	3,225.5	5,065.5	
HIRS/3	Off	.0	.0	.0	.0	5.0	5.0	1.0	3.7	3.7	
	Operating	290.0	290.0	520.0	2,000.0	5.0	5.0	1.0	813.7	2,293.7	2A pulse @ retrace
	Scan Only	175.0	175.0	450.0	450.0	5.0	5.0	1.0	628.7	628.7	
	delta Outgas Heater	.0	.0	1,100.0	1,100.0	.0	.0	.0	1,100.0	1,100.0	
	delta Cooler Door	.0	.0	.0	2,000.0	.0	.0	.0	.0	2,000.0	

TABLE 4.6.4-3. ORBIT AVERAGE POWER REQUIREMENTS

Subsystem	Component	Operating Mode	S/C Orbit Avg Power (Watts) at 28V Regulator	Comments
C&CS	SCU	100% dc	.09	
	CPU1	Control - 100% dc	8.49	
	CPU2	Backup - 100% dc	8.49	
	CIU	100% dc	6.34	
	CXU	100% dc	.35	
	RXO	100% dc	3.92	Includes typical heater power
	DAU	100% dc	5.49	
Subtotal			33.17	
ADACS	SSA	100% dc	1.28	
	ESA	100% dc	1.17	
	XRWA		7.80	
	YRWA		7.80	
	ZRWA		7.80	
	SRWA	Off	.05	
	PTC	3.0% DC	.22	
	RYC	17.3% DC	2.08	
	IMU	100% dc	33.70	Includes typical heater power
Subtotal			61.90	
Data Handling	TIP	100% dc	2.71	
	MIRP	100% dc	5.89	
	XSU	Per Orbit Timeline	7.06	
	SATCU	100% dc	.78	
	TLM	100% dc	1.40	S/C pressure, temp. TLM
	AIP	100% dc	3.33	
Subtotal			21.18	
Communications	STX-1	100% dc	25.77	
	STX-2	14.8% dc	3.81	
	STX-3	24.6% dc	6.34	
	STX-4	Off	.15	
	VTX-1	100% dc	19.50	VTX-1 + RF Switch
	VTX-2	Off	.04	

TABLE 4.6.4-3. ORBIT AVERAGE POWER REQUIREMENTS (Continued)

Subsystem	Component	Operating Mode	S/C Orbit Avg Power (Watts) at 28V Regulator	Comments
Communications (Con't)	BTX-1	100% dc	7.74	BTX-1 + RF Switch
	BTX-2	Off	.04	
	GRD	24.6% dc	2.94	2 Receivers on
Subtotal			66.33	
Power	ADE/SAD	100% dc	10.14	
	PSE/BCA	100% dc	12.66	Loads are shunt losses
Subtotal			22.80	
Thermal	GAMMA = 0		161.98	
	GAMMA = 28		91.28	
	GAMMA = 50		102.20	
	GAMMA = 80		80.08	
GFE	AVHRR/3	100% dc	27.17	
	DCS-2	100% dc	29.30	
	SEM/2	100% dc	9.89	
	SBUV/2	100% dc	15.69	Grating Mode 1
	SARR	100% dc	43.78	All Receivers On
	SARP-2	100% dc	21.24	
	DTR-1	Per Orbit Timeline	4.57	GAC Record/Playback
	DTR-2	Per Orbit Timeline	1.43	LAC Record/Playback
	DTR-3	Per Orbit Timeline	4.57	GAC Record/Playback
	DTR-4	Per Orbit Timeline	8.80	AMSU/TIP Record/Playback
	DTR-5	Off	.00	
	AMSU-A1	100% dc	90.34	
	AMSU-A2	100% dc	40.33	
	AMSU-B	100% dc	90.31	
	HIRS/3	100% dc	22.78	
	Contingency		39.79	
Subtotal			450.00	
Totals	GAMMA = 0		817.36	
	GAMMA = 28		746.66	
	GAMMA = 50		757.58	
	GAMMA = 80		735.46	

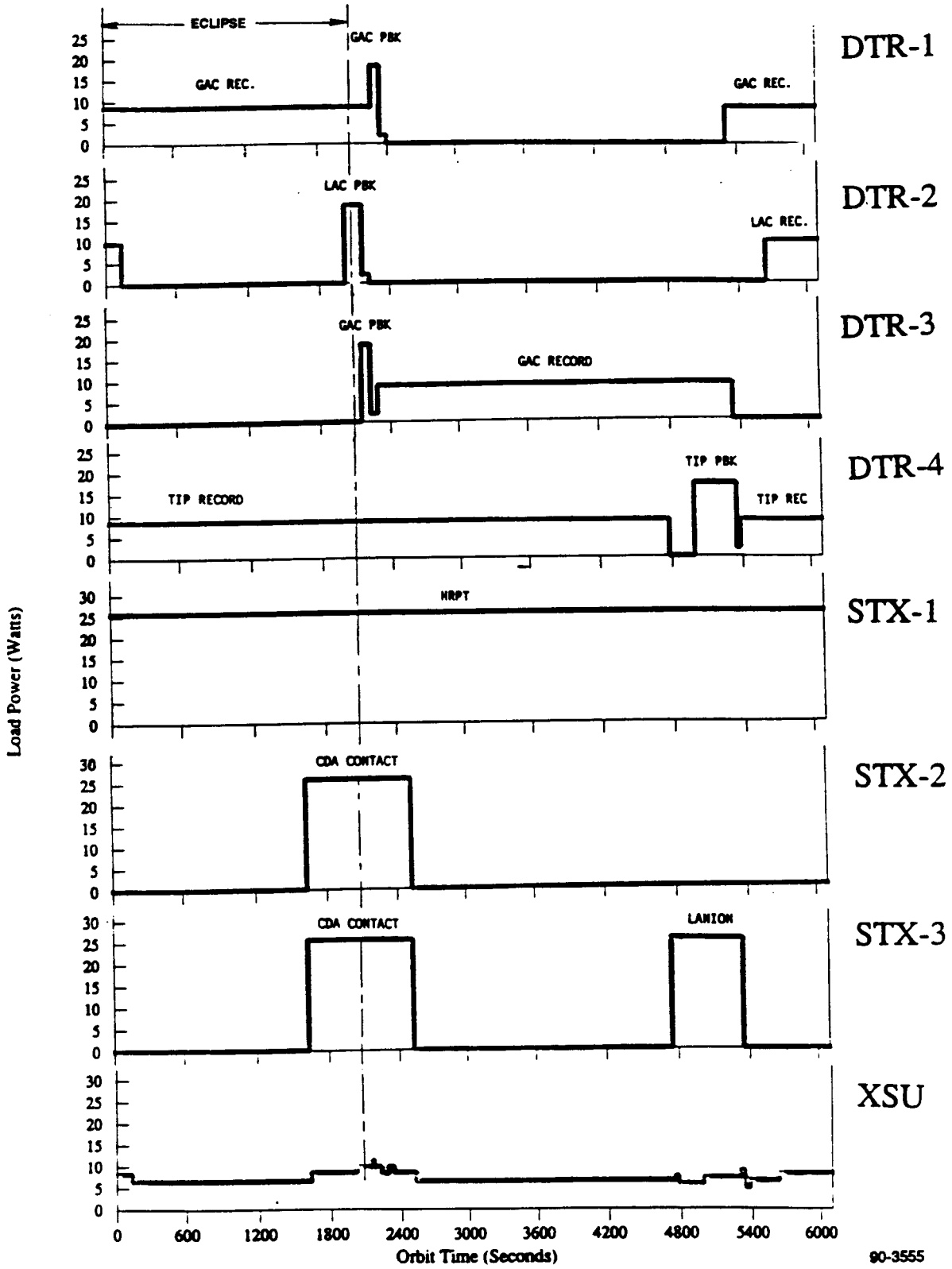

Figure 4.6.4-2. Orbit Time-Line Used for Load Analysis

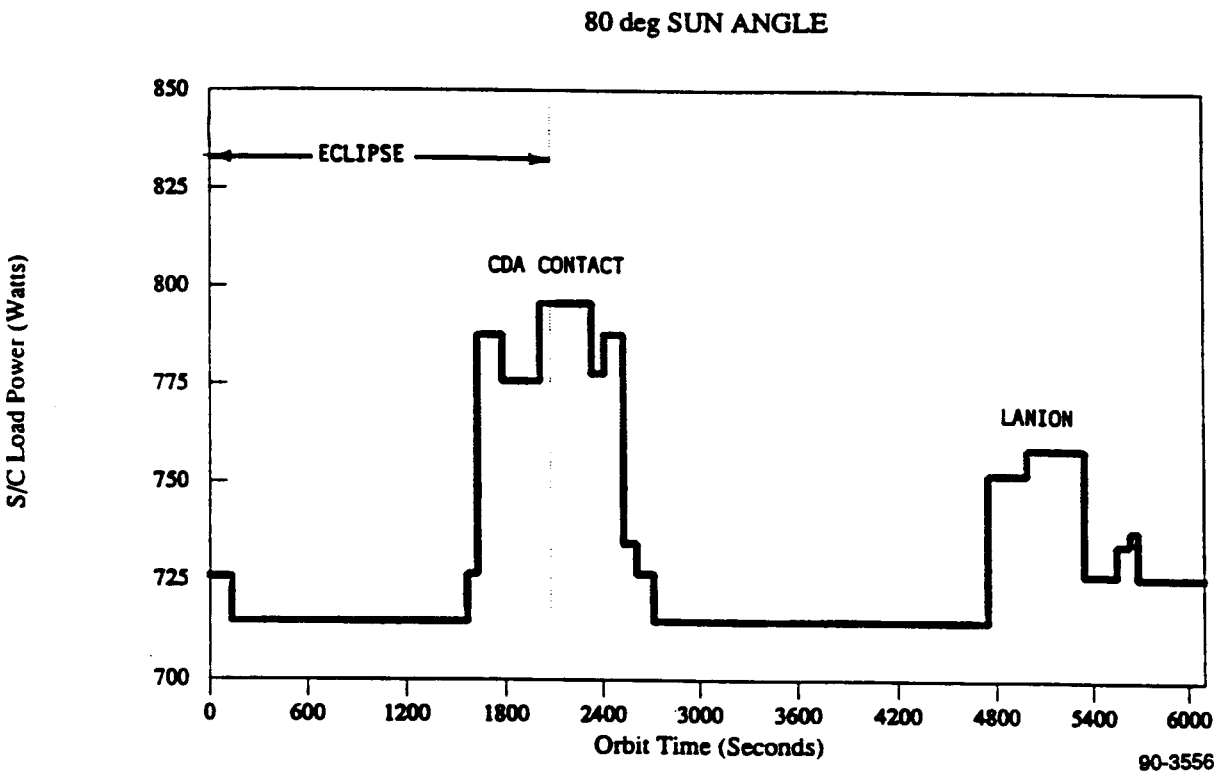

Figure 4.6.4-3. Power Profile for a Typical Orbit

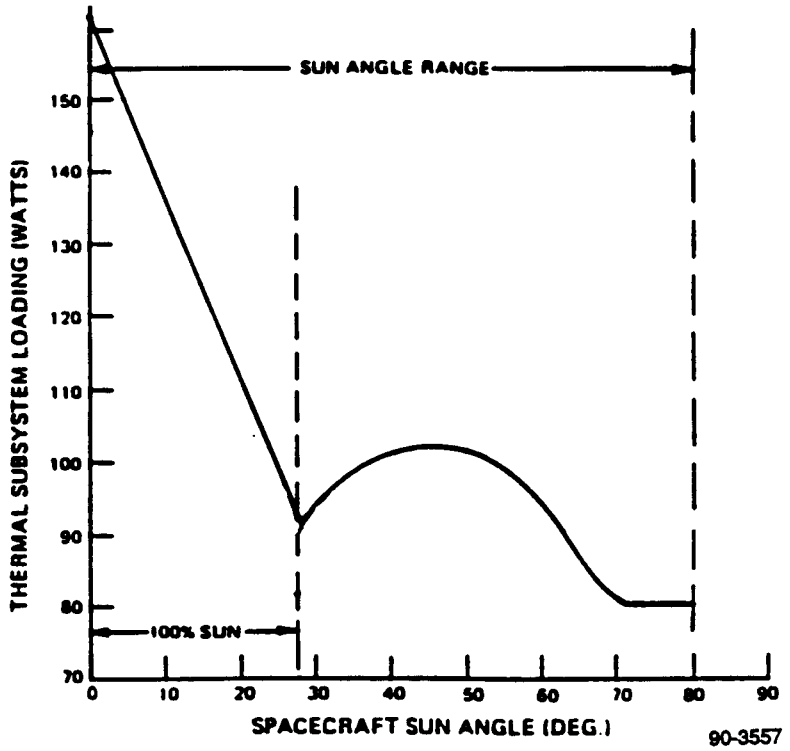

Figure 4.6.4-4. Thermal Subsystem Electrical Loading

The orbital lifetime requirement for the NOAA-KLM spacecraft is two years. The spacecraft will operate in either a 450 or 470 nautical mile, circular sun synchronous orbit. The spacecraft sun angle design range is 0 to 80 degrees. The 100 percent suntime sun angle boundary is 27.8 degrees. At angles above 27.8 degrees the spacecraft will spend some portion of each orbit cycle in earth eclipse. A tabulation of eclipse time duration versus spacecraft sun angle is presented in Table 4.6.4-4 for the 450 nautical mile orbit. At this altitude, the orbital time period is 101.6 minutes.

TABLE 4.6.4-4. ECLIPSE TIME DURATION VERSUS SPACECRAFT SUN ANGLE (450 Nautical Mile Orbit Altitude)

Sun Angle (Degrees)	Eclipse Time (Minutes)
28	3.4
30	11.8
32	15.9
34	18.8
36	21.1
38	22.9
40	24.5
42	25.8
44	26.9
46	27.9
48	28.8
50	29.6
52	30.2
54	30.9
56	31.4
58	31.9
60	32.3
62	32.7
64	33.1
66	33.4
68	33.7
70	33.9
72	34.1
74	34.3
76	34.5
78	34.6
80	34.8

On-orbit power subsystem load capability is derived by computer analysis using the subsystem model and calculation procedures described below. Computer inputs for the analysis are summarized in Table 4.6.4-5. In the computer analysis, all loads were considered constant throughout the orbit.

TABLE 4.6.4-5. COMPUTER INPUTS FOR POWER ANALYSIS

Computer Parameters	Values Used
Solar Array	
Solar Cell I-V Curve	Nominal BOL (Baseline), Figure 4.6.5-6
Solar Cell Temp. Coefficients	EOL Data, Table 4.6.5-7
Solar Cell Layout	90 series cells, 210 parallel strings
Array Operating Point Voltage	32 volts
Array Sun Incidence Angles	Figure 4.6.5-1
Array Temperatures	Thermal properties, Table 4.6.5-8 Temp vs sun angle, Figure 4.6.5-10
Battery	
Capacity	141.0 ampere-hour
Series Cells	17
Temperature	2°C
Storage Cell Voltage Charac.	2 year, +2°C data; Figure 4.6.5-51
Charge Current Limit	30.0 amperes (10.0 A/battery)
Charge Voltage Limit	VT1 - 25.55V Figure 4.6.5-54 VT3 - 25.21V Figure 4.6.5-54
C/D Ratio	1.04 minimum @ +5°C Figure 4.6.5-53
Electronics	
Regulated Bus Voltage	+28 volts
Boost Regulator Efficiency	90%
Shunt Loss	200 mA (5.6 watts)
Array Bus Voltage Drop	4 volts
Battery Bus Voltage Drop	2 volts

Figure 4.6.4-5 shows the power subsystem model used for power budgeting on the ATN-KLM satellite. Conventional current flow is always in the direction shown, with bi-directional flow only in the batteries. The solar array operating-point voltage (Vsa) is held at approximately 32 volts by the action of the various regulatory elements. When the solar array current availability exceeds the load requirement plus the battery charge current limit, the excess array current is diverted through the partial shunts by a process which ultimately results in Isa matching the current demand at the array (Isa = Ibc + Ir).

The battery and charge regulator combination in Figure 4.6.4-5 is a system composite. The battery capacity is 141.0 ampere-hours with 17 series cells. The charge regulator during normal recharge is a constant current device which supplies charge current to the batteries at one of the three selectable current limits: 30.0, 22.5, or 2.5 amperes. If solar array current availability is not large enough to meet the chosen regulator current limit, then the battery charge current is simply the difference between the array current available and the load (Ibc = Isa - Ir).

When the battery approaches full charge, the charge regulator becomes a constant voltage device, limiting Vb to 1 of the 16 selectable battery voltage limits. During voltage limiting, the battery charge current, Ibc, tapers back to a fixed level as dictated by the overcharge characteristics of the battery.

Whenever the load requirement exceeds the solar array current availability, the battery supplies power to the load. Power is transferred to the regulated bus via the discharge diodes and a boost regulator. For power budgeting calculations, the voltage drop in the discharge path Vd is fixed at 2.0 volts for diode and wiring losses. The boost regulator is a device which transfers power at a relatively constant efficiency.

Battery discharge current in amperes (Ibd) is determined by:

$$Ibd = \frac{Vr\ (Ir - Isa)}{Ebr\ (Vb - Vd)}$$

where Ebr is the boost regulator efficiency factor. The remaining variables are defined in Figure 4.6.4-5.

All system voltages, except battery voltage Vb, are considered constant over the orbit cycle. If prior definition of solar array current availability and load requirements over the orbit cycle is assumed, then only the battery voltages and currents are unknowns.

To find the maximum load that the power subsystem can support, the dc level of the load profile is incrementally increased for a given set of orbital conditions. Load iterations are continued until a load condition is found which just permits proper battery recharge. This maximum load, averaged over the orbit cycle, is presented in Figure 4.6.4-6 as a function of spacecraft sun angle.

A comparison of the load power data presented in Table 4.6.4-3 with the curve of load capability demonstrates ample power margin with regard to the GFE requirement. Table 4.6.4-6 provides a summary of these power margins at both the 0-degree and 80-degree sun angle boundaries as well as at the intermediary sun angles of 28 and 50 degrees.

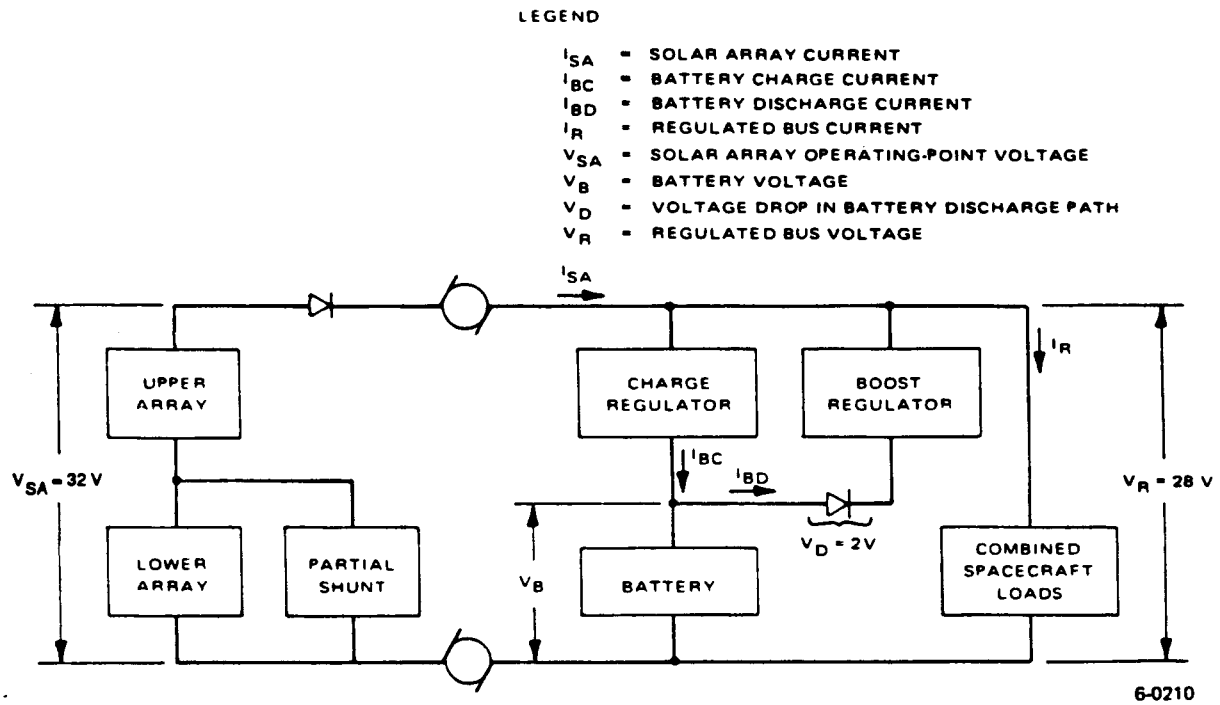

Figure 4.6.4-5. Energy Balance Computer Model

4.6.4.2.3 Peak Current Requirements

The maximum peak current requirements have been estimated in order to establish the ratings for the +28-volt regulator design. The highest current conditions are expected to occur during spacecraft contact with a CDA station. Table 4.6.4-7 lists the values of maximum and peak currents attributed to each component. These values are assumed to be time-coincident during the busiest portion of the station contact profile shown in Figure 4.6.4-2 and therefore represent a worst-case situation.

As shown in the table, when at the zero degree spacecraft sun angle (100% sun), the regulator must be capable of supplying up to 54.7 amperes from the solar array aided by the batteries and BVR. At a sun angle of 50 degrees, The BVR alone must supply a W.C. peak current requirement of 44.1 amperes during an eclipse period. Both of these requirements are met by the regulator design.

4.6.4.2.4 Bus Performance

The Power Subsystem provides four different regulated buses which are distributed throughout the satellite for operation of components as needed:

- +28-volt main bus for primary regulated power needs.
- +28-volt pulse load bus for stepper motors and other transient circuits.
- +28-volt switched telemetry bus.
- +10-volt common bus for standard interface circuits.

MORNING ORBIT

37 DEGREE CANT

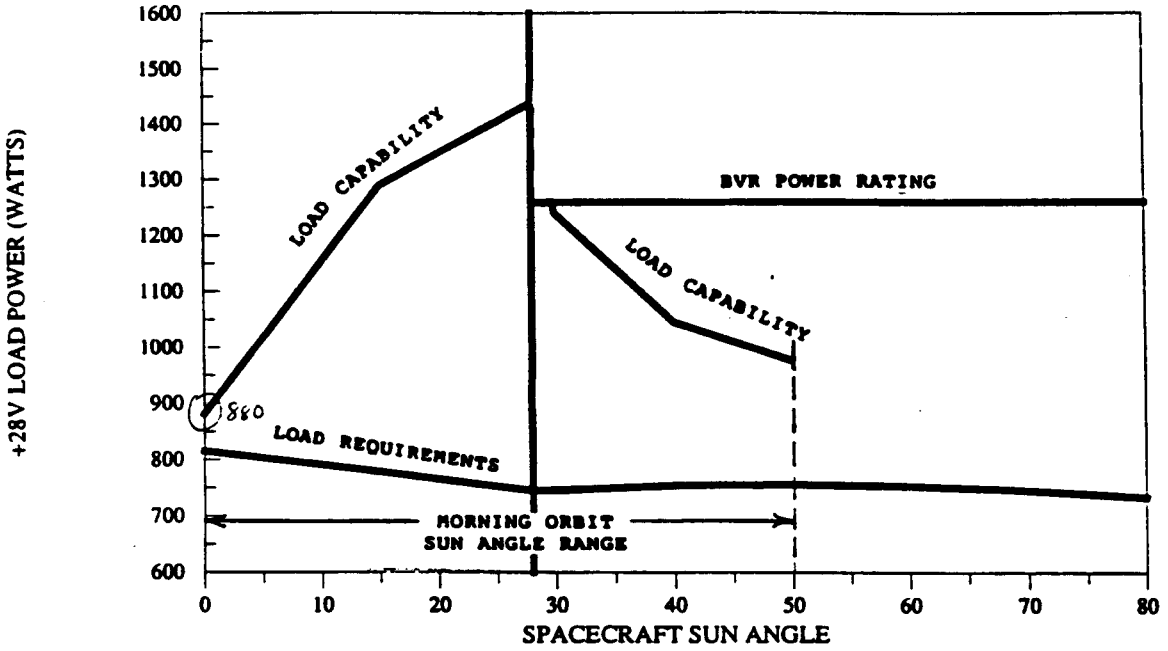

AFTERNOON ORBIT

22 DEGREE CANT

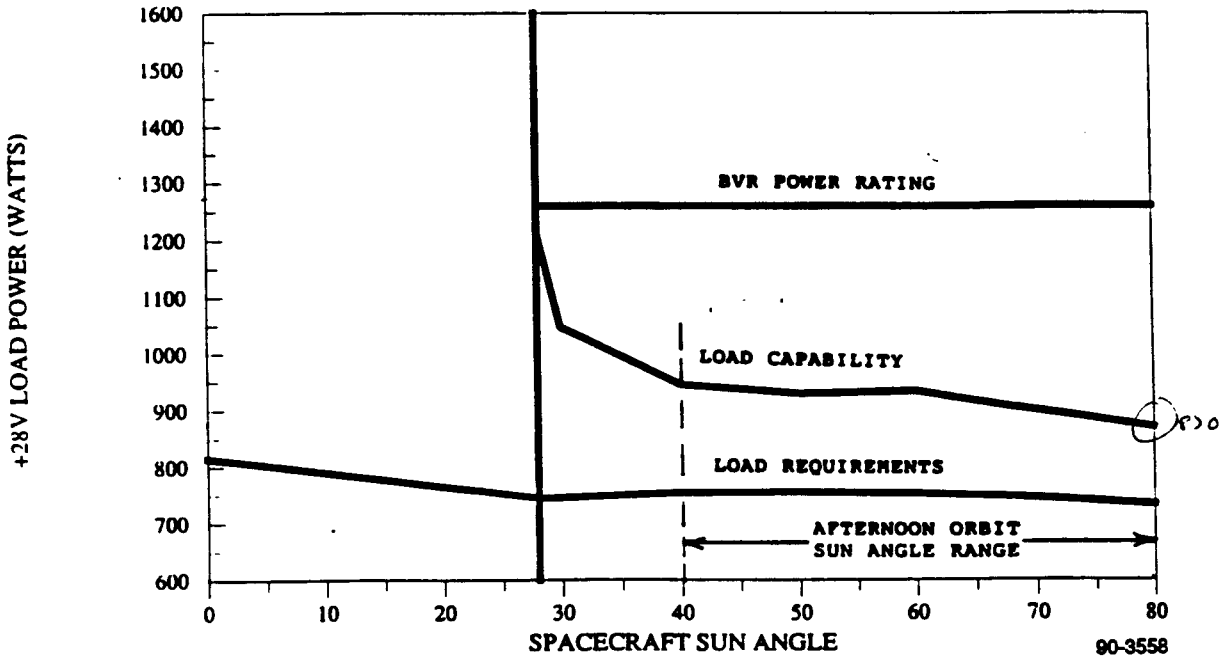

Figure 4.6.4-6. Power Subsystem Load Capability

TABLE 4.6.4-6. TIROS KLM POWER SUMMARY

	S/C Orbit Avg Power @ 28V (Watts)				S/C Peak Power @ 28V (Watts)			
Subsystem/Gamma	0	28	50	80	0	28	50	80
C&CS	33.17	33.17	33.17	33.17	47.82	47.82	47.82	47.82
ADACS	61.90	61.90	61.90	61.90	217.25	217.25	217.25	217.25
Data Handling	21.18	21.18	21.18	21.18	25.44	25.44	25.44	25.44
Communications	66.33	66.33	66.33	66.33	107.98	107.98	107.98	107.98
Power	22.80	22.80	22.80	22.80	27.78	27.78	27.78	27.78
Thermal	161.98	91.28	102.20	80.08	472.78	155.68	173.74	136.08
Subtotal	367.36	296.66	307.58	285.46	899.06	581.96	600.02	562.36
GFE	427.22	427.22	427.22	427.22	633.53	633.53	633.53	633.53
GFE Contingency	22.78	22.78	22.78	22.78	-	-	-	-
Subtotal	450.00	450.00	450.00	450.00	633.53	633.53	633.53	633.53
Total S/C Load	817.36	746.66	757.58	735.46	1532.59	1215.49	1233.55	1195.89
Avg Load Cap.	879.90	1438.40	929.60	869.80	-	-	-	-
Power Margin (W)	62.54	691.74	172.02	134.34	N/A	N/A	N/A	N/A
% Margin	7.65%	92.64%	22.71%	18.27%	N/A	N/A	N/A	N/A

NOTE: 0 degree and 28 degree sun angles have 37 degree solar array cant
50 degree and 80 degree sun angles have 22 degree solar array cant

TABLE 4.6.4-7. PEAK CONTINUOUS CURRENT IN CDA CONTACT

Subsystem	Component	Operating Mode	At +28V Regulator (mA) Max Avg 1	(mA) Peak 1	Comments
C&CS	SCU	On	3.1	26.1	
	CPU1	Maximum Program	520.9	520.9	
	CPU2	Normal Program	303.3	520.9	
	CIU	On	226.4	226.4	300 mA on 10V common
	CXU	On	12.6	12.6	
	RXO	On (Max Heater)	204.9	204.9	Includes full on heater power
	DAU	On	196.0	196.0	
Subtotals (Amps)			1.5	1.7	
ADACS	SSA	On	45.9	45.9	
	ESA	On	41.7	74.7	
	RWA(R)	1000 RPM	111.6	111.6	
	RWA(P)	2000 RPM	141.6	141.6	
	RWA(Y)	Max Torque	2,501.6	5,001.6	Assumes only one RWA @ max torque
	SRWA	Off	101.6	141.6	
	PTC	On	286.0	307.0	
	RYC	On	429.0	461.0	
	IMU	On (Nominal)	1,203.7	1,473.7	Includes typical heater power
Subtotals (Amps)			4.9	7.8	
Data Handling	TIP	On	96.9	96.9	
	MIRP	On	210.2	210.2	
	XSU	3 STX, 2 DTRr, 2 DTRp	404.5	404.5	
	SATCU	On	28.0	28.0	
	S/C TLM	On	50.0	50.0	S/C pressure, temp. TLM
	AIP	On (AMSU/TIP)	119.1	119.1	
Subtotals (Amps)			0.9	0.9	
Communications	STX-1	On	920.5	920.5	
	STX-2	On	920.5	920.5	
	STX-3	On	920.5	920.5	
	STX-4	Off	5.5	5.5	
	VTX-1	On	696.4	696.4	VTX-1 + RF switch

TABLE 4.6.4-7. PEAK CONTINUOUS CURRENT IN CDA CONTACT (Continued)

Subsystem	Component	Operating Mode	At +28V Regulator (mA) Max Avg 1	(mA) Peak 1	Comments
Communications (Continued)	VTX-2	Off	1.4	1.4	
	BTX-1	On	276.4	276.4	BTX-1 + RF switch
	BTX-2	Off	1.4	1.4	
	GRD	Active	114.1	114.1	Demodulating with 2 receivers on
Subtotals (Amps)			3.9	3.9	
Power	SAD/ADE	Normal/Slew	362.1	540.1	
	PSE/BCA	On	452.2	452.2	Loads are shunt losses
Subtotals (Amps)			0.8	1.0	
Thermal	GAMMA = 0		5,785.0	16,885.0	
	GAMMA = 28		3,260.0	5,560.0	
	GAMMA = 50		3;650.0	6,205.0	
	GAMMA = 80		2,860.0	4,860.0	
GFE	AVHRR/3	Operating	970.3	970.3	
	DCS-2	RPU + 8 DRU	1,046.5	1,046.5	
	SEM/2	DPU + MEPED + TED	353.2	353.2	
	SBUV/2	On (Discrete)	560.5	1,049.5	Grating Mode 1
	SARR	On	1,563.7	1,563.7	All receivers on
	SARP-2	RPU + 3 DRU	758.5	758.5	
	DTR 1	Record 66.5 kB	308.0	308.0	GAC record
	DTR 2	Playback 2661.6 kB	658.0	658.0	LAC playback
	DTR 3	Playback 2661.6 kB	658.0	658.0	GAC playback
	DTR 4	Record 16.4 kB	308.0	308.0	AMSU/TIP record
	DTR 5	Standby	70.0	70.0	
	AMSU-A1	On	3,226.5	4,512.5	
	AMSU-A2	On	1,440.5	3,010.5	
	AMSU-B	On	3,225.5	5,065.5	
	HIRS/3	Operating	813.7	2,293.7	Spec calls 2A pulse @ retrace
Subtotals (Amps)			16.0	22.6	
Totals (Amps)	GAMMA = 0		33.7	54.7	
	GAMMA = 28		31.1	43.4	
	GAMMA = 50		31.5	44.1	
	GAMMA = 80		30.7	42.7	

The characteristics of these various bus interfaces at their source are summarized in Table 4.6.4-8. Values shown are valid for battery operation within the range of 18 to 26 volts.

The +28-volt switched telemetry bus is derived from the +28-volt main bus and therefore is not shown separately in the table. The switched +28-volt bus is provided to power analog telemetry circuits in the instruments. This permits specific housekeeping functions, such as housing temperatures, to be monitored while the instruments are turned OFF. Since the power source for the switched telemetry bus is the +28-volt main bus at the PSE, both buses possess similar characteristics.

TABLE 4.6.4-8. REGULATED BUS INTERFACE CHARACTERISTICS

Parameter	+28-V Main Bus	Pulse Load Bus	+10-V Common Bus
Bus Voltage	+28.0 V	+28.0 V	+10.0 V
Regulation	+0.56/-0.30 V	±0.56	±0.5 V
Output Impedance	< 0.16Ω (dc to 100 kHz)	< 0.2Ω (dc to 100 MHz)	< 1.0Ω (dc to 10 MHz)
Load Current	45.0A* max. from BVR alone 57.0A* max. from BVR and SA	0-23.25 A	100-800 mA
Voltage Ripple	150 mV p-p or 200 mV p-p including dead bands (dc to 100 kHz)	200 mV p-p (dc to 100 kHz)	250 mV p-p (dc to 10 MHz)
Transient Response	500 mV p-p for 7.5A ΔI	600 mV p-p for 2.1 A ΔI; 1.6 V p-p for 6.0 A ΔI	1 V pk
Voltage Range	+16 V to +38 V	+16 V to +38 V	+9 V to +15 V
Redundancy	Automatic Failure Detection & switchover for: • Mode Controller • Phase Control Circuit • Charge Regulator 4 out of 5 BVR Chan. Redundancy	Same as Main Bus	Redundant Converters; Diode OR'ed
Source Unit	PSE	PSE	CPC

*Includes Pulse Load Current

4.6.5 EQUIPMENT DESCRIPTION

4.6.5.1 Solar Array

4.6.5.1.1 General Description

The solar array is the primary source of satellite power. It provides electrical current to the regulated bus for operation of other satellite components and to charge the 3 batteries as required. During short periods of peak satellite load, energy from the batteries may also be used to supplement the current available from the solar array.

The solar array is an assembly of 10 coplanar solar panels. The solar array surface is canted with respect to the satellite Z axis (37° for morning orbits, 22° for afternoon orbits). The array is rotated about an axis parallel to the Z axis once per orbit by the solar array drive. The flat face of the solar array therefore "tracks" the sun to maintain an almost constant sun incidence angle around the orbit. The value of sun incidence angle is a function of the orbit sun angle as shown in Figure 4.6.5-1.

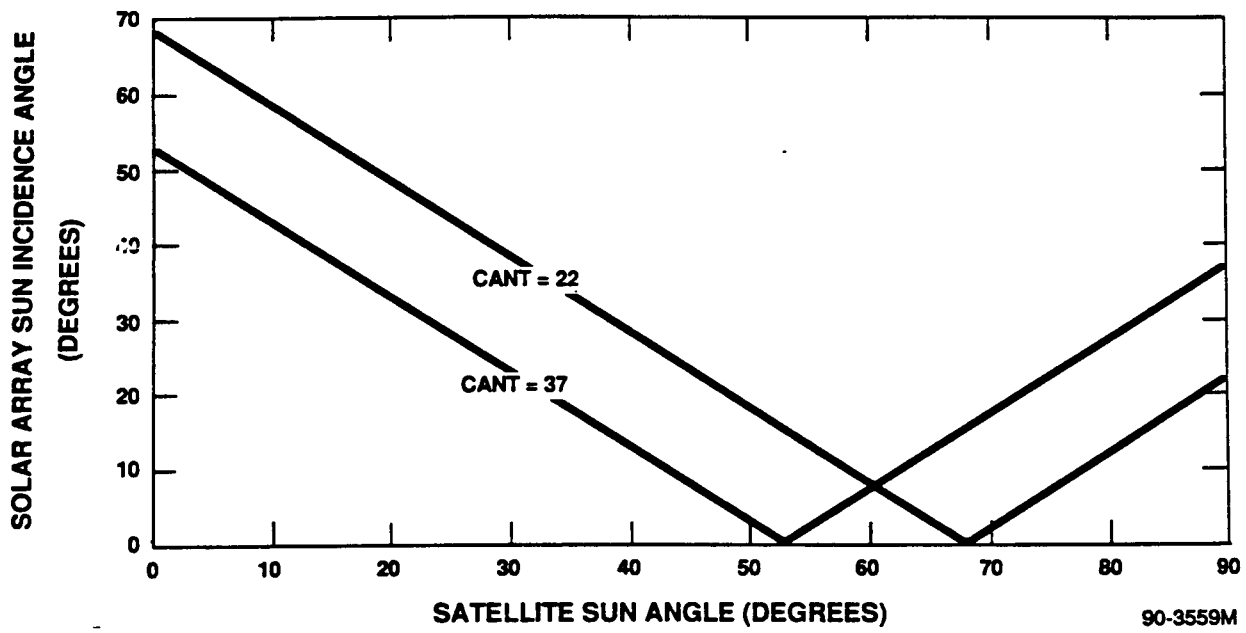

Figure 4.6.5-1. Incidence Angle vs. Sun Angle - No Rotational Offset

The equation for determining the solar array sun incidence angle is:

$$A = \cos^{-1} (\cos \gamma \cos [90 - \alpha] + \sin \gamma \sin [90 - \alpha] \cos \theta)$$

where A is the sun incidence angle,
γ is the spacecraft sun angle,
α is the cant angle (α = 37° or 22°),
and θ is the offset tracking angle (rotational angle).

Slip rings inside the solar array drive provide power and signal connections from the solar array to the satellite.

The series-parallel solar cell configuration for the array has been defined using minimum End Of Life (EOL) solar cell performance estimates. Each of the 10 array panels has 7 solar cell electrical circuits containing three parallel cells. On the eight inboard panels, there are 90 series-connected cells in each circuit, and on the outboard panels, there are 89 series-connected cells. The 70 individual array circuits are connected in parallel through individual isolation diode groups.

Each panel also contains seven partial shunt circuits and seven individual shunt drivers. The partial shunts are connected across 58 series cells, with each shunt assigned to its own solar cell circuit. The partial shunt dissipates the excess available solar array power in response to control signals from the mode controller in the PSE.

The cross section of the solar panel is given in Figure 4.6.5-2. The nominal solar cell dimensions are 0.797 x 1.591 x 0.010 inches. The solar cells are fabricated from one to three ohm-cm base resistivity, N-on-P silicon wafers with a 22 mil wide N strip and have solderless silver-paladium-titanium contacts. The cell has a multi-layer anti-reflective coating on the negative surface.

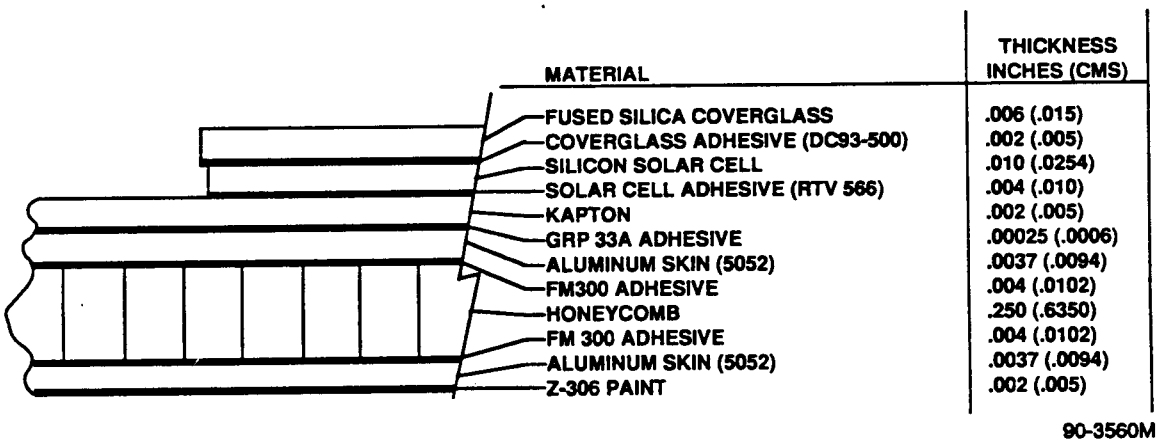

Figure 4.6.5-2. Aluminum Skin Solar Panel Cross Section

The solar cells are protected by a 6 mil thick fused silica platelet (coverglass) bonded to the active surface. Each filter platelet has an ultraviolet rejection coating (with a 350 nm cut-on)* applied to the cell-facing surface and a MgF_2 anti-reflecting coating applied to the sun-facing surface. Each filter platelet (coverglass) is bonded to the solar cells using Dow Corning 93-500, a clear silicone adhesive. The solar cells in turn are bonded to the panel substrate using RTV 566 silicone rubber adhesive with GE SS4004 primer.

The solar cell interconnects are made with 0.002 inch thick expanded silver mesh. The mesh is oriented to provide stress relief between parallel-connected cells, while a formed hump provides stress relief between series-connected cells. Solder joints to solar cells are made using eutectic solder containing two percent silver.

4.6.5.1.2 Cell Degradation Considerations

Charged particle irradiation is the major cause of solar cell degradation in orbit. Because of the multi-energy level, omnidirectional nature of space radiation, it is virtually impossible to duplicate the space environment in the laboratory. In order to predict solar cell degradation in space, GE ASD has used the concept of "damage equivalence." By applying damage coefficients (which are a function of particle energy, the type of particle, and the density of the solar cell shielding material), the space environment is translated into a damage equivalent, normally incident (DENI) 1 MeV electron fluence. The changes in solar cell parameters with normally incident, 1 MeV electron irradiation are well known from a variety of laboratory tests, hence the calculated DENI 1 MeV data can be coupled with the laboratory data to characterize the solar cell degradation in orbit.

The omnidirectional space radiation for the 99 degree inclined, 852 km circular orbit is defined for the NOAA-KLM program in GSFC X-600-87-11. This data, based on the August 1987 update of the radiation environment by E. G. Stassinopoulos, is repeated in Tables 4.6.5-1 through 4.6.5-3.

The radiation resistance model for the solar cell includes 6 mils of coverglass on the front side and approximately 18.4 mils of equivalent aluminum backshielding. To allow for the self-shielding effect for cells irradiated from the rear, seven mils of the actual solar cell thickness was included in the backshield model. The electron and proton damage coefficients for the solar cells are presented in Figures 4.6.5-3 and 4.6.5-4**. Using the damage coefficients and the radiation environment from Tables 4.6.5-1, 4.6.5-2, and 4.6.5-3 (the yearly alpha particle flux is considered to be five percent of the flare proton flux), the DENI 1 MeV electron fluences have been calculated and are presented in Table 4.6.5-4.

---

*The wavelength or "cut-on" point at which the solar cell coverglass begins transmission of light is defined as the point at which transmission is 50 percent.

**From "Solar Cell Radiation Handbook," JPL Publication 82-69, dated November 1, 1982.

TABLE 4.6.5-1. TRAPPED PROTON ENVIRONMENT

(Orbit-Integrated, Omnidirectional, Integral Fluxes) Perigee = 852 KM, Apogee = 852 KM, Inclination = 99°	
Energy (MeV)	Averages No. of Particles/cm^2-day
2	2.453E07
3	2.051E07
4	1.801E07
5	1.632E07
6	1.512E07
8	1.371E07
10	1.262E07
15	1.128E07
20	1.022E07
25	9.613E06
30	9.057E06
35	8.623E06
40	8.216E06
45	7.832E06
50	7.470E06
60	6.786E06
80	5.625E06
100	4.685E06
150	2.877E06
200	1.798E06
250	1.112E06
300	6.918E05
350	4.333E05
400	2.724E05
500	1.088E05

Data Source: "METSAT Charged Particle Environment Study" Revised Edition, Method 2, August 1987, by E.G. Stassinopoulos, J.M. Barth, R.L. Smith, GSFC X-600-87-11.

TABLE 4.6.5-2. TRAPPED ELECTRON ENVIRONMENT

(Orbit-Integrated, Omnidirectional, Integral Fluxes) Inclination = 99°, Circular Orbit, Altitude 852 km			
	Averaged No. of Particles/cm^2-day		
Energy (MeV)	Inner Zone L,<2.8	Outer Zone L,>2.8	Total
0.10	3.100E10	8.057E09	3.906E10
0.50	6.615E08	1.432E08	2.094E09
0.80	1.446E08	6.879E08	8.326E08
1.00	7.467E07	4.701E08	5.447E08
1.25	4.532E07	3.071E08	3.523E08
1.50	2.761E07	2.023E08	2.298E08
1.75	1.828E07	1.321E08	1.504E08
2.00	1.213E07	8.667E07	9.879E07
2.25	8.173E06	5.772E07	6.590E07
2.50	5.517E06	3.861E07	4.412E07
2.75	2.265E06	2.441E07	2.667E07
3.00	9.458E05	1.547E07	1.642E07
3.25	2.945E05	9.632E06	9.927E06
3.50	9.349E04	6.010E06	6.104E06
3.75	3.060E04	3.473E06	3.505E06
4.00	8.320E04	2.019E06	2.027E06
4.50	1.890E02	5.956E05	5.958E05
5.00	0.00	1.628E05	1.629E05
5.50	0.00	3.594E04	3.594E04
6.00	0.00	5.152E04	5.151E03
6.50	0.00	6.242E01	6.243E01
7.00	0.00	0.00	0.00

TABLE 4.6.5-3. ORBIT ATTENUATED SOLAR FLARE PROTON FLUENCES

for Cutoff Dipole Shell of 5 Earth Radii (Omnidirectional, Integral intensities) Circular Orbit, Inclination 99° Solar Maximum, Altitude 852 km (460.0 nautical miles)			
	Total No. of Particles/cm^2 for a Mission Duration of 2 Years		
	Confidence level Q (%)*		
	80-87	88-96	97-99
Energy (MeV)	No. of Anomalously Large Events Predicted (1)	(2)	(3)
10.0	3.402E09	6.804E09	1.021E10
20.0	2.479E09	4.958E09	7.437E09
30.0	1.791E09	3.582E09	5.373E09
40.0	1.279E09	2.558E09	3.837E09
50.0	9.058E08	1.812E09	2.717E09
60.0	6.369E08	1.274E09	1.911E09
70.0	4.474E08	8.948E08	1.342E09
80.0	3.135E08	6.269E08	9.404E08
90.0	2.189E08	4.379E08	6.568E08
100.0	1.527E08	3.054E08	4.581E08

*Q denotes the degree of confidence assigned to the results, namely that for the specified mission duration; the calculated fluences are the smallest values that will not be exceeded by actually encountered intensities.

Data Source: "METSAT Charged Particle Environment Study" Revised Edition, Method 2, August 1987, by E.G. Stassinopoulos, J.M. Barth, R.L. Smith, GSFC X-600-87-11.

The solar cell degradation factors given in Table 4.6.5-5 are used to generate maximum BOL, nominal EOL and minimum EOL solar cell performance characteristics. Data is obtained by orthogonal translation of the baseline solar cell I-V curve in accordance with the current and voltage products of the factors in the table. The solar cell EOL charged particle losses listed in the table are obtained from the data in Figure 4.6.5-5 generated from radiation tests on G-STAR cells. The Solar Cell Radiation Handbook gives the charged particle damage factors for the 10 mil thick silicon coverglass. Tests on the SATCOM KU covering are the source for the coverglass adhesive degradation due to ultraviolet radiation.

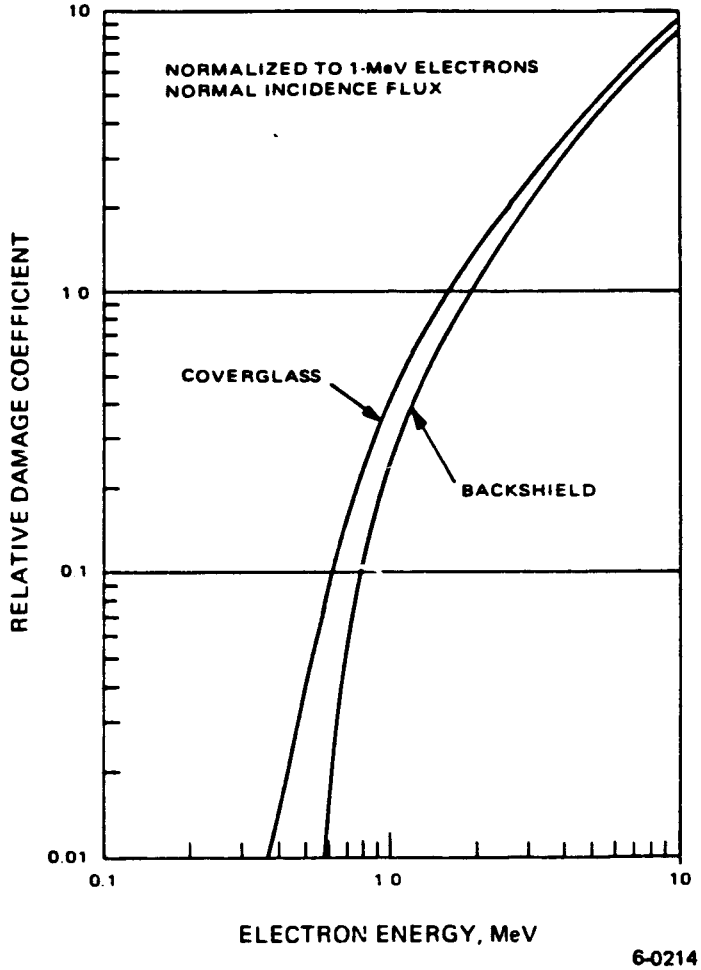

Figure 4.6.5-3. Solar Cell Electron Damage Coefficients

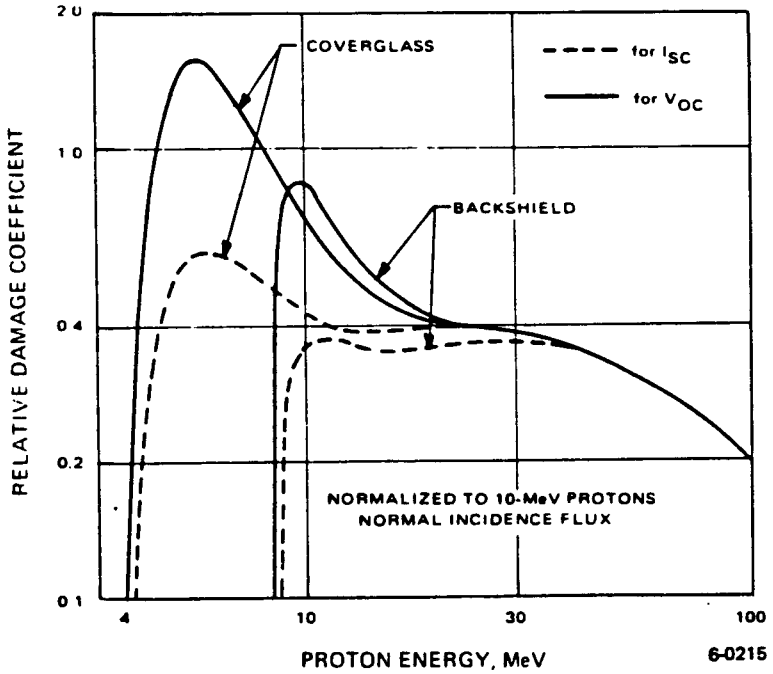

Figure 4.6.5-4. Solar Cell Proton Damage Coefficients

TABLE 4.6.5-4. TIROS KLM SOLAR-CELL FLUENCE - TWO-YEAR MISSION*

	(6-mil Coverglass and 10-mil Solar Cell)					
	Front Thickness 0.0467 GM/CM**2		Back Thickness 0.1258 GM/CM**2		Total Fluence	
Particle Type	I_{sc}	V_{oc}	I_{sc}	V_{oc}	I_{sc}	V_{oc}
Protons	1.186E+13	1.737E+13	8.131E+12	9.944E+12	1.991E+13	2.731E+13
Solar Protons	7.497E+12	8.193E+12	7.014E+12	8.345E+12	1.451E+13	1.654E+13
Solar Alphas	1.334E+12	2.405E+12	6.328E+11	1.052E+12	1.968E+12	3.457E+12
Electrons	5.900E+11	5.900E+11	2.970E+11	2.970E+11	8.807E+11	8.807E+11
Total Fluence	2.128E+13	2.856E+13	1.607E+13	1.964E+13	3.727E+13	4.819E+13

1-MeV-Equivalent-Electron Fluence for I_{sc} = 3.727E+13 E/CM**2
1-MeV-Equivalent-Electron Fluence for V_{oc} = 4.819E+13 E/CM**2

*METSAT Environment X-600-87-11

TABLE 4.6.5-5. SOLAR ARRAY DEGRADATION FACTORS

Degradation Factor	Maximum BOL	Nominal BOL	Nominal 2 Year	Minimum 2 Year
ISC Factors				
1. SA Assembly Loss	0.978	0.978	0.978	0.978
2. Coverglass Charged Particle Damage	1.00	1.00	0.995	0.995
3. Coverglass Adhesive UV Degradation	1.00	0.975	0.975	0.975
4. Sun Intensity Variation	1.034	1.00	1.00	0.966
5. Solar Cell Charged Particle Damage	1.00	1.00	0.962	0.962
Maximum Power Factors				
1. SA Assembly Loss	0.980	0.980	0.980	0.980
VOC Factors				
1. Coverglass Adhesive UV Degradation	1.00	0.995	0.995	0.995
2. Solar Cell Charged Particle Damage	1.00	1.00	0.973	0.973

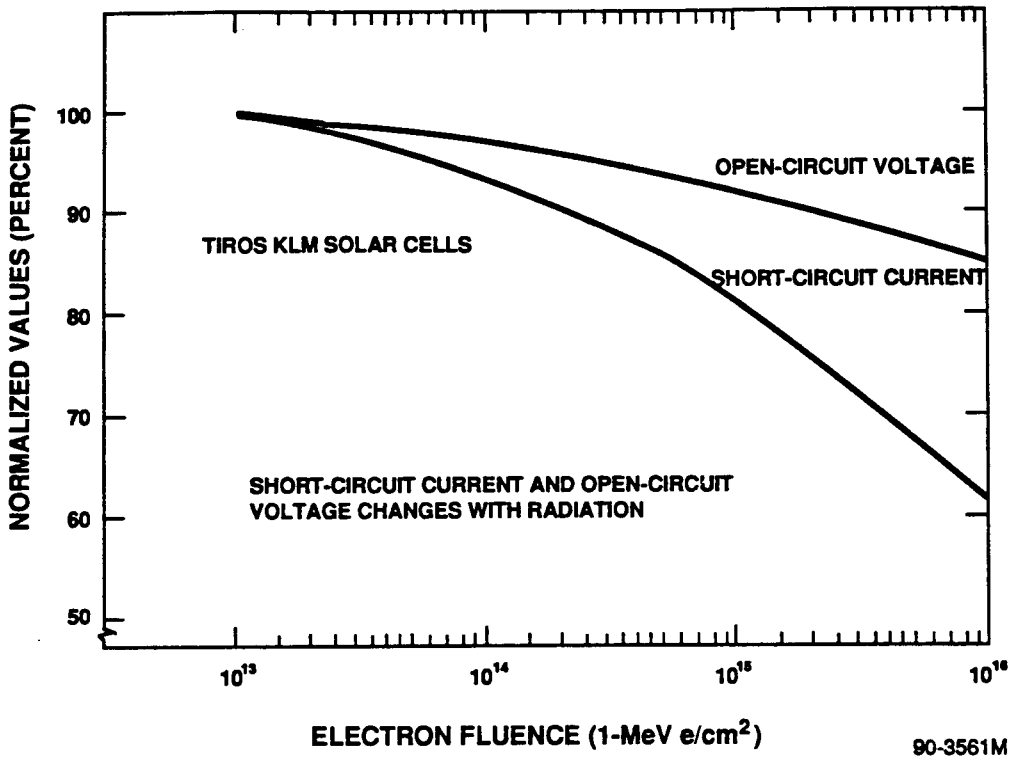

Figure 4.6.5-5. Short-Circuit Current and Open-Circuit Voltage Changes with Radiation

4.6.5.1.3 Design Characteristics

The solar array design characteristics are summarized in Table 4.6.5-6.

The baseline solar cell I-V curve for the NOAA solar array is presented in Figure 4.6.5-6. This curve is generated from vendor supplied data and cell selection from GE 2629104-1 high efficiency cells. The cell selection procedure assigns available cells to modules so that array output is optimized.

Maximum BOL, nominal EOL, and minimum EOL solar cell I-V curves shown in Figure 4.6.5-7 complete the family of design curves for the NOAA-KLM program. The degradation factors shown in Table 4.6.5-5 were used to generate the data.

The solar array current availability curves in Figure 4.6.5-8 were derived from the solar cell I-V characteristics presented herein. The minimum EOL solar cell I-V curve was used for the load capability analysis described in Section 4.6.4.2.2.

Table 4.6.5-7 presents the solar cell temperature coefficients which were used in the NOAA-KLM solar array design. These coefficients are developed from data in the JPL Solar Cell Radiation Handbook.

TABLE 4.6.5-6. SOLAR ARRAY PARAMETERS

Parameter	Value
Orientation System	Sun oriented, single degree of freedom
Array Configuration	10 coplanar panels
Array Position (Deployed)	Array normal 68° or 53° from spacecraft +Z axis
Array Temperature	+74.3°C maximum at $\gamma = 80°$ -80.6°C minimum at $\gamma = 80°$ (end of eclipse)
Array Operating Point Voltage	31 volts
Array Power availability at 32 V	1993 watts maximum BOL at $\gamma = 68°$ (22° Cant angles) 951 watts minimum EOL at $\gamma = 0°$ (22° Cant angles)
Solar Cell Design	N on P silicon - high efficiency cell 4.04 x 2.02 cm 0.254 mm thickness 1 to 3 ohm-cm base resistivity
Solar Cell "Tree"	89 series cells per circuit (outboard 2 panels) 90 series cells per circuit (all other panels) 3 parallel cells per circuit 7 circuits per panel 10 panels per array
Total Solar Cells	18,858 (does not include cells for patch telemetry)
Coverglass Design	Fused silica material 0.152 mm thickness MgF_2 anti-reflective coating 350 nm cut-on filter
Partial Shunt-Solar Cell Configuration	Tap-off point at 58 series cells (inboard), 57 series cells (outboard)
Maximum Shunt Power Dissipation, Each Shunt Circuit	16.0 watts at $\gamma = 68°$ (BOL, No load)
Total Number of Shunt Circuits	70 (Fig. 4.6.5-11)
Solar Array Size	Each panel 107.5 x 24.2 inches
Solar Array Weight	Each panel 18.8 pounds maximum

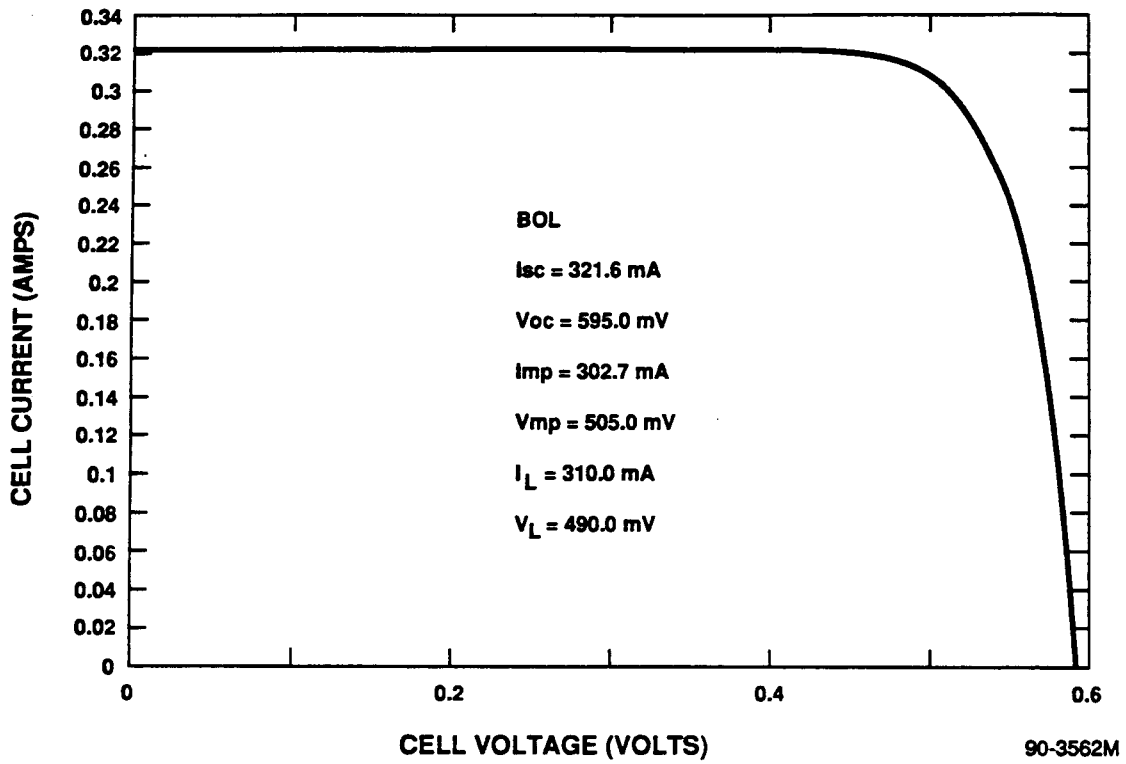

Figure 4.6.5-6. Baseline Solar Cell I-V Characteristics @ 28°C

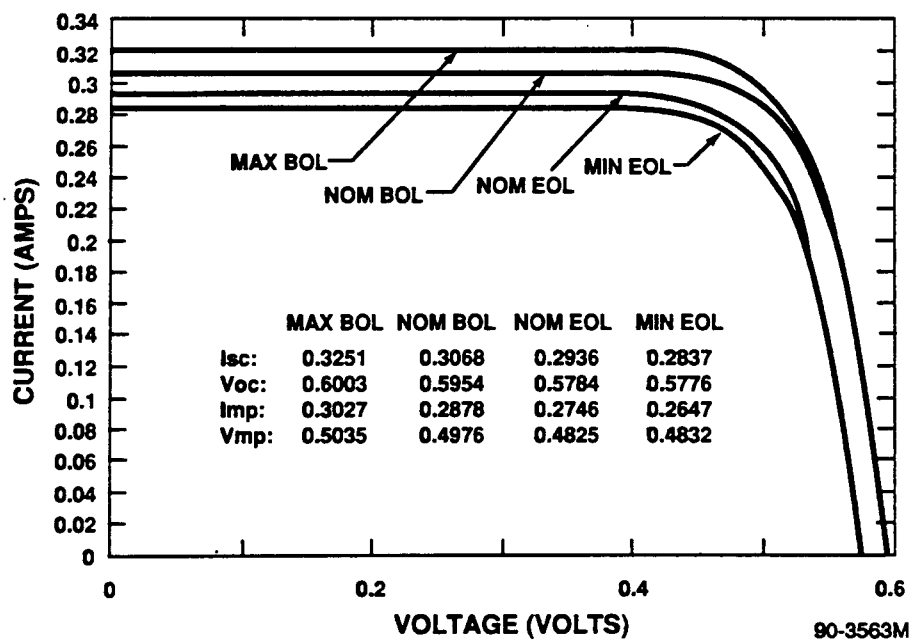

Figure 4.6.5-7. Degraded Solar Cell I-V Curves @ 28°C

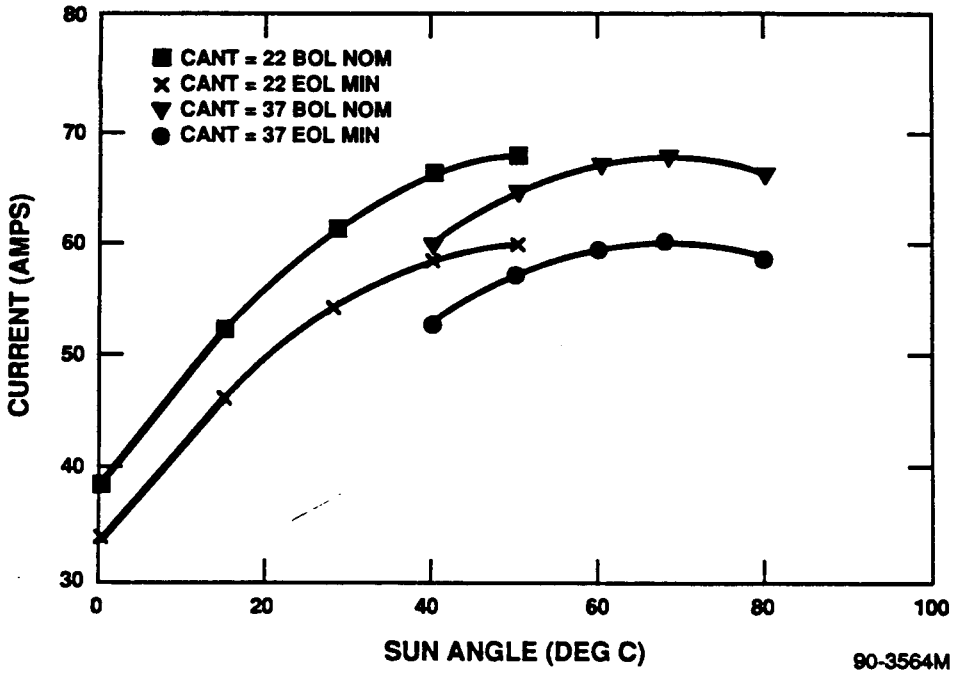

Figure 4.6.5-8. Solar Array Current Availability

TABLE 4.6.5-7. SOLAR CELL TEMPERATURE COEFFICIENTS

Factor	Coefficient	
	BOL	EOL
dI_{SC}/dT (μA/°C)	162	198
dV_{OC}/dT (mV/°C)	2.10	2.16

dI_{SC} = change in short circuit current
dV_{OC} = change in open circuit voltage
dT = change in temperature

The solar array thermal properties are presented in Table 4.6.5-8. The front side absorptance and emittance data have been adjusted for the materials and spacing between solar cells. The emittance is primarily a function of the coverglass material; for NOAA-KLM, the coverglass is fused silica. The array panel back sides are covered with black paint to provide high emissivity and reduce reflections.

The solar array temperature-time profile at the design-boundary sun angles is shown in Figure 4.6.5-9. The temperatures were calculated by a specialized

TABLE 4.6.5-8. SOLAR ARRAY THERMAL PROPERTIES

Effective Thermal Properties	Value
Front side absorptance	0.700
Front side emittance	0.810
Back side absorptance	0.960
Back side emittance	0.910

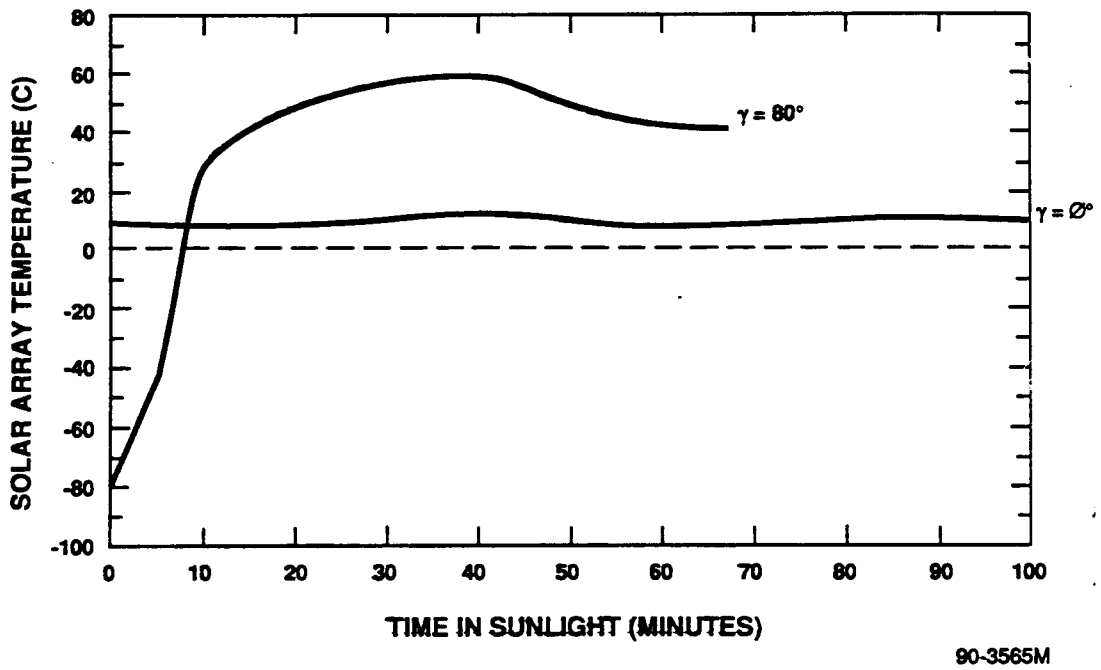

Figure 4.6.5-9. Solar Array Temperatures at Boundary Sun Angles

computer program written for the TIROS/5D-2 power subsystem. The computer models the solar array as a single panel (two surfaces) and only considers the interaction of direct sunshine, reflected sunshine from earth, and the earth emitted radiation.

The temperature time profile at an 80 degree sun angle shows the lowest temperature (-80.6°C) anticipated for the NOAA-KLM solar cells. The maximum temperatures, as a function of sun angle, are presented in Figure 4.6.5-10. These temperature profiles were used for the array electrical characterization given in Figure 4.6.5-8.

Each solar cell circuit has a tap point at the negative side of the 32nd cell from the circuit positive. There is a separate shunt circuit associated with each tap point, shown in Figure 4.6.5-11, which consists of two redundant shunt transistors and one common driver transistor. The drive power is

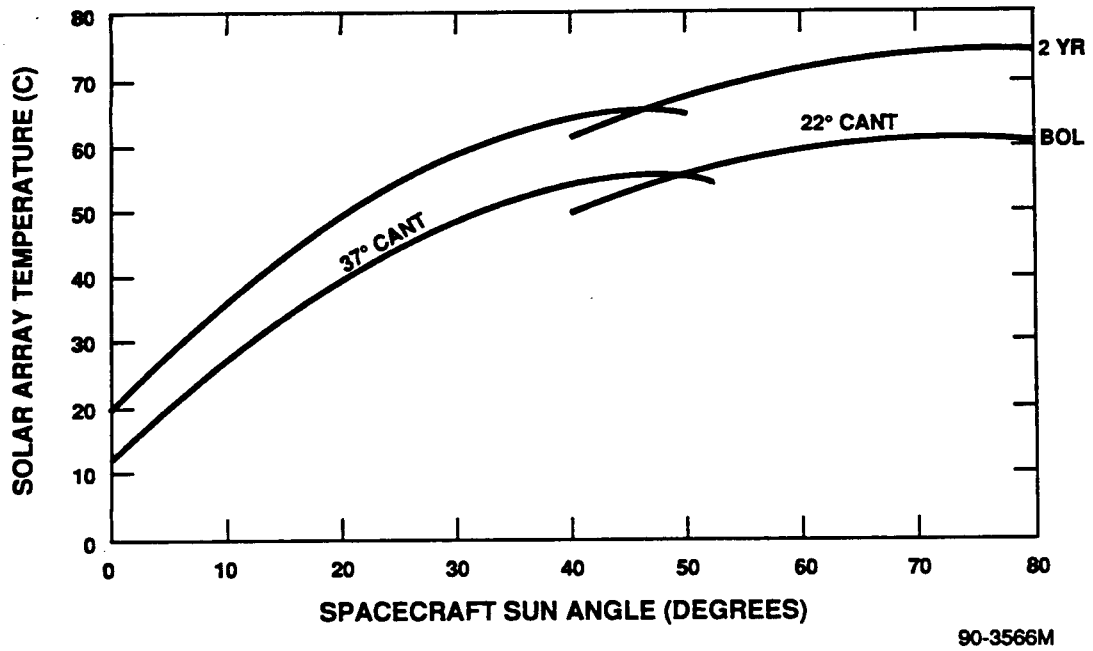

Figure 4.6.5-10. Maximum Solar Array Temperature Versus Sun Angle

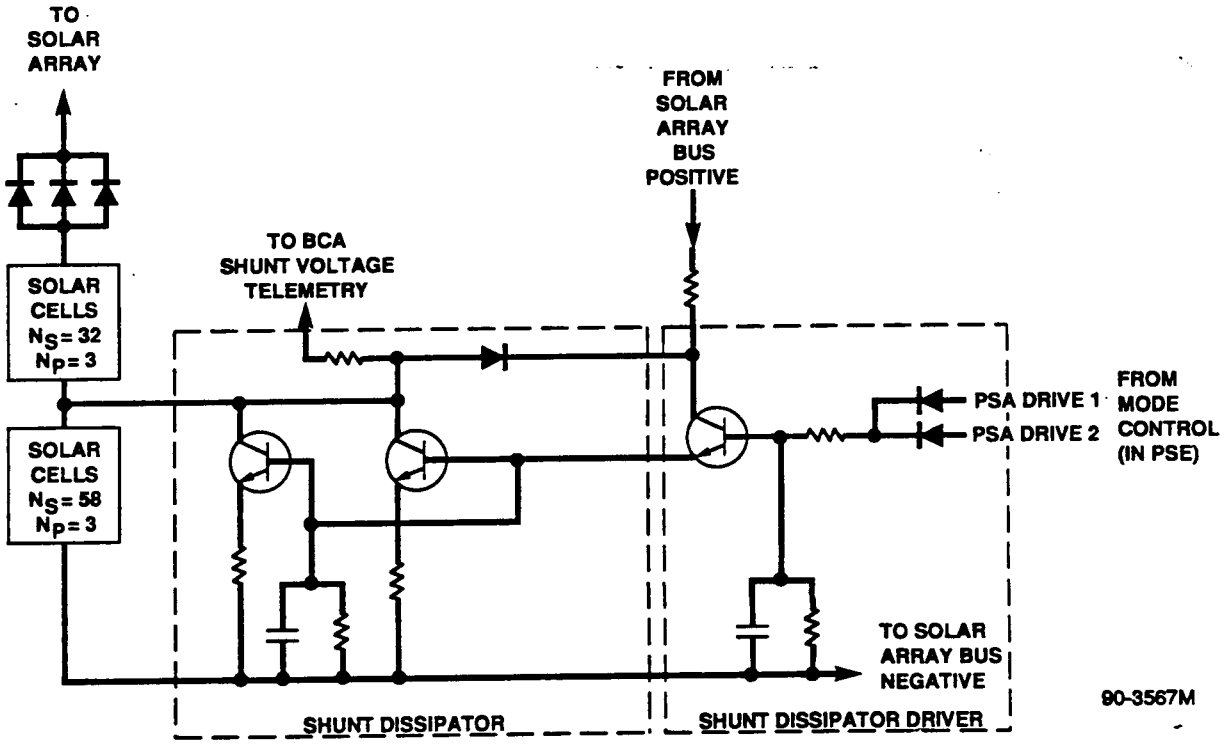

Figure 4.6.5-11. Solar Array Partial Shunt Regulator Circuits

obtained directly from the solar array power bus on the panels. The control signals from the PSE are transmitted to the driver via a redundant slip ring arrangement.

The partial shunt performance depends strongly on the solar cell circuit characteristics. Figure 4.6.5-12 presents the shunt performance as a function of solar cell circuit current output at each of the solar array temperature extremes. The characteristics are modeled at the 0 degree sun incidence angle using the maximum BOL I-V curve from Figure 4.6.5-7. Maximum shunt heat dissipation occurs at the highest array temperature with zero loading; minimum voltage across the shunt occurs at the lowest array temperature, also with zero loading. The maximum shunt circuit heat dissipation as a function of satellite sun angle is plotted in Figure 4.6.5-13. This curve incorporates changes in solar array sun incidence angle and maximum temperature, both of which vary with satellite sun angle.

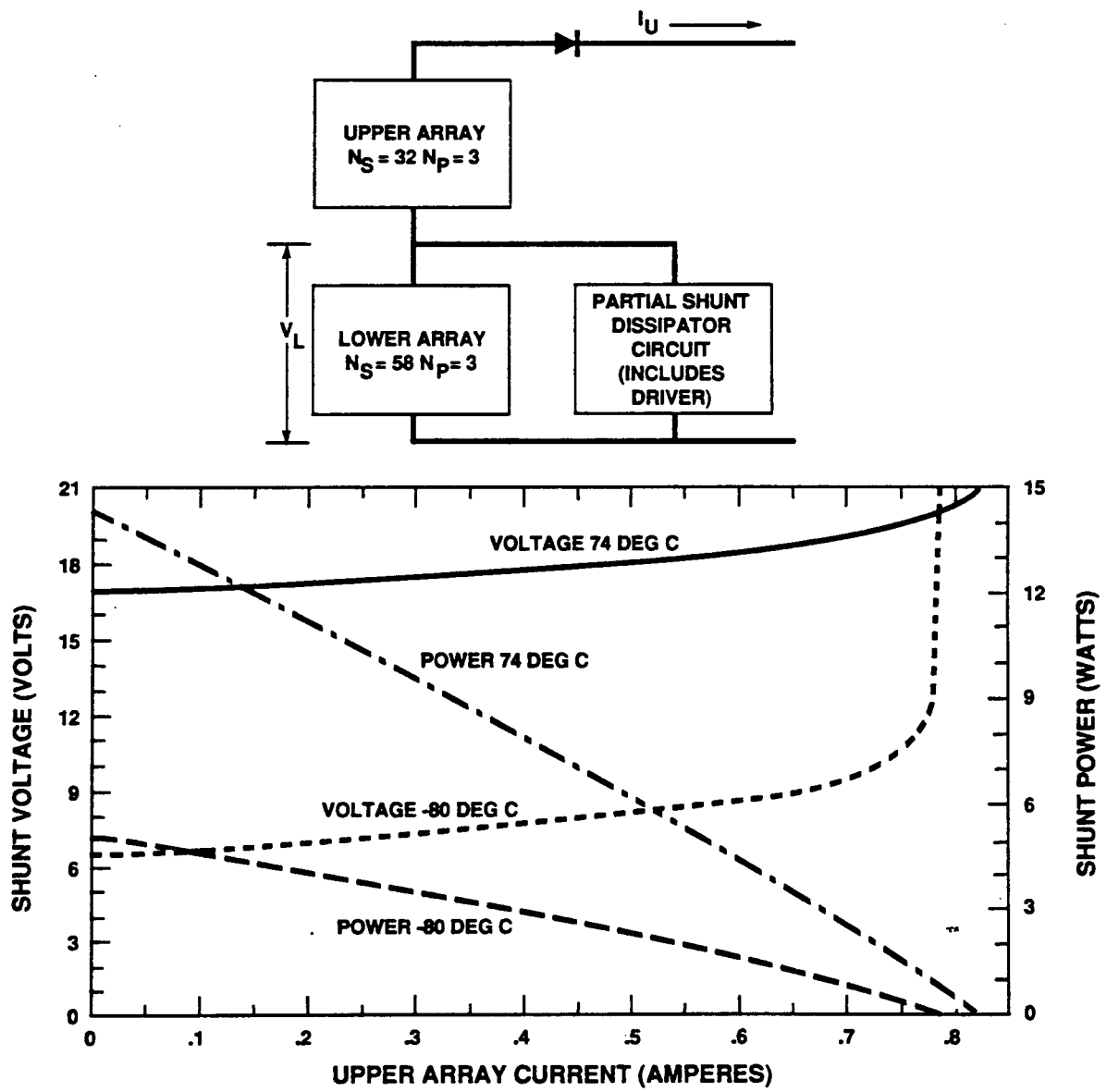

Figure 4.6.5-12. Partial Shunt Performance

90-3568M

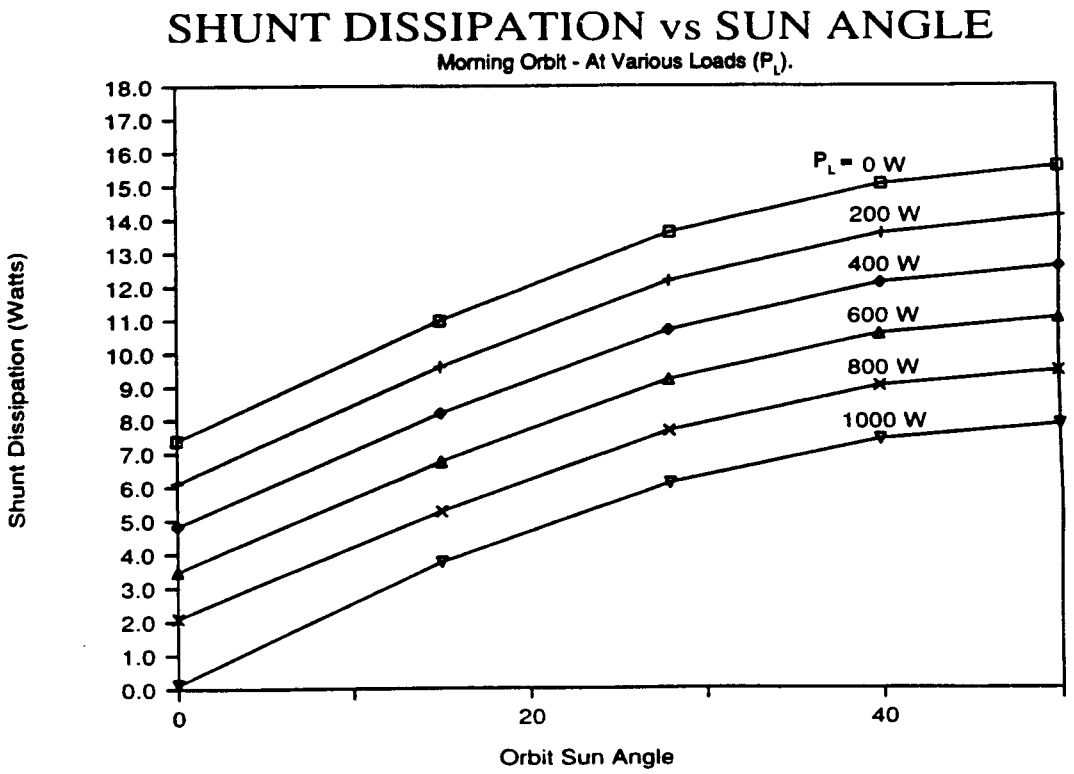

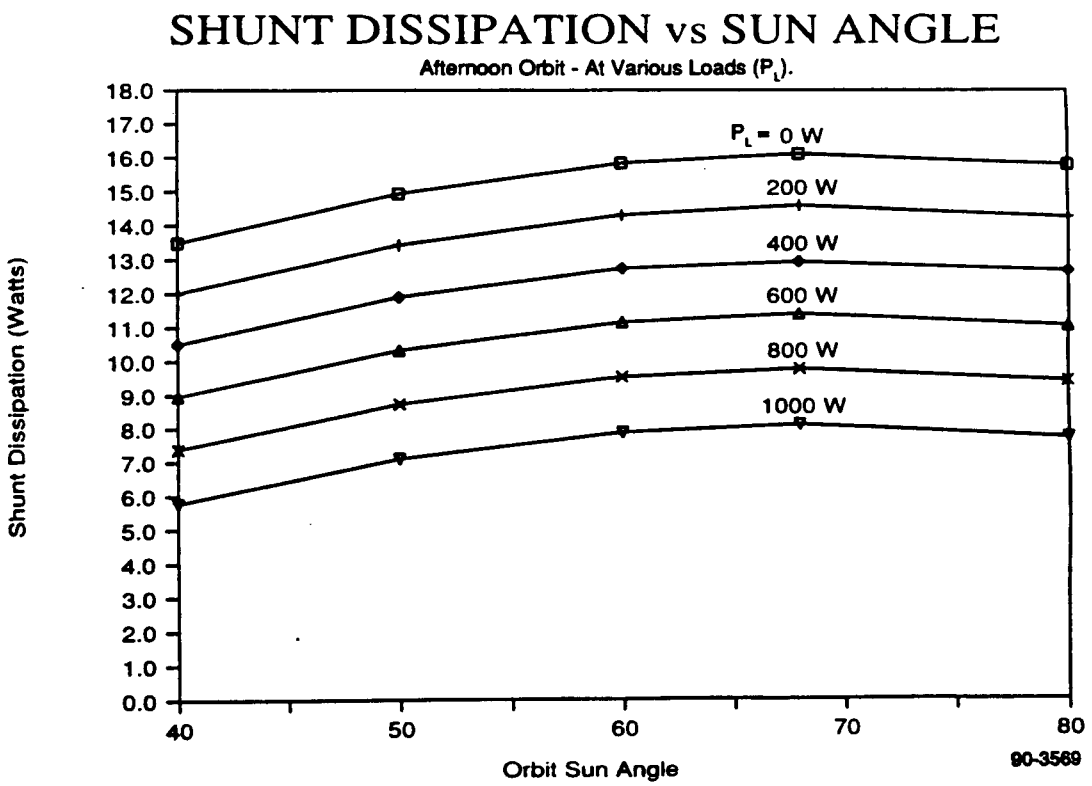

Figure 4.6.5-13. Maximum Partial Shunt Heat Dissipation

4.6.5.1.4 Solar Array Telemetry

The telemetry sensors associated with the Solar Array are listed in Table 4.6.5-9. Figure 4.6.5-14 shows the panel locations of these sensors.

A description of these sensors and their associated conditioning networks is given in the sections that follow.

TABLE 4.6.5-9. SOLAR ARRAY TELEMETRY

Sensor Function	Abbreviation
Solar Array Partial Shunt Voltage	VPSH
Solar Array Short Circuit Current (Panel 10)	ISC
Solar Cell Load Current 1 (Panel 9)	ISCL1
Solar Cell Load Voltage 1 (Panel 9)	VSCL1
Solar Cell Load Current 2 (Panel 4)	ISCL2
Solar Cell Load Voltage 2 (Panel 4)	VSCL2
Solar Array Operating Voltage	VSA
Solar Array Unreg Bus Voltage	VSB
Solar Array Position Sensor 1 (Panel 1)	APS1
Solar Array Position Sensor 2 (Panel 10)	APS2
Solar Array Panel 4 High Temperature	TSAH2
Solar Array Panel 4 Low Temperature	TSAL2
Panel 4 Shunt Heat Sink High Temperature	TSHH
Panel 4 Shunt Heat Sink Low Temperature	TSHL
Solar Array Panel 10 High Temperature	TSAH3
Solar Array Panel 10 Low Temperature	TSAL3
Solar Array Panel 9 High Temperature	TSAH1
Solar Array Panel 8 Low Temperature	TSAL1
Solar Array Hinge 1 Deployment	Hinge 1
Solar Array Hinge 2 Deployment	Hinge 2
Solar Array Hinge 3 Deployment	Hinge 3
Solar Array Hinge 4 Deployment	Hinge 4
Solar Array Hinge 5 Deployment	Hinge 5
Solar Array Hinge 6 Deployment	Hinge 6
Solar Array Hinge 7 Deployment	Hinge 7
Solar Array Hinge 8 Deployment	Hinge 8
Solar Array Hinge 9 Deployment	Hinge 9
Solar Array Hinge 10 Deployment	Hinge 10
Solar Array Mast Cant Deployment	CANT

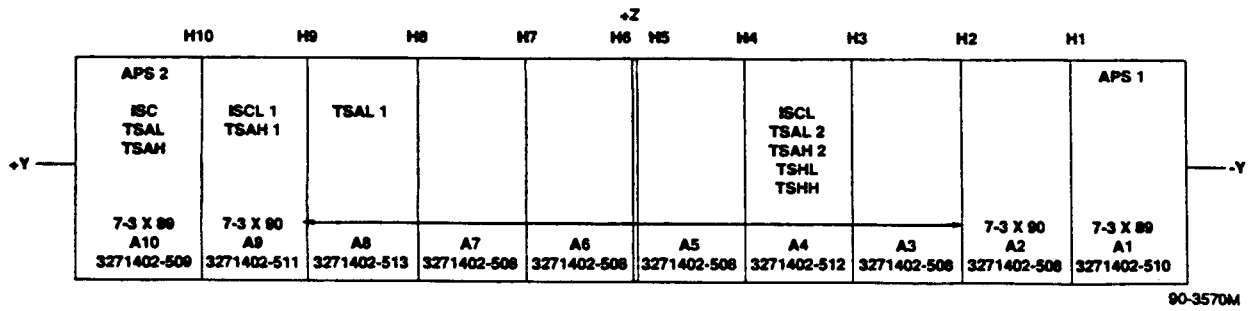

Figure 4.6.5-14. NOAA KLM Solar Array Telemetry Locations

4.6.5.1.4.1 Solar Array Position Sensor (APS). These telemetry channels provide measurement of the position of the solar array relative to the sun. Each sensing element consists of two dedicated solar cells mounted on opposite sides of an angled bracket that is located on the outboard solar panels. The active conditioning circuit for each array-position sensor is a null detection circuit contained in the SATCU. A circuit diagram of the APS is shown in Figure 4.6.5-15. The nominal telemetry voltage for zero solar array pointing error is 2.25 V.

With appropriate software, these telemetry channels can provide a method of orienting the solar array that is independent of ephemeris and unaffected by SAD two-pole resolver failure.

4.6.5.1.4.2 Solar Cell Load Current Sensor. These telemetry channels provide a measurement of the current produced by two series solar cells operating at approximately 0.70 V. The sensing elements are pairs of dedicated solar cells located on solar array panels 4 and 9; the active conditioning circuits are contained in the SATCU. A circuit diagram of the solar cell load current sensor is shown in Figure 4.6.5-16.

The purpose of these telemetry channels is to indicate the load current at the operating voltage on a per-cell basis. The cell load current telemetry, in conjunction with the cell load voltage sensor, allows accurate tracking of solar cell degradation with time. In sunlight, the nominal solar cell load current should be 225 to 275 mA.

4.6.5.1.4.3 Solar Cell Load Voltage Sensor. These telemetry channels provide measurement of the voltage across the solar cells of the ISCL sensors and are shown in Figure 4.6.5-16.

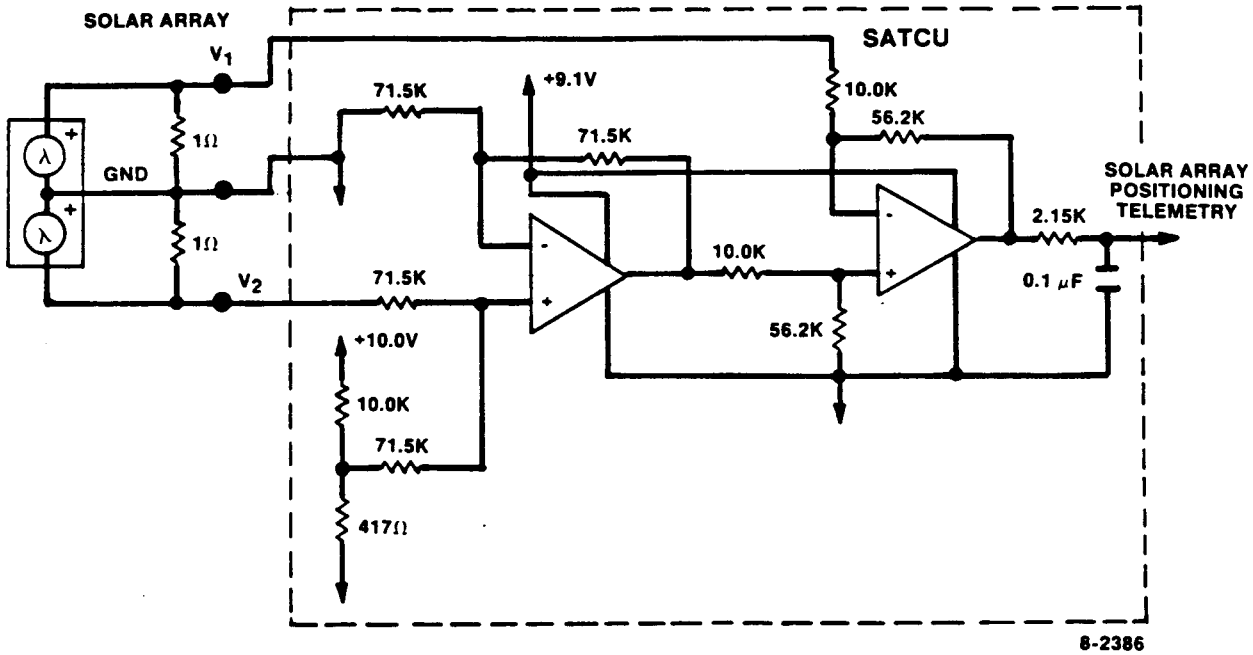

Figure 4.6.5-15. APS Sensor Circuit

4.6.5.1.4.4 Solar Array Operating Voltage Sensor. This telemetry channel provides a measurement of the average operating voltage of the actual solar-cell circuits that make up the full array. This information, when combined with the partial shunt voltage sensor information, permits determination of the average upper solar cell circuit operating point. 70 resistors located on the solar panels are used to sample and average the voltages from each of the 70 solar cell circuits that comprise a full array. The 70 sampling resistors are on the solar array; the passive conditioning circuit is located in the SATCU. A circuit diagram for the solar array voltage sensor is shown in Figure 4.6.5-17.

The upper solar array voltage is expected to vary from zero volts during eclipse to a maximum value of approximately 32 volts during sunlight.

4.6.5.1.4.5 Solar Array Unregulated Bus Voltage Sensor. This telemetry channel provides measurement of the unregulated solar array bus voltage. The passive conditioning circuit is located in the SATCU. This information, along with the regulated bus voltage, allows determination of the power losses between the solar array bus and the control point within the PSE. This signal can also be used in conjunction with the upper solar array voltage telemetry to determine the voltage drop across the solar array isolation diodes. A circuit diagram of the solar array bus voltage sensor is shown in Figure 4.6.5-18.

The solar array bus voltage is expected to have a maximum value of approximately 31 V during sunlight.

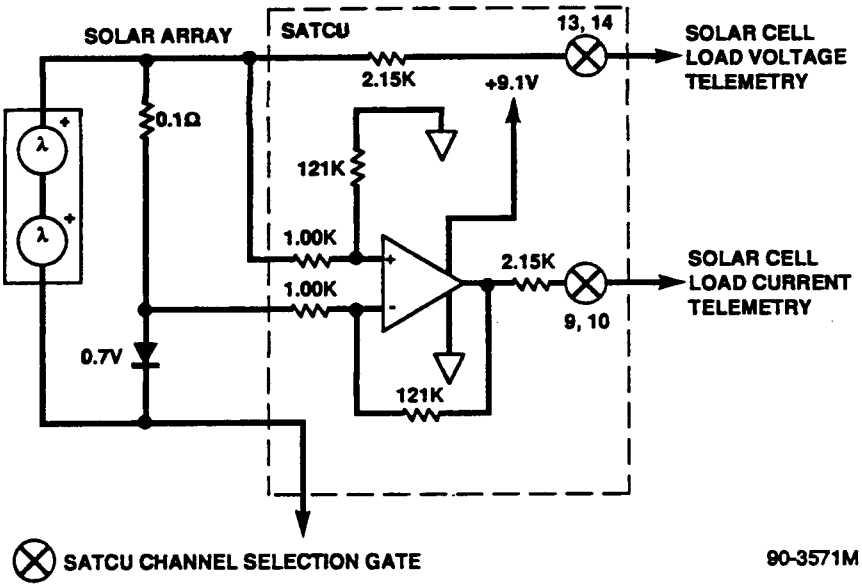

Figure 4.6.5-16. Solar Cell Load Current and Load Voltage Sensor Circuits

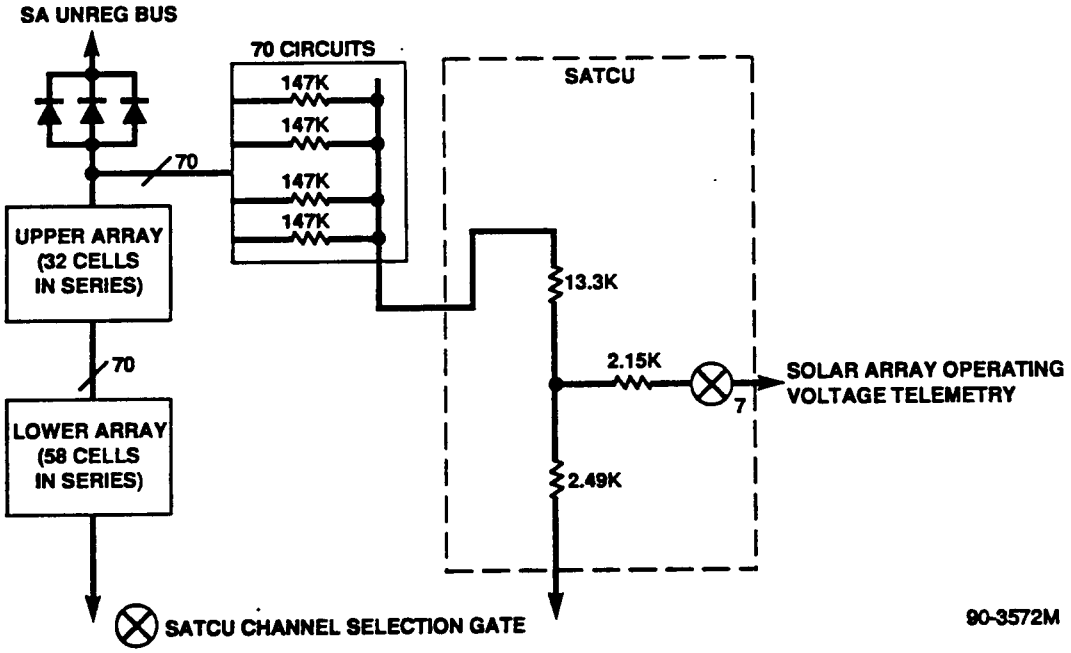

Figure 4.6.5-17. Solar Array Voltage Sensor Circuit

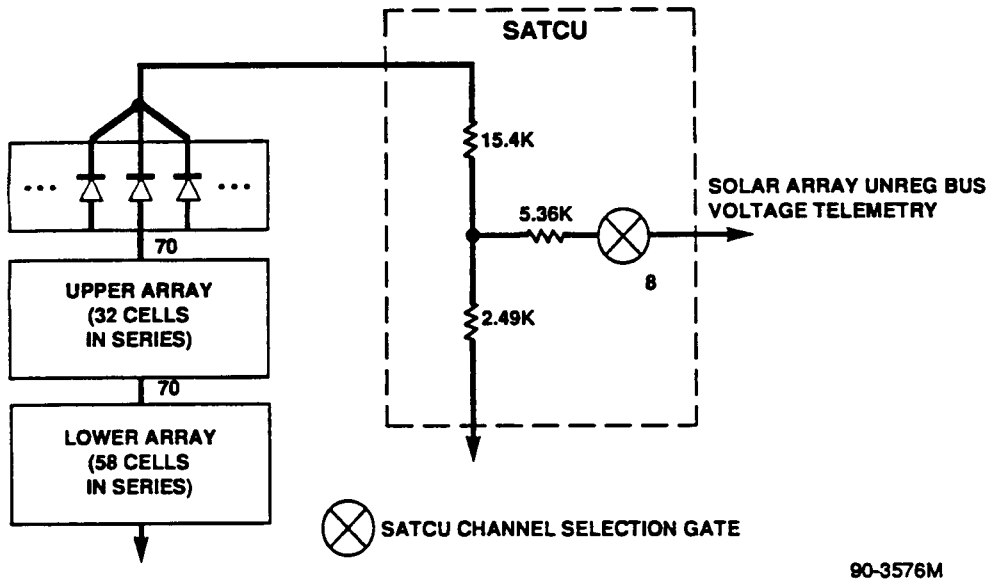

Figure 4.6.5-18. Solar Array Bus Voltage Sensor Circuit

4.6.5.1.4.6 Solar Array Hinge Deployment Sensors. These telemetry channels monitor the amount of rotation of the solar array panel hinges, and therefore indicate the angles of the solar panels with respect to each other. The sensing elements are potentiometers mounted to each solar array hinge pin. A circuit diagram of the solar array hinge deployment sensors is shown in Figure 4.6.5-19.

4.6.5.1.4.7 Solar Array High Temperature Sensors. These telemetry channels provide high-range temperature measurements of the solar array. The thermistor sensing circuits 1 through 3 are located on the back of array panels 9, 4, and 10, respectively. A circuit diagram of the solar array high temperature sensor circuit is shown in Figure 4.6.5-20.

4.6.5.1.4.8 Solar Array Low Temperature Sensors. These telemetry channels provide low-range temperature measurements of the solar array. The thermistor sensing circuits 1 through 3 are located on the back of array panels 8, 4, and 10, respectively. A circuit diagram for the solar array low temperature sensors is shown in Figure 4.6.5-21.

Solar array temperatures are expected to vary widely, from as low as -80.6°C at the end of eclipse to as high as +74.3°C near spacecraft noon. TSAL1 through TSAL3 are used in conjunction with TSAH1 through TSAH3 to measure the complete temperature range.

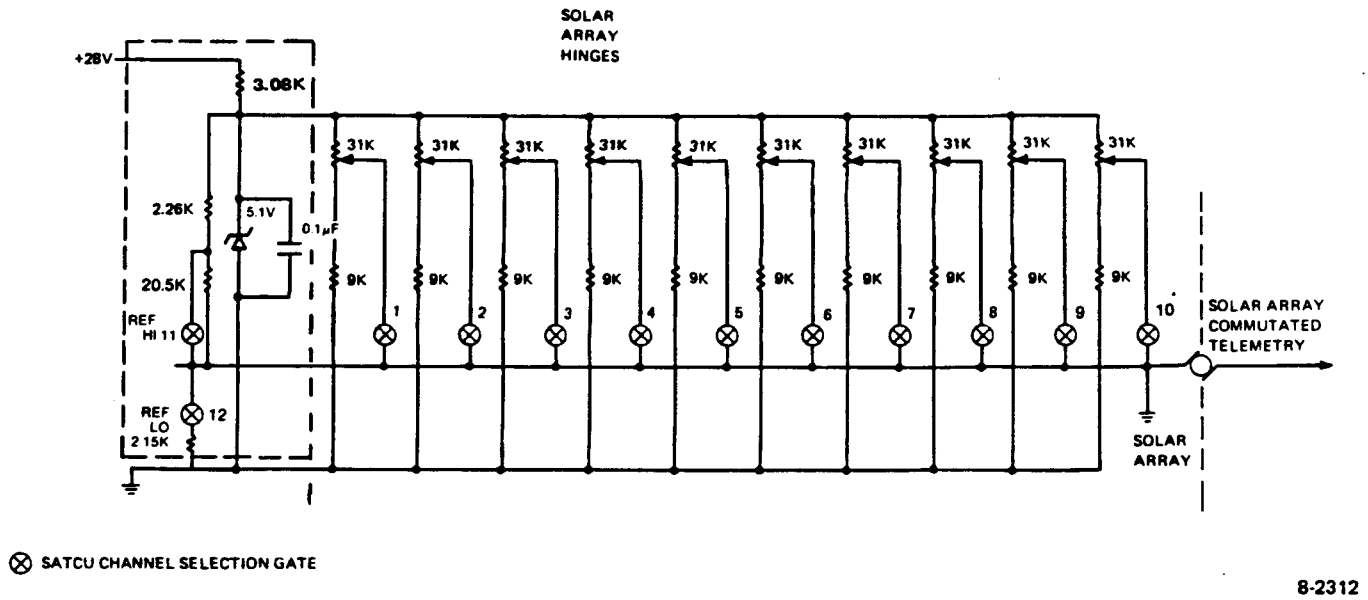

Figure 4.6.5-19. Solar Array Hinge Deployment Sensor Circuits

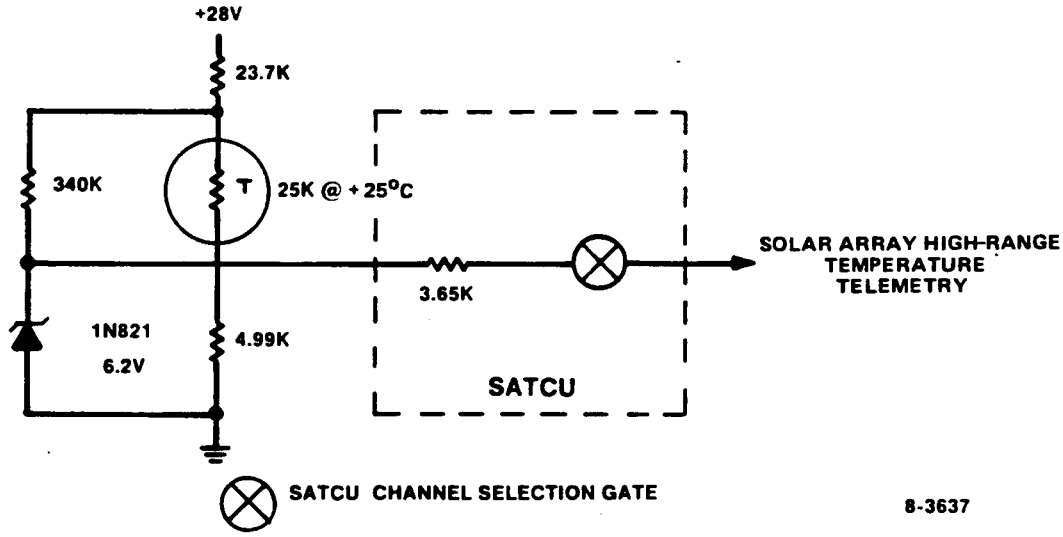

Figure 4.6.5-20. Solar Array High Temperature Sensor Circuit

4.6.5.1.4.9 Solar Cell Short Circuit Current. This telemetry channel provides a measurement of the short-circuit current available from a dedicated solar-cell patch. The sensing element is a test set of two solar cells mounted on outboard panel 10; the active conditioning circuit is located in the SATCU. This telemetry channel is included to enable the measurement of solar cell degradation as a function of time. A circuit diagram of the solar cell short circuit current sensor is shown in Figure 4.6.5-22.

The nominal beginning-of-life short circuit current should be 250-300 mA in sunlight, and is predicted to degrade with time.

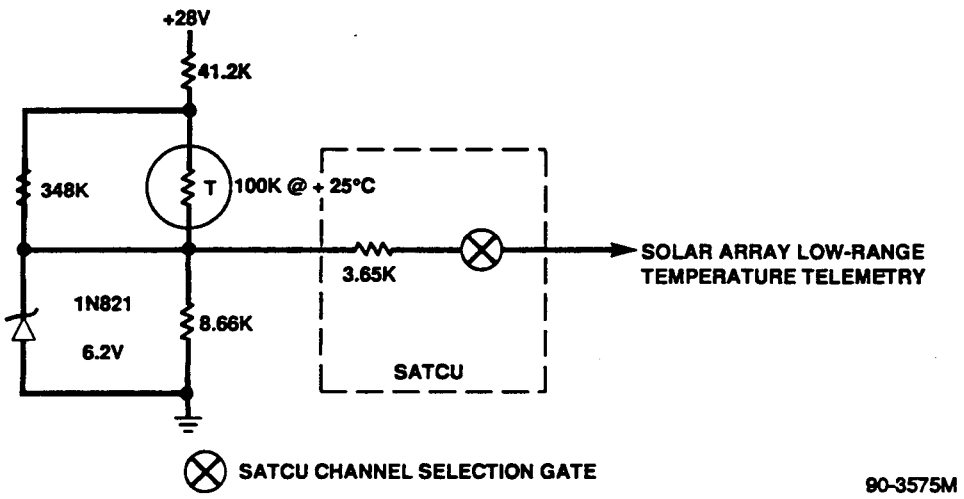

Figure 4.6.5-21. Solar Array Low Temperature Sensor Circuit

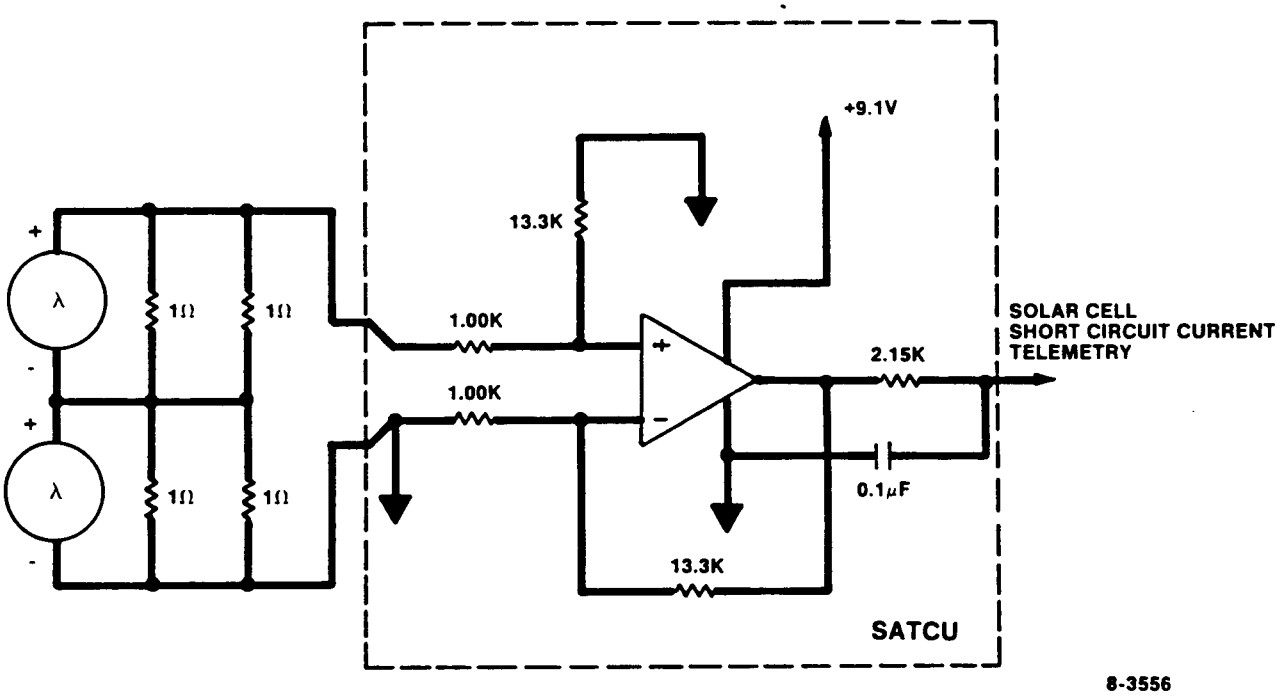

Figure 4.6.5-22. Solar Cell Short Circuit Current Sensor Circuit

4.6.5.1.4.10 Partial Shunt Voltage Sensor. This telemetry channel provides an indication of the average operating voltage of the lower solar cell circuits. This information permits determination of the average lower solar cell circuit operating point. The 70 sampling resistors are on the solar array; the summation resistors and RC filter are in the SATCU. A circuit diagram of the partial shunt voltage sensor is shown in Figure 4.6.5-23.

The partial shunts dissipate a portion of the excess solar array power; this channel is therefore also a gross indicator of the output power capability of the solar array. The partial shunt voltage is expected to vary from zero during eclipse to a maximum value of approximately 21 volts during entry to or exit from sunlight.

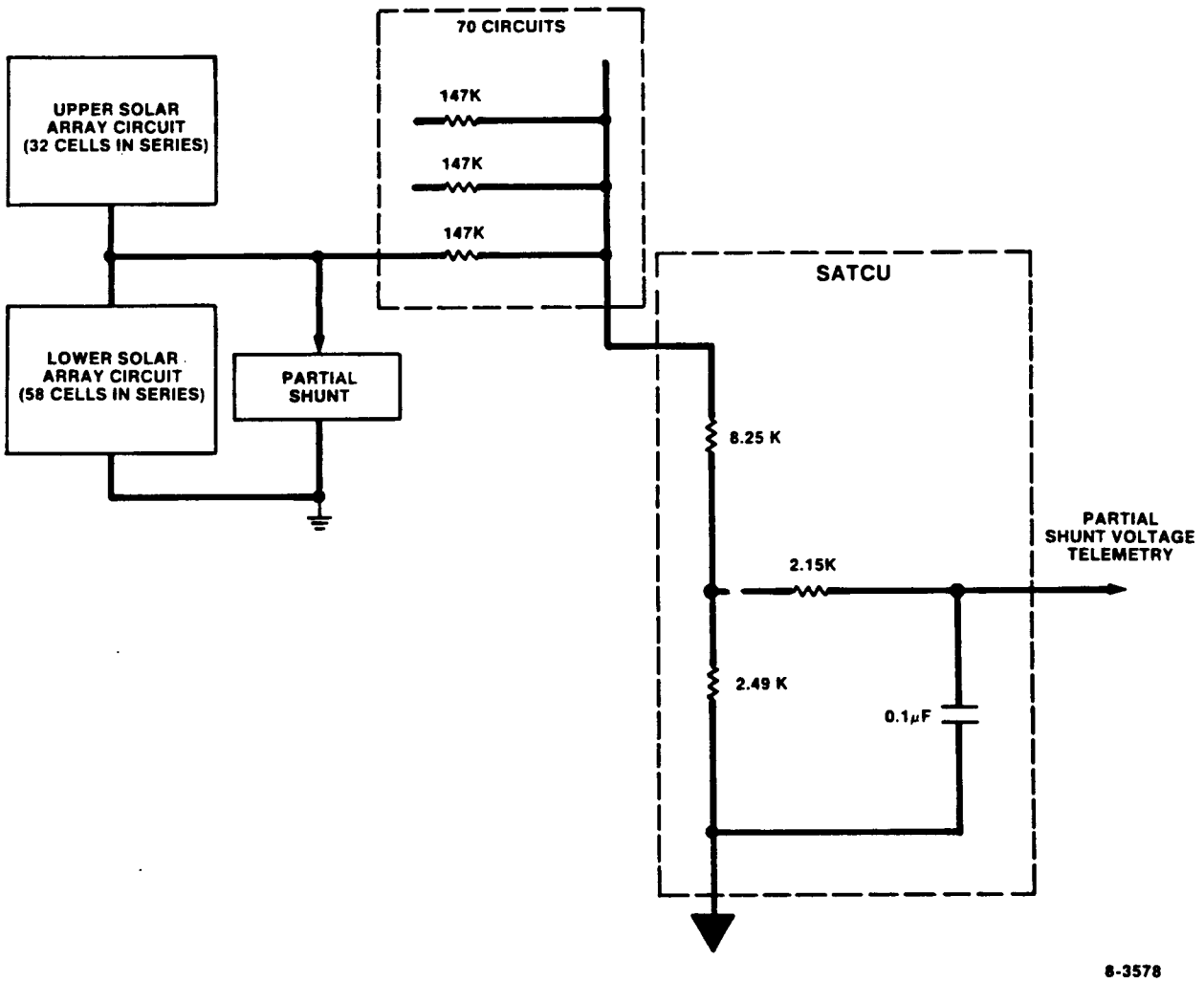

Figure 4.6.5-23. Partial Shunt Voltage Sensor Circuit

4.6.5.1.4.11 Shunt Heat Sink Temperature Sensors. These telemetry channels provide both a high-range and a low-range temperature measurement of one of the seven shunt heat sinks mounted on the back of solar panel 4. A circuit diagram of the shunt heat sink high temperature sensor is shown in Figure 4.6.5-24. The low temperature sensor circuit is shown in Figure 4.6.5-25. Shunt heat sink temperatures are expected to vary widely, from as low as -65°C at the end of eclipse to as high as +100°C near spacecraft noon.

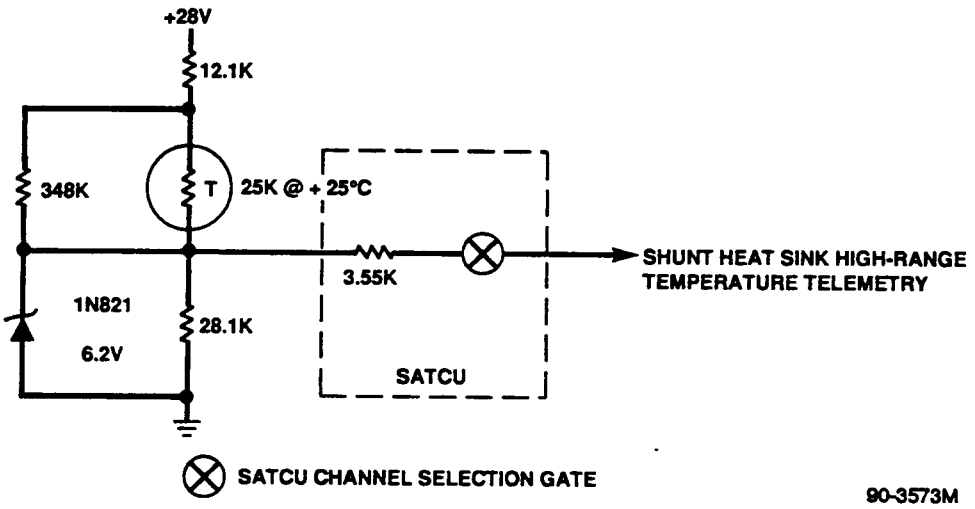

Figure 4.6.5-24. Shunt Heat Sink High Temperature Sensor Circuit

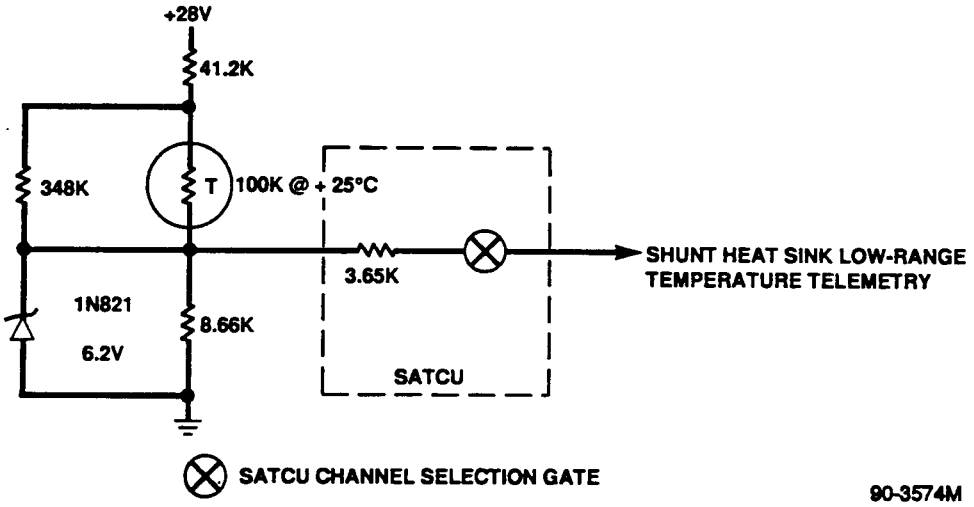

Figure 4.6.5-25. Shunt Heat Sink Low Temperature Sensor Circuit

4.6.5.2 Solar Array Drive/Array Drive Electronics

The Solar Array Drive (SAD) and Array Drive Electronics (ADE) provide the means for rotating the solar array, under the control of the Command and Control Subsystem (C&CS). An interface block diagram of the SAD/ADE is shown in Figure 4.6.5-26.

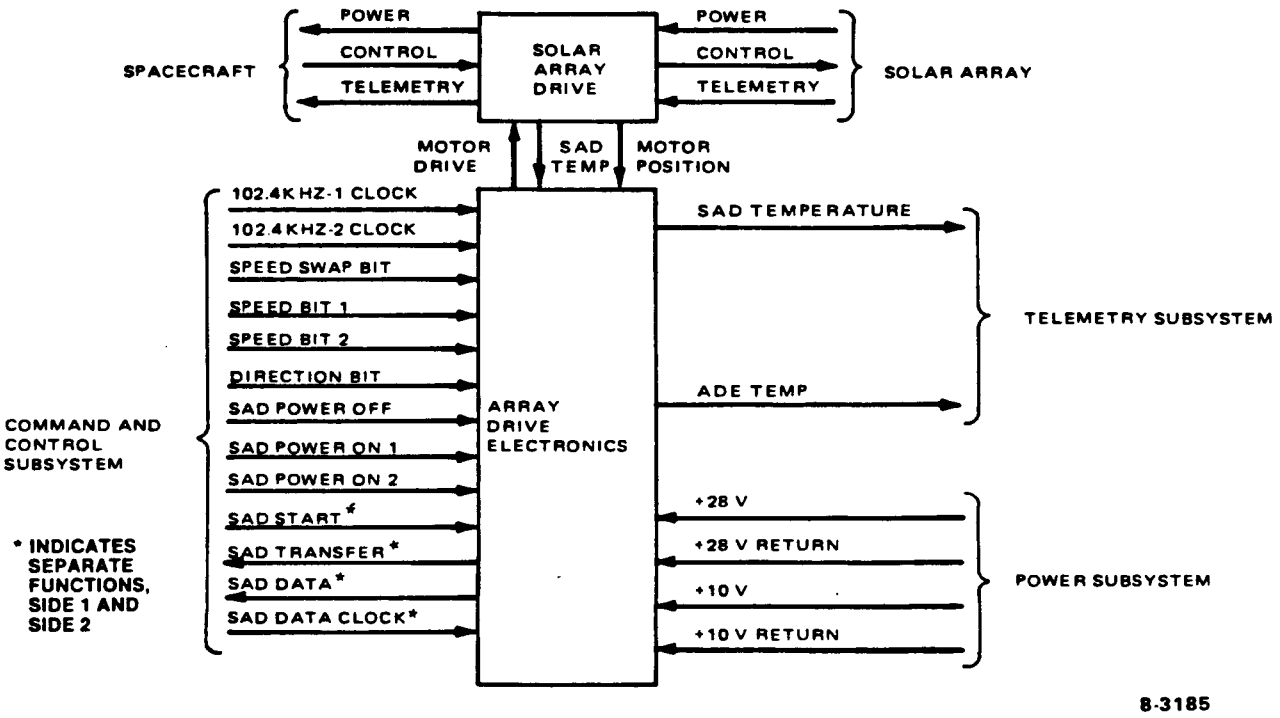

Figure 4.6.5-26. Solar Array Drive/Array Drive Electronics Interface Diagram

The SAD rotates the solar array at any one of several precise, constant speeds, permitting the C&CS to continually face the solar array toward the sun. The SAD contains slip rings for transferring power from the rotating solar array to the satellite and for providing conduction paths for control and telemetry signals associated with the solar array.

The ADE contains all the electronics required for operation of the SAD. Motor drive signals are provided to the SAD in accordance with the speed select signals received from the C&CS. The required speed select signals are derived in the C&CS based on the present orbital position of the satellite and the SAD motor shaft position and status information provided from the ADE.

4.6.5.2.1 Design Description

A functional block diagram of the SAD is shown in Figure 4.6.5-27. As shown, the SAD consists of a housing containing an actuator (stepper motor and harmonic drive), a gear train and clutch, a set of slip rings, and a two-pole resolver. The torque for rotating the solar array is provided by the stepper

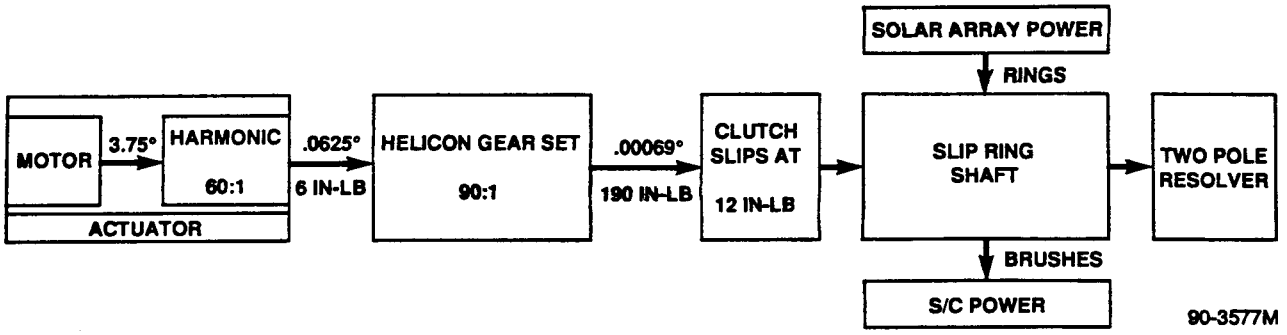

Figure 4.6.5-27. SAD Functional Block Diagram

motor. Angular information on the motor shaft position is provided to the ADE by the two-pole resolver. The slip rings provide conductive paths between the rotating solar array and the remainder of the satellite. The only redundancy in the SAD is the redundant motor windings.

A functional block diagram of the ADE is shown in Figure 4.6.5-28. The ADE contains two completely redundant sets of electronics. Each section consists of a command decoder and clock generator, a serial output buffer, a sequence generator, bridge circuits, and a resolver interface. In addition, each side has a +10V regulator to provide power for the CMOS logic. Only CIU interface logic is powered by +10V CIU power. Relays on each side select either set of redundant electronics.

4.6.5.2.1.1 Design Characteristics. The design characteristics of the SAD and ADE, individually and in combination, are summarized in Tables 4.6.5-10 through 4.6.5-12.

4.6.5.2.1.2 Physical Description

4.6.5.2.1.2.1 Array Drive Electronics. The ADE is packaged within a special electronics box containing four circuit boards and a harness board. The major construction features are shown in Figure 4.6.5-29. External connections are made directly to board-mounted connectors, which project through openings in the cover.

The ADE case was designed to comply with the TIROS unique requirements for radiated emissions. In order to accomplish this goal, the housing was designed as an assembly consisting of a unitized dip brazed central shell with front and rear covers. The shell is provided with flanges and mating electrically conductive flexible gaskets for reliable EMI suppression when both covers are installed.

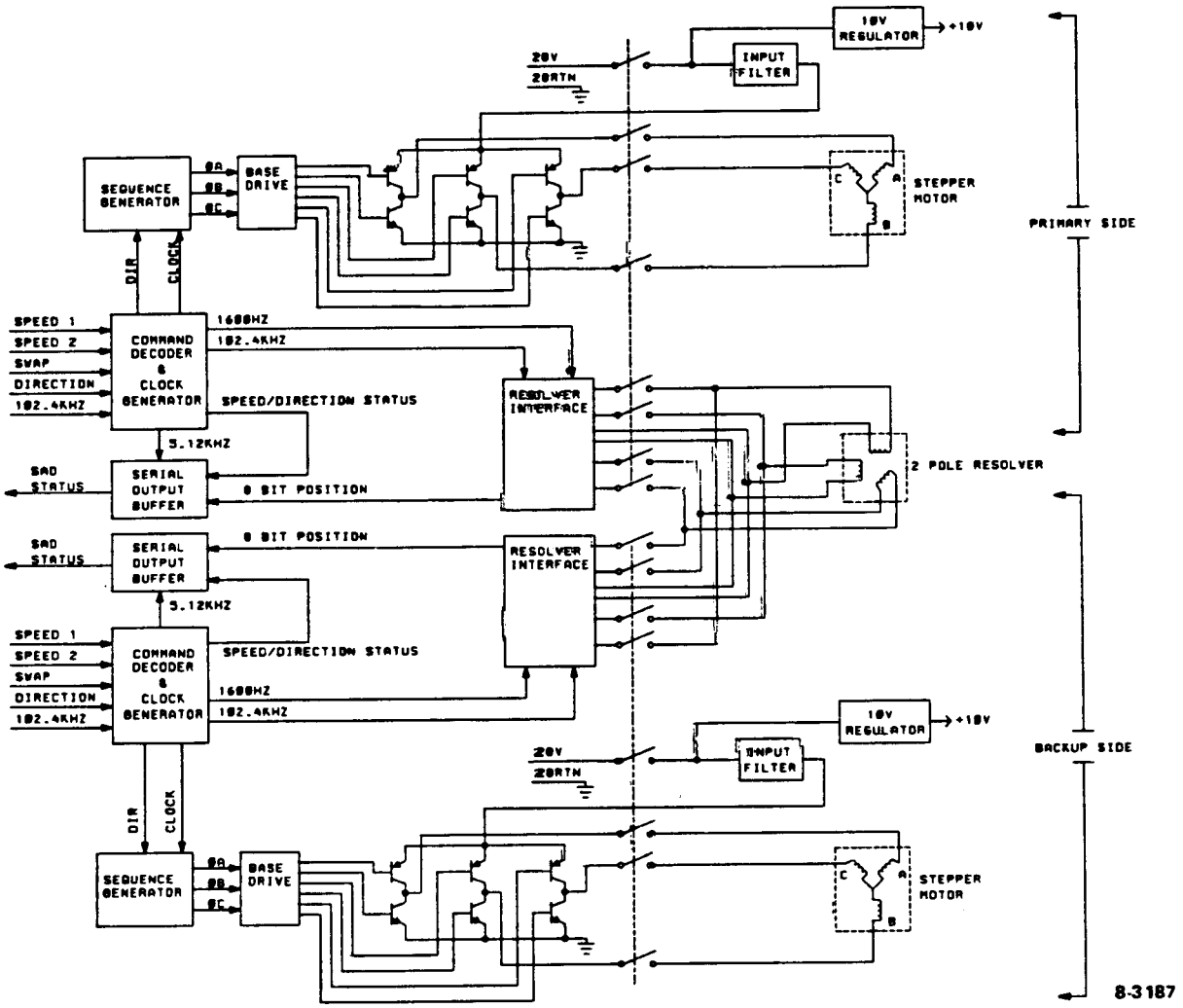

Figure 4.6.5-28. ADE Functional Block Diagram

The circuit boards include a printed circuit analog board and a printed circuit digital board for ADE side 1 as well as an identical analog board and digital board for ADE side 2. The printed circuit harness board provides the required interconnections between the circuit boards.

All four component circuit boards use multilayer printed wiring. Special adjustable angle brackets are used for mounting external D-subminiature (rectangular) connectors to the printed wiring boards and to the front cover with gasketing in order to ensure a tight EMI connector-to-cover seal.

The ADE temperature is controlled within a range of 0 to 50°C through the use of an insulating blanket and a TCE-controlled heater.

TABLE 4.6.5-10. SOLAR ARRAY DRIVE/ARRAY DRIVE ELECTRONICS PERFORMANCE SUMMARY

Parameter	Value
Motor Operating Speed	
Fast	1.047 mrad/sec
Normal	1.030 mrad/sec
Slow	1.013 mrad/sec
Slew (Acquisition)	5.234 mrad/sec
Shaft Position Reporting	
Format	8 bits, binary
Resolution	24.54 mrad
+28 V Power Requirements	< 10.1 watts
+10 V Power Requirements	< 0.02 watt

TABLE 4.6.5-11. ARRAY DRIVE ELECTRONICS CHARACTERISTICS

Parameter	Value
Design Concept	Clock controlled, precision motor speed control. Electronics completely redundant, selectable by command.
Construction	Standard Electronics box 2 Analog Boards (PC) 2 Digital Boards (PC) 1 Harness Board (PC)
Size	5.3 x 7.7 x 9.6 in.
Weight	5.6 lb

4.6.5.2.1.2.2 Solar Array Drive. The solar array drive configuration is shown in Figure 4.6.5-30. The slip rings are installed on a titanium shaft which rotates in a magnesium alloy housing on a set of stainless steel bearings. The bearing set consists of a preloaded DF pair and a trailer bearing supported and loaded by a beryllium-copper diaphragm. The diaphragm permits differential thermal expansion between the shaft and housing.

The solar array is attached mechanically to the SAD shaft by a flange. Thermal insulation between the SAD and solar array is provided by a polycarbofil washer.

TABLE 4.6.5-12. SOLAR ARRAY DRIVE CHARACTERISTICS

Parameter	Value
Motor	Permanent magnet Schaeffer actuator - 3.75 stepper with 60:1 harmonic
2-Pole Synchro	Kearfott size 11 brushless resolver synchro
Slip Rings	Polyscientific, modified gold on gold, redundant flat cantilever brush, V-groove rings
Bearings	
Main Bearings	DF pair angular contact
Trailer Bearing	Angular contact
Lubricant	Wet VacKote TNDE, highly refined mineral oil, Ball Brothers 86234
Lubricant Reservoirs	Nylasint, quantity of five
Dynamic Seals	Labyrinth, non-contacting
Structural Materials	
Housing	ZK60A-T5 magnesium
Shaft	TI-6AL-4V titanium
Bearings	440C stainless steel
Size	6-inch diameter by 13.4-inch length
Weight	10.6 lb (15.9 lb with attached harnesses)

The solar array drive is driven relative to the SAD housing by a stepper-driven gear train. The drive actuator consists of a 3.75° permanent magnet stepper driving a 60:1 harmonic and is coupled to the slip ring shaft through a 90:1 single-pass gear train. The motor is directly coupled to an alloy steel pinion that meshes with a non-metallic self-lubricating helicon. Motor performance parameters and drive train characteristics are shown in Table 4.6.5-13. The motor is illustrated in Figure 4.6.5-31.

A Kearfott two-pole brushless resolver synchro is attached to the satellite end of the housing. This synchro is rotated by the SAD shaft through a flexible bellows coupling and is used to indicate the position of the solar array to the C&CS.

One end of the SAD housing is attached to a mast; the other end is attached to and supported by the satellite. Thermal insulation between the SAD housing and the mast is provided by a polycarbofil washer.

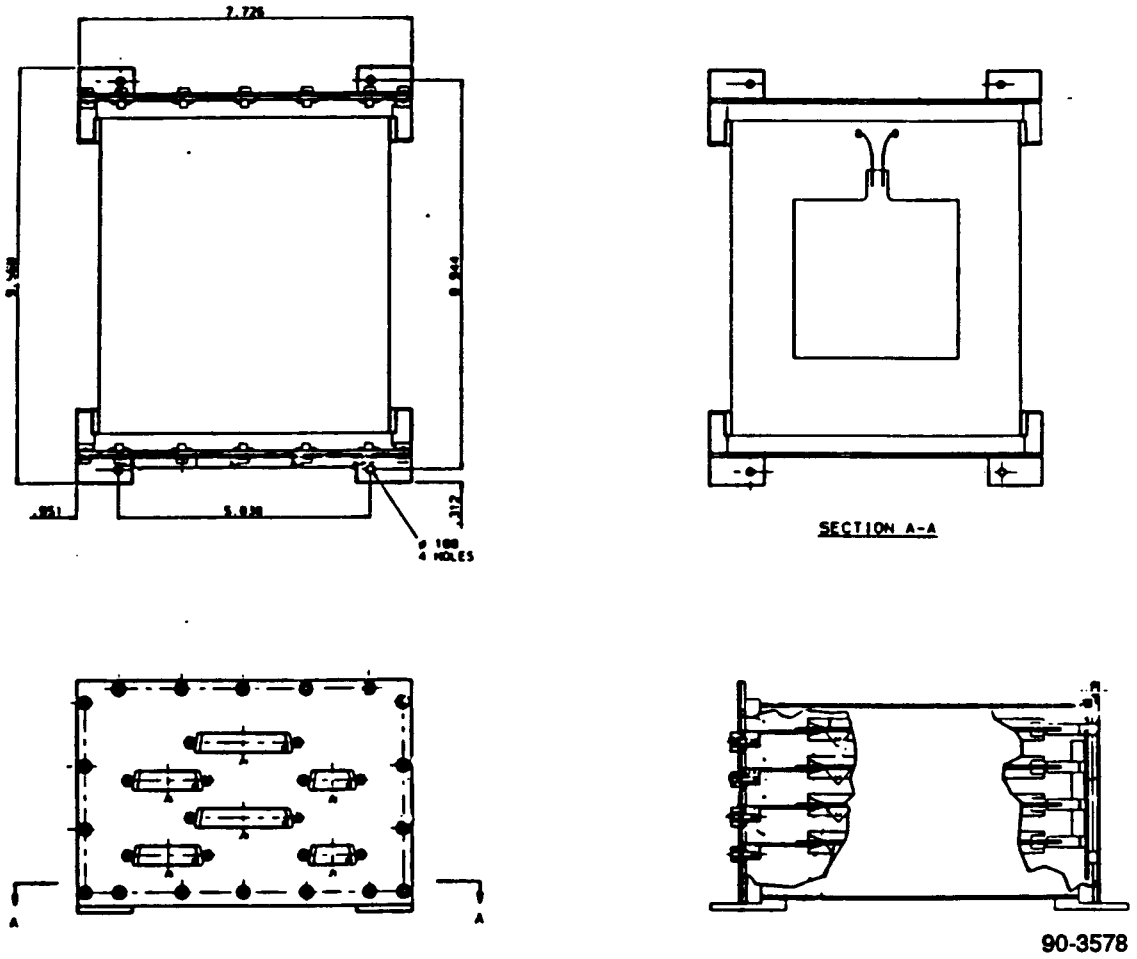

Figure 4.6.5-29. Array Drive Electronics Construction

A failsafe slip clutch is incorporated at the output shaft to preclude damage from excessive back-driving torques that are possible during installation and test operations.

The hard gold V-groove slip rings and flat cantilever Ney Ore 28A gold-alloy brushes carry power from the solar array to the satellite and provide signal connections for the control and monitoring of the array. The primary slip ring characteristics are summarized in Table 4.6.5-14.

The slip ring brushes are carried by two brush blocks, one on each side of the housing. The brushes, slip rings, and bearings are in a chamber sealed by a labyrinth against loss of lubricant to space.

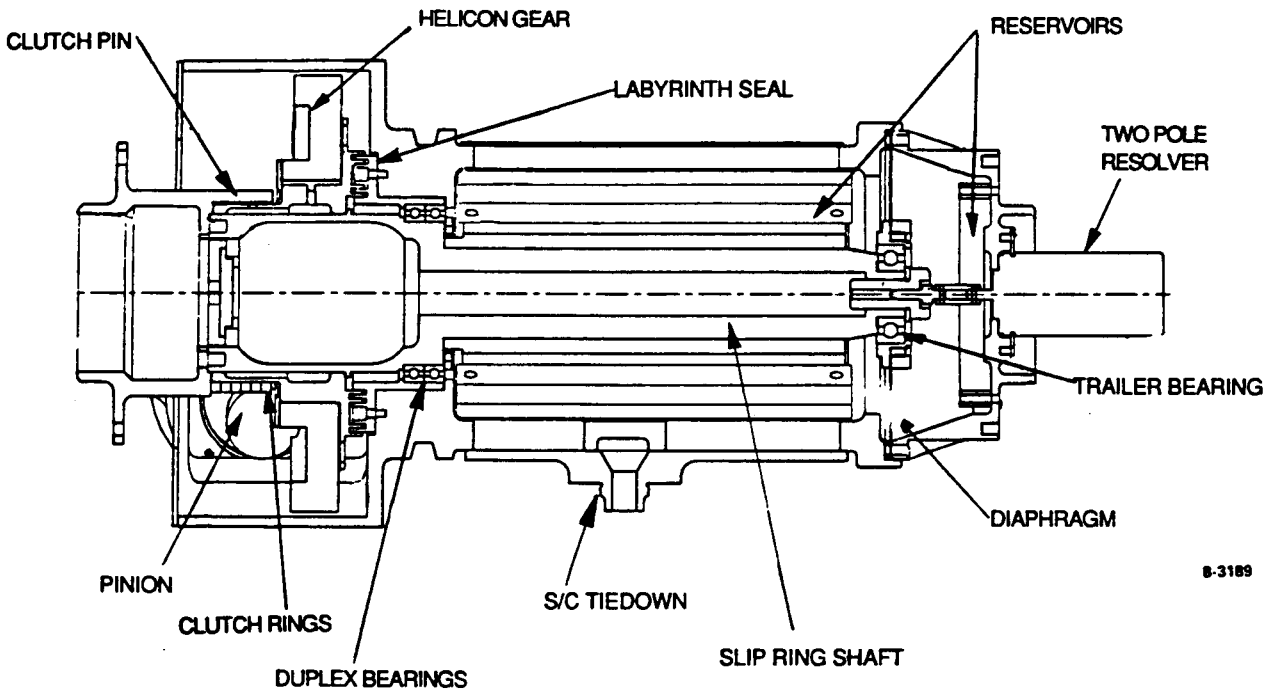

Figure 4.6.5-30. Solar Array Drive

TABLE 4.6.5-13. SOLAR ARRAY DRIVE TRAIN PARAMETERS

Parameter	Value
Schaeffer Actuator Drive Motor	• Three phase, redundant windings • 3.75° steps • 0.217 in-lb output torque
Integral Harmonic	• 60:1 ratio • 0.0625° step • 6 in-lb output torque
Helicon Gear	• 90:1 ratio torque multiplication factor • Torque-limiting slip clutch, 12 in-lb
	Loss Parameters
Slip Rings and Bearings	2.18 in-lb EOL 1.75 in-lb BOL

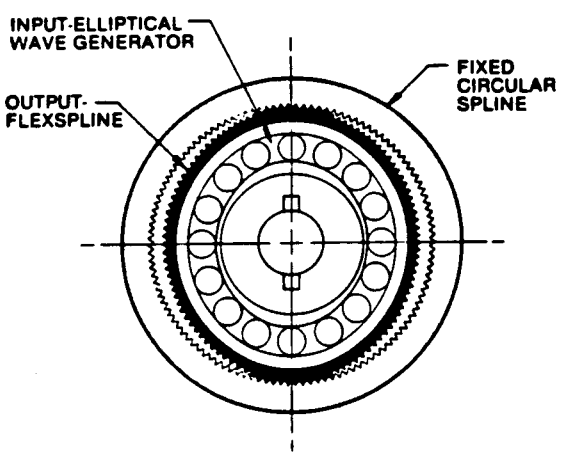

HARMONIC DRIVE PRINCIPLE
Rotation of the elliptical wave generator results in a greatly reduced motion at the toothed output members due to differential action between teeth on flexspline and circular spline.

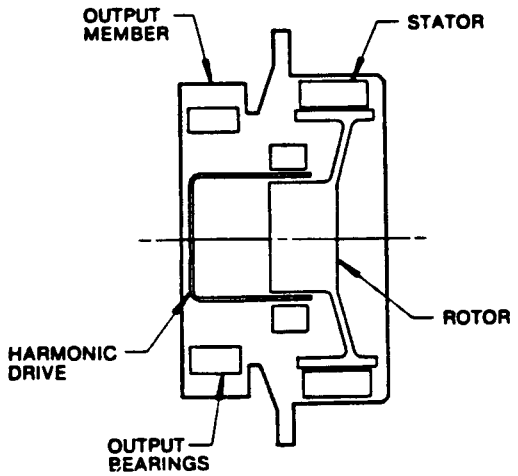

MECHANICAL SCHEMATIC
Schematic representation of actuator illustrating stepper motor, Harmonic Drive and thin section output bearings.

THE SMI ROTARY ACTUATOR EMPLOYS A SMALL ANGLE PERMANENT MAGNET MOTOR TO DIRECTLY DRIVE AN INTEGRAL HARMONIC DRIVE SPEED REDUCER. 8-3190

Figure 4.6.5-31. SAD Actuator

TABLE 4.6.5-14. SOLAR ARRAY DRIVE SLIP RING CHARACTERISTICS

Parameter	Value
Type	Polyscientific, modified gold on gold, redundant flat cantilever brush, V-groove ring
Power and Power Return Slip Rings	
Quantity	36
Brushes per ring	4
Current rating (in air)	10.3 amperes per ring
Current derating	5 amperes per ring
Control and Signal Slip Rings	
Quantity	12
Brushes per ring	2
Current rating (in air)	2 amperes per ring
Current derating	1 ampere per ring

The slip ring configuration is shown in Figure 4.6.5-32. There are a total of 48 slip rings; 30 of these carry solar array power at currents up to five amperes each, 14 carry control and monitoring signals at currents up to one ampere each, two are provided as spare power slip rings, and two are provided as spare signal rings.

Each power slip ring consists of two V-shaped grooves with two brushes for each groove and is rated in air to carry 10.3 amperes. Each signal slip ring consists of a single V-shaped groove with two brushes and is rated in air to carry two amperes. Inspection ports on the housing can be uncovered to check that all the brushes are properly seated in the V-grooves of the slip rings.

The ball bearings and slip rings are lubricated using Ball Brothers wet VacKote process 86234. Synthane grade LBB ball retainers are impregnated with lubricant after assembly of the race. Primary lubricant reservoirs are located in the slip ring and brush chamber; a secondary reservoir is located in the chamber outboard from the trailer bearing. These reservoirs are made of Nylasint impregnated with lubricant, which is provided to critical surfaces by molecular transfer. The supply of VacKote lubricant is adequate for several times the SAD design life. The miniature precision ball bearings in the two pole synchro are dry lubricated by the Barden Bar-temp process.

The slip rings are connected to the solar array through a 31-pin connector mounted to the slip ring shaft. The SAD slip rings, motor, and synchros are connected to the satellite through two eight-foot cables.

The SAD temperature is controlled within the range of +5 to +35°C by an insulating blanket, by radiating surfaces on the brush blocks and motor housing, and by a TCE-controlled heater.

The overall component flow during manufacturing of the SAD is depicted in Figure 4.6.5-33.

4.6.5.2.2 Functional Description

Functional block diagrams for the SAD and ADE are shown in Figures 4.6.5-27 and 4.6.5-28.

4.6.5.2.2.1 Command Decoder and Clock Generator. A block diagram of the command decoder and clock generator is shown in Figure 4.6.5-34.

The inputs from the C&CS are direction, Swap, Speed-1, and Speed-2. These signals are decoded to determine desired SAD speed and direction. This status information is input to a 16-bit register interfacing to the serial output buffer. The decoded commands will address a four-to-one multiplexer that supplies the rate clock to the step sequence generator. The multiplexer inputs are four clock signals, generated by dividing down the 102.4-kHz system clock (provided by the C&CS), that correspond to the step rates required for the slew, fast, normal, and slow rates of the SAD.

In addition, the 102.4 kHz is divided down to 5.12 kHz and 1.6 kHz. The 1.6 kHz and the 102.4 kHz are routed to the resolver interface, while the 5.12 kHz is used for the serial output buffer sequencer logic.

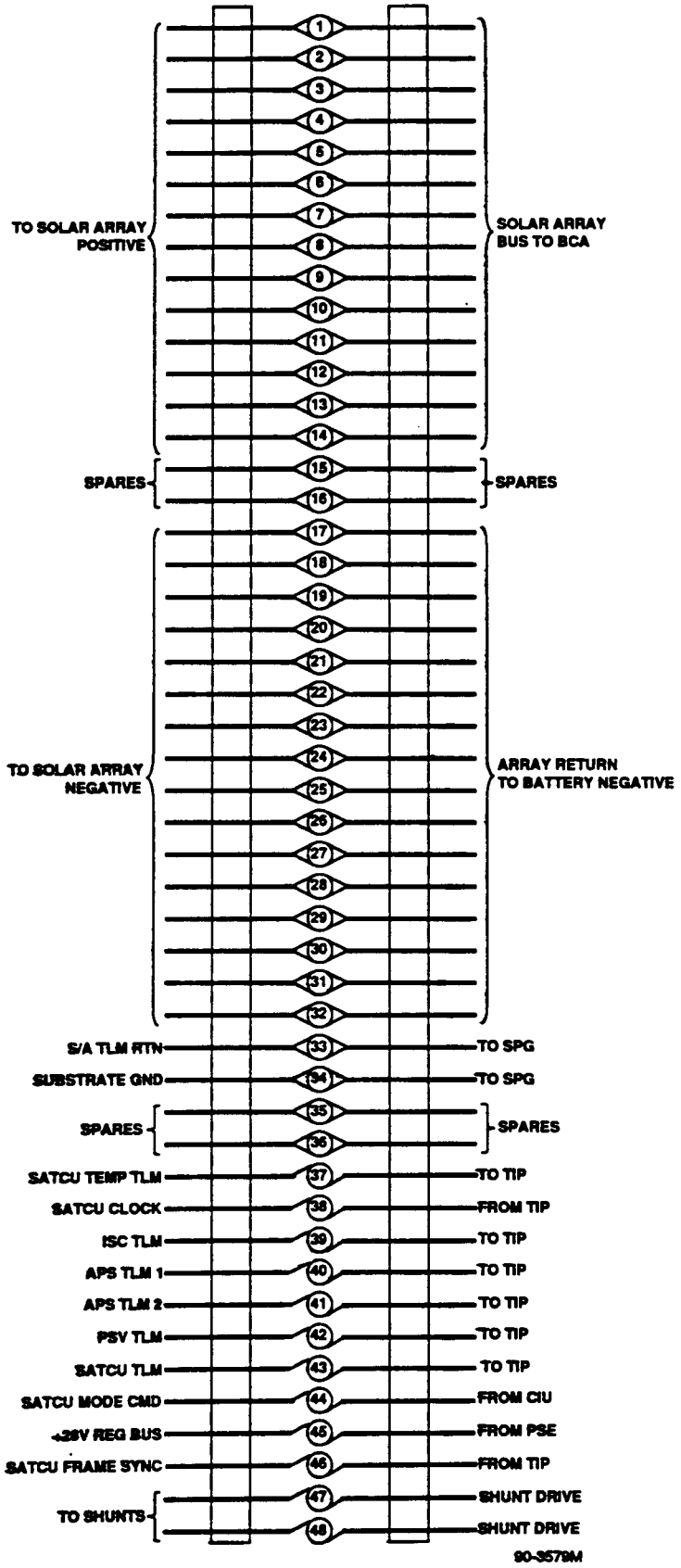

Figure 4.6.5-32. Slip Ring and Brush Configuration

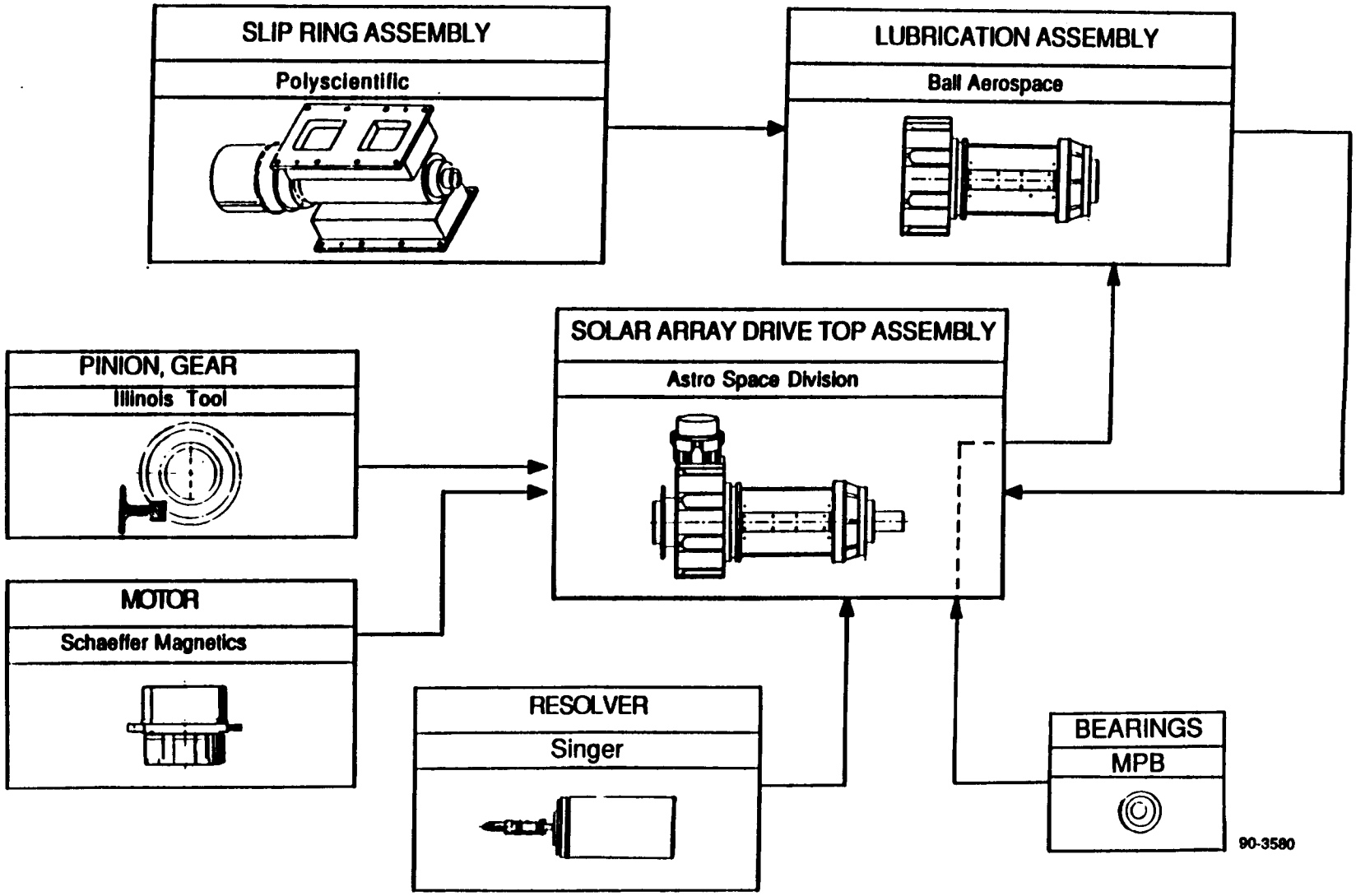

Figure 4.6.5-33. SAD Component Flow

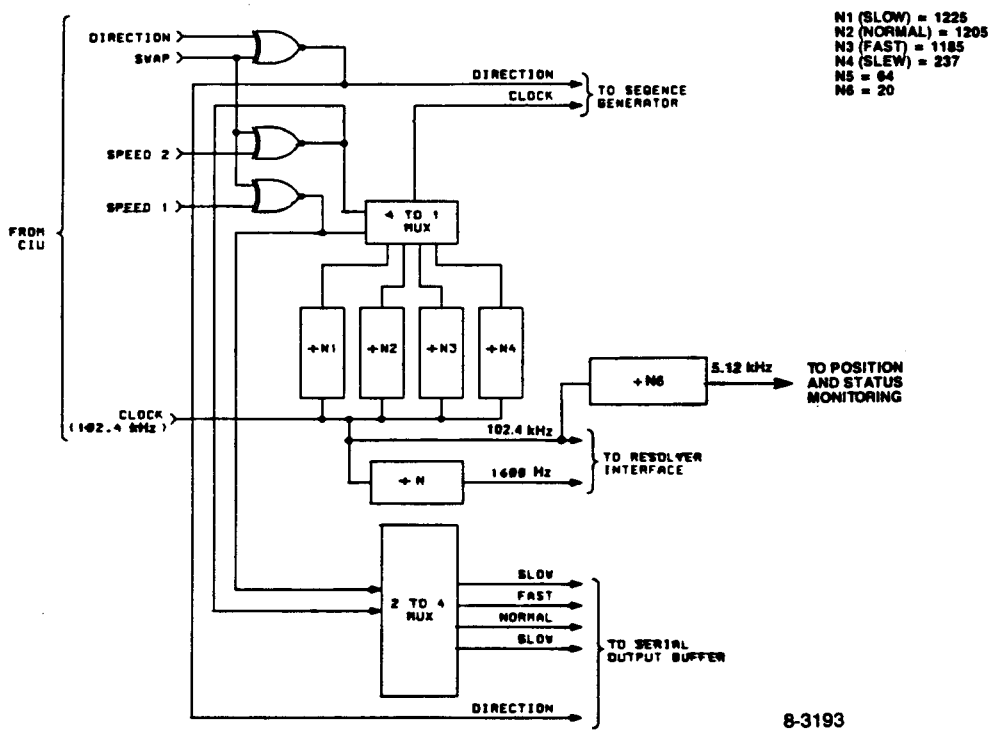

Figure 4.6.5-34. Command Decoder and Clock Generator

4.6.5.2.2.2 Resolver Interface. A block diagram of the resolver interface is shown in Figure 4.6.5-35. The two-pole resolver used for position feedback represents a nonredundant element in the SAD. A relay is used to switch the resolver windings from ADE side 1 to ADE side 2, depending on which side has been turned on. The relay will switch by the "power on" signals.

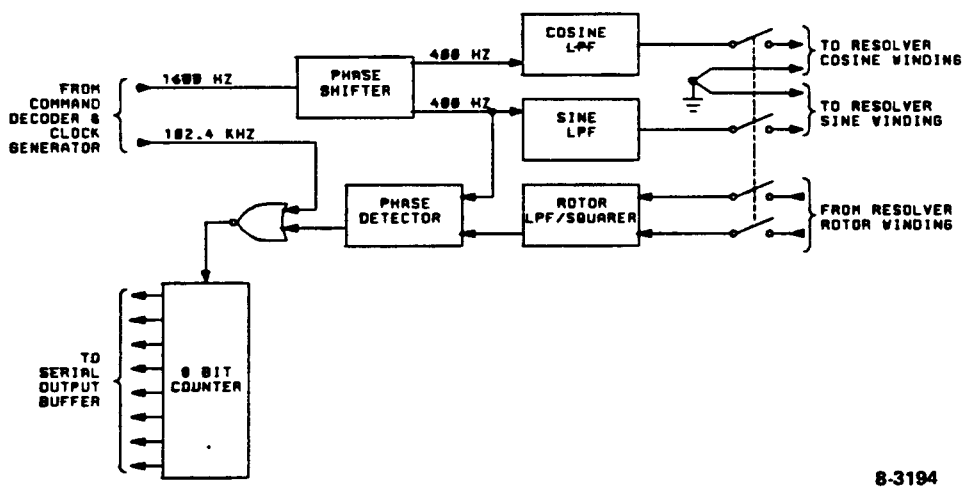

Figure 4.6.5-35. Resolver Interface

The resolver requires a sine input and a cosine input at 400 Hz. The sine and cosine signals are generated by dividing the system clock down to 1600 Hz and using a divide by four Johnson counter to generate the 400 Hz sine and cosine square waves. Low-pass filtering supplies the required 400 Hz sinusoids to the resolver windings. The resolver rotor signals are low-pass filtered to eliminate noise and then fed to a squaring circuit. By comparing the squared rotor output to the squared 400-Hz sine wave, position of the SAD can be determined. The phase difference between the two signals is indicative of SAD position. The position decode circuit will convert the phase error to an eight-bit position word to be used as part of the 16-bit serial telemetry.

4.6.5.2.2.3 Sequence Generator. A block diagram of the sequence generator is shown in Figure 4.6.5-36. The step sequence generator has been designed to generate the six-state sequence required to step the motor. The generator was designed using JK flip flops with external gating. A common clock to the three flip flops ensures synchronous operation. The sequence generator will step in either direction, enabling bidirectional motion of the motor. The step sequence generator requires two inputs from the command section of the ADE: the rate clock and the direction select.

A block diagram of forward/reverse state diagrams is shown in Figure 4.6.5-37.

4.6.5.2.2.4 Base Drive Bridge Circuits. A block diagram of one of the three base drive bridge circuits is shown in Figure 4.6.5-38. The stepper motor is wired in a Y configuration and requires a six-state sequence to be repeated for motor rotation. Each phase of the motor is required to either sink or source current at some point during the six-state sequence. This motor configuration requires the power stage to be a three-phase bridge. The bridge uses bipolar transistors as switches.

There exists a deadband in this base drive bridge circuit to prevent cross-conduction during switching. Flyback diodes D1 and D2 provide a path for motor current during switching.

4.6.5.2.2.5 Position and Status Monitoring. The position and status monitoring circuits are shown in Figure 4.6.5-39. These circuits generate two 8-bit words that indicate the solar array angular position and the status of the ADE, as shown in Table 4.6.5-15. This information is serially read out into the Controls Interface Unit (CIU).

The status bits are derived from the speed and direction decoder outputs and from the power switching relay contacts and are parallel loaded into the output register. The position information bits are generated using a two-pole brushless resolver, a sequencer, and an eight-bit counter; the contents of the counter digitally represent the synchro shaft angle as shown in Table 4.6.5-16.

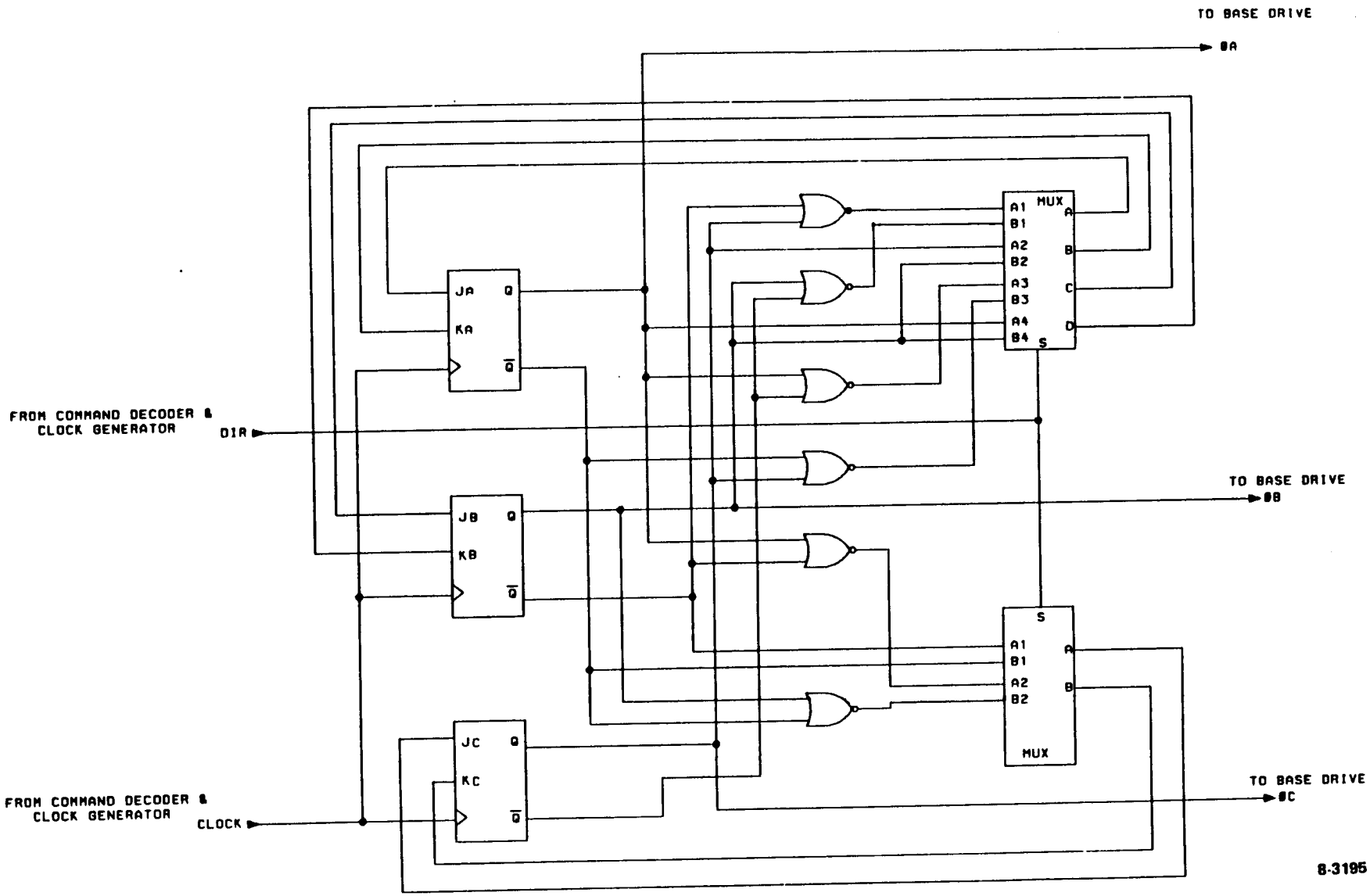

Figure 4.6.5-36. Sequence Generator

STATE DIAGRAM FOR THE FORWARD DIRECTION

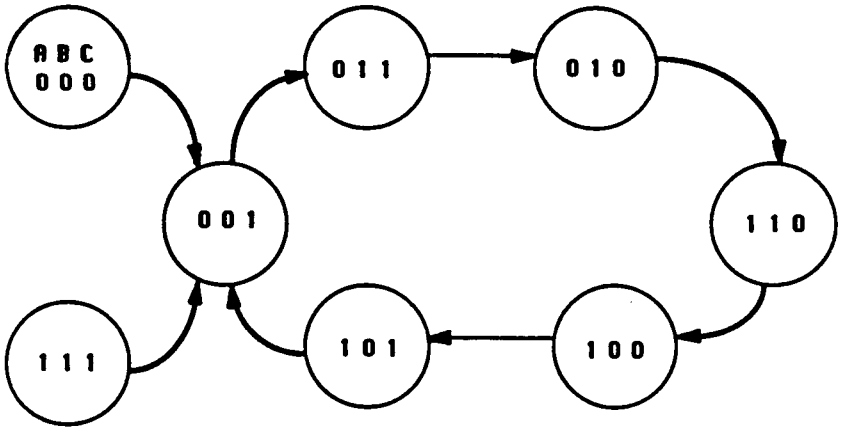

STATE DIAGRAM FOR THE REVERSE DIRECTION

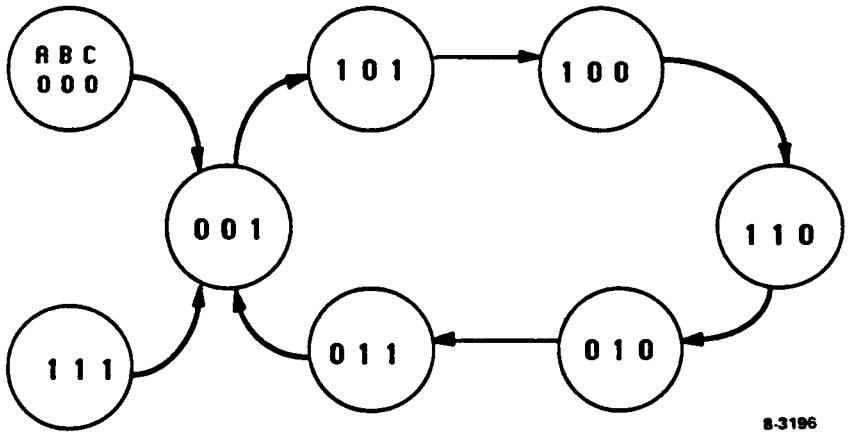

Figure 4.6.5-37. Forward/Reverse State Diagrams

The counter contents are parallel transferred to the output register, then serially read out.

The windings of the two-pole synchro are excited by 400-Hz sine wave voltages in phase quadrature. The output of the synchro is a constant amplitude 400-Hz sine wave, but shifted in phase from the input voltage by the shaft angle. The synchro output is squared, divided by two, and then compared to a reference square wave by the sequencer. The sequencer enables the counter to count clock pulses for a time period proportional to the shaft angle.

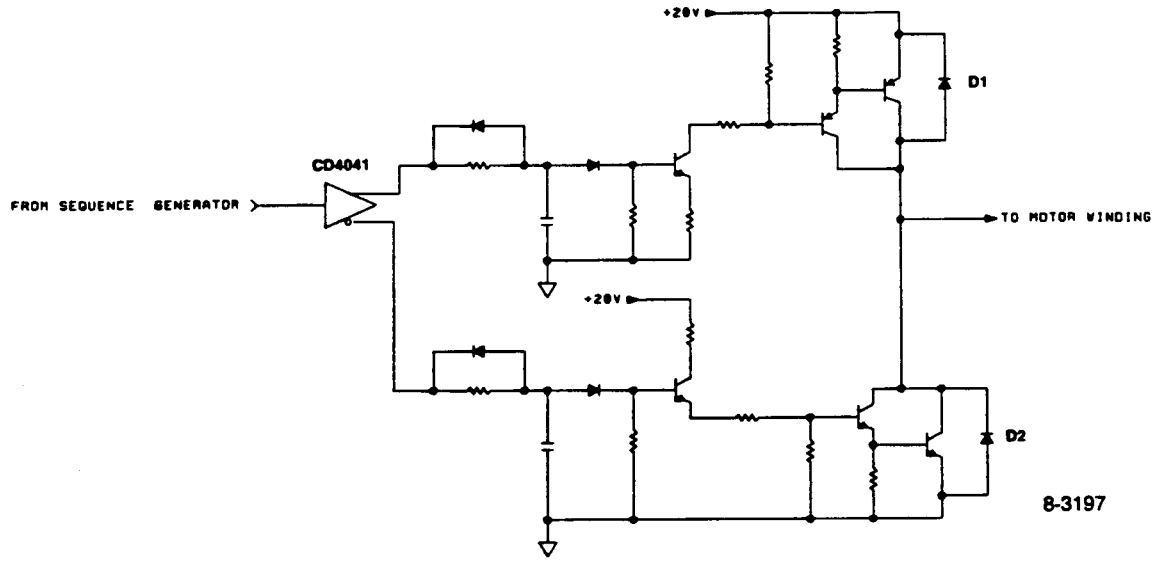

Figure 4.6.5-38. Base Drive Bridge Circuit

The sequencer state diagram is shown in Figure 4.6.5-40; timing diagrams are shown in Figure 4.6.5-41. The sequencer starts its cycle in state 0; the counter has been reset in the previous cycle. When the synchro output goes high, the sequencer is clocked at the 51.2-kHz rate to state 1 if the reference is high, or to state 3 if the reference is low. If the sequencer is clocked to state 1, it will be clocked to state 3 when the reference goes low. While the sequencer is in either state 1 or 3, the counter is enabled and is counting clock pulses. The sequencer is clocked from state 3 to state 7 when the reference goes high and the counter is then disabled. The counter contains a binary number equal to the time from the leading edge of the resolver output signal to the leading edge of the reference signal. This time difference is directly proportional to the SAD shaft angle.

If the data register contents are being transferred to the CIU, the sequencer remains in state 7 until the transfer is completed. Once the transfer is completed, or if no transfer has started, the sequencer is clocked to state 6. In this state, during the first half of the 51.2-kHz clock pulse, the contents of the counter and the status information bits are parallel shifted into the output register. On the next clock pulse, the sequencer is clocked to state 4, releasing the register to provide a serial output and generating a signal to reset the counter. The sequencer remains in state 4 until the synchro output pulse is low, at which time the sequencer is clocked to state 0, where it is ready to start a new cycle.

The data register is read out serially to the CIU. Readout is initiated by the Array Status Start signal, which may occur at any time. Therefore, a pulse generator receives the signal and generates two pulses, shown in Figures 4.6.5-39 and 4.6.5-42. The Transfer Data Inhibit signal prevents the sequencer from loading the data register during the readout cycle; the array status transfer pulse is sent to the CIU to signify that the data register may

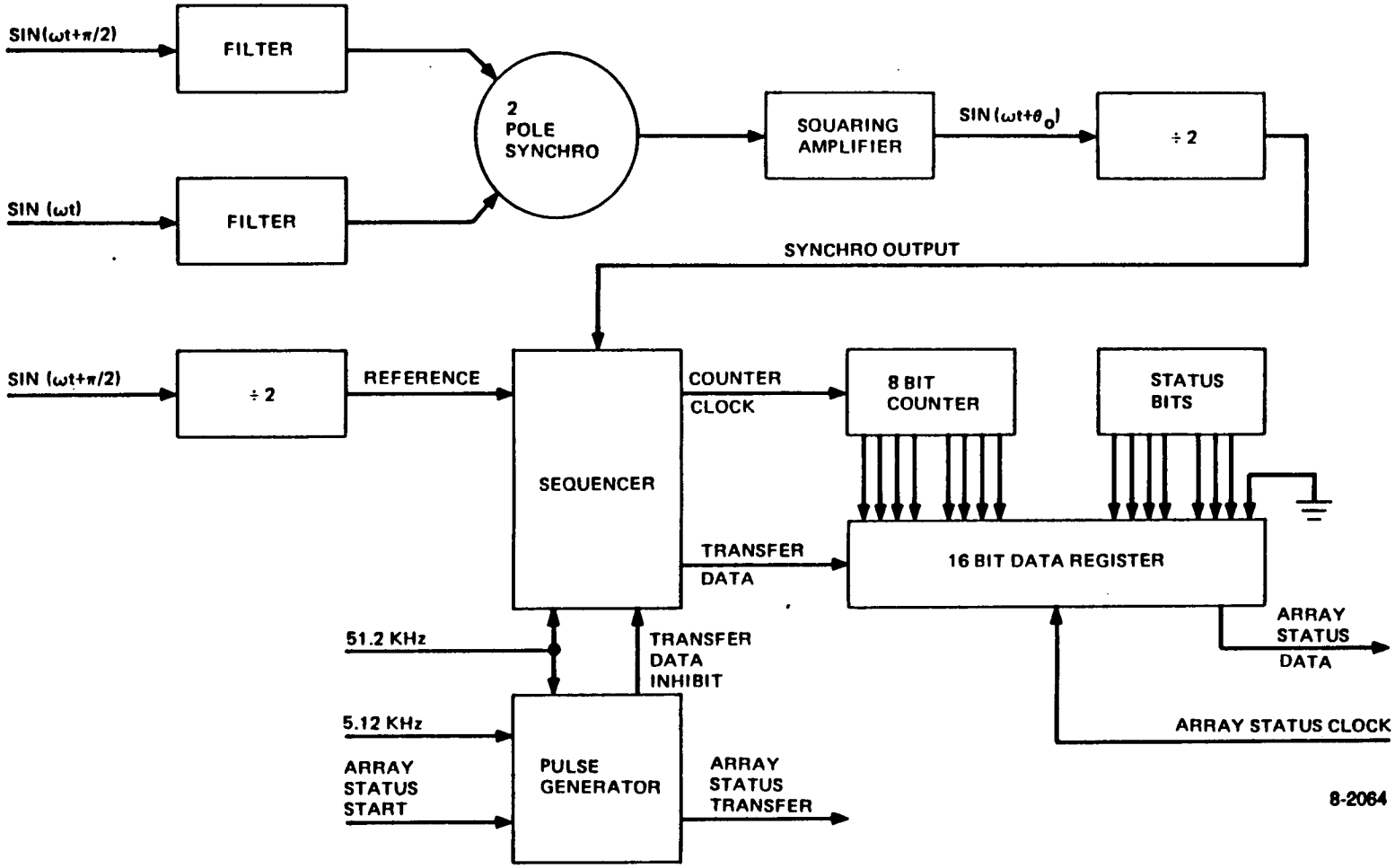

Figure 4.6.5-39. Position and Status Monitoring Block Diagram

TABLE 4.6.5-15. SAD STATUS FORMAT

Bit	Function
1	0 (Dummy Bit)
2	SAD/ADE 1 Powered
3	SAD/ADE 2 Powered
4	SAD Forward/Reverse
5	SAD Slew
6	SAD Fast
7	SAD Normal
8	SAD Slow
9 MSB	
10	
11	
12	
13	Array Position
14	
15	
16 LSB	

Bit 4 status bit, forward = 0, reverse = 1; all other status bits, active = 1

TABLE 4.6.5-16. SOLAR ARRAY ANGLE OUTPUT CODE

Shaft Angle		Output Code
Degrees	Radians	MSB LSB
0	0	0 0 0 0 0 0 0 0
1.41	0.02454	0 0 0 0 0 0 0 1
45	$\pi/4$	0 0 1 0 0 0 0 0
90	$\pi/2$	0 1 0 0 0 0 0 0
135	$3\pi/4$	0 1 1 0 0 0 0 0
180	π	1 0 0 0 0 0 0 0
225	$5\pi/4$	1 0 1 0 0 0 0 0
270	$3\pi/2$	1 1 0 0 0 0 0 0
315	$7\pi/4$	1 1 1 0 0 0 0 0
358.59	$2\pi - 0.02454$	1 1 1 1 1 1 1 1
360	2π	0 0 0 0 0 0 0 0

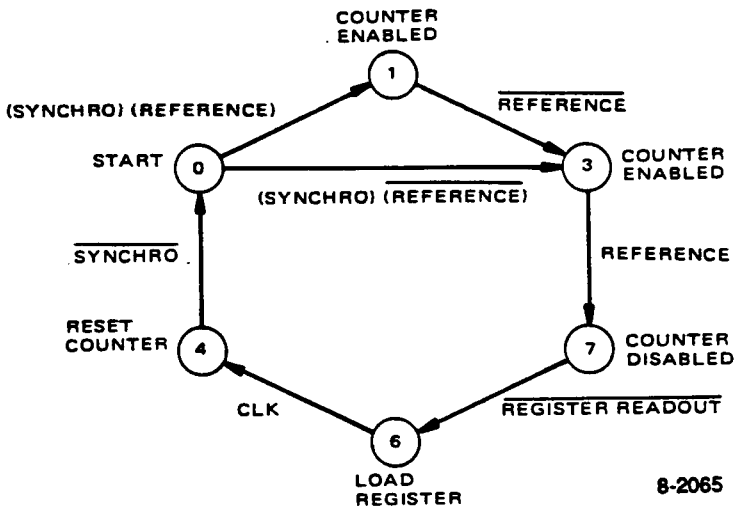

Figure 4.6.5-40. Sequencer State Diagram

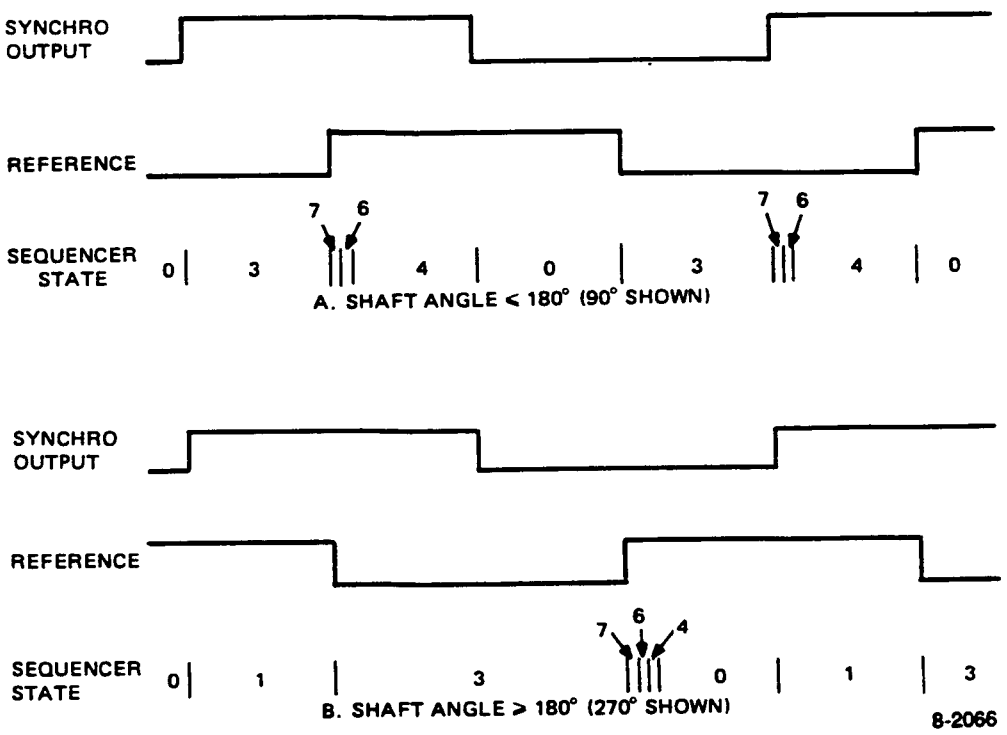

Figure 4.6.5-41. Sequencer Timing Diagram

be read out. The CIU then terminates the Array Status Start signal and sends 16 clock pulses (Array Status Clock) to the data register at a 102.4-kHz rate. The data in the register is serially shifted to the array status data output in synchronism with the positive-going edge of the array status clock.

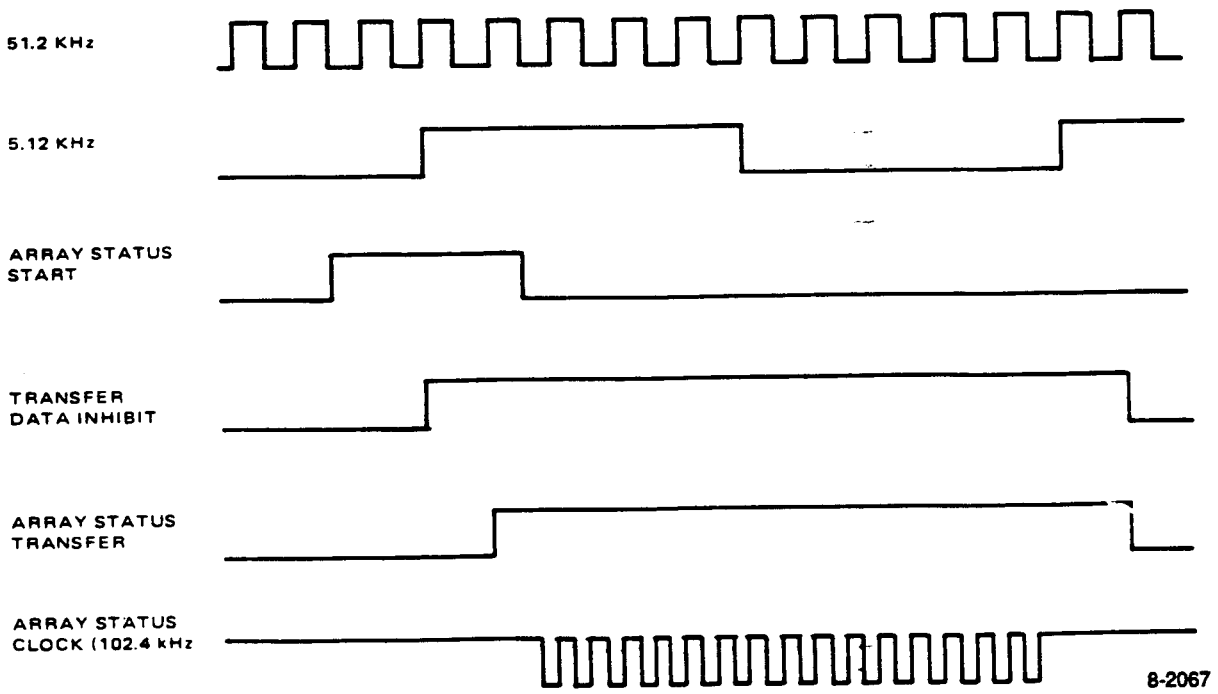

Figure 4.6.5-42. Pulse Generator Timing Diagram

The pulse generator output is generated from the 5.12-kHz clock. Therefore, the pulses are terminated approximately 30 microseconds after the last Array Status Clock pulse, ensuring that the data has been read out before allowing new data to be transferred into the register.

4.6.5.2.3 Telemetry

4.6.5.2.3.1 SAD Temperature Telemetry. A thermistor attached to the central housing in the SAD provides an indication of SAD slip ring temperature. The remainder of the SAD temperature telemetry circuit is located on the motor driver board of the ADE.

4.6.5.2.3.2 ADE Temperature Telemetry. A thermistor is located on each of the two motor driver boards in the ADE. Both thermistors are active irrespective of the selected ADE side.

4.6.5.2.4 Commands

4.6.5.2.4.1 Side Select Commands. A block diagram of the power switching is shown in Figure 4.6.5-43. SAD/ADE side selection is controlled by commands from the CIU. The three commands used are SAD Power On 1, SAD Power On 2, and SAD Power Off. The SAD Power On 1 command activates a relay coil drive circuit to connect the latching relays on side 1 and disconnect the latching relays on side 2. The SAD Power On 2 command performs the same function for side 2. The side 2 latching relays are connected, whereas the side 1 latching relays are disconnected.

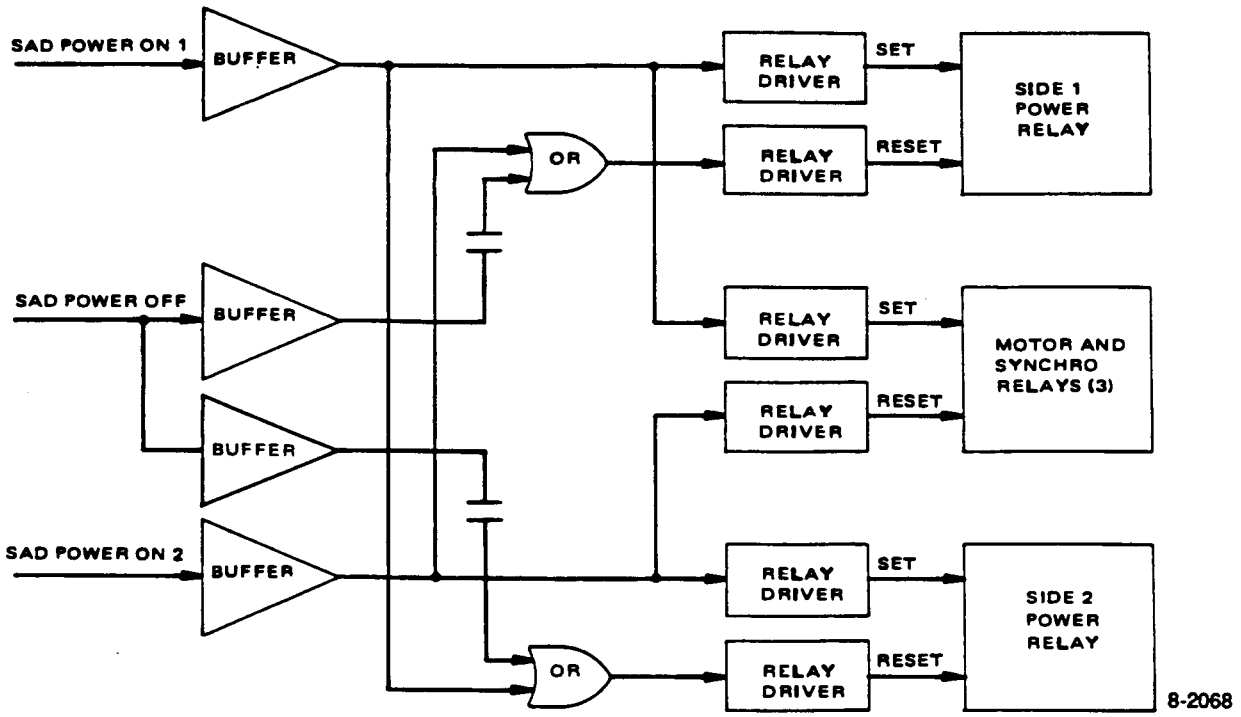

Figure 4.6.5-43. Power Switching Functional Block Diagram

The SAD Power Off command activates two relay coil drive circuits. Each disconnects the latching relays on the respective sides. The Power Off command is capacitively coupled to its drivers so that in the event of an active state failure both sides will not be locked off. If one of the Power On commands should fail, the other "On" command will still activate its side and the Power Off command will deactivate both sides.

4.6.5.2.4.2 Speed and Direction Commands. The SAD speed and direction is controlled in response to four control signals received from the C&CS:

- SAD Direction
- SAD Speed Bit 1
- SAD Speed Bit 2
- SAD Speed Swap Bit

These signals are decoded to control motor rotation as shown in Table 4.6.5-17. If any one control signal fails in either the high or the low sense, the remaining three bits can be used to select any speed and either direction. There are two complementary bit patterns for each condition. Error detection and correction is automatically provided by an algorithm in the C&CS software.

TABLE 4.6.5-17. SAD SPEED AND DIRECTION CONTROL

Direction Bit	Speed Swap Bit	Condition and Speed Speed Bits 1, 2				Direction
		0,0	0,1	1,1	1,0	
0	0	Slew	Slow	Normal	Fast	Reverse
0	1	Normal	Fast	Slew	Slow	Forward
1	1	Normal	Fast	Slew	Slow	Reverse
1	0	Slew	Slow	Normal	Fast	Forward

4.6.5.3 Solar Array Telemetry Commutator Unit (SATCU)

4.6.5.3.1 General Description

The Solar Array Telemetry Commutator Unit (SATCU) is a non-redundant unit that subcommutates and/or conditions analog telemetry derived from circuits on the solar array. A total of 32 telemetry signals are made available to the TIROS Information Processor (TIP) by the SATCU, 28 of which are arranged into subcom frames by the commutator and four of which are given separate, direct inputs to the TIP. Commutation of the majority of these signals is required because of the limited number of slip rings available for the solar array telemetry signals.

Many of the solar array signals handled by the SATCU are provided with active or passive conditioning circuits to make them compatible with the telemetry subsystem electrical requirements. In addition to these telemetry conditioning circuits, the SATCU also provides voltage references and ground returns that power some of the sensors on the solar array.

The SATCU is continuously powered by the spacecraft 28V regulated bus and uses spacecraft power ground for its signal ground. A 1-Hz clock (minor frame sync), major frame sync, and a Mode-Select command for operation of the commutator are derived from the spacecraft interface. The SATCU interface diagram is shown in Figure 4.6.5-44.

The SATCU is a single-board unit that uses a PC trace to provide connection between components. The unit assembly is mounted on the array mast between the solar panels. The physical configuration of the SATCU is shown in Figure 4.6.5-45.

4.6.5.3.2 SATCU Design and Functional Description

A functional block diagram of the SATCU is shown in Figure 4.6.5-46; the design parameters are summarized in Table 4.6.5-18.

4.6.5.3.2.1 SATCU Commutator. The SATCU Commutator (Figure 4.6.5-47) provides inputs for 28 telemetry signals and can operate in two distinct modes designated "A" and "B". These 28 signals are divided into three unique groups by the commutator, two of which contain 12 signals each and are used exclusively in mode "A" or mode "B" operation, and a third which is composed of the remaining signals and is common to both modes of operation. A SATCU

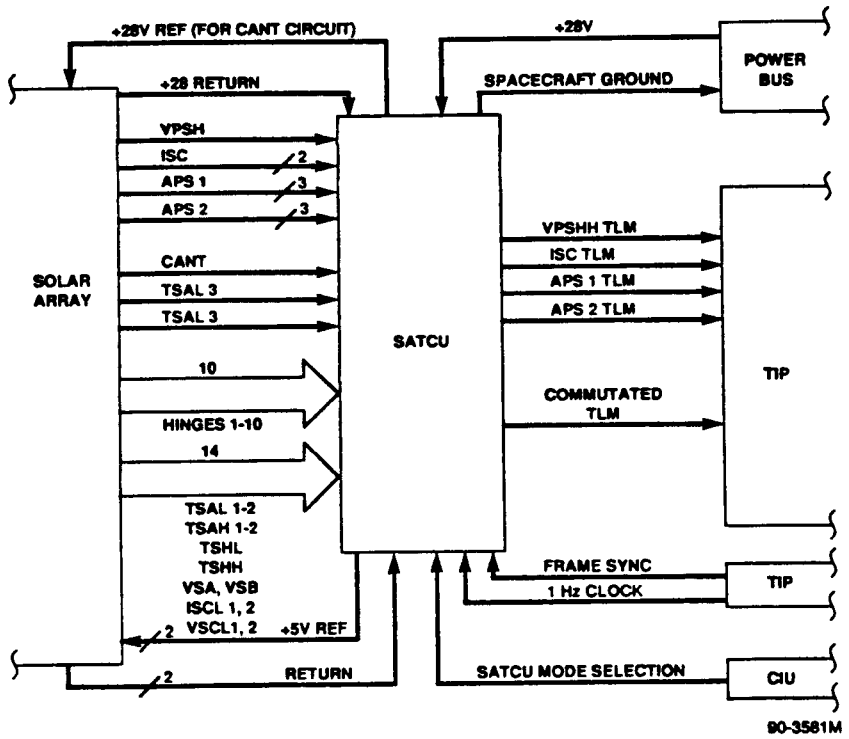

Figure 4.6.5-44. SATCU Interface Diagram

frame length is defined as 16 advancements of a 1-Hz external clock (from the CIU). Each data frame is composed of the 16 commutator inputs (Group A or B) sequentially gated to the output at a rate of one channel per clock period. The mode "A" data mostly consists of solar array hinge deployment telemetry, and is primarily useful during ascent and early orbit operations. The mode "B" data consists mostly of solar array temperatures, voltages, and current telemetry signals, and is used throughout the life of the spacecraft. The commutated data sequence is shown in Table 4.6.5-19.

The commutation process is achieved by sequentially activating channels from a series of five analog multiplexers which are tied to a common output. Selection of the appropriate multiplexer and desired channel address are controlled by logical combinations of the outputs of a binary ripple counter and the Mode-Select Command. Reset of the counter is synchronous with the frame sync pulse.

4.6.5.3.2.2 SATCU Telemetry Conditioning Circuits

4.6.5.3.2.2.1 Array Positioning Sensors (APS1, 2). This conditioning circuit performs a differential comparison between the outputs of two cells mounted on opposite sides of an angled bracket on the solar array. By determining which cell is operating at a higher output, it will become possible to adjust the array so that light incidence becomes uniform. Two of these circuits are provided by the SATCU and their outputs are given direct line to the TIP.

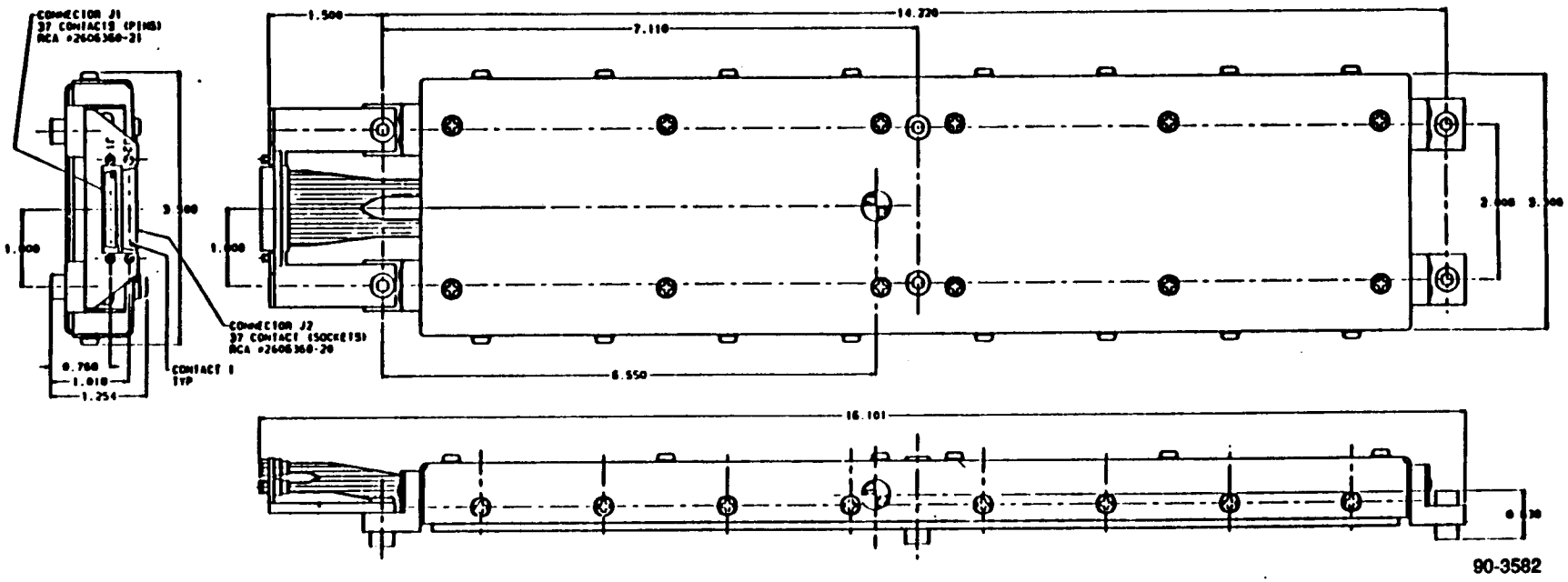

Figure 4.6.5-45. SATCU Physical Configuration

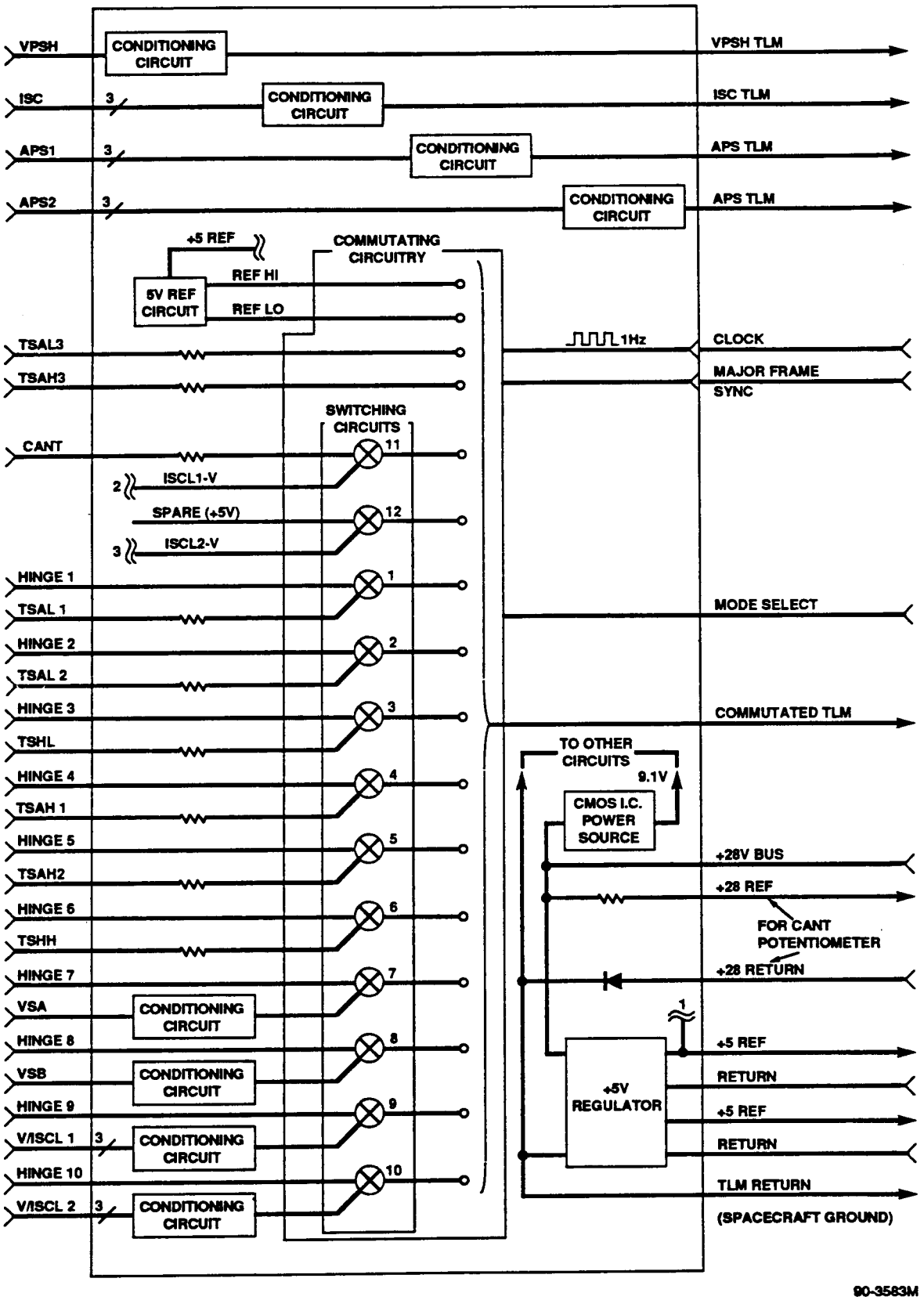

Figure 4.6.5-46. SATCU Functional Block Diagram

TABLE 4.6.5-18. SATCU DESIGN PARAMETERS

Parameter	Value
Supply Current (from 28V Bus)	27 mA
Power Dissipation	0.70 mW
Output Signal Range	0 to 5.1V
Operating Temperature	-35° to +75°C
Weight	1.16 lb Max

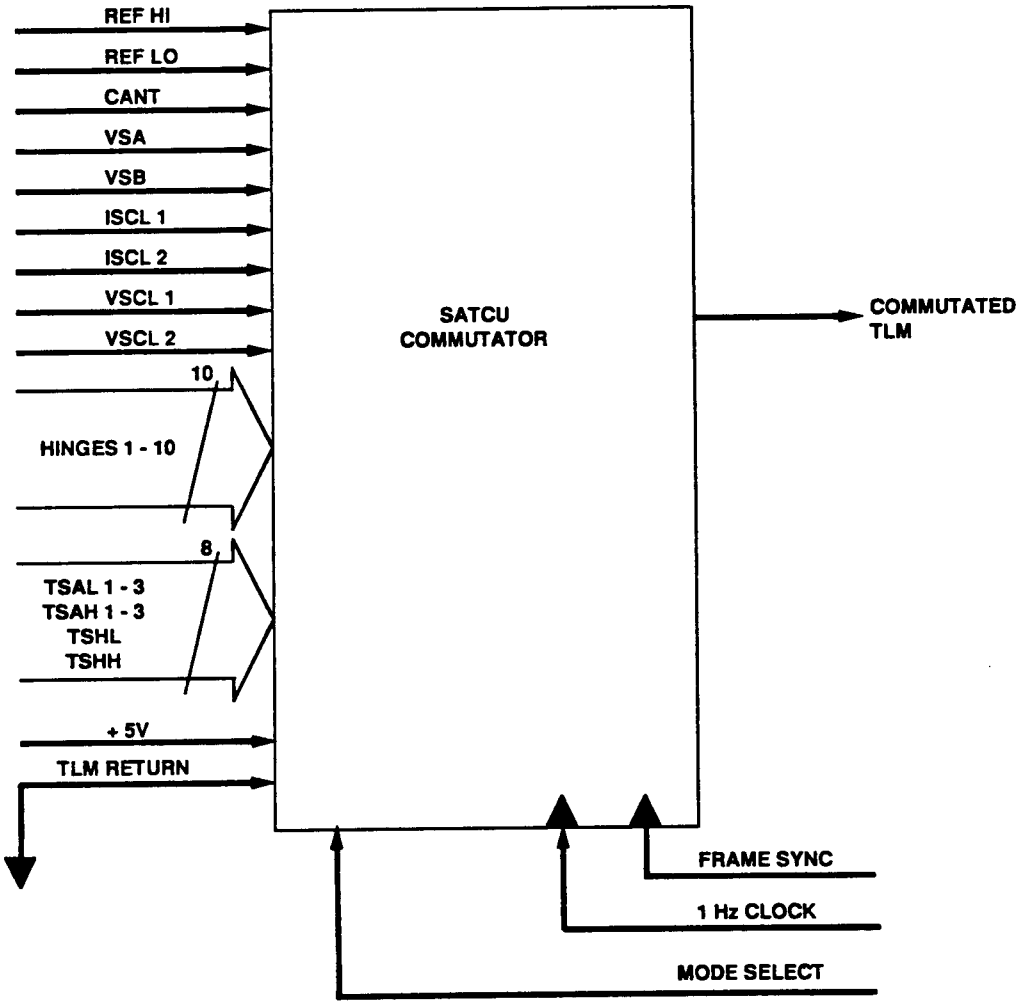

Figure 4.6.5-47. SATCU Commutator Block Diagram

90-3584M

TABLE 4.6.5-19. SATCU COMMUTATED TELEMETRY SEQUENCE

Subchannel Slot	Mode A Telemetry*	Mode B Telemetry*
1	Hinge 1	TSAL 1
2	Hinge 2	TSAL 2
3	Hinge 3	TSHL
4	Hinge 4	TSAH 1
5	Hinge 5	TSAH 2
6	Hinge 6	TSHH
7	Hinge 7	VSA
8	Hinge 8	VSB
9	Hinge 9	ISCL 1
10	Hinge 10	ISCL 2
11	REF HI (+5.1V)	REF LO (0V)
12	REF LO (0V)	REF HI (+5.1V)
13	CANT	VSCL 1
14	TSAL 3	TSAL 3
15	TSAH 3	TSAH 3
16	Spare (+5.1V)	VSCL 2

*Abbreviations used in this table are defined in Table 4.6.5-9.

The conditioning circuits are composed of two op-amp stages, the first being a unity gain adder and the second a differential amplifier ($V_{out} = A[V_x - V_1]$). Stage 1 exists to add a dc offset (V_{dc}) to V_2 so that V_x ($=V_2 + V_{dc}$) will never be less than V_1. This addition is necessary because no negative voltage is supplied to the SATCU and thus no negative signal values are possible.

4.6.5.3.2.2.2 Solar Cell Load Current (ISCL1, 2). This circuit monitors the output current of a pair of solar cells (mounted on the array) which are held at an operating potential of approximately 0.34V (per cell). Measurement of the desired current is achieved by placing the cells in series with a diode and a 0.1-ohm resistor (also on the array) and making a differential measurement (op-amp differential amplifier) across the resistor. The diode's function is to maintain a relatively constant 0.7V potential across the solar cells. Because of the 0.1-ohm resistor, the total drop across the cells will be slightly dependent on their output current; however, even at full output (350 mA), the additional drop is only 35 mV.

4.6.5.3.2.2.3 Solar Cell Load Current Voltage (VSCL1, 2). This telemetry signal is an accompaniment to the ISCL circuit. It gives an accurate measurement of the voltage across the two cells used as the ISCL sensor. By measuring this value, more accurate estimates of solar cell degradation with time can be made.

4.6.5.3.2.2.4 Solar Cell Short Circuit Current (ISC). The ISC circuit provides a measurement of the short circuit current available from a dedicated solar cell patch on the array. Load resistors mounted on the patch provide a

signal voltage for making this measurement. The conditioning circuit employed is an op-amp-based differential amplifier that provides voltage gain to the signal. Like the APS telemetry, this signal is given its own direct line to the TIP.

4.6.5.3.2.2.5 <u>+5V Reference Telemetry (Ref-Hi)</u>. This circuit is a resistive voltage divider network acting on the 5V reference which the SATCU provides to the array hinge potentiometers. Its purpose is to give an indication of the actual value of this 5V signal throughout the spacecraft lifetime. The proportionality constant for the divider is approximately 0.9V.

4.6.5.3.2.2.6 <u>Partial Shunt Voltage (VPSH)</u>. This circuit makes a measurement of the voltage at the partial shunts of the solar array. The input signal is provided through an equivalent series resistance of 2.1 Kohm (70 147Kohm isolation resistors in parallel). A voltage division is then made by the circuit to bring the telemetry into the 0-5.1V range. This signal has its own dedicated path to the TIP.

4.6.5.3.2.2.7 <u>Array Operating Voltage (VSA)</u>. This circuit provides a measurement of the operating voltage of the upper solar cells on the solar array. Like the VPSH telemetry, this signal is passed to the conditioning circuit through an equivalent 2.1-Kohm resistance and conditioned with a voltage divider.

4.6.5.3.2.2.8 <u>Array Operating Voltage (VSB)</u>. The VSB telemetry circuit measures the unregulated solar array bus voltage. Unlike the other array operating voltage measures, this signal is received without a series resistance. Once again the conditioning circuit is a voltage divider.

4.6.5.3.2.2.9 <u>+5V Voltage Reference</u>. Two 5V lines are provided by the SATCU to power the 10 array hinge potentiometers. This voltage is generated by a zener regulator. Also provided by the SATCU are the ground return lines for these potentiometers.

4.6.5.3.2.2.10 <u>+28V (Cant) Voltage Reference</u>. The signal designated +28V Ref. is the 28V bus fed through a 17.8-Kohm resistor. This line powers the array Cant potentiometer. In addition to the 28V Ref. signal, the SATCU also provides a diode protected return line to ground for the Cant hinge.

4.6.5.4 <u>Batteries</u>

The nickel-cadmium batteries are the source of all electrical power for satellite functions during the night portions of the orbit, and of supplementary electrical power during daylight when the satellite load demands exceed the solar array capability.

The battery system consists of three 47-ampere-hour rated batteries to provide a combined capacity of 141 ampere hours. This value of battery capacity is consistent with the GSFC specified requirement for a minimum mission life of 12,000 orbital charge/discharge cycles.

4.6.5.4.1 Design Description

4.6.5.4.1.1 Design Approach. The NOAA KLM battery configuration is three parallel 47-ampere-hour batteries, each with 17 series-connected storage cells. The three batteries are charged separately by separate charge regulators in the BCA and PSE, but are discharged together through the discharge isolation diodes.

A functional block diagram for one of the three identical NOAA KLM batteries is presented in Figure 4.6.5-48. As shown, the storage cells are packaged in a nine-cell pack and an eight-cell pack.

Each pack contains two thermistors for the battery Voltage/Temperature (V/T) limiting reference circuit in the PSE. Thermistors bonded to the end surface of cells 6A and 2B provide a combined voltage proportional to temperature for the primary control circuit, and thermistors bonded to the end surface of cells 2A and 5B provide the combined output voltage for the backup control circuit.

Thermistors bonded to the end surface of cells 5A and 4B provide a separate temperature telemetry signal for each pack. Those bonded to 4A and 4B provide a separate temperature telemetry signal used during ground test. Thermistors bonded to the side of cells 5A and 4B are provided as the sensing element for the Thermal Control Electronics (TCE), which control each pack temperature through a strip heater or a cooling louver.

In addition to the temperature sensing and control circuits, the battery packs include a diode for protection when the battery is charged externally during spacecraft level checkout and an isolation resistor for monitoring battery voltage during ground tests.

Each battery pack temperature is held at a nominal battery operating temperature of 0 to 2°C by the TCE, which actively controls the temperature by using a heater for heating the pack or louvers for cooling the pack. The lower temperature limit is for heater turn-on, and the upper limit is for louver operation.

4.6.5.4.1.2 Design Characteristics. The design characteristics for each of the three batteries are listed in Table 4.6.5-20. The design characteristics of the TCE may be found in Section 4.5.

4.6.5.4.1.3 Physical Description. The 47-ampere-hour storage cell is a standard prismatic, hermetically sealed nickel-cadmium aerospace cell manufactured by Gates Aerospace Batteries in Gainesville, Florida. The cell case is a stainless steel (304L) container with 0.019-inch wall thickness with the top, bottom, and side faces corrugated for additional pressure resistance on these unsupported surfaces. Both the positive and negative cell terminals are electrically isolated from the case by means of an all nickel brazed butt-type ceramic seal. The separator is non-woven nylon. Both positive and negative plates are a sintered nickel structure; the positive plate is impregnated with nickel hydroxide active material and the negative plate with cadmium hydroxide active material. The plates are die cut with corner radii and coined edges to prevent shorting. The cell design includes a thin Teflon impregnation on the

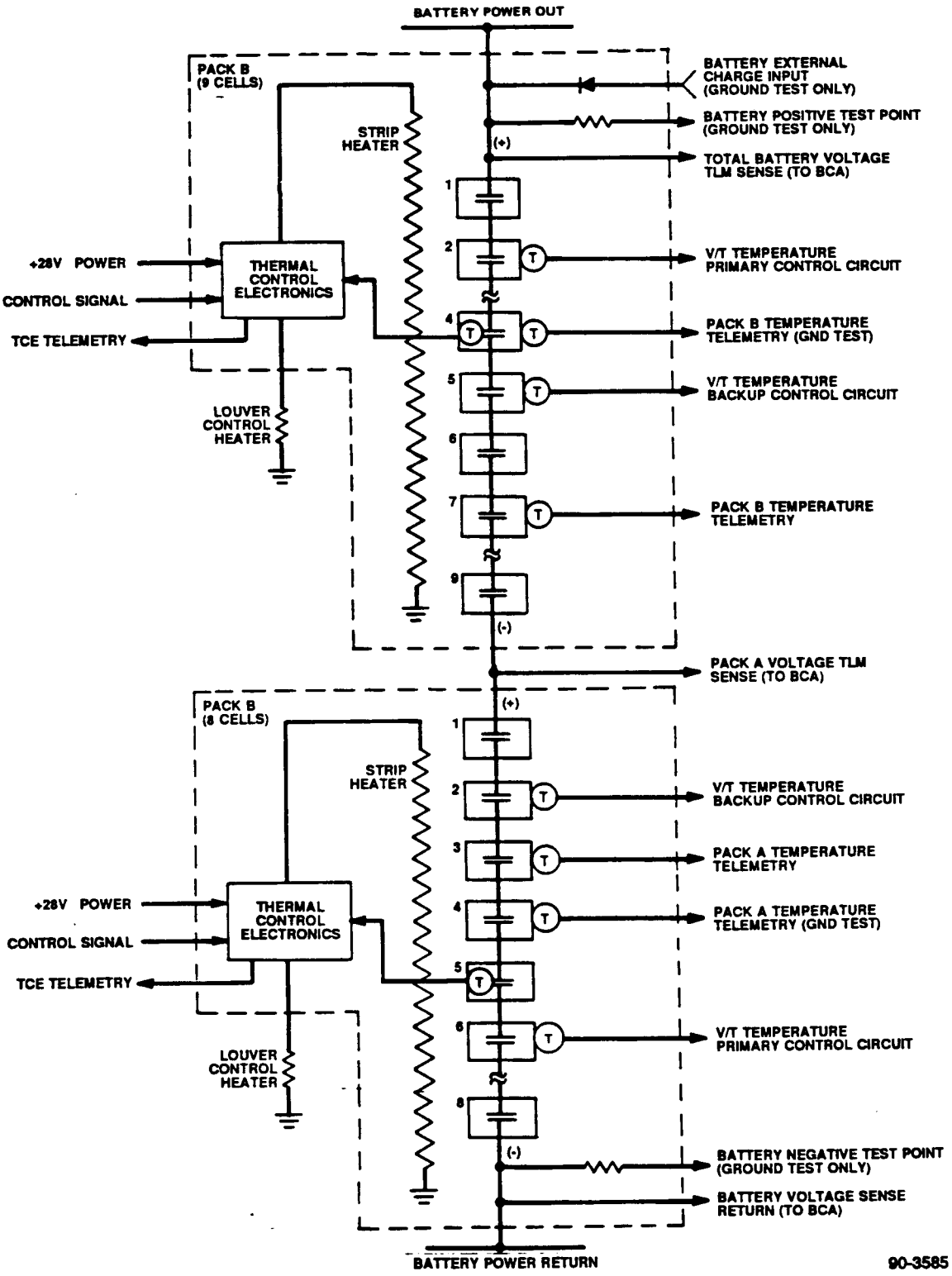

Figure 4.6.5-48. Battery Functional Block Diagram

TABLE 4.6.5-20. BATTERY CHARACTERISTICS

Parameter	Value (For Nominal 17-Cell Battery)
Battery Type	Nickel-Cadmium
Battery Voltage	
Minimum Discharge	See Table 4.6.5-21
Maximum Full Charge*	25.84 volts
Battery Capacity**	47 (141) ampere-hours
Cell Quantity**	17 (51)
Packaging	9-cell pack and 8-cell pack
Size	
8-cell pack	15.2 x 8.1 x 7.4 inches
9-cell pack	16.1 x 8.1 x 7.4 inches
Weight	
8-cell pack	39.6 pounds
9-cell pack	43.6 pounds

*At minimum temperature
**Numbers in parentheses are for the entire battery configuration.

surface of each negative plate. This feature extends operational life by enhancing oxygen recombination and retarding cadmium migration. The cells are manufactured in accordance with NHB 8073.1, specification for NASA STD Aerospace nickel-cadmium cells.

The individual cells are assembled in a basic module as shown in Figure 4.6.5-49. Machined magnesium shells are bonded to each cell using RTV 566 silicone rubber. The interior walls of the magnesium shells are anodized to provide electrical insulation without impeding heat transfer. The magnesium shells perform the following functions:

- Insulate cell cases from each other and from the end plates
- Provide mounting flanges for each cell
- Provide a heat transfer path to the radiating surface
- Provide flat and parallel cell module surfaces for stacking

The cell module design was dictated largely by the need to remove large amounts of heat energy from the battery. Heat generated within the cell is transferred through the RTV to the magnesium shells, and then down to the connecting flanges. During normal charge-discharge cycling, the temperature gradient between the hottest cell and the mounting surface will be no more than 1°C. During worst-case continuous overcharging, the thermal gradient is less than 3°C.

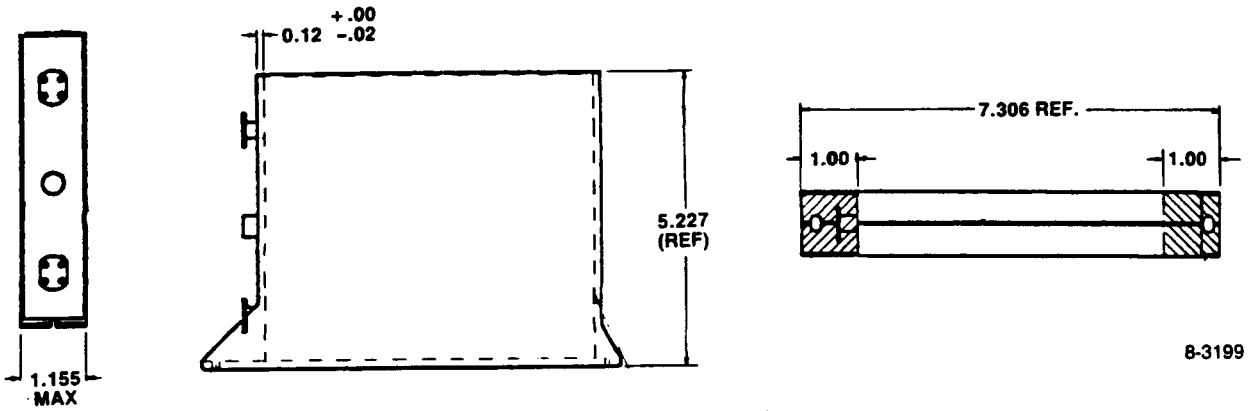

Figure 4.6.5-49. Battery Bonded Cell Module

The bonded cell modules are assembled into a battery pack as shown in Figure 4.6.5-50. The cell modules are stacked side by side and held together by tension stringers attached to milled end plates. The primary purpose of the end plates is to hold the assembly together and to restrain the cells from bulging (cells can develop an internal pressure as high as 60 psig during extended overcharging). The battery cell voltage, temperature, and telemetry signals are brought out to multiple-pin connectors. A separate multipin connector on each pack provides a two-wire connection to each cell for reconditioning operations.

The battery packs are mounted externally around the RSS, with the bottoms oriented toward the spacecraft +X axis. Each pack is attached directly to the window frame brackets at the bonded cell module tiedown flanges.

Thermal control of each pack is accomplished by rectangular "venetian-blind" louvers in the pack mounting bracket (which allows cooling by direct radiation to space) and by a strip heater installed across the bottom of the pack. A complete description of the thermal controls is contained in Section 4.5.

4.6.5.4.2 Functional Description

4.6.5.4.2.1 Voltage Characteristics. The relationship of charge voltage to state of recharge for the nickel-cadmium cells is highly complex, depending upon many factors other than the obvious ones of temperature and charge rate. Among such factors are the following:

- Depth of discharge immediately preceding the charging
- Immediate past history of the cell (repetitive cycling, continuous overcharge, open circuit, etc.)
- The age of the cell
- Long-range past history (type of usage and temperature)

Because of these factors, there is at present no general model relating cell voltage and state of recharge. However, a limited model applicable to the NOAA KLM batteries has been developed on the basis of test data; the curves

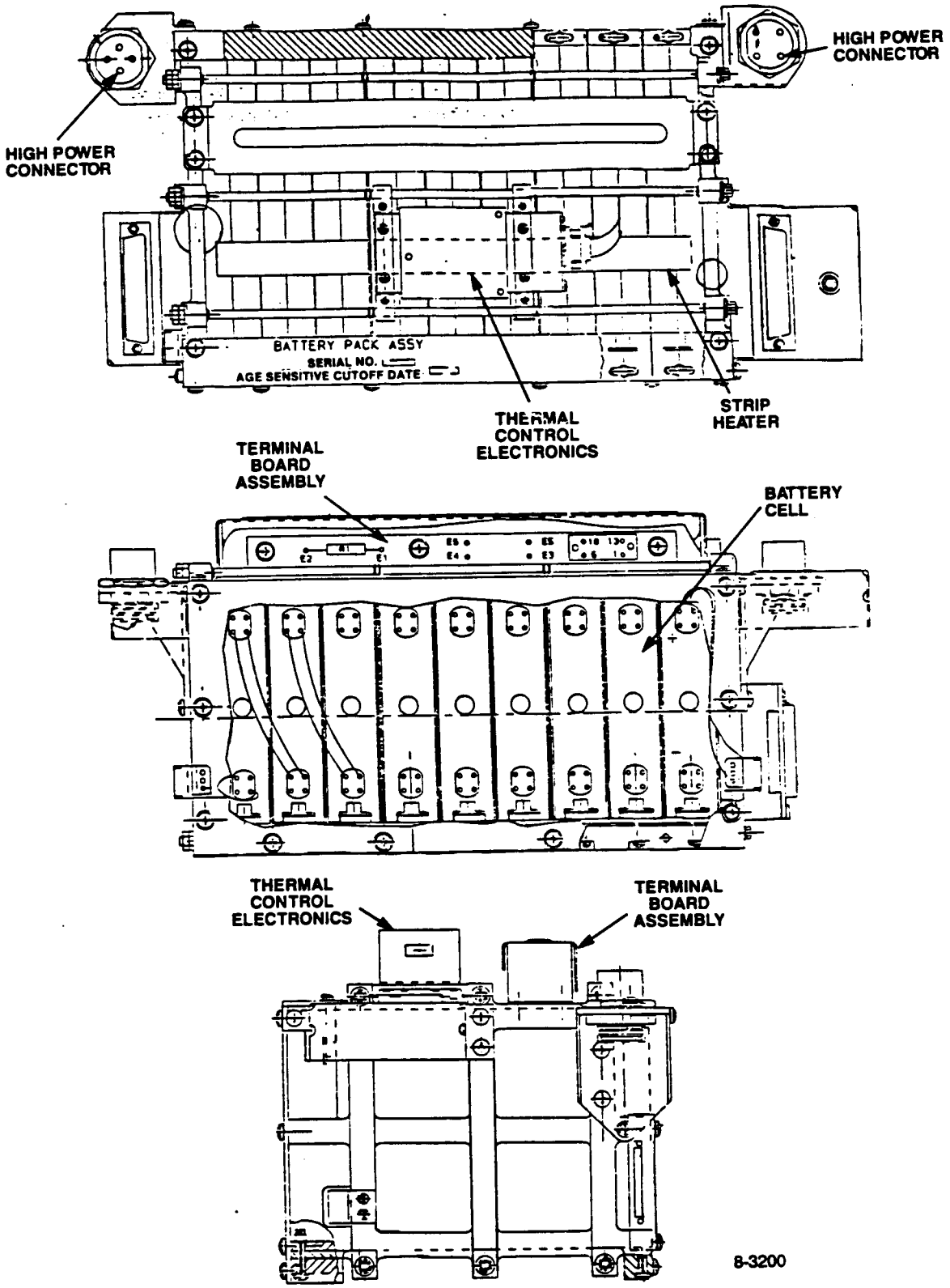

Figure 4.6.5-50. Typical Battery Pack Physical Configuration

shown in Figure 4.6.5-51 represent this model. Both charge and discharge (negative currents) curves are shown in the figure, since discharge voltages must be considered when determining discharge currents in a DET system. One open circuit voltage curve is shown to be used for interpolation for charge currents.

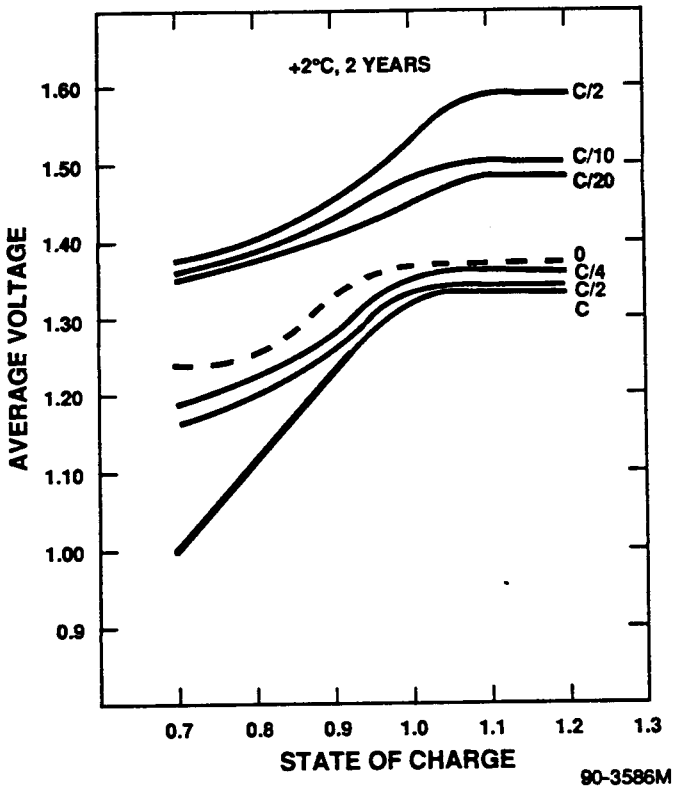

Figure 4.6.5-51. Battery Cell Voltage

4.6.5.4.2.2 Temperature Characteristics. The sealed nickel-cadmium cell is a temperature sensitive device with the following characteristics:

- The charge voltage decreases with increasing temperature.
- The maximum tolerable overcharge current decreases with decreasing temperature.
- The cycle life of a cell (as determined by its discharge voltage) decreases with increasing temperature (see Figure 4.6.5-52).
- The thermal dissipation within a cell normally increases with increasing temperature.
- The recharge efficiency of a cell increases with decreasing temperature (see Figure 4.6.5-53).

In light of these considerations, optimum cell performance is obtained by operating the batteries in a narrow temperature range near 0°C. Below 0°C, battery voltages may become too high for proper charger circuit operation. Also, cell equilibrium pressure tends to increase. These concerns dictate the low end temperature limit.

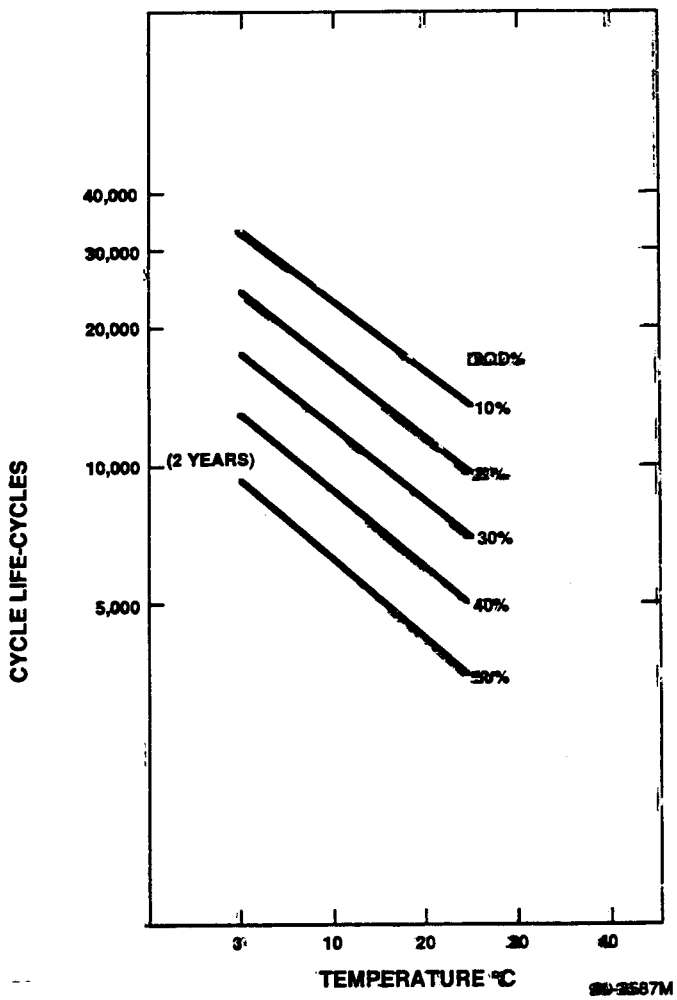

Figure 4.6.5-52. Life Prediction of NiCd Batteries in Low Earth Orbit

Battery temperatures are maintained in the desirable range between 0°C and +2°C by an active thermal control system which utilizes a dual heater/louver TCE.

4.6.5.4.2.3 Charge Protection. The charge protection plan for the NOAA KLM batteries is current limiting at 10 amperes/battery and multi-level voltage limiting during normal recharge and commanded trickle charge in overcharge.

The NOAA KLM system has four ground-commandable charge current limits. The two normal limits are either 0.85 ampere for continuous sunlight orbits or 10.0 amperes for those orbits that require recharge after the eclipse discharge. The third limit, at 7.5 amperes, is included to accommodate orbits requiring a low charge rate due to lower than expected power demands. The fourth limit, at 12.5 amperes, is reserved for two-battery operation or reconditioning charging. The charge rates are individually commandable for each battery.

Overcharge protection is accomplished by voltage limiting at or near full charge and C/D ratio controlled command to trickle charge once full charge has

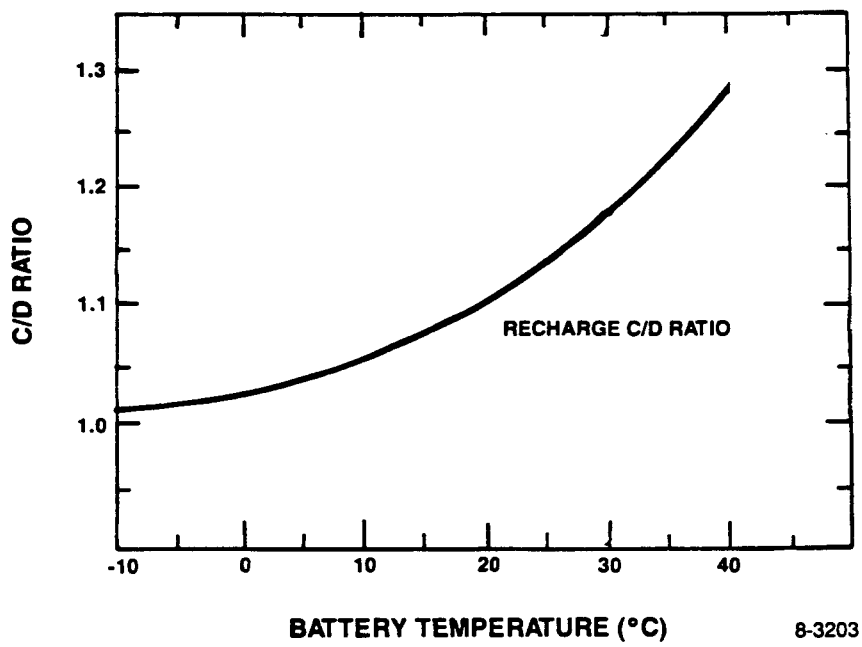

Figure 4.6.5-53. Minimum Charge/Discharge Ratios

been achieved. The ground command structure is such that different voltage limits can be applied separately to each battery. When a battery reaches one of the 16 limits shown in Figure 4.6.5-54, its current is reduced by a tapering action so that battery voltage is maintained at the preset level. When a low limit is selected, the charge current can be decreased to a rate that is both safe and practical for extended overcharge. For those higher sun angle orbits where overcharge is limited, a higher voltage level suitable for meeting the energy balance requirements can be used. The minimum ampere-minute charge to discharge ratio required for ensuring energy balance is presented in Figure 4.6.5-53.

Further overcharge protection is provided by the C/D ratio control feature in Power Management Software (PMS). With this feature the desired C/D ratio is based on battery temperature telemetry and the charge rate is automatically shifted to 0.85 ampere when the required charge input in ampere-minutes has been achieved.

The shape of each of the 16 voltage limit curves has been purposely depressed at temperatures above +10°C to remove any chance for thermal runaway when the batteries cannot be accessed from the ground. This high temperature depression of the voltage limit curves will not hamper battery energy balance if the active thermal controls fail. In this event (or if the TCEs are turned off) passive temperature controls will limit the batteries to approximately +17°C under normal operating conditions.

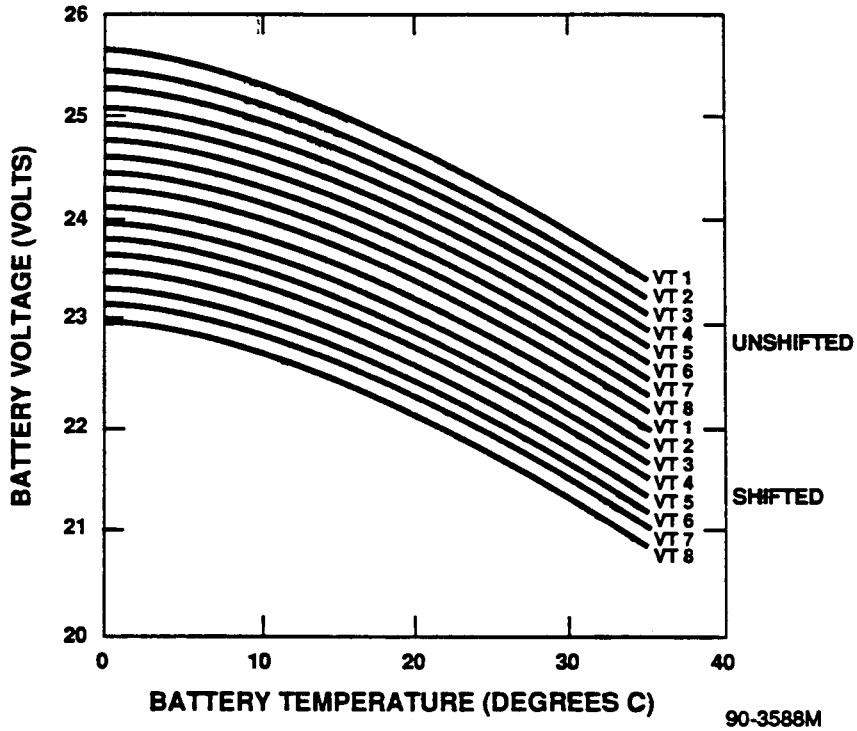

Figure 4.6.5-54. Nominal Battery Voltage Limits

4.6.5.4.3 Battery Performance

The battery performance at the beginning of life and at the end of a 2-year mission life is summarized in Table 4.6.5-21. This table shows battery Depth-of-Discharge (DOD) and end-of-discharge voltages and currents for each of the following four conditions:

1. Normal three-battery operation

2. One battery with a shorted cell

3. Two batteries each with a shorted cell

4. Two normal batteries on line such as during reconditioning of the third battery.

As shown, the depth of discharge for normal three-battery operation is less than 20%. With two batteries on line the DOD increases to 32%. Even with this higher DOD, the cycle life prediction curves for NiCd batteries presented in Figure 4.6.5-52 indicate a high degree of confidence in exceeding the 2-year mission requirements for the spacecraft.

TABLE 4.6.5-21. NOAA KLM BATTERY PERFORMANCE

Period	No. of Cells Per Battery			Battery No. 1			Battery No. 2			Battery No. 3		
	1	2	3	DOD %	Voltage (Volts)	EOD I (Amps)	DOD %	Voltage (Volts)	EOD I (Amps)	DOD %	Voltage (Volts)	EOD I (Amps)
Begin. of Life (BOL)	17	17	17	19.3	21.34	14.52	19.3	21.34	14.52	19.3	21.34	14.52
	17	17	16	22.8	21.07	16.68	22.8	21.07	16.89	13.6	20.59	10.81
	17	16	16	26.8	20.74	19.63	16.9	20.25	13.13	16.9	20.25	13.13
	17	17	--	31.1	20.39	23.64	31.1	20.39	23.64	--	--	--
End of Life (EOL)	17	17	17	19.8	20.57	15.16	19.8	20.57	15.16	19.8	20.57	15.16
	17	17	16	23.3	20.30	17.26	23.3	20.30	17.26	14.3	19.89	12.09
	17	16	16	27.2	20.00	19.87	17.7	19.56	14.00	17.7	19.56	14.00
	17	17	--	31.9	19.69	24.73	31.9	19.69	24.73	--	--	--

Battery Capacity used in analysis - 42AH

Based on 843W load, 0.057 ohm harness resistance, and quad diodes/30°C for 35 minute discharge

4.6.5.4.4 Telemetry

The following telemetry indicators are available for each battery:

- Battery Voltage (High Range)
- Battery Voltage (Low Range)
- Battery Pack A Voltage
- Battery Charge Current (Sensed in BCA)
- Battery Discharge Current (Sensed in BCA)
- Battery Pack A Temperature
- Battery Pack B Temperature
- Battery Pack A TCE Operation
- Battery Pack B TCE Operation

Battery voltage telemetry conditioning circuits are physically located in the BCA.

4.6.5.5 Battery Reconditioning Unit (BRU)

The Battery Reconditioning Unit (BRU) provides the means for spacecraft battery reconditioning. The reconditioning process consists of a full discharge followed by a recharge of all battery cells.

Battery reconditioning minimizes the reduction in battery performance due to memory effect and unequal cell voltages, thereby extending battery life. The spacecraft has three BRUs, one dedicated to each of three 17-cell nickel cadmium batteries. The three batteries are reconditioned sequentially, one battery at a time. To discharge the selected battery, the BRU switches in individual let-down resistors across each cell of the battery. Once the battery is discharged, the BRU switches out the let-down resistors and switches in a series pull-up resistor between the +28.0-V bus and the discharged battery. This initiates the recharge cycle. Switching of the BRU let-down and pull-up resistors is accomplished by latching relays within the BRU. The relay drive signals are provided by the PSE in response to command signals from the CIU. The BRU is a new assembly that has not been used on previous TIROS spacecraft. Figure 4.6.5-55 shows a functional block diagram of the BRU.

4.6.5.5.1 Design Description

The BRU assembly contains the battery cell let-down resistors, pull-up resistors, switching relays, and telemetry circuits for indicating relay status configuration and BRU temperature. The let-down resistors are implemented by two resistors in parallel and the pull-up resistors are implemented by four resistors in parallel. The let-down and pull-up resistors are switched in or out by two latching relay contacts in series on two separate relays.

The two relays used to provide the two series connected relay contacts for the let-down resistors are designated as Group A and Group B. Each of the series

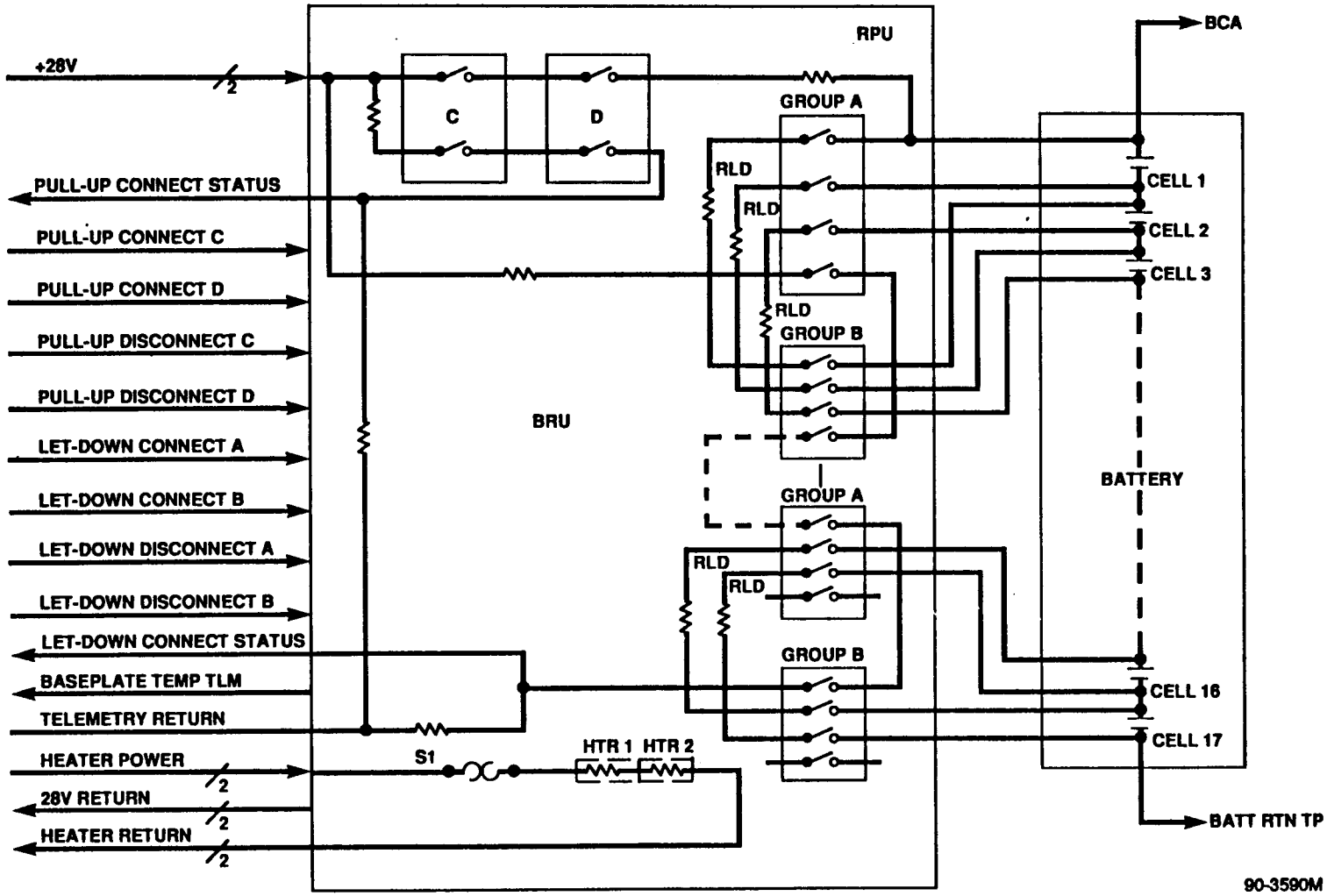

Figure 4.6.5-55. BRU Functional Block Diagram

relays, designated A and B, are activated by separate relay drive signals from the PSE. Similarly, the two relays used to provide the two series connected relay contacts for the pull-up resistor are designated as Group C and Group D. Again, each of the series relays, designated C and D, are activated by separate relay drive signals from the PSE. The above relay configurations are shown in Figure 4.6.5-55.

Even though the let-down resistors and pull-up resistors have parallel redundancy and there are two relay contacts in series for both, the BRU is not a truly redundant function. The two relay contacts in series are provided to ensure that a single point failure will not result in a permanent connection of the let-down or pull-up resistors. If the BRU does experience a single-point failure, the mission life will not be endangered, although the ability to recondition the associated battery may be lost.

To ensure that the piece part component temperatures stay above -55°C, a thermostatically controlled heater is mounted to the BRU baseplate. The controlling transducer for the thermostat is a thermistor, also mounted on the baseplate.

4.6.5.5.1.1 Design Characteristics. The design characteristics for the BRU are listed in Table 4.6.5-22.

4.6.5.5.1.2 Physical Description. The BRU consists of two subassemblies:

- Radiator Assembly
- Printed Circuit Board (PCB) Assembly

The radiator assembly shown in Figure 4.6.5-57 provides the means to dissipate the heat from the let-down and pull-up resistors during battery reconditioning. The radiator is fabricated from 0.090 thick, 6061-T6 Aluminum plate and is finished with a white high emissivity paint (S-13G/LO) on its exterior surface to enhance thermal radiation. The resistors are spread out over the radiator surface and bonded with RTV-566. Two heating strips are located between the resistors and are bonded to the radiator plate along with the thermostat and two thermistors. The thermostat controls the heater strips so that the box temperature is maintained within the operational limits of the electrical components. The heating strips and the thermostat are bonded to the radiator plate using RTV-566. The two thermistors are bonded to the radiator plate using thermally conductive epoxy 828/V140.

The PCB shown in Figure 4.6.5-56 is a four layer, 0.062 thick board containing the BRU electrical components with the exception of those mentioned above. The PCB mounts to the radiator plate through eight aluminum spacers which provide the heat transfer path. A right angle 37 pin connector and a 25 pin solder cup connector interface the BRU to the battery and spacecraft. A small wiring harness provides the interconnection between the PCB and the radiator mounted components. Any large components are staked using Blue Solithane and the PCB is conformally coated with Conathane CE-1155.

TABLE 4.6.5-22. BRU DESIGN CHARACTERISTICS

Parameter	Value
Pull-up Resistance	4- 689 ohm resistors in parallel R_{eq} = 174.5 ±2.8% ohms
Let-down Resistance	2- 3.01 ohm resistors in parallel R_{eq} = 1.505 ±2.8% ohms
Heater Resistance	139 ±15% ohms
Input Supply Voltage	+28.0-Volt Regulated Bus
Input Power (+28.0V) - During Relay Switching - During Standby - Heater Requirements	 I_{max} = 400 mA; Duration ≤ 70 msec I_{max} = 5 mA I_{max} = 241.7 mA
Packaging	BRU consists of two sub-assemblies • Radiator assembly • 1- printed circuit board assembly
Size (in.)	
Radiator Assembly	6.75 x 12.80 x 0.09
PCB Assembly (see Figure 4.6.5-56)	4.20 x 6.68 x 0.062
BRU Overall (see Figure 4.6.5-57)	6.75 x 13.00 x 2.165
Weight BRU Overall (lb.)	3.35 Max.

The unit is enclosed with an aluminum cover (Figure 4.6.5-57), fabricated from 0.040 thick, 6061-T4 and heat treated to a T6 state Aluminum alloy. The cover protects the electronic parts. The BRU is mounted with six #6-32 screws to a bracket extending from the RSS. Shoulder bushings and washers made of Polycarbofil (G-50/40) thermally isolate the BRU from its mounting bracket. The BRU is oriented such that the side of the radiator with no components is facing space, while the box side is facing the spacecraft. The side facing the spacecraft will be blanketed to minimize the heat exchange between the BRU and the spacecraft. A grounding strap will connect the BRU chassis to the spacecraft.

4.6.5.5.2 Functional Description

The BRU's function is to switch in and out the let-down and pull-up resistors as commanded via the PSE. The BRU sends status telemetry signals to the TIROS

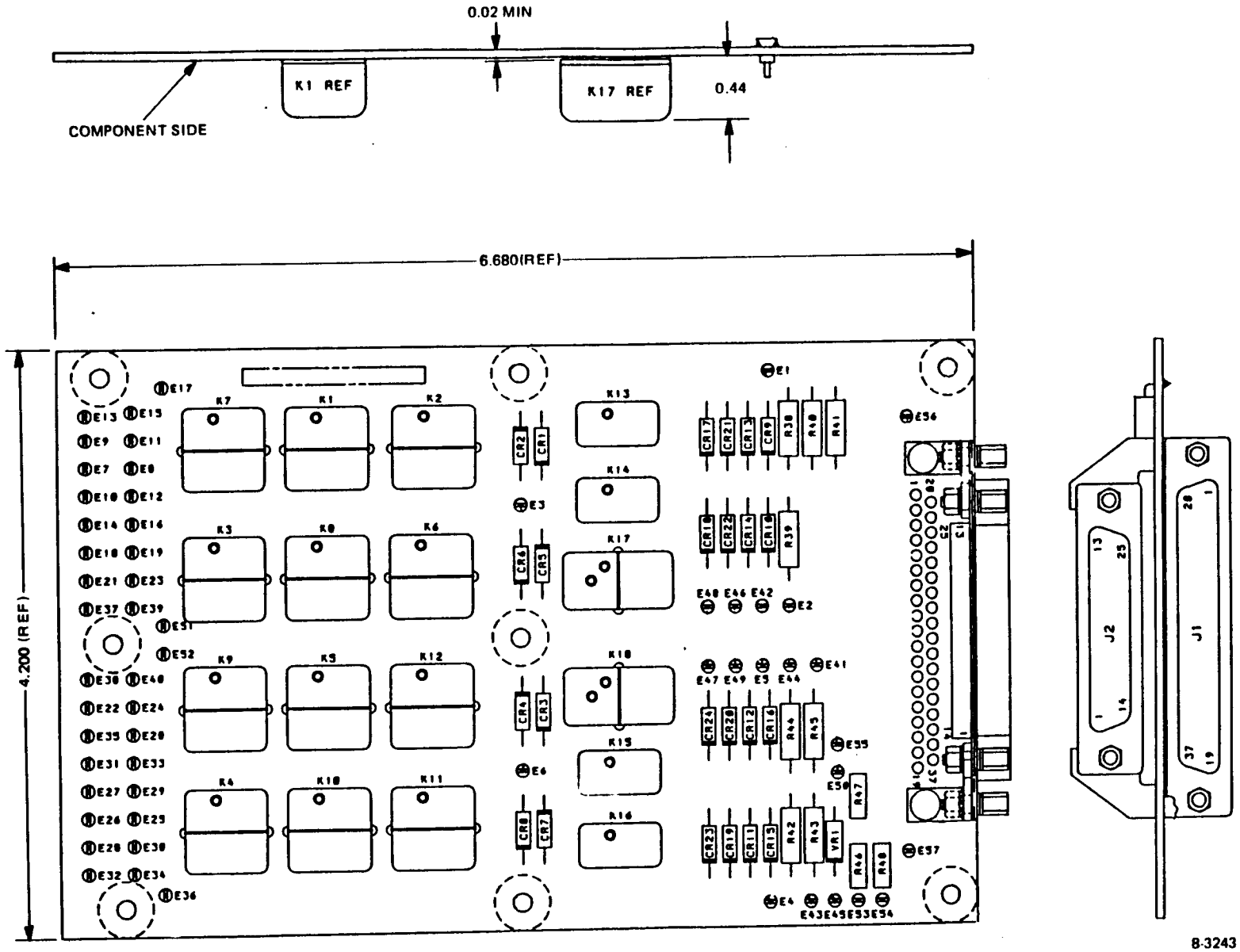

Figure 4.6.5-56. PCB Assembly Outline

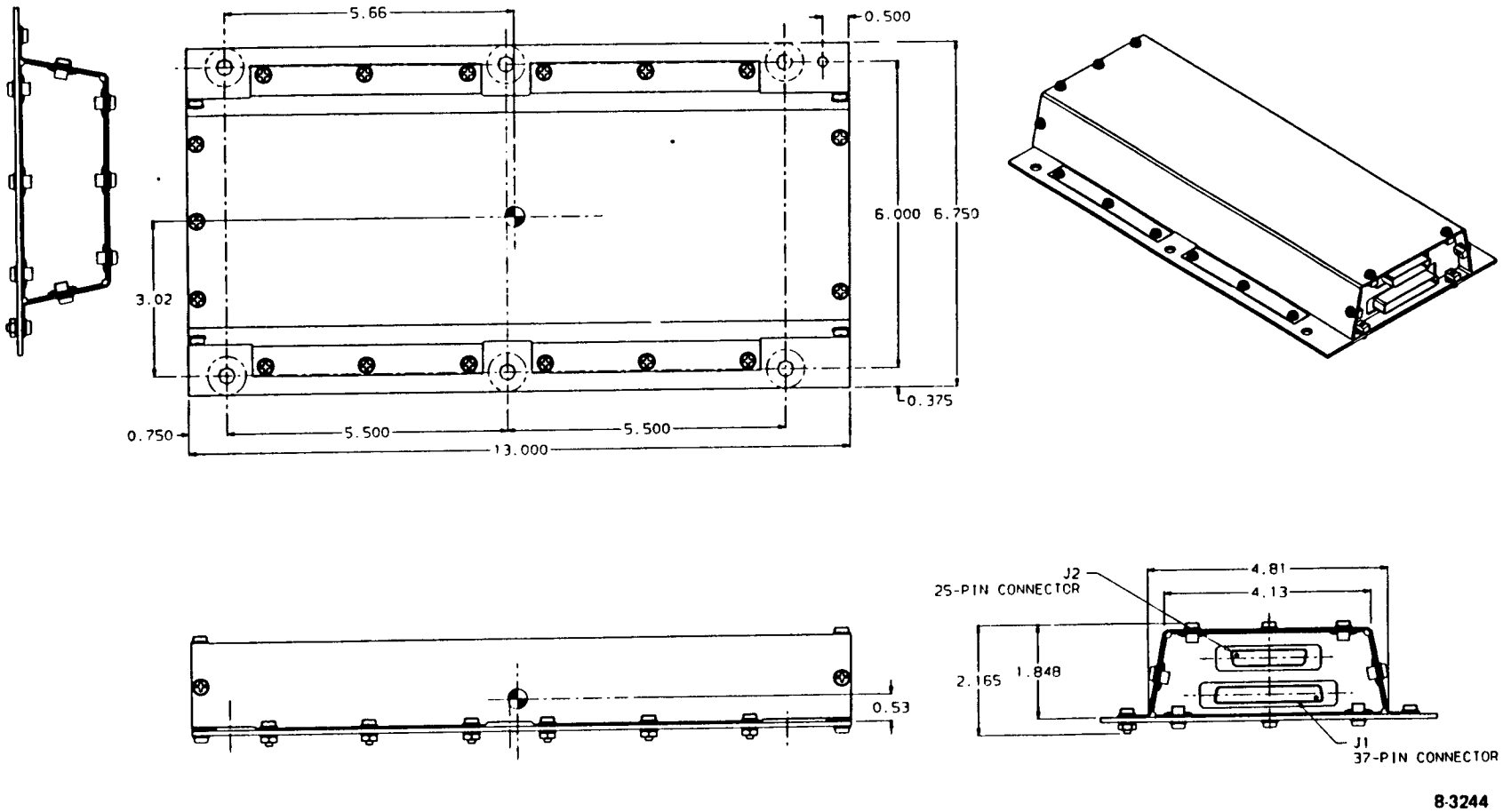

Figure 4.6.5-57. BRU Outline Drawing

Information Processor (TIP) continuously to determine the actual relay status and baseplate temperature to ensure the BRU has performed the commands sent and that the resulting baseplate temperature is within limits. Figure 4.6.5-58 is the interface diagram of the BRU and shows the input commands and telemetry signal lines provided.

4.6.5.5.3 Telemetry

A list of the telemetry signals provided by the BRU to the TIP is given Table 4.6.5-23. All associated telemetry conditioning circuitry is located in the BRU.

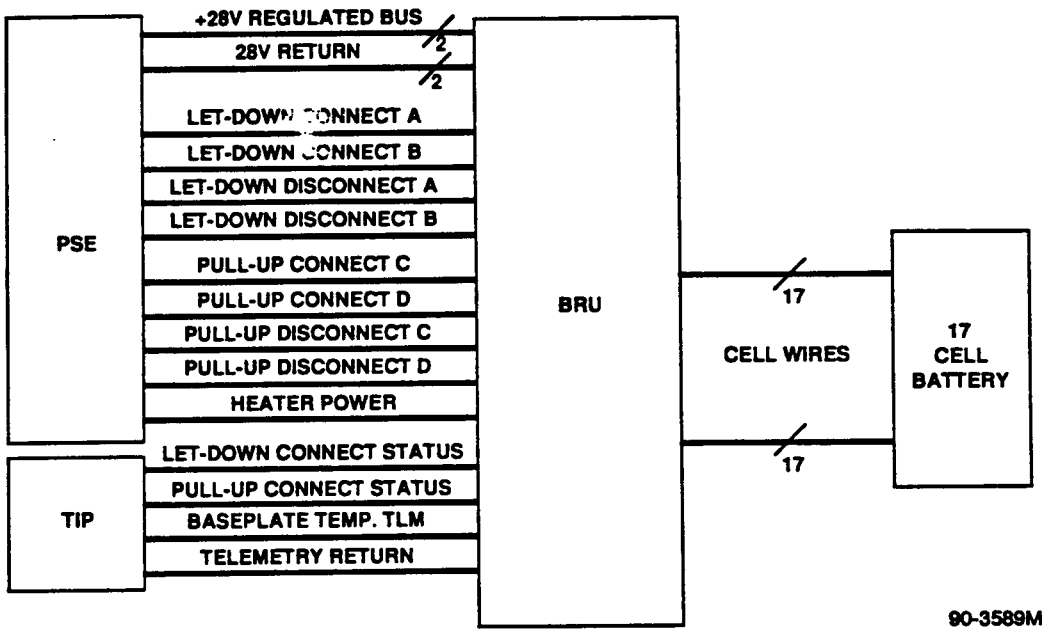

Figure 4.6.5-58. BRU Interface Diagram

TABLE 4.6.5-23. BRU TELEMETRY

Telemetry Signal	Signal Type
Let-down Resistor Connection Status	Discrete
Pull-up Resistor Connection Status	Discrete
BRU Baseplate Temperature	Analog

4.6.5.5.4 Commands

The BRU receives the following let-down and pull-up relay drive signals from the PSE:

- Let-down Connect A
- Let-down Connect B
- Let-down Disconnect A
- Let-down Disconnect B
- Pull-up Connect C
- Pull-up Connect D
- Pull-up Disconnect C
- Pull-up Disconnect D

The BRU Let-down Connect A and BRU Let-down Connect B relay drive signals cause let-down relay groups A and B to close and thereby enable the battery let-down function. The BRU Let-down Disconnect A and BRU Let-down Disconnect B relay drive signals cause let-down relay groups A and B to open and thereby disable the battery let-down function. The BRU Pull-up Connect C and BRU Pull-up Connect D relay drive signals cause pull-up relays C and D to close and thereby enable the battery pull-up function. The BRU Pull-up Disconnect C and Pull-up Disconnect D relay drive signals cause pull-up relays C and D to open and thereby disable the pull-up function.

The characteristics of the relay drive signal from the PSE are summarized in Table 4.6.5-24.

TABLE 4.6.5-24. BRU RELAY DRIVE SIGNAL CHARACTERISTICS

Signal Characteristics	Value
Active Level	Switched Ground, -0.5 to +2.5 volts
Inactive Level	Open Circuit
Active Sink Capability	50 mA (max)
Pulse Width	60 ±10 msec

4.6.5.6 Power Control Electronics (PCE)

The Power Control Electronics (PCE) consists of the following major components: Power Supply Electronics (PSE), Battery Charge Assembly (BCA), and Partial Shunt Assembly (PSA). The function of the PCE is to accept power inputs from the solar array and batteries and provide a regulated output voltage of +28.0 Vdc. This regulated output voltage is maintained with load currents of up to 57.0 amperes when the solar array is illuminated by the sun, and up to 45.0 amperes when the array is shaded. The +28.0 volt regulated power is distributed to spacecraft loads as two separate buses: the Main Bus and the Pulse Load Bus.

A functional block diagram for the PCE is shown in Figure 4.6.5-59. A description of the PCE's major assemblies follows:

PSE - The PSE consists of three redundant charger control circuits, redundant mode control circuitry, a 5-channel Boost Voltage Regulator (BVR), redundant phase control circuitry for the BVR, a 33-volt boost bias generator, failure detection circuitry and automatic switchover for the functions mentioned above, and a fuse board. The PSE is the source of all commands to the BCA, PSA, and BRU.

BCA - The BCA consists of three independent redundant battery charge regulators, resistive shunt circuitry providing charge current feedback to the PSE for each charge regulator, and relays for connecting and disconnecting each charge regulator and battery discharge path.

PSA - The PSA is comprised of 70 partial shunt dissipators and drive circuitry. The PSA drive circuitry, located on the 10 solar panels, is controlled by the PSE.

The PSE, BCA, and PSA assemblies are functionally integrated to supply regulated +28 volt power to the remainder of the satellite. The units are physically separated due to power handling and thermal considerations. The BCA and PSA contain many of the high-current circuits and are placed outside of the spacecraft structure near the solar array and batteries. For a cohesive presentation of material in this section, however, the PSE, BCA and PSA cannot be easily separated. The material is therefore based on the combined operation of these assemblies. For convenience, the PSE, BCA, and PSA will be referred to as the PCE for the remainder of this section. The PSE, BCA, or PSA will be specifically mentioned only where it is appropriate.

4.6.5.6.1 Design Description

The major elements contained within the PCE are shown in the functional block diagram, Figure 4.6.5-59.

Each charge regulator passes a charge current from the Solar Array bus to the associated battery. The battery charge rate is defined by the mode controller based on the sensed Voltage/Temperature (V/T) signal from the battery, and by the maximum allowable charge rate as defined by ground command.

The boost regulator supplies energy from the batteries to the +28 volt regulated bus during periods when the Solar Array output is not adequate to supply load current demands. The battery voltage is boosted as required to maintain the regulated bus at +28 volts.

The partial shunts reduce the current output from the Solar Array when full output is not required for satisfying satellite load requirements and for charging the battery.

The mode controller activates the boost regulator, the charge regulator, and the partial shunts as required to maintain the regulated bus at +28 volts.

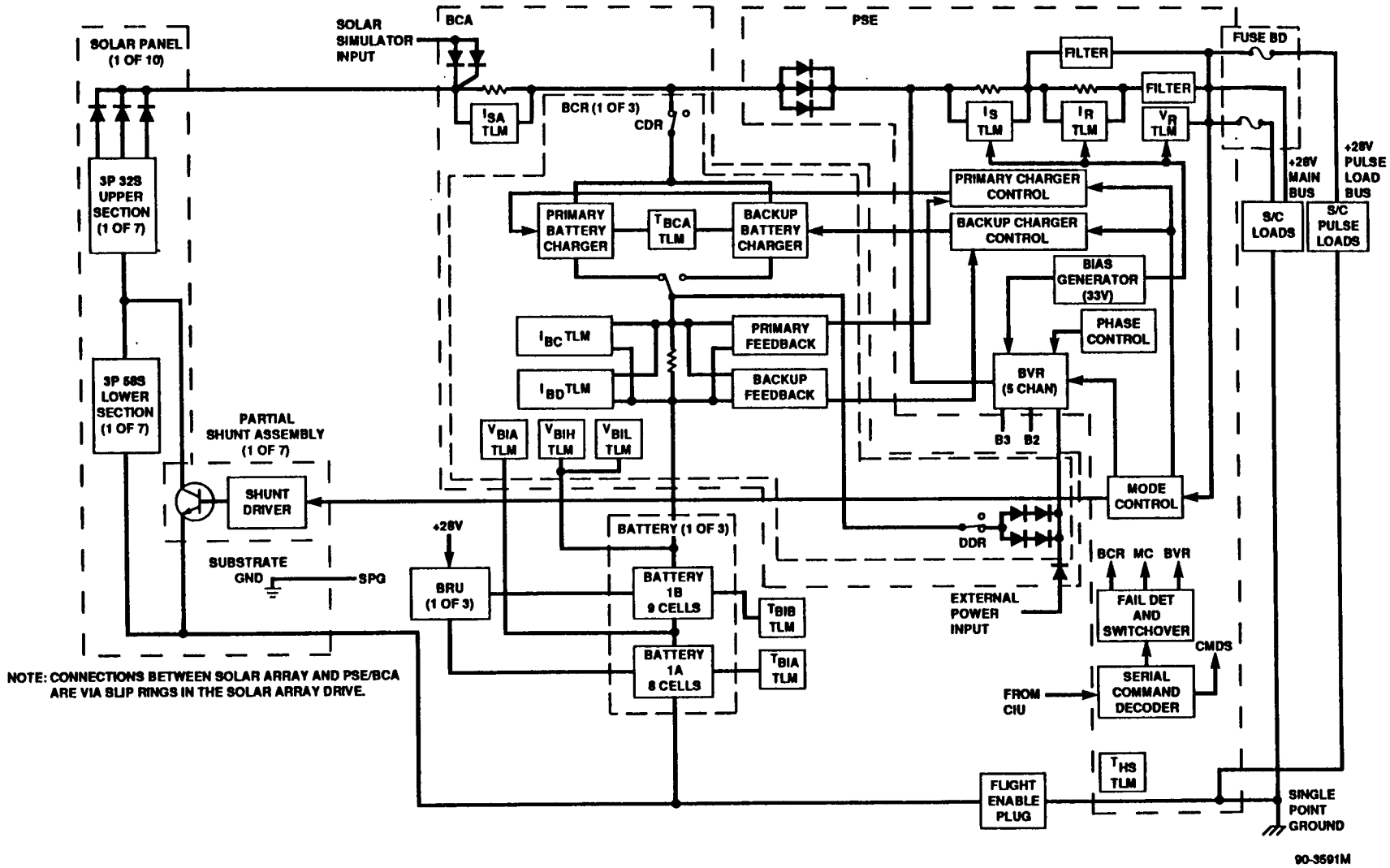

Figure 4.6.5-59. PCE Functional Block Diagram

The failure detection circuits continuously monitor the operation of the charge regulator, boost regulator, and mode controller. If a failure is detected, automatic switchover from the primary to the backup function (only) is provided. Either the primary or backup function may also be selected by ground command.

Complete independent operational redundancy is provided in the PCE design as follows:

- The PCE contains two independent charge regulators per battery, five boost regulators, and two mode control units. Automatic switchover from the primary to the backup circuits is provided; either the primary or backup circuit may also be selected by command. In the case of the BVR, a failed channel is automatically shut down. Only four out of five channels are required to support mission requirements.

- The PCE contains charge sensing circuits for controlling the battery charge. Complete battery charge protection is maintained by a fully redundant, multiple Voltage/Temperature (V/T) limit control.

- Redundancy in the partial shunts is provided by the multiplicity of parallel shunting paths (140) and shunt drivers (70).

- Due to the large volume and weight of the BVR power components (capacitors, inductors, and diodes), completely redundant backup circuits are not provided. Instead, five parallel channels provide four out of five channel redundancy.

- The failure detection circuits are not redundant; however, these circuits are designed such that any failure can result only in a loss of automatic failure detection or a false switchover to the backup circuit. In the event of false switchover, the primary can be selected by ground command.

4.6.5.6.2 Operating Modes

The operating modes of the PCE are controlled by both internally generated signals and external control signals from the Command and Control Subsystem (C&CS) generated in response to ground or software commands. The external control signals are serial 16-bit command words provided by the CIU. The command format is such that the mode identification is contained in bits 1 through 4. The mode identification identifies a specific mode command to be executed by the PCE as summarized in Table 4.6.5-25. The remaining 12 bits (5 through 16) will compose the data portion of the command and contain command specific information, as summarized in the following sections..

The modes controlled within the PCE include the selection of the basic operating modes (BVR mode, charge regulator mode, partial shunt mode) and selection of the backup circuits after detection of a primary circuit failure. These internal operating modes are described fully in Section 4.6.5.6.5.

TABLE 4.6.5-25. PCE CONTROL SIGNALS

Mode I.D. (HEX)	Control Signal	Response
1	VT Limit Set-Battery 1 only	Selects 1 of 16 VT Limit curves for Battery 1 only
2	VT Limit Set-Battery 2 only	Selects 1 of 16 VT Limit curves for Battery 2 only
3	VT Limit Set-Battery 3 only	Selects 1 of 16 VT Limit curves for Battery 3 only
4	VT Limit Set-All Batteries	Selects 1 of 16 VT Limit curves for all Batteries
5	Charge Rate Limit Set-Battery 1 only	Selects maximum charge rate for Battery 1 only
6	Charge Rate Limit Set-Battery 2 only	Selects maximum charge rate for Battery 2 only
7	Charge Rate Limit Set-Battery 3 only	Selects maximum charge rate for Battery 3 only
8	Charge Rate Limit Set-All Batteries	Selects maximum charge rates for all batteries
9	Charge/Discharge Path Set	Connects or disconnects the charge regulator relays and discharge path relays in the BCA for each battery
A	Redundant Function Select Command	Selects primary or backup charge regulators, mode control, and BVR phase control
B	Battery Reconditioning Command	Commands Battery Reconditioning Unit (BRU) to connect or disconnect pull-up and let-down resistors for each battery (see Section 4.6.5.5.)
C	BVR, PSA Drive, and BRU Commands	Commands BRU heaters ON or OFF, resets BVR channels, and selects connections between the PSA drive lines and control amplifiers

4.6.5.6.2.1 V/T Limit Selection. At a given temperature, the maximum charge voltage to which each battery is allowed to rise during charging is controlled in response to the last 12 bits (5 through 16) of a 16-bit V/T limit command word provided by the CIU as follows:

- Bits 5 through 8, Battery 1 V/T Limit Set
- Bits 9 through 12, Battery 2 V/T Limit Set
- Bits 13 through 16, Battery 3 V/T Limit Set

These control signal bits are decoded by the PCE as shown in Table 4.6.5-26; the decoded signals define the maximum allowable battery voltage. When this voltage is reached, the charge current is automatically tapered to maintain battery voltage at the selected value.

TABLE 4.6.5-26. V/T LIMIT SIGNAL RESPONSE

V/T Limit Set Code 4 Bits Per Battery				PCE Response	
				V/T Limit Set	Voltage Limit at +10°C
5,9,13	6,10,14	7,11,15	8,12,16	Unshifted 1	25.330
0	0	0	0	2	25.155
0	0	0	1	3	24.980
0	0	1	0	4	24.805
0	0	1	1	5	24.630
0	1	0	1	6	24.455
0	1	1	0	7	24.280
0	1	1	1	8	24.105
1	0	0	0	Shifted 1	23.880
1	0	0	1	2	23.705
1	0	1	0	3	23.530
1	0	1	1	4	23.355
1	1	0	0	5	23.180
1	1	0	1	6	23.005
1	1	1	0	7	22.830
1	1	1	1	8	22.655

4.6.5.6.2.2 Charge Current Rate Control. The maximum current rate at which each battery may be charged is controlled in response to the last 12 bits (5 through 16) of a 16-bit charge rate limit command word provided by the CIU as follows:

- Bits 5 through 8, Battery 1 Charge Rate
- Bits 9 through 12, Battery 2 Charge Rate
- Bits 13 through 16, Battery 3 Charge Rate

These control signal bits are decoded by the PCE as shown in Table 4.6.5-27. The PCE then sets the maximum allowable battery charge rate for both the primary and backup charge regulators of each battery.

TABLE 4.6.5-27. CHARGE RATE CONTROL SIGNAL RESPONSE

Charge Rate Select Code 4 Bits Per Battery				Maximum Charge Current Level (amperes)
5,9,13	6,10,14	7,11,15	8,12,16	
0	0	0	0	10.0 ±0.50
0	0	0	1	7.5 ±0.50
0	0	1	0	12.5 ±0.60
0	0	1	1	0.85 ±0.25

All combinations of the 10.0A, 7.5A, and 0.85A charge rates are commandable for the three batteries. At least one battery must be commanded to the 0.85A rate before either or both of the other two batteries can be commanded to the 12.5A rate.

4.6.5.6.2.3 Battery Charge/Discharge Path Relay Operation. The configuration of the battery connect/disconnect relays is controlled in response to the last 12 bits (5 through 16) of the associated 16-bit command word provided by the CIU as shown in Table 4.6.5-28.

The solar array bus is connected to or disconnected from charge regulator 1 in response to the Battery 1 Charge Connect or Battery 1 Charge Disconnect signals, respectively, thus enabling or disabling the charge path to battery 1. Similarly, the battery 1 bus is connected to or disconnected from the discharge diodes in response to the Battery 1 Discharge Connect or Battery 1 Discharge Disconnect signals, respectively, thus enabling or disabling the battery 1 discharge path through the discharge diodes to the BVR. In an analogous manner, the charge and discharge paths to and from battery 2 and/or battery 3 are controlled in response to battery 2 and/or battery 3 charge/discharge connect/disconnect signals. A hardware interlock prevents more than two batteries from being disconnected from their discharge paths at the same time.

4.6.5.6.2.4 Redundant Equipment Selection. The primary and backup sections of the mode controller, charge regulators, and boost regulator phase control circuits are selected in response to the last 12 bits (5 through 16) of the associated 16-bit command word provided by the CIU as shown in Table 4.6.5-29.

On receipt of the Mode Control Primary control signal, the primary mode control is switched into the system and the backup mode control is switched out. On receipt of the Mode Control Backup control signal, the backup mode control is switched into the system and the primary mode control is switched out. In an analogous manner, receipt of the Phase Control Circuit Primary or Phase Control Circuit Backup signal results in selection of the primary or backup phase control circuit. Receipt of the Charge Regulator Primary or Charge Regulator Backup control signal results in selection of the primary or backup charge regulator for the associated battery.

TABLE 4.6.5-28. BATTERY CONNECT/DISCONNECT RELAY CONTROL SIGNAL RESPONSE

Data Bit	Level	PCE Response
5	1	(CC) - Connect Battery 1 Charge Regulator
	0	No Action
6	1	(DC) - Disconnect Battery 1 Charge Regulator
	0	No Action
7	1	(DC) - Connect Battery 1 Discharge Path
	0	No Action
8	1	(DD) - Disconnect Battery 1 Discharge Path
	0	No Action
9	1	(CC) - Connect Battery 2 Charge Regulator
	0	No Action
10	1	(DC) - Disconnect Battery 2 Charge Regulator
	0	No Action
11	1	(DC) - Connect Battery 2 Discharge Path
	0	No Action
12	1	(DD) - Disconnect Battery 2 Discharge Path
	0	No Action
13	1	(CC) - Connect Battery 3 Charge Regulator
	0	No Action
14	1	(DC) - Disconnect Battery 3 Charge Regulator
	0	No Action
15	1	(DC) - Connect Battery 3 Discharge Path
	0	No Action
16	1	(DD) - Disconnect Battery 3 Discharge Path
	0	No Action

Under normal conditions the primary circuits will be selected, which enables automatic switchover to the backup circuits after detection of a failure. Switchover from the backup circuit to the primary circuit occurs only on receipt of the proper ground initiated control signal from the CIU.

4.6.5.6.3 PCE Design Specifications

The design specifications of the PSE and BCA are shown in Table 4.6.5-30.

TABLE 4.6.5-29. REDUNDANT EQUIPMENT SELECTION CONTROL SIGNAL RESPONSE

Data Bit	Level	PCE Response
5	X	No Action
6	X	No Action
7	1	Connect Charge Regulator 1 Primary & Disconnect Backup
	0	No Action
8	1	Connect Charge Regulator 1 Backup & Disconnect Primary
	0	No Action
9	1	Connect Charge Regulator 2 Primary & Disconnect Backup
	0	No Action
10	1	Connect Charge Regulator 2 Backup & Disconnect Primary
	0	No Action
11	1	Connect Charge Regulator 3 Primary & Disconnect Backup
	0	No Action
12	1	Connect Charge Regulator 3 Backup & Disconnect Primary
	0	No Action
13	1	Connect Mode Control Primary & Disconnect Backup
	0	No Action
14	1	Connect Mode Control Backup & Disconnect Primary
	0	No Action
15	1	Connect Phase Control Primary & Disconnect Backup
	0	No Action
16	1	Connect Phase Control Backup & Disconnect Primary
	0	No Action

4.6.5.6.4 Physical Description

The BCA contains the high-current circuitry for battery charge control and sensing. Relays for connecting and disconnecting the charge regulators and battery discharge paths are also contained within the BCA. The remaining electronic circuitry, including the mode control, PWM boost regulators, phase control, battery charge regulators, and the 33-volt boost bias generator, are located in the PSE. The BCA and PSE also contain telemetry circuitry.

4.6.5.6.4.1 Battery Charge Assembly. The BCA consists of four baseplate electronics assemblies (BPEs) shown in Figure 4.6.5-60 which are mounted to the BCA radiator assembly, three circuit boards for battery current/voltage telemetry/feedback, and one board containing the solar array telemetry circuitry.

Three of the BPEs are dedicated one-for-one to the three batteries. Each of these BPEs contain one driver/temperature board, one current sense board, and three diode boards, for a total of five circuit boards. The remaining BPE is referred to as the auxiliary BPE and contains a meter shunt used as a solar array current telemetry transducer and test diodes.

The battery disconnect relays are high-current magnetic latching relays. Contacts in the battery charge path are rated at 25 amperes; in the battery discharge path, the contacts are rated at 50 amperes. The relays are interlocked such that no more than two batteries can be disconnected from the discharge paths at the same time.

TABLE 4.6.5-30. PSE AND BCA DESIGN SPECIFICATIONS

Parameter	Value
Main Bus	
Voltage	+28 Vdc
Current	45.0 amperes max (night) } less current used by Pulse Load Bus 57.0 amperes max (day)
Regulation	+560 mV/-300 mV
Internally Generated Voltage Ripple	<50 mV p-p
Output Impedance	<0.16 ohms, dc to 100 kHz
Transient Response	0.5V p-p for maximum step load change of 7.5 amperes at any rate not exceeding 100 mA/μsec
Pulse Load Bus	
Voltage	+28 Vdc
Current	23.25 amperes max.
Regulation	±560 mV
Internally Generated Voltage Ripple	<50 mV p-p
Output Impedance	<0.20 ohms, dc to 100 kHz
Transient Response	1.6V p-p for maximum step load change of 6.0 amperes
Boost Regulator	
Regulator Efficiency (for 16 Volt Input)	90% minimum, 5 to 45 amperes
Fault Current Capability	14 amperes for 5 seconds above maximum regulator current rating
Battery Bus	+16.0 to +26.0V at input to BVR
Shunt Losses	<450 mA

TABLE 4.6.5-30. PSE AND BCA DESIGN SPECIFICATIONS (Continued)

Parameter	Value
Battery Charge Control	
Charge Rates	12.5 ±0.60 A (Two Batteries only) 10.0 ±0.50 A 7.5 ±0.50 A 0.85 ±0.25 A
Charge Rate Sensing	Voltage and Temperature (V/T)
Charge Voltage Limit	V/T Limits 1-8 Unshifted V/T Limits 1-8 Shifted
Redundancy	Three 47.0 AH batteries. Dual-mode control, boost voltage regulator, and charge regulator circuits, with automatic failure detection and switchover. Multiple path bus diodes and partial shunts
Size (in.)	
PSE	25.0 x 13.8 x 12.0
BCA (Not Including Radiator)	15.5 x 10.5 x 5.0
BCA Radiator Plate	16.5 x 26.7 x 0.25
Weight (lb)	
PSE	43.0
BCA and Radiator Plate	25.5

The BCA is thermally bonded to a flat, large area radiator, which is attached to the RCE Support Structure near the spacecraft +X axis between the battery packs. The major construction features of the BCA and radiator assembly are shown in Figures 4.6.5-60 and 4.6.5-61.

4.6.5.6.4.2 Power Supply Electronics. The PSE enclosure was designed to meet the TIROS unique requirements for radiated emissions.

The PSE consists of an electronics box containing 1 harness board, 22 printed circuit boards, 1 fuse board, and the inductors, capacitors, power transistors, and diodes required in the boost voltage regulator and for output voltage filtering. The major construction features of the PSE are shown in Figures 4.6.5-62 and 4.6.5-63.

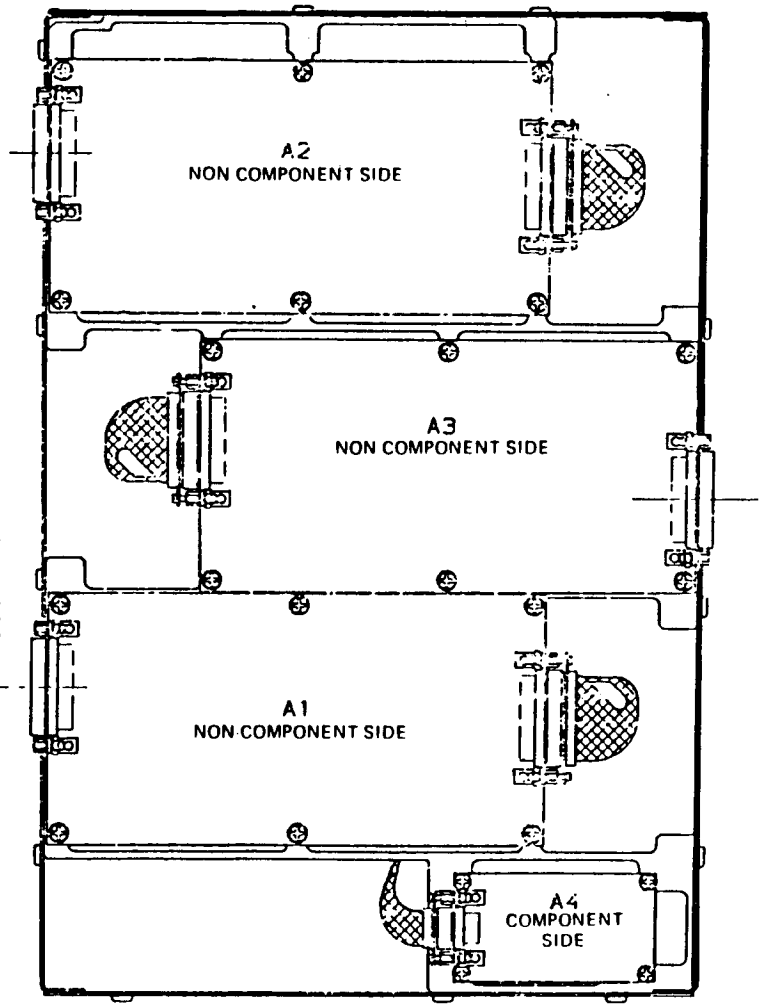

COMPONENT BOARD A1, A2, A3

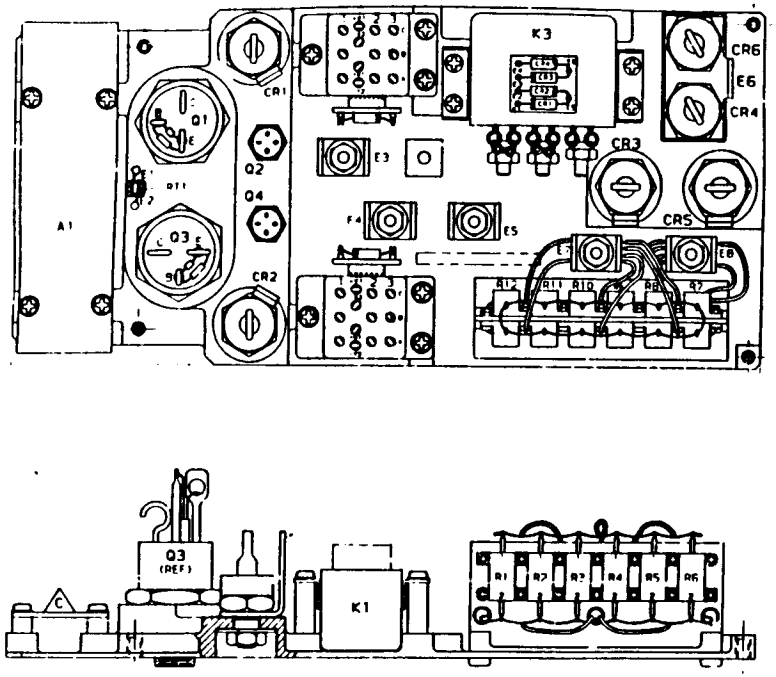

8-3204

Figure 4.6.5-60. Battery Charge Assembly Construction

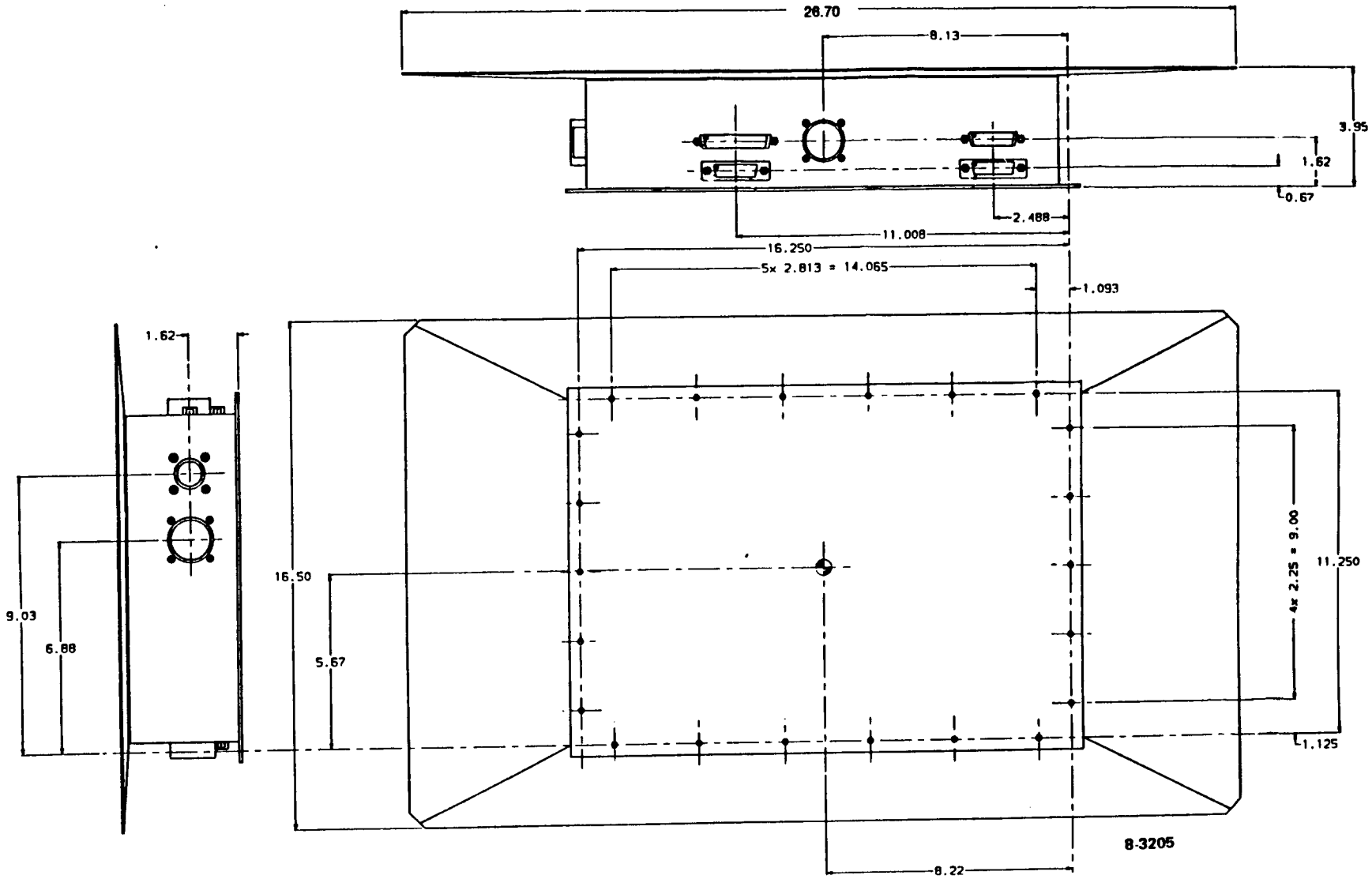

Figure 4.6.5-61. BCA Radiator Construction

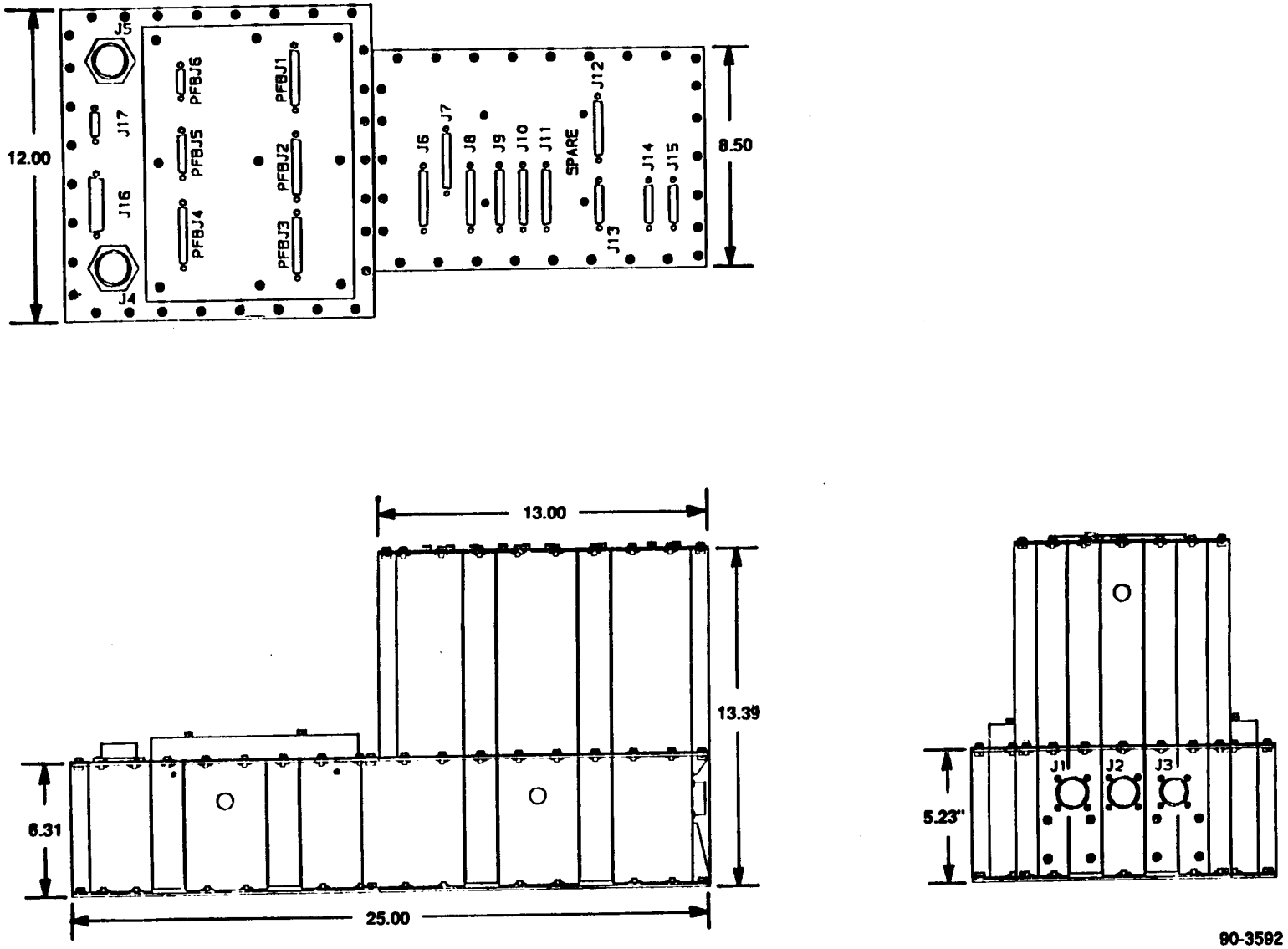

Figure 4.6.5-62. Power Supply External Construction

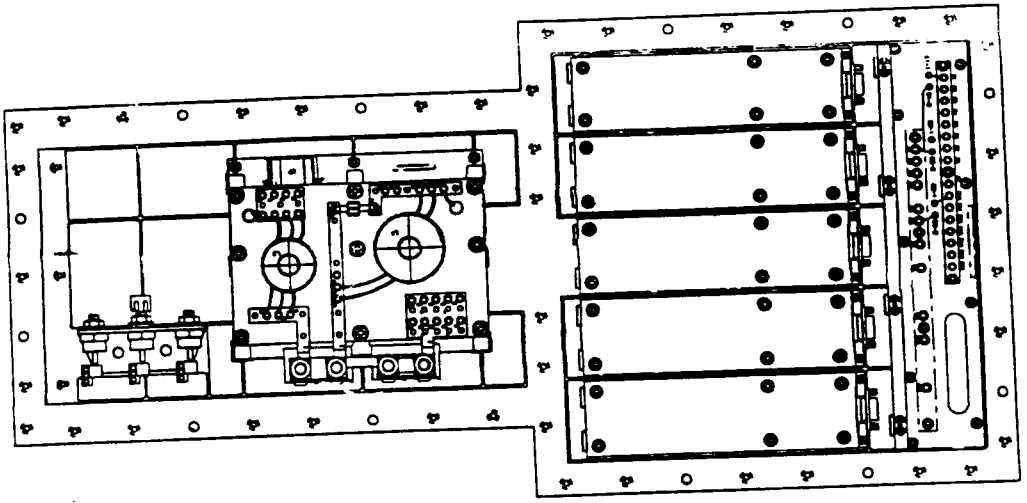

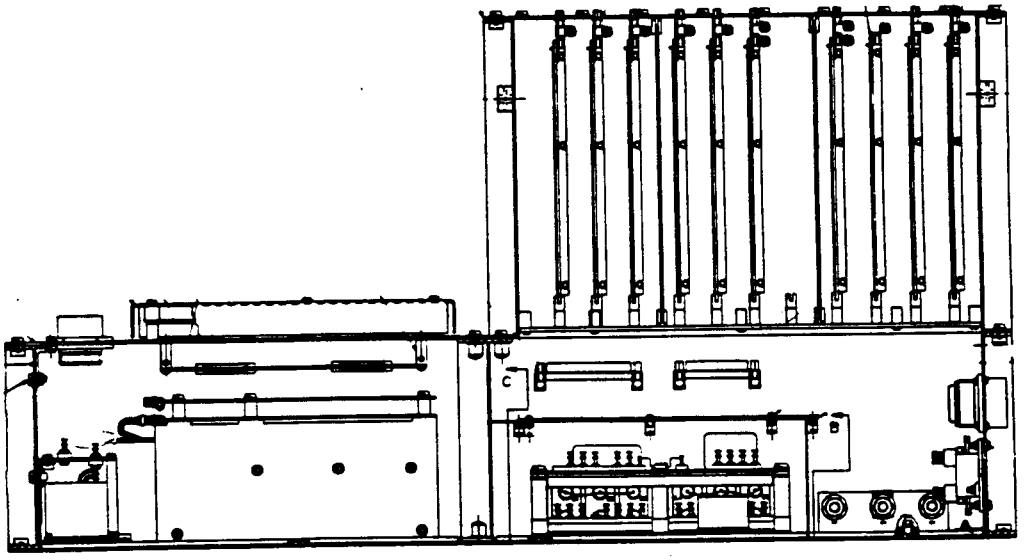

90-3593

Figure 4.6.5-63. Power Supply Internal Construction

The Power Supply Electronics enclosure consists of a baseplate, two dip brazed housings (upper and lower) and two covers. The upper housing contains 10 plug-in printed circuit boards, 1 harness board, EMI gasket mounting flanges for each p.c. connector and a cover. The 10 plug-in p.c. boards are 6.500" wide x 6.600" long and are mounted in "Burtcher Loktainer" card retainers. Three boards are of welded wire construction and seven are multilayer printed circuit construction. The p.c. mounted connectors protrude through the cover of the upper housing to which they are attached with an EMI gasket seal.

The lower housing contains several baseplate mounted assemblies and components. The baseplate mounted assemblies include the output filter assembly, input filter assembly and five BVR baseplate assemblies. Each BVR baseplate assembly consists of two p.c. boards mounted on standoffs above the BVR baseplate as well as the BVR power components mounted on the baseplate assembly itself. One other p.c. board is mounted on standoffs in the lower housing to provide BVR Status Telemetry.

A single fuse board is mounted on the outside cover of the lower PSE housing.

4.6.5.6.5 Functional Description

Functionally, the PCE can be divided into five major blocks: partial shunts, charge regulator, boost voltage regulator, the mode control that sequences the first three functions to maintain the proper bus voltage, and the failure detectors and switchover control logic. Each function is redundant, except for the failure detectors. The failure detectors automatically sense failures and switch over to the backup circuit.

4.6.5.6.5.1 Mode Control. The mode control consists of three differential amplifiers (U4,U2,U3) plus an amplifier (U1) that is common to the three modes, as shown in Figure 4.6.5-64. Each of the 3 differential amplifiers has a different turn-on or "threshold" voltage. All output stages are biased to activate sequentially the boost voltage regulator, the charge regulator, and the partial shunts as the solar array output current varies from zero to maximum, as shown in Figure 4.6.5-65. A resistive voltage divider (R49, R50, R51) at the inputs to the three differential amplifiers has bias values such that there is a dead-band (no overlap) between the thresholds of operation of one mode and the next. The dead-bands as referred to the +28 V bus are reduced by the voltage gain to the output of the common differential amplifier U1.

Note that the charge regulator circuit contains three drivers used for driving the three charge regulators in the BCA in parallel. To maintain loop stability, charge lockout occurs when the system switches to the boost voltage regulator mode.

During satellite night, when the solar array current is zero, the battery is supplying discharge current to the load through the boost voltage regulator. The gain of the mode control circuitry is such that the differential dc amplifier will control the duty cycle of the boost voltage regulator to maintain the +28V regulated bus. The boost voltage regulator also supplies load power during satellite day when the solar array cannot satisfy the load requirements. During operation of the boost voltage regulator, output signals to the charge

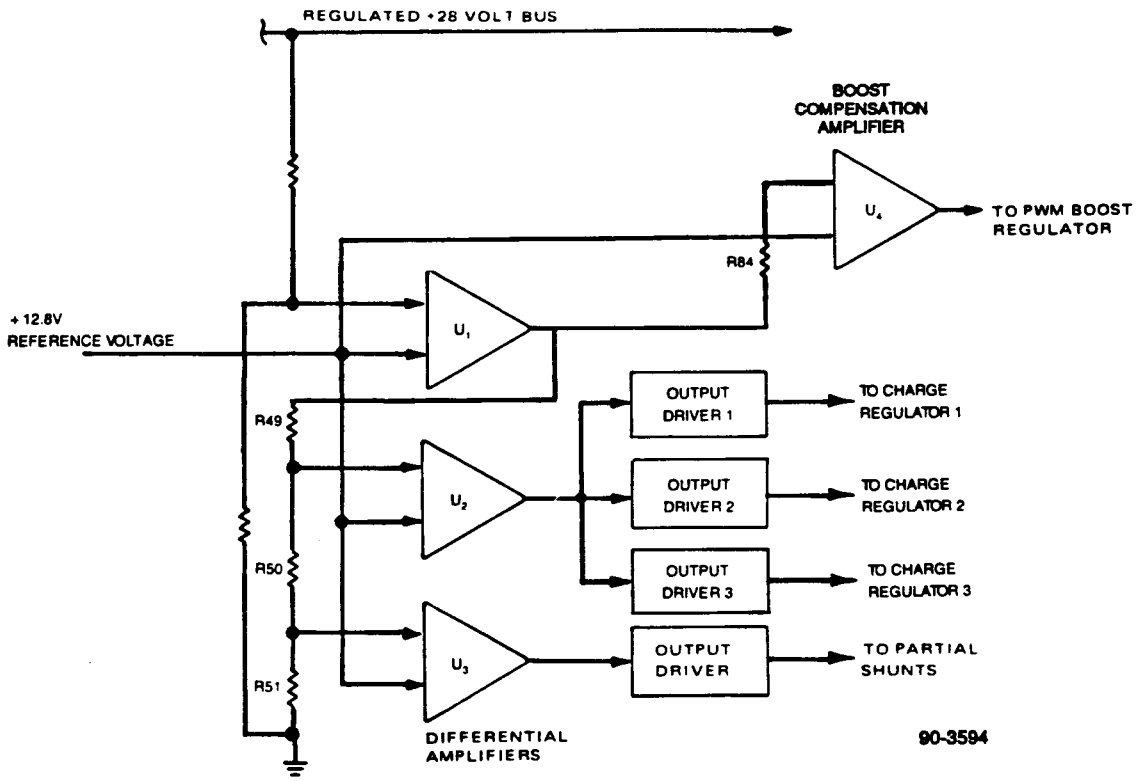

Figure 4.6.5-64. Mode Control Functional Block Diagram

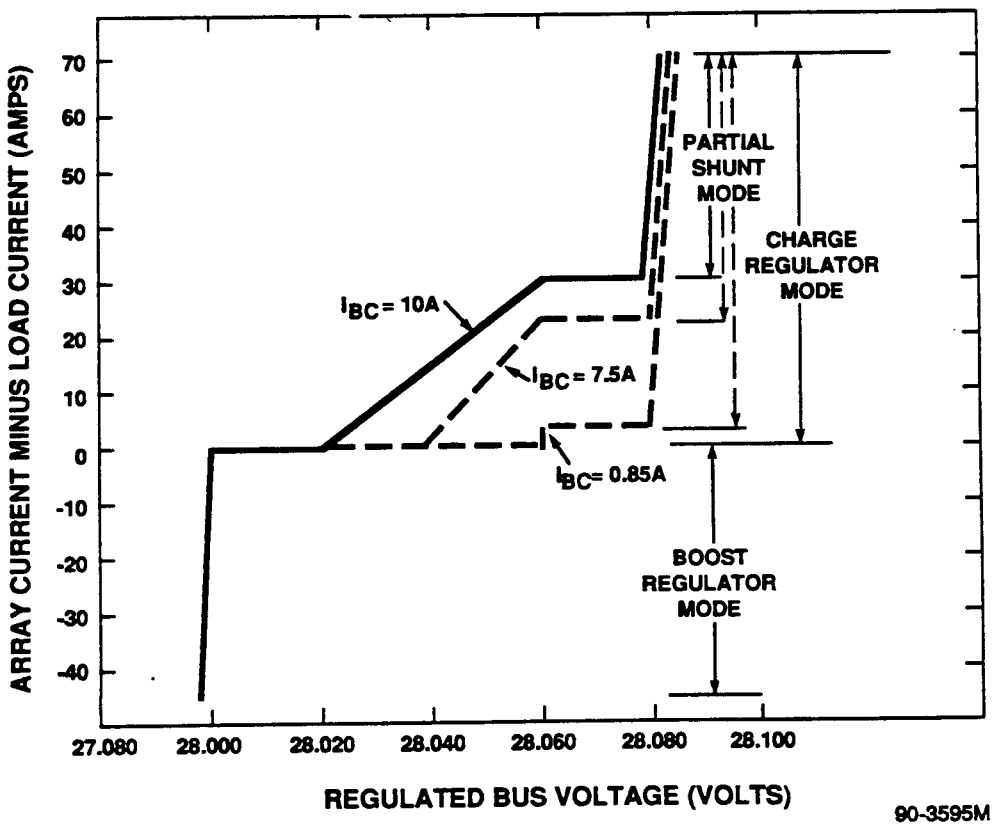

Figure 4.6.5-65. Regulated +28V Bus I-V Characteristics

regulators and partial shunts make them inactive. The battery charge and shunt currents are therefore zero, and the PSE is operating in the boost voltage regulator mode.

As the regulated bus voltage increases due to a decrease in load demand and/or an increase in solar array current, the mode control drive signal to the boost voltage regulator reduces the regulator duty cycle and maintains the +28V regulated bus to within a small voltage range. As the regulated +28V bus voltage rises still further, a point is reached at which the boost voltage regulator is completely inhibited and all required load current is being supplied by the solar array.

As the regulated +28V bus continues to rise in response to an increase in solar array power or a decrease in load requirements, a finite "dead band" is crossed. This dead band is provided to prevent simultaneous operation of the boost voltage regulator and the charge regulator due to tolerance buildup or variations due to temperature or component degradation.

As the regulated +28V bus continues to rise, the charge regulator mode is entered. The charge regulator is turned on and allowed to pass a progressively greater charge current to the battery, thus maintaining the regulation of the +28V bus. As the bus voltage continues to rise, the battery charge current also rises until the maximum allowable charge rate is reached (as selected by ground command, Power Management Software (PMS), or limited by V/T charge sensing conditions).

As the regulated +28V bus continues to rise, a second dead band is crossed and the partial shunt mode is entered. The partial shunts are turned on and allowed to shunt a progressively greater amount of current, thus maintaining the regulation of the +28V bus. During operation of the partial shunts, the battery is always being charged at the maximum permissible rate as determined by ground command, PMS, or V/T limiting. The regulated +28V bus I-V characteristic shown in Figure 4.6.5-65 gives the values of the regulated bus voltage at the voltage sense terminals within the PSE. The +28V bus I-V characteristic at the load terminals will be the same as shown in Figure 4.6.5-65, but will be shifted to the left (reduced +28V bus voltage) by a voltage equal to 0.0016 plus PSE-to-load harness resistance multiplied by the load current. The 0.0016 figure is the approximate resistance in ohms of the wiring within the PSE from the voltage sense terminals to the PSE output connectors J1 and J2.

4.6.5.6.5.2 <u>Boost Voltage Regulator</u>. A switching regulator is used to boost the battery voltage (+16 to +26 volts at the PSE input terminals) up to the regulated bus level of +28 volts, over a satellite load range up to 45 amperes. Voltage regulation is accomplished using Pulse Width Modulation (PWM) techniques. The dc input is switched (chopped) to produce a square current pulse train of constant frequency, which is rectified and filtered and supplied to the load. By varying the duty cycle of the pulse train (i.e., modulating its pulse width), the load voltage is controlled.

A simplified block diagram of the boost voltage regulator is shown in Figure 4.6.5-66. This circuit is referred to as a current-fed, constant frequency,

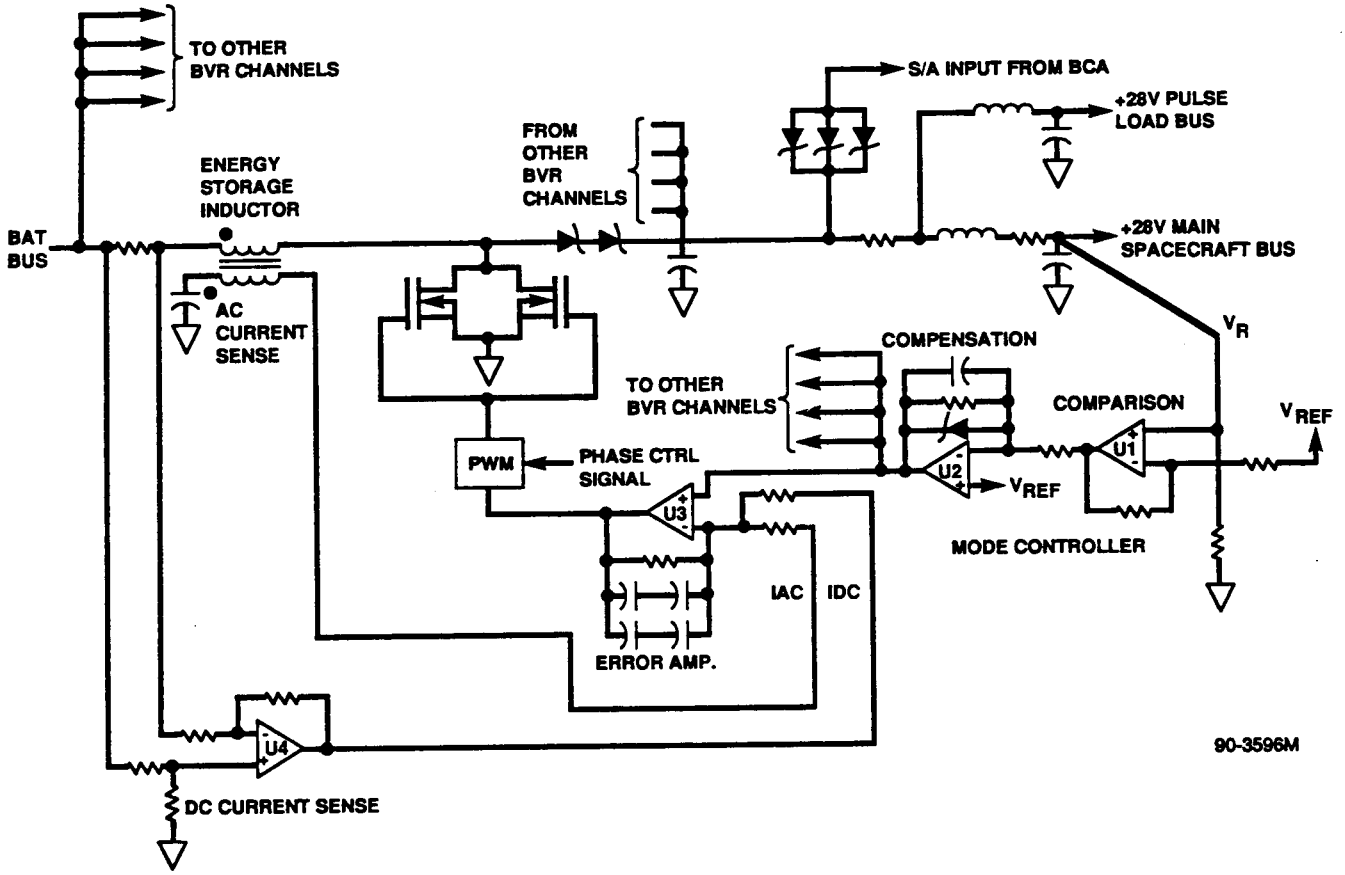

Figure 4.6.5-66. BVR Functional Block Diagram

pulse-width-modulated voltage regulator because constant frequency is maintained by a master oscillator and only the pulse width is varied as a function of error voltage. The complete boost voltage regulator is composed of the following sections:

- Power inductors and diodes
- Energy storage capacitors
- Transistor power switches
- Switch drive circuitry
- Pulse width modulator
- Duty cycle limit and voltage limit circuitry
- Sawtooth oscillator
- AC and DC current sense feedback circuitry
- Comparison amplifier
- Compensation amplifier
- Voltage reference
- Output filter
- PWM error amplifier

The power switches are N-channel, enhancement mode, MOSFET power transistors that are alternately turned on and off. During the on time of the switch, current is conducted through inductor L and the switch to ground. During the off time, inductor L continues this conduction, delivering current through the diode to the load. The output capacitor acts as an energy storage device, supplying current to the load during the time the power switch is on.

Assuming V_R is maintained essentially constant by the output capacitor permits a simplified analysis of the boost voltage regulator to be made. The on time of the power switch is defined as αT, and the off time is defined as $(1 - \alpha)T$, where α is the duty cycle of the switch. During the switch on time, the change in current through inductor L is defined by

$$di_{L1} = \frac{V_B}{L} \, dt_1$$

where

$$dt_1 = \alpha T$$

$$V_B = \text{Battery Voltage}$$

When the switch turns off, the change in current through the inductor L is defined by

$$di_{L2} = \frac{V_L}{L} \, dt_2$$

where

$$dt_2 = (1 - \alpha)T$$

$$V_L = V_R - V_B$$

To maintain system equilibrium, the net change in inductor current must be zero; therefore,

$$di_{L1} = di_{L2}$$

and

$$V_R = \frac{1}{1 - \alpha} \, V_B$$

The last equation indicates that the output voltage is a function of the duty cycle α. Because α must be less than 1.0, the output is boosted to a voltage greater than the input. Therefore, a mechanism for controlling α is all that is necessary to boost and regulate the output voltage.

The operating waveforms of this regulator are illustrated in Figure 4.6.5-67. Assume that at time $t = 0$, the transistor switch is closed because of the presence of the signal from the switching circuits. The output is now completely disconnected from the input by the diode so that the output voltage V_R, maintained by capacitor C, decays exponentially. When the switch opens, the output capacitor is charged by the inductor current. Because of these charge and discharge cycles, there is a small ripple voltage on the output bus.

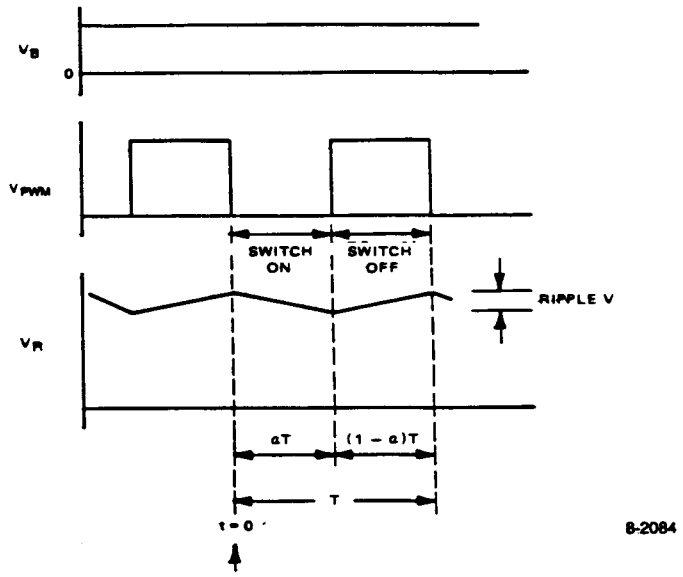

Figure 4.6.5-67. PWM Boost Regulator Waveforms

As shown in Figure 4.6.5-66, the differential amplifier U1 compares the regulated output voltage V_R with a stable reference voltage and amplifies the error voltage. U1 is part of the +28V regulator feedback loop during all three modes of regulator operation: boost, charge regulation, and partial shunt. When the regulator is in charge regulation mode or in partial shunt mode, the feedback error voltage, after amplification through U1 and the compensation amplifier U2, forces the U2 input to the Pulse Width (PW) modulator error amplifier U3 to become negative with respect to the dc current sense amplifier output, and PW modulation becomes zero (no boost). During boost mode operation, the error input voltage to the Pulse Width Modulator (PWM) error amplifier is positive, and a rectangular pulse train of constant frequency and appropriate duty cycle for voltage regulation is generated at the PWM output. The phase control circuit provides a 96 $\pm$9.6 kHz oscillator output to each of the five BVR channels with phase differences of approximately 72 degrees. The phasing of the BVR channels results in a regulated bus ripple of 480 kHz. The phasing performed yields better output ripple and less electromagnetic interference.

The dc current sense amplifier and ac sense inputs to the PWM error amplifier are provided to eliminate the effect of the right half plane zero on the feedback loop. The current sense inputs permit a relatively wider loop bandwidth, good ac stability, and faster transient responses. An additional feature of the current sense inputs is to provide a feedback signal which forces the five parallel BVR channels to share load current.

Curves showing typical boost regulator power conversion efficiency as a function of load and battery voltage are shown in Figure 4.6.5-68.

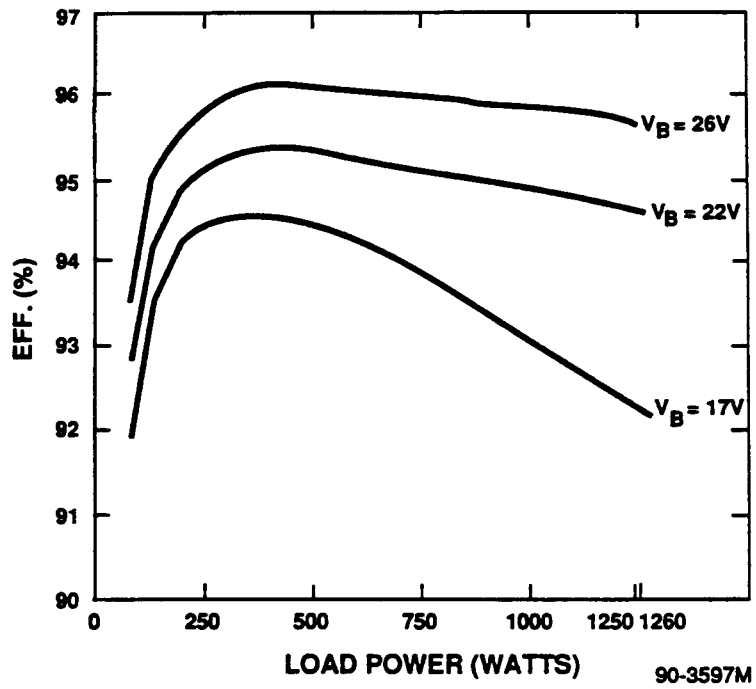

Figure 4.6.5-68. Typical Boost Regulator Efficiency

4.6.5.6.5.3 Charge Regulator. The charge regulator protects the battery from overcurrent and overvoltage conditions during charge by monitoring and operating upon the following parameters:

- Battery charge current
- Battery terminal voltage
- Battery temperature

The charge regulator control signal from the mode control proportionately changes the battery charge current to maintain regulation on the +28V bus. The charge regulator circuitry accepts signal inputs corresponding to each of the above parameters and compares these inputs with built-in references. Deviations of error signals in the feedback loop are amplified and ultimately adjust battery charge current to decrease the error by modifying the feedback ratio of the current regulator. A functional block diagram of the charge regulator is shown in Figure 4.6.5-69.

There are two modes in which the charge regulator operates:

- Current limiting mode
- Voltage/Temperature mode (V/T)

The maximum battery charge current may be limited to one of four levels selectable by ground command or PMS as defined in Table 4.6.5-27. In the current limiting mode, the selected charge current is maintained in the battery, and any excess current is controlled by the mode control using the partial shunts.

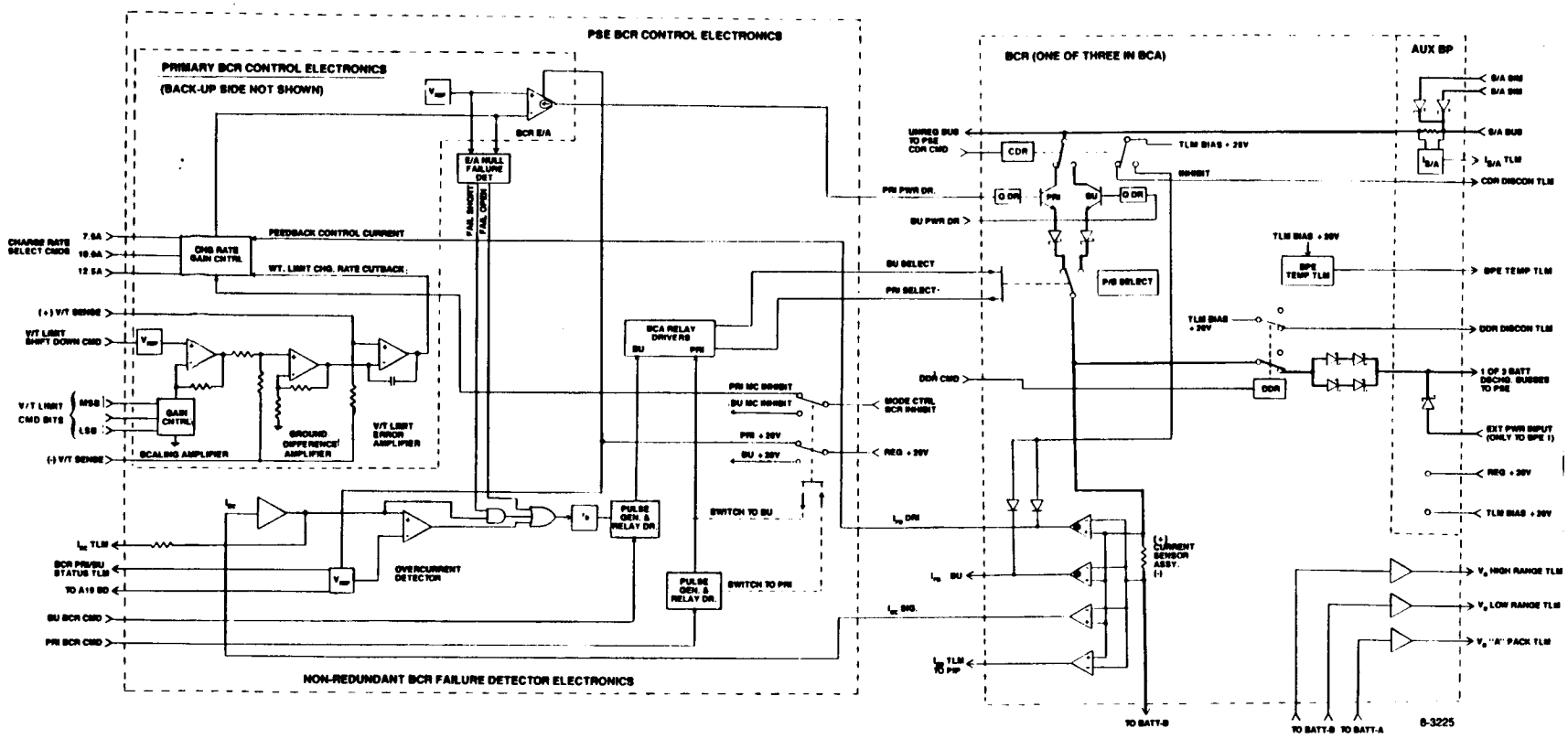

Figure 4.6.5-69. Charge Regulator Functional Block Diagram

As full charge is reached, battery charge current is reduced by voltage/temperature control. If battery voltage and temperature reach a given limiting curve, as shown in Figure 4.6.5-70, charge current is reduced (tapered) as required to maintain the battery voltage limit. The charge regulator acts as a battery voltage regulator in the V/T mode.

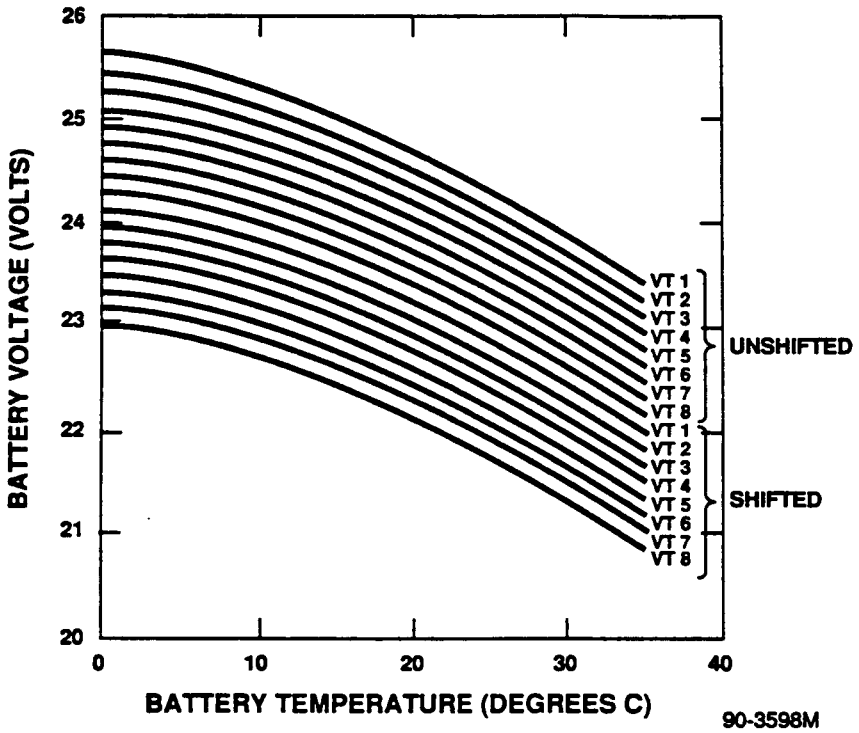

Figure 4.6.5-70. Nominal Battery Voltage Limits

There are 16 selectable levels of voltage/temperature control in each charge controller. Any 1 of the 16 levels given in Table 4.6.5-26 may be selected independently for each battery by command. The V/T Limit Select signals from the CIU are processed by the V/T limit decoder to set the regulator in the proper voltage limiting mode.

When charge current is reduced by the V/T control, the mode control causes the partial shunts to reduce the available solar array current accordingly.

Battery protection is provided by the shape of the V/T characteristic, which is designed to reduce battery dissipation and temperature rise in overcharge by reducing the end-of-charge voltage for battery temperatures above +10°C.

4.6.5.6.5.4 Partial Shunts. When the solar array current supply exceeds the requirements of satellite load and battery charging, the excess current is controlled by a system of partial shunts. Each of the 70 parallel circuits of solar cells (7 circuits on each of 10 panels) is tapped for connection to a partial shunt circuit, as shown in Figure 4.6.5-71.

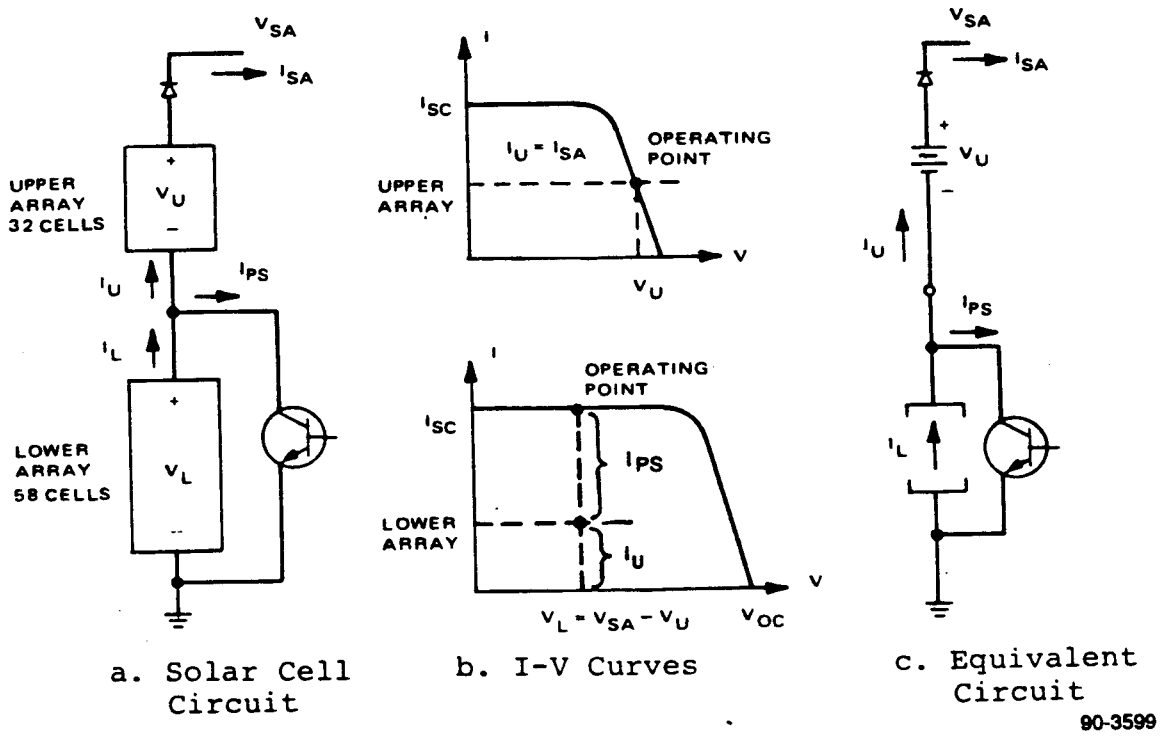

Figure 4.6.5-71. Partial Shunt Operations

When the shunts are operating they force the lower array to operate in the current source region of its I-V characteristic, so that the net current available from the lower array exactly matches the satellite requirement. This is depicted in Figure 4.6.5-71. Thus, applying Kirchoff's current law at the array tap,

$$I_{SA} = I_L - I_{PS} = I_U$$

Since this current is less than the short circuit value, the operating point of the upper array is in the voltage source region of its characteristic. The voltage across the lower array assumes whatever value is necessary to maintain system regulated bus voltage. Thus, by Kirchoff's voltage law,

$$V_L = V_{SA} - V_U$$

The proper partial shunt current is determined by the mode control so as to maintain the +28V bus regulation in the PSE.

The partial shunt performance is illustrated in Figure 4.6.5-72. The maximum partial shunt current is 70 amperes with peak transistor dissipation of 1100 watts distributed over 70 devices. Each panel has seven redundant partial shunts and seven partial shunt driver circuits.

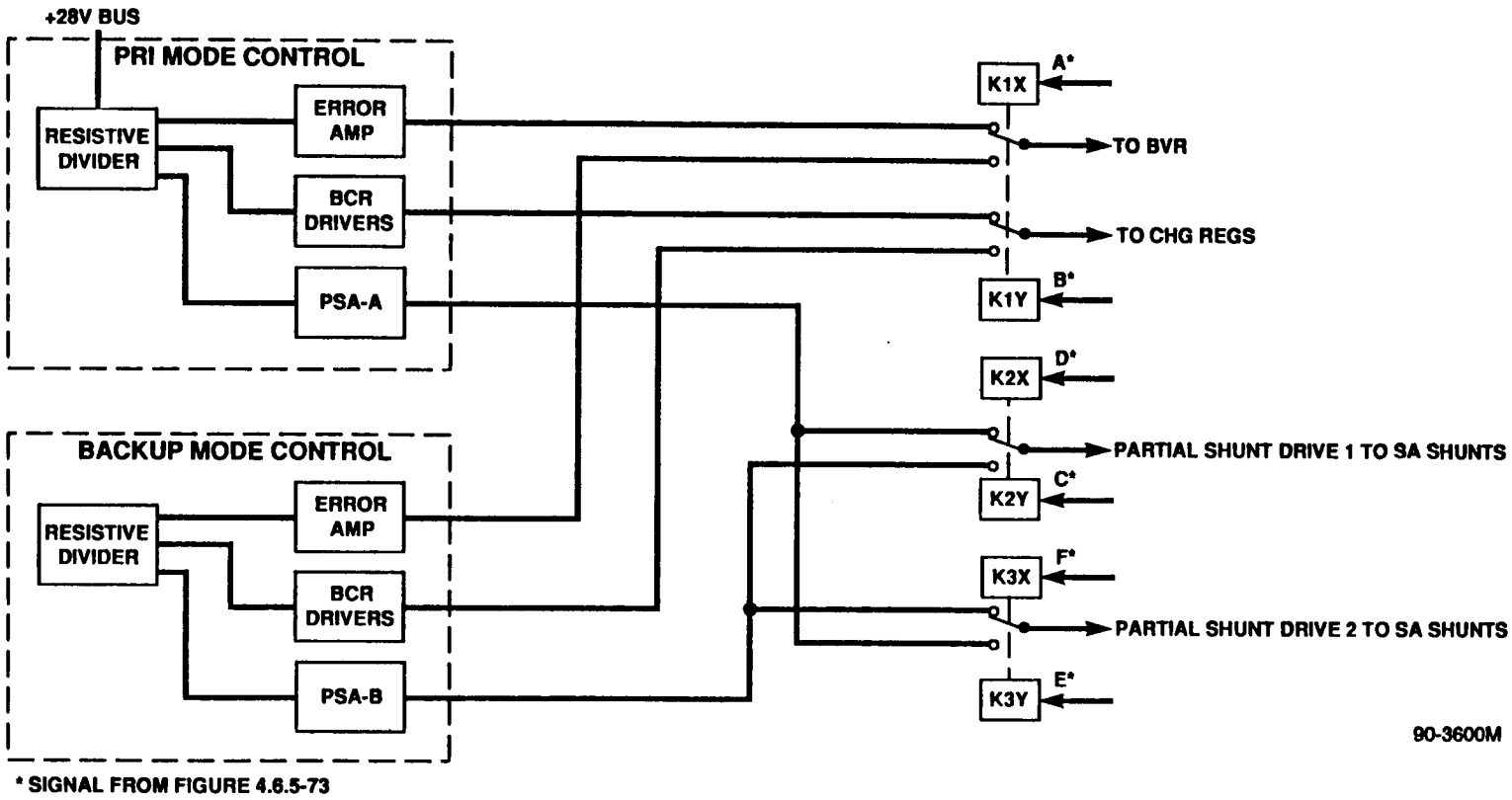

Figure 4.6.5-72. Mode Control Functional Block Diagram

4.6.5.6.5.5 Failure Detectors

4.6.5.6.5.5.1 Mode Control. The Mode Control primary and backup configuration is shown functionally in Figure 4.6.5-72 while the mode control failure detection logic is shown in Figure 4.6.5-73.

The mode control failure detector monitors the operation of the mode controller and the +28V regulated bus voltage. If a failure is sensed, the failure detector automatically switches the appropriate relays thus disconnecting the failed element and connecting the backup element. As shown in Figure 4.6.5-73, the mode controller failure detector operates by sensing the +28V regulated bus (for overvoltage or undervoltage) as well as the BVR error signal, the three BCR inhibit signals, and the two Partial Shunt Amplifier (PSA) drive signals. The undervoltage or overvoltage condition of this +28V bus is detected by operational amplifiers connected as threshold detectors.

If an undervoltage (less than 27.00 volts) or overvoltage (greater than 29.50 volts) is sensed, the mode controller is switched to backup and PSA-A is disconnected so that both Partial Shunt Drive 1 and Partial Shunt Drive 2 are provided drive signals from PSA-B. With an undervoltage condition, a time delay of 2.0 $\pm$0.5 seconds in the sensing circuits prevents short duration perturbations from causing false or premature switching. For an overvoltage condition, a time delay of 130 milliseconds at the threshold of 29.50 volts decreases with increasing voltage becoming approximately 100 milliseconds if the bus voltage exceeds 30.50 volts. This delay prevents false or premature switching and in conjunction with the on-line redundancy of the partial shunt amplifiers, assures that the bus voltage cannot exceed 38.0 volts. On-line redundancy is provided by powering both PSA-A (in the primary MC) and PSA-B (in the backup MC) at all times with their outputs OR'ed at the input to the shunt circuits on the solar array. If the primary MC is driving the BVR or the battery chargers and PSA-B is erroneously driving the shunts, PSA-B will be disconnected from the partial shunt drive lines after a 0.5 second delay.

The mode control overlap detector senses the BVR error signal, the primary BCR inhibit signals, and the PSA signals, and switches to the backup functions if the PSAs or the BCRs are active when the BVR is active. As shown in Figure 4.6.5-73, the same two-second time delay used for undervoltage is imposed. As indicated in Figures 4.6.5-72 and 4.6.5-73, switching from primary to backup functions can be implemented by ground command or by the failure detectors. However, switching from backup to primary can only be accomplished by ground initiated commands. Connecting or disconnecting of PSA drives may be done by ground command.

4.6.5.6.5.5.2 BVR Failure Detection. Failure detection in the BVR is provided by a phase control circuit failure detector and by individual channel shutdown control.

The phase control circuitry contains a failure detector which senses the primary clock generator frequency and a failure detector which senses the phase difference between channels. If the 96 kHz frequency of the primary clock generator drops below 82.5 kHz or exceeds 108.5 kHz, the failure

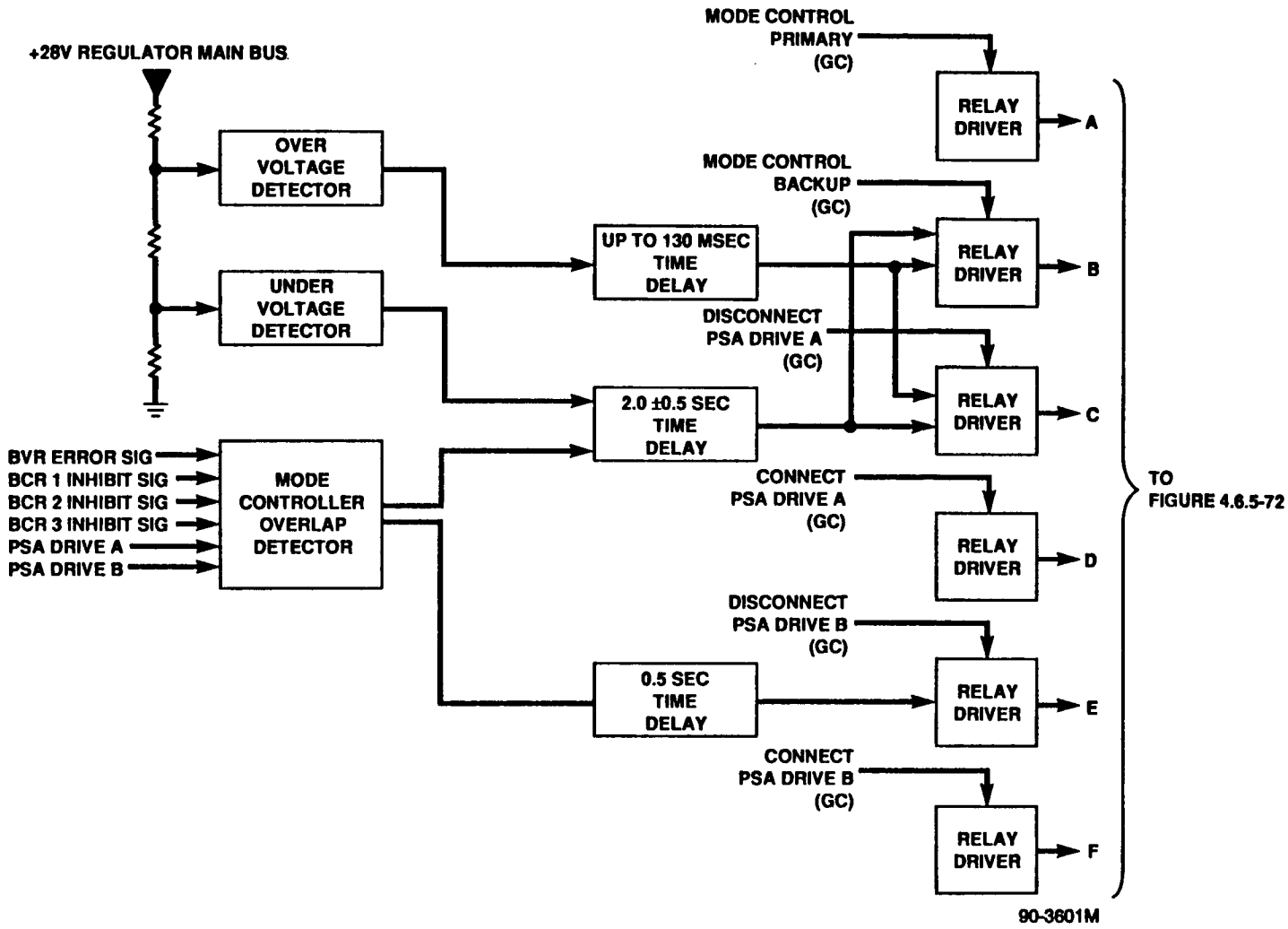

Figure 4.6.5-73. Mode Control Failure Detector Functional Block Diagram

detector causes a switch to the backup clock generator and phase control circuits. If the phase control failure detector senses a change of more than 10% in the phase difference between channels, the backup clock generator and phase control circuits are selected. A ground command is required to return to primary operation.

Failure detectors within each channel sense the dc current, the control loop error voltage signal, and the mode control error signal. An out-of-limits condition in any of the three will cause the drive to be removed from the Hex Fet switches in that channel. Shutdown of a single channel is an acceptable operation since there is five for four channel redundancy in the BVR. Return to normal operation is achieved automatically when an overcurrent out-of-limit condition has returned to the operating range. However, loop failure or channel failure have a latch off feature which requires a ground command to bring the channel back into normal operation.

An additional failure detector senses the main bus voltage and shuts down the switch drive to all BVR channels when the voltage exceeds 34 volts. Channel operation is resumed when the bus voltage decreases to 30 volts or less.

4.6.5.6.5.5.3 Charge Regulator Failure Detector. The charge regulator failure detector monitors the primary charge regulator and, if a failure is sensed, switches automatically to the backup charge regulator. As shown in Figure 4.6.5-74, the charge regulator failure detector operates by sensing an open or shorted condition in the charge rate controller or by sensing an excessive battery charge current level of 13.6 $\pm$0.5 amperes or greater for more than 130 milliseconds.

An open or shorted condition in the charge rate controller is indicated by an out-of-null condition of the differential amplifier controlling the battery charge rates. If the normally present null condition changes to an unbalanced state in one direction, a Fail Open signal results; if the null condition changes to an unbalanced state in the other direction, a Fail Short signal results.

The primary charge regulator is switched out and the backup charge regulator switched in after the detection of any failure or on receipt of a Charge Regulator Backup control signal from the CIU. When a failure is detected, a 200-millisecond switching delay is incorporated for noise immunity and to avoid false tripping due to momentary signal excursions.

Switching from the backup to the primary charge regulator occurs only on receipt of the Charge Regulator Primary control signal from the CIU.

4.6.5.6.6 +28V Fuse Board

Both fused and unfused spacecraft loads are connected to the +28-V regulated bus through a +28V fuse board. As shown in Figure 4.6.5-62, the fuse board (A19) is located on top of the PSE under a dust cover, permitting easy access for fuse replacement as well as shortened cable runs to minimize voltage drops. A list of available fuses in the PSE fuse board is given in Table 4.6.5-31.

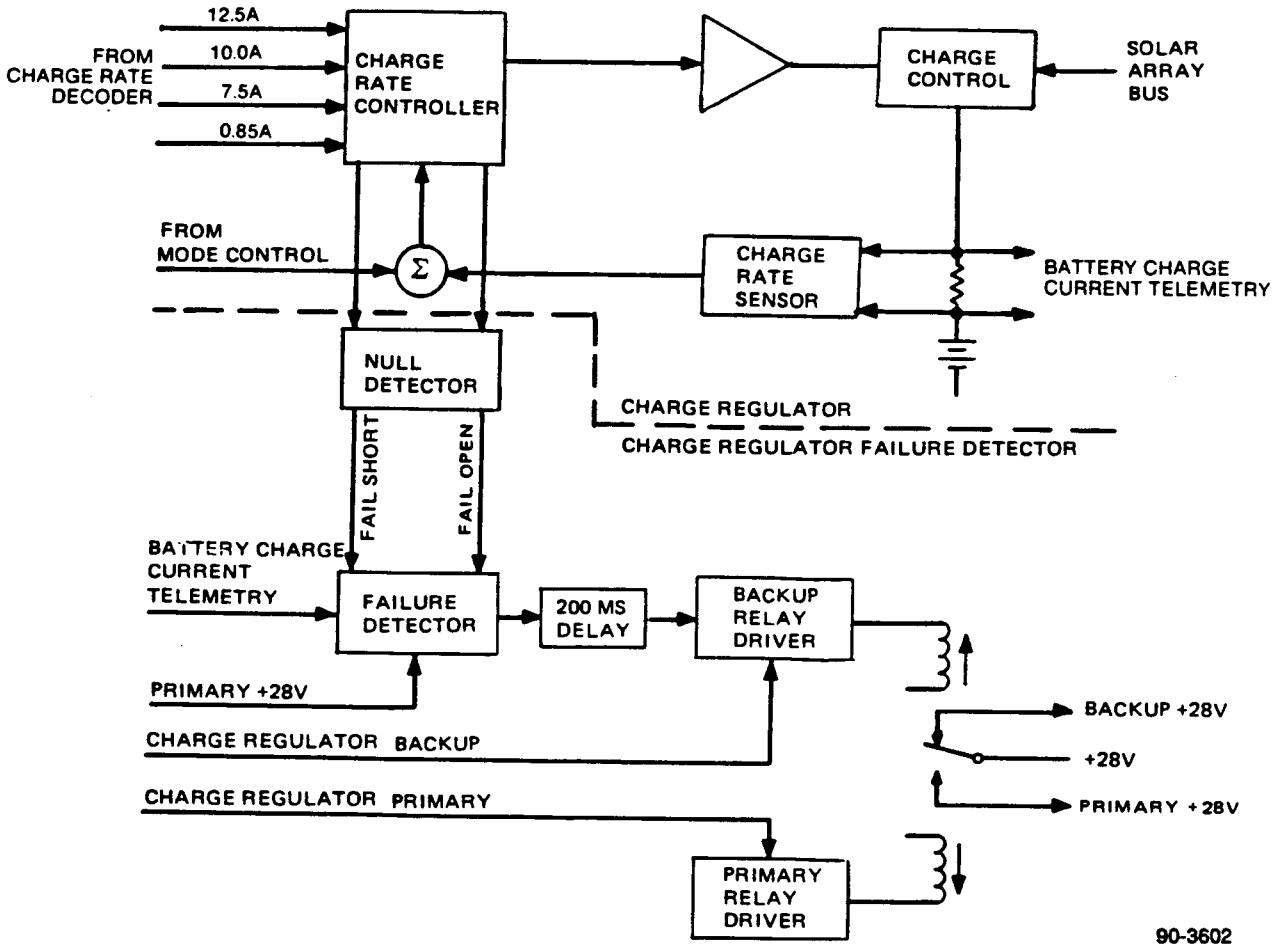

Figure 4.6.5-74. Charge Regulator Failure Detector Functional Block Diagram

TABLE 4.6.5-31. AVAILABLE FUSED POWER FROM PSE

Power Bus	Fuse Rating	No. of Fuses
+28V Main Bus	5A 7A	75 12
Pulse Load Bus	5A 7A	43 2
Switched +28V Telemetry Bus	1.5A	2 in Parallel

4.6.5.6.7 Telemetry

4.6.5.6.7.1 Analog Telemetry. The analog telemetry signals provided by the PCE are listed in Table 4.6.5-32.

TABLE 4.6.5-32. PCE ANALOG TELEMETRY

TLM Description	Input Range	Sensing Element Location	Signal Processing Unit
PSE +28V Total Reg Current	0 to 60A	PSE	PSE
PSE +28V Main Bus Voltage	25 to 32V	PSE	PSE
PSE +28V Main Bus Current	0 to 60A	PSE	PSE
PSE Heat Sink Temp.	-5 to +55°C	PSE Heat Sink	PSE
PSA Drive 1	0 to 14V	PSE	PSE
PSA Drive 2	0 to 14V	PSE	PSE
B1 Charge Current	0 to 20A	BCR1	PSE
B2 Charge Current	0 to 20A	BCR2	PSE
B3 Charge Current	0 to 20A	BCR3	PSE
Solar Array Current	0 to 70A	BCA	BCA
B1 Voltage (High Range)	14 to 27V	Across B1	BCA
B1 Pack A Voltage	7 to 13V	Across B1 Pack A	BCA
BCA1 Heat Sink Temp.	-25 to +85°C	BCA1 Heat Sink	BCA
B2 Voltage (High Range)	14 to 27V	Across B2	BCA
B2 Pack A Voltage	7 to 13V	Across B2 Pack A	BCA
BCA2 Heat Sink Temp.	-25 to +85°C	BCA2 Heat Sink	BCA
B3 Voltage (High Range)	14 to 27V	Across B3	BCA
B3 Pack A Voltage	7 to 13V	Across B3 Pack A	BCA
BCA3 Heat Sink Temp.	-25 to +85°C	BCA3 Heat Sink	BCA
B1 Discharge Current	0 to 45A	BCR1	BCA
B2 Discharge Current	0 to 45A	BCR2	BCA
B3 Discharge Current	0 to 45A	BCR3	BCA
B1 Voltage (Low Range)	0 to 14V	Across B1	BCA
B2 Voltage (Low Range)	0 to 14V	Across B2	BCA
B3 Voltage (Low Range)	0 to 14V	Across B3	BCA
Partial Shunt Voltage	0 to 25V	PSA	SATCU

Current telemetry is provided by meter shunt circuitry. The meter shunt sensing elements for solar array current, and the battery charge and battery discharge currents are located in the BCA. The telemetry conditioning circuitry for solar array current and the battery currents is contained within the BCA. The regulated bus current sensors and conditioning circuitry are located in the PSE.

Except for the telemetered measurement of partial shunt drive voltage, which is accomplished via a resistor divider, voltage telemetry measurements are made differentially via suppressed zero circuitry which results in expanded scale telemetry around the region of interest. Battery and partial battery voltage telemetry conditioning circuitry is located in the BCA; +28V bus and partial shunt drive voltage telemetry conditioning circuitry is located in the PSE.

Temperature telemetry is sensed by thermistors bonded to the surface of interest. The temperature points provided are as follows:

- PSE heat-sink temperature
- BCA heat-sink 1 temperature

- BCA heat-sink 2 temperature
- BCA heat-sink 3 temperature

4.6.5.6.7.2 Multi-Level Status Telemetry. The Multi-level status telemetry signals provided by the PCE are given in Table 4.6.5-33.

TABLE 4.6.5-33. PCE MULTI-LEVEL ANALOG TELEMETRY

TLM Description	Status TLM	Output (V)	Sensing Element Location	Signal Processing Unit
CHARGE RATE STATUS (One per BCR)	0.85A	1.0 ±0.20	PSE	PSE
	7.5A	2.0 ±0.20		
	10.0A	3.0 ±0.20		
	12.5A	4.0 ±0.20		
V/T LIMIT STATUS (One per BCR)	1	1.0 ±0.10	PSE	PSE
	2	1.5 ±0.15		
	3	2.0 ±0.20		
	4	2.5 ±0.20		
	5	3.0 ±0.20		
	6	3.5 ±0.20		
	7	4.0 ±0.20		
	8	4.5 ±0.20		
BVR CHANNEL STATUS (# of operating channels)	0	0.45 ±0.04	PSE	PSE
	1	1.28 ±0.10		
	2	2.11 ±0.17		
	3	2.94 ±0.24		
	4	3.77 ±0.30		
	5	4.60 ±0.40		

Analog status telemetry is provided to reflect the command and operating mode states of each battery charge regulator circuit. Each individual telemetry circuit uses a resistor-diode matrix to transform operating states or modes into an analog voltage level.

Since there are several Boost Voltage Regulator (BVR) PWM power stages in parallel, boost channel telemetry is provided within the PSE for the purpose of verifying the number of boost channels that are operative when in boost mode. Six state levels of telemetry are provided for the five-channel PSE, with a 0.83-V increment between one state and the next.

All analog status telemetry circuitry is located in the PSE.

4.6.5.6.7.3 Discrete Telemetry. The discrete telemetry provided by the PSE and BCA is shown in Table 4.6.5-34.

4.6.5.7 Controls Power Converter

The Controls Power Converter (CPC) is a dual dc-to-dc converter, as shown in Figure 4.6.5-75. Each converter accepts +28 volts and provides output voltages of +10 and -10 volts. The output voltages from converter A are

TABLE 4.6.5-34. PCE DISCRETE TELEMETRY

TLM Output				
TLM Description	Status	Logic Level/Volts	Sensing Element Location	Signal Processing Unit
BCR1 STATUS	PRI B/U	0/5V 1/0V	PSE	PSE
BCR2 STATUS	PRI B/U	0/5V 1/0V	PSE	PSE
BCR3 STATUS	PRI B/U	0/5V 1/0V	PSE	PSE
PHASE CTRL STAT.	PRI B/U	0/5V 1/0V	PSE	PSE
MC STATUS	PRI B/U	0/5V 1/0V	PSE	PSE
B1 V/T STATUS	UNSHIFTED VT1 TO VT8 SHIFTED VT9 TO VT16	0/5V 1/0V	PSE	PSE
B2 V/T STATUS	UNSHIFTED VT1 TO VT8 SHIFTED VT9 TO VT16	0/5V 1/0V	PSE	PSE
B3 V/T STATUS	UNSHIFTED VT1 TO VT8 SHIFTED VT9 TO VT16	0/5V 1/0V	PSE	PSE
INTERFACE SIDE SELECT STATUS	SIDE-1 SIDE-2	0/5V 1/0V	PSE	PSE
B1 CHARGE CONN. STATUS	CONNECT DISCONNECT	0/5V 1/0V	BCA	BCA
B2 CHARGE CONN. STATUS	CONNECT DISCONNECT	0/5V 1/0V	BCA	BCA
B3 CHARGE CONN. STATUS	CONNECT DISCONNECT	0/5V 1/0V	BCA	BCA
B1 DISCHARGE CONN STATUS	CONNECT DISCONNECT	0/5V 1/0V	BCA	BCA

TABLE 4.6.5-34. PCE DISCRETE TELEMETRY (Continued)

TLM Output				
TLM Description	Status	Logic Level/Volts	Sensing Element Location	Signal Processing Unit
B2 DISCHARGE CONN STATUS	CONNECT DISCONNECT	0/5V 1/0V	BCA	BCA
B3 DISCHARGE CONN STATUS	CONNECT DISCONNECT	0/5V 1/0V	BCA	BCA
BRU1 HEATER CONN. STATUS	CONNECT DISCONNECT	0/5V 1/0V	PSE	PSE
BRU2 HEATER CONN. STATUS	CONNECT DISCONNECT	0/5V 1/0V	PSE	PSE
BRU3 HEATER CONN. STATUS	CONNECT DISCONNECT	0/5V 1/0V	PSE	PSE
PSA DRIVE 1 CONN STATUS	CONN. TO PSA-CTRL-A	0/5V	PSE	PSE
	CONN. TO PSA-CTRL-B	1/0V		
PSA DRIVE 2 CONN STATUS	CONN. TO PSA-CTRL-B	0/5V	PSE	PSE
	CONN. TO PSA-CTRL-A	1/0V		

provided to CPU1 and to the CIU logic dedicated to CPU1; output voltages from converter B are provided to CPU2 and to the CIU logic dedicated to CPU2. A +10-volt common bus is also provided through a diode OR gate from either converter. This uninterruptible bus is provided to all spacecraft units requiring +10-volt interface power. Telemetry indications are provided for the CPC operating mode and for the voltage levels of the +10-volt common, -10-volt A, and -10-volt B buses.

4.6.5.7.1 Controls Power Converter Description

The CPC consists of two identical dc-to-dc converters. As shown in Figure 4.6.5-76, each converter consists essentially of an input filter, a switching regulator, an over-voltage protect circuit, a chopper feeding a transformer, and a pair of rectifiers and filters.

The line filter removes some of the noise on the +28-volt input line and inhibits the reflection of chopper noise back onto the +28-volt bus. The line filter also contains a transistor switch that is initially used to limit surge

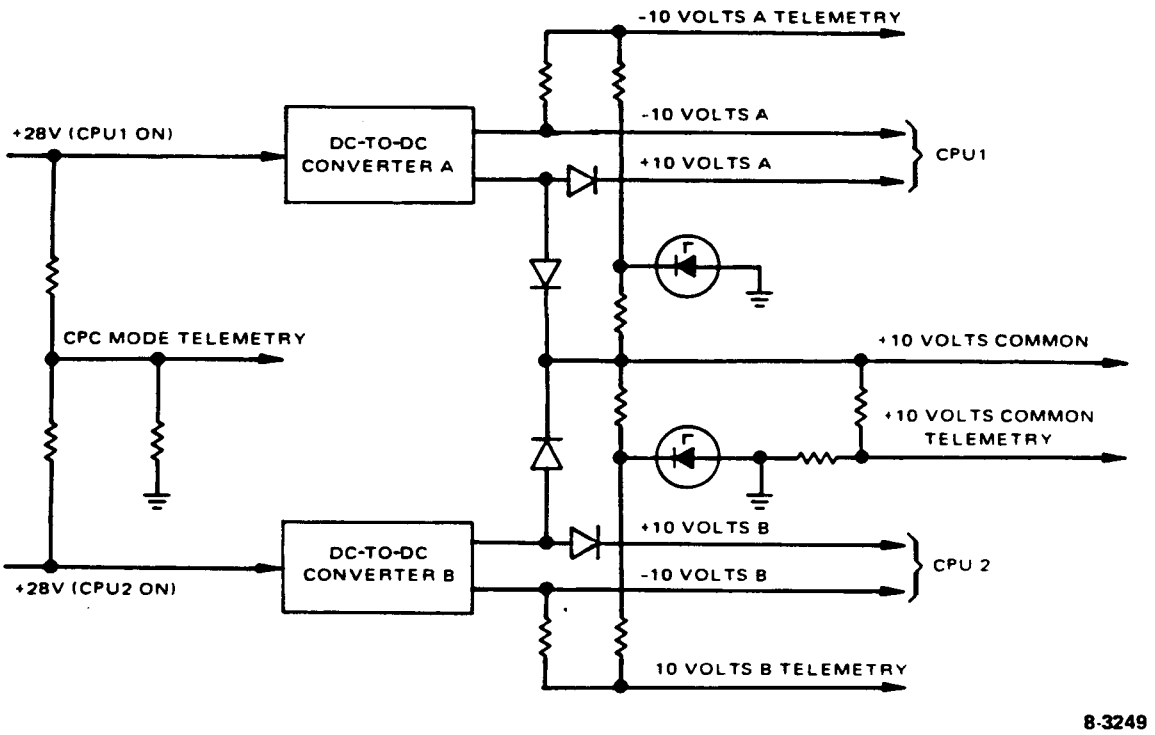

Figure 4.6.5-75. Controls Power Converter Functional Block Diagram

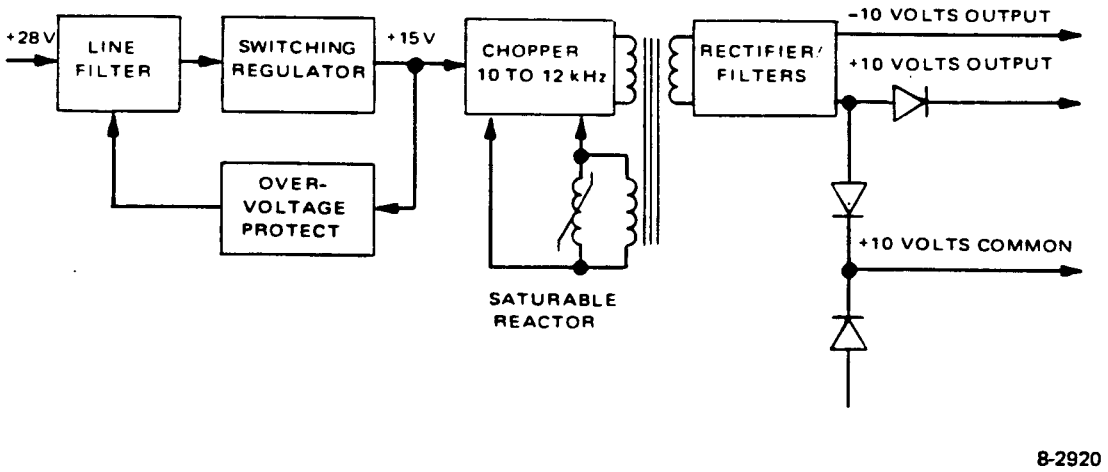

Figure 4.6.5-76. DC-to-DC Converter Functional Block Diagram

current at turn-on. This switch is also opened if the voltage out of the switching regulator rises too high (to prevent over-voltage at the +10-volt output terminals).

The switching regulator accepts the +28-volt bus input (which may, under transient failure conditions, be anywhere in the range of 17 to 38 volts) and provides regulated +15-volt power to the chopper.

The over-voltage protect circuit monitors the output voltage from the switching regulator to protect the CIU and CPU from over-voltages. If this voltage goes too high (approximately 16 volts), then the over-voltage protect circuit latches up and opens the line filter transistor switch, removing power from the switching regulator. The over-voltage protect circuit remains latched up until power is removed and re-applied, after which operation returns to normal until an excessive voltage again trips the latch.

The chopper is a free-running inverter, with the operating frequency controlled by the saturable reactor. The transformer saturates at a frequency of approximately 6 kHz. Operating the inverter at from 10 to 12 kHz thus ensures that the transformer does not saturate, which minimizes switching transients and spikes and maximizes conversion efficiency.

A pair of full-wave rectifiers operating from a single transformer secondary convert the ac input voltage into two dc output voltages. The output filters remove the switching spikes and transients from the output and minimize the effects of load current switching.

4.6.5.7.1.1 Design Approach. The design of the CPC is conventional. Each dc-to-dc converter consists essentially of a switching regulator and a power oscillator followed by rectifiers and filters to provide the desired output voltages. The CPC is configured to protect the CIU and CPU from any abnormal voltage deviation on the spacecraft +28-volt bus and from abnormal operations within either converter.

4.6.5.7.1.2 Operating Modes. The operating modes are as follows:

- Off (Inhibited in SCU)
- Mode A
- Mode B
- Mode AB

The operating mode is controlled by the presence or absence of the +28-volt CIU power applied to each converter. If the +28 volts is present, then that converter is operating and providing output voltages.

The +28-volt CPC power is controlled by the SCU, which turns CPC power 1 on or off and turns CPC power 2 on or off in accordance with control signals received from the CPC. Circuits in the SCU are interlocked such that CPC power 1 and CPC power 2 can never be turned off at the same time, that is, the CPC Off mode cannot occur.

4.6.5.7.1.3 Performance Summary. The performance characteristics of the CPC are listed in Table 4.6.5-35.

4.6.5.7.1.4 Physical Description. The CPC is a single rectangular assembly, as shown in Figure 4.6.5-77.

TABLE 4.6.5-35. CONTROLS POWER CONVERTER DESIGN CHARACTERISTICS

Parameter	Value
Input Voltage	+17 to +38 V (+28 V nominal)
Output Voltages	
Converter A	+10 V +0.50 -10 V -0.45
Converter B	+10 V +0.50 -10 V -0.45
Common	+10 V +0.50 -0.45
Output Current	
+10V (A or B)	200 to 1200 mA
-10V (A or B)	15 to 75 mA
+10V (common)	100 to 800 mA
Output Ripple	<50 mV p-p
Conversion Efficiency	63% (EOL)
Size	5.0 x 10.0 x 1.0
Weight	<2.25 lb

4.6.5.7.2 Telemetry

There are four telemetry signals provided by the CPC:

- CPC Mode Telemetry
- -10-Volt A Telemetry
- -10-Volt B Telemetry
- +10-Volt Common Telemetry

The CPC mode telemetry provides a level discrete output signal indicating the operating mode of the CPC. The operating modes are listed in Table 4.6.5-36, along with the resulting converter states and associated telemetry values.

The -10-volt telemetry circuits provide an analog indication of the -10-volt output voltage level. This signal is nominally +1.3 volts at a normal output level of -10 volts and +4.4 volts at an output level of 0 volts.

The +10-volt telemetry circuit provides an analog indication of the +10-volt bus output voltage level. This signal is nominally +3.88 volts at a normal output level of +10 volts.

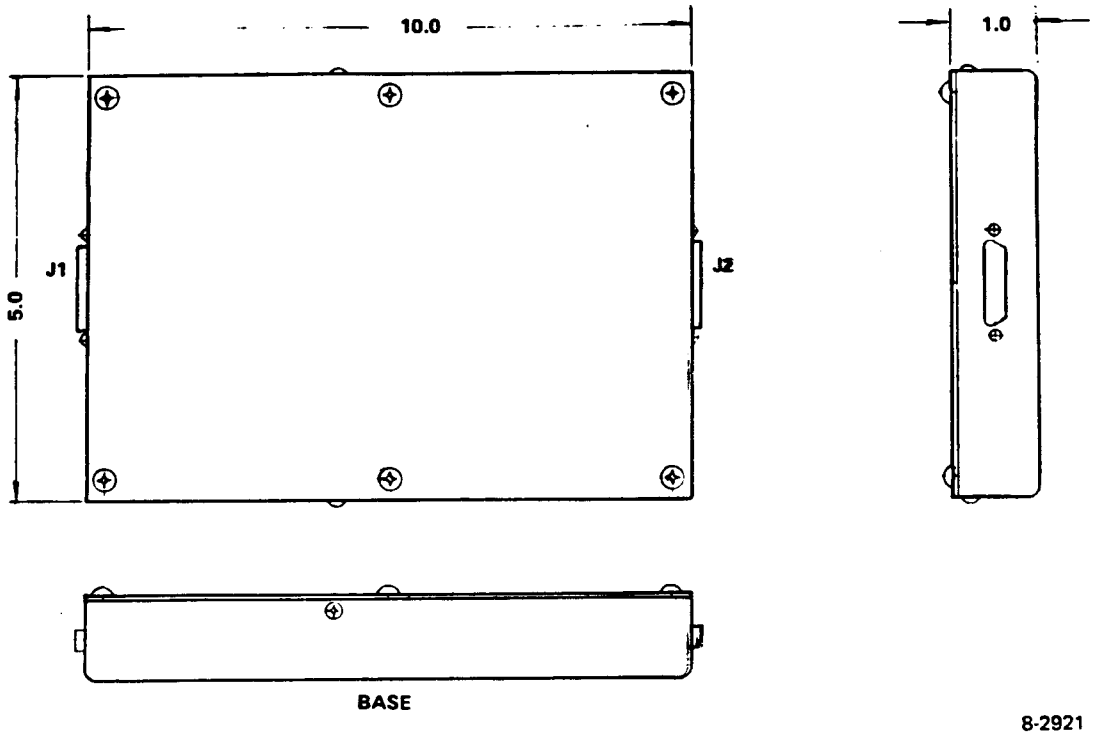

Figure 4.6.5-77. Controls Power Converter Outline Drawing

TABLE 4.6.5-36. TYPICAL CPC MODE TELEMETRY

CPC Mode	Converter State		Telemetry Value (V)
	A	B	
Off	Off	Off	0
B	Off	On	1.62
A	On	Off	3.33
AB	On	On	4.59